NOVEL HUMANIZED MOUSE MODELS OF MULTIPLE SCLEROSIS TO ELUCIDATE VIRAL AND HOST RISK FACTORS OF DISEASE

by

JESSICA R. ALLANACH

B.Sc. Honours, Mount Allison University, 2015

A DISSERTATION SUBMITTED IN PARTIAL FULFILLMENT OF
THE REQUIREMENTS FOR THE DEGREE OF

DOCTOR OF PHILOSOPHY

in

THE FACULTY OF GRADUATE AND POSTDOCTORAL STUDIES

(Microbiology and Immunology)

THE UNIVERSITY OF BRITISH COLUMBIA

(Vancouver)

December 2023

The following individuals certify that they have read, and recommend to the Faculty of Graduate and Postdoctoral Studies for acceptance, the dissertation entitled:

Novel humanized mouse models of multiple sclerosis to elucidate viral and host risk factors of disease

submitted by Jessica R. Allanach in partial fulfillment of the requirements for

the degree of Doctor of Philosophy

in Microbiology and Immunology

Examining Committee:

Dr. Marc S. Horwitz, Professor, Dept. of Microbiology & Immunology, UBC
Supervisor

Dr. Lisa C. Osborne, Assistant Professor, Dept. of Microbiology & Immunology, UBC
Supervisory Committee Member

Dr. Cheryl Wellington, Professor, Dept. of Pathology and Laboratory Medicine, UBC
University Examiner

Dr. John Priatel, Assistant Professor, Dept. of Pathology and Laboratory Medicine, UBC
University Examiner

Additional Supervisory Committee Members:

Dr. Soren Gantt, Professor, Dept. of Microbiology, Infectiology & Immunology, Université de Montréal
Supervisory Committee Member

Dr. Laura M. Sly, Professor, Dept. of Pediatrics – Div. of Gastroenterology, UBC
Supervisory Committee Member

Abstract

Multiple sclerosis (MS) is a neuroinflammatory autoimmune disease of the central nervous system (CNS) caused by environmental triggers in genetically susceptible individuals. Previous infection with Epstein-Barr virus (EBV) is a strong risk factor for the development of MS, however, studying the mechanisms underlying this association is experimentally challenging because of the latent virus' narrow host tropism for human B cells and subsequent lack of experimental models that support EBV infection directly. To evaluate the immunomodulatory effects of EBV infection in a murine model of MS, we induced experimental autoimmune encephalomyelitis (EAE) with myelin oligodendrocyte glycoprotein in humanized mice reconstituted with peripheral blood mononuclear cells (PBMC) from individuals with or without a history of EBV infection and/or a diagnosis of relapsing MS (RRMS). EAE-induced humanized PBMC (HuPBMC) mice recapitulate key clinical and immunopathological aspects of the disease more closely than regular EAE models. In the HuPBMC EAE model, we observed clinical symptoms typical of EAE in regular mice, including ascending paralysis and weight loss. Our findings indicate that demyelination of the brain and spinal cord in this model occurs through the coordinated cytotoxic actions of human $IFN\gamma^{+}CD4^{+}$ (Th1) and $IFN\gamma^{+}GzmB^{+}CD8^{+}$ cytotoxic T cells, in conjunction with the phagocytic activity of murine macrophages. HuPBMC EAE mice generated from EBV^{-} healthy donor samples were less susceptible to developing clinical symptoms than EBV^{+} healthy donor and EBV^{+} RRMS recipient cohorts, with reduced disease severity and delayed symptom onset. The EBV and RRMS status of the PBMC donors did not affect the degree of human B cell infiltration of the CNS in recipient HuPBMC EAE cohorts, though significant T cell immunomodulation was observed. Donor EBV seropositivity and RRMS diagnosis led to a significant incremental increase in the number of CNS infiltrating effector T cells, in the absence of viral reactivation, due to enhanced proliferation of proinflammatory T cells and reduced expansion of regulatory T cells. The data indicate that a history of EBV infection, further compounded by a diagnosis of RRMS, promotes T cell-mediated disease in a novel humanized mouse model of MS.

Lay Summary

Epstein-Barr virus (EBV) infection is a strong risk factor for the development of multiple sclerosis (MS). Experimental investigation of the mechanisms behind this risk factor has been hampered by the inability of EBV to infect established rodent models of MS. To overcome this species limitation, we developed a humanized mouse model of MS, wherein immunocompromised mice are reconstituted with human immune cells obtained from blood donors with or without a history of EBV infection and are then induced with an MS-like disease. This new humanized MS model reproduced many aspects of the disease process in humans, including myelin damage caused by inflammatory T cells. Blood donor history of EBV infection worsened disease symptoms by skewing the balance of harmful and protective T cells in the brain and spinal cord. These results reveal an immunomodulatory mechanism by which EBV infection could predispose a person to the development of MS.

Preface

All work presented in this thesis was conducted at the Life Sciences Institute and the Modified Barrier Facility at the University of British Columbia, Point Grey Campus (Vancouver, Canada), with blood sampling performed at the Fraser Health Multiple Sclerosis Clinic (Burnaby, Canada) and the Life Sciences Institute. Dr. Marc Horwitz is the supervisory author of all work herein. All animal work was approved by the University of British Columbia Animal Care Committee; protocol numbers A17-0105, A21-0145, A13-0234, A17-0266, A13-0116, A17-0184, A21-0282, and A21-0228. Human ethics approval was obtained from the University of British Columbia's Research Ethics Board; certificate numbers H12-02480 and H16-02338.

A subset of the findings presented in Chapters 4 and 5 has been submitted for publication (Jessica R. Allanach, Naomi M. Fettig, Blair K. Hardman, Ariel R. Rosen, Vina Fan, Erin J. Goldberg, Zachary J. Morse, Iryna Shanina, Galina Vorobeychik, Lisa C. Osborne, Marc S. Horwitz. (2023) "Epstein-Barr virus promotes T cell dysregulation in a humanized mouse model of multiple sclerosis") and pre-published on bioRxiv (DOI: 10.1101/2022.02.23.481716). JRA designed and performed experiments, analyzed data, and prepared the manuscript. NMF designed and performed ex vivo cellular assays. BKH designed and performed immunofluorescent imaging analysis. VF performed serum ELISAs. ARR performed myelin staining and quantification. NMF and EJG produced rhMOG protein. EJG and ZJM facilitated donor sample collection. IS coordinated phlebotomy, mouse breeding, and aided with in vivo procedures. JRA, NMF, BKH, VF, ARR, EJG, ZJM, and IS processed tissues for cellular analysis. GV recruited and assessed donors with RRMS and provided input for the study design. LCO oversaw immunofluorescent imaging and ex vivo cellular assays and provided input for the study design. JRA and MSH conceptualized the study, designed the methodology, and interpreted results for discussion. MSH oversaw the study and manuscript preparation.

The following individuals are acknowledged for their aid in supplying reagents, optimizing protocols and/or providing technical assistance for the studies completed in this thesis. Dr. Soren Gantt and Karen Simmons for providing the EBV *BALF5* qPCR protocol; Dr. John Priatel for providing the B95-8 EBV^+ cell line; Dr. Jennifer Gommerman, Dr. Nancy Ruddle, and Dr. Christopher Linington for providing the rhMOG-producing *E. coli* plasmid and expression protocols; Dr. Angela Lin, Guillermo Caballero, Dr. Natalie Strynadka, and Dr. Michael Murphy

for assistance with rhMOG protein production; Tanya Kadach for organizing blood donations and clinical evaluations at the Fraser Health MS Clinic; the staff at the Modified Barrier Facility for animal husbandry; the veterinary staff at UBC Animal Care Services for technical training; Yu Gu for ELISA protocol development; Iryna Shanina, Brankica Culibrk, and Philma Molina for phlebotomy; Justin Wong and Andrew Johnson for assistance with flow cytometry and FACS; Virginie Jean-Baptiste, Dr. Isobel Mouat, Ariel Rosen, and Erin Goldberg for assistance with animal monitoring; Dr. Christina Farr-Zuend for developing the protocol and surgical technique to generate the humanized bone marrow-liver-thymus mice; Iryna Shanina and Virginie Jean-Baptiste for human $CD34^+$ stem cell isolation; Dr. Citlali Marquez for providing γHV68 virion stocks. We acknowledge and are thankful for technical support from the Life Sciences Institute Cores (ubcFLOW) supported by the UBC GREx Biological Resilience Initiative. We further express our gratitude to the blood donors for providing their time and samples to the studies. All other reagents provided by external research groups and institutions are indicated in the materials and methods.

Table of Contents

List of Tables

List of Figures

List of Abbreviations

ABC	Age-associated B cell
ADEM	Acute disseminated encephalomyelitis
Ag	Antigen
AIDS	Acquired immunodeficiency syndrome
ANOVA	Analysis of variance
APC	Antigen presenting cell
APRIL	A proliferation-inducing ligand
ATCC	American Type Culture Collection
BAFF	B-cell activating factor (also termed B lymphocyte stimulator, BLyS)
BALF5	*BamHI* A left frame transcript 5
BBB	Blood-brain barrier
BCR	B cell receptor
BHK	Baby hamster kidney (fibroblasts)
BL	Burkitt's lymphoma
BM	Bone marrow
BRG	Immunodeficient BALB/c *Rag2*$^{-/-}$*IL-2Rγc*$^{-/-}$ (mouse strain)
BRGS	Immunodeficient BALB/c *Rag2*$^{-/-}$*IL-2Rγc*$^{-/-}$*sirpa*$^{NOD/human}$ (mouse strain)
BTK	Bruton's tyrosine kinase
B6-RGS^{human}	Immunodeficient C57Bl/6 *Rag2*$^{-/-}$*IL-2Rγc*$^{-/-}$*sirpa*^{human} (mouse strain)
B6-TKO	Immunodeficient C57Bl/6 *Rag2*$^{-/-}$*IL-2Rγc*$^{-/-}$*CD47*$^{-/-}$ triple knock out (mouse strain)
CAEBV	Chronically active Epstein-Barr virus
CalHV3	*Callitrichine herpesvirus* 3
CD	Cluster of differentiation
CFA	Complete Freund's adjuvant
CFSE	Carboxyfluorescein succinimidyl ester
CIHR	Canadian Institutes of Health Research (CAN)
CIS	Clinically isolated syndrome
CLIP	Cytoplasmic linker protein
CMAH	CMP-N-acetylneuraminic acid hydroxylase
CMV	Cytomegalovirus
CNS	Central nervous system
CSF	Cerebrospinal fluid
CSPG	Chondroitin sulfate proteoglycan

CTL	Cytotoxic T lymphocyte (also referred to as Tc)
CTLA-4	Cytotoxic T lymphocyte associated protein 4
DAPI	Diamidino-2-phenylindole
DC	Dendritic cell
DKO	Double knockout
DLBCL	Diffuse large B cell lymphoma
DMT	Disease modifying therapy
dNTP	Deoxynucleoside triphosphate
DPI	Day post-induction/immunization or day post-infection
dsDNA	Double-stranded deoxyribonucleic acid
EA	Early antigen
EAE	Experimental autoimmune encephalomyelitis
EBERs	Epstein-Barr virus (EBV)-encoded small RNAs
EBNA	Epstein-Barr nuclear antigen
EBV	Epstein-Barr virus
EC	Epithelial cell
EDSS	Expanded disability status scale
EDTA	Ethylenediaminetetraacetic acid
ELISA	Enzyme-linked immunosorbent assay
EnC	Endothelial cell
EOMES	Eomesodermin
EtBr	Ethidium bromide
FACS	Fluorescence-activated cell sorting
FBS	Fetal bovine serum
Fc	Fragment crystallizable
FLT3L	FMS (Feline McDonough Sarcoma)-like tyrosine kinase 3 ligand
FMO	Full minus one
FMT	Fecal microbiome transfer
FOXP3	Forkhead box P3/ scurfin
GA	Glatiramer acetate
GAPDH	Glyceraldehyde 3-phosphate dehydrogenase
GC	Germinal center
G-CSF	Granulocyte colony-stimulating factor
GM-CSF	Granulocyte-macrophage colony-stimulating factor
gMFI	Geometric median fluorescence intensity
GFP	Green fluorescent protein
gp	Glycoprotein

GvHD	Graft-versus-host disease
Gy	Gray (unit)
GzmB	Granzyme B
HBV	Hepatitis B virus
HCV	Hepatitis C virus
HD	Healthy donor
HEPES	N-2-hydroxyethylpiperazine-N-2-ethane sulfonic acid
HERV	Human endogenous retrovirus
HHV	Human herpesvirus
HIS	Human immune system
HIV	Human immunodeficiency virus
HL	Hodgkin's lymphoma
HLA	Human leukocyte antigen
HLH	Hemophagocytic lymphohistiocytosis
HRP	Horseradish peroxidase
HSC	Hematopoietic stem cell
HSV	Herpes simplex virus
Hu	Human/Humanized
HuBLT	Humanized bone marrow-liver-thymus (mouse model)
HuHSC	Humanized $CD34^+$ hematopoietic stem cell (mouse model)
Hu-PBL-SCID	Humanized peripheral blood leukocyte SCID (mouse model)
HuPBMC	Humanized peripheral blood mononuclear cell (mouse model)
HuProBLT	Humanized propagated bone marrow-liver-thymus (mouse model)
IBD	Inflammatory bowel disease
ID	Identifier
IFA	Incomplete Freund's adjuvant
IFN	Interferon
IFNAR	Interferon alpha receptor
Ig	Immunoglobulin
IHC	Immunohistochemistry
IL	Interleukin
IL-2Rγc	Interleukin 2 receptor gamma chain (also denoted as IL2rg)
IM	Infectious mononucleosis
IN	Intranasal
IP	Intraperitoneal
IPTG	Isopropyl ß-D-1-thiogalactopyranoside
ISH	In-situ hybridization

IV	Intravenous
JAX	Jackson Laboratory
JCV	John Cunningham virus
JPEG	Joint photographic experts group
kb	Kilobase (unit)
kDa	Kilodalton (unit)
KO	Knockout
KSHV	Kaposi sarcoma herpesvirus
LANA	Latency-associated nuclear antigen
LCL	Lymphoblastoid cell line
LCMV	Lymphocytic choriomeningitis virus
LCV	Lymphocryptovirus
LED	Light-emitting diode
Lin	Lineage
LMP	Latent membrane protein
LOD	Limit of detection
LPC	Lysophosphatidylcholine (lysolethicin)
LPD	Lymphoproliferative disorder/disease
LPL	Lamina propria lymphocyte
Mac	Macrophage
MBP	Myelin basic protein
M-CSF(-1)	Macrophage colony-stimulating factor (-1)
MCMV	Murine cytomegalovirus
MEM	Minimum essential media
MHC	Major histocompatibility complex
MHV	Mouse hepatitis virus
MI	Myelination index
miRNA	Micro ribonucleic acid
MISTRG-6	Immunodeficient BALB/c/129 *Rag2*$^{-/-}$*IL-2Rγc*$^{-/-}$ with transgenic human *M-CSF, IL-3, GM-CSF, SIRPα, TPO* and *IL-6* (mouse strain)
MOG	Myelin oligodendrocyte glycoprotein
MRI	Magnetic resonance imaging
MS	Multiple sclerosis
MSRV	Multiple sclerosis-associated retrovirus
Mu	Murine
MWCO	Molecular weight cut-off
N/A	Not applicable

NBF	Neutral buffered formalin
NCG	Immunodeficient NOD-*scid IL-2Rγc*^{null} [NOD-*Prkdc*^{em26Cd52}*Il2rg*^{em26Cd22}/NjuCrl] (mouse strain, Charles River Laboratories)
NEAA	Non-essential amino acid
NHP	Non-human primate
NIH	National Institutes of Health (USA)
NK	Natural killer
NKT	Natural killer T cell
NOD	Non-Obese Diabetic (mouse strain)
NOD-*scid*	Non-obese diabetic-severe combined immunodeficiency, NOD-*Prkdc*^{scid} (mouse strain)
NOG	Immunodeficient NOD-*scid IL-2Rγc*^{null} [NOD.Cg-*Prkdc*^{scid}*Il2rg*^{tm1Sug}/Jic] (mouse strain, Taconic Biosciences)
NOG-EXL	NOG with transgenic human *IL-3* and *GM-CSF* (mouse strain) [NOD.Cg-*Prkdc*^{scid} *Il2rg*^{tm1Sug} Tg(SV40/HTLV-IL3,CSF2)10-7Jic/JicTac]
NPC	Nasopharyngeal carcinoma
NRG	Immunodeficient NOD *Rag*^{null} *IL-2Rγc*^{null} [NOD-*Rag1*^{tm1Mom} *Il2rg*^{tm1Wjl}/SzJ] (mouse strain)
NSG	Immunodeficient NOD-*scid IL-2Rγc*^{null} [NOD.Cg-*Prkdc*^{scid} *Il2rg*^{tm1Wjl}/SzJ] (mouse strain, The Jackson Laboratory)
NSG-SGM3	NSG with transgenic human *IL-3*, *GM-CSF* and *SCF* (*KITLG)* (mouse strain) [NOD.Cg-*Prkdc*^{scid}*Il2rg*^{tm1Wjl}Tg (CMV-IL3,CSF2,KITLG)1Eav/MloySzJ]
OCB	Oligoclonal band
OCT	Optimal cutting temperature
OPC	Oligodendrocyte precursor cell
OR	Odds ratio
ORF	Open reading frame
OVA	Ovalbumin
PBMC	Peripheral blood mononuclear cell (also called peripheral blood leukocytes, PBL, or peripheral mononuclear cells)
PBS	Phosphate-buffered saline
PBT	Phosphate-buffered saline with 0.2% Triton X-100
PCR	Polymerase chain reaction
PD-1	Programmed cell death protein 1
PD-L1 (/2)	Programmed cell death ligand 1 or 2
pDC	Plasmacytoid dendritic cell
PFU	Plaque forming unit
PLP	Proteolipid protein

PMA	Phorbol myristate acetate
pNF-H	Phosphorylated neurofilament heavy chain
PPMS	Primary progressive multiple sclerosis
PrKdc	Protein kinase, DNA activated, catalytic polyprotein
PRR	Pathogen recognition receptor
PTLD	Post-transplant lymphoproliferative disorder
PTx	Pertussis toxin
qPCR	Quantitative polymerase chain reaction
RA	Rheumatoid arthritis
RAG	Recombination activating gene
RBC	Red blood cell
RGB	Red, green, blue
rhMOG	Recombinant human myelin oligodendrocyte glycoprotein
RPMI-1640	Roswell Park Memorial Institute media 1640
RORγt	Retinoic acid receptor-related orphan receptor gamma
RRMS	Relapsing remitting multiple sclerosis
RT	Room temperature
S1PR	Sphingosine-1-phosphate receptor
SAP	Signaling lymphocytic activation molecule-associated protein
SCID	Severe combined immunodeficiency
SCF	Stem cell factor (c-KIT receptor ligand)
SD	Standard deviation
SDS-PAGE	Sodium dodecyl sulphate–polyacrylamide gel electrophoresis
SEM	Standard error of the mean
SIRPα	Signal regulatory protein α
SJL	Swiss James Lambert (mouse strain)
SLE	Systemic lupus erythematosus
SPMS	Secondary progressive multiple sclerosis
SQ	Subcutaneous
ssRNA	Single stranded RNA
TAE	Tris-acetate-EDTA
Tc1	$IFN\gamma^+$ and/or Granzyme B^+ $CD8^+$ cytotoxic T cell (also referred to as CTL)
TCR	T cell receptor
Tg	Transgenic
Th	Helper T cell
Th1	$IFN\gamma^+CD4^+$ helper T cell

Th2	IL-4^{+}CD4^{+} helper T cell
Th17	IL-17A^{+}CD4^{+} helper T cell
TKO	Triple knockout
TLT	Tertiary lymphoid tissue
TLR	Toll-like receptor
TMB	3,3',5,5'-Tetramethylbenzidine
TMEV	Theiler's murine encephalomyelitis virus
TNF	Tumor necrosis factor
TPA	Tiglian 12-O-tetradecanoylphorbol-13-acetate
TPO	Thrombopoietin
Treg	Regulatory T cell
TSLP	Thymic-stromal-cell-derived lymphopoietin
T1D	Type 1 diabetes
UBC	University of British Columbia
UCB	Umbilical cord blood
UV	Ultraviolet
VCA	Viral capsid antigen
V(D)J	Variable (diversity) joining
VLP	Virus-like particle
VZV	Varicella zoster virus
w/o	Weeks old
WT	Wild type
xGvHD	Xenogeneic graft-versus-host disease
XLP	X-linked lymphoproliferative disorder
β2m	β2-microglobulin
γc	Common gamma chain
γHV68	Murine gammaherpesvirus-68

Acknowledgments

I would first like to acknowledge Dr. Marc Horwitz for providing me with the opportunity to pursue this research project in his lab. I am thankful even more so for his ongoing support, guidance, and advice, and to have worked with such a wonderful supervisor and friend. Further, I am thankful to the members of my thesis committee, Dr. Lisa Osborne, Dr. Laura Sly, and Dr. Soren Gantt, for their advice, guidance, and enthusiasm for the project. I thank the funders of the study, listed in detail in the preface, with notable acknowledgment of the MS Society of Canada and endMS Training Program for their continued financial support and opportunity for professional development. I am grateful to the members of the Horwitz Lab for their intellectual insights and comradery over the years. In particular, I thank Iryna Shanina for her technical support and for being a fantastic lab manager. I also thank Dr. Christina Farr-Zuend and Dr. Citlali Marquez for taking the time to train me and advise my initial studies. Moreover, I am appreciative to all of the graduate students listed in the preface for their scientific contributions and support, as well as the members of the Osborne, Harder, Abraham, Johnson, Perona-Wright, Tropini, and Tokuyama labs for their indispensable help and input. I also extend my gratitude to the many veterinary and technical staff members who supported this research. Finally, I am incredibly grateful and humbled to say that there are frankly too many family members and friends to acknowledge individually for their endless moral support, encouragement, and positivity during my time in graduate school. I would especially like to thank my parents, Bill and Karen, for all they have done for me. Last, and certainly not least, I acknowledge my dog, Clover 'Sweet pea' Allanach, for being the most delightful and joyful member of the very large support network that saw me through to the finish line.

This work was supported by funding from the Multiple Sclerosis Society of Canada (MSSC, grant ID #3631), the National Multiple Sclerosis Society (NMSS, grant ID #PP-1707-28236), the University of British Columbia (UBC) and the Canadian Institutes of Health Research (CIHR, grant ID #168967, #178298) granted to Dr. Marc Horwitz. Graduate student funding was provided by the MSSC's endMS personnel award program – master's and doctoral studentship (ID #2955), CIHR Frederick Banting and Charles Best Canada Graduate Scholarship, Master's (CGS-M), as well as the Theodore E. Arnold Fellowship and Shaughnessy Hospital Volunteer Society Fellowship in Health Care awarded through UBC.

Dedicated to beloved family members who have passed but whose support and lessons remain,

Samuel Frederick Allanach

Eileen Kathleen (Atkinson) Allanach

Peter Anthony 'Tony' Shanley

Kimberley Jon DeWare, MD

George Henry Tulk

Bruce Frederick Allanach

Chapter 1 – Introduction

1.1 Multiple sclerosis

Multiple sclerosis (MS) is a chronic autoinflammatory disease of the central nervous system (CNS) characterized by lesions of demyelinated nerve axons, infiltration of autoreactive T cells, and neurodegeneration of the brain and spinal cord, resulting in physical and mental disability[1]. The first annotated descriptions of MS lesions were illustrated by J. Cruveilhier and R. Carswell in 1835. Numerous cases of neurological disease, now suspected to be MS, date back even earlier in 19th century Europe[2–4]. A few decades later, the clinical and anatomical features of MS were defined by J. M. Charcot, establishing MS as a unique and distinct neurological disease[5,6]. Continual advances in medical technology have allowed for more precise diagnosis of cases of MS, as well as the identification of distinct disease subtypes and the elucidation of autoimmune and neurodegenerative processes that lead to inflammatory demyelination of the CNS. Though considerable progress has been made to dissect and define the complex pathological processes underpinning the disease, the mechanistic cause(s) of MS remain elusive.

1.1.1 Epidemiological and clinical overview

MS is one of the leading causes of disability among young people worldwide, as disease usually onsets in the late 20s to early 30s[7], though it does affect children in 2 – 5% of cases[8]. MS is especially prevalent among women, for whom there is a heavy bias in incidence of 3:1 relative to men[9,10]. MS shows a strong latitudinal gradient in incidence toward the northern and southern poles (Figure 1.1), especially in North American and European countries, and adults tend to retain the risk associated with their region of origin unless migration occurred before adulthood[11–14]. Epidemiological patterns can be attributed to multiple confounding variables, including socio-economic status, age, environment, and ethnicity. Of the over 2.8 million people currently affected by MS, more than 100,000 are Canadian, making Canada one of the highest risk countries for MS in the world[11,15,16]. The number of Canadians affected by MS is also predicted to rise to over 133,000 by 2030[17]. For individuals affected by MS, symptoms can vary widely but typically involve some combination of loss of coordination and sensation, muscle weakness, vision impairment, fatigue, pain, and cognitive impairment, among others[15,18]. The onset of a debilitating neurological condition in young adulthood creates significant economic burden and reduces the quality of life for individuals affected, due to personal and occupational costs associated with

disability and the lifelong uncertainty surrounding relapses, progression, and functional impairment[19]. As a result, the co-occurrence of severe disease symptoms, unemployment, and depression is common[19,20].

Clinical presentation among affected individuals is heterogeneous, with disease courses ranging from relapsing to progressive with intermediate phenotypes that can morph over time (Figure 1.2)[1]. The first symptomatic demyelinating episode commonly observed prior to the establishment of MS is called clinically isolated syndrome (CIS); a 24-hour MS-like attack often defined by transient optic neuritis and/or numbness in the lower limbs without fever or other signs of infection [21]. At this stage, the overall burden of MS-like abnormalities in the CNS, as measured by magnetic resonance imaging (MRI), is predictive of the likelihood of the condition converting to full MS[21]. In ~80% of cases, MS begins as a phasic relapsing-remitting condition, characterized by distinct waves of symptoms followed by periods of resolution, that then slowly shifts into a secondary progressive phenotype, which is characterized by fewer, less distinct periods of remission and continuous accruement of disability[19]. Among a smaller proportion of cases (~10 – 15%), disease symptoms are progressive from the onset. Relapsing and progressive forms are hypothesized to result from different aetiologies, owing to different pathobiological processes observed among these subtypes (see following section).

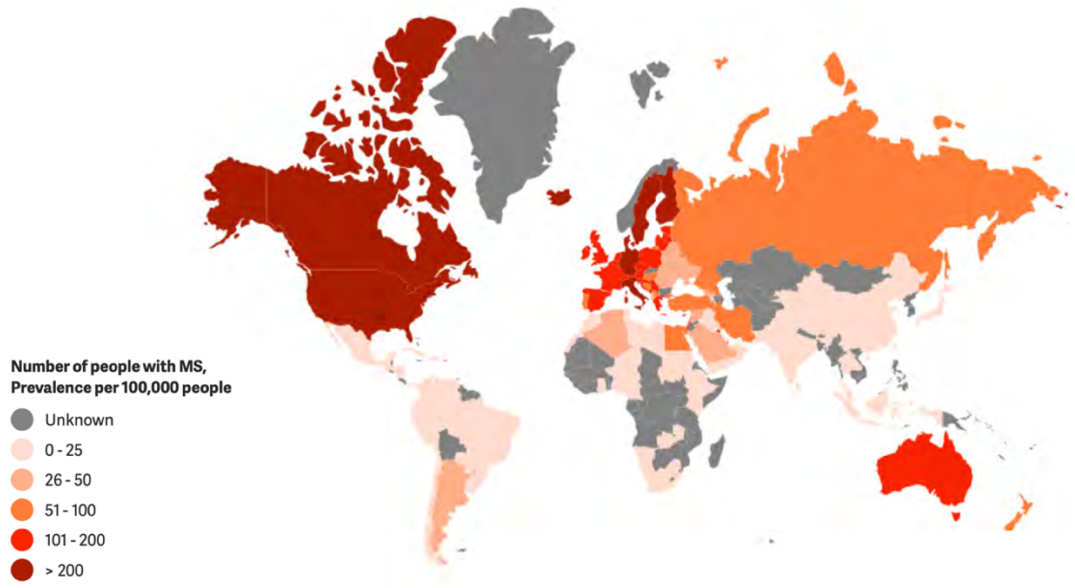

Figure 1.1 Geographic distribution of MS

Prevalence of multiple sclerosis (MS) per 100,000 people. Reproduced from the Atlas of MS 2020 ©[16].

MS is a clinically defined disorder with no single diagnostic test available to definitively confirm the condition. A diagnosis of relapsing-remitting (RRMS), primary progressive (PPMS), or secondary progressive (SPMS) is therefore made based on the criteria outlined by the Poser and McDonald reports[22–24]. Generally, diagnosis is dependent on the formation of disseminated lesions in multiple regions of the CNS over time, which can be ascertained by neurological exams, as well as more sensitive clinical tests, including MRI of lesions and a lumbar spinal tap to assess the presence of oligoclonal bands (OCBs) in the cerebrospinal fluid (CSF), which are composed of intrathecal antibodies produced by infiltrating plasma cells in response to CNS injury and infection[25,26]. Due to overlapping symptomologies and pathological features with other neurodegenerative and inflammatory CNS conditions, such as acute disseminated encephalomyelitis (ADEM), myelin oligodendrocyte glycoprotein (MOG) antibody disease, and neuromyelitis optica spectrum disorder, definitively diagnosing MS is dependent on these more disease specific tests[27,28]. The fact that lesions have already formed and are visible by MRI at diagnosis indicates that pre-symptomatic diseases process begin months or years prior to the first attack.

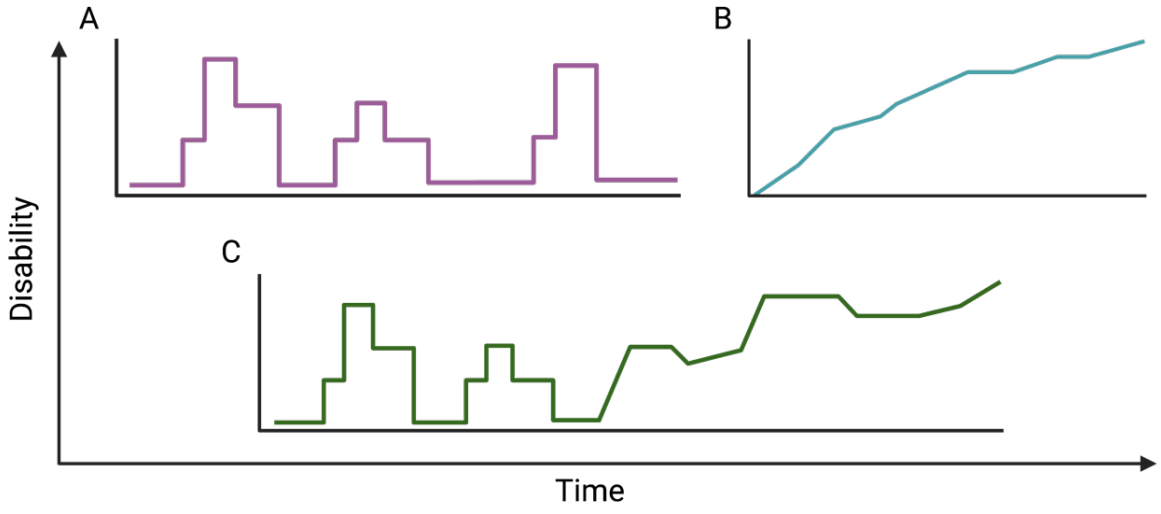

Figure 1.2 Clinical phenotypes of MS

The three most common clinical courses of MS from symptom onset: (A) relapsing-remitting, (B) primary progressive, and (C) secondary progressive. Adapted from Klineova and Lublin[21]. Created using BioRender.

1.1.2 Disease pathology and treatment

The hallmark feature of MS is the presence of demyelinated lesions, also called sclerotic plaques, in the CNS. These lesions tend to form throughout the CNS, but often occur in the periventricular regions, the optic nerve, and in inferior anatomical regions, such as the brain stem, cerebellum, and spinal cord[29]. MS is not a disease associated with immune suppression, which indicates that an intact immune response is required for development. Our understanding of the mechanisms of the autoimmune response and neurodegenerative and remyelinating events that occur in MS is derived mainly from animal models (Section 1.1.5), in addition to MRI and post-mortem analyses of CNS tissues. Demyelinated lesions are considered to be caused by infiltrating autoinflammatory immune cells, including T cells, B cells, natural killer (NK) cells, neutrophils, and macrophages, as well as CNS-resident microglia and astrocytes. Infiltrating leukocytes cross the normally tightly adjoined and relatively immune privileged blood-brain barrier (BBB) through the choroid plexus, the meninges, and/or in post-capillary venules[30]. Upregulated expression of selectins and chemoattractants results in immune cell accumulation at the perivascular cuffs, where matrix metalloproteinases break down the tight junctions to allow entry[30]. Once infiltration occurs, lesions are characterized by significant apoptosis of oligodendrocytes that each myelinate multiple metabolically linked axons, and subsequently, neuroaxonal transection, which leads to reduced viability, saltatory conduction, and signal potentiation among affected neurons[31,32].

Using biopsy and autopsy samples, Lucchinetti and colleagues described the occurrence of four phenotypically distinct lesions that occur variably in the CNS of MS patients[33]. Type I lesions were characterized by T cell, activated microglia, and/or macrophage mediated demyelination, type II by complement and antibody mediated demyelination, type III by hypoxic tissue injury rather than oligodendrocyte cell death, and type IV by oligodendrocyte loss with minimal inflammation[33]. Immune responses within active lesions (gadolinium-enhancing by MRI) follows a heterogenous temporal pattern involving the upregulation of major histocompatibility complex (MHC) expression locally, reduced regulatory control, and the presence of IFNγ (Th1) and IL-17A (Th17) producing helper $CD4^+$ T cells, cytotoxic $CD8^+$ T cells, B cells, and NK cells[34–39]. The relative contribution of Th1 and Th17 cells and their antigenic specificity, especially early on, is unclear and still deliberated[40]. $CD8^+$ T cells far outnumber $CD4^+$ T cells within and around MS lesions and exhibit evidence of clonal expansion[38]. The infiltrating $CD8^+$ T cells are cytotoxic and display an activated memory phenotype, suggestive of a direct role in demyelinating axons[38]. B

cells are able to contribute through multiple canonical inflammatory mechanisms, including autoantibody secretion, presentation of autoantigens, and cytokine and chemokine expression[41]. Complement dependent cytotoxicity is also occurs in some lesions, whereby recognition of complement and Fc complexes results in phagocytosis of myelin by activated microglia[42]. Astrocytes and microglia, present in active and chronic lesions, can contribute to destruction and regenerative processes through expression of pro- and anti-inflammatory products (Figure 1.3), including neurotrophic factors, cytokines, and growth factors, as well as through antigen presentation to infiltrating T cells[43,44]. Lesions in which active inflammation has mostly resolved and are experiencing a chronic, low level of activity are termed 'smoldering'[45]. Lesions in which immune activity has completely resolved are considered 'inactive' and are characterized by the formation of a gliotic scar[32,43]. To some extent, neuroregenerative processes can fully or partially reverse the inflammatory damage, through phagocytic clearance of myelin debris and removal of inhibitory factors, creating formerly active, remyelinated 'shadow plaques'[46]. The sum consequence of the inflammatory and neurodegenerative process occurring in the MS brain is an accelerated rate of global atrophy compared unaffected individuals, leading to profound neurological disability that cannot be restored by current treatment and management options[47,48].

The initiating events that lead to the BBB breach and immune infiltration in MS are debated. The two predominant theories to explain the triggers that lead to onset of MS are inside-out and outside-in, referring to the sequence of initial and subsequent pathological mechanisms that cause demyelination. Inside-out describes a scenario in which a spontaneous or induced local CNS injury, neuroaxonal dysfunction, or a demyelinating event leads to CNS antigen drainage into external lymph nodes, peripheral presentation and priming of the immune response, and secondary inflammatory infiltration that then worsens lesion formation[42]. The outside-in mechanism suggests infiltration of peripheral immune cells into the CNS is the initiating event that triggers lesion formation, suspected to result from an environmental and/or genetic CNS-external factor that promotes dysregulated autoreactive immune cells to develop and migrate to the susceptible, but otherwise healthy, CNS[49]. Subsets and variations of these theories have also been proposed[18,50]. Both of the proposed causative theories are supported by different animal models that recapitulate distinct aspects of MS pathology (Section 1.1.5). Both mechanisms have also been supported by the cellular composition of lesions in MS brain tissues. As mentioned above, type I and II lesions are predominantly T cell containing, while types III and IV indicate glial and oligodendrocyte

dysfunction in the absence of peripheral immune infiltration[33]. Though four different lesion types have been described, individual cases of MS seem to present with one dominant lesion type[33].

Early stages of RRMS are defined by inflammatory lesions, whereby consecutive attacks lead to an eventual failure of oligodendrocyte differentiation and remyelination, as well as cumulative neuronal damage and loss of motor function, resulting in transition to SPMS with more subdued chronic inflammation[51]. Transition to progressive disease is thus considered an age-related neurodegenerative process following years of autoimmune mediated damage that surpasses a threshold of neuronal dysfunction and loss[32]. In cases of SPMS, but not RRMS or PPMS, tertiary lymphoid-like structures containing germinal centers composed of B cells and dendritic cells (DCs) form in the meningeal tissues of the brain, suggesting ongoing and chronic local inflammation[52]. PPMS tends to occur at an older age and mainly involves spinal cord atrophy with less inflammation, considered to result from different pathological mechanisms than SPMS[10,53]. The theory has therefore been proposed that cases of RRMS are predominantly a consequence of outside-in mechanisms and PPMS a result of inside-out mechanisms of disease initiation, whereby the resulting disease phenotypes are both classified as MS but are in fact distinct neuropathological disorders[54]. The efficacy of immunomodulatory drugs in RRMS but not in PPMS highlights the discrepancies in the underlying pathological processes that occur in these two subtypes of MS.

Current treatments mainly address the adaptive immune cell mediated component of MS to reduce CNS inflammation. The first disease modifying therapy (DMT) approved for use in MS was interferon-β (IFNβ) in 1993. Treatment of RRMS with IFNβ was shown to reduce relapse frequency, whereas IFNγ promoted relapses by stimulating pathogenic Th1 cells[18]. The effectiveness of IFNβ has seen been ascribed to its role in promoting DC expression of IL-27 and suppressing IL-17A, thereby increasing regulatory T cell expansion while reducing pathogenic Th17 cell numbers[55]. Another first line DMT, approved in 1996, is glatiramer acetate (GA), an amino acid copolymer designed to act as structural mimic to tolerize myelin basic protein (MBP) reactive T cells[56]. Fingolimod, or FTY720, is a broad sphingosine-1-phosphate (S1P) receptor agonist that prevents general T cell egress from lymph nodes and reduces T cell traffic to the CNS, in addition to other immunomodulatory properties[57–60], and provides significant clinical benefit that is not matched by direct depletion of $CD4^+$ T cells[61].

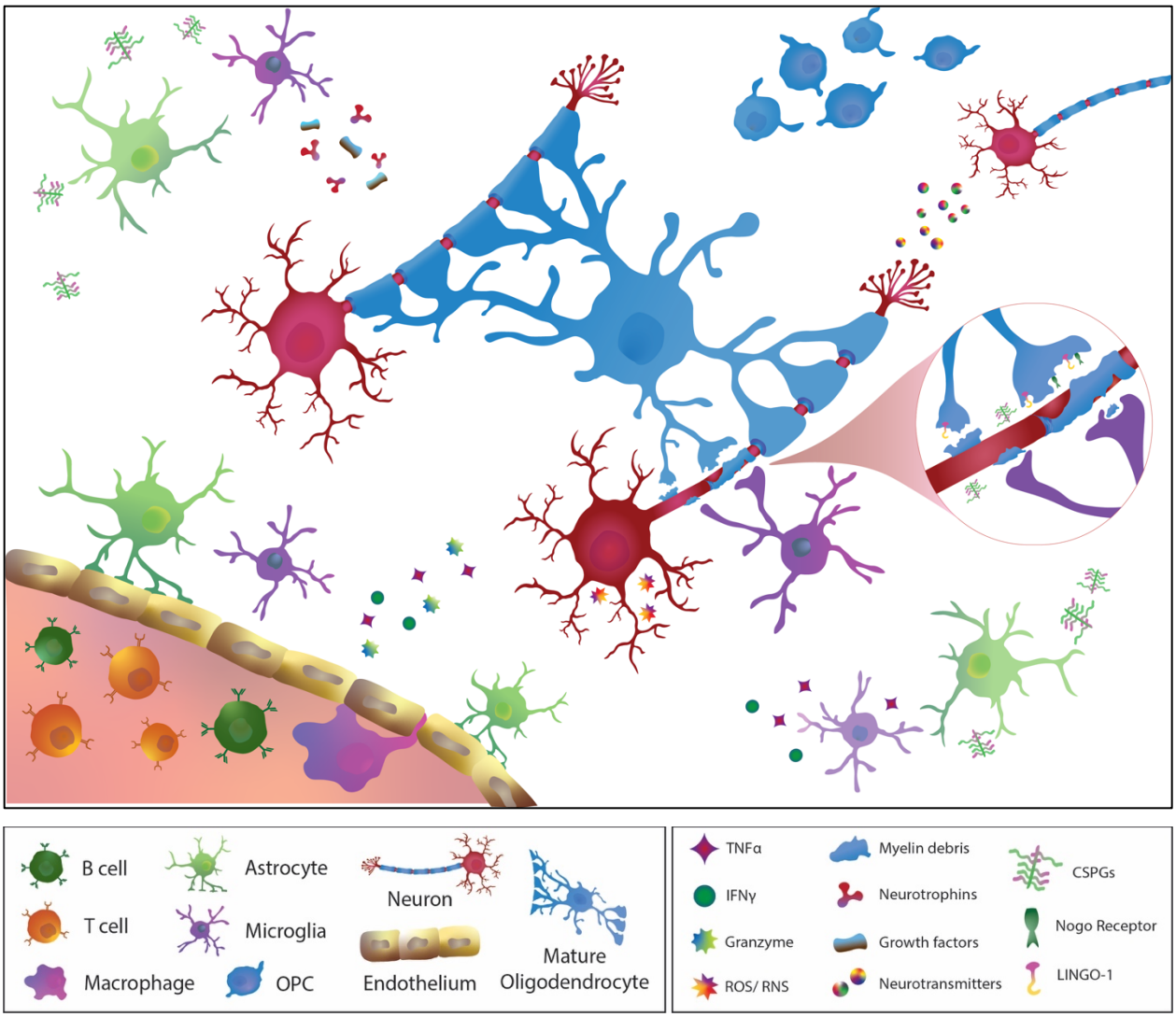

Figure 1.3 Neurodegenerative and inflammatory processes in an MS lesion

Peripheral immune cells, including T cells, B cells, and macrophages, cross the blood-brain barrier and generate pro-inflammatory cytokines. Activated microglia, in conjunction with infiltrating macrophages, phagocytose myelin on damaged neural axons, leading to denudation, compromised neuron integrity, and loss of signal propagation. Oligodendrocyte precursor cells (OPCs) are recruited to the site of damage to differentiate into mature oligodendrocytes and facilitate remyelination. Remyelination is locally impaired by the expression of inhibitory receptors, such as leucine-rich repeat and immunoglobin-like domain-containing protein 1 (LINGO-1) and neurite outgrowth inhibitory protein (Nogo), as well as inhibitory extracellular matrix components like chondroitin sulfate proteoglycans (CSPGs), associated with myelin debris. Pathogenic microglia and astrocytes also secrete cytokines and reactive oxygen/nitrogen species (ROS/RNS), which are counteracted by the production of protective growth factors and neurotrophins by other subsets. Adapted from Allanach et al.[62]. Created using Adobe Illustrator.

The first line DMTs typically reduce relapse rate by 30% or more if started upon presentation of CIS[50]. Newer generation DMTs mainly target immune cells by depleting populations (i.e. anti-CD20 rituximab and anti-CD52 alemtuzumab monoclonal antibodies) or inhibiting migration (i.e. anti-CD49d natalizumab or the S1PR1/5 modulator siponimod)[63–65]. A more recently developed approach to treat unresponsive and aggressive MS is complete immune system ablation and autologous hematopoietic stem cell transplantation; typically employed as a last resort[66]. In general, immunomodulatory DMTs that show benefit in RRMS have reduced clinical effectiveness over time as disability accumulates, with only minimal benefit in cases of established SPMS and PPMS[67]. It is believed that the systemic effects of many immunomodulatory DMTs for MS are ineffective in progressive forms of MS where there is less autoimmune mediated damage and more neurodegenerative processes, as well as a more intact BBB that limits the ability of drugs to cross into the site of disease[68]. Continued investigation will be required to dissect the mechanisms underlying distinct subtypes of MS and to tailor effective DMTs appropriately.

1.1.3 Genetic risk factors and sex bias in MS

Although the exact etiology of MS is unclear, development of the disease is considered to be a multifactorial consequence of environmental triggers in genetically susceptible individuals[69]. The familial recurrence rate of MS is ~20%[18] and people with family members affected by MS are at a 20 – 50-fold greater risk of developing the disease themselves compared to individuals without a first-degree relative with MS[70–72]. There is also a higher concordance rate between monozygotic twins (25 – 30%) compared to dizygotic twins and siblings (4 – 5%)[73]. Ethnicity is a predisposing factor for MS, which further suggested a heritable component of disease risk, though it is not considered a result of Mendelian or mitochondrial inheritance[29]. Most MS patients, however, do not have a family history of the disease, and most forms of MS are only partially heritable[74]. Through linkage analyses and sequencing studies, most risk genes for MS have been identified as encoding components of or regulating the immune system. Like other autoimmune diseases, the primary genetic risk for MS has been linked to loci encoding genes for MHC and with particular human leukocyte antigen (HLA) gene combinations. In MS, the strongest risk is associated with the HLA-DRB1*1501 allele, which increases the risk 3-fold in heterozygous carriers and 6-fold in individuals homozygous for the allele[75]. In high incidence countries, 14 – 30% of the population carries the HLA-DRB1*1501 allele[74]. In Caucasian populations, the HLA-DR15 haplotype

(DRB1*1501, DRB5*0101, DQA1*0102, DQB1* 0602) accounts for up to 60% of the genetic risk for MS[76]. Other haplotypes, including DR3 (DRB1*0301) and DR4 (DRB1*0405, DQA1*0301, DQB1*0302), and population-specific alleles such as those seen in the Sardinian MS population, also confer risk for developing the disease[74,77].

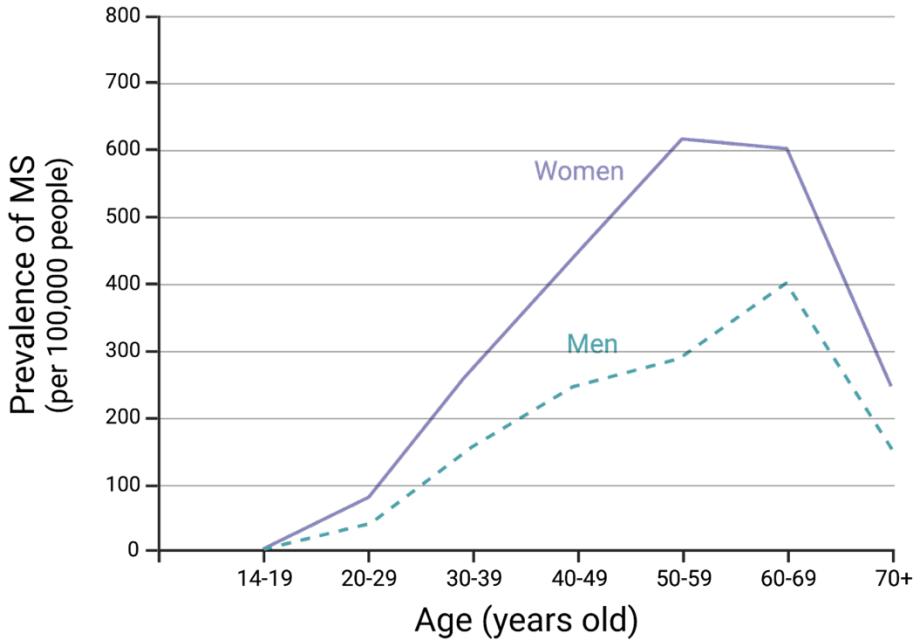

Figure 1.4 Prevalence of MS by age and sex

Mean prevalence rate of multiple sclerosis (MS) in Hordaland, Norway (2013). Adapted from Grytten et al.[78]. Created using BioRender.

The link between certain HLA alleles and risk for autoimmunity has been proposed to be due to ineffective negative selection of autoreactive T cells due to incomplete or 'wobbly' self-peptide affinity to some MHC binding pockets, though this mechanism has been debated due to the presence of autoreactive T cells in the repertoire of both MS and unaffected individuals with differing HLA haplotypes[79]. Wang and colleagues recently provided evidence to support the notion that HLA-DR15 haplotype confers risk by presenting cross-reactive foreign and auto-antigens on B cell MHC II complexes to $CD4^+$ T cells in MS[80]. Other non-MHC related gene variants have also been identified as risk factors for MS, including genes encoding innate immune system components, such as complement proteins, as well as in less strictly immune related loci such as the *CYP27B1* gene encoding 25-hydroxyvitamin D-1α hydroxylase, which converts the vitamin D

precursor into its active form[72,74]. MS is especially prevalent among women, for whom there is a heavy bias in incidence (2 – 3:1 women to men)[9], similar to most autoimmune diseases. Though MS on the whole is woman-bias in its incidence, PPMS cases are less sex-biased, showing a 1.3:1 female: male incidence ratio[10]. Additionally, cases of pediatric MS show a less substantial sex bias that becomes more pronounced toward women after the onset of puberty (Figure 1.4)[81]. Sex bias in autoimmunity is explained in part by sex specific hormone expression, notably estrogens, incomplete X chromosome inactivation leading to epigenetic dysregulation and overexpression of immune related genes, and lifestyle differences due to social and gender-related behaviours[9].

1.1.4 Environmental risk factors of MS

Initial epidemiological evidence supporting a role for environmental triggers in MS was largely derived from migration studies and the geographic distribution of cases. Geographical areas where MS is prevalent are predominantly populated by northern European and descendant populations, which can conflate environment and genetics. Migration studies, however, point to environmental factors, as individuals tend to retain the risk associated with their region of origin up until adolescence (i.e. migrating from a high risk area to a low risk area in childhood confers a more reduced risk than had the individual remained in the originating high risk area)[12]. The individual environmental factors most strongly linked to MS are listed and discussed in this section, though it is noted that these variables do not act independently and can influence one another in a positive or negative way to compound or alleviate cumulative risk[69]. Understanding the integrated risk of genetic factors and environmental exposures early in life is critical to determining effective preventative strategies.

A lack of ultraviolet (UV) radiation exposure and low serum vitamin D levels are associated with an increased risk for MS both epidemiologically and clinically[74,78,82–84]. The geographical concentration of cases of MS in higher latitudes countries implicates reduced UV exposure with increased disease susceptibility, which is further supported by the preponderance of cases among individuals who were born in the springtime months, suggestive of an effect of seasonal and maternal sun exposure that persists into adulthood[74,82]. The role of UV exposure has been attributed to its essential role in converting precursor vitamin D to its active form[69]. Additional data suggest vitamin D supplementation is protective in MS[82,83]. The underlying mechanism of how vitamin D contributes to disease is still unclear, though is suspected to modulate

immune responses, particularly among T cells, toward a less proinflammatory and more regulatory state[74,84]. Moreover, the promoter region of HLA-DRB1*15 haplotype contains a vitamin D response element, and functional analyses have shown that vitamin D can regulate the expression levels of HLA-DRB1*1501 class II molecules[85]. Two environmental risk factors associated with MS strongly point to adolescence as a critical age window for disease development, obesity and physical brain trauma[69,86]. Obesity during adolescence is a particularly strong risk factor for earlier onset of MS when adjusted for confounding factors[69]. The mechanism relating obesity to MS are thought to be immune related, as adipose tissue can cause chronic, low grade inflammation through production of leptin and proinflammatory cytokines[69]. Vitamin D can also be sequestered in adipose tissue, reducing bioavailability and further contributing to cumulative risk through an overlapping pathway[87]. Additionally, the incidence of physical brain trauma as a result of concussions has been reported to be a risk factor for the development of MS, specifically for men in adolescence[86]. Physical injury to the brain may be the initial trigger leading to peripheral immune cell infiltration and temporary disruption of the BBB could allow previously primed autoreactive T cells to enter the CNS[86]. Smoking is suspected to contribute to the onset of MS in men especially and is predictive of worse long-term cognitive function[74,83]. The effects of smoking tobacco may be related to multiple pathways involved in MS pathogenesis, though the risk is much lower for chewing tobacco, indicating a critical role for lung inflammation[74,88]. Likewise, air pollution is suspected to cause general oxidative stress and generate proinflammatory cytokines as a result[69,89].

The role of dietary factors and the intestinal microbiome has been investigated in many clinical and experimental studies of MS. Individuals with MS have notable dysbiosis of fecal microbial populations compared to unaffected controls, characterized by the diminishment of suspected beneficial species and the expansion of potentially pathogenic species, as well as overall reduced bacterial diversity[90,91]. Experimentally, fecal microbiome transfers (FMTs) from individuals with MS worsened disease severity and reduced regulatory T cell expansion in spontaneous and actively induced EAE models compared to FMTs from unaffected controls[92,93]. Moreover, alterations to the diet can produce beneficial effects on autoimmune outcomes in EAE mice[94] and in people with MS[95]. The intestinal microbiome is a dominant producer of bacterial metabolites, such as short chain fatty acids, amino acids, neurotransmitters, and vitamins, as well as immunomodulatory products that influence autoimmune processes locally and systemically[96].

Furthermore, gut-associated lymphoid tissues play a role in immunological education and establishing commensal tolerance during development[95]. The various aspects of gut-brain-immune axis communication and their potential role in CNS disease are reviewed in detail by Wang and Kasper in[97]. More generally, the role of microbial exposure, or lack thereof, has been suspected to play a role in allergic and autoimmune condition susceptibility[98]. The 'hygiene hypothesis', also called the 'microbial deprivation hypothesis', suggests that avoiding exposures to benign and pathogenic microbes can predispose for immunological disorders due to a lack of immune training, reduced tolerance, and an imbalance within the helper T cell response[98]. Evidence to support the hygiene hypothesis includes the prevalence of MS is 'Westernized' regions where sanitation, socioeconomic, and healthcare measures reduce interaction with and pathology resulting from exposure to microbes from a young age[74,98]. Moreover, the potentially beneficial effects of helminthic infection in MS, which are less prevalent in Western countries, may result from skewing the proinflammatory Th1 response toward a more balanced Th2 response; an example of the 'old friends hypothesis' that suggests co-development with microbial communities is required for proper immunoregulation[98,99]. The hygiene hypothesis, however, does not apply to all microbial exposures, most notably to certain viral infections[74].

A key case study pointing to the role of a transmissible agent in causing MS is that of the Faroe Islands. The first known case of MS on the Faroe Islands was observed in 1943, following British military occupation of the island starting in 1940[100]. The apparent lack of cases prior to this time among the native population, and the sudden surge in cases rising to the level of epidemic in occupied areas, strongly suggested an infectious pathogen was introduced to the native residents by members of the British military[100]. Though not a conclusive example, several viruses have since been proposed to play a role in MS onset, most notably with persistent, lifelong infections, such as those established by the herpesviruses Epstein-Barr virus (EBV), herpes simplex virus (HSV), varicella zoster virus (VZV), cytomegalovirus (CMV), and human herpesvirus-6 (HHV-6), John Cunningham virus (JCV), and human endogenous retroviruses (HERVs)[82,101]. Conflicting reports suggest that early childhood infections are or are not associated with increased risk for MS, including rubella, measles, HSV, and VZV[82]. Many of the intrathecal antibodies produced in the CSF of MS patients recognize and cross react with multiple different viruses, especially herpesviruses, though the interpretation of this specificity is unclear (i.e. is the presence of antibodies due to a response to local infection or due to nonspecific recruitment and bystander

activation of cells from the periphery in an inflamed CNS)[26,102,103]. Infections are also known to bring about inflammatory relapse, either through transient infection such as with upper respiratory tract infections (hit-and-run), or through reactivation of latent or chronically persistent viruses within the host due to cellular stress or general inflammation[82,104]. To note, many clinical and epidemiological studies focused on viral infections in MS susceptibility utilize retrospective and serological analyses[82], which each present with limitations for interpretation of the significance of the results and inferring cause or consequence.

Due to their neurotropism and ability to incite encephalitis, the herpesviruses VZV and HSV have been investigated as potential risk factors for MS onset and relapse, producing mixed findings[82,105,106]. Disease activity has been correlated with increased humoral immune responses to these HHVs in established cases of MS[105,107,108]. Infection with CMV has generally not been associated with disease outcomes in MS and antibody responses to CMV have been correlated with reduced disease severity over time[109–112]. The virus most consistently and strongly linked with an increased risk for developing MS is EBV, discussed in greater detail below. The next most strongly linked infections are with HHV-6 and HERVs; the evidence for which is covered in detail by Meier and colleagues in[101]. HHV-6 reactivation has been associated with disease activity in RRMS and SPMS, and there are reports of direct CNS infection in MS brain tissues[101]. The dysregulation expression of elements of HERV-W and HERV-K has also been implicated, most notably with the pathogenic HERV-W member MS-associated retrovirus (MSRV)[101,113,114]. MSRV envelope protein expression has been detected in various immune cells within MS lesions, and therapies that directly or indirectly reduce HERV-W activity exhibit clinical benefit[101,115]. Viral infections generally incite an inflammatory response that can contribute to ongoing autoimmunity but may not be specifically required for disease initiation. With increased understanding of the prodromal period that precedes onset of clinically evident MS[116], determining the mechanistic contribution of infections prior to and following autoimmune disease initiation will be necessary to introduce effective preventative strategies that target viruses.

In summary, many of the environmental risk factors associated with MS are known generate persistent systemic inflammation, which cumulatively increases the likelihood for autoimmune disease to develop. It is possible that MS is a group of similar diseases caused by genetic variants compounded by environmental triggers that, when combined in a timing specific manner in certain populations, exceeds an inflammatory threshold for regulation, breaks

immunological tolerance, and leads to an autoimmune response to the CNS that causes symptomatic disease. To quote Compston and Coles, "The cause of multiple sclerosis involves environmental exposure and genetic susceptibility. Arguing the merits of one faction versus the other is unproductive. Each is clearly implicated, together with the cultural condition of age at which the interplay between genes and the environment occurs"[18]. In order to dissect the independent and co-operative mechanisms underlying the genetic and environmental exposures that contribute to disease onset and progression, multiple animal models have been generated that each recapitulate distinct aspects of the pathobiology of MS.

1.1.5 Animal models for preclinical assessments in MS

Most of our understanding of the pathogenesis of MS in patients comes from longitudinal MRI studies, epidemiological data, clinical samples, and post-mortem CNS tissues, often obtained after many years of chronic disease. These studies are often limited by the years long delay between the triggering events and symptom onset and the limited ability to analyze CNS tissues during active disease. Animal models can help elucidate early factors associated with onset and allow for mechanistic molecular and cellular interrogation during different stages of disease. Models are just that, however, and each have their pros and cons in terms of which aspects of MS subtypes and pathologies they most closely reproduce. Animal models of MS generally fall into two groups: chemically induced, which reflect the neurodegenerative and regenerative aspects of MS, and immune-mediated, which reflect the systemic and neuroinflammatory aspects of MS.

1.1.5.1 Chemical and viral-induced demyelination

Chemically and virally induced demyelination models involve direct damage to the CNS as the inciting event, coupled with or without subsequent immune infiltration and local inflammation. The chemically induced models of MS that specifically minimize peripheral immune involvement include injectable detergents and destabilizing agents, such as lysophosphatidylcholines (LPC), ethidium bromide, and anti-galactosidase antibodies, as well as orally administered demyelinating agents such as cuprizone. These models are most useful for studies focused directly on neurodegenerative, protective, and remyelinating processes within the CNS. In a systematic review of preclinical assessments of therapies evaluated for neuro-regenerative effects in MS, cuprizone was the most employed agent to induce demyelination,

followed by active EAE induction (discussed in the next section) and localized injections of LPC or ethidium bromide[62].

Ethidium bromide (EtBr) is a DNA intercalating agent used to induce focal demyelinated areas with minimal systemic inflammation[117]. EtBr destroys glial cells, and especially their highly proliferative precursors, by compromising DNA replication. EtBr causes nonspecific apoptosis within the injection site and subsequent demyelination and remyelination of the lesion, though is considered a less attractive substance than LPC due to its carcinogenic effects[62]. Models that employ lysolethicin, also called LPC, involve the injection of this phospholipid activator with membrane detergent-like properties into a predetermined site within the CNS[118]. The resulting disruption to the myelin sheaths creates demyelinated lesions within 2 – 3 days, mainly surrounded by macrophages and activated microglia, that both mediate demyelination and remove myelin debris during oligodendrocyte precursor mediated remyelination, with very few adaptive immune cells present in the area[118]. Cuprizone is a copper chelator that specifically and selectively causes mitochondrial stress and apoptosis of mature oligodendrocytes in particular regions of the brain, notably the corpus callosum, though the exact mechanism(s) underlying this specificity is unclear[42]. Demyelination in this model occurs with an intact BBB and minimal peripheral immune cell infiltration, creating lesions with a type III composition[33,42]. Short-term or long-term administration of cuprizone in the diet leads to acute or chronic demyelination, respectively, along with activation of glial cells. Similar to LPC lesions, cessation of the cuprizone diet leads to spontaneous remyelination that proceeds in a highly reproducible spatiotemporal pattern.

Viral demyelination models are similar to EAE models in that peripheral immune cells infiltrate and demyelinate the CNS. The site of the initial trigger, however, is similar to chemical models, wherein intracranial inoculation with a neurotropic strain causes demyelination to occur secondarily to axonal damage (inside-out mechanism). Two predominant positive sense single-stranded RNA [(+)ssRNA] viruses are utilized for this purpose, Theiler's murine encephalomyelitis virus (TMEV, a picornavirus) and mouse hepatitis virus (MHV, a coronavirus). TMEV injection into the CNS causes acute encephalitis and peripheral T cell infiltration to clear the virus, which results in nonspecific CNS damage and initiates autoantigen recognition[119]. In the Swiss James Lambert (SJL) mouse strain, viral clearance is incomplete and results in a persistent infection within macrophages and glial cells, resulting in further epitope spreading and chronic inflammation[120,121]. Similar to the TMEV model, MHV produces axonal damage and chronic

demyelination throughout the CNS after intracranial inoculation[122]. Demyelination is a result of incomplete viral clearance by infiltrating peripheral immune cells responding to infection. The neurotropic demyelinating strains A59 and JHMV are most commonly used to model clinical and histopathological aspects of MS[122].

1.1.5.2 Experimental autoimmune encephalomyelitis

In 1935, Rivers and colleagues demonstrated that a clinically overt encephalitic demyelinating disorder resembling ADEM could be produced in rhesus macaques following repeated injection with normal rabbit brain extract in the absence of an infectious agent[123]. This study followed case reports of accidental induction of CIS-like paralysis in people after administration of the rabies vaccine, which was derived from rabbit CNS tissue, as well as previous reports of human spinal cord homogenate injections inducing paralysis and functional deficits in rabbits[123–125]. The process of inducing this novel disease model became more efficient with the addition of a new adjuvant created by Freund[126]. The EAE model, in which disease is initiated by CNS autoantigen recognition in the periphery, occurs by primary demyelination that results in axonal damage and clinical symptoms (outside-in mechanism). Various EAE models have been developed to each recapitulate specific aspects of MS. While no one agent has been determined to produce MS in humans in the way EAE can be artificially induced in animals, nor does any single EAE model reproduce all aspects of MS, the resulting immunopathology provides insights into pathogenic mechanisms within the CNS early in disease that would otherwise be unknown[41,127].

1.1.5.2.1 Inducing EAE

EAE models can be divided into three main groups based on the induction method: active, passive, and spontaneous. Active EAE is generated by immunizing animals with myelin peptide or protein (or spinal cord homogenate, though this is less commonly used due to the many potential epitopes in the injection) emulsified with an adjuvant, in order to elicit a CNS-directed and predominantly $CD4^+$ T cell mediated autoimmune response[50,128]. Some of the earlier attempts to generate EAE in rodents using a single antigen involved the use of MBP and led to the development of GA[41], though many encephalitic epitopes have since been identified. Priming of the adaptive immune response occurs in the periphery (the induction phase), followed by lymphocyte migration and infiltration of the CNS, which may be aided by administering blood-

brain barrier permeating agents like pertussis toxin, and secondary recruitment and activation of local and infiltrating cells that go on to demyelinate axons (the effector phase)[129]. A modified version of active EAE induction is focal or targeted EAE induction. A predetermined site in the CNS of an EAE mouse is injected with interferon-γ and tumor necrosis factor (TNF)-α to preferentially 'target' peripherally activated leukocytes to a single lesion following active immunization[118]. Focal induction directs the pathology to specific areas of the CNS, including those that may be less commonly affected by regular induction protocols.

Passive EAE is induced by the adoptive transfer of ex vivo stimulated and expanded myelin reactive $CD4^+$ or $CD8^+$ T cells, isolated from the peripheral lymphoid organs (draining lymph nodes and spleen) of actively induced donors[130,131]. T cell transfer to a naïve, syngeneic recipient results in a disease with the same clinical and immunopathological characteristics as the actively induced donor, but that bypasses the initial priming step (bypasses the induction phase)[129]. The resulting disease tends to onset more consistently between animals, with greater symptom severity and incidence[129]. Passive induction is helpful for differentiating the effects of an intervention on the initial priming of the autoimmune response versus the effects on leukocyte migration and CNS-localized pathogenic mechanisms. The ex vivo stimulation step also allows for manipulation of the cell phenotypes and characteristics (Th1 or Th17 polarization, modification by gene editing, etc.). Passive transfer of murine or human derived autoreactive antibodies alone is not sufficient to induce EAE in recipient mice, though pathogenic antibodies can exacerbate damage in an ongoing T cell mediated EAE[132].

Spontaneous EAE models refer to those in which the genes encoding the T cell receptor (TCR) and/or B cell receptor (BCR) are genetically engineered to recognize an encephalitogenic epitope[41]. The 2D2 C57BL/6 (H-2^b)/MOG_{35-55} TCR transgenic $CD4^+$ T cell model is one of the most widely employed spontaneous models[133]. Typically, the class II recognizing TCR is modified, though autoreactive class I restricted $CD8^+$ T cell-mediated and B cell-mediated transgenic models have also been reported[134,135]. For example, the IgH_{MOG} mouse contains a MOG-specific Ig heavy chain knock-in on the 2D2 TCR background[135]. Spontaneous disease will develop at 5 – 8 weeks old, though rates are generally low (~4%) and highly dependent on housing conditions[133]. The additional use of an active or passive immunization step in transgenic strains results in high disease incidence and severity characterized by an earlier onset than non-transgenic controls[41,129]. In other models, the transgenic TCRs are human HLA restricted, though these strains

do require active or passive immunization to generate symptoms[129]. The end consequence of these induction methods is the development of widespread demyelination and clinically measurable neurological deficits, most notably an ascending paralysis that affects the tail and hind limbs.

1.1.5.2.2 Immunopathology of murine EAE models

Active immunization with myelin peptide is the most widely used method to induce EAE in mice and is the most comprehensively described of any EAE model. The injection of complete Freund's adjuvant (CFA) emulsion containing an encephalitogenic peptide, desiccated *M. tuberculosis*, and mineral oil, stimulates DC maturation through toll-like receptors (TLRs) and other pattern recognition receptors, which then promotes presentation of the peptide to $CD4^+$ T cells[136,137]. The sequence of immunological and neurological processes that drive the effector phase of EAE are as follows: Primed $CD4^+$ T cells migrate to and extravasate across the BBB (which has been compromised by administration of pertussis toxin in some strains), are reactivated locally by microglia presenting myelin antigens as normal, and then produce proinflammatory cytokines and chemokines to further permeabilize the BBB and activate and recruit other peripheral immune cells (including macrophages, B cells and some $CD8^+$ T cells). Local glial cells also become activated by these cytokines, which, in conjunction with infiltrating macrophages, demyelinate axons[129,138].

The role of T cells, particularly of $CD4^+$ T cells, has been extensively studied in EAE models. The role of B cells has also been investigated and is discussed in the next section. EAE can be passively induced by the adoptive transfer of myelin reactive Th1 or Th17 polarized cells, and knocking either of the Th1 or Th17 pathways does not protect mice from EAE susceptibility[138]. Passive immunization can also be accomplished with $CD8^+$ cytotoxic T cells in some strains, though generally, $CD8^+$ T cells are underrepresented in murine EAE models compared to human disease[37,139]. $CD4^+FOXP3^+$ regulatory T cells are also known to control the movement and proliferation of pathogenic T cells within the CNS of EAE mice[140]. Despite the preclinical evidence suggesting a key role for effector $CD4^+$ T cells in driving disease, a clinical trial of ustekinumab (an IL12/23 p40 antibody that inhibits the differentiation of both Th1 and Th17 cells), showed no benefit in RRMS[141], confirming that once MS is established, $CD4^+$ T cell depletion is not a viable treatment strategy[61]. Other important discrepancies between the neuroimmunological

aspects of MS and EAE have been noted[128]. Murine EAE models are more spinal cord dominant, whereas inflammatory forms of MS, such as in RRMS, predominantly involve the brain[128].

1.1.5.2.3 Mouse strain and antigen-dependent outcomes

The clinical phenotype and the involvement of different components of the immune system in EAE models varies depending on the susceptibility of the induced mouse strain and the ability of the encoded MHC variants to form a stable complex with the immunizing antigen[50,129,142]. The most common EAE model uses the peptide MOG_{35-55} to induce C57Bl/6 mice, which produces a chronic progressive phenotype[129], while BALB/c mice are generally resistant[143]. SJL mice immunized with proteolipid protein $(PLP)_{139-151}$ without pertussis toxin develop a relapsing remitting disease course (Figure 1.5) characterized by epitope spreading and a female sex bias[129]. Both male and female non-obese diabetic (NOD) mice immunized with MOG_{35-55} develop a relapsing phenotype that shifts to a secondary progressive course[139,144,145]. In other strains, mice can develop an acute episode of paralytic symptoms followed by resolution (i.e. MOG_{35-55} or MBP_{1-9} induction of H-2^u strains such as PL/J and B10.PL) or can develop a relapsing progressive disease (i.e. MOG_{8-21} or spinal cord homogenate induction in Biozzi ABH mice)[129,146–148].

Though these combinations of strains and antigens are typically used, altering the dose and sequence of the inducing myelin antigen, as well as using full length proteins rather than immunodominant peptides, can result in temporally different clinical and immunohisto-pathological outcomes[149–151]. For instance, varying the antigen or dose of MOG_{35-55} used to induce C57Bl/6 mice can produce a monophasic or mild relapsing disease rather than a chronic, hyper acute phenotype[152–154]. MOG protein induced EAE in C57Bl/6 mice produces a similar clinical phenotype as MOG_{35-55} immunization but with differential activation and involvement of adaptive immune cells in disease pathology. The immunological differences elicited by peptide and protein MOG EAE in C57Bl/6 has illuminated the diverse roles B cells can play in disease onset and progression through distinct and specific mechanisms that depend on the inflammatory context. Full length recombinant MOG protein contains multiple encephalitogenic determinants as well as conformational epitopes that generate greater numbers of infiltrating MOG-reactive B cells that can present antigen and secrete autoantibodies[41,149,155]. B cell deficient mice are resistant to EAE induction with MOG protein but not with MOG_{35-55} peptide, indicating that B cells are necessary for the induction of EAE by intact protein[155]. The authors noted that B cell deficiency in the MOG

protein model did not prevent the processing or presentation of MOG generally[155] though antigen processing of MOG protein by B cells may result in the presentation of distinct epitopes to T cells and the generation of pathogenic antibodies[41,156]. The clinical relevance of these findings is highlighted by the efficacy of anti-CD20 B cell depletion therapies in MOG protein induced EAE model and relapsing MS in people, but the aggravation of disease in MOG peptide induced EAE, suggesting the involvement of regulatory B cell mechanisms in the latter model[41,157].

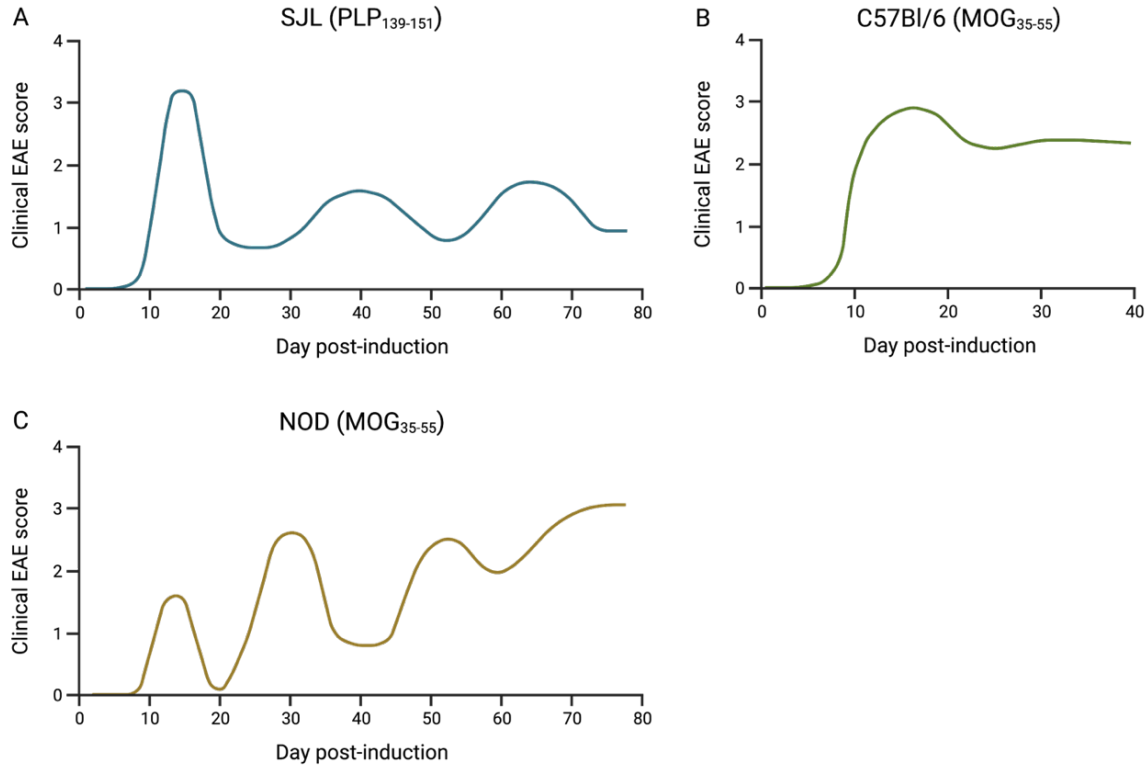

Figure 1.5 Clinical EAE disease courses for common mouse strains and antigens

Paralytic symptom kinetics of experimental autoimmune encephalomyelitis (EAE) induced in (A) Swiss James Lambert (SJL) mice with proteolipid protein $(PLP)_{139-151}$, (B) C57Bl/6 mice with myelin oligodendrocyte $(MOG)_{35-55}$, and (C) non-obese diabetic (NOD) mice with MOG_{35-55}. Adapted from our data and[129,144]. Created using BioRender.

1.1.5.2.4 Non-human primate models of EAE

EAE was first established in non-human primates (NHP) and has provided insights into disease processes in MS with greater translational relevance to humans than conventional laboratory mice. NHP EAE model studies typically utilize colonies of marmoset monkeys

(*Callithrix jacchus*) or Japanese macaques (*Macaca fuscata*)[49,158]. In marmosets, a progressive MS-like pathology can be induced using MOG_{34-56} emulsified in complete or incomplete Freund's adjuvant, the latter of which cannot induce EAE in rodents in the absence of mycobacterium[49,159]. Relapsing disease can also be generated by modifying the induction procedure. The resulting CNS pathology resembles human MS more closely than in murine EAE models, including demyelination of the white matter and cortical grey matter in the brain and spinal cord, microglial activation, oxidative stress leading to mitochondrial dysfunction, iron redistribution, necrotic hemorrhage, and the presence of neutrophils in the CSF[49,158]. The autoimmune response is predominantly driven by Th1 cells (restricted by monomorphic MHC class II/Caja-DRB*W1201), with IL-17A expression contributing to progression alongside MHC-I restricted T cells that numerically dominate the lesions[49,159]. NHP EAE models are advantageous over murine EAE models in that NHP colonies are pathogen-exposed and outbred, and the genetic loci relevant to MS, especially MHC encoding regions, are more similar to humans[160].

1.1.5.2.5 Applicability and limitations

A large variety of EAE models have been developed since the first reports of an ADEM-like disease in NHPs, especially among laboratory rodents. The EAE model has even been extended to zebrafish for rapid drug screening[161]. The increasing number of EAE models that have become available for mechanistic and therapeutic assessments of MS has also generated an increasing number of caveats for their use[42]. No single mouse model of EAE accurately recapitulates all aspects of the disease, and while NHP EAE models show greater similarity to human MS, their use is limited by relatively small numbers of offspring and long gestational periods, as well as ethical and welfare considerations. Apprehension to using EAE models on the basis that it is externally induced, unlike spontaneously occurring MS in humans, and therefore inherently imprecise, can arguably be extended to many animal models of human disease[152]. Careful consideration must thus be given when selecting an EAE model to interrogate a specific pathway or mechanism, and especially so when being employed for preclinical assessments of therapies (summarized in detail in[50]). In this case, the use of multiple different EAE models may better predict the efficacy and potential detrimental side effects of treatments in subtypes of MS.

1.2 Epstein-Barr virus

EBV was the first oncogenic human virus to be identified, following its discovery in 1964 in Burkitt's lymphoma biopsy samples[162]. The use of the new technique of electron microscopy drew skepticism at the time that the observation of virus particles in cancer cells was not accurate and was simply an artifact or contaminant[163]. The isolated biopsy cells, however, were also able to propagate ex vivo, which caused the authors manuscript to "…encounter serious problems when submitted for publication from reviewers who were unwilling to believe that human lymphoid cells could be grown in culture at all"[163]. EBV is now recognized as a near universally prevalent gammaherpesvirus that can cause malignant disease in predisposed individuals.

1.2.1 Human herpesviruses

Herpesviridae is an expansive group of highly conserved, species-specialized viruses known to infect most mammals, which arose nearly 200 million years ago. Their broad host range and near ubiquity is ascribed to the infection of a common ancestor and continual evolution and speciation alongside their hosts over the last 80 million years[164]. The extensive co-evolution of herpesviruses with their host has significant ramifications for host immune system development and health, as herpesviruses form part of the larger virome responsible for immunological training and modulation of responses to other pathogens[165,166]. Nine herpesviruses known to infect humans (HHVs) are classified into three main groups based on tropism, replication strategy, and genomic structure[167]. The α-herpesviruses include the neurotropic HHVs herpes simplex 1 (HSV-1, or HHV-1), herpes simplex 2 (HSV-2, or HHV-2) and varicella zoster virus (VZV, or HHV-3). The β-herpesviruses comprise cytomegalovirus (CMV, or HHV-5), HHV-6A, HHV-6B, and HHV-7. The γ-herpesviruses are Epstein-Barr virus (EBV, or HHV-4, of the lymphocryptovirus genus) and Kaposi Sarcoma herpesvirus (KSHV, or HHV-8, of the rhadinovirus genus). The latter two groups are predominantly but not exclusively leukotropic. All humans are exposed to and infected with multiple HHVs in their lifetime, typically early in childhood due to intrafamilial transmission[168]. Most HHVs transmit horizontally through direct oral contact and/or infection at mucosal barriers, with the main exceptions being VZV, which can transmit through aerosol, and CMV, which can transmit vertically in utero on rare occasions[168,169]. The hallmark characteristic of herpesviruses is their dual infectious modes, beginning with lytic primary infection, followed by the establishment of latency in a specialized host cell type to evade immune clearance, and intermittent reactivation

back into a lytic cycle for propagation to new hosts. Though generally quiescent, herpesviruses are double stranded DNA (dsDNA) viruses that establish a lifelong, persistent infection that can cause a spectrum of malignancies and clinical conditions if host immune control is compromised.

1.2.2 EBV transmission and epidemiology

EBV predominately transmits through the oral route in saliva but can also transmit horizontally through close contact, transfusions, and tissue transplants[170]. Acquisition typically occurs in childhood through mastication of food[171] or indirect contact with shared items like toys[172], though the exact nature and age of acquisition is dependent socioeconomic and cultural differences in familial behaviour, childcare practices, etc. A person's likelihood of transmitting EBV fluctuates also over time, with the proportion of adults shedding detectable levels of EBV in oropharyngeal secretions varying between ~25% and 80% at a given time[168,173]. In developing countries, children generally acquire EBV and seroconvert by 3 – 4 years old, whereas a bimodal distribution is observed in developed countries wherein peaks of seroconversion occur both under 5 years of age and above 10 years of age[172]. In all regions, however, EBV has a prevalence rate of 90% or higher among adults[172]. During primary infection, EBV infects epithelial cells (ECs) in the oropharynx and subsequently disseminates and infects memory B cells, within which the virus establishes latency and persists for the life of the host. the transcriptional programs employed by EBV to establish and switch between the lytic and latent forms of infection are highly attuned to the immune microenvironment, making EBV a highly efficient and successful human pathogens.

The two subtypes of EBV, types I and II, exhibit distinct geographical distributions. The two strains are thought to have arisen from a recombination event between a proto-EBV strain and another lymphocryptovirus that then diverged into the now circulating EBV subtypes[174,175]. Though most populations are preferentially infected with one of the two types, they do not appear to behave differently as far as their ability to cause disease, and, with the exception of Epstein-Barr nuclear antigen (EBNA)-2 and EBNA-3A/B/C encoding genes, most sequences remain highly conserved[172,174,176]. Immunocompromised individuals can be superinfected with multiple strains of EBV, though superinfection is common in healthy individuals as well, and it is suspected that EBV subtypes can recombine during dual infection[174,177–179]. The sequence by which multiple strains of EBV are acquired is unclear, in terms of whether there is simultaneous infection with

multiple strains at primary exposure, acquisition of different strains over time, or divergence from a single strain due to reactivation and reinfection within the same host[177].

1.2.3 Lifecycle

EBV contains a 172 kbp dsDNA genome encoding over 80 viral proteins and multiple noncoding EBV RNAs (EBERs) and microRNAs (miRNAs)[180]. Similar to other HHVs, EBV forms a bilayer enveloped mature virion of 120 – 180 nm diameter, wherein the genome is encased in a capsid and surrounded by tegument proteins (Figure 1.6)[167]. The envelope contains up to 11 glycoproteins that coordinate attachment and entry into target cells[181]. The attachment, fusion/entry, and replication strategies differ between ECs and B cells in order to facilitate re-seeding between these cell types and transmission to new hosts. The attachment of EBV to B cells involves contact between the gp350/gp220 glycoproteins and CD21 (also called C3d receptor, encoded by the complement receptor 2 gene) on the membrane surface (Figure 1.6B)[181]. The core glycoproteins gH/gL form a trimer with gp42 to bind HLA class II, and, along with gB, fuse the virion membrane with the target B cell membrane. ECs, however, lack both CD21 and HLA II expression under normal circumstances, and thus rely on the glycoprotein BMRF2 to bind β1, α5, and α3 integrins on the cell surface of ECs (Figure 1.6C)[182]. The gH/gL/gB complex then facilitates fusion to the EC cell membrane, without gp42, by interacting with the Ephrin receptor A2[181,183]. EC infection was debated for a long time in favor of intraepithelial B lymphocytes, though both populations may be targets in the oropharynx[163]. EBV is still shed from the throat in B cell lymphoma patients treated with anti-CD20 B cell depletion, indicating the presence a second reservoir of infected cells, most likely being the oral epithelium[184].

The lipid bilayer surrounding new virions is derived from host cell membranes when capsids bud out and there is evidence indicating that new virions produced by infected B cells lack gp42 expression, while expression of gp42 is present on the surface by EC-derived virions, in order to switch tropism and effectively re-infect the other cell type; presumably as a survival strategy to maintain the two tissue reservoirs[185,186]. After membrane fusion with the membrane of either a B cell or EC, the nucleocapsid is released into the cytoplasm, where it is dissolved, and the genome transported to the cell nucleus for lytic replication and/or the establishment of a latent episomal infection[187]. A series of temporal transcriptional programs determine if and when a lytic or latent infection strategy is implemented. During lytic infection of B cells and ECs, EBV employs a

sequential series of three lytic gene expression profiles divided into immediate-early, early, and late-stage products[187]. The early-stage genes encode products required to replicate the virus, modulate host metabolism, and reduce antigen processing and presentation to the immune system. The later stage genes encode mainly for structural proteins to form new virions and to continue the immune evasion tactics[187]. This phase of the EBV lifecycle can be inhibited with acyclovir and derivative nucleoside analogues by disrupting the elongation of the genome by the viral encoded DNA polymerase (encoded by EBV's *BALF5* gene)[188–190]. After approximately 2 weeks, lytic genes are CpG methylated and silenced in B cells to establish latency[191,192]. In normal epithelium, EBV infection is restricted to the differentiated layers where it is chronically lytic and does not form a stable latent infection[191].

With the caveat in mind that most of our understanding of infected B cell behaviour is derived from in vitro studies of lymphoblastoid cell lines (LCLs), the latent transcriptional profiles expressed in human B cells has been studied and documented extensively. During latency, the viral genome is maintained as multiple copies of extra-chromosomal episomes that do not, except in rare cases, integrate with the host genome[192]. These heterochromatinized episomes contain host derived histones and replicate alongside the host chromosome using the host DNA polymerase[192]. To ensure replication alongside its host's genome, EBV encodes the latency protein EBNA-1, which can oligomerize into filaments and form DNA-binding dimer complexes that tether the episome to the host chromosome[192,193]. Other gene products expressed during latency can include more EBNAs (EBNA-1/2/3A/3B/3C/LP), latent membrane protein (LMP-1/2A/2B), and EBERs 1 and 2[193,194]. After initial infection of a B cell in vivo, EBV is thought to go through progressively more restricted latency profiles, defined by specific latent gene expression combinations, to avoid detection and deletion[192]. The most profound latency profile is type 0, where no EBV proteins are expressed at all. Next is latency type I, where only EBNA-1 and EBERs are expressed. In type II latency, EBNA-1, LMP1, and LMP2 are expressed. Type III latency is the least restricted profile, where all latent genes are expressed, and is typically observed in LCL cultures in the absence of immune control[192]. The main functions of the latent proteins and miRNAs is to ensure survival of the infected B cell by supressing apoptosis, downregulating the expression of surface antigen presentation complexes, regulating the cell cycle, and epigenetically modifying the viral genome to sense the microenvironment for changes that would favour reactivation[192,195]. A thorough review of EBV encoded lytic and latent genes is discussed by Kanda, Murata, and colleagues in[194,196].

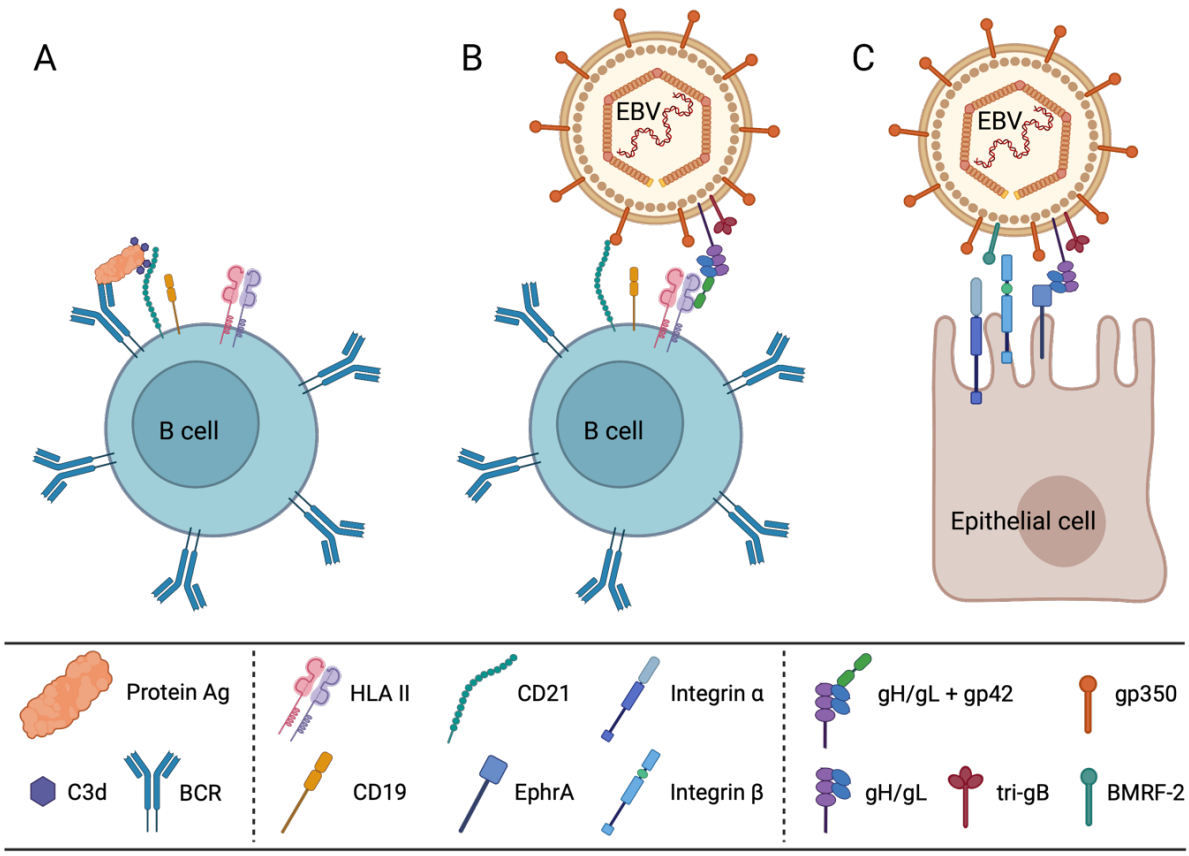

Figure 1.6 EBV virion attachment to B cells and epithelial cells

(A) Cognate protein antigen recognition by B cell receptors (BCR) and co-stimulation of CD21 binding via C3d complement protein complexed with antigen (Ag). (B) B cell attachment of Epstein-Barr virus (EBV) is mediated by glycoprotein (gp) 350 binding to CD21 and gH/gL + gp42 + trimeric gB complex attachment to human leukocyte antigen (HLA) class II molecules. CD21 binding by C3d or gp350 causes phosphorylation of the intracellular tail of CD19 to increase signaling 1,000 – 10,000-fold and results in B cell activation. (C) Epithelial cell attachment of EBV is mediated by gH/gL + trimeric gB complex to Ephrin receptor A (EphrA) and viral BMFR-2 to integrins on the cell surface. Adapted from[197,198]. Created using BioRender.

The shift from lytic infection to latency during primary infection can be observed though repeated serological testing for viral capsid antigen (VCA), early antigen (EA), and EBNA-1 specific IgM and IgG levels over time (Figure 1.7)[187,199–201]. In symptomatic cases of EBV infection, IgG antibodies to EBNA-1 do not develop in most individuals until about 3 months post-symptom onset[193,202]. Though EBNA-1 is required for episomal maintenance during latency, it also facilitates binding to the viral origin of replication to shift back into a lytic replication state[203,204]. Reactivation in B cells is triggered by host B cell activation by BCR antigen recognition

and differentiation into a plasma cell, or by acute cellular stress[205,206]. Once plasma cell differentiation is initiated, the BCR signaling-responsive promoter of the *BZLF1* gene is activated to transcribe and express the proteins Z and R in methylated episomes in B cells and unmethylated episomes in oral epithelial cells, respectively[191]. Similar to other DNA viruses, EBV encoded gene products compact and relocate the cellular chromosome to the periphery of the nucleus once lytic genes are re-expressed[192,207]. In culture and humanized mice, subtype I and II EBV strains differ in their predilection to establish a more lytic or latent infection in B cells, wherein type I strains (B95-8, Akata, Mutu, M81, GD1, etc.) are typically more latent and type II strains (AG876, BL5, P3HR-1, Jijoye, etc.) are initially highly lytic strains that become increasingly latent with LCL passage due to differential lytic *BZLF1* gene promoter usage and BCR-associated transcription factor activity[208–211]. Type II EBV strains from the BL5 and Jijoye cell lines have also been shown to latently infect primary $CD8^+$ T cells in culture, unlike the type I strains from B95-8 and Akata cell lines[212] (information in Table 1.5).

The main viral reservoir for latent EBV is long-lived, hypermutated, and class-switched memory B cells, which comprise only a small proportion of the total B cell population[213,214]. In immunocompetent individuals, only 5 to 3000 per 10^7 memory B cells (0.0000005 – 0.0003%) are infected with the virus[215]. Two main models of B cell persistence have been proposed to explain how EBV ultimately establishes an infection in such a specialized and numerically infrequent subset of B cells: the direct infection model and the germinal center (GC) model[216]. The GC model of persistence suggests that EBV infection of memory B cells occurs via infection of naïve B cells that are then driven to differentiate into a memory phenotype by the expression of viral genes that mimic the natural GC-dependent maturation process[217]. This model is supported by the finding that different subsets of B cells express increasingly restricted latency profiles as they become more differentiated (i.e. activated naïve B cells express type III genes, induced B cell differentiation leads to type II latency, and dividing memory B cells exhibit type I latency)[217–219]. Moreover, EBV encodes multiple gene products that mimic B cell receptors to engage B cell survival and differentiation pathways, such as in the case of LMP1, which mimics CD40 co-stimulation by structurally resembling a TNF receptor family domain[220,221]. The direct infection model, as the name entails, suggests that EBV infects already differentiated memory B cells in the oropharynx without mimicking GC-dependent maturation[216]. Though generally this model is discounted on the basis that there is scant evidence to support it, interesting evidence backing this

model of persistence has been reported by Chaganti and colleagues, indicating EBV directly infected non-class-switched memory B cell population (IgD^+CD27^+) cells rather than driving them through GC-like maturation steps[222]. The GC persistence model is generally favored and is perhaps more likely to occur given the low number of differentiated memory B cells in the oropharynx of infants. It is also entirely possible that one or both mechanisms are opportunistically utilized to establish latent infection depending on the available populations. In both scenarios, EBV infection of B cells leads to a state of constitutive activation that alters the responses, functions, and immune control of infected cells.

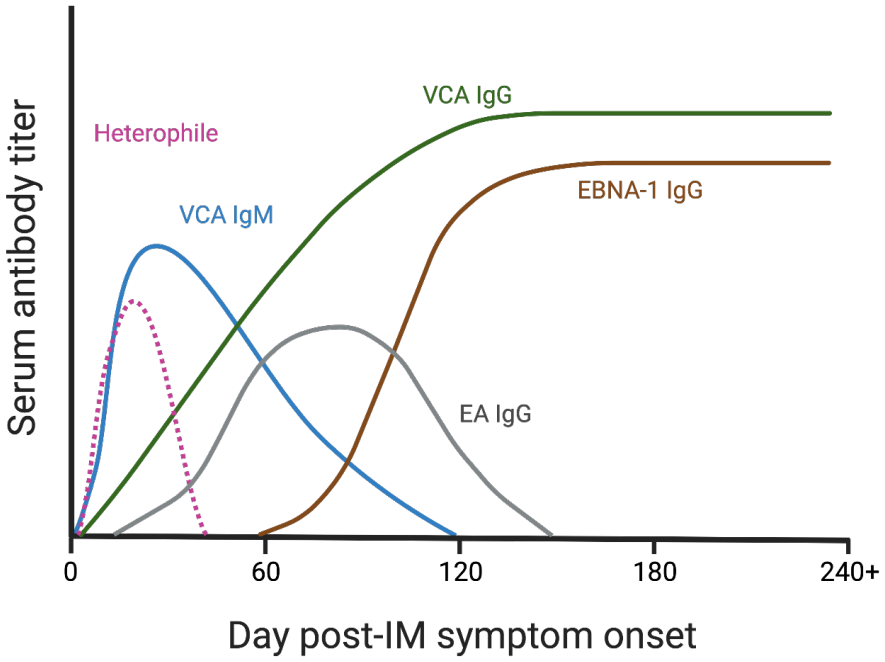

Figure 1.7 Temporal serology of symptomatic primary EBV infection

Viral capsid antigen, VCA; early antigen, EA; Epstein-Barr nuclear antigen, EBNA; infectious mononucleosis, IM. Adapted from[187,200]. Created using BioRender.

1.2.4 Host immune control of EBV infection

Given the sophisticated replication, persistence, and evasion strategies EBV has evolved to employ to maintain a life-long infection in its host, the host has correspondingly evolved several redundant and specialized strategies to control and limit infection, since complete clearance is not achievable. Most of what is known about immune responses to primary infection is derived from symptomatic cases of infectious mononucleosis (IM), as asymptomatic primary infections in

children are difficult to identify[170]. Both innate and adaptive immunity is involved in supressing the replication within and outgrowth of EBV infected B cells. Though the immune responses engaged during the earliest stages of primary EBV are mostly unknown, the virus is presumed to elicit a strong type I interferon (IFN) response very early on and can be detected approximately 2 weeks prior to symptom onset in young adults[223]. EBV engages multiple TLRs (2, 3, 7, and 9) which can promote the type I IFN response[224]. To counteract this response, EBV encodes a lytic protein, BGLF5, that promotes TLR9 RNA transcript degradation to reduce expression within the infected cell[225]. The latency protein LMP1 is also upregulated by IFNα which has an antiproliferative effect and helps maintains latency[226]. Contributing to EBV control through IFN expression is plasmacytoid dendritic cells (pDCs), which secret large quantities of type I interferons in response to infection[227]. Evidence also suggests these pDCs may play a larger role in priming T cell responses than conventional DCs that are responsive to EBERs[227].

To avoid detection by cytotoxic $CD8^+$ T cells, EBV induces downregulation of MHC expression on the host cell surface[228]. Downregulation of MHC expression by viruses activates NK cell mediated lysis, and therefore, EBV expresses the BILF1 encoding gene to downregulate surface HLA-A and -B molecule expression but not NK cell-inhibitory HLA-C molecule expression[228]. The role of NK cells in limiting early lytic replication is reflected by increased proliferation during IM and an inverse correlation between NK cell counts and IM symptom severity[187,229]. NK cells within tonsillar tissues are also more efficient than peripheral NK cells at targeting EBV infected cells[230]. As discussed above, IgM and IgG antibodies to both lytic and latent antigens are generated as EBV progresses through its lifecycle. Antibodies specific to the gp350 envelope protein have been shown to prevent binding of EBV particles to the receptor CD21, indicating an important role for antibody responses in limiting the spread of infection[231]. The humoral immune response, alike other responses, is dependent on the age of the host. EBV seropositive infants present with high titers, as do individuals above 50 years old, suggesting reduced effective immune control of the virus in these age groups[172]. During IM, peripheral $CD4^+$ T cell counts do not increase substantially, though they do recognize lytic antigens and are maintained in the blood at the low levels after acute infection resolves[232]. Latent EBNA-1 specific $CD4^+$ T cells develop correspondingly with the appearance of anti-EBNA-1 IgG several weeks after symptom onset[232].

Investigations of the T cell response to EBV has revealed a critical role for cytotoxic T cells (CTLs) in controlling lytic infection and eliminating latently infected cells. In the early phase of primary infection, serum IL-2 levels and $CD8^+$ T cell counts specific to structural and early lytic EBV antigens (such as gp350, gH/gL, gB, BZLF1, and BRLF1) rise dramatically[170,187,233]. As actively replicating cells are eliminated by these CTLs and more B cells form a latent infection, the numbers of lytic antigen specific CTLs declines while latent antigen specific (e.g., EBNA-2 and -3) cell counts increase[234]. Antibody and CTL responses to EBNA-1 generally tend to be less robust than to other EBNAs due to the low levels at which it is expressed in latently infected cells and the presence of protease resistant motifs within the protein[101,170]. Mathematical modeling of persistence and CTL responses to EBV suggests that when EBV infected B cells deviate from their resting memory B cell phenotype (during early infection, GC maturation, or reactivation), they are acted upon by CTLs, which selectively pressures EBV to maintain increasingly restricted forms of latency with low antigenicity[217]. To counter CTL responses to infection, EBV encodes gene products designed to dampen the ability of CTLs to recognize and kill infected B cells, including a homologue of human IL-10 (BCRF1) as well as viral proteins and miRNAs that reduce the expression of IL-12, lysosomal proteases, and MHC class I and II molecules[235,236]. In immune competent hosts, immune control by innate and adaptive mechanisms is sufficient to remove active EBV-infected B cells and restrict infection to a minimally antigenic latent form within very few resting memory B cells. Dysregulation or impairment of host immune functions, however, can lead to proliferation of infected B cells, uncontrolled replication, and clinically overt malignancy[237].

1.2.5 EBV-associated diseases

EBV infection is associated with a broad spectrum of seemingly very distinct diseases that can occur at high rates in certain populations while occurring very infrequently in others. The varied pathological consequences of EBV infection are attributed to host-specific differences in immune responses to infection dictated by age, genetic predispositions, cellular micro-environment, and previous and concurrent environmental exposures[172]. Though infection with EBV is normally asymptomatic, some individuals experience the symptomatic condition IM after primary exposure. In individuals with genetic or acquired immunodeficiency, EBV can cause lymphoproliferative disorders and cancers in both the epithelial and B cell compartments. EBV

infection is also linked to immunological disorders due to ineffective immune control and chronic infection, as well as to multiple autoimmune diseases.

1.2.5.1 Infectious mononucleosis

Infectious mononucleosis (IM) is a clinical entity characterized by a common set of symptoms, including sore throat, cervical lymph node enlargement, hepatosplenomegaly, and fatigue and fever[170]. In 90% of cases, IM is caused by EBV infection, though it can also be caused by CMV infection (and rarely by human immunodeficiency virus (HIV) or *toxoplasma* infection)[238]. The determination that EBV was the cause of IM was an expected discovery best described by Michael A. Epstein in the article "historical background"[163]: "Another event in EBV research whose history merits recording relates to the recognition of the causal relationship between the virus and infectious mononucleosis (IM). Not only did this come about entirely by chance, but the circumstances provide a perfect example of Pasteur's classic 1854 affirmation that `dans les champs de l'observation le hasard ne favorise que les esprits pre¨ pare¨ s' (`Where observation is concerned, chance favours only the prepared mind'). Shortly after the discovery of EBV the virus was sent for study to a number of laboratories, including, for reasons already explained (Epstein, 1999), that of Werner and Brigitte Henle in Philadelphia. There, sera from many different sources were being screened for antibodies to EBV in a search for disease associations and a young female technician was using samples of her own serum as a negative control in the tests. At this stage she developed IM and, when she returned to work a few weeks later, her serum was found no longer to be negative but to have developed antibodies to EBV. This hint was rapidly followed up by the Henles who drew on the resources of a serum bank collected over many years from students with IM at Yale University. It did not take long to work out that all were seronegative to EBV before their attacks of IM and developed specific antibodies to EBV during the disease, indicating causation by the virus (Henle et al, 1968; Crawford, this issue)." Most aspects of infectious mononucleosis briefly covered in this section have been reviewed extensively by Balfour and colleagues in [187] and [170].

During early childhood, acute infection with EBV is considered to be generally or at least mostly asymptomatic[170]. When EBV infection is delayed to adolescence or young adulthood, the risk of developing symptomatic IM after primary EBV increases[170], though children can also present with symptoms of IM in some cases[239]. The incubation period between initial EBV

infection and IM symptom onset of 32–49 days was determined through case reports of initially seronegative undergraduate students who recalled, with disconcerting accuracy, the day when they were likely exposed to a salivary transmission event[170,240]. Due to the nature of these transmission events, infection via genital contact or sexual intercourse could not be ruled out entirely, though 'deep kissing' was a noted contributing factor in all cases[170]. Though no seasonal variation in IM incidence has been reported in the general population, a peak in cases of IM tends to occur 6 weeks after freshmen arrive on university campuses[170]. Diagnosis of IM traditionally and often still depends on a positive heterophile antibody test, often called the monospot test[241]. Heterophile antibodies are derived from IgM expressing B cells with seemingly no specificity to EBV antigens but that can react with and agglutinate sheep erythrocytes[187,242]. Despite their unrelatedness to the pathogenesis of IM, they were found to be produced at high levels for over a year after the initial inflammatory phase of IM (in 86% of adolescents and adults) but not in other conditions[187,242]. In their report, Paul and Bunnell defined heterophile antibodies as "having the capacity to react to certain antigens, which are quite different from, and phylogenetically unrelated to the one instrumental in producing the antibody response"[242]. A positive monospot test is therefore not an EBV induced IM-specific test[241]. Heterophile antibodies are notably unreliable for use as diagnostic tests in children, where only 40% will test positive during primary infection, and thus specific EBV serological assays are recommended to more definitively determine and diagnose cases of EBV induced IM[187].

Sprunt and Evans first described and named IM after observing that patient samples contained large, atypical lymphocytes, also referred to as Downey cells, which we now recognize as $CD8^+$ CTLs that have expanded in response to viral antigens[170,243]. Serum viral loads peak during the first week of symptoms and decline thereafter, though they continue to remain higher than in individuals who did not experience IM for over 6 months post-onset in the blood and in saliva[244]. CTL counts also follow a similar declining trend during convalescence[170]. Infected B cells tend to exhibit a type II or III latency program and neutralizing gp350 antibody titres peak after 180 days post-IM onset[219,245,246]. The symptoms and physical effects of IM are attributed to excessive production of IFNs and other cytokines during the immune response to EBV infected B cells[231]. There is no specific treatment currently approved for use in IM, though vancyclovir has been used to manage symptoms[170]. Following an extended period of malaise and fatigue, infectious

mononucleosis generally resolves on its own and does not require treatment[187]. Following resolution of IM, recurrent cases are uncommon, as memory responses limit EBV reactivation[187].

The age relatedness of IM after primary EBV infection has led to investigations as to the underlying cause of asymptomatic versus symptomatic presentation depending on the age at acquisition. The theory has been proposed that children are exposed to lower quantities of virus through indirect salivary exchange with family and peers, whereas adolescents and young adults may receive a larger inoculum during salivary transmission events, which would result in higher viral loads and a greater CTL response[170]. A second perspective proposes that age related differences in immune development and maturity of the T cell response is responsible for differences between EBV infection in children and adults[170]. Evidence to support this theory comes from reports demonstrating a contraction of NK cells in adults compared to children, which could be important in cell mediated responses to EBV early in life while CTL responses are either not yet fully effective in childhood or are less engaged during NK cell-mediated control[170,229]. Immune response-based differences in susceptibility to IM are also supported by the inconsistency of heterophile antibody production in children with primary EBV infection, suggesting alternate inflammatory mechanisms are at play in infancy and childhood. The age relatedness of EBV and IM, which is in itself a risk factor for many diseases[170], is an important aspect of EBV pathobiology to dissect in order to develop preventative interventions.

1.2.5.2 Cancers and lymphoproliferative disorders

EBV infection is a group 1 carcinogen associated with 9 different cancers that accounts for over 1% of the worldwide cancer burden and causes more than 150,000 deaths per year[170,181]. Most cancers caused by EBV are rare but severe, and are identified by the expression of EBERs within biopsy samples[247]. The oncogenes encoded by EBV to infect, transform, and immortalize B cells are at the route of its carcinogenic potential[162,248]. EBV-associated B cell malignancies include Burkitt's lymphoma, Hodgkin's lymphoma, post-transplant lymphoproliferative disorder (PTLD), and diffuse large B cell lymphoma (DLBCL)[249]. Less frequently, EBV causes tumor formation in epithelial tissues in susceptible people, most commonly nasopharyngeal carcinoma (NPC) and gastric cancers[249]. In rare cases, EBV can infect and cause T and NK cell lymphomas[172]. The development of EBV associated cancers is considered to be due to high levels of lytic replication during early infection and horizontal transfer between B cells in a given host, which then causes

chromosomal instability during reactivation, and increases the likelihood of infecting and immortalizing a proto-oncogenic B cell[191,247,250,251]. In immunodeficient mice and in cell culture, lytic replication deficient EBV mutants have a reduced ability to generate tumors[252,253]. EBV encodes several oncogenes, including the CD40 mimic LMP1, the BCR signal mimic LMP2A, and the anti-apoptotic bcl-2 protein mimic BHRF1, which all act to promote the activation and survival of infected B cells[174,220,221,254].

Once EBV has established a latent infection in a susceptible B cell, impaired immune control by the host can lead to preferential and unrestricted outgrowth of the clone[253,255]. The specific factors that lead to the development of certain lymphomas and carcinomas, however, are more variable and complex. Burkitt lymphoma is a monoclonal cancer caused by the translocation and constitutive expression of the *c-myc* oncogene; an independent genetic event that becomes clinically pathogenic when the affected B cell has been infected with EBV[256]. The geographical distribution and prevalence of EBV positive BL overlaps closely with the African geographical area comprising the "malaria belt", where children are repeatedly exposed to and infected with *Plasmodium* species due to holoendemic transmission[172,257]. Repeated infection with malaria, or potentially any source of chronic antigen exposure, is suspected to continually reactivate EBV from infected *Plasmodium* reactive B cells, and/or to impair CTL control of latently infected B cells, leading to a greater chance of horizonal transmission to a B cell containing the *c-myc* gene translocation[191,258,259]. This theory is supported by findings that peaks in EBV viral loads in the blood are concurrent with episodes of malaria in young children[258,260]. Cases of EBV induced lymphoma that occur due to non-genetic factors often involve some form of acquired immunodeficiency. In transplant settings, EBV infection is major risk factor for poor outcomes due to the immune suppression administered to recipients and resulting inability to control reactivation of infection[172]. The risk of developing PTLD is especially high when tissues from an EBV seropositive donor are transferred to a priorly EBV seronegative recipients, where primary infection within the recipient can cause severe disease[172].

1.2.5.3 Other disorders due to aberrant infection and ineffective immune control

Complications of EBV infection resulting from chronically active infections that cannot be controlled are often severe and life threatening. Most cases are related to a genetic predisposition and the only long term treatment known to be effective is complete hematopoietic stem cell

transplant[261]. A very rare complication of IM is chronic active EBV (CAEBV) disease, where EBV preferentially infects T and/or NK cells beyond the typically low levels observed in IM, rather than infecting B cells during primary infection[261,262]. Inappropriate control of viral replication ensures, leading to elevated antibody titres to EBV and excessively high viral loads that can cause lethal viremia[261]. No known genetic immunodeficiency has yet been identified as a common cause[262]. One clear case of an isolated genetic immunodeficiency causing EBV associated disease is that of X-linked lymphoproliferative (XLP) disease, a form of hemophagocytic lymphohistiocytosis (HLH) hyperinflammatory syndrome[263]. XLP is a very rare hereditary condition caused by a deletion of or mutation within the *SH2D1A* gene that encodes for the signalling lymphocytic activation molecule-associated protein (SAP)[264]. The lack of SAP activity causes broad defects in the functions of T cells and NK cells, resulting in the inability of B cells to class switch[264] and ineffective CTLs that cannot eliminate EBV infected B cells[265].

1.2.6 Vaccine development

Based on the extensive association of EBV with multiple illnesses, often characterized by high viral loads and improper immune control, the administration of a vaccine to the general population could have a substantial impact on reducing the rates of these diseases[170]. To date, a sterilizing vaccine has not been developed to prevent EBV infection, though preliminary trials have demonstrated therapeutic benefit[266,267]. The first EBV gp350 subunit vaccine designed by Epstein and colleagues in 1985 did not prevent infection in cottontop tamarins but did protect immunized animals from the development of lymphoma[268]. A phase II trial of recombinant gp350 with adjuvant also reduced the rates of IM in the immunized group but did not prevent asymptomatic primary infection altogether[269]. The takeaway lessons from initial animal and clinical studies indicated that a sterilizing vaccine against this HHV may not be viable, nor would it be necessary to curb the incidence of IM, which is in turn a risk factor for lymphomas and autoimmune disease[267]. To improve the efficacy of EBV-targeted vaccines, nanoparticle and mRNA vaccines to both lytic and latent antigen targets are under investigation to boost CTL mediated immune responses to infection[266,267].

Currently, two EBV vaccines are in the early phases of clinical trials. Cohen and colleagues with the National Institutes of Health (NIH) have developed a gp350 nanoparticle vaccine modeled on the human papillomavirus and hepatitis B virus (HBV) vaccines[270]. In their formulation, gp350

is fused to each monomer of a ferritin core-containing nanoparticle to enable more effective BCR cross linking and antigen presentation than soluble gp350[270]. This vaccine produced high and persistent levels of anti-gp350 antibody titres after immunization in an ongoing 2020 initiated phase I trial (ClinicalTrials.gov: NCT04645147, J. Cohen conference communication). Separately, Moderna has recently initiated a phase I trial to test an mRNA-1189 vaccine to gp350 and gH/gL/gp42, which each account for most neutralizing antibodies detected after primary infection and may provide better protection against EC infection (ClinicalTrials.gov: NCT05164094)[271].

In addition to known side effects caused by vaccines, the main potential concern for unintended consequences of an EBV vaccine is the potential waning of immunity after administration in childhood (when individuals are EBV seronegative), leading to delayed acquisition of the virus to an age of increased risk for developing IM[267]. To circumvent this issue, selective vaccination of at-risk populations, such as transplant candidates and EBV seronegative adolescents, rather than universal vaccine, has been proposed[166], though already immune-compromised individuals may not respond well to vaccination[267]. In EBV seropositive individuals, a therapeutic vaccine may be beneficial for improving EBV specific immune control and reduce EBV-associated disease. To reiterate the perspective of Jeffrey Cohen, "trials of an EBV vaccine to reduce the incidence of Hodgkin lymphoma, multiple sclerosis, or Burkitt lymphoma would be difficult but feasible. Importantly, such a vaccine might definitively demonstrate (or refute) a causative role of EBV in multiple sclerosis"[267].

1.2.7 Gammaherpesvirus infection models

Despite mounting epidemiological and clinical evidence suggesting EBV infection is a co-factor in autoimmune diseases, as well as a known causative factor in malignancies and immunological disorders, experimental investigation has been limited due to the high prevalence of EBV in the general population and, since EBV exclusively infects humans, a lack of suitable animal models. Some animal species are variably susceptible to EBV, though do not necessarily generate human-representative immune responses to infection[49,272]. In lieu of direct EBV infection of laboratory animals, researchers have identified natural gammaherpesviruses amongst most mammalian species that share conserved properties with both EBV and KSHV, including in NHPs and rodents[273]. A list of these representative gammaherpesvirus animal models is presented by Shigeyoshi Fujiwara in the book chapter[273].

1.2.7.1 Non-human primate models

Gammaherpesviruses that infect NHPs are, unsurprisingly, very similar to EBV and KSHV. Lymphocryptoviruses (LCVs) that naturally infected new-world and old-world NHPs[274] share latent EBV's tropism for memory B cells, lifecycle features, and transforming capacity, where they can be used to generate LCLs ex vivo[273]. NHP models are also advantageous over rodent models in that LCLs establish infections in both the epithelial and B cell compartments like EBV[170]. The two most commonly reported LCVs studied in NHPs are CalHV-3 (*Callitrichine herpesvirus 3*) in marmosets[275] and rhesus LCV (*Macacine herpesvirus 4*) in rhesus macaques[273]. In the marmosets colony maintained by Bert 't Hart and colleagues, over half of adults are naturally infected with CalHV-3[49]. Rhesus LCV shares high sequence homology with EBV[276] and produces similar effects after oral inoculation of seronegative individuals, including the generation of lymphadenopathy, a CTL and humoral response, latent infection of B cells, and salivary shedding[277]. Similar to NHP EAE models, the clear advantages to studying LCV infection in NHPs can often be outweighed by the limitations of these models, including high costs, low cohort numbers, lengthy rearing times, and ethical concerns. Moreover, the endangerment of certain NHP species, such as the cottontop tamarin, has resulted in bans for their use in research[278].

The laboratory of A. Tang has also recently described the use of Chinese tree shrews (*Tupaia belangeri chinensis*) as hosts for in vivo studies of EBV infection directly[279–282]. Tree shrews are rodent sized animals with phylogenetic similarity to NHPs, including conserved homology with the EBV gp350 binding regions of the human CD21 viral receptor[282]. The Tang group demonstrated that healthy tree shrews could be intravenously inoculated with the B95-8 strain of EBV, resulting in a persistent infection marked by EBER positive cells in the spleens and lymph nodes of recipients[279]. During acute infection, some animals experienced transient weight loss, fever, and neutropenia akin to IM in people[279,282]. Acute infection was also associated with changes in the composition of the fecal microbiome and metabolomic profile[281]. Following administration of cyclosporin A to previously infected tree shrews, EBV reactivation was detected one week post treatment, and in vitro treatment of tree shrew PBMCs resulted in enhanced EBV induced proliferation, though the development of overt lymphoma was not reported[280]. While tree shrews are becoming increasingly used as models for human viral infections, the authors noted a number of current limitations to their use, including few commercially available reagents for detection of tree shrew immune cell and tissue analysis[279]. At present, it is unclear if EBV can

infect tree shrews via oral inoculation and/or epithelial cells or if tree shrews are already naturally infected with a species-specific lymphocryptovirus[279]. Thus, rodent models of EBV infection have been the focus of most recent studies.

1.2.7.2 Rodent models

Gammaherpesvirus-68 (γHV68, also called murid herpesvirus-4 or -68 by some groups but will not be herein to avoid confusion with neurotropic demyelinating strains of MHV used to model MS) is a natural rhadinovirus of wild rodents that was originally identified during a field study of rodent arboviruses in Slovakia[283,284]. In this initial report and in studies since, γHV68 has been found to reliably infect common strains of laboratory mice[283,284]. γHV68 is phylogenetically more closely related to KSHV than EBV, though it shares similarities with both HHVs[174,285]. For example, EBV's EBNA-1, KSHV's latency-associated nuclear antigen (LANA), and γHV68's LANA protein all function primarily to maintain viral episomes in latently infected B cells[286]. Much of what is known about the early stages of gammaherpesvirus infection, especially prior to when IM symptom onset occurs in people, has thus been derived from studies using γHV68 infection of mice.

The natural route of infection for γHV68 in wild mice, and therefore the similarity of its transmission route to EBV, has been debated. Mice are susceptible to both oral and intranasal (IN) infection with γHV68, and despite evidence indicating mice do sneeze and cough, albeit quietly, the relevance of these routes for transmission among wild mice remains unclear[287,288]. Evidence also suggests γHV68 may propagate naturally through sexual transmission[289], though in experimental settings, γHV68 is generally inoculated through IN, intraperitoneal (IP), or intravenous (IV) routes, which each result in different dissemination patterns and pathogenesis. IN infection results in lytic infection within the nasal and lung epithelium, as well as nearby lymph nodes, which then disseminates systemically via B cell, DC, and macrophage infection[283,284]. Lytic infection can also be established in the intestinal epithelium by gastric inoculation to investigate EBV's role in gastric carcinomas[290]. Bypassing the EC infection stage can be accomplished by IP or IV infection[283,291]. In most cases, regardless of route or dosing[283], acute infection is resolved by 14 – 16 days post inoculation, and the long-term reservoir for latent γHV68 infection is class-switched B cells within the spleen, from which it intermittently reactivates[292,293]. The peak of viral latency in the spleen coincides with notable splenomegaly and an IM-like lymphoproliferative

syndrome[294]. After resolution of acute infection by IP inoculation, γHV68 can also be detected within peritoneal macrophages and splenic DCs, wherein it forms an incomplete latency program susceptible to frequent lytic reactivation, though this latency reservoir shrinks over time[293,295].

Similar to EBV, the total number of infected B cells becomes increasingly reduced over time as γHV68 establishes a latent infection within 1 of every 10,000 naïve B cells by 3 months post-infection[283,292]. The tendency for γHV68 to reactivate is also modulated by virally encoded proteins and stimulated by infected B cell differentiation into a plasma cell[296,297,298]. During the IM-like phase post-γHV68 inoculation, adaptive and innate immune responses proceed similarly to those observed in cases of EBV-induced IM, though the effectiveness of immune control depends on the mouse strain[294,299]. The IM-like syndrome is characterized by $CD4^+$ T cell-mediated expansion of B cells and $V\beta4^+CD8^+$ T cells[298], the latter of which follow two distinct kinetic patters corresponding to the lytic and latent phases of infection[300]. Immunization of BALB/c mice with a gp150 targeted vaccine, comparable to the gp350 EBV vaccines, reduced IM-like lymphoproliferation without preventing seroconversion or latent γHV68 infection, demonstrating similarity to findings in human trials of EBV vaccines[298]. Studies of γHV68 infection in mice have also demonstrated a role for existing latent infection in providing transient protection against subsequent viral, parasitic, and bacterial challenge[301], which could inform as to how EBV influences the education and responsiveness of the immune system in people.

γHV68 encodes host immunoregulatory factors, such as a Bcl-2 homologue to prevent infected B cell apoptosis, though it does not encode EBV equivalents for EBNAs and LMPs that are required for transforming host B cells[285,302]. As such, modeling EBV-induced B cell and epithelial tumorigenesis in mice is limited by the lack of naturally oncogenic rodent herpesviruses. High dose γHV68 infection of immunocompetent mice can result in B cell lymphomas forming in ~10% of mice, following a persistent infection characterized by the IM-like syndrome[298], though very few of the lymphoma cells actually contain γHV68[291]. The rates of γHV68-induced B cell lymphomas are reported to be increased in immunocompromised mouse strains[291]. Two transgenic mouse strains generated by Joanna Wilson and colleagues have partially addressed the minimal tumorigenesis of rodent herpesviruses by knocking in EBV oncogenes to generate B cell lymphoma and skin epithelial carcinomas[303–305]. In summary, rodent models of gammaherpesvirus infection present with many advantages over NHP models, including low costs, high cohort numbers, and short breeding times, despite a lack of similarity with some aspects of EBV infection.

1.2.8 EBV infection as a causal factor in autoimmune diseases

In addition to its role in various malignancies, EBV infection is associated with the development of several autoimmune diseases, including rheumatoid arthritis (RA), systemic lupus erythematosus (SLE), Sjögren's syndrome, autoimmune thyroiditis, Guillain-Barré syndrome, and MS[249,306], which suggests the existence of a common mechanism by which EBV predisposes for autoimmunity. Excluding type I diabetes (TID), MS (CNS-targeted), RA (synovium and joint-targeted), and SLE (nuclear antigen-targeted) collectively account for most cases of autoimmune disease, and individuals who develop these diseases exhibit higher serum antibody titres to EBV antigens, higher seroconversion rates, higher viral loads, and impaired adaptive immune control of infection prior to symptom onset compared to unaffected controls[306–308]. All three diseases are also associated with polymorphic HLA risk genes and do not appear to associate as strongly with other herpesviruses infections[109,306,309–311]. Proposed mechanisms for the association between EBV and autoimmunity that share commonality between these diseases include molecular mimicry of EBV proteins, latent infection of autoreactive B cells, and infection-induced dysregulation of the immune system that increases susceptibility to disease[306,307]. Various epidemiological, clinical, and experimental studies report findings that support each of these potential mechanisms in MS.

1.2.8.1 Clinical and epidemiological evidence

The earliest studies that pinpointed EBV as a potential risk factor for MS came from epidemiological analyses that demonstrated a striking overlap in cases of IM and MS in terms of geographical incidence, age, and ethnicity[74,312]. Numerous studies have since strongly and consistently linked EBV infection with the development of MS[82,313–315]. Individuals who are EBV seronegative (EBV^-) have a relatively low risk for MS, whereas asymptomatically infected individuals have a moderate risk, and those who have previously developed IM from primary EBV infection have a significantly higher risk for MS than those who acquired the virus asymptomatically (Figure 1.8)[315,316]. This association between IM and MS was found to be more specific than with other infections and diseases[317]. Additionally, nearly all adult (~99%) and pediatric (~83%) MS patients are EBV seropositive[8,318,319]. In cases of pediatric MS, where seroconversion rates have been reported to be lower than in adult MS[318,320], it has been noted seronegative cases may not be due to MS, but rather to a related disorder, which can often be more challenging to distinguish in children[321].

MS patients show higher EBV-specific antibody titers than age-matched controls in the years preceding disease onset[314] and individuals who have experienced IM have increased serum anti-EBNA-1 antibody levels compared to those that acquired EBV asymptomatically[322]. MS patients also show increased frequencies of EBV-specific T cells in the blood compared to unaffected individuals with a similar viral load, some of which are cross reactive to MBP antigens and produced IFNγ[323,324]. Individuals with CIS present with higher anti-EBNA-1 IgG levels in the blood, which strongly and specifically correlates with lesion burden, disability, and the risk of conversion to MS[325]. In a discordant monozygotic twin study, peripheral blood $CD8^+$ T cells from twins with MS were found to respond to more EBV derived antigens than T cells from unaffected twins, "consistent with an ongoing anti-EBV immune reaction in MS"[326]. Another report further demonstrated that MS-derived $CD8^+$ T cells, while numerically increased in affected individuals, have decreased reactivity to infected B cells compared to healthy donor T cells, likely due to exhaustion following uncontrolled expansion and reactivation of infected B cells[327]. Generally, these studies collectively point to a dysregulated T cell response to EBV in cases of MS.

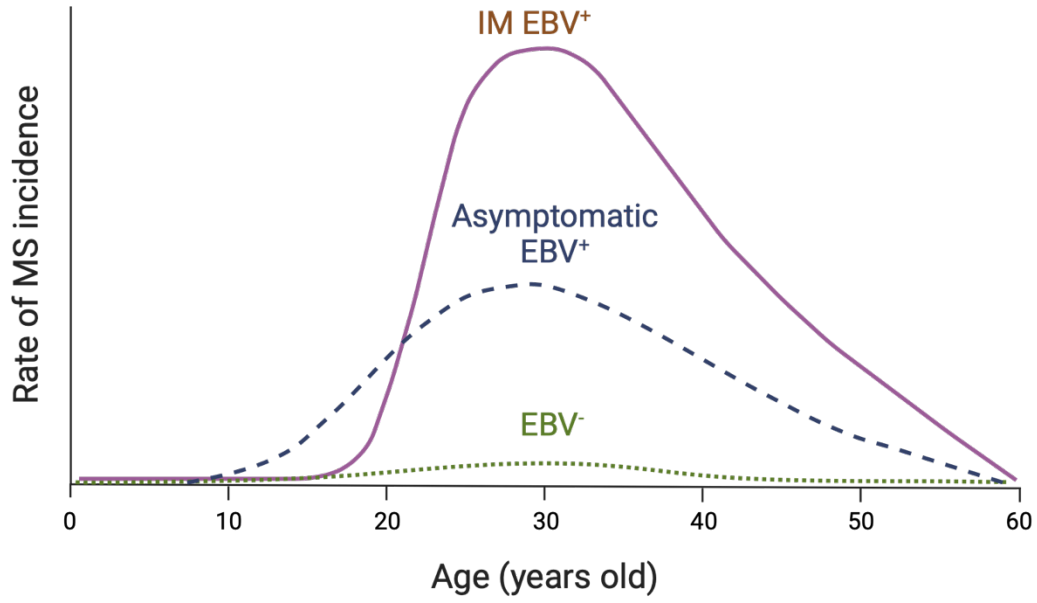

Figure 1.8 Schematic representation of MS incidence with age and EBV infection

Epstein-Barr virus, EBV; infectious mononucleosis, IM; multiple sclerosis, MS. Adapted from[315]. Created using BioRender.

The strength of the association between EBV infection and MS is emphasized by the relatively lower contribution of other known environmental factors to disease risk. In a meta-analysis, the odds ratio for EBV infection in MS was reported to be ~3.6, while the next two strongest risk factors, smoking and low vitamin D levels, were ~1.6 and 1.4, respectively,[69]. Recently, a longitudinal case-matched study demonstrated a 32-fold increased risk for MS and significant upregulation of a biomarker of axonal degeneration in individuals with MS, specifically following EBV seroconversion in young adulthood[109]. The authors noted that the strength of the association likely could not be matched by any other known or suspected risk factor for disease[109]. The role of the two EBV subtypes in MS is unclear due to the confounding influence of EBV type I prevalence in areas with high MS incidence, though data suggests patients can be infected with both types[328–330]. The efficacy of anti-CD20 B cell depletion therapies in treating inflammatory MS further suggests clinical benefit may result from elimination of the viral reservoir[65,159,331,332]. Anti-CD20 therapies work quickly and effectively in MS without altering the presence of Ig in serum or OCBs in CSF samples, which is attributed to the lack of CD20 expression on plasma cells generally[333,334]. CD20 is, however, highly expressed on memory B cells[334].

The notion that specialized B cell populations can have an outsized impact on disease pathology is supported by the failed trial of Atacicept, an anti-BAFF/APRIL expressing B cell depletion therapy that worsened disease outcomes in MS[335]. B cell activating factor (BAFF, also called BLyS) and a proliferation-inducing ligand (APRIL) are B cell survival factors expressed in many subsets, including potentially protective plasma and regulatory B cells, but that are not required for the survival of memory B cells[336–338]. Jagessar and colleagues evaluated the effects of anti-CD20, anti-BAFF, and anti-APRIL antibody depletion on the reservoir of CalHV3-infected B cells in marmosets and observed a significant reduction in viral loads in the peripheral lymphoid organs of animals treated with anti-CD20 but not in those treated with anti-BAFF or anti-APRIL antibodies [159]. In an active EAE model, anti-CD20 treatment was shown to target and eliminate IL-6 producing B cells[339], a cytokine known to be produced by EBV immortalized B cells in culture[340]. Moreover, Bruton's tyrosine kinase (BTK) inhibitors are currently under investigation for use clinically in MS[341]. Intriguingly, BTK is activated downstream of BCR signalling, a pathway that EBV's LMP2A protein mimics to promote survival of infected B cells[342]. These data indicate a critical role of pathogenic B cells in perpetuating disease activity in established MS, though more analysis will be required to determine if these effects are specifically due to removal

infected memory B cells specifically or to suppression of separate functions, such as antigen presentation and inflammatory cytokine expression[104].

In addition to many other studies that were not expressly mentioned herein, the data collectively demonstrates a consistent association between prior EBV infection and an increased risk of autoimmune disease, particularly MS, developing later in life. EBV has thus been described as a "*condicio sine qua non*", an indispensable condition, for the development of MS. The main counterargument to the supposition that EBV is a causal factor in MS is the fact that MS is a relatively rare disease (affecting ~0.04% of the global population), whereas EBV is not a rare pathogen (infecting >90% of the global population). This line of reasoning, however, can be applied to any EBV-associated disorder, including the above-mentioned subtypes of cancers, which are not universally EBV-positive. The general consensus is that EBV is a cofactor in disease development, but that other environmental and/or genetic factors determine the consequent pathological outcome, i.e., cancer, chronic active infection, autoimmune disease, etc. In this regard, MS can be considered as a rare sequelae of EBV infection in genetically susceptible individuals. By this view, IM could be considered a symptomatic precursor phase to the subclinical and prodromal MS phases that lead up to onset and diagnosis. The potential mechanism(s) underlying this association are still unclear, though numerous interwoven theories are currently under active investigation.

1.2.8.2 Proposed mechanisms for causation and experimental evidence

Many of the mechanisms that have been proposed to explain the role of EBV infection in autoimmune disease generally fall into two categories, pointing to a pathogenic function of EBV-infected B cells themselves and/or immune activity resulting from the response to EBV-infected B cells. Experimental evidence for each hypothesis has been reported, and the main mechanisms that have been suggested and investigated are discussed in this section. It is important to note, however, these mechanisms are not necessarily mutually exclusive, nor do they fit into only one category, and therefore determination of which mechanisms are at play at different stages of disease development (initiation vs potentiation) and in different phenotypic subsets of MS will be crucial to developing effective therapeutic interventions.

1.2.8.2.1 Hygiene hypothesis

The 'hygiene hypothesis' proposes that reduced exposure to childhood infections and microbial antigens predisposes to the development of autoimmune disease due to the absence of fundamental immunological tolerance mechanisms and education typically provided by these exposures that restrains aberrant proinflammatory responses to subsequent challenges[98]. The classical hygiene hypothesis does not reasonably apply to EBV infection in MS, as reasoned by Alberto Ascherio and Kassandra Munger, because based on this theory, EBV seronegative individuals, who are more 'hygienic' in this context than seropositive individuals, should have the greatest risk for developing MS[343]. EBV seronegative individuals are more protected from MS, as the odds ratio (OR) for MS among seropositive populations that experienced early childhood infection is ~1, whereas groups who remain seronegative by avoiding childhood EBV infection have a substantially lower OR of ~0.1[313,344]. Conversely, seropositive individuals that escaped early childhood infection but acquired EBV later in life, resulting in IM, have an OR of 2.3[315].

Ascherio and colleagues thus formulated the hypothesis that individuals who have not been infected with EBV will not develop MS unless they are first infected with EBV[109]. To test their hypothesis, they retrospectively evaluated medical records and serial serological samples collected over time from thousands of U.S. military service members[109]. Among a nested group of 35 initially EBV seronegative individuals at baseline who went on to be diagnosed with MS later in life (one third being women and two thirds being men), all but one person (a white male) seroconverted prior to disease development with a 5 – 7.5 year delay between EBV infection and MS onset[109]. The importance of age at infection in these data is intriguing as well, since military recruits are at youngest 18 years old when baseline samples are obtained, which indicates that the strong calculated risk for MS of 32-fold after primary infection derived from this group could be more of a consequence of delayed infection (or IM, which was not reported in the medical records) than EBV infection generally. In a second group of individuals who were diagnosed with MS later in life but who had entered the military with existing EBV seropositivity, the calculated risk was lower, at 26-fold[109], further supporting existing data that primary infection in early childhood is less of a risk for MS than acquiring EBV in adulthood. Generally, these data demonstrate that EBV infection is a significant risk factor for developing MS overall, regardless of age at acquisition.

1.2.8.2.2 Molecular mimicry

One of the first and, arguably, most intuitive mechanisms to have been proposed to account for EBV-mediated risk in autoimmune disease is molecular mimicry, wherein linear peptide sequences or conformational epitopes of viral proteins share sufficient homology with host tissue antigens to trigger immunological cross reactivity to self-tissues following infection[345]. Conserved and similar sequence motifs have been identified for many viruses and corresponding target antigens[101,346]. In 1996, Vaughan and colleagues identified cross-reactive anti-EBNA-1 antibodies in the serum of some Norwegian MS and SLE patients that also recognized proteins from neuroglial cells[347]. MS-derived autoantibodies to transaldolase, expressed by oligodendrocytes, have also been shown to cross react with EBV and HSV capsid antigens[348], though most studies investigating molecular mimicry have consistently identified EBNA-1 as a predominant source of cross-reactive epitopes. In RA samples, EBNA-1 antibodies were able bind to the same peptide as rheumatoid arthritis nuclear antigen antibodies, and the same citrullinated fibrinogen peptides recognized by anti-citrullinated protein/peptide antibodies are also recognized by anti-EBNA-1 antibodies[306]. Different anti-EBNA-1 antibodies have also been shown to cross react with the SLE autoantigens SmB, SmD, and Ro, as well as with dsDNA[309]. Jog and colleagues have demonstrated the presence of $EBNA_{411–426}$ specific antibodies in the serum of MS patients that are not detectable in unaffected controls, and, in nearly half of patients, they are cross-reactive to epitopes of MBP[349]. The authors also noted that IFNβ treatment reduced anti-$EBNA_{411–426}$ IgG binding, and that titres were higher in SPMS than PPMS and CIS sera[349]. This latter finding appears to suggest ongoing inflammation is the potential reason for elevated IgG titres (SPMS > CIS), however, the group was able to demonstrate that the $EBNA_{411–426}$ epitope was capable of generating MBP reactive antibodies and of inducing clinical symptoms in immunized SJL mice when mixed with CFA alone[349]. Further analysis of the immunophenotypic alterations induced by EBNA-1 EAE in SJL mice, especially of the CNS-infiltrating $CD4^+$ and $CD8^+$ T cells, would also be informative.

Recently, Lanz and colleagues demonstrated the presence of a cross-reactive antibody clone from MS CSF samples that recognizes a proline-arginine rich motif within both $EBNA\text{-}1_{386–405}$ and a phosphorylated epitope of the intracellular domain of glial cell adhesion molecule ($GlialCAM_{370–389}$), following extensive sequencing and biochemical analyses[26]. In plasma samples from over 100 individuals with MS from three separate cohorts, 20 – 25% showed the presence of and elevated IgG titres to $EBNA\text{-}1_{386–405}$, $GlialCAM_{370–389}$, and phosphorylated $GlialCAM_{370–389}$

compared to unaffected controls (CSF samples was not assessed)[26]. Moreover, phosphorylated GlialCAM$_{370–389}$ could block the reactivity of anti-EBNA-1$_{386–405}$ IgG in some highly reactive samples[26]. Interestingly, Bjornevik and colleagues also found that pre-onset MS serum samples contained higher levels of antibodies responsive to EBNA-1$_{365–420}$ relative to control sera than any other EBV antigen derived peptide[109]. The subset of MS patients with seropositivity to the EBNA-1/ GlialCAM epitopes in this study was 20 – 25% (albeit the rate could be higher if the CSF was analyzed), whereas >99% of individuals with MS are EBV seropositive[26,319].

Lanz and colleagues further demonstrated a functional role for this cross-reactivity using a RRMS model of EAE. SJL mice were pre-immunized with a scrambled peptide or the EBNA-1$_{386–405}$ peptide emulsified in Incomplete Freund's adjuvant (IFA) and CpG. Three weeks later, mice were immunized with PLP$_{139-151}$ mixed with the same EBNA-1 or scrambled peptide emulsified in CFA, containing *M. Tuberculosis*, to induce EAE[26]. Peripheral blood samples obtained from the EBNA-1 immunized mice demonstrated robust antibody reactivity to the GlialCAM intracellular domain without altering the reactivity of the humoral or T cell responses to PLP[26]. Interestingly, the EBNA-1-PLP immunized group experienced more severe clinical EAE relapses than the scramble-PLP immunized group, corresponding to increase T cell infiltration and demyelination of the spinal cord in this group[26]. Though this report indicates a potentially important role for viral mimicry in potentiating CNS activity in individuals with existing MS, while the data is less clear as to how this cross-reactivity could initiate disease. Immunization of SJL mice with the EBNA-1 epitope with IFA and CpG was in itself not sufficient to induce EAE (or if it was sufficient with only CpG or *M. Tuberculosis*, this data was not shown), and required a further immunization step with the known EAE-inducing epitope of PLP[26]. Time to symptom onset was also unaffected. These findings suggest this EBNA-1/ GlialCAM cross-reactivity contributes to disease severity once already initiated in the SJL EAE model but does not initiate disease on its own. EBNA-1/ GlialCAM cross-reactivity could potentially promote disease activity through epitope spreading since the identified GlialCAM epitope is a component of the protein's intracellular domain. Repetition of this induction scheme in an EAE model with minimal epitope spreading, such as in C57Bl/6 mice, could provide further insight into this mechanism. Other limitations and considerations for the interpretation of the data in this study are noted by Bar-Or and colleagues[350].

In an ideal, yet logistically challenging scenario, a similar analysis performed on prodromal cases, or even at-risk cases that are followed up for MS after primary EBV infection (IM), could

reveal more information about the initiation versus potentiation of MS via antigenic mimicry. Evidence for a functional role of cross-reactive antibodies and immune cells in MS and other diseases is currently lacking due to the existence of autoreactive immune cells in healthy individuals and the necessary condition that immunological tolerance break in their presence to initiate autoimmune disease[345,346,351,352]. Additional investigation into the role of autoantibodies in initiating and perpetuating disease will be necessary to select vaccine antigen formulas that avoid exacerbating any existing cross-reactive responses, such as to EBNA-1[353]. The fact that animal models, using phylogenetically related viruses encoding distinct genes, recapitulate many aspects of the immunological changes observed in people argues against the requirement for a single cross-reactive epitope to influence susceptibility to autoimmune diseases with unrelated antigens[166].

1.2.8.2.3 Infection of B cells in the brain

Another mechanism by which EBV could prompt autoimmunity is by directly infecting cells within the affected tissue, or by infecting the cells infiltrating the affected tissue, thereby acting to promote damage directly or by drawing virus-responsive immune cells into the area that then inflict bystander damage[104]. The detection of clonally expanded B cells and somatically hypermutated IgG within the CSF that recognize EBV antigens suggests chronic stimulation of these cells is due to local exposure and subsequent maturation in the draining lymph nodes, from which there is bi-directional exchange with the CNS[354,355]. There are quite a few routes by which EBV infected B cells could enter the CNS, including through lymphatic vessels in the meninges and choroid plexus[30], though whether there is preferential BBB transmigration of infected versus uninfected B cells is not clear. Direct infection of B cells residing within the CNS tissues of post-mortem MS samples has been inconsistently reported across multiple studies, depending on the technique used to analyze samples[101,356]. The timeline of publication of these studies and their conflicting results are reviewed thoroughly by Meier and colleagues in[101].

The presence of B cell aggregates resembling ectopic follicles containing GC-like structures, also called tertiary lymphoid tissues (TLTs), have been found within the meninges of late-stage SPMS post-mortem brain samples by multiple research groups[52,101,357]. These TLTs have been found to contain T cells, plasma cells, follicular DCs, and proliferating B cells, indicative of ongoing GC reactions[357]. Serafini and colleagues detected EBERs by in situ hybridization (ISH) in a substantial portion of BAFF-expressing B cells and plasma cells (40 – 90%) in nearly all MS

CNS samples, especially within the meningeal TLTs, but not in samples obtained from other inflammatory CNS diseases[355,358]. The distribution of lytic and latent EBV-encoded proteins coincident with pDCs and cytotoxic $CD8^+$ T cells varied by anatomical region and lesion activity[355,358]. As the authors noted, "Whether homing of EBV-infected B cells to the CNS is a primary event in MS development or the consequence of a still unknown disease-related process, we interpret these findings as evidence that EBV persistence and reactivation in the CNS play an important role in MS immunopathology"[355].

Other groups have attempted and failed to reproduce these findings, even when using the same tissue samples as the 2007 study[359–361], or, have detected EBV products within both MS and control brain samples[362,363]. A separate study detected EBERs in 82% of MS brain samples and 24% of control non-MS disease brain samples, however they did not detect follicular clusters of infected cells (as seen in TLTs previously) and they also detected EBER-ISH staining in a small proportion of activated astrocytes and microglia in some MS samples (theorized to be due to uptake of $EBER^+$ exosomes from infected B cells)[364]. The inconsistent findings obtained by each group likely reflects methodological and technical differences, as well as the heterogeneity of the MS samples that may have been analyzed in each study. Serafini and colleagues have also since provided evidence for lytic EBV reactivation and CTL responses in the inflammatory MS brain in a case of fulminant natalizumab withdrawal[365]. EBV-specific $CD8^+$ memory T cells have also been isolated from the CSF of MS patients, though they were also present in healthy control CSF samples with a different Tm phenotype[326]. More recently, this group has detected latent infection and low-level EBV reactivation associated with local T cell activation and EBV-specific $CD8^+$ T cell responses within laser-cut lesion samples from progressive MS brain samples[366,367]. EBV-specific $CD8^+$ T cells in these sections comprised 0.5 – 2% of total infiltrating CTLs, compared to ≤0.3% that were CMV-specific[366]. EBV has also been detected within the synovial lesions of RA joint tissues[307], indicating a potential role for tissue-specific infection in promoting local inflammation and bystander damage. In an interesting case study, the occurrence of a spontaneous demyelinating encephalomyelitis was associated with infection of a previously unknown rhadinovirus (also called simian gamma-2-herpesvirus) in 1 – 3% of Japanese macaques within a long-term colony, which was isolated directly from the white matter lesions of affected animals[158].

Working under the assumption that EBV infected B cells are present within the brain in most cases of MS, their presence alone does not establish causation[368]. As with other EBV-

associated illnesses, other genetic and environmental factors may prompt or influence their infiltration of the brain, leading to EBV infected B cells migrating into the brain as a secondary consequence of ongoing disease processes. Similar to the molecular mimicry theory, determining the timing of EBV infected B cell appearance in the MS brain relative to the sequence of other pathogenic processes will be crucial for establishing the role of direct infection in initiating and/or promoting established disease. Theorized mechanisms by which EBV infected B cells within the MS brain could directly contribute to disease vary from the production of proinflammatory cytokines, the infection of CNS autoreactive B cells, and antigen presentation of auto- or neo-antigens to T cells, among others.

1.2.8.2.4 Autoreactive B cell infection

The autoreactive B cell infection theory has been proposed to explain how many different autoimmune diseases could result from infection with EBV. The lead proponent of this theory, M. Pender, suggests EBV could latently infect autoreactive B cells, which are more abundant within individuals who are genetically susceptible to their generation and/or persistence due to ineffective elimination[369,370]. EBV infection then prevents their apoptosis and removal through normal tolerogenic mechanisms and CTL killing by expressing virally encoded survival and immune evasion factors[369,370]. These EBV-immortalized autoreactive B cells then travel to the tissue expressing the target antigen and promote pathogenesis by recruiting and acting as antigen presenting cells to autoreactive T cells, as well as by producing cytokines to promote inflammatory responses, and by secreting autoantibodies[104,369]. This theory thus closely aligns with the direct CNS infection theory, whereby the arrival of infected B cells into the CNS is a consequence of infecting CNS autoreactive B cells that then migrate into the brain and promote disease.

The low probability counterargument to this theory suggests there is only a minimal likelihood that an autoreactive B cell happens to be latently infected with EBV, migrates to and expands within the CNS, and promotes inflammation to the extent that clinically measurable disease ensues. The rarity of MS relative to the commonality of EBV infection suggests this series of events may be plausible in genetically susceptible populations where autoreactive B cells escape into the periphery more frequently. Autoantibodies are characteristic of most autoimmune diseases, including MS, RA, and SLE, and tend to appear prior to clinical onset[79,371–374], indicating the presence of these cells early in disease development. In a study of six RA patients, Samuels

and colleagues demonstrated that autoreactive B cells were not effectively removed from circulation and comprised a larger proportion of the mature naïve B cell population (35 – 52%) compared to healthy controls (20%), some which were polyreactive, indicating an impairment of central and peripheral B cell tolerance[373]. EBV-infected autoreactive plasma cells have also been detected in the synovium of RA samples[104,370]. In individuals with MS, editing of autoreactive BCRs also appears inefficient[375], suggesting an increased availability of autoreactive B cells susceptible to infection with EBV within individuals with reduced capacity to modify the specificity of these B cells after autoantigen encounter. Tracy and colleagues, however, have shown that EBV infected memory B in the peripheral blood of individuals with IM are typically less self- and poly-reactive to MOG compared to uninfected memory B cells[376], though the potential added genetic risk factors associated with MS were not disclosed for this cohort.

Additional perturbations in CTL control of latently infected B cells could lead to frequent lytic reactivation of EBV, thereby increasing the likelihood over time of infecting a neighbouring autoreactive B cell within the same individual[104,377]. In this case, immunization of at-risk populations to improve CTL recognition of EBV infected B cells could remove autoreactive cell reservoirs as a preventative measure, whereas administration of EBV-specific CTLs to individuals with existing MS could remove these pathogenic cells directly. A potential issue with targeting EBV infected B cells specifically in the CNS is the inefficiency of episomal EBV replication with the host cell, which can lead to previously infected cells becoming EBV-free after multiple rounds of division[378,379]. Targeting pathogenic B cell subsets more generally may be necessary to clear clonally expanded autoreactive B cells in CNS if EBV is lost from a large enough proportion of these cells. Despite this potential issue, a phase I trial of autologous EBV-specific $CD8^+$ T cell therapy produced sustained clinical benefit in some individuals with progressive MS[380,381]. Two phase I/II trials using autologous and allogeneic EBV-specific $CD8^+$ T cell therapies in SPMS and PPMS have since been initiated (ClinicalTrials.gov: NCT03283826, NCT02912897).

1.2.8.2.5 B cell dysfunction and neoantigenic responses

The B cell dysfunction mechanism of EBV-induced autoimmunity suggests that viral gene expression within infected cells can lead to dysregulation of the functionality and specificity of host B cells by modulating host gene expression enough to breaching tolerance. This theory precludes the need for EBV to be present within the CNS, as EBV infected B cells could promote

autoreactive T cell responses in the periphery that trafficking to and cause damage in the CNS[104]. For instance, EBV-induced expression of proinflammatory cytokines such as TNF, IL-6, and granulocyte-macrophage colony-stimulating factor (GM-CSF) by infected B cells could promote autoreactive T cell responses[104]. Interference with the activity and number of regulatory B cells, which have been shown to be suppressed during MS relapses, could be due to the expression of the virally-encoded IL-10 homologue interfering with host signaling[104,382]. Multiple reports have shown that the latently expressed EBV protein EBNA-2 can alter the expression of autoimmune risk genes by binding to transcription factors that regulate their promoters[383–385]. Furthermore, EBNA-2 was able to the remodel chromatin structure at these risk loci in cultured B cells[383], which implicates direct EBV modulation of host genes as a cause of B cell dysfunction in autoimmunity.

A related phenomenon has been proposed to occur, wherein self-antigens become modified by infected B cells and subsequently recognized as foreign antigens by interacting T cells. In this scenario, EBV infection leads to altered processing of antigens (post-translational modifications, alternative splicing, selective peptide protection, etc.) to generate neoantigens that are presented by infected B cells to T cells that would have not been exposed to such antigens during selection[49,79,386]. Consistent with the autoreactive B cell theory, 't Hart and colleagues have demonstrated that EBV modulates myelin antigen processing in infected B cells through autophagy and citrullination of peptides that are then cross-presented to $CD8^+CD56^+$ cytotoxic T cells[49,160,386]. The efficacy of B cell depletion therapies in MS could therefore be a result of eliminating inflammatory and pathogenic antigen presenting EBV^+ B cells from circulation[104].

1.2.8.2.6 Lytic reactivation

The EBV reactivation mechanism suggests that disease onset and/or progression is due to frequent and high levels of lytic viral replication, either peripherally or locally, which then promotes disease activity through secondary anti-EBV inflammation-induced mechanisms[101]. Higher EBV-specific CTL activation and expansion has been observed in MS patients compared to unaffected controls, as well as the expansion of EBV-specific $CD4^+$ T cells and lytic antigen-specific CTLs during inflammatory relapses[327,387]. Moreover, EBV-directed T cell responses may contribute to disease activity within the brain, as lytic EBV antigen-specific CTLs have been found in the CSF of MS patients[388]. Individuals with highly active RA are at an increased risk of developing lymphoma, which is also known to be promoted by lytic EBV replication[191,251,306].

Frequent viral reactivation, especially within the CNS, could lead to increased T cell inflammation and bystander damage, and could increase the likelihood that an autoreactive B cell becomes infected with viral progeny.

Despite the increased number of EBV-specific CTLs in the blood of individuals with MS, these CTLs are less functional and exhibit an exhausted phenotype[327]. The temporal sequence of EBV-induced CTL exhaustion and lytic reactivation remains unknown. An EBV-intrinsic deficiency in the establishment and maintenance of latency, such as with genetic variants of EBNA-1, could lead to a greater propensity for EBV to reactivate from latently infected B cells, triggering an expansion of CTLs and eventual exhaustion through repeated cycles. Conversely, an intrinsic deficiency in the ability of the host's T cells to mount an effective response to EBV could lead to less restricted latency programs and more opportunity for lytic replication, increasing viral loads and leading to CTL exhaustion as well. In the latter scenario, increased lytic reactivation during relapses could be a consequence of defective immune control in the periphery as a consequence of anatomically faraway CNS inflammation caused by an unrelated mechanisms. The notion that lytic EBV infection and reactivation perpetuates disease activity is supported by the efficacy of IFNβ therapy, which is a potent antiviral cytokine[382,389]. Affected tissues in many autoimmune diseases, including MS, RA, SLE, and type 1 diabetes (T1D), show a common upregulation of genes within the type I and II IFN pathways, indicative of local immune responses [390]. Upregulation of local IFN responses could be due to increased lytic EBV replication but could also be due to other viruses infecting the target tissue.

1.2.8.2.7 Viral transactivation and superantigenic stimulation

One way in which EBV infection has been proposed to promote inflammatory disease activity is by transactivating other exogenous or endogenous viruses within the affected tissue, which can then cooperate to induce or exacerbate autoimmunity via aforementioned mechanisms, such as molecular mimicry and bystander damage[101,391]. Support for this theory comes from reproduced, though not unanimous, evidence showing that HERVs and HHV-6A are both present within MS brain lesions[101,392]. HHV-6A is a neurotropic virus that infects astrocytes and can promote the transformation of EBV-infected B cells in the CNS[104]. HERV-W envelope protein has also been shown to promote lytic EBV gene expression in latently infected B cells, indicating multidirectional interactions between these viruses[101,393]. The numerous ways in which EBV,

HHV-6A, and HERVs independently and jointly cooperate to promote pathogenesis in MS is extensively reviewed by Meier and colleagues in[101]. Direct infection of astrocytes by EBV or the release of pro-inflammatory cytokines and exosomes by EBV-infected B cells could also promote transactivation of HERVs, and specifically HERV-W/MSRV[101,104]. EBV also has been shown to transactivate the *HERV-K18* gene within LCLs, leading to the expression of an encoded superantigen and T cell activation in vitro[394]. Superantigenic stimulation occurs when antigenic binding outside the classical peptide binding site leads to polyclonal Vβ TCR-driven activation. Though certain *HERV-K18* variants have since been shown to increase genetic risk for MS[395], studies examining this phenomenon within MS lesions have not yet been reported. Responders to IFNβ therapy show reduced peripheral HHV-6A and MSRV viral loads and reduced T cell reactivity to EBNA-1, suggesting a potentially broad effect of reducing inflammatory MS by suppressing viral activity[101].

1.2.8.2.8 Bystander activation and epitope spread

Bystander activation describes the process by which immunological tolerance to self-antigens breaks due to excessive inflammation, leading to activation of immune cells with unrelated specificities, which can perpetuate autoimmune disease[396]. In the case of EBV, primary infection leads to massive cytokine production and the proliferation of $CD4^+$ and $CD8^+$ T cells at the direction of proinflammatory antigen presenting cells (APCs) that have been stimulated via TLRs and other pathogen recognition receptors (PRRs)[396]. Subsequent tissue damage due to local infection, and the immune response to the infection, could also release normally sequestered self-antigens[397]. These self-antigens can be presented by activated APCs to autoreactive T cells, which exist normally within otherwise healthy individuals, leading to intra- and/or inter-molecular epitope spreading[396,397]. The generation of responses to antigens through epitope spreading is an adaptive process to eliminate infections that may escape through gene expression changes or mutations if only one epitope is recognized, and thus this mechanism could plausibly activate T cells with reactivity to CNS antigens that were not eliminated during thymic selection[397]. Regulatory T cell dysfunction may also increase bystander activation as well[307,398]. The 'mistaken-self' hypothesis proposes a similar effect whereby EBV induces the expression of the heat-shock protein αB-crystallin in infected B cells, which is then presented to T cells in the context of pathogenic infection, and is subsequently recognized on oligodendrocytes in the CNS[399].

1.2.8.3 Gammaherpesvirus infection in animal models of MS

Experimental studies using gammaherpesvirus infections of animal models have provided insights into the potential mechanisms by which EBV could incite or promote MS activity that would otherwise not be feasibly obtained from human subjects. The long incubation period between EBV infection and symptomatic manifestations, as well as the lengthy delay between primary infection and the onset of autoimmune disease, makes investigation of often confounding risk factors very challenging for researchers. Animal models, despite presenting with various limitations to their use, are advantageous compared to retrospective and patient case studies in that interventions can be administered in a temporally controlled manner and the immune response followed sequentially both systemically and at the site of disease. Thus, direct infection of laboratory animals with EBV and species-specific gammaherpesvirus infections has been used to model the effect EBV infection may exert on the host immune response to initiate or perpetuate autoimmune disease.

1.2.8.3.1 Direct EBV infection of animal models

Hassani and colleagues recently reported CNS infection of rabbits with a cultured EBV strain[400]. B95-8 EBV, when administered intravenously as virions to naïve wild-type rabbits, persisted asymptomatically within splenocytes up to day 14 post-infection and prompted cellular aggregates to form within the brain and spinal cord in 2 of 8 healthy infected animals[400]. Histologically, the center of these aggregates, composed of mainly $CD8^+$ T cells, B cells, macrophages, neutrophils, and activated glia, were devoid of myelin staining[400]. The formation of CNS immune aggregates corresponded to peak peripheral cell-associated viral loads, and 6 of 8 EBV-infected healthy animals had detectable EBER staining within B cells in the brain independent of the presence of immune cell aggregates, suggesting EBV entered the CNS via infected B cells[400]. Latent gene expression was also associated with proinflammatory cytokine expression, and minimal lytic gene expression was observed[400]. None of the infected animals developed overt neurological signs similar to MS despite CNS infection and cellular aggregate formation in some[400]. The authors noted that 7 of 9 EBV-infected animals co-administered the immunosuppressive drug cyclosporin A developed these CNS immune cell aggregates as well[400]. The use of cyclosporin A, while suppressing cytokine expression and immune cell function in a relatively broad manner[401], could mimic potential intrinsic defects in EBV immunity that could

predispose certain individuals to CNS infection and ensuing bystander damage. Further assessments of the innate and adaptive immune response to EBV by the rabbit immune system will hopefully shed light on the mechanisms by which EBV enters the CNS.

In a separate study, Polepole and colleagues demonstrated an exacerbated EAE phenotype in wild-type mice pre-treated with human EBV LCLs before myelin immunization[402]. EBV LCLs derived from an individual with SPMS (MS-LCL), exhibiting a type III latency similar to that observed during IM, were twice injected IP into C57Bl/6 mice 3 – 5 weeks before MOG_{35-55} EAE induction, which enhanced EAE symptom severity compared to cell-free controls[402]. Furthermore, administering a third dose of MS-LCLs during the chronic phase of disease induced a relapse[402]. C57Bl/6 mice tolerated multiple injections (5 – 7) with high doses of LCLs (10^7 infected B cells per inoculation) without developing any signs of illness, and their administration alone did not generate EAE-like disease[402]. The authors also noted that utilizing healthy donor derived EBV LCLs resulted in a similar effect, though this data was not shown or discussed in detail[402]. The authors posit that over-proliferation of B cells is a risk factor for MS, rather than EBV itself, *per se*, but that the former event is driven by EBV infection of B cells[402]. The relevance of murine immune control mechanisms when using human LCLs is not entirely clear, as individuals with MS are seemingly not at a higher risk of developing lymphomas, outside of certain familial forms of MS[403]. Determining the specificity of this exacerbation would also be informative, as human B cells infected with HHV-6A or KSHV may produce similar effects as an indirect consequence of generally increased inflammation following foreign body recognition. Though MRI analysis of animals was performed to assess the integrity of the BBB, which was actually increased in MS-LCL treated EAE mice[402], immunological assessments of the murine T and B cell responses could provide greater insight into how MS-LCLs enhance disease severity in EAE. To circumvent uncertainties surrounding infecting animals with human viruses, animal models of natural gammaherpesvirus infection in NHP and rodent models of MS have been reported to reflect many key pathological features of disease in humans.

1.2.8.3.2 Lymphocryptovirus infection of NHP EAE models

Bert ‘t Hart and colleagues have published numerous studies characterizing the effects of NHP LCV infection on EAE and neuroinflammatory disease pathology[49,159,160,272,386,404–407]. In one of their studies, Haanstra and colleagues demonstrated that LCLs derived from a NHP LCV

infection could drive CNS pathology in naïve animals when pre-pulsed with a modified immunodominant epitope of MOG[272]. In this study, autologous NHP LCLs were generated using a closely related LCV to that of rhesus macaques, *Herpesvirus papio*, which were then pre-pulsed in culture with either the immunodominant $MOG_{34–56}$ epitope, a citrullinated version of this epitope, or a CMV-derived mimic peptide, and thrice administered intravenously to recipient rhesus monkeys[272]. The authors noted they were not able to include LCV-negative, untransformed B cells as controls in this study due to logistical limitations in obtaining sufficient numbers of autologous B cells over time from the same animals. Administration of autologous LCLs generated an IM-like lymphoproliferation of T cells, but none of the pre-pulsed LCLs generated clinical neurological symptoms in recipients on their own by day 98[272]. The $MOG_{34–56}$ and CMV LCL recipient groups were then immunized with $MOG_{34–56}$ emulsified in IFA and compared to the unimmunized citrullinated $MOG_{34–56}$ LCL recipient group for neuropathological changes. The two immunized groups displayed histological features consistent with mild inflammation seen with previous immunizations with MOG/IFA that did not suggest a significant additional effect was mediated by the regular peptide pulsed LCLs. In the unimmunized citrullinated $MOG_{34–56}$ LCL recipient group, however, the CNS contained perivascular and meningeal infiltrates (composed mainly of $CD3^+$, $CD68^+$, and some $CD20^+$ cells) similar to those seen in MS patients, suggesting post-translational modification of a self-antigen presented by infected B cells elicited T cell driven neuroinflammation[272].

Further expanding on these findings, Jagessar and colleagues demonstrated the beneficial effects of anti-CD20 B cell depletion therapy in marmoset EAE models was associated with a reduction in CalHV3 viral loads in peripheral lymphoid organs[159]. To determine if infected B cells themselves could present to and activate $MOG_{34–56}$-specific T cells, B cells were isolated from five pairs of marmosets and transformed into LCLs using the EBV B95-8 strain[159]. Within each of the pairs, one marmoset received autologous LCLs as is, and the other received autologous LCLs pre-pulsed with $MOG_{34–56}$ (without a later immunized step to induce EAE). No clinical signs of EAE were observed in either of the groups infused with autologous LCLs, however $MOG_{34–56}$ LCL infusion induced the activation of proinflammatory cytotoxic $CD8^+$ T cells, and in 2 of 5 $MOG_{34–56}$ LCL recipients, $CD3^+$ and $CD20^+$ lymphocytes were detected in the meninges[159]. To investigate how LCV-infected B cells may alter the processing and presentation of self-antigens to autoreactive T cells that are normally present in the naïve immune repertoire of NHPs, the team

evaluated MOG presentation by class I and II molecules on LCV-LCLs[408]. In the marmoset model, immunization with $MOG_{34–56}$ led to activation of Caja-E (MHC-E)–restricted autoreactive $CD8^+CD56^+$ CTLs recognizing $MOG_{40–48}$[407,408]. When marmosets are immunized with full length MOG protein, Caja-DRB*W1201–restricted $CD4^+$ Th1 cells recognizing $MOG_{24–36}$ are activated in the absence of these MOG_{40-48} CTLs, suggesting this epitope is not preserved nor presented to $CD8^+$ T cells following antigen processing[407,408]. As the authors note, B cells typically do not cross-present via MHC I to $CD8^+$ T cells like DCs, but based on previous findings they hypothesized that "LCV infection of B cells leads to limited processing of the exogenous encephalitogenic peptide $MOG_{34–56}$ in such a way that the $MOG_{40–48}$ epitope remains available for loading on MHC-E molecules and presentation to core pathogenic $CD8^+$ T cells in the primate EAE model"[408].

Using both marmoset and rhesus macaque LCV infected-LCLs, the authors reported significant changes to the expression of genes involved in antigen cross-presentation that would be expected to be observed in professional $CD8\alpha^+$ mouse DCs, including upregulation of MHC I and costimulatory molecules, as well as modified expression of genes in the autophagy pathway[408]. In normal primary B cells, the MOG_{40-48} epitope of $MOG_{34–56}$ is destroyed by the endolysosomal protease cathepsin G, however, in LCV^+ LCLs, citrullination of the protease target site within MOG_{40-48} protects it from cleavage following endocytosis[408]. The authors suggest protection of the protease target site by citrullination following modulation of the host B cell's gene expression by LCV (including the enzyme responsible for citrullination) enables the MHC-E restricted cross-presentation of this epitope to autoreactive CTLs, which then mediate CNS pathology in the marmoset EAE model[408]. In 2017, Morandi and colleagues elaborated these findings in human B cells and concluded that "EBV infection switches MOG processing in B cells from destructive to productive and facilitates cross-presentation of disease-relevant epitopes to $CD8^+$ T cells"[386]. These studies collectively provide a clear and detailed pathway in which antigen processing and presentation of CNS antigens by EBV-infected B cells can alter cytotoxic T cell responses that mediate MS-like pathology in the brain following challenge. A notable caveat with the use of NHP EAE models the high prevalence of LCVs within group-housed captive colonies, as well as undetectable levels of virus in the blood during latency, which, combined with a lack of validated serological test for these LCVs, limits the identification and use of seronegative animals as controls[159,409]. Though this high prevalence of LCVs in the NHP populations is an important feature of primate gammaherpesvirus infection that closely reflects the epidemiology of human

EBV, it also restricts investigation of EAE in the absence of prior infection, which can be readily modeled in laboratory rodents that are exogenously infected with murine gammaherpesvirus.

1.2.8.3.3 Gammaherpesvirus-68 infection of rodent EAE models

Latent gammaherpesvirus infection is known to modulate immune responses relevant to autoimmunity, promoting downregulation of B cell apoptosis, suppression of regulatory T cell function and production of an interferon-I response[220,410,411]. As such, γHV68 has been used to interrogate the effects of EBV infection in murine models of autoimmunity. Though some studies have investigated the effects of intracerebral inoculation of γHV68[412–414], our group and others have used peripheral infection routes to better reflect EBV transmission in humans[283,415–417]. In 2003, Peacock and colleagues reported the exacerbation of disease severity in an RRMS EAE mouse model following infection with γHV68[416]. In their study, SJL mice were infected intranasally with γHV68 or UV-inactivated γHV68 and immunized with $PLP_{139–151}$ two days later. Infected mice experienced high mortality rates, whereas control mice recovered[416]. These findings were then replicated by passive EAE induction of Lewis rats using MBP-specific T cells 7 – 10 days after recipients were infected with γHV68[416]. Following either acute or latent infection, EAE symptoms were more severe compared to uninfected control rats, which correlated with increased immune infiltration of CNS tissues by histological analysis but without any detectable local γHV68 infection[416]. EAE induction also did not affect latent viral loads in the spleen[416]. Consistent with previous findings, γHV68 infection alone was not reported to generate neurological symptoms in their study. The authors surmised that “if γHV68 does not enter the CNS to any significant extent, then the mechanisms required for exacerbation of EAE must occur in peripheral tissues”, which they attribute to a virally induced "immunological dissonance"[416].

To investigate the underlying immunomodulatory mechanisms that occur in the periphery and at the site of disease, the Horwitz lab has extensively studied the effects of latent γHV68 infection in models of EAE and RA[389,415,417–421]. In the standard γHV68-EAE model (Figure 1.9), wild-type C57Bl/6 mice are infected with γHV68 by IP or IN inoculation. Following a five-week incubation period, during which the virus firmly establishes a latent infection in the periphery to mimic the delay between EBV infection and MS onset in humans, mice are then immunized with MOG_{35-55} peptide to induce EAE[415]. In this model, mice infected with γHV68 prior to EAE induction experience a severe pathology more alike MS than uninfected EAE mice[415]. The

enhanced MS-like disease observed in γHV68-EAE mice is characterized by greater clinical scores with earlier symptom onset, as well as a loss of myelin and infiltration of activated macrophages/ microglia, cytotoxic $CD8^+$ T cells, and Th1-skewed $CD4^+$ T cells into the brain and spinal cord[415]. Clinically, γHV68 infected EAE mice displayed additional atypical symptoms on top of the more severe ascending paralysis compared to uninfected EAE mice, including ataxic movement and a loss of the righting reflex[415].

Within the CNS, greater proportions and numbers of $CD8^+$ T cells were measured, including within the brain, which typically remains minimally infiltrated compared to the spinal cord in uninfected EAE mice[128,415]. These infiltrating $CD8^+$ T cells expressed granzyme B, and a similar proportion of them recognized viral proteins in the CNS and periphery, suggesting the response to infection was not preferentially enriched or expanded in the CNS[415]. The brains of γHV68-EAE mice also contained greater numbers of $CD4^+$ T cells and $F4/80^+$ myeloid cells than uninfected EAE mice, and had formations of small lesions wherein demyelination had occurred, notably in the cerebellum and corpus callosum[415]. Infiltrating $CD4^+$ T cells were heavily Th1 skewed in γHV68-EAE mice compared to uninfected EAE mice, wherein an increased proportion produced IFNγ with a concomitant reduction in the proportion expressing IL-17A in both the CNS and periphery[415]. $CD4^+FOXP3^+$ regulatory T cell (Treg) frequencies were also significantly decreased in the CNS and spleen of infected EAE mice, a regulatory deficiency also noted to occur in individuals with MS and reported in other models of γHV68 infection[39,410,415,422]. These immunopathological features of the γHV68-EAE model are hallmark characteristics of MS that are either far less pronounced or absent in classical EAE models[128,131], which strongly indicates EBV might contribute to similar aspects of the pathogenesis of MS in humans.

Moreover, these effects were exclusive to latent γHV68 infection, as acute infection or infection with other viruses, including murine cytomegalovirus (MCMV) and lymphocytic choriomeningitis (LCMV) virus, was not able to enhance EAE[415]. Pre-infection of mice with either LCMV, which is cleared 8 days post-inoculation, or MCMV, which establishes a persistent infection for months following acute phase resolution, five weeks before EAE induction resulted in clinical outcomes similar to uninfected EAE mice[415,423–426]. Clearance of acute γHV68 infection and the absence of replication was confirmed by negative splenic plaque assays collected day 35 post-infection, and the extent of ex vivo splenic reactivation was determined to be similar between EAE-induced and uninduced controls at days 7 and 14 post-immunization[415]. To confirm the

absence of lytic viral replication as a contributing factor to EAE enhancement, γHV68-EAE mice were co-administered the anti-viral drug cidofovir and found to exhibit comparable clinical outcomes as untreated γHV68-EAE mice[415]. At endpoint, all brain and spinal cord samples were negative for γHV68 DNA by PCR, indicating direct infection of the CNS did not occur[415]. When EAE was induced during the acute phase of infection (day 2 post-inoculation), the onset of EAE symptoms was delayed to 14 days post-inoculation, once latency was established[418]. Furthermore, infection with a latency-free version of γHV68 that is cleared following the acute phase, resulted in clinical and immunological EAE outcomes similar to uninfected EAE mice, indicating a crucial role for viral latency in mediating enhancement of disease[415,418]. Collectively, these data indicated the effects of γHV68 infection on symptomology and pathology in the EAE was a consequence of latent infection, rather than an acute or lytic reactivated infection, which mimics the delay between primary EBV infection and onset of MS in people.

Figure 1.9 Experimental design for the γHV68-EAE model

C57Bl/6 mice are infected with 10^4 plaque forming units (PFU) of wild type gammaherpesvirus-68 (γHV68 WUMS strain) by IP injection (or 10^{2-3} PFU by IN inoculation). Following a five-week incubation period, during which the virus firmly establishes a latent infection in the periphery, mice are then actively immunized with myelin oligodendrocyte glycoprotein peptide MOG_{35-55} emulsified in complete Freund's adjuvant (CFA) and co-administered pertussis toxin (PTx). Methodological details are included in sections 2.5 and 2.13.

Interestingly, EAE symptoms could be induced in γHV68-infected C57Bl/6 mice without the co-administration of pertussis toxin (PTx), which is required, alongside MOG_{35-55} peptide emulsified in CFA, to generate reproducible CNS infiltration in naïve C57Bl/6 mice[129,415]. γHV68-infected C57Bl/6 mice induced with MOG and CFA without PTx developed an EAE disease course similar to naïve EAE mice, though paralysis was less severe than γHV68-infected C57Bl/6 mice induced with PTx (i.e., removing PTx eliminated the enhancement of symptoms caused by

infection)[415]. These findings indicated a potential role of γHV68 in functioning in a similar way as PTx to increase BBB permeability, which then allows T cell infiltration of the CNS to proceed in C57Bl/6 mice[129]. In a separate study, the B95-8 strain of EBV was able to directly infect cultured human brain-derived endothelial cells (EnCs)[421]. Infection of brain EnCs increased their expression of pro-inflammatory factors and promoted peripheral immune cell adhesion, providing a potential mechanism by which infection could alter BBB permeability to promote MS[421].

The Th1 polarization skew measured following EAE induction of infected mice was also associated with an increased ratio of anti-MOG IgG2a/IgG1 isotype response in serum after EAE induction, though total anti-MOG IgG levels were similar between groups regardless of pre-infection[415]. Despite no change in the strength of the anti-MOG humoral response, γHV68 infected mice did have elevated IgG levels to whole brain extract, potentially indicative of increased epitope spreading[415]. Peripheral $CD11b^+CD11c^+$ myeloid cells from γHV68-EAE mice were also more pro-inflammatory compared to uninfected EAE mice, exhibiting increased expression of STAT1, CD40, and IFNγ, despite themselves not being infected with the virus directly at this later stage of latency[415,418]. $CD11b^+CD11c^+$ cells were also shown to act as APCs to MOG-specific T cells, and they were not able to generate as strong of a Th1 response when isolated from EAE mice pre-infected with the latency-deficient variant of the virus due to a lack of CD40 upregulation on these APCs that occurs with latent γHV68 infection[415,418]. Since STAT1 was also upregulated $CD11b^+$ $CD11c^+$ cells, the role of IFN signaling in mediating APC-induced Th1 enhancement was investigated using a global IFNα receptor knock-out mouse strain ($IFNAR^{-/-}$)[389]. Despite having an important role in establishing and maintaining γHV68 latency, $IFNAR^{-/-}$ mice did not exhibit significant differences compared to wild-type mice in the γHV68-EAE model[389,427]. Adoptive transfer mature B cells ($CD19^+IgD^-$) from γHV68 infected mice, however, did generate enhanced EAE in naïve recipients, despite the relatively few cells among these transferred cells are themselves latently infected by the virus[419]. This finding suggested a broad immunomodulatory effect of γHV68 on the host's B cell population, without directly infecting them.

In recent studies, our group has demonstrated that a B cell subset termed age-associated B cells (ABCs), or atypical memory B cells, are modulated by and modulators of γHV68 infection and autoimmunity in mice[417,420,428]. These $CD19^+CD11c^+$T-bet^+ B cells are known to expand and persist long-term following viral infections and in autoimmune disease, especially in females[420]. In the EAE model, MOG_{35-55} immunization of naïve mice promoted a regulatory phenotype among

ABCs[420]. However, latent γHV68 infection was shown to promote a pro-inflammatory phenotype among the ABC population, characterized by increased IFNγ and TNFα expression with reduced IL-17A expression[420]. In γHV68-EAE mice, the ABC population was thusly split between pathogenic and regulatory phenotypes[420]. Using a CD19 specific T-bet KO mouse strain, the pathogenic ABCs were shown to be required to enhance EAE following latent γHV68 infection, even though they are not preferentially infected compared to other B cell subsets[420,428]. In human blood samples, we also observed an expansion in the proportion of ABCs among total activated B cells in EBV seropositive people compared to seronegative people[420]. Moreover, the proportions were further increased in EBV seropositive RRMS derived samples compared to unaffected EBV seropositive controls[420]. The role of ABCs in driving enhanced autoimmune disease following γHV68 infection was replicated in a collagen-induced arthritis model of RA as well[417]. Similar to the γHV68-EAE model, latent γHV68 infection of mice prior to CIA induction exacerbated disease symptoms and promoted a pathogenic Th1 and cytotoxic T cell response while reducing Tregs abundance in the joint synovium[417]. This immunomodulatory effect was specific to latent γHV68 infection and enhancement did not occur with latency-free virus infection prior to immunization, nor when immunizing ABC KO mice latently infected with γHV68[417].

1.2.8.4 Summary

In conjunction with genetic risk factors and concomitant environmental exposures, EBV infection appears to promote a chronic and dysregulated inflammatory state that increases the risk of developing autoimmunity[397]. Epidemiological, clinical, and experimental data all support the notion that EBV infection, through its viral gene expression programs, immune evasion and modulation tactics, and persistence and B cell transforming capacities, acts as a susceptibility factor for the development of MS[104,397]. The collective understanding of how EBV influences autoimmune disease is predicated on the concept that critical interactions occur between infected B cells and autoreactive T cells, though the underlying mechanisms that determine these interactions are still debated[104]. Elucidation of the autoimmune processes affected by EBV infection prior to and during disease will be critical to the development of effective and safe preventative measures to eliminate or reduce inciting mechanisms that prompt disease onset, and to develop efficacious treatments that target pathological mechanisms perpetuated by persistent infection once disease has been established.

Important caveats and considerations for the interpretation of the studies described above are eloquently summarized by Münz and colleagues in[397]: "Models in which infection directs autoreactive responses to distinct tissues provide a simple system in which to study the pathological mechanisms of infection-induced autoimmunity. However, in most cases a robust immune response to a pathogenic infection in the target organ is usually not associated with the development of autoimmunity in humans. None of the proposed mechanisms for the development of infection-induced autoimmunity excludes the possibility that disease can occur temporally and/or spatially distal from the site of the initiating infection. Similarly, pathogen infected lymphocytes could preferentially migrate to inflamed tissues and this localization could be erroneously interpreted as a contribution of the pathogen in the autoimmune pathology, whereas it reflects in reality only the normal migratory behavior of infected host cells. Therefore, the enrichment of both pathogen-specific and pathogen-infected lymphocytes at sites of autoimmunity might be informative with respect to the migration behaviour of pathogen-infected host cells and lymphocytes targeting them, rather than indicating the involvement of the respective pathogens in the immunopathology of autoimmune diseases"[397].

The experimental evidence accumulated by the Horwitz Lab using the murine orthologue of EBV broaches and describes many of these considerations and has led us to propose an alternative hypothesis for the role of EBV infection in MS susceptibility. We theorize that latent EBV infection establishes a precondition within the host that skews the systemic immune responses to subsequent challenges, including to self-antigens, toward an exacerbated pathogenic Th1 and cytotoxic T cell response that then promotes the development of autoimmune disease[382]. Rather than infecting autoreactive immune cells or affected tissues directly, latently infected B cells act as necessary co-factors in the periphery to modulate autoimmune responses after a secondary challenge, which, along with genetic factors, directs a site-specific reaction determined by the nature of the secondary challenge[382]. In this case EBV acts as an enabling immunomodulator, or a first hit, and the resulting specify of an immune response to the CNS in MS occurs at the directive of a second hit, and explains how one structurally and mechanistically conserved virus is associated with the development of many antigenically and pathologically distinct autoimmune diseases[382]. This theory is predicated on the findings that in the γHV68-EAE model, broad but profound immunomodulatory changes are reproducibly observed without direct infection of the CNS tissues[415,418,420]. Although this modeling approach has been educational, a

more complete understanding of how EBV modifies MS susceptibility could be gained from improved modeling of host-viral interactions. In the current work, we utilized humanized mice, whereby EBV infection of human immune cells can be studied in an in vivo model of MS.

1.3 Humanized mouse models of infectious disease and autoimmunity

The term humanized mouse is generally applied to mice containing genetic sequences or tissues derived from human sources, which could include human transgenes, engrafted human tissues or cells, and/or transplanted human microbiomes[93,133,429]. In this work, humanized mice refer specifically to mice reconstituted with human immune system (HIS) components, which are derived by engrafting immunodeficient mice with mature peripheral immune cells or HSCs, with or without fetal hematopoietic tissues. Given many of the limitations of using NHP models in biomedical research, including high infrastructure and maintenance costs, reduced genetic manipulability and low cohorts numbers, in addition to ethical concerns, humanized mice offer an alternative to NHP models that replicate human immunity more closely than inbred lab mice[430]. Certain immunological differences between rodents and humans, including genetic divergence and discrepancies in key development and activation mechanisms, present major challenges to the adaptation and translation of data from preclinical mouse models to human disease[431,432]. As summarized by Koboziev and colleagues, "Major differences between the two species include hematopoietic activity of the spleen, circulating levels of lymphoid and myeloid leukocytes, innate immune mechanisms [e.g. Toll Like Receptors, NOD Like Receptors, defensins], T cell signaling pathways, B cell function, IgA production and isotype, intestinal intraepithelial and lamina propria cell composition, gut-associated dendritic cell and Natural Killer T (NKT) cell subsets and inducible nitric oxide synthase"[431]. Moreover, rodent strains do not always express the target or disease of interest or are not susceptible to infection with human-specific viruses. Humanized mice have therefore been used to investigate hematopoiesis, immuno-oncology, infectious disease, and autoimmunity, among other immunological processes[429,433]. Though many immunocompromised mouse strains and humanization methodologies are still actively under development, the collective prior and recent advances to improve the reproducibility and utility of humanized mice has enabled functional analyses of human immunity in a tractable system that would, otherwise, be infeasible[429,433,434].

1.3.1 Immunocompromised mouse strains

The generation of severely immunocompromised strains of mice arose through chance findings followed by the application of accrued knowledge about the genetic basis of immune cell development and function, which ultimately produced inbred lines with profound deficiencies in the murine innate and adaptive immune lineages to support more efficient and complete reconstitution of a HIS.

1.3.1.1 Discovery and critical advancements

In the 1960s, N. R. Grist noted the appearance of hairless pups in a colony of albino mice housed in their virology lab, which were then described to present with many other phenotypic abnormalities, including lacking a thymus, due to a mutation in the *Foxn1* transcription factor gene[431,435–437]. The absence of T cells in the athymic nude strain (*Foxn1*^{nu}) allowed for engraftment of human tissues without murine immune system mediated rejection, though the engraftment of HIS cells was inefficient due to the continued presence of murine NK and other innate immune cells[431,438]. In 1983, a spontaneous mutation in a litter of C.B-17 mice was discovered to result in an inability to produce Ig by some of the pups, which were then selectively bred to generate homozygous C.B-17-*scid/scid* mice[439]. The severe combined immune deficiency (SCID) phenotype of the mice reflected the often fatal and rare congenital disorder observed in infants, wherein mature T and B cells fail to develop, rendering the individual highly susceptible to common infections[439]. In the C.B-17-*scid/scid* mouse, the affected gene *Prkdc*, encodes the catalytic subunit of the DNA-dependent protein kinase that mediates double-stranded DNA break repair during V(D)J recombination of the TCR and BCR encoding genes; an essential developmental process required for the survival and maturation of both cell types[440]. C.B-17-*scid/scid* mice could also be engrafted with primary human tissues and cell, but likewise exhibited poor hematopoietic cell engraftment due to residual murine NK cell activity[433].

In 1995, the *Prkdc*^{scid} mutation was backcrossed onto the NOD background, generating the immunodeficient NOD-*scid* strain[441]. The NOD is a unique strain that possesses many immune-related polymorphisms that make them susceptible to spontaneous development of T cell-mediated diabetes[442,443]. NOD mice present with defective NK cell-mediated cytotoxicity, macrophage and DC-mediated APC functions, and the inability to generate membrane attack complexes due to a 2 bp mutation in the hemolytic complement C5-encoding gene[441,444–447]. Consequently, NOD-

scid mice have reduced murine innate immune function compared to the BALB/c related C.B-17-*scid/scid* strain, which enhanced the engraftment and expansion of human hematopoietic cells[441]. Moreover, NOD mice express a variant of the signal regulatory protein alpha (SIRPα) homologous to that of humans, and thus NOD macrophages can recognize CD47 expressed on the engrafted human cells to transmit the 'don't eat me' signal, which further reduces phagocytotic clearance of human immune cells[441,448]. The main drawback to using *scid* strains was the incidence of thymic lymphomas due to *scid* 'leakiness' that resulted in partial murine T and B cell development, and was especially common in C.B-17-*scid/scid* mice with increasing age (>10%)[449–451]. This 'leakiness' is due to residual functional TCR and BCR gene rearrangement and recombination, though the underlying mechanisms leading to leaky *scid* mice are unclear[450–453]. Immunodeficient mouse strains bearing nullifying mutations in the recombination activating genes 1 or 2 (*Rag1* or *Rag2*) display similar deficiencies in the mature T and B cell populations due to abrogation of V(D)J recombination, but by targeting the enzymes that mediate initial single-stranded knicks to the DNA upstream of the kinase-mediated break repair steps, the pathway cannot be initiated at all, and thus *Rag*^{null} mice are not leaky and more resistant to radiation and genotoxic drug treatment than *Prkdc*^{scid} mice[454].

Improvements in the engraftment and reconstitution of diverse lineages of the HIS were observed in immunodeficient mice (either NOD-*scid* or BALB/c-*Rag*^{null} mice) with an additional nullification of the IL2 receptor common gamma chain gene (*IL-2Rγc*^{null}), which further reduced murine innate immune cell functioning[455–459]. IL-2Rγc (CD132) is a common domain in the receptors for IL-2, IL-4, IL-7, IL-9, IL-15, and IL-21 (Figure 1.10)[460]. The absence of IL-15 signaling, in particular, greatly improved multilineage HIS engraftment by eliminating the key signal for host NK cell survival, even compared to engraftment of NK cell-depleted NOD-*scid* mice[457,461,462]. The abrogation of IL2-Rγc based signaling led to other benefits and disadvantages as well. NOD-*scid IL-2Rγc*^{null} mice are resistant to thymic lymphoma development, since T cell survival is IL-2 dependent, which restored their longevity compared to the precursor NOD-*scid*[441,455,457]. Immunodeficient mice with the *IL-2Rγc*^{null} mutation also required injection of fewer cells per recipient to achieve high levels of engraftment compared to the *scid* only precursor strains[429,463]. A negative consequence of this mutation was the elimination of IL-7 signaling, which impairs lymph node development and structural organization in the mouse; the downstream effects of which can only be partially reversed by administering exogenous human IL-7[464–467]. The lack

of lymph node development hampers B and T cell interactions needed for B cell maturation and Ig class-switching, and thus humanized *IL-2Rγc* ^{null} mice produce very little class switched antibody in response to antigenic challenge[465,468].

1.3.1.2 Next-generation strain development

Three dominant strains bearing the *IL2rγc* ^{null} mutation became commonly used: BALB/c-*Rag2*^{null}*IL2rγc*^{null} (BRG), NOD/Lt-*scidIL2rγc*^{null} (NSG), and NOD/Shi-*scidIL2rγc*^{null} (NOG). The NSG and NOG strains were derived from independent NOD-*Prkdc*^{scid} colonies, and both contain mutations that functionally eliminate IL-2Rγc signaling[429]. The NSG contains a complete IL-2Rγc null mutation (*IL2rg*^{tm1Wjl}, available from The Jackson Laboratory) and the NOG contains a truncating mutation of the intracellular domain of IL-2Rγc (*IL2rg*^{tm1Su}, available from Taconic Biosciences)[429]. In the NOG, the extracellular portion of the receptor is expressed, which can form complexes and binds cytokines, but cannot transmit signals due to the absence of the intracellular portion[469]. Though considered to be functionally equivalent genetically, differences in HIS reconstitution between the NSG and NOG have been reported to favor the NSG with certain humanization protocols[469]. Similar commercially available variants include the NCG (NOD-*Prkdc*^{em26Cd52} *Il2rg*^{em26Cd22}/NjuCrl, Charles River Laboratories), and the NRG, bearing the *Rag1*^{null} mutation instead of *Prkdc*^{scid} (NOD.Cg-*Rag1*^{tm1Mom} *Il2rg*^{tm1Wjl}/SzJ, The Jackson Laboratory).

The NOG and NSG strains were initially exhibited superior reconstitution of HIS subsets compared to the BRG strain, despite bearing functionally equivalent genetic mutations[433,470]. This difference was due to the variant of the *Sirpα* allele expressed by BALB/c, as well as C57Bl/6 mice, which was not compatible with human CD47, and therefore murine host macrophages phagocytosed the 'non-self' engrafted human immune cells[433,471]. Updated BRG-SIRPa strains (e.g., BRGS) have since been developed, wherein a human or NOD *Sirpα* transgene is knocked in to address this issue[471]. Moreover, a variant on the C57Bl/6 *Rag2*^{null} background has been generated wherein CD47 is knocked out entirely (triple knock out (TKO), B6.129S-*Rag2*^{tm1Fwa} *Cd47*$^{tm1Fp\ l}$*Il2rg*^{tm1Wjl}/J, The Jackson Laboratory), since macrophages that develop in a CD47^{null} environment fail to recognize its expression on engrafted cells[472–474].

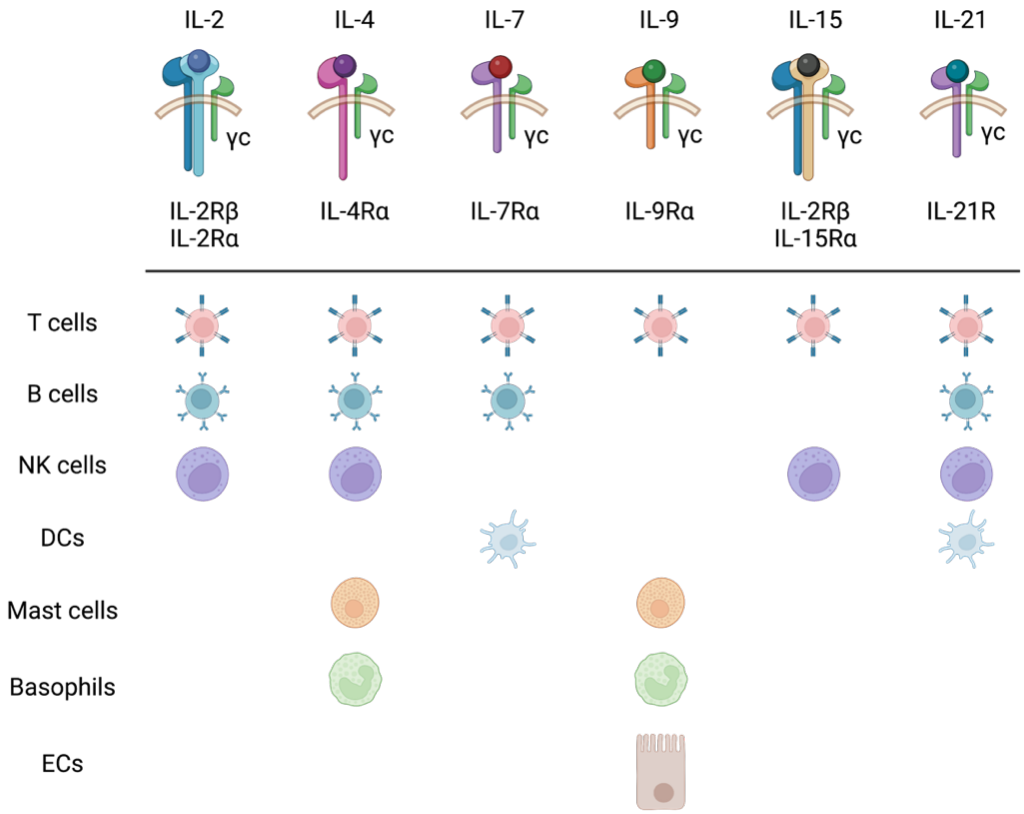

Figure 1.10 Common gamma chain bearing interleukin receptors and cell subset expression

Interleukin, IL; gamma chain, γc; natural killer, NK; dendritic cell, DC; epithelial cell, EC. Adapted from[431]. Created using BioRender.

Given the extensive degree of murine immunodeficiency seen with most new generation strains, selection of a NOD, BALB/c, or C57Bl/6 based immunocompromised strain is now more of a choice to be made based on the nature of the intended study and experimental aims, the potential complications associated with each host's genetic background, the purchasing and acquisition options, and the availability of derivative strains with specific knockouts and human transgenes that promote reconstitution of immune subsets of interest. While over 50 different immunocompromised strains have been reported to date[434,475], we focus here on a few examples that represent the types of transgenic improvements and derivatizations shown to enhance engraftment of HIS subsets.

To overcome the *IL-2Rγc* null mutation's effect of abolishing IL-7 signaling and hindering the functions of lymphoid tissue inducer cells needed for proper lymphoid tissue development, Li and colleagues have generated a BRGS derivative strain expressing murine thymic stromal cell

derived lymphopoietin (TSLP)[468]. The BRGST mouse develops large and abundant lymph nodes that are highly reconstituted with HIS cells following HSC engraftment compared to the BRGS[468]. The humanized BRGST lymph nodes were also noted to contain follicular structures with human B cell zones reconstituted with human follicular helper T cells and plasma cells, and the BRGST mice also had increased circulating levels of IgG and IgA, in addition to the usual IgM produced in the BRGS[468]. Another potential advantage of using BALB/c and C57Bl/6 immunocompromised strains over the NOD counterparts is the presence of hemolytic complement activity, which is an essential component of many immunological disease, including MS and EAE[445,476,477]. A complement sufficient NSG variant was generated in 2017, in which a functional, intact C5 gene was backcrossed on to the NSG background (NSG-*Hc*^{1}, The Jackson Laboratory)[476].

In addition to addressing some of the functional and structural issues within the murine host caused by the *IL-2Rγc* null mutation, genetic modifications to immunocompromised strains have been performed with the intent to improve the representation of minor HIS lineages, especially innate immune lineages, and to promote the maturation and ordinary functionality of reconstituted cells. For example, the NSG-SGM3 mouse has been made available for purchase by The Jackson Laboratory (~ NOG-EXL, Taconic Biosciences), wherein the inclusion of the human transgenes for stem cell factor (SCF), GM-CSF, and IL-3 promotes the engraftment of myeloid and regulatory T cells[478,479]. The NSG and NSG-SGM3 strains have both since been upgraded to include the human IL-15 transgene to support NK cell development, which can be further supported by simultaneous expression of a human IL-7 transgene[480]. On the BALB/c background, Rongvaux and colleagues have generated a BRGS derivative, called the MISTRG-6 mouse, expressing human transgenes that replace the murine equivalents of M-CSF, IL-3, GM-CSF, IL-6, thrombopoietin (TPO), and SIRPα[481,482]. The MISTRG-6 strain also exhibits high engraftment levels of myeloid cells, including within peripheral tissues, and improved T, B, and NK cell development[481,483]. BRG, NRG, NSG, and NSG-SGM3 mice have also been modified to knock out murine FMS (Feline McDonough Sarcoma)-like tyrosine kinase 3 ligand (FLT3) to further suppress the mouse innate immunity and/or to express a human FLT3 ligand encoding transgene, in order to improve human dendritic cell reconstitution and the function and abundance of NK cells and innate lymphoid cells (e.g., NSG-mFlt3KO-hFLT3LG-Tg, Jackson Laboratory)[434,484,485].

Important considerations for the insertion and deletion of human and murine cytokine encoding genes in immunodeficient mice are noted by Shultz and colleagues in[465]: “A caveat

associated with expressing human factors in immunodeficient mice is that although some murine cytokines do not function on human cells, many of the human factors cross-react with murine cells. This could cause unexpected phenotypic changes. For example, transgenic expression of a factor used to increase levels of human innate immunity following human HSC engraftment could upregulate mouse innate immunity and reduce levels of human engraftment. In addition, even cross-reactive mouse cytokines that work *in vitro* may have lower *in vivo* potency than their corresponding human cytokines". Practical examples of this issue have since been reported[481,486]. In the MISTRG strain, the nullifying mutation in the murine TPO gene, and replacement with the human TPO and GM-CSF genes, resulted in poor mouse erythropoiesis following irradiation, resulting in progressive lethal anemia that limits the study duration to 2 – 3 weeks post-irradiation[481]. In a separate study, the development of macrophage activation syndrome was reported to occur following viral infection of humanized NSG-SGM3 mice, but not with humanized NSG mice, presumably due to excessive myeloid cell cytokine expression[486].

Another modification designed to improve HIS functioning in humanized mice was the introduction of human HLA transgenes to enable HSC differentiation into human HLA-restricted T cells, rather than their development occurring on host thymic tissue resulting in murine MHC restriction[487,488]. Homozygous expression of HLA-A class I molecules (*A0201) in NSG mice generates functionally mature, cytotoxic HLA-A2 restricted $CD8^+TCR\alpha\beta^+$ T cell responses and enhanced reconstitution of $CD8^+TCR\gamma\delta^+$ T cells[487]. In NSG-HLA-A2/HHD mice, HLA-A2 molecule expression was detected on the surface of murine epithelial cell adhesion molecule positive ($EpCAM^+$) thymic ECs at equivalent levels as human fetal thymic ECs, which enabled the development of Th17 $CD4^+$ T cells alongside Th1 and Th2 cells[487,488]. NSG strains with HLA class II molecule expression have also been generated (i.e., NSG-HLA-DR1, -DR4, - DQ8), which has been demonstrated to improve human T-B cell interactions and Ig class switching[465,489–491]. More recently developed strains bear combinations of human HLA class I and II transgenes with or without murine MHC I or II deletions to replace their mouse counterparts[492,493]. For example, HUMAMICE ($HLA\text{-}A2^{+/+}/DR1^{+/+}/H\text{-}2\text{-}\beta_2m^{-/-}/IA\beta^{-/-}/Rag2^{-/-}/IL2r\gamma^{-/-}/Perf^{-/-}$ mice) are C57Bl/6 background immunodeficient *RAG* KO mice with such dual replacement of murine MHC I and II genes with human HLA transgenes encoding HLA-A2 and HLA-DR1 molecules[492]. The key limitation of using HLA transgenic mice, especially class I and II combinatorial strains, is the identification of donor cells expressing that combination of HLA genes[434]. A non-exhaustive

summary of genetic modifications that have been reported in immunocompromised mouse strains for improved humanization is presented in Table 1.1, and multiple reviews provide additional information concerning the utility and limitations of these and other strains[475,494,495].

1.3.2 Methods for humanizing the immune system of mice

Various protocols for generating humanized HIS mice using different tissue and cell sources have been reported, though they generally fall into one of three main categories: humanized peripheral blood mononuclear cell (HuPBMC), humanized hematopoietic stem cell (HuHSC), and humanized bone marrow-liver-thymus (HuBLT). In every case, humanized HIS mice are created individually by engrafting human immune tissues and/or cells in severely immunodeficient mice[457,495]. Humanized mouse model generation using the NSG recipient strain has been reported most often compared to other immunodeficient strains and will therefore serve as the baseline strain to compare the humanization methods below, unless otherwise stated. Logistical, methodological, and immunological considerations and expected outcomes for each of the three main humanized mouse models are summarized in Table 1.2 – Table 1.4.

1.3.2.1 HuPBMC model

HuPBMC mice are generated by engrafting immunocompromised mice with peripheral blood mononuclear cells (PBMCs) from blood donors with a phenotype of interest and reconstitute predominantly with mature T cells and some myeloid, NK and B cells[433]. Practically, the HuPBMC model is the simplest to execute, as HuPBMC mice can be generated by isolating PBMCs from adult blood donors with relatively few institutional and technical barriers (Table 1.2). Mosier and colleagues first demonstrated in 1988 that IP injection of human PBMC into C.B-17-*scid/scid* mice (Hu-PBL-SCID model) resulted in reconstitution and continued functionality of those cells following challenge[496]. In NSG mice, engraftment of PBMCs from an individual blood donor leads to highly reproducible engraftment and response kinetics, and different PBMC donors exhibit variable responses to challenge, which can enable assessments of a single intervention in mice derived from genetically and phenotypically diverse populations[463,497]. HuPBMC mice also present with the advantage of, in some cases, being able to recall blood donors of interest to obtain additional PBMC samples for further characterization and engraftment. HuPBMC mice can therefore be considered to reflect an immunological snapshot of the donor, such that modifications

to the immunophenotype of an individual can be assessed before and after an intervention or environmental exposure.

Typically, drawing 75 – 150 mL of blood per donor, with an expected frequency of ~10^6 cells/mL from healthy donors, can yield sufficient cell numbers to humanize 10 – 25 NSG mice from one individual when injecting 5 – 20 x 10^6 PBMCs per mouse (Table 1.3)[429]. PBMCs are typically isolated by density gradient centrifugation and injected IV into recipient mice after being freshly isolated or thawed from cryopreservation[429]. The IV route is generally considered most effective for engrafting donor PBMCs, though IP and intrasplenic injections are also used by some[429,463]. Due to xenogeneic recognition of mouse MHC by the engrafted mature T cells (discussed below), the experimental window duration for study is typically between 4 – 8 weeks post-PBMC injection at most, depending on the number of PBMCs initially injected per recipient[429]. Given the accelerated rate at which human T cells expand following PBMC injection, certain experiments can commence at a lower initial reconstitution levels (5 – 10% $hCD45^+$ relative to $mCD45^+$ cells in peripheral blood) compared to HSC-based models (15% or more).

The composition of engrafted cell subsets changes over time following PBMC injection, ultimately favoring mature effector T cells (Table 1.4). In the first week or so post-PBMC injection, human B cells, NK cells, and myeloid cells can be detected in circulation and in the spleen at low levels, though by 4 weeks post-injection, they are almost entirely undetectable[429,465]. Among the reconstituted T cells, most are activated $CD45RO^+$ effector/memory subsets with equivalent proportions of $CD4^+$ and $CD8^+$ T cells detected by 3 weeks post-injection, though $CD4^+$ T cells are predominant at earlier times[429,463]. Human $CD19^+$ B cells typically comprise 0.5 to 1.0% of human $CD45^+$ cells in the spleen, but exogenous administration of recombinant human BAFF/BLyS can improve B cell survival[429,465,498]. Pre-depletion of naïve $CD45RA^+CD4^+$ T cells from transferred PBMCs can also promote the survival of human B cells, including that of splenic $CD138^+$ plasmablasts[499], as can the pre-irradiation of MHC I/II DKO NSG mice prior to PBMC engraftment (J. Keck, conference communication). The main limitation when assessing adaptive immune responses in the HuPBMC model is the HLA-MHC mismatch between the donor and recipient tissues, as human T cells are selected on the donor's human HLA during development and transferred to murine MHC expressing recipients[465,492]. Utilizing HLA-matched donor PBMC and MHC KO NSG mice can partially circumvent this issue[465,492].

Table 1.1 Genetic modifications of immunodeficient mouse strains

Modification(s)	Purpose	Strain	References
Prkdc^{scid} *Rag*^{null} *IL-2γc*^{null}	Eliminate mouse T, B, and NK cells, impair innate immunity	• Next-generation strains (NOD, C57Bl/6, and BALB/c backgrounds)	455,471,500
Human/NOD *SIRPa* Tg or *CD47*$^{-/-}$	Inhibit murine myeloid cell phagocytosis of human cells	• BALB/c-RGS • C57Bl/6-RGS^{human} • C57Bl/6-TKO	471,500,501
Hc^{1} C5 gene (Tg)	Enable hemolytic complement activity on NOD background	• NSG-*Hc1*	476
Murine *TSLP* Tg	Improve lymph node structure	• BALB/c-RGST	468
Murine *FLT3*, *CMAH*, *TLR4*, and *c-kit* deletions	Improve HIS reconstitution by reducing murine innate immunity, preclude need to irradiate mice	• BALB/c-RG(S)F • NBSGW • NSG-TLR4KO, etc.	484,502–504
Murine MHC class I and/or II deletion	Reduce xenogeneic GvHD	• NSG-$K^bD^{b\ null}$ or (NOG) $\beta2m^{null}$ and/or IA^{null}, etc.	493,505,506
Human HLA class I and/or II expression (Tg)	Human HLA restricted T cells, improve antigenic responses	• NSG(-SGM3)-A2 • NSG-*Ab*^{o} • NRG-DRAGA • NSG-DR1/DR4/DQ8, etc.	470,487,490,491,507,508
Both murine MHC gene deletions and human HLA class I/II expression (Tg)	Reduce xenogeneic GvHD and improve antigenic responses by human HLA T cell restriction	• NSG-*Ab*^{o} DR4 • HUMAMICE, etc.	491,492
Human cytokines (Tg) (IL-6, BAFF, SCF, IL-3, GM-CSF, M-CSF, IL-34, FLT3L, TPO, IL-15, etc.)	Enhance specific HIS subset engraftment (myeloid cells, NK cells, DCs etc.)	• NSG-SGM3 • NSG-Quad • NSG(-SGM3)-IL-15 • NSG-mFlt3KO-hFLT3LG • BALB/c-MISTRG-6, etc.	480–482,509–511 (JAX #033367)
Other mouse gene deletions and human Tg expression	Promote niche tissue engraftment (human hepatocytes, human pancreatic islets, microglia, etc.)	• NSG-*PiZ* • NSG *Gcg1-29*KO • NSG-*hHGF*ki, etc.	512–514
eGFP (Tg)	Fluorescent labeling of host murine cells and tissues	• NSG-eGFP	515

1.3.2.2 HuHSC model

HuHSC mice are generated by engrafting immunocompromised mice with human HSCs derived from one of multiple sources, in order to generate a HIS from scratch within the recipient. Human HSCs, marked by the expression of the CD34 glycoprotein, can be isolated from human fetal liver, umbilical cord blood (UCB), or granulocyte colony-stimulating factor (G-CSF) mobilized adult donor peripheral blood or bone marrow (BM), depending on the availability of

these sources and the need to pre-select phenotypes or genotypes of interest (Table 1.2)[494]. In the case of UCB cells, $CD34^+$ cells can be positively selected for injection or total T cell depleted UCB cells can be engrafted directly[429]. The degree of 'stem-ness' among the $CD34^+$ HSCs isolated from each tissue source has been reported to differ (i.e., adult HSCs are less pluripotent so recipient mice exhibit reduced HIS diversity, produce fewer Tregs, etc.), though for the purposes of generating a HIS mouse model to study major immune lineages, normalizing transferred cell counts per mouse and utilizing transgenic recipient strains could mitigate this issue[457,516,517].

The number of $CD34^+$ HSCs injected per recipient varies from 1×10^4 to 2×10^5 cells or more, but usually follows a pre-conditioning step for murine myeloablation, unless using a strain of mouse designed to eliminate this step (e.g., NBSGW)[429,502,517]. The dose of irradiation also depends on the recipient strain (e.g., *scid* mice tolerate lower doses compared to *Rag*$^{-/-}$ mice) and the radiation source (e.g., X-ray, gamma, or UV)[518–520]. Following irradiation, a delay period of 6 – 20 hours before HSC injection is recommended so that increased stromal derived factor-1 expression facilitates homing of human HSCs to the mouse bone marrow[429,521]. The number of mice produced per HSC sample is dependent on the source; fetal liver tissue generally contains the highest $CD34^+$ cell abundance of any source and can produce as many as 40 mice per cohort, compared to just 10 – 20 mice from UCB-derived HSCs[434]. An additional consideration when generating HuHSC mice is the sex of the recipient mice, as female mice can exhibit superior engraftment and quicker T cell development compared to males in some research groups[522].

Engraftment of recipient immunocompromised mice can occur by intrahepatic or intracardiac injection of neonates, or via IV injection of adults[429]. Though reconstitution of newborns can present with practical limitations regarding breeding and technique, HIS reconstitution is generally superior, especially for developing functional human T cells due to the ability of engrafted $CD34^+$ HSCs to select on murine MHC expressing thymic tissue before its atrophy in young adulthood (Table 1.3)[429,488]. Unless HSCs are engrafted onto a human HLA transgenic expressing recipient strain, the T cells that develop in HuHSC mice are entirely murine MHC restricted, which can impede analysis of specific antigenic responses, such as to human infections[429,487]. The benefit of this murine MHC restriction is tolerance of the engrafted HIS to the host tissue. HuHSC mice rarely develop xenogeneic graft-versus-host disease and thus the study duration window can be months long (>48 weeks in some labs)[429]. High levels of peripheral blood reconstitution (20% or greater $hCD45^+$ relative to $mCD45^+$ cells) is observed 12 – 15 weeks

post-HSC injection for many cell types, mainly comprising B and T cells (Table 1.4)[429]. NK cells also reconstitute in HuHSC mice (Table 1.4) but are functionally deficient in NSG mice, which can be improved by engrafting human IL-15 and HLA class I transgene bearing NSG strains[465].

1.3.2.3 HuBLT model

HuBLT mice are created by implanting human fetal liver and thymus tissue under the kidney capsule of immunodeficient mice, followed by engraftment of $CD34^+$ HSCs isolated from autologous liver[523,524]. The liver/thymus tissue implant forms a thymus-like organoid that allows for human HLA-restricted selection of T cells derived from engrafted HSCs and comprehensive reconstitution of blood, lymphoid, and mucosal tissues with various innate and adaptive immune cell subsets[433,523,524]. The precursor to the HuBLT, the SCID-Hu model, involving co-implantation of human fetal and liver thymus tissues, enabling the assessment of local thymic processes and T cell development, but was hampered by low peripheral reconstitution of non-T cell subsets and limited cellular functionality[465,525–527]. With subsequent injection of autologous HSCs, a robust multilineage HIS develops (>20% $hCD45^+$ relative to $mCD45^+$ cells in peripheral blood by 9 – 12 weeks post-injection) that extends to the mucosa, which has enabled intravaginal infections of human $CD4^+$ T cells with HIV as well as inoculation of other human pathogens via peripheral routes (Table 1.4)[433,528,529]. Though the exact procedural sequence varies by lab, HuBLT mice are typically generated by surgical insertion of the fetal thymus and liver tissues (~1 mm^3 in size) under the kidney capsule of adult NSG mice, followed by a recovery period of approximately 3 weeks, after which the mice are irradiated and injected with $>10^5$ $CD34^+$ autologous HSCs each[523,524,528,530]. The HuBLT model presents with more logistical and practical barriers than the HuHSC model, including more technical expertise required for the surgical component of the model that can limit the number of mice generated from a single donation (n = 15 – 40 mice/cohort), as well as restricted access to fetal tissues in some regions (Table 1.2)[434,465]. To minimize the former barrier, Smith and colleagues have reported a method of propagating HuBLT mice to generate larger cohorts of mice (termed HuProBLT mice) from one fetal tissue donor by dividing and transferring bone marrow cells and human thymic implant tissue from a fully reconstituted HuBLT mouse to 4 – 5 naïve recipient mice[531].

The inclusion of the thymic and liver implant in the HuBLT model precludes the need for for HLA typing and matching with transgenic mice in order for human T cells to develop with

human HLA restriction (Table 1.3). The disadvantage of this strategy is the development of a graft-versus-host-like wasting disease in long-term experiments (>3 months after reconstitution), presumably due to eventual loss of human HLA-restricted T cell tolerance to murine MHC expressed on the host tissue[457]. HuBLT mice (or HuHSC mice) can also be implanted with additional tissues to evaluate specific localized responses or to enable infections with certain tissue-tropic pathogens[434]. Examples include implantation of human dorsal root ganglia to permit infection with VZV, engraftment of human hepatocytes to enable infection with hepatitis viruses, and implantation of human lung tissue for Zika and coronavirus infection[434,526,532,533]. In both the HuHSC and HuBLT models, HSCs can be genetically or phenotypically modified prior to their engraftment for specific studies[534–536]. Similar to the other two humanized models, HuBLT mice also suffer from incomplete T-B cell interactions that limit Ig class-switching and differentiation[434]. Blood samples from HuBLT mice contain greater proportions of phenotypically immature and transitional B cell subsets compared to human PBMCs[537]. Co-implantation of autologous spleen tissue (or bone fragments) has been shown to promote follicular lymphoid structures within the implant that improve GC-based B cell maturation and functionality in HuBLT mice[434,538–540]. HuBLT mice generated on the NSG-SGM3 background also develop greater numbers of mature human B cells compared to regular NSG mice, which then produce higher levels of IgM and IgG[509]. As an alternative to the NSG, B6-TKO mice ($CD47^{-/-}$) reportedly have better HIS reconstitution when humanized via the HuBLT method[500].

1.3.2.4 Considerations for and limitations of humanized mouse models

Most of the considerations when selecting one or more methods of humanization to employ for a particular research study are dependent on the intended aims of the study, the logistical and practical limitations to acquiring different tissues, relevant technical expertise and equipment, and the availability of suitable immunocompromised mouse strains that can generate relevant human immune cell subsets and functions. In general, humanized mouse models need to be specifically tailored around precise questions concerning human immunity, hematopoiesis, and pathogenesis with the awareness that not all aspects of the process can be recapitulated by any one model. As mentioned above, most humanized mouse models suffer from disorganized follicular lymphoid structures within shrunken secondary lymphoid tissues, which impairs human T-B cell contact[465,541]. Transgenic expression of human cytokines and HLA molecules, murine TSLP

expression, and implantation of human spleen tissue, have each improved human B cell function in humanized mice, but further improvements will be needed to match the complexity of the humoral response to challenge seen in humans[434,490,509,538]. Introducing further deficiencies in the murine innate immune system may also provide more complete HIS reconstitution and activity[433,457]. Moreover, hematopoietic lineages such as human neutrophils, granulocytes, and erythrocytes are often lacking or minimally reconstituted in humanized mice, so the addition of human transgenes to many current immunodeficient strains are intended to address these deficiencies[479,481,482,484,542]. Ultimately, HIS-containing mice will always be human-mouse chimeras, which will inevitably require careful consideration, methodological optimization, and thorough characterization to infer accurate conclusions. To promote and ensure reproducibility of humanized mouse studies between research groups, a list of key reporting items for publications has been proposed by an international committee of researchers, termed the "Minimal Information for Standardization of Humanized Mice" (MISHUM) checklist[434].

1.3.3 Modeling EBV infection and pathogenesis in humanized mice

One of the first human restricted pathogens studied in humanized mice was HIV. C.B-17-*scid/scid* mice were found to be susceptible to infection when engrafted with human PBMCs or a thymic tissue implant (SCID-hu model)[543,544]. Since then, many leukotropic viruses have been evaluated for their ability to infect different humanized mouse models, including all of the HHVs, many HERVs, human T-cell lymphotropic virus, JCV, influenza, Dengue virus, Ebola virus, hepatitis viruses, adenoviruses, and coronaviruses, as well as bacteria and parasites. The full list of human pathogens that have been investigated using humanized mice is extensive, diverse, and constantly growing, and has been thoroughly reviewed elsewhere[457,545–548]. Reports of successful EBV infection of humanized mice followed not long after the development of *scid* mice and have included studies using all three major model types. Due to the narrow tropism of latent EBV for human B cells, and resulting inability to infect murine immune cells, EBV infection of humanized mice has provided direct assessment of many aspects of gammaherpesvirus immune control, gene expression programs, tumorigenesis, associated disease pathologies, and vaccination strategies.

1.3.3.1 Early EBV studies and methodology

In 1992, Mosier and colleagues demonstrated that engraftment of C.B-17-*scid/scid* mice with 25 – 50 x 10^6 PBMCs IP per mouse from EBV seropositive blood donors led to spontaneous development of EBV positive lymphomas akin to PTLD[549]. As the authors noted, depending on the seropositive donor sample, the derivative cohorts of mice remained entirely tumor-free, had tumors develop in only a fraction of the recipient mice over time, or had tumors develop in all of the recipient mice relatively quickly[549]. Given that T cells reconstituted these mice very poorly compared to B cells and the varying ability of donor PBMCs to generate tumors, the resulting tumor burden likely depended on the initial infected B cell load in the transferred PBMC inoculum[549]. Similar studies of EBV lymphoproliferative disease (LPD) were subsequently performed using the HuPBMC model[550,551]. Islas-Ohlmayer and colleagues later reported successful experimental infection of HSC-reconsituted NOD-*scid* mice with cultured EBV strains, which resulted in high peripheral viral loads and the formation of $CD20^+$ and $EBER^+$ tumors[552]. These lymphoma-derived cells exhibited type II latency and generated LCLs ex vivo[552].

The same year, Traggiai and colleagues infected BRG mice with increasing doses of EBV to assess the utility of *IL-2Rγc* ^{null} mice as immundeficient hosts for HSC engraftment and functional HIS reconstitution[456]. They observed consistent infection and the generation of an EBV-specific CTL response in inoculated mice, and noted a dose-dependent effect on resulting tumor burden[456]. The dose-dependent oncogenic outcomes of EBV infection in inoculated humanized mice was later confirmed by Yajima and colleagues using HuHSC NOG mice[553]. High dose infections caused B cell lymphoma while low dose infections produced an asymptomatic persistent infection similar to what is seen in immunocompetent individuals after primary EBV infection[553]. At all doses, inoculation generated an EBV-specific CTL and IgM response[553]. EBV infection of HuBLT mice produced on the NOD-*scid* background was used to assess and validate the utility of the NOD/SCID-HuBLT model by Melkus and colleagues in 2006[524].

Table 1.2 Logistical considerations for generating humanized mouse models

Model	Human tissue source	Selectable features of donor tissue	Tissue accessibility	Cost to acquire tissue and humanize mice	Technical difficulty to generate
HuHSC	Fetal liver tissue, umbilical cord blood, or mobilized adult peripheral blood	Sex of cells, HLA type, immunogenetics, introduced variables by $CD34^+$ HSC manipulation	Moderate: easier through cord or peripheral blood donations; limited for fetal liver tissue due to ethical and political barriers	Low – moderate: depending on tissue source, some equipment required (irradiator), lengthy housing time	Easy – moderate: irradiation followed by single IV injection; intrahepatic injection of newborns for some protocols
HuBLT	Fetal liver and thymic tissues	Sex of tissue, gestational period (typically 16 – 24 weeks), introduced variables by $CD34^+$ HSC manipulation	Limited: frequency of procedures varies; ethical and political barriers to acquisition	Moderate to high: depending on tissue source, some equipment required (irradiator), technical and material surgical costs, lengthy housing time	Difficult: requires surgical technique, in addition to irradiation and IV injection
HuPBMC	Adult volunteer blood donors	Immunogenetics, HLA type, sex, age, medical history, etc.	Easy – moderate: depending on selection criteria and availability of chosen donors	Low: small reimbursement for donors, minimal phlebotomy costs, short animal housing time during reconstitution	Easy: single IV injection

Table 1.3 Immunological and experimental considerations for humanized mouse models

Model	Duration of reconstituted period*	T cell selection (MHC restriction)	Distribution in mouse tissues	Number of mice per donor	GvHD incidence
HuHSC	Long: 10 – 50+ weeks post-HSC injection	Murine MHC: on mouse lymphoid tissue (unless human HLA transgenic strain used)	Blood, spleen, bone marrow, lymph nodes†, thymus (newborns), as well as non-hematopoietic tissues (liver, lung)	• 15 – 40 mice per fetal liver tissue • 10 – 15 mice per cord blood unit • 20 – 40+ mice per G-CSF treated blood sample Depending on total HSC yield	Low: extended study window before onset
HuBLT	Moderate: 8 – 20 weeks post-HSC injection	Human HLA: within implanted fetal tissue organoid	Blood, spleen, bone marrow, lymph nodes†, mucosal sites, as well as non-hematopoietic tissues (liver, lung) and the implanted human organoid	• 15 – 40 mice per fetal liver tissue Depending on surgical efficiency and resources (can be increased by propagating into 3 – 5X more HuProBLT mice)	Moderate: long study window before onset, wasting symptoms typically begin after 20 weeks
HuPBMC	Short: 2 – 8 weeks post-PBMC injection	Human HLA: within blood donor	Blood, spleen, and lymph nodes, as well as non-hematopoietic tissues targeted by mouse MHC recognition/ GvHD (liver, intestines, skin)	• 10 – 30 mice from 80 – 100 mL of whole blood • 100+ mice from leukopak samples	High: time to onset dependent on PBMC donor and dose (accelerated by irradiation)

* Given same immunocompromised recipient strain used (NSG) and typical methods are used to humanize without additional tissue modifications
† Lymph nodes do not contain structurally functional follicles needed for B cell hypermutation and Ig class switching in germinal centres; addition of fetal splenic tissue in HuBLT mice reported to improve B cell maturation

Table 1.4 Reconstitution of immune subsets in peripheral blood of humanized mice

Model	%hCD45$^+$* (Relative to %mCD45$^+$)	%hCD45$^+$ in blood to begin experiments	T cells* (hCD3$^+$)	Regulatory T cells (Treg)* (hFOXP3$^+$)	B cells† (hCD19$^+$)	NK cells* (hCD56$^+$)	Myeloid cells* (hCD14$^+$)	Other innate immune subsets
HuHSC	Moderate – high: depending on HSC dose and length of reconstitution time	10 – 20% or more	Low – moderate: CD4$^+$ and CD8$^+$ T cells increase with reconstitution‡; fewer of both compared to B cells	Low – moderate: few natural Treg develop on murine thymus; functional peripherally induced Treg responses	High: similar % to donor PBMC and greater than T cells; ~95% express CD20; ~25% express CD21	Absent – low: reduced compared to donor PBMC (<0.2% of total leukocytes)	Low – moderate: similar % as CD4$^+$ T cells in cohort	Absent – low: human DCs detectable (mainly in the bone marrow)
HuBLT	Moderate – high: depending on HSC dose and length of reconstitution time	10 – 20% or more	Expected: CD4$^+$ and CD8$^+$ T cell frequencies closely reflect relative proportions in donor PBMC (superior % to HuHSC)	Expected: Treg frequencies closely reflect proportions of CD4$^+$ T cells in donor PBMC	Expected: frequencies closely reflect T cell-relative proportions in donor PBMC; ~80% express CD20 but few express any CD21	Low: reduced compared to donor PBMC (<0.1% of total leukocytes)	Low: reduced compared to donor PBMC (<0.5% of total leukocytes)	Absent – low: human DCs detectable (mainly in the bone marrow)
HuPBMC	Low – high: depending on PBMC dose/ donor, and length of reconstitution time	5 – 15% or more (higher % increases risk of GvHD)	High: majority of engrafted cells are mature CD4$^+$ and CD8$^+$ T cells (effector/memory)	Low – expected: frequencies closely reflect proportions of CD4$^+$ T cells in donor PBMC, but lower abundance	Low: >10X fewer compared to donor PBMC; decrease with reconstitution; Most do not express CD21; ~20% express CD20	Absent – low: decrease with extended reconstitution (<0.1% of total leukocytes)	Absent – low: decrease with extended reconstitution	Absent – low: NK-T cells decrease with extended reconstitution

* Improved with engraftment of transgenic human cytokine and hematopoietic factor-expressing NSG mice (NSG-SGM3)
† Lymph nodes do not contain structurally functional follicles needed for B cell maturation and Ig class switching in germinal centres, and thus generate IgM to novel antigens
‡ T cell reconstitution in HuHSC mice superior in newborn NSG mice compared to adults for the same donor source

Human T cells isolated from various organs of EBV-infected HuBLT mice produced IFNγ in response to co-cultured EBV$^+$ LCLs, and this response could be blocked by antibodies to human HLA class I and II molecules, demonstrating the generation of EBV-specific T cell responses in the model[524].

Data from these studies and others has highlighted some key aspects of EBV biology to consider when selecting a method of infecting humanized mice. Using HuPBMC mice, EBV can be studied in the context of endogenous infection, wherein the transplanted immune system has experienced EBV infection naturally. The likelihood with which an active infection is transferred to inoculated mice, however, is low and quite inconsistent between healthy donors with highly variable peripheral viral loads[549]. As such, other groups have performed 'superinfections' of EBV seropositive donor derived HuPBMC mice by exogenous inoculation with a cultured EBV strain following engraftment[554]. Alternatively, endogenous EBV isolated from selected blood donors can be propagated using LCLs[555], which can then be used to generate infectious particles and inoculate humanized mice at a consistent pre-determined dose. Well-characterized strains of EBV grown in cell culture were originally derived from patient biopsies, and the selection of a particular strain can have an impact on subsequent infection kinetics and disease pathogenesis in humanized mice[209,556]. Characteristics of common laboratory strains are summarized in Table 1.5[208,209,557].

1.3.3.2 Immune control of EBV infection in humanized mice

Humanized mouse models have recapitulated various aspects of the viral immune response to EBV infection and EBV-associated immunopathology observed in humans, including adaptive and innate immune control of lytic and latent infections[470,524,553]. Most studies have focused on the role of T cells, and in particular CTLs, in humanized NSG or NOG strains, though other studies have investigated NK cell mediated control of infection and the role of pDCs [554,558–561]. Using the HuHSC NOG model, Yajima and colleagues noted the degree of T cell reconstitution among individual mice correlated strongly with survivability following infection with EBV, and direct depletion of either CD3$^+$ or CD8$^+$ T cells reduced their lifespan[237]. CD8$^+$ T cell counts expanded with increased viral loads and, ex vivo, these CD8$^+$ T cells reacted to autologous EBV$^+$ LCLs[237]. In HuHSC NSG mice, Heuts and colleagues demonstrated that EBV-induced tumors contained infected B cells exhibiting different viral latency programs depending on the presence of CD4$^+$ T cells[560]. The team determined that CD8$^+$ T cell depletion, which resulted in a consequent expansion

of $CD4^+$ T cells, or vice versa, led to distinct, preferential viral promoter usage among infected B cells that modulated latency and gene expression profiles[560]. They further noted that $CD4^+$ T cell depleted mice did not develop visible tumors, while most $CD8^+$ T cell depleted mice did, suggesting a distinct but overlapping role for each T cell subset in eliminating lytic and proliferating infected B cells ($CD8^+$ T cells) and driving latently infected B cells into deeper forms of latency ($CD4^+$ T cells)[560]. These findings, demonstrating both $CD4^+$ and $CD8^+$ T cell mediated control of EBV infected B cells in humanized mice, have been reproduced by other groups[237,470].

Table 1.5 EBV producing cell lines used in culture and humanized mouse studies

Strain	Original source	Characteristics	Genetics	References
B95-8	Infectious mononucleosis (USA)	• Prototypical type I strain • Preferentially latent • Marmoset lymphocyte cell line (TPA or *BZLF1* activation induces virions) • Efficiently generates human LCLs in culture	• Full genome sequenced • Deletion of miRNA-encoding 12 kbp region (added back from Raji – EcoRI C fragment) • GFP-tagged variant	189,562–566
Akata	Burkitt lymphoma (Japan)	• Type I strain • Preferentially latent (latency program 1) • IgG^+ human B cell line (anti-IgG induces virions)	• Full genome sequenced • GFP-tagged variant • Closely related to GD1	176,209,211,567–569
Mutu	Burkitt lymphoma (Kenya)	• Type I strain • Preferentially latent (latency program 1) • IgM^+ human B cell line (anti-IgM induces virions)	• Full genome sequenced	176,209,211,570
M81	Nasopharyngeal carcinoma (China)	• Type I strain • Preferentially lytic • Prone to frequent reactivation in vivo • Highly tropic for epithelial cells	• Full genome sequenced	571–575
GD1	Nasopharyngeal carcinoma (China)	• Type I strain	• Full genome sequenced	176,557
AG876	Burkitt lymphoma (Ghana)	• Type II strain • Less B cell transforming in culture than type I EBVs • More lytic in B cells than type I strain	• Full genome sequenced	209,211,576,577
BL5	Burkitt lymphoma/ AIDS	• Type II strain • Infects primary $CD8^+$ T cells in culture (inconsistent finding) • More lytic in B cells than type I strain	• Gene expression of infected LCLs partially characterized	209,211,212,578,579

As noted above, a disadvantage of utilizing HuHSC models on the regular NSG or NOG backgrounds is the development of murine MHC-restricted human T cells, which may skew the binding and reactivity of EBV epitope-specific T cells that develop following infection compared to human HLA-restricted T cells[470]. To this end, two similar HLA class I transgenic NSG strains were developed that express the A*0201 class I variant, one of the most prevalent genotypes in human populations, and were infected with EBV following HSC engraftment[470,487]. Consistent with other reports, Strowig and colleagues observed a massive expansion of $CD45RO^+HLA\text{-}DR^+CD8^+$ T cells following infection of regular HuHSC NSG mice with EBV (strain not specified), similar to what occurs in IM[470]. The team, however, suspected human T cell restriction on murine MHC in the HuHSC NSG model may bias recognition of specific EBV antigens, and thus compared T cell responses to EBV using regular NSG mice as well as NSG-A2 transgenic mice[470]. By evaluating IFNγ production by T cells from each model in response to EBV peptides, they determined that NSG-A2 derived T cells were strongly responsive to all lytic peptides and had relatively reduced but consistent responses to latent peptides, while the NSG derived T cells did not respond to either set of peptides ex vivo, despite similar overall responses of both NSG and NSG-A2 T cell populations to autologous LCLs[470]. The authors therefore concluded that the restriction of T cells to murine MHC or human HLA biased the recognition of specific viral epitopes, which has important consequences for modeling and targeting the EBV specific T cell responses that would be observed in humans[470].

Separately, Shultz and colleagues developed the NSG-HLA-A2/HHD strain for similar purposes[487]. EBV infection of HuHSC NSG and NSG-HLA-A2/HHD mice resulted in EBV-induced lymphoma in both strains, though the distribution and localization of B cell tumors and responding $CD3^+$ T cells differed[487]. Consistent with Strowig et al., the team observed significant $CD45RO^+HLA\text{-}DR^+CD8^+$ T cell expansion following EBV infection of HuHSC NSG-HLA-A2/HHD mice[487]. $CD8^+$ T cells derived from infected HuHSC NSG-HLA-A2/HHD mice also recognized specific EBV peptides bound to HLA-A2 tetramers, while this was not the case with $CD8^+$ T cells isolated from infected HuHSC NSG mice[487]. To further characterize the functions of lytic antigen specific $CD8^+$ T cells, which are known to predominate over latent specific T cells in people after IM, Antsiferova and colleagues generated lytic and latent antigen specific HLA-A2 restricted $CD8^+$ T cells clones[170,470,561]. CTL clones expanded ex vivo were then adoptively transferred into HuHSC NSG-A2 mice one day prior to high dose EBV infection[561]. CTL clones

specific to the lytic antigen BMLF-1 reduced the incidence of high viremia at 3 weeks post-infection (peak lytic replication), whereas CTL clones specific to latent antigen LMP2 had no effect compared to controls[561]. In all of these studies, EBV infection of humanized mice led to an inversion of the CD4:CD8 ratio as a result of $CD8^+$ CTL expansion, which mimics cases of IM, and suggests boosting CTL control of infected B cells could be an effective approach to treating EBV-associated LPD[237,471,487,561,580].

Strategies aimed at improving CTL mediated control of EBV-induced disease LPD by targeting inhibitory PD-1/CTLA-4 pathways have been attempted in humanized mouse models and produced conflicting results depending on the humanization method use and the timing of interventions[573]. In four separate studies, EBV^+ lymphoma cells in humanized mice were determined to express PD-1, PD-L1 and/or PD-L2, and $CD8^+$ T cells from these infected mice correspondingly expressed or upregulated PD-1[573,581–583]. Using B95-8 or M81 EBV infected cord blood humanized mice, Ma and colleagues demonstrated that targeting either the PD-L1–PD-L2 or PD-1–CTLA-4 axis by antibody blockade prior to initial development of lymphoma reduced overall tumor growth and infected B cell counts compared to untreated infected controls, specifically by increasing EBV specific T cell responses and tumor infiltration[583]. Chatterjee and colleagues later showed that during acute primary infection of HuHSC NSG-A2 mice with B95-8 EBV, inhibitory PD-1 expression on CTLs correlated with viral loads and $PD\text{-}1^+CD8^+$ CTLs were functionally responsive to infected B cells[582]. Interestingly, when PD-1 antibody blockade treatment was initiated 3 weeks post-high dose infection, treated mice exhibited higher viral loads and tumor burden, suggesting PD-1 expression on CTLs is required to effectively control EBV infection during the primary acute phase[582]. In a follow up study, Volk and colleagues specifically compared the differences observed between these two studies in detail and repeated PD-1 blockade in humanized mice to determine the effects on EBV induced LPD[573]. In a third model, HuHSC NRG mice were infected with either B95-8 or M81 EBV and treated with PD-1 antibody blockade (pembrolizumab) starting at 2 weeks post-infection[573]. Corroborating the findings of Chatterjee et al., PD-1 antibody blockade increased viral loads, dissemination, and tumor burden, and in this case, even resulted in $EBER^+$ LPD within the CNS of treated mice with phenotypic resemblance to CNS PTLD seen in patients[573]. Volk and colleagues also observed a more pathogenic effect of PD-1 antibody blockade with M81 infected mice compared to B95-8 infected mice, further confirming that impaired CTL control of lytic infection and frequent reactivation are key factors

in the development of EBV lymphoma[573]. As all three of these studies were performed during acute infection, specific analysis of PD-1 antibody blockade in humanized mice with more developed EBV$^+$ LPD (5 – 8 weeks post-high dose infection) could shine light on the role of PD-1 expressing CTLs in controlling outgrowth of latently infected B cells once acute infection is resolved. These studies collectively highlight how the method of humanization, the resulting HIS subset composition, and the temporal sequence of infection and treatment can significantly skew results and lead to contradictory or misleading outcomes in humanized mouse models.

In a recent study specifically investigating the role of EBV infection in MS, Zdimerova and colleagues described a mechanistic relationship between the major risk HLA haplotype for MS and T cell responses to EBV infection[584]. In HuHSC NSG mice humanized with HLA-DR15 class II risk haplotype expressing HSCs, baseline CD4$^+$ and CD8$^+$ T cell activation was higher compared to HLA-DR4$^+$ HSC humanized mice. In response to infection with high dose B95-8 EBV, activated HLA-DR15 restricted CD8$^+$ T cells proliferated to a greater degree than non-HLA-DR15 restricted CTLs due to higher viral loads in mice with the former haplotype, while no significant difference among activated CD4$^+$ T cells was observed[584]. These data, in addition to ex vivo LCL assays, suggested EBV infection was less effectively controlled by T cells derived from HLA-DR15 expressing HSCs[584]. HLA-DR15 restricted splenic CD4$^+$ T cells derived and expanded from EBV infected mice responded strongly to MBP antigens, whereas less MBP reactivity was observed with EBV experienced, HLA-DR4 restricted CD4$^+$ T cells[584]. In addition to this apparent myelin cross-reactivity, HLA-DR15 restricted CD4$^+$ T cells from EBV infected mice appeared more promiscuous generally and exhibited higher levels of HLA alloreactivity, as determined by increased recognition of EBV$^+$ LCLs expressing other HLA molecules and reduced inflammatory responses to HLA matched EBV$^+$ LCLs[584]. The authors therefore conclude that "these findings point to both diminished immune control of EBV and its proinflammatory effects, as well as increased cross-reactivity of the CD4$^+$ T-cell compartment that is more activated by the poorly controlled EBV infection in the context of HLA-DR15. In this way, EBV-induced immune responses could synergize with HLA-DR15 to enhance MS." [584]. The authors did not report any assessments of the CNS localized T cell responses to myelin or EBV infection.

Alongside T cells, NK cells have been shown to control viral replication during the acute phase of EBV infection in humanized mice[558]. Chijioke and colleagues demonstrated in HuHSC NSG mice that human NK cell numbers increased two-fold by four weeks post-high dose B95-8

EBV infection and NK cell counts followed a temporal kinetic response similar to that observed in IM, as contraction of the early differentiated NK cell population occurred concurrently with CTL expansion[558]. Pre-depletion of human NK cells before EBV infection resulted in increased effector/memory CTL expansion and more severe IM-like symptoms, including increased viral loads and splenomegaly, and, eventually, increased tumor burden[558]. Notably, expansion of more differentiated NK cells reduced EBV control, indicating early differentiated NK cells were critical to the initial control of infection[558]. Specifically, NK cells responded to lytic antigens on infected B cells in vitro, which exhibited reduced MHC I expression[558]. Using a reactivation deficient EBV mutant, which can only remain in latency once established, NK cell depletion was shown to be detrimental only during lytic EBV replication but not during latency[558]. The authors surmise that NK cells play a crucial and complimentary role in limiting lytic replication of reactivated EBV infected B cells and the consequently high viral loads associated with the acute symptomatic phase of IM[558]. The role of NKT cells has also been investigated using a modified SCID-hu model of EBV infection[585]. Yuling and colleagues humanized NOD-*scid* mice by implanting fetal liver tissue under the kidney capsule, then injecting NKT cell-depleted human fetal thymic cells into the recipient mouse thymus (termed hu-thym-SCID chimeras), which were then challenged with EBV intrathymically (viral strain not specified)[585]. EBV infection preferentially expanded IFNγ producing human $CD8^+$ NKT cells relative to IL-4 expressing $CD4^+$ NKT cells in the thymus and peripheral tissues, which respectively promoted Th1 and Th2 responses ex vivo[585]. In mice mouse bearing xenotransplanted HL or NPC-derived tumor cells, adoptive transfer of $CD8^+$ NKT cells from the EBV challenged hu-thym-SCID mice reduced tumor size compared to transfer of only $CD4^+$ NKT cells, though co-transfer of both $CD8^+$ and $CD4^+$ NKT cells was synergistically protective against tumor formation and increased overall survival[585].

As mentioned above, pDCs are an innate immune cell subset involved in the control of lytic EBV infection through production of type I interferon[227]. Lim and colleagues studied how pDCs affected EBV induced LPD development in the HuPBMC model, wherein NOD-*scid* mice were engrafted with PBMCs isolated from EBV seropositive donors[554]. In HuPBMC mice engrafted with pDC-depleted PBMC, significantly higher mortality was observed compared to bulk PBMCs due to latent EBV transfer and dissemination[554]. In contrast, superinfection of PBMCs with B95-8 EBV led to higher rates of tumor formation in engrafted recipients[554]. PBMC exposure to EBV virions resulted in pDC TLR9 stimulation, cellular maturation, and increased

IFNα production, which then promoted NK cell and CTL cytotoxicity through cell-cell contact[554]. Pre-enriching superinfected PBMCs with pDCs prior to engraftment reduced recipient mortality compared to unenriched bulk PBMC control mice[554]. More recently, the role of pDCs was interrogated over time in B95-8 EBV infected HuHSC NSG mice by Gujer and colleagues[559]. Shortly after high dose infection (18 hr), significant levels of serum IFNα were detected, whereas IL-12 production indicative of classical DC involvement was not observed[559]. Daily exogenous administration of IFNα to EBV infected HuHSC mice reduced initial viral loads (3 weeks post-infection), splenomegaly, and splenic $CD8^+$ T cell counts, but did not affect viral load at later time points (4 – 5 weeks post-infection), which suggests a role for IFNα-producing pDCs specifically in limiting the early phase of viral replication[559]. Moreover, treatment of HuHSC mice with plasmacytoid DC and conventional DC-expanding FLT3L before EBV infection also reduced subsequent viral loads and $CD8^+$ T cell counts at 3 weeks post-infection[559]. Pre-depletion of $CD303^+$ pDCs from HuHSC mice prior to EBV infection, however, did eliminate the initial production of IFNα but did not impact viral loads or $CD8^+$ T cell expansion over time, indicating pDCs can transiently improve control of EBV infection but are not required to do so[559].

1.3.3.3 The role of oncogenic and regulatory viral genes in LPD

In addition to evaluating the functions of HIS cell subsets in controlling and modulating EBV infection and LPD, humanized mice have also been employed to investigate how the expression of virally encoded genes can influence infected B cell regulation and host immune responses. Humanized mouse studies of EBV-encoded genes have largely relied on single gene knockout (KO) mutant strains of EBV; some have evaluated the contributions of EBV oncogenes to development of LPD[221,252,561,586], while others have revealed the presence of virally encoded tumor suppressor genes that protect the host from LPD[575,587,588]. Ma and colleagues showed that infection of HuBLT NSG mice with a lytic replication deficient EBV (BZLF1-KO) resulted in lower tumor incidence compare to wild type (WT) B95-8 virus[252]. Antsiferova and colleagues also noted a site-specific reduction in tumor burden outside secondary lymphoid tissues (i.e., in the liver) with BZLF1-KO EBV infection of HuHSC NSG-A2 mice compared to WT EBV, despite producing similar viral loads[561]. Whitehurst and colleagues demonstrated the oncogenicity of the late lytic protein BPLF1 using an EBV KO strain in a HuHSC BRG model[586]. By eliminating the deubiquitinating activity of the protein, EBV BPLF1-KO mutant virus was less infectious than

WT B95-8 virus, and as a consequence, BPLF1-KO infected mice had reduced PTLD-like tumor formation and increased survival[586]. Using single and double EBV-KO B95-8 virus mutants to infect cord blood humanized NSG mice, Ma and colleagues demonstrated that the latent oncogenes LMP1 and LMP2A, the former of which mimics CD40 signaling and the latter BCR signaling, are cooperative contributors to LPD incidence but are not essential to the transformation of B cells[221].

In contrast, Zhang and colleagues demonstrated how another EBV protein, EBNA2, promotes B cell immortalization and the establishment of long-term latency while preventing oncogenesis, likely by restricting lytic reactivation[587]. Inoculation of HuHSC NSG mice EBNA2 mutant viruses resulted in increased viral loads, tumor burden, and mortality compared to WT virus[587]. Similarly, White and colleagues revealed the importance of the EBNA3C latency protein in suppressing tumor formation[588]. HuHSC NSG mice infected with a moderate dose of EBNA3C-KO virus developed DLBCL-like splenic tumors, whereas at this dose, B95-8 WT virus infected mice did not[588]. EBNA3C-KO infected B cells in these mice exhibited gene expression profiles similar to PTLD-derived tumor cells with a natural *EBNA3C* mutation[588]. In another study, Lin and colleagues used the M81 strain of EBV to investigate the role of EBV encoded miRNAs in the BART region, which is absent in the B95-8 WT strain, on viral replication and LPD in HuHSC NSG-A2 mice[575]. At 5 weeks post-infection, inoculation with the miR-BART KO virus generated much higher viral loads, increased tumor incidence, and reduced overall survival, compared to the M81 WT strain[575]. The authors determined that the BART miRNAs reduce EBV induced tumor formation by suppressing spontaneous lytic replication and decreasing LMP1 expression[575]. The findings of these studies have collective revealed the importance of a balance between lytic and latent gene expression in generating long term, asymptomatic latency within the host and that aberrant viral gene expression can cause or exacerbate EBV induced LPD.

1.3.3.4 Cofactors that affect EBV pathogenesis in humanized mice

Environmental cofactors that influence the pathogenic outcomes of EBV infection and LPD formation have also been evaluated in humanized mice. Accardi and colleagues showed that chronic exposure of HuHSC NSG mice to fungal aflatoxin B1 before and during B95-8 EBV infection increased peripheral viral loads and tumor burden compared to infected mice that were not exposed to aflatoxin B1[589]. Spleens from aflatoxin B1 treated mice exhibited elevated lytic gene expression, suggesting increased viral replication[589]. These findings implicate aflatoxin

exposure from contaminated food, which is common in regions where Burkitt's lymphoma is prevalent, promotes EBV induced tumor formation by stimulating lytic reactivation[589]. Two studies from the Münz lab have also investigated co-infection of leukotropic viruses in humanized mouse models of EBV-induced LPD. To model the pathogenesis of primary effusion lymphoma, McHugh and colleagues dual infected HuHSC NSG mice with B95-8 EBV and KSHV[590]. Dual infection reduced humanized mouse survival compared to EBV only infected mice, concurrent with increased EBV viral loads and tumor burden[590]. KSHV infection alone did not generate visible pathology and KSHV detection was sustained in the presence of ongoing EBV infection, indicating increased KSHV persistence[590]. Further histopathological analysis revealed that KSHV and EBV co-infected the same transformed B cells and these dually infected cells exhibited gene expression patterns similar to human primary effusion lymphoma cell lines[590]. Concomitant infection of B cells by KSHV and EBV resulted in a plasma cell phenotype and increased lytic *BZLF1* gene expression, and thus, since plasma cell differentiation of B cells reactivates EBV, the authors concluded KSHV infection of EBV-infected B cells promotes tumorigenesis by inducing lytic replication[590]. In the second study, McHugh and colleagues demonstrated that human B cells infected with B95-8 EBV could then co-infected with HIV in HuHSC NSG-A2 mice[591]. The authors noted that HIV infection of EBV^+ B cells did not alter EBV gene expression, but that "despite a comparable $CD8^+$ T-cell expansion in EBV and EBV/HIV dual-infected mice, T cells from a dual-infected environment did not seem to react to EBV-infected cells as efficiently"[591].

1.3.3.5 Modeling non-LPD pathologies associated with EBV

The spontaneous development of HLH, a rare condition often caused by uncontrolled active EBV infection in patients, has been reported in a study of EBV infected humanized mice that was attempting to generate LPD[486,592]. In HuHSC NOG mice, Sato and colleagues demonstarted that Akata EBV infection resulted in "hemophagocytosis, erythrocytopenia, thrombocytopenia, hypercytokinemia, $CD8^+$ T-cell activation/ proliferation and organ infiltration, and histiocyte proliferation. Moreover, the disease severity, IFN-γ production, and $CD8^+$ T-cell activation correlated with EBV DNA production"[592]. The authors noted that their experimental design differed from most studies of EBV infection in HuHSC NOG mice in that most of the engrafted and infected mice were male (boys are more prone to HLH than girls), which exhibited more severe disease than females in the same cohort, while other studies have only used female

NOG recipients[264,592,593]. They further suspected that the relatively earlier age at which the HuHSC NOG mice (13-16 weeks of age) were inoculated with EBV may have contributed to this alternative outcome[592]. Another research group has reported the occurrence of a spontaneous RA-like disease in EBV infected HuHSC NOG mice[594,595]. In 2011, Kuwana and colleagues described the incidence of erosive arthritis characterized by synovial joint membrane proliferation, T cell infiltration, and pannus formation in 65% of EBV infected mice[594]. In their experimental design, HuHSC mice were generated by engrafting non-irradiated adult female NOG mice with UCB $CD34^+$ HSC via IV injection, which were then infected with log-fold different doses of Akata EBV an average of 145 days after engraftment[594]. In a follow up study, Nagasawa and colleagues demonstrated the ex vivo development of human osteoclasts, which are responsible for the degradation of bone tissue, from the bone marrow of EBV infected HuHSC NOG mice, which the authors suggest could be triggered by human immune infiltration of joints in this model[595]. These data collectively demonstrate the importance of carefully choosing model parameters when designing experiments to reflect the disease and/or pathological outcomes of interest (age and sex of donor cells and recipient mice, timing of EBV infection, etc.).

1.3.3.6 Vaccination strategies

Recently, multiple different vaccine formulas have been evaluated for their efficacy in protecting humanized mice from EBV infection, either by directly enhancing T cell control of infection or by passively transferring protective antibodies[227,278,596–598]. In 2018, van Zyl and colleagues created non-infectious EBV virus-like particles (VLPs) expressing multiple capsid antigens to stimulate CTLs[596]. In HuHSC NSG-A2 mice, immunization with VLPs expressing EBNA-1 reduced detectable blood viral loads by 86% at 8 weeks post-challenge compared to unimmunized controls, whereas regular VLPs reduced detection by only 38%[596]. As the authors note, "vaccines that include antigens which predominate throughout the EBV life cycle are likely to enhance their ability to protect against EBV infection"[596]. In 2021, Cui and colleagues reported that a purified protein vaccine, composed of the gH/gL + gB trimeric complex required for both EC and B cell infection, produced neutralizing antibodies in immunized rabbits, which could be transferred to humanize mice to protect them from lethal EBV infection[278]. In this study, HuHSC NOG mice were administered pooled rabbit serum by IP injection, and infected with high dose

Akata EBV two hours later[278]. At 75 days post-infection, unimmunized serum recipients exhibited 100% mortality, whereas all trimeric complex immunized serum recipients survived[278].

Two more recent reports have described the development and protective capacity of nanoparticle vaccines by targeting the EBV envelope and attachment proteins gp350, gH/gL, and gp42[597,598]. In both cases, passive transfer of antibodies was evaluated since humanized mice "do not efficiently generate antibody responses to immunization" [598]. Malhi and colleagues developed a 60-mer nanoparticle vaccine displaying gH/gL, which was used to elicit neutralizing antibodies in WT C56Bl/6 mice[598]. The purified, pooled IgG antibodies were then passively transferred into HuHSC NSG mice two days before inoculation with a lethally high dose of Akata EBV[598]. At endpoint, all animals that received gH/gL 60-mer IgG survived infection, while none of the unimmunized IgG recipients survived[598]. The authors noted that neither 60-mer or monomer immunization provided sterilizing immunity[598]. In a second study, Wei and colleagues developed a bivalent gp350 and gH/gL/gp42 nanoparticle vaccine[597]. The vaccine was determined to elicit anti-EBV immune responses in immunized mice, ferrets, and NHPs and antibodies derived from these models prevented B cell and EC entry in vitro[597]. In their experimental design, purified IgG was isolated from the serum of immunized or control BALB/c mice, which was then transferred to HuHSC NSG mice infected with a moderate dose of B95-8 EBV[597]. They noted that all control IgG recipient humanized mice became infected but only one immunized IgG recipient had detectable EBV infection[597]. Moreover, immunized IgG recipient tissues were all EBER negative and none developed EBV^+ LPD, whereas half of the control IgG recipients did[597].

1.3.3.7 Outstanding topics

A key aspect of EBV infection that is not recapitulate in HIS humanized mice is infection of and replication within oral ECs, an important reservoir for the virus, highlighted by the finding that patients treated with B cell depleting antibodies still shed virus in the saliva[170,184,598]. In order to study EC infection and immune control of tumor cells, Liu and colleagues engrafted NPC biopsies from patients into HuHSC NSG mice[599]. Though not a model of homeostatic, non-pathogenic EBV infection of ECs seen in most healthy carriers, the EC xenograft method could represent a means of including the oropharyngeal component of natural EBV infection in humanized mouse studies. Moreover, oral or IN infection of humanized mice may be possible with improved mucosal reconstitution of human B cells, such as in HuBLT mice. As with all humanized

mouse models reported to date, nuanced humoral and antibody responses are typically lacking or absent following EBV infection, which can limit the applicability of findings to humans[600,601].

1.3.4 Humanized mouse models of autoimmune and neurodegenerative disease

Humanized HIS mice have been increasingly utilized as models for the study of immunological tolerance, graft reactivity, and autoimmune disease[602]. With the introduction of genetically enhanced immunodeficient mouse strains, many of the mechanisms underlying tolerance and various autoimmune diseases have been recapitulated in humanized mice[602,603]. A comprehensive description of humanized mouse studies of autoimmunity was recently compiled by Alves de Costa and colleagues in[602]. Studies that have investigated the development of autoimmune diseases in humanized mice have primarily focus on T1D, SLE, and RA, though other reports detail specific phenotypes alike human pathologies, including neurological disorders.

1.3.4.1 Immunological tolerance in humanized mice

Given the nature of humanizing a host expressing foreign species-specific antigens, questions arose as to whether and how human immune cells could be selected on murine MHC expressing tissues and if immunological tolerance mechanisms proceeded in a similar manner as in human primary lymphoid tissues. In non-transgenic immunocompromised mouse strains, such as the NSG, engraftment of newborn mice with $CD34^+$ HSCs results in human T cell maturation within the mouse thymus, resulting in murine MHC restriction[488,602]. Numerous studies have demonstrated that human T and B cells undergo both positive and negative selection in NSG mice, and the resulting TCR and BCR repertoires are similar in diversity and composition to human samples, though some divergent elements have also been noted[488,602,604–606]. By comparing HuHSC NSG mouse thymus tissue to human fetal thymic tissue, Halkias and colleagues demonstrated "that both conventional T-cell development and intra-thymic migration patterns in humanized mice closely resemble human thymopoiesis" and that "expression of an HLA-A2 transgene by murine thymic ECs does not dramatically improve T-cell development"[488], which has also confirmed using the BRG strain[488,604]. The temporal pattern of human thymocyte migration, indicative of cell-cell interactions during T cell selection, was also similar[488]. Halkias et al. concluded that these findings "further support the notion of efficient thymocyte: stromal interspecies crosstalk"[488].

Noted differences between these tissues, however, included reduced EOMES$^+$CD8$^+$ T cell and FOXP3$^+$ Treg counts in the HuHSC thymus compared to human fetal thymus, which could be due to the absence of specialized structures or signals required for their development that are not effectively reproduced in the murine thymic environment[488,604,607]. Interestingly, while thymic Tregs were scarce, peripheral Tregs were abundant, suggesting a specific deficiency in natural Treg development[488]. The authors hypothesize that "since development of FOXP3$^+$ T cells is thought to require stronger TCR signals compared with conventional T-cell development, it is possible that interspecies TCR:MHC interactions are unable to provide sufficient TCR signal strength required for efficient FOXP3$^+$ T-cell development"[488]. In a HuBLT NOD-*scid* model, natural Treg development occurred within the implanted human thymus tissue and displayed phenotypic markers in the periphery similar to those seen in people[606], corroborating this supposition. In a modified HuBLT NSG model (wherein mice were first thymectomized to remove the host murine thymus, then human fetal thymus tissue was implanted under the kidney capsule without liver tissue), Khosravi-Maharlooei and colleagues also demonstrated the production of a diverse TCR repertoire by positive selection within the implanted thymic tissue[608].

In theory, HLA transgenic NSG humanized with HSC, or NSG mice transplanted with human thymic tissue, will generate human T cells that are partially HLA restricted if murine MHC is co-expressed, or fully HLA-restricted if murine MHC has been deleted[470,487,488]. Halkias et al. noted that while peripheral MHC/HLA class I-restricted CTL responses to EBV infection have been shown to differ in the presence of the HLA-A2 transgene[471,487,488], the development and maturation of human CD8$^+$ T cells in the thymus of HuHSC NSG mice was unaffected by transgene expression, though they do suggest "the HLA-A2 transgene could enhance both negative and positive selection, thus producing a similar overall thymic output"[488]. Ehx and colleagues also reported in HuPBMC mice that TCR sequencing analysis showed that "productive clonality was comparable in the spleen and in the lungs on day 14 after transplantation but was slightly lower (meaning more diversity) in NSG-HLA-A2/HHD than in NSG mice suggesting that additional antigens were recognized by donor CD8$^+$ T cells in NSG-HLA-A2/HHD mice. In contrast, productive clonality was comparable in CD4$^+$ T cells from NSG and NSG-HLA-A2/HHD mice"[609]. The potential for atypical human thymocyte: thymocyte interactions in generating non-conventional T cell lineages was also briefly discussed by Halkias et al. but would require further assessment to determine the incidence and relevance to HIS reconstitution of HuHSC NSG

mice[488]. Negative selection of self-reactive T cells by engrafted human APCs has also been suggested to occur in non-transgenic HuHSC BRG mice, as T cells that develop in these mice are tolerant to both human HLA and murine MHC[456,602,607].

In addition to the presence of effective T cell tolerance mechanisms in humanized mice, the Pelanda lab has published multiple studies showing that central B cell tolerance is intact in HuHSC mice[510,541,601,602,610]. In HuHSC BRG mice, human B cell development within the mouse BM appeared similar to development in human BM, but subsequent maturation upon entering secondary lymphoid tissues was ineffective[541]. To determine if expression of human BAFF could improve B cell maturation, the team generated BRGS mice expressing human BAFF in place of mouse BAFF[510]. In both HuPBMC and HuHSC BRGS mice, human BAFF transgene expression did not alter the total B cell counts, though a noted skew within the B cell population away from plasma cells toward memory or naïve B cells was observed, concomitant with reduced total serum IgG levels[510]. Overall, transgenic human BAFF expression, on its own, was insufficient to ameliorate B cell development in the periphery of humanized mice[510]. Lang and colleagues further assessed the removal of autoreactive B cells during selection in HuHSC BRG mice expressing a synthetic self-antigen and concluded that "similar to mouse B cell development, central tolerance for human B cells is extremely efficient", as autoreactive clones are generally eliminated[602,610].

1.3.4.2 Xenogeneic graft-versus-host disease

Immunodeficient mouse strains humanized with human HLA-restricted T cells are known to present with varying levels of graft reactivity depending on the model, due to a lack of tolerance to murine MHC expressing cells[457]. HuBLT NSG mice, which express murine MHC on host tissues and human HLA on implanted thymic tissue, exhibit signs of a chronic xenogeneic graft-versus-host disease (xGvHD) many weeks after HSC engraftment, suspected to be due to eventual loss of tolerance toward the host tissues[537]. HuPBMC NSG mice, however, can exhibit a more swift and severe form of acute xGvHD, depending on the humanization protocol, that is typically lethal by 20 – 50 days post-PBMC injection due to the engraftment of fully human HLA restricted mature T cells from human blood donors[493,505]. As noted by Schroeder and DiPersio, "the same model of aGvHD can vary between investigators because of differences in radiation dose and delivery rate, differences in pathogens between animal facilities, and differences in T-cell dose and sources of T cells." Though generally considered a disadvantage of the HuPBMC model that

confounds and limits the duration of studies post-engraftment (~4 weeks at high doses of PBMCs per mouse), the mechanisms underlying xGvHD have been investigated in this model and applied more broadly to alloreactivity in human cases of transplant rejection and GvHD[429,493,505,609,611].

1.3.4.2.1 Acute xGvHD

In 2009, King and colleagues reported a highly reproducible model of xGvHD using irradiated NSG mice engrafted with human PBMCs[493]. xGvHD symptoms included "a gradual weight loss, hunched posture, anaemia, decreased platelet counts, decreased mobility and ruffled fur"[493]. King et al. determined that increasing the number of injected PBMCs from any donor, as well as pre-conditioning mice with low-dose irradiation, resulted in more rapid onset of xGvHD [463,493]. Ali and colleagues further demonstrated that "NSG mice develop GvHD significantly faster than BRG mice" due to quicker and higher human $CD3^+$ effector memory T cell reconstitution in the NSG compared to the BRG following PBMC engraftment[612]. Development of xGvHD was in part dependent on the recognition of murine MHC I and II molecules by the engrafted T cells, as NSG mice with genetic deficiencies in the expression of either MHC class delayed onset of xGvHD compared to regular NSG mice following PBMC engraftment[493,613]. In MHC II KO NSG mice, xGvHD onset was just as severe but slightly delayed compared to HuPBMC NSG mice, whereas MHC I KO NSG were significantly more protected from xGvHD compared to either regular or MHC II KO NSG mice, indicating a critical role for human $CD8^+$ T cell recognition of murine MHC I in generating xGvHD symptoms in HuPBMC mice[493]. Expansion and reconstitution of PBMC in MHC KO NSG mice was also reduced compared to regular NSG mice, and the deletion of MHC I led to an increased $CD4^+$:$CD8^+$ T cell ratio, whereas a reduction $CD4^+$:$CD8^+$ T cell ratio as observed in MHC II KO mice, indicative of compensatory expansion[493,505]. MHC I/II DKO NSG mice, however, reconstituted with a similar $CD4^+$: $CD8^+$ T cell ratio as regular NSG mice[505]. Using an allograft rejection assay, human T cells engrafted in HuPBMC MHC I/II DKO mice, although quantitatively fewer, were shown to be functionally responsive[505]. MHC I/II DKO NSG mice exhibited even greater protection and increased survivability of xGvHD compared to single MHC KO strains and regular NSG mice following PBMC engraftment[505]. Interestingly, treatment of HuPBMC MHC I/II DKO NSG mice with high doses of human IL-2 resulted in the activation of engrafted T cells and the generation of xGvHD

symptoms in these mice, indicating that while murine MHC recognition is a major driver of xGvHD, it is not the only xeno-antigenic T cell response involved[505].

Ehx and colleagues also investigated xGvHD as a model of human allogeneic GvHD by comparing outcomes in NSG and transgenic NSG-HLA-A2/HHD mice engrafted with HLA-A2$^+$ PBMC[609]. The team determined via gene expression profiling that PBMC-derived T cell expansion in NSG and NSG-HLA-A2 mice was driven comparably in both strains by IL-2 expression, TCR stimulation, and co-stimulatory signals[609]. Engraftment of NSG-HLA-A2 mice with HLA-A2$^+$ donor PBMCs resulted in a reduced CD4$^+$:CD8$^+$ T cell ratio compared to control NSG mice in all tissues, indicative of increased CD8$^+$ T cell expansion and differentiation with matched HLA class I expression[609]. Expression of the HLA-A2/HHD transgene in NSG mice resulted in greater TCR diversity and exacerbated symptoms of xGvHD compared to regular HuPBMC NSG mice, potentially due to co-expression of human HLA and murine MHC in these mice[609]. Antibody blockade of HLA-A2 molecules expressed on engrafted human donor A2$^+$ T cells in the HuPBMC NOG model also reduced xGvHD and improved survival by eliminating mismatched T cells[614]. On the C57Bl/6 background HUMAMICE strain, where mice have both dual human HLA I/II expression and dual murine MHC I/II elimination, HLA-matched HIS engraftment does not result in any "allo-like or xeno-like rejection reactions"[492].

Although human CD8$^+$ T cells have been shown to play a larger role in xGvHD development in HuPBMC NSG models, in CB.17-*scid/scid* mice, the opposite skew toward human CD4$^+$ T cells that recognized murine MHC II was more predominant than human CD8$^+$ T cells that recognized murine MHC I, suggesting experimental conditions, engraftment efficiency, and strain use can affect the xenoreactivity of T cell subsets[615]. Covassin and colleagues demonstrated the relative contribution of human CD4$^+$ T cells to xGvHD, showing that purified CD4$^+$ T cells also produced symptoms of xGvHD in NSG mice by recognizing murine MHC class II, but with reduced severity and delayed onset compared to whole PBMCs[491]. Moreover, HLA-mismatching of engrafted human CD4$^+$ T cells generated allogeneic-like GvHD in NSG mice expressing an HLA-DR4 transgene (without murine MHC II), which could be used to model human HLA-mismatch transplant cases more closely than typical xGvHD models[431,491]. Removing naïve CD4$^+$ T cells from PBMCs prior to engraftment of NSG mice has also been reported to prevent xGvHD-associated mortality and improve human B cell class switching and Ig production[499]. Human CD4$^+$ T cells are generally considered to mediate acute xGvHD through Th1 and Th17 driven responses,

though $CD4^+CD25^+$ Treg are also significant contributors to the suppression of xGvHD[431,616,617]. In the HuPBMC BRG model, Mutis and colleagues demonstrated that $CD4^+CD25^+$ Tregs were able to suppress incidence of xGvHD, since anti-CD25 pre-depletion of PBMCs worsened xGvHD symptoms and increased mortality, whereas enrichment with autologous $CD25^+$ Treg had the opposite effect in reducing xGvHD by limiting the expansion of effector T cells[616]. The authors noted that "protection from x-GvHD by Treg cells was associated with a significant reduction of human T cells from the circulation and with a significant increase in plasma levels of IL-10 and IFNγ"[616]. Recently, Reading and colleagues demonstrated that Tregs expanded ex vivo using multipotent adult progenitor cells could be therapeutically co-administered to NSG mice alongside whole PBMCs to reduce xGvHD mortality to a greater extent than regular Tregs[617].

1.3.4.2.2 Chronic xGvHD

Longer term HSC-based humanized mouse models have been used to model a more chronic xGvHD, which is characterized by both overlapping and distinct immunopathological processes compared to acute xGvHD seen in HuPBMC models[431]. The kinetics of symptom onset of acute and chronic xGvHD are temporally distinct, reflected by the respective terminology, and tend to model the incidence of acute and chronic GvHD observed in post-transplant cases on a contracted timescale[618,619]. HuBLT mice are most commonly investigated for the development of a spontaneous chronic xGvHD approximately 4 months post-HSC engraftment, without prior occurrence of acute xGvHD, though HuHSC mice have also been reported to display signs of chronic xGvHD after 5 months post-engraftment[537,607,618,620]. Chronic xGvHD elicited by HSC engraftment of human IL-6 transgenic NSG mice resulted in a pathology mediated by Th2 skewed $CD4^+$ T cells and activated human macrophages, which was also observed in HuBLT NSG mice, whereas acute xGvHD generated by engrafting regular NSG mice with CD34-depleted cord blood (containing T and B cells) resulted in rapid symptom onset characterized by increased clonal Th1 and Tc1 activation and expansion without human macrophage involvement[607,618–620]. Chronic xGvHD in HuHSC and HuBLT NSG mice resembles human chronic GvHD histopathologically as well, characterized by sclerodermatous skin, alopecia, multiorgan fibrosis, and immune infiltration dominated by $CD4^+$ T cells, though these features are also observed following acute xGvHD in HuPBMC BRG mice, suggesting the recipient strain immunogenetics may also play a role in disease pathogenesis[607,618,619].

HuBLT NSG mice have also been reported to develop a chronic xGvHD due to a gradual and spontaneous HIS activation that is not dependent on the presence of murine MHC molecules nor on reduced peripheral blood Treg counts[537]. Treg levels within the human thymic implant, however, have been shown to negatively correlate with chronic xGvHD severity in HuBLT NSG mice[618]. Covassin and colleagues suspected, "it is possible that the levels of mouse cells within the human thymic organoid are not sufficient to enable the negative selection of human T cells that are reactive with mouse MHC"[537]. Lockridge and colleagues noted that the chronic xGvHD histopathology seen in HuBLT NSG mice resembled sclerodermatous GvHD that can arise in mice transferred with minor histocompatibility antigen mismatched T cells[618]. They also noted the co-implantation of fetal liver tissue alongside thymus tissue delayed onset of chronic xGvHD in HuBLT NSG mice compared to those that received only a thymus tissue implant[618]. Sonntag and colleagues speculate that chronic xGvHD occurs in HuHSC mice due to "a peptide repertoire-specific T-cell reactivity in $CD34^+$ cGvHD NSG mice rather than responsiveness to xenogeneic MHC complex"[607]. Human B cell and plasma cell involvement has been suggested to potentially contribute to disease pathology in some models, but the collective evidence has not pointed to a primary role for B cells in inciting or promoting either acute or chronic xGvHD[537,607,618,620].

Though the generation of xGvHD can confound interpretation of humanized mouse models of autoimmune disease, many autoreactive pathologies have been recapitulated and studied in both HuPBMC and HSC-based humanized mice[431,602]. Interestingly, Sonntag and colleagues observed that $CD34^+$ HSCs expressing risk HLA haplotypes associated with autoimmune type I psoriasis and RA in humans were more likely to generate xGvHD in recipient engrafted NSG mice due to clonal T cell expansion in affected tissues[607]. The authors asserted "that the huCD34$^+$ NSG model may serve as a platform to study the role of human susceptibility and risk factors in the break of tolerance and autoimmunity"[607]. These studies suggest intertwined and overlapping mechanisms underpinned by intolerant HLA:TCR interactions are shared between the development of xGvHD and autoimmunity in humanized mice, also referred to as "(xeno-) autoimmunity"[607].

1.3.4.3 Type 1 diabetes

Humanized mouse models of T1D have been used to investigate immunological mechanisms of islet rejection, the pathogenic functions of beta cell reactive T cells, and therapeutic interventions to restore pancreatic function and normoglycemia[431,602,621]. In 2008, King and

colleagues applied the streptozotocin model of beta cell toxicity to HuPBMC NSG mice to evaluate the role of immune mediated islet destruction[463]. They found that injection of HuPBMC NSG mice with streptozotocin caused hyperglycemia, which could be rescued by transplantation of human islets[463,622]. Hyperglycemia could then be reinduced following allogeneic human T cell destruction of the human islets by co-transplanting HLA mismatched PBMC[463]. Zhao and colleagues further showed that human PBMCs from people with T1D could damage beta cells following injection of engrafted NSG mice containing diabetic NOD mouse derived irradiated splenocytes, which acted to prompt insulitis and recruit human T and NKT cells to the pancreas[623]. Though not a humanized model, adoptive transfer of different NOD donor T cell clones into recipient NSG mice variably induces diabetes and can be mitigated by Treg activity, which the authors interpret to "indicate that NSG-based models may be good recipients for studies entailing the transfer of ß-cell autoreactive T-cell clones or lines from human donors"[489].

A humanized diabetes model was also generated by Brehm and colleagues by introducing the *Akita* mutation in the insulin 2 gene to NRG mice, which causes metabolic stress and death specifically in beta cells[622]. NRG-Akita mice developed spontaneous hyperglycemia that could be reversed by transplanting human islets[622]. In HuHSC humanized NRG-Akita mice, allogeneic human islet transplants were rejected by the engrafted HIS, resulting in hyperglycemia[622]. Subsequent studies have utilized various methods to direct a human T cell response to beta cells in humanized mice, including engrafting NSG mice that express diphtheria toxin in insulin producing cells and generating NSG mice expressing the T1D risk allele HLA-DQ8, among other HLA transgenes[507,621,624]. In one such study, engraftment of NSG HLA-A2 transgenic mice with matched donor PBMC from individuals with T1D promoted islet infiltration and insulitis involving diabetogenic $CD8^+$ T cell clones, while PBMCs from unaffected control donors did not[625].

1.3.4.4 Systemic lupus erythematosus

The two main humanized mouse models have been utilized to study SLE, the HuPBMC and the HuHSC model[626]. Some groups have administered pristane to HuHSC mice, which is a hydrocarbon oil that induces multi-specific autoantibody production and an SLE-like syndrome [626,627]. Most studies, however, have used SLE patient-derived PBMCs to model disease in recipient immunocompromised mice[626,628]. Andrade and colleagues demonstrated that humanization of BRG mice with PBMCs from active SLE patients, but not with PBMCs from unaffected controls,

resulted in autoantibody generation, human T and B cell infiltration of the kidney glomeruli, nephritis, renal IgG complex deposition, and proteinuria[628]. The peripheral T cell ratio was also skewed toward $CD8^+$ T cells compared to $CD4^+$ T cells and active SLE HuPBMC BRG mice had reduced longevity compared to control HuPBMC BRG mice[628]. Pathology comparable to human cases was also observed in HuPBMC NSG mice derived from SLE patients[629].

1.3.4.5 Rheumatoid arthritis

As detailed by Schinnerling and colleagues in[621], five distinct methods have been used to generate RA-like disease in humanized mice, involving both the HuPBMC and HuHSC models. In the HuPBMC model, and variants thereof, RA has been modelled by engrafting mice with RA patient derived PBMCs, synovial tissue components, and/or synovium infiltrating immune cells[621]. O'Boyle and colleagues induced arthritic inflammation in HuPBMC mice by creating an air pouch in the backs of NSG mice, which produced a lining resembling the synovial membrane infiltrated by human T cells[630]. Using donor PBMCs pre-depleted of naïve $CD4^+$ T cells, Ishikawa and colleagues showed that engraftment of NSG mice with memory $CD4^+$ memory T cells and B cells from RA patients resulted in the generation of IgM-rheumatoid factor antibodies, indicating transfer of antigen specific pathogenic T cells from the donor[499]. NSG have also been subcutaneously transplanted with human synovial tissue, and more severe inflammation within these tissue implants was driven by the engraftment of naïve $CD4^+$ T cells derived from RA patients compared to unaffected controls[631,632]. To direct a site-specific inflammation within the joint tissues of recipient mice, Misharin and colleagues injected CFA into the knee or ankle joints of HuHSC NSG mice[633]. Following CFA immunization, arthritic inflammation and bone erosion within the injection site was observed alongside human immune cell infiltration[633]. Administration of the RA-approved TNF inhibitor Etanercept ameliorated these outcomes and reduced pannus formation[633]. In other HuHSC studies of RA, local and systematically inoculated infectious agents have been shown to induce synovial inflammation[594,634]. Chang and colleagues showed in the HuHSC NOD-*scid* (pre-NK-depleted) model that humanization with osteoarthritis derived bone marrow HSCs could mediate synovial inflammation following injection of the articular joint bone with *Chlamydia trachomatis*[634]. As mentioned above, Kuwana and colleagues reported the spontaneous development of inflammatory erosive arthritis in the knee and ankle joints of HuHSC NOG mice infected with EBV[594].

1.3.4.6 Autoimmune syndromes and neurological disorders

Numerous studies have demonstrated the utility of humanized mice in modeling many other autoimmune diseases, including inflammatory bowel disease (IBD) and syndromes with less prevalent or less direct human counterparts[431,602,621]. Humanization of NSG mice with PBMCs derived from individuals with Sjogren's syndrome, a systemic autoimmune disorder that predominantly affects the salivary and lacrimal glands, resulted in increased pro-inflammatory cytokine levels in recipient serum compared to PBMCs from unaffected controls[635]. Also using the HuPBMC model, Unterweger and colleagues engrafted NSG mice with PBMCs derived from ulcerative colitis and Crohn's disease affected patients and observed more extensive remodeling of the intestinal mucosa following ethanol challenge compared to mice that received unaffected control PBMCs [636]. Taconic has reported that HuHSC NOG mice induced with dextran sulfate sodium develop IBD, though the model reportedly did not respond to known effective treatments for IBD and was not pursued further[637]. Little and colleagues demonstrated that treatment of HuHSC NSG mice with anti-proteinase-3 IgG antibodies from patients with systemic vasculitis produced a similar pathology in recipients[638]. Vudattu and colleagues also described a generalized autoimmune disease "characterized by hepatitis, adrenalitis, sialitis, anti-nuclear antibodies, and weight loss" in HuHSC NSG mice treated with the anti–CTLA-4 antibody ipilimumab, presumably due to a loss of systemic Treg function[639].

Although less commonly utilized for studies of neurological disorders, humanized mouse models present with the unique advantage of modeling inflammatory components of CNS disorders in the context of relevant HIS cell subsets[430]. For instance, the role of HIV-infected macrophages in the CNS has been investigated in humanized mice (mainly HuHSC and HuBLT NSG mice) to investigate the effects of long-term infection on HIV associated encephalitis and neurocognitive impairment[430,530,640]. In one study, Manocha and colleagues evaluated neuroinflammation in HuHSC NSG mice that were treated with a neurotoxin known to induce Parkinson's disease-like lesions and symptoms[641]. Damage to dopaminergic neurons could be attenuated with an established treatment, which corresponded to reduced local pro-inflammatory cytokine levels[641]. Dash and colleagues further reported in their 2021 review that they observed no synergistic effect of prior, acute HIV infection on dopaminergic neurodegeneration in this neurotoxin induced humanized mouse model of Parkinson's disease[430].

1.3.4.8 Humanized mouse models of MS

To date, most humanized mouse models of MS have been based on the introduction of human HLA transgenes, rather than full HIS reconstitution, or on humanizing the gut microbiota through FMT of patient and control samples[92,93,133,642]. Two previous attempts at generating MS-like pathology in humanized mice have utilized PBMC engraftment, though they employed different strategies to generate CNS disease[643,644]. El Behi and colleagues sought to evaluate in vivo remyelination efficiency in the presence of an adaptive HIS derived from either MS patients or unaffected, otherwise healthy control donors (HD)[643]. To do so, the team generated lesions in the spinal cords of athymic nude mice (*Foxn1*^{null}) by LPC injection, and 48 hours later, grafted pre-activated PBMCs from HD and MS donors into the lesion site[643]. At 3 weeks post-activated PBMC engraftment, HLA$^+$ leukocytes were mainly found to be distributed in the lesion centers and borders, often associated with blood vessels[643]. Interestingly, the number of human HLA$^+$ cells and murine oligodendrocytes in the lesions was comparable whether PBMCs were derived from HD or MS donors[643]. However, the proportion of oligodendrocytes within the lesions expressing the precursor (OPC) differentiation marker CC1$^+$ was significantly reduced in the lesions grafted with MS donor PBMCs compared to both HD and unengrafted control mice[643]. The authors noted that "these results demonstrate that multiple sclerosis lymphocytes did not interfere with OPC recruitment, but impeded OPC differentiation" at the site of injury and "this concurs with the observations that in demyelinated multiple sclerosis lesions a high number of OPCs are present, a pattern underlining a failure of differentiation rather than recruitment"[643]. Furthermore, the effect of PBMC engraftment on remyelination also differed between these donor groups despite observing similar proportions of T and B cell subsets following stimulation in culture[643].

HD-grafted lesions and unengrafted lesions exhibited similar remyelination patterns, whereas MS grafted lesions fell into two groups based on the donor PBMCs: the first exhibited similarly effective remyelination as controls and the second showed reduced remyelination efficacy compared to controls and the first MS subgroup[643]. The authors summarized that "while lymphocytes from some of the patients induced a pro-regenerative microglia activation that led to proper OPC differentiation and successful remyelination *in vivo*, other patients' lymphocytes induced a hostile environment for remyelination, a pattern suggesting that the intrinsic capacity to induce remyelination is specific to each patient"[643]. Overall, their findings indicate a functional crosstalk between mature human lymphocytes and murine glial cells within the inflamed and

demyelinated CNS, demonstrating feasibility and relevance of humanized mice in modelling pathogenic immune processes in MS. A key advantage of the humanized LPC mouse model detailed by El Behi and colleagues is the development of spatiotemporally reproducible lesions wherein select donor PBMCs can be introduced locally under consistent conditions. The main criticism of chemically induced lesion models generally is the lack of BBB breach and peripheral immune infiltration observed in many inflammatory forms of MS[33,118].

Zayoud and colleagues took the EAE induction approach to generate CNS inflammation by immunizing HuPBMC mice with multiple myelin antigens[644]. In their study, Zayoud et al. engrafted NSG mice with HD PBMCs pre-mixed with autologous myelin antigen-pulsed monocyte-derived DCs (expanded and matured ex vivo) to promote presentation of myelin antigens to the engrafted human T cells[644]. Individual myelin antigens were used to pulse aliquots of the autologous DCs, which were then combined in equal amounts for engraftment[644]. Antigens included peptides and protein domains from PLP, MBP, and MOG, typically used in classical murine EAE models, or nonspecific antigens such as ovalbumin (OVA) for control immunizations[644]. Six days later, the engrafted HuPBMC NSG mice were then subcutaneously (SQ) injected with a second dose of non-pulsed immature DCs to promote antigen presentation, and 12 hours later, mice were immunized SQ with the same myelin peptides emulsified in CFA[644]. At day 24 post-immunization, subclinical inflammatory infiltration of the brain and spinal cord was observed, comprised of human $CD4^+$ and $CD8^+$ T cells, though no clinical EAE symptoms developed in any group[644]. Human $CD4^+$ T cells isolated from the spleens of the immunized mice were found to specifically proliferate and secrete proinflammatory cytokines in response to rat MOG protein when cultured with syngeneic pulsed DCs, but not to the other myelin antigens, and $CD8^+$ T cells did not respond to any of the immunizing antigens[644]. In two of four independent cohorts, they measured anti-rat MOG IgG in serum, suggesting administration of autologous human DCs promoted B cell survival, maturation, and class switching in at least some HuPBMC NSG mice[644]. The authors therefore concluded that "T and B cells from healthy human beings, which are specific for the MOG protein, are clonally expanded and readily activated when properly primed and migrate into their target tissue"[644]. The authors noted that the number of donor cells required to engraft each recipient mouse was prohibitively too high to generate cohorts with MS patient derived PBMCs, and thus MS PBMCs were not evaluated in the model. Overall, the data

presented by Zayoud, El Behi, and colleagues, suggests that human T cell responses can be directed to the CNS of humanized mice to produce MS-like immunopathology.

1.4 Research aims and rationale

Of great interest to our research group is the development of mouse models that recapitulate the intersection of immunopathological processes underpinning autoimmune, infectious, and neuroinflammatory diseases. Though classical murine EAE models have been informative in many regards, the significance of the evolutionary gap between the mouse and human immune system is emphasized by reports of promising therapeutics tested in murine EAE models that fail to be effective in MS patients, and in some cases, worsen inflammatory symptoms[50,335,645–647]. Direct EBV infection of mice with human immune systems has closely mimicked the pathology of various human diseases, and humanized mice are becoming increasingly recognized for their utility as preclinical models for therapeutic assessments in infectious disease. Despite the known caveats associated with current humanized mouse models of EBV infection, humanized mice present with advantages over classical EAE models, including the use of genetically diverse donor tissues that reflect variation in the human population more closely than inbred strains of mice[50]. By creating a human immune system within mice, we can more accurately model what occurs in people and examine environmental and genetic aspects of MS currently out of our reach experimentally. Moreover, the development of a humanized EAE model could be used to identify additional autoimmune mechanisms, therapeutic targets, and biomarkers of disease. We therefore applied the principles of mouse EAE induction and EBV infection of humanized mice, in addition to mechanistic and technical knowledge acquired from the γHV68-EAE model, to analyze the immunomodulatory effects of EBV infection directly on CNS autoimmunity in vivo.

The aim of the work presented herein was to develop a humanized EAE model in mice that is immunopathologically representative of MS in humans, such that we could interrogate the influence of latent EBV infection on disease initiation and development. Broadly, the aims of this work were, sequentially:

Aim 1 – Develop a humanized EAE model using HuPBMC, HuHSC, and/or HuBLT mice

Aim 2 – Characterize the immunopathology of CNS disease in HuPBMC EAE mice and determine donor and recipient specific parameters and limitations of the model

Aim 3 – Evaluate the immunomodulatory role of latent EBV infection in a humanized mouse model of MS by comparing clinical and immunological outcomes in HuPBMC EAE mice derived from donors with or without a history of infection and a diagnosis of relapsing MS

Chapter 2 details the methodology and procedures for generating humanize mice, inducing EAE, and measuring the immunological outcomes of infection and CNS disease used throughout the following three data chapters. The goals of Chapters 3 and 4 were collectively to develop a humanized EAE model of MS and to define the relevant parameters and limitations for subsequent investigation of EBV infection, which is detailed in Chapter 5. In Chapter 3, we describe preliminary assessments of EAE susceptibility, symptomology, and immunopathology in the three main humanized mouse models used to study EBV infection: HuPBMC, HuHSC, and HuBLT mice. The main finding of this chapter was that EAE induction of HuPBMC mice generated aspects of disease observed in classical EAE models that warranted further development. Chapter 4 outlines the immunopathological features of the HuPBMC EAE model, including characterization of the peripheral and CNS localized immune responses compared to classical EAE models, technical considerations for EAE immunization, sex bias in EAE susceptibility, and the relative chimeric contributions of human immune cell subsets and murine myeloid cells in mediating disease. In chapter 5, we assessed the differential capacity of PBMCs from healthy EBV seropositive and negative individuals, as well as from RRMS patients, to mediate disease in the HuPBMC EAE model. We determined that a PBMC history of EBV exposure, in the absence of an active infection, led to greater effector T cell accumulation in the CNS with reduced regulatory T cell expansion, suggesting a pathogenic priming of the T cell response to autoimmune challenge following EBV infection of the host. The data collectively reveal a critical immunomodulatory co-factor role for EBV in mounting susceptibility to MS years after primary infection.

Chapter 2 – Materials and Methods

2.1 Human participants

2.1.1 Blood donations

Blood donation by human participants was approved by the University of British Columbia's Clinical Research Ethics Board and by the Fraser Health Authority. Women with RRMS, aged 19 – 39 years old, were recruited at the Fraser Health MS Clinic (Burnaby, BC) under the supervision of Dr. Galina Vorobeychik under protocol H16-02338. Donors with a definite RRMS diagnosis, according to Poser or 2010 McDonald criteria, and disease duration of less than 10 years, were confirmed as treatment naïve prior to donation (no previous use of any disease modifying therapies during lifetime). RRMS donors underwent a neurological exam the day of blood donation to assess Expanded Disability Status Scale (EDSS) score. Individuals with a progressive MS diagnosis or EDSS >4, that were male, pregnant, outside of the designated age range, or undergoing treatment, were excluded from the present study. Unaffected, otherwise healthy female and male donors, aged 19 – 39 years old, were recruited at the Life Sciences Center (University of British Columbia) under protocol H12-02480. All donors provided written informed consent prior to enrolment in the study. Blood donor demographic information and serology is summarized in Table 2.1. For the comparative analysis in chapter 5, donors included were all female (mean age 31.5 ± 6.1 years for RRMS donors and 26.4 ± 6.2 years for HDs) and were enrolled in the study between November 2018 to August 2021.

2.1.2 Tissue donations

Human fetal liver and thymus tissue was obtained from women undergoing elective abortion during the second gestational trimester (19 or 20 weeks in this study). Written informed consent was obtained by the clinic, as outlined in protocol H12-02480. Fetal tissues were procured by Advanced Biosciences Resources Inc. (Alameda, California, USA). Serum testing of maternal blood samples by enzyme immunoassays was performed by LABS Inc. (Centennial, Colorado, USA) to confirm that tissue donors were negative for HBV, HCV, and HIV-1/HIV-2.

Table 2.1 Blood donor demographic information and serology

Donor ID	Age (years)	Biological sex	Country of birth and age of immigration to Canada	Age (years) at MS symptom onset	EDSS score	Disease duration	EBV IgG serostatus		CMV IgG serostatus	Serum 25-OH (ng/mL)
MS-01	24	F	Country: United Kingdom Age: 5 years old	24	2.5	4 months	VCA EBNA-1	+ +	+	29.7
MS-02	31	F	Country: Afghanistan Age: 20 years old	31	2.5	6 months	VCA EBNA-1	+ -	+	34.9
MS-03	32	F	Country: Canada Age: N/A	26	2.0	5 years	VCA EBNA-1	+ +	-	19.9
MS-04	39	F	Country: Canada Age: N/A	31	2.0	7 years	VCA EBNA-1	+ +	-	66.5
MS-05	37	F	Country: Canada Age: N/A	37	3.5	4 months	VCA EBNA-1	/ /	N/A	N/A
HD-01	39	F	Country: Canada Age: N/A	N/A	N/A	N/A	VCA EBNA-1	+ +	-	27.7
HD-02	25	F	Country: Canada Age: N/A	N/A	N/A	N/A	VCA EBNA-1	- -	-	35.0
HD-03	26	F	Country: Canada Age: N/A	N/A	N/A	N/A	VCA EBNA-1	- -	-	29.8
HD-04	23	F	Country: Canada Age: N/A	N/A	N/A	N/A	VCA EBNA-1	+ +	+	37.5
HD-05	19	F	Country: Canada Age: N/A	N/A	N/A	N/A	VCA EBNA-1	- -	+	18.9
HD-06	25	F	Country: Canada Age: N/A	N/A	N/A	N/A	VCA EBNA-1	+ -	+	38.4
HD-07	28	F	Country: Canada Age: N/A	N/A	N/A	N/A	VCA EBNA-1	+ +	-	27.5
HD-08	25	M	Country: Canada Age: N/A	N/A	N/A	N/A	VCA EBNA-1	+ +	-	28.9
HD-09	24	M	Country: Canada Age: N/A	N/A	N/A	N/A	VCA EBNA-1	+ -	-	42.0
HD-10	53	M	Country: Canada Age: N/A	N/A	N/A	N/A	VCA EBNA-1	+ +	+	33.1
HD-11	41	M	Country: Canada Age: N/A	N/A	N/A	N/A	VCA EBNA-1	- -	-	38.4
HD-12	32	M	Country: Canada Age: N/A	N/A	N/A	N/A	VCA EBNA-1	+ +	-	23.1
HD-13	27	M	Country: Canada Age: N/A	N/A	N/A	N/A	VCA EBNA-1	+ +	-	30.8

2.2 Human sample processing

2.2.1 Peripheral blood mononuclear cells

Human blood samples were obtained by venipuncture and assigned an alphanumeric code to protect donor identity. Whole blood (80 mL) was processed for PBMC isolation by Lymphoprep density gradient separation (STEMCELL Technologies, #07801), according to the manufacturer's instructions (by gently underlaying whole blood), within an hour of collection in K_2-ethylene-diaminetetraacetic acid (EDTA) coated vacutainer tubes (BD, #366643). Donor PBMCs were

immediately injected into recipient mice (not frozen prior to engraftment). A subsample of freshly isolated PBMCs was retained for DNA isolation and flow cytometric analysis. A second subsample of PBMCs was stored in autologous plasma with 10% dimethyl sulfoxide and placed in a Mr. Frosty™ Freezing Container (Thermo Fisher, #5100-0001) for controlled cooling to -80°C, followed by transfer to liquid nitrogen for long-term storage. Serum was obtained by centrifugation of blood (15 min at 1300 x g) collected in uncoated vacutainers (BD, #367820) and frozen at -80°C prior to analysis. Genomic DNA was isolated from a maximum of 4×10^6 donor PBMCs per donor using the PureLink™ Genomic DNA Minikit (Invitrogen, #K1820), according to the manufacturer's instructions, quantified using a Nanodrop Lite Spectrophotometer (Thermo Scientific, firmware version 1.02), and stored at -80°C. Donor DNA samples were HLA genotyped by The Sequencing Center (Fort Collins, Colorado, USA) using GenDx NGSengine® software for HLA typing (v.2.27.1).

2.2.2 Hematopoietic stem cells

Single cell suspensions were generated from human fetal liver by manually dissecting and passing the tissue through a 70-µm cell strainer with a syringe insert. Filters were flushed with Roswell Park Memorial Institute (RPMI)-1640 media supplemented with L-glutamine (Gibco, #11875-093) and 10% fetal bovine serum (FBS). Lymphocytes were isolated by Lymphoprep density gradient separation (STEMCELL Technologies, #07801), according to the manufacturer's instructions (by gently overlaying the liver cell suspension). Buffy coat cells were isolated and processed for HSC isolation using the EasySep™ Human Cord Blood CD34 Positive Selection Kit II, following the RoboSep™ protocol according to the manufacturer's instructions (STEMCELL Technologies, #17896). $CD34^+$ HSCs (comprising ~3% of total fetal liver lymphocytes), as well as an aliquot of the $CD34^-$ cell fraction, were frozen in human serum with 10% dimethyl sulfoxide and placed in a Mr. Frosty™ Freezing Container (Thermo Fisher, #5100-0001) for controlled cooling to -80°C and stored for 3 weeks prior to injection of NSG (-SGM3) mice.

2.3 Animals

Animal work was approved by the Animal Care Committee of the University of British Columbia, under regulation of the Canadian Council of Animal Care, under protocols for breeding (A17-0105 and A21-0145), and studies for humanization (A13-0234, A17-0266, and A21-0282) and autoimmunity (A13-0116, A17-0184, and A21-0228). Adult female or male NSG (NOD.Cg-*Prkdc*^{scid} *Il2rg*^{tm1Wjl}/SzJ, JAX #005557), NSG-SGM3 (NOD.Cg-*Prkdc*^{scid}*Il2rg*^{tm1Wjl}Tg (CMV-IL3, CSF2, KITLG) 1Eav/MloySzJ, JAX #013062), NOD (JAX #001976), and C57Bl/6 (JAX #000664) mice, originally sourced from the Jackson Laboratory, began experiments at 6 – 14 weeks old. NSG mice were bred in three facilities in Vancouver, British Columbia (BC Cancer Animal Resource Centre, Centre for Disease Modelling, and Modified Barrier Facility) to minimize any potential facility-specific outcomes (as has been priorly reported to be a factor in EAE studies[648,649]) and housed in the same specific pathogen-free facility at the University of British Columbia for the duration of experiments (Modified Barrier Facility). NOD, C57Bl/6, and NSG-SGM3 mice were bred in the Modified Barrier Facility. Mice were housed in groups up to five animals per cage on corn cob bedding (Bed-o'Cobs, The Andersons) and fed ad libitum with PicoLab Rodent Diet 20 (#5053) standard irradiated chow. NOD and C57Bl/6 mice were given free access to standard reverse osmosis-treated water. NSG (-SGM3) mice were given free access to autoclaved acidified water (pH 3 – 4), which has been shown not to affect EAE susceptibility compared to regular drinking water[650]. NSG (-SGM3) mice were kept on designated immunocompromised cage racks, separate from the immunocompetent C57Bl/6 and NOD mice. All housing rooms were set at 22 – 25°C with a humidity range of 50 – 70% and maintained on a 14.5 – 9.5-hour light-dark cycle with sunrise at 5:30 am and sunset at 8:00 pm.

2.4 Humanized mouse models

2.4.1 HuHSC model

Adult NSG (-SGM3) were pre-conditioned with 100 cGy sub-lethal irradiation from an X-ray source (48 seconds, RS-2000 Biological System small animal irradiator, RAD Source Technologies) and provided with nutritional gel. The following morning (~16 hours post-irradiation), pre-conditioned mice were then IV injected with 1 x 10^5 viable $CD34^+$ human HSCs each in phosphate-buffered saline (PBS) from a single tissue donor (thawed after 3 weeks in freezer storage and counted using trypan blue staining). All NSG (-SGM3) mice in the same cohort

received the same number and source of donor cells (cells were never mixed between multiple donors). Cages were switched from acidified water to antibiotic water (0.2 mg/mL enrofloxacin, Baytril®, Bayer Corp.) three days prior to irradiation to prevent microbial translocation in these immunocompromised mice and were maintained on treated water for a total of 4 weeks, after which the cages were returned back to acidified water. As EAE development can be abrogated by antibiotic treatment before induction[97], soiled bedding from naïve breeding room cages of NSG (-SGM3) mice was twice transferred, once every two weeks, into sex-matched HuHSC recipient cages to promote reconstitution of the intestinal flora following return to acidified drinking water. Following a 15-week reconstitution period, circulating human $CD45^+$ immune cell repopulation was confirmed by saphenous vein blood sampling and flow cytometric analysis, followed by EAE induction.

2.4.2 HuBLT model

To prepare for surgical implantation of a human organoid, fetal thymus and liver tissues were dissected into ~1 mm^3 sized fragments. Two pieces of liver surrounding one piece of thymus tissue (liver-thymus-liver) were loaded into a sterile trocar tool. Adult NSG (-SGM3) mice were anesthetized with 2% inhaled isoflurane (Fresnius Kabi Canada, #CP0406V2) and subcutaneously administered 2 mg/kg bupivacaine locally (Marcaine®, Pfizer), as well as 5 mg/kg meloxicam (Metacam®, Boehringer Ingelheim), 0.1 mg/kg buprenorphine (Buprenex®, Indivior Inc.), and 1 mL sterile saline to provide analgesia and fluids. The incision site was prepared by shaving the area and sterilizing the skin with iodine and isopropanol. Two small skin and muscle incisions were made to briefly expose the kidney, which was hydrated with fluids and implanted with the tissues just under the outer kidney capsule using the loaded trocar. The muscle and skin incision were closed with continuous and single interrupted patterns, respectively, using braided Vicryl-coated 5-0 sutures (Ethicon, #J303H), and secured with Vetbond™ tissue glue (3M, #1469SB). Surgical tools supplied by Roboz Surgical Instrument Co. (Gaithersburg, MD, USA) and Fine Science Tools (North Vancouver, BC, Canada) were heat sterilized between surgeries using a glass bead sterilizer (Germinator 500, CellPoint Scientific). Post-surgical mice were regularly provided with additional analgesia (meloxicam and buprenorphine SQ) and specific supportive care as needed during recovery, such as wound cleaning and maintenance, SQ fluids, cage heating, and nutritional gel.

Three weeks post-surgery, implant recipient mice were pre-conditioned with 100 cGy sub-lethal irradiation from an X-ray source (48 seconds, RS-2000 Biological System small animal irradiator, RAD Source Technologies) and provided with nutritional gel. Cages were maintained on acidified drinking water to reduce potential effects of microbial depletion on EAE induction. The following morning (~16 hours post-irradiation), pre-conditioned mice were then IV injected with 1.35 x 10^5 viable autologous $CD34^+$ human HSCs each in PBS (thawed after 3 weeks in freezer storage and counted using trypan blue staining). Subsamples were retained for flow cytometric analysis of the thawed $CD34^+$ and $CD34^-$ fetal liver cell fractions. Following a 10-week reconstitution period, circulating human $CD45^+$ immune cell repopulation was confirmed by saphenous vein blood sampling and flow cytometric analysis, followed by EAE induction.

2.4.3 HuPBMC model

NSG (-SGM3) mice were engrafted with 5×10^6 live donor PBMCs each in PBS by intravenous tail vein injection (viability confirmed by trypan blue counting with a hemacytometer), which were freshly isolated from a single donor (i.e., cells were never mixed from multiple donors and were not frozen prior to engraftment). Unengrafted controls received blank PBS. Twelve to thirty mice per donor were randomly assigned to recipient mouse groups based on PBMC yield and available stock on the day of blood donation. Cages were maintained on acidified drinking water for the entirety of the experiment. Following a three-week reconstitution period, circulating human $CD45^+$ immune cell repopulation was confirmed by saphenous vein blood sampling and flow cytometric analysis, followed by EAE induction.

2.5 EAE induction

Humanized mice, as well as un-engrafted control NSG and immunocompetent C57Bl/6 and NOD mice for some experiments, were actively induced with EAE on day 0 by SQ injection of 100 µL complete Freund's adjuvant containing 400 µg desiccated *M. Tuberculosis H37Ra* (DIFCO, #DF3114-338) in incomplete Freund's adjuvant (DIFCO, #DF0639-60-6) emulsified with one or more of the following myelin antigens: 200 µg MOG_{35-55} peptide (GenScript), 100 µg recombinant human MOG ($rhMOG_{1-120}$ prepared in-house), or 50 µg human MBP (Creative Biomart, #MBP-6947H). On days 0 and 2 post-immunization, mice received an intraperitoneal injection of 200 ng pertussis toxin in 200 µL of PBS (List Biological Laboratories, #179A). The

mice were monitored and scored daily for EAE symptoms. Clinical EAE scoring was based on the following 5-point scale: 0, no overt signs of disease; 0.5, partially limp tail; 1, limp tail; 1.5 limp tail and hind limb weakness; 2, loss of coordinated movements; 2.5, one hind limb paralyzed; 3, both hind limbs paralyzed; 3.5, hind limbs paralyzed and weakness in forelimbs; 4, forelimbs paralyzed; 5, moribund state or death by EAE. EAE studies were performed in a biosafety containment level 2 facility. Clinical outcome assessors of HuPBMC EAE mice were blinded to the viral serostatus of the blood donors. Onset was defined by the occurrence of tail paralysis (score 0.5 or higher) for two consecutive days. Cumulative EAE scores were calculated by summing daily clinical scores from the day of onset until endpoint. Mice with motor impairments, weight loss, and signs of illness were provided supportive care, including administration of SQ fluids and cage heating, and provisions of wet food and nutritional gel. Humane endpoint was defined by an EAE score of 4 or greater, or a clinical health score of 4 or greater, as defined by the Animal Care Committee based on body condition, weight loss and signs of pain.

2.6 Xenogeneic graft-versus-host disease

Symptomatic onset of xGvHD in HuPBMC NSG (-SGM3) mice was defined by the appearance and persistence or worsening of skin dryness, redness, discoloration (jaundice), and/or hair loss. Due to intragroup variability in EAE symptom onset and ongoing xGvHD and wasting following the resolution of EAE symptoms, HuPBMC EAE mice could not be maintained longer than approximately ten days post-symptom onset. HuBLT and HuHSC mice were not maintained for a sufficiently extended period of time for symptoms of chronic xGvHD to develop.

2.7 Recombinant human MOG protein

The extracellular domain of recombinant human myelin oligodendrocyte protein ($rhMOG_{1-120}$) was expressed from an *Escherichia coli* BL21 vector (pQE-30) obtained from Drs. Christopher Linington and Nancy Ruddle[149,651], and the protocol was modified from that of Dr. Jennifer Gommerman. The vector expresses a 15.8 kDa His-tagged rhMOG protein under the control of a lac operon. Following isopropyl ß-D-1-thiogalactopyranoside (IPTG) induction, the cells were lysed to release the protein product from inclusion bodies. The protein was subsequently purified using a Ni^{2+}-His-bind resin column (5 mL HisTrap FF, Cytiva, #17525501) and the protein fractions were analyzed by SDS-PAGE gel electrophoresis and stained with Coomassie blue. The

fractions containing sufficiently pure protein of the correct molecular weight were pooled and diluted to a protein concentration of <0.5 mg/mL in preparation for partial refolding in cellulose dialysis tubing (6 – 8 kDa molecular weight cut-off, MWCO). The refolded protein product was concentrated by centrifugation in 3K MWCO Amicon tubes (EMD Millipore, #UFC900324) until a final concentration of at least 4 mg/mL was reached. The final concentration was determined using a Nanodrop Lite Spectrophotometer (Thermo Scientific, firmware version 1.02) (MW = 15.5 kDa, e/1000 = 12.09). Protein samples were aliquoted, and flash frozen in liquid nitrogen prior to storage at -80ºC. The purified and concentrated rhMOG protein was confirmed to elicit an encephalitogenic response by induction of EAE symptoms in C57Bl/6 mice.

2.8 Tissue collection

Mice were euthanized at endpoint by isoflurane overdose. Blood was collected by cardiac puncture, followed by perfusion with 20 mL of sterile PBS for collection of CNS tissues. Brains, spinal cords, and spleens were dissected whole and kept in cold sterile PBS or in 10% neutral buffered formalin (NBF) for further processing. Spinal cords were straightened, placed onto filter paper, and submerged in NBF for histological analyses. The presence of intact emulsion was confirmed by examining the skin at the injection site. Serum was extracted from untreated blood samples by centrifugation (13 min at 8000 rpm) and stored at -80°C prior to analysis. To isolate peripheral blood cells, blood samples were treated with K2-EDTA for further processing. Tissues from animals in each recipient cohort were included for analysis regardless of the occurrence of clinically visible EAE symptoms to account for differences in incidence and severity among donor groups.

2.9 Histological analysis

2.9.1 Immunohistochemistry

Perfused, intact organs collected for analysis of cellular infiltration by immunohistochemistry (IHC) were stored in 10% NBF for 2 hours at room temperature (RT). At 2 hours, brains were halved by sagittal division and incubated for another 2 hours along with the spinal cords (4 hours total in NBF at RT). CNS organs were washed in cold PBS for 1 hour at 4°C to remove remaining NBF, then placed in 15% sucrose solution overnight at 4 °C for cryoprotection. Organs were then placed in a 30% sucrose solution overnight at 4°C, then placed

overnight at 4°C in a 25% sucrose solution containing 50% optimal cutting temperature compound (OCT, VWR Clear Frozen Section Compound, #CA95057-838). Cryoprotected organs were segmented in the case of spinal cords, and oriented in cryomolds containing OCT medium and frozen on a partially submerged aluminum block equilibrated in liquid nitrogen, then stored at -80°C for sectioning. Brain and spinal cord tissues were cut at -19°C into 12-µm sagittal and coronal sections, respectively, using a Shandon Cryotome® FSE (Thermo), and placed onto Superfrost Plus microscope slides (Fisher Scientific, #12-550-15). Sections were taken at least 30-µm apart and obtained from one of either brain hemispheres, or from four equally distant points along the length of the spinal cord. Sections were rehydrated in PBS for 10 min at RT, followed by blocking in 3% mouse serum in PBS overnight at 4°C. Sections were thrice washed in PBS (5 min per wash) and incubated with rabbit anti-human CD8 primary antibody (stock diluted 1:200 – Table 2.2) and/or goat anti-mouse/human Iba-1 primary antibody (0.5 mg/mL stock diluted 1:300) in 3% mouse serum in PBS for 2 hours at 4°C. A rat IgG isotype primary (Abcam, #ab27478) was used to confirm the specificity of the secondary antibody binding to anti-human CD8. Sections were then thrice washed and incubated with AlexaFluor 680-conjugated donkey anti-rabbit IgG secondary antibody (2 mg/mL stock diluted 1:600) or DyLight594-conjugated mouse anti-goat IgG secondary antibody (1 mg/mL stock diluted 1:300) in 3% mouse serum in PBS for 2 hours at 4°C. Sections were thrice washed with PBS then incubated for 20 min at RT in PBS containing 0.2% Triton X-100 (PBT solution). CNS sections were incubated 20 min at RT in a PBT master mix containing FluoroMyelin™ Green, NeuroTrace™ 530/615 and diamidino-2-phenylindole (DAPI) (BrainStain™ Imaging Kit, Invitrogen #B34650). Sections were then thrice washed in PBT (15 min per wash) to remove excess stain. Slides were mounted with ProLong™ Diamond Antifade Mountant medium (Invitrogen, # P36961), sealed, allowed to cure for 24 hours at room temperature, and then stored at 4°C until imaged.

2.9.2 Demyelination

Perfused, intact spinal cords collected for analysis of myelination were stored in 10% NBF overnight at RT, then moved to 70% ethanol and sent to Wax-it Histology Services Inc. for paraffin embedding. To quantify myelination throughout the organ, a total of 6 – 9 consecutive 10-µm coronal sections were taken from of 4 – 6 equally distanced regions along the length of the spinal cord using a Shandon Finesse 325 microtome (Thermo Scientific). Sections were mounted on

Superfrost Plus microscope slides (Fisher Scientific, #12-550-15), dried at 37°C for one hour, and then air dried overnight at RT. Sections were washed in 3 changes of xylene for 10 minutes each, then treated in 3 changes of absolute ethanol for 3 minutes each and hydrated in 95% ethanol for 5 minutes. Slides were incubated in eriochrome cyanine R (Sigma-Aldrich, #3564-18-9) staining solution (0.22% w/v ferric chloride, 0.5% v/v sulfuric acid and 0.2% w/v eriochrome cyanine R CI 43820) for 20 minutes, run under tap water for 30 seconds, and incubated in differentiating solution (5.6% w/v ferric chloride) for 5 – 10 minutes until only the white matter retained the stain. Slides were washed under running tap water for 5 minutes, then dehydrated in 3 changes of 100% ethanol for 30 seconds each (with agitation) and cleared in 3 changes of xylene for 30 seconds each (with agitation). Coverslips were mounted with VectaMount Permanent Mounting Medium (Vector Laboratories, #H-5000).

2.9.3 Imaging and analysis

Histology sections were imaged using a Zeiss Axio Observer 7 epi-fluorescent microscope outfitted with a motorized stage (x, y, z mobility) and five LED channels. Whole organ immunofluorescent sections were imaged at x20/0.65 NA air objective using an Axiocam 702 mono CMOS camera at room temperature. Isotype staining was used to set LED voltages and exposures across slides per imaging experiment. Immunofluorescent images were stitched and Z-stack (3 stacks of 1.2 µm each) fusion was performed using a wavelet transform in Zen2.6 Pro (blue edition, Zeiss). Brightfield images of EC-stained spinal cord sections were acquired at 10X/0.3 NA air objective magnification using an Axiocam 105 colour CMOS camera. Stitching and subsequent analysis of images was performed using Zen 2.6 Pro. For EC sections, single RBG images were saved as JPEG files and quantitative analysis of staining was performed using ImageJ 1.53c (NIH). Default color thresholding method was used to first select the area of stained myelin and then the total area of the spinal cord. Hue, saturation, and brightness thresholds were set based on fully myelinated NSG control sections and applied across all other sections. The Area measurement function was used to acquire the area of the selected regions in μm^2, relative to a 200-µm scale bar. Myelination was expressed as fraction of myelin-stained area of total area of the spinal cord section. Replicate sections (6 – 9 consecutive sections per region) were averaged to generate 4 – 6 regional myelination indices (MI) per spinal cord.

2.10 Flow cytometric analysis

2.10.1 Sample processing

Brains, spinal cords, and spleens were kept in sterile PBS on ice, then processed into single cell suspensions by passing the tissue through a 70-µm cell strainer with a sterile syringe insert. Splenocyte suspensions were incubated in red blood cell (RBC) lysis buffer (150 mM NH_4Cl, 10 mM $KHCO_3$, 0.1 mM Na_2-EDTA) for 10 min on ice. Whole EDTA-treated blood samples were incubated in pre-warmed red blood cell lysis buffer for 15 min at RT. Brain and spinal cord samples specifically processed for the detection of intracellular MBP within phagocytic cells were predigested with 0.5 mg/mL Collagenase/Dispase® (Roche, #11097113001), 0.02 mg/mL DNase I (Sigma-Aldrich, #D5025) and 2% FBS in 10 mL RPMI per sample for 45 min shaking at 180 rpm and 37°C. CNS cells were further isolated by resuspension in 40% isotonic Percoll™ solution (Cytiva, #17089101) and centrifugation (15 min at 1400 rpm) to remove lipid debris. Samples analyzed for cytokine expression were incubated at 37°C (5% CO_2) for 4 hours at 1 – 2×10^6 splenocytes or total isolated CNS cells per 200 µL of stimulation media, containing 10% FBS, 10 ng/mL phorbol 12-myristate 13-acetate (PMA, Sigma-Aldrich, #P1585), 500 ng/mL ionomycin (Thermo Fisher, #I24222) and 1 µL/mL GolgiPlug™ Protein Transport Inhibitor (containing Brefeldin A, BD Biosciences, #555029) in minimum essential medium (MEM, Gibco, #11095-080). Cell suspensions were washed between each step with sterile PBS containing 2% FBS (FACS buffer).

2.10.2 Cell sorting and co-culture

For interspecies antigen presentation assays, splenocytes were isolated from female HD PBMC-engrafted male NSG (n = 4) and B6-TKO mice (n = 5) at 4 weeks post-injection, as described above. Splenocytes from the same background strain were combined to generate two suspensions, which were each stained with fluorochrome-labelled anti-mCD45, anti-hCD4, and anti-hCD8 antibodies (Table 2.2) and positively selected using a BD Influx™ cell sorter. For mCD45: hCD8 co-culture wells, sorted cells were resuspended to 3 – 4×10^4 $mCD45^+$ cells with 3 – 4×10^5 $hCD8^+$ cells (1:10 ratio) per well in 200 µL complete tissue culture medium (RPMI-1640 plus FBS, L-glutamine, penicillin/streptomycin, MEM NEAA, sodium pyruvate, HEPES, β-mercaptoethanol), supplemented with or without 20 µg/mL rhMOG protein. For mCD45: hCD4 co-culture wells, sorted cells were resuspended to 3 – 7×10^4 $mCD45^+$ cells with 3 – 7×10^5 $hCD4^+$

cells (1:10 ratio) per well in 200 µL complete tissue culture medium supplemented with or without 20 µg/mL MOG_{35-55} peptide. All wells were incubated for 65 hours at 37°C (5% CO_2). Cells were then refreshed with pre-warmed culture medium (with same respective rhMOG or MOG_{35-55} media treatments) containing 1 µL/mL GolgiPlug™ Protein Transport Inhibitor and incubated for another 5 hours at 37°C (5% CO_2). Following 70 hours total incubation time, cells were washed with serum-free PBS and stained for flow cytometric analysis as described below.

2.10.3 T cell bead stimulation assay

Donor PBMC samples previously stored in autologous plasma with 10% dimethyl sulfoxide were thawed from liquid nitrogen for activation analysis. Total PBMCs (5 x 10^6 cells/ mL) were stained with 2.5 µM carboxyfluorescein succinimidyl ester (CFSE, Sigma #21888-25MG-F) in the dark at 4°C for 8 minutes prior to quenching with newborn calf serum. An unstimulated and PMA/ionomycin-stimulated subset of each sample was analyzed for baseline marker expression (PMA stimulation conditions described above under 'sample processing'). Duplicate wells of 200,000 CFSE-stained cells per sample were then incubated for 91 hours at 37°C (5% CO_2) at a 1:2 bead-cell ratio with Human T-Activator CD3/CD28 DynaBeads™ (Thermo Fisher, #11161D) and 1 U/mL of recombinant human IL-2 (BioLegend, #589102) in 200 µL of complete culture medium (see above for media components). The media did not contain any factors to specifically influence polarization or activation. Cells were then refreshed with pre-warmed culture medium containing 1 µL/mL GolgiPlug™ Protein Transport Inhibitor and incubated for another 5 hours at 37°C (5% CO_2). Following 96 hours total incubation time, cells were washed with serum-free PBS and stained for flow cytometric analysis as described below.

2.10.4 Antibody and tetramer staining and analysis

Cells were stained with 1X eBioscience™ Fixable Viability Dye eFluor™ 506 (Thermo Fisher, #65-0866-14) for 20 min at 4°C in serum-free PBS. Cells were then washed in FACS buffer, and preincubated with human and mouse Fc block (Table 2.2) in FACS buffer for 10 minutes at RT. For detection of epitope specific $CD4^+$ T cells, MHC class II tetramers, provided by the NIH Tetramer Core Facility at Emory University, were incubated with the cell suspensions for 3 hours at RT at a 1:300 dilution (4 – 4.5 µg/mL) in FACS buffer (Table 2.3). Cells were washed again and incubated with fluorochrome-labelled antibodies specific to extracellular makers

(Table 2.2) in FACS buffer for 30 minutes at 4°C. Cells were washed and treated with transcription factor fixation and permeabilization reagent (Thermo Fisher, #00-5521-00) for 30 min at 4°C, followed by a wash with permeabilization buffer (Thermo Fisher, #00-8333-56). Cells were incubated with fluorochrome-labelled antibodies specific to intracellular makers (Table 2.4) in permeabilization buffer for 30 min at RT. Cells were washed with permeabilization and FACS buffer and resuspended in FACS buffer with 2 mM EDTA for acquisition. Frozen human PBMC samples were stained as detailed above for use as titration, compensation, and gating controls for all experiments. Stained cell suspensions were acquired on an Attune NxT flow cytometer (Thermo Fisher) and analyzed using FlowJo™ v10.8 Software (BD Life Sciences).

2.11 Serology

Endogenous antibodies to EBV, CMV, and rhMOG were detected using indirect enzyme-linked immunosorbent assays (ELISA). Nunc Maxisorp 96-well microtiter ELISA plates (Thermo Fisher, #439454) were coated overnight at 4°C with 1 μg/well of the peptide or protein of interest (Table 2.5, produced by ScenicBio) in 0.05 M carbonate buffer. For EBV EBNA-1 and CMV, epitope peptides 1 and 2 were mixed prior to well coating. The following day, the plates were washed thrice with PBS and wash buffer (PBS + 0.05% Tween-20), followed by a two-hour blocking step at RT using wash buffer + 3% bovine serum albumin. Plates were washed again, then incubated with serum samples serially diluted in blocking buffer to generate duplicate 6-point curves (1:100 – 1:5000 for human donor serum and 1:50 – 1:2500 for mouse serum). After a two-hour RT incubation with serum dilutions, the plates were washed, then incubated with HRP-labelled anti-human IgG antibody (Table 2.2) diluted 1:3000 in blocking buffer, or HRP-labelled anti-human IgM diluted 1:4000, for 1 hour at 37°C. The plates were then washed with PBS prior to the addition of 100 μL/well TMB substrate (BD Biosciences, #555214). Fifteen minutes after the addition of substrate, 100 μL stop solution (2 N sulfuric acid) was added to each well. The plates were read at 450 nm on a VarioSkan Plate Reader (Thermo Fisher), or on an Epoch Microplate Spectrophotometer (BioTek), within 10 min of adding stop solution. Donor serum diluted 1:1000 was used to determine seropositivity to EBV and CMV antigens. The lower limit of detection for positive IgG and IgM values was set based on the level of nonspecific background signal in negative control samples (full reaction minus antigen and/or serum). Human donor serum vitamin D levels were quantified using a 25-OH Vitamin D ELISA assay test kit, according to the

manufacturer's instructions (Eagle Biosciences, #VID31-K01). Mouse serum neurofilament levels were determined using a Phosphorylated Neurofilament H (pNF-H) Sandwich ELISA kit with a 1:10 sample dilution, according to the manufacturer's instructions (EMD Millipore, #NS170).

2.12 EBV viral load

Genomic DNA was isolated from a maximum of 4×10^6 donor PBMCs or HuPBMC mouse splenocytes, per sample using the PureLink™ Genomic DNA Minikit (Invitrogen, #K1820), according to the manufacturer's instructions, quantified using a Nanodrop Lite Spectrophotometer (Thermo Scientific, firmware version 1.02), and stored at -80°C. A *BamHI* A left frame transcript 5 (*BALF5*) viral DNA polymerase gene qPCR protocol adapted from Kimura et al. was used to measure EBV load in DNA samples[190]. The forward and reverse primer and fluorogenic probe sequences are listed in Table 2.6 (produced by Integrated DNA Technologies), along with the *BALF5* gene fragment sequence used for standard curve generation. qPCR reactions comprised 300 ng genomic DNA, 0.4 μM each primer, 0.2 μM probe, and 1X QuantiNova Probe PCR master mix (Qiagen, #208256). An EBV^+ B95-8 cell line extract (100 ng per reaction) was used as a positive control for EBV detection. Blank water was used in negative control reactions. An 8-point standard curve was generated with 1 to 10^7 *BALF5* gBlock copies per reaction. Reactions were made up in Mx3000P 96-well plates (Agilent Technologies, #401333) and data were acquired using a CFX96 Real-Time System C1000 Thermal Cycler (Bio-Rad) and CFX manager 3.1 software for HEX detection. The cycler parameters were set according to the Qiagen QuantiNova Probe PCR protocol – 2 min at 95°C to activate DNA polymerase then 45 repeats of 5 sec at 95°C and 5 sec at 60°C. Sample copies per reaction were determined by interpolation of the standard curve using triplicate-averaged reaction threshold values (C_T), which were then used to calculate viral load. The lower limit of detection was determined by interpolating the C_T value for the lowest detectable standard point per plate and was normally ~30 EBV copies/μg DNA.

2.13 Gammaherpesvirus-68

2.13.1 Virion generation and infection of C57Bl/6 mice

Wild type gammaherpesvirus-68 (γHV68, WUMS strain) was purchased from the American Type Culture Collection (ATCC, #VR-1465) and propagated on baby hamster kidney fibroblasts (BHK-21, ATCC, #CCL-10). Virion production and quantification of viral titres was

adapted from[652]. Briefly, γHV68 was produced by infecting BHK-21 cells at 40 – 50% confluence with a multiplicity of infection of 0.1. Two days later, the virion-containing supernatant was collected and concentrated by ultracentrifugation. Viral stocks were quantified using a Vero cell-based plaque assay. C57Bl/6 mice (8 – 12 weeks old) were infected IP with 10^4 plaque forming units (PFU) in 200 µl of MEM or with blank MEM for uninfected controls. Experiments involving γHV68 infections were performed in a biosafety containment level 2 facility. MOG_{35-55} or rhMOG EAE was induced 35 days post-infection to allow for the establishment of latency prior to initiation of CNS autoimmunity.

2.13.2 PCR confirmation of systemic infection

Genomic DNA was isolated from a maximum of 4×10^6 mouse splenocytes (RBC-lysed) using the PureLink™ Genomic DNA Minikit (Invitrogen, #K1820), according to the manufacturer's instructions, quantified using a Nanodrop Lite Spectrophotometer (Thermo Scientific, firmware version 1.02), and stored at -80°C. Infection of splenocytes at EAE endpoint was confirmed by nested PCR for the *ORF50* viral gene[653] using the primer sequences in Table 2.7 (produced by Integrated DNA Technologies) and positive control gBlock, containing the target gene sequence, cloned into a TOPO vector. The first PCR reaction contained 0.4 µM of both the outer forward and reverse primers, 0.16 mM of each dNTP (New England BioLabs, #N0440S – N0443S), 0.6 U of DreamTaq DNA polymerase (Thermo Fisher, #EP0702), and 400 ng genomic DNA in Crimson Taq Reaction buffer (New England BioLabs, #B0324S). Reactions were substituted with 1 µl of blank water as a negative control or *ORF50* gene plasmid for a positive control. A quality control reaction for each genomic DNA sample was also included using housekeeping glyceraldehyde 3-phosphate dehydrogenase (*GAPDH*) gene primers at 0.4 µM (Table 2.8). PCR reactions were completed using a T100™ ThermalCycler (Bio-Rad) and the cycling parameters: 2 min at 94°C, followed by 34 cycle repeats of [1 min at 94°C, 1 min at 62°C, 1 min at 72°C], and 5 min at 72°C. For the second (nested) PCR reaction, 5 µL of the corresponding first reaction PCR products was combined with dNTPs, Taq, and reaction buffer as in the first reaction with 0.4 µM of both the inner forward and reverse primers and incubated using the same cycler parameters. PCR reaction products were electrophoresed through a 2% TAE-agarose gel (FroggaBio Agarose, #A87-G) stained with 1X SYBR Safe DNA gel strain (Invitrogen, #533102), alongside a 100 bp DNA ladder (GeneDirex, #DM001-R500S), using a Bio-Rad PowerPac Basic

system. The expected 293 bp band for *ORF50* and the 248 bp band for *GAPDH* were visualized using the MultiImage Light Cabinet (Alpha Innotech Corp.).

2.14 Software and statistical analyses

Data were collated using Microsoft Excel, then graphed and statistically analyzed using GraphPad Prism software 9.2.0 (GraphPad Software Inc.). Figure panels and graphical illustrations were generated in Adobe Illustrator V24.3 and/or BioRender (license #2959-1014). Most graphs present group means with standard error (SEM) or standard deviation (SD) unless otherwise stated in the figure legend. No inclusion or exclusion criteria were used for analyses and groups include all mice from the cohort regardless of the incidence of clinical EAE symptoms, unless otherwise stated. Two normally distributed groups of data were analyzed by two-tailed, unpaired t-test with Welch's correction. For three or more groups, normally distributed data were analyzed by ordinary one-way analysis of variance (ANOVA) with Tukey's multiple comparisons test or Brown-Forsythe and Welch ANOVA with Dunnett's T3 multiple comparisons test. If group data did not pass the Kolmogorov–Smirnov normality test (or Shapiro-Wilk test when group N too small to compute KS distance), a nonparametric Mann-Whitney test or Kruskal-Wallis with Dunn's multiple comparisons test was used. A Log-rank (Mantel-Cox) test was used for incidence curve analysis, simple linear regression analysis for cell count correlations, and ordinary two-way ANOVA for group comparisons with two variables (i.e., EAE scores over time and ELISA absorbance readings with serum dilution), where the column factor p value is reported. Specific statistical tests used for each assay are noted in the figure legends, along with the number of animals or replicates per group. Significance is indicated by asterisks: ****$p<0.0001$, ***$p<0.001$, **$p<0.01$, and *$p<0.05$.

2.14.1 Determination of group sizes

In order to determine the group sizes for EBV^- HD, EBV^+ HD, and EBV^+ RRMS donors (number of volunteers to enrol) for the analysis performed in chapter 5, we employed a resource equation approach. A full power analysis to determine the number of donors to evaluate per group could not be performed prior to initiation of this study, as the potential clinical and immunological outcomes that differed, as well as the size and relevance of those differences, between HuPBMC EAE mice humanized with PBMCs from $EBV^{+/-}$ and/or RRMS donors were yet unknown in this

new model. Compared to typical murine models, there is additional variability between donors independent of EBV status (genetics, history of exposures, etc.), as well as variability between mice within a cohort engrafted with the same donor PBMC due to differential reconstitution of immune cell subsets. As such, we opted not to use a power analysis at this early stage of model development and testing to determine the number of donors to enrol.

Based on the resource equation, to obtain E = 10 – 20 (degrees of freedom in ANOVA), the total experimental units minus the number groups should fall between 10 and 20. On the upper limit of E = 20, with 3 donor groups: total number of donors is 20 – 3 = 17 donors, split between 3 groups gives ≅ 6 donors/group. For the lower limit of E = 10, with 3 donor groups: total number of donors is 10 – 3 = 7 donors, split between 3 groups gives ≅ 2 donors/group. Therefore, our best estimate at this stage was to enrol 2 – 6 blood donors/group. Ultimately, we were able to enrol 3 EBV^- HD, 4 EBV^+ HD, and 4 EBV^+ RRMS female donors for the experiments in chapter 5 (E = 14). Given that human PBMC and HSC yield per donor limited recipient cohort size, no statistical methods were used to predetermine humanized mouse group numbers in any of the chapters.

Table 2.2 Antibodies for extracellular targets

Target antigen	Clone	Species reactivity	Application	Source	Identifier
CD3	OKT3	Human	Flow cytometry	Thermo Fisher	56-0037-42
CD3ε	eBio500A2	Mouse	Flow cytometry	Thermo Fisher	48-0033-82
CD4	RPA-T4	Human	Flow cytometry	BD Biosciences	555347
CD4	RPA-T4	Human	Flow cytometry	Thermo Fisher	47-0049-42
CD4	RM4-5	Mouse	Flow cytometry	Thermo Fisher	45-0042-82
CD4	RM4-5	Mouse	Flow cytometry	Thermo Fisher	11-0042-85
CD4	RM4-5	Mouse	Flow cytometry	Thermo Fisher	56-0042-82
CD4	RM4-5	Mouse	Flow cytometry	Thermo Fisher	64-0042-82
CD8	SP16	Human	IHC-F	Thermo Fisher	MA5-14548
CD8	RPA-T8	Human	Flow cytometry	Thermo Fisher	11-0088-42
CD8	RPA-T8	Human	Flow cytometry	BD Biosciences	563821
CD8α	53-6.7	Mouse	Flow cytometry	Thermo Fisher	12-0081-82
CD8α	53-6.7	Mouse	Flow cytometry	BioLegend	100762
CD11b	M1/70	Mouse	Flow cytometry	Thermo Fisher	17-0112-82
CD11c	N418	Mouse	Flow cytometry	Thermo Fisher	11-0114-85
CD14	63D3	Human	Flow cytometry	BioLegend	367142
CD14	61D3	Human	Flow cytometry	Thermo Fisher	11-0149-42
CD19	HIB19	Human	Flow cytometry	Thermo Fisher	47-0199-42
CD19	eBio1D3	Mouse	Flow cytometry	Thermo Fisher	12-0193-82
CD20	2H7	Human	Flow cytometry	BioLegend	302328
CD21	HB5	Human	Flow cytometry	Thermo Fisher	12-0219-42
CD25	CD25-4E3	Human	Flow cytometry	Thermo Fisher	11-0257-42
CD25	BC96	Human	Flow cytometry	Thermo Fisher	45-0259-42
CD25	PC61.5	Mouse	Flow cytometry	Thermo Fisher	47-0251-82
CD27	LG.3A10	Human/Mouse	Flow cytometry	BioLegend	124216
CD34	4H11	Human	Flow cytometry	Thermo Fisher	17-0349-42
CD38	HIT2	Human	Flow cytometry	BioLegend	303529
CD38	HIT2	Human	Flow cytometry	Thermo Fisher	12-0389-42
CD40	3/23	Mouse	Flow cytometry	Thermo Fisher	MA5-17855
CD44	IM7	Human/Mouse	Flow cytometry	BioLegend	103012
CD45	HI30	Human	Flow cytometry	Thermo Fisher	MHCD4517
CD45	HI30	Human	Flow cytometry	BD Biosciences	557748
CD45	30-F11	Mouse	Flow cytometry	Thermo Fisher	45-0451-82

CD45	30-F11	Mouse	Flow cytometry	Thermo Fisher	48-0451-82
CD45	30-F11	Mouse	Flow cytometry	Thermo Fisher	56-0451-82
CD45RA	HI100	Human	Flow cytometry	Thermo Fisher	48-0458-42
CD56	TULY56	Human	Flow cytometry	Thermo Fisher	17-0566-42
CD90 (Thy-1)	ebio5E10	Human	Flow cytometry	Thermo Fisher	45-0909-42
CD137	4B4-1	Human	Flow cytometry	BioLegend	309818
CD154 (40L)	24-31	Human	Flow cytometry	BioLegend	310823
F4/80	BM8	Mouse	Flow cytometry	Thermo Fisher	47-4801-82
F4/80	BM8	Mouse	Flow cytometry	Thermo Fisher	25-4801-82
Fc receptor (CD16/CD32)	2.4G2	Mouse	Flow cytometry	BD Biosciences	553142
Fc receptor	Fc1.3216	Human	Flow cytometry	BD Biosciences	564220
HLA-DR	L243	Human	Flow cytometry	Thermo Fisher	17-9952-42
Iba-1	Polyclonal	Mouse	IHC-F	Thermo Fisher	PA5-18039
IgG (H+L)	Polyclonal	Goat	IHC-F	Jackson ImmunoResearch	205-585-108
IgG (γ chain)	Polyclonal	Human	ELISA	Thermo Fisher	62-8420
IgG (H+L)	Polyclonal	Rabbit	IHC-F	Thermo Fisher	A10043
IgG2b	m2b-25G4	Mouse	Flow cytometry	Thermo Fisher	11-4220-82
IgM (μ chain)	Polyclonal	Human	ELISA	Thermo Fisher	A18841
Lineage cocktail	Multiple	Human	Flow cytometry	BioLegend	348801

Table 2.3 MHC Class II I-A^{g7} tetramers

Antigen	**Peptide sequence**	**Format**	**[Stock] (mg/ml)**	**[Staining] (μg/mL)**
$OVA_{141-160}$	CARELINSWVESQTNGIIRN	APC	1.41	4.65
MOG_{42-55}	SPFSRVVHLYRNGK	PE	1.39	4.59
PLP_{56-70}	DYEYLINVIHAFQYV	BV421	1.21	3.99
MBP_{74-85}	SRPGLCHMYKDS	BV421	1.22	4.03
MBP_{73-92}	RSRPGLCHMYKDSHTRTTHY	BV421	1.24	4.09
$CLIP_{87-101}$	PVSKMRMATPLLMQA	PE	1.38	4.55
$CLIP_{87-101}$	PVSKMRMATPLLMQA	APC	1.40	4.62
$CLIP_{87-101}$	PVSKMRMATPLLMQA	BV421	1.18	3.89

Table 2.4 Antibodies for intracellular targets

Target antigen	Clone	Species reactivity	Application	Source	Identifier
CD68	Y1/82A	Human	Flow cytometry	BioLegend	333825
EOMES	WD1928	Human	Flow cytometry	Thermo Fisher	11-4877-41
FOXP3	236A/E7	Human	Flow cytometry	Thermo Fisher	17-4777-42
FOXP3	FJK-16S	Mouse	Flow cytometry	Thermo Fisher	11-5773-82
Granzyme B	QA16A02	Human/Mouse	Flow cytometry	BioLegend	372214
IFNγ	4S.B3	Human	Flow cytometry	Thermo Fisher	48-7319-42
IFNγ	XMG1.2	Mouse	Flow cytometry	Thermo Fisher	45-7311-82
IL-17A	eBio64DEC17	Human	Flow cytometry	Thermo Fisher	25-7179-42
IL-17A	TC11-18H10.1	Mouse	Flow cytometry	BioLegend	506938
IL-17A	eBio17B7	Mouse	Flow cytometry	Thermo Fisher	17-7177-81
Ki-67	Ki-67	Human	Flow cytometry	BioLegend	350516
MBP	MBP101	Mouse	Flow cytometry	Abcam	ab62631
RORγt	AFKJS-9	Human	Flow cytometry	Thermo Fisher	12-6988-80
T-bet	4B10	Human	Flow cytometry	Thermo Fisher	45-5825-82
TNFα	MAb11	Human	Flow cytometry	Thermo Fisher	17-7349-82
TNFα	MP6-XT22	Mouse	Flow cytometry	Thermo Fisher	416-7321-82
TNFα	MP6-XT22	Mouse	Flow cytometry	BioLegend	506324

Table 2.5 Antigen sequences for endogenous antibody detection by ELISA

Antigen	Sequence
EBV VCA p18[201]	ASAGTGALASSAPSTAVAQSATPSVSSSISSLRAATSGATAAAAVDTGS GGGGQPHDTAPRGARKKQ
EBV EBNA-1[201]	Epitope 1: RSPSSQSSSSGSPPRRPPPGRRPFFHPVG
	Epitope 2: DYFEYHQEGGPDGEPDVPPGAIEQGPADDPGEGPSTGPRG
rhMOG$_{(1-120)}$[149]	MASLSRPSLPSCLCSFLLLLLLQVSSSYAGQFRVIGPRHPIRALVGDEVE LPCRISPGKNATGMEVGWYRPPFSRVVHLYRNGKDQDGDQAPEYRG RTELLKDAIGEGKVTLRIRNVRFS
CMV pp28 (UL99)[654]	CETDDLDEEDTSIYLSPPPVPPVQVVAKRLPRPDTPRT
CMV pp150 (UL32)[654]	KSGTGPQPGSAGMGGAKTPSDAVQNILQKIEKIKNTEE

Table 2.6 DNA sequences for EBV *BALF5* qPCR assay

Component	Sequence (5' to 3')
Primer P1[190]	CGGAAGCCCTCTGGACTTC
Primer P2[190]	CCCTGTTTATCCGATGGAATG
Probe P3[190]	/5HEX/TGTACACGC/ZEN/ACGAGAAATGCGCC/3IABkFQ/
BALF5 gene standard (gBlock)	ACC GAG ACC CGG CAG GGG GTC CTG CGG TCG AAG GTG CTG GCC TTG AGG GCG CTG AGG ACT GCA AAC TCC ACG TCC AGA CCC TGA GGC GCG CTG GCG TAG AAG TAG GCC TGC TGC CCA AAC ACG TTC ACA CAC ACG CTG GCC CCA TCG GCC TTG CGC CGG CCC AGT AGC TTG ATG ACG ATG CCA CAT GGC ACC ACA TAC CCC TGT TTA TCC GAT GGA ATG ACG GCG CAT TTC TCG TGC GTG TAC ACC GTC TCG AGT ATG TCG TAG ACA TGG AAG TCC AGA GGG CTT CCG TGG GTG TCT GCC TCC GGC CTT GCC GTG CCC TCT TGG GCA CGC TGG CGC CAC CAC ATG CCC TTT CCA TCC TCG TCA CCC CCC ACC ACC GTC AGG GAG TCT TGG TAG AAG CAC AGG GGG GGC TGA GGC CCC CGC ACA TCC ACC ACC CCT GCG GCG CCT GGT GTC TGG AAA CAC TTG GGA ATG AGAC GCA GGT ACT CCT TGT CAG GCT TTT TC

Table 2.7 DNA sequences for gammaherpesvirus-68 *ORF50* PCR assay

Component	Sequence (5' to 3')
Outer forward primer	GATGGAAACAGAAAACGAGCCC
Outer reverse primer	TCGCTTGTTTCTGGGGAGGTTT
Inner forward primer	AAAAGTTCTGCATCCCAGACCC
Inner reverse primer	AGGGCTAATGGGTGAAAATGGC
ORF50 gene standard (gBlock) GenBank: U97553.2	TTT ATC AGC ACG CCA TCA ACA TCC CAC CAG ACT GTG TAC CCA GCT GTA CTA TTG GAG ATG GAA ACA GAA AAC GAG CCC CCC ACG GTT CGC TAT ACA GTA AAG ACA TAT CCT CAC AAA AGT TCT GCA TCC CAG ACC CCC TGT TTG CTT CTC CCA CAG AAC CAG GGT TGG GGG AGT TGC ATA GGG GTA ATA TGG CAC ATT TGC TGC AGA ACC CAG AAG AAA TCA TTA ACC TGG ACC CTC TAC ACA ATA CCA CTG AAC CCT GTT TGT ATC AAA TGT TTT CAG AGG CGG TGA CAA ACC CCT CTA AAA AAA GAT GGC TTT CTT CTT TCA ACA TGG TCT TTT CAG GAC TGT CTC CGA GAG CTC GGC CAG AGA CCA CTT ATG AAC CAT TGG GGC CAT TTT CAC CCA TTA GCC CTG GCC CTT CTT CCG CCA CAG AAG AGT TCC AGT TTG AAT TTA GCC CTT CTC CTC AAA CCT CCC CAG AAA CAA GCG AGC AGA GCT ACA TAC CTA CT

Table 2.8 DNA sequences for *GAPDH* PCR assay

Component	Sequence (5' to 3')
Forward primer	GTGTTCCTACCCCCAATGTGT
Reverse primer	ATTGTCATACCAGGAAATGAGCTT

Chapter 3 – Modeling autoimmune multiple sclerosis in mice with humanized immune systems

3.1 Rationale

Although rodents share approximately 85% gene homology with humans, species specific divergence can present issues for disease modeling and performing preclinical drug testing for therapies that are highly target specific, such as antibodies, which often require NHP models to achieve sufficient homology[432,655]. In February 2022, the U.S. Food and Drug Administration advised that due to a shortage of NHPs resulting from the COVID-19 pandemic, preclinical drug testing should aim to reduce NHP usage in favor of appropriate alternative models "e.g., species-specific surrogates in rodents, genetically modified rodents, when scientifically justified." To do so, however, representative disease models must be developed in laboratory rodents. Humanized EAE mouse models could address multiple limitations of human-specific environmental and genetic components absent from animal homologues used in preclinical MS studies, though EAE induction in humanized mice leading to clinical symptoms has not yet been reported[50,602,643,644]. Various HIS humanized mouse models have been developed, each with their respective benefits, uses, and limitations[434,465].

To address different aspects of EBV infection and other human-specific risk factors in MS, we aimed to induce EAE in adult donor immune cell engrafted and/or HSC-reconstituted mice. The former humanization method would be used to determine the effect of donor PBMC history of naturally occurring endogenous EBV infection on MS-like disease outcomes with genetic variability and other risk factors at play. HuPBMC mice are easy to generate, are cost-effective, and can be personalized for individual analyses based on the donor's medical history, such as an MS diagnosis. They are limited, however, in terms of the short experimental window before clinical xGvHD onsets[505]. Genetic variability in this model conferred by donor PBMCs is advantageous in that an effect consistently observed with multiple donor cohorts is more likely to represent a broad effect within a population that is not specific to only a few individuals.

The latter humanization methods, involving HSC engraftment, would be used to normalize immunophenotype and donor genetics to introduce EBV exogenously as an isolated variable and assess the specific influence of infection on CNS autoimmunity with a consistent background.

HSC humanized mice (HuHSC and HuBLT) have a longer experimental window, where disease severity, maintenance, and relapses could also be studied over time[429,537]. Moreover, PBMC and HSC reconstituted humanized mouse models differ in their reconstitution of various cell subsets by abundance and tissue distribution, which could influence disease induction. The three models also differ in the complexity and costs of the methods to produce them, which can impact feasibility and utility for future studies. This chapter compares HIS reconstitution and EAE induction in the three main humanized immune system mouse models: HuPBMC, HuHSC, and HuBLT (Table 1.2 – Table 1.4). These tractable experimental models will allow us to explore the interplay of environmental and genetic influences on EBV infection directly during MS-like autoimmune disease.

3.2 Experimental design

For initial assessment of humanized mouse susceptibility to EAE induction, three cohorts of humanized mice were generated using adapted protocols for the HuHSC, HuBLT, and HuPBMC models, described in detail in the methods (Section 2.4). Briefly, HuHSC mice were produced by injecting adult, irradiated NSG or NSG-SGM3 mice intravenously with $CD34^+$ HSCs isolated from fetal liver (Section 2.4.1). HuBLT mice were generated by surgically implanting fetal thymic and liver tissue under the kidney capsule of adult NSG mice, followed by a 3-week recovery period. Post-surgery mice were then irradiated and intravenously injected with autologous liver $CD34^+$ HSCs (Section 2.4.2). To improve human HSC engraftment of the recipient mouse bone marrow and differentiation into T cells, sublethal whole body irradiation is recommended prior to HSC injection[537]. Though irradiation can impact EAE incidence, the reconstitution period delay between irradiation and EAE induction of 10 weeks minimum in HSC-based humanized mouse models is expected to nullify irradiation dependent effects on later EAE susceptibility[656–658]. All HuHSC and HuBLT recipient mice received 1 – 1.4 x 10^5 HSCs each (Table 3.1). The number of injected HSCs has been shown not to significantly impact subsequent reconstitution of total human immune cells and human T cells in the blood as long as each mouse receives between 1 and 5 x 10^5 HSCs[537].

Table 3.1 Humanized mouse model generation

Abbreviations: F, female; M, male; w/o, weeks old.

	HuHSC	**HuBLT**	**HuPBMC**
Date of human tissue donation	2018 March 16	2019 October 30	2018 June 29
Tissue source	Fetal liver tissue (ID XXX102)	Fetal liver and thymus tissue (ID XXX001)	Healthy adult blood donors (HD-01 and HD-03)
Age of donor/tissue	20 weeks gestation	19 weeks gestation	39 and 25 years old
Sex of donor cells	Male	Female	Female
Recipient mice (Strain, sex, age)	• 8 adult mice, 9-10 w/o at irradiation • 2F and 2M NSG-SGM3; 2F and 2M NSG	• Adult mice, 10 w/o at surgery • 5M NSG	• 7-11 w/o at PBMC engraftment • HD-01: 2F and 3M NSG-SGM3; 3F and 4M NSG • HD-03: 3F and 4M NSG-SGM3; 2F and 5M NSG
Number of cells engrafted per mouse	1 x 10^5 $CD34^+$ HSCs	1.35 x 10^5 autologous $CD34^+$ HSCs	5 × 10^6 donor PBMCs

HuPBMC mice were generated by intravenous injection of adult NSG or NSG-SGM3 mice with whole human PBMCs from two healthy blood donors (HD) (Section 2.4.3). Preliminary analysis comparing the survival of different immune cell subsets from the same donor's freshly isolated PBMCs to aliquots of frozen and stored PBMC demonstrated a loss of $CD14^+$ monocytes, $CD8^+$ T cells, and $CD56^+$ NK cells with PBMC freeze-thaw (data not shown). Therefore, for all HuPBMC model generation going forward, freshly isolated PBMCs obtained from blood samples processed within an hour of collection were used to engraft recipient immunocompromised mice to maximize engraftment of all subsets. For the three humanized mouse cohorts described in this chapter, NSG or NSG-SGM3 mice were used as the recipient immunocompromised strains. The NSG mouse (or functional NOD background equivalents like the NOG and NRG) is the most commonly reported background strain used to generate humanized mice and the many NSG variants available through the Jackson Laboratory would enable more extensive humanized EAE model manipulation and investigation in future studies[434,475,659]. One such variant is the NSG-

SGM3, which transgenically expresses human stem cell factor, GM-CSF and IL-3, shown to promote myeloid, B cell, and Treg development in HSC humanized models[479,509]. We therefore also used NSG-SGM3 mice to determine if altered or improved human immune subset reconstitution could impact EAE susceptibility or modify symptom development following HSC or PBMC engraftment. A summary of the donor tissue and humanization parameters for each of the three model cohorts is included in Table 3.1. Individual donor PBMC composition and the number of human PBMCs injected per recipient mouse in each cohort is available in Appendix 1. The humanized mice were then each incubated for the respective model's appropriate period of time before HIS reconstitution of the peripheral blood was assessed and EAE induced.

3.3 Reconstitution of humanized mouse peripheral blood

3.3.1 Donor PBMC composition

Assessment of the efficiency and diversity of human immune cell reconstitution of the peripheral blood of humanized mice was made in comparison to the typical composition of human donor PBMCs (Figure 3.1). For the purposes of clarifying whether human or murine immune cell markers are being described, they are prefaced with either an h- or m-, respectively. For antibodies cross reactive to epitopes for both species, upstream gating on $mCD45^+$ or $hCD45^+$ immune cells first segregated cells by species of origin. Figure 3.2 illustrates the gating scheme used to identify and quantify human immune cell subsets in donor PBMC and humanized mouse tissue samples.

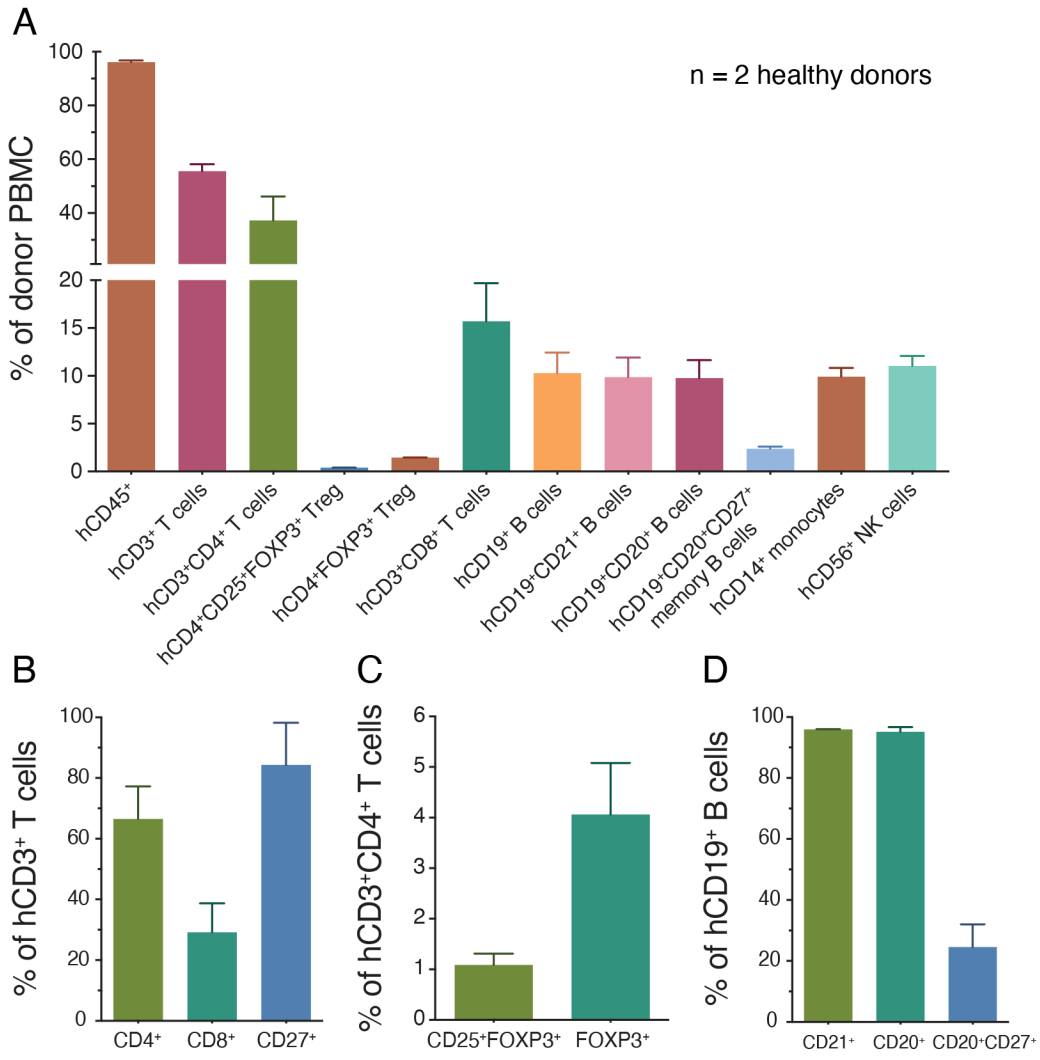

Figure 3.1 Human immune cell composition of healthy blood donor PBMCs

(A) Relative composition of human immune cell lineages in the PBMCs of adult donors as a percentage of total leukocytes immediately after isolation from whole blood. (B) Proportions of T cell subsets among hCD3$^+$ T cells. (C) Proportions of regulatory T cell (Treg) subsets among hCD3$^+$CD4$^+$ T cells. (D) Proportions of B cell subsets among hCD19$^+$ B cells. Data are combined from HD-01 and HD-03 donor PBMC samples and are presented as mean with SEM.

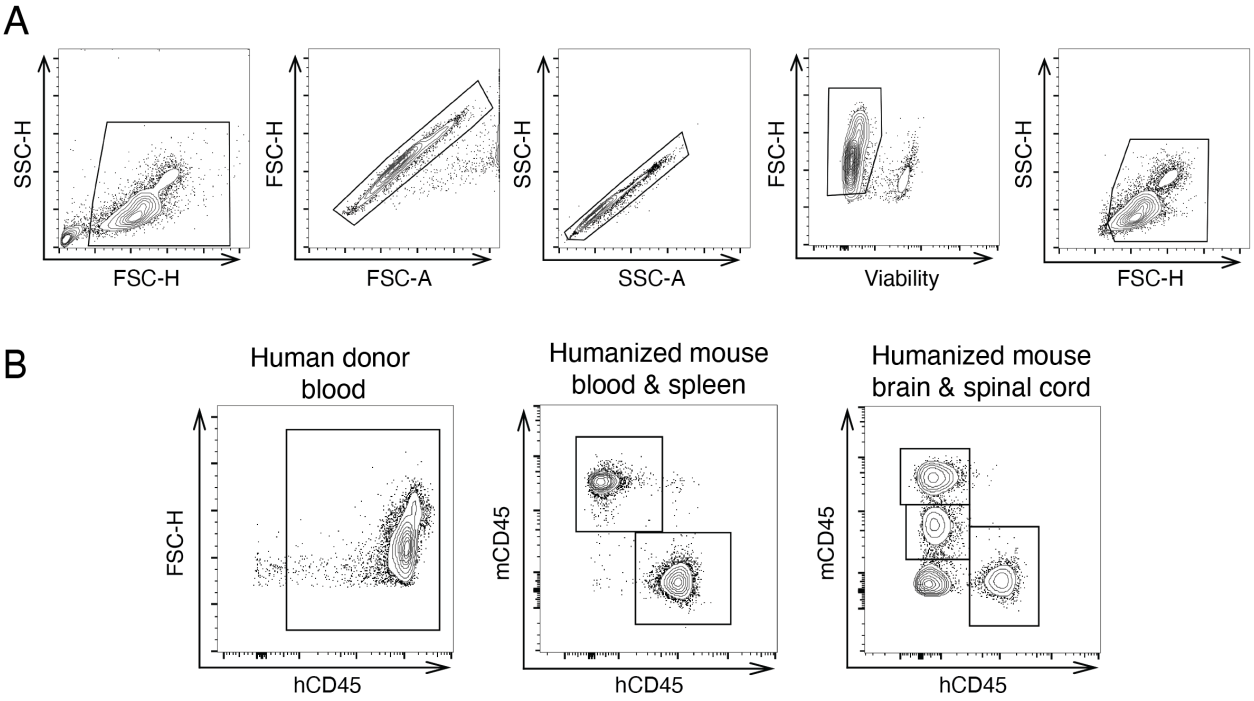

Figure 3.2 Gating strategy for flow cytometric analysis of human immune cells in donor PBMCs and humanized mouse tissues

(A) General cleanup steps applied to all samples. Gates were drawn successively from left to right: exclusion of cellular debris and doublets, by both size and complexity, followed by selection of viable cells and leukocytes. (B) Identification of human (h) and mouse (m) $CD45^{+/hi/lo}$ cell subsets based on source tissue. (C) Major human T cell, B cell, NK cell, and monocyte/ macrophage subsets by marker. CNS tissues were perfused prior to cell isolation. Intracellular staining was performed to detect FOXP3 and CD68 (see Tables 2.2 and 2.4 for complete marker information). The parent population for each representative plot is noted above.

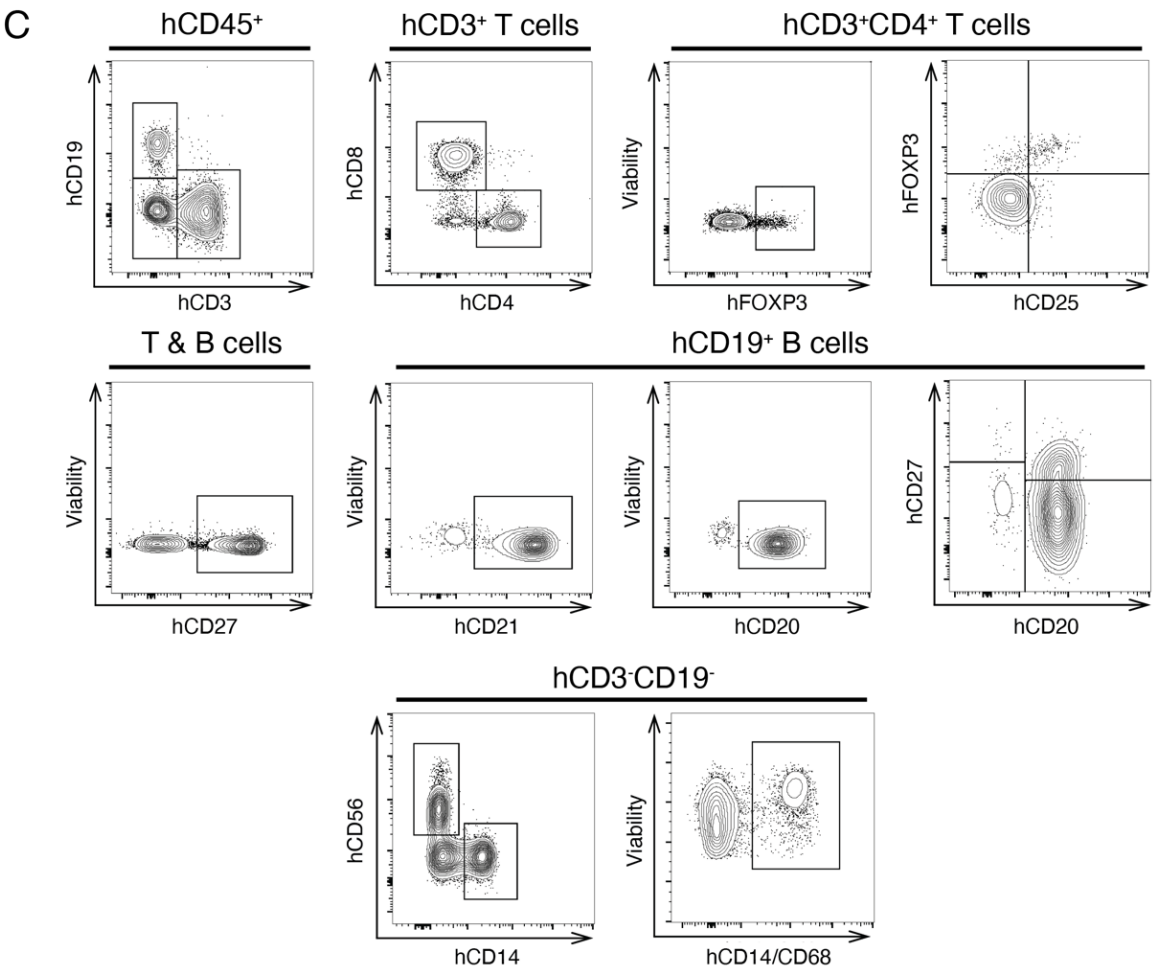

Figure 3.2 continued

3.3.2 HuHSC mice

For the HuHSC cohort, reconstitution of peripheral blood was measured in saphenous vein samples at 15 weeks post-CD34$^+$ HSC injection (Figure 3.3), based on published reports indicating that consistent reconstitution typically occurs after 12 weeks post-injection[429]. See Appendix 4 for CD34$^+$ HSC purity analysis following isolation from fetal liver tissue. Six of eight mice reconstituted to >15% hCD45$^+$ at this timepoint, while the remaining two of eight mice contained ~5% hCD45$^+$ cells (Figure 3.3A). Most of these hCD45$^+$ cells were B cells expressing hCD19 and hCD20 (Figure 3.3B). hCD3$^+$CD4$^+$ T cells and hCD14$^+$ monocytes had secondarily reconstituted (Figure 3.3C). Compared to human donor PBMCs and the HuHSC B cell levels, T cell and NK cell reconstitution in blood was quite low. Among hCD3$^+$ T cells, the relative proportions of hCD4$^+$, hCD8$^+$, and hCD27$^+$ subsets were similar to donor PBMC frequencies (Figure 3.3D),

whereas Treg proportions among hCD3$^+$CD4$^+$ T cells were also similar on average but dichotomously absent or higher than expected (Figure 3.3E). Among hCD19$^+$ B cells, most expressed hCD20 (>85%), similar to donor PBMCs, however, far fewer B cells expressed the markers hCD21 (5 – 50%) and hCD27 (<5%) (Figure 3.3F). To determine if there was a difference between the reconstitution of NSG and NSG-SGM3 mice following HSC engraftment, data were also segregated by recipient strain (Figure 3.4). At 15 weeks post-engraftment in the blood, there was no clear advantage to one strain over the other, though NSG-SGM3 mice may have better hCD3$^+$CD4$^+$FOXP3$^+$ Treg reconstitution than NSG mice and increasing numbers per group may show smaller but significant differences in future cohorts (Figure 3.4E).

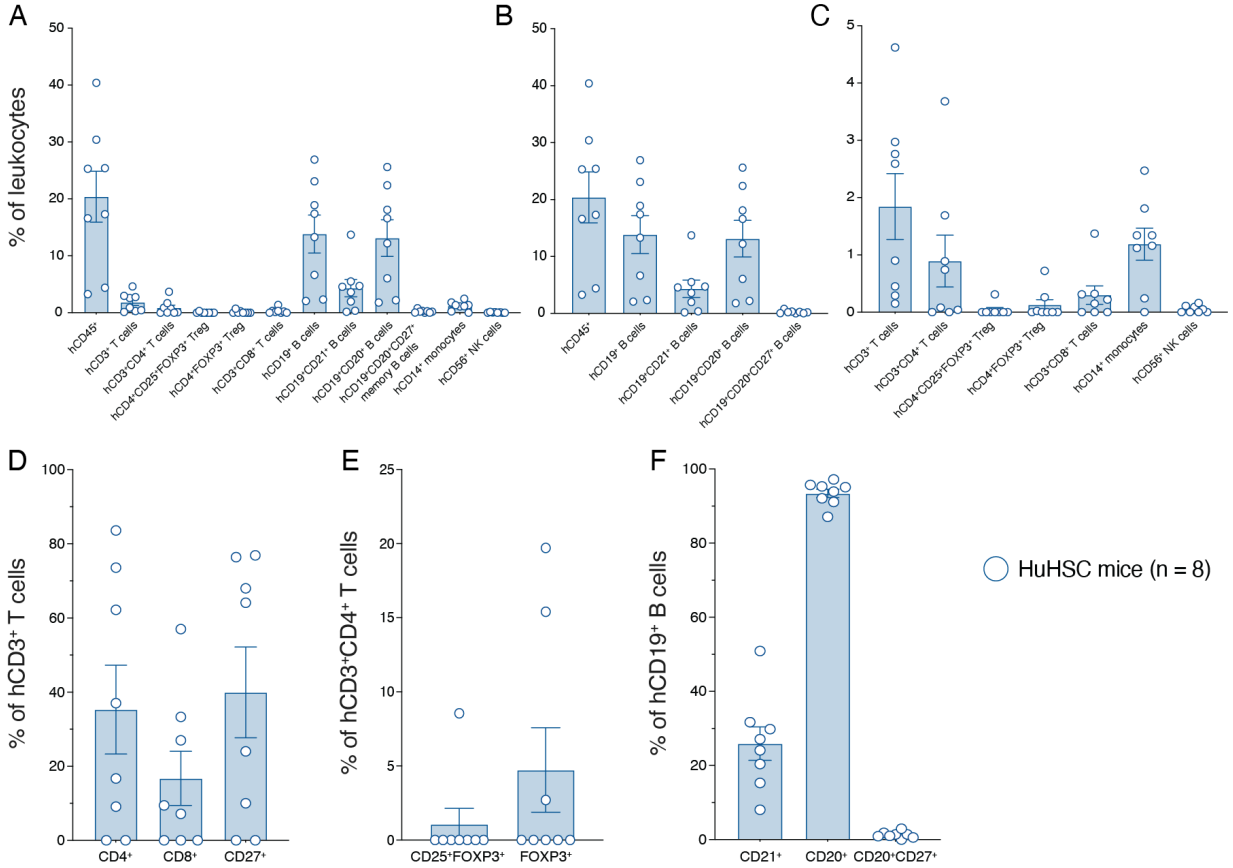

Figure 3.3 Peripheral blood reconstitution of adult HuHSC mice

(A) Relative proportions of all measured human immune cell lineages are shown as a proportion of total leukocytes (murine and human) in peripheral blood at 15 weeks post-HSC engraftment. These data are then subdivided into (B) predominantly engrafted immune cell lineages and (C) minorly engrafted immune cell lineages to better illustrate relative frequencies. (D) Proportions of T cell subsets among hCD3$^+$ T cells. (E) Proportions of regulatory

T cell (Treg) subsets among hCD4$^+$ T cells. (F) Proportions of B cell subsets among hCD19$^+$ B cells. Data are shown as mean with SEM for 8 mice total.

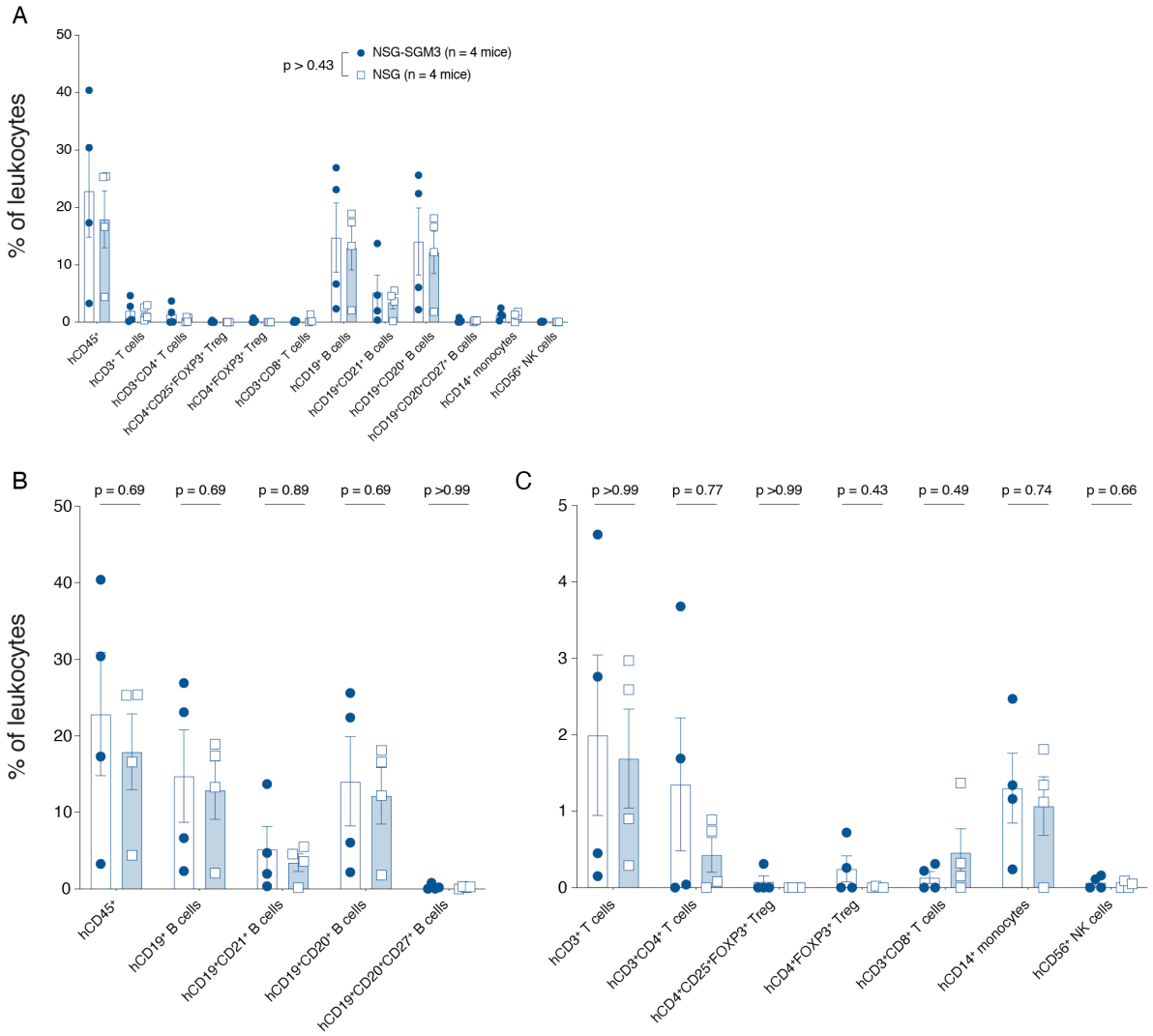

Figure 3.4 Peripheral blood reconstitution of adult HuHSC mice on the NSG and NSG-SGM3 background

(A) Relative proportions of all measured human immune cell lineages are shown as a proportion of total leukocytes (murine and human) in peripheral blood of HSC-engrafted NSG and NSG-SGM3 mice at 15 weeks post-HSC engraftment. These data are then subdivided into (B) predominantly engrafted immune cell lineages and (C) minorly engrafted immune cell lineages to better illustrate relative frequencies. (D) Proportions of T cell subsets among hCD3$^+$ T cells. (E) Proportions of regulatory T cell (Treg) subsets among hCD4$^+$ T cells. (F) Proportions of B cell subsets among hCD19$^+$ B cells. Data are shown as mean with SEM for 4 mice per strain group and were analyzed by Mann-Whitney test.

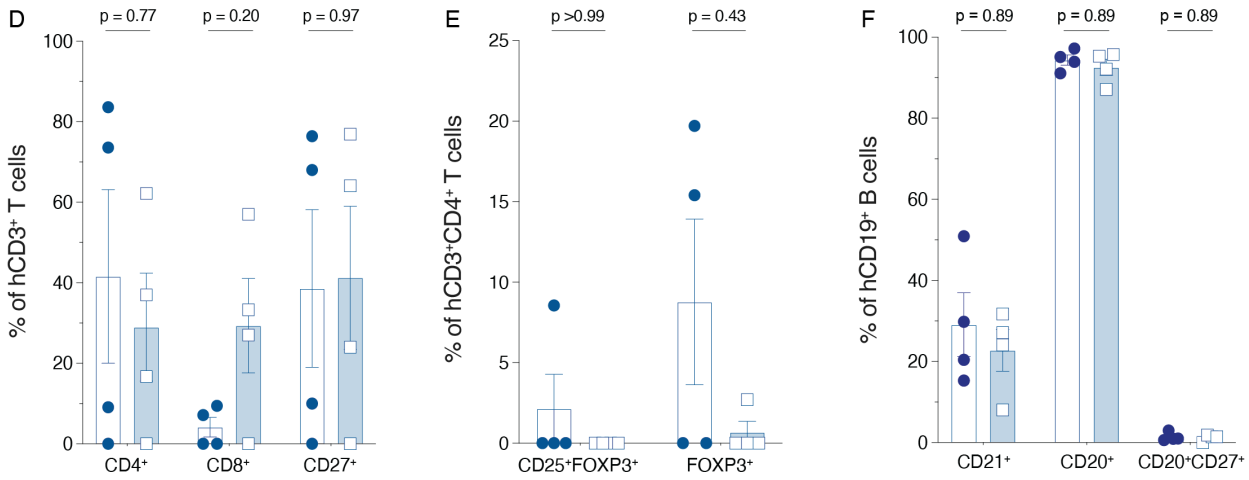

Figure 3.4 continued

3.3.3 HuBLT mice

Analysis of saphenous vein blood samples from five male HuBLT NSG mice (#1002 – 1006) showed that four of five mice reconstituted with 5 – 20% hCD45$^+$ cells at 11 weeks post-HSC engraftment (Figure 3.5). See Appendix 4 for CD34$^+$ HSC purity analysis following isolation from fetal liver tissue. One of the five mice (#1005) did not reconstitute, exhibited low weight, piloerection, and paleness, indicative of radiation-induced illness, and was therefore euthanized. A sixth HuBLT mouse (female #990) from the same donor cohort was included as a reconstitution control to remain uninduced. In terms of relative proportions, reconstitution of major human T cell and B cell subsets (hCD4$^+$, hCD8$^+$, hCD19$^+$, and hCD20$^+$) was very similar to the relative composition of donor PBMCs (Figure 3.6A–C). Within hCD3$^+$ T cells, subset expression of hCD4, hCD8, and hCD27, as well as regulatory T cell marker hCD25 and hFOXP3 expression on hCD4$^+$ T cells, was consistent with donor PBMCs (Figure 3.6D–E). Among hCD19$^+$ B cells, expression of hCD20 as high and consistent with donor PBMCs, however, very few expressed hCD21, the B cell receptor for EBV (Figure 3.6F). Though hCD20$^+$CD27$^+$ dual expressing B cells were present, they composed only half of the B cell population frequency expected for peripheral blood. In contrast to T and B cells, reconstitution of monocytes and NK cells was much lower than in donor PBMCs, each comprising less than the proportion of hCD4$^+$ Treg among total leukocytes (Figure 3.6C).

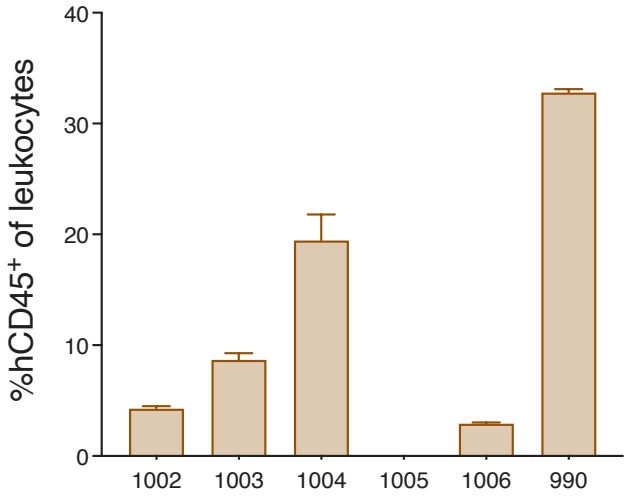

Figure 3.5 Human immune cell reconstitution of HuBLT mouse peripheral blood

The proportion of hCD45$^+$ cells among total leukocytes (murine and human) in peripheral blood at 11 weeks post-HSC engraftment of NSG mice implanted with a fetal thymic and liver tissue organoid. Duplicate samples were analyzed for each sample. Data are shown as mean with SEM.

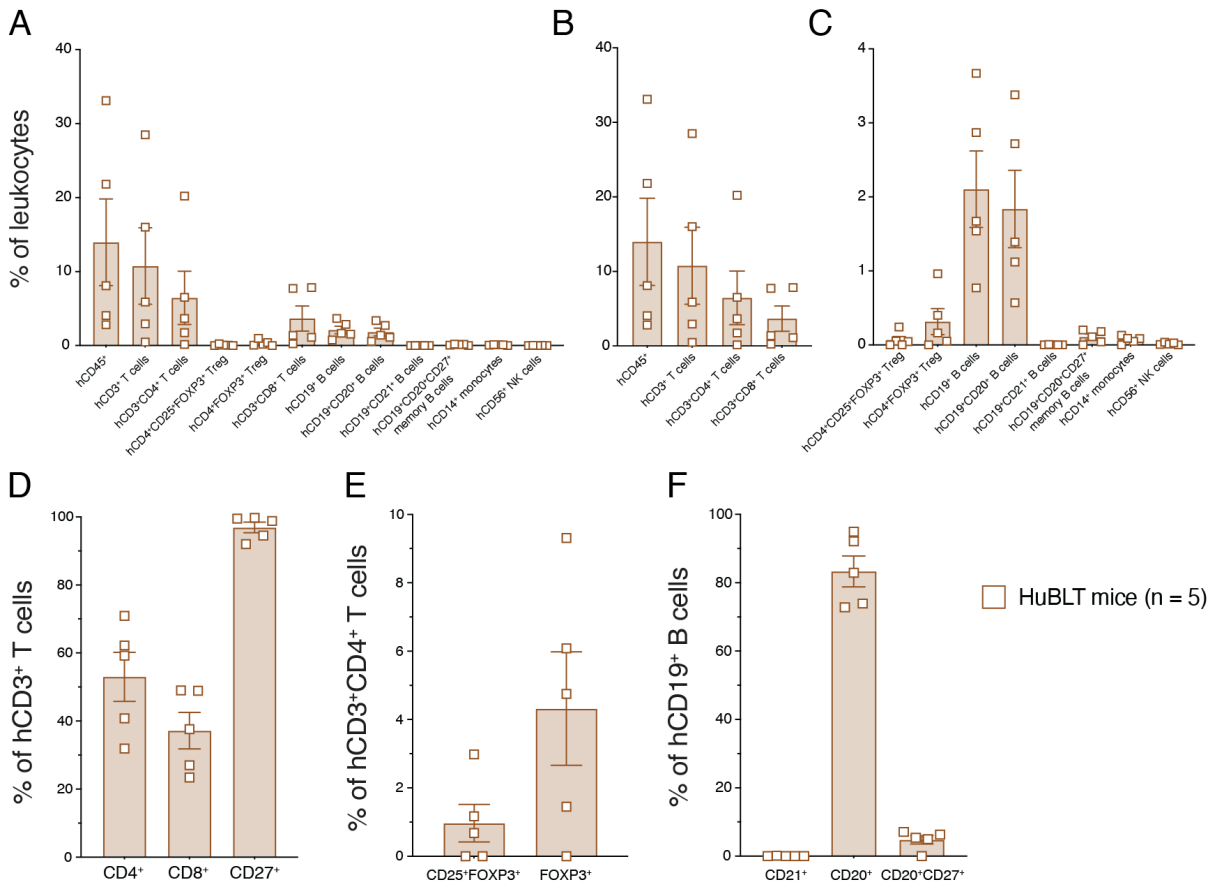

Figure 3.6 Peripheral blood reconstitution of HuBLT mice

(A) Relative proportions of all measured human immune cell lineages are shown as a proportion of total leukocytes (murine and human) in peripheral blood at 11 weeks post-HSC engraftment of NSG mice implanted with a fetal thymic and liver tissue organoid. These data are then subdivided into (B) predominantly engrafted immune cell lineages and (C) minorly engrafted immune cell lineages to better illustrate relative frequencies. (D) Proportions of T cell subsets among $hCD3^+$ T cells. (E) Proportions of regulatory T cell (Treg) subsets among $hCD4^+$ T cells. (F) Proportions of B cell subsets among $hCD19^+$ B cells. Data are shown as mean with SEM for 5 HuBLT mice total (unreconstituted #1005 excluded).

3.3.4 HuPBMC mice

Using a common density gradient separation protocol to isolate PBMCs from approximately 80 mL of donated blood, we obtained 92 x 10^6 cells from HD-01 (1.3 x 10^6 cells/mL) and 142.5 x 10^6 cells from HD-03 (1.78 x 10^6 cells/mL), which were both within the expected range of 1 – 2 x 10^6 cells/mL blood for healthy donors. Each recipient mouse received 5 x 10^6 freshly isolated PBMCs, composed of mainly T cells (2.5 – 3 x 10^6), as well as B cells (4 – 6 x 10^5), monocytes (4.5 – 5.5 x 10^5), and NK cells (5 – 6 x 10^5), based on the individual donor PBMC composition (Figure 3.7).

Reconstitution of saphenous blood samples was analyzed for all mice in HD-01 and HD-03 recipient cohorts (numbered HuPBMC cohort 8 and 9, respectively) at 2.5 weeks post-PBMC injection, as determined based on the analysis presented in section 4.2. At this timepoint, both HuPBMC cohorts reconstituted to a very similar extent with equivalent immune cell subset prevalence and relative proportions in blood (Figure 3.8A – B). These trends were also consistent between the cohorts for NSG and NSG-SGM3 engrafted recipient mice (Figure 3.8C – D) and were therefore combined for a more representative analysis of HuPBMC mouse blood reconstitution in Figure 3.9. At 2.5 weeks post-engraftment, $hCD45^+$ cells comprised 5% of total leukocytes on average. Consistent with previous reports, HIS reconstitution of HuPBMC mice was predominated by $hCD3^+$ T cells, both $hCD4^+$ and $hCD8^+$, wherein very few $hCD45^+$ cells were $hCD3^-$ (Figure 3.9A – B) [493,505]. Among total leukocytes, $hCD4^+FOXP3^+$ Tregs and $hCD19^+$ B cells each represented ~0.1% of cells, whereas B cell subsets, monocytes, and NK cells were either less than 0.1% of cells or absent entirely at this timepoint (Figure 3.9C). Within the $hCD3^+$ T cells, the proportion of cells expressing hCD4, hCD8, and hCD27 was pretty similar to donor PBMCs, with the exception that $hCD4^+$ and $hCD8^+$ T cells were represented at equivalent frequencies, whereas $hCD4^+$ T cells typically outnumber $hCD8^+$ T cells in donor PBMCs (Figure 3.9D). hCD25

and hFOXP3 expressing Tregs comprised a similar if slightly higher proportion of $hCD4^+$ T cells on average compared to donor PBMCs (Figure 3.9E). Among the few $hCD19^+$ B cells, ~20% expressed hCD20, whereas few to none expressed hCD21 or hCD27 (Figure 3.9F).

Compared to HuPBMC NSG mice, HuPBMC NSG-SGM3 mice had generally greater human $CD45^+$ and T cell reconstitution levels at this timepoint, though the relative frequencies of HIS lineages between HuPBMC mice on the same background was consistent regardless of NSG or NSG-SGM3 engraftment (Figure 3.10A – B). All measured T cell subsets were elevated in NSG-SGM3 mice than NSG mice that had received the same donor PBMCs, as well as a moderately increased average NK cell frequency, with no effect on total B cell proportions. (Figure 3.10B – C). Within the T cell, Treg and B cell populations, the frequency of distinct subsets was not affected by the recipient strain, suggesting using the NSG-SGM3 mice can generate higher reconstitution levels quicker after PBMC engraftment but does not result in altered subset HIS reconstitution (Figure 3.10D – F). A more comprehensive, retrospective assessment of blood reconstitution of HuPBMC mice on the NSG and NSG-SGM3 background prior to EAE induction and in the spleen at endpoint is presented in section 4.4.2.

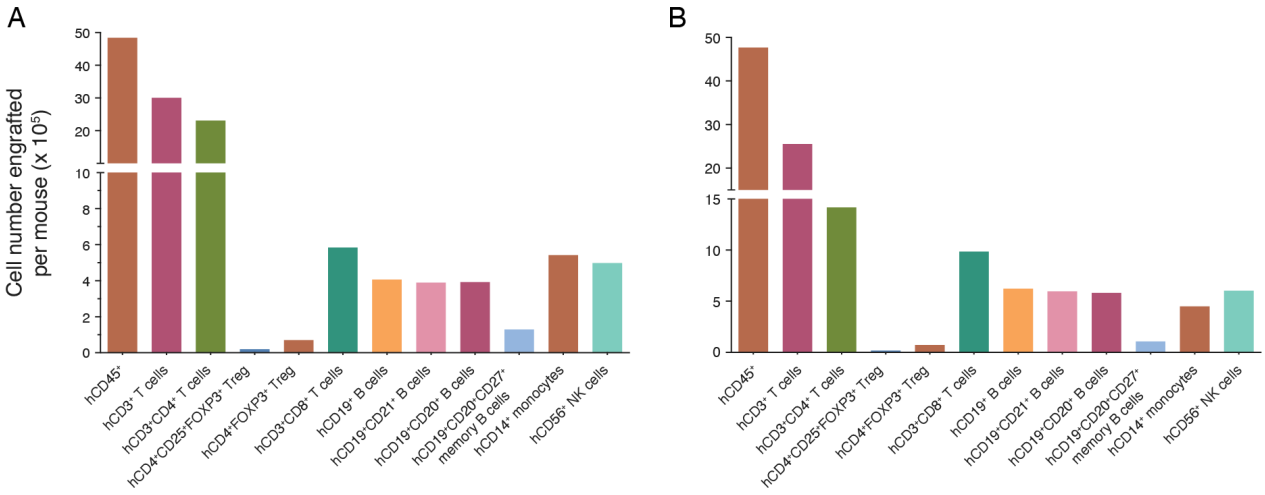

Figure 3.7 Human immune cell counts engrafted per HuPBMC recipient mouse

Absolute human immune cell subset counts injected per recipient NSG or NSG-SGM3 mouse from a total of 5 x 10^6 PBMCs derived from donor (A) HD-01 or (B) HD-03 to generate HuPBMC mouse cohorts 8 and 9, respectively.

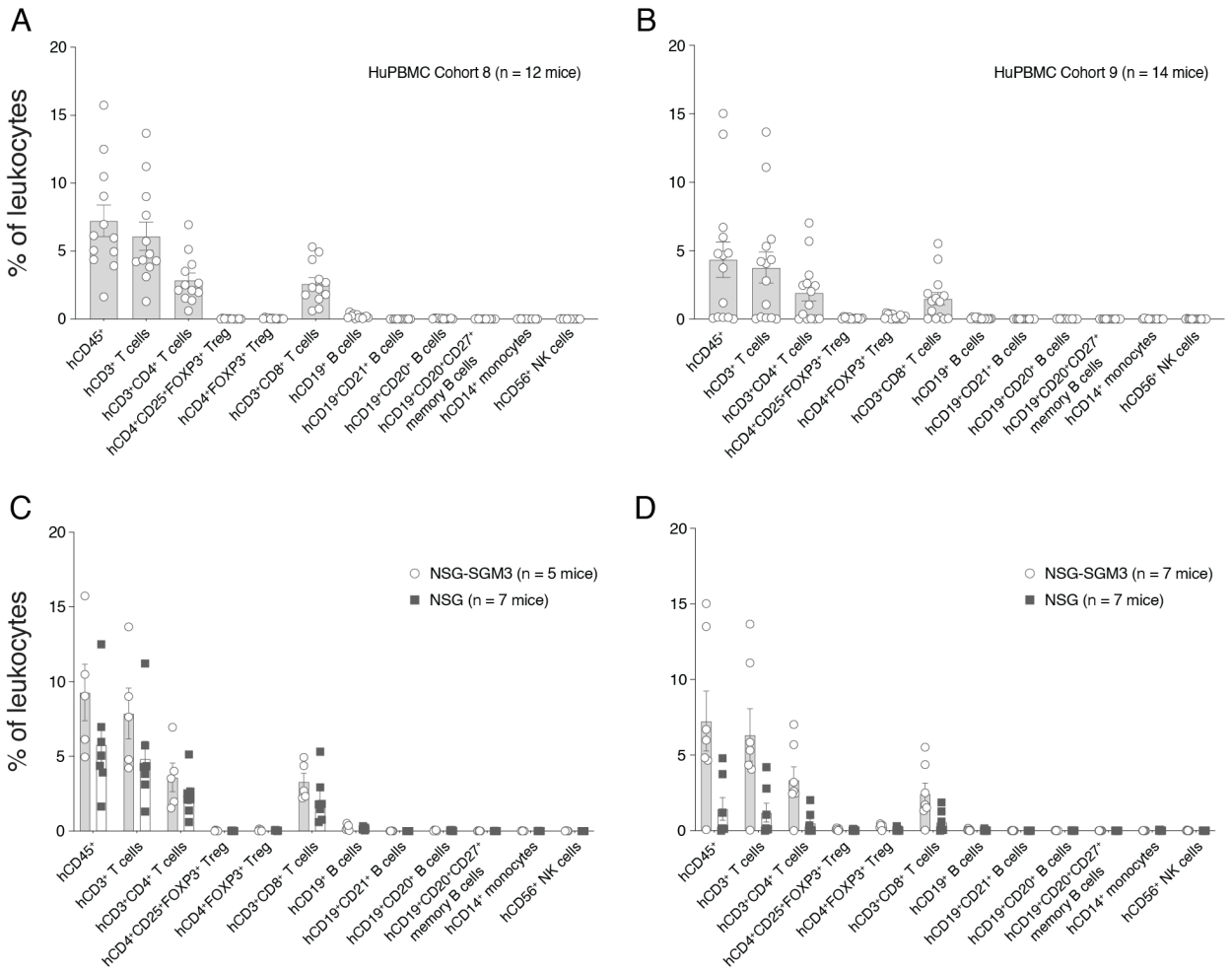

Figure 3.8 Peripheral blood reconstitution of HuPBMC mice per donor

Relative proportions of all measured human immune cell lineages are shown as a proportion of total leukocytes (murine and human) in peripheral blood of HuPBMC mice engrafted with HD-01 PBMCs (A; cohort 8, n = 12 mice) and HD-03 PBMCs (B; cohort 9, n = 14 mice) at 2.5 weeks (18 days) post-PBMC engraftment. HuPBMC mice generated on the NSG and NSG-SGM3 backgrounds were further separated for cohort 8 (C; n = 5 – 7 mice/strain) and cohort 9 (D; n = 7 mice/strain). Data are shown as mean with SEM.

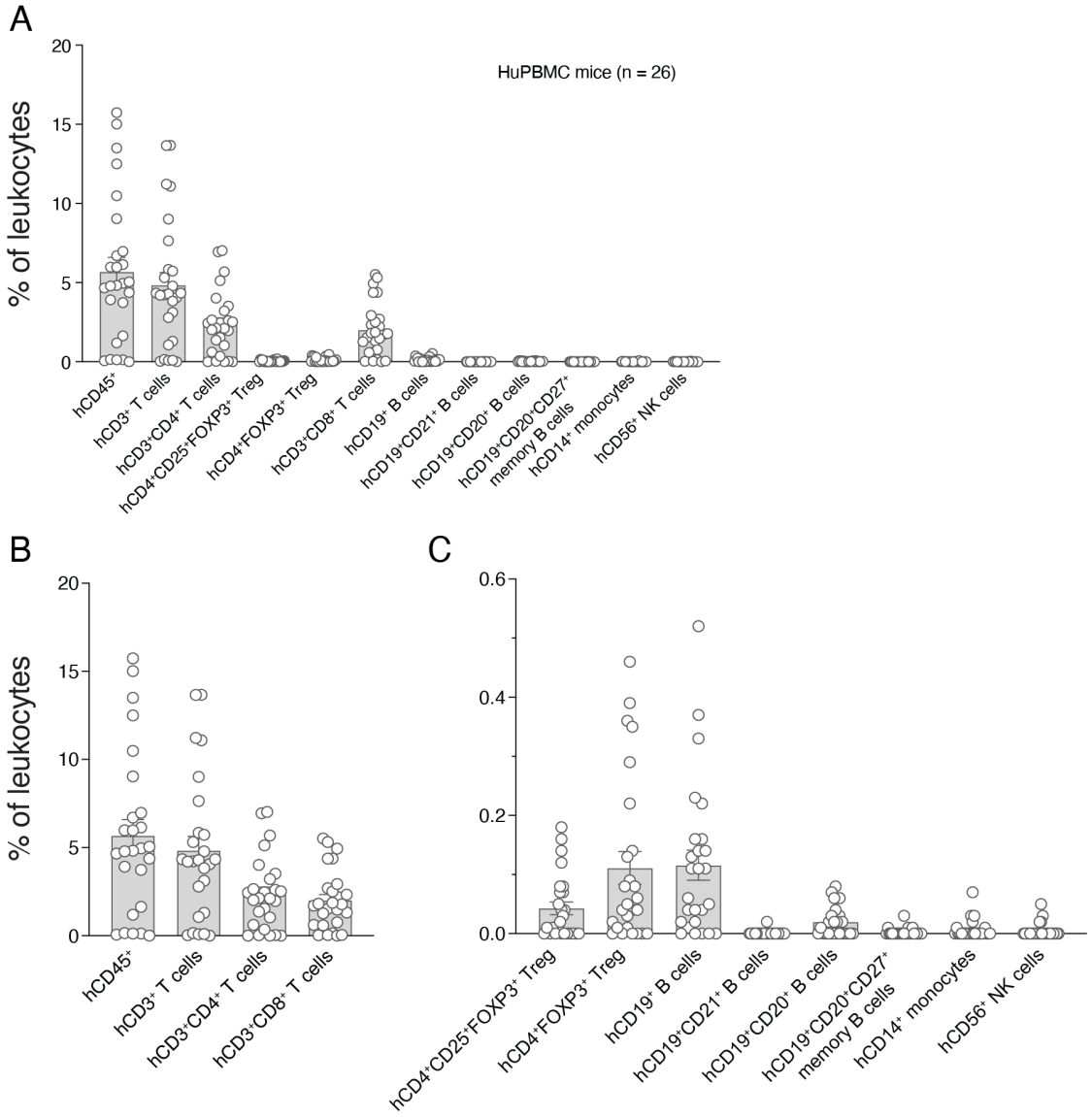

Figure 3.9 Peripheral blood reconstitution of HuPBMC mice derived from healthy donors

(A) Relative proportions of all measured human immune cell lineages are shown as a proportion of total leukocytes (murine and human) in peripheral blood at 2.5 weeks (18 days) post-PBMC engraftment. These data are then subdivided into (B) predominantly engrafted immune cell lineages and (C) minorly engrafted immune cell lineages to better illustrate relative frequencies. (D) Proportions of T cell subsets among $hCD3^+$ T cells. (E) Proportions of regulatory T cell (Treg) subsets among $hCD4^+$ T cells. (F) Proportions of B cell subsets among $hCD19^+$ B cells. Data are shown as mean with SEM for 26 mice total (cohorts 8 and 9 combined) engrafted with PBMCs from one of two healthy adult female donors (HD-01 or HD-03).

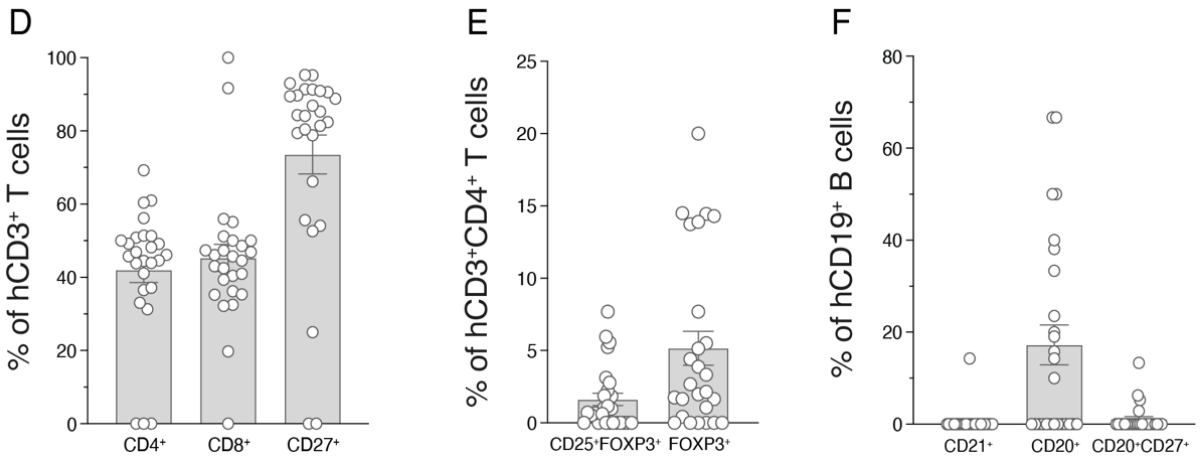

Figure 3.9 continued

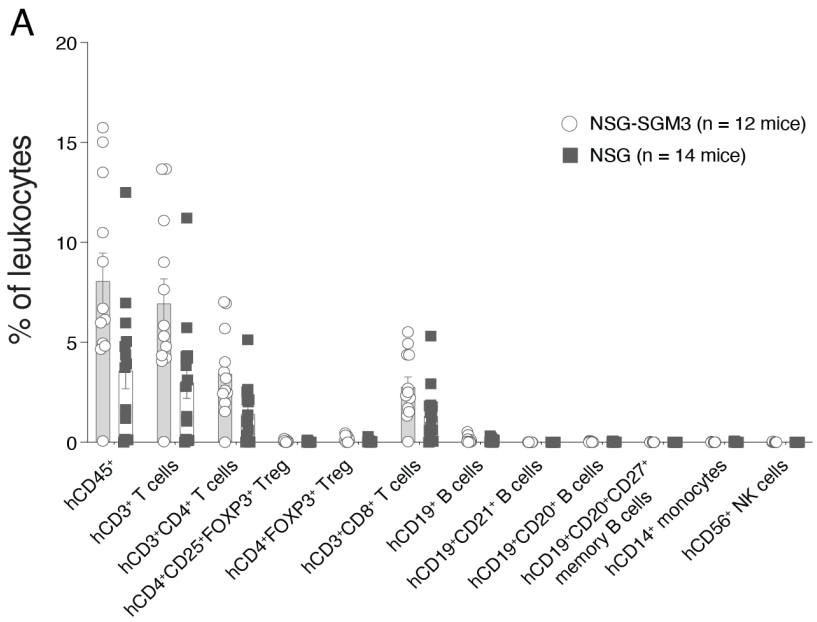

Figure 3.10 Peripheral blood reconstitution of HuPBMC mice on the NSG and NSG-SGM3 background

(A) Relative proportions of all measured human immune cell lineages are shown as a proportion of total leukocytes (murine and human) in peripheral blood of healthy donor PBMC-engrafted NSG and NSG-SGM3 mice at 2.5 weeks (18 days) post-PBMC engraftment. These data are then subdivided into (B) predominantly engrafted immune cell lineages and (C) minorly engrafted immune cell lineages to better illustrate relative frequencies. (D) Proportions of T cell subsets among $hCD3^+$ T cells. (E) Proportions of regulatory T cell (Treg) subsets among $hCD4^+$ T cells. (F) Proportions of B cell subsets among $hCD19^+$ B cells. Data are shown as mean with SEM for 12 – 14 mice per strain group and were analyzed by Mann-Whitney test.

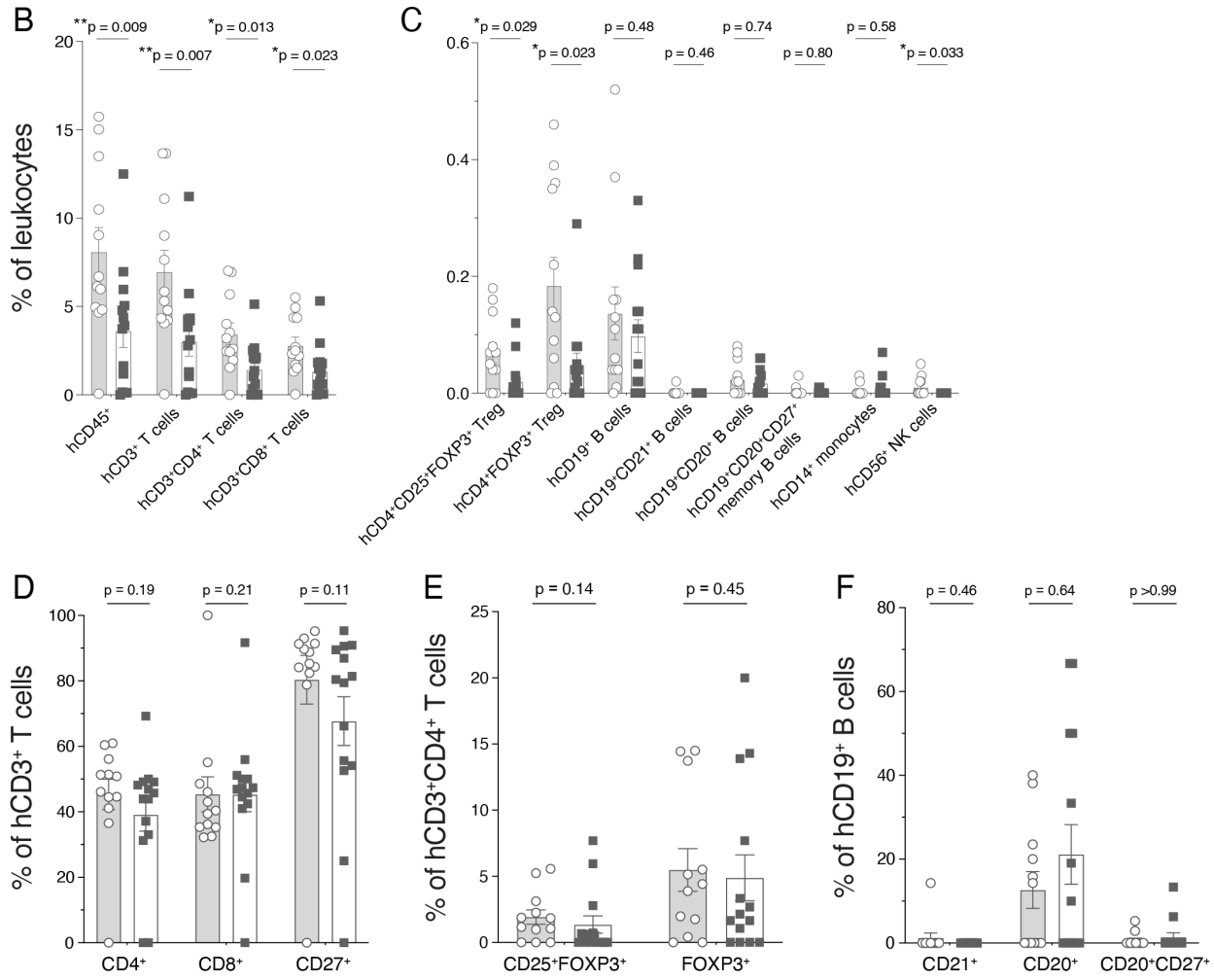

Figure 3.10 continued

3.3.5 Model comparison of human immune cell lineage reconstitution of blood

Direct comparison of HIS lineage repopulation of NSG (-SGM3) mouse blood following each of the three humanization methods is summarized in Table 3.2. In general, engraftment of HSCs requires a longer reconstitution period (10+ weeks) than PBMC engraftment (2 – 4 weeks), and, therefore, reconstitution of peripheral blood in each model was measured at the earliest timepoint where hCD45$^+$ cell engraftment was consistently measured and EAE could be reliably induced. In all three humanized mouse cohorts, regardless of humanization method, reconstitution was highly variable between individual mice engrafted with the same donor cells/tissues.

Table 3.2 Peripheral blood reconstitution of humanized mice before EAE induction

Data are shown as group average frequencies of total leukocytes (murine and human) with standard deviation for each cohort.

	HuHSC	**HuBLT**	**HuPBMC**
Reconstitution timepoint (weeks post-engraftment)	15	11	2.5
Cohort size (n)	8	5	26
%hCD45$^+$	20.4 (± 12.7)	14.0 (± 13.1)	5.68 (± 4.64)
%hCD3$^+$ T cells	1.84 (± 1.63)	10.8 (± 11.5)	4.84 (± 4.07)
%hCD19$^+$ B cells	13.8 (± 9.39)	2.10 (± 1.15)	0.12 (± 0.13)
%hCD14$^+$ monocytes	1.19 (± 0.79)	0.070 (± 0.049)	0.007 (± 0.016)
%hCD56$^+$ NK cells	0.051 (± 0.062)	0.015 (± 0.015)	0.005 (± 0.012)

The overall proportion of human CD45$^+$ immune cells in circulation was higher in HSC-engrafted models compared to the HuPBMC model at these timepoints, though all groups showed an average engraftment level of over 5% prior to induction of EAE (Figure 3.11A). hCD3$^+$ T cell reconstitution was statistically similar between the models, though average T cell engraftment was lower for HuHSC mice compared to both HuBLT and HuPBMC mice (Figure 3.11B). hCD3$^+$CD8$^+$ T cell engraftment was also comparable between HuBLT and HuPBMC mice, with average reconstitution of HuBLT mice being slightly greater than that of HuPBMC mice, but which was significantly lower in HuHSC mice (Figure 3.11C). The relative proportion of hCD3$^+$CD4$^+$ T cells followed this same trend, but differences were not significant (Figure 3.11D). Likewise, hCD25 and hFOXP3 expressing Treg levels were statistically indifferent between groups and, overall, quite low, but generally did not appear to expand at all in many HuHSC blood samples compared to at least half of the HuBLT and HuPBMC samples that had detectable Treg levels in blood at this time (Figure 3.11E – F).

In contrast, HuHSC mice had far superior reconstitution and significant expansion of human B cells expressing hCD19, hCD21, and hCD20 compared to both other models (Figure 3.11G – I). HuPBMC blood samples generally did not contain consistently measurable levels of engrafted human B cells, whereas HuBLT blood contained low but consistent levels of B cell reconstitution. hCD19$^+$CD20$^+$CD27$^+$ B cell reconstitution was similarly low but detectable in the

HuHSC and HuBLT samples, and nearly absent from the HuPBMC samples (Figure 3.11J). $hCD14^+$ monocyte expansion was slightly higher in HuHSC mice compared to HuBLT mice, and significantly so compared to HuPBMC mice (Figure 3.11K). A similar trend was observed for $hCD56^+$ NK cells, however NK cell expansion was less consistent in HuHSC mice and more frequent in the HuBLT and HuPBMC mice (Figure 3.11L). Reconstitution of human NK cells and monocytes was below expected levels for blood samples in all three models.

Among $hCD3^+$ T cells, the proportion expressing hCD4 was quite similar between all three models, comprising 30 – 55% of T cells, though individual frequencies were highly variable in the HuHSC cohort (Figure 3.12A). The frequency of hCD8 and hCD27 expressing T cells was also similar between HuBLT and HuPBMC mice, but significantly lower on average and highly disparate in HuHSC mice. The proportion of $hCD4^+$ T cells expressing the regulatory markers hCD25 and/or hFOXP3 was statistically indifferent between all three models (Figure 3.12B). In general, the data indicate that the main T cell subsets are present to varying degrees within the reconstituted peripheral blood T cell population of all three humanized mouse models at the measured timepoints, but that total T cell abundance is greater in the HuBLT and HuPBMC mice compared to the relatively low levels detected in HuHSC mice (Figure 3.11 and Figure 3.12).

Among $hCD19^+$ B cells, expression of subset markers was quite variable depending on the method of humanization (Figure 3.12C). HuHSC mice showed the best reconstitution of B cells between the three models, including ~20 – 25% that expressed hCD21, whereas samples from neither the HuBLT nor HuPBMC mice contained $hCD21^+$ B cells. For hCD20, however, HuHSC and HuBLT B cells all mostly expressed this key marker, as expected, whereas many HuPBMC B cells expressed hCD20 less frequently or did not express it at all. Dual expression of hCD20 and hCD27 was consistently low among B cells in all three models at this timepoint, likely due to the naivety of the immune system in newly reconstituted HSC-engrafted mice and the inefficiency of B cell engraftment in the HuPBMC model. In general, HuHSC mouse blood contained far greater B cell levels, including those expressing the EBV receptor, HuBLT mice had moderate B cell reconstitution, and HuPBMC mice were nearly devoid of human B cell engraftment (Figure 3.11 and Figure 3.12).

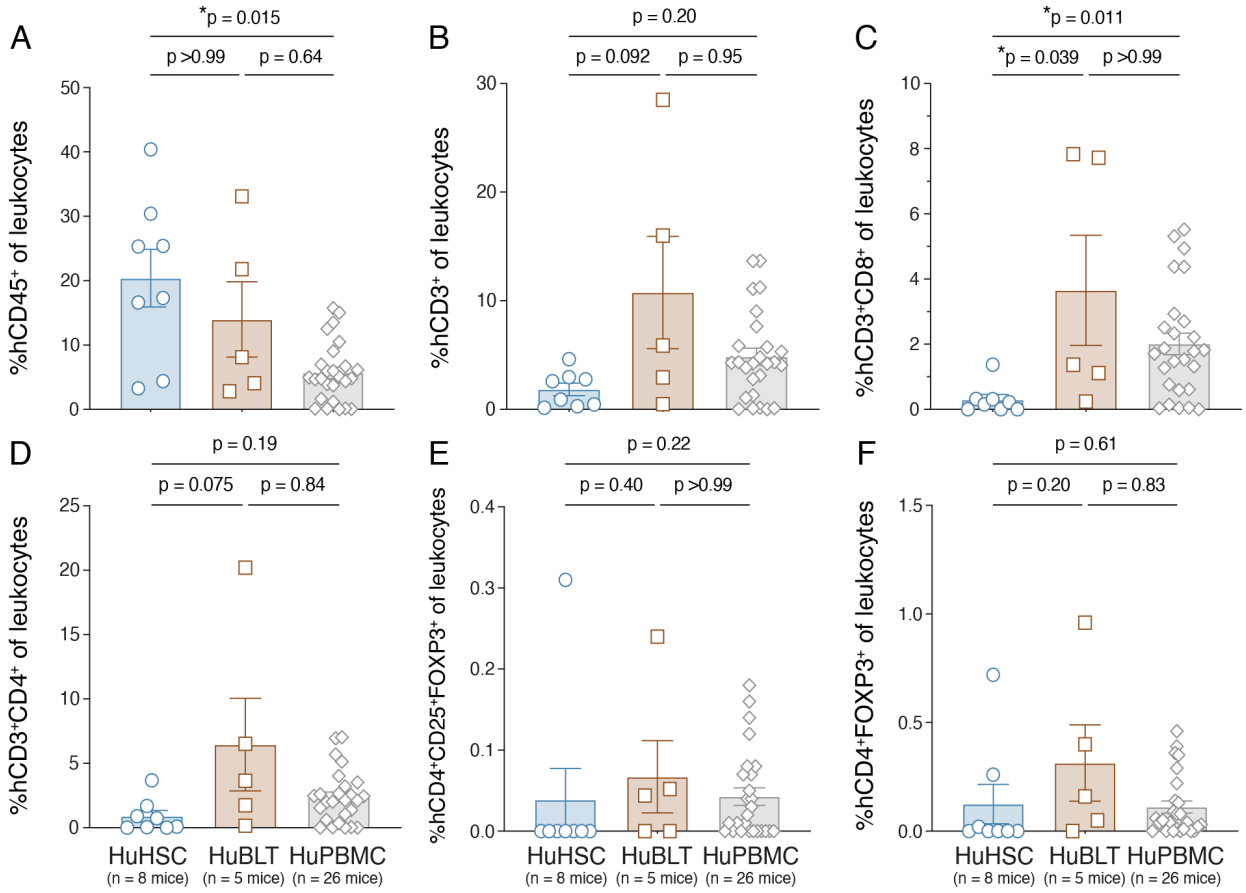

Figure 3.11 Model comparison of humanized mouse reconstitution of peripheral blood

Relative proportions of all measured human immune cell lineages shown as a proportion of total leukocytes (murine and human) in the peripheral blood of HuHSC mice (n = 8) at 15 weeks post-HSC engraftment, HuBLT mice (n = 5) at 11 weeks post-HSC engraftment, and HuPBMC mice (n = 26) at 2.5 weeks post-PBMC engraftment. (A) $hCD45^+$ immune cells, (B) $hCD3^+$ T cells, (C) $hCD3^+CD8^+$ T cells, (D) $hCD3^+CD4^+$ T cells, (E) $hCD3^+CD4^+CD25^+FOXP3^+$ regulatory T cells (Treg), (F) $hCD3^+CD4^+FOXP3^+$ Treg, (G) $hCD19^+$ B cells, (H) $hCD19^+CD21^+$ B cells, (I) $hCD19^+CD20^+$ B cells, (J) $hCD19^+CD20^+CD27^+$ B cells, (K) $hCD14^+$ monocytes, and (L) $hCD56^+$ NK cells. All engrafted NSG and NSG-SGM3 mice per cohort are combined for this analysis. Data are shown as mean with SEM and were analyzed by Kruskal-Wallis test with Dunn's multiple comparisons.

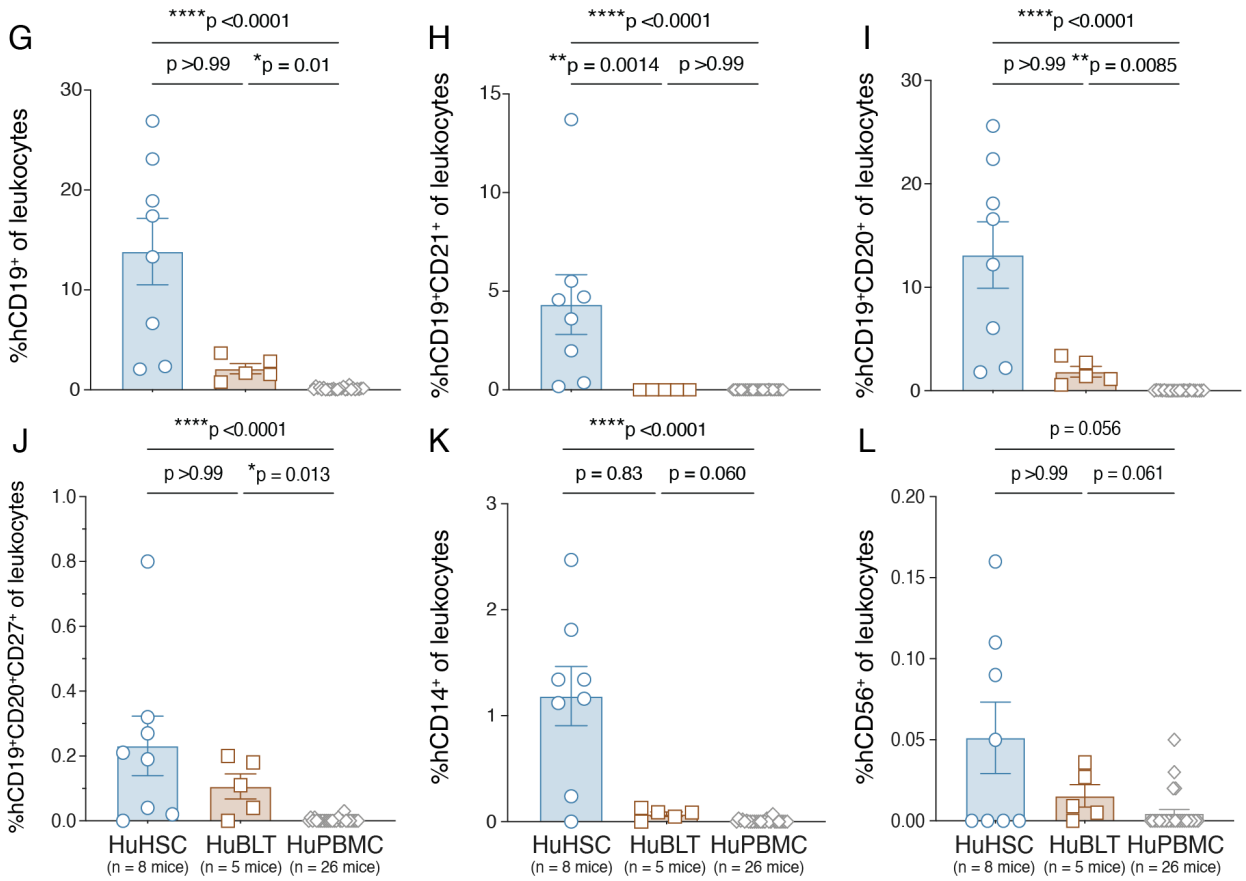

Figure 3.11 continued

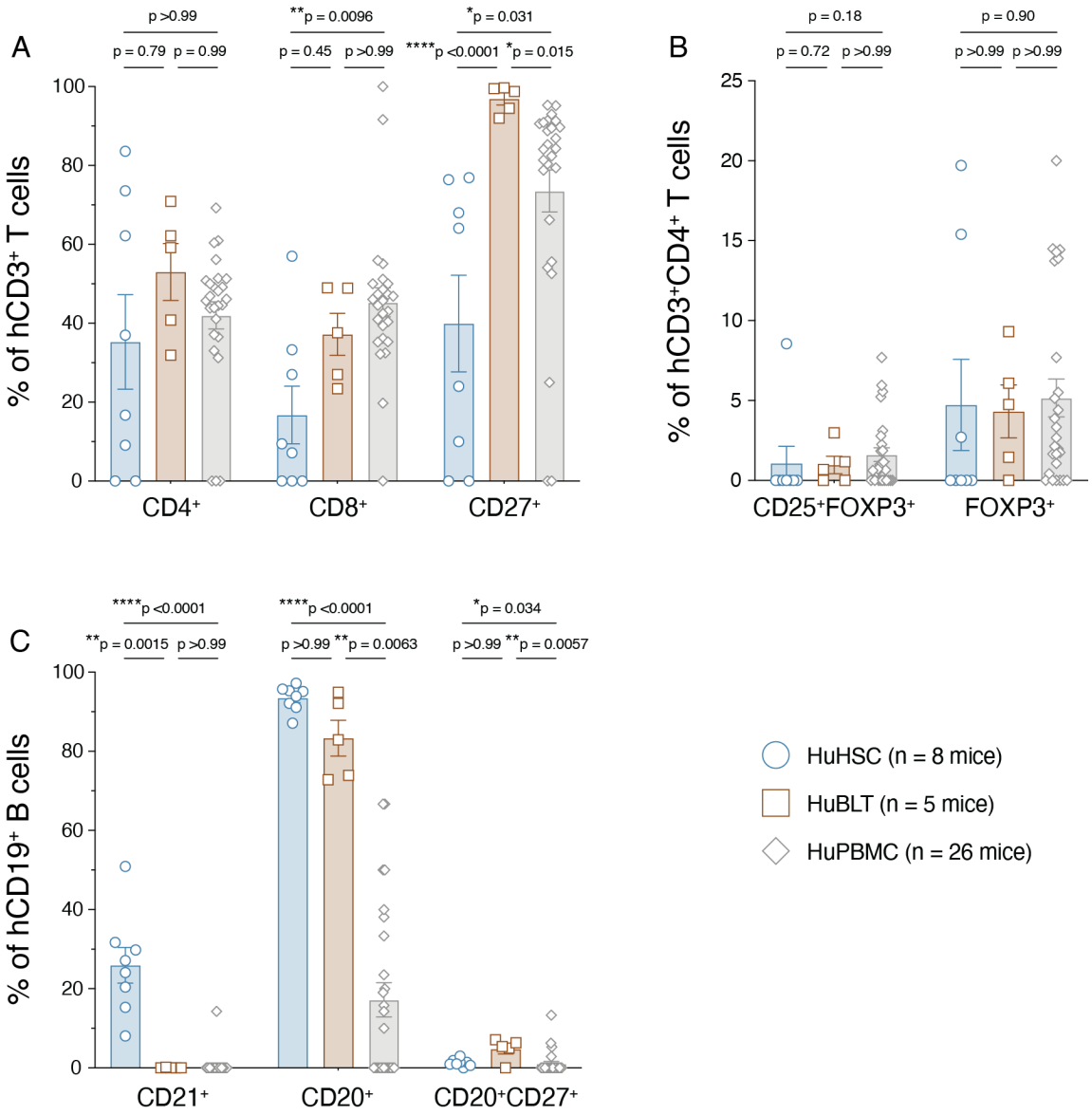

Figure 3.12 Model comparison of human T and B cells in the peripheral blood of humanized mice

Relative proportions of all measured human T cell (A), regulatory T cell (Treg) (B), and B cell (C) subsets shown as a proportion of the parent population in the peripheral blood of HuHSC mice (n = 8) at 15 weeks post-HSC engraftment, HuBLT mice (n = 5) at 11 weeks post-HSC engraftment, and HuPBMC mice (n = 26) at 2.5 weeks post-PBMC engraftment. All engrafted NSG and NSG-SGM3 mice per cohort are combined for this analysis. Data are shown as mean with SEM and were analyzed by Kruskal-Wallis test with Dunn's multiple comparisons.

3.4 EAE susceptibility of humanized mouse models

3.4.1 Clinical EAE outcomes

Following confirmation of sufficient hCD45$^+$ cell reconstitution of peripheral blood in each humanized mouse cohort, EAE was induced using the extracellular domain of human MOG (rhMOG$_{1\text{-}120}$). The order in which the three humanized mouse cohorts were generated for this analysis was dependent on the timing of donor tissue and blood sample acquisition, and as such, the HuHSC and HuPBMC mice were generated first. Model development with other HuPBMC cohorts was ongoing during these experiments due to the shorter duration of the HuPBMC model, which informed subsequent modification to the emulsion formulation given to the HuBLT cohort that included both peptide as well as the full domain recombinant protein. HuHSC mice (at 16 weeks post-HSC engraftment) and HuPBMC mice (at 3 weeks post-PBMC engraftment) were therefore induced with 100 µg rhMOG$_{1\text{-}120}$, and the HuBLT mice (at 11 weeks post-HSC engraftment) were induced with 100 µg rhMOG protein plus 200 µg MOG$_{35\text{-}55}$ per mouse. In every case, MOG antigens were emulsified in 100 µL CFA injected SQ, and two doses of PTx were injected IP on days 0 and 2, as described in detail in method Section 2.5. In order to account for variability in subset reconstitution levels within and between humanized model cohorts, all mice, regardless of their overall %hCD45$^+$ cells in the blood prior to immunization, were included for EAE induction and analysis.

Following immunization, EAE symptoms were scored daily based on the degree and progression of paralysis using a standard 5-point scale. In the HuHSC cohort, symptoms indicative of EAE, including paralysis, continued weight loss, and poor physical condition, were not observed up to day 15 post-induction. HuHSC mice were therefore given a third PTx dose to promote migration of myelin reactive to the CNS, however, clinical signs of EAE were not observed out to day 30 post-induction (Figure 3.13A – B). On days 20 and 26, two mice were lost to nonspecific illness, characterized by weight loss and diarrhea, but had not shown any indication of EAE related disease, and the remaining mice exhibited temporary weight loss after immunization but recovered afterward (Figure 3.13C). At endpoint, the presence of visible CFA bubbles under the skin was confirmed in all mice to ensure the induction itself was not a technical failure. Similarly, none of the 4 induced HuBLT mice developed symptoms of EAE up to day 26 and were therefore induced a second time using 200 µg MOG$_{35\text{-}55}$ (no protein) in CFA with two booster doses of PTx, with the same doses, volumes, and timing as the first induction. Despite receiving an additional

immunization, induced HuBLT mice remained asymptomatic out to day 41 (Figure 3.13). At endpoint, all HuBLT mice had visibly enlarged kidney capsule implants, and the induced mice contained two intact CFA bubbles under the skin. No clinical complications were observed beyond the transient weight loss expected to occur in all mice following both rounds of immunization (i.e., no diarrhea, etc.).

In the HuPBMC cohort, however, typical paralytic EAE symptoms were observed in five mice (4 males and 1 female representing 25% overall incidence) starting asynchronously on days 13 – 16 post-induction (Figure 3.13A–B). EAE symptoms included tail and hind limb paralysis reaching scores of 1.5 – 2.5, which eventually resolved in a monophasic course (Figure 3.13A). Symptom onset for these five mice coincided with progressive weight loss in all HuPBMC EAE mice, beyond the transient immunization induced weight loss and regardless of the occurrence clinically measurable symptoms in most mice (Figure 3.13C). In this cohort, three mice developed other symptoms of GvHD (hair loss, skin redness, hunching), and some mice had to be euthanized due to excessive weight loss. The duration of the experiment was limited to 24 days post-induction, when the presence of intact CFA bubbles under the skin was confirmed in all EAE induced mice.

3.4.2 Tissue reconstitution and infiltration at EAE endpoint

3.4.2.1 HuHSC mice

Spleen reconstitution of human immune cells was assessed at day 30 post-EAE induction in the remaining HuHSC mice. As none of the mice had developed clinical symptoms of EAE, the CNS tissues from this cohort had not been analyzed for the presence of human immune cells. Of the six remaining EAE-induced HuHSC mice, five contained engrafted $hCD45^+$ cells in the spleen, though they were numerically fewer than $mCD45^+$ cells at endpoint (Figure 3.14A). The majority of $hCD45^+$ immune cells were $hCD19^+$ (~40%) and $hCD20^+$ (~30%) B cells (Figure 3.15A–B). In half of the spleens, hCD27 expressing $hCD3^+$ T cells were detected at moderate levels (Figure 3.15C). Reconstitution of non-T cells was consistently observed, with greater proportions of $hCD14^+$ monocytes compared to $hCD3^+CD4^+$ T cells and similar frequencies of $hCD56^+$ NK cells and $hCD8^+$ T cells (Figure 3.15C). Among engrafted $hCD3^+$ T cells, an ~30% expressed hCD4 while ~20% expressed hCD8 (Figure 3.15D). In half of the HuHSC mice, splenic $hCD3^+$ T cells also either mostly expressed CD27 (~90%) or very few expressed this marker (~10%) (Figure 3.15D). Two spleens did not contain Tregs, though those that did exhibited high proportions

FOXP3$^+$ hCD4$^+$ T cells (15 – 40%) (Figure 3.15E). As expected, hCD20 was expressed on most hCD19$^+$ B cells (~50 – 90%), but hCD21 was only expressed on ~10 – 60% of B cells. Very few (<10%) dually expressed CD20 and CD27 (Figure 3.15F). The data indicate that despite an overall skew toward human B cell engraftment compared to T cell engraftment, all major human immune lineages were variably present in the spleens of reconstituted HuHSC mice following EAE induction.

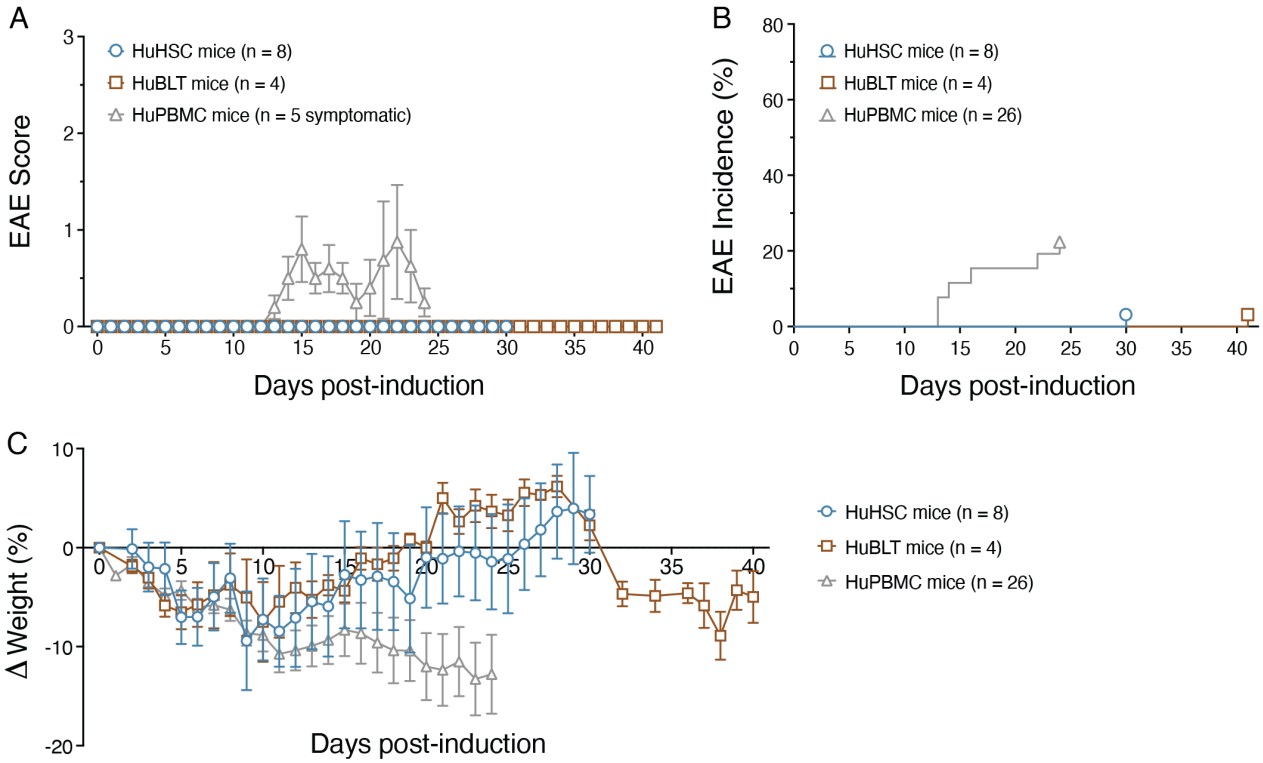

Figure 3.13 Clinical outcomes of MOG EAE induction in humanized mice

(A) Clinical EAE disease scores post-induction for symptomatic EAE-induced HuPBMC mice and all EAE-induced HuHSC and HuBLT mice. Data are shown as mean with SEM (n = 4 – 8 mice/group). (B) Incidence of clinical EAE symptoms post-induction in each humanized mouse cohort. Data are shown as the cumulative percentage of the group (n = 4 – 26 mice/group). (C) Weight loss post-EAE induction in each humanized mouse cohort. Data are shown as mean with SEM (n = 4 – 26 mice/group).

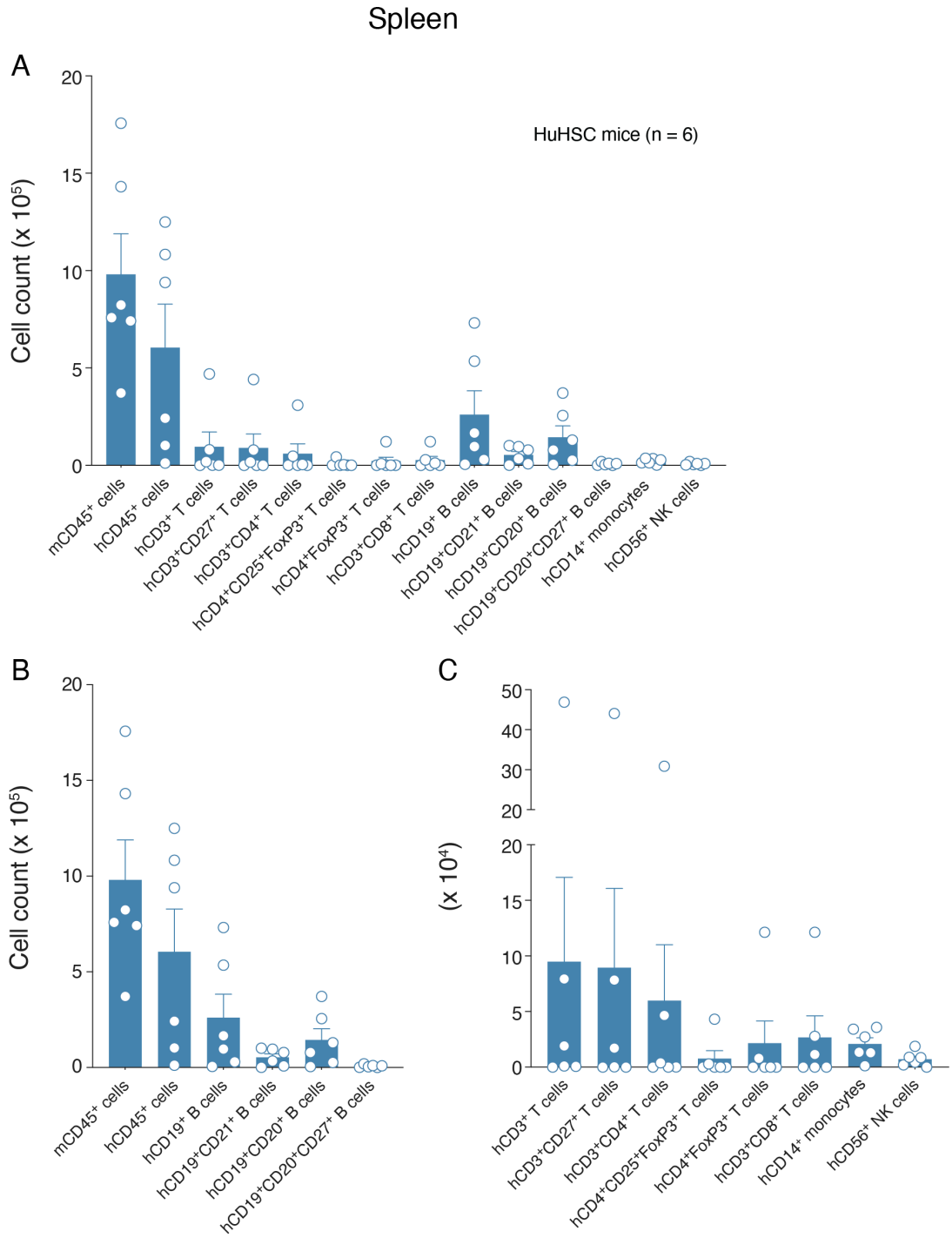

Figure 3.14 Reconstituted human immune cell abundance in HuHSC spleens at EAE endpoint

(A) Total cell counts for all measured human immune cell lineages in the spleen at day 30 post-EAE induction. These data are then subdivided into (B) predominantly engrafted immune cell lineages and (C) minorly engrafted immune cell lineages to better illustrate relative abundance. Data are shown as mean with SEM for 6 HuHSC mice total.

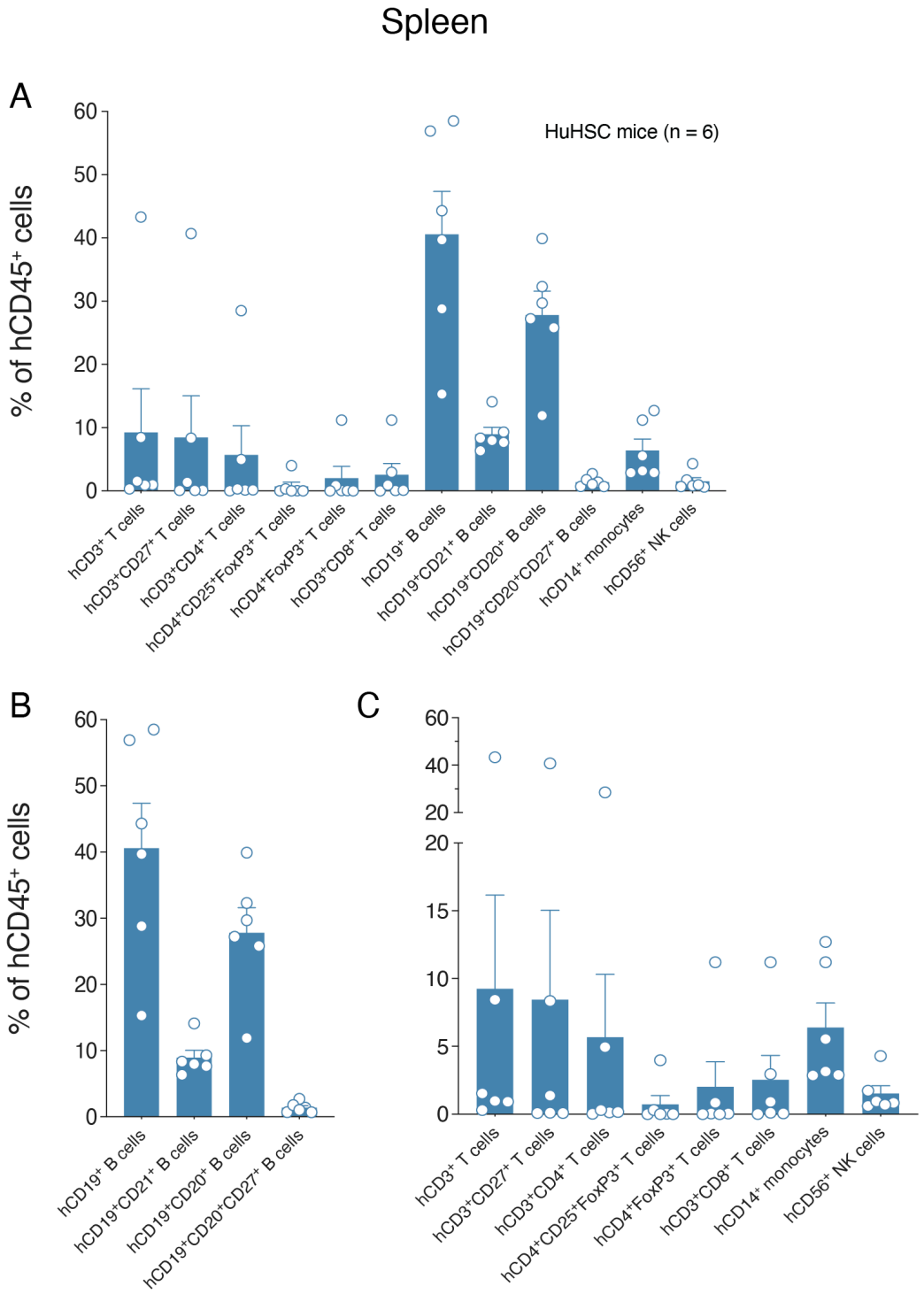

Figure 3.15 Reconstituted human immune cell frequencies in HuHSC spleens at EAE endpoint

(A) Relative proportions of all measured human immune cell lineages are shown as a proportion of engrafted hCD45$^+$ cells in the spleen at day 30 post-EAE induction. These data are then subdivided into (B) predominantly engrafted immune cell lineages and (C) minorly engrafted immune cell lineages to better illustrate relative frequencies. (D) Proportions of T cell subsets among hCD3$^+$ T cells. (E) Proportions of regulatory T cell (Treg) subsets among

hCD4$^+$ T cells. (F) Proportions of B cell subsets among hCD19$^+$ B cells. Data are shown as mean with SEM for 6 HuHSC mice total.

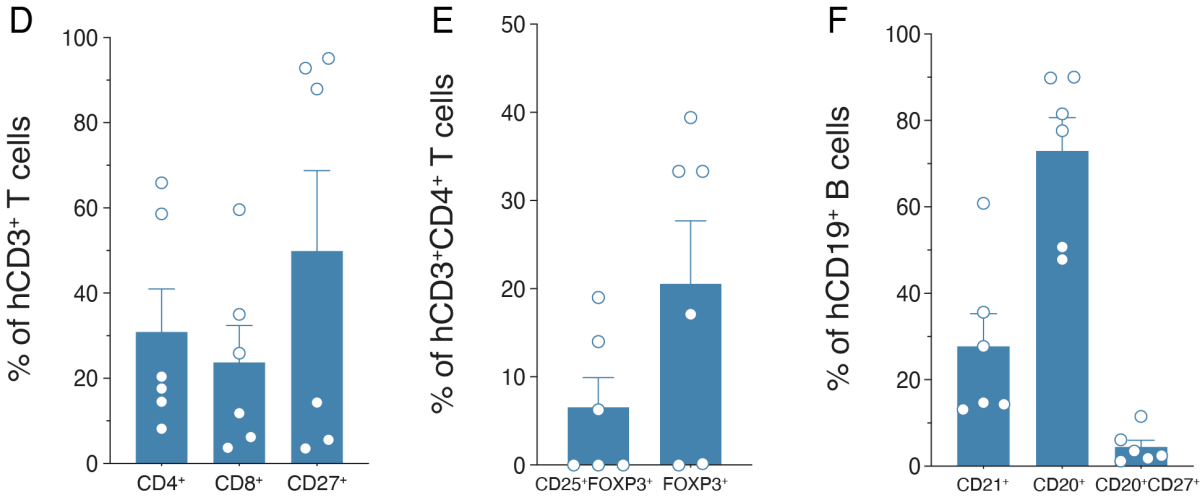

Figure 3.15 continued

Endpoint levels of human immune cell subsets, determined by both numerical abundance (Figure 3.16) and by the proportion of engrafted hCD45$^+$ cells (Figure 3.17), were not statistically different based on the recipient mouse being on the NSG or NSG-SGM3 background, as there was greater variability between individuals than between strains. In one of the HuHSC NSG-SGM3 mice, human T cell engraftment was far superior compared to all other mice in the cohort, attaining relative levels similar to donor PBMCs (Figure 3.17C). This one NSG-SGM3 engrafted HuHSC spleen also contained the expected proportions of hCD4, hCD8, and hCD27 expressing hCD3$^+$ T cells (Figure 3.17D). All three NSG-SGM3 mouse spleens consistently contained greater Treg proportions among total hCD4$^+$ T cells, despite low total Treg counts in two of three mice owing to low levels of hCD4$^+$ T cells generally, and NSG-SGM3 mice tended toward higher expression of hCD21 and hCD20 on hCD19$^+$ B cells (Figure 3.17E–F). The data suggest the NSG-SGM3 could be preferable to the NSG for supporting physiologically representative human T cell reconstitution, though additional cohorts would need to be assessed to determine their superiority for the HuHSC EAE model.

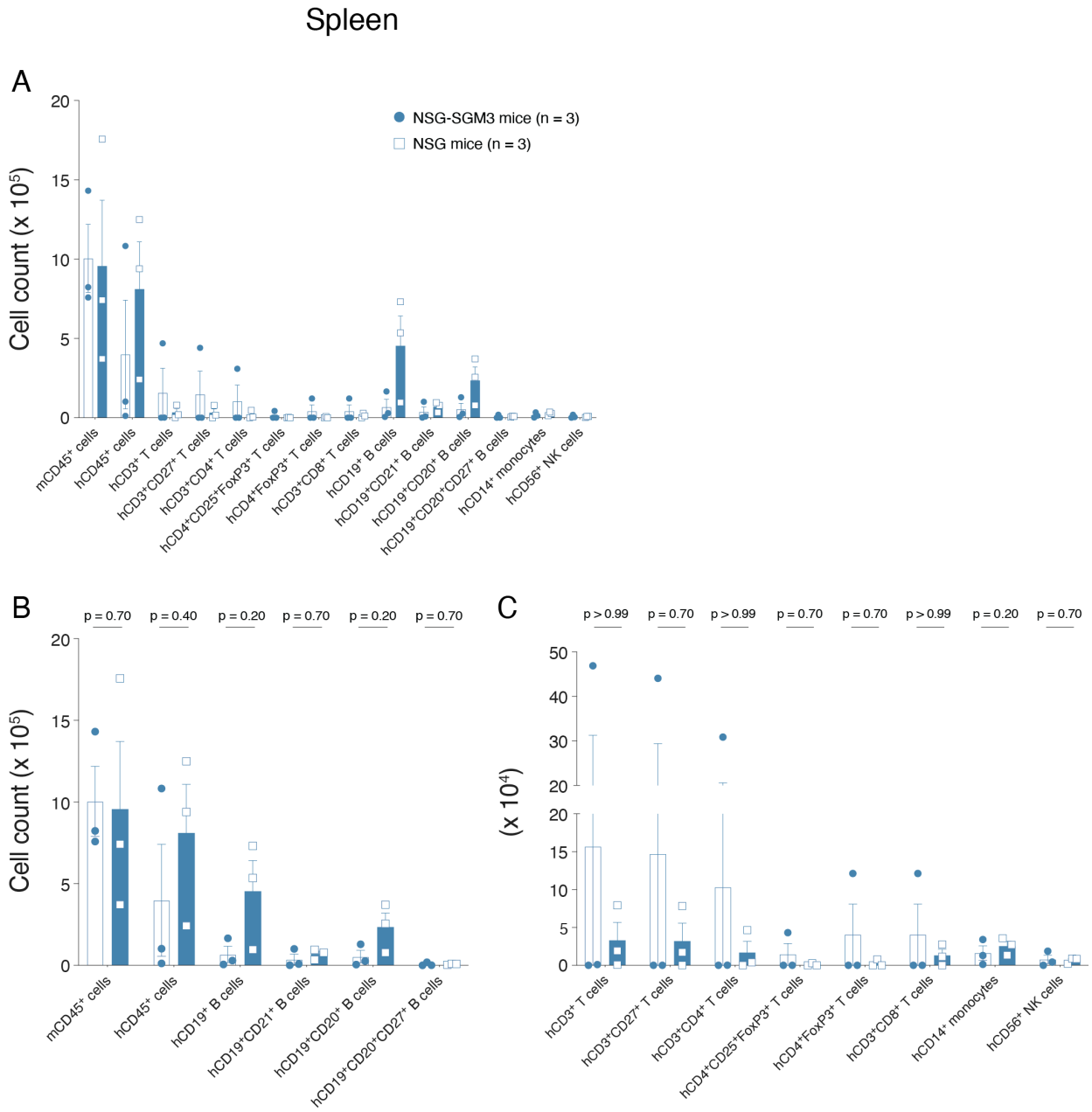

Figure 3.16 Reconstituted human immune cell abundance in HuHSC spleens on the NSG and NSG-SGM3 background at EAE endpoint

(A) Total cell counts for all measured human immune cell lineages in the spleen at day 30 post-EAE induction of HuHSC NSG and NSG-SGM3 mice. These data are then subdivided into (B) predominantly engrafted immune cell lineages and (C) minorly engrafted immune cell lineages to better illustrate relative abundance. Data are shown as mean with SEM for 3 HuHSC mice per strain and were analyzed by Mann-Whitney test.

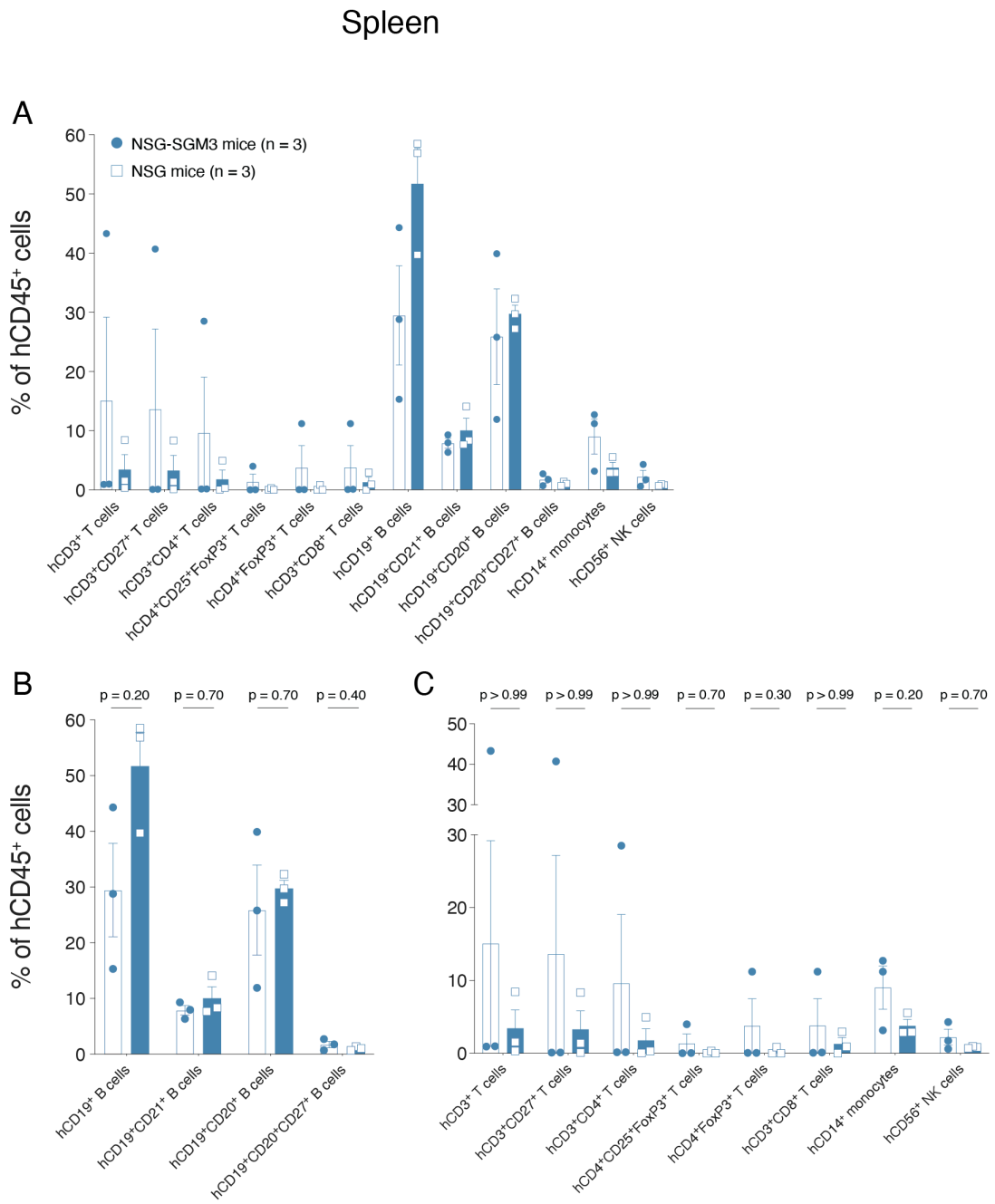

Figure 3.17 Reconstituted human immune cell frequencies in HuHSC spleens on the NSG and NSG-SGM3 background at EAE endpoint

(A) Relative proportions of all measured human immune cell lineages are shown as a proportion of engrafted hCD45$^+$ cells in the spleen at day 30 post-EAE induction of HuHSC NSG and NSG-SGM3 mice. These data are then subdivided into (B) predominantly engrafted immune cell lineages and (C) minorly engrafted immune cell lineages to better illustrate relative abundance. (D) Proportions of T cell subsets among hCD3$^+$ T cells. (E) Proportions of regulatory T cells (Treg) subsets among hCD4$^+$ T cells. (F) Proportions of B cell subsets among hCD19$^+$ B cells. Data are shown as mean with SEM for 3 HuHSC mice per strain and were analyzed by Mann-Whitney test.

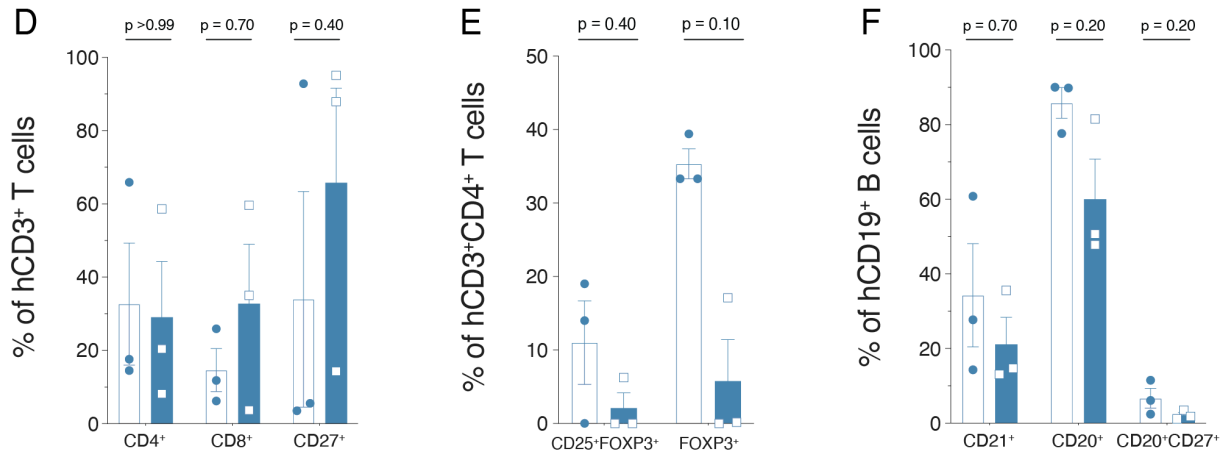

Figure 3.17 continued

3.4.2.2 HuBLT mice

EAE induction of HuBLT mice, similar to adult HuHSC mice, did not result in clinical symptoms consistent with classical EAE models that would suggest CNS localized inflammation occurred post-induction. The splenic analysis of EAE-induced HuHSC mice, however, revealed the absence of clinical symptoms was not due to an absence of effector cells in the system that would be required to generate EAE pathology following immunization. Therefore, perfused brain and spinal cord tissues from the HuBLT mice were analyzed for total levels of human immune cell infiltration, alongside splenic reconstitution, at day 41 post-EAE induction. Reconstitution analysis of the spleen indicated that all EAE-induced HuBLT mice contained the expected relative proportions of T and B cells compared to donor PBMCs (Figure 3.18A – C). EAE induction appeared to promote T cell expansion in the spleen of HuBLT mice compared to the uninduced control HuBLT mouse, resulting in an associated reduction in the proportion of B cells, but did not appear to impact the relative expression of hCD4 and hCD8 among these T cells (Figure 3.18D). EAE induction also appeared to promote the expansion of $hCD14^+CD68^+$ macrophages in the spleen (Figure 3.18C), though as only one uninduced control HuBLT mouse was available for this preliminary study, statistical analyses could not be performed. Regulatory T cell proportions among $hCD4^+$ T cells were also similar to donor PBMC frequencies, and some T and B cells expressed T-bet, occurring at frequencies comparable to $hCD4^+$ Tregs (~2 – 5%) (Figure 3.18E – F). hCD20 expression among total $hCD19^+$ B cells was somewhat reduced compared to donor PBMC derived B cells, though generally remained high (~70%) (Figure 3.18F). Spleen analysis

overall determined that the HuBLT mice contained the expected proportions of human immune cell subsets following EAE induction.

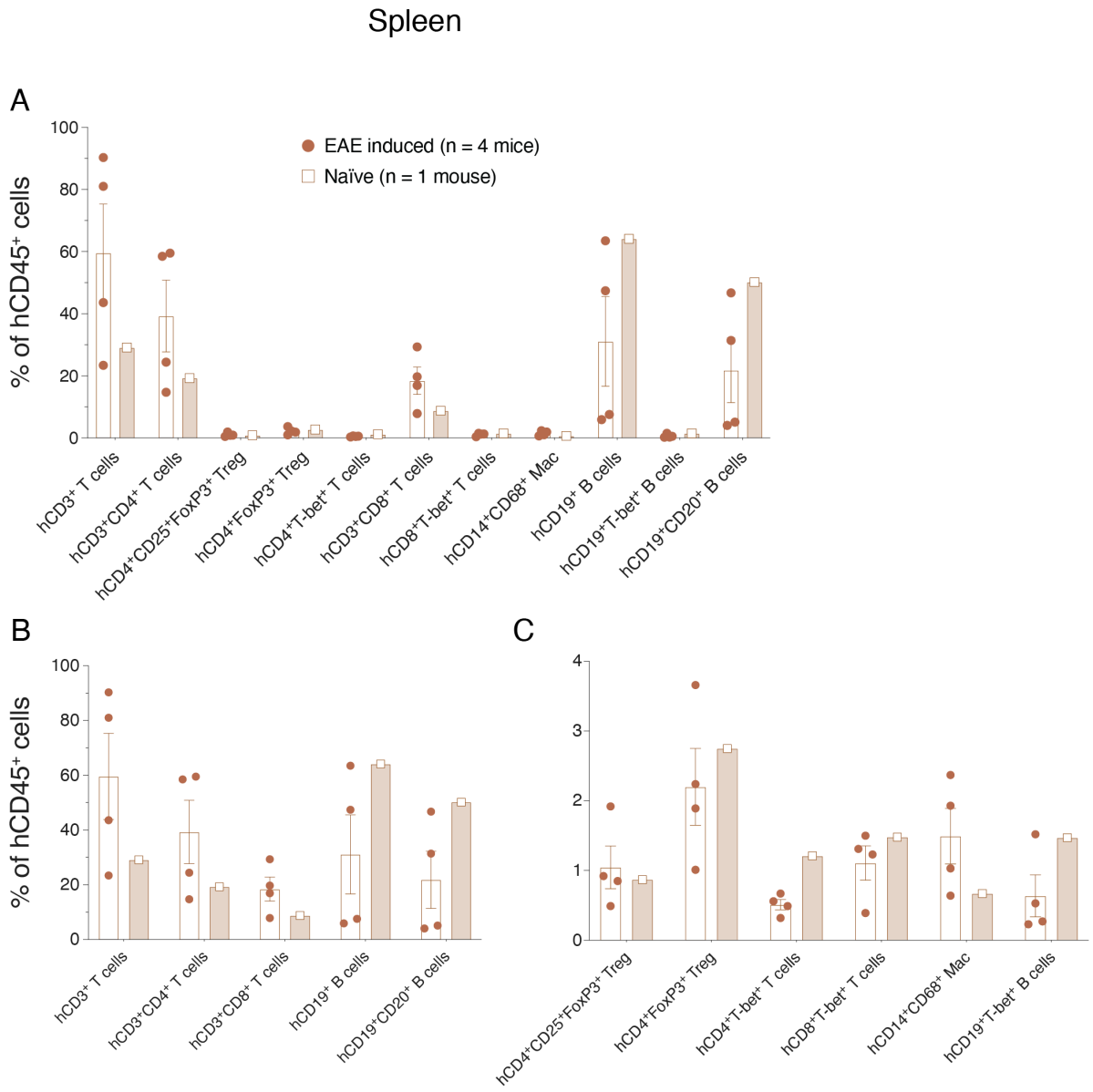

Figure 3.18 Reconstituted human immune cell frequencies in HuBLT spleens at EAE endpoint

(A) Relative proportions of all measured human immune cell lineages are shown as a proportion of engrafted hCD45$^+$ cells in the spleen at day 41 post-EAE induction. These data are then subdivided into (B) predominantly engrafted immune cell lineages and (C) minorly engrafted immune cell lineages to better illustrate relative frequencies. (D) Proportions of T cell subsets among hCD3$^+$ T cells. (E) Proportions of regulatory T cell (Treg) subsets among hCD4$^+$ T cells. (F) Proportions of B cell subsets among hCD19$^+$ B cells. Data are shown as mean with SEM for 4 EAE-induced HuBLT mice and for one uninduced control (naïve) HuBLT mouse. Abbr: Mac, macrophage.

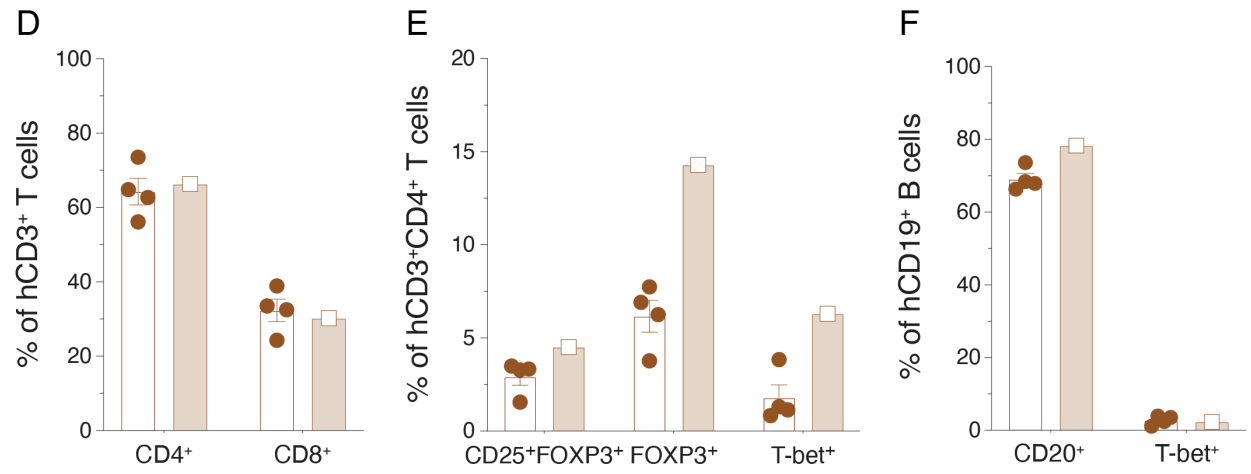

Figure 3.18 continued

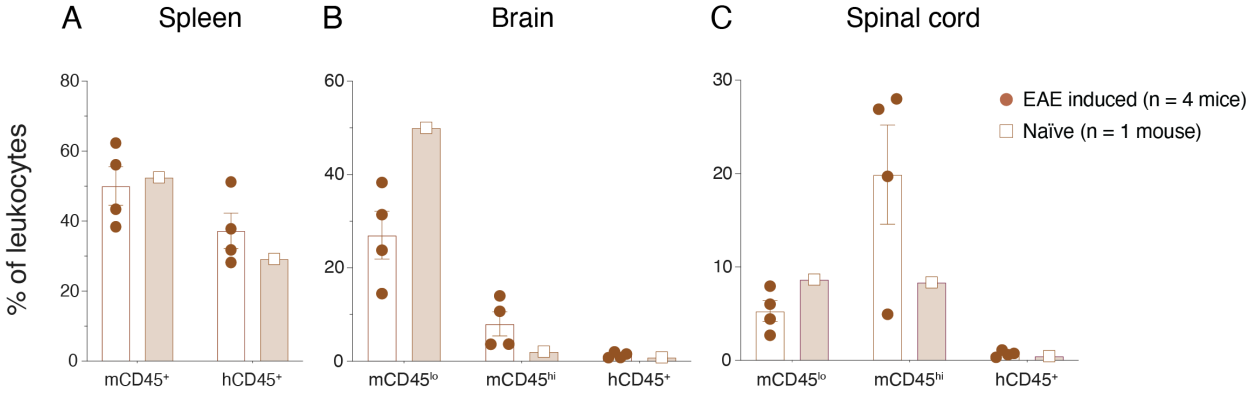

Figure 3.19 Murine and human immune cells in the CNS and peripheral tissues of HuBLT mice at EAE endpoint

Relative proportions of human hCD45^{+} and murine mCD45$^{hi/lo}$ immune cells of total leukocytes (murine and human) in the (A) spleen, (B) brain, and (C) spinal cord at day 41 post-EAE induction. Relative proportions of all measured human immune cell lineages are shown as a proportion of engrafted hCD45^{+} cells in the (D) spleen, (E) brain, and (F) spinal cord. Total cell counts of all measured immune cell lineages in the (G) spleen, (H) brain, and (I) spinal cord. Brain and spinal cord tissues were perfused prior to cell isolation. Data are shown as mean with SEM for 4 EAE-induced HuBLT mice and for one uninduced control (naïve) HuBLT mouse. Abbr: Mac, macrophage.

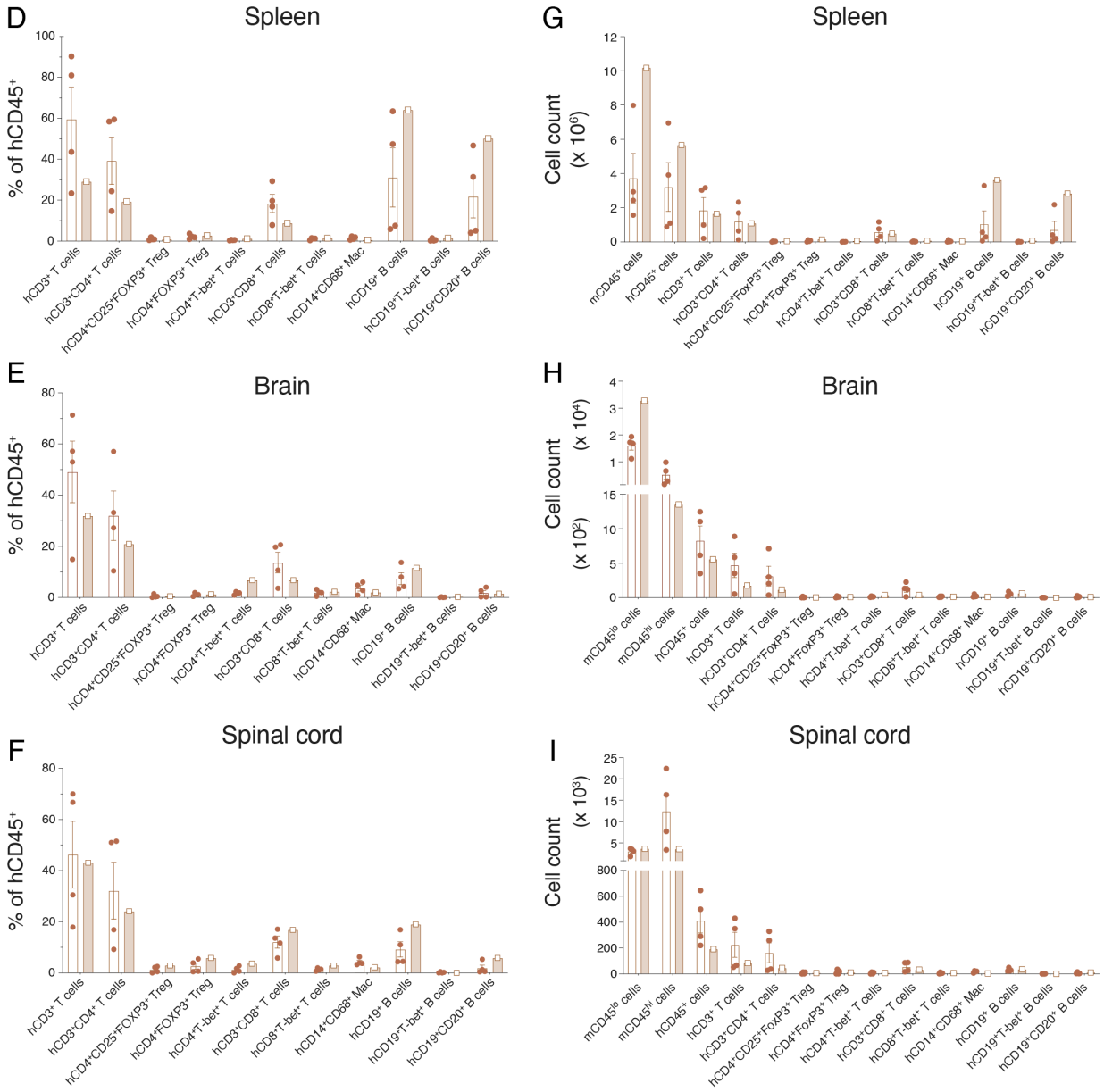

Figure 3.19 continued

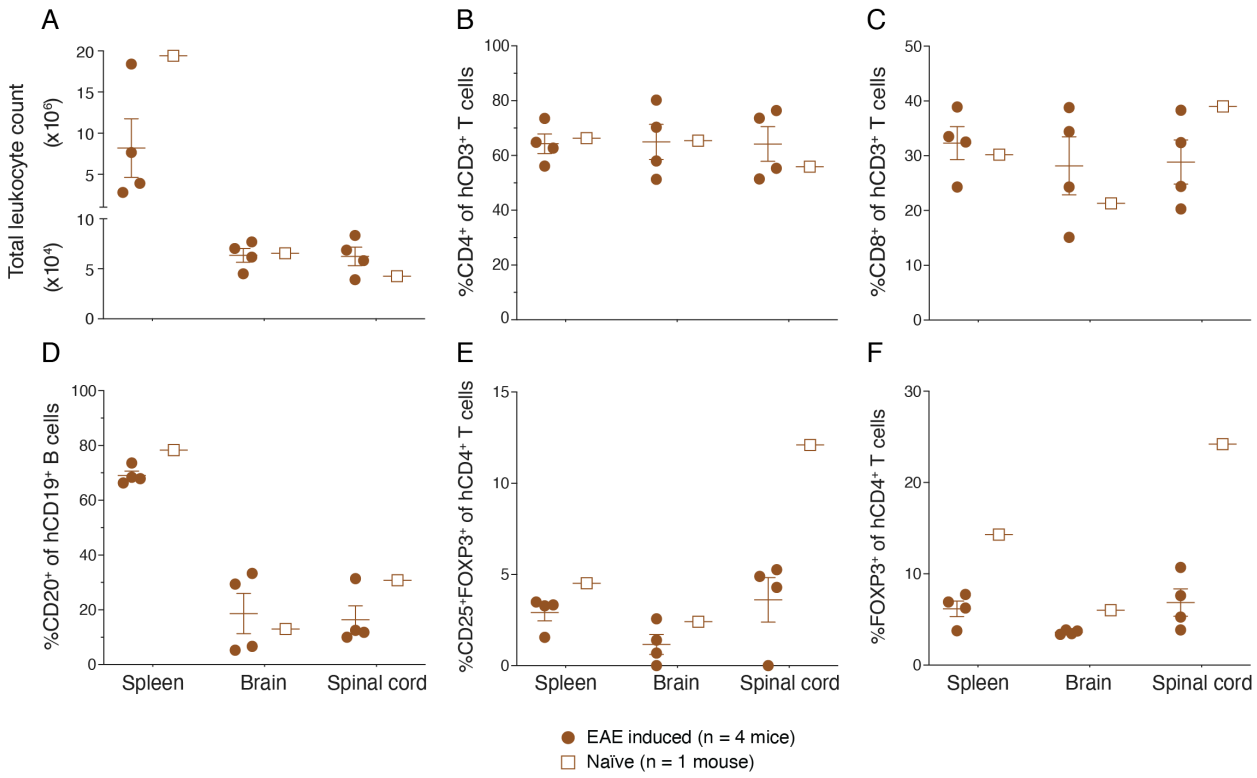

Figure 3.20 Human immune cell subset composition in the CNS and spleens of HuBLT mice at EAE endpoint

Total leukocyte counts (A) and the proportions of $CD4^+$ of $hCD3^+$ T cells (B), $CD4^+$ of $hCD3^+$ T cells (C), $CD20^+$ of $hCD19^+$ B cells (D), $CD25^+FOXP3^+$ of $hCD3^+CD4^+$ T cells (E), and $FOXP3^+$ of $hCD3^+CD4^+$ T cells (F) in the spleen, brain, and spinal cord at day 41 post-EAE induction. Brain and spinal cord tissues were perfused prior to cell isolation. Data are shown as mean with SEM for 4 EAE-induced HuBLT mice and for one uninduced control (naïve) HuBLT mouse.

Human immune cell frequencies were similar but somewhat smaller than those of $mCD45^+$ cells in the spleens of all HuBLT mice and did not appear to be impacted substantially by EAE induction (Figure 3.19A). EAE induction, however, did result in a notable increase in the proportion of infiltrating $mCD45^{hi}$ immune cells in the brain and especially the spinal cord, producing a concomitant decrease in the proportion of resident $mCD45^{lo}$ cells, despite a very small proportion of $hCD45^+$ cells comprising total immune cells in the CNS (Figure 3.19B – C). The scarcity of $hCD45^+$ cells in the CNS following EAE induction was emphasized by the relatively few total numbers of human immune cells in the brain (~700 $hCD45^+$ vs. ~7500 $mCD45^{hi}$ cells) and spinal cord (~400 $hCD45^+$ vs. ~1 x 10^4 $mCD45^{hi}$) compared to the spleen (~ 4 x 10^6 of both

hCD45$^+$ and mCD45$^+$ cells), though these values were slightly greater than the uninduced HuBLT control (Figure 3.19 right column). Within the CNS-infiltrating hCD45$^+$ cell population, the relative proportions of T cell subsets reflected those in the spleen, indicating there was not a preferential migration of one T cell subset over another into the CNS following immunization, whereas very few human B cells infiltrated the CNS (Figure 3.19).

EAE induction led to a moderate increase in the total cell counts in the spinal cord compared to the uninduced control with an associated contraction in the spleen (Figure 3.20A). The proportion of infiltrating hCD3$^+$ T cells expressing hCD4 and hCD8 was consistent between the CNS and spleen (Figure 3.20B – C), though hCD19$^+$ B cells that entered the CNS were preferentially hCD20 negative compared to splenic B cells (Figure 3.20D). In all three tissues, but most notably in the spinal cord, fewer of the infiltrating hCD4$^+$ T cells expressed regulatory markers hCD25 and hFOXP3 (Figure 3.20E – F). Overall, EAE induction did not produce substantial human immune cell infiltration of the CNS of HuBLT mice compared to the uninduced control sufficient to produce clinical EAE symptoms, despite exhibiting comprehensive HIS reconstitution in the periphery.

3.4.2.3 HuPBMC mice

Unlike the HuHSC and HuBLT cohorts, EAE induction of HuPBMC mice derived from two healthy female adult blood donors did result in clinical symptoms consistent with classical models in ~20% of the mice. Spleen reconstitution was assessed for 20 remaining HuPBMC mice derived from both donors at 24 days post-EAE induction and, as expected, was predominated by hCD3$^+$ T cells, which comprised 80 – 100% of hCD45$^+$ cells in most samples (Figure 3.21A). hCD19$^+$ B cells were also present in some samples, but most spleens contained fewer than 0.5% human B cells among all engrafted hCD45$^+$ cells (Figure 3.21B). Quantitatively, mCD45$^+$ immune cells and hCD45$^+$/CD3$^+$ T cells were present in equivalent amounts (Figure 3.21C). Multiple spleens contained detectable but low levels of hCD56$^+$ NK cells, whereas hCD14$^+$ cells could not be reliably measured in the samples (Figure 3.21D). Four of the 20 spleen samples were obtained from mice that had developed clinically measurable EAE symptoms, though the composition of engrafted human immune cells (Figure 3.22A) and the total number of each (Figure 3.22B) did not statistically differ between the mice that did or did not develop symptoms, suggesting absolute

human T cell reconstitution in the periphery was not the sole factor determining symptom onset following EAE induction.

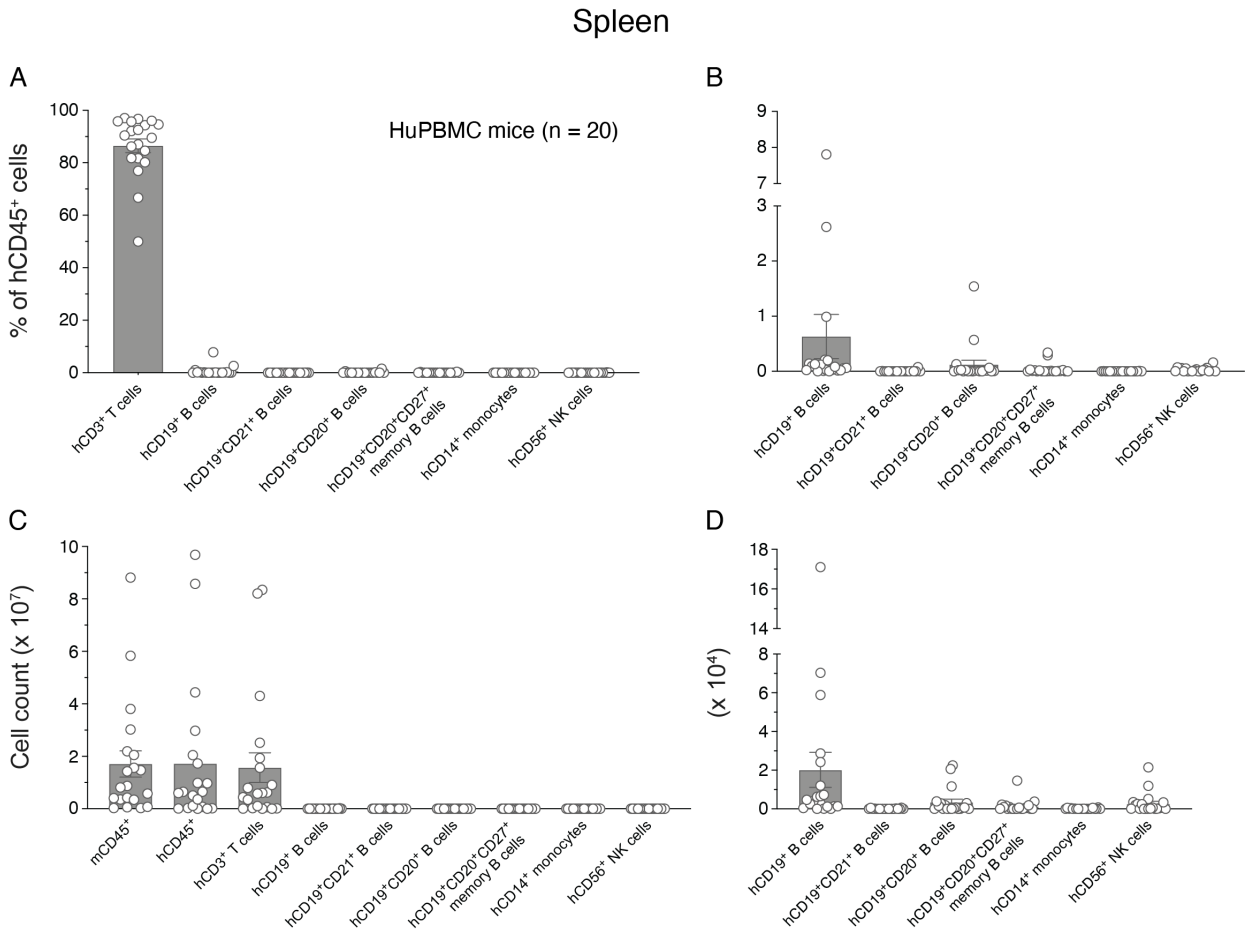

Figure 3.21 Reconstitution of human immune cells in HuPBMC spleens at EAE endpoint

(A) Relative proportions of all measured human immune cell lineages shown as a proportion of engrafted hCD45$^+$ cells in the spleen at day 24 post-EAE induction, (B) with the minorly engrafted immune cell lineages graphed separately to better illustrate abundance. (C) Total cell counts for all measured immune cell lineages in the spleen, (D) with the minorly engrafted human immune cell lineages graphed separately to better illustrate abundance. Data are shown as mean with SEM for 20 mice total (cohorts 8 and 9 combined) engrafted with PBMCs from one of two healthy adult female donors (HD-01 or HD-03) and induced with EAE.

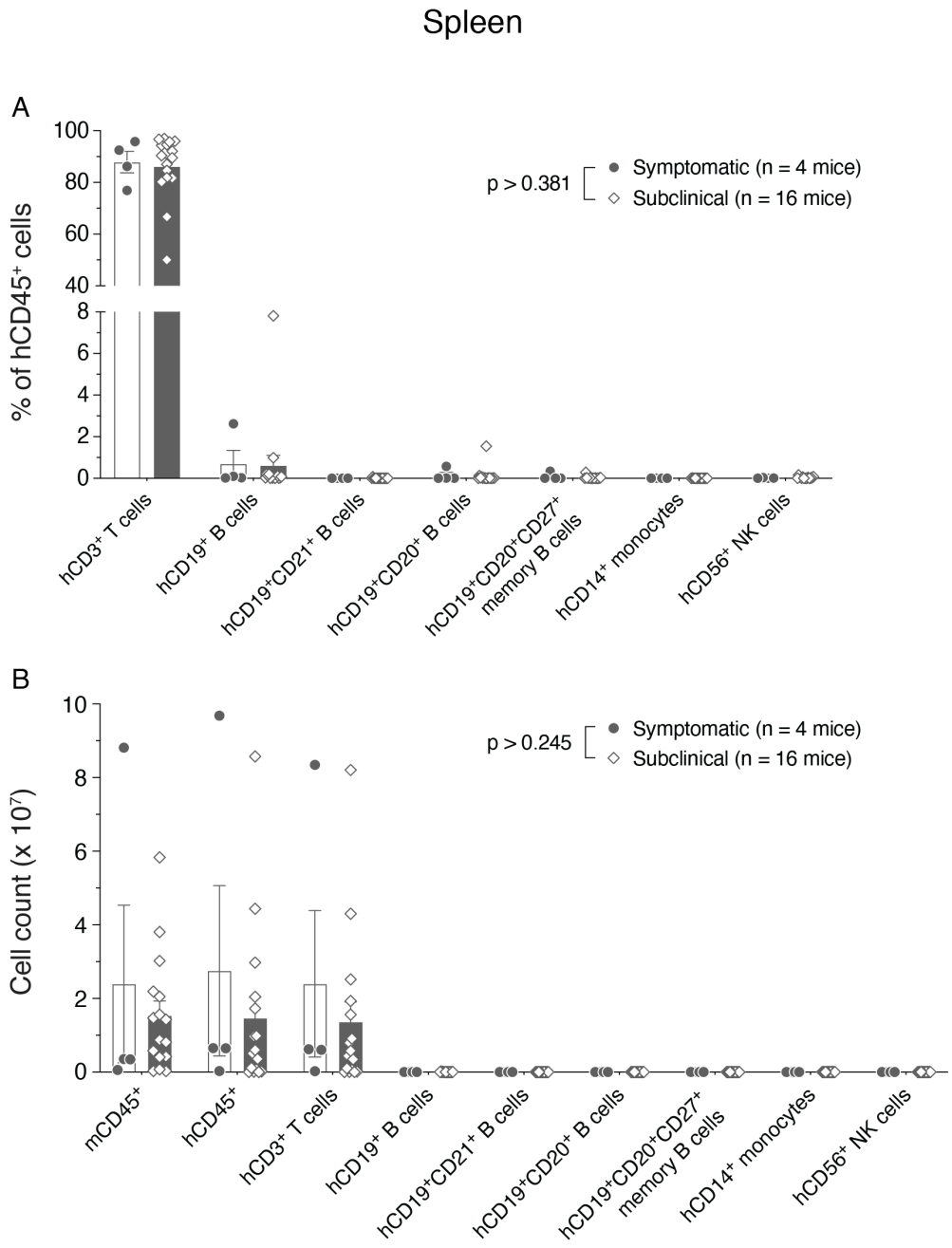

Figure 3.22 Reconstitution of human immune cells in HuPBMC spleens at EAE endpoint by symptom presentation

(A) Relative proportions of all measured human immune cell lineages shown as a proportion of engrafted hCD45$^+$ cells and (B) total cell counts in the spleen at day 24 post-EAE induction. Data are shown as mean with SEM for 4 clinically symptomatic mice and 16 subclinical HuPBMC EAE mice (cohorts 8 and 9 combined) engrafted with PBMCs from one of two healthy adult female donors (HD-01 or HD-03). Data for each cell subset were analyzed by Mann-Whitney test.

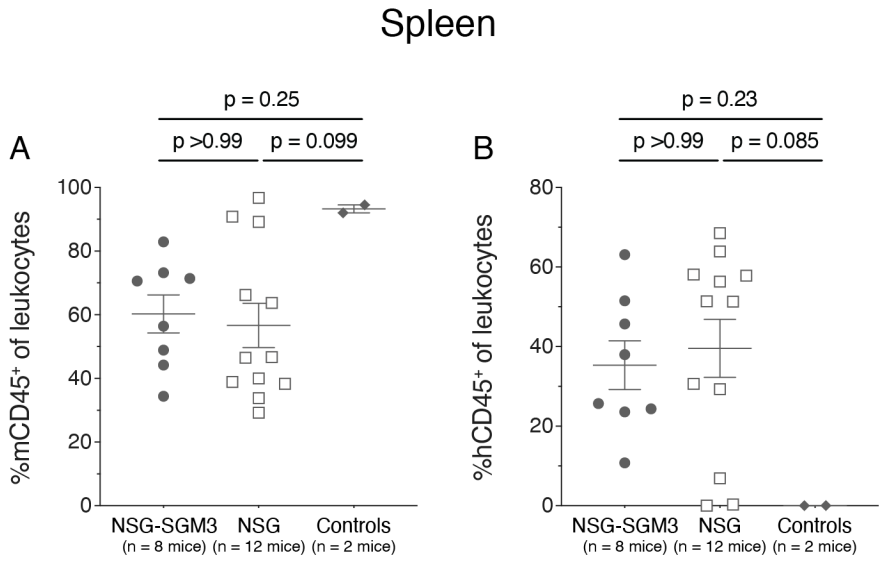

Figure 3.23 Murine and human immune cells in the spleens of HuPBMC mice on the NSG and NSG-SGM3 background at EAE endpoint

Relative proportions of murine mCD45$^+$ (A) and human hCD45$^+$ (B) immune cells of total leukocytes (murine and human) in the spleen at day 24 post-EAE induction. Data are shown as mean with SEM for 12 NSG and 8 NSG-SGM3 mice (cohorts 8 and 9 combined) engrafted with PBMCs from one of two healthy adult female donors (HD-01 or HD-03), alongside 2 NSG mice that remained as unengrafted control, induced with EAE. Data were analyzed by Kruskal-Wallis test with Dunn's multiple comparisons.

Of the five HuPBMC mice that developed paralytic symptoms after EAE induction, 4 were PBMC-engrafted NSG mice, and the other was an NSG-SGM3 mouse, suggesting the use of NSG-SGM3 mice did not provide any additional advantage in terms of promoting EAE symptom onset. In the spleen at EAE endpoint, mCD45$^+$ and hCD45$^+$ levels were statistically equal between NSG and NSG-SGM3 engrafted mice (Figure 3.23). Furthermore, human immune cell subset composition (Figure 3.24A) and abundance (Figure 3.24B) in the spleen did not statistically differ between these recipient background strains at endpoint. A more comprehensive analysis of PBMC engrafted NSG and NSG-SGM3 in section 4.4 further confirms the relative similarity of both strains as recipients for the HuPBMC EAE model. The proportions of hCD19$^+$ B cells expressing the EBV receptor hCD21 was notably low in the spleen at endpoint (<10%) and hCD20 expression was not consistently observed on all human B cells but was detected on ~10 – 40% of B cells if present (Figure 3.25A). Approximately half of the hCD19$^+$CD20$^+$ B cells also expressed the activation marker hCD27 (Figure 3.25A), though none of the B cell subsets were impacted by the

use of NSG or NSG-SGM3 mice as PBMC recipients (Figure 3.25B), nor did the occurrence of clinical symptoms relate to B cell subset levels (Figure 3.25C).

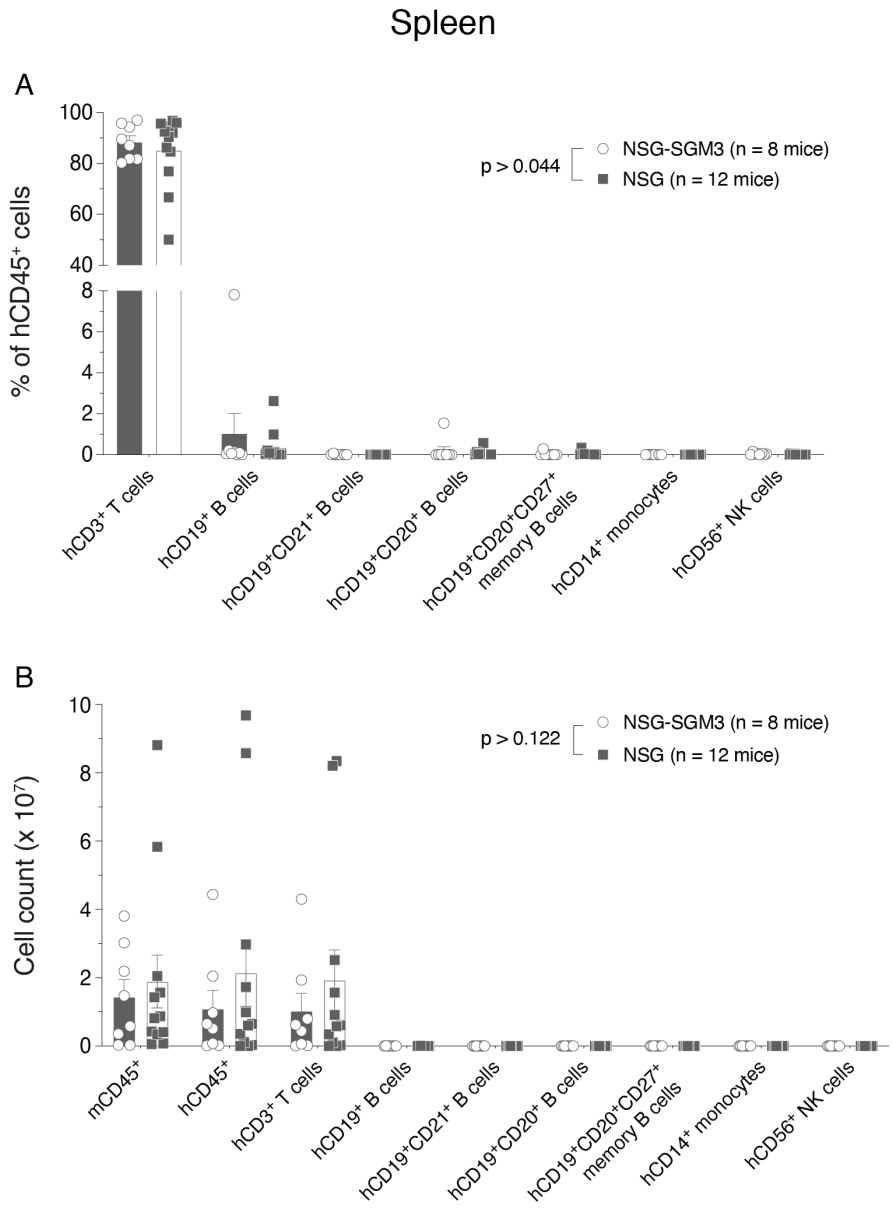

Figure 3.24 Reconstitution of human immune cells in the spleens of HuPBMC mice on the NSG and NSG-SGM3 background at EAE endpoint

(A) Relative proportions of all measured human immune cell lineages shown as a proportion of engrafted $hCD45^+$ cells and (B) total cell counts in the spleen at day 24 post-EAE induction. Data are shown as mean with SEM for 12 NSG and 8 NSG-SGM3 mice (cohorts 8 and 9 combined) engrafted with PBMCs from one of two healthy adult female donors (HD-01 or HD-03) and induced with EAE. Data for each cell subset were analyzed by Mann-Whitney test.

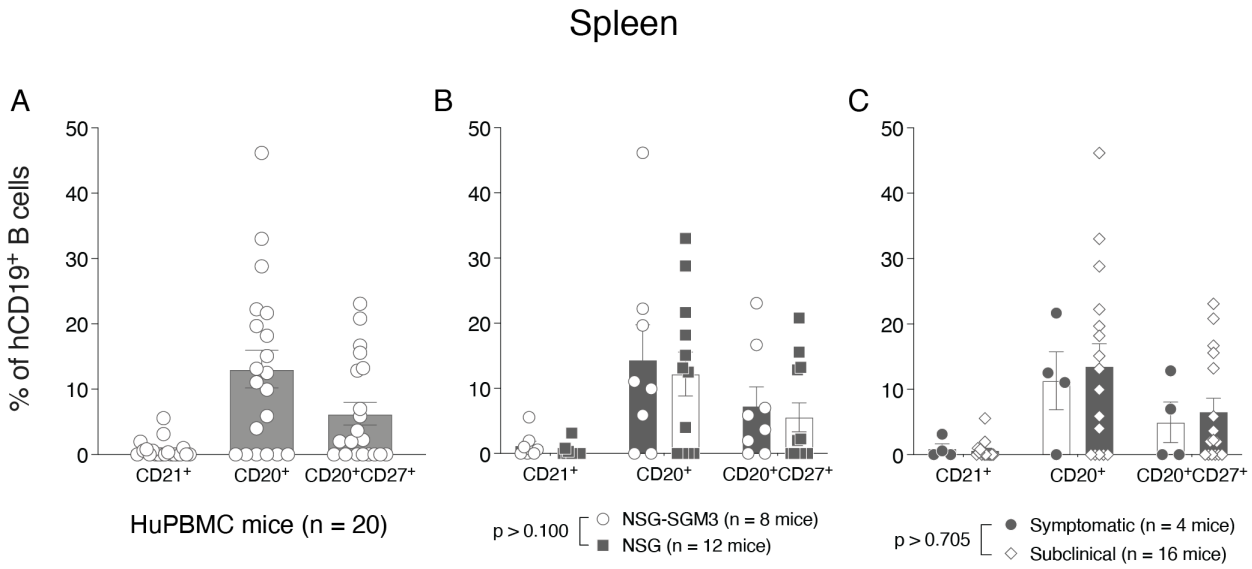

Figure 3.25 Human B cell subset reconstitution of the spleens of HuPBMC mice at EAE endpoint

Proportions of human B cell subsets among $hCD19^+$ B cells in the spleen at day 24 post-induction of (A) all HuPBMC EAE mice (n = 20 mice combined from cohorts 8 and 9, engrafted with PBMCs from one of two healthy adult female donors (HD-01 or HD-03)), (B) for NSG (n = 12 mice) and NSG-SGM3 (n = 8 mice) engrafted HuPBMC EAE mice, and (C) for HuPBMC EAE mice grouped based on clinical symptom presentation (n = 4 symptomatic mice) or lack thereof (n = 16 subclinical mice). Data are shown as mean with SEM and (B – C) were analyzed by Mann-Whitney test.

Cells isolated from the spleens of all 20 EAE-induced HuPBMC mice as well as from whole brain and spinal cord samples from 13 mice (cohort 9, derived from donor HD-03) were also stimulated ex vivo with PMA and ionomycin to assess T cell infiltration and cytokine expression in the CNS and periphery. Though there were insufficient numbers of CNS samples to compare mice that did or did not develop clinical symptoms in this preliminary analysis, a statistical assessment of CNS infiltration in symptomatic and subclinical mice is presented in section 4.7.2. As noted above, engraftment and EAE induction of HuPBMC mice resulted in $hCD45^+$ immune cell reconstitution of the spleen (Figure 3.26A), wherein $hCD45^+$ and $mCD45^+$ immune cells expanded to a correspondingly similar extent in the periphery (Figure 3.26B). EAE induction of HuPBMC mice also led to a moderate increase in the number of $mCD45^{lo}$ and $mCD45^{hi}$ cells in the brain and spinal cord compared to unengrafted NSG control mice, though $hCD45^+$ cell infiltration was even greater and numerically surpassed $mCD45^{lo}$ and $mCD45^{hi}$ counts in some CNS samples (Figure 3.26C – F).

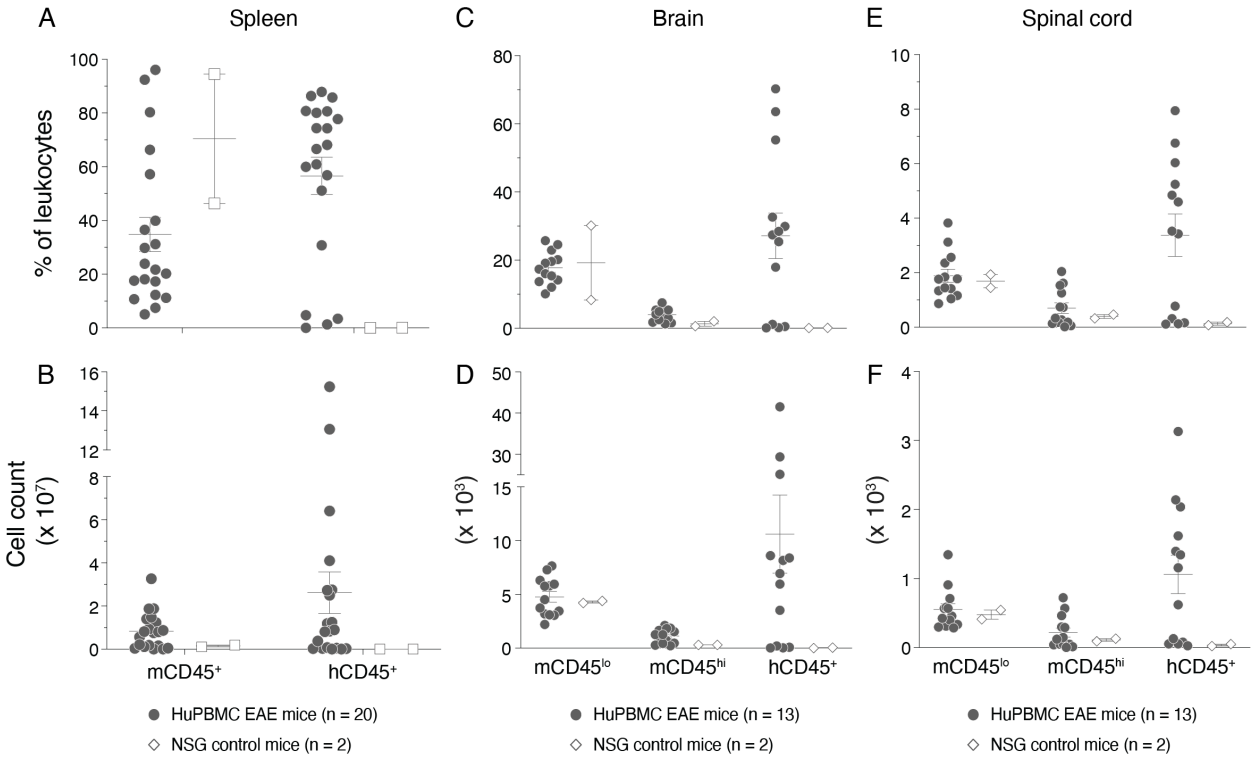

Figure 3.26 Murine and human immune cells in the CNS and peripheral tissues of HuPBMC mice at EAE endpoint

Relative proportions of human hCD45^{+} and murine mCD45$^{hi/lo}$ immune cells of total leukocytes (murine and human, top row) as well as total cell counts (bottom row) in the spleen (A–B), brain (C–D), and spinal cord (E–F) at day 24 post-EAE induction. Brain and spinal cord tissues were perfused prior to cell isolation. Data are shown as mean with SEM for 13 – 20 HuPBMC mice (cohorts 8 and 9 combined) engrafted with PBMCs from one of two healthy adult female donors (HD-01 or HD-03), alongside 2 NSG mice that remained as unengrafted control, induced with EAE.

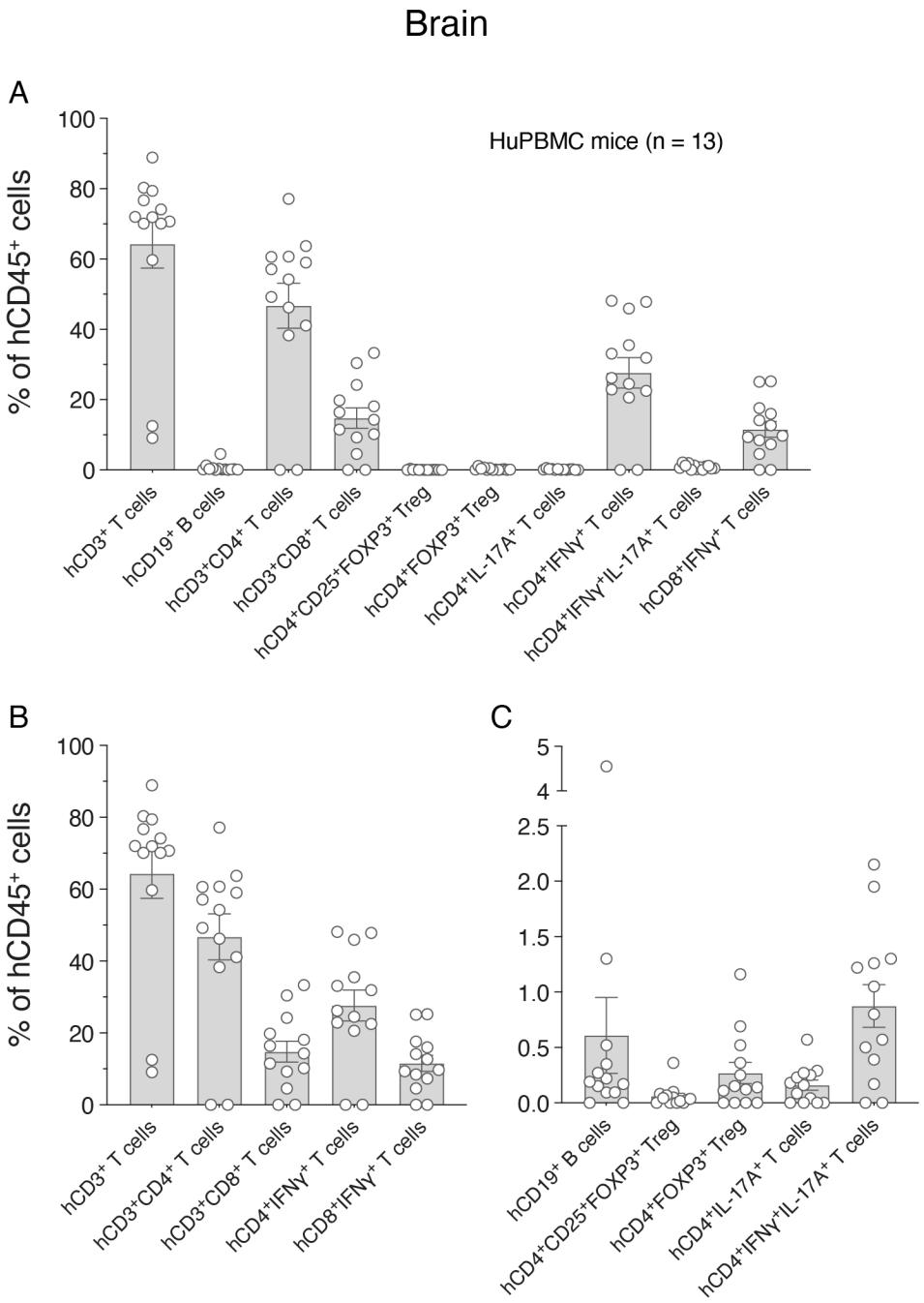

Figure 3.27 Human immune cell frequencies in HuPBMC brains at EAE endpoint

(A) Relative proportions of all measured human T and B cell subsets are shown as a proportion of infiltrating hCD45$^+$ cells in the brain of HuPBMC mice at day 24 post-EAE induction. These data are then subdivided into (B) predominantly infiltrating immune cell subsets and (C) minorly infiltrating immune cell subsets to better illustrate relative frequencies. Cells isolated from perfused brains were stimulated with PMA and ionomycin to measure cytokine expressing T cells (note that single positive hCD4$^+$IFNγ$^+$ T cells are IL-17A$^-$ and vice versa). Data are shown as mean with SEM for 13 mice total (cohort 9) engrafted with PBMCs from a healthy adult female donor (HD-03) and induced with EAE.

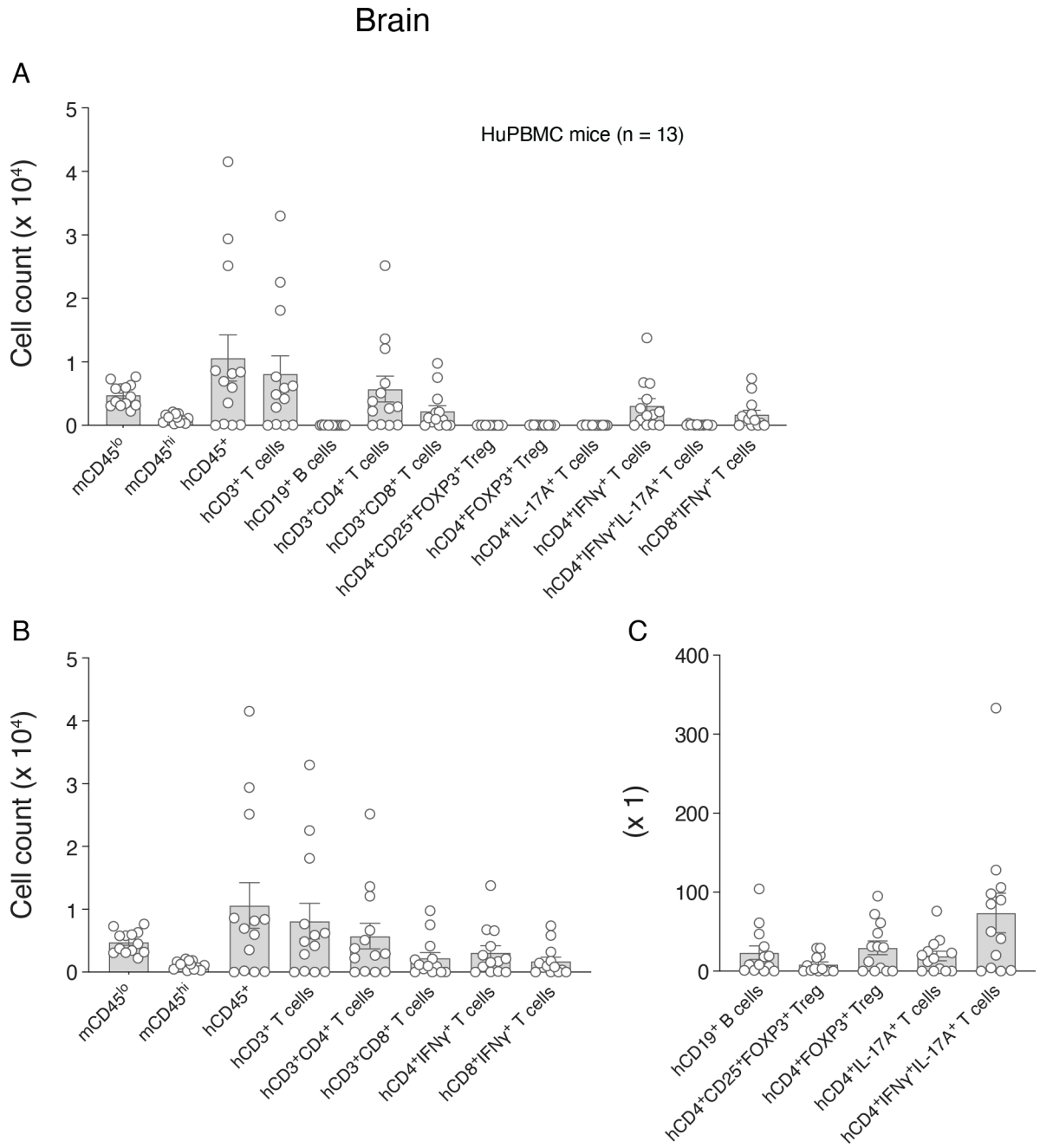

Figure 3.28 Murine and human immune cell abundance in HuPBMC brains at EAE endpoint

(A) Total cell counts for all measured murine and human immune cell subsets in the brain of HuPBMC mice at day 24 post-EAE induction. These data are then subdivided into (B) predominantly infiltrating immune cell subsets and (C) minorly infiltrating immune cell subsets to better illustrate relative frequencies. Cells isolated from perfused brains were stimulated with PMA and ionomycin to measure cytokine expressing T cells (note that single positive $hCD4^+IFN\gamma^+$ T cells are IL-$17A^-$ and vice versa). Data are shown as mean with SEM for 13 mice total (cohort 9) engrafted with PBMCs from a healthy adult female donor (HD-03) and induced with EAE.

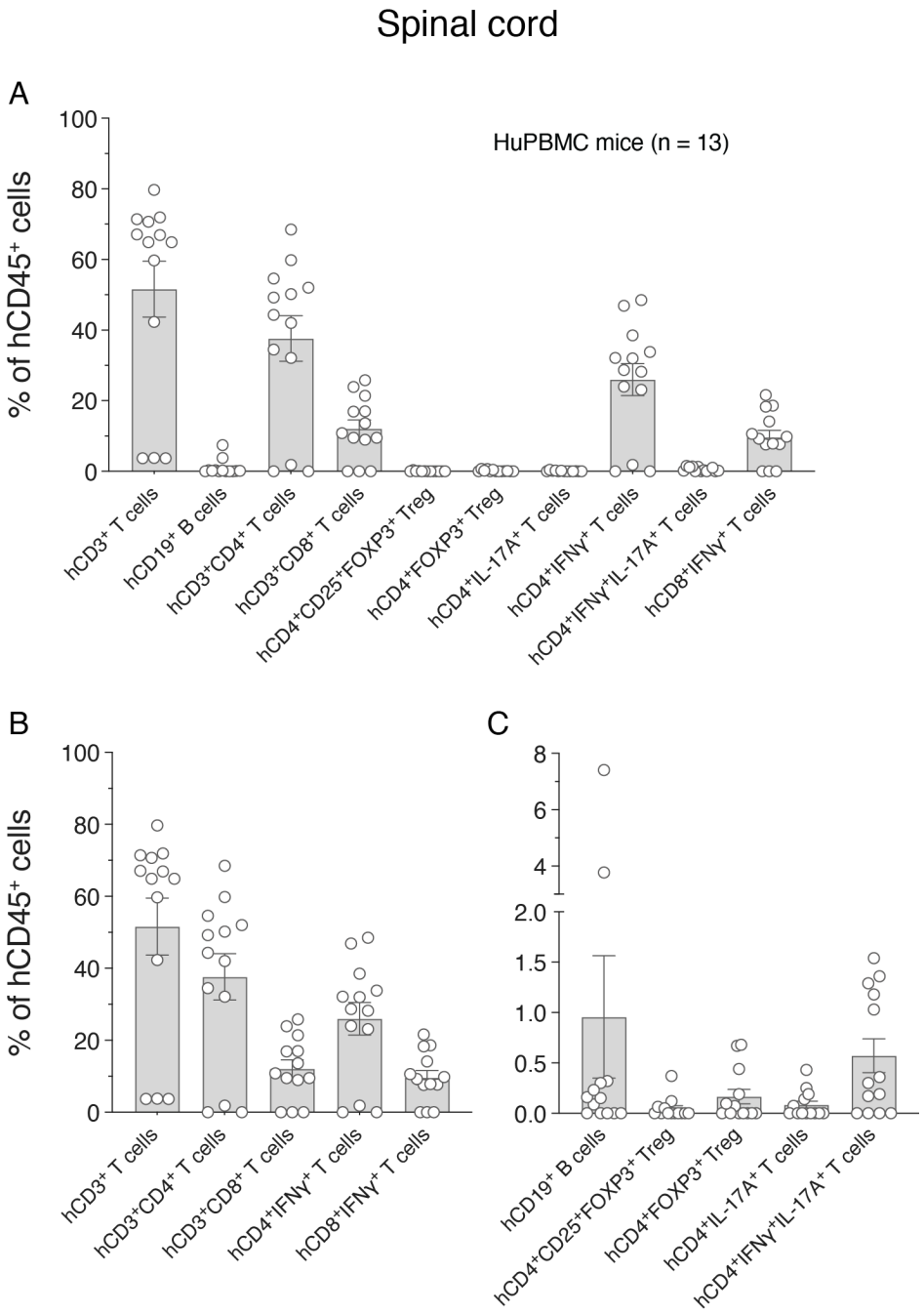

Figure 3.29 Human immune cell frequencies in HuPBMC spinal cords at EAE endpoint

(A) Relative proportions of all measured human T and B cell subsets are shown as a proportion of infiltrating hCD45$^+$ cells in the spinal cord of HuPBMC mice at day 24 post-EAE induction. These data are then subdivided into (B) predominantly infiltrating immune cell subsets and (C) minorly infiltrating immune cell subsets to better illustrate relative frequencies. Cells isolated from perfused spinal cords were stimulated with PMA and ionomycin to measure cytokine expressing T cells (note that single positive hCD4$^+$IFNγ$^+$ T cells are IL-17A$^-$ and vice versa). Data are shown as mean with SEM for 13 mice total (cohort 9) engrafted with PBMCs from a healthy adult female donor (HD-03) and induced with EAE.

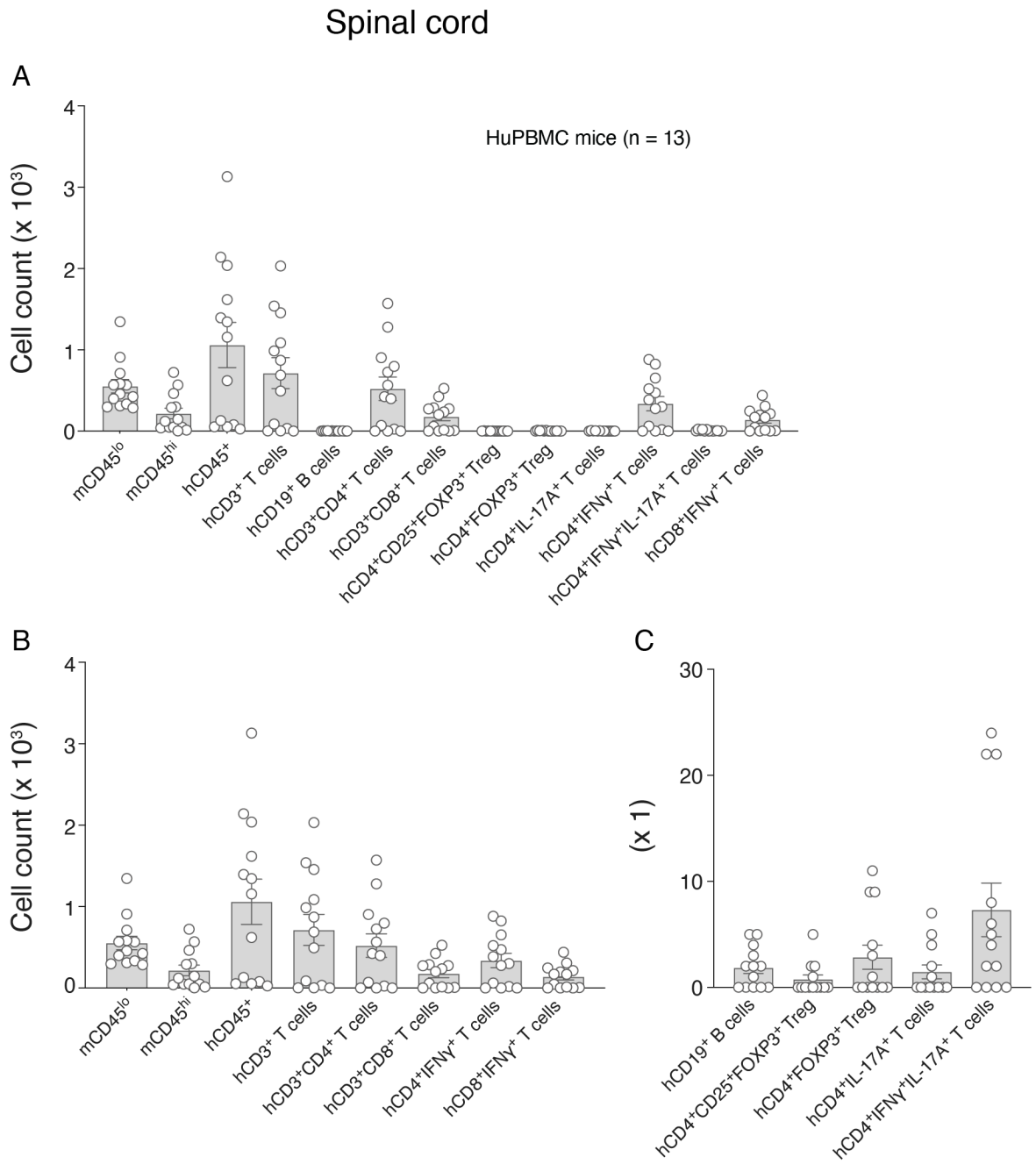

Figure 3.30 Murine and human immune cell abundance in HuPBMC spinal cords at EAE endpoint

(A) Total cell counts for all measured murine and human immune cell subsets in the spinal cord of HuPBMC mice at day 24 post-EAE induction. These data are then subdivided into (B) predominantly infiltrating immune cell subsets and (C) minorly infiltrating immune cell subsets to better illustrate relative frequencies. Cells isolated from perfused spinal cords were stimulated with PMA and ionomycin to measure cytokine expressing T cells (note that single positive $hCD4^+IFN\gamma^+$ T cells are $IL\text{-}17A^-$ and vice versa). Data are shown as mean with SEM for 13 mice total (cohort 9) engrafted with PBMCs from a healthy adult female donor (HD-03) and induced with EAE.

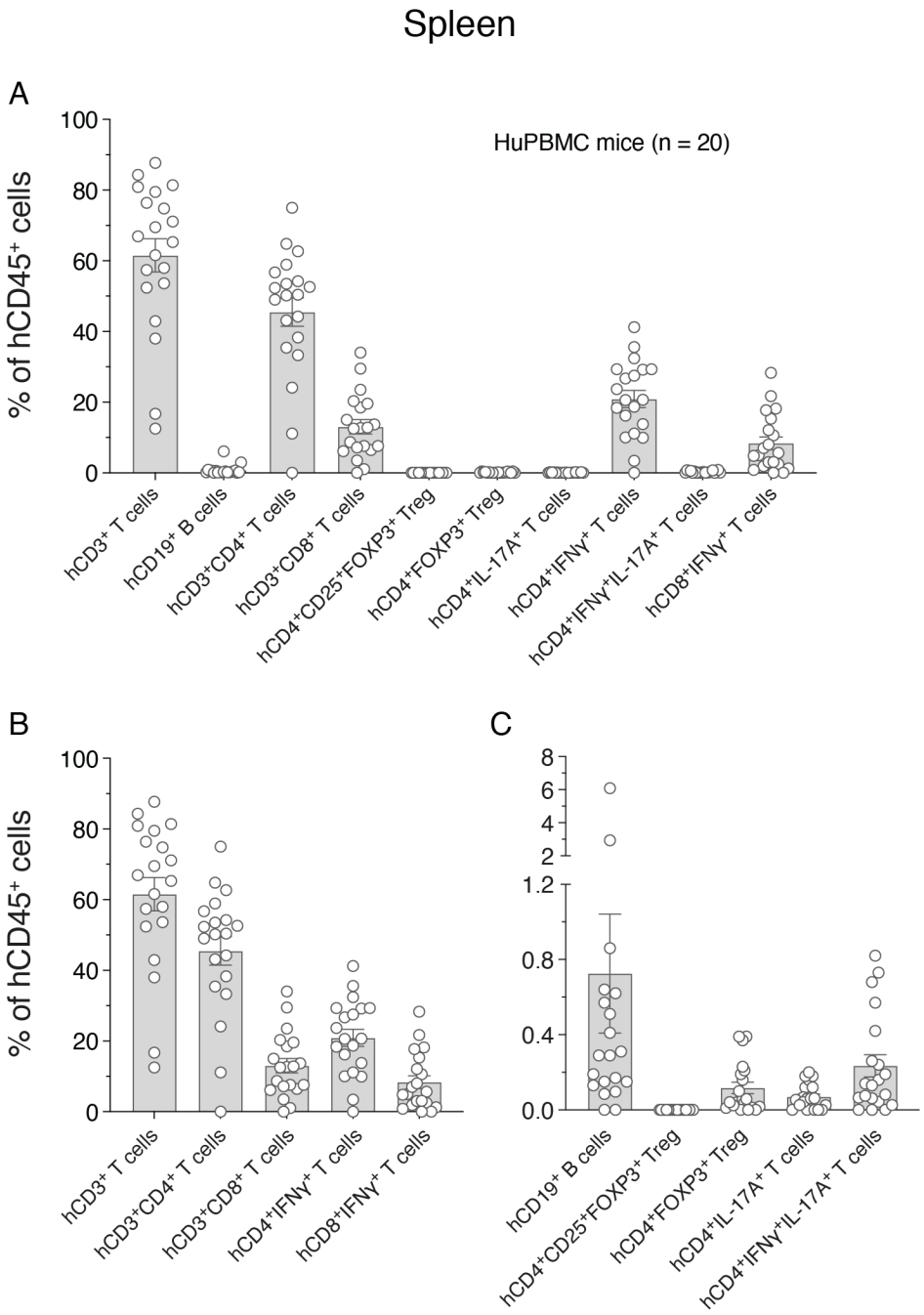

Figure 3.31 Human immune cell frequencies in HuPBMC spleens at EAE endpoint

(A) Relative proportions of all measured human T and B cell subsets are shown as a proportion of engrafted $hCD45^+$ cells in the spleen of HuPBMC mice at day 24 post-EAE induction. These data are then subdivided into (B) predominantly engrafted immune cell subsets and (C) minorly engrafted immune cell subsets to better illustrate relative frequencies. Cells isolated from spleens were stimulated with PMA and ionomycin to measure cytokine expressing T cells (note that single positive $hCD4^+IFN\gamma^+$ T cells are IL-$17A^-$ and vice versa). Data are shown as mean with SEM for 20 mice total (cohorts 8 and 9 combined) engrafted with PBMCs from one of two healthy adult female donors (HD-01 or HD-03) and induced with EAE.

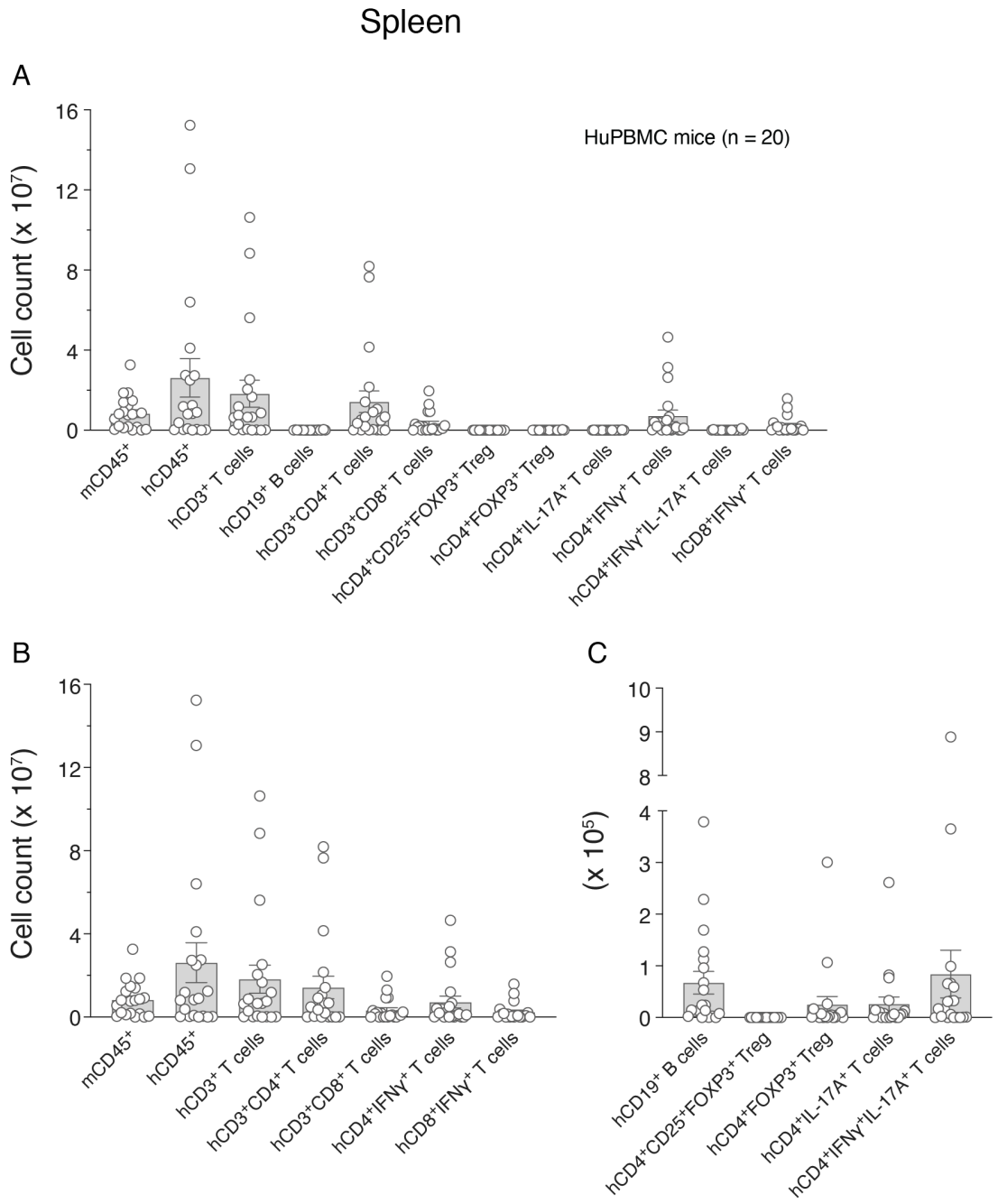

Figure 3.32 Murine and human immune cell abundance in HuPBMC spleens at EAE endpoint

(A) Total cell counts for all measured murine and human immune cell subsets in the spleen of HuPBMC mice at day 24 post-EAE induction. These data are then subdivided into (B) predominantly engrafted immune cell subsets and (C) minorly engrafted immune cell subsets to better illustrate relative frequencies. Cells isolated from spleens were stimulated with PMA and ionomycin to measure cytokine expressing T cells (note that single positive $hCD4^+IFN\gamma^+$ T cells are IL-$17A^-$ and vice versa). Data are shown as mean with SEM for 20 mice total (cohorts 8 and 9 combined) engrafted with PBMCs from one of two healthy adult female donors (HD-01 or HD-03) and induced with EAE.

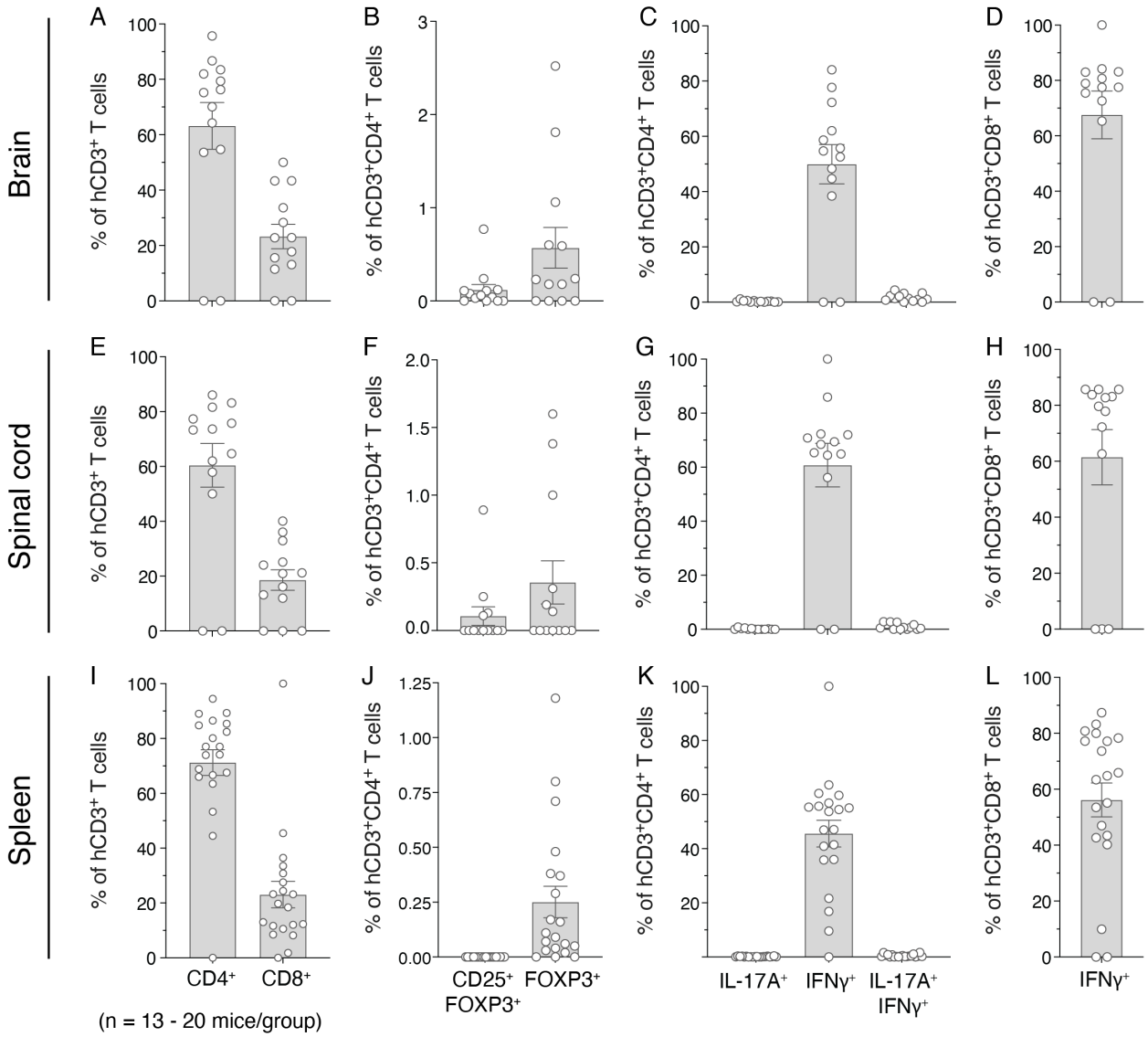

Figure 3.33 Human T cell subsets in the CNS and peripheral tissues of HuPBMC mice at EAE endpoint

Relative proportions of human regulatory and effector T cell subsets among parent T cell populations in the brain (A – D, n = 13), spinal cord (E – H, n = 13), and spleen (I – L, n = 20). Brain and spinal cord tissues were perfused prior to cell isolation. Cells isolated from each tissue were stimulated with PMA and ionomycin to measure cytokine expressing T cells (note that single positive $hCD4^{+}IFN\gamma^{+}$ T cells are IL-$17A^{-}$ and vice versa). Data are shown as mean with SEM for HuPBMC mice (cohorts 8 and 9 combined) engrafted with PBMCs from one of two healthy adult female donors (HD-01 or HD-03) and induced with EAE.

Similar to the composition of spleen engrafted $hCD45^+$ cells in HuPBMC mice, most brain infiltrating $hCD45^+$ cells were $hCD3^+$ T cells (~60 – 90%), including both $hCD4^+$ and $hCD8^+$ T cells expressing IFNγ (Figure 3.27A – B). IL-17A and FOXP3 expressing T cells occurred at similarly low levels as $hCD19^+$ B cells, each comprising <1% of $hCD45^+$ cells in most brain samples (Figure 3.27C). The proportional distribution of T and B cells was further reflect by the total number of each subset present in the brain, where $mCD45^{lo}$ CNS resident immune cell counts were similar to $hCD45^+CD3^+$ T cell counts at ~ 1 x 10^4 per brain (Figure 3.28A – B), which were both far more abundant than regulatory T cells, IL-$17A^+$ T cells, and $hCD19^+$ B cells at less than ~100 cells each per brain (Figure 3.28C). The HuPBMC EAE spinal cords contained a nearly identical relative composition of T cell subsets among $hCD45^+$ immune cells as the brains (Figure 3.29), though with approximately 10X fewer of each cell type in the physically smaller spinal cords than the brain (Figure 3.30). The spleens also contained the same relative composition of T cell subsets among $hCD45^+$ immune cells as the CNS tissues (Figure 3.31), suggesting there was not a preferential migration or expansion of certain subset from the periphery into the CNS. The spleens did, however, contain consistently higher frequencies (Figure 3.31C) and larger numbers of $hCD19^+$ B cells than the CNS (Figure 3.32C). Within each T cell population, the proportions of $hCD4^+$ and $hCD8^+$ T cells (Figure 3.33 first column), $hCD4^+$ regulatory T cells (second column), $hCD4^+$ effector T cells (third column), and $hCD8^+$ effector T cells (last column) were detected consistently in the brain (Figure 3.33A – D), spinal cord (Figure 3.33E – H), and spleen samples (Figure 3.33I – L).

3.4.2.4 Model comparison of human immune cell reconstitution of the spleen

Freshly isolated splenocytes from all EAE-induced HuHSC (day 30 post-induction), HuBLT (day 41 post-induction), and HuPBMC mice (day 24 post-induction) were compared at endpoint for reconstitution of major human immune cell lineages to provide insight as to how EAE induction influenced HIS engraftment and whether this effect promoted EAE symptom development in the HuPBMC mice but not in the HuHSC or HuBLT mice. Both the proportions of $hCD45^+$ immune cells, $hCD19^+$ B cells, $hCD3^+$ T cells, $hCD14^+$ monocytes, and $hCD56^+$ NK cells, and their total quantities in the spleen are reported in Table 3.3 for reference. hCD56, hCD21, and hCD27 expression was not measured in HuBLT spleens at endpoint, and for these cell subsets, HuHSC and HuPBMC spleen samples are compared.

Table 3.3 Splenic reconstitution of humanized mice at EAE endpoint

Data are shown as cohort average cell counts, percentages of total leukocytes (murine and human), or percentages of $hCD45^+$ cells for engrafted subsets with standard deviation.

	HuHSC	**HuBLT**	**HuPBMC**
EAE induction (Weeks post-engraftment)	16	11	3
EAE endpoint (Day post-induction)	30	41	24
Cohort size (n)	6	4	20
Total leukocyte count in spleen	1.78×10^6 ($\pm 8.16 \times 10^5$)	1.04×10^7 ($\pm 7.95 \times 10^6$)	3.55×10^7 ($\pm 5.12 \times 10^7$)
$\%hCD45^+$ cells of leukocytes	30.9 (± 27.6)	35.6 (± 9.47)	37.9 (± 22.0)
$hCD45^+$ cell count	6.05×10^5 ($\pm 5.46 \times 10^5$)	3.71×10^6 ($\pm 2.70 \times 10^6$)	1.72×10^7 ($\pm 2.78 \times 10^7$)
$\%hCD3^+$ T cells of $hCD45^+$	9.25 (± 17.0)	53.5 (± 30.5)	86.5 (± 11.7)
$hCD3^+$ T cell count	9.48×10^4 ($\pm 1.86 \times 10^5$)	1.81×10^6 ($\pm 1.29 \times 10^6$)	1.57×10^7 ($\pm 2.53 \times 10^7$)
$\%hCD19^+$ B cells of $hCD45^+$	40.6 (± 16.6)	37.7 (± 29.1)	0.63 (± 1.79)
$hCD19^+$ B cell count	2.60×10^5 ($\pm 3.00 \times 10^5$)	1.57×10^6 ($\pm 1.74 \times 10^6$)	2.02×10^4 ($\pm 4.05 \times 10^4$)
$\%hCD14^+$ monocytes of $hCD45^+$	6.39 (± 4.45)	1.33 (± 0.78)	0.001 (± 0.002)
$hCD14^+$ monocyte count	2.08×10^4 ($\pm 1.37 \times 10^4$)	4.81×10^4 ($\pm 5.00 \times 10^4$)	130 (± 230)
$\%hCD56^+$ NK cells of $hCD45^+$	1.52 (± 1.42)	---	0.028 (± 0.039)
$hCD56^+$ NK cell count	7.12×10^3 ($\pm 6.69 \times 10^3$)	---	2.71×10^3 ($\pm 5.23 \times 10^3$)

Relative proportions of $hCD45^+$ immune cells among total leukocytes (murine and human) in the spleen was consistent between all three humanized mouse models (Figure 3.34A – B). Within the engrafted $hCD45^+$ splenocyte population, $hCD3^+$ T cells comprised an average of only ~10% in HuHSC mice, significantly lower than the averages of ~60% in HuBLT and >80% in HuPBMC mice (Figure 3.34C). In contrast, $hCD19^+$ B cells comprised ~40% of $hCD45^+$ cells in spleens of HuHSC mice, ~30% of HuBLT $hCD45^+$ cells, and <5% of HuPBMC $hCD45^+$ cells (Figure 3.34D). Similarly, $hCD14^+$ monocytes made up 1 – 15% of $hCD45^+$ splenocytes in HuHSC and HuBLT mice, significantly greater than the near absence of monocytes in HuPBMC spleens (Figure 3.34E). Though $hCD56^+$ NK cells were not entirely absent from HuPBMC splenocytes, they composed a significantly smaller proportion of total $hCD45^+$ cells compared to the HuHSC model. All of these proportions mostly reflect the relative composition of blood-derived leukocytes in each model prior to EAE induction (Figure 3.11), indicating that blood sampling prior to EAE induction is an appropriate indicator of available HIS subset reconstitution.

In terms of total cell abundance, HuBLT and HuPBMC spleens generally contained greater numbers of $hCD45^+$ cells than the HuHSC spleens at EAE endpoint, and some HuPBMC spleens were significantly enlarged compared to the other samples, which corresponded to the number of $mCD45^+$ immune cells (Figure 3.35A – B). HuPBMC mouse spleens often contained more $hCD3^+$ T cells than the other two models, though on average, T cell quantities were not significantly greater than in the HuBLT spleens (Figure 3.35C). Consistent with the frequency data, HuHSC spleens contained far fewer $hCD3^+$ T cells than the other two models (Figure 3.35C). $hCD19^+$ B cell and $hCD14^+$ monocyte counts were comparable between HuHSC and HuBLT spleens, both of which had significantly greater quantities than HuPBMC spleens, where they were mostly or entirely lacking (Figure 3.35D – E). $hCD56^+$ NK cell counts in the spleen were not statistically different between the HuHSC and HuPBMC mice, though the HuHSC spleens more reliably contained some NK cells, whereas HuPBMC mice either contained a similar amount of NK cells as the HuHSC mice or did not contain any at all (Figure 3.35F). Based on the blood reconstitution analysis prior to EAE induction (Figure 3.11), we anticipate that HuBLT spleens would likely contain similar numbers of human NK cells as those from HuHSC mice.

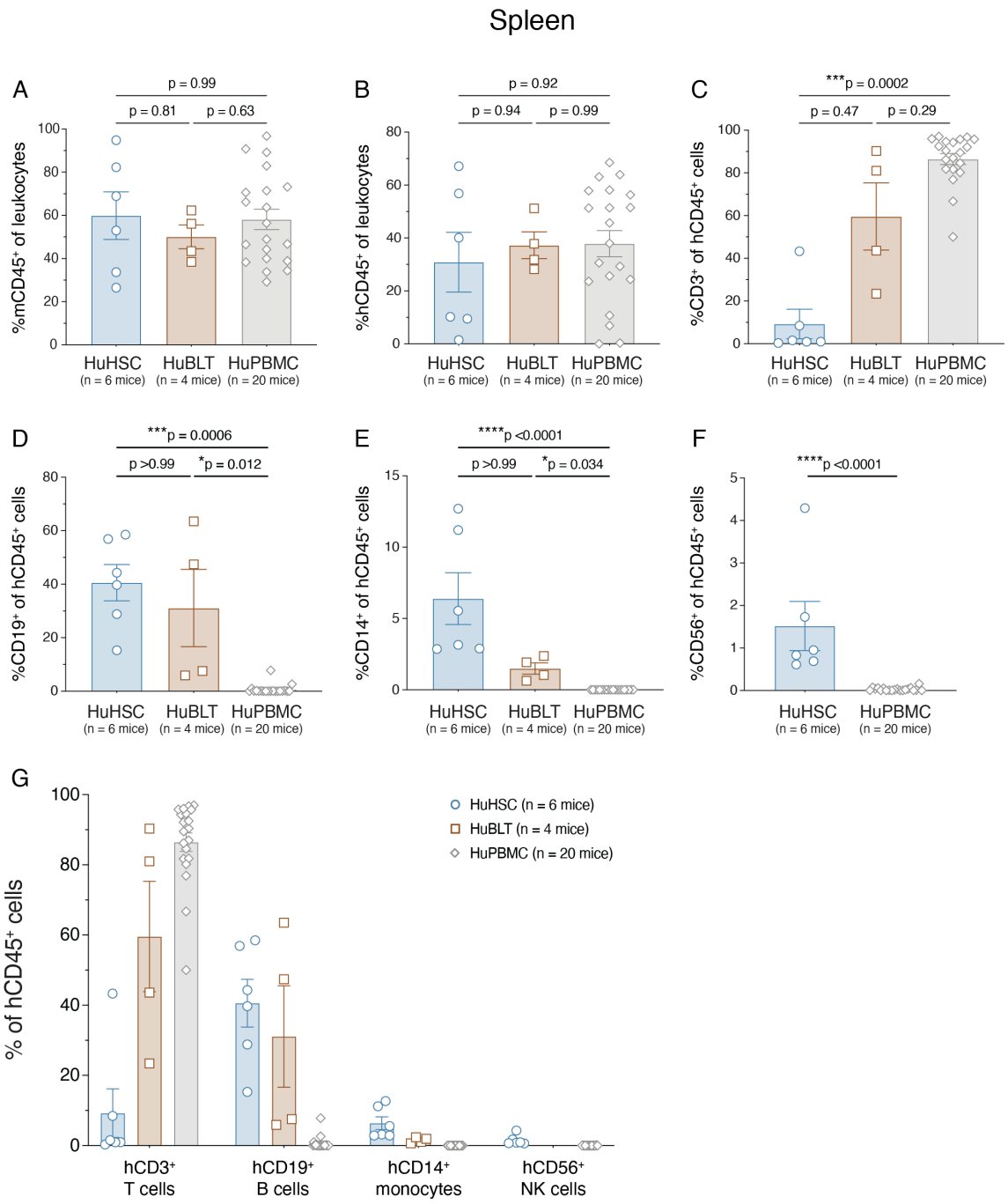

Figure 3.34 Model comparison of reconstituted human immune cell frequencies in humanized EAE mouse spleens

Proportions of (A) murine and (B) human immune cells among total leukocytes in the spleens of HuHSC mice (n = 6) day 30 post-EAE induction, HuBLT mice (n = 4) day 41 post-EAE induction, and HuPBMC mice (n = 20) day 24 post-EAE induction. Proportions of (C) hCD3$^+$, (D) hCD19$^+$, (E) hCD14$^+$, and (F) hCD56$^+$ immune cell lineage reconstitution among engrafted hCD45$^+$ cells, grouped in (G) to illustrate relative abundance. All engrafted NSG and NSG-SGM3 mice per cohort are combined for this analysis. Data are shown as mean with SEM and were

analyzed by Brown-Forsythe test with Dunnett's T3 multiple comparisons (A and B), Kruskal-Wallis test with Dunn's multiple comparisons (C – E), or Mann-Whitney test (F).

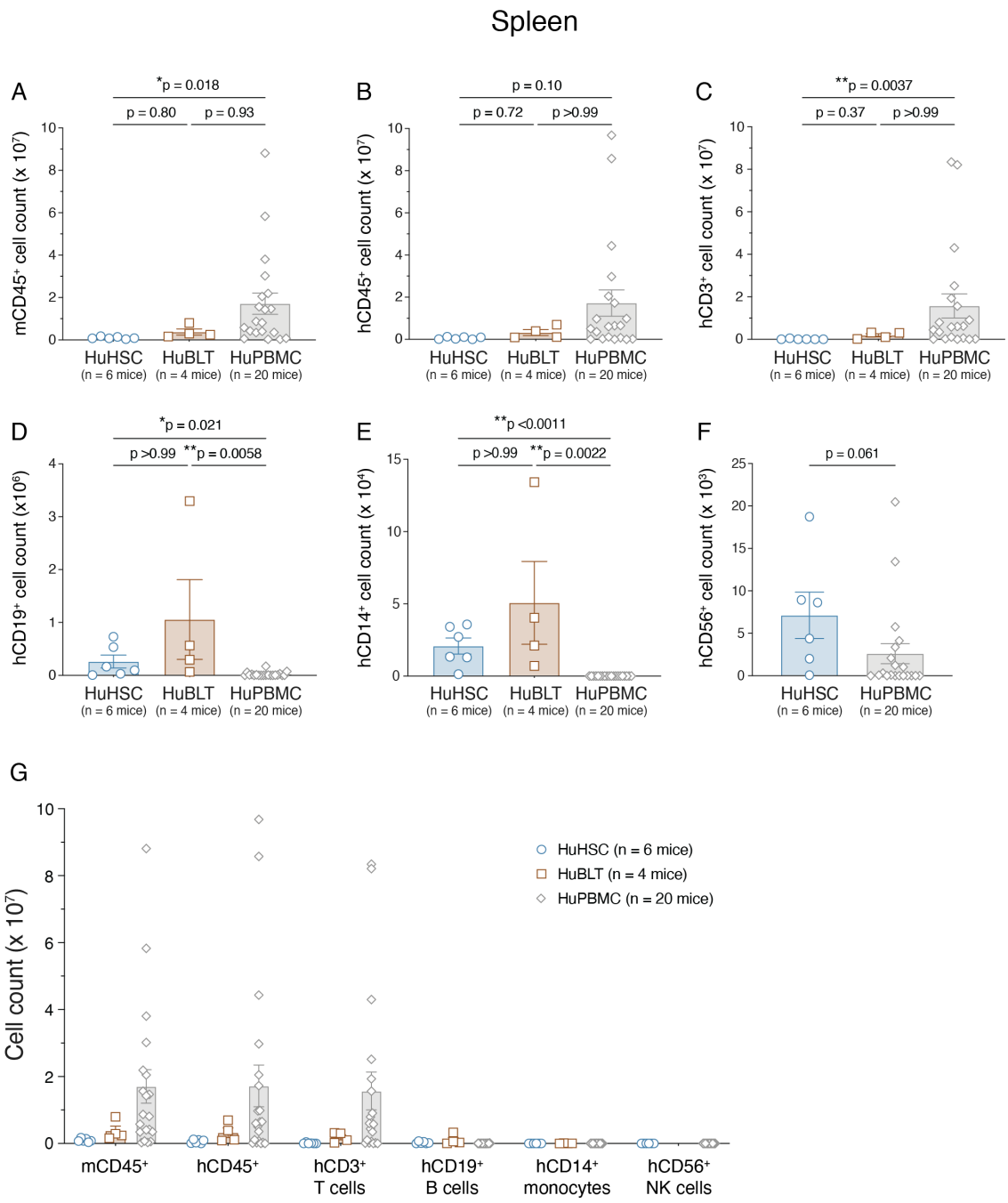

Figure 3.35 Model comparison of reconstituted human immune cell abundance in humanized EAE mouse spleens

Total cell counts of (A) mCD45$^+$, (B) hCD45$^+$, (C) hCD3$^+$, (D) hCD19$^+$, (E) hCD14$^+$, and (F) hCD56$^+$ immune cells in the spleens of HuHSC mice (n = 6) day 30 post-EAE induction, HuBLT mice (n = 4) day 41 post-

EAE induction, and HuPBMC mice (n = 20) day 24 post-EAE induction. Data are grouped in (G) to illustrate relative abundance. All engrafted NSG and NSG-SGM3 mice per cohort are combined for this analysis. Data are shown as mean with SEM and were analyzed by Kruskal-Wallis test with Dunn's multiple comparisons (A – E) or by Mann-Whitney test (F).

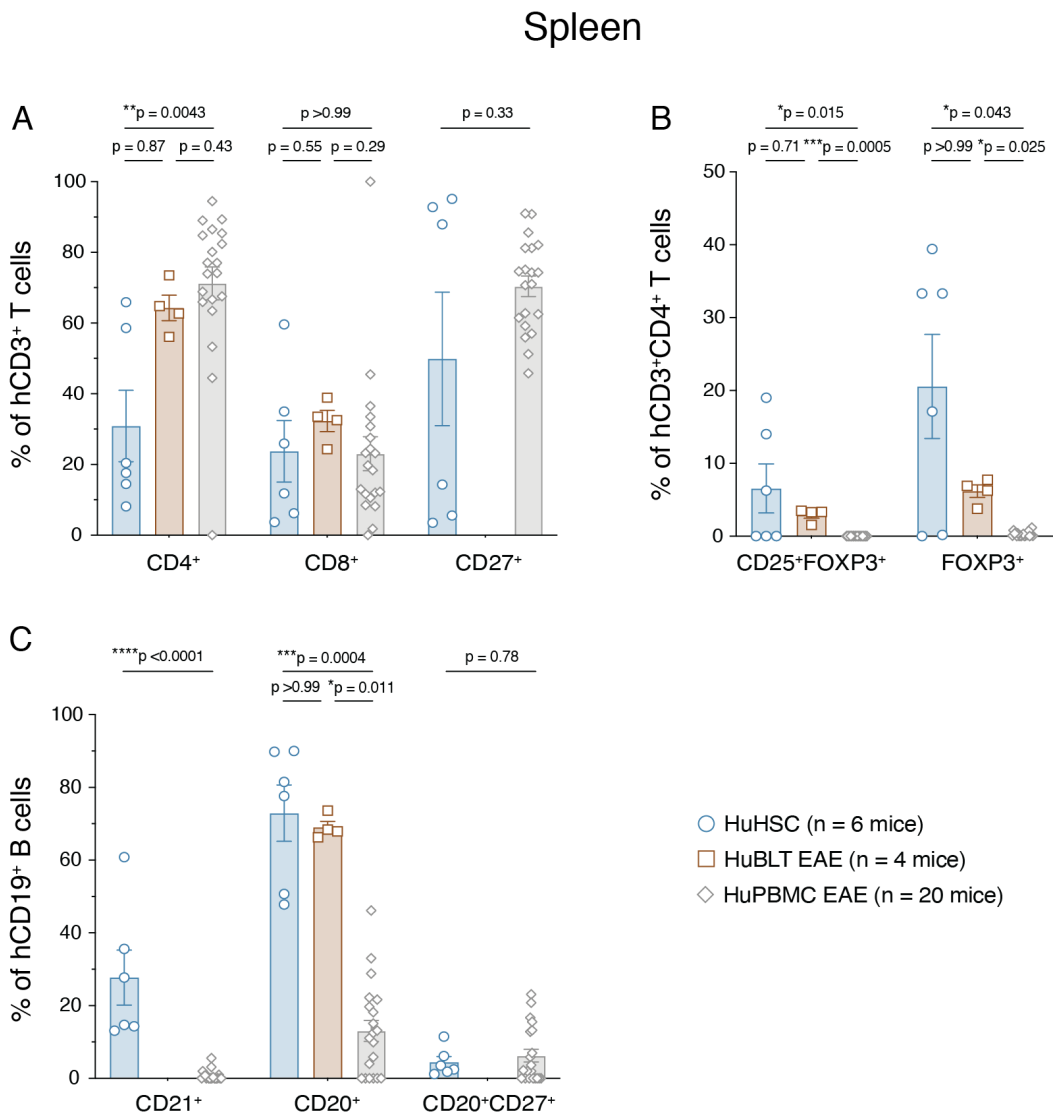

Figure 3.36 Model comparison of human T and B cell subsets in the spleens of humanized EAE mice

Relative proportions of all measured human T cell (A), regulatory T cell (Treg) (B), and B cell (C) subsets shown as a proportion of the parent population in the spleens of HuHSC mice (n = 6) day 30 post-EAE induction, HuBLT mice (n = 4) day 41 post-EAE induction, and HuPBMC mice (n = 20) day 24 post-EAE induction. All engrafted NSG and NSG-SGM3 mice per cohort are combined for this analysis. Data are shown as mean with SEM and were analyzed by Kruskal-Wallis test with Dunn's multiple comparisons or by Mann-Whitney test.

Within the spleen-engrafted hCD3$^+$ T cell population, HuHSC and HuBLT mice maintained relative expression levels of hCD4, hCD8, and hCD27 (Figure 3.36A) similar to that of the blood samples before EAE induction (Figure 3.12A). In the HuPBMC mice, however, the blood samples pre-EAE contained more or less even proportions of hCD4$^+$ and hCD8$^+$ T cells (Figure 3.12A), whereas EAE endpoint spleen samples were skewed toward hCD4$^+$ T cells relative to hCD8$^+$ T cells, suggesting preferential expansion of the former in this tissue (Figure 3.36A). hCD27 expression on hCD3$^+$ T cells in HuPBMC spleens also remained high (average ~70%), though was slightly reduced compared to pre-EAE blood samples (>80% in most samples). EAE induction resulted in a considerable contraction of hCD4$^+$ T cells expressing regulatory markers in the spleens of HuPBMC mice, which was significant compared to the other two models (Figure 3.36B) and may indicate reduced Treg control in this system enabled CNS damage sufficient for clinical symptom development. hCD19$^+$ B cells in the spleens of HuHSC and HuBLT mice mostly expressed hCD20 (~70%), while only ~20% of HuPBMC spleen B cells did (Figure 3.36C). The relative expression of hCD21, hCD20, and hCD27 among human B cells remained similar to pre-induction blood levels (Figure 3.12), suggesting EAE did not affect B cell phenotype persistence or expansion in the spleen.

Overall, HuHSC spleens skewed toward reconstitution of non-T cell engraftment (human B cells and monocytes), whereas HuPBMC spleens were comprised almost entirely of human T cells. HuBLT mouse spleens contained the most representative and greatest diversity of human immune subsets, producing values comparable to the dominantly engrafted subsets among both the HuHSC and HuPBMC splenocytes. These findings are consistent with literature reports for each of these humanization methods for adult NSG mice[429,493,524] and indicates that EAE induction does not result in major deviations in subset engraftment in the periphery at the respective timepoints of immunization.

3.4.2.4 Model comparison of human immune cell infiltration of the CNS

Reconstitution analysis of the spleen indicated that while HuPBMC mice contained more T cells in the periphery at EAE endpoint than the other two humanized mouse models, HuBLT mice also reconstituted with a physiologically appropriate level of human T cells, which are known to mediate inflammation in the CNS during MS and in classical EAE models[38,79,131,660]. Therefore, to determine why HuPBMC mice developed clinical EAE symptoms while HuBLT mice did not,

we compared murine and human immune cell infiltration of the brain and spinal cord between HuBLT at day 41 post-induction and HuPBMC mice at day 24 post-induction.

By both proportion of all leukocytes and total cell counts in the brain and spinal cord, HuPBMC mouse CNS samples contained fewer resident $mCD45^{lo}$ (Figure 3.37A – B, G – H) and infiltrating $mCD45^{hi}$ cells (Figure 3.37 C – D, I – J) than HuBLT mice, whereas HuBLT CNS tissues contained significantly fewer infiltrating $hCD45^{+}$ cells (Figure 3.37E – F, K – L) than HuPBMC mice. The spinal cord of HuBLT mice, the main site of infiltration and demyelination in classical EAE models[128], consistently contained ~500 $hCD45^{+}$ cells (Figure 3.37L) compared to ~1 x 10^4 $mCD45^{hi}$ (Figure 3.37J) and ~3 x 10^3 $mCD45^{lo}$ cells (Figure 3.37H) in the same samples. EAE induction thus appeared to promote microgliosis and murine macrophage infiltration of the CNS in HuBLT mice more so than human immune cell infiltration. The spinal cords of HuPBMC mice, however, contained either very few or more than ~1 x 10^3 $hCD45^{+}$ cells, doubling the average number measured in the HuBLT spinal cords (Figure 3.37L). Similar but less significant differences in the resident and infiltrating murine and human immune cell populations were observed in the brain between models at endpoint (Figure 3.37A–F).

Within the brain infiltrating $hCD45^{+}$ cell population, $hCD3^{+}CD4^{+}$ and $hCD3^{+}CD8^{+}$ T cell proportions were not significantly different between HuBLT and HuPBMC mice, though HuPBMC brain infiltrates did skew towards more hCD4 expressing T cells compared to HuBLT mice (Figure 3.38A – B). Quantitatively, $hCD3^{+}CD4^{+}$ and $hCD3^{+}CD8^{+}$ T cells were more abundant, though not significantly, in the HuPBMC brains (Figure 3.39A – B). HuBLT brains exhibited a greater proportion of $hCD3^{+}CD4^{+}$ T cells expressing the regulatory marker FOXP3 than HuPBMC brain samples, but these $hCD4^{+}$ Tregs comprised at most 2.5% of brain infiltrating $hCD45^{+}$ cells in both models (Figure 3.38C). Consistent with the relative peripheral engraftment of human B cells, $hCD19^{+}$ B cells were significantly more abundant in the brains of HuBLT mice than HuPBMC mice (Figure 3.38C). Despite higher frequencies of human Tregs and B cells in HuBLT brains, the numerically larger quantity of $hCD45^{+}$ cells in the HuPBMC brains resulted in statistically similar numbers in the brains of both humanized mouse cohorts (Figure 3.39C). Nearly identical relative proportions of human immune cell subsets were also measured in the spinal cords (Figure 3.40A – C). Unlike in the brain samples, HuBLT spinal cord infiltrating $mCD45^{hi}$ cells were more abundant than resident $mCD45^{lo}$ cells, which, as noted above, were both significantly expanded compared to murine immune cells in the HuPBMC spinal cords (Figure 3.41A – B).

HuPBMC spinal cords also contained significantly greater numbers of $hCD3^+CD4^+$ and $hCD3^+CD8^+$ T cells than HuBLT spinal cords (Figure 3.41A – B). Consistent with the brain samples, HuBLT spinal cords contained greater numbers of human Tregs and B cells than the HuPBMC spinal cords (Figure 3.41C).

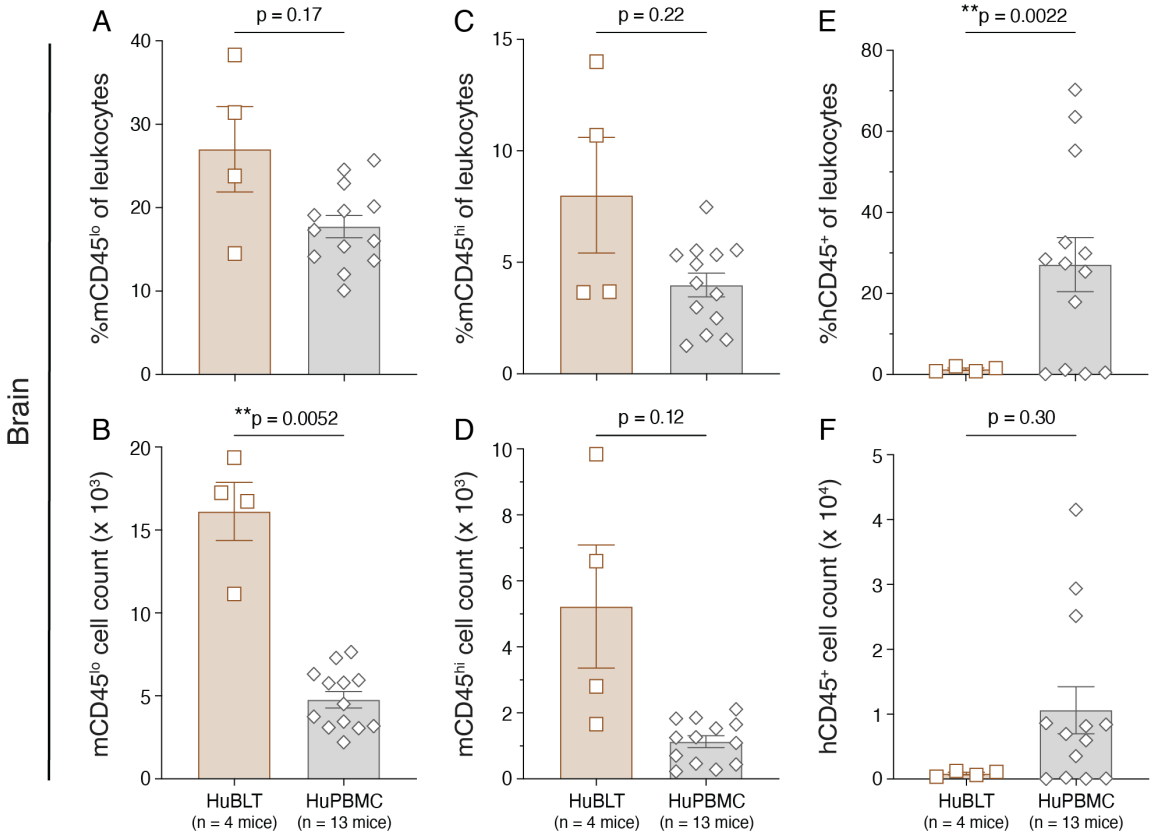

Figure 3.37 Murine and human immune cells in the CNS of humanized EAE mice

Relative proportions among all leukocytes (top row) and total cell counts (bottom row) of $mCD45^{lo}$, $mCD45^{hi}$, and $hCD45^+$ cells in the brain (A – F) and spinal cord (G – L) of HuBLT mice (n = 4) day 41 post-EAE induction and HuPBMC mice (n = 13) day 24 post-EAE induction. All engrafted NSG and NSG-SGM3 mice per cohort are combined for this analysis. Brain and spinal cord tissues were perfused prior to cell isolation. Data are shown as mean with SEM and were analyzed by Welch's unpaired t test or by Mann-Whitney test.

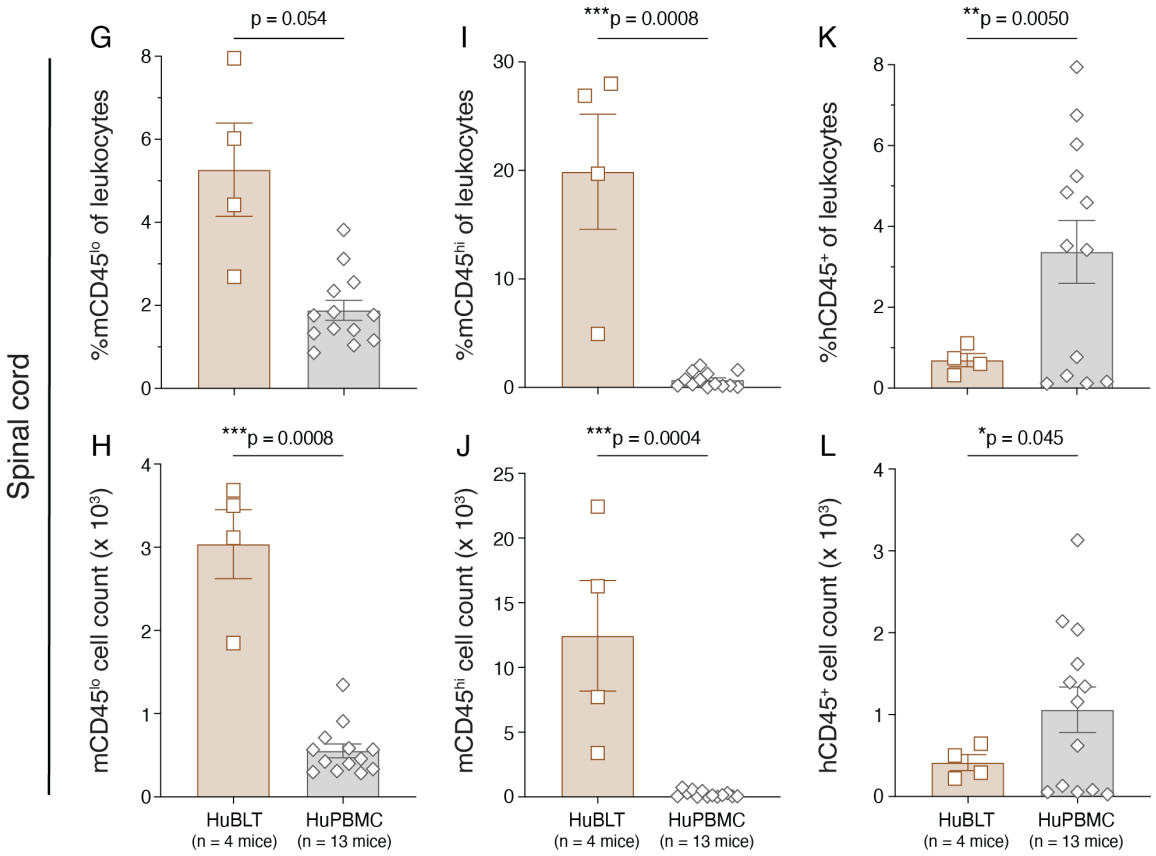

Figure 3.37 continued

Within the CNS-infiltrating human T cell population, the proportions of hCD3$^+$ T cells expressing hCD4 and hCD8 were similar in samples from both models (Figure 3.42A – B, E – F), suggesting EAE induction results in similar subset migration to and/or expansion in the CNS of mice engrafted using both humanization methods. There was a significant increase, however, in the proportions of infiltrating hCD3$^+$CD4$^+$ T cells expressing regulatory markers hCD25 and hFOXP3 in HuBLT CNS samples compared to HuPBMC samples (Figure 3.42C – D, G – H), which may have impeded pro-inflammatory cytokine secretion necessary to demyelinate the CNS following EAE immunization. Overall, the combination of greater numbers of CNS infiltrating T cells and reduced proportions of those T cells expressing regulatory markers likely explains the occurrence of clinical EAE symptoms in the HuPBMC mice but not in the HuBLT mice for these preliminary cohorts.

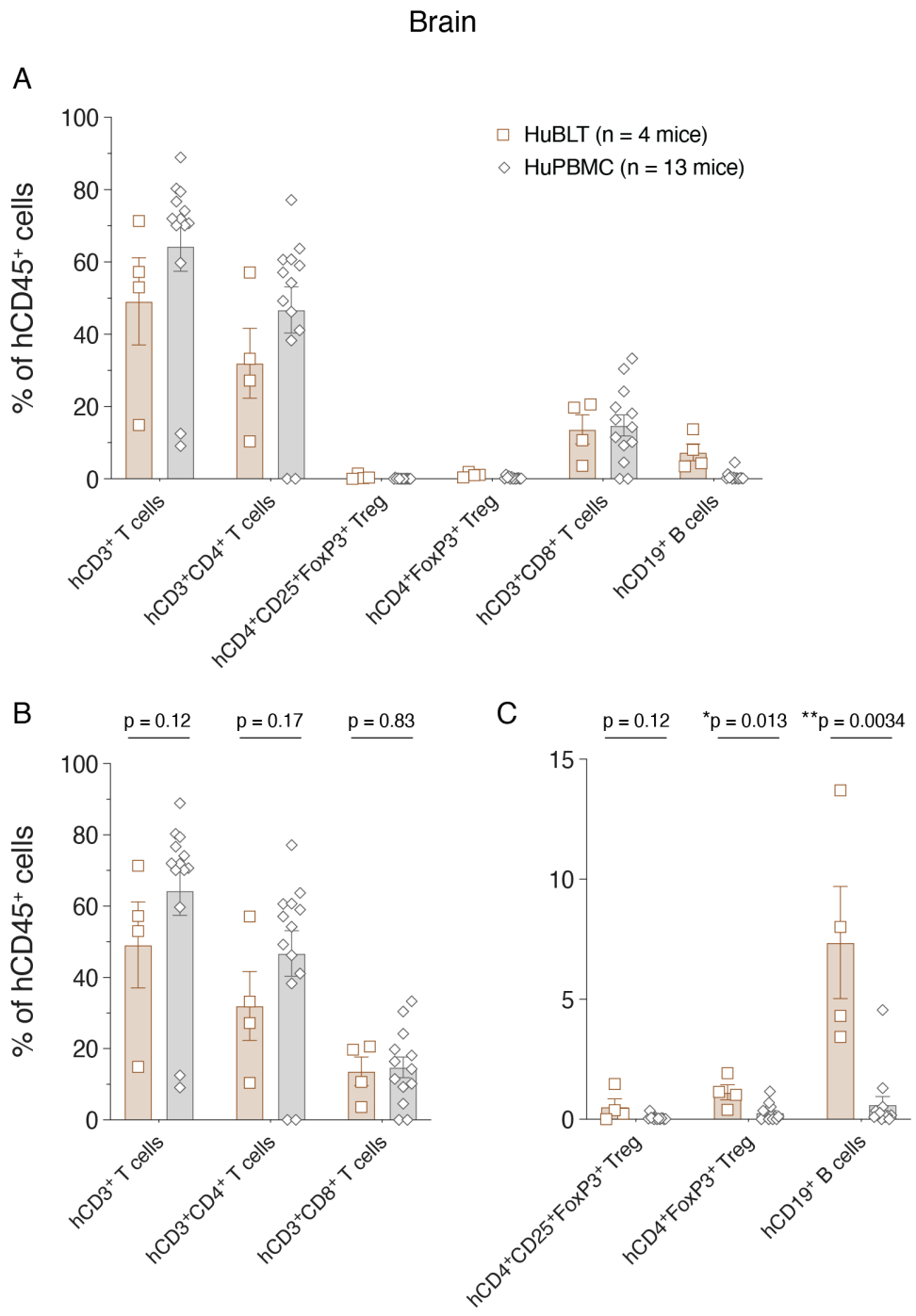

Figure 3.38 Brain infiltrating human immune cell frequencies in humanized EAE mice

(A) Relative proportions of all measured human T and B cell subsets are shown as a proportion of infiltrating hCD45$^+$ cells in the brain of HuBLT mice (n = 4) day 41 post-EAE induction and HuPBMC mice (n = 13) day 24 post-EAE induction. These data are then subdivided into (B) predominantly infiltrating immune cell subsets and (C) minorly infiltrating immune cell subsets to better illustrate relative frequencies. All engrafted NSG and NSG-SGM3 mice per cohort are combined for this analysis. Brain tissues were perfused prior to cell isolation. Data are shown as mean with SEM and were analyzed by Welch's unpaired t test or by Mann-Whitney test.

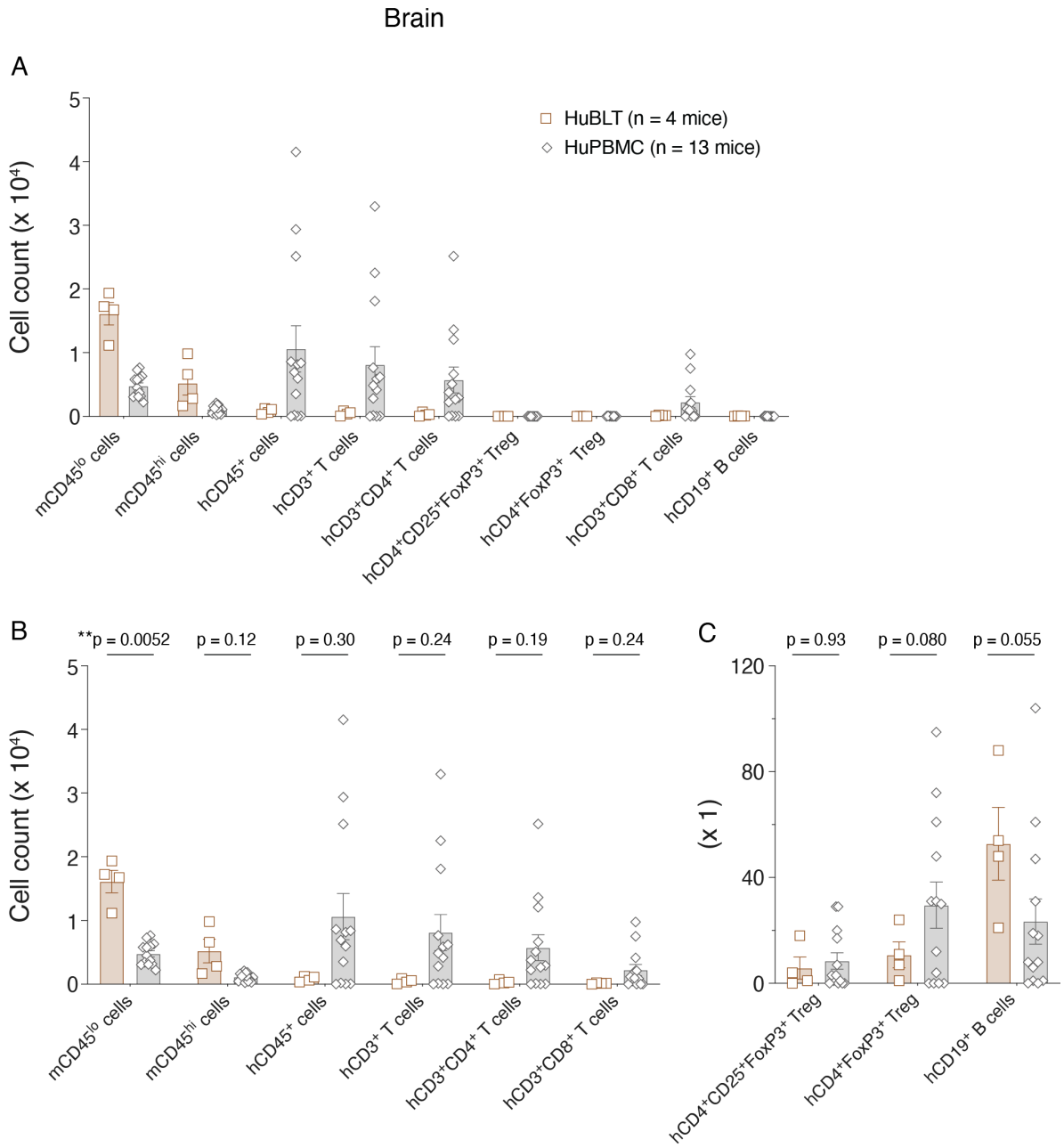

Figure 3.39 Brain resident and infiltrating immune cell abundance in humanized EAE mice

(A) Total cell counts for all measured murine and human immune cell subsets within the brain of HuBLT mice (n = 4) day 41 post-EAE induction and HuPBMC mice (n = 13) day 24 post-EAE induction. These data are then subdivided into (B) predominantly infiltrating immune cell subsets and (C) minorly infiltrating immune cell subsets to better illustrate relative frequencies. All engrafted NSG and NSG-SGM3 mice per cohort are combined for this analysis. Brain tissues were perfused prior to cell isolation. Data are shown as mean with SEM and were analyzed by Welch's unpaired t test or by Mann-Whitney test.

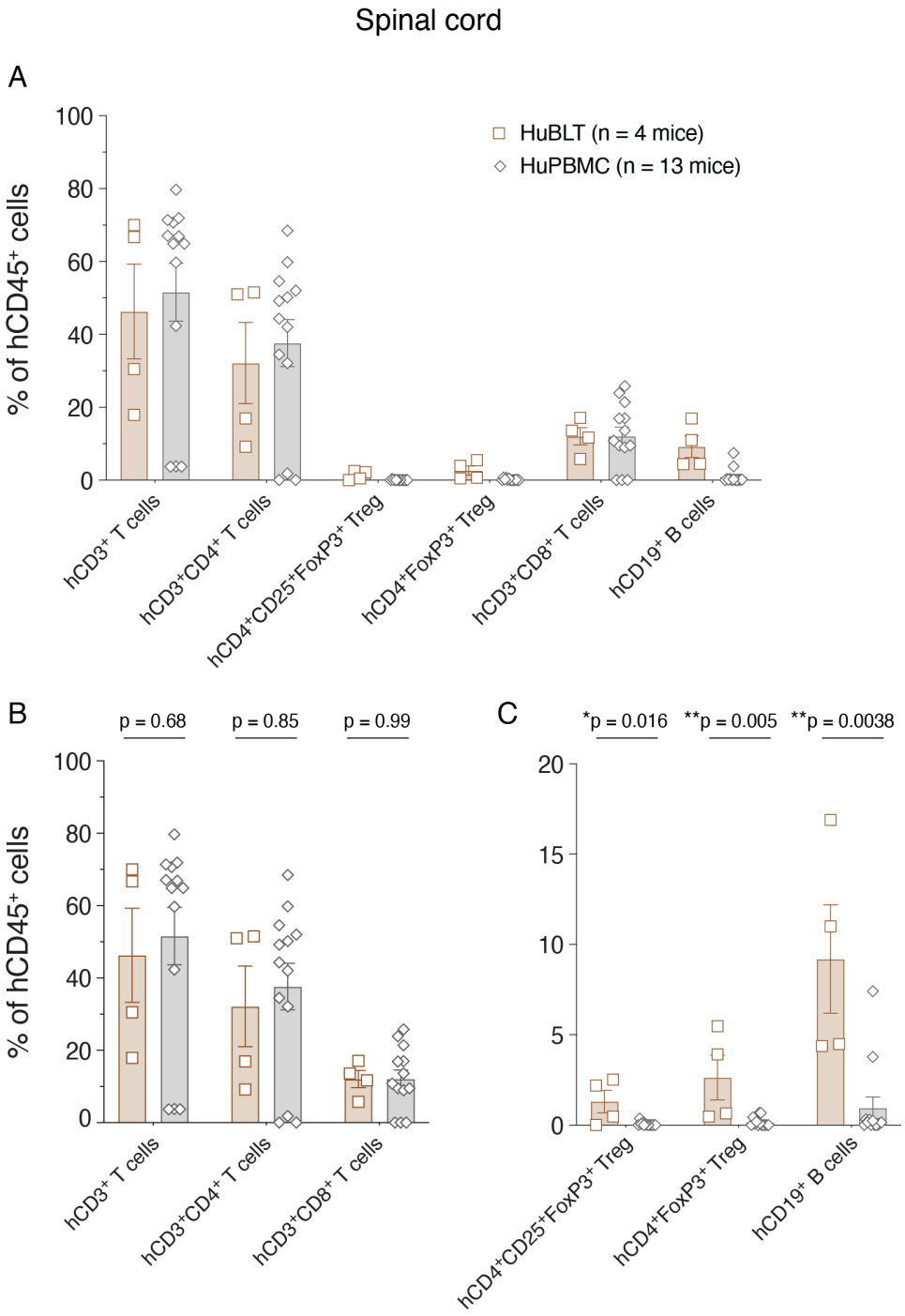

Figure 3.40 Spinal cord infiltrating human immune cell frequencies in humanized EAE mice

(A) Relative proportions of all measured human T and B cell subsets are shown as a proportion of infiltrating hCD45$^+$ cells in the spinal cord of HuBLT mice (n = 4) day 41 post-EAE induction and HuPBMC mice (n = 13) day 24 post-EAE induction. These data are then subdivided into (B) predominantly infiltrating immune cell subsets and (C) minorly infiltrating immune cell subsets to better illustrate relative frequencies. All engrafted NSG and NSG-SGM3 mice per cohort are combined for this analysis. Spinal cord tissues were perfused prior to cell isolation. Data are shown as mean with SEM and were analyzed by Welch's unpaired t test or by Mann-Whitney test.

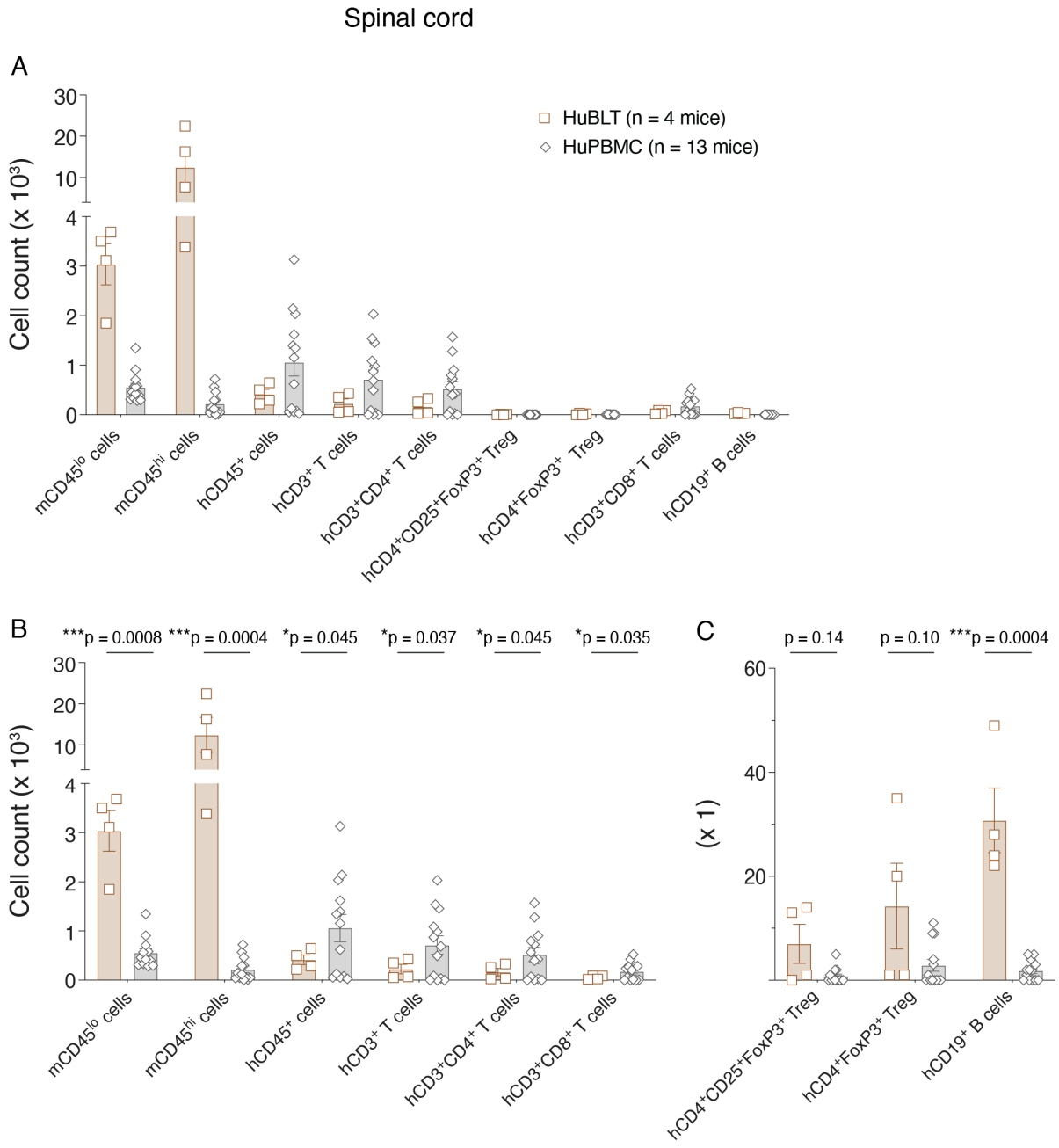

Figure 3.41 Spinal cord resident and infiltrating immune cell abundance in humanized EAE mice

(A) Total cell counts for all measured murine and human immune cell subsets within the spinal cord of HuBLT mice (n = 4) day 41 post-EAE induction and HuPBMC mice (n = 13) day 24 post-EAE induction. These data are then subdivided into (B) predominantly infiltrating immune cell subsets and (C) minorly infiltrating immune cell subsets to better illustrate relative frequencies. All engrafted NSG and NSG-SGM3 mice per cohort are combined for this analysis. Brain tissues were perfused prior to cell isolation. Data are shown as mean with SEM and were analyzed by Welch's unpaired t test or by Mann-Whitney test.

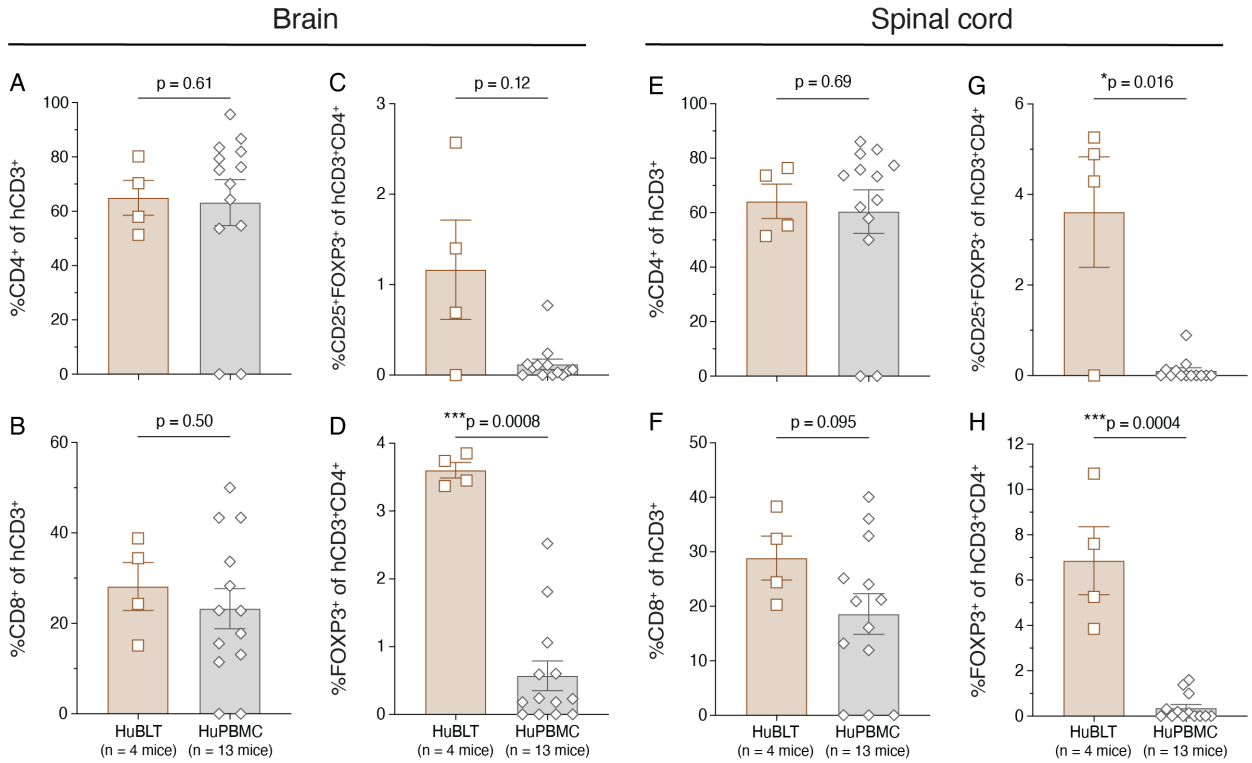

Figure 3.42 Human T cell subsets in the CNS of humanized EAE mice

Relative proportions of all measured human T cell subsets shown as a proportion of the parent population in the brain (A – D) and spinal cord (E – H) of HuBLT mice (n = 4) day 41 post-EAE induction and HuPBMC mice (n = 13) day 24 post-EAE induction. All engrafted NSG and NSG-SGM3 mice per cohort are combined for this analysis. Brain and spinal cord tissues were perfused prior to cell isolation. Data are shown as mean with SEM and were analyzed by Welch's unpaired t test or by Mann-Whitney test.

3.5 Summary and discussion of findings

Of the three humanized mouse models generated in this study, EAE induction resulted in clinically measurable deficits and CNS infiltration only in the HuPBMC model, and not in the HSC-engraftment based HuHSC or HuBLT models. Reconstitution analysis of peripheral blood prior to EAE induction and of the spleen post-EAE induction demonstrated expected patterns of HIS subset engraftment for these established humanization protocols that are consistent with published findings[429,493,499,505,509,524,531,552]. In the HuHSC model, we observed predominant engraftment of hCD19$^+$ B cells with relatively few hCD3$^+$ T cells, which was in contrast to the human T cell dominant engraftment of HuPBMC mice that were mostly lacking in human B cells. The HuBLT model most accurately reproduced the expected proportions of HIS lineages measured

in human PBMCs, reliably comprising human T cells, B cells, monocytes, and NK cells. The main finding of this chapter is that MOG immunization is sufficient to generate EAE symptoms in PBMC humanized NSG mice, which points to a critical role for human T cells in mediating myelin damage. While a reconstitution cut-off level was not specified for these experiments, it is advisable that a minimum proportion of $hCD45^+$ and/or $hCD3^+$ immune cells among total circulating leukocytes be determined to ensure reproducibility in the future, as only mice with sufficient levels of human immune cells will proceed with EAE induction.

Engraftment of adult NSG mice with $hCD34^+$ HSCs is known to be less efficient in generating human T cell subsets than engraftment of newborn NSG mice with an intact thymus, and thus results in a greater skew toward human B cell reconstitution[429,661]. Moreover, $CD34^+$ HSC humanized athymic *Foxn1*^{null} NSG mice do not generate human T cells, whereas BLT humanized NSG *Foxn1*^{null} mice reconstitute with T cells at levels similar to typical NSG recipient mice (M. Brehm, conference communication, JAX European Breakthrough Series 2020), highlighting the importance of murine thymus in human T cell development in the HuHSC model. The relatively reduced T cell expansion at the assessed timepoint (15 weeks post-HSC injection) and comparatively large population of $hCD21^+$ B cells also presents potential issues for exogenous infection with EBV in future EAE studies, where the occurrence of lymphoma needs to be minimized. The engraftment of neonatal NSG mice with human HSCs could improve human T cell selection on murine thymus, prior to its involution starting at 4 weeks of age[662], and potentially facilitate encephalitogenic T cell development following immunization with MOG. Alternatively, increasing the reconstitution period delay between HSC engraftment and EAE induction of adult NSG mice to >20 weeks may improve infiltration and clinical symptom generation, as human B cells tend to predominate in HuHSC mice early on post-HSC injection while human T cells slowly attain comparable frequencies over time[429,663]. Assuming T cell levels can be adequately increased via neonatal NSG engraftment, the HuHSC model presents with a notable advantage over the other two humanized models in that human T cells are selected on murine MHC, wherein known immunodominant epitopes of MOG presented by the NSG I-A^{g7} MHC haplotype can be probed specifically using existing reagents[144,664,665].

Though it is perhaps not surprising that MOG immunization did not result in clinical EAE symptoms in the adult HuHSC model with so few reconstituted T cells, the reasons underpinning the lack of symptom development in the T cell replete HuBLT model are less apparent. HuHSC

mice in this study were created by engrafting both female and male adult NSG mice with male sexed fetal liver HSCs. In subsequent studies using the HuPBMC model, however, the sex of the donor cells and recipient NSG mice was shown to impact EAE incidence (Section 4.3), and therefore HuBLT mice were generated using male NSG mice engrafted with female sexed fetal liver HSCs. In the event that enrofloxacin treated water had abrogated EAE induction weeks after irradiation in the HuHSC model, the potential side effects of antibiotic treatment on humanized mice post-irradiation and engraftment were entirely eliminated from this cohort, as HuBLT mice were maintained on acidified water like the HuPBMC cohort. Since only 4 HuBLT mice were available to be included in this preliminary cohort, increasing the total number of MOG immunized mice using different tissue donors may also improve our ability to measure EAE symptoms in HuBLT mice, assuming similar incidence rates as the HuPBMC model.

Analysis of HuBLT and HuPBMC model splenocytes demonstrated that while mice in both cohorts contained substantial peripheral levels of human HLA selected T cells, only those in the HuPBMC model trafficked to and entered (and/or expanded within) the CNS in sufficient numbers to generate inflammation and clinical symptoms, as evidenced by the scant number of $hCD45^{+}$ cells in the CNS tissues of HuBLT mice, despite similar levels of murine myeloid cells ($mCD45^{lo}$ and $mCD45^{hi}$) in the CNS of both models. As PBMC derived T cells are obtained from adult blood donors with years of immunological experience and engraftment of NSG mice results in extensive T cell activation, the lack of EAE in the otherwise naïve HuBLT mice may be due to the absence of pre-existing or concurrent immune exposures that promote T cell activation upon challenge with MOG antigen. MS is a disease that generally occurs in early-mid adulthood specifically after EBV seroconversion, and is associated with multiple environmental factors and exposures, suggesting pro-inflammatory priming or exacerbation of the autoimmune response is a necessary requisite for disease[74,109]. As noted about the HuBLT model by Covassin and colleagues, "T cells from NSG mice that were irradiated and injected with HSC only were consistently lower in the expression of CD45RA compared to mice also implanted with thymic tissues, consistent with a recently published study, suggesting that the development of human T cells on human thymic tissue helps to maintain a naïve phenotype of human T cells"[537]. Overcoming the propensity of T cells to maintain a naïve phenotype may therefore enable induction of overt EAE in the HuBLT model. To determine if insufficient T cell activation and/or trafficking underlies the lack of EAE development in HuHSC and HuBLT mice, human T cell activation, proliferation, chemokine

expression, and MOG specificity before and after immunization in the periphery and CNS should be analyzed specifically. Based on the finding that PBMCs from genetically unrelated blood donors can produce EAE symptoms in the HuPBMC model, it is less likely, though not improbable, that HuBLT mice failed to exhibit EAE symptoms due to human HLA: TCR incompatibility in presenting or recognizing local MOG (Section 4.9.3).

The use of HuHSC and HuBLT models should not be ruled out for future development of humanized mouse models of EAE based on our preliminary findings, as further optimization could improve the generation of CNS inflammation, demyelination, and clinical symptoms. The reconstitution of various HIS subsets in HSC based models could be highly informative in assessing mechanistic contributions of these lesser represented subsets to the immunopathogenesis of MS. Moreover, while HuBLT mouse cohort sizes are typically limited by tissue availability, individual HuBLT mice or entire cohorts can be propagated to generate greater numbers of HuProBLT recipient mice, bearing the same tissue donor immunogenetics and phenotype as the original HuBLT donors (see Appendix 5 for HuProBLT model generation). Specific steps to improve EAE development in HSC engrafted models should aim to reflect what we know about how MS proceeds in humans and apply methods known to improve T cell reconstitution and EAE induction as determined using HuPBMC mice (see chapter 4). Such steps could include engrafting neonatal NSG mice for the HuHSC model, using male NSG (or NSG-SGM3) mice as fetal tissue and/or HSC recipients, maintaining cages on acidified water (no antibiotic use), pre-infection of humanized mice with EBV and/or administering other immune stimuli to promote otherwise naïve T cells to activate and proliferate following EAE induction, as well as multiple rounds of myelin antigen immunization over a longer study period to mimic repeated antigenic challenges in people that impair self-tolerance over time. Due to the success of generating MS-like disease symptoms and human immune cell infiltration of the brain and spinal cord in the HuPBMC model, HuPBMC EAE mice were further characterized in relation to existing EAE models in chapter 4 and employed to determine the impact of previous EBV infection on CNS autoimmunity in chapter 5.

Chapter 4 – Immunopathological features of experimental autoimmune encephalomyelitis in peripheral blood mononuclear cell humanized mice

4.1 Background and preliminary findings

Our initial assessment of the susceptibility of different humanized mouse models to EAE induction revealed that MOG immunization of PBMC engrafted NSG mice produced clinical deficits, including paralysis and motor imbalance, that were associated with proinflammatory T cell infiltration of the CNS, as expected for an EAE model[131]. Since HuPBMC mice are cost effective to generate, can be reproduced using multiple short-term cohorts, and can be personalized based on the genetic and phenotypic characteristics of the donor, we focused on further developing the HuPBMC EAE model. Initially, we attempted EAE induction of HuPBMC mice using both male and female recipient NSG and NSG-SGM3 mice and immunized reconstituted mice at 3 weeks post-injection with one or both of the peptide and protein antigen versions of MOG. In these preliminary experiments (Table 4.1), we observed preferentially robust outcomes using certain combinations of reagents and donor and recipient characteristics, some of which are known to vary considerably among established murine EAE models[50,128]. Individual donor PBMC composition and the number of human PBMCs injected per recipient mouse in each cohort is available in Appendix 1. This chapter (4) is focused on addressing specific technical aspects and immunopathological features of HuPBMC EAE mice that were investigated and optimized to generate an autoimmune MS model that could enable investigation of EBV infection directly in the next chapter (5).

Table 4.1 Results from preliminary HuPBMC EAE studies

All mice were humanized by IV injection of 5 x 10^6 healthy female donor PBMC (n = 4 unrelated donors aged 23 – 39 years) and induced by subcutaneous injection of specified antigen with 400 μg of *M. Tuberculosis* in 100 μL of CFA. Onset and peak scores are shown as average with standard deviation for symptomatic mice. Abbreviations: F, female; M, male.

Cohort ID	HuPBMC mice (strain and sex use)	EAE antigen (per mouse)	EAE symptom incidence		EAE symptom onset (day post-induction)	Peak EAE score	Summary
			Proportion	%			Effect & Result
5	NSG: 3F, 7M	87.6 μg rhMOG	3/7 M 0/3 F	42.8 0.00	22.7 ± 5.51	1.17 ± 0.29	Symptoms: Mild, delayed Incidence: Low Sex bias: Male Strain bias: N/A
6	NSG: 3F, 3M NSG-SGM3: 3F, 2M	100 μg rhMOG	NSG: 1F+1M /6 total NSG-SGM3: 1F+2M /5 total	33.3 60.0	20.8 ± 2.59	0.90 ± 0.42	Symptoms: Mild Incidence: Moderate Sex bias: None Strain bias: None
7	NSG: 3F, 3M NSG-SGM3: 3F, 3M	200 μg MOG_{35-55}	NSG: 1F /6 total NSG-SGM3: 1M /6 total	16.7 16.7	25.5 ± 0.71	1.00 ± 0.00	Symptoms: Mild, delayed Incidence: Low Sex bias: None Strain bias: None
8	NSG: 3F, 4M NSG-SGM3: 2F, 3M	100 μg rhMOG	NSG: 1F+2M /7 total NSG-SGM3: 0/5 total	42.8 0.00	16.0 ± 5.20	1.33 ± 0.29	Symptoms: Mild Incidence: Low Sex bias: Male Strain bias: NSG
9	NSG: 2F, 5M NSG-SGM3: 3F, 4M	100 μg rhMOG	NSG: 1M /7 total NSG-SGM3: 1M /7 total	14.3 14.3	15.0 ± 1.41	2.00 ± 0.71	Symptoms: Normal Incidence: Low Sex bias: Male Strain bias: None
10	NSG: 3M NSG-SGM3: 3F, 5M	100 μg rhMOG + 200 μg MOG_{35-55}	NSG: 2/3 M NSG-SGM3: 1F+3M /8 total	66.7 50.0	12.3 ± 4.18	1.88 ± 0.74	Symptoms: Normal Incidence: Moderate Sex bias: Male Strain bias: None

4.2 Timeline to reconstitution of human PBMCs in NSG mice

4.2.1 Rationale and experimental design

The reconstitution kinetics of NSG mice humanized with blood donor derived PBMCs is dependent on the initial number of cells injected and the subsequent time delay for engraftment and expansion of human immune cells, as once hCD45$^+$ cells are detected in circulation, T cells rapidly expand[493,611,628]. The main goal of engrafting NSG mice with human PBMCs for this study was to generate a consistent, detectable level of reconstitution in the peripheral blood at a set timepoint post-injection in order to induce EAE once sufficient cell numbers had engrafted and could therefore mount a response capable of producing clinical symptoms after myelin antigen immunization, but that was also sufficiently early such that symptoms of xGvHD did not significantly confound the clinical course of EAE. When considering the engraftment of EBV seropositive donor derived PBMCs, we also aimed to identify the minimum total cell inoculum needed to reliably reconstitute and induce EAE in HuPBMC mice while also reducing the potential for spontaneous lymphoma via outgrowth of transferred EBV-infected B cells. Furthermore, reducing the number of cells injected per recipient increases the size of the cohort that can be derived from a single blood donation, which is a particularly important consideration for patient donors who may begin a disease modifying therapy shortly after donating. Ideally, as few cells as possible are injected per mouse and sufficient time allowed to reconstitute such that myelin antigen reactive T cells can be activated, proliferate, and migrate to the CNS following EAE induction before nonspecific murine antigen reactive T cells become highly abundant and outcompete naïve T cells with other specificities. To achieve a balance between T cell reconstitution and nonspecific graft reactivity, we sought to identify the timepoint post-PBMC injection at which hCD45$^+$ cells could be reliably detected in peripheral blood samples at relatively low levels, prior to rapid T cell expansion.

Most published studies employing HuPBMC mice inject NSG mice with 5 – 20 x 10^6 whole PBMCs or more, and begin experimentation at 2 – 6 weeks post-injection once the frequency of hCD45$^+$ cells reach >20% of all leukocytes in recipient tissues[429,493,611,628]. In a report by Andrade and colleagues using PBMCs derived from individuals with SLE, a condition commonly marked by lymphopenia, 3 – 5 x 10^6 PBMCs were engrafted per BRG mouse, half via IP injection and half via IV injection without providing a comparison of the routes[628]. Engraftment with 3 – 5 x 10^6

SLE and HD PBMCs per BRG was noted to consistently result in 50 – 80% hCD45$^+$ cells among total blood leukocytes 4 weeks post-injection, and was sufficient to produce immunophenotypic characteristics consistent with the disease in humans, including proteinuria, IgG complex deposition in the kidneys, and reduced survival[628]. As noted in Section 1.3.4.2, irradiation of NSG mice prior to PBMC engraftment enhances the release of murine antigens and subsequent xGvHD severity[493], and therefore, NSG mice were not irradiated prior to PBMC engraftment for all of our studies. Both IV and IP injections have been used to humanized NSG mice with donor PBMCs, though IV injection has been more favorably reportedly for improved distribution of human immune cells throughout peripheral tissues[429,493]. Therefore, both injection routes were assessed to determine which would provide the most consistent levels of reconstitution between NSG mice in a cohort engrafted with PBMCs from the same healthy female donor.

4.2.2 Reconstitution analysis

Five NSG mice were injected IV and three NSG mice were injected IP with 5 x 10^6 PBMCs each in 100 µL of PBS. Three unengrafted NSG control mice were injected IP with 100 µL of blank PBS. Reconstitution of the peripheral blood was analyzed weekly for 4 weeks by measuring hCD45$^+$ cell frequencies in saphenous vein blood samples (Figure 4.1A – C). At 4 weeks post-PBMC injection, the spleen was analyzed for endpoint reconstitution of human T and B cells (Figure 4.1D – G). Despite an initial bump at week 1 post-injection, the level of hCD45$^+$ cells in blood remained mostly below 4% of total leukocytes until 4 weeks post-injection for both injection routes (Figure 4.1A). On the fourth week, however, two PBMC engrafted NSG mice, one IV injected and one IP injected, displayed a large spike in HIS reconstitution compared to the prior third week, reaching 20% and 40% hCD45$^+$, respectively (Figure 4.1B – C). We therefore construed that 3 weeks post-injection was an early timepoint post-PBMC engraftment at which reconstitution is observed in the blood prior to significant human T cell expansion indicative of graft reactivity.

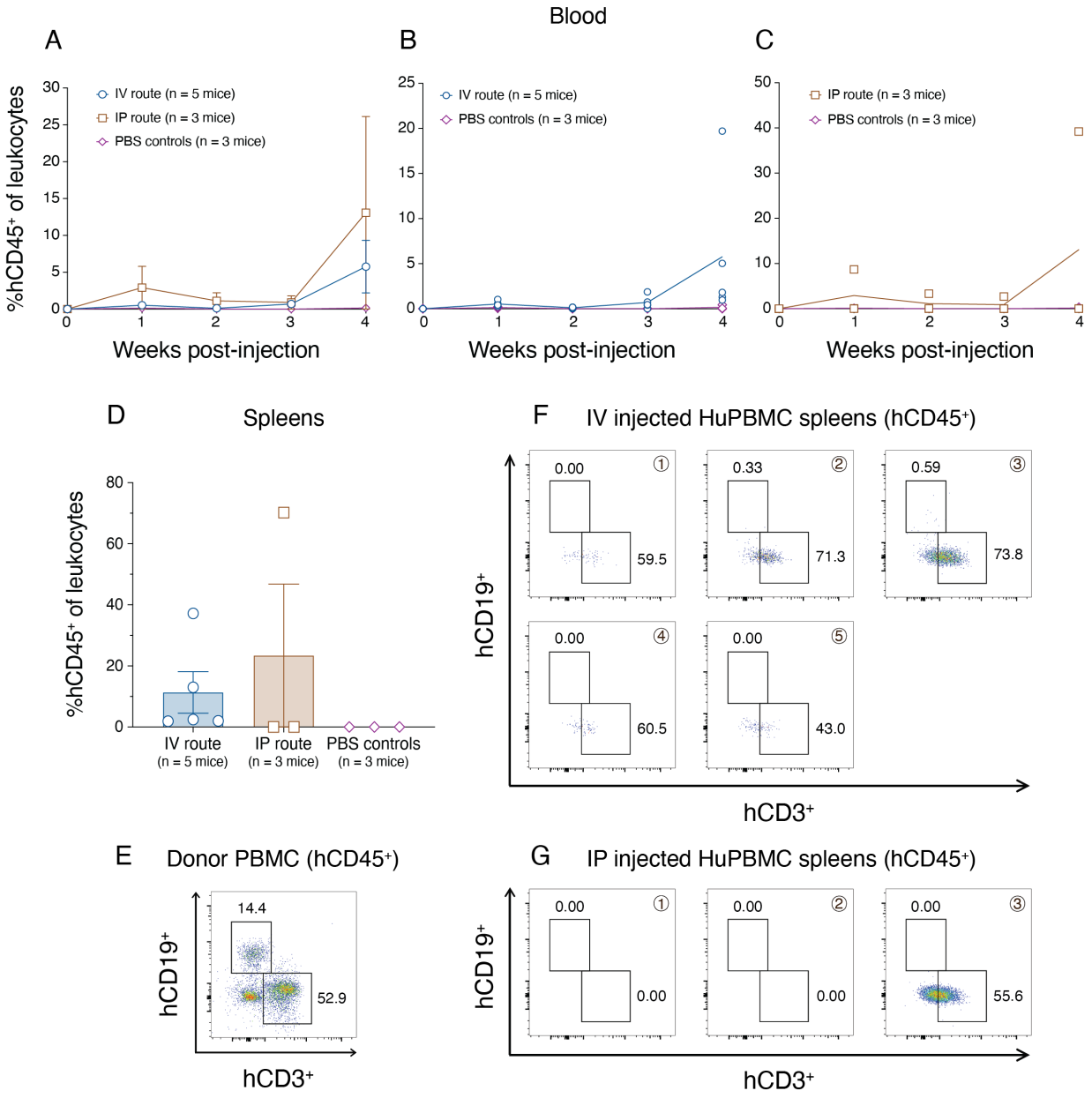

Figure 4.1 PBMC reconstitution of IV and IP injected NSG mice over time

Figure shows (A) weekly average proportions of hCD45$^+$ cells among total leukocytes in the peripheral blood of NSG mice engrafted with healthy female blood donor derived PBMCs (1 donor) via intravenous (IV, n = 5 mice) or intraperitoneal (IP, n = 3 mice) injection over 1 – 4 weeks compared to unengrafted PBS injected controls (n = 3 mice). Data are shown as mean with SEM per group and as individual mice for IV injected (B) and IP injected (C) HuPBMC-NSG mice to illustrate group variability. (D) Proportions of hCD45$^+$ cells among total leukocytes in the spleens of NSG mice at 4 weeks post-PBMC injection. Data are down as mean with SEM. (E) Reference flow cytometry gates for human donor PBMCs used to measure hCD3$^+$ T cells and hCD19$^+$ B cells. These gates were then applied to measure and visualize individual spleen samples from NSG mice engrafted with PBMCs via IV (F) and IP (G) injection. Numbers within the gated populations denotes the frequency among total hCD45$^+$ cells in each sample.

Though neither IV nor IP injection of donor PBMCs led to considerable engraftment of $hCD19^+$ B cells in the spleen after 4 weeks, the IV injection route was determined to be preferable to IP due to more consistent $hCD3^+$ T cell engraftment (Figure 4.1D – G). Although one of the IP injected mice was highly reconstituted, the other two IP injected mice failed to reconstitute at all (33.3% success rate), whereas all five IV injected mice variably engrafted to some extent by endpoint (100% success rate) (Figure 4.1D).

4.2.3 Summary and discussion of findings

The primary conclusion of this reconstitution timing pilot is that the EAE should be induced in the HuPBMC-NSG model at the earliest 3 weeks post-PBMC injection of 5 million PBMCs via the intravenous route. We would anticipate a cohort average of approximately 5% $hCD45^+$ cells in the blood at this timepoint, with all engrafted NSG mice containing at least some human immune cells, as beyond this time, substantial murine antigen reactive T cell expansion may occur and result in clinical xGvHD. Our findings are consistent with Ajith and colleagues, who also identified 3 weeks post-intravenous PBMC injection to result in optimal, consistent reconstitution of NSG mice in order to introduce an allogeneic challenge[611]. Following an injection of 5 million PBMCs, the spleens of their engrafted NSG mice contained ~4% $hCD45^+$ cells, compared to over 35% $hCD45^+$ when injected with 8 or 10 million PBMCs each[611]. Injecting 5 million donor PBMCs per mouse is therefore likely sufficient to reconstitute the mice while minimizing extensive nonspecific T cell proliferation prior to EAE induction. The team also noted that at 3 weeks post-PBMC injection, nearly half of engrafted human T cells displayed a naïve phenotype ($CD62L^+CD45RA^+$), after which, they observed a decrease in the proportion of naïve to effector memory cells[611]. Minimal signs of xGvHD had been observed in their HuPBMC mice. They concluded that "the NSG mouse allowed efficient engraftment of human PBMCs while maintaining lymphocytes in a naïve state prime for activation in response to suitable stimuli. These observations make our humanized-NSG-PBMC model an efficient novel method for investigating allogeneic immune responses between recipient and donors"[611].

4.3 Sex bias in the HuPBMC EAE model

4.3.1 Background

Preliminary analyses of the susceptibility of HuPBMC-NSG mice to EAE induction revealed a potential bias in the incidence and severity of disease symptoms depending on the sex of the recipient NSG (Table 4.1). As MS is a disease with a well-documented sex bias in overall and subtype incidence[10], we assessed the impact of blood donor PBMC sex and recipient NSG mouse sex on clinical outcomes in the HuPBMC EAE model to inform future study design.

4.3.2 Assessment of recipient NSG sex bias in EAE symptom susceptibility

To assess recipient NSG sex bias in EAE susceptibility while controlling for any potential donor sex bias, we humanized cohorts of male and female recipient NSG and NSG-SGM3 mice (NSG/SGM3, used interchangeably, Section 4.4) with only female donor PBMCs derived from four genetically unrelated, healthy individuals, aged 19 – 40 years old (included the six cohorts listed in Table 4.1). EAE was then induced in all HuPBMC mice at 3 weeks post-PBMC injection by immunizing CFA emulsion containing rhMOG protein and/or MOG_{35-55} peptide. Incidence of clinical EAE symptoms was defined by the onset and continued presence or progression of paralysis of the tail and hind limbs. Incidence of xGvHD was defined by the onset and continuation/progression of skin redness and dryness, hair loss, and/or sudden weight loss indicative of acute xGvHD. When separating clinical outcomes measured in our preliminary experiments by the sex of the recipient NSG mouse, we observed a significantly greater and earlier incidence of EAE paralysis in PBMC humanized male recipients compared to female recipient NSG/SGM3 mice (Figure 4.2A). The opposite bias was observed for symptoms of xGvHD, where female recipients were more susceptible to developing clinical xGvHD (Figure 4.2B). To account for potential donor PBMC variability in EAE and/or xGvHD susceptibility, the proportion of female and male recipient mice that developed clinical symptoms of either were grouped by cohort and showed the same effect of recipient sex on overall incidence (Figure 4.2C). The absolute incidence of EAE for mice in all cohorts combined was 16/42 males = 38.1% and 5/28 females = 17.9% (Figure 4.2D).

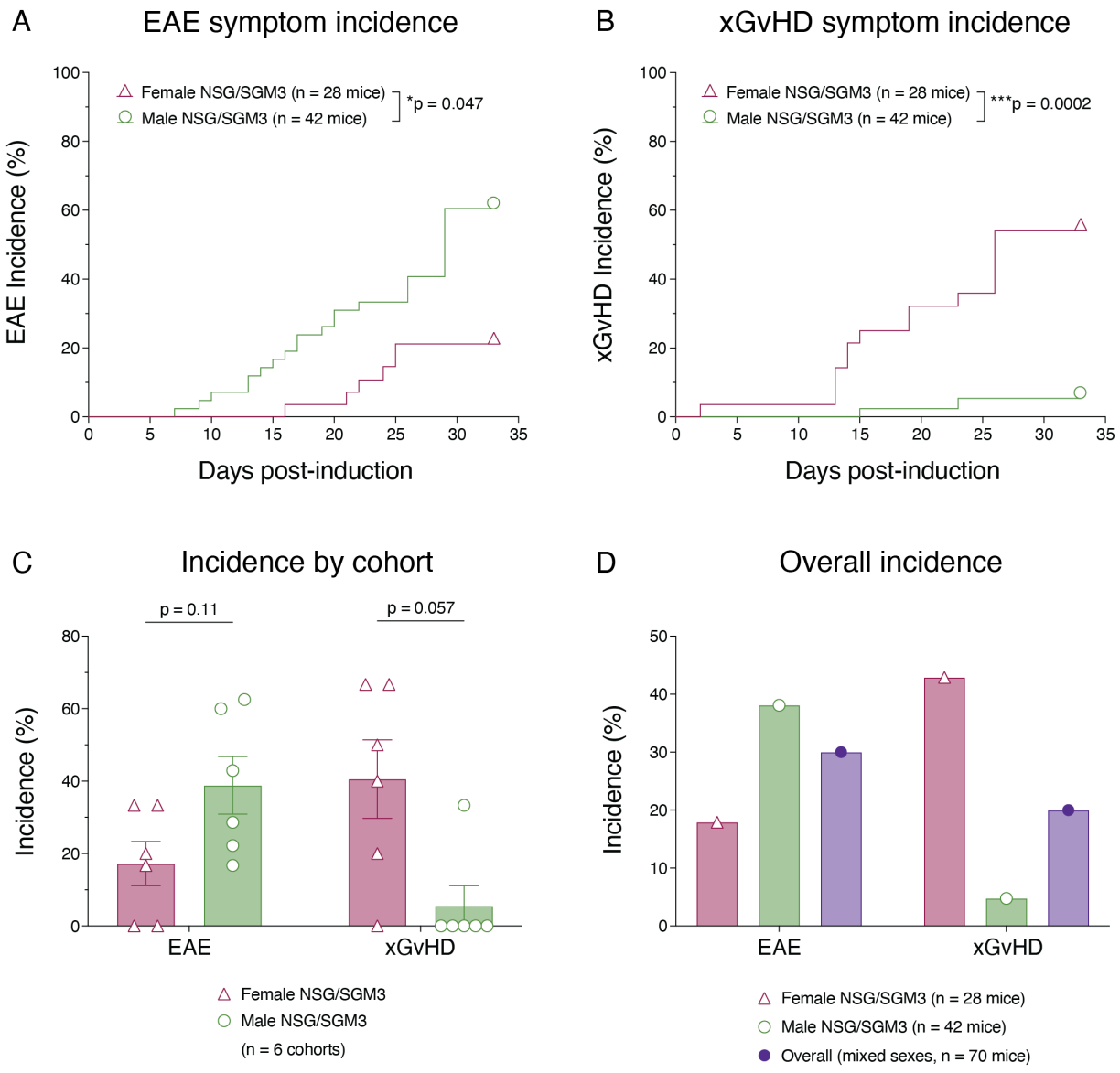

Figure 4.2 Effect of recipient NSG sex on EAE and xGvHD symptom incidence in the HuPBMC model

Clinical EAE (A) and xenogeneic (x)GvHD (B) symptom incidence over time as a proportion of all female recipient (n = 28) and male recipient (n = 42) NSG/SGM3 mice post-rhMOG and/or MOG_{35-55} EAE induction. Recipient NSG and NSG-SGM3 mice were grouped together (treated interchangeably) and are denoted as NSG/SGM3. Data shown are combined from six separate HuPBMC cohorts engrafted with unrelated healthy female donor PBMCs (n = 4 HDs) and were analyzed by Log-rank (Mantel-Cox) test. (C) Recipient sex-based incidence of EAE and xGvHD symptoms for each of the six HuPBMC cohorts, shown as mean with SEM and analyzed by Mann-Whitney test, as well as the (D) overall recipient sex-based incidence of EAE and xGvHD symptoms for all HuPBMC mice combined. HuPBMC cohorts included: 5, 6, 7, 8, 9, and 10.

4.3.3 Assessment of donor sex bias in EAE symptom susceptibility

To evaluate potential bias in clinical EAE symptom incidence in the HuPBMC model due to the sex of the PBMC donor while controlling for recipient mouse sex bias, male recipient NSG/SGM3 mice were each injected with 5 x 10^6 PBMCs from either a male or female human donor (as specified on their birth certificate). The use of only male NSG/SGM3 mice herein was predicated on the observation of higher EAE and reduced xGvHD incidence (Figure 4.2). Cohorts of male recipient NSG/SGM3 mice were engrafted with PBMCs derived from one of four healthy female and four healthy male blood donors, aged 19 – 55 years old, which were all genetically unrelated (see Appendices 2 and 3 for individual blood donor serological information and HLA genotyping). At 3 weeks post-PBMC injection, all mice were immunized with mixed rhMOG/MOG_{35-55} containing emulsion.

The composition of the injected PBMCs based on donor sex indicated that statistically similar proportions and total numbers of all measured human immune cell subsets were introduced into recipient mice regardless of the sex of the blood donor (Figure 4.3). Consistent with previous reports, we did observe a mild skew toward increased hCD4 expression compared to hCD8 expression (higher $CD4^+$:$CD8^+$ T cell ratio) among the female donor $hCD3^+$ T cells relative to male donors[666], though this difference was not statistically significant (Figure 4.3C). We therefore did not expect to observe an effect on clinical EAE outcomes due to variation in the injected male versus female donor PBMC composition, though this analysis does not reflect the functional capacity of these cells which may differ.

The clinical course of EAE symptoms in female and male donor derived HuPBMC mice immunized with MOG antigens was compared to control immunocompetent NOD WT EAE mice (Figure 4.4). Clinical EAE curves were not significantly different between symptomatic mice in the male and female donor groups (Figure 4.4A) and weight loss proceeded similarly (Figure 4.4B), though it appeared somewhat worse on average in the male donor HuPBMC EAE mice early on because one of the donor cohorts (HuPBMC cohort 32) experienced earlier symptom onset. Among immunized HuPBMC mice that developed EAE symptoms, female donor mice attained peak EAE scores at a distribution similar to NOD controls, while male donor mice had overall milder peak disease (Figure 4.4C). HuPBMC EAE symptom incidence was generally lower compared to NOD EAE mice but onset over time at a similar rate for male and female donor groups (Figure 4.4D). By overall EAE incidence, however EAE symptoms developed in half as many

male donor HuPBMC mice (~20%) compared to female donor HuPBMC mice (~40%) (Figure 4.4E). Time to EAE symptom onset was also similar between all groups but somewhat earlier in the male donor mice compared to female donor mice due to increased and earlier incidence in male donor HuPBMC cohort 32 (Figure 4.4F).

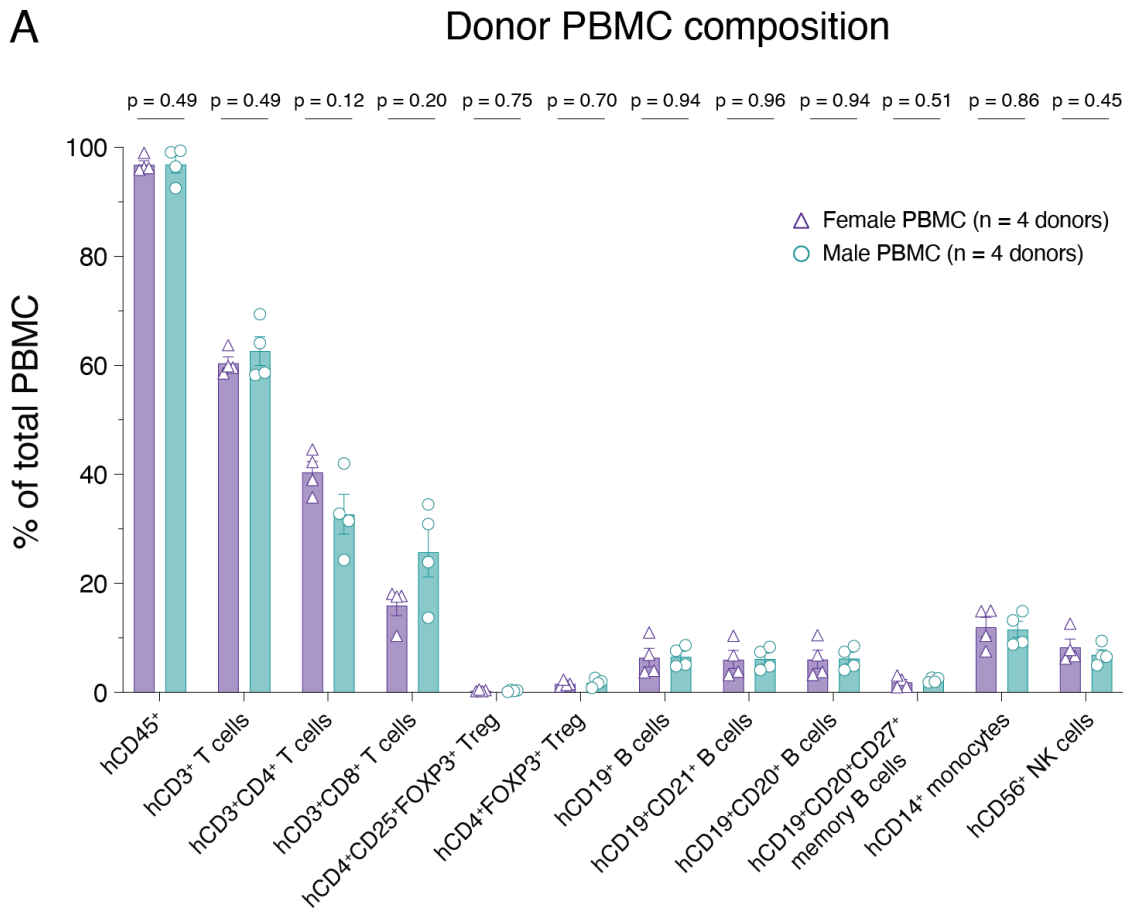

Figure 4.3 Sex differences in blood donor PBMC composition

(A) Relative composition of human immune cell lineages in the PBMCs of healthy adult female and male donors as a percentage of total leukocytes immediately after isolation from whole blood. (B) Total number of human immune cell subsets injected per recipient NSG/SGM3 mouse from each donor group. (C) Proportions of T cell subsets among hCD3$^+$ T cells in each donor group. (D) Proportions of regulatory T cell (Treg) subsets among hCD3$^+$CD4$^+$ T cells in each donor group. (E) Proportions of B cell subsets among hCD19$^+$ B cells in each donor group. PBMC samples are grouped from 4 female donors (HD-01, HD-04, HD-06, and HD-07) and 4 male donors (HD-10, HD-11, HD-12, and HD-13). Data are presented as mean with SEM and were analyzed by Welch's unpaired t test or by Mann-Whitney test.

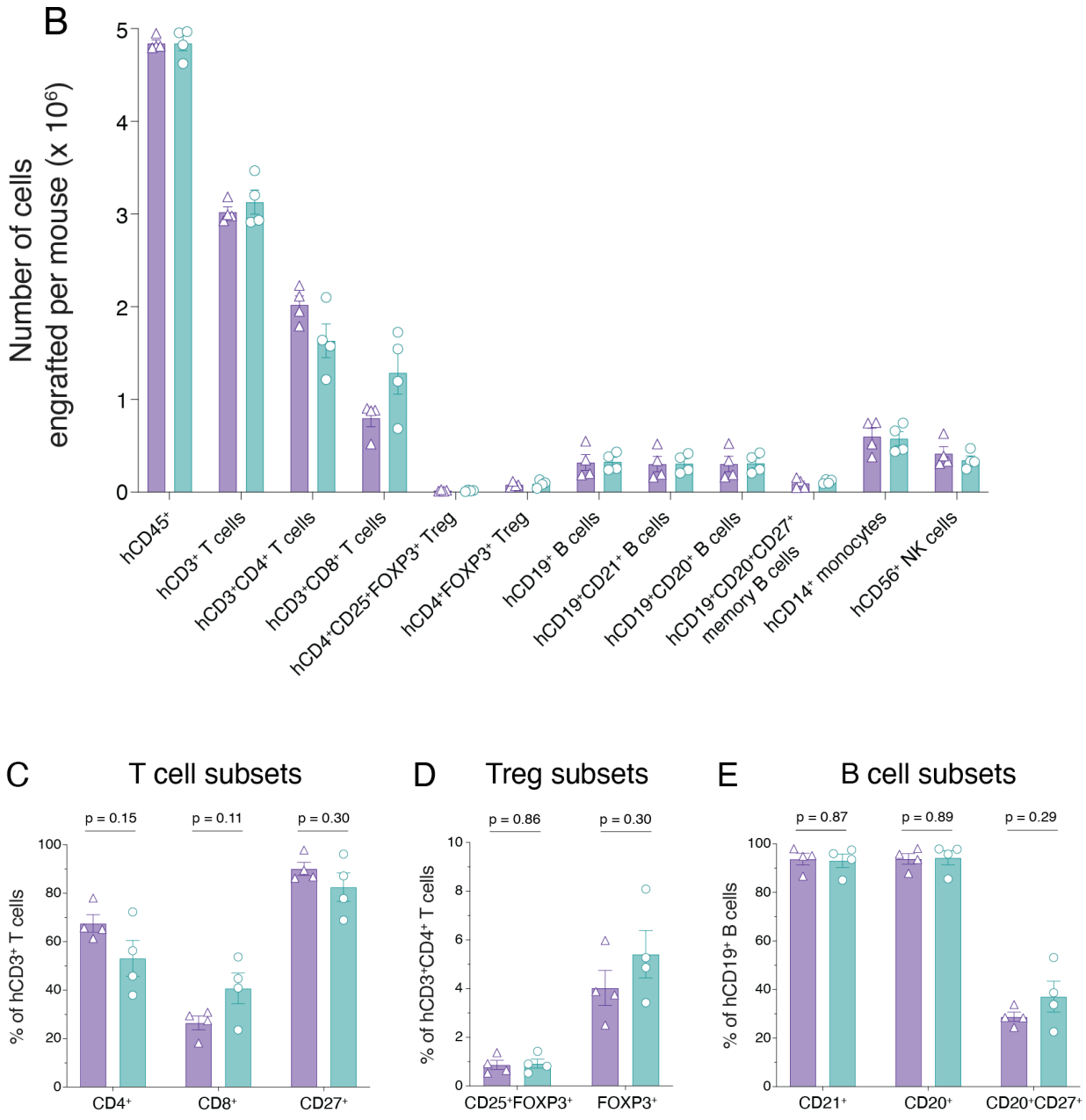

Figure 4.3 continued

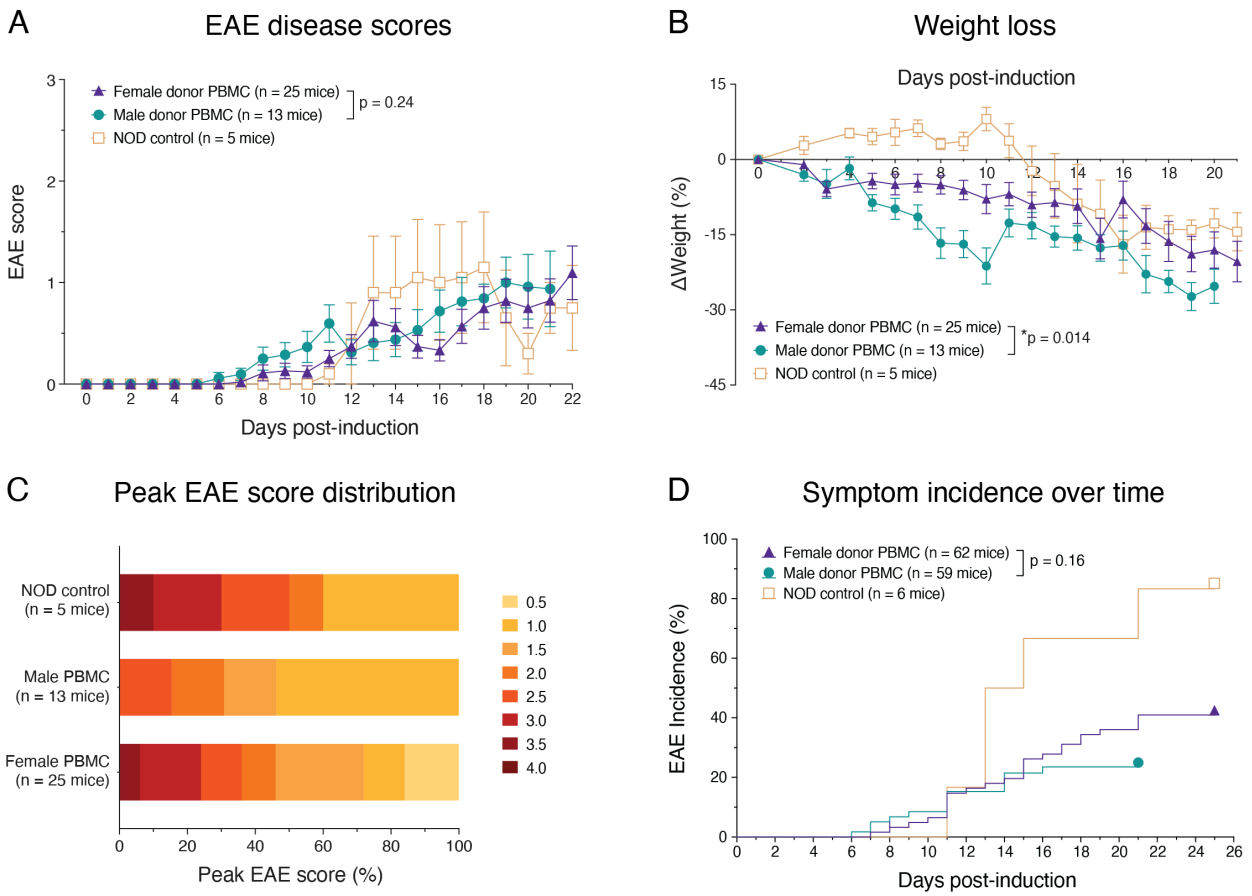

Figure 4.4 Effect of PBMC donor sex on clinical outcomes in the HuPBMC EAE model

Figure shows (A) clinical EAE scores, (B) weight loss, and (C) proportions of peak EAE disease scores attained by symptomatic female donor HuPBMC-NSG/SGM3 mice (n = 25 derived from 4 F HDs), male donor HuPBMC-NSG/SGM3 mice (n = 13 derived from 4 M HDs), and control NOD mice (n = 5) post-rhMOG/MOG_{35-55} EAE induction. For A and B, data are shown as mean with SEM and curves were analyzed using a mixed-effects two-way model. (D) Incidence of EAE symptoms over time among all EAE induced female donor HuPBMC mice (n = 62 derived from 4 F HDs), male donor HuPBMC mice (n = 59 derived from 4 M HDs), and control NOD mice (n = 6) post-EAE induction. Data are shown as percentage of the group and curves were analyzed by Log-rank (Mantel-Cox) test. (E) Overall EAE symptom incidence for each HuPBMC cohort (n = 4 HDs of both sexes) compared to a NOD control cohort. Data are shown as mean with SEM and were analyzed by Mann-Whitney test. (F) Day of EAE symptom onset post-induction (DPI) for symptomatic mice in each group. Distribution of individual data are shown with median and quartiles (dashed lines) and were analyzed by Brown-Forsythe and Welch ANOVA with Dunnett's T3 multiple comparisons. HuPBMC cohorts included: 10, 18, 19, 21, 24, 26, 31, and 32.

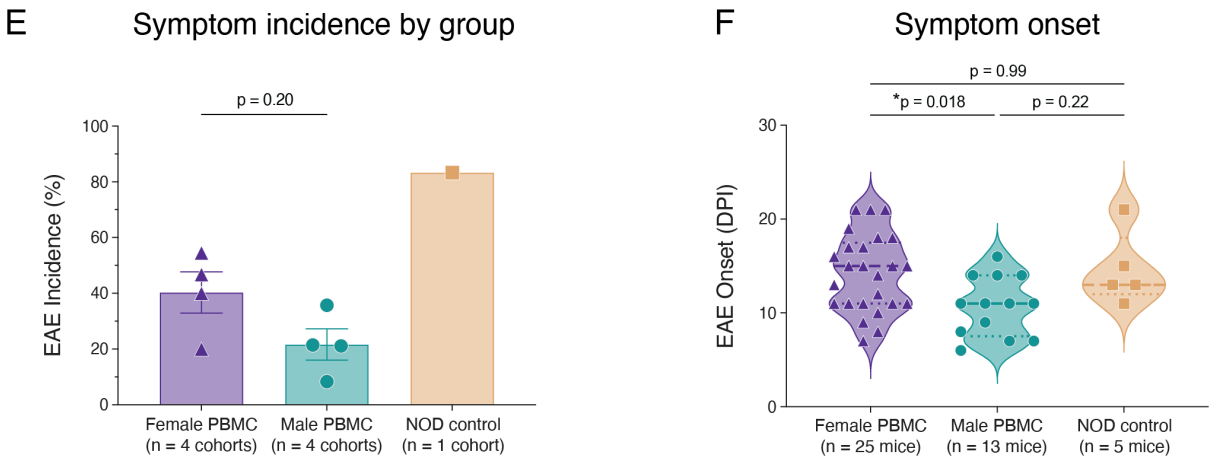

Figure 4.4 continued

4.3.4 Summary and discussion of findings

Based on the results of six preliminary HuPBMC EAE cohorts all derived from healthy female donor PBMCs, male recipient NSG and NSG-SGM3 mice were significantly more susceptible to myelin antigen immunization resulting in clinical EAE paralysis than female recipient mice, whereas female recipient mice were far more prone to developing symptoms of xGvHD. In NOD mice, increased EAE severity has been reported to occur following pathogenic chromosomally male MOG-specific Th17 cell transfer compared to female Th17 cells[477]. The absence of endogenous murine T cells in the immunocompromised NSG mouse, however, suggests the enhanced, more severe EAE disease seen in male recipient HuPBMC-NSG mice is due to host differences independent of the T cell intrinsic responses reported by Doss and colleagues. Male recipient HuPBMC-NSG mice may possibly develop EAE more frequently due to increased permeabilization of the BBB following CFA immunization and pertussis toxin administration, since many female recipient HuPBMC-NSG mice developed xGvHD symptoms indicative of peripheral inflammation while typically remaining free of paralytic symptoms caused by CNS localized inflammation. Specific assessments would be required to determine if BBB integrity differs with recipient sex post-EAE induction in HuPBMC-NSG mice. There is also the possibility that the recipient sex bias observed in the preliminary experiments would be different had male donor PBMCs been used to engraft the recipients, though this appears unlikely given the similarity in HuPBMC EAE outcomes based on blood donor sex in the subsequent analysis.

Bias resulting from the sex of the engrafted PBMCs was observed in some but not all included clinical measurements in male recipient HuPBMC-NSG EAE mice. In particular, the average overall EAE incidence of male PBMC-engrafted mice was approximately half of that in female PBMC engrafted mice, though once the mice did develop symptoms, they tended to proceed similarly regardless of blood donor sex. The data suggest that male donor PBMCs are less efficient in driving EAE following immunization. Despite a similar composition of human immune cell subsets having been injected into recipients from male and female PBMC donors, the functions and activation status of these cells may have differed initially and following engraftment and immunization. To determine the immunological basis for the reduced disease incidence in male donor engrafted HuPBMC-NSG EAE mice, the inclusion of more blood donors that are serotyped and demographically matched would allow for a more complete assessment of any differences in HIS engraftment kinetics, CNS infiltration and distribution, and/or T cell activation and functionality that account for inter-donor variability.

Ultimately, our preliminary data indicates that the optimal combination of donor and recipient sex moving forward is engraftment of male NSG/SGM3 recipient mice with female blood donor PBMCs, in order to maximize the incidence of EAE symptoms and to minimize sex bias as a confounding factor for investigating viral infection specifically in the HuPBMC EAE model.

4.4 Differences in HuPBMC EAE on the NSG and NSG-SGM3 background

4.4.1 Rationale and experimental design

While many different strains of immunocompromised mice have been developed for the purposes of generating a representative HIS in a small animal model, the NSG mouse is a standard, frequently used background for efficient humanization (Section 1.3.1). The derivative strain NSG-SGM3 has the same host genetics as the NSG but also transgenically express three human cytokines (SCF, GM-CSF, and IL-3), which have been shown to promote the engraftment of non-T cells (especially myeloid cells) and Tregs when humanized with hCD34$^+$ HSCs[479,509]. It is unclear, however, what is the impact of transgenic human cytokine expression on the level and composition of human PBMC engraftment in the NSG-SGM3 mouse. Data from the preliminary HuPBMC cohorts induced with EAE (Table 4.1) indicated that NSG and NSG-SGM3 mice developed EAE paralysis to similar extents, though differences in HIS subset had not yet been

evaluated. As changes to immune cell subset populations could impact the development of EAE, and potentially enhance incidence and/or severity of clinical symptoms in recipient derived from some or all PBMCs donors, we sought to determine if one or both strains should be preferentially used in generating the HuPBMC EAE model. To do so, we retrospectively analyzed peripheral blood HIS reconstitution before EAE induction, clinical EAE outcomes following MOG antigen immunization, and splenic HIS reconstitution at endpoint for NSG and NSG-SGM3 mice derived from the same four genetically unrelated healthy female PBMC donors.

4.4.2 Peripheral blood reconstitution

On days 18 – 22 post-PBMC injection of 5 x 10^6 healthy female donor cells, HIS reconstitution in the peripheral blood of four separate cohorts of male recipients (each comprised of some of both NSG and NSG-SGM3 mice) was analyzed to assess strain-based differences in engrafted immune composition. As a proportion of total leukocytes in the blood, none of the major or minor human immune cell subsets measured differed between HuPBMC NSG or NSG-SGM3 samples (Figure 4.5). PBMC engraftment of both NSG and NSG-SGM3 mice also led to similar reconstitution of T cell and B cell subsets prior to EAE induction (Figure 4.6). At 3 weeks post-PBMC injection, engraftment of NSG and NSG-SGM3 mice was comparable.

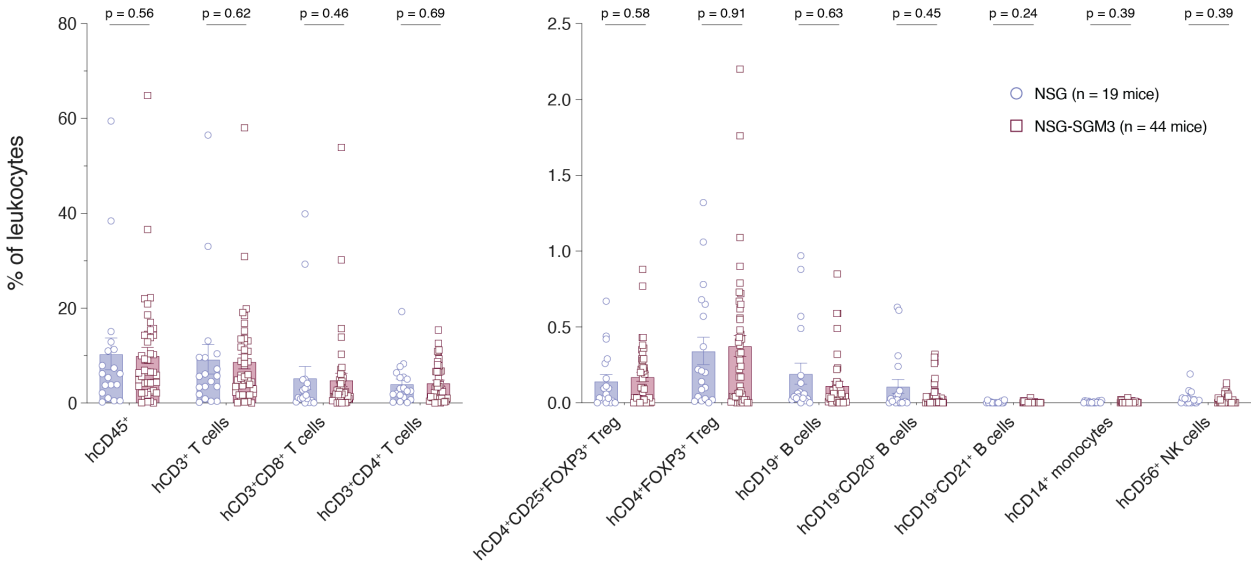

Figure 4.5 Peripheral blood reconstitution of PBMC engrafted NSG and NSG-SGM3 mice

Relative proportions of all measured human immune cell lineages are shown as a proportion of total leukocytes (murine and human) in the peripheral blood days 18 – 22 (3 weeks) post-PBMC engraftment of male NSG

mice (n = 19) and NSG-SGM3 mice (n = 44) derived from 4 healthy female donors (HD-01, HD-04, HD-06, and HD-07). Subsets are subdivided into predominantly engrafted immune cell lineages (left) and minorly engrafted immune cell lineages (right) to better illustrate relative frequencies. Data are shown as mean with SEM and were analyzed by Mann-Whitney test. HuPBMC cohorts included: 10, 18, 24, and 26.

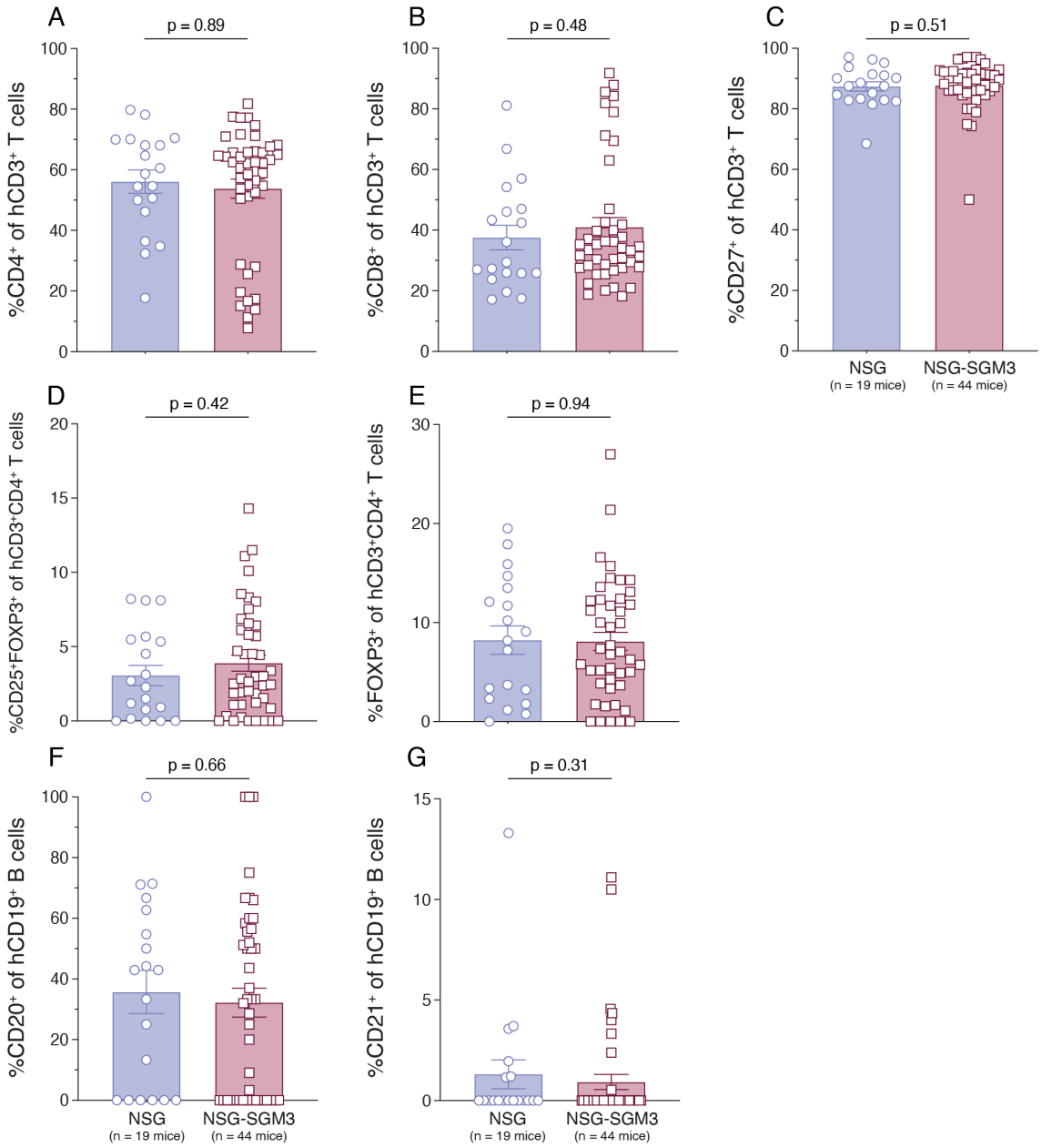

Figure 4.6 Human T and B cell subsets in the peripheral blood of PBMC engrafted NSG and NSG-SGM3 mice

Human T and B cell subset frequencies in the peripheral blood days 18 – 22 (3 weeks) post-PBMC engraftment of male NSG (n = 19) and NSG-SGM3 mice (n = 44) derived from 4 healthy female donors (HD-01, HD-

04, HD-06, and HD-07). Proportions of (A) hCD4, (B) hCD8, and (C) hCD27 expressing subsets among $hCD3^+$ T cells. Proportions of (D) both hCD25 and hFOXP3, and (E) hFOXP3 expressing $hCD3^+CD4^+$ regulatory T cell (Treg) subsets. Proportions of (F) hCD20 and (G) hCD21 expressing subsets among $hCD19^+$ B cells. Data are shown as mean with SEM and were analyzed by Welch's unpaired t test or by Mann Whitney test. HuPBMC cohorts included: 10, 18, 24, and 26.

4.4.3 Clinical EAE outcomes

Following immunization with mixed rhMOG protein and MOG_{35-55} peptide, PBMC-engrafted NSG and NSG-SGM3 mice presented with statistically similar outcomes for all measured aspects of clinical disease, including EAE symptom incidence, onset, disease course and weight loss, as well as the incidence of xGvHD symptoms (Figure 4.7). The data indicate that use of either NSG or NSG-SGM3 mice as PBMC recipients comparably represents the immunophenotype of the donor.

4.4.4 Spleen reconstitution at EAE endpoint

At EAE endpoint (days 15 – 22 post-immunization), spleen reconstitution of HuPBMC mice on the NSG and NSG-SGM3 backgrounds was nearly identical, with activated T cells comprising most of the engrafted $hCD45^+$ cells (Figure 4.8, symptomatic and subclinical mice combined for analysis). Transgene expression in the NSG-SGM3 mouse did not statistically increase the relative proportions or quantities of non-T cells in the spleen, which reconstituted at comparably low levels (Figure 4.8, Figure 4.9). Proportionally, humanized NSG-SGM3 mice had a statistically higher level of $hCD45^+$ cell reconstitution compared to NSG mice (Figure 4.8C), however, by numerical abundance, HuPBMC NSG and NSG-SGM3 mouse spleens contained similar quantities of $hCD45^+$ cells (Figure 4.9A) Further, EAE-induced HuPBMC NSG and NSG-SGM3 mice did not have any differences in $hCD3^+$ T cell activation level or $hCD19^+$ B cell marker expression (Figure 4.8). As CNS tissues from each cohort were processed and analyzed differently, infiltration levels could not be compared between strains.

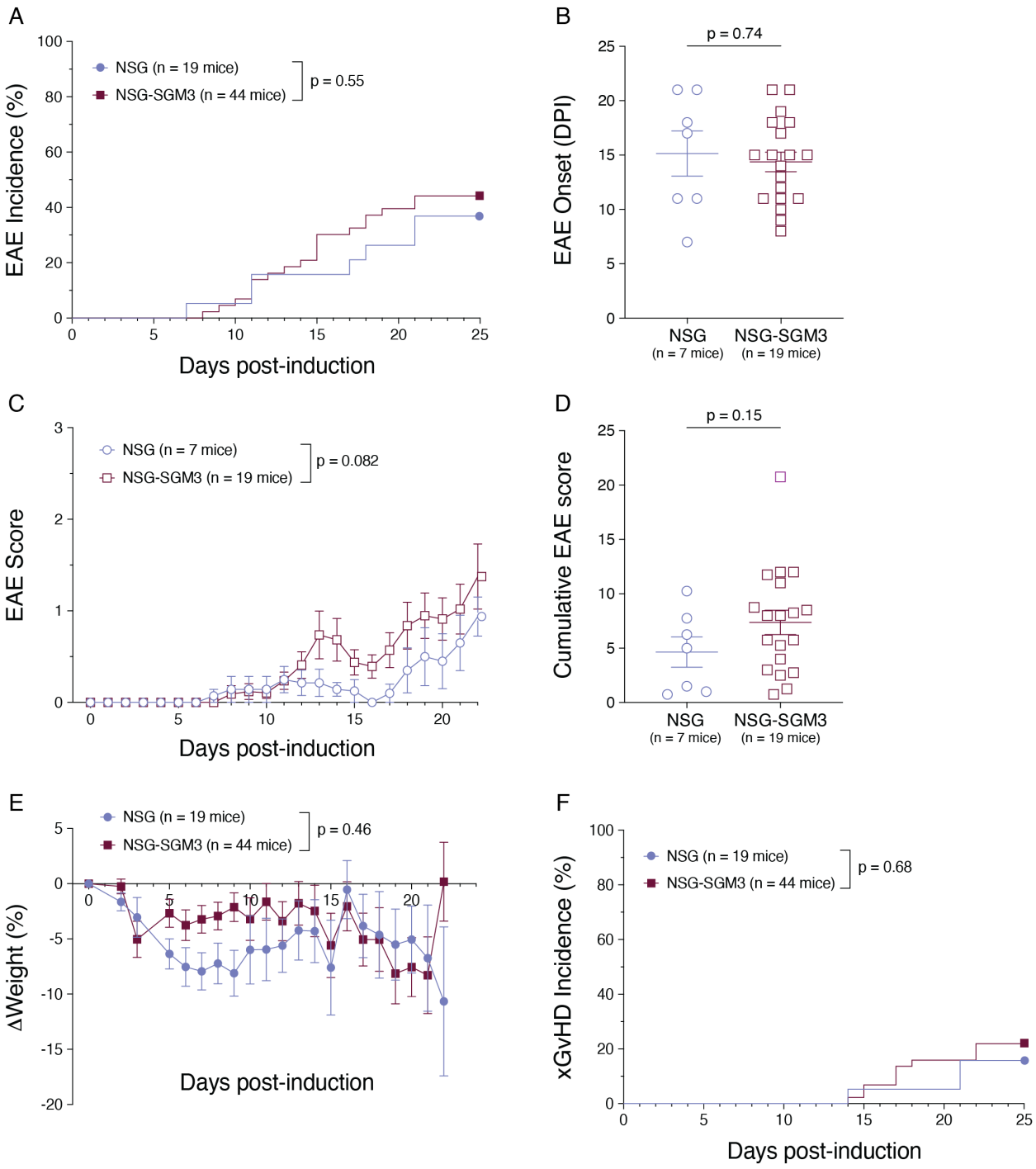

Figure 4.7 Clinical EAE outcomes for PBMC engrafted NSG and NSG-SGM3 mice

Figure shows (A) incidence of EAE symptoms over time among all mixed rhMOG/MOG$_{35-55}$ immunized PBMC engrafted male NSG mice (n = 19) and NSG-SGM3 mice (n = 44) derived from 4 healthy female donors (HD-01, HD-04, HD-06, and HD-07). Data are shown as percentage of the group and curves were analyzed by Log-rank (Mantel-Cox) test. Among the HuPBMC NSG (n = 7) and NSG-SGM3 mice (n = 19) that developed symptoms of EAE, figure shows (B) day of EAE symptom onset post-induction (DPI), (C) clinical EAE scores over time, and (D)

cumulative EAE scores for each strain group. Data are shown as mean with SEM. Data in B and D were analyzed by Welch's unpaired t test, data in C were analyzed using a mixed-effects two-way model. Among all EAE induced HuPBMC NSG (n = 19) and NSG-SGM3 mice (n = 44), figure shows (E) weight loss and (F) symptoms of xGvHD over time for each strain group. Data in E are shown as mean with SEM and were analyzed using a mixed-effects two-way model. Data in F are shown as percentage of the group and curves were analyzed by Log-rank (Mantel-Cox) test. HuPBMC cohorts included: 10, 18, 24, and 26.

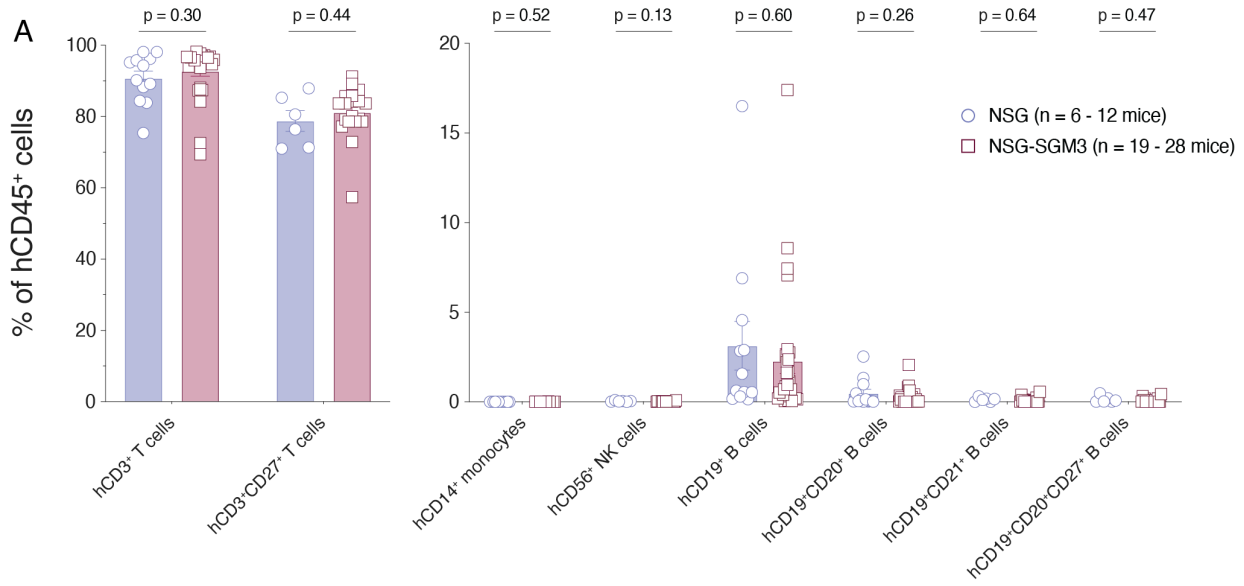

Figure 4.8 Proportional spleen reconstitution of PBMC-engrafted NSG and NSG-SGM3 mice at EAE endpoint

(A) Relative proportions of all measured human immune cell lineages are shown as a proportion of engrafted hCD45$^+$ leukocytes in the spleen days 15 – 22 post-rhMOG/MOG$_{35-55}$ EAE induction of male HuPBMC NSG mice (n = 6 – 12) and NSG-SGM3 mice (n = 19 – 28) derived from 3 healthy female donors (HD-01, HD-04, and HD-06). Subsets are subdivided into predominantly engrafted immune cell lineages (left) and minorly engrafted immune cell lineages (right) to better illustrate relative frequencies. Figure shows proportions of (B) mCD45$^+$ and (C) hCD45$^+$ cells among total leukocytes (murine and human), as well as proportions of (D) hCD27 expressing hCD3$^+$ T cells, and (E) hCD21, (F) hCD20, and (G) hCD20 and hCD27 dual expressing hCD19$^+$ B cells. Data are shown as mean with SEM and were analyzed by Welch's unpaired t test or by Mann-Whitney test. HuPBMC cohorts included: 10, 18, and 24.

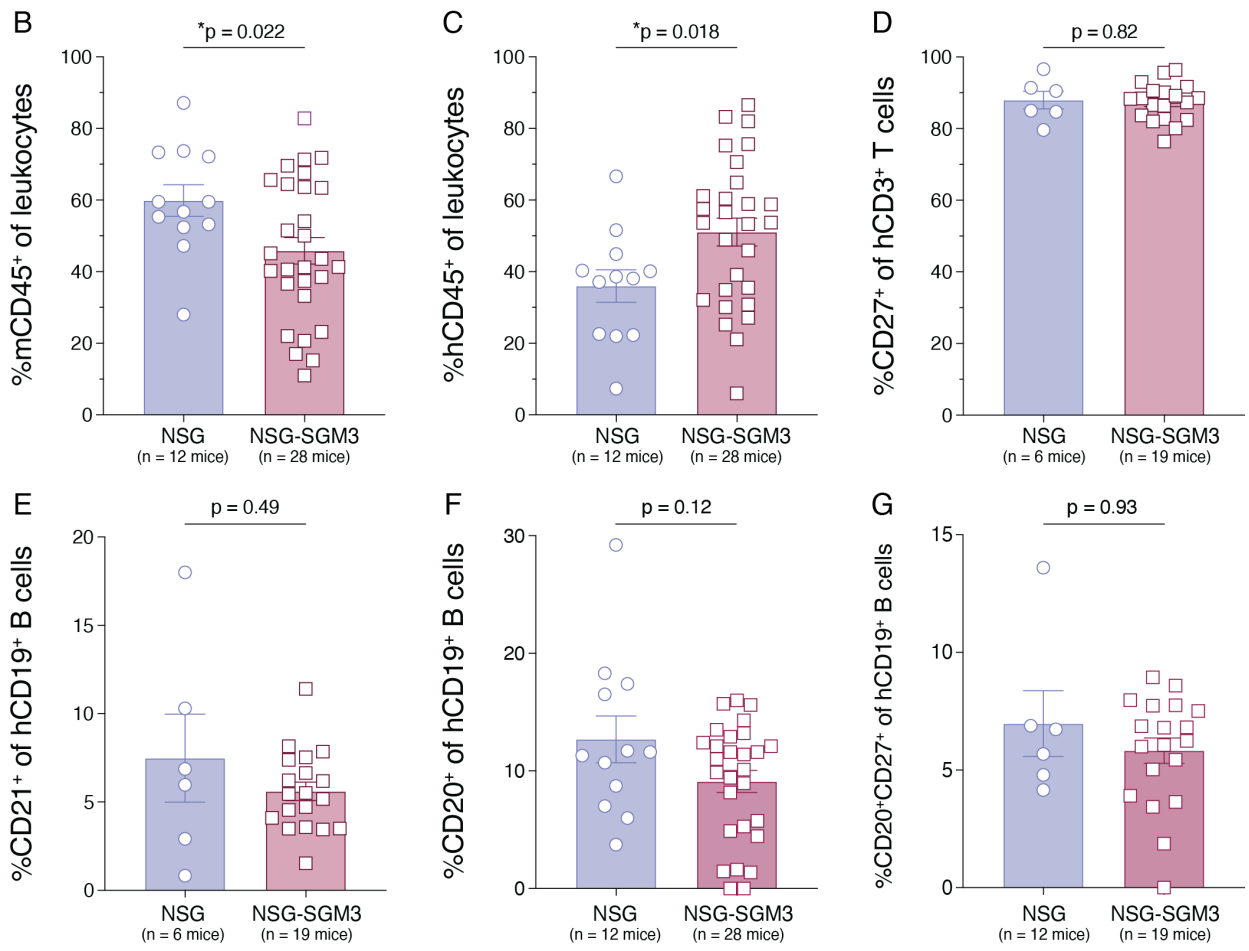

Figure 4.8 continued

4.4.5 Summary and discussion of findings

Peripheral blood and spleen reconstitution of human immune cell lineages was comparable between PBMC-engrafted and EAE induced NSG and NSG-SGM3 mice. Unlike what has been observed in HuHSC mice[479,509], PBMC engraftment of NSG-SGM3 did not improve myeloid cell or Treg reconstitution compared to the NSG to a statistically measurable degree. Moreover, clinical EAE outcomes were similar for the same PBMC donors regardless of which recipient strain was engrafted prior to MOG immunization. The HuPBMC NSG-SGM3 EAE mice did exhibit a slightly more severe average EAE disease course, though none of the individual days were significantly different, and had increased numbers of NSG mice been available to engraft (only half as many as NSG-SGM3 mice in this analysis), this difference may have been negligible. In conclusion, there was no clear advantage to using NSG-SGM3 mice over NSG mice for the

HuPBMC EAE model, and therefore both strains were used interchangeably to generate recipient cohorts (denoted as NSG/SGM3).

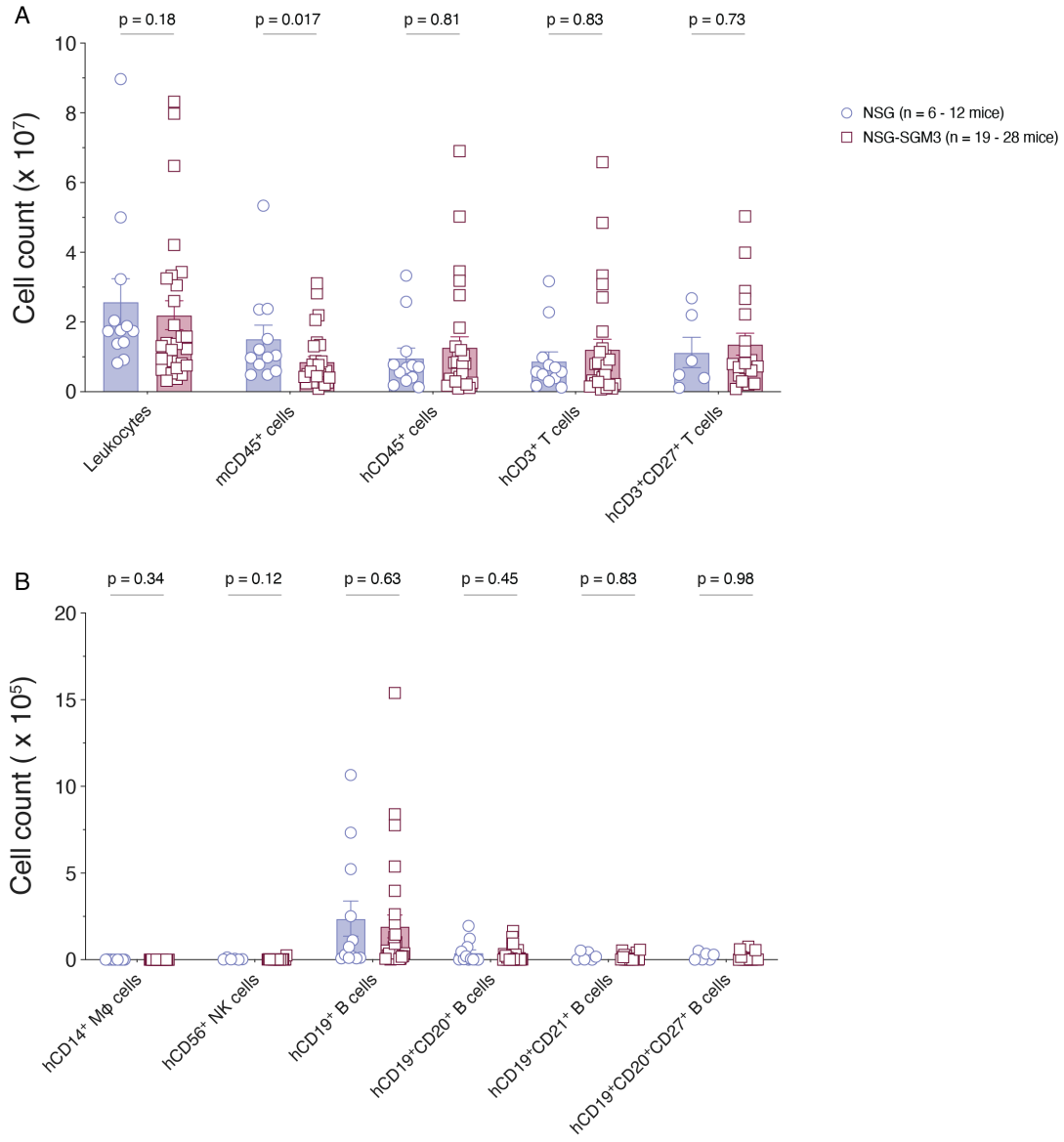

Figure 4.9 Quantified spleen reconstitution of PBMC engrafted NSG and NSG-SGM3 mice at EAE endpoint

Relative abundance of all measured human immune cell lineages in the spleen days 15 – 22 post-rhMOG/MOG$_{35-55}$ EAE induction of male HuPBMC NSG mice (n = 6 – 12) and NSG-SGM3 mice (n = 19 – 28) derived from 3 healthy female donors (HD-01, HD-04, and HD-06). Subsets are subdivided into predominantly engrafted immune cell lineages (A) and minorly engrafted immune cell lineages (B) to better illustrate relative frequencies. Data are shown as mean with SEM and were analyzed by Mann-Whitney test. HuPBMC cohorts included: 10, 18, and 24.

4.5 Antigenic differences in EAE induction of HuPBMC mice

4.5.1 Rationale and experimental design

Genetically distinct strains of laboratory mouse are differentially susceptible to active EAE induction with certain protein and peptide myelin antigenic epitopes (Table 4.2), as determined by each strain's chemokine expression patterns, MHC haplotype, and non-MHC genetic regional variance[152,153,667,668]. For example, C57Bl/6 mice are highly susceptible to EAE induction with MOG peptides, but not so with MBP peptides[152]. The same epitopes can also produce variable clinical courses in the same stain just by altering the dose of antigen administered. In C57Bl/6 mice, some reports have shown that lower doses of MOG_{35-55} in CFA emulsion produce a mildly relapsing disease course, whereas higher doses of MOG_{35-55} typically result in a chronic monophasic course, though this finding has not been consistently observed between independent studies[128,154,669].

The peptide antigen MOG_{35-55} has been most commonly reported to induce EAE in both C57Bl/6 and NOD mice, the latter of which serves as the background for the NSG/SGM3 strain[129,139,144]. EAE induction of C57Bl/6 mice with MOG_{35-55} generates a preferentially $CD4^+$ T cell mediated disease as the peptide 40-55 is efficiently processed loaded into H-2b MHC II complexes[148]. The extracellular domain of MOG protein (1-120) with rat, mouse, and human sequences can also induce a predominantly B cell dependent or independent response in C57Bl/6 mice depending on the species[149,155,670–672]. Though the effectiveness of using recombinant MOG proteins to induce B cell dependent EAE in NOD mice is not yet known, recombinant MOG induced a severe chronic relapsing form of EAE alike MOG_{35-55} immunization[673]. For the purposes of inducing EAE in HuPBMC-NSG/SGM3 mice, expressing the same MHC haplotype as the NOD, we initially attempted active induction using one or both of MOG_{35-55} peptide and $rhMOG_{1-120}$ (Table 4.1).

Unpublished findings from the laboratory of Hervé Perron (GeNeuro Innovation) indicated that PBMC humanized NOD-*scid/scid* mice were susceptible to induction with recombinant human MBP combined with an immunodominant peptide epitope of MBP, which they determined to share increased structural homology with host MBP that improved interspecies antigen recognition (personal communication). It was therefore unclear which myelin epitopes were most effective at facilitating interspecies antigen presentation of myelin epitopes and producing

clinically measurable immunopathology in HuPBMC-NSG/SGM3 model, in addition to how the disease progresses compared to typical murine EAE models. In sections 4.5 and 4.6, differences in the susceptibility of HuPBMC-NSG/SGM3 mice to EAE induction with individual myelin peptide and protein antigens, as well as the pathological differences in clinical and immunological disease outcomes compared to classical EAE models, were investigated, respectively. Herein, two separate donations from the same healthy female blood donor were used to humanize recipient male NSG/SGM3 mice with 5 million PBMCs each, and at 3 weeks post-engraftment, mice were immunized with one of three antigen formulations using standard doses: mixed rhMOG protein + MOG_{35-55} peptide, MOG_{35-55} peptide only, or rhMBP protein only.

Table 4.2 Mouse strain-based differences in active EAE inducing myelin antigen susceptibility

Abbr: Myelin basic protein, MBP; Myelin oligodendrocyte glycoprotein, MOG; Pertussis toxin, PTx; Proteolipid protein (PLP). See Table 15.1.1 in [129] for a more comprehensive list.

Strain	Susceptible antigens	PTx used?	Clinical outcomes	References
C57Bl/6	▪ MOG_{35-55} ▪ rMOG protein ▪ rMBP protein (less effective) ▪ PLP peptides (less effective) ▪ MBP-PLP fusion protein	Yes	▪ Chronic, severe, monophasic ▪ Low doses and some antigens produce mild disease symptoms ▪ Histopathology differs by antigen ▪ Similar incidence by sex	129,152,153
NOD	▪ MOG_{35-55} ▪ rMOG protein ▪ PLP_{56-70} (less effective)	Yes	▪ Relapsing-remitting then secondary chronic progressive ▪ Similar incidence by sex	144,145,673–675
SJL/J	▪ rPLP protein ▪ $PLP_{139-151}$ ▪ rMBP protein ▪ MBP peptides ▪ MOG peptide (less effective)	Not for PLP Yes for MBP	▪ Relapsing-remitting, severe ▪ Females more susceptible ▪ Epitope spreading	129,676

4.5.2 Peripheral blood reconstitution of HuPBMC cohorts

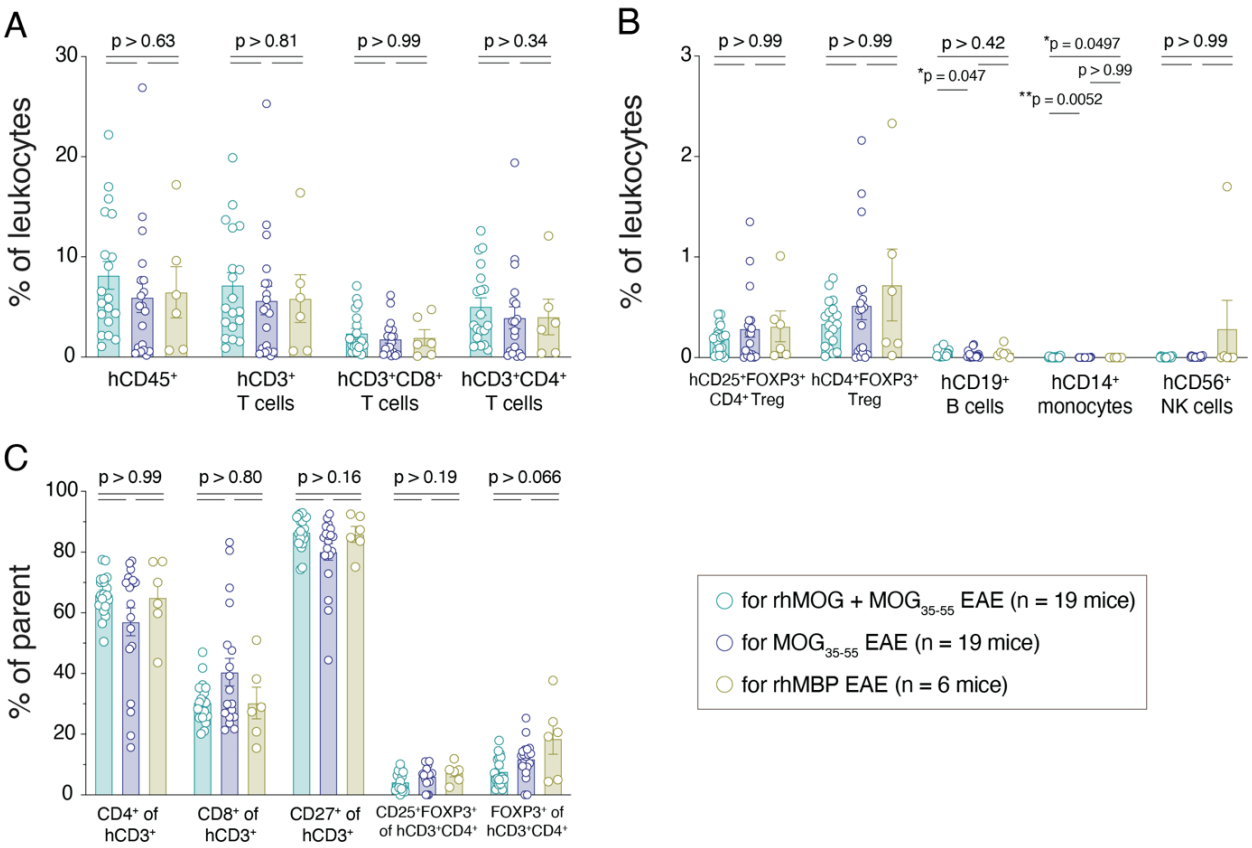

Figure 4.10 Peripheral blood reconstitution of HuPBMC cohorts prior to EAE induction

Figure shows (A – B) relative proportions of all measured human immune cell lineages are shown as a proportion of total leukocytes (murine and human) and (C) human T cell subset proportions in the peripheral blood days 19 – 20 post-PBMC engraftment of male NSG/SGM3 mice (n = 6 or 19/cohort) derived from a healthy female donor (HD-04). Subsets are subdivided into predominantly engrafted immune cell lineages (A) and minorly engrafted immune cell lineages (B) to better illustrate relative frequencies. Data are shown as mean with SEM and were analyzed by Brown-Forsythe and Welch ANOVA with Dunnett's T3 multiple comparisons or by Kruskal-Wallis test with Dunn's multiple comparisons. HuPBMC cohorts included: 18 and 35.

As NSG/SGM3 mice had to be humanized in two separate cohorts to obtained sufficient numbers of HuPBMC mice from the same blood donor, peripheral blood reconstitution of all mice at 3 weeks post-PBMC injection was assessed to ensure comparability in engraftment between mice randomly assigned to be immunized with each antigen formulation. Flow cytometric analysis of saphenous vein blood samples confirmed that engraftment of PBMCs derived from the same

blood donor resulted in variable but statistically similar HIS subset reconstitution in all recipient NSG/SGM3 mice (Figure 4.10).

4.5.3 Clinical and immunological EAE outcomes

At 3 weeks post-PBMC injection, HuPBMC-NSG/SGM3 mice were immunized with myelin antigens emulsified in a standard volume and dose of CFA (as specified in the legend of Figure 4.11). Consistent with our preliminary HuPBMC EAE cohort findings (Table 4.1), the inclusion of rhMOG protein in the emulsion led to earlier onset of EAE paralysis compared to MOG_{35-55} peptide alone, wherein the first wave of symptoms was more evident (Figure 4.11A – B). Immunization with MOG_{35-55} peptide or rhMBP protein resulted in similar delays to symptom onset (Figure 4.11A – B), though rhMBP induced mice attained more severe disease scores compared to both MOG antigen immunized groups (Figure 4.11A, E). It is currently unclear if rhMBP would induce a phasic/relapsing phenotype similar to MOG immunization in HuPBMC-NSG/SGM3 mice, as the cohort could not be maintained longer post-induction due to development of xGvHD. Overall incidence of clinically evident paralysis was similar between groups by endpoint (Figure 4.11C), suggesting a PBMC donor dependent effect on the proportion of mice that developed symptoms post-induction rather than an inducing antigen dependent effect. Consistent with this observation, similar patterns of weight loss indicated that pre-clinical or subclinical disease pathology proceeded in a similar manner regardless of the inducing antigen (Figure 4.11D). The main takeaway from these data was that immunizing HuPBMC-NSG/SGM3 mice with mixed rhMOG/MOG_{35-55} antigen formulation resulted in clinical EAE symptoms that outpaced the onset of symptoms of xGvHD (Figure 4.11C), which makes this antigen combination preferable for use in the HuPBMC EAE model.

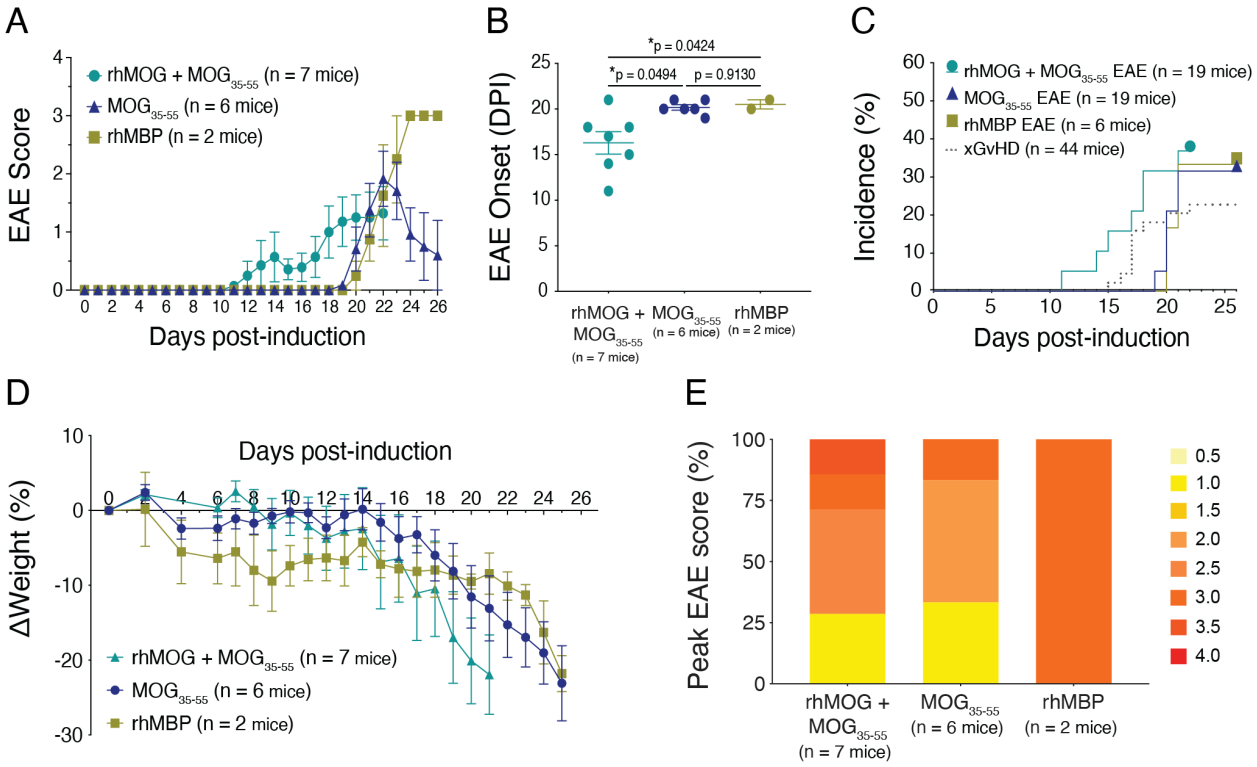

Figure 4.11 Clinical EAE outcomes in HuPBMC mice induced with different myelin antigens

Figure shows (A) clinical EAE scores, (B) day of EAE symptom onset post-induction (DPI), (D) weight loss, and (E) proportions of peak EAE disease scores attained by symptomatic HuPBMC-NSG/SGM3 mice (all males engrafted with HD-04 female PBMCs) induced with mixed 100 µg rhMOG protein + 200 µg MOG_{35-55} peptide (n = 7 mice), 200 µg MOG_{35-55} peptide (n = 6 mice), or 50 µg rhMBP protein (n = 2 mice). (C) The incidence of EAE symptoms over time for all EAE induced mice per antigen (n = 6 or 19 mice induced per group), as well as the incidence of xGvHD symptoms over time for all HuPBMC EAE cohorts combined (n = 44 mice total). In A, B, and D, data are shown as mean with SEM. Data in B were analyzed by Brown-Forsythe and Welch ANOVA with Dunnett's T3 multiple comparisons. Data in C and E are shown as percentage of the group. HuPBMC cohorts included: 18 and 35.

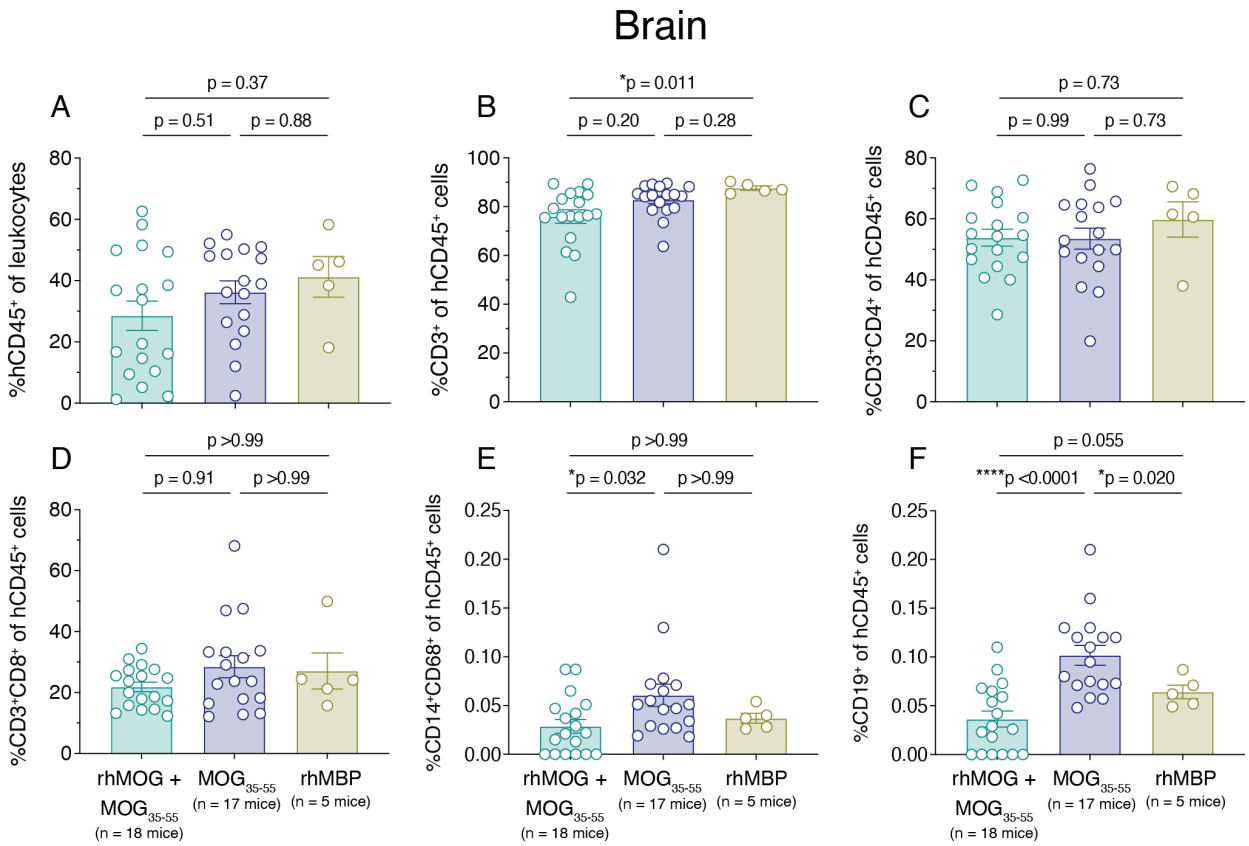

Figure 4.12 Human immune cell infiltration of the brains of HuPBMC EAE mice induced with different myelin antigens

Figure shows proportions of (A) hCD45$^+$ cells among total leukocytes (murine and human), as well as (B) hCD3$^+$ T cells, (C) hCD3$^+$CD4$^+$ T cells, (D) hCD3$^+$CD8$^+$ T cells, (E) hCD14$^+$CD68$^+$ macrophages, and (F) hCD19$^+$ B cells among all hCD45$^+$ immune cells infiltrating the brain of HuPBMC-NSG/SGM3 mice (all males engrafted with HD-04 female PBMCs) induced with mixed 100 µg rhMOG protein + 200 µg MOG$_{35-55}$ peptide (n = 18 mice) day 22 post-EAE induction, 200 µg MOG$_{35-55}$ peptide (n = 17 mice) day 26 post-EAE induction, or 50 µg rhMBP protein (n = 5 mice) day 26 post-EAE induction. Brain tissues were perfused prior to cell isolation. Data are shown as mean with SEM and were analyzed by Brown-Forsythe and Welch ANOVA with Dunnett's T3 multiple comparisons or by Kruskal-Wallis test with Dunn's multiple comparisons. HuPBMC cohorts included: 18 and 35.

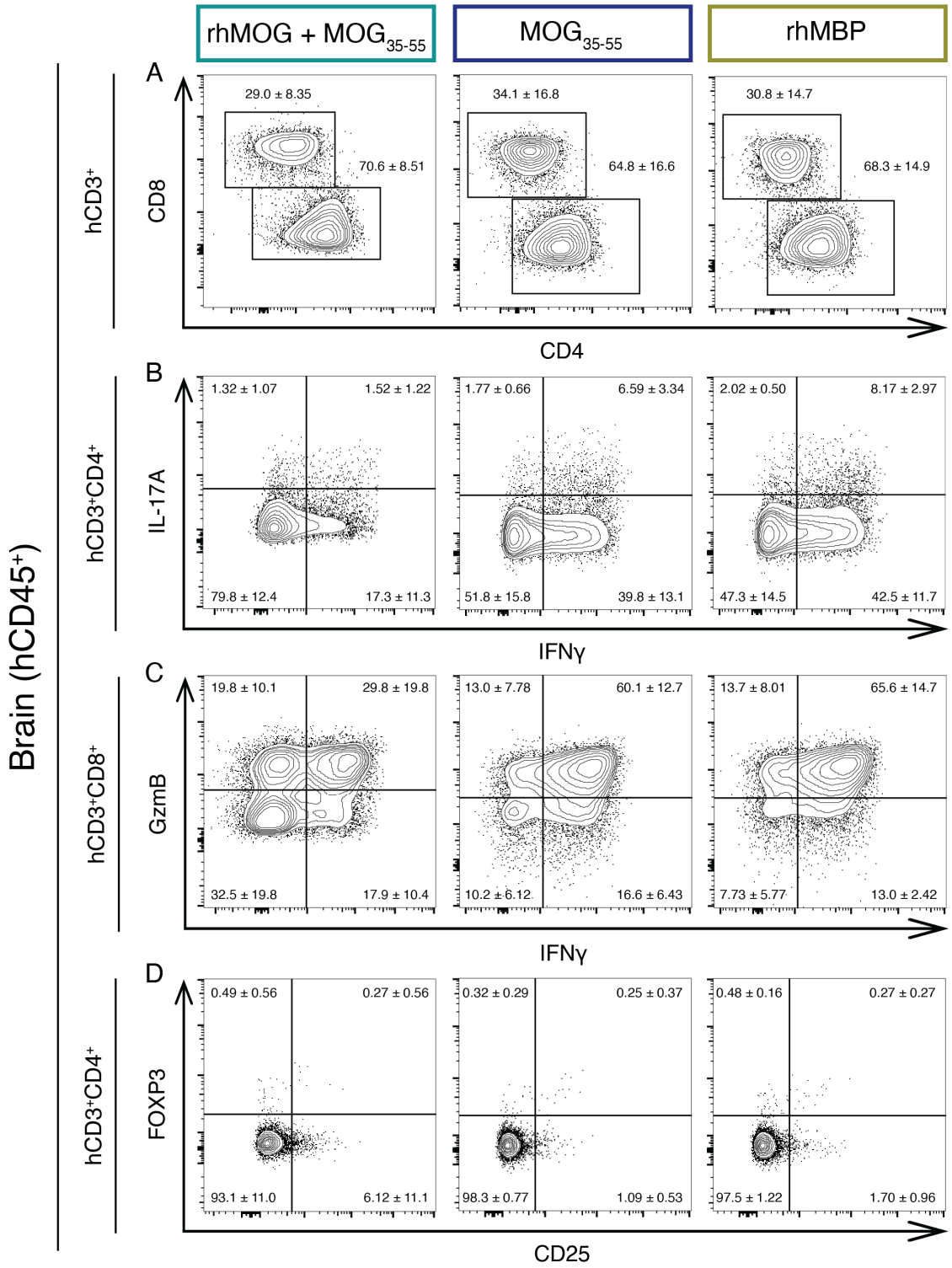

Figure 4.13 Brain infiltrating human T cell subsets in HuPBMC EAE mice induced with different myelin antigens

Figure shows concatenated flow cytometric plots for human T cell subsets infiltrating the brain of HuPBMC-NSG/SGM3 mice (all males engrafted with HD-04 female PBMCs) induced with mixed 100 µg rhMOG protein +

200 µg MOG_{35-55} peptide (n = 18 mice) day 22 post-EAE induction, 200 µg MOG_{35-55} peptide (n = 17 mice) day 26 post-EAE induction, or 50 µg rhMBP protein (n = 5 mice) day 26 post-EAE induction. Cells isolated from perfused brains were stimulated with PMA and ionomycin to measure cytokine expression. Data are shown as mean with SD for proportions of (A) CD4 and/or CD8 expressing $hCD3^+$ T cells, (B) IFNγ and/or IL-17A expressing $hCD3^+CD4^+$ T cells, (C) IFNγ and/or GzmB expressing $hCD3^+CD8^+$ T cells, and (D) CD25 and/or FOXP3 expressing $hCD3^+CD4^+$ T cells. HuPBMC cohorts included: 18 and 35.

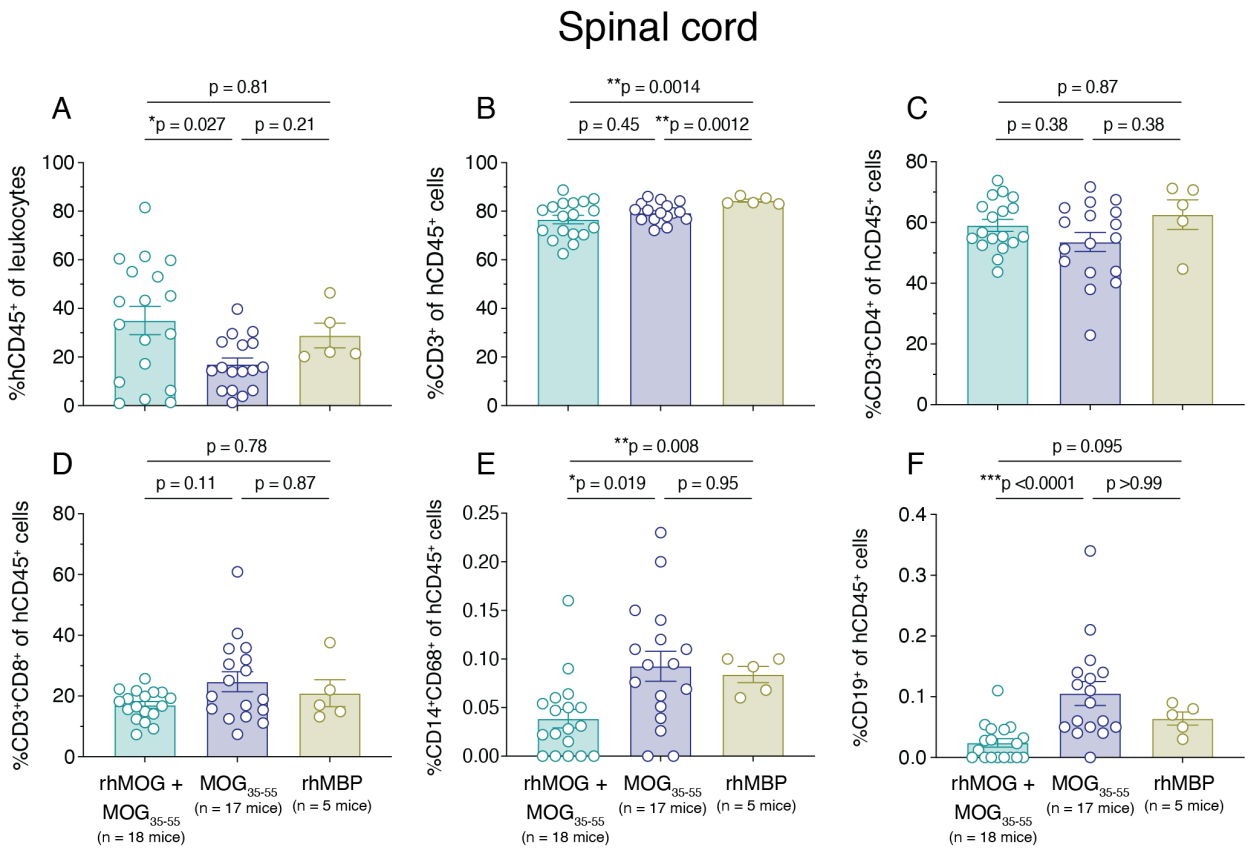

Figure 4.14 Human immune cell infiltration of the spinal cords of HuPBMC EAE mice induced with different myelin antigens

Figure shows proportions of (A) $hCD45^+$ cells among total leukocytes (murine and human), as well as (B) $hCD3^+$ T cells, (C) $hCD3^+CD4^+$ T cells, (D) $hCD3^+CD8^+$ T cells, (E) $hCD14^+CD68^+$ macrophages, and (F) $hCD19^+$ B cells among all $hCD45^+$ immune cells infiltrating the spinal cord of HuPBMC-NSG/SGM3 mice (all males engrafted with HD-04 female PBMCs) induced with mixed 100 µg rhMOG protein + 200 µg MOG_{35-55} peptide (n = 18 mice) day 22 post-EAE induction, 200 µg MOG_{35-55} peptide (n = 17 mice) day 26 post-EAE induction, or 50 µg rhMBP protein (n = 5 mice) day 26 post-EAE induction. Spinal cord tissues were perfused prior to cell isolation. Data are shown as mean with SEM and were analyzed by Brown-Forsythe and Welch ANOVA with Dunnett's T3 multiple comparisons or by Kruskal-Wallis test with Dunn's multiple comparisons. HuPBMC cohorts included: 18 and 35.

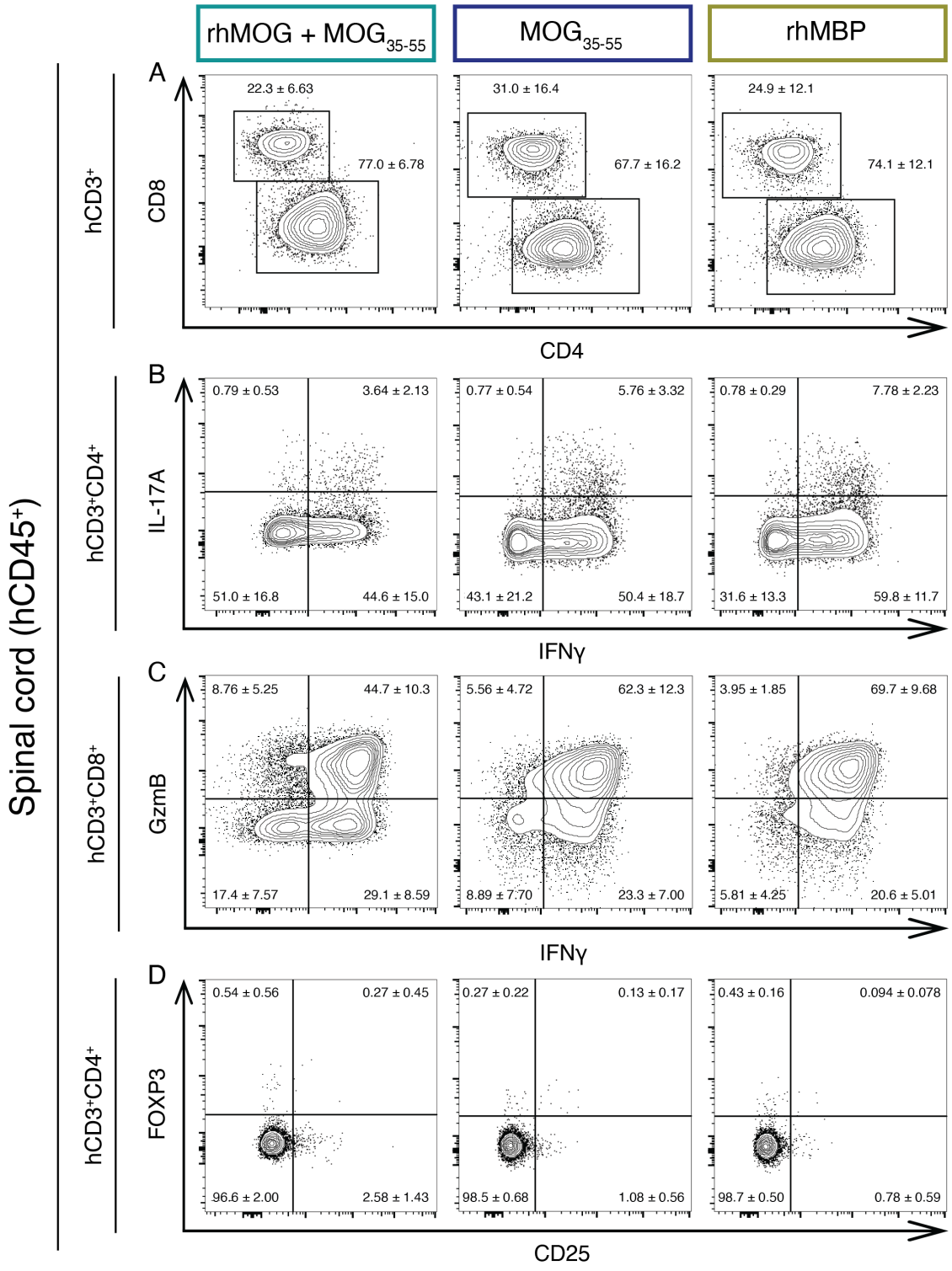

Figure 4.15 Spinal cord infiltrating human T cell subsets in HuPBMC EAE mice induced with different myelin antigens

Figure shows concatenated flow cytometric plots for human T cell subsets infiltrating the spinal cord of HuPBMC-NSG/SGM3 mice (all males engrafted with HD-04 female PBMCs) induced with mixed 100 µg rhMOG

protein + 200 µg MOG_{35-55} peptide (n = 18 mice) day 22 post-EAE induction, 200 µg MOG_{35-55} peptide (n = 17 mice) day 26 post-EAE induction, or 50 µg rhMBP protein (n = 5 mice) day 26 post-EAE induction. Cells isolated from perfused spinal cords were stimulated with PMA and ionomycin to measure cytokine expression. Data are shown as mean with SD for proportions of (A) CD4 and/or CD8 expressing $hCD3^+$ T cells, (B) IFNγ and/or IL-17A expressing $hCD3^+CD4^+$ T cells, (C) IFNγ and/or GzmB expressing $hCD3^+CD8^+$ T cells, and (D) CD25 and/or FOXP3 expressing $hCD3^+CD4^+$ T cells. HuPBMC cohorts included: 18 and 35.

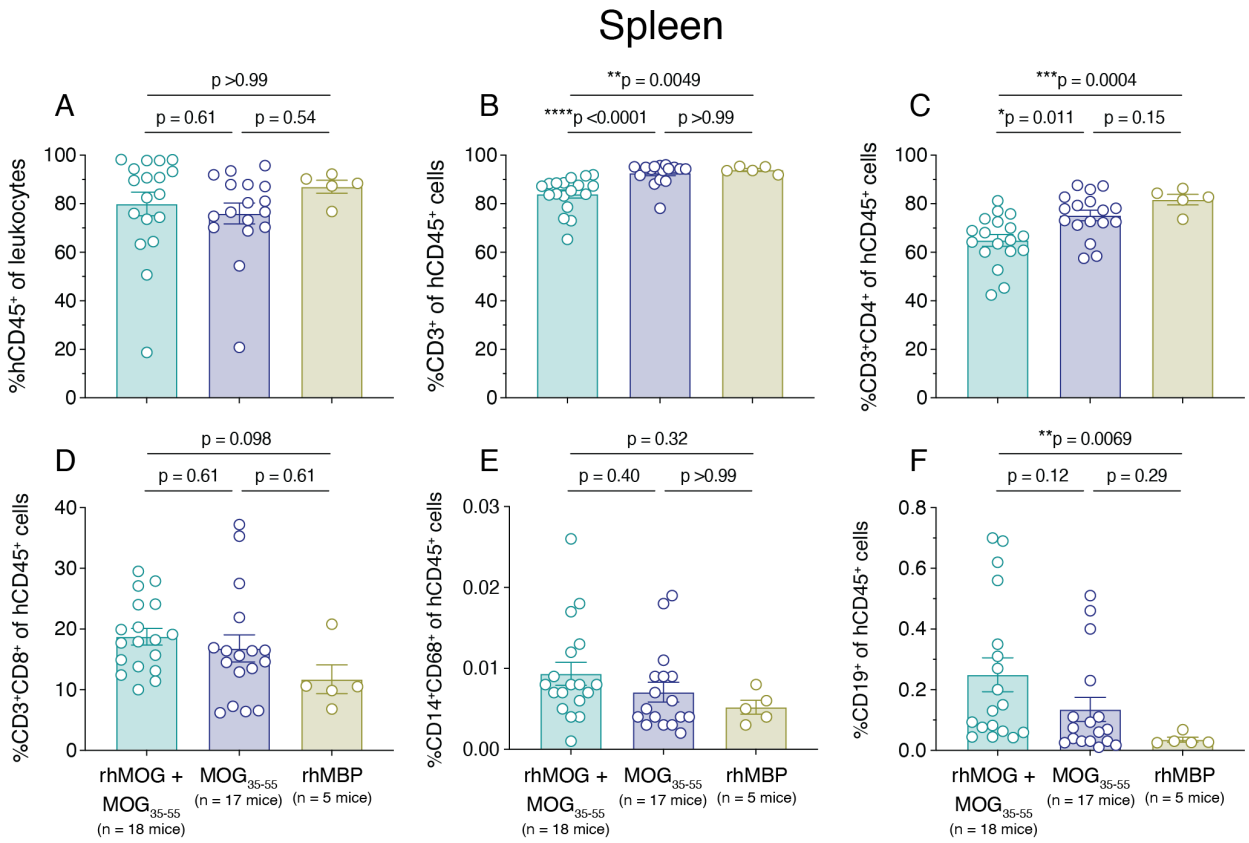

Figure 4.16 Human immune cell reconstitution of the spleens of HuPBMC EAE mice induced with different myelin antigens

Figure shows proportions of (A) $hCD45^+$ cells among total leukocytes (murine and human), as well as (B) $hCD3^+$ T cells, (C) $hCD3^+CD4^+$ T cells, (D) $hCD3^+CD8^+$ T cells, (E) $hCD14^+CD68^+$ macrophages, and (F) $hCD19^+$ B cells among all $hCD45^+$ immune cells reconstituting the spleens of HuPBMC-NSG/SGM3 mice (all males engrafted with HD-04 female PBMCs) induced with mixed 100 µg rhMOG protein + 200 µg MOG_{35-55} peptide (n = 18 mice) day 22 post-EAE induction, 200 µg MOG_{35-55} peptide (n = 17 mice) day 26 post-EAE induction, or 50 µg rhMBP protein (n = 5 mice) day 26 post-EAE induction. Data are shown as mean with SEM and were analyzed by Brown-Forsythe and Welch ANOVA with Dunnett's T3 multiple comparisons or by Kruskal-Wallis test with Dunn's multiple comparisons. HuPBMC cohorts included: 18 and 35.

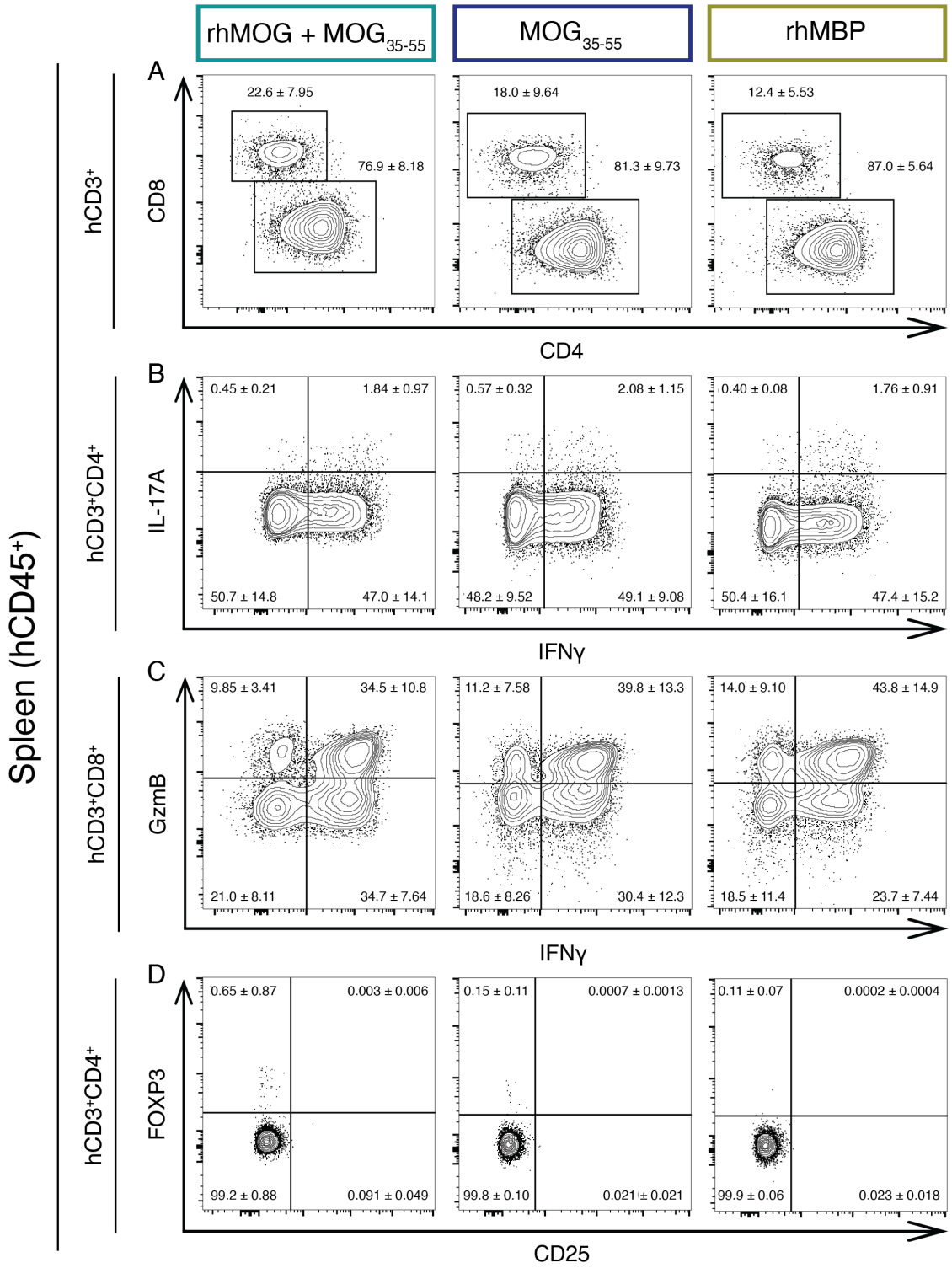

Figure 4.17 Spleen reconstituting human T cell subsets in HuPBMC EAE mice induced with different myelin antigens

Figure shows concatenated flow cytometric plots for human T cell subsets reconstituting the spleen of HuPBMC-NSG/SGM3 mice (all males engrafted with HD-04 female PBMCs) induced with mixed 100 µg rhMOG

protein + 200 μg MOG_{35-55} peptide (n = 18 mice) day 22 post-EAE induction, 200 μg MOG_{35-55} peptide (n = 17 mice) day 26 post-EAE induction, or 50 μg rhMBP protein (n = 5 mice) day 26 post-EAE induction. Cells isolated from spleens were stimulated with PMA and ionomycin to measure cytokine expression. Data are shown as mean with SD for proportions of (A) CD4 and/or CD8 expressing $hCD3^+$ T cells, (B) IFNγ and/or IL-17A expressing $hCD3^+CD4^+$ T cells, (C) IFNγ and/or GzmB expressing $hCD3^+CD8^+$ T cells, and (D) CD25 and/or FOXP3 expressing $hCD3^+CD4^+$ T cells. HuPBMC cohorts included: 18 and 35.

CNS tissues and spleens were collected from mice in each cohort approximately 1 week from symptom onset to analyze the composition of the human immune infiltrates and peripheral engraftment (Figure 4.12 – 4.17). In the brains, spinal cords, and spleens, variable but consistent proportions of the infiltrating/reconstituting human immune cells in each antigen immunized group were $hCD3^+$ T cell subsets (typically >80% of $hCD45^+$ cells) (Figure 4.12, Figure 4.14, and Figure 4.16), expressing similar patterns of proinflammatory cytokines and regulatory markers (Figure 4.13, Figure 4.15, and Figure 4.17). Consistent with the findings of Ajith and colleagues, tissue-infiltrating cytotoxic $hCD8^+$ T cells expressed GzmB and IFNγ [611]. In the MOG_{35-55} peptide and rhMBP cohort derived CNS tissues (Figure 4.13B, Figure 4.15B), a greater proportion of the infiltrating $hCD3^+CD4^+$ T cells were double IFNγ and IL-17A expressing than in mixed rhMOG/MOG_{35-55} cohort samples. Adoptively transferred double Th1/Th17 T cells have been associated with increased xGvHD severity in HuPBMC-NSG mice [677] and their increased expansion seen here is likely related to the later timepoint post-induction (day 26) when these samples were collected compared to the mixed rhMOG/MOG_{35-55} immunized mice (day 22).

Proportions of $hCD14^+CD68^+$ macrophages and $hCD19^+$ B cells were statistically lower in the mixed rhMOG/MOG_{35-55} CNS tissue samples compared to the two other antigen groups (Figure 4.12E – F, and Figure 4.14E – F), whereas the opposite trend was observed in the spleen (Figure 4.16E – F). Given that the mixed rhMOG/MOG_{35-55} cohort samples were collected earlier than samples from the other two antigen groups, the delayed endpoint may have allowed these subsets to migrate from the periphery into the CNS to a greater extent, though their relatively small overall abundance suggests these subsets are less likely to contribute to phenotypic differences in clinical EAE outcomes than the predominant T cell populations.

4.5.4 Summary and discussion of findings

Clinical and immunopathological EAE outcomes following immunization of HuPBMC-NSG/SGM3 mice with different myelin antigen formulations revealed that the time to onset and peak severity of symptoms can be influenced by the choice of immunizing antigen, while CNS infiltration and polarization of human T cells appeared largely dependent on the blood donor PBMCs and the duration of time to experimental endpoint rather than the inducing antigen(s). In this experiment, we observed that mixed rhMOG/MOG_{35-55} EAE induction of HuPBMC-NSG/SGM3 mice was preferable to the use of MOG_{35-55} peptide only or rhMBP protein, mainly because of the earlier onset of EAE paralysis that outpaced the onset of clinical symptoms of xGvHD. Though the inclusion of greater numbers of rhMBP-induced HuPBMC mice may have revealed more nuanced group differences in the clinical and/or immunological data, the cost limitation associated with acquiring human-brain derived purified or recombinant MBP protein was cost prohibitive ($990 per mg), compared to MOG_{35-55} peptide ($35 per mg) and rhMOG protein, which is expressed from an *E. coli* vector and purified in-house. Moreover, the effectiveness of MOG antigens for inducing EAE on the NSG/SGM3 background aligns with reports showing susceptibility of NOD mice with rMOG and MOG_{35-55} peptide EAE immunization[139,144,673] and increases our options for using existing epitope specific reagents. The difference in time to onset observed when immunizing mice with MOG_{35-55} emulsion with or without rhMOG protein could be due to the presence of additional immunodominant epitopes in the extracellular domain of MOG [see Figure 5 in[386]] that may have activated responsive T cells more rapidly, though specific interrogation of the immunodominant epitopes in rhMOG recognized in PBMC humanized NSG/SGM3 EAE mice would be required to evaluate this hypothesis. Any discrepancies in the CNS distribution patterns of demyelination would also need to be investigated to make a more comprehensive determination of the utility of different myelin antigens for inducing EAE in the HuPBMC-NSG/SGM3 model.

4.6 EAE in murine and humanized PBMC models

4.6.1 Rationale and experimental design

Having established that MOG is a suitable myelin antigen to induce EAE in HuPBMC-NSG/SGM3 mice, we sought to compare the HuPBMC EAE model to well established and characterized murine EAE models induced with MOG to determine any conserved or unique clinical features (phenotype, progression, incidence) and immune cell subset involvement (proportions, polarization) known to contribute to strain specific phenotypes of disease that mimic different aspects of MS in humans[128,131,139,144]. We compared the clinical course of C57Bl/6 mice (naïve WT), NOD mice (naïve WT), and HuPBMC mice (female donor PBMC engraftment of male NSG/SGM3 recipient mice), induced with either mixed rhMOG/MOG_{35-55} or MOG_{35-55} peptide only, to evaluate the resemblance of the HuPBMC EAE phenotype to the most commonly used strain for EAE studies (i.e., C57Bl/6) and the background strain for the HIS recipient (i.e., NOD). To compare effector T cell phenotype between these EAE models, CNS infiltrates and splenoyctes from mixed rhMOG/MOG_{35-55} immunized mice were then assessed by flow cytometry.

4.6.2 Clinical outcomes in different EAE models

As EAE induction of C57Bl/6 and NOD mice most often involves immunization with MOG_{35-55} peptide, we first compared clinical outcomes of these strains to HuPBMC-NSG/SGM3 EAE mice following peptide immunization (Figure 4.18). Symptoms of EAE in C57Bl/6 MOG_{35-55} immunized mice consistently onset earlier than in NOD and HuPBMC-NSG/SGM3 mice and reached experimental endpoint on day 15 (Figure 4.18A – C). Peak EAE scores were generally less severe in NOD and HuPBMC-NSG/SGM3 mice than in C57Bl/6 mice, where most developed scores greater than 2 (Figure 4.18D). As has been reported for NOD MOG_{35-55} EAE mice, symptoms onset variably and remitted following an initial mild phase of disease for some mice, after which, a more severe relapsed began around day 27 that affected twice as many mice as the first wave (Figure 4.18A). Symptoms in HuPBMC-NSG/SGM3 MOG_{35-55} EAE mice appeared to reflect the clinical course and the onset, incidence, and peak score distributions of NOD EAE mice more closely than C57Bl/6 EAE mice, as anticipated given the shared host genetics of the NSG and NOD (Figure 4.18A – D). The first phase of clinically evident symptoms in HuPBMC-

NSG/SGM3 MOG_{35-55} EAE mice, all derived from one healthy female blood donor, began approximately day 18 post-immunization (Figure 4.18A, B). Despite being unable to follow the clinical course of EAE in HuPBMC-NSG/SGM3 mice beyond day 26 due to the onset of xGvHD symptoms, the clinical phenotype appears to be an asynchronous relapsing course alike the NOD mouse. By day 26 for HuPBMC-NSG/SGM3 mice, day 35 for NOD mice, and day 14 for C57Bl/6 mice post-MOG_{35-55} immunization, all cohorts attained statistically similar cumulative EAE disease burden (Figure 4.18E).

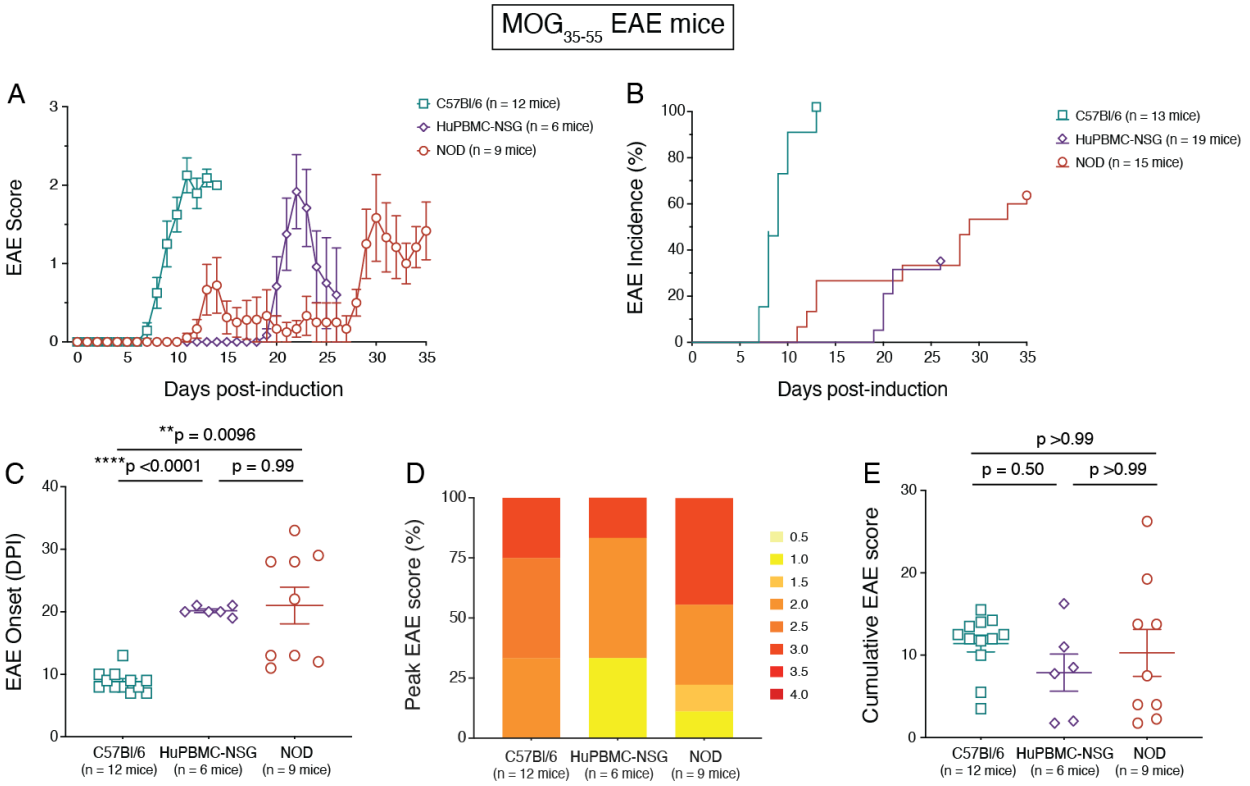

Figure 4.18 Clinical EAE outcomes in NOD, C57Bl6, and HuPBMC mice induced with MOG_{35-55} peptide

Figure shows (A) clinical EAE scores over time for symptomatic C57Bl6 mice (n = 12 WT mixed sex), NOD mice (n = 9 WT mixed sex), and HuPBMC-NSG/SGM3 mice (n = 6 males engrafted with HD-04 female PBMCs, HuPBMC cohort 35) immunized with 200 µg MOG_{35-55} peptide. (B) Incidence of EAE symptoms over time for all EAE induced mice per strain (n = 13 – 19 mice/group). (C) Day of EAE symptom onset post-induction (DPI), (D) proportions of peak EAE scores, and (E) cumulative EAE scores attained by symptomatic mice per strain (n = 6 – 12 mice/group). In A, C, and E, data are shown as mean with SEM. Data in C were analyzed by Brown-Forsythe and Welch ANOVA with Dunnett's T3 multiple comparisons test. Data in E were analyzed by Kruskal-Wallis with Dunn's multiple comparisons test. Data in B and D are shown as percentage of the group.

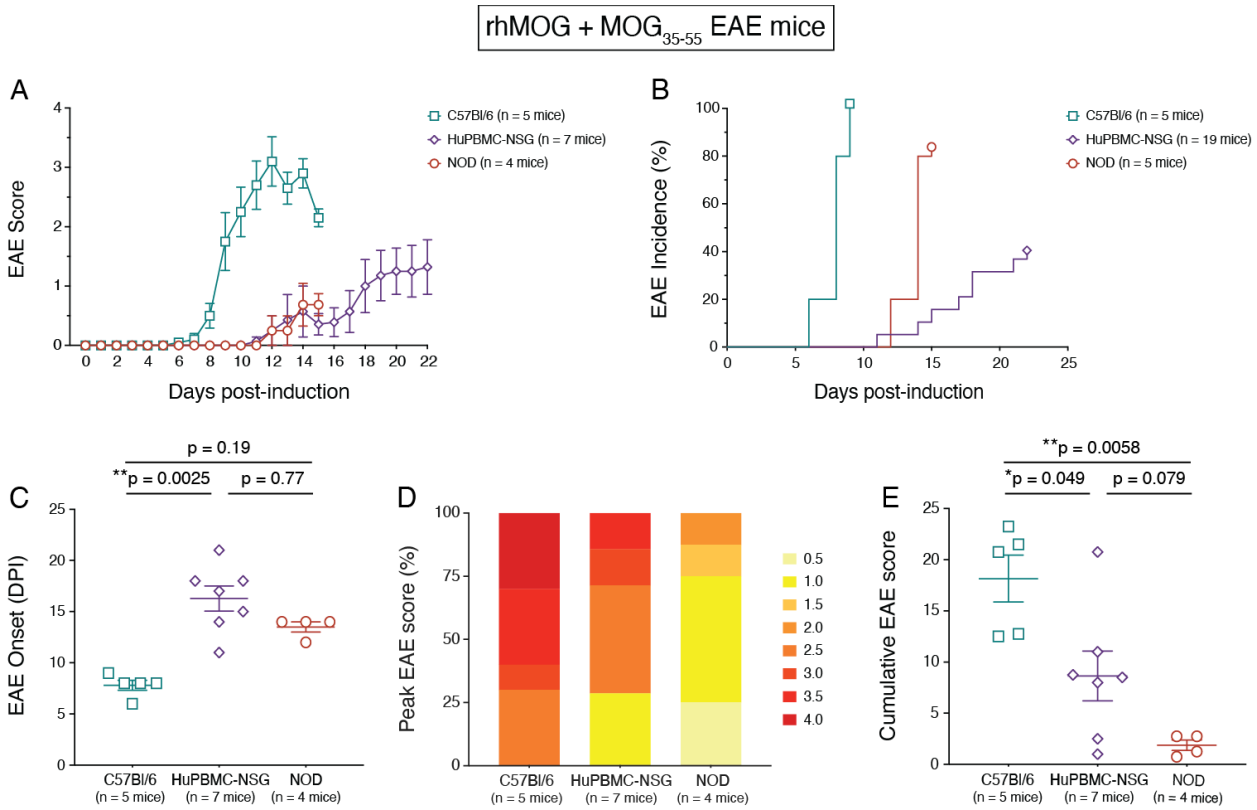

Figure 4.19 Clinical EAE outcomes in NOD, C57Bl6, and HuPBMC mice induced with mixed rhMOG protein and MOG_{35-55} peptide

Figure shows (A) clinical EAE scores over time for symptomatic C57Bl6 mice (n = 5 WT males), NOD mice (n = 4 WT males), and HuPBMC-NSG/SGM3 mice (n = 7 males engrafted with HD-04 female PBMCs, HuPBMC cohort 18) immunized with 100 µg rhMOG protein and 200 µg MOG_{35-55} peptide mixed. (B) Incidence of EAE symptoms over time for all EAE induced mice per strain (n = 5 – 19 mice/group). (C) Day of EAE symptom onset post-induction (DPI), (D) proportions of peak EAE scores, and (E) cumulative EAE scores attained by symptomatic mice per strain (n = 4 – 7 mice/group). In A, C, and E, data are shown as mean with SEM. Data in C were analyzed by Kruskal-Wallis with Dunn's multiple comparisons test. Data in E were analyzed by Brown-Forsythe and Welch ANOVA with Dunnett's T3 multiple comparisons test. Data in B and D are shown as percentage of the group.

Following immunization with both $rhMOG_{1-120}$ protein and MOG_{35-55} peptide combined, clinical EAE symptoms in all three strains appeared to follow similar patterns as MOG_{35-55} peptide induced mice (Figure 4.18, Figure 4.19). Interestingly, both antigen formulations produced similar symptom onset timing in C57Bl/6 and NOD mice, but significantly reduced the time to onset for HuPBMC-NSG mice when mixed protein and peptide induction was used instead of peptide only (5 days earlier on average) (Figure 4.18C, Figure 4.19C). By all clinical measures of disease

assessed, EAE symptoms in C57Bl/6 mice were very similar with both antigen formulations (Figure 4.18, Figure 4.19). In NOD mice, EAE incidence was higher and onset earlier in mice that were immunized with mixed MOG antigens compared to peptide only (Figure 4.18B, Figure 4.19B). Mixed rhMOG/MOG_{35-55} immunization led to nearly identical time to onset for NOD and HuPBMC-NSG/SGM3 mice (Figure 4.19A, C), though HuPBMC-NSG/SGM3 mice had reduced incidence overall compared to NOD and C57Bl/6 mice (Figure 4.19B).

As the clinical course and immune cell behaviour following rhMOG induction of NOD mice has not yet been reported (qualitative descriptions of phenotype in[673]), we collected CNS tissues from NOD and C57Bl/6 mice day 15 post-rhMOG/MOG_{35-55} immunization, and from HuPBMC-NSG/SGM3 mice day 22 post-induction, in order to compare T cell infiltration and polarization during the initial symptomatic phases of EAE for each strain. At these respective timepoints, the NOD cohort had fewer mice attain peak EAE scores of 2 or greater (Figure 4.19D) compared to the C57Bl/6 cohort, leading to comparatively reduced cumulative EAE scores (Figure 4.19E). Though we would likely observe greater total disease burden if the NOD EAE cohort had entered the second phase of symptoms, since HuPBMC EAE cohorts cannot be extended beyond the first relapse due to xGvHD, we collected samples from all NOD-based mice during their first relapse for comparison. The data generally indicate that MOG induced EAE in HuPBMC-NSG/SGM3 mice is phenotypically similar to NOD mice.

4.6.3 CNS infiltration and T cell polarization in different EAE models

Single cell suspensions, isolated from whole CNS and spleen samples collected day 15 from C57Bl/6 WT and NOD WT mice (referred to together as B6/NOD) and day 22 from HuPBMC-NSG/SGM3 mice post-rhMOG/MOG_{35-55} immunization, were stimulated with PMA and ionomycin to compare total immune cell infiltration and effector T cell polarization between strains. Only males of each strain were included in this analysis to minimize potential sex differences between each model. In general, HuPBMC-NSG/SGM3 EAE mouse tissues contained fewer total peripheral murine immune cells ($mCD45^{hi}$) and CNS resident microglia ($mCD45^{lo}$) compared to the immunocompetent B6/NOD EAE mice (Figure 4.20A – E). However, HuPBMC-NSG/SGM3 $hCD45^{+}$ and B6/NOD $mCD45^{hi}$ cell counts were statistically similar in all tissues, indicating successful niche replacement of the $mCD45^{hi}$ immune cells in HuPBMC-NSG/SGM3 EAE mice with $hCD45^{+}$ immune cells (Figure 4.20A – C).

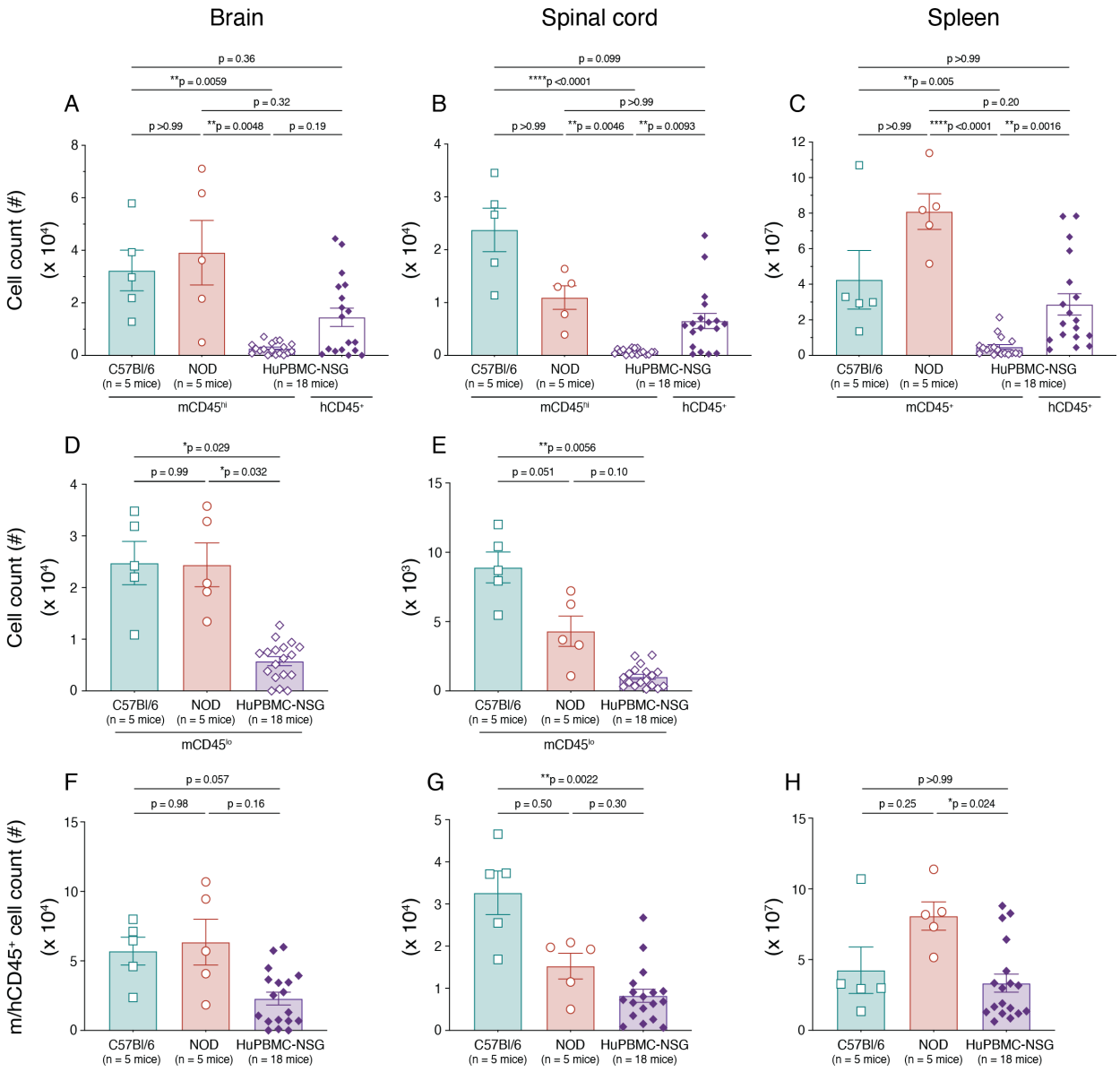

Figure 4.20 Murine and human immune cell abundance in the CNS and periphery of murine and humanized EAE models

Figure shows total mCD45^{hi} and hCD45^{+} immune cell counts in the brain (A), spinal cord (B), and spleen (C), total mCD45lo cell counts in the brain (D) and spinal cord (E), and total leukocyte counts (murine and human combined) in the brain (F), spinal cord (G), and spleen (H) of C57Bl/6 mice (n = 5 WT males) and NOD mice (n = 5 WT males) at day 15 post-EAE induction, and HuPBMC-NSG/SGM3 mice (n = 18 males engrafted with HD-04 female PBMCs, HuPBMC cohort 18) at day 22 post-rhMOG/MOG$_{35-55}$ EAE induction. Brain and spinal cord tissues were perfused prior to cell isolation. For NOD and C57Bl/6 samples, infiltrating immune cells are gated on mCD45^{hi} cells, and for HuPBMC samples infiltrating immune cells are gated on either hCD45^{+} cells or mCD45^{hi} cells. Data are shown as mean with SEM and were analyzed by Brown-Forsythe and Welch ANOVA with Dunnett's T3 multiple comparisons test or by Kruskal-Wallis with Dunn's multiple comparisons test.

In the CNS, expansion of $mCD45^{lo}$ microglia was reduced in HuPBMC-NSG/SGM3 EAE mice compared to the murine EAE strains, but mostly fell within the same log fold count range (i.e., counts were lower but not log folds lower) (Figure 4.20D – E). As far as total immune cell counts (summation of $CD45^{hi/lo/+}$ populations of both murine and human lineages in each organ), the HuPBMC-NSG/SGM3 EAE mice had comparable levels of infiltration in both the brain and spinal cord to NOD EAE mice (Figure 4.20F – G). All three strains showed nonsignificant differences in total immune cell counts in the brain (Figure 4.20F), whereas C57Bl/6 EAE mice contained more immune cells than NOD and HuPBMC-NSG/SGM3 EAE mice in the spinal cord at these timepoints (Figure 4.20G). The spleens of NOD EAE mice contained slightly more total immune cells than C57Bl/6 or HuPBMC-NSG/SGM3 EAE mice, likely due to the early endpoint during the first symptomatic phase for NODs, but all tissue counts fell within a similar range to one another regardless of background strain (Figure 4.20H). Taken together, the reduced numbers of murine immune cells in HuPBMC-NSG EAE mouse tissues appears to be due at least in part to a compensatory expansion of $hCD45^{+}$ cells in each of the organs.

In contrast to B6/NOD EAE mice, all HuPBMC-NSG/SGM3 EAE tissues contained practically no $hCD19^{+}$ B cells (Figure 4.21, Figure 4.22A – C). All tissues from C57Bl/6 and NOD EAE mice contained detectable and statistically comparable levels of $mCD19^{+}$ B cells (Figure 4.21, Figure 4.22A – C). $CD3^{+}$ T cell counts, however, were very similar between the strains, with no significant differences in any tissue (Figure 4.22D – F). As previously noted, nearly all CNS infiltrating and spleen reconstituting $hCD45^{+}$ cells in HuPBMC-NSG/SGM3 EAE mice were $hCD3^{+}$ T cells (frequently >80%), whereas the relative proportions of B and T cells were similar in each tissue between NOD and C57Bl/6 EAE mice (Figure 4.21).

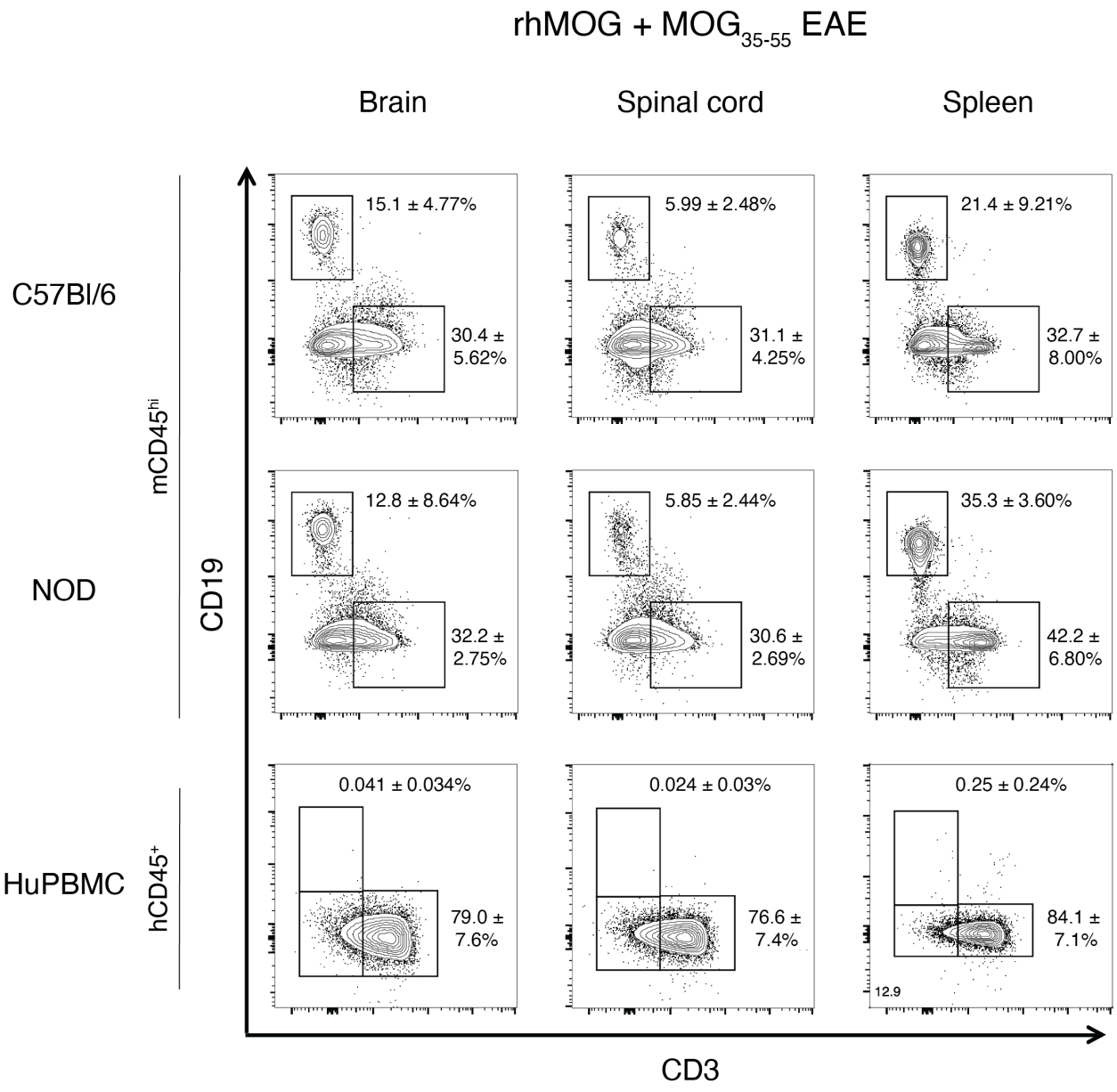

Figure 4.21 T and B cell proportions in the CNS and periphery of murine and humanized EAE models

Figure shows concatenated flow cytometric plots for murine and human $CD3^+$ T cells and $CD19^+$ B cells in the brains (left column), spinal cords (middle column), and spleens (right column) of C57Bl/6 mice (n = 5 WT males) and NOD mice (n = 5 WT males) at day 15 post-EAE induction, and HuPBMC-NSG/SGM3 mice (n = 18 males engrafted with HD-04 female PBMCs, HuPBMC cohort 18) at day 22 post-rhMOG/MOG_{35-55} EAE induction. Brain and spinal cord tissues were perfused prior to cell isolation. Data are shown as mean with SD for proportions of $mCD45^{hi}$ cells for NOD and C57Bl/6 mice, and proportions of $hCD45^+$ cells for HuPBMC mice.

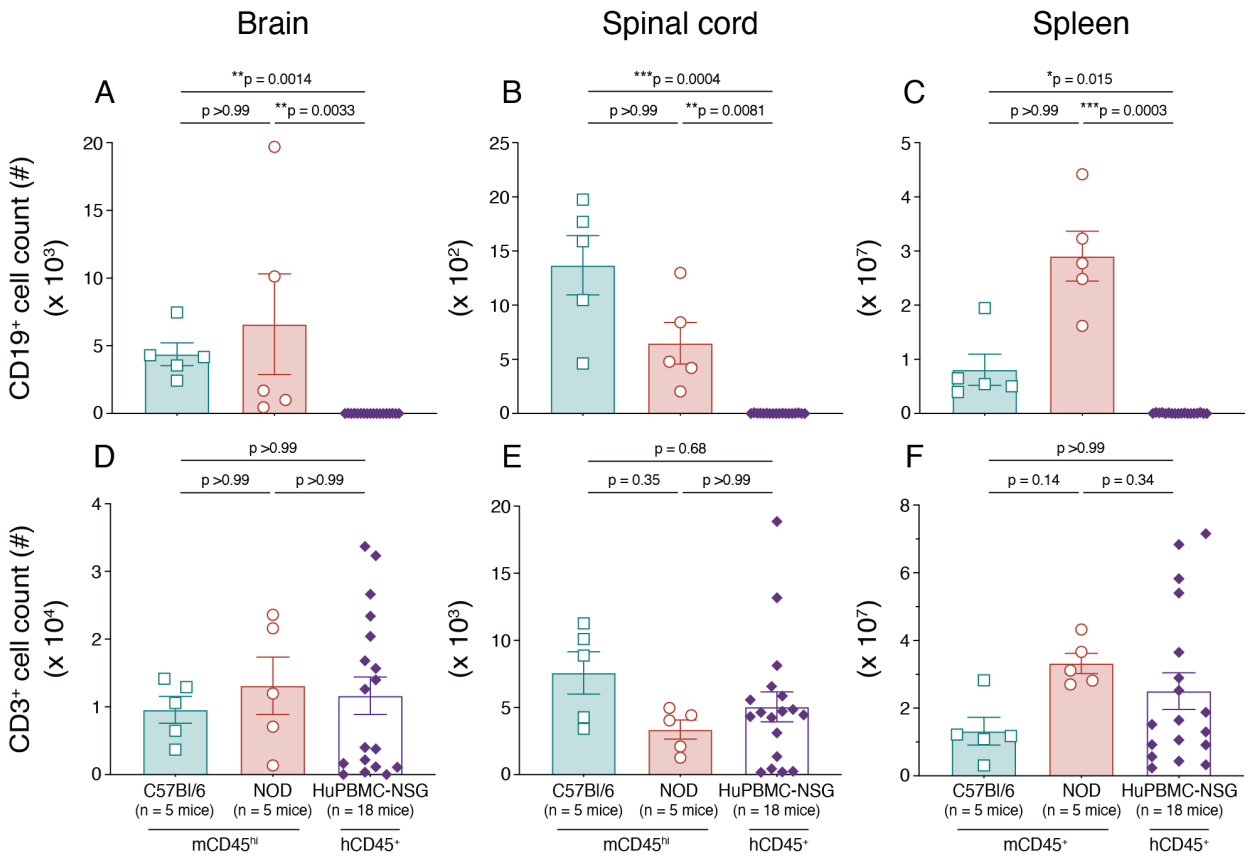

Figure 4.22 T and B cell abundance in the CNS and periphery of murine and humanized EAE models

Figure shows total murine and human $CD19^+$ B cell and $CD3^+$ T cell counts in the brain (A, D resp.), spinal cord (B, E resp.), and spleen (C, F resp.) of C57Bl/6 mice (n = 5 WT males) and NOD mice (n = 5 WT males) at day 15 post-EAE induction, and HuPBMC-NSG/SGM3 mice (n = 18 males engrafted with HD-04 female PBMCs, HuPBMC cohort 18) at day 22 post-rhMOG/MOG_{35-55} EAE induction. Brain and spinal cord tissues were perfused prior to cell isolation. For NOD and C57Bl/6 samples, subsets are gated on $mCD45^{hi}$ cells, and for HuPBMC samples subsets are gated on $hCD45^+$ cells. Data are shown as mean with SEM and were analyzed by Kruskal-Wallis with Dunn's multiple comparisons test.

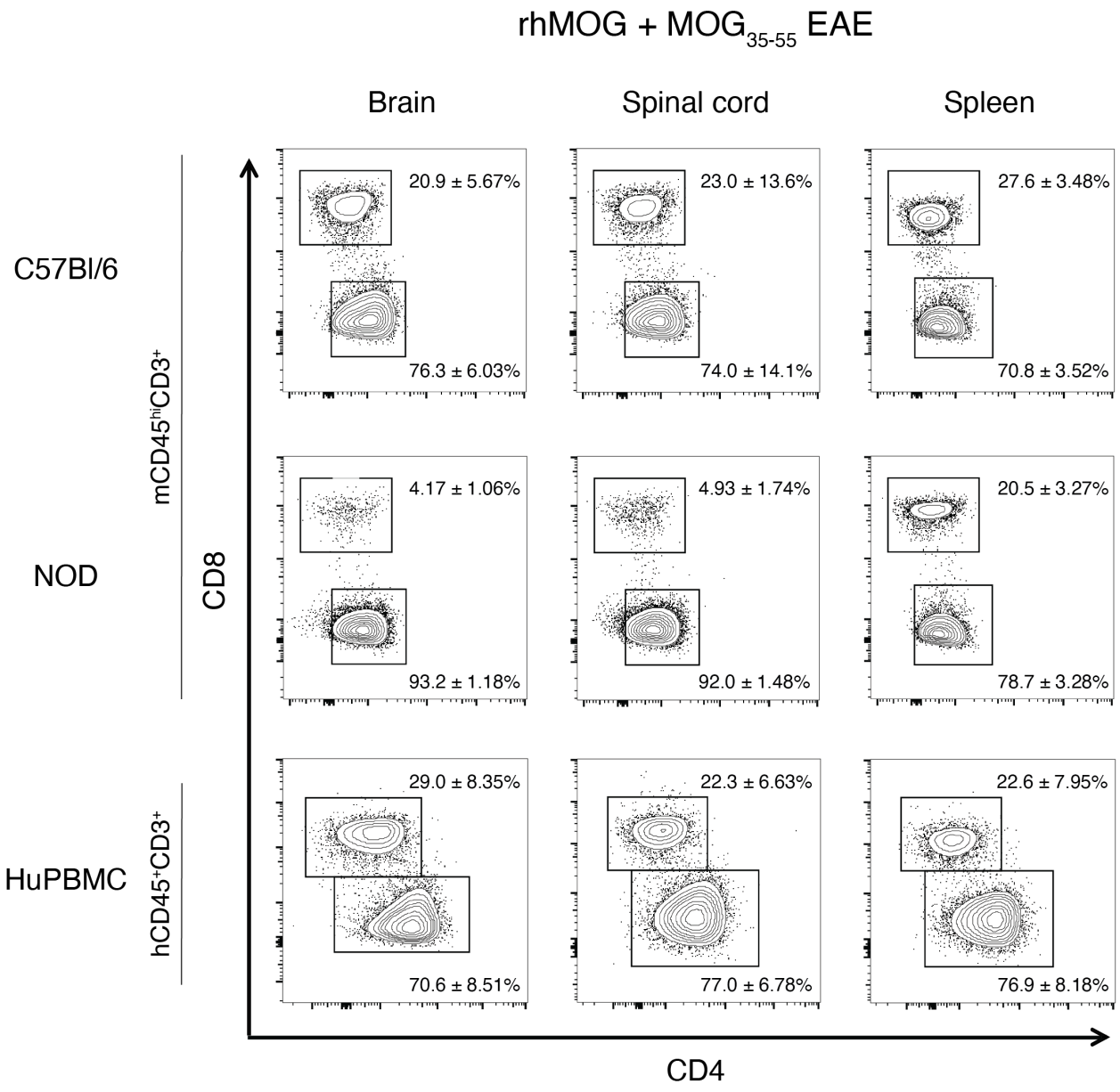

Figure 4.23 T cell subset proportions in the CNS and periphery of murine and humanized EAE models

Figure shows concatenated flow cytometric plots for murine and human $CD4^+$ and $CD8^+$ T cells in the brains (left column), spinal cords (middle column), and spleens (right column) of C57Bl/6 mice (n = 5 WT males) and NOD mice (n = 5 WT males) at day 15 post-EAE induction, and HuPBMC-NSG/SGM3 mice (n = 18 males engrafted with HD-04 female PBMCs, HuPBMC cohort 18) at day 22 post-rhMOG/MOG_{35-55} EAE induction. Brain and spinal cord tissues were perfused prior to cell isolation. Data are shown as mean with SD for proportions of $mCD45^{hi}CD3^+$ cells for NOD and C57Bl/6 mice, and proportions of $hCD45^+CD3^+$ cells for HuPBMC mice.

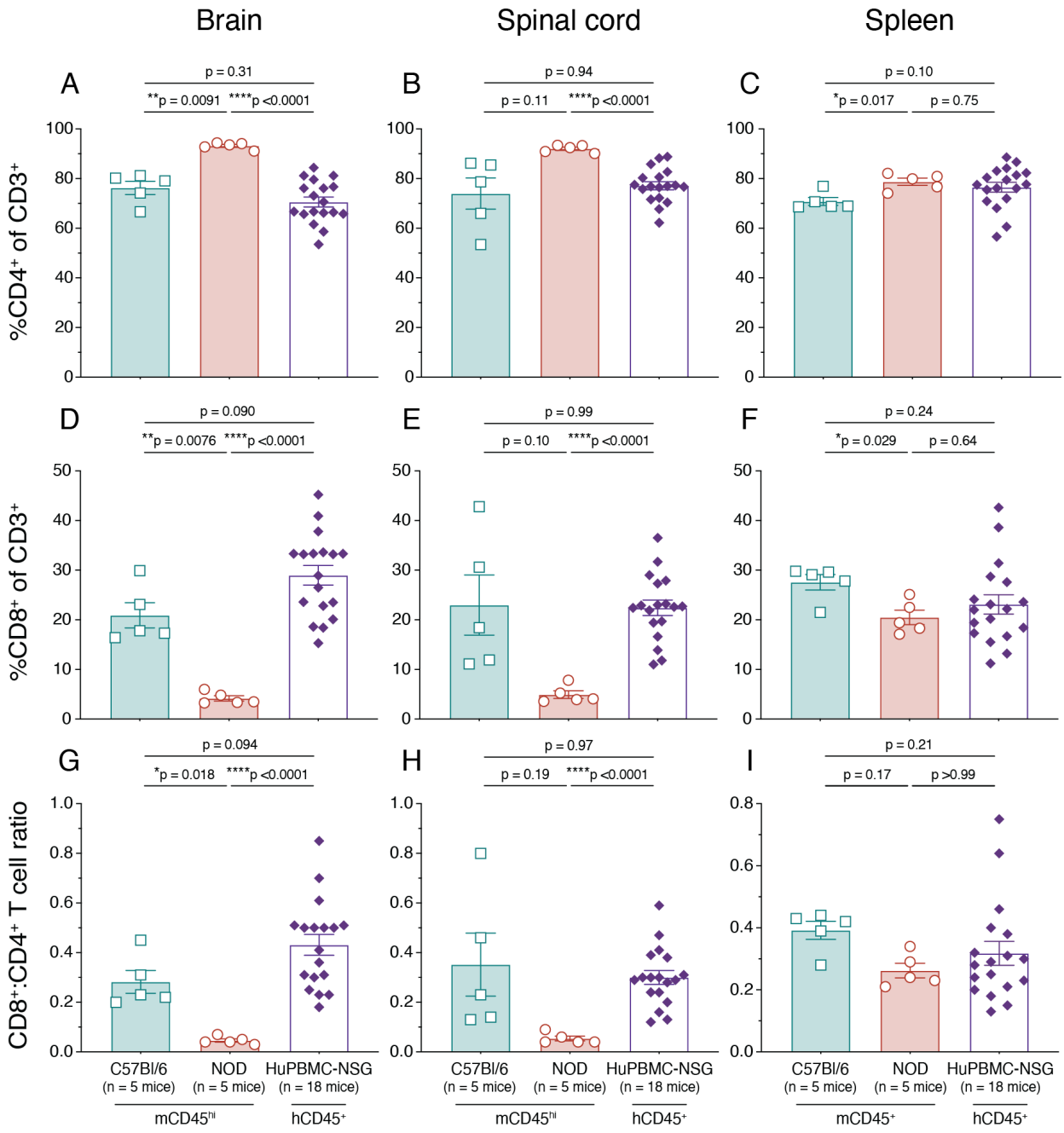

Figure 4.24 Relative T cell subset frequencies in the CNS and periphery of murine and humanized EAE models

Figure shows the quantified relative proportions of murine and human CD4 and CD8 expressing $CD3^+$ T cells and the ratio of $CD8^+$ to $CD4^+$ T cells in the brain (A, D, G resp.), spinal cord (B, E, H resp.), and spleen (C, F, I resp.) of C57Bl/6 mice (n = 5 WT males) and NOD mice (n = 5 WT males) at day 15 post-EAE induction, and HuPBMC-NSG/SGM3 mice (n = 18 males engrafted with HD-04 female PBMCs, HuPBMC cohort 18) at day 22 post-rhMOG/MOG_{35-55} EAE induction. Brain and spinal cord tissues were perfused prior to cell isolation. For NOD and C57Bl/6 samples, subsets are gated on $mCD45^{hi}$ cells, and for HuPBMC samples subsets are gated on $hCD45^+$

cells. Data are shown as mean with SEM and were analyzed by Brown-Forsythe and Welch ANOVA with Dunnett's T3 multiple comparisons test or by Kruskal-Wallis with Dunn's multiple comparisons test.

Despite minor statistical differences in T cell subset frequencies among total $CD3^+$ T cells between the C57Bl/6 and NOD EAE cohorts, the spleens of all three strains contained comparable relative proportions of $CD4^+$ and $CD8^+$ T cells, suggesting a similar global T cell response to MOG immunization in the periphery of these models (Figure 4.23, quantified in Figure 4.24 right column). At endpoint, the CNS tissues of C57Bl/6 and HuPBMC-NSG/SGM3 EAE mice contained similar relative proportions and ratios of $CD8^+$ to $CD4^+$ T cells, whereas NOD EAE CNS tissues were predominated by $CD4^+$ T cell infiltration with fewer $CD8^+$ T cells, likely due to the reduced disease burden attained in this cohort by the day 15 endpoint (Figure 4.23, quantified in Figure 4.24 left and middle columns). On day 35 post-MOG_{35-55} peptide immunization of NOD mice, $mCD8^+$ cell proportions were substantially increased in the CNS during the second wave of symptoms compared to day 15 post-rhMOG/MOG_{35-55} immunization during the first wave of symptoms (Figure 4.25, data obtained from a separate experiment), indicating prolonged symptom duration is driven by and/or promotes $CD8^+$ T cell expansion within the CNS in all three models.

By total cell counts, $CD4^+$ T cell infiltration of the CNS and expansion in the spleen was numerically comparable in all three EAE models (Figure 4.26A – C). Consistent with the proportional subset data post-rhMOG/MOG_{35-55} induction (Figure 4.24D – F), $CD8^+$ T cell abundance in the spleens of all three strains was statistically similar, though the CNS tissues of NOD EAE mice contained fewer total $CD8^+$ T cells than the other two groups (Figure 4.26D – F). Total cell abundance was highly variable amongst HuPBMC-NSG/SGM3 EAE mice derived from the same donor, which was not unexpected as mice that both did and did not develop EAE symptoms were included for analysis. The data suggest that similar proportions and quantities of $CD4^+$ and $CD8^+$ T cell subsets migrated to and/or expanded within the CNS of all three strains post-MOG immunization.

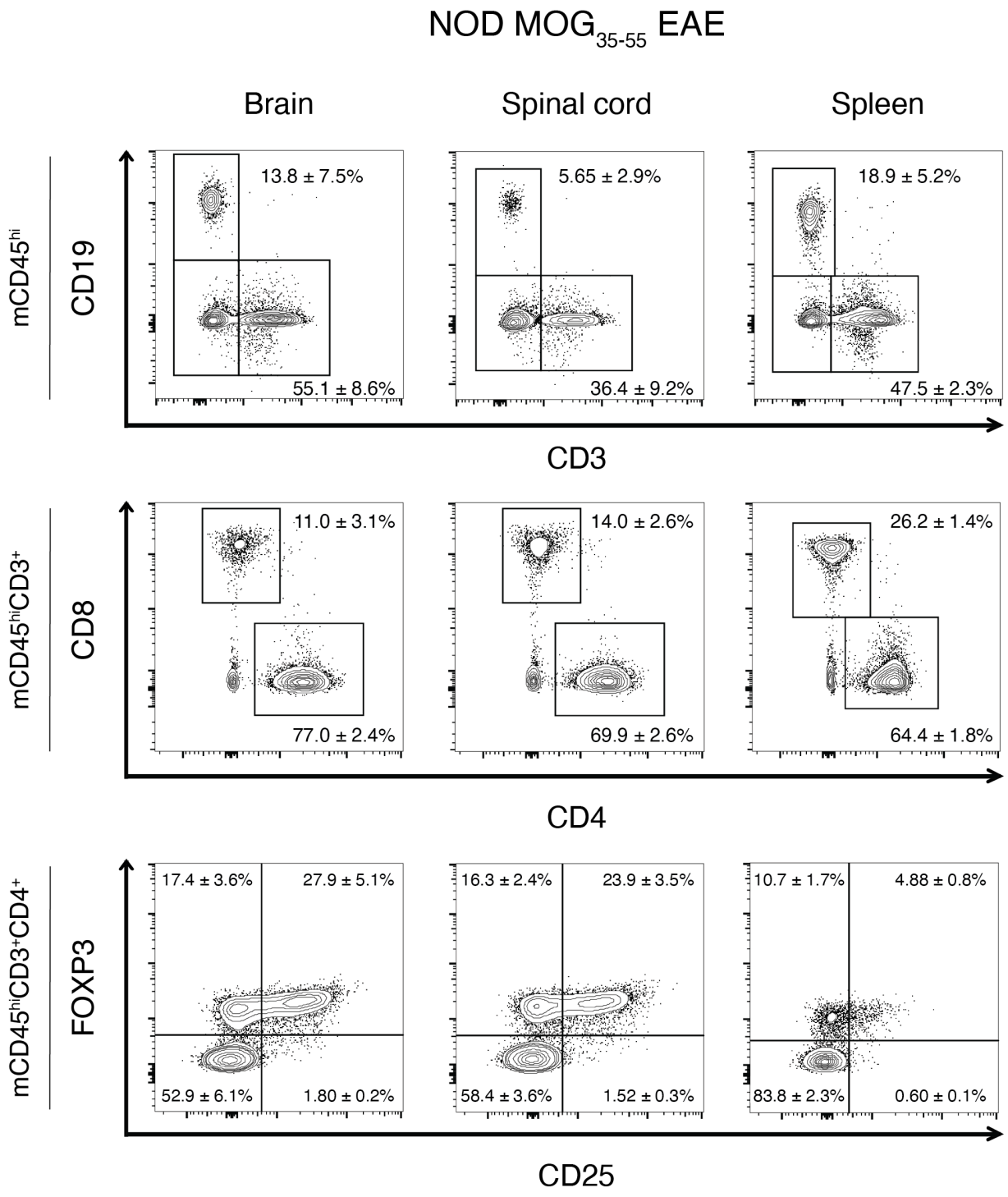

Figure 4.25 Immune cell proportions in the CNS and periphery of NOD mice on day 35 post-MOG_{35-55} peptide induction

Figure shows concatenated flow cytometric plots for murine T and B cells in the brains (left column), spinal cords (middle column), and spleens (right column) of symptomatic NOD mice (n = 6 WT males) at day 35 post-EAE induction with MOG_{35-55} peptide emulsion. Brain and spinal cord tissues were perfused prior to cell isolation. Data are

shown as mean with SD for proportions of CD3 and CD19 expressing mCD45^{hi} cells (top row), CD4 and CD8 expressing mCD45^{hi}CD3^{+} cells (middle row), and CD25 and FOXP3 expressing mCD45^{hi}CD3^{+}CD4^{+} cells (bottom row).

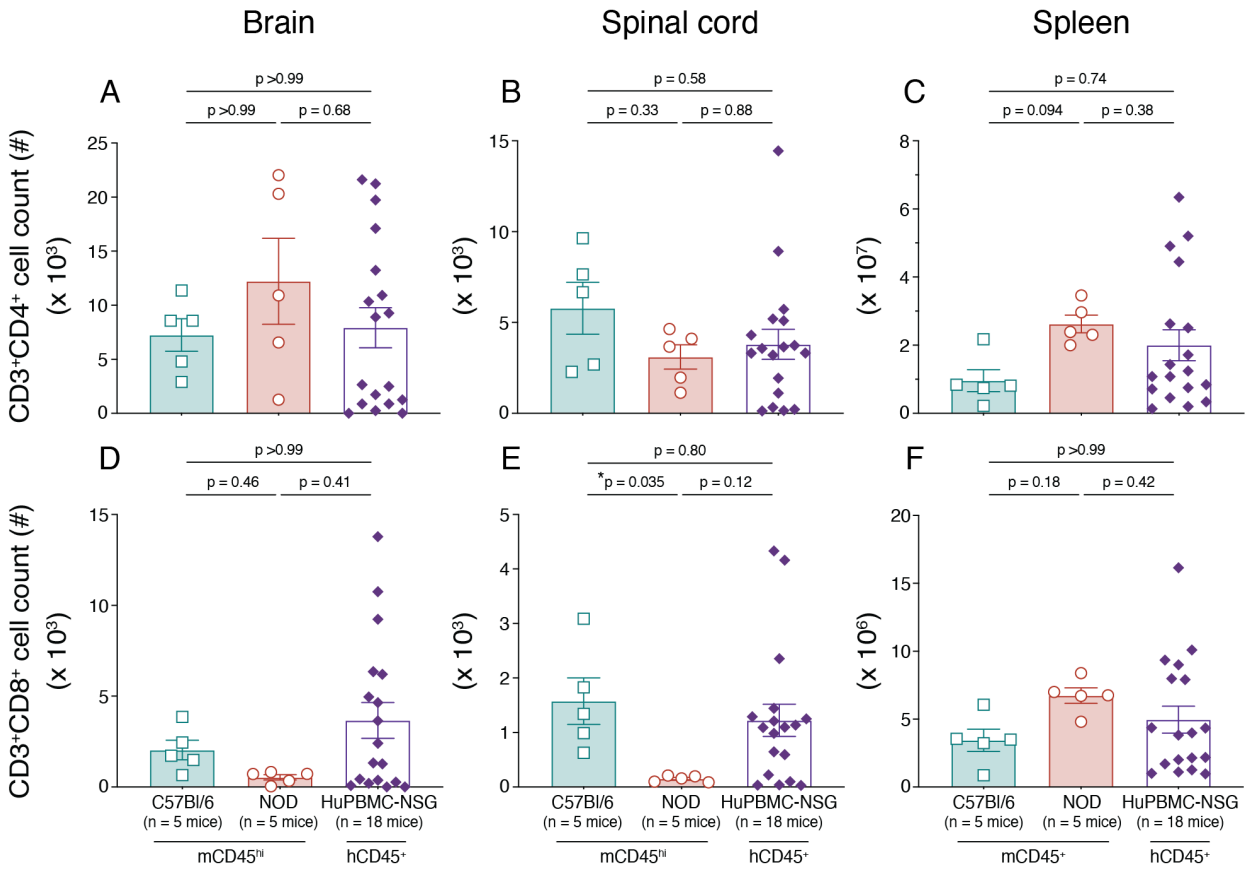

Figure 4.26 T cell subset abundance in the CNS and periphery of murine and humanized EAE models

Figure shows total murine and human CD3^{+}CD4^{+} and CD3^{+}CD8^{+} T cell counts in the brain (A, D resp.), spinal cord (B, E resp.), and spleen (C, F resp.) of C57Bl/6 mice (n = 5 WT males) and NOD mice (n = 5 WT males) at day 15 post-EAE induction, and HuPBMC-NSG/SGM3 mice (n = 18 males engrafted with HD-04 female PBMCs, HuPBMC cohort 18) at day 22 post-rhMOG/MOG$_{35-55}$ EAE induction. Brain and spinal cord tissues were perfused prior to cell isolation. For NOD and C57Bl/6 samples, subsets are gated on mCD45^{hi} cells, and for HuPBMC samples subsets are gated on hCD45^{+} cells. Data are shown as mean with SEM and were analyzed by Brown-Forsythe and Welch ANOVA with Dunnett's T3 multiple comparisons test or by Kruskal-Wallis with Dunn's multiple comparisons test.

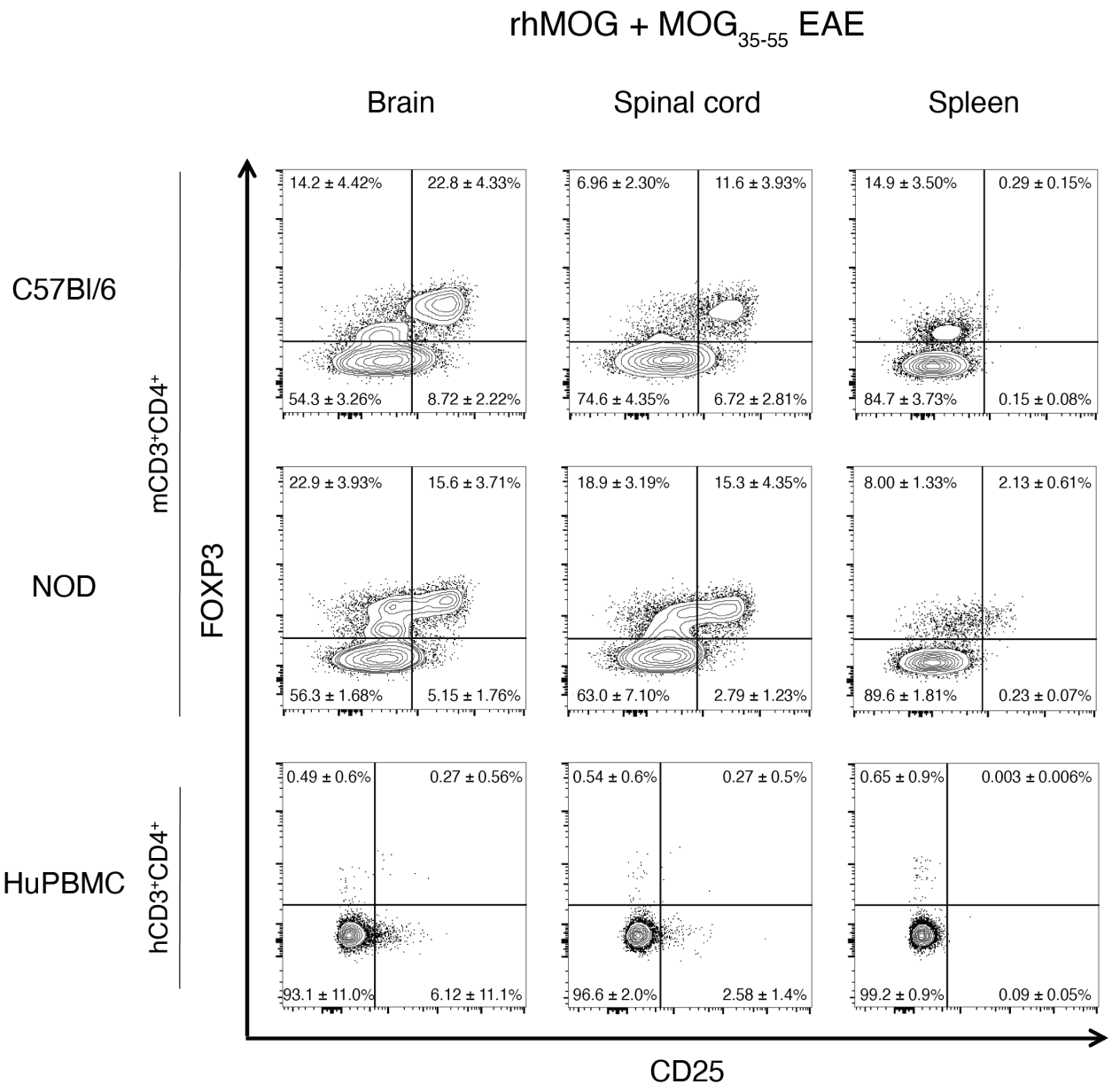

Figure 4.27 Regulatory T cell subset proportions in the CNS and periphery of murine and humanized EAE models

Figure shows concatenated flow cytometric plots for murine and human $CD4^+$ regulatory T cells in the brains (left column), spinal cords (middle column), and spleens (right column) of C57Bl/6 mice (n = 5 WT males) and NOD mice (n = 5 WT males) at day 15 post-EAE induction, and HuPBMC-NSG/SGM3 mice (n = 18 males engrafted with HD-04 female PBMCs, HuPBMC cohort 18) at day post-rhMOG/MOG_{35-55} EAE induction. Brain and spinal cord tissues were perfused prior to cell isolation. Data are shown as mean with SD for proportions of CD25 and FOXP3 expressing $mCD45^{hi}CD3^+CD4^+$ cells for NOD and C57Bl/6 mice, and proportions of $hCD45^+CD3^+CD4^+$ cells for HuPBMC mice.

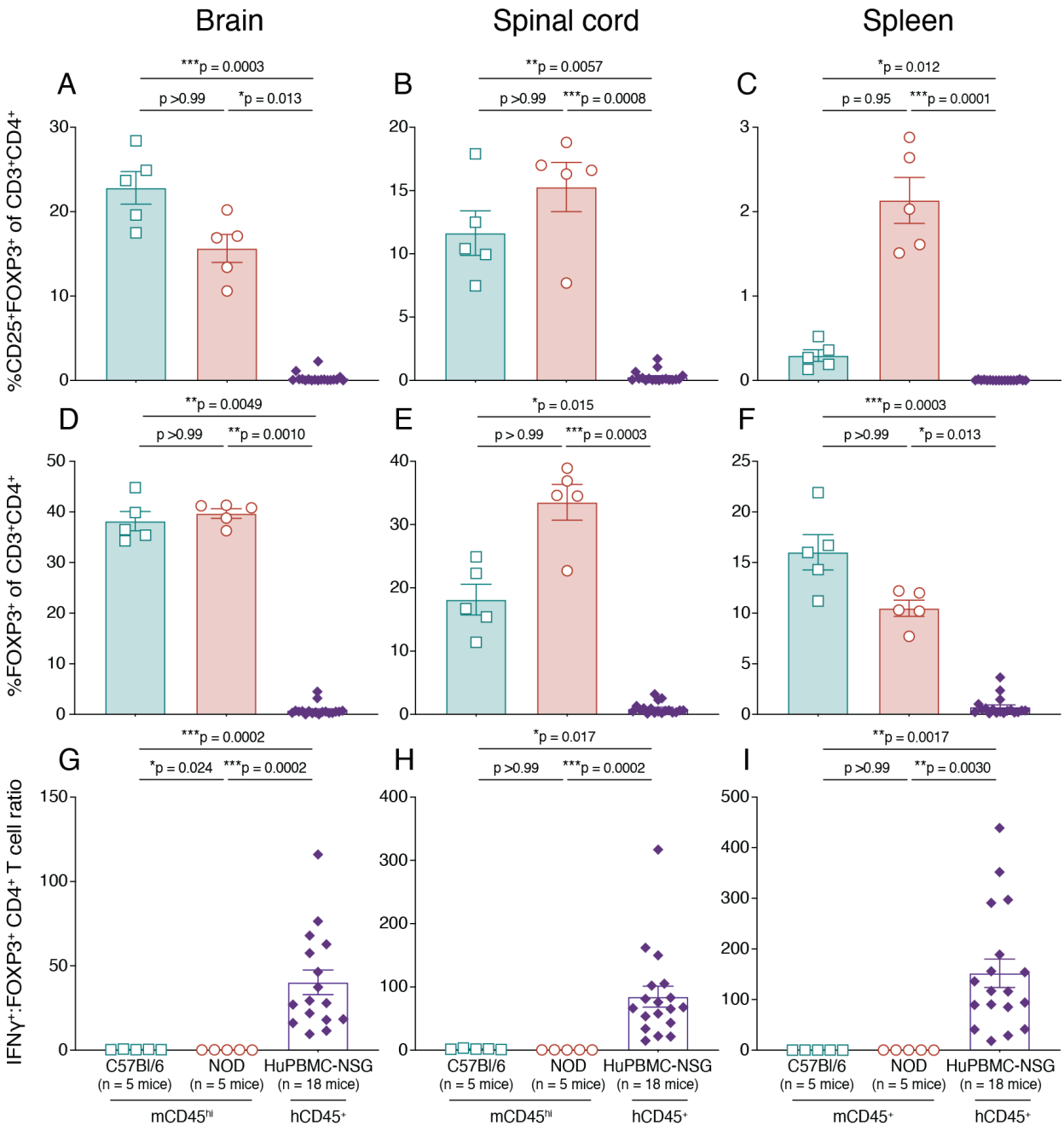

Figure 4.28 Relative regulatory T cell subset frequencies in the CNS and periphery of murine and humanized EAE models

Figure shows the quantified relative proportions of murine and human CD25 and/or FOXP3 expressing $CD3^+CD4^+$ T cells and the ratio of $IFN\gamma^+$(IL-$17A^-$) to $FOXP3^+$ $CD4^+$ T cells in the brain (A, D, G resp.), spinal cord (B, E, H resp.), and spleen (C, F, I resp.) of C57Bl/6 mice (n = 5 WT males) and NOD mice (n = 5 WT males) at day 15 post-EAE induction, and HuPBMC-NSG/SGM3 mice (n = 18 males engrafted with HD-04 female PBMCs, HuPBMC cohort 18) at post-rhMOG/MOG_{35-55} EAE induction. Cells isolated from perfused brains, spinal cords, and spleens were stimulated with PMA and ionomycin to measure cytokine expression. For NOD and C57Bl/6 samples,

subsets are gated on mCD45^{hi} cells, and for HuPBMC samples subsets are gated on hCD45^{+} cells. Data are shown as mean with SEM and were analyzed by Brown-Forsythe and Welch ANOVA with Dunnett's T3 multiple comparisons test or by Kruskal-Wallis with Dunn's multiple comparisons test.

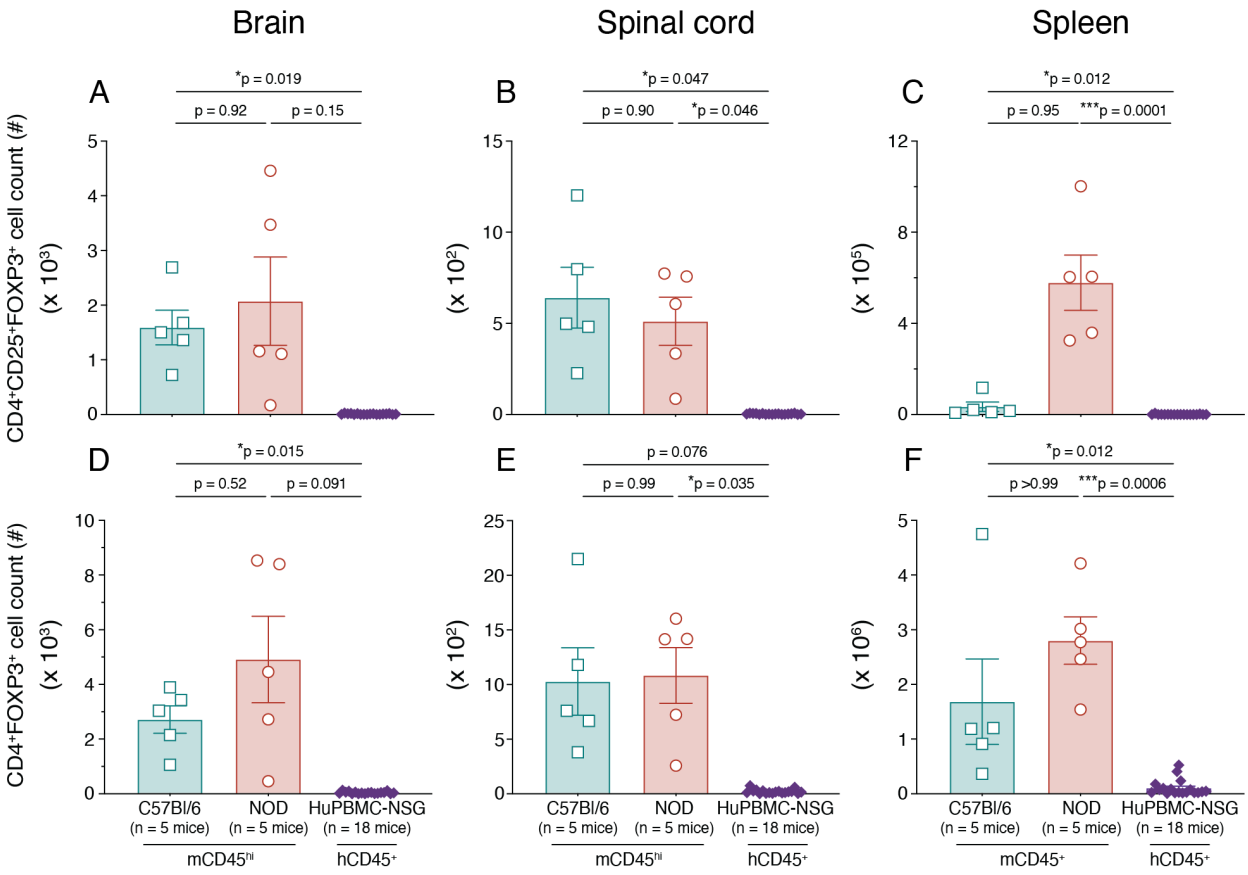

Figure 4.29 Regulatory T cell subset abundance in the CNS and periphery of murine and humanized EAE models

Figure shows total murine and human CD25 and FOXP3 expressing CD3^{+}CD4^{+} T cell counts in the brain (A, D), spinal cord (B, E), and spleen (C, F) of C57Bl/6 mice (n = 5 WT males) and NOD mice (n = 5 WT males) at day 15 post-EAE induction, and HuPBMC-NSG/SGM3 mice (n = 18 males engrafted with HD-04 female PBMCs, HuPBMC cohort 18) at day 22 post-rhMOG/MOG$_{35-55}$ EAE induction. Brain and spinal cord tissues were perfused prior to cell isolation. For NOD and C57Bl/6 samples, subsets are gated on mCD45^{hi} cells, and for HuPBMC samples subsets are gated on hCD45^{+} cells. Data are shown as mean with SEM and were analyzed by Brown-Forsythe and Welch ANOVA with Dunnett's T3 multiple comparisons test or by Kruskal-Wallis with Dunn's multiple comparisons test.

HuPBMC-NSG/SGM3 EAE mice did not reconstitute with nearly as many FOXP3 expressing $hCD4^+$ regulatory T cells as seen in B6/NOD EAE mice (Figure 4.27, quantified in Figure 4.28A – F). In all three strains, however, CD25 expression on $CD4^+FOXP3^+$ T cells was higher in the CNS compared to the spleen, consistent with site-specific inflammation (Figure 4.27, Figure 4.28A – F). In both murine EAE cohorts, the brains contained a greater proportion of $CD4^+$ T cells expressing regulatory markers compared to the corresponding spinal cords (Figure 4.27, Figure 4.28A – F) Human Treg proportions, though much lower than in B6/NOD EAE mice, were similar in the brains and spinal cords of HuPBMC-NSG/SGM3 EAE mice (Figure 4.27). The CNS and spleens of HuPBMC-NSG/SGM3 EAE mice, as a consequence of harboring so few human Tregs, had proportionally far greater numbers of effector $IFN\gamma^+CD4^+$ Th1 cells compared to B6/NOD EAE mice (Figure 4.28G – I). Quantitatively, both C57Bl/6 and NOD EAE tissues contained similar numbers of murine Tregs, which were numerically far more abundant than human Tregs in all tissues collected from HuPBMC-NSG/SGM3 EAE mice (Figure 4.29A – F).

For both murine EAE models, a proportion of $mCD4^+$ T cells infiltrating the CNS expressed IL-17A or IFNγ (Th17 or Th1, respectively), with a relatively smaller proportion expressing both cytokines simultaneously (double Th1/Th17) (Figure 4.30, quantified in Figure 4.31). The CNS tissues of NOD EAE mice generally contained a greater or similar proportion of Th17 cells relative to Th1 cells, whereas the opposite trend was observed in C57Bl/6 EAE mice, where Th1 cells predominated over Th17 cells (Figure 4.30, Figure 4.31A – E). In HuPBMC-NSG/SGM3 EAE tissues, effector $hCD4^+$ T cells were majority Th1 (Figure 4.30, Figure 4.31D – F) and the IL-17A expressing $hCD4^+$ T cells were mostly double positive for IFNγ (Figure 4.30, Figure 4.31G – I), consistent with predisposition toward Th1 cell activation seen in NOD background mice[678]. The main difference between the murine and the humanized EAE groups was the significantly reduced frequencies of Th17 cells in the CNS of HuPBMC-NSG/SGM3 mice, but which overall resembled the $mCD4^+$ T cell composition in C57Bl/6 EAE tissues more closely than in NOD EAE mice at this timepoint.

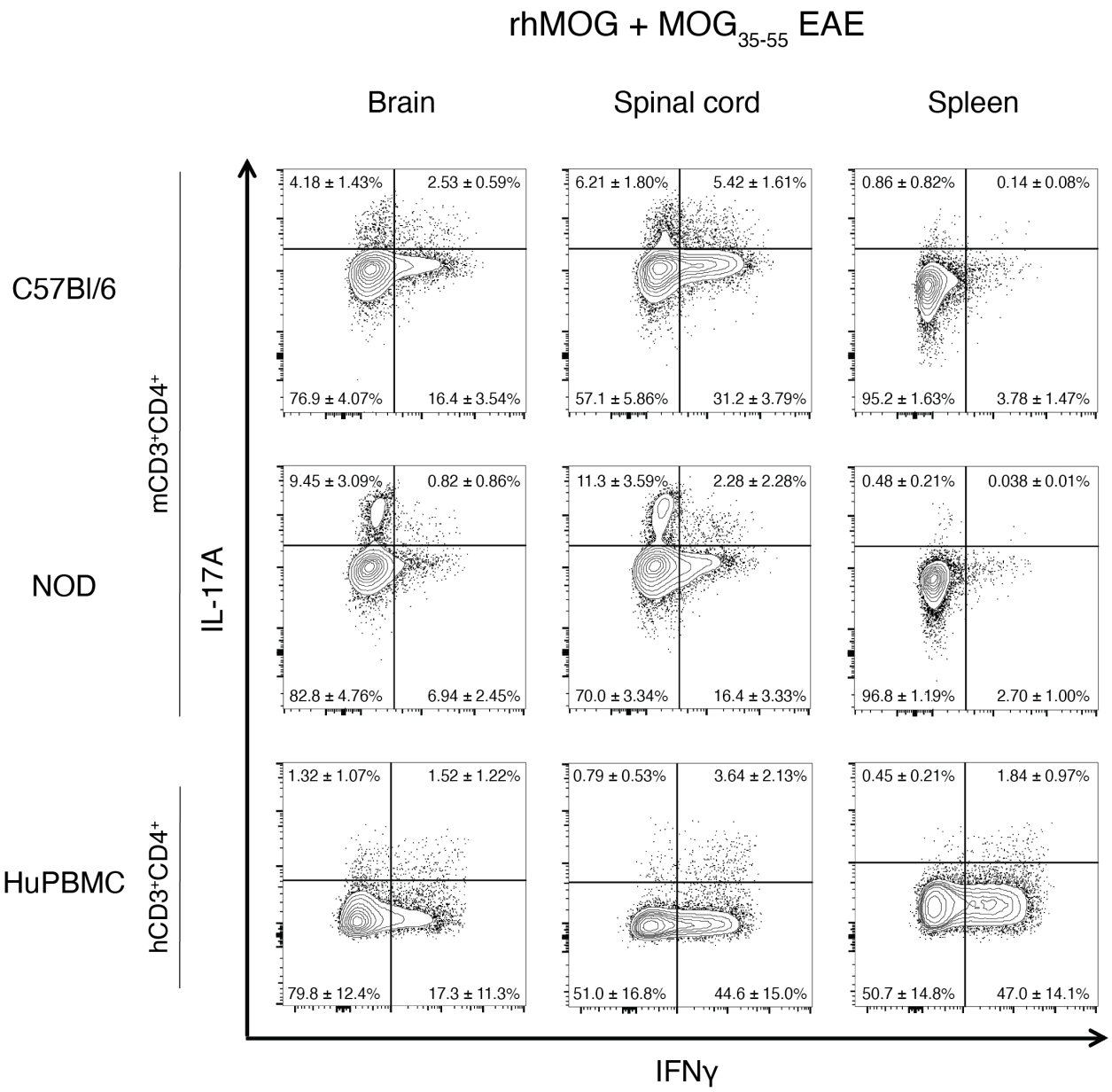

Figure 4.30 Effector $CD4^+$ T cell subset proportions in the CNS and periphery of murine and humanized EAE models

Figure shows concatenated flow cytometric plots for murine and human $CD4^+$ effector T cells in the brains (left column), spinal cords (middle column), and spleens (right column) of C57Bl/6 mice (n = 5 WT males) and NOD mice (n = 5 WT males) at day 15 post-EAE induction, and HuPBMC-NSG/SGM3 mice (n = 18 males engrafted with HD-04 female PBMCs, HuPBMC cohort 18) at post-rhMOG/MOG_{35-55} EAE induction. Cells isolated from perfused brains, spinal cords, and spleens were stimulated with PMA and ionomycin to measure cytokine expression. Data are shown as mean with SD for proportions of IFNγ and IL-17A expressing $mCD45^{hi}CD3^+CD4^+$ cells for NOD and C57Bl/6 mice, and proportions of $hCD45^+CD3^+CD4^+$ cells for HuPBMC mice.

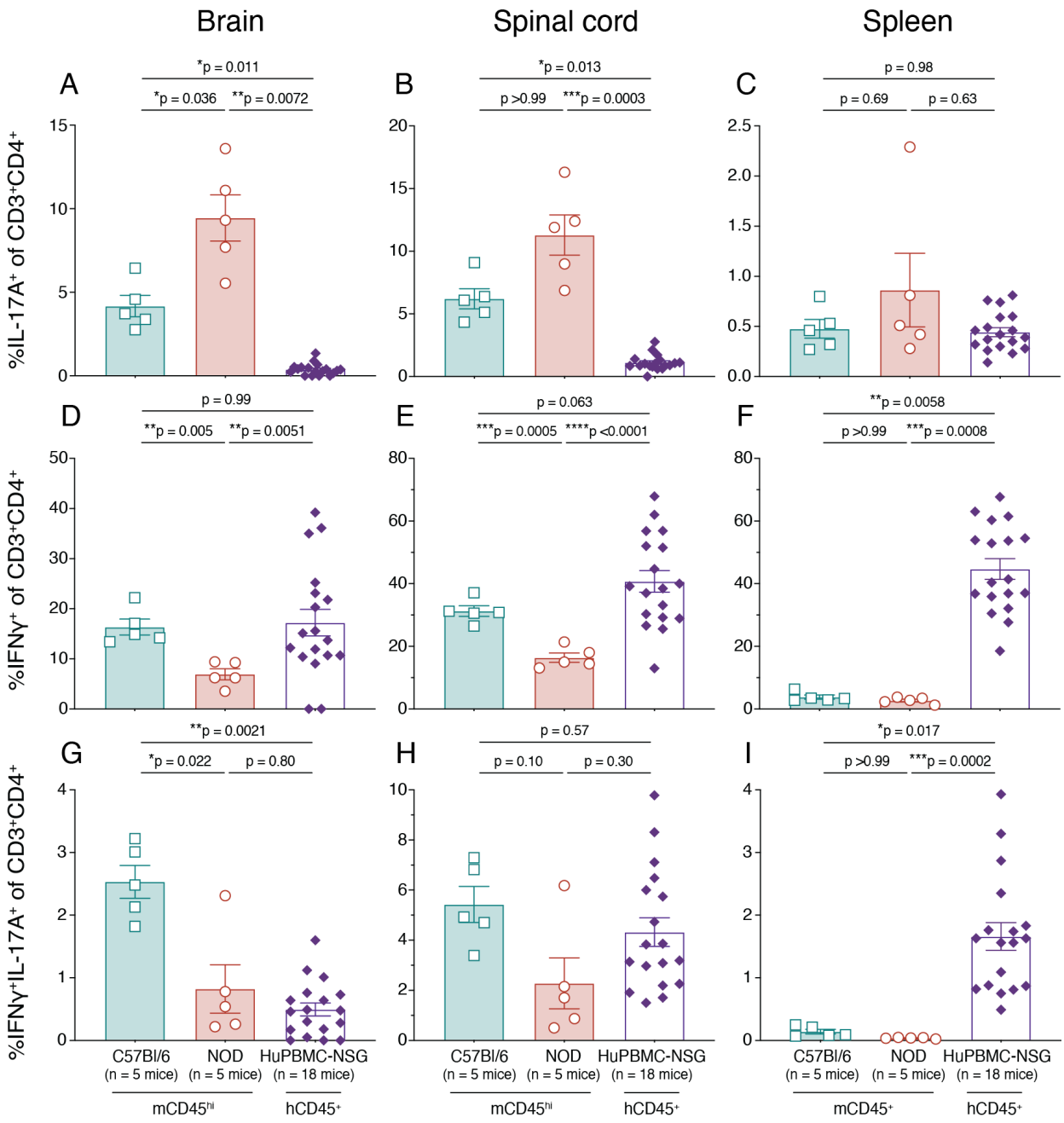

Figure 4.31 Relative effector CD4$^+$ T cell subset frequencies in the CNS and periphery of murine and humanized EAE models

Figure shows the quantified relative proportions of murine and human (A – C) IL-17A$^+$(IFNγ$^-$), (D – F) IFNγ$^+$(IL-17A$^-$), and (G – I) IFNγ$^+$IL-17A$^+$ CD3$^+$CD4$^+$ T cells in the brain (left column), spinal cord (middle column), and spleen (right column) of C57Bl/6 mice (n = 5 WT males) and NOD mice (n = 5 WT males) at day 15 post-EAE induction, and HuPBMC-NSG/SGM3 mice (n = 18 males engrafted with HD-04 female PBMCs, HuPBMC cohort 18) at day 22 post-rhMOG/MOG$_{35-55}$ EAE induction. Cells isolated from perfused brains, spinal cords, and spleens were stimulated with PMA and ionomycin to measure cytokine expression. For NOD and C57Bl/6 samples, subsets

are gated on mCD45^{hi} cells, and for HuPBMC samples subsets are gated on hCD45^{+} cells. Data are shown as mean with SEM and were analyzed by Brown-Forsythe and Welch ANOVA with Dunnett's T3 multiple comparisons test or by Kruskal-Wallis with Dunn's multiple comparisons test.

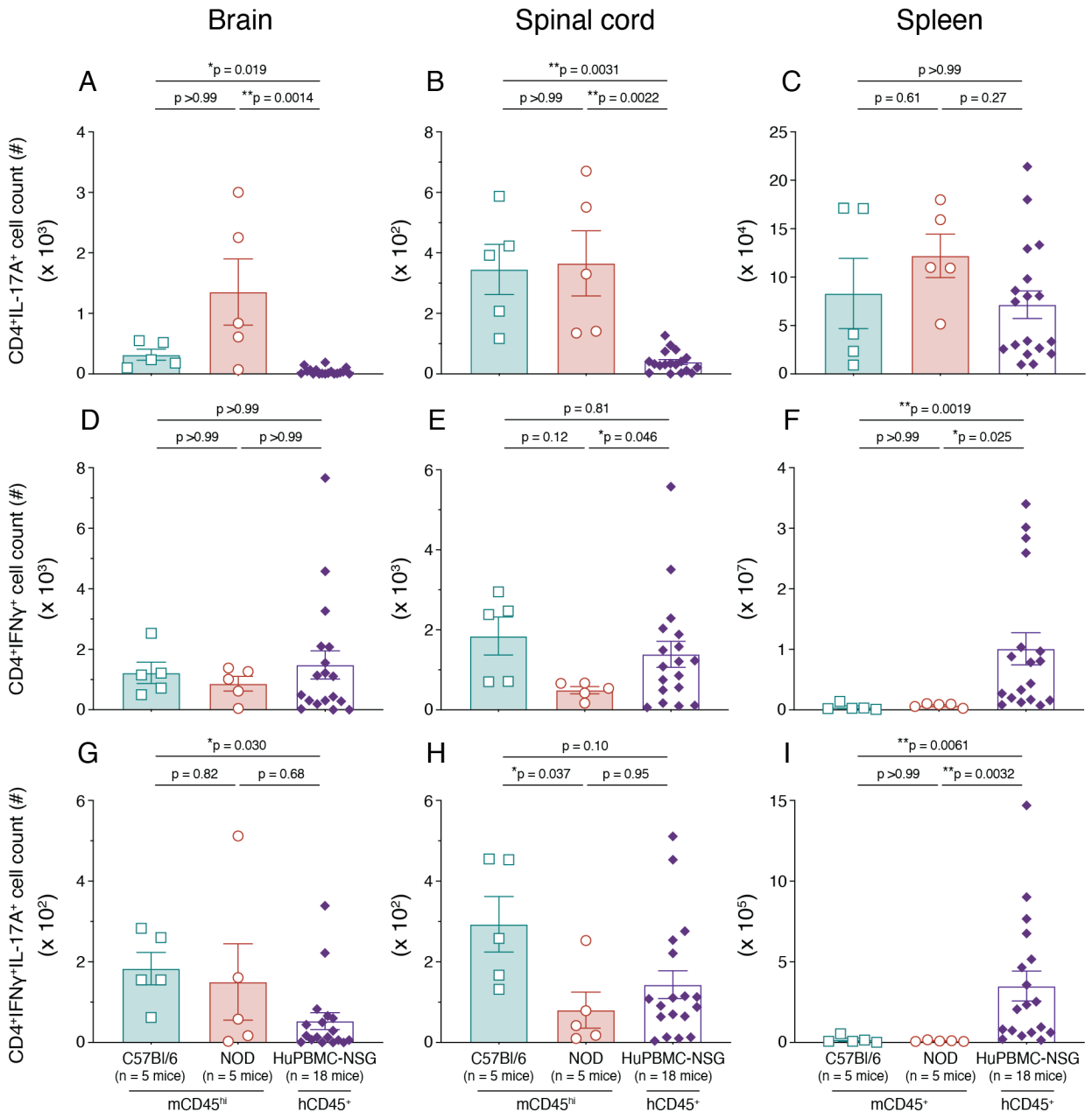

Figure 4.32 Effector CD4^{+} T cell subset abundance in the CNS and periphery of murine and humanized EAE models

Figure shows total murine and human (A – C) IL-17A^{+}(IFNγ^{-}), (D – F) IFNγ^{+}(IL-17A^{-}), and (G – I) IFNγ^{+}IL-17A^{+} CD3^{+}CD4^{+} T cell counts in the brain (left column), spinal cord (middle column), and spleen (right column) of

C57Bl/6 mice (n = 5 WT males) and NOD mice (n = 5 WT males) at day 15 post-EAE induction, and HuPBMC-NSG/SGM3 mice (n = 18 males engrafted with HD-04 female PBMCs, HuPBMC cohort 18) at day 22 post-rhMOG/MOG_{35-55} EAE induction. Cells isolated from perfused brains, spinal cords, and spleens were stimulated with PMA and ionomycin to measure cytokine expression. For NOD and C57Bl/6 samples, subsets are gated on $mCD45^{hi}$ cells, and for HuPBMC samples subsets are gated on $hCD45^+$ cells. Data are shown as mean with SEM and were analyzed by Brown-Forsythe and Welch ANOVA with Dunnett's T3 multiple comparisons test or by Kruskal-Wallis with Dunn's multiple comparisons test.

Consistent with the proportional data, HuPBMC-NSG/SGM3 EAE CNS tissues contained numerically far fewer Th17 cells than B6/NOD EAE CNS tissues, but all three models contained similar amounts in the spleen (Figure 4.32A – C). In the CNS, HuPBMC-NSG/SGM3 EAE Th1 cell counts were similar to both of the murine strains, but were much higher in the spleen, likely due to nonspecific graft reactivity in the periphery of the PBMC humanized recipients (Figure 4.32D – F). Double Th1/Th17 cell counts were similar in the CNS of all strains (G, H), but greater numbers were measured in the spleens of HuPBMC-NSG/SGM3 EAE mice than B6/NOD EAE mice (Figure 4.32G – I). The total numbers of Th17, Th1, and double Th1/Th17 $mCD4^+$ T cells was similar between C57Bl/6 and NOD EAE mice in all tissues, though NOD EAE mice at this time point skewed more Th17 relative to Th1 compared to C57Bl/6 EAE mice (Figure 4.32).

In C57Bl/6 and NOD EAE CNS tissues, IFNγ and/or GzmB expression patterns among infiltrating $mCD8^+$ T cells were quite similar, though with slightly fewer NOD $mCD8^+$ T cells expressing GzmB than in C57Bl/6 mice (Figure 4.33, quantified in Figure 4.34 left and middle columns). The reduced cytotoxicity of NOD derived $mCD8^+$ T cells was likely due to the reduced relative proportions and quantities of Th1 $mCD4^+$ T cells at this timepoint compared to C57Bl/6 mice. As expected, $mCD8^+$ T cells expressed very little of either IFNγ or GzmB in the spleens of B6/NOD EAE mice (Figure 4.33, Figure 4.34 right column). In HuPBMC-NSG/SGM3 EAE tissues, $hCD8^+$ T cells were highly cytotoxic in all organs, wherein ~75% expressed either IFNγ and/or GzmB (Figure 4.33), which correlated with the corresponding abundance of Th1 $hCD4^+$ T cells in these tissues. Accordingly, splenic activation of cytotoxic $hCD8^+$ T cells in HuPBMC-NSG/SGM3 EAE mice was also likely due to nonspecific graft reactivity in the periphery.

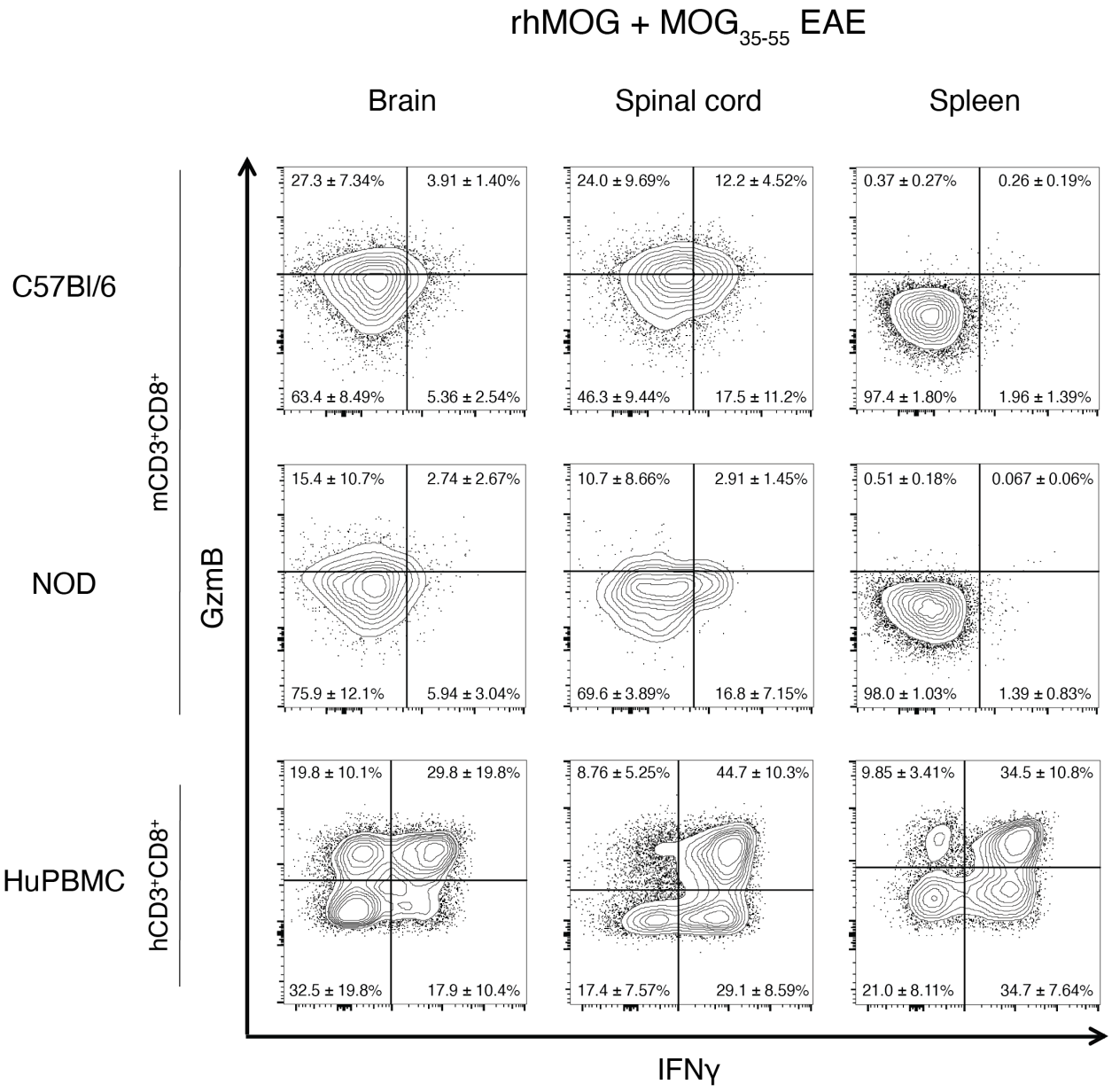

Figure 4.33 Cytotoxic CD8$^+$ T cell subset proportions in the CNS and periphery of murine and humanized EAE models

Figure shows concatenated flow cytometric plots for murine and human CD8$^+$ cytotoxic T cells in the brains (left column), spinal cords (middle column), and spleens (right column) of C57Bl/6 mice (n = 5 WT males) and NOD mice (n = 5 WT males) at day 15 post-EAE induction, and HuPBMC-NSG/SGM3 mice (n = 18 males engrafted with HD-04 female PBMCs, HuPBMC cohort 18) at day 22 post-rhMOG/MOG$_{35-55}$ EAE induction. Cells isolated from perfused brains, spinal cords, and spleens were stimulated with PMA and ionomycin to measure cytokine expression. Data are shown as mean with SD for proportions of IFNγ and granzyme B (GzmB) expressing mCD45^{hi}CD3$^+$CD8$^+$ cells for NOD and C57Bl/6 mice, and proportions of hCD45$^+$CD3$^+$CD8$^+$ cells for HuPBMC mice.

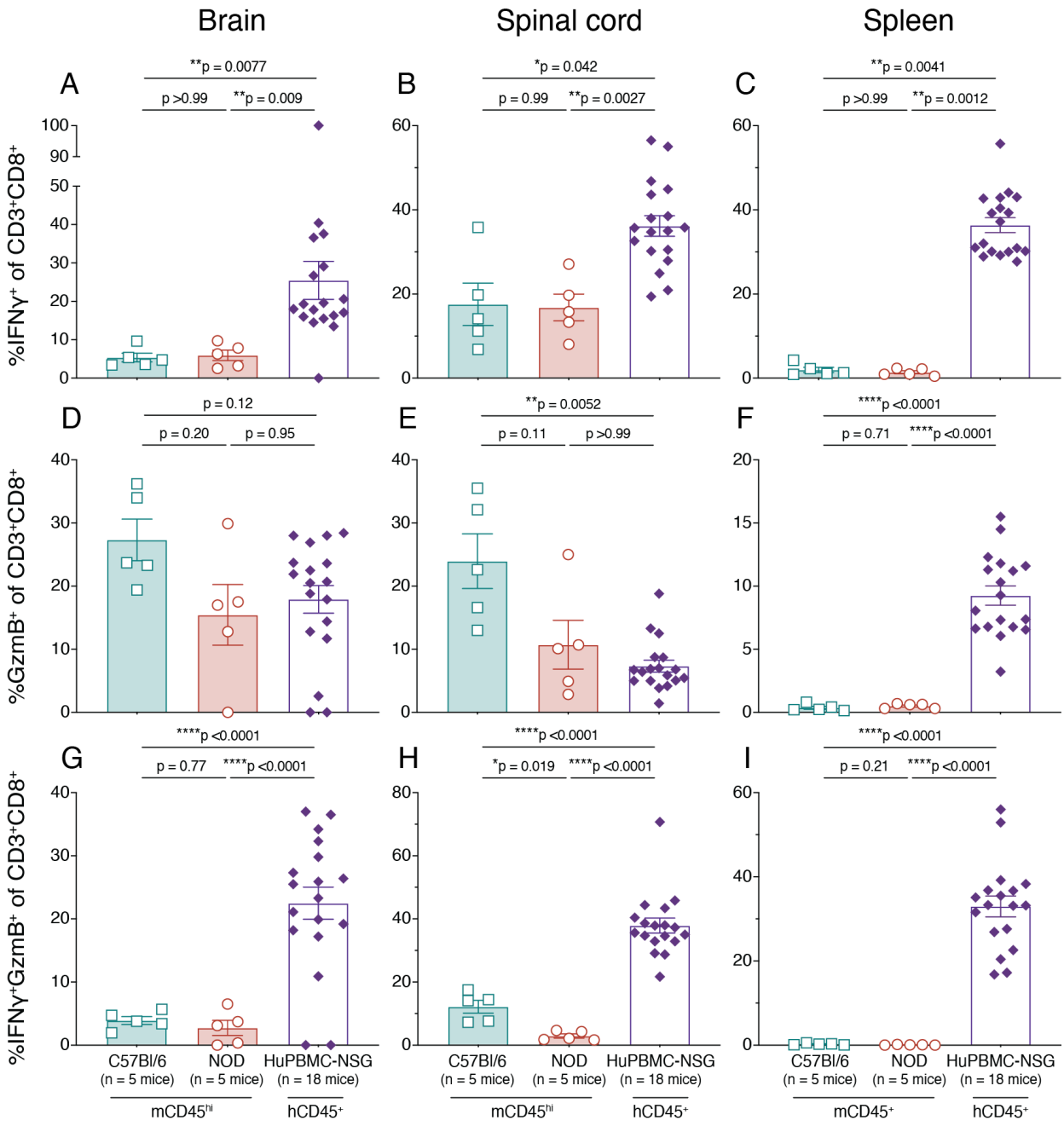

Figure 4.34 Relative cytotoxic CD8$^+$ T cell subset frequencies in the CNS and periphery of murine and humanized EAE models

Figure shows the quantified relative proportions of murine and human (A – C) IFNγ$^+$(GzmB$^-$), (D – F) GzmB$^+$(IFNγ$^-$), and (G – I) IFNγ$^+$GzmB$^+$ expressing CD3$^+$CD8$^+$ T cells in the brain (left column), spinal cord (middle column), and spleen (right column) of C57Bl/6 mice (n = 5 WT males) and NOD mice (n = 5 WT males) at day 15 post-EAE induction, and HuPBMC-NSG/SGM3 mice (n = 18 males engrafted with HD-04 female PBMCs, HuPBMC cohort 18) at post-rhMOG/MOG$_{35-55}$ EAE induction. Cells isolated from perfused brains, spinal cords, and spleens were stimulated with PMA and ionomycin to measure cytokine expression. For NOD and C57Bl/6 samples, subsets

are gated on mCD45^{hi} cells, and for HuPBMC samples subsets are gated on hCD45^{+} cells. Data are shown as mean with SEM and were analyzed by Brown-Forsythe and Welch ANOVA with Dunnett's T3 multiple comparisons test or by Kruskal-Wallis with Dunn's multiple comparisons test.

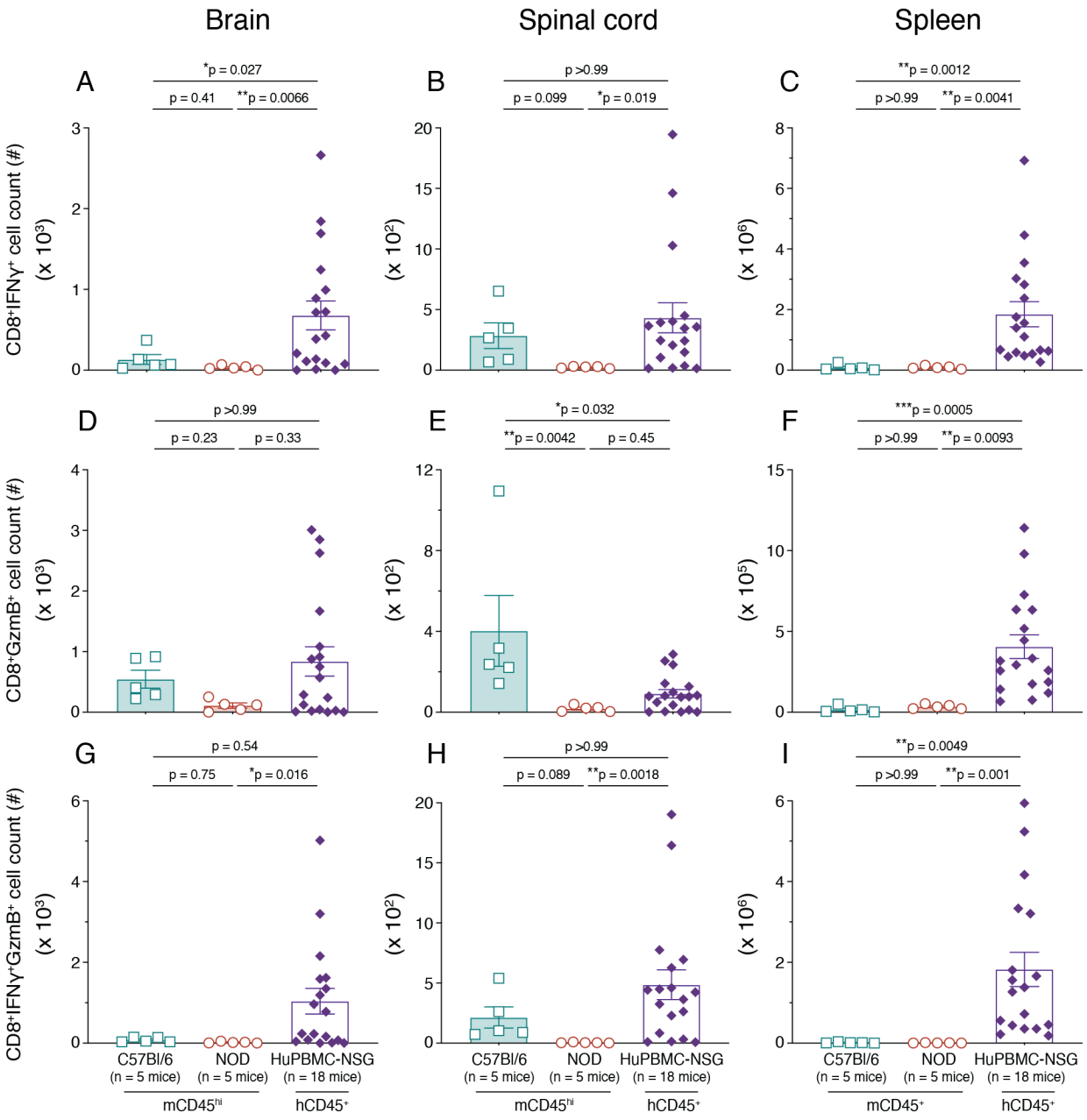

Figure 4.35 Cytotoxic CD8^{+} T cell subset abundance in the CNS and periphery of murine and humanized EAE models

Figure shows total murine and human (A – C) IFNγ^{+}(GzmB^{-}), (D – F) GzmB^{+}(IFNγ^{-}), and (G – I) IFNγ^{+}GzmB^{+} CD3^{+}CD8^{+} T cell counts in the brain (left column), spinal cord (middle column), and spleen (right

column) of C57Bl/6 mice (n = 5 WT males) and NOD mice (n = 5 WT males) at day 15 post-EAE induction, and HuPBMC-NSG/SGM3 mice (n = 18 males engrafted with HD-04 female PBMCs, HuPBMC cohort 18) at day 22 post-rhMOG/MOG_{35-55} EAE induction. Cells isolated from perfused brains, spinal cords, and spleens were stimulated with PMA and ionomycin to measure cytokine expression. For NOD and C57Bl/6 samples, subsets are gated on $mCD45^{hi}$ cells, and for HuPBMC samples subsets are gated on $hCD45^{+}$ cells. Data are shown as mean with SEM and were analyzed by Brown-Forsythe and Welch ANOVA with Dunnett's T3 multiple comparisons test or by Kruskal-Wallis with Dunn's multiple comparisons test.

Quantitively, the CNS and spleens of B6/NOD EAE mice contained fewer cytotoxic $CD8^{+}$ T cells than in HuPBMC-NSG/SGM3 EAE mice, though cytotoxic $CD8^{+}$ T cell counts in the spinal cords of C57Bl/6 EAE mice during the chronic phase of disease (day 15 post-induction) were more similar to the counts measured in HuPBMC-NSG/SGM3 EAE mice (day 22 post-induction) than in NOD EAE mice during the first wave of symptoms (day 15 post-induction) (Figure 4.35). Importantly, the brains of HuPBMC-NSG/SGM3 EAE mice contained on average greater numbers of cytotoxic $CD8^{+}$ T cells than both murine EAE models; a feature that more closely resembles the $hCD8^{+}$ T cell replete brain lesions seen in MS patients than classical EAE models[38,128].

4.6.4 Summary and discussion of findings

Clinically, symptoms of EAE in HuPBMC-NSG/SGM3 mice reflected the disease course and onset and incidence patterns observed in NOD EAE mice post-immunization with both MOG_{35-55} peptide and mixed rhMOG/MOG_{35-55} emulsion. The monophasic relapsing phenotype observed in HuPBMC-NSG/SGM3 EAE mice may represent the first symptomatic wave of a relapsing remitting disease course that unfortunately cannot be extended to the second relapse due to the limiting onset of xGvHD. Comparative analysis of the phenotype of effector T cells in the CNS and periphery of all three strains revealed the immunopathological process underpinning EAE in HuPBMC-NSG/SGM3 post-rhMOG/MOG_{35-55} immunization was (1) predominantly Th1 $hCD4^{+}$ T cell mediated, generating (2) numerically very few regulatory human T cells, and (3) large numbers of numbers of cytotoxic $hCD8^{+}$ T cells in the CNS, especially the brain. The data collectively indicate that, similar to typical murine EAE models, substantial human T cell infiltration of the CNS following MOG induction results in an MS-like disease in HuPBMC-NSG/SGM3 mice.

4.7 Human $CD8^+$ cytotoxic T cells coordinate with murine myeloid cells to demyelinate the CNS of HuPBMC EAE mice

4.7.1 Rationale and experimental design

The relative contributions of different immune cell populations to the immunopathology of MS is an ongoing and evolving area of investigation[1,337,679,680]. Murine EAE models also present with a range of distinct disease symptomologies, CNS pathology, and constituent autoimmune processes based on the induction method and strain used[50,129,673]. Traditionally, $CD4^+$ T cells have been pinned as the primary mediators of disease[129,680]. However, $CD8^+$ T cells often far outnumber $CD4^+$ T cells within the lesions of the brain parenchyma in MS and transfer of MOG-specific $CD8^+$ T cells can also induce EAE in C57Bl/6 and NOD mice[139,681,682]. Infiltrating and resident myeloid cells that phagocytose myelin are another key group of immune cells that act to demyelinate the CNS in EAE models[44,683]. In humanized mouse models, both endogenous murine and engrafted human myeloid cells reconstitute and can co-exist within the CNS, depending on the humanization method and interventions applied[530,640]. We therefore sought to determine the interactions that occur between the engrafted HIS and the host murine innate immune cells in HuPBMC NSG EAE mice that lead to CNS immunopathology and clinical symptoms. In this section, all HuPBMC mice were generated by engrafting male recipient NSG/SGM3 mice with female blood donor PBMCs and inducing EAE at 3 weeks post-injection with mixed rhMOG/MOG_{35-55} emulsion, unless otherwise specified.

4.7.2 Proinflammatory T cell infiltration and symptom incidence in HuPBMC EAE mice

Based on results obtained from multiple healthy female blood donor derived HuPBMC-NSG/SGM3 EAE cohorts, the incidence of clinically measurable symptoms post-rhMOG/MOG_{35-55} immunization was determined to be approximately 30 – 50%, depending on the donor (refer to Figure 4.7). It remained unclear which human immune cell subsets determined which mice became clinically symptomatic and which remained subclinical, despite the fact that all engrafted HuPBMC mice induced with EAE demonstrated some degree of human immune cell infiltration of the CNS (Figure 4.36). To summarize our understanding so far of human T cell involvement in HuPBMC EAE model pathology, Figure 4.36 shows the CNS infiltrating and spleen reconstituting

T cell phenotype seen in a representative cohort. We observed substantial spinal cord infiltration of both $hCD4^+$ (3802 ± 3525 cells/ spinal cord) and $hCD8^+$ T cells (1225 ± 1262 cells/ spinal cord), which each produced high levels of proinflammatory cytokines (Figure 4.36A – B). Over 20% of spinal cord infiltrating T cells expressed IFNγ, IL-17A, granzyme B, or some combination thereof (Figure 4.36A – B). Though the level of T cell reconstitution and infiltration was variable among tissues derived from the same recipient cohort, the pattern of cytokine expression was similar in the periphery and in the CNS (Figure 4.36A – B). Though human T cell infiltration was detected in the CNS of all EAE induced HuPBMC mice regardless of the development of clinically visible EAE symptoms, the ratio of $hCD8^+$ to $hCD4^+$ T cells was notably higher in the CNS tissues of symptomatic mice compared to subclinical mice (Figure 4.36C).

The brains and spleens of EAE induced HuPBMC mice that did or did not develop symptoms contained similar numbers of all measured HIS subsets at endpoint (Figure 4.37). The spinal cords of mice that developed clinical symptoms, however, contained significantly greater numbers of $hCD45^+$ immune cells, including both total $hCD3^+CD8^+$ T cells and activated $hCD8^+CD137^+$ T cells, than mice that remained subclinical (Figure 4.37A – D). Interestingly, the spinal cords of all immunized mice contained similar numbers of $CD137^+$ activated and $FOXP3^+$ regulatory $hCD3^+CD4^+$ T cells (Figure 4.37E – G), suggesting a critical role for cytotoxic $hCD8^+$ T cells specifically in mediating demyelination and tissue damage that results in clinically overt symptomology in HuPBMC EAE mice. Though the spinal cords of symptomatic HuPBMC mice contained a nonsignificant greater number of $hCD14^+CD68^+$ macrophages and $hCD19^+$ B cells, their abundance was relatively low (~100 cells of each per spinal cord) (Figure 4.37H – I), consistent with other reports noting PBMC humanization of NSG mice generally favors the engraftment of T cells over innate immune subsets[493,537,684]. In all tissues, host $mCD45^{hi}CD11b^{hi}F4/80^+$ macrophage counts significantly dwarfed the numbers of human macrophages, indicating they would likely have a greater role in axonal demyelination following EAE induction than the few engrafted human macrophages (Figure 4.38A).

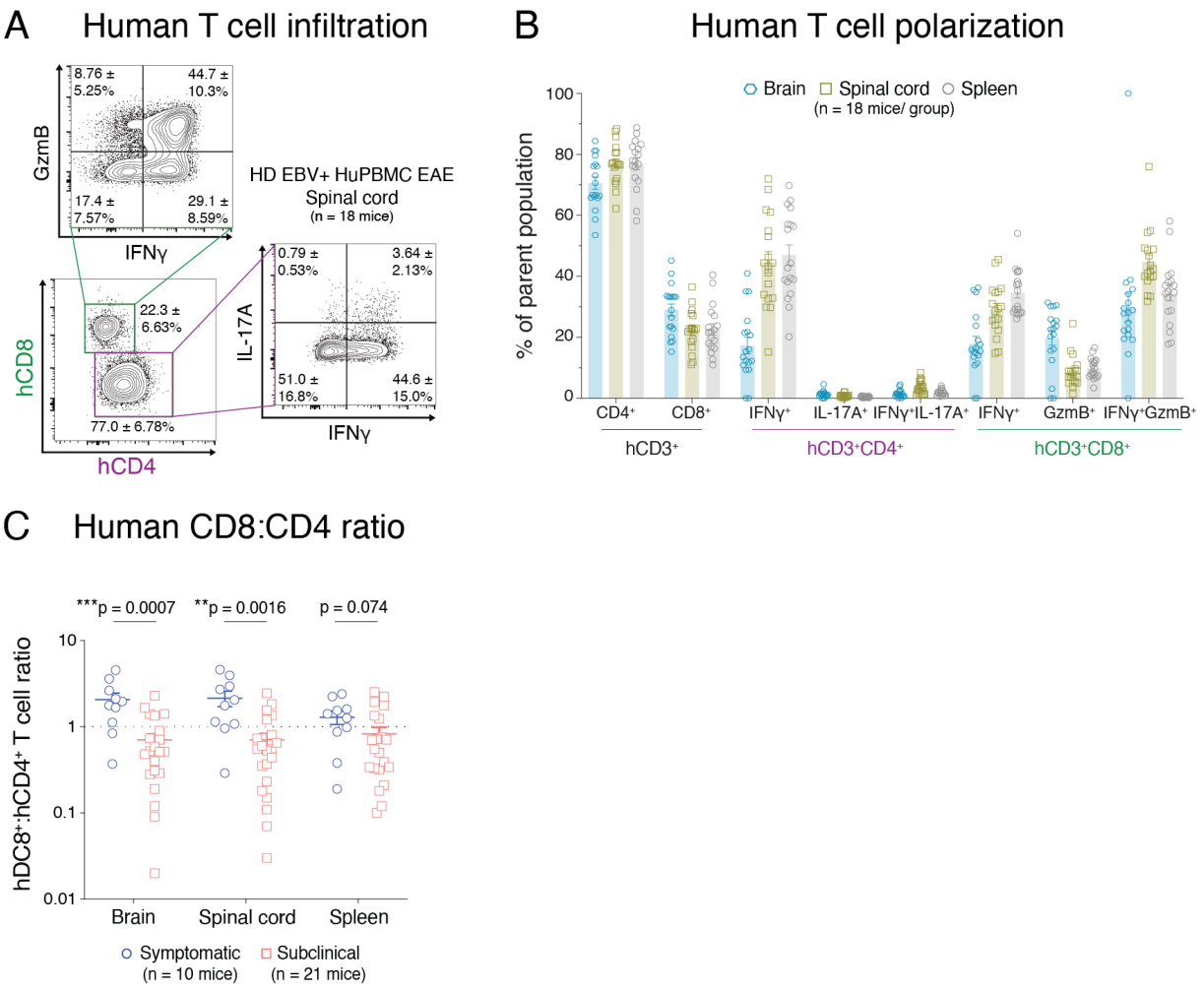

Figure 4.36 Effector human T cell infiltration of the CNS of HuPBMC EAE mice

Figure shows (A) concatenated flow cytometric plots of spinal cord infiltrating hCD3$^+$CD4$^+$ and hCD3$^+$CD8$^+$ T cells and their respective IFNγ, IL-17A, and granzyme B (GzmB) expression and (B) human T cell subsets frequencies in the brain, spinal cord, and spleen, of individual HuPBMC EAE mice (n = 18 symptomatic and subclinical combined) derived from a healthy female donor (HD-04) day 22 post-induction. (C) Ratio of hCD3$^+$CD8$^+$ to hCD3$^+$CD4$^+$ T cells in the brain, spinal cord, and spleen of HuPBMC EAE mice that either developed clinical symptoms (n = 10) or remained subclinical (n = 21) out to day 14 – 24 post-induction. Plotted data are combined from three separate cohorts each derived from a healthy female donor: HD-04, HD-06, and HD-07). All mice represented in A – C were induced with mixed rhMOG/MOG$_{35-55}$ emulsion. Cells isolated from perfused brains, spinal cords, and spleens were stimulated with PMA and ionomycin to measure cytokine expression. HuPBMC samples subsets are gated on hCD45$^+$ cells. Data in A are shown as shown as mean frequency of the parent population with SD, and data in B and C are shown as mean with SEM. Data in C were analyzed by Mann-Whitney test.

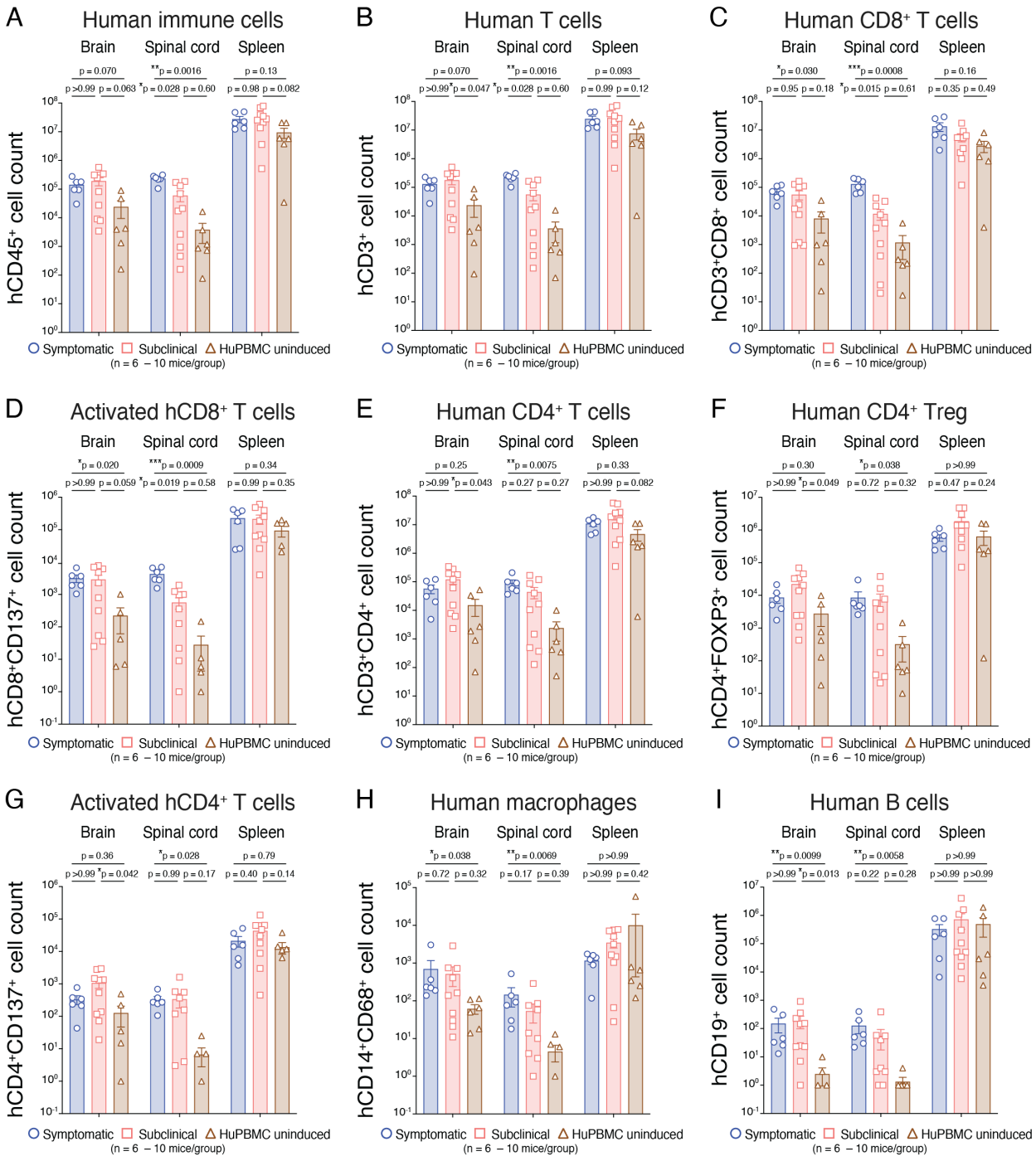

Figure 4.37 Human immune cell infiltration of the CNS in symptomatic and subclinical HuPBMC EAE mice

Figure shows total numbers of human (A) hCD45$^+$ immune cells, (B) hCD3$^+$ T cells, (C) hCD3$^+$CD8$^+$ T cells, (D) activated hCD3$^+$CD8$^+$CD137$^+$ T cells, (E) hCD3$^+$CD4$^+$ T cells, (F) hCD3$^+$CD4$^+$FOXP3$^+$ regulatory T cells, (G) activated hCD3$^+$CD4$^+$CD137$^+$ T cells, (H) hCD14$^+$CD68$^+$ macrophages and (I) hCD19$^+$ B cells, in the brain, spinal cord, and spleen of uninduced HuPBMC mice (n = 6) and EAE-induced HuPBMC mice that either developed

symptoms (n = 6) or remained subclinical (n = 10) until endpoint. Cells from perfused tissues were isolated days 14 and 24 post-rhMOG/ MOG_{35-55} induction of recipient cohorts derived from two unrelated healthy female donors (HD-04 and HD-07), and data were combined for analysis. Data are shown as mean with SEM and were analyzed by Brown-Forsythe and Welch ANOVA with Dunnett's T3 multiple comparisons test or by Kruskal-Wallis with Dunn's multiple comparisons test.

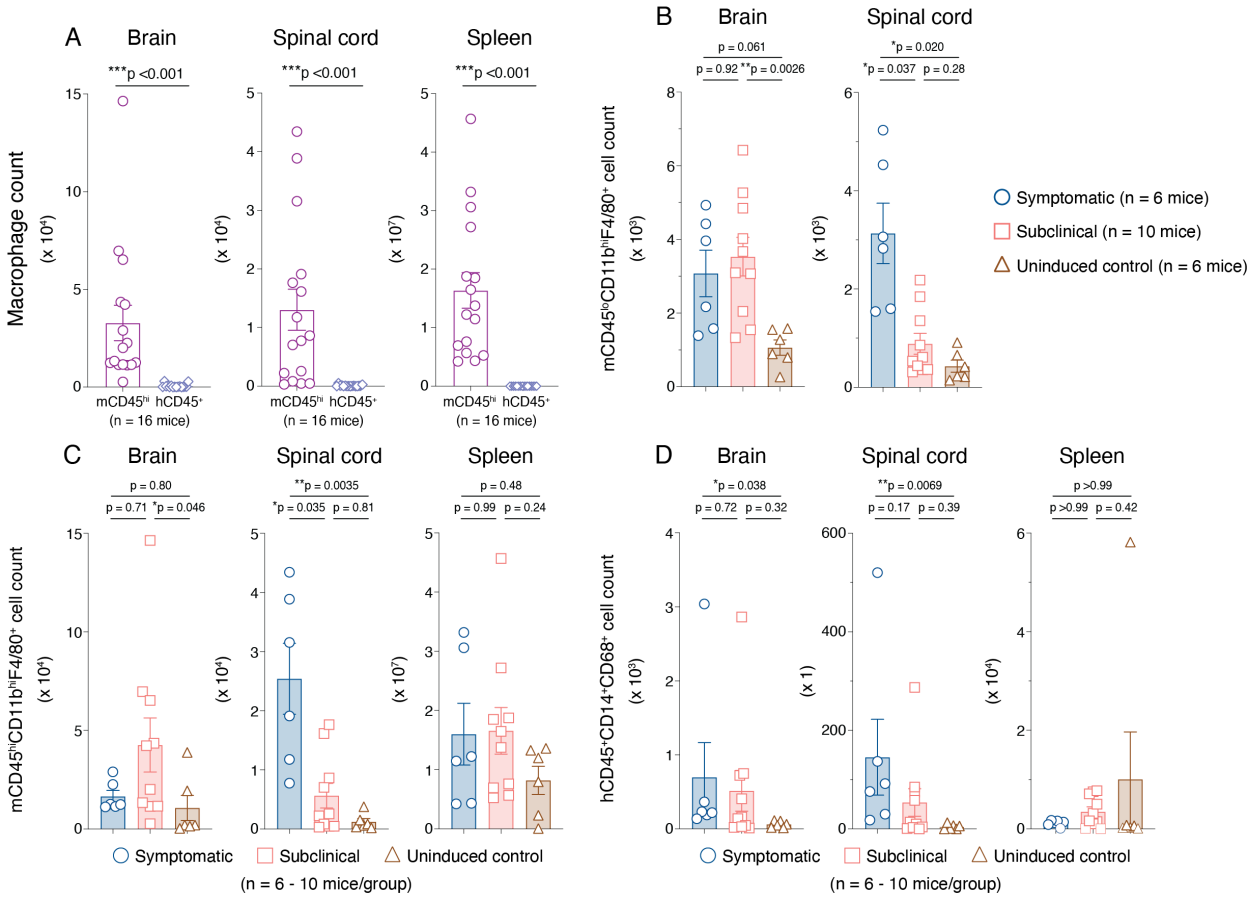

Figure 4.38 Murine and human macrophage infiltration of the CNS in HuPBMC EAE mice

Figure shows (A) relative total cell counts of murine $mCD45^{hi}CD11b^{hi}F4/80^{+}$ and human $hCD45^{+}CD14^{+}CD68^{+}$ macrophages in the brain, spinal cord, and spleen of HuPBMC EAE mice (n = 16 symptomatic and subclinical mice combined). Total cell counts of (B) CNS resident murine $mCD45^{lo}CD11b^{hi}F4/80^{+}$ microglia, (C) infiltrating murine $mCD45^{hi}CD11b^{hi}F4/80^{+}$ macrophages, and (D) infiltrating human $hCD45^{+}CD14^{+}CD68^{+}$ macrophages in the brain, spinal cord, and spleen of uninduced HuPBMC mice (n = 6) and EAE-induced HuPBMC mice that either developed symptoms (n = 6) or remained subclinical (n = 10). Cells from perfused tissues were isolated days 14 and 24 post-rhMOG/MOG_{35-55} induction of recipient cohorts derived from two unrelated healthy female donors (HD-04 and HD-07), and data were combined for analysis. For A, Data are shown as mean with SEM and were analyzed by Mann-Whitney test. For B – D, data are shown as mean with SEM and were analyzed by Brown-Forsythe and Welch ANOVA with Dunnett's T3 multiple comparisons test or by Kruskal-Wallis with Dunn's multiple comparisons test.

rhMOG/MOG_{35-55} EAE induction of HuPBMC mice resulted in a general expansion of murine and human myeloid cells in the CNS tissues compared to uninduced controls (Figure 4.38). Consistent with the relative abundances of human T cells, resident $mCD45^{lo}CD11b^{hi}F4/80^{+}$ microglia counts and infiltrating $mCD45^{hi}CD11b^{hi}F4/80^{+}$ macrophage counts were similar between MOG immunized HuPBMC mice that did or did not develop clinically measured symptoms of disease in both the brain and the spleen (Figure 4.38B – C). In the spinal cord, however, symptomatic HuPBMC EAE mice contained significantly greater numbers of murine myeloid cells than subclinical mice (Figure 4.38B – C). As the spinal cord is the predominant site of demyelination in murine EAE models, and damage to which is known to produce EAE paralysis, the data suggest that infiltrating cytotoxic human $CD8^{+}$ T cells and both resident and infiltrating murine myeloid cells contribute most to demyelination in the HuPBMC EAE model.

4.7.3 Myelin phagocytosis by murine macrophages and microglia in the CNS

Demyelination of the CNS in persons with MS and in murine EAE models results in elevated levels of neurofilament protein subunits in the serum, which is often used as a biomarker of axonal degeneration[109,685–687]. In serum samples from HuPBMC EAE mice, pNF-H levels were as equivalently elevated as NOD EAE controls compared to normal NSG serum (Figure 4.39). To confirm that myelin damage in the CNS occurred following MOG EAE induction of HuPBMC mice, intracellular MBP-specific antibody staining was performed on CNS tissues that were pre-digested with collagenase, dispase, and DNase I to the increase yield of myeloid cells that may have contributed to the denuding of myelinated axons and/or phagocytosing myelin debris following axonal injury.

Flow cytometric analysis of MBP phagocytosis by myeloid cells specifically due to EAE induced demyelination was first validated using samples obtained from C57Bl/6 EAE mice (see Appendix 6). The gating strategy to identify murine ($mCD45^{lo}$ and $mCD45^{hi}$) and human ($hCD45^{+}$) myeloid cells that have phagocytosed myelin (i.e., stained positive for MBP) in the CNS of HuPBMC EAE mice is shown in Figure 4.40. We also confirmed that MBP staining was specific to the CNS tissues, as a fraction of $mCD45^{hi}CD11b^{hi}F4/80^{+}$ macrophages in both the brain and spinal cord contained intracellular myelin protein, whereas the spleen for the same HuPBMC EAE mouse does not (Figure 4.41). Quantification in each tissue revealed that approximately 5 – 35% of $mCD45^{hi}CD11b^{hi}F4/80^{+}$ (Figure 4.42A) and 5 – 45% of $mCD45^{hi}CD11b^{lo}F4/80^{-}$ (Figure 4.42B)

CNS infiltrating myeloid cells contained intracellular MBP, whereas nearly none of the cells in either of these populations stained positive for MBP in the spleen. These data further confirm that flow cytometric detection of intracellular MBP is indicative of local CNS myelin processing by myeloid cells.

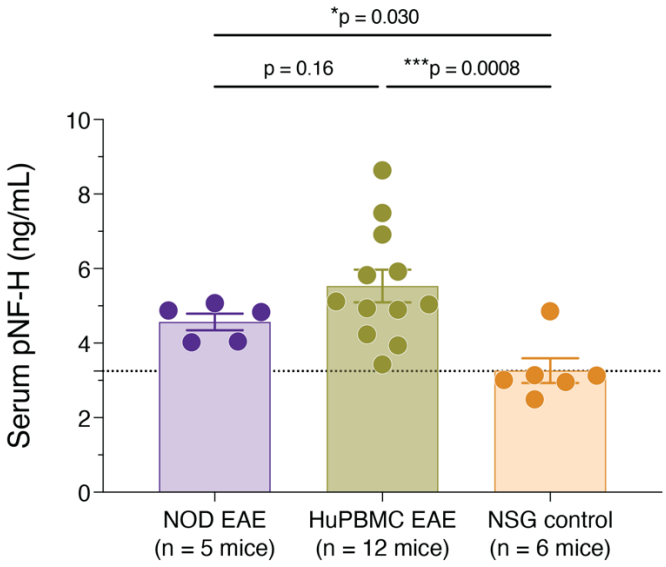

Figure 4.39 Serum neurofilament levels in HuPBMC and NOD mice at EAE endpoint

Figure shows serum levels of phosphorylated neurofilament heavy chain (pNF-H) in NOD mice (n = 5 WT males and females mixed), HuPBMC mice (n = 12 NSG/SGM3 males derived from healthy female donors HD-02, HD-03, and HD-07; symptomatic and subclinical combined), and unengrafted control NSG mice (n = 6 males and females mixed) on days 14 – 25 post-immunization with rhMOG/MOG$_{35-55}$ EAE. Data are shown as mean with SEM and were analyzed by multiple Mann-Whitney tests. The dashed line indicates the NSG group mean level of 3.25 ng/mL pNF-H in normal serum. HuPBMC cohorts included: 13, 14, and 26.

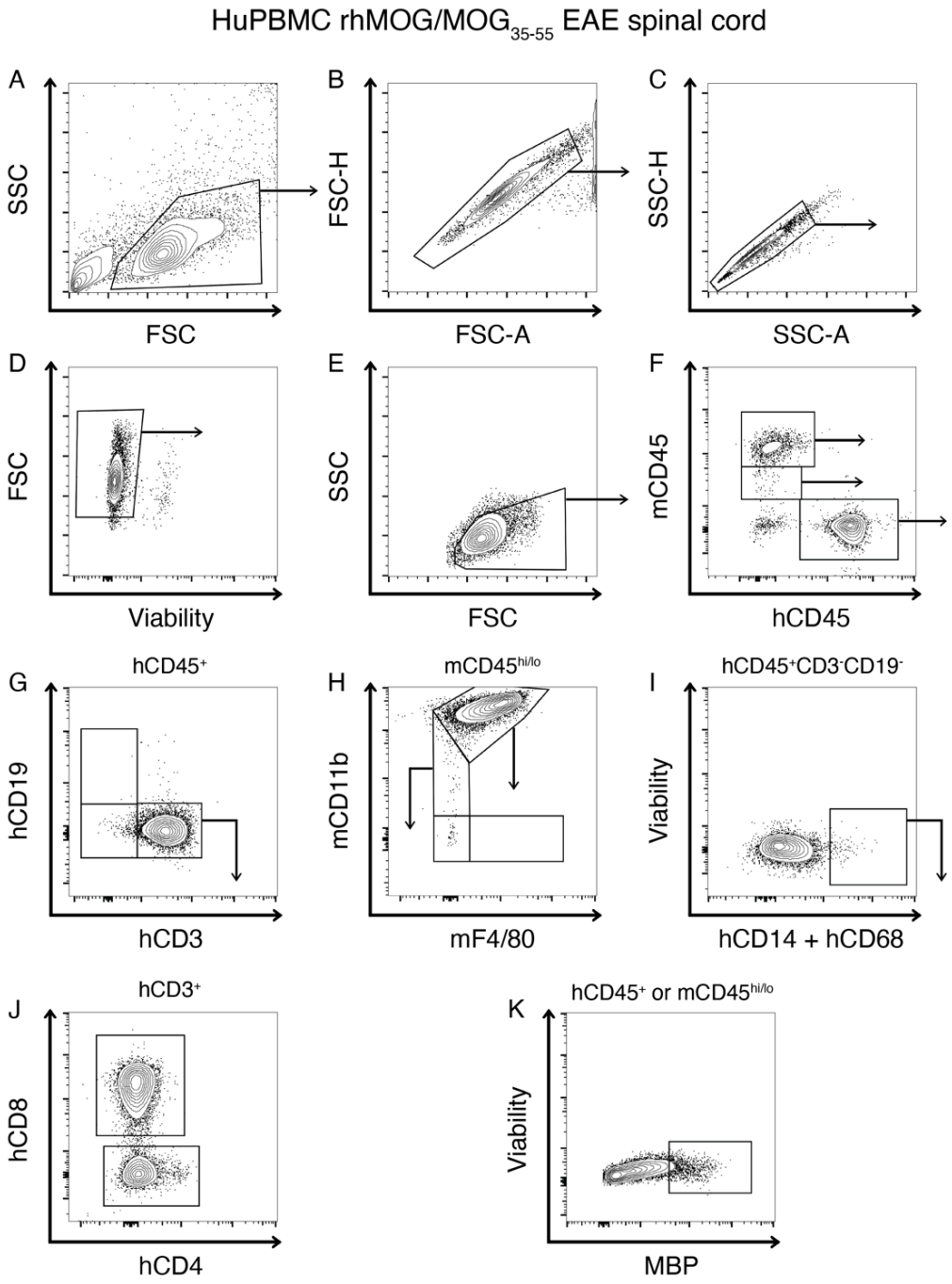

Figure 4.40 Gating strategy for flow cytometric analysis of myelin phagocytosing myeloid cells in the spinal cord of HuPBMC EAE mice

Figure shows (A – E) general cleanup steps applied to all samples. Gates were drawn successively from left to right: exclusion of cellular debris and doublets, by both size and complexity, followed by selection of viable cells and leukocytes. (B) Identification of human (h) and mouse (m) $CD45^{+/hi/lo}$ cell subsets in the spinal cord of a HuPBMC EAE mouse derived from healthy female donor HD-07 post-rhMOG/MOG_{35-55} induction. (G) Within $hCD45^{+}$ cells, $hCD3^{+}$ T cells, $hDC19^{+}$ B cells, and double negative non-T/B cells were gated. (J) Human T cell subsets expressing

hCD4 or hCD8 among $hCD3^+$ T cells sub-gated from (G). Note that enzymatic treatment of CNS tissues by a combination of collagenase, dispase, and DNAse I to release myeloid cells resulted in the cleavage of hCD4 from the T cell surface, and therefore $hCD8^-$ cells were considered $hCD4^+$ (I) $hCD14^+CD68^+$ macrophages derived from the double negative non-T/B cell sub-gate from (G). (H) mF4/80 and mCD11b expression on $mCD45^{hi}$ and $mCD45^{lo}$ cells identified macrophage and microglial populations, respectively. (K) Myelin basic protein (MBP) positive human $hCD14^+CD68^+$ macrophages and murine $mCD45^{hi/lo}CD11b^{hi/lo}F4/80^{+/-}$ myeloid cells. Spinal cord tissues were perfused prior to cell isolation. The parent population for each representative plot is noted above.

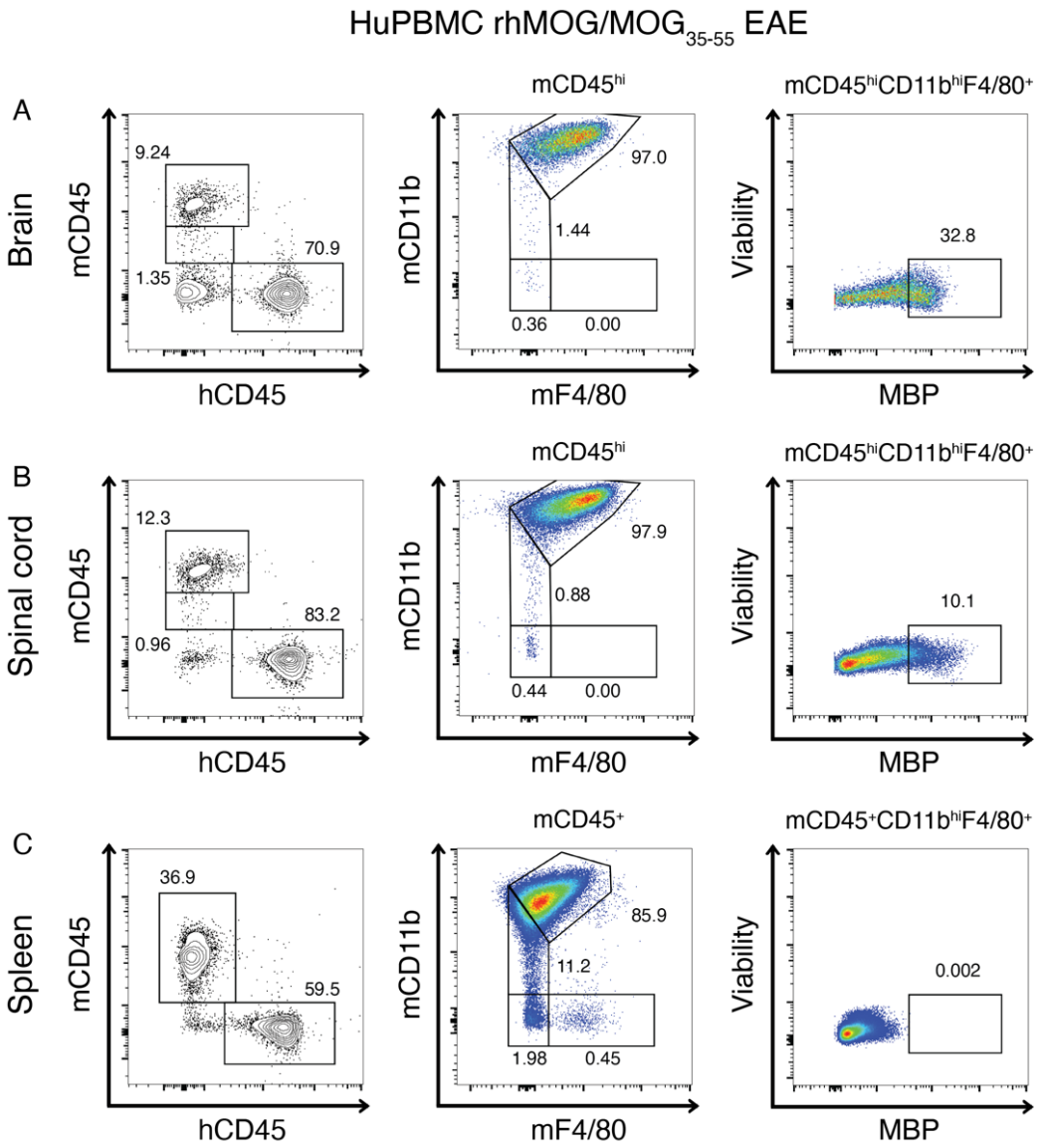

Figure 4.41 Tissue specific staining of myelin phagocytosing murine macrophages in HuPBMC EAE mice

To demonstrate CNS specificity of myelin staining, figure shows gates were drawn successively from left to right in the (A) brain, (B) spinal cord, and (C) spleen that identify peripherally derived/ infiltrating murine mCD45^{hi}CD11b^{hi}F4/80^{+} macrophages that have phagocytosed myelin basic protein (MBP) in a HuPBMC EAE mouse derived from healthy female donor HD-07 post-rhMOG/MOG$_{35-55}$ induction. Brain and spinal cord tissues were perfused prior to cell isolation. The parent population for each representative plot is noted above and the numbers above or adjacent to each gate show the frequency of the subset among the parent population.

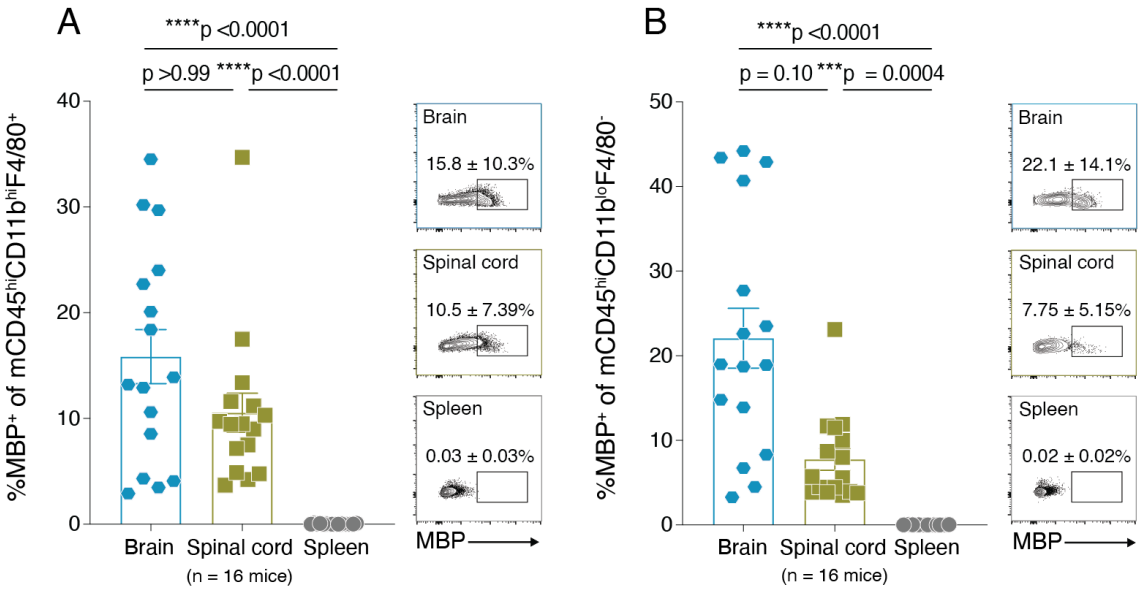

Figure 4.42 Macrophage mediated phagocytosis of myelin in the CNS of HuPBMC EAE mice

Figure shows the frequency of infiltrating murine mCD45^{hi} CD11b^{hi}F4/80^{+} (A) and CD11b^{lo}F4/80^{-} (B) macrophages containing intracellular myelin basic protein (MBP^{+}) in the brain, spinal cord, and spleen of HuPBMC EAE mice (n = 16 symptomatic and subclinical mice combined). Concatenated flow cytometric plots show the mean frequency of MBP co-staining with CD11b^{hi}F4/80^{+} (left) and CD11b^{lo}F4/80^{-} (right) macrophage populations in each tissue with SD. Total cell counts of MBP^{+} myelin containing (C) infiltrating mCD45^{hi}CD11b^{hi}F4/80^{+} macrophages, (D) resident mCD45^{lo}CD11b^{hi}F4/80^{+} microglia, and (E) infiltrating hCD45^{+}CD14^{+}CD68^{+} macrophages in the brain and spinal cord of uninduced HuPBMC mice (n = 6) and EAE-induced HuPBMC mice that either developed symptoms (n = 6) or remained subclinical (n = 10). Cells from perfused tissues were isolated days 14 and 24 post-rhMOG/MOG$_{35-55}$ induction of recipient cohorts derived from two unrelated healthy female donors (HD-04 and HD-07, HuPBMC cohorts 25 – 27), and data were combined for analysis. All graphed data are shown as mean with SEM and were analyzed by Brown-Forsythe and Welch ANOVA with Dunnett's T3 multiple comparisons test or by Kruskal-Wallis with Dunn's multiple comparisons test.

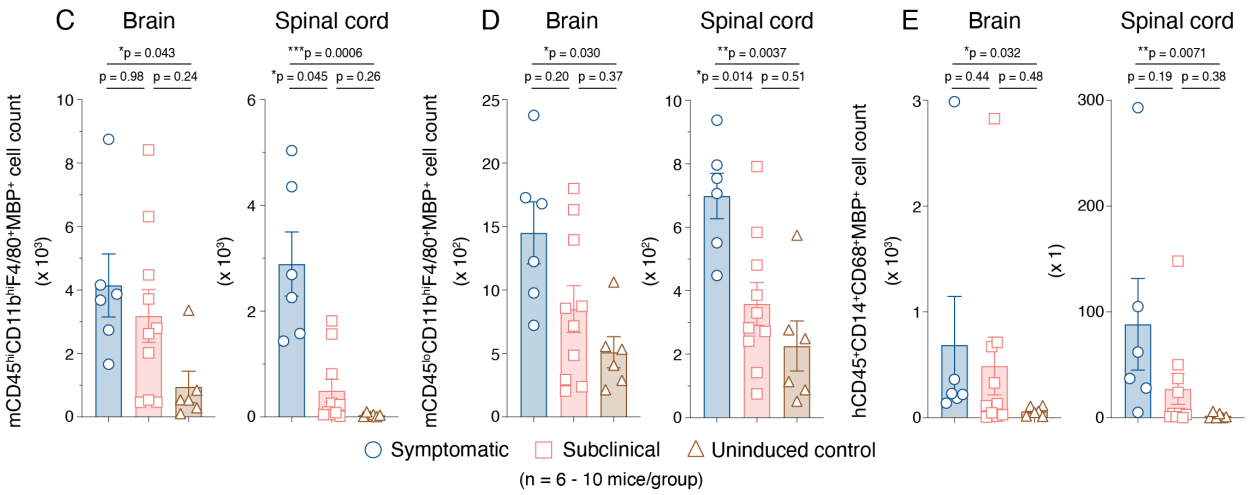

Figure 4.42 continued

Consistent with the increased total numbers of murine myeloid cells in the spinal cords of symptomatic EAE induced HuPBMC mice compared to subclinical mice, spinal cords from symptomatic mice also contained significantly greater numbers of host myelin-phagocytosing (MBP^+) macrophages and microglia ($mCD45^{hi/lo}CD11b^{hi}F4/80^+$) (Figure 4.42C – D). Brain tissues from symptomatic mice also displayed a nonsignificant increase in MBP^+ murine myeloid cells compared to those from subclinical mice (Figure 4.42C – E). Infiltrating human macrophages containing myelin ($hCD45^+CD14^+CD68^+MBP^+$) also trended toward increased relative numbers in the CNS tissues of symptomatic mice compared to subclinical HuPBMC EAE mice, though the quantities did not differ significantly and in symptomatic mice, were numerically less abundant (~100 MBP^+ engrafted cells per spinal cord) than the MBP^+ murine myeloid cells (~3000 MBP^+ host cells per spinal cord) (Figure 4.42C – E), suggesting murine macrophages and microglia demyelinate the CNS sufficiently to produce clinical symptoms in this model.

Given that symptomatic HuPBMC EAE CNS tissues contained increased numbers of both $hCD3^+$ T cells and myeloid cells compared to subclinical mice, we analyzed the relative abundance of these different populations within the same samples to assess any close correlations indicative of cooperative activity. Total numbers of infiltrating $hCD4^+$ and $hCD8^+$ T cells correlated positively with murine microglia counts (Figure 4.43A – D) and infiltrating murine macrophage counts (Figure 4.43E – H) in the brain and the spinal cord of MOG immunized HuPBMC mice, regardless of EAE symptom incidence. The strongest correlations were observed between spinal cord infiltrating $hCD8^+$ T cells and both murine microglial (R^2 = 0.70) and macrophage

populations ($R^2 = 0.88$) (Figure 4.43B, F), similar to MS brain lesions where infiltrating cytotoxic T cells and macrophages are positively correlated with the extent of axonal damage[31].

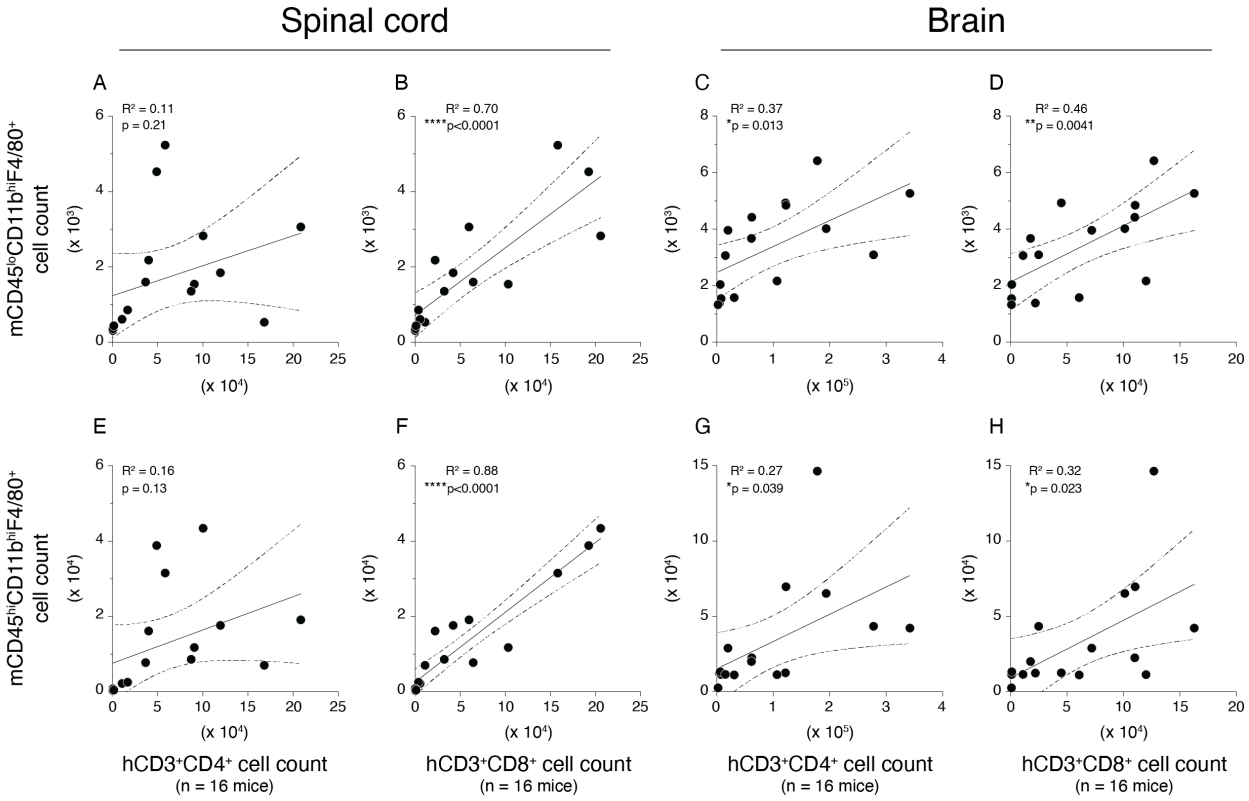

Figure 4.43 Correlation between CNS infiltrating human T cell subsets and murine macrophage and microglia populations in HuPBMC EAE mice

Figure shows correlations between total cell counts of human $hCD3^+CD4^+$ or $hCD3^+hCD8^+$ T cells with murine $mCD45^{lo}CD11b^{hi}F4/80^+$ microglia (A – D) or $mCD45^{hi}CD11b^{hi}F4/80^+$ infiltrating macrophages (E – H) in the spinal cords (left) and brains (right) of HuPBMC EAE mice (n = 16 symptomatic and subclinical mice combined). Cells from perfused tissues were isolated days 14 and 24 post-rhMOG/MOG_{35-55} induction of recipient cohorts derived from two unrelated healthy female donors (HD-04 and HD-07, HuPBMC cohorts 25 – 27), and data were combined for analysis. Data were analyzed by simple linear regression (solid line). Goodness of fit is indicated by the R^2 value, and the 95% confidence interval by dashed lines.

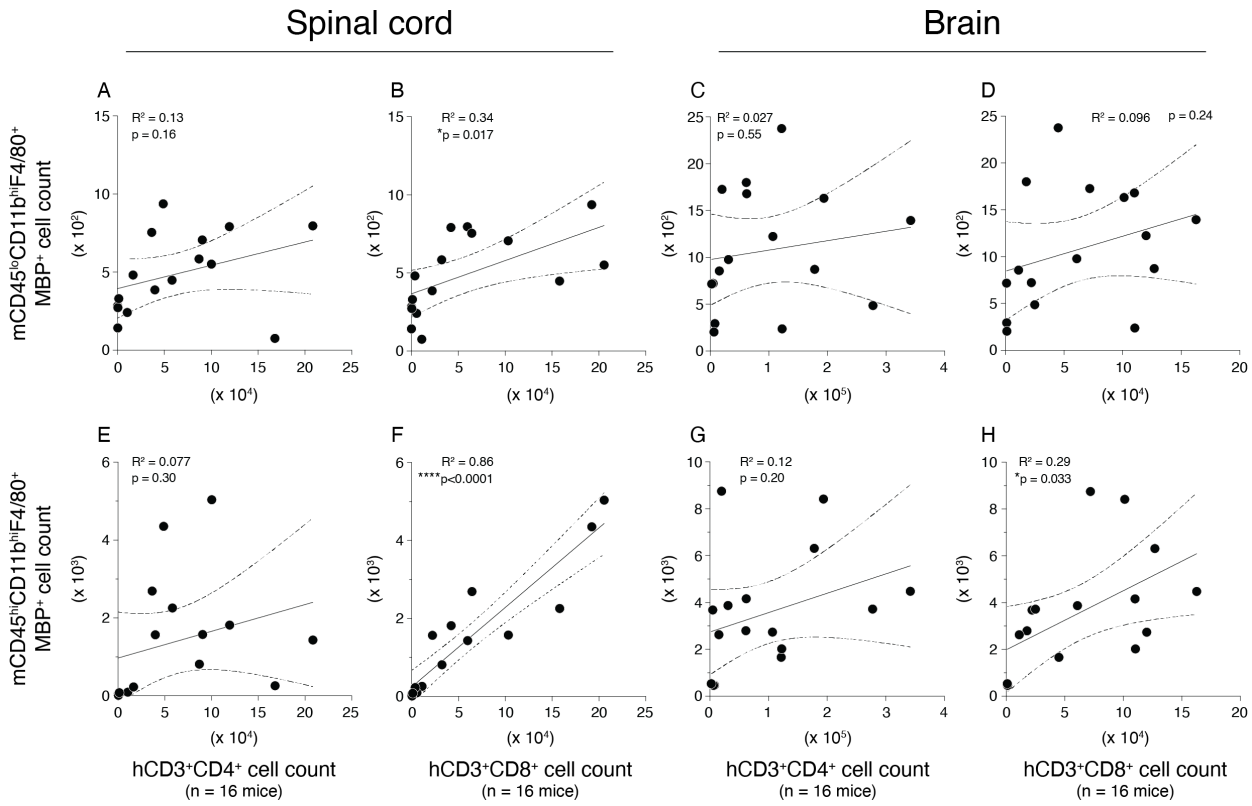

Figure 4.44 Correlation between CNS infiltrating human T cell subsets and myelin phagocytosing murine macrophage and microglia populations in HuPBMC EAE mice

Figure shows correlations between total cell counts of human $hCD3^+CD4^+$ or $hCD3^+hCD8^+$ T cells with myelin containing murine $mCD45^{lo}CD11b^{hi}F4/80^+MBP^+$ microglia (A – D) or $mCD45^{hi}CD11b^{hi}F4/80^+MBP^+$ infiltrating macrophages (E – H) in the spinal cords (left) and brains (right) of HuPBMC EAE mice (n = 16 symptomatic and subclinical mice combined). Cells from perfused tissues were isolated days 14 and 24 post-rhMOG/MOG_{35-55} induction of recipient cohorts derived from two unrelated healthy female donors (HD-04 and HD-07, HuPBMC cohorts 25 – 27), and data were combined for analysis. Data were analyzed by simple linear regression (solid line). Goodness of fit is indicated by the R^2 value, and the 95% confidence interval by dashed lines.

Correlations between the numbers of CNS infiltrating human T cell and murine myeloid cells that contained intracellular MBP were similarly though less strongly positive (Figure 4.44), with the exception being an equally strong association between $hCD8^+$ T cells and MBP^+ infiltrating murine macrophages in the spinal cord (R^2 = 0.86) (Figure 4.44F). Spinal cord infiltrating $hCD4^+$ T cells and MBP^+ murine myeloid cells were only weakly correlated (Figure 4.44A, D). All human T cell and murine myeloid cell correlations in the brain were moderately positive (Figure 4.44 right columns). In contrast to the positive correlations between human T cells

and murine myeloid cells in HuPBMC EAE CNS tissues, human T cells did not correlate with total infiltrating human macrophages (Figure 4.45A, B) nor with human macrophages containing intracellular MBP (Figure 4.45C, D). Overall, the data show that infiltrating human T cells, and specifically $hCD8^+$ T cells, correlate strongly with infiltration of murine macrophages and phagocytosis of myelin by those macrophages in the spinal cord, suggesting these subsets work in tandem to damage myelin in HuPBMC EAE mice.

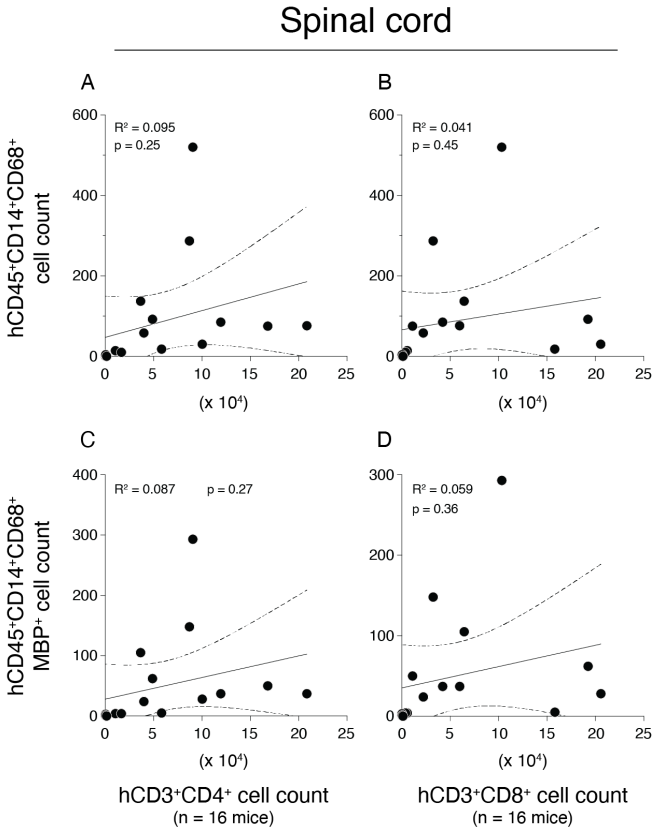

Figure 4.45 Correlation between CNS infiltrating human T cell subsets and human macrophage populations in HuPBMC EAE mice

Figure shows correlations between total cell counts of human $hCD3^+CD4^+$ (left column) or $hCD3^+hCD8^+$ T cells (right column) with total infiltrating human $hCD45^+CD14^+CD68^+$ macrophages (top row) as well as myelin containing human $hCD45^+CD14^+CD68^+MBP^+$ macrophages (bottom row) in the spinal cord of HuPBMC EAE mice (n = 16 symptomatic and subclinical mice combined). Cells from perfused tissues were isolated days 14 and 24 post-rhMOG/MOG_{35-55} induction of recipient cohorts derived from two unrelated healthy female donors (HD-04 and HD-07, HuPBMC cohorts 25 – 27), and data were combined for analysis. Data were analyzed by simple linear regression (solid line). Goodness of fit is indicated by the R^2 value, and the 95% confidence interval by dashed lines.

These findings are in contrast to numerous studies showing that mCD4^{+} helper T cells are the main drivers of myelin damage following MOG immunization in classical murine EAE models[665,688,689]. Accordingly, we observed that the numbers of infiltrating murine T cells and myeloid cells were mostly positively correlated in the CNS tissues of C57Bl/6 MOG$_{35-55}$ EAE mice (Figure 4.46, Figure 4.47). Statistically significant correlations between the numbers of resident microglia (mCD45^{lo}CD11b^{hi}F4/80^{+}) and infiltrating macrophages (mCD45^{hi}CD11b^{hi} F4/80^{+}) were specifically seen with mCD4^{+} T cells, but not with mCD8^{+} T cells, in both the brain and spinal cord of C57Bl/6 EAE mice (Figure 4.47C, E, G).

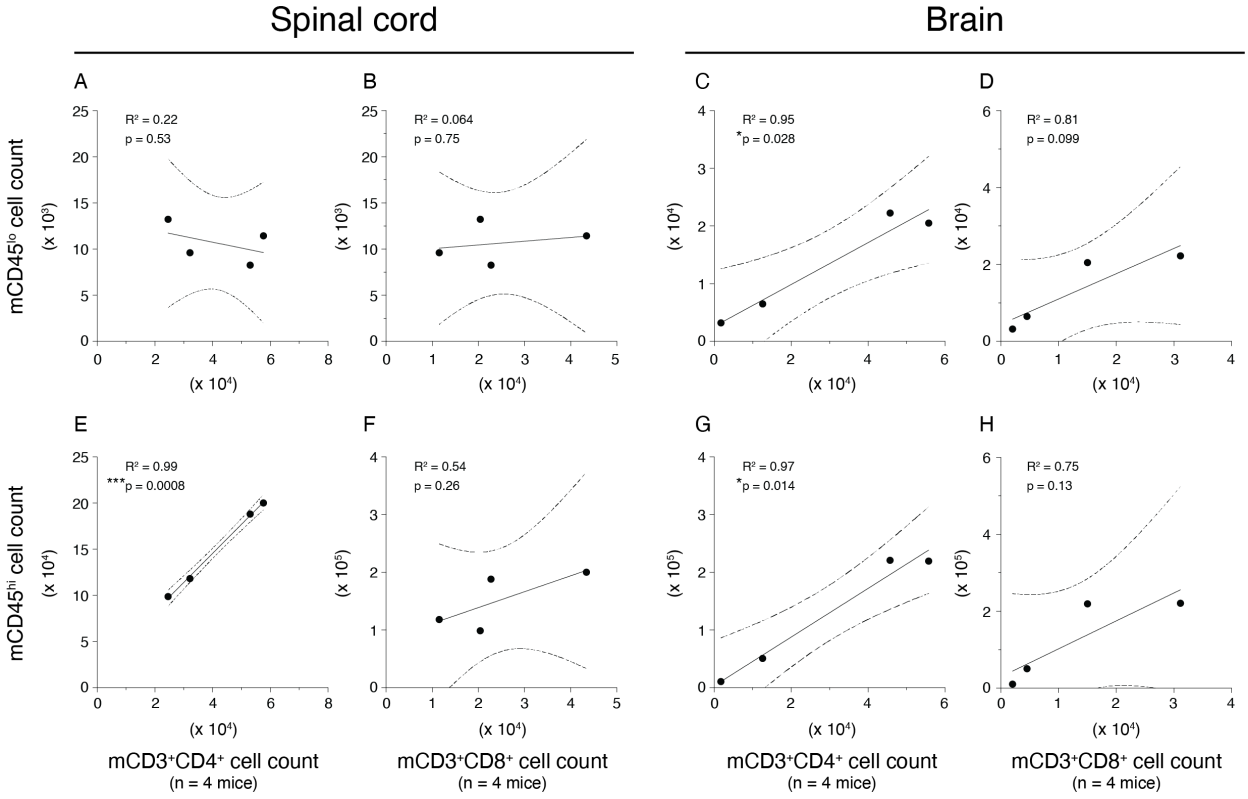

Figure 4.46 Correlation between CNS infiltrating T cell subsets and myeloid cell populations in C57Bl/6 EAE mice

Figure shows correlations between total cell counts of murine mCD3^{+}CD4^{+} or mCD3^{+}hCD8^{+} T cells with mCD45^{lo} microglia (A – D) or mCD45^{hi} infiltrating macrophages (E – H) in the spinal cords (left) and brains (right) of C57Bl/6 EAE mice (n = 4 symptomatic WT males). Cells from perfused tissues were isolated day 15 post-MOG$_{35-55}$ EAE induction. Data were analyzed by simple linear regression (solid line). Goodness of fit is indicated by the R^2 value, and the 95% confidence interval by dashed lines.

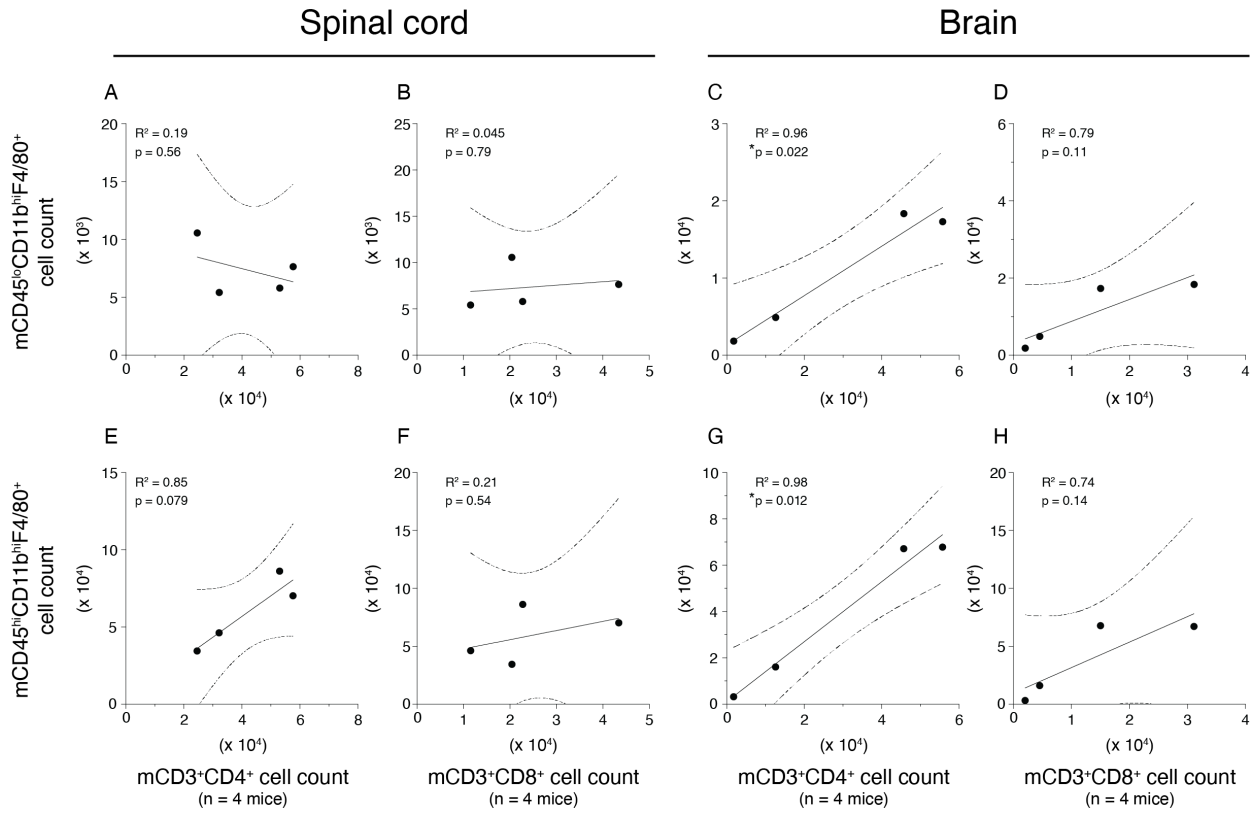

Figure 4.47 Correlation between CNS infiltrating T cell subsets and macrophage and microglia populations in C57Bl/6 EAE mice

Figure shows correlations between total cell counts of murine $mCD3^+CD4^+$ or $mCD3^+hCD8^+$ T cells with $mCD45^{lo}CD11b^{hi}F4/80^+$ microglia (A – D) or $mCD45^{hi}CD11b^{hi}F4/80^+$ infiltrating macrophages (E – H) in the spinal cords (left) and brains (right) of C57Bl/6 EAE mice (n = 4 symptomatic WT males). Cells from perfused tissues were isolated day 15 post-MOG_{35-55} EAE induction. Data were analyzed by simple linear regression (solid line). Goodness of fit is indicated by the R^2 value, and the 95% confidence interval by dashed lines.

Strong correlations were also observed in the brain and spinal cord between the numbers of $mCD4^+$ T cells and macrophages that contained intracellular MBP (Figure 4.48), suggesting $mCD4^+$ T cells are more involved than $mCD8^+$ T cells in promoting the recruitment and/or expansion of phagocytic myeloid cells in the CNS of C57Bl/6 EAE mice. Overall, the data indicate that, unlike in classical murine EAE models, demyelination, and symptom incidence in HuPBMC EAE mice is driven by $hCD8^+$ T cell infiltration and cooperation with the murine host myeloid cells that phagocytose myelin.

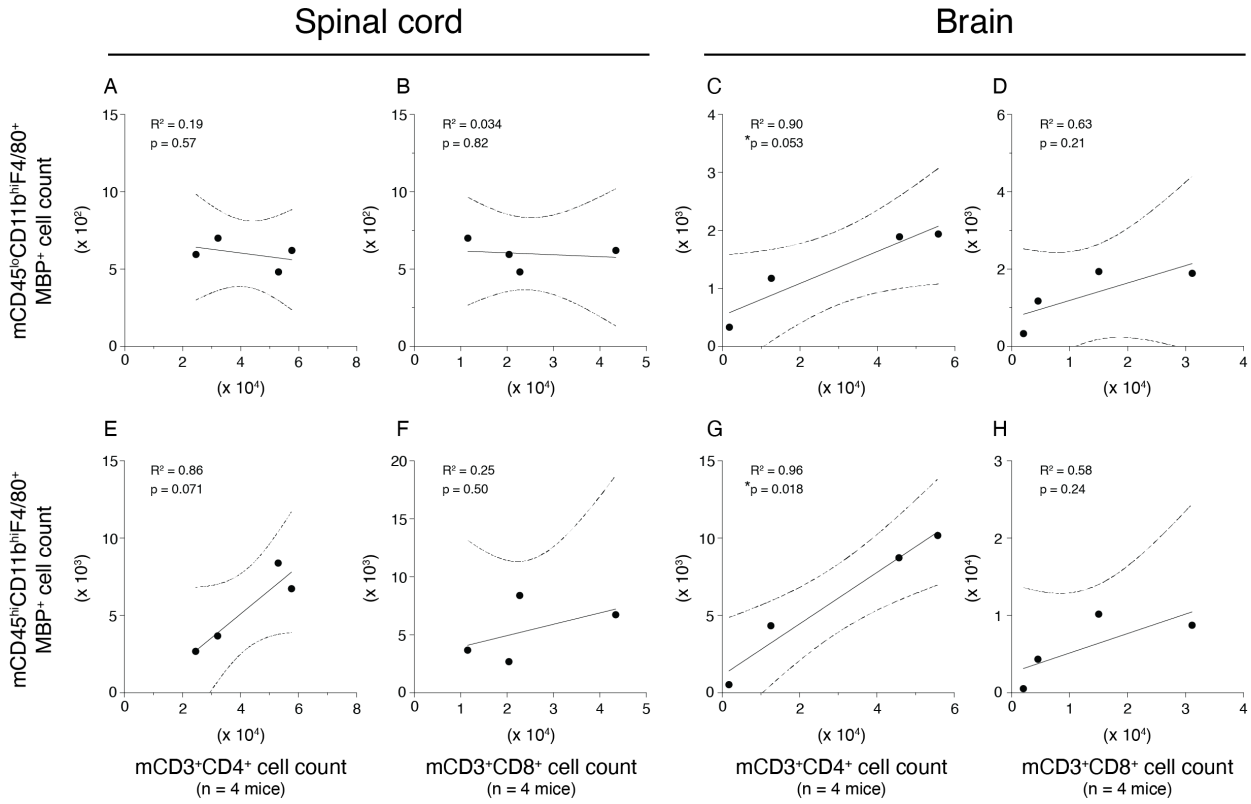

Figure 4.48 Correlation between CNS infiltrating T cell subsets and myelin phagocytosing macrophage and microglia populations in C57Bl/6 EAE mice

Figure shows correlations between total cell counts of murine $mCD3^+CD4^+$ or $mCD3^+hCD8^+$ T cells with $mCD45^{lo}CD11b^{hi}F4/80^+MBP^+$ microglia (A – D) or $mCD45^{hi}CD11b^{hi}F4/80^+MBP^+$ infiltrating macrophages (E – H) in the spinal cords (left) and brains (right) of C57Bl/6 EAE mice (n = 4 symptomatic WT males). Cells from perfused tissues were isolated day 15 post-MOG_{35-55} EAE induction. Data were analyzed by simple linear regression (solid line). Goodness of fit is indicated by the R^2 value, and the 95% confidence interval by dashed lines.

4.7.4 CNS distribution of human $CD8^+$ T cells and murine microglia in demyelinated areas

Based on the results of the prior analyses, we suspected functional interspecies interactions occurred between the engrafted human and host murine immune cell subsets in the CNS of HuPBMC EAE mice. Specifically, we observed a strong correlation between $hCD8^+$ T cell and murine myeloid cell counts in the CNS, which were both increased in the CNS of symptomatic mice compared to subclinical mice in the same recipient cohorts. We therefore performed qualitative immunohistochemical imaging of HuPBMC EAE CNS tissues, derived from a female

blood donor with a diagnosis of RRMS, in order to visualize the distribution and co-localization of infiltrating hCD8^{+} T cells and murine microglia with demyelinated areas of the CNS.

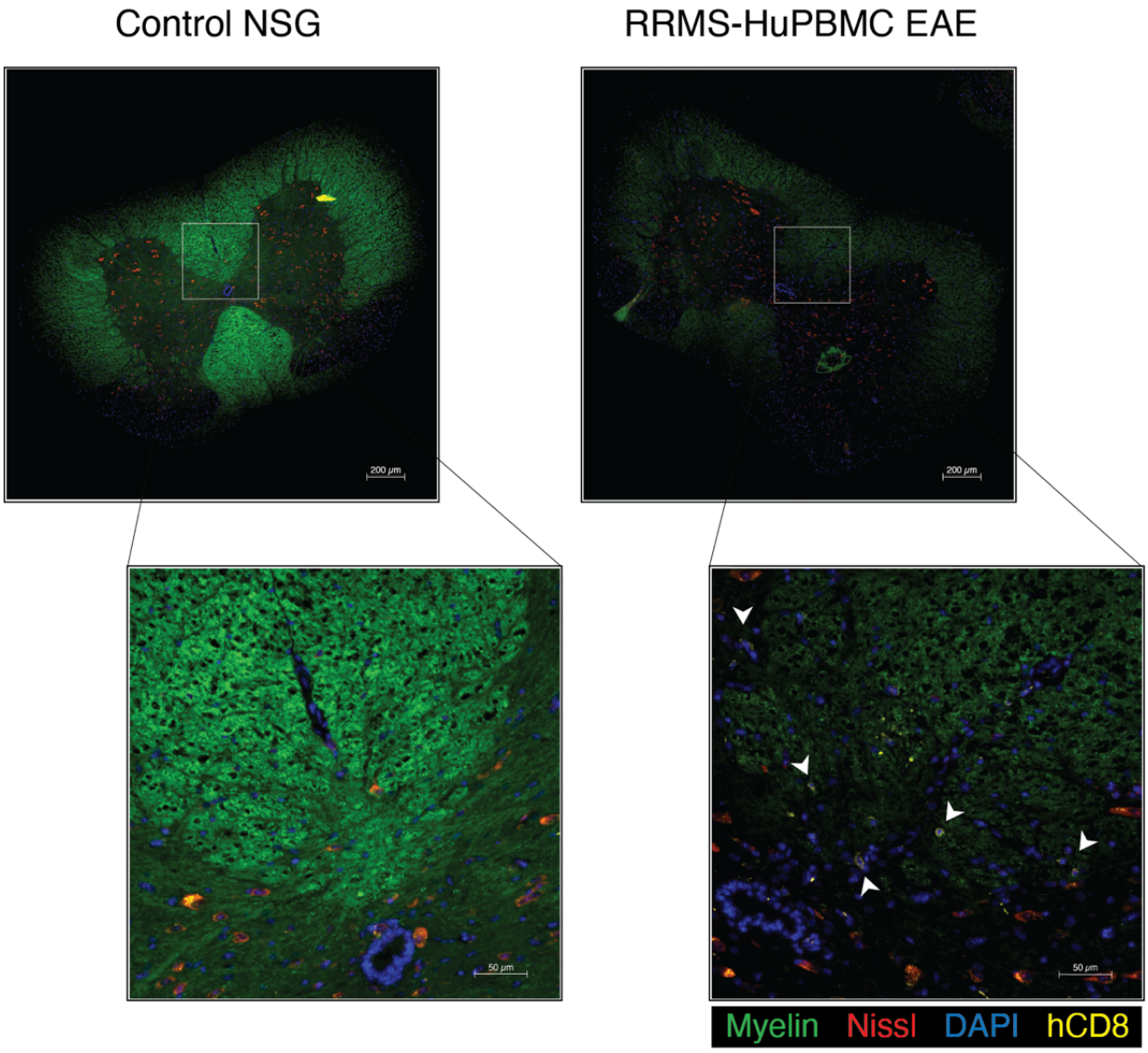

Figure 4.49 Demyelination and human T cell infiltration of the HuPBMC EAE spinal cord

Representative images of lumbar spinal cord sections from an unengrafted NSG control mouse (left) and a symptomatic HuPBMC EAE mouse (right) derived from a female donor with RRMS (MS-05). Perfused tissues were collected day 15 post-rhMOG/MOG$_{35-55}$ EAE induction (day 4 post-symptom onset). Sections were labelled with FluoroMyelin (green), NeuroTrace 530/615 (red), DAPI (blue), and anti-hCD8 (yellow). Example hCD8^{+} T cells are indicated by white arrows. Scale bars indicate size as specified per panel, showing 200 µm sections and 50 µm insets.

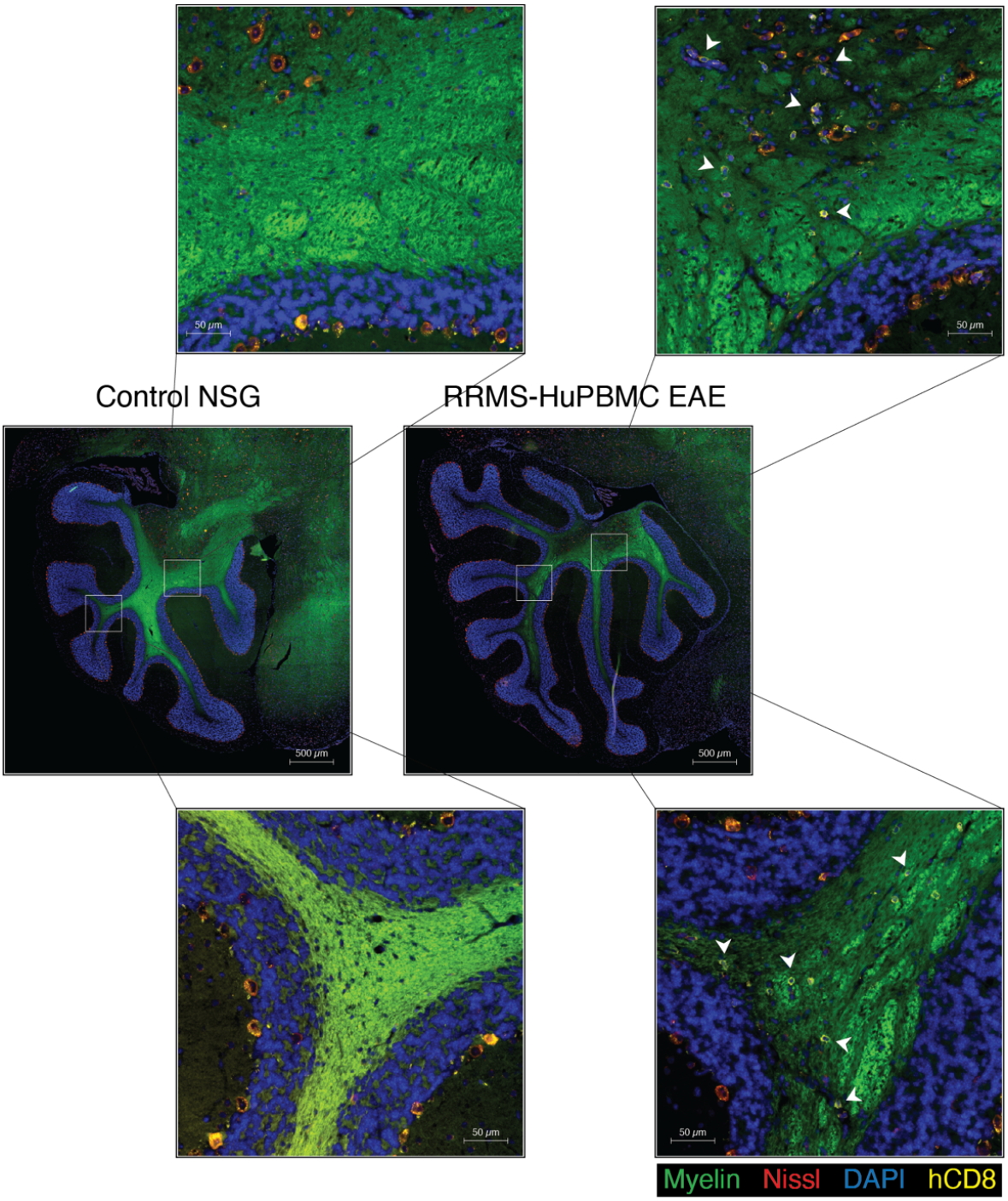

Figure 4.50 Demyelination and human T cell infiltration of the HuPBMC EAE cerebellum

Representative images of cerebellar sections from an unengrafted NSG control mouse (left) and a symptomatic HuPBMC EAE mouse (right) derived from a female donor with RRMS (MS-05). Perfused tissues were collected day 15 post-rhMOG/MOG_{35-55} EAE induction (day 4 post-symptom onset). Sections were labelled with FluoroMyelin (green), NeuroTrace 530/615 (red), DAPI (blue), and anti-hCD8 (yellow). Example $hCD8^+$ T cells are indicated by white arrows. Scale bars indicate size as specified per panel, showing 500 µm sections and 50 µm insets.

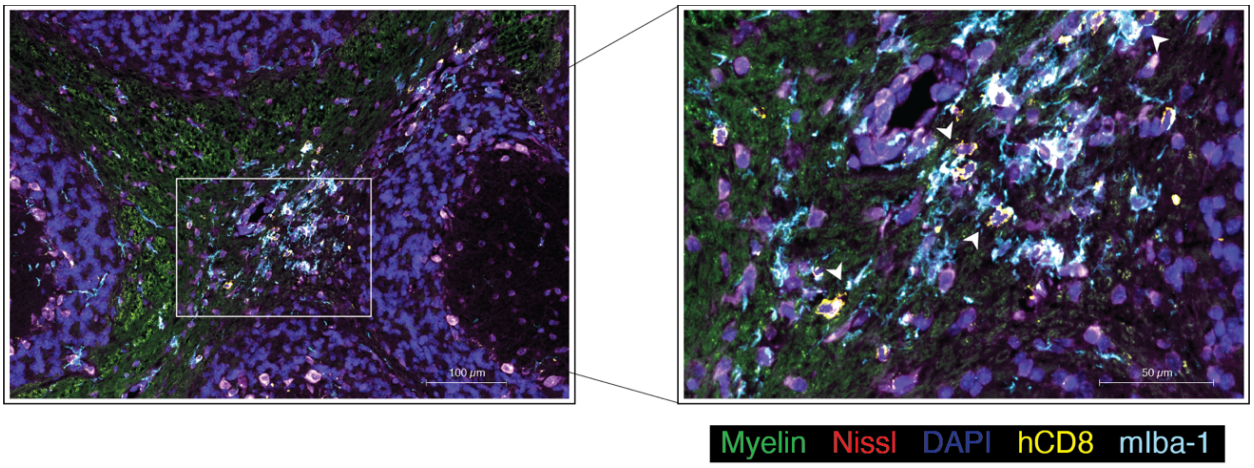

Figure 4.51 Human T cell and murine microglia co-localization in the HuPBMC EAE cerebellum

Representative image of a cerebellar section from a symptomatic HuPBMC EAE mouse derived from a female donor with RRMS (MS-05). Perfused tissues were collected day 15 post-rhMOG/MOG_{35-55} EAE induction (day 4 post-symptom onset). Sections were labelled with FluoroMyelin (green), NeuroTrace 530/615 (red), DAPI (blue), anti-hCD8 (yellow), and anti-Iba-1 (light blue). Example $hCD8^+$ T cells in proximity to Iba-1^+ cells are indicated by white arrows. Scale bars indicate size as specified per panel, showing a 100 µm section and a 50 µm inset.

We detected a notable accumulation of $hCD8^+$ T cells in the white matter of both the lumbar spinal cord (Figure 4.49) and the cerebellum (Figure 4.50) of HuPBMC EAE mice engrafted with RRMS donor PBMCs (see Appendix 7, Figure A.33 for isotype staining control), demonstrating that engrafted human T cells can infiltrate CNS regions typically demyelinated in classical EAE models. Myelin fibers stained less brightly and appeared more fragmented in these regions compared to unaffected NSG control tissues, showing that inflammatory immune subsets were present specifically in areas with damaged myelin (Figure 4.49, Figure 4.50). Moreover, we observed an inflammatory lesion within the cerebellum marked by microgliosis, as indicated by concentrated Iba-1 staining that co-localized with $hCD8^+$ T cells (Figure 4.51). Spinal cord demyelination and brain lesion infiltrates composed of macrophages and $CD8^+$ T cells are consistent with CNS immunopathology seen in both EAE models and MS, respectively[38,131]. Unlike in MS, however, the corpus callosum of HuPBMC EAE mice was mostly devoid of individual or clusters of $hCD8^+$ T cells and demyelinated lesions that were seen in the cerebellar area of the same samples[690], though the distribution may vary with PBMC donor and would require a more systematic analysis to confirm preferential anatomical localization of infiltrating human T cells.

4.7.5 Summary and discussion of findings

The main findings of this section collectively indicate that infiltrating hCD4$^+$ T cells direct a Th1 polarized response in the CNS of HuPBMC EAE mice that leads to hCD8$^+$ T cell-mediated myelin damage and subsequent or concurrent phagocytosis by murine macrophages and microglia. Though some infiltrating human macrophages are detected in the CNS, the preponderance of human T cells and murine myeloid cells points to their combined activity producing clinically measurable paralysis in the HuPBMC EAE model. The correlated abundance and anatomical co-localization of myelin phagocytosing murine myeloid cells with cytotoxic hCD8$^+$ T cells supports their cooperative role in mediating demyelination, as well as potentially in presenting the inducing MOG antigen to engrafted human T cells, which is examined in sections 4.8 and 4.9. These data highlight the interspecies nature of the immunopathology of the HuPBMC EAE model. Ultimately, human and murine immune cell subset transfer and/or depletion experiments would best determine the pathogenicity of individual populations, though we anticipate logistical difficulty in performing these types of experiments due to confounding graft reactivity[616] as well as the limited numbers of HuPBMC recipients obtained per blood donor and the short duration of experiments to onset of xGvHD. Importantly, and unlike in typical murine EAE models, hCD8$^+$ T cells were equally if not more abundant than hCD4$^+$ T cells in the brain and spinal cord of HuPBMC EAE mice, a key feature of MS lesions[38,131,665,688,689], which supports its use as a model of MS.

4.8 Effects of adjuvant on human T cell infiltration in the HuPBMC EAE model

4.8.1 Rationale and experimental design

We have established that active EAE induction of HuPBMC mice with MOG antigens is associated with human T cell infiltration of the CNS, myelin damage, and symptoms of paralysis consistent with regular murine EAE models. In these classical EAE models, different components of the immunization formulation are needed to activate myelin reactive T cells and enable their migration into the CNS of certain stains. For example, PTx is not required for symptom development in SJL mice immunized with PLP antigens but is required to generate paralysis in C57Bl/6 and NOD mice immunized with MOG antigens (Table 4.2)[129,691]. Moreover, the use of CFA containing *M. Tuberculosis* as an immune stimulant influences the polarization of responding T cells toward Th1 through TLR 2, 4, and 9 signalling, among other PRRs, and via the induction

of IL-2 expression[136,691–694]. It is therefore unclear how the use of the different components of the inducing formulation (i.e., CFA, PTx, and MOG) affects the expansion and reconstitution of HIS subsets and the subsequent disease outcomes in the HuPBMC EAE model.

Further complicating analyses of EAE induction in HuPBMC mice is the concurrence of nonspecific graft reactivity, wherein engrafted human $CD8^+$ and $CD4^+$ T cells mediate xGvHD by recognizing MHC I and II molecules, respectively, on the surface of the murine host cells[491,505]. Therefore, in addition to how each adjuvant component affects disease outcomes, it remained unclear which proportion, if any, of the responding human T cells recognized the inducing MOG antigen or other myelin antigens following EAE induction, or if CNS infiltrating T cells simply recognized foreign MHC when given access to the CNS and effectively caused bystander damage resulting in paralysis. The monophasic nature of the disease course seen in HuPBMC EAE mice, where remission occurs after the peak of symptom severity (see Figure 4.18), suggests that graft reactivity is not the sole perpetrator of CNS damage, since xGvHD is generally aggressive, progressive, and eventually lethal, once initiated[493,505,609,612,677]. It is unclear, however, if the regulatory mechanisms at play in the CNS that cause remission would apply to a nonspecific graft response or only to a myelin antigen specific response in this interspecies model.

To begin to address some of the unknowns surrounding the role of inducing antigen and adjuvant in modulating the human T cell response in HuPBMC EAE mice, we performed preliminary experiments in this section aimed at answering the following two questions: (1) Does successful induction of clinical EAE symptoms in HuPBMC mice require the additional provision of PTx? (2) Is MOG antigen required to generate paralytic symptoms, or is nonspecific graft reactivity in the CNS sufficient? To address these questions, a cohort of HuPBMC mice was produced by engrafting NSG mice with healthy female donor PBMCs, obtained from a single donation. Subgroups of the cohort were then induced with varying combinations of the immunization formulation to determine their necessity and sufficiency to produce symptoms of EAE and xGvHD in HuPBMC mice. At endpoint, CNS and peripheral tissues from all groups were assessed for human T cell infiltration indicative of disease induction.

4.8.2 HuPBMC cohort humanization and EAE induction

At 3 weeks post-injection of 5 x 10^6 PBMCs, reconstitution of the peripheral blood of recipient male NSG mice resembled the typical engraftment profile of other donor-derived cohorts

(Figure 4.52). Variably reconstituted groups of 4 – 8 HuPBMC mice were then randomly assigned to be immunized with one or more of the inducing adjuvant components (CFA, PTx, and/or MOG), as noted in Table 4.3. All unengrafted NSG mice (PBS injected) were induced with the usual mixed MOG EAE induction formula to serve as negative controls for human T cell involvement generally.

4.8.3 Clinical EAE outcomes

Clinically measurable EAE paralysis was observed in 4 of 8 HuPBMC mice (50%) induced with the complete formulation (CFA + MOG + PTx), as well as in 1 of 5 HuPBMC mice (20%) that received blank CFA and PTx without myelin antigen in the emulsion (Table 4.4). EAE paralysis was not observed in any of the other treatment groups. The incidence of xGvHD symptoms in this cohort, whether they remained mild or became fully established by the day 19 – 22 endpoint, occurred in well over half of the HuPBMC mice in most groups regardless of the inducing adjuvant components administered (see Table 4.4 for xGvHD symptom descriptions). The clinical course of EAE symptoms proceeded similarly among all HuPBMC mice that developed paralysis following immunization with either blank CFA/PTx or complete MOG emulsion (Figure 4.53A – B). These data demonstrated that the inclusion of MOG antigen promoted increased overall incidence of EAE symptoms compared to myelin antigen-free formulations (Figure 4.53C), but that blank CFA and PTx combined were still able to generate CNS damage sufficient to cause paralysis in a smaller fraction of immunized HuPBMC mice.

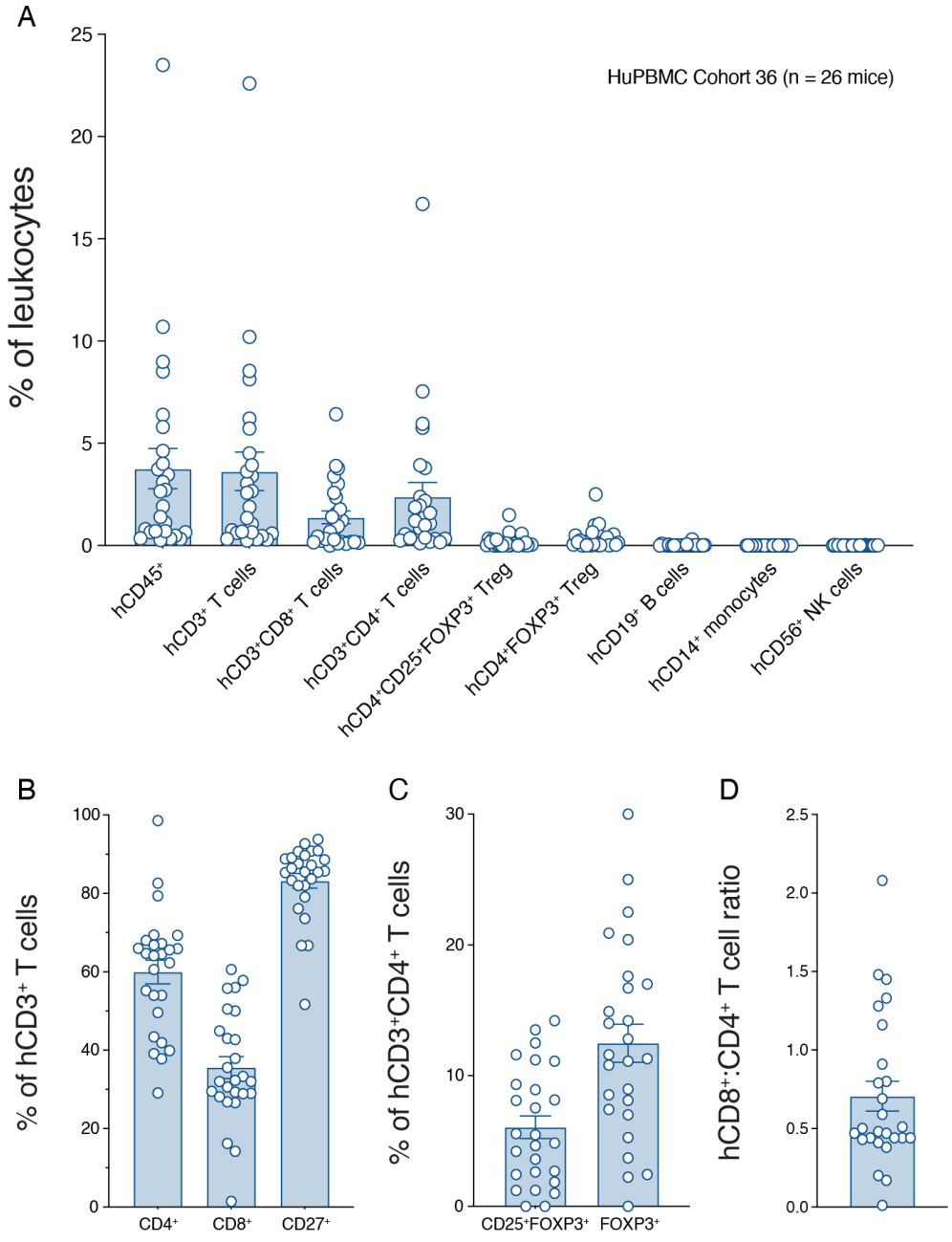

Figure 4.52 Peripheral blood reconstitution of mice in HuPBMC cohort 36

(A) Relative proportions of all measured human immune cell lineages are shown as a proportion of total leukocytes (murine and human) in the peripheral blood day 19 (3 weeks) post-PBMC engraftment of male NSG mice (n = 26) derived from healthy female donor HD-04. (B) Proportions of T cell subsets among $hCD3^+$ T cells. (C) Proportions of regulatory T cell (Treg) subsets among $hCD3^+CD4^+$ T cells. (D) $hCD3^+CD8^+$ to $hCD3^+CD4^+$ T cell ratio. Data are shown as mean with SEM.

Table 4.3 Induction of HuPBMC mice with individual and combined EAE adjuvant components

Seven cages of NSG mice (n = 26 males) were humanized by IV injection of 5 x 10^6 healthy female donor PBMCs (HD-04, HuPBMC cohort 36). One cage of NSG mice (n = 4 males) received blank PBS by IV injection (control, ctrl). Subgroups of 4 – 8 mice were induced by 100 μL subcutaneous injection of blank CFA emulsion (100 μL IFA with 400 μg of M. Tuberculosis) or mixed MOG CFA emulsion containing 100 μg rhMOG and 200 μg MOG_{35-55} antigen. An intraperitoneal injection of 200 ng pertussis toxin (PTx) was administered days 0 and 2 to specified groups. Peripheral blood reconstitution of human immune cells day 19 post-PBMC injection is noted for individual mice as well as the average proportions per subgroup with standard deviation prior to induction.

Mouse ID	Engraftment	Induction treatment	Group size	%hCD45$^+$ of leukocytes	Group %hCD45$^+$ of leukocytes	
					Average	Standard deviation
1	PBS ctrl	Mixed MOG EAE	4	0.00	0.00	0.00
2				0.00		
3				0.00		
4				0.00		
5	PBMC	Mixed MOG EAE	8	0.83	6.10	7.90
6				7.23		
7				25.0		
8				3.76		
9				3.26		
10				1.11		
11				4.85		
12				2.77		
13	PBMC	PTx only (no antigen or CFA)	4	9.91	6.32	5.71
14				2.20		
15				0.75		
16				12.4		
17	PBMC	CFA + mixed MOG (no PTx)	5	0.35	2.00	1.97
18				0.66		
19				4.02		
20				4.27		
21				0.69		
22	PBMC	CFA only (no antigen or PTx)	4	0.32	1.31	1.15
23				2.84		
24				1.55		
25				0.53		
26	PBMC	CFA + PTx (no antigen)	5	0.34	3.41	4.22
27				6.47		
28				0.29		
29				0.62		
30				9.33		

Separately administering either blank CFA emulsion, MOG-replete CFA emulsion, or PTx alone did not generate any clinical symptoms of EAE in HuPBMC recipients (Figure 4.53A – C), indicating that both an immune stimulant and a BBB permeabilizing agent, or perhaps the synergistic effect from the combination of adjuvants, was necessary. The occurrence of xGvHD symptoms and the degree of weight loss, which are immunopathological consequences of graft reactivity influenced mainly by the blood donor in HuPBMC models[695,696], proceeded variably but were not selectively exacerbated in groups with EAE paralysis, suggesting symptomatic EAE and xGvHD incidence were not interdependent events (i.e., immunized HuPBMC mice could develop symptoms of EAE without xGvHD, or vice versa, or develop both/neither) (Figure 4.53D – E). The data also suggest that CFA and PTx both had similar effects on the magnitude of nonspecific graft reactivity in the periphery, as no one group was particularly affected by xGvHD, which would be expected if one or both of the adjuvants significantly promoted general human T cell activity in PBMC engrafted NSG mice.

Table 4.4 Incidence of EAE and xGvHD symptoms in HuPBMC mice induced with different EAE adjuvant components

Groups of unengrafted male NSG mice (n = 4 PBS controls) and HuPBMC mice (n = 4 – 8 male NSG mice/ group, 3 weeks post-engraftment with healthy female HD-04 PBMCs) were induced with one or more EAE adjuvant components (CFA, MOG and/or PTx) and scored daily for symptoms of EAE paralysis or xenogeneic (x)GvHD inflammation until day 19 – 22. Mild xGvHD was determined by the appearance of pink colored skin on the ears and face indicative of local inflammation that did not progress beyond this symptom (early sign). Established xGvHD was determined by the appearance of red inflamed skin, dry skin, abdominal/ facial hair loss, and/or jaundice that persisted until endpoint. MOG = 100 μg rhMOG$_{1-120}$ protein and 200 μg MOG$_{35-55}$ peptide mixed.

Humanization	Induction	EAE symptom incidence	Mild xGvHD incidence	Established xGvHD incidence
PBS control	CFA + MOG + PTx	0 / 4	0 / 4	0 / 4
PBMC	CFA + MOG + PTx	**4 / 8**	1 / 8	6 / 8
PBMC	CFA + MOG	0 / 5	1 / 5	3 / 5
PBMC	CFA + PTx	**1 / 5**	1 / 5	1 / 5
PBMC	CFA	0 / 4	3 / 4	1 / 4
PBMC	PTx	0 / 4	0 / 4	3 / 4

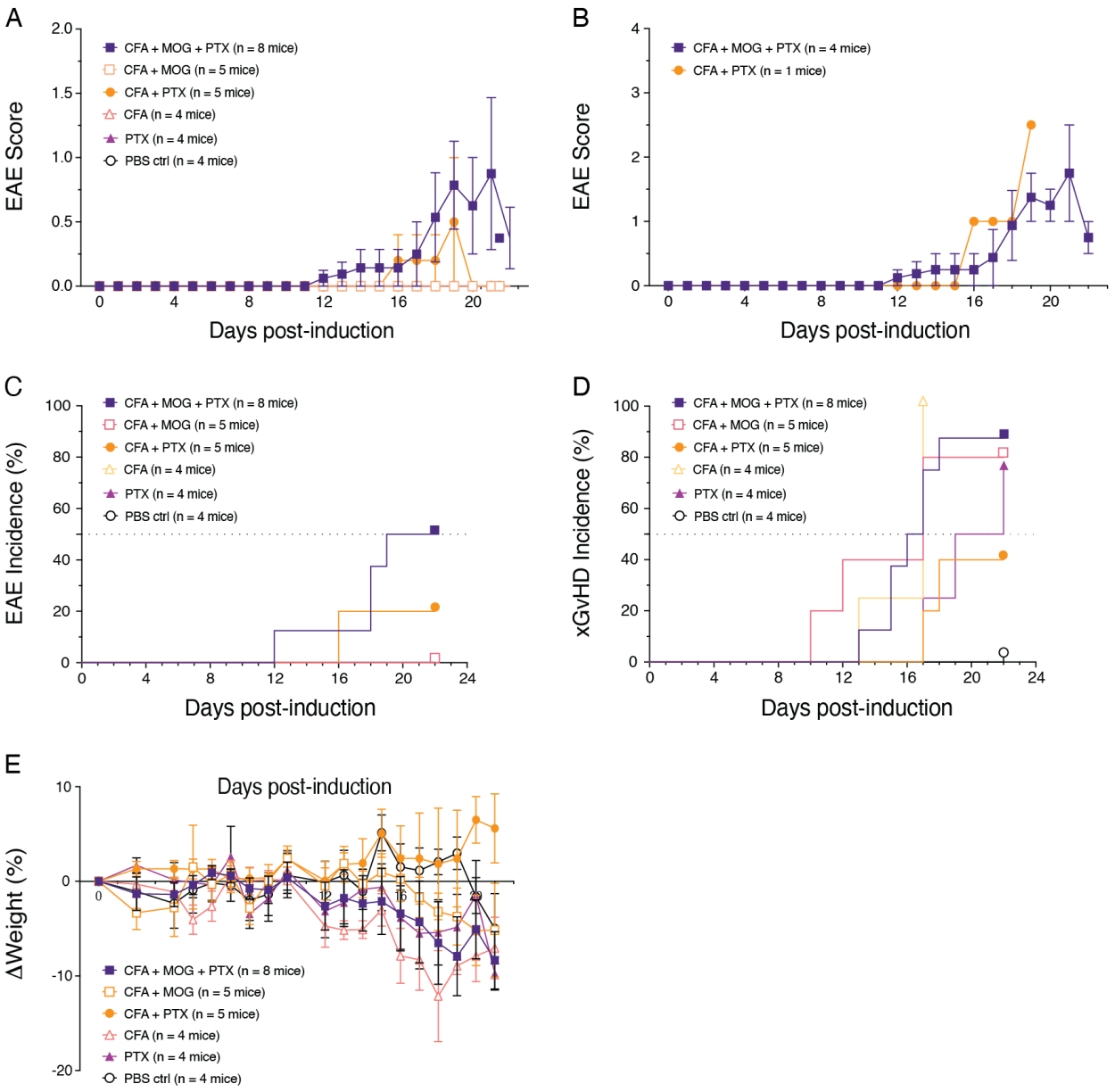

Figure 4.53 Clinical EAE and xGvHD outcomes for HuPBMC mice induced with different EAE adjuvant components

Figure shows (A) clinical EAE scores for all variably induced HuPBMC cohort 36 mice (n = 4 – 8/ group, derived from HD-04 female PBMCs) and (B) clinical EAE scores for symptomatic mice only (n = 4 of 8 full CFA + MOG + PTx induced mice and n = 1 of 5 antigen-free CFA + PTx induced mice). Data are shown as mean with SEM. (C) The incidence of paralytic EAE symptoms and (D) inflammatory xenogeneic (x)GvHD symptoms over time for all variably induced mice (n = 4 – 8 mice/group). Data are shown as percentage of the group. (E) Weight loss over time for all variably induced HuPBMC mice (n = 4 – 8/ group). Data are shown as mean with SEM.

4.8.4 Influence of antigen and adjuvant components on tissue infiltration post-induction

The quantities of murine and human immune cells in the brain, spinal cord, spleen, liver, and intestinal lamina propria were compared between HuPBMC groups to assess the effects of each immunization component on CNS and peripheral tissue infiltration due to EAE and/or graft reactivity (Figure 4.54 – Figure 4.63). Given that only 3 – 7 mice per group from a single blood donation cohort could be immunized with each adjuvant component combination, and the fact that highly variable engraftment is observed among mice in the same HuPBMC cohort (Figure 4.52), statistical significance between treatment groups could not be reliably determined in this preliminary analysis. Despite this limitation, we observed a general trend of greater average leukocyte abundance in the brain and spinal cord tissues from treatment groups in which PTx was administered, whereas this trend was not evident in peripheral tissues (Figure 4.54), suggesting PTx specifically promoted CNS infiltration without enhancing immune cell proliferation systemically. $mCD45^{lo}$ CNS resident microglia counts followed the same trend as the general leukocyte counts (Figure 4.55). The proportions of these microglia expressing high or low levels of CD11b was not differentially altered by any of the inducing formulations (Appendix 8, Figure A.35). Though we measured slightly greater uptake of MBP by $CD11b^{lo}$ microglia in the brain in the full EAE induction group (CFA + MOG + PTx) compared to the other groups (Figure 4.56C), the individual and combined induction components did not appear to determine the proportion of microglia subsets that contained intracellular MBP following immunization (Figure 4.56).

Consistent with total leukocyte quantities, $mCD45^{hi}$ myeloid cell infiltration followed the same trend of greater numbers in the CNS tissues of groups in which PTx was administered, but not in the corresponding peripheral tissues (Figure 4.57). Likewise, separate induction components did not selectively skew the proportions of $mCD45^{hi}$ myeloid cells expressing high or low levels of CD11b in any of the examined tissues (Appendix 8, Figure A.36 – Figure A.38). In all immunization groups, the proportion of CNS infiltrating $mCD45^{hi}CD11b^{hi}$ macrophages that had phagocytosed MBP was comparable, though some full EAE induced mouse brains contained greater proportions of $mCD45^{hi}CD11b^{hi}MBP^{+}$ cells (Figure 4.58A – B). As expected, less than 1% of $mCD45^{hi}CD11b^{hi}$ macrophages in peripheral tissues contained intracellular MBP (Figure 4.58C – E). Generally, relative leukocyte subset abundance by treatment group showed an inverse pattern between the corresponding spleen and liver tissues, suggesting trafficking of these cells from the

spleen to the liver post-immunization consistent with nonspecific graft reactivity, though confirming this possibility would require a more tailored assessment.

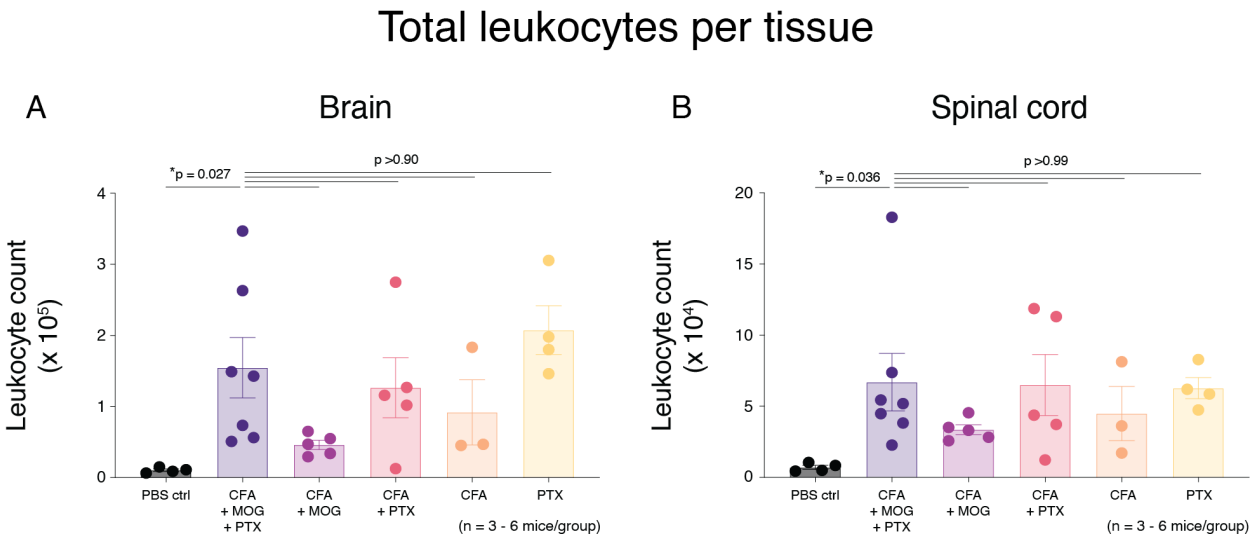

Figure 4.54 Quantification of total leukocytes in the CNS and periphery of HuPBMC mice induced with different EAE adjuvant components

Figure shows the total number of leukocytes (murine and human) in the (A) brain, (B) spinal cord, (C) spleen, (D) liver, and (E) intestinal lamina propria on days 19 – 22 post-immunization of PBS engrafted control NSG mice induced with the full mixed MOG EAE immunization containing rhMOG and MOG_{35-55} antigen emulsified in CFA, co-administered PTx (PBS ctrl, n = 4 mice) and HuPBMC mice (n = 26 mice all derived from HD-04 female PBMCs) induced with full mixed EAE immunization (CFA + MOG + PTx, n = 7 mice), mixed MOG emulsion without PTx (CFA + MOG, n = 5 mice), blank CFA emulsion and PTx without antigen (CFA + PTx, n = 5 mice), blank CFA emulsion only without antigen or PTx (CFA, n = 3 mice), or PTx only without emulsion (PTx, n = 4 mice). Tissues were perfused prior to cell isolation. Data are shown as mean with SEM and were analyzed by Brown-Forsythe and Welch ANOVA with Dunnett's T3 multiple comparisons test or by Kruskal-Wallis with Dunn's multiple comparisons test.

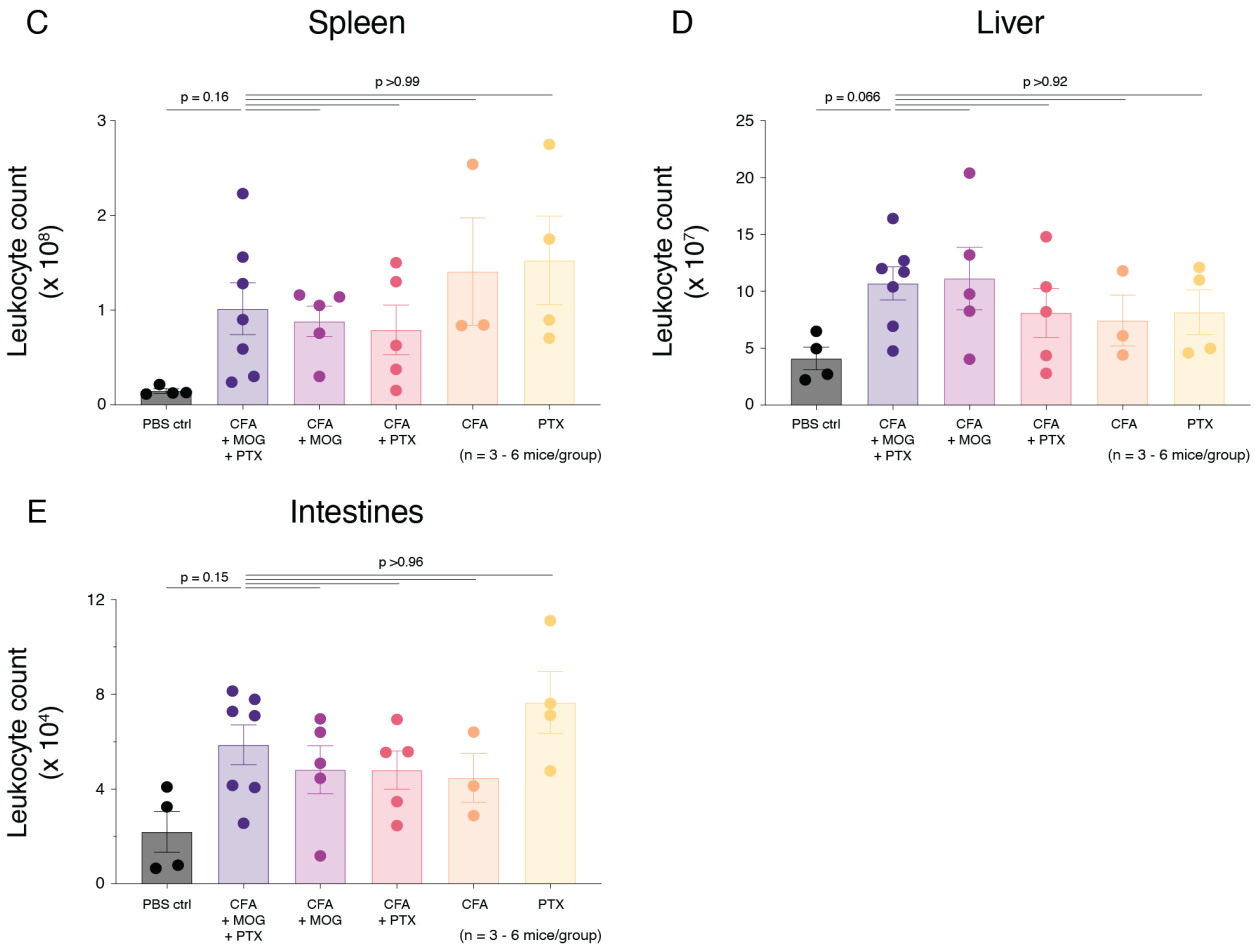

Figure 4.54 continued

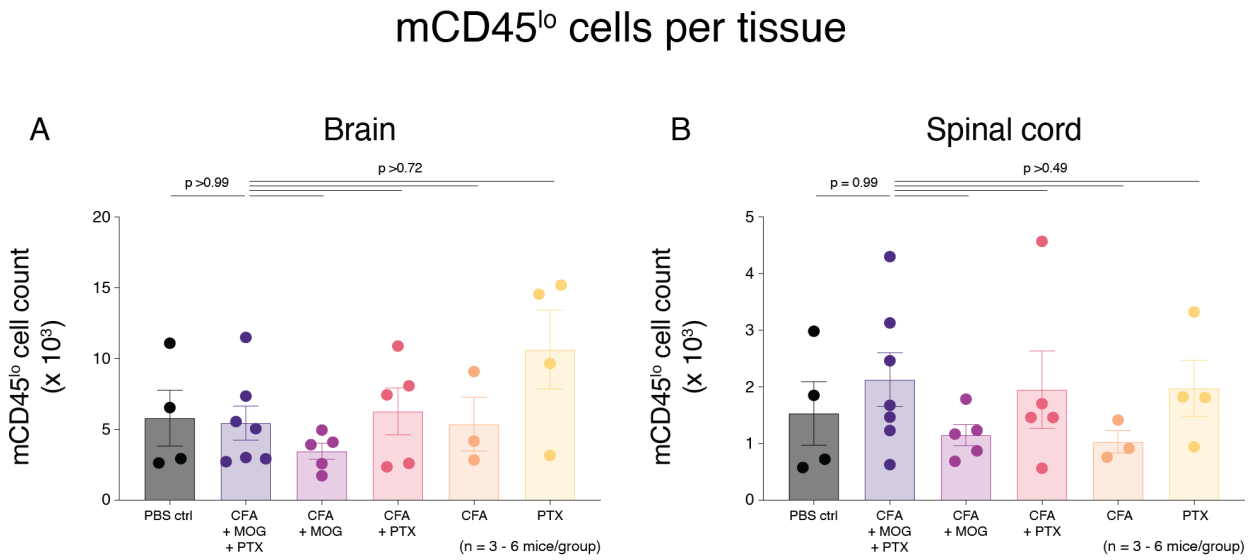

Figure 4.55 Quantification of CNS resident murine myeloid cells in HuPBMC mice induced with different EAE adjuvant components

Figure shows the total number of resident murine mCD45^{lo} myeloid cells in the (A) brain and (B) spinal cord on days 19 – 22 post-immunization of PBS engrafted control NSG mice induced with the full mixed MOG EAE immunization containing rhMOG and MOG_{35-55} antigen emulsified in CFA, co-administered PTx (n = 4 mice) and HuPBMC mice (n = 26 mice all derived from HD-04 female PBMCs) induced with full mixed EAE immunization (CFA + MOG + PTx, n = 7 mice), mixed MOG emulsion without PTx (CFA + MOG, n = 5 mice), blank CFA emulsion and PTx without antigen (CFA + PTx, n = 5 mice), blank CFA emulsion only without antigen or PTx (CFA, n = 3 mice), or PTx only without emulsion (PTx, n = 4 mice). Tissues were perfused prior to cell isolation. Data are shown as mean with SEM and were analyzed by Brown-Forsythe and Welch ANOVA with Dunnett's T3 multiple comparisons test or by Kruskal-Wallis with Dunn's multiple comparisons test.

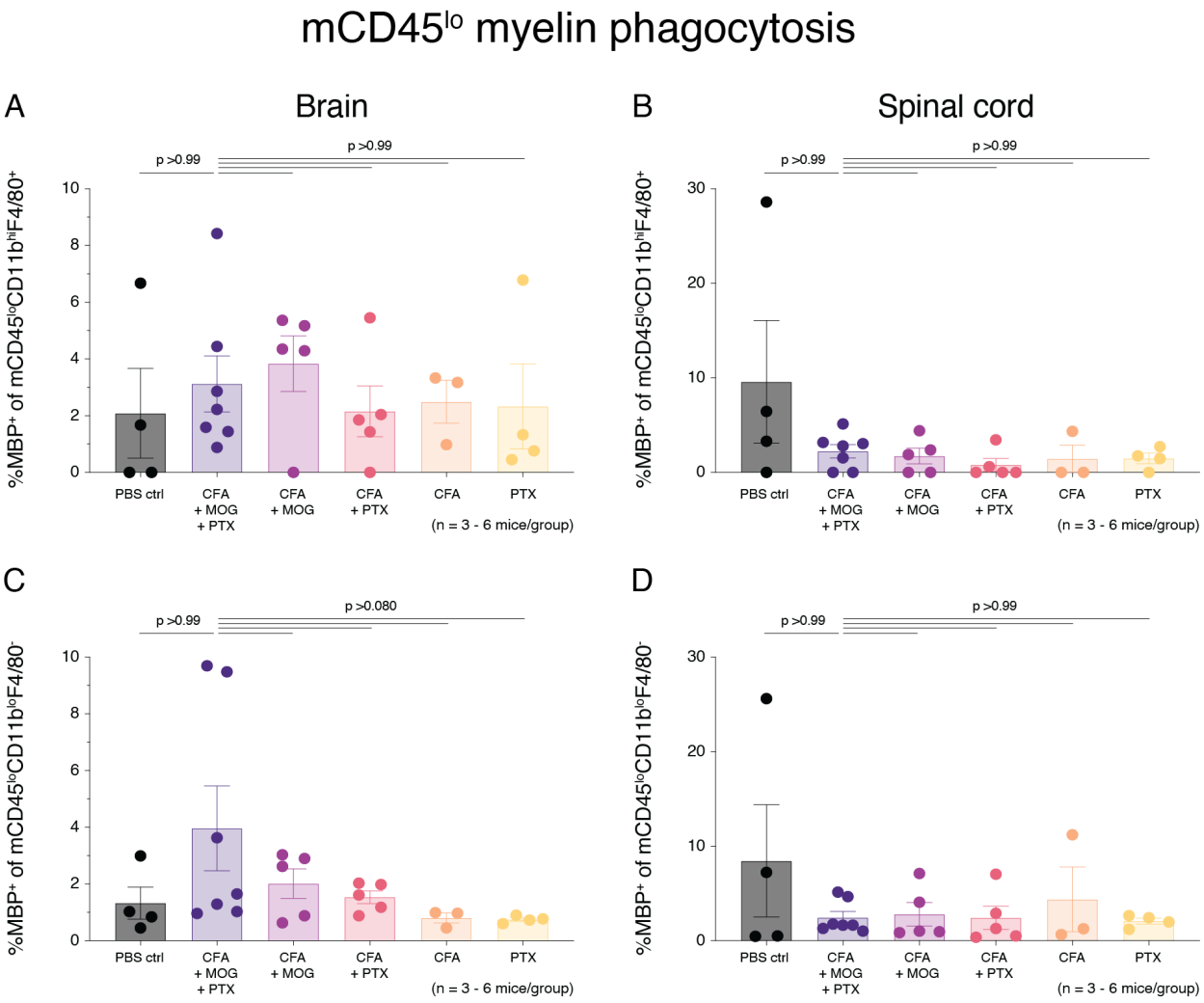

Figure 4.56 Myelin phagocytosis by CNS resident murine myeloid cells in HuPBMC mice induced with different EAE adjuvant components

Figure shows the proportion of resident murine mCD45^{lo} CD11b^{hi}F/40^{+} (A – B) and CD11b^{lo}F4/80^{-} (C – D) myeloid cells in the brain (left) and spinal cord (right) containing intracellular myelin basic protein (MBP^{+}) on days 19 – 22 post-immunization of PBS engrafted control NSG mice induced with the full mixed MOG EAE immunization containing rhMOG and MOG$_{35-55}$ antigen emulsified in CFA, co-administered PTx (n = 4 mice) and HuPBMC mice (n = 26 mice all derived from HD-04 female PBMCs) induced with full mixed EAE immunization (CFA + MOG + PTx, n = 7 mice), mixed MOG emulsion without PTx (CFA + MOG, n = 5 mice), blank CFA emulsion and PTx without antigen (CFA + PTx, n = 5 mice), blank CFA emulsion only without antigen or PTx (CFA, n = 3 mice), or PTx only without emulsion (PTx, n = 4 mice). Tissues were perfused prior to cell isolation. Data are shown as mean with SEM and were analyzed by Brown-Forsythe and Welch ANOVA with Dunnett's T3 multiple comparisons test or by Kruskal-Wallis with Dunn's multiple comparisons test.

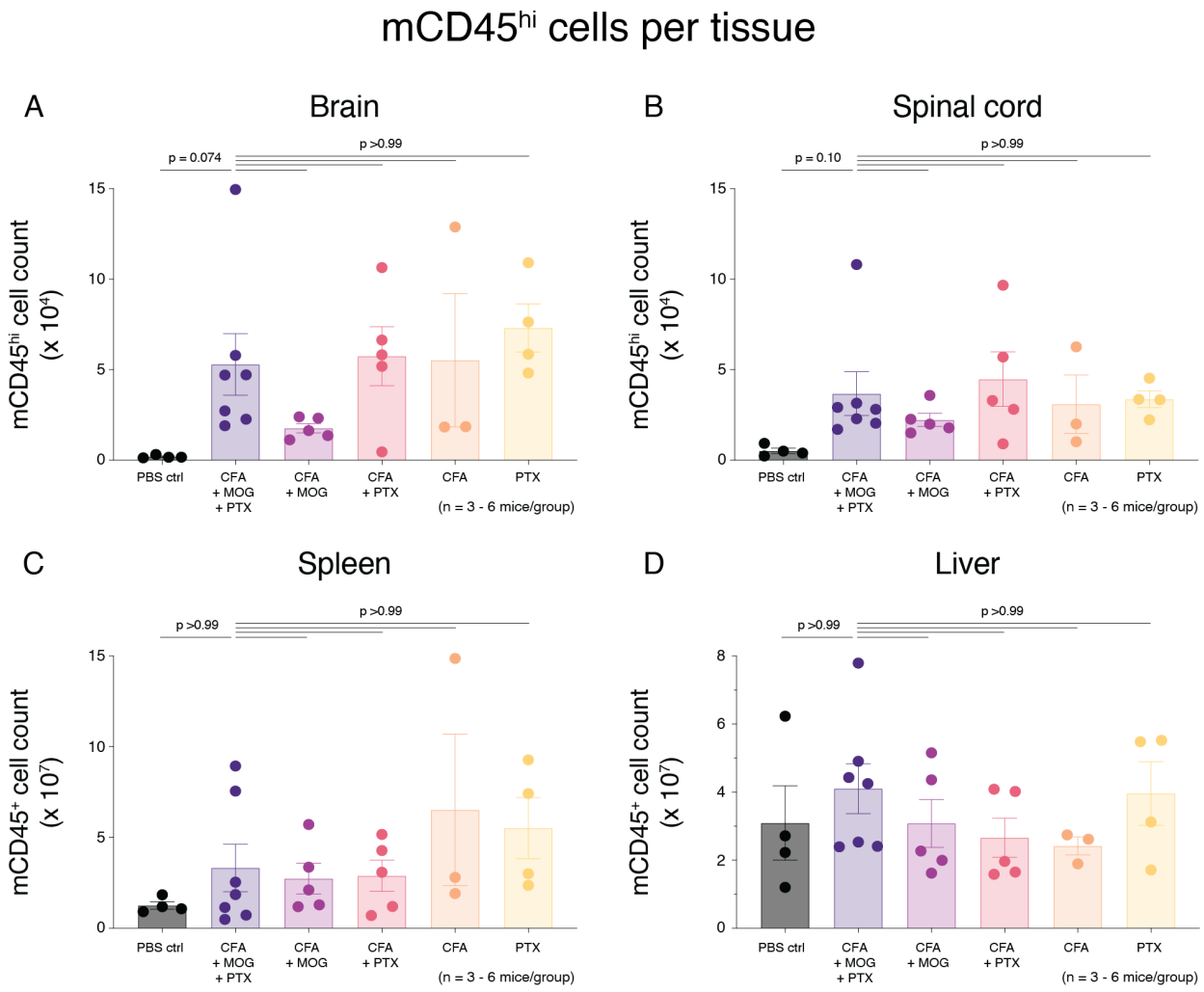

Figure 4.57 Quantification of murine myeloid cells in the CNS and periphery of HuPBMC mice induced with different EAE adjuvant components

Figure shows the total number of murine mCD45$^{hi/+}$ myeloid cells in the (A) brain, (B) spinal cord, (C) spleen, (D) liver, and (E) intestinal lamina propria on days 19 – 22 post-immunization of PBS engrafted control NSG mice induced with the full mixed MOG EAE immunization containing rhMOG and MOG$_{35-55}$ antigen emulsified in CFA with PTx co-administered (PBS ctrl, n = 4 mice) and HuPBMC mice (n = 26 mice all derived from HD-04 female PBMCs) induced with full mixed EAE immunization (CFA + MOG + PTx, n = 7 mice), mixed MOG emulsion without PTx (CFA + MOG, n = 5 mice), blank CFA emulsion and PTx without antigen (CFA + PTx, n = 5 mice), blank CFA emulsion only without antigen or PTx (CFA, n = 3 mice), or PTx only without emulsion (PTx, n = 4 mice). Tissues were perfused prior to cell isolation. Data are shown as mean with SEM and were analyzed by Brown-Forsythe and Welch ANOVA with Dunnett's T3 multiple comparisons test or by Kruskal-Wallis with Dunn's multiple comparisons test.

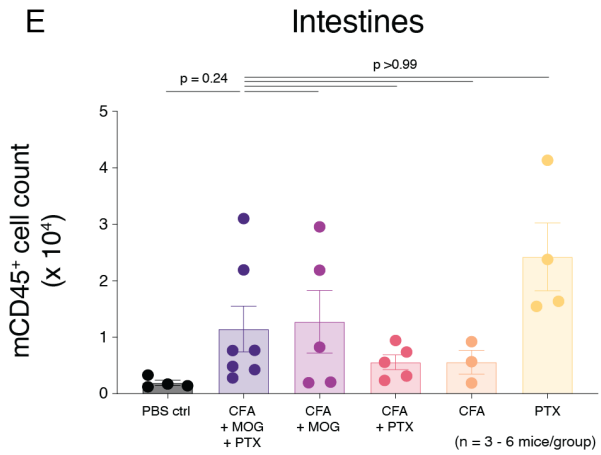

Figure 4.57 continued

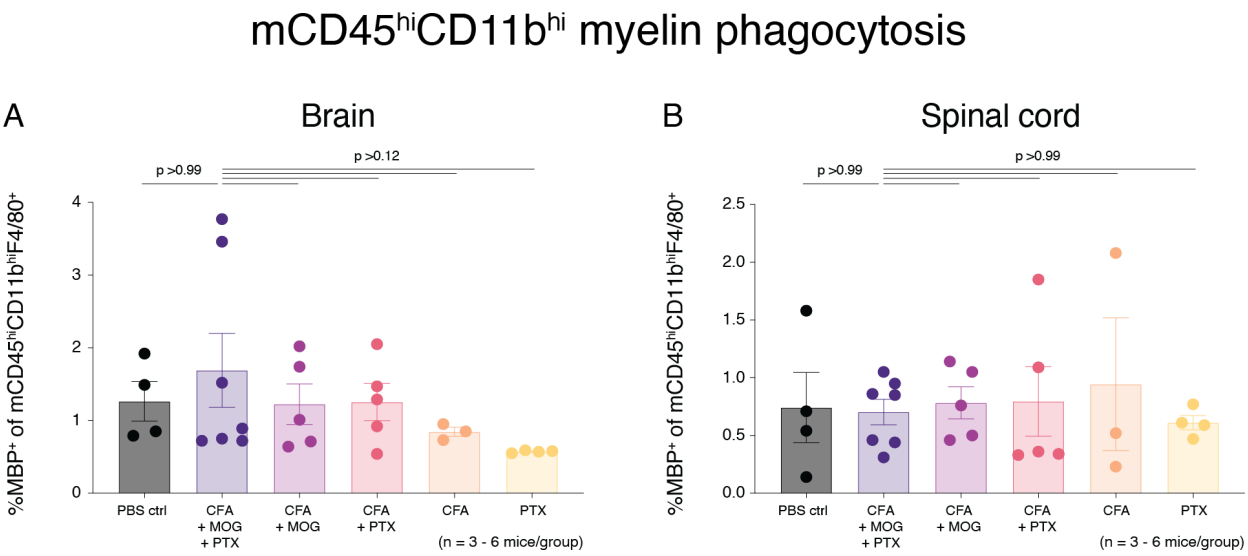

Figure 4.58 Myelin phagocytosis by murine myeloid cells in the CNS and periphery of HuPBMC mice induced with different EAE adjuvant components

Figure shows the proportion of murine mCD45$^{hi/+}$CD11b^{hi}F/40^{+} myeloid cells in the (A) brain, (B) spinal cord, (C) spleen, (D) liver, and (E) intestinal lamina propria containing intracellular myelin basic protein (MBP^{+}) on days 19 – 22 post-immunization of PBS engrafted control NSG mice induced with the full mixed MOG EAE immunization containing rhMOG and MOG$_{35-55}$ antigen emulsified in CFA, co-administered PTx (n = 4 mice) and HuPBMC mice (n = 26 mice all derived from HD-04 female PBMCs) induced with full mixed EAE immunization (CFA + MOG + PTx, n = 7 mice), mixed MOG emulsion without PTx (CFA + MOG, n = 5 mice), blank CFA emulsion and PTx without antigen (CFA + PTx, n = 5 mice), blank CFA emulsion only without antigen or PTx (CFA, n = 3 mice), or PTx only without emulsion (PTx, n = 4 mice). Tissues were perfused prior to cell isolation. Data are shown

as mean with SEM and were analyzed by Brown-Forsythe and Welch ANOVA with Dunnett's T3 multiple comparisons test or by Kruskal-Wallis with Dunn's multiple comparisons test.

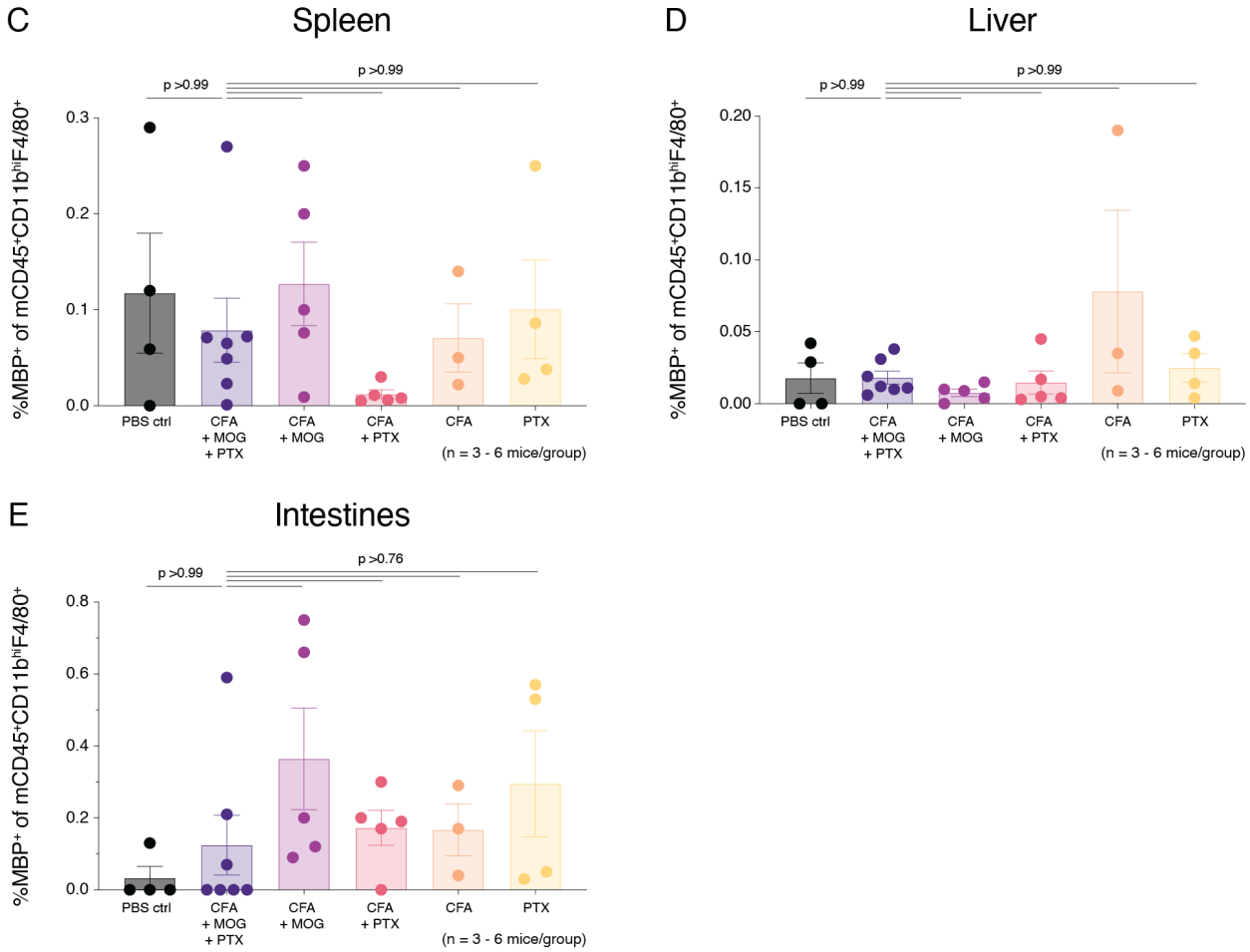

Figure 4.58 continued

PTx administration promoted hCD45$^+$ immune cell infiltration and/or expansion in the CNS tissues even more so than for murine myeloid cell populations (Figure 4.59A – B), while the peripheral tissues again contained similar numbers of hCD45$^+$ cells (>90% of which were hCD3$^+$ T cells) regardless of the components included in the immunization formulation (Figure 4.59C – E; Appendix 8, Figure A.40). The separate immunization components also did not substantially influence the relatively low abundance of hCD45$^+$CD14$^+$CD68$^+$ macrophages in most tissues, though total counts did follow the increased trend with PTx in the brain and the inverse decreased trend in the spleen (Figure 4.60). In all treatment groups, very few of the CNS infiltrating human

macrophages contained intracellular MBP, and, as expected, none were detected in the peripheral tissues (Appendix 8, Figure A.39).

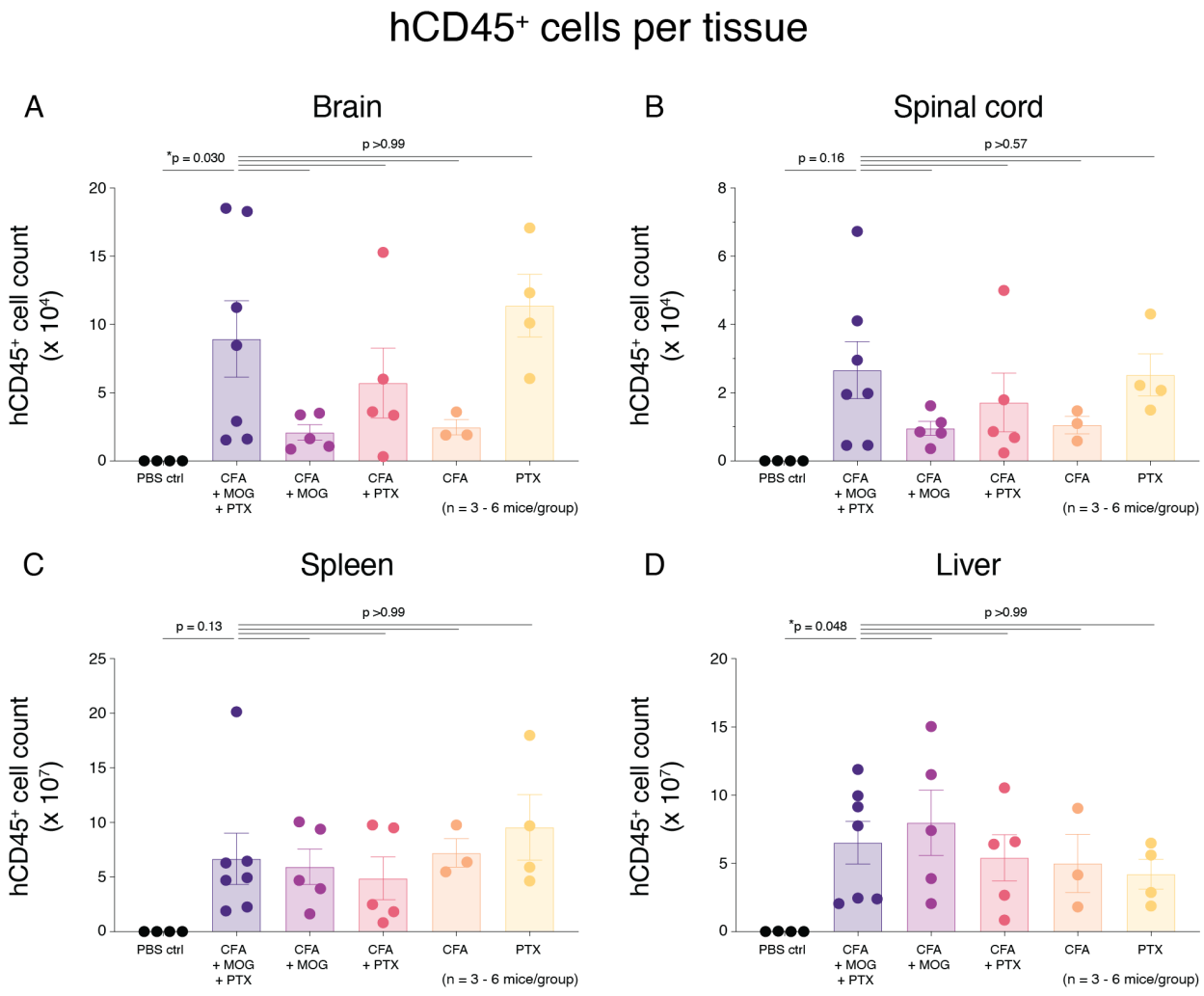

Figure 4.59 Quantification of total human immune cell numbers in the CNS and periphery of HuPBMC mice induced with different EAE adjuvant components

Figure shows the total number of human hCD45$^+$ immune cells in the (A) brain, (B) spinal cord, (C) spleen, (D) liver, and (E) intestinal lamina propria on days 19 – 22 post-immunization of PBS engrafted control NSG mice induced with the full mixed MOG EAE immunization containing rhMOG and MOG$_{35-55}$ antigen emulsified in CFA with PTx co-administered (PBS ctrl, n = 4 mice) and HuPBMC mice (n = 26 mice all derived from HD-04 female PBMCs) induced with full mixed EAE immunization (CFA + MOG + PTx, n = 7 mice), mixed MOG emulsion without PTx (CFA + MOG, n = 5 mice), blank CFA emulsion and PTx without antigen (CFA + PTx, n = 5 mice), blank CFA emulsion only without antigen or PTx (CFA, n = 3 mice), or PTx only without emulsion (PTx, n = 4 mice). Tissues were perfused prior to cell isolation. Data are shown as mean with SEM and were analyzed by Brown-Forsythe and

Welch ANOVA with Dunnett's T3 multiple comparisons test or by Kruskal-Wallis with Dunn's multiple comparisons test.

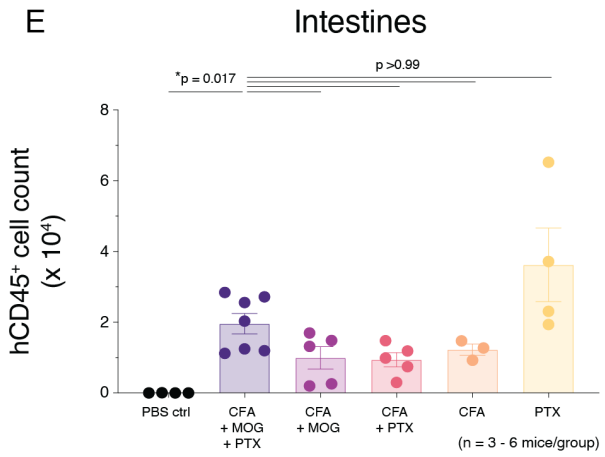

Figure 4.59 continued

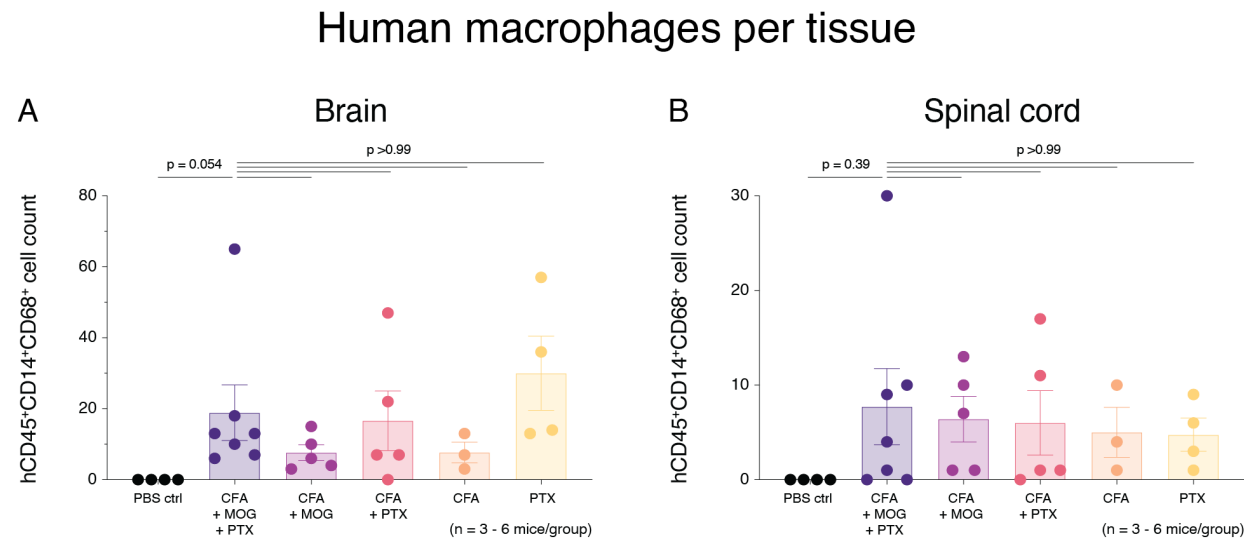

Figure 4.60 Quantification of human macrophages in the CNS and periphery of HuPBMC mice induced with different EAE adjuvant components

Figure shows the total number of human $hCD45^+CD14^+CD68^+$ macrophages in the (A) brain, (B) spinal cord, (C) spleen, (D) liver, and (E) intestinal lamina propria on days 19 – 22 post-immunization of PBS engrafted control NSG mice induced with the full mixed MOG EAE immunization containing rhMOG and MOG_{35-55} antigen emulsified in CFA with PTx co-administered (PBS ctrl, n = 4 mice) and HuPBMC mice (n = 26 mice all derived from HD-04 female PBMCs) induced with full mixed EAE immunization (CFA + MOG + PTx, n = 7 mice), mixed MOG emulsion without PTx (CFA + MOG, n = 5 mice), blank CFA emulsion and PTx without antigen (CFA + PTx, n = 5 mice),

blank CFA emulsion only without antigen or PTx (CFA, n = 3 mice), or PTx only without emulsion (PTx, n = 4 mice). Tissues were perfused prior to cell isolation. Data are shown as mean with SEM and were analyzed by Brown-Forsythe and Welch ANOVA with Dunnett's T3 multiple comparisons test or by Kruskal-Wallis with Dunn's multiple comparisons test.

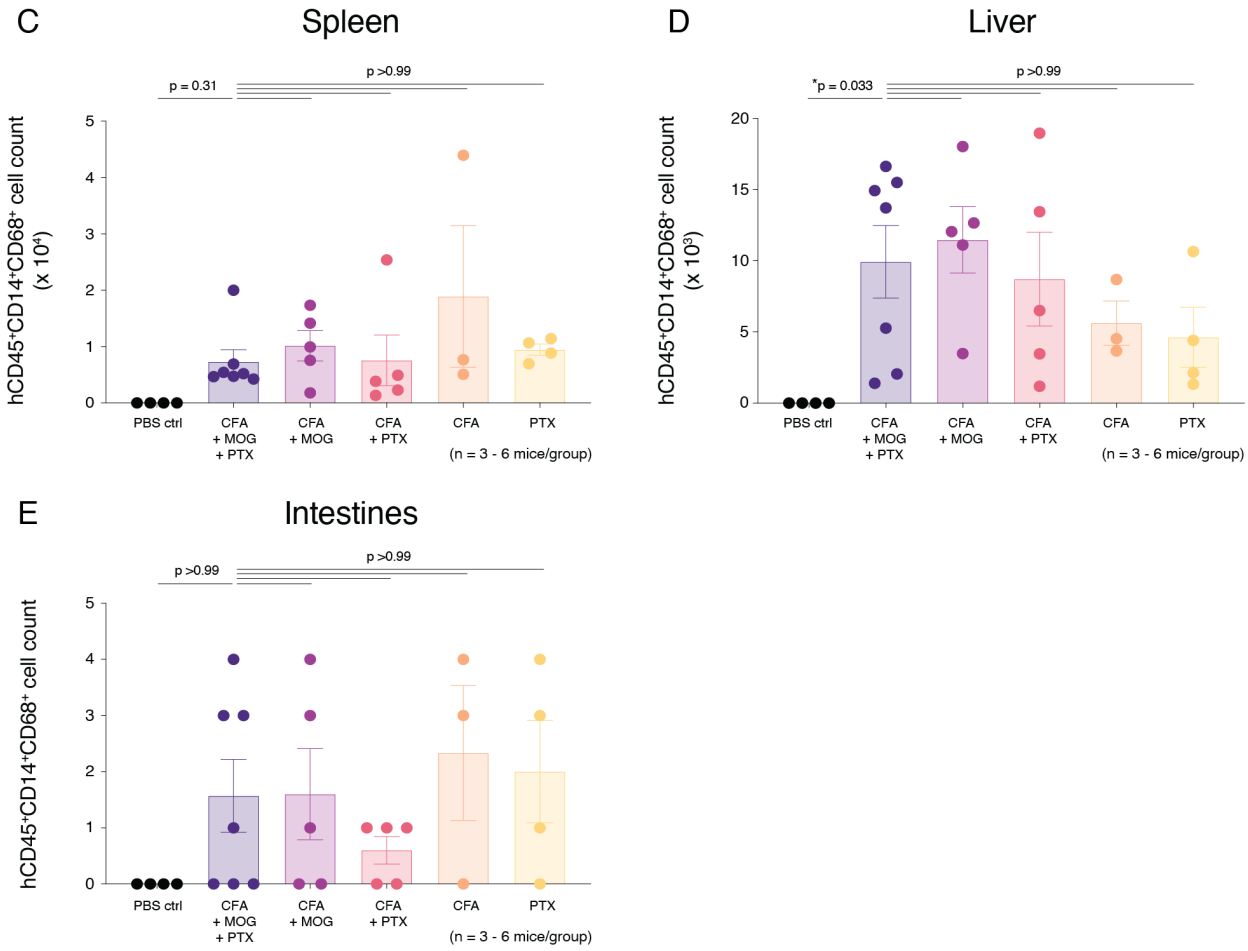

Figure 4.60 continued

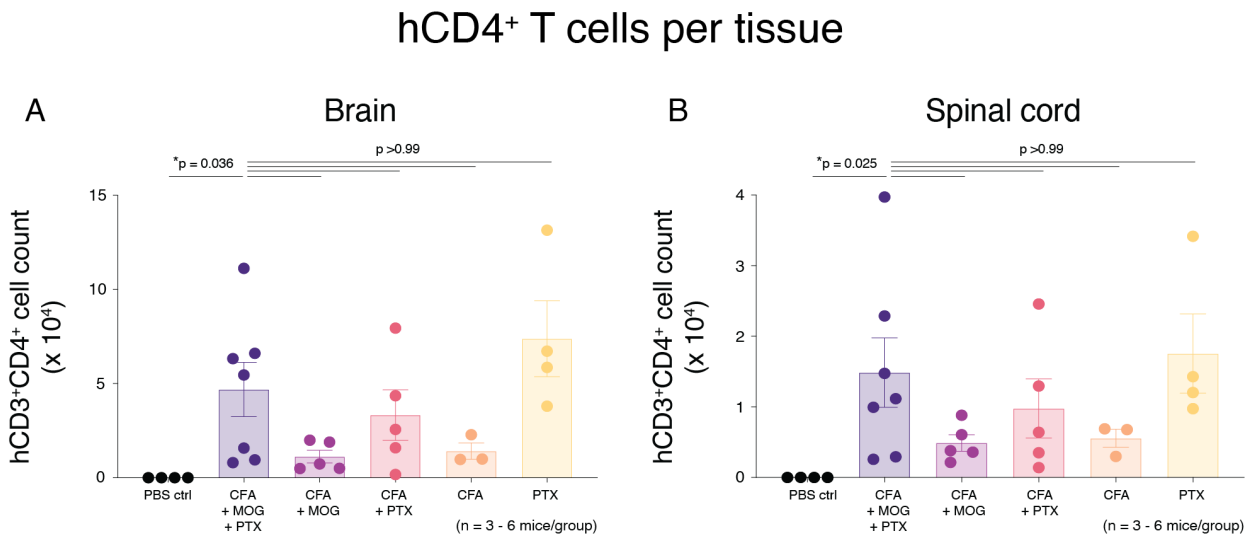

Figure 4.61 Quantification of human CD4$^+$ T cells in the CNS and periphery of HuPBMC mice induced with different EAE adjuvant components

Figure shows the total number of human hCD45$^+$CD3$^+$CD4$^+$(CD8$^-$) T cells in the (A) brain, (B) spinal cord, (C) spleen, (D) liver, and (E) intestinal lamina propria on days 19 – 22 post-immunization of PBS engrafted control NSG mice induced with the full mixed MOG EAE immunization containing rhMOG and MOG$_{35-55}$ antigen emulsified in CFA with PTx co-administered (PBS ctrl, n = 4 mice) and HuPBMC mice (n = 26 mice all derived from HD-04 female PBMCs) induced with full mixed EAE immunization (CFA + MOG + PTx, n = 7 mice), mixed MOG emulsion without PTx (CFA + MOG, n = 5 mice), blank CFA emulsion and PTx without antigen (CFA + PTx, n = 5 mice), blank CFA emulsion only without antigen or PTx (CFA, n = 3 mice), or PTx only without emulsion (PTx, n = 4 mice). Tissues were perfused prior to cell isolation. Data are shown as mean with SEM and were analyzed by Brown-Forsythe and Welch ANOVA with Dunnett's T3 multiple comparisons test or by Kruskal-Wallis with Dunn's multiple comparisons test.

Among hCD3$^+$ T cells in each tissue, the proportions expressing hCD4 or hCD8 were not altered by any of the EAE inducing components (Appendix 8, Figure A.41, Figure A.42). To note, the enzymatic digestion protocol used to process intestinal tissues for isolation of lamina propria lymphocytes (LPLs) resulted in the cleavage of hCD4 on the surface of hCD3$^+$ T cells, and therefore hCD4$^+$ T cells were identified by their negative expression of hCD8 (hCD3$^+$CD8$^-$) in intestinal samples. Both hCD3$^+$CD4$^+$ and hCD3$^+$CD8$^+$ T cell counts followed the same general increasing trend in the CNS with PTx administration but were otherwise comparable between immunization groups (Figure 4.61, Figure 4.62). Accordingly, none of the immunization formulations differentially skewed the relative ratio of hCD8$^+$ and hCD4$^+$ T cells in any of the

peripheral tissues (Figure 4.63C – E), though a slight decrease in the $hCD8^+$:$CD4^+$ T cell ratio was observed in the CNS tissues from groups given PTx (Figure 4.63A – B).

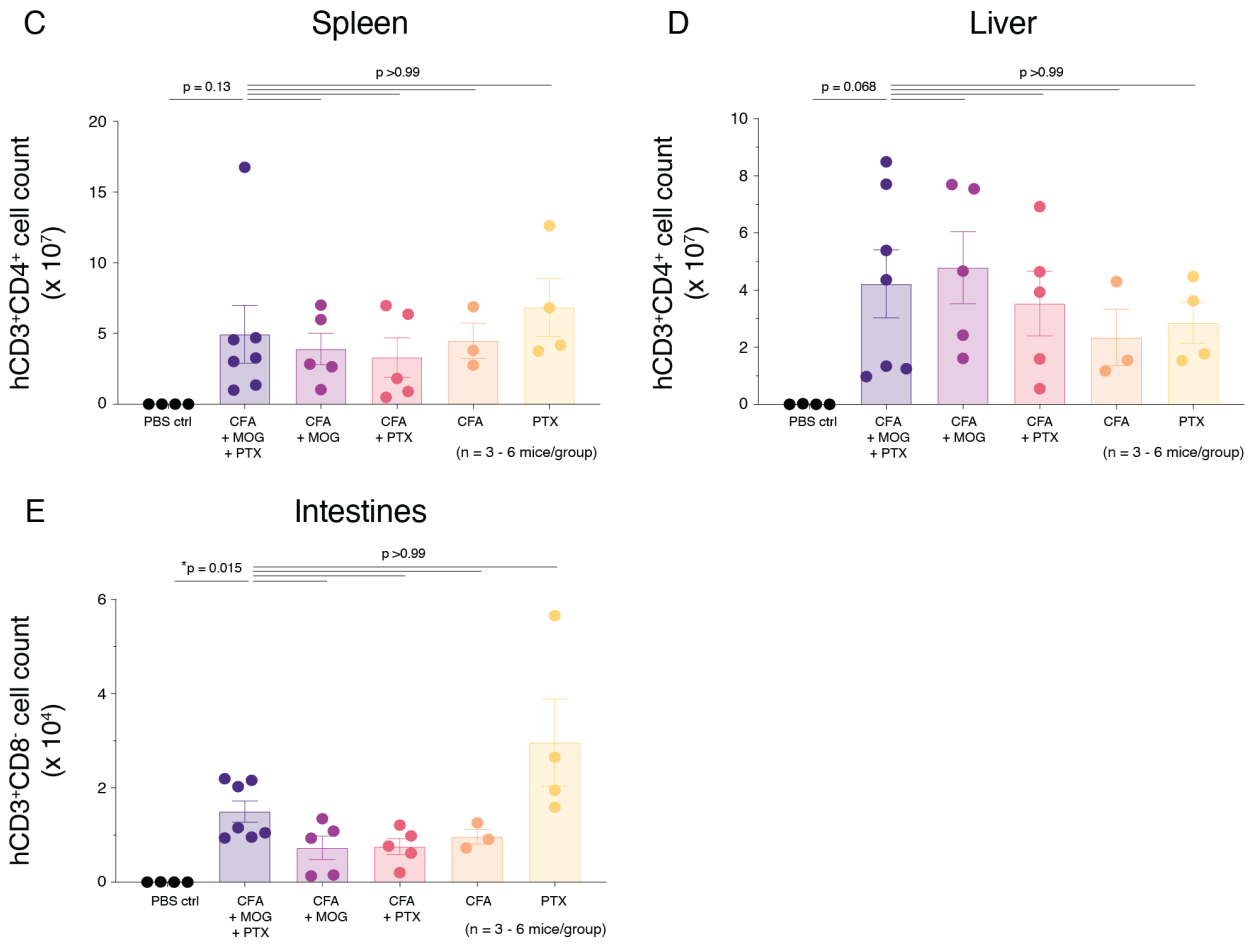

Figure 4.61 continued

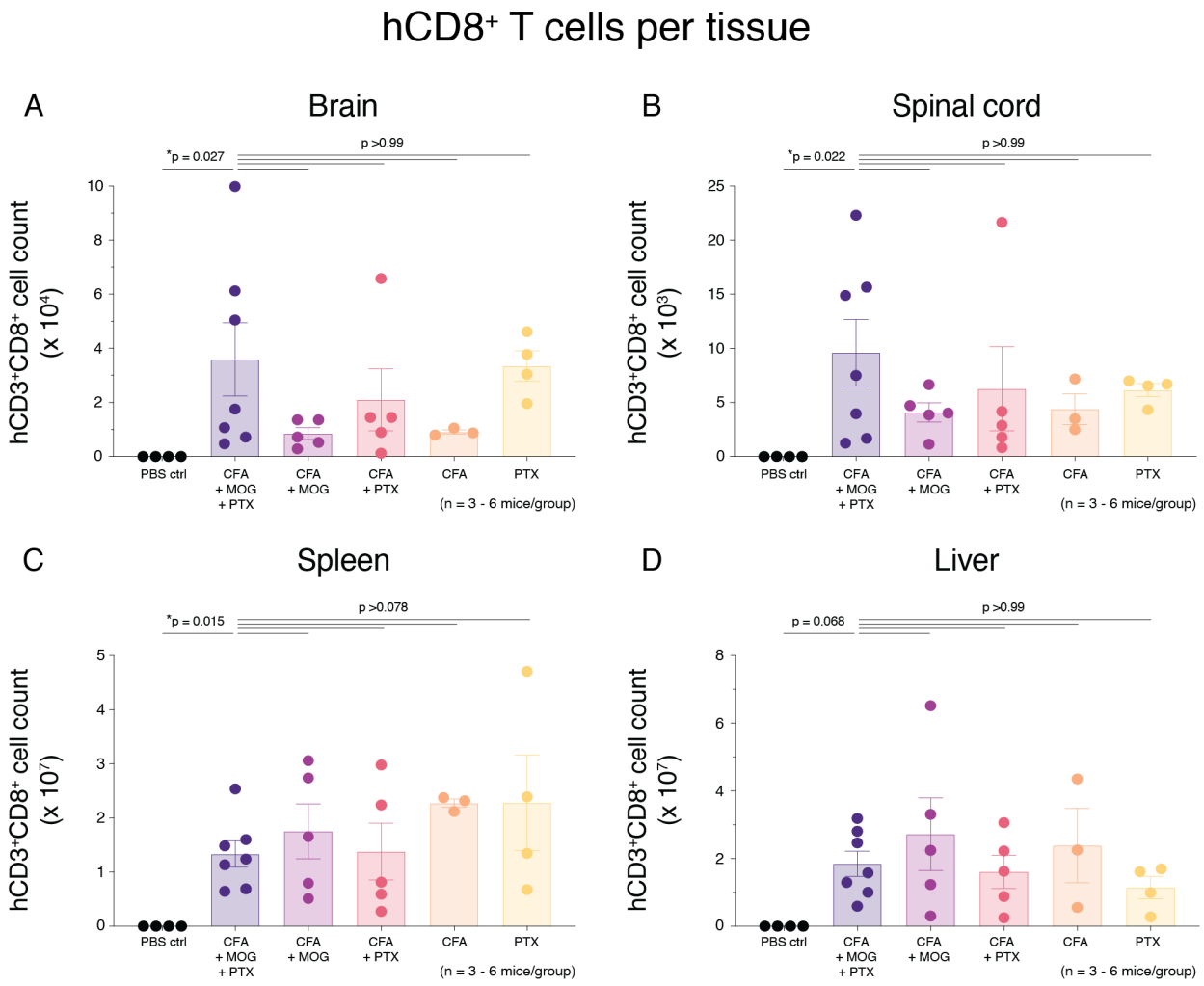

Figure 4.62 Quantification of human CD8$^+$ T cells in the CNS and periphery of HuPBMC mice induced with different EAE adjuvant components

Figure shows the total number of human hCD45$^+$CD3$^+$CD8$^+$(CD4$^-$) T cells in the (A) brain, (B) spinal cord, (C) spleen, (D) liver, and (E) intestinal lamina propria on days 19 – 22 post-immunization of PBS engrafted control NSG mice induced with the full mixed MOG EAE immunization containing rhMOG and MOG_{35-55} antigen emulsified in CFA with PTx co-administered (PBS ctrl, n = 4 mice) and HuPBMC mice (n = 26 mice all derived from HD-04 female PBMCs) induced with full mixed EAE immunization (CFA + MOG + PTx, n = 7 mice), mixed MOG emulsion without PTx (CFA + MOG, n = 5 mice), blank CFA emulsion and PTx without antigen (CFA + PTx, n = 5 mice), blank CFA emulsion only without antigen or PTx (CFA, n = 3 mice), or PTx only without emulsion (PTx, n = 4 mice). Tissues were perfused prior to cell isolation. Data are shown as mean with SEM and were analyzed by Brown-Forsythe and Welch ANOVA with Dunnett's T3 multiple comparisons test or by Kruskal-Wallis with Dunn's multiple comparisons test.

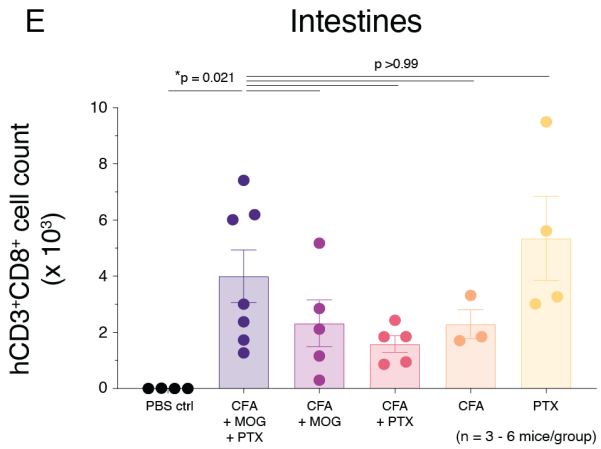

Figure 4.62 continued

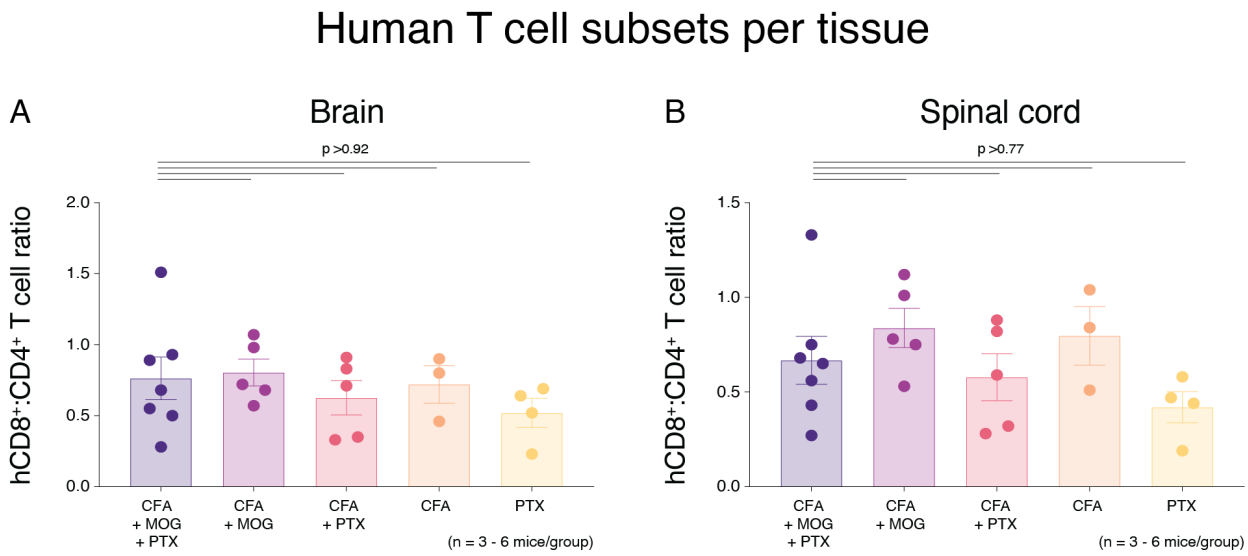

Figure 4.63 Ratio of human $CD8^+$ to $CD4^+$ T cells in the CNS and periphery of HuPBMC mice induced with different EAE adjuvant components

Figure shows the ratio of human $hCD45^+CD3^+CD8^+(CD4^-)$ T cells to $hCD45^+CD3^+CD4^+(CD8^-)$ T cells in the (A) brain, (B) spinal cord, (C) spleen, (D) liver, and (E) intestinal lamina propria on days 19 – 22 post-immunization of PBS engrafted control NSG mice induced with the full mixed MOG EAE immunization containing rhMOG and MOG_{35-55} antigen emulsified in CFA with PTx co-administered (PBS ctrl, n = 4 mice) and HuPBMC mice (n = 26 mice all derived from HD-04 female PBMCs) induced with full mixed EAE immunization (CFA + MOG + PTx, n = 7 mice), mixed MOG emulsion without PTx (CFA + MOG, n = 5 mice), blank CFA emulsion and PTx without antigen (CFA + PTx, n = 5 mice), blank CFA emulsion only without antigen or PTx (CFA, n = 3 mice), or PTx only without emulsion (PTx, n = 4 mice). Tissues were perfused prior to cell isolation. Data are shown as mean with SEM and were analyzed by Brown-Forsythe and Welch ANOVA with Dunnett's T3 multiple comparisons test or by Kruskal-Wallis with Dunn's multiple comparisons test.

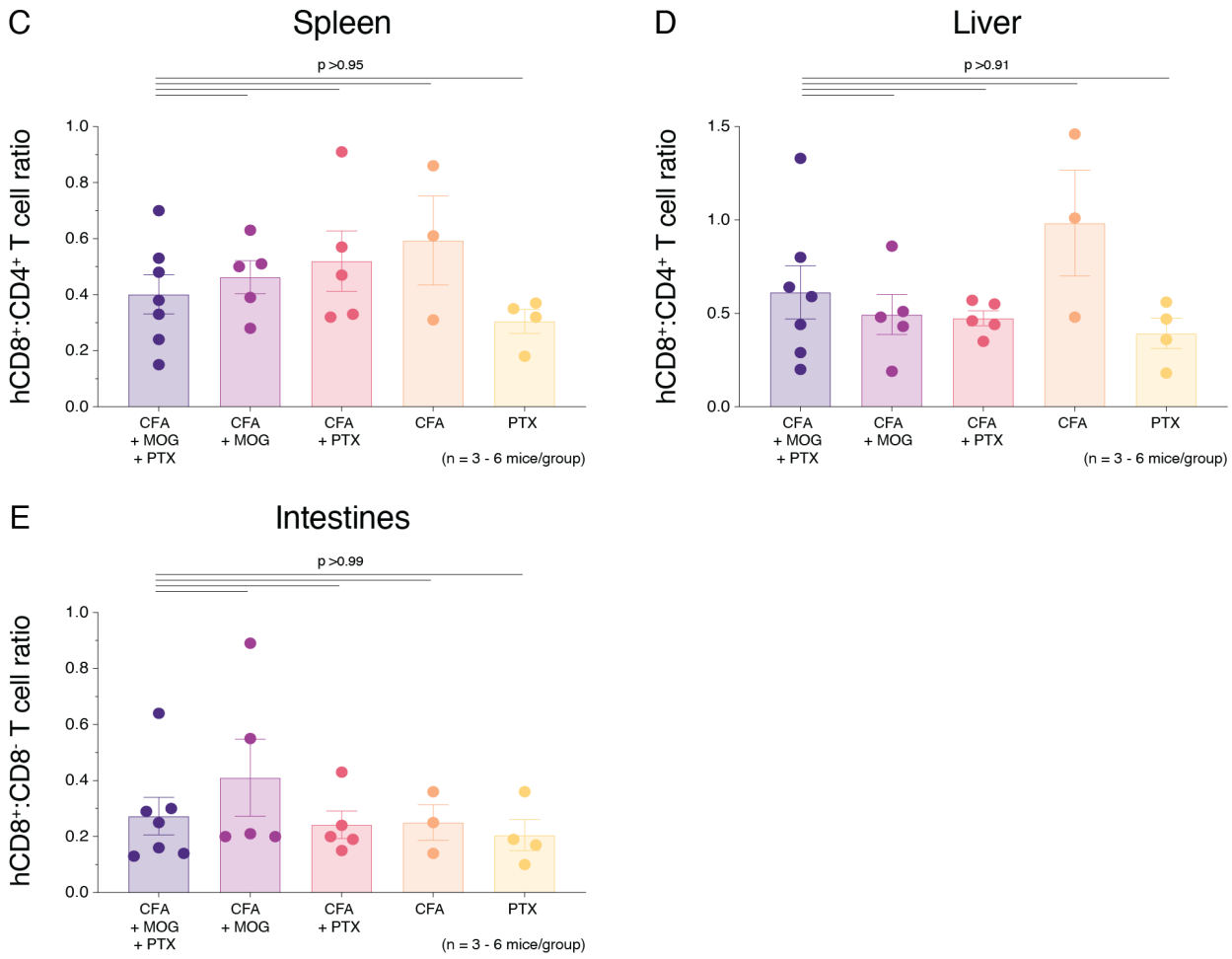

Figure 4.63 continued

The data indicate that overall, no one adjuvant component, or combinations thereof, in the EAE immunization protocol preferentially influenced tissue infiltration of major murine myeloid or human T cell subsets, but PTx did appear to permeabilize the BBB and enable sufficient human T cell trafficking into the CNS to generate myelin damage and cause paralysis when administered alongside MOG-replete CFA emulsion.

4.8.5 Comparison of HuPBMC EAE tissue-specific infiltration to NOD EAE mice

In HuPBMC EAE mice, peripheral tissue infiltration may be a result of engrafted human T cells filling an empty niche in immunocompromised NSG mice, rather than being due solely to nonspecific graft reactivity. We therefore compared the quantity of immune cells in each tissue between NOD and HuPBMC mice to determine what the expected relative abundance of T cells

in the CNS and peripheral tissues of HuPBMC mice should be post-MOG immunization when both CFA and PTx are administered.

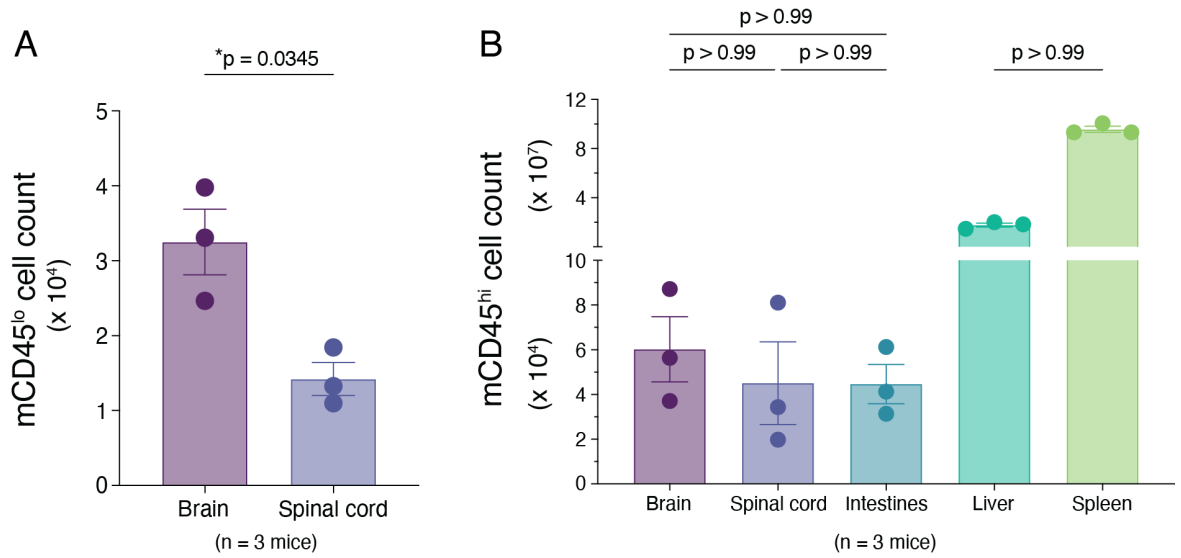

Figure 4.64 Murine immune cell abundance in the CNS and periphery of typical NOD EAE mice

Figure shows the total number of (A) mCD45^{lo} and (B) mCD45^{hi} immune cells in the brain, spinal cord, intestinal lamina propria, liver, and spleen on day 24 post-immunization of NOD WT mice induced with 200 µg MOG_{35-55} antigen emulsified in CFA with PTx co-administered (n = 3 immunized mice). Tissues were perfused prior to cell isolation. Data are shown as mean with SEM and were analyzed by (A) Welch's unpaired t test and by (B) Kruskal-Wallis with Dunn's multiple comparisons test.

In EAE induced NOD mice, total CNS resident mCD45^{lo} cell counts and peripherally derived mCD45^{hi} immune cell counts (innate and adaptive combined) were compared between tissues (Figure 4.64). The same analysis was performed using samples obtained from EAE induced HuPBMC mice (all derived from the same blood donor) to quantify mCD45^{lo} and mCD45^{hi} myeloid cell counts, as well as hCD45^{+} immune cell counts, most of which were hCD3^{+} T cells (Figure 4.65). The brains of both NOD and HuPBMC EAE mice contained greater numbers of mCD45^{lo} microglia than the corresponding spinal cords, as expected for these organs (Figure 4.64A, Figure 4.65A). Total mCD45^{lo} cell counts were generally lower in HuPBMC CNS samples (~1 – 11 x 10^3 cells/ tissue) compared to NOD CNS samples (~1 – 4 x 10^4 cells/ tissue) at endpoint (Figure 4.64A, Figure 4.65A). Within NOD EAE mice, the brain, spinal cord, and intestinal lamina propria each contained similar numbers of mCD45^{hi} immune cells (Figure 4.64B). Similar relative

abundances of mCD45^{hi} myeloid and hCD45^{+} immune cells were present in these tissues from HuPBMC EAE mice as well (Figure 4.65B – C). See Appendix 8 for supplemental data (Figure A.43 – Figure A.48).

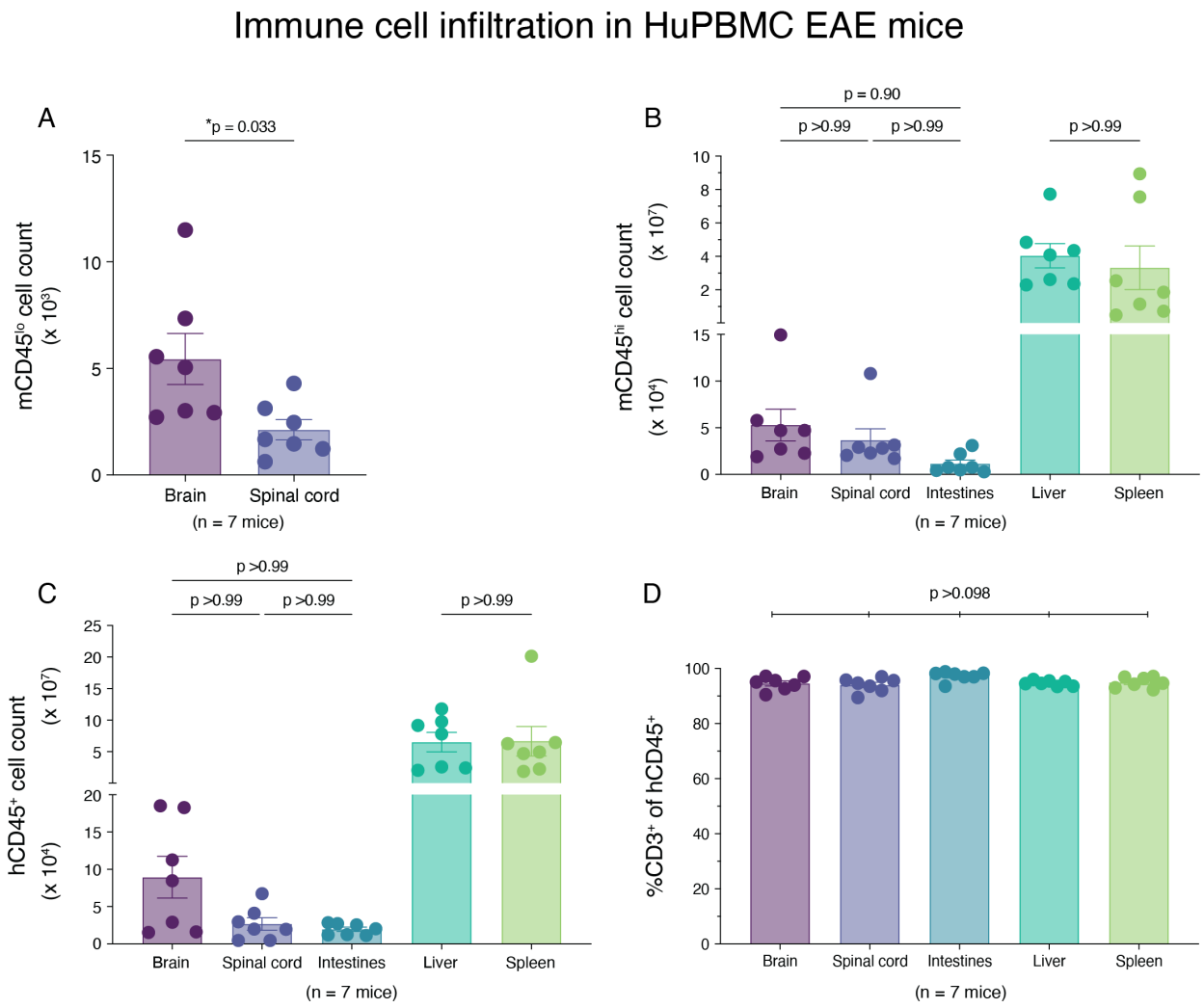

Figure 4.65 Human and murine immune cell abundance in the CNS and periphery of HuPBMC EAE mice

Figure shows (A) the total number of murine mCD45^{lo} CNS resident myeloid cells, (B) the total number of murine mCD45^{lo} myeloid cells, (C) the total number of hCD45^{+} immune cells, and (D) the proportion of hCD3^{+} T cells among hCD45^{+} immune cells, in the brain, spinal cord, intestinal lamina propria, liver, and spleen on days 19 – 22 post-immunization of HuPBMC mice (n = 7 males derived from HD-04 female PBMCs) induced with the full mixed MOG EAE immunization containing rhMOG and MOG$_{35-55}$ antigen emulsified in CFA with PTx co-administered. Tissues were perfused prior to cell isolation. Data are shown as mean with SEM and were analyzed by (A) Welch's unpaired t test or by (B – D) Kruskal-Wallis with Dunn's multiple comparisons test.

Though not statistically significant, spleens from NOD EAE mice contained greater numbers of $mCD45^{hi}$ immune cells than respective liver samples (Figure 4.64B), whereas similar numbers of both $mCD45^{hi}$ myeloid cells and $hCD45^{+}CD3^{+}$ T cells were present in the livers and spleens of HuPBMC EAE mice (Figure 4.65B – C), which indicated that the livers of HuPBMC mice contained more immune cells than would be expected post-EAE induction compared to NOD mice. Immune cell counts in the livers and spleens of both strains generally fell between 2 and 12 x 10^7, with an anticipated higher variability observed among the HuPBMC samples (Figure 4.64B, Figure 4.65B – C). Individual murine and human immune cell subset abundance in the liver and spleen was then compared directly between strains (Figure 4.66, Figure 4.67) to determine if human immune cell presence in the HuPBMC EAE tissues could be attributed to inflammatory infiltration rather than niche replacement in these organs.

Total leukocyte counts, including both murine myeloid cell and human T cell subset counts, were significantly higher in the livers of HuPBMC EAE mice compared to naïve and EAE induced NOD livers, on average (Figure 4.66A – E), which suggests nonspecific inflammation beyond just niche occupation occurred in HuPBMC EAE mouse livers. EAE induced NOD and HuPBMC spleens, however, contained statistically similar numbers of murine myeloid cells and human T cell subsets (Figure 4.67), which did suggest empty niche occupation without substantial graft reactivity in HuPBMC EAE spleens. Excessive, nonspecific T cell infiltration of the liver above the levels seen in NOD mice occurred in over half of the HuPBMC EAE mice at endpoint (approximately 4/7) (Figure 4.66A – E), though the ratio of $CD8^{+}$ to $CD4^{+}$ T cell subsets was only moderately elevated in HuPBMC EAE livers on average (Figure 4.66F). The increased numbers of T cells and murine macrophages in the livers of HuPBMC EAE mice, but not in the spleens, compared to NOD EAE mice, indicates additional infiltration of the liver beyond simply filling an empty niche and indicates nonspecific graft reactivity of human immune cells to the peripheral host tissues in EAE immunized HuPBMC mice (i.e., the response was not directed exclusively by the MOG inducing antigen).

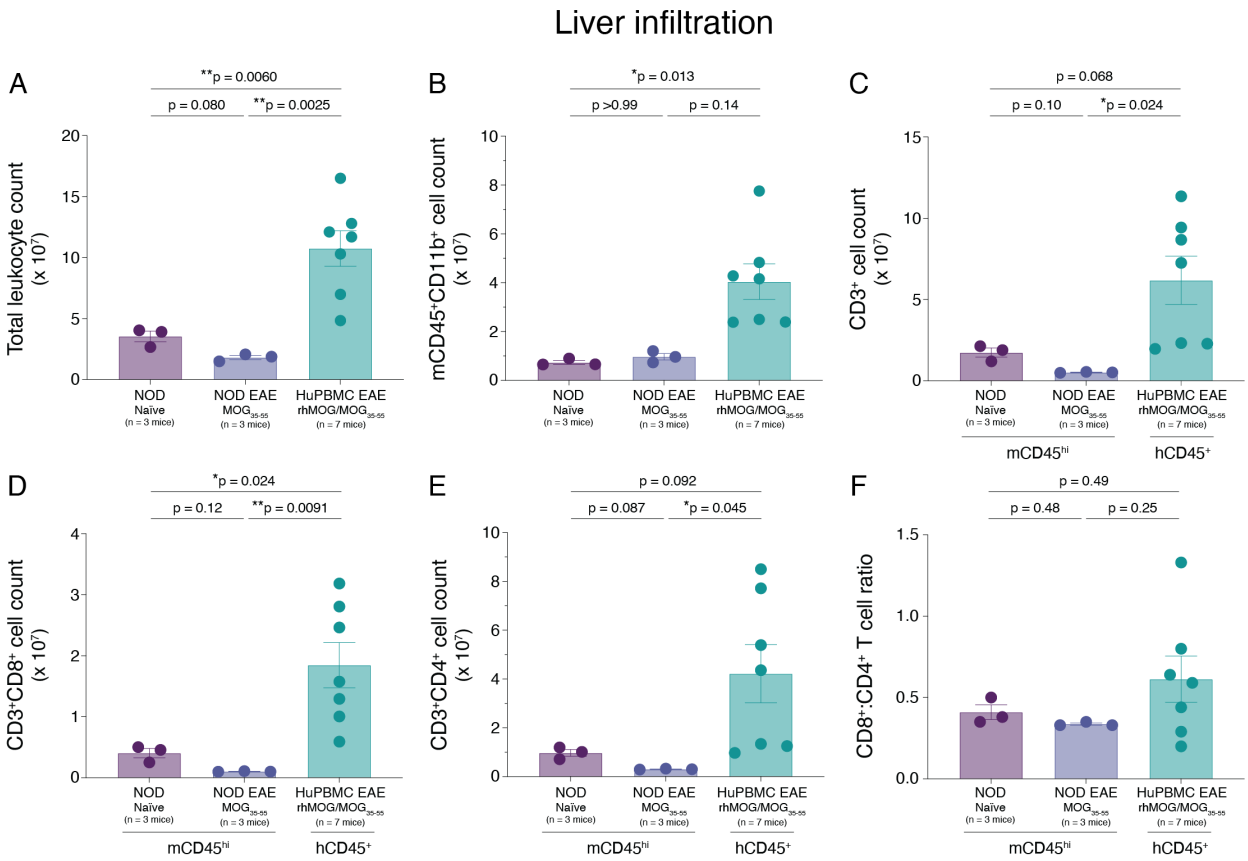

Figure 4.66 Immune infiltration of the liver of EAE induced NOD and HuPBMC mice

Figure shows the total numbers of (A) all leukocytes (murine and human), (B) mCD45$^+$CD11b$^+$ myeloid cells, (C) m/hCD3$^+$ T cells, (D) m/hCD3$^+$CD8$^+$ T cells, (E) m/hCD3$^+$CD4$^+$ T cells, and (F) the ratio of m/hCD3$^+$CD8$^+$ to m/hCD3$^+$CD4$^+$ T cells in the liver of naïve (untreated) NOD mice (n = 3 WT), MOG$_{35-55}$ EAE induced NOD mice (n = 3 WT) day 24 post-immunization, and mixed rhMOG/MOG$_{35-55}$ EAE induced HuPBMC mice (n = 7 derived from HD-04 female PBMCs) day 19 – 22 post-immunization. Tissues were perfused prior to cell isolation. Data are shown as mean with SEM and were analyzed by Brown-Forsythe and Welch ANOVA with Dunnett's T3 multiple comparisons test or by Kruskal-Wallis with Dunn's multiple comparisons test.

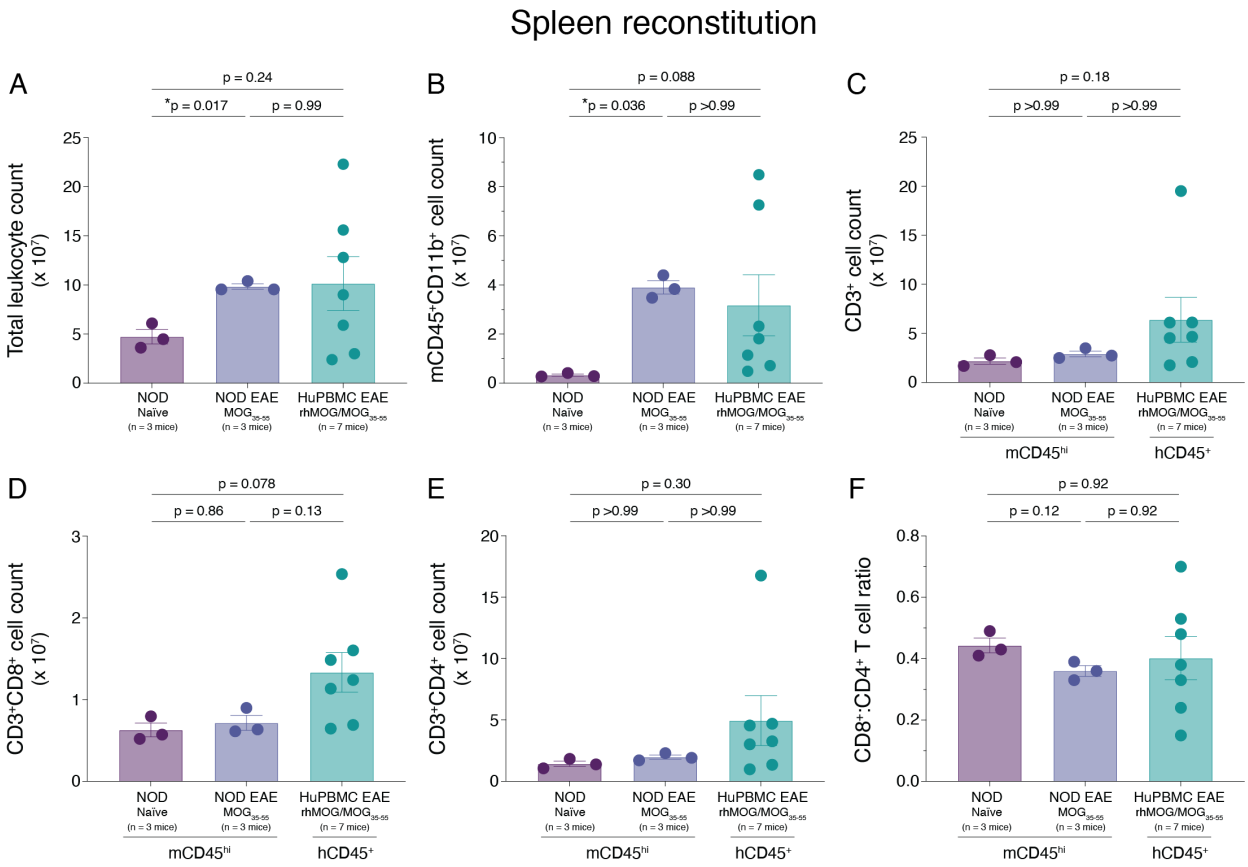

Figure 4.67 Immune composition of the spleen of EAE induced NOD and HuPBMC mice

Figure shows the total numbers of (A) all leukocytes (murine and human), (B) mCD45$^+$CD11b$^+$ myeloid cells, (C) m/hCD3$^+$ T cells, (D) m/hCD3$^+$CD8$^+$ T cells, (E) m/hCD3$^+$CD4$^+$ T cells, and (F) the ratio of m/hCD3$^+$CD8$^+$ to m/hCD3$^+$CD4$^+$ T cells in the spleens of naïve (untreated) NOD mice (n = 3 WT), MOG$_{35-55}$ EAE induced NOD mice (n = 3 WT) day 24 post-immunization, and mixed rhMOG/MOG$_{35-55}$ EAE induced HuPBMC mice (n = 7 derived from HD-04 female PBMCs) day 19 – 22 post-immunization. Tissues were perfused prior to cell isolation. Data are shown as mean with SEM and were analyzed by Brown-Forsythe and Welch ANOVA with Dunnett's T3 multiple comparisons test or by Kruskal-Wallis with Dunn's multiple comparisons test.

4.8.6 Summary and discussion of findings

The results of this preliminary experiment suggest that immunization of HuPBMC mice with MOG replete CFA emulsion with PTx preferentially directs the graft response to the CNS, resulting in EAE immunopathology. Administration of CFA, PTx, or MOG individually, or in combination, did not differentially affect major T cell subset ratios in any tissue, nor did the ratio differ from pre-induction levels in the blood, suggesting transferred T cells retained their tendency to skew regardless of which adjuvant was given (consistent with a donor specific). PTx treatment

of HuPBMC mice, with or without additional CFA, however, produced greater human and murine immune cell infiltration of the CNS compared to otherwise comparable HuPBMC mice given only MOG and/or CFA. We therefore suspect that PTx administration to HuPBMC mice, regardless of the use of any other immunization components, is necessary and sufficient to allow human T cells to infiltrate the CNS.

The second question we posed for this analysis was: is MOG antigen required to generate paralytic symptoms, or is nonspecific graft reactivity in the CNS sufficient? EAE symptom incidence was zero in HuPBMC mice administered PTx without CFA and/or MOG antigen. The use of CFA and PTx without myelin antigen, however, did result in T cell infiltration of the CNS and tissue damage sufficient to produce clinical EAE symptoms in one immunized mouse, but the symptom incidence was much lower than when MOG was also added to the CFA emulsion, indicating the graft response was preferentially directed to the CNS when immunized with CFA containing myelin antigen. The importance of MOG antigen in promoting EAE pathology was highlighted by the similar average numbers of each immune cell subset in the CNS tissues of all PTx treated groups, and as such, the lack of symptom incidence in groups without MOG could not be attributed simply to insufficient infiltration. If the incidence of EAE was dependent simply on enabling the entry of xenoreactive human T cells into the mouse CNS, we would expect to see equal or at least similar rates of paralysis in all PTx treated HuPBMC mice. These findings suggest the infiltrating human T cells in CFA and PTx immunized groups were less reactive to the murine CNS tissues (reduced encephalitogenicity) when MOG was not included in the CFA emulsion.

Extricating the relative contributions of graft xenoreactivity murine antigens from graft xenoreactivity specifically in the context of murine MOG antigens is experimentally very challenging. In the brain, spinal cord, spleen, and intestinal lamina propria, total immune cell counts per tissue were statistically similar between NOD and HuPBMC mice post-immunization, suggesting CFA and PTx had a consistent effect in the EAE induction of humanized mice as it did with the background strain (i.e. there was no evidence of notably greater barrier breach in one strain over the other) nor that general, nonspecific graft reactivity resulted in substantially greater CNS infiltration and/or local immune cell expansion in HuPBMC EAE mice above what could be expected for typical murine EAE models. The livers of HuPBMC EAE mice, however, contained far more immune cells (both murine myeloid and human T cells) in over half of the group, demonstrating the presence of nonspecific tissue recognition (xenoreactivity), that was not myelin

antigen specific, beyond simply filling an empty niche in the NSG tissues. Moreover, the consistently higher incidence of clinical symptoms of xGvHD in all immunized HuPBMC mice, independent of whether these mice also or separately developed EAE paralysis, indicates that while xGvHD is an unavoidable feature of using the HuPBMC model, CNS immunopathology likely cannot be attributed only to brain and spinal cord localized xGvHD. Rather, our findings indicate that the nonspecific recognition of murine MHC by engrafted human T cells is a feature we can harness in order to present an introduced myelin antigen that boosts CNS specific inflammation, leading to greater paralytic symptom incidence. Assessments of cell-cell interactions between human T cells and murine MHC expressing myeloid cells is further examined in section 4.9.3.

4.9 Murine macrophage-mediated human T cell activation in HuPBMC EAE mice

4.9.1 Background and rationale

Macrophages in classical EAE models are known to participate in both the peripheral T cell activation phase of disease induction and in T cell recruitment, demyelination, and myelin debris clearance in the CNS[697–699]. The requirement for human T cell infiltration of the CNS to generate EAE symptoms in HuPBMC mice was fairly clear, however it remained unclear how MOG was presented to these human T cells when so few professional human APCs reconstituted NSG mice following PBMC transfer (i.e., human myeloid and B cells). Likewise, it was unclear if peripheral or CNS localized murine myeloid cells, which numerically corresponded to cytotoxic human T cell counts in the CNS following immunization, were acting as APCs in the periphery by priming priorly naïve human T cells with the inducing antigen and/or in the CNS by restimulating infiltrating T cells. The findings from previous sections pointed to murine myeloid cells acting as APCs to engrafted human T cells, given the relative dearth of human APCs, and increased clinical symptom incidence with MOG antigen immunization than with blank CFA. However, a specific consideration for the HuPBMC EAE model is that activated human T cells express MHC II and can act as atypical APCs to one another, whereas activated mouse T cells generally do not express MHC II[700,701].

B6 triple knockout (B6-TKO) mice are effectively a C57Bl/6 background version of the NSG, with functional knockouts reproducing those of the latter strain. B6-TKO mice (JAX strain #025730) bear nullifying mutations in the genes encoding RAG2, IL-2Rγ, and CD47[500]. The CD47 mutation provides an additional advantage over the NSG in that humanized B6-TKO recipients are more resistant to xGvHD than similarly treated NSG recipients[500,702]. CD47 is an integrin associated protein that acts as a 'marker of self' that, when bound to SIRPα expressed on macrophages, transmits a 'don't eat me' signal to inhibit phagocytosis of healthy host cells[448,703]. NOD mice express an allelic variant of SIRPα that is compatible with and transduces a 'don't eat me' signal when bound to human CD47, which promotes macrophage tolerance to HIS transplantation in NSG mice[501]. C57Bl/6 mice, however, express a variant of SIRPα that does not recognize human CD47, resulting in poor HIS engraftment of C57Bl/6-*Rag2*^{null}*IL2Rγ*^{null} mice[501,704]. Therefore, knocking out the expression of host CD47 in C57Bl/6-*Rag2*^{null}*IL2Rγ*^{null} mice results in murine macrophages that are nonresponsive to murine or human CD47 on transplanted immune cells[472], enabling humanization of the B6-TKO. While tolerizing murine host macrophages in the B6-TKO to human CD47, nullifying mutations in the gene encoding CD47 also result in defective phagocytosis and antigen processing[472].

SIRPα-CD47 interactions have been investigated to some extent in the context of MS and EAE models[36,474,699,705]. In active MS lesions, CD47 transcript and protein expression levels have been found to be downregulated, which, in culture, has been shown to promote myelin phagocytosis by macrophages and suggests a role for SIRPα-CD47 in demyelinating axons[36,474,705]. Wang and colleagues showed that antibody blockade of the SIRPα-CD47 signaling axis post-EAE symptom onset impairs clinical recovery, due to the inability of CNS infiltrating monocytes to differentiate into mature macrophages, which, alongside resident microglia, could not phagocytose and clear myelin debris; a critical step in the remyelination process[699]. This finding had been reproduced by Han and colleagues, who also demonstrated that splenocytes from CD47$^{-/-}$ single KO C57Bl/6 mice failed to activate following MOG_{35-55} immunization and were therefore resistant to EAE[474]. The authors noted that "there was impaired proliferation with WT T cells when co-cultured with irradiated CD47$^{-/-}$ splenocytes, suggesting that both T cells and APCs lacking in CD47 were defective in generating encephalitogenic T cells"[474].

To examine the role of host murine macrophage functions in driving immunopathology in the HuPBMC EAE model, we compared clinical and immunological EAE outcomes between

PBMC humanized NSG/SGM3 and B6-TKO mice, in which murine macrophages are respectively functional or defective as APCs and phagocytes, but which both retain murine MHC and co-stimulatory molecule expression. Furthermore, we assessed the ability of human T cells derived from HuPBMC mice to respond to MOG antigen when supplied with murine macrophages from each of these strains for comparison to regular murine EAE model pathogenesis.

4.9.2 HuPBMC EAE on the B6-TKO and NSG/SGM3 background

4.9.2.1 Experimental design

Two cohorts of HuPBMC mice were generated by engrafting NSG/SGM3 and B6-TKO mice with 5 x 10^6 PBMCs each from the same healthy female blood donor and were induced with mixed rhMOG/MOG_{35-55} EAE at 3 weeks post-PBMC injection. Reconstitution of the blood prior to EAE induction and of the spleen at EAE endpoint was compared between NSG/SGM3 and B6-TKO recipients, in addition to differences in clinical EAE outcomes and CNS infiltration, to assess the importance of CD47-SIRPα mediated macrophage functions in a humanized mouse model of CNS autoimmune disease.

4.9.2.2 Peripheral blood reconstitution

PBMC engraftment of B6-TKO mice resulted in similar HIS reconstitution of peripheral blood as HuPBMC NSG/SGM3 mice in terms of relative proportions of immune cell subsets, which comprised mainly $hCD3^+$ T cells and very few human B cells, myeloid cells, and NK cells (Figure 4.68A). HuPBMC B6-TKO mice, however, showed overall lower levels of engraftment of $hCD4^+$ and $hCD8^+$ T cells and regulatory $hCD4^+FOXP3^+$ T cells compared to NSG/SGM3 mice at 3 weeks post-PBMC injection (Figure 4.68B – C). Though neither strain reconstituted with many $hCD19^+$ B cells or $hCD14^+$ monocytes, HuPBMC NSG/SGM3 mouse samples contained significantly greater frequencies among total leukocytes compared to HuPBMC B6-TKO mice, whereas no difference was seen in human NK cell proportions (Figure 4.68C). Among $hCD3^+$ T cells, the relative proportion of $hCD4^+$ and $hCD8^+$ T cell subsets was statistically similar in both strains (Figure 4.68D – E). The proportion of engrafted human T cells expressing the activation marker CD27, however, was significantly lower in HuPBMC-B6-TKO mice compared to HuPBMC NSG/SGM3 (Figure 4.68F), which is consistent with reports of reduced xGvHD

susceptibility in PBMC humanized B6-TKO mice[702]. FOXP3$^+$ Treg subsets made up a significantly smaller proportion of total hCD3$^+$CD4$^+$ T cells in humanized B6-TKO mice compared to the NSG-SGM3 group, also suggestive of reduced inflammation from xGvHD.

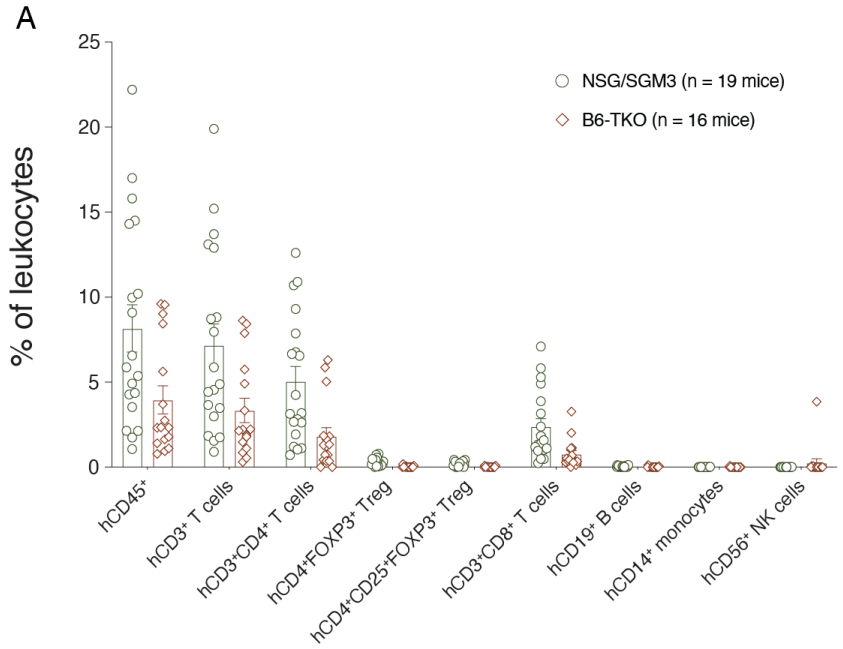

Figure 4.68 Peripheral blood reconstitution of PBMC engrafted NSG/SGM3 and B6-TKO mice

Figure shows (A) relative proportions of all measured human immune cell lineages are shown as a proportion of total leukocytes (murine and human) in the peripheral blood days 19 – 20 (3 weeks) post-engraftment of NSG/SGM3 mice (n = 19 males) and B6-TKO mice (n = 16 females and males mixed) with 5 x 10^6 PBMCs derived from a healthy female donor (HD-04). Subsets are subdivided into predominantly engrafted immune cell lineages (B) and minorly engrafted immune cell lineages (C) to better illustrate relative frequencies. Figure also shows the proportional expression of hCD4 (D), hCD8 (E), and hCD27 (F) on hCD3$^+$ T cells, as well as hCD25 and/or hFOXP3 on hCD3$^+$CD4$^+$ T cells (G – H). Data are shown as mean with SEM and were analyzed by Welch's unpaired t test or by Mann-Whitney test. HuPBMC cohorts included: 18 and 28.

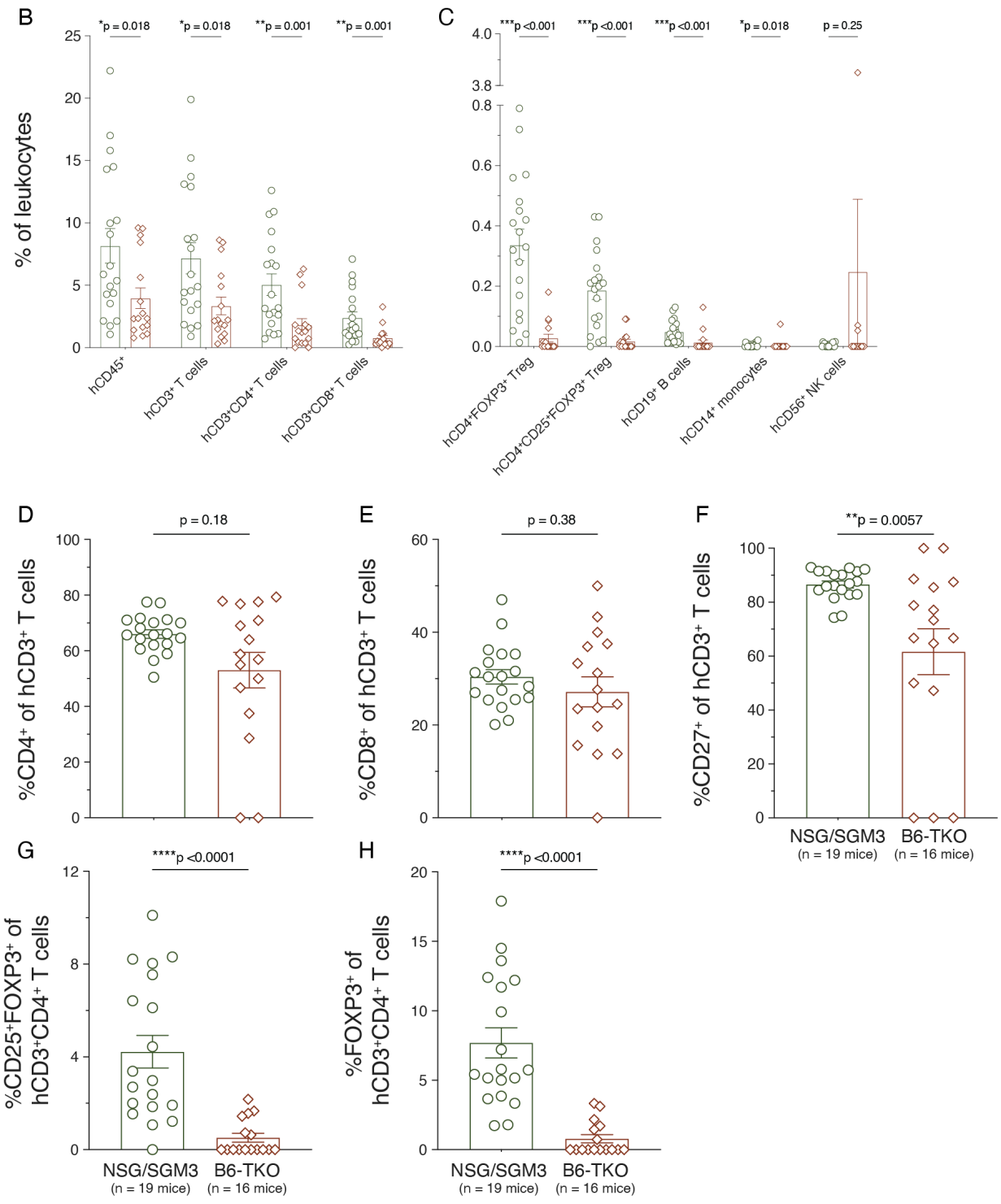

Figure 4.68 continued

4.9.2.3 Clinical EAE outcomes

All HuPBMC B6-TKO mice immunized with mixed MOG antigen emulsion remained clinically asymptomatic out to day 23 post-induction (Figure 4.69A – B). EAE resistance was observed for both male and female recipient B6-TKO mice, and assessments of infiltration at endpoint indicated minimal to no sex bias in EAE susceptibility for PBMC engrafted B6-TKO mice (see Appendix 9, Figure A.49 – Figure A.51). Therefore, recipient B6-TKO mice of both sexes were included in these analyses unless otherwise specified. Starting around day 14, HuPBMC NSG/SGM3 EAE mice on average began to gradually lose weight, whereas weight in the HuPBMC B6-TKO EAE group remained stable following a brief dip around days 7 – 10 (Figure 4.69C). None of the HuPBMC B6-TKO mice in this cohort developed clinical symptoms of xGvHD by the day 23 endpoint, though one mouse did present with mild liver cirrhosis at endpoint. In a second HuPBMC B6-TKO cohort derived from the same PBMC donor, signs of xGvHD, including facial hair loss and liver cirrhosis, affected two female recipients by the day 33 endpoint. These data suggested that graft reactivity was reduced but not entirely absent in HuPBMC-B6-TKO mice, despite a simultaneous lack of EAE paralysis that would likely occur at a similar rate if nonspecific xGvHD was the main driver of CNS damage in HuPBMC mice post-immunization.

In C57Bl/6 $Rag1^{-/-}$ $CD47^{+/+}$ mice, adoptive transfer of murine T cells renders recipients susceptible to EAE induction with MOG_{35-55} peptide[689,706]. To verify that the absence of clinical EAE symptoms in HuPBMC-B6-TKO mice was a result of the CD47 deletion, we also compared clinical outcomes of MOG immunization in HuPBMC-B6-TKO mice to C57Bl/6 WT mice and B6-TKO mice reconstituted with sex-matched syngeneic C57Bl/6 WT derived splenocytes to normalize for potential C57Bl/6 background-human interspecies interactions, or lack thereof, that may confound effects specific to CD47 loss. C57Bl/6 WT mice developed EAE symptoms approximately 1-week post-immunization, whereas both humanized B6-TKO mice (Hu B6-TKO) and murine immune cell reconstituted B6-TKO mice (Mu B6-TKO) remained asymptomatic beyond day 30 post-induction (Figure 4.70A – B). Symptom onset occurred in all immunized C57Bl/6 WT mice and coincided with considerable weight loss (Figure 4.70B – C). Both reconstituted B6-TKO groups maintained stable weight throughout the experiment (Figure 4.70C), indicating CD47 loss was the protective factor against disease. These findings were supported by flow cytometric analysis showing that all three groups demonstrated significant T cell infiltration

of the CNS tissues at EAE endpoint, indicating immunization was otherwise successful (see Appendix 10, Figure A.52 – Figure A.61).

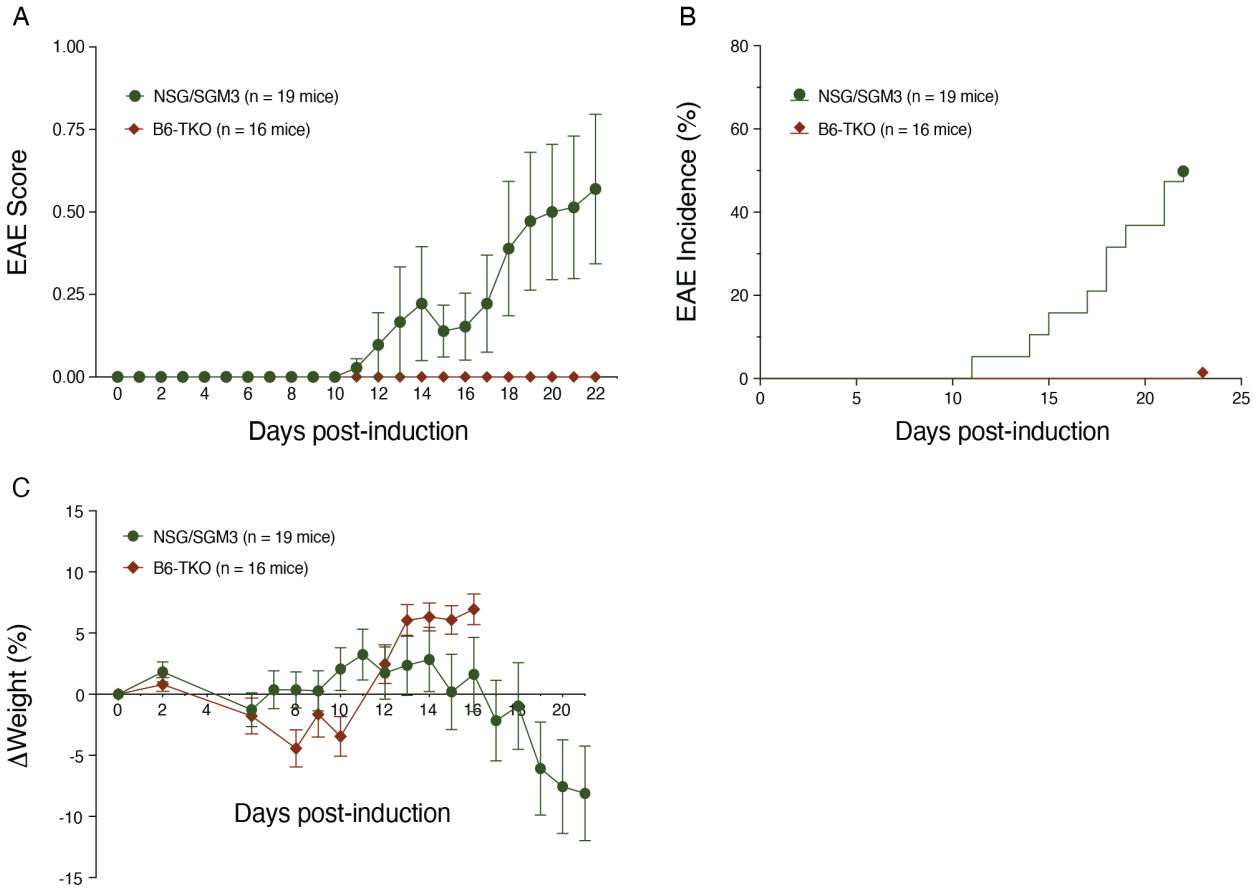

Figure 4.69 Clinical EAE outcomes for PBMC engrafted NSG/SGM3 and B6-TKO mice

Figure shows (A) clinical EAE scores, (B) incidence of EAE symptoms, and (C) weight loss over time among all rhMOG/MOG$_{35-55}$ EAE induced PBMC engrafted NSG/SGM3 mice (n = 19 males), and B6-TKO mice (n = 16 females and males mixed) derived from a healthy female donor (HD-04). In A and C, data are shown as mean with SEM. In B, data are shown as percentage of the group. HuPBMC cohorts included: 18 and 28.

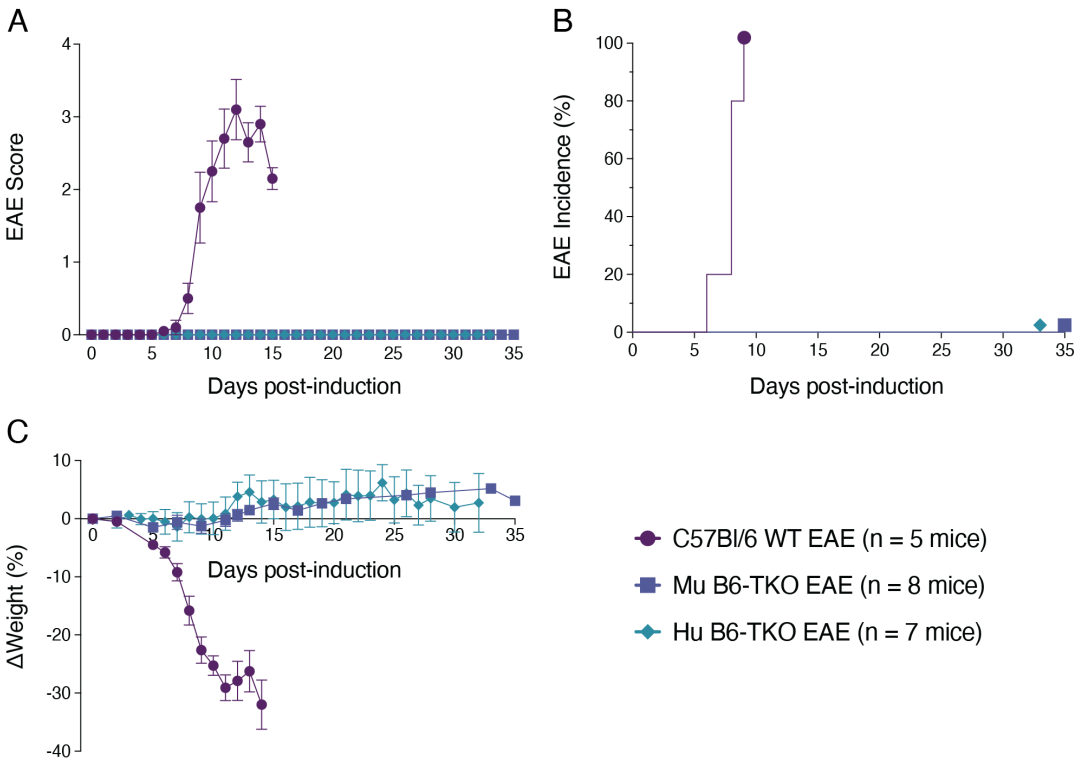

Figure 4.70 Clinical EAE outcomes for B6-TKO mice reconstituted with a murine or human immune system

Figure shows (A) clinical EAE scores, shown as mean with SEM, (B) incidence of EAE symptoms, shown as percentage of the group, and (C) weight loss, shown as mean with SEM, over time among all EAE induced mice. Groups include immunocompetent C57Bl/6 mice (n = 5 WT males) induced with rhMOG/MOG_{35-55} EAE, B6-TKO mice engrafted with sex-matched syngeneic C57Bl/6 WT derived splenocytes (n = 8 males and females mixed engrafted with 5 x 10^6 cells each) induced with MOG_{35-55} EAE, and human PBMC engrafted B6-TKO mice (n = 7 females and males mixed derived from healthy female donor HD-04, cohort 23) induced with rhMOG/MOG_{35-55} EAE.

4.9.2.4 Spleen reconstitution and humoral responses

Among HuPBMC-NSG/SGM3 EAE mice, there were no significant differences in splenic reconstitution of any cell types between mice that did or did not develop clinical EAE symptoms, so all mice per strain were grouped together. For HuPBMC B6-TKO EAE mice, females and males were similarly reconstituted and resistant to EAE and were thus analyzed together (Appendix 9, Figure A.49 – Figure A.51). Under the same donor PBMC engraftment and EAE induction parameters, B6-TKO mice had greater $mCD45^+$ cell proportions and correspondingly reduced $hCD45^+$ cell proportions among total leukocytes in the spleen at endpoint compared to NSG/SGM3

mice (Figure 4.71A – B). Within the engrafted hCD45$^+$ cell population, both strains contained similar proportions of reconstituted activated human T cells, which made up 80 – 90% of all engrafted human immune cells (Figure 4.71C – E). NSG/SGM3 mouse spleens, however, contained a relatively greater engrafted proportion of non-T cell subsets than B6-TKO mice (Figure 4.71E). Among hCD19$^+$ B cells, those from NSG/SGM3 spleens had greater expression levels of key markers than those in B6-TKO spleens (Figure 4.71F).

Numerically, splenic abundance of each human immune cell subset reflected the total proportions, comprising mostly hCD3$^+$ T cells in both strains (Figure 4.72A). mCD45$^+$ immune cell counts were comparable, however fewer total human cells engrafted in the B6-TKO group by endpoint (Figure 4.72B). Accordingly, the total number of activated human T cells was also much lower in the spleens of B6-TKO mice (Figure 4.72C). For all minor HIS lineages, including hCD19$^+$ B cells, hCD14$^+$ monocytes, and hCD56$^+$ NK cells, NSG/SGM3 mice reconstituted with significantly more of each cell type than the B6-TKO mice (Figure 4.72D – F). As a result of reduced human B cell reconstitution in the periphery, PBMC engrafted B6-TKO mice generated significantly lower levels of serum anti-rhMOG IgM in response to immunization compared to matched NSG/SGM3 mice (Figure 4.73).

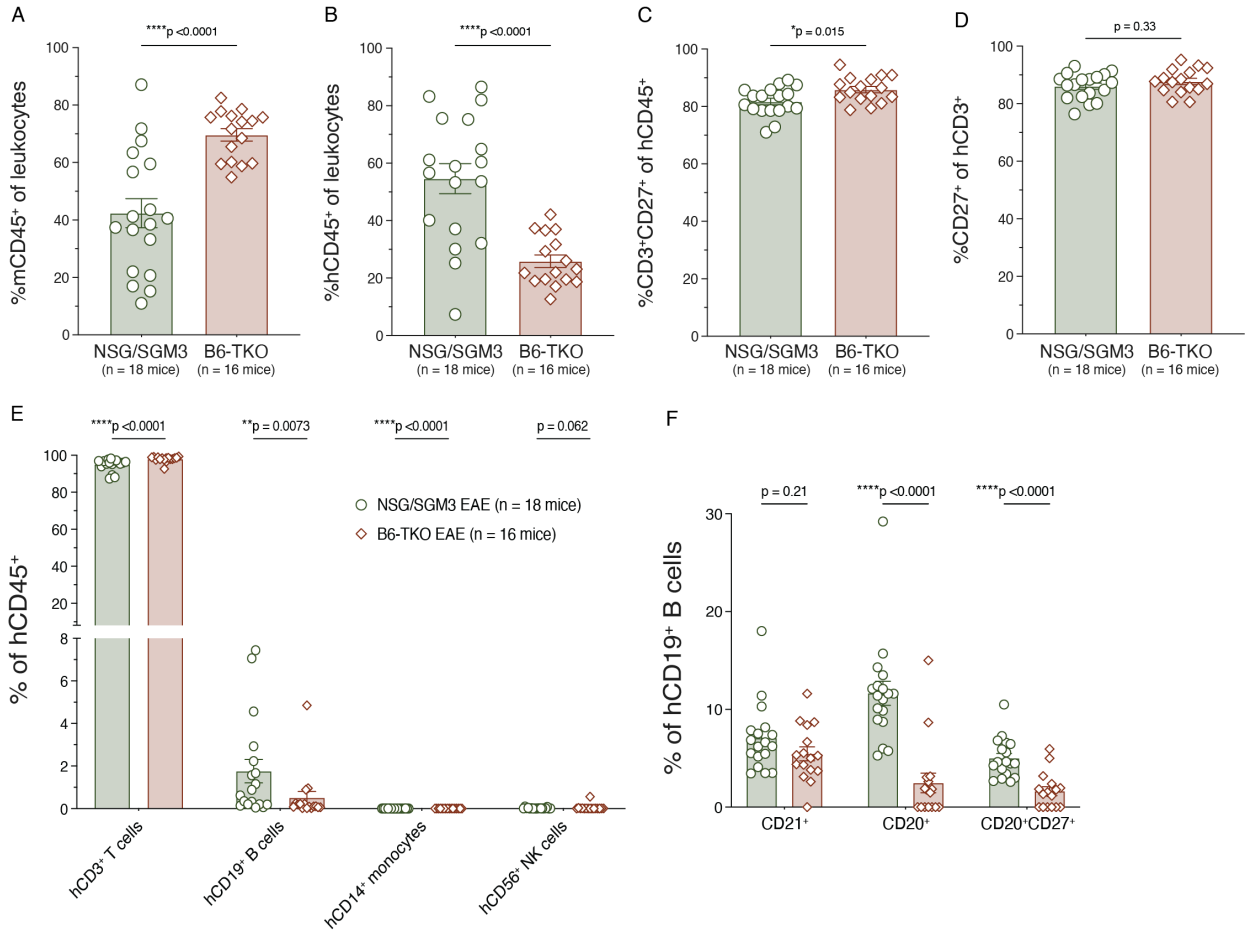

Figure 4.71 Human immune cell frequencies reconstituting the spleens of PBMC engrafted NSG/SGM3 and B6-TKO mice at EAE endpoint

Figure shows the proportions of (A) murine $CD45^+$ cells among all leukocytes, (B) human $CD45^+$ cells among all leukocytes, (C) $hCD3^+CD27^+$ T cells among engrafted $hCD45^+$ cells, and (D) $hCD27^+$ T cells among $hCD3^+$ T cells, as well as (E) the relative proportions of major human immune cell lineages among all $hCD45^+$ cells and (F) the relative proportions of hCD21, hCD20 and/or hCD27 expressing $hCD19^+$ B cell subsets in the spleen of PBMC-engrafted NSG/SGM3 mice (n = 18 males) and B6-TKO mice (n = 16 females and males mixed) derived from a healthy female donor (HD-04) day 22 – 23 post-rhMOG/MOG_{35-55} EAE induction. Data are shown as mean with SEM and were analyzed by Welch's unpaired t test or by Mann-Whitney test. HuPBMC cohorts included: 18 and 28.

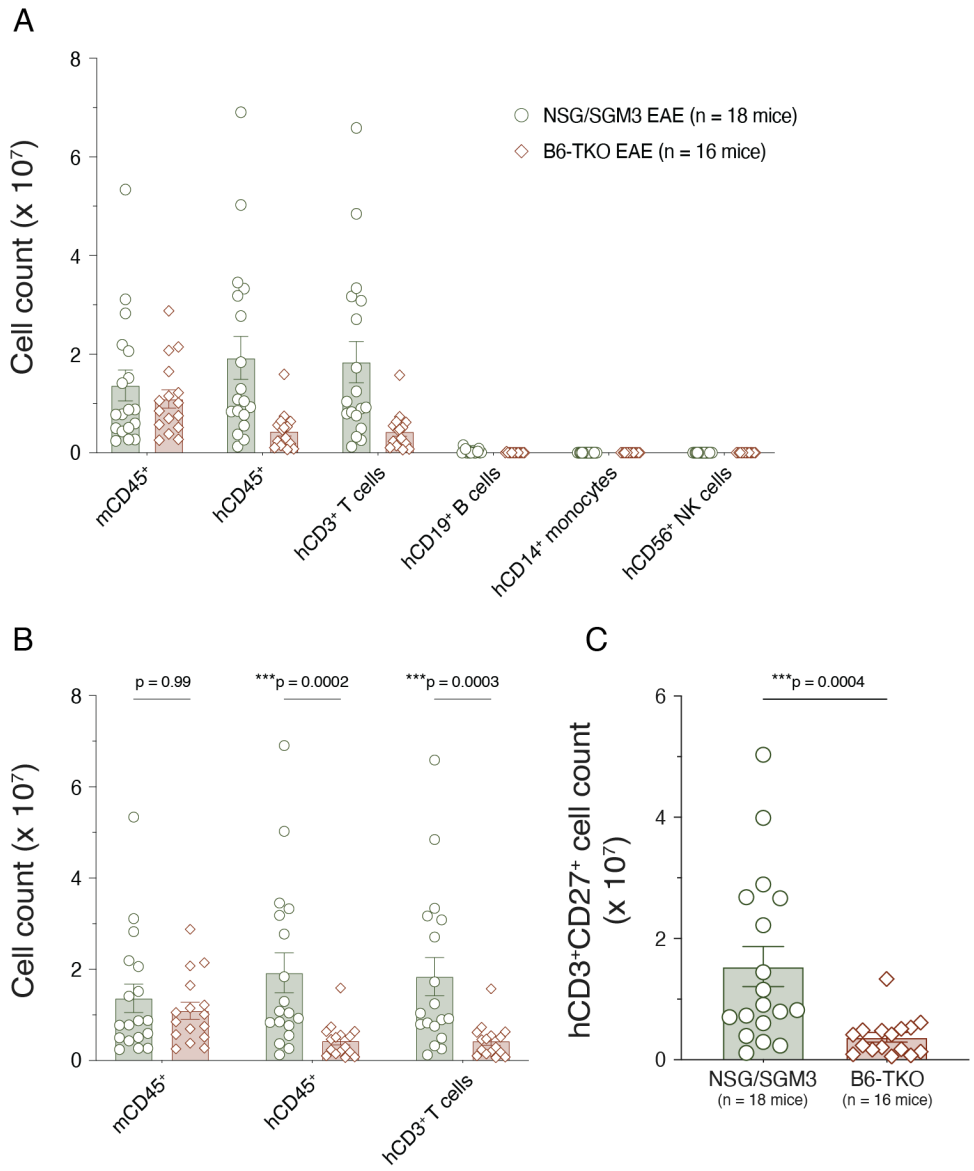

Figure 4.72 Human immune cell abundance in the spleens of PBMC engrafted NSG/SGM3 and B6-TKO mice at EAE endpoint

Figure shows (A) the total numbers of murine leukocytes and human immune cell subsets in the spleens of PBMC-engrafted NSG/SGM3 mice (n = 18 males), and B6-TKO mice (n = 16 females and males mixed) derived from a healthy female donor (HD-04) day 22 – 23 post-rhMOG/MOG$_{35-55}$ EAE induction. The relative abundance of predominantly engrafted subsets is shown in (B) to better illustrate quantities. The figure also shows total splenic cell counts for minorly engrafted subsets: (C) hCD3^{+}CD27^{+} T cells, (D) hCD9^{+} B cells, (E) hCD14^{+} monocytes, and (F) hCD56^{+} NK cells. Data are shown as mean with SEM and were analyzed by Mann-Whitney test. HuPBMC cohorts included: 18 and 28.

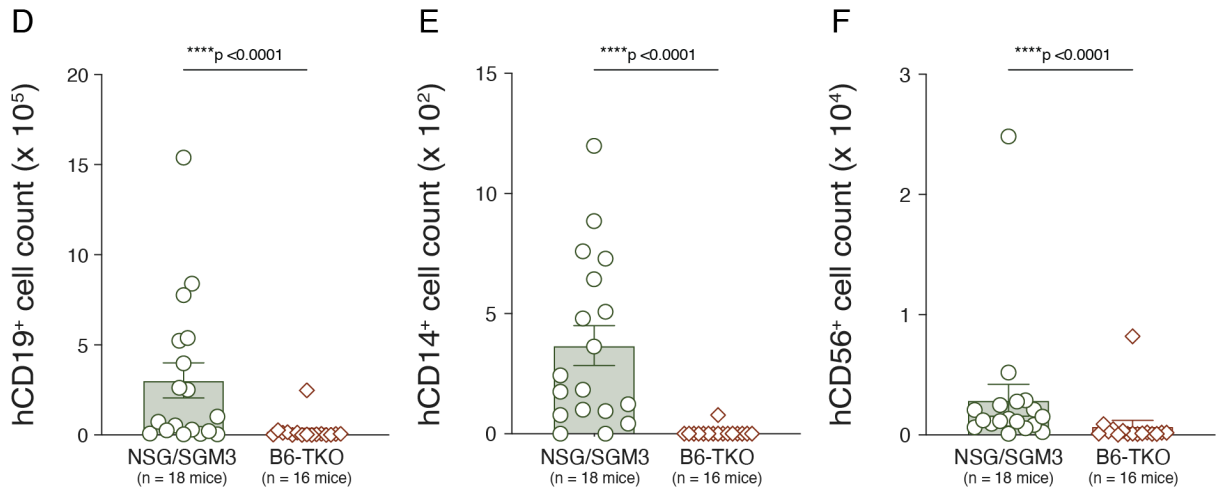

Figure 4.72 continued

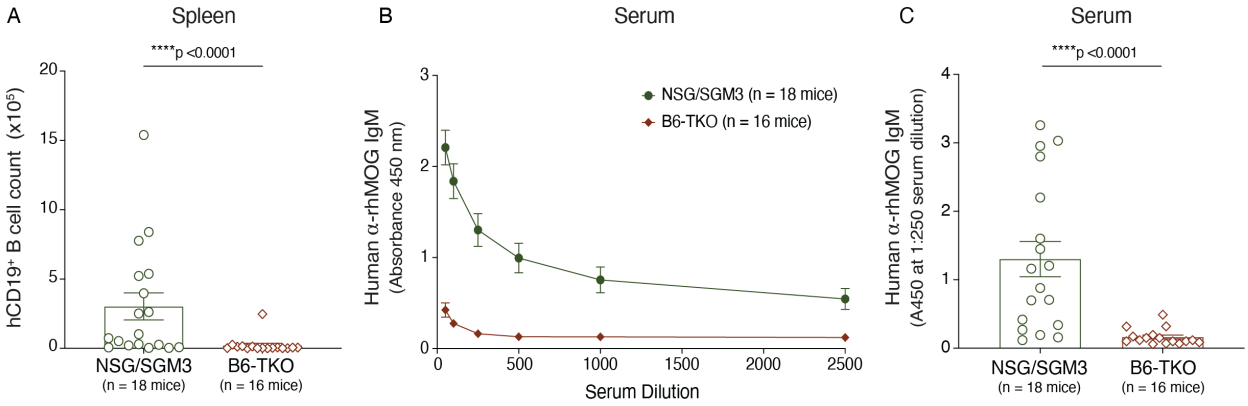

Figure 4.73 Peripheral human B cell engraftment and IgM responses to EAE induction of PBMC engrafted NSG/SGM3 and B6-TKO at endpoint

Figure shows (A) the total hCD19^{+} B cell count in the spleens of PBMC-engrafted NSG/SGM3 mice (n = 18 males) and B6-TKO mice (n = 16 females and males mixed) derived from a healthy female donor (HD-04) day 22 – 23 post-rhMOG/MOG$_{35-55}$ EAE induction, as well as (B) the human anti-rhMOG IgM levels in the serum for increasing dilutions, and (C) the human anti-rhMOG IgM level at a 1:250 serum dilution specifically. In B and C, data show the average of two duplicate wells per sample. Data are shown as mean with SEM and, in A and C, were analyzed by Mann-Whitney test. HuPBMC cohorts included: 18 and 28.

4.9.2.5 CNS infiltration at endpoint

Within the HuPBMC NSG/SGM3 EAE group, there were significant differences in CNS infiltration of some HIS cell subsets between mice that either did or did not develop clinical symptoms (see Figure 4.37), so they were separated into two groups for comparison to HuPBMC B6-TKO EAE mice, which were all asymptomatic. For this analysis, we only included the male recipient B6-TKO mice, despite recipient B6-TKO seemingly not showing a similar sex bias as seen in HuPBMC NSG/SGM3 EAE mice (Appendix 9, Figure A.49 – Figure A.51), to normalize for this potential factor and its influence on HIS subset phenotypes. In the CNS, total immune cell counts (murine + human cells combined) were higher in EAE induced HuPBMC B6-TKO mice than NSG/SGM3 mice, whereas this trend was inverted in the spleen (Figure 4.74A – C). This increased abundance in the B6-TKO CNS was accounted for by the relatively high numbers of murine myeloid cells, including both resident mCD45^{lo} and infiltrating mCD45^{hi} immune cells (Figure 4.74D – H, Figure 4.75), suggesting more severe gliosis occurred in the HuPBMC B6-TKO EAE mice consistent with previous observations from CD47$^{-/-}$ mice[707]. mCD45^{+} myeloid cell counts in the spleen were comparable between strains (Figure 4.74I).

In the CNS at endpoint, the proportions of hCD45^{+} cells among all leukocytes were reduced in B6-TKO mice compared to symptomatic NSG/SGM3 mice but were statistically similar to subclinical NSG/SGM3 mice (Figure 4.76A – B). Though infiltrating hCD45^{+} counts were similar in the brain between strains (Figure 4.76A D), the spinal cords and spleens of B6-TKO mice contained fewer human immune cells than the symptomatic NSG/SGM3 samples (Figure 4.76E – F). The majority of reconstituting and CNS infiltrating hCD45^{+} cells were hCD3^{+} T cells (Figure 4.76G – I), and thus, the same cell count trends applied (Figure 4.76J – L). Among CNS infiltrating and spleen reconstituting hCD3^{+} T cells, the proportions expressing hCD4 (Figure 4.77A – C) and hCD8 (Figure 4.77D – F) were similar in all tissues between NSG/SGM3 and B6-TKO mice, indicating a donor specific effect on T cell subset ratios that was not skewed specifically by the engrafted recipient strain. Among the hCD3^{+}CD4^{+} T cells, regulatory FOXP3^{+} cells also occurred at similar frequencies between groups in all tissues (Figure 4.77G – I).

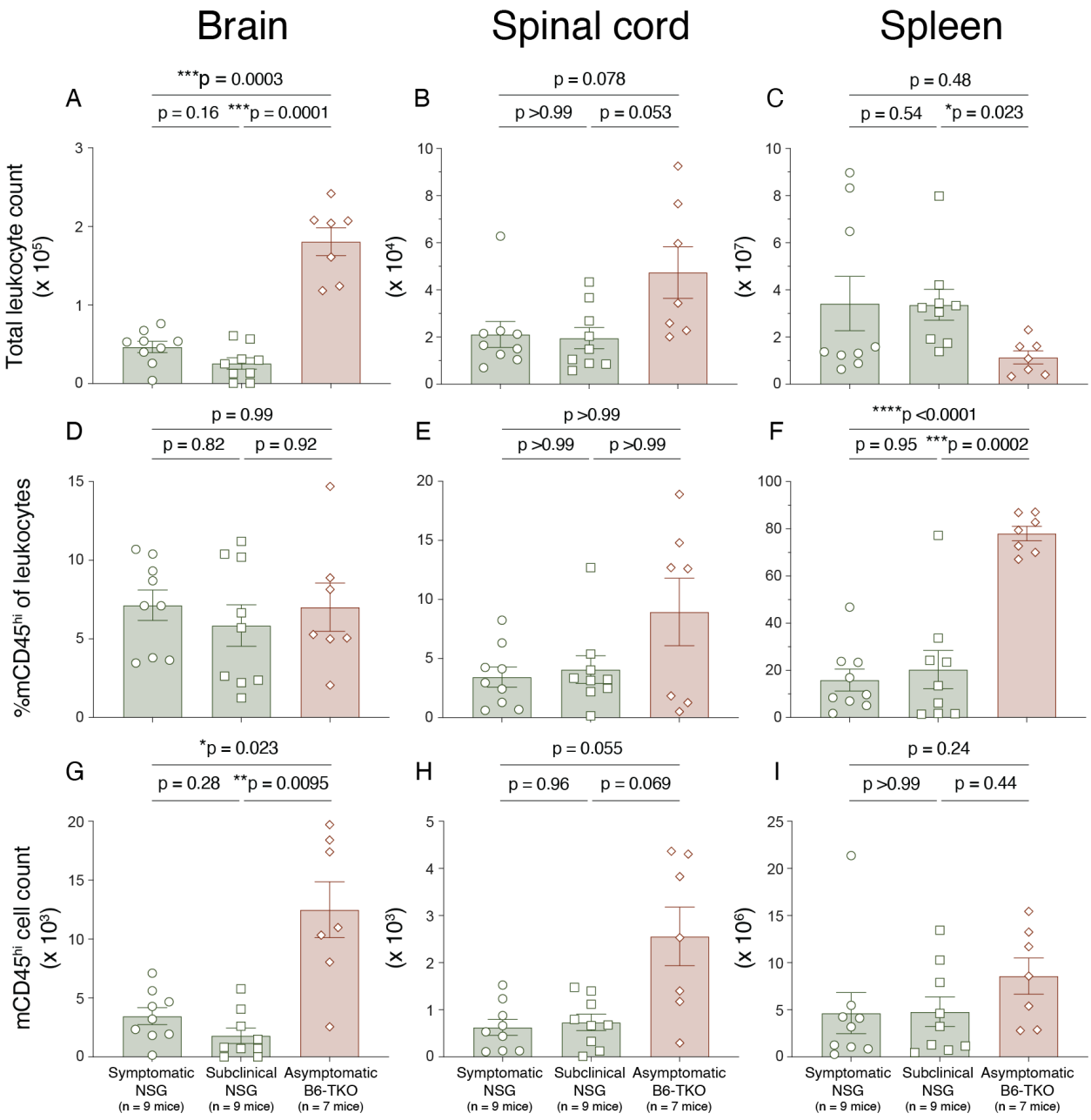

Figure 4.74 Murine macrophages in the CNS and spleens of PBMC engrafted NSG/SGM3 and B6-TKO mice at EAE endpoint

Figure shows the total number of leukocytes (murine and human, A – C), the proportion of mCD45^{hi} cells among all leukocytes (D – F), and the total number of mCD45^{hi} cells (G – I) in the brains (left column), spinal cords (middle column), and spleens (right column) of PBMC-engrafted NSG/SGM3 mice (separated into n = 9 symptomatic males and n = 9 subclinical males) and B6-TKO mice (n = 7 asymptomatic males) derived from a healthy female donor (HD-04) day 22 – 23 post-rhMOG/MOG$_{35-55}$ EAE induction. Tissues were perfused prior to cell isolation. Data are shown as mean with SEM and were analyzed by Brown-Forsythe and Welch ANOVA with Dunnett's T3 multiple comparisons or by Kruskal-Wallis test with Dunn's multiple comparisons test. HuPBMC cohorts included: 18 and 28.

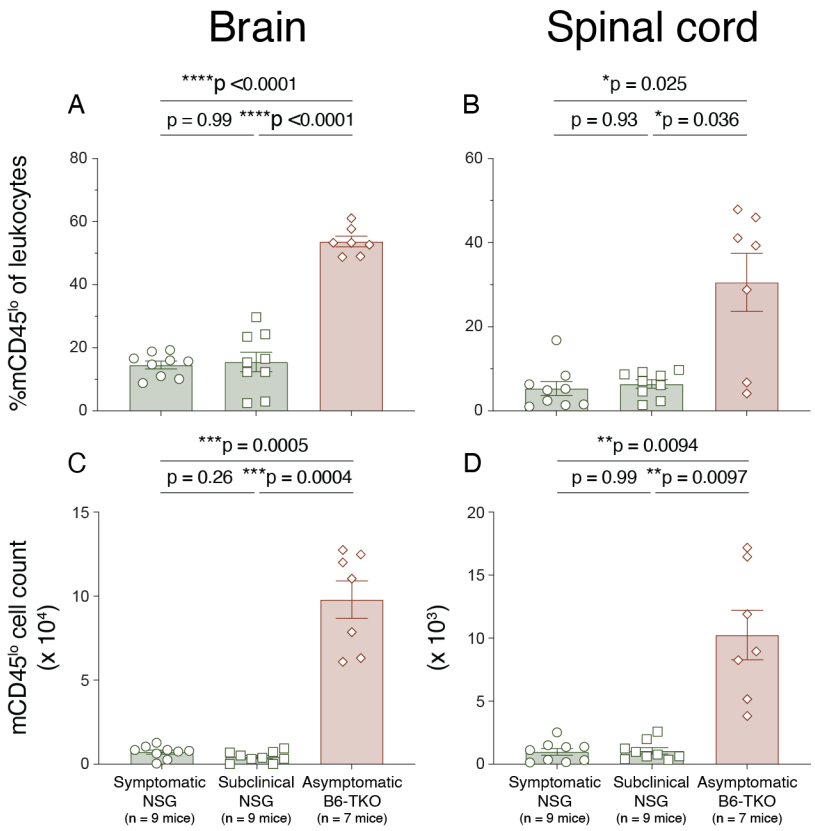

Figure 4.75 Murine microglia in the CNS of PBMC engrafted NSG/SGM3 and B6-TKO mice at EAE endpoint

Figure shows the proportion of mCD45^{lo} cells among all leukocytes (A – B) and the total number of mCD45^{lo} cells (C – D) in the brains (left column) and spinal cords (right column) of PBMC-engrafted NSG/SGM3 mice (separated into n = 9 symptomatic males and n = 9 subclinical males) and B6-TKO mice (n = 7 asymptomatic males) derived from a healthy female donor (HD-04) day 22 – 23 post-rhMOG/MOG$_{35-55}$ EAE induction. Tissues were perfused prior to cell isolation. Data are shown as mean with SEM and were analyzed by Brown-Forsythe and Welch ANOVA with Dunnett's T3 multiple comparisons or by Kruskal-Wallis test with Dunn's multiple comparisons test. HuPBMC cohorts included: 18 and 28.

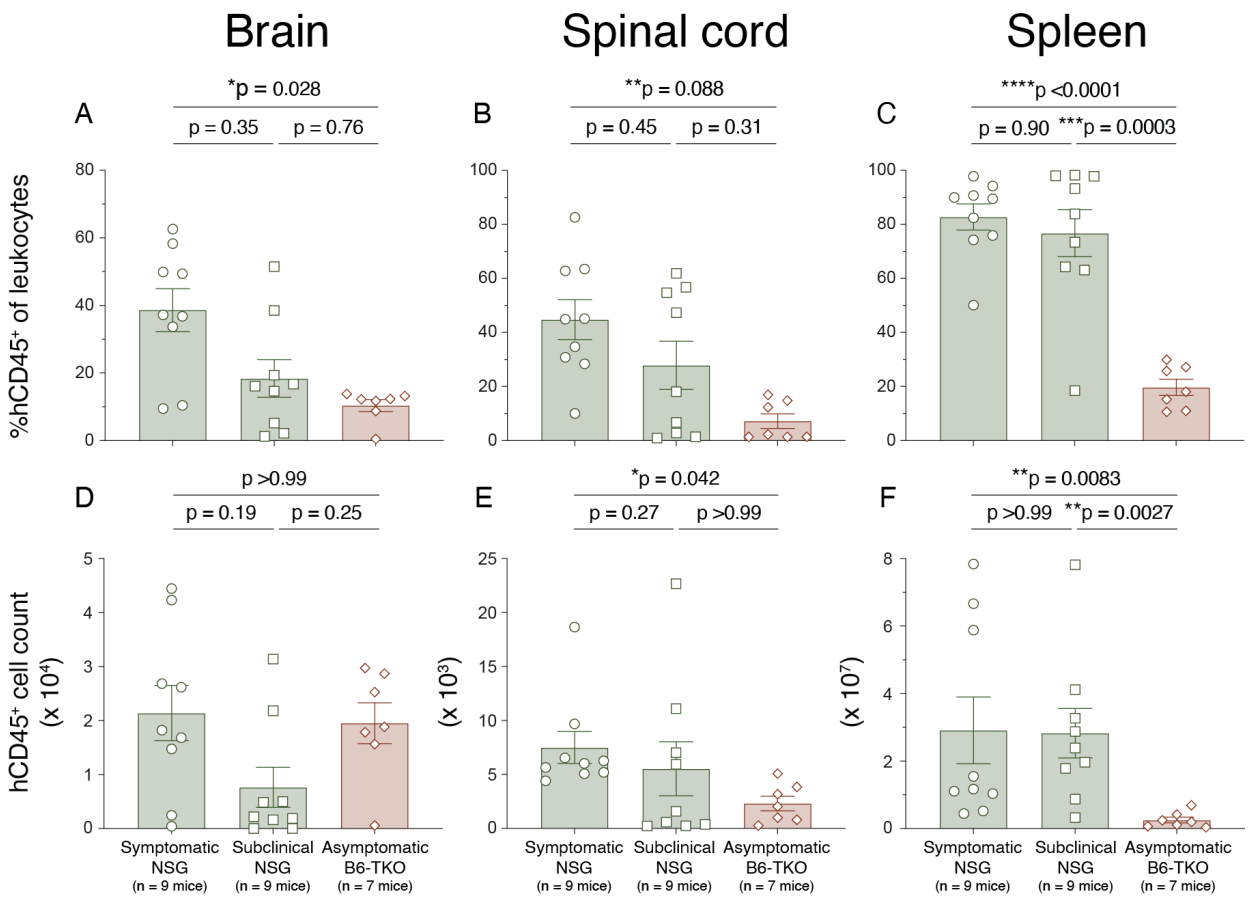

Figure 4.76 Human immune cells in the CNS and spleens of PBMC engrafted NSG/SGM3 and B6-TKO mice at EAE endpoint

Figure shows the proportion of $hCD45^+$ cells among all leukocytes (A – C), the total number of $hCD45^+$ cells (D – F), the proportion of $hCD3^+$ T cells among $hCD45^+$ cells (G – I), and the total number of $hCD45^+CD3^+$ T cells (J –L) in the brains (left column), spinal cords (middle column), and spleens (right column) of PBMC-engrafted NSG/SGM3 mice (separated into n = 9 symptomatic males and n = 9 subclinical males) and B6-TKO mice (n = 7 asymptomatic males) derived from a healthy female donor (HD-04) day 22 – 23 post-rhMOG/MOG_{35-55} EAE induction. Tissues were perfused prior to cell isolation. Data are shown as mean with SEM and were analyzed by Brown-Forsythe and Welch ANOVA with Dunnett's T3 multiple comparisons or by Kruskal-Wallis test with Dunn's multiple comparisons test. HuPBMC cohorts included: 18 and 28.

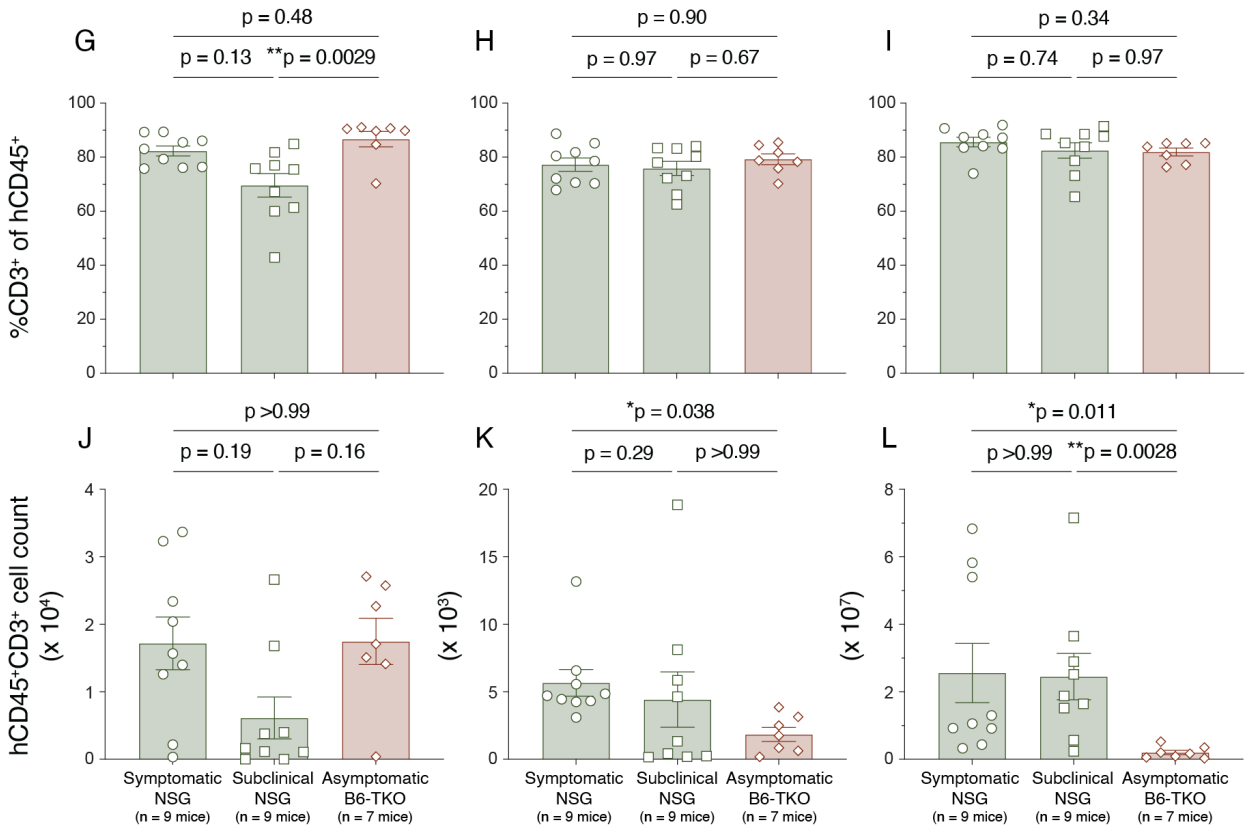

Figure 4.76 continued

In the brain, all groups contained similar numbers of hCD3$^+$CD4$^+$ and hCD3$^+$CD8$^+$ T cells, though the B6-TKO spinal cords and spleens contained significantly fewer in total than the corresponding symptomatic NSG/SGM3 mice (Figure 4.78). Consistent with the proportional data, the overall reduction in infiltrating hCD45$^+$ counts in the B6-TKO spinal cord and spleen samples appeared to apply to both T cell subsets equally (Figure 4.78). Correspondingly, the brains in each group contained similar numbers of regulatory CD4$^+$FOXP3$^+$ T cells (Figure 4.79D), whereas there were fewer total Tregs in the B6-TKO spinal cords and spleens compared to both NSG/SGM3 groups, as a result of fewer total h CD3$^+$CD4$^+$ T cells in these organs (Figure 4.79E – F). The spinal cords of B6-TKO mice, however, did show a nonsignificant skew toward slightly fewer hCD3$^+$CD8$^+$ T cells relative to hCD3$^+$CD4$^+$ T cells, a trend that was inverted in the spleens (Figure 4.79G – I).

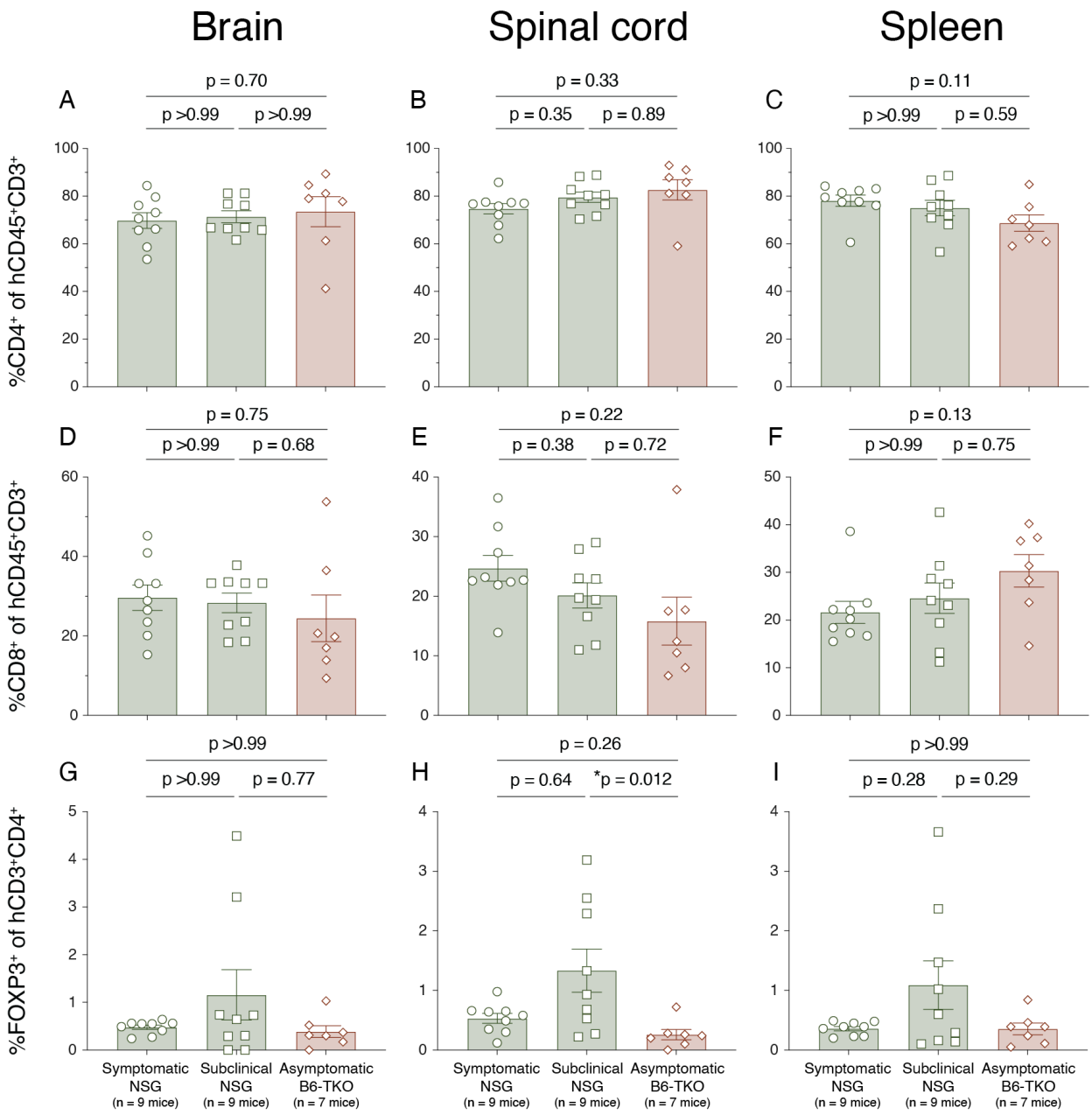

Figure 4.77 Human T cell subsets in the CNS and spleens of PBMC engrafted NSG/SGM3 and B6-TKO mice at EAE endpoint

Figure shows the proportions of $hCD4^+$ cells among $hCD3^+$ T cells (A – C), $hCD8^+$ cells among $hCD3^+$ T cells (D – F), $FOXP3^+$ cells among $hCD3^+CD4^+$ T cells (G – I) in the brains (left column), spinal cords (middle column), and spleens (right column) of PBMC-engrafted NSG/SGM3 mice (separated into n = 9 symptomatic males and n = 9 subclinical males) and B6-TKO mice (n = 7 asymptomatic males) derived from a healthy female donor (HD-04) day 22 – 23 post-rhMOG/MOG_{35-55} EAE induction. Tissues were perfused prior to cell isolation. Data are shown as mean with SEM and were analyzed by Brown-Forsythe and Welch ANOVA with Dunnett's T3 multiple comparisons or by Kruskal-Wallis test with Dunn's multiple comparisons test. HuPBMC cohorts included: 18 and 28.

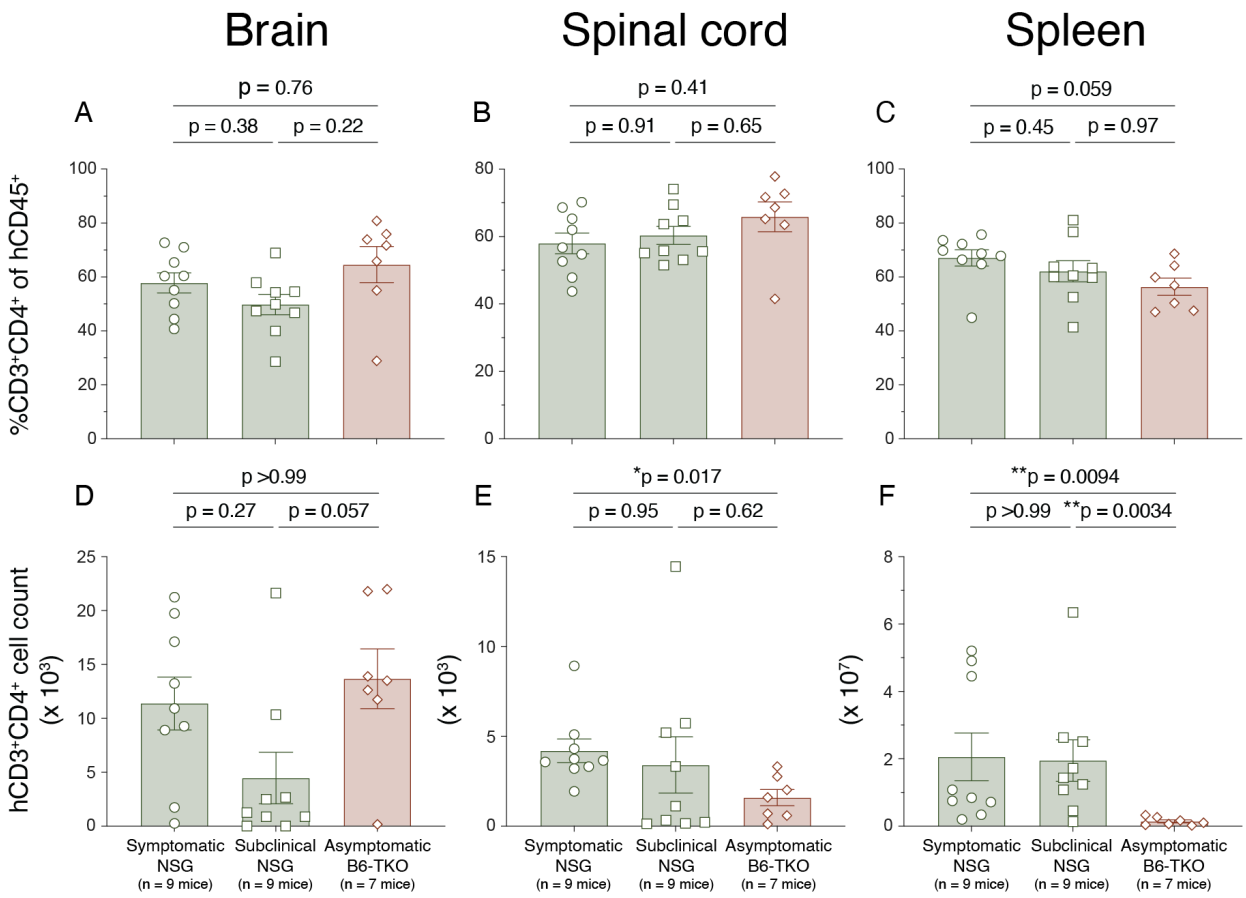

Figure 4.78 Human T cell abundance in the CNS and spleens of PBMC engrafted NSG/SGM3 and B6-TKO mice at EAE endpoint

Figure shows the proportion of $hCD3^+CD4^+$ T cells among $hCD45^+$ cells (A – C), the total number of $hCD3^+CD4^+$ T cells (D – F), the proportion of $hCD3^+CD8^+$ T cells among $hCD45^+$ cells (G – I), and the total number of $hCD3^+CD8^+$ T cells (J – L) in the brains (left column), spinal cords (middle column), and spleens (right column) of PBMC-engrafted NSG/SGM3 mice (separated into n = 9 symptomatic males and n = 9 subclinical males) and B6-TKO mice (n = 7 asymptomatic males) derived from a healthy female donor (HD-04) day 22 – 23 post-rhMOG/MOG_{35-55} EAE induction. Tissues were perfused prior to cell isolation. Data are shown as mean with SEM and were analyzed by Brown-Forsythe and Welch ANOVA with Dunnett's T3 multiple comparisons or by Kruskal-Wallis test with Dunn's multiple comparisons test. HuPBMC cohorts included: 18 and 28.

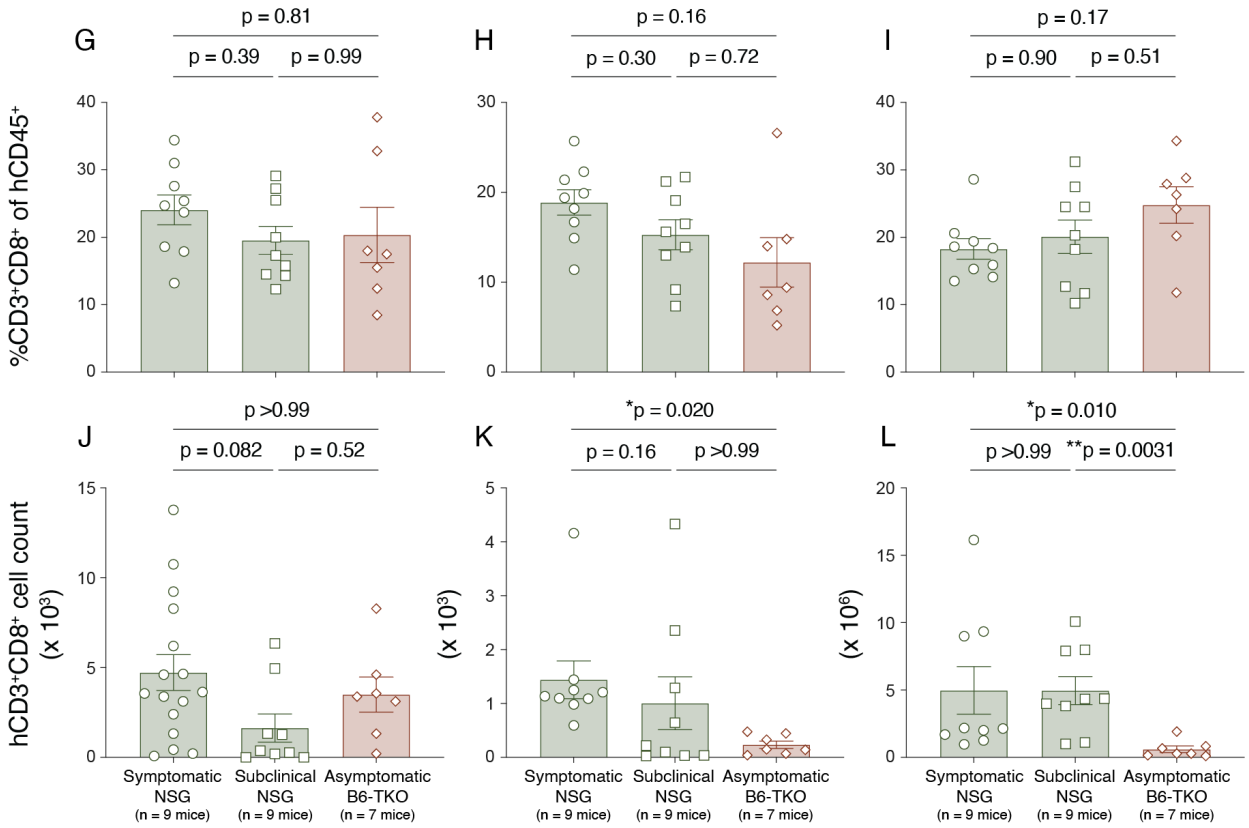

Figure 4.78 continued

Cytokine expression by engrafted and CNS infiltrating human T cells was measured to determine if hCD3$^+$CD4$^+$ and hCD3$^+$CD8$^+$ T cells reconstituting both recipient strains were primed and functionally capable of mediating EAE inflammation following MOG immunization. In the CNS, a significantly greater proportion of infiltrating human immune cells in B6-TKO mice were hCD3$^+$CD4$^+$IFNγ$^+$ Th1 polarized compared to all NSG/SGM3 mice, though Th1 frequency was similar in the spleens across groups (Figure 4.80A – C). Furthermore, a greater proportion of infiltrating hCD45$^+$ cells were hCD3$^+$CD4$^+$IL-17A$^+$ Th17 cells in the brains of B6-TKO mice, with similar proportions occurring in the spinal cords and spleens (Figure 4.80G – I). Despite overall reduced numbers of hCD3$^+$CD4$^+$ T cells in the spinal cords of B6-TKO mice compared to symptomatic NSG/SGM3 mice (Figure 4.78E), the increased proportion of B6-TKO CNS infiltrating T cells expressing proinflammatory cytokines resulted in similar numbers of Th1 and Th17 cells in the spinal cords between groups (Figure 4.80 middle column). In the brain, there were quantitively more effector Th1 and Th17 cells in the B6-TKO mice than both NSG/SGM3 groups (Figure 4.80 left column), whereas fairly equivalent proportions in the spleen resulted in

fewer total splenic effector hCD3$^+$CD4$^+$ T cell counts in the B6-TKO mice compared to NSG/SGM3 mice (Figure 4.80 right column).

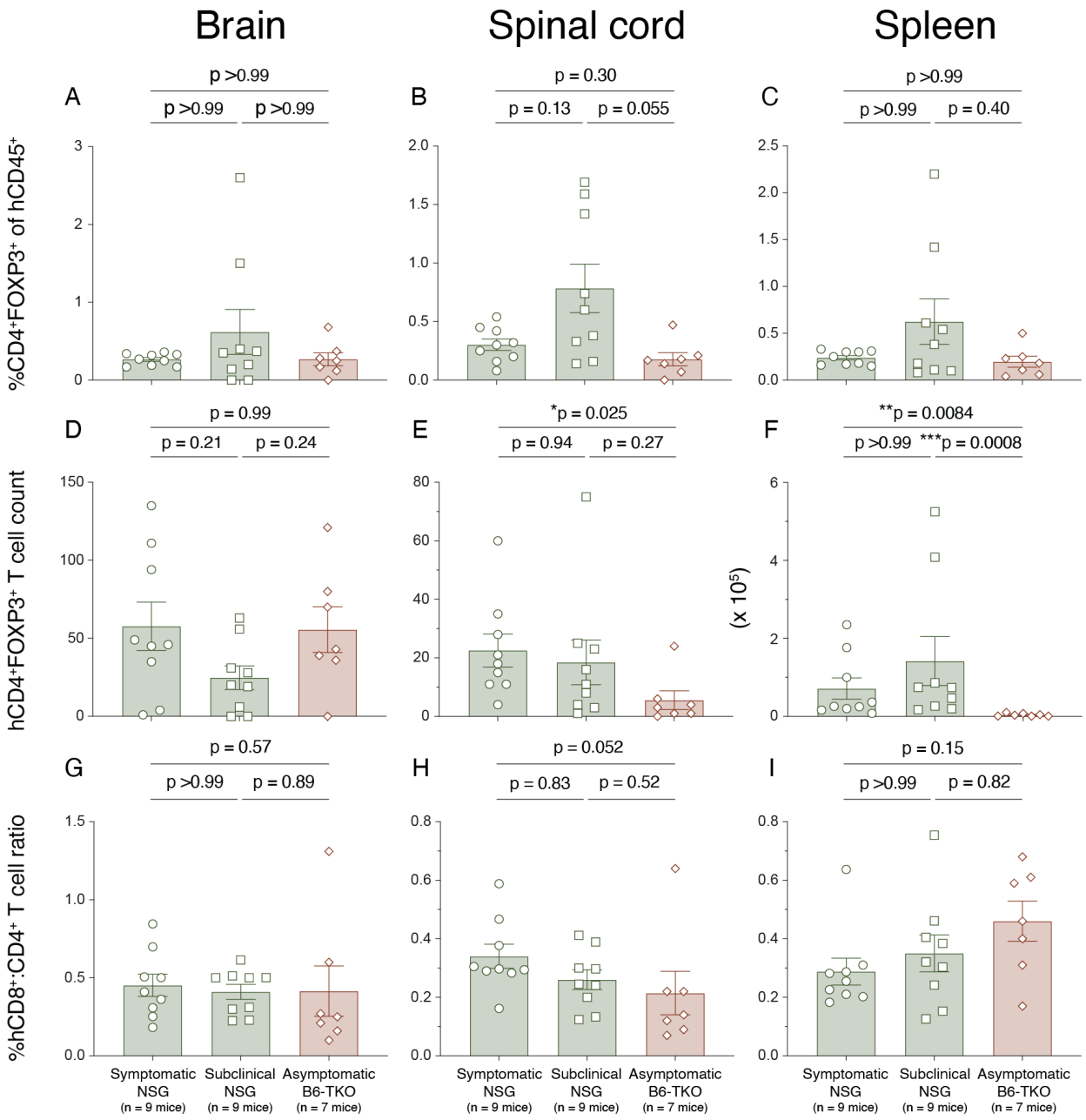

Figure 4.79 Human T cell subsets in the CNS and spleens of PBMC engrafted NSG/SGM3 and B6-TKO mice at EAE endpoint

Figure shows the proportion of FOXP3$^+$ cells among hCD3$^+$CD4$^+$ T cells (A – C), the total number of hCD3$^+$CD4$^+$FOXP3$^+$ T cells (D – F), and the ratio of hCD3$^+$CD8$^+$ T cells to hCD3$^+$CD4$^+$ T cells (G – I) in the brains (left column), spinal cords (middle column), and spleens (right column) of PBMC-engrafted NSG/SGM3 mice

(separated into n = 9 symptomatic males and n = 9 subclinical males) and B6-TKO mice (n = 7 asymptomatic males) derived from a healthy female donor (HD-04) day 22 – 23 post-rhMOG/MOG$_{35-55}$ EAE induction. Tissues were perfused prior to cell isolation. Data are shown as mean with SEM and were analyzed by Brown-Forsythe and Welch ANOVA with Dunnett's T3 multiple comparisons or by Kruskal-Wallis test with Dunn's multiple comparisons test. HuPBMC cohorts included: 18 and 28.

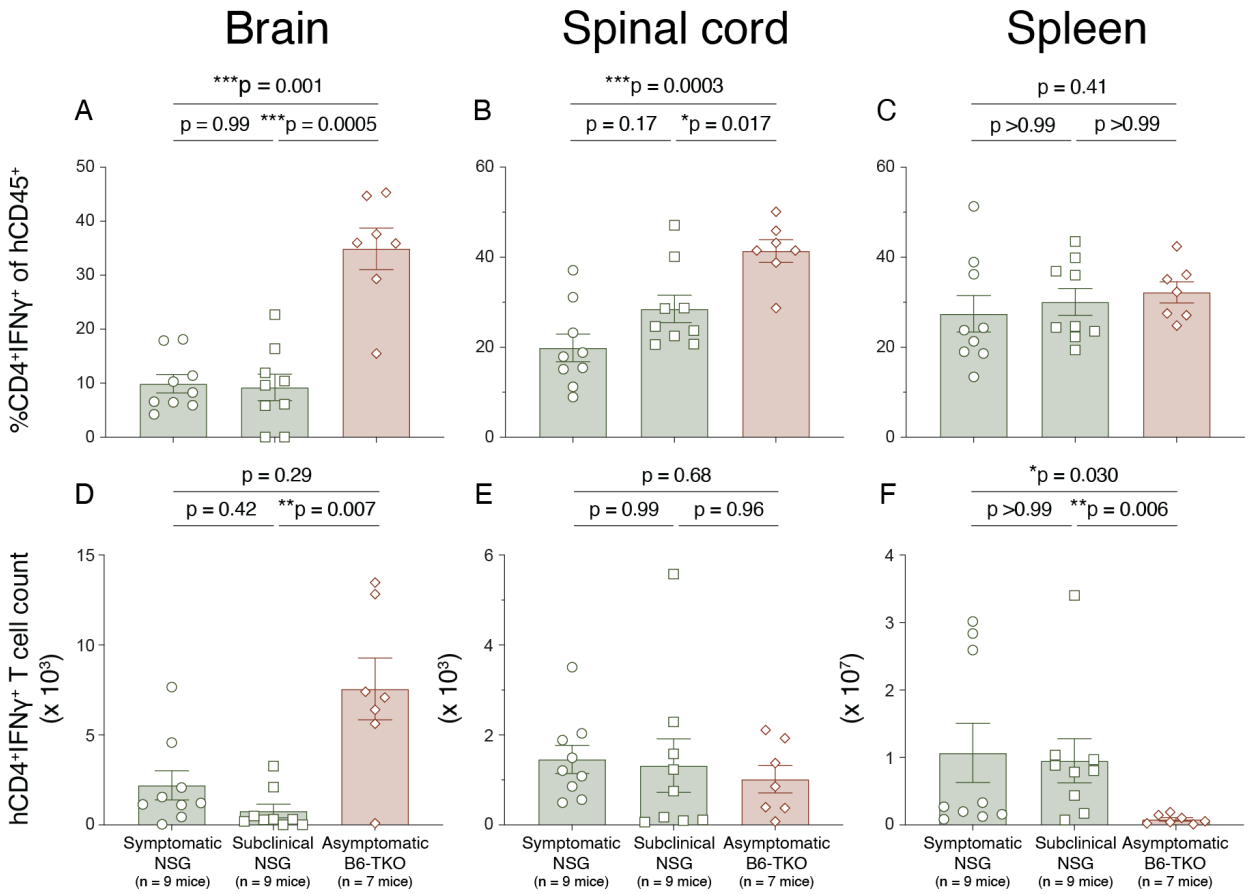

Figure 4.80 Human Th1 and Th17 abundance in the CNS and spleens of PBMC engrafted NSG/SGM3 and B6-TKO mice at EAE endpoint

Figure shows the proportion of hCD4$^+$IFNγ$^+$(IL-17A$^-$) Th1 cells among hCD45$^+$ cells (A – C), the total number of hCD4$^+$IFNγ$^+$(IL-17A$^-$) Th1 cells (D – F), the proportion of hCD4$^+$IL-17A$^+$(IFNγ$^-$) Th17 cells among hCD45$^+$ cells (G – I), and the total number of hCD4$^+$IL-17A$^+$(IFNγ$^-$) Th17 cells (J – L) in the brains (left column), spinal cords (middle column), and spleens (right column) of PBMC-engrafted NSG/SGM3 mice (separated into n = 9 symptomatic males and n = 9 subclinical males) and B6-TKO mice (n = 7 asymptomatic males) derived from a healthy female donor (HD-04) day 22 – 23 post-rhMOG/MOG$_{35-55}$ EAE induction. Cells isolated from perfused tissues were stimulated with PMA and ionomycin to measure cytokine expression. Data are shown as mean with SEM and were analyzed by Brown-Forsythe and Welch ANOVA with Dunnett's T3 multiple comparisons or by Kruskal-Wallis test with Dunn's multiple comparisons test. HuPBMC cohorts included: 18 and 28.

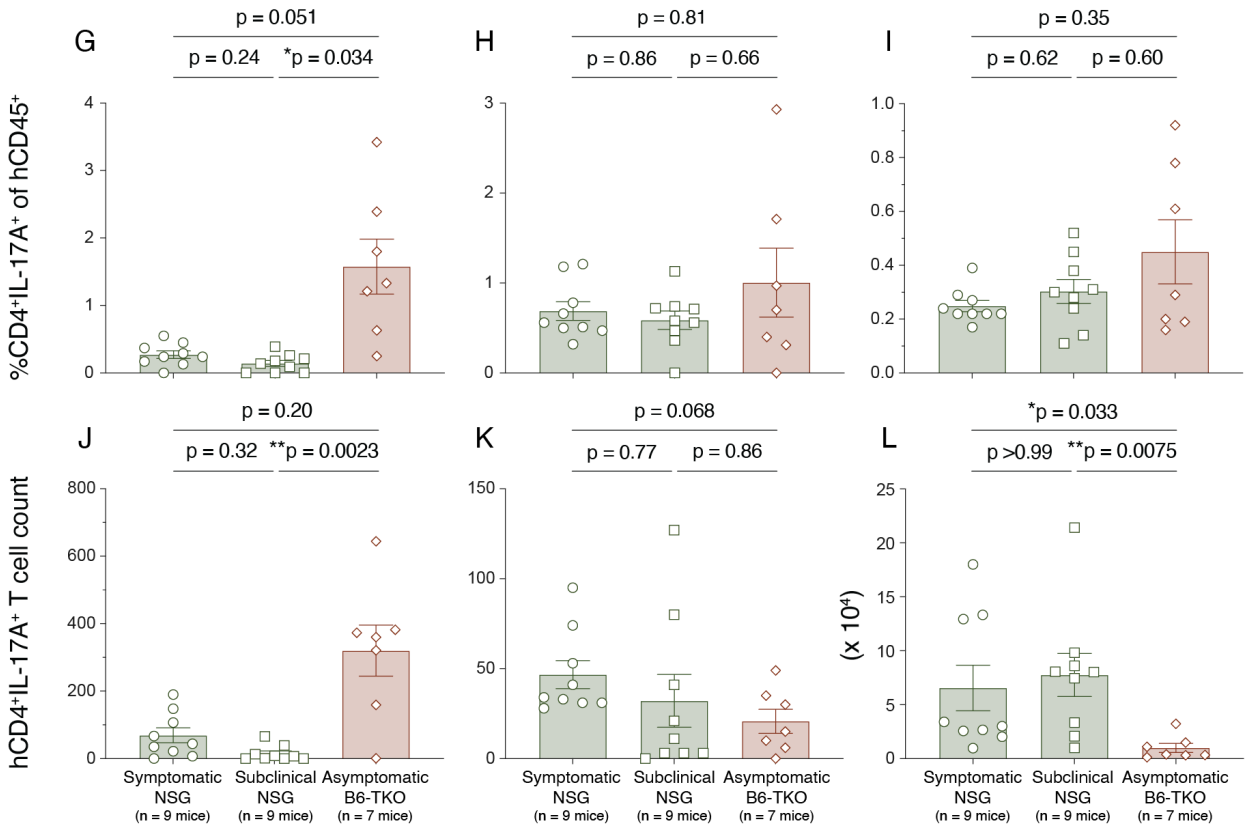

Figure 4.80 continued

The proportion of infiltrating hCD3$^+$CD4$^+$ T cells that were double IFNγ$^+$IL-17A$^+$ (Th1/Th17) was also higher in all tissues from HuPBMC EAE B6-TKO mice compared to NSG/SGM3 mice regardless of symptom incidence (Figure 4.81A – C). Double Th1/Th17 counts were similar or increased in the CNS tissues of B6-TKO mice, and reduced in the spleens, compared to NSG/SGM3 mice (Figure 4.81D – F). The data indicated that while fewer hCD3$^+$CD4$^+$ T cells infiltrated the CNS of asymptomatic B6-TKO mice compared to symptomatic NSG/SGM3 mice following PBMC engraftment and MOG EAE induction, a greater proportion of B6-TKO CNS infiltrating hCD3$^+$CD4$^+$ T cells expressed proinflammatory cytokines, generating comparable total numbers of effector cells in the brains and spinal cords of both strains. Therefore, the absence of EAE symptom incidence in HuPBMC B6-TKO EAE mice could not be attributed to a deficiency in the development of effector hCD3$^+$CD4$^+$ T cell responses and proinflammatory polarization at the site of disease.

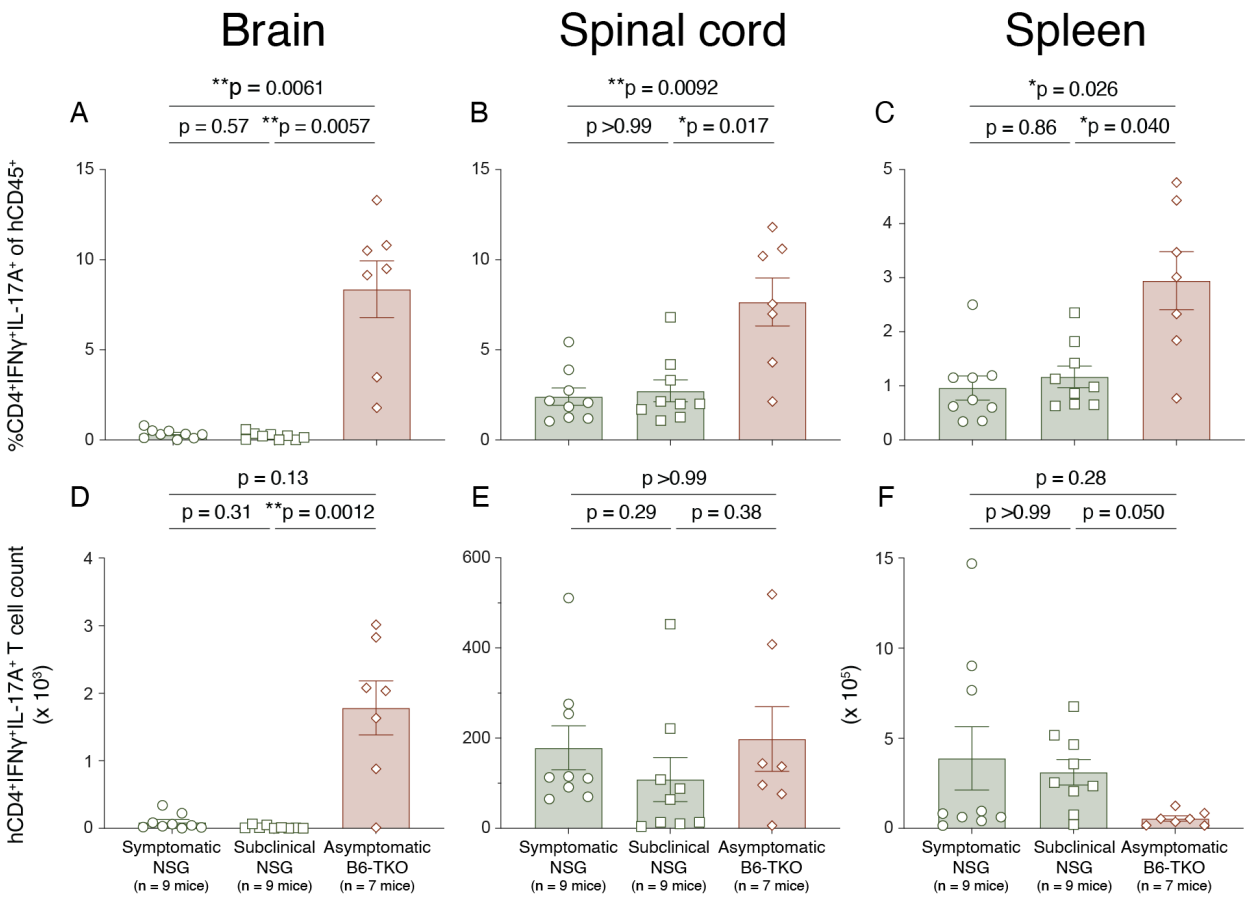

Figure 4.81 Dual Th1/Th17 human T cell abundance in the CNS and spleens of PBMC engrafted NSG/SGM3 and B6-TKO mice at EAE endpoint

Figure shows the proportion of hCD4$^+$IFNγ$^+$IL-17A$^+$ Th1/Th17 cells among hCD45$^+$ cells (A – C) and the total number of hCD4$^+$IFNγ$^+$IL-17A$^+$ Th1/Th17 cells (D – F) in the brains (left column), spinal cords (middle column), and spleens (right column) of PBMC-engrafted NSG/SGM3 mice (separated into n = 9 symptomatic males and n = 9 subclinical males) and B6-TKO mice (n = 7 asymptomatic males) derived from a healthy female donor (HD-04) day 22 – 23 post-rhMOG/MOG$_{35-55}$ EAE induction. Cells isolated from perfused tissues were stimulated with PMA and ionomycin to measure cytokine expression. Data are shown as mean with SEM and were analyzed by Brown-Forsythe and Welch ANOVA with Dunnett's T3 multiple comparisons or by Kruskal-Wallis test with Dunn's multiple comparisons test. HuPBMC cohorts included: 18 and 28.

In the CNS, $hCD3^+CD8^+IFN\gamma^+$ T cells comprised a similar proportion of infiltrating $hCD45^+$ immune cells in all three groups, though the proportion was somewhat lower in the spleens of HuPBMC B6-TKO EAE mice (Figure 4.82A – C). $hCD3^+CD8^+IFN\gamma^+$ T cell counts were similar in the brain, but lower in the spinal cord and spleen of B6-TKO mice compared to NSG/SGM3 mice (Figure 4.82D – F), due to reduced total $hCD8^+$ T cell counts in these tissues (Figure 4.78K – L). Despite being present at similar or lower levels in the CNS, $hCD3^+CD8^+IFN\gamma^+$ T cells expressed, on average, a greater amount of IFNγ per cell in the brains and spinal cords of B6-TKO mice (Figure 4.82G – H), whereas per cell expression was comparable in the spleens (Figure 4.82I), indicating that CNS infiltrating $hCD8^+$ T cells were just as capable if not more so of producing IFNγ in B6-TKO recipients than NSG/SGM3 recipients.

In contrast, $hCD3^+CD8^+GzmB^+$ T cells comprised a smaller proportion of CNS infiltrating $hCD45^+$ cells in subclinical NSG/SGM3 and B6-TKO mice than symptomatic NSG/SGM3 mice (Figure 4.83A – B), resulting in reduced total numbers per tissue in the former groups (Figure 4.83D – E). Similar proportions were measured in the spleens of all groups (Figure 4.83AC), though B6-TKO spleens contained significantly fewer than both NSG/SGM3 group samples (Figure 4.83F). Per cell expression of GzmB by $hCD3^+CD8^+$ T cells followed a consistently decreasing trend from symptomatic to subclinical NSG/SGM3 mice then asymptomatic B6-TKO mice in all tissues (Figure 4.83G – I) and was significantly lower in the CNS of B6-TKO mice (Figure 4.83G – H). Double $hCD8^+IFN\gamma^+GzmB^+$ T cells comprised variably similar proportions of CNS infiltrating human immune cells in all three groups but were more frequent in the spleens of B6-TKO mice compared to NSG/SGM3 mice (Figure 4.84A – C). The brains from each group therefore contained similar numbers of $hCD8^+IFN\gamma^+GzmB^+$ T cells, whereas the spinal cords and spleens of B6-TKO mice contained fewer total than the NSG/SGM3 mice (Figure 4.84D – F).

Overall, $hCD3^+CD8^+$ T cells infiltrating the CNS of HuPBMC B6-TKO EAE mice shifted toward greater IFNγ, with a concomitant decrease in GzmB expression, compared to HuPBMC NSG-SGM3 EAE mice. Despite this polarization skew in the cytotoxic $hCD8^+$ T cell population, PBMC engrafted B6-TKO mice appeared just as effective in generating CNS localized effector $hCD8^+$ T cell responses as similarly treated NSG/SGM3 mice.

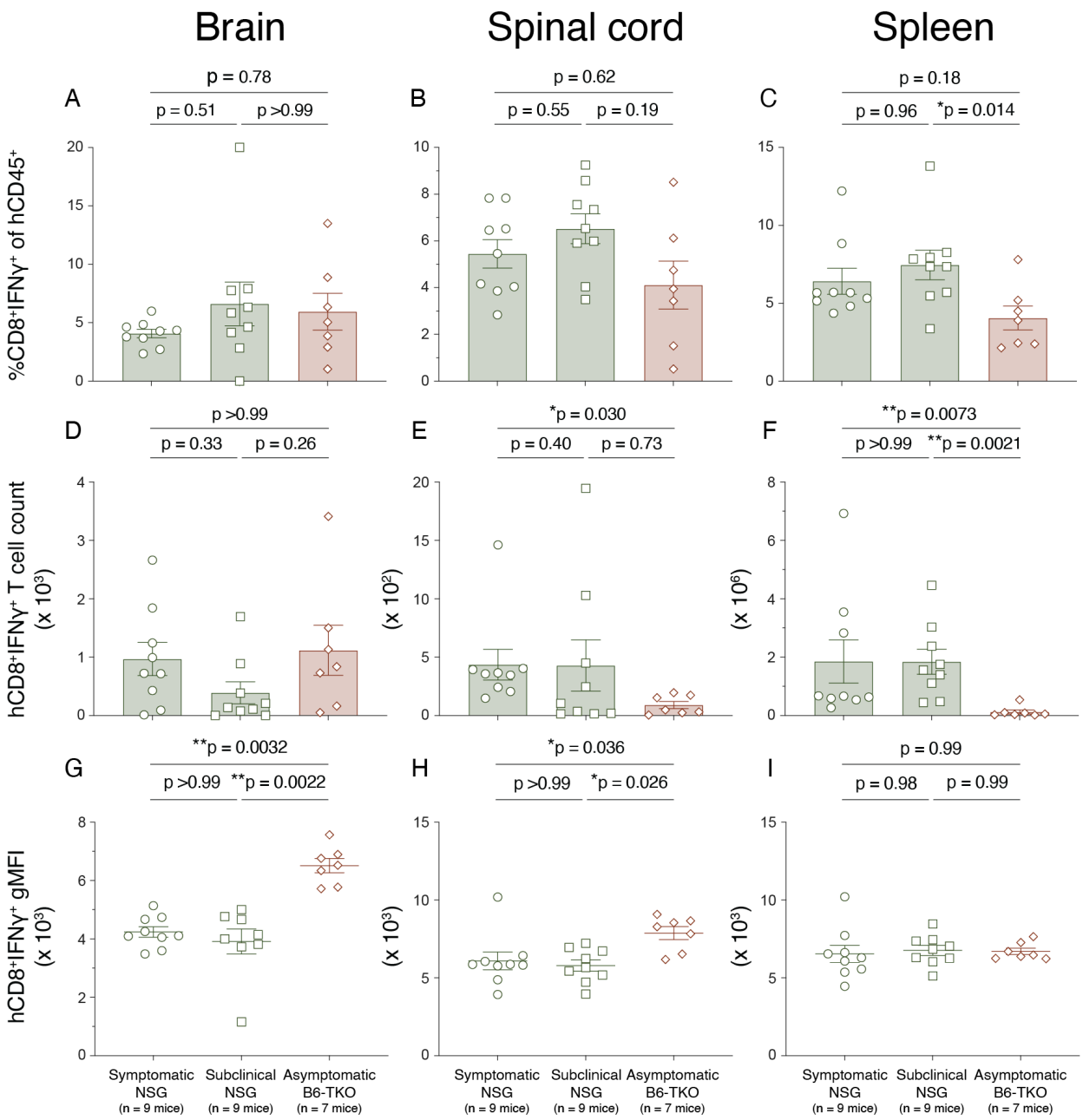

Figure 4.82 IFNγ expressing human CD8$^+$ T cells in the CNS and spleens of PBMC engrafted NSG/SGM3 and B6-TKO mice at EAE endpoint

Figure shows the proportion of hCD8$^+$IFNγ$^+$(GzmB$^-$) T cells among hCD45$^+$ cells (A – C), the total number of hCD8$^+$IFNγ$^+$(GzmB$^-$) T cells (D – F), and the mean per cell expression of IFNγ on hCD3$^+$CD8$^+$ T cells (G – I) in the brains (left column), spinal cords (middle column), and spleens (right column) of PBMC-engrafted NSG/SGM3 mice (separated into n = 9 symptomatic males and n = 9 subclinical males) and B6-TKO mice (n = 7 asymptomatic males) derived from a healthy female donor (HD-04) day 22 – 23 post-rhMOG/MOG$_{35-55}$ EAE induction. Cells isolated from perfused tissues were stimulated with PMA and ionomycin to measure cytokine expression. Data are

shown as mean with SEM and were analyzed by Brown-Forsythe and Welch ANOVA with Dunnett's T3 multiple comparisons or by Kruskal-Wallis test with Dunn's multiple comparisons test. HuPBMC cohorts included: 18 and 28.

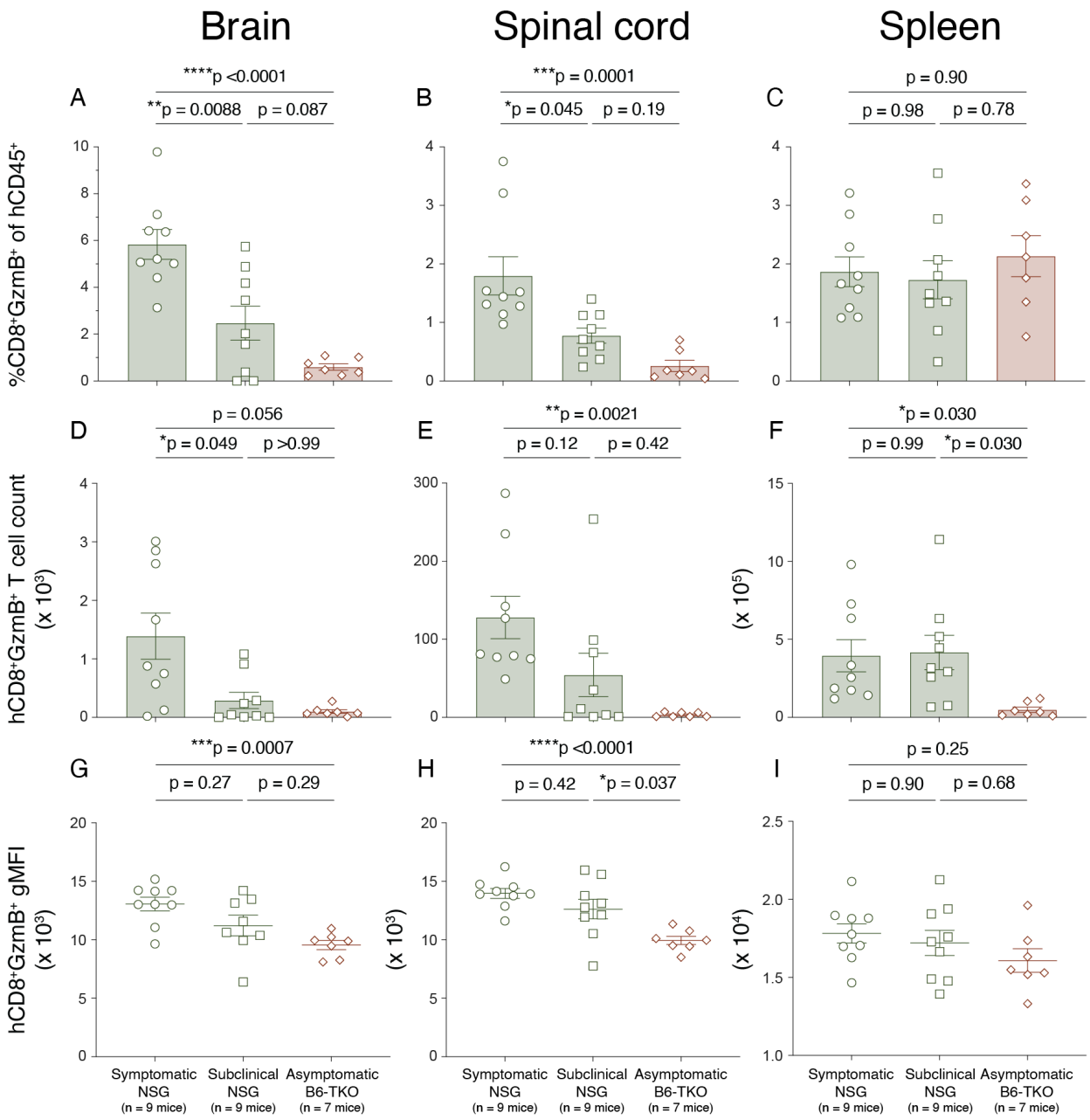

Figure 4.83 Granzyme B expressing human CD8$^+$ T cells in the CNS and spleens of PBMC engrafted NSG/SGM3 and B6-TKO mice at EAE endpoint

Figure shows the proportion of hCD8$^+$GzmB$^+$(IFNγ$^-$) T cells among hCD45$^+$ cells (A – C), the total number of hCD8$^+$GzmB$^+$(IFNγ$^-$) T cells (D – F), and the mean per cell expression of granzyme B (GzmB) on hCD3$^+$CD8$^+$ T cells (G – I) in the brains (left column), spinal cords (middle column), and spleens (right column) of PBMC-engrafted

NSG/SGM3 mice (separated into n = 9 symptomatic males and n = 9 subclinical males) and B6-TKO mice (n = 7 asymptomatic males) derived from a healthy female donor (HD-04) day 22 – 23 post-rhMOG/MOG$_{35-55}$ EAE induction. Cells isolated from perfused tissues were stimulated with PMA and ionomycin to measure cytokine expression. Data are shown as mean with SEM and were analyzed by Brown-Forsythe and Welch ANOVA with Dunnett's T3 multiple comparisons or by Kruskal-Wallis test with Dunn's multiple comparisons test. HuPBMC cohorts included: 18 and 28.

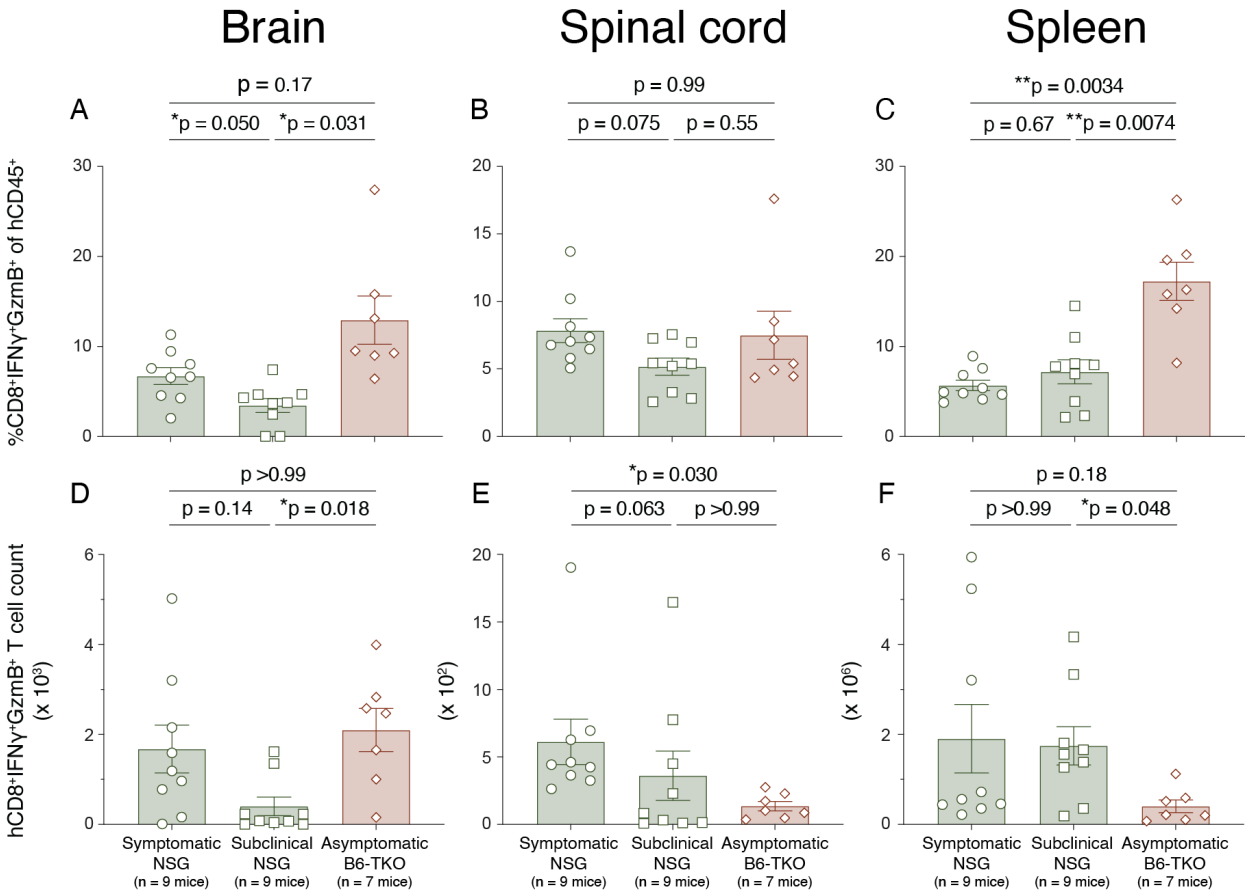

Figure 4.84 Dual IFNγ and granzyme B expressing human CD8$^+$ T cells in the CNS and spleens of PBMC engrafted NSG/SGM3 and B6-TKO mice at EAE endpoint

Figure shows the proportion of hCD8$^+$IFNγ$^+$GzmB$^+$ T cells among hCD45$^+$ cells (A – C) and the total number of hCD8$^+$IFNγ$^+$GzmB$^+$ T cells (D – F) in the brains (left column), spinal cords (middle column), and spleens (right column) of PBMC-engrafted NSG/SGM3 mice (separated into n = 9 symptomatic males and n = 9 subclinical males) and B6-TKO mice (n = 7 asymptomatic males) derived from a healthy female donor (HD-04) day 22 – 23 post-rhMOG/MOG$_{35-55}$ EAE induction. Cells isolated from perfused tissues were stimulated with PMA and ionomycin to measure cytokine expression. Data are shown as mean with SEM and were analyzed by Brown-Forsythe and Welch ANOVA with Dunnett's T3 multiple comparisons or by Kruskal-Wallis test with Dunn's multiple comparisons test. HuPBMC cohorts included: 18 and 28.

These data collectively indicate that the resistance of HuPBMC B6-TKO mice to EAE induction was not due to differences in regulatory T cell expansion or strain-based skewing of reconstituted human T cell subsets, but rather, at least in part, to insufficient numbers of human T cells engrafting the spleen and entering the spinal cord. Despite the HuPBMC B6-TKO CNS tissues containing far greater numbers of both resident microglia and infiltrating myeloid cells than the NSG/SGM3 mice, the inability of the murine myeloid cells to phagocytose myelin and present antigen to infiltrating human T cells may have prevented the amplification and perpetuation of inflammation required to recruit additional effector T cells, as well as by precluding SIRPα expressing cells from mediating demyelination in the CNS[698,708,709].

4.9.3 Presentation of MOG antigen to human T cells by murine MHC expressing myeloid cells

4.9.3.1 Experimental design

Though previously it had been assumed that murine and human immune cells did not recognize the peptide-MHC complexes presented by the other's species[710,711], there have been many recent reports, especially from humanized mouse models, suggesting otherwise [488,493,505,609,712,713]. Evidence from xGvHD models in HuPBMC mice has repeatedly indicated that human T cells do in fact recognize both murine MHC class I and II molecules[493,712]. During hematopoietic development, there is no means for a human immune system to select against human T cell recognition of foreign MHC without the genes that encode them, and structurally, both murine and human MHC molecules are very similar[714,715]. As noted by Koyama and Hill, "a scenario can occur whereby the molecular complex of a peptide and mismatched MHC is structurally sufficiently similar to that of another peptide and matched MHC to activate a donor T cell", a form of molecular mimicry resulting from the promiscuity of TCR:MHC antigen recognition[712]. Rather, when both options are given in culture assays, human T cells will preferentially interact with human HLA over murine MHC expressing cells[711,712]. In $CD34^+$ HuHSC mice, differentiating human T cells can bind murine MHC with enough affinity to undergo conventional selection on mouse thymus tissue, though they exhibit impaired natural Treg reconstitution, suggesting the murine thymic environment does mimic some aspects of that in humans[488]. Halkias and colleagues speculated that "since development of $Foxp3^+$ T cells is thought

to require stronger TCR signals compared with conventional T-cell development, it is possible that interspecies TCR: MHC interactions are unable to provide sufficient TCR signal strength required for efficient Foxp3$^+$ T-cell development"[488].

In the HuPBMC-NSG model, however, very few human HLA expressing APCs survive beyond a week post-engraftment of human donor PBMCs[493,537,712]. To expand upon our findings suggesting human T cells cooperate with murine macrophages to demyelinate the CNS of HuPBMC EAE mice, we analyzed whether hCD4$^+$ and/or hCD8$^+$ T cells could be presented to (and potentially locally restimulated) by host derived, murine MHC bearing antigen presenting myeloid cells that are either functional or defective as APCs. To do so, we compared the ability of splenic mCD45$^+$ cells from NSG mice to present rhMOG or MOG_{35-55} peptide to hCD8$^+$ and hCD4$^+$ T cells, respectively, relative to B6-TKO derived splenic mCD45$^+$(*CD47*$^{-/-}$) cells, engrafted with the same human donor PBMCs. As noted by Han and colleagues, "T cells and APCs from CD47$^{-/-}$ mice failed to express markers of activations (CD27 and CD44 on T cells, and CD80 and CD86 on APCs) in response to active immunization with $MOG_{35–55}$ peptide in Freund's adjuvant"[474]. To eliminate the potential contribution of the few reconstituting (human originating) professional APCs, mCD45$^+$, hCD8$^+$, and hCD4$^+$ cells were fluorescence-activated cell sorted (FACS) from the spleens of PBMC engrafted NSG and B6-TKO mice after 4 weeks of engraftment (Figure 4.85). mCD45$^+$ splenoyctes were then co-cultured with strain-respective hCD4$^+$ or hCD8$^+$ T cells in blank media or in media supplemented with myelin antigen, and after three days, subsets were analyzed for the expression of markers indicative of productive human T cell antigen recognition of murine MHC expressing myeloid cells. The flow cytometric gating schemes to confirm FACS purity of sorted cell populations, co-receptor expression on hCD3$^+$ T cell subsets, as well as activation marker and cytokine expression by human T cell and murine myeloid cell subsets are included in Appendix 12 (Figure A.69 – Figure A.72).

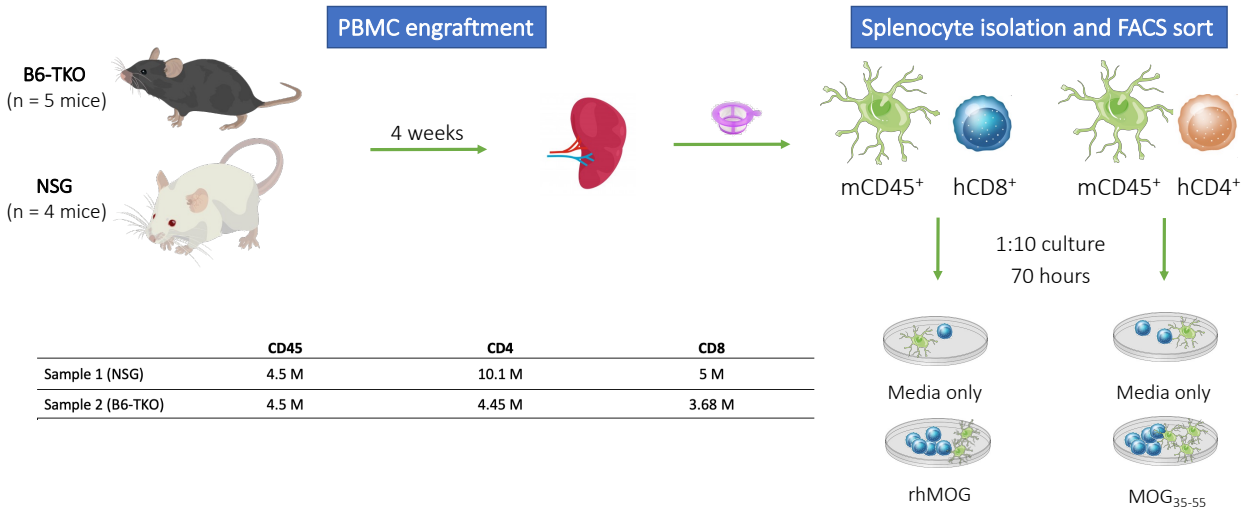

	CD45	CD4	CD8
Sample 1 (NSG)	4.5 M	10.1 M	5 M
Sample 2 (B6-TKO)	4.5 M	4.45 M	3.68 M

Figure 4.85 Interspecies antigen presentation assay design for HuPBMC mice

To assess the ability of murine host antigen presenting cells (APCs) from NSG and B6-TKO mice to activate human donor T cells with MOG antigens in HuPBMC mice, total splenocytes were isolated from NSG (n = 4 males) and B6-TKO mice (n = 5 males) at 4 weeks post-engraftment of 5 x 10^6 PBMC each derived from the same healthy female donor (HD-04, HuPBMC cohort 30). HuPBMC B6-TKO and NSG splenocytes were then combined by strain, to account for any individual mice with poor HIS reconstitution, and labelled with anti-mCD45, hCD4, and hCD8 conjugated antibodies to FACS sort the populations individually. The sorted yield of each of these three subsets is noted in the table by strain. Splenic mCD45$^+$ cells were co-cultured at a 1:10 ratio with either hCD8$^+$ or hCD4$^+$ T cells in complete culture media containing rhMOG or MOG_{35-55}, respectively, and compared to replicate control wells incubated in blank media without antigen for APC and T cell responses.

4.9.3.2 hCD8$^+$ T cells respond to MOG antigen presentation by murine immune cells

Changes in cell marker expression following protein antigen exposure in culture were assessed for mCD45$^+$ cells (Figure 4.86) and hCD8$^+$ T cells (Figure 4.87) derived from either HuPBMC NSG or B6-TKO spleens. rhMOG addition to the culture media led to a significant expansion of all murine myeloid cell types from both NSG and B6-TKO spleens compared to blank media (Figure 4.86 left column). The degree of expansion of mCD11b$^+$ and mF4/80$^+$ cells was lower in the NSG wells compared to the B6-TKO wells, though mCD11c$^+$ expansion was similar between strains, indicating the lack of CD47 expression differentially influenced mCD11b$^+$ and mF4/80$^+$, but not mCD11c$^+$, myeloid cell subset expansion in the presence of rhMOG antigen. Among mCD11c$^+$ cells, the proportion expressing mCD40 was significantly higher on NSG than B6-TKO derived cells following rhMOG exposure (Figure 4.86B).

In contrast, fewer mCD11b$^+$ cells from both strains expressed mCD40 after rhMOG exposure, though the mCD40 expressing mCD11b$^+$ cell proportion was still considerably higher in NSG wells regardless of media treatment (Figure 4.86E). mCD40$^+$ proportions of mF4/80$^+$ cells from both strains were modestly increased with rhMOG antigen, though again, the fraction of mF4/80$^+$ cells from NSG mice expressing mCD40 was much higher than those from B6-TKO mice with either media treatment (Figure 4.86H). The data show that mCD40 expression on mCD45$^+$ myeloid cells from NSG mice was consistently high (>40% with rhMOG media), whereas mCD45$^+$(*CD47*$^{-/-}$) myeloid cells from B6-TKO mice did not express mCD40 as frequently (<10% regardless of media). For all three myeloid subsets from both strains, mTNFα expression was only slightly elevated with protein antigen addition compared to blank media and the positive proportions remained quite low in all wells (typically <2%) (Figure 4.86 right column).

Whereas mCD45$^+$ myeloid cell counts increased in wells from both strains with the addition of rhMOG to the media, and even more so for B6-TKO wells (Figure 4.86), the total numbers of hCD45$^+$ cells derived both strains decreased in wells with rhMOG media (Figure 4.87A). Confirming that the sorting procedure to isolate hCD8$^+$ T cells removed potential professional human APCs, less than two hCD14$^+$CD68$^+$ cells per well were detected at endpoint (Figure 4.87B). While the FACS sort removed most hCD19$^+$ B cells, leaving <5 – 10 cells per well, the addition of rhMOG resulted in an expansion of those few remaining human B cells to ~30 cells per well from both strains (Figure 4.87C).

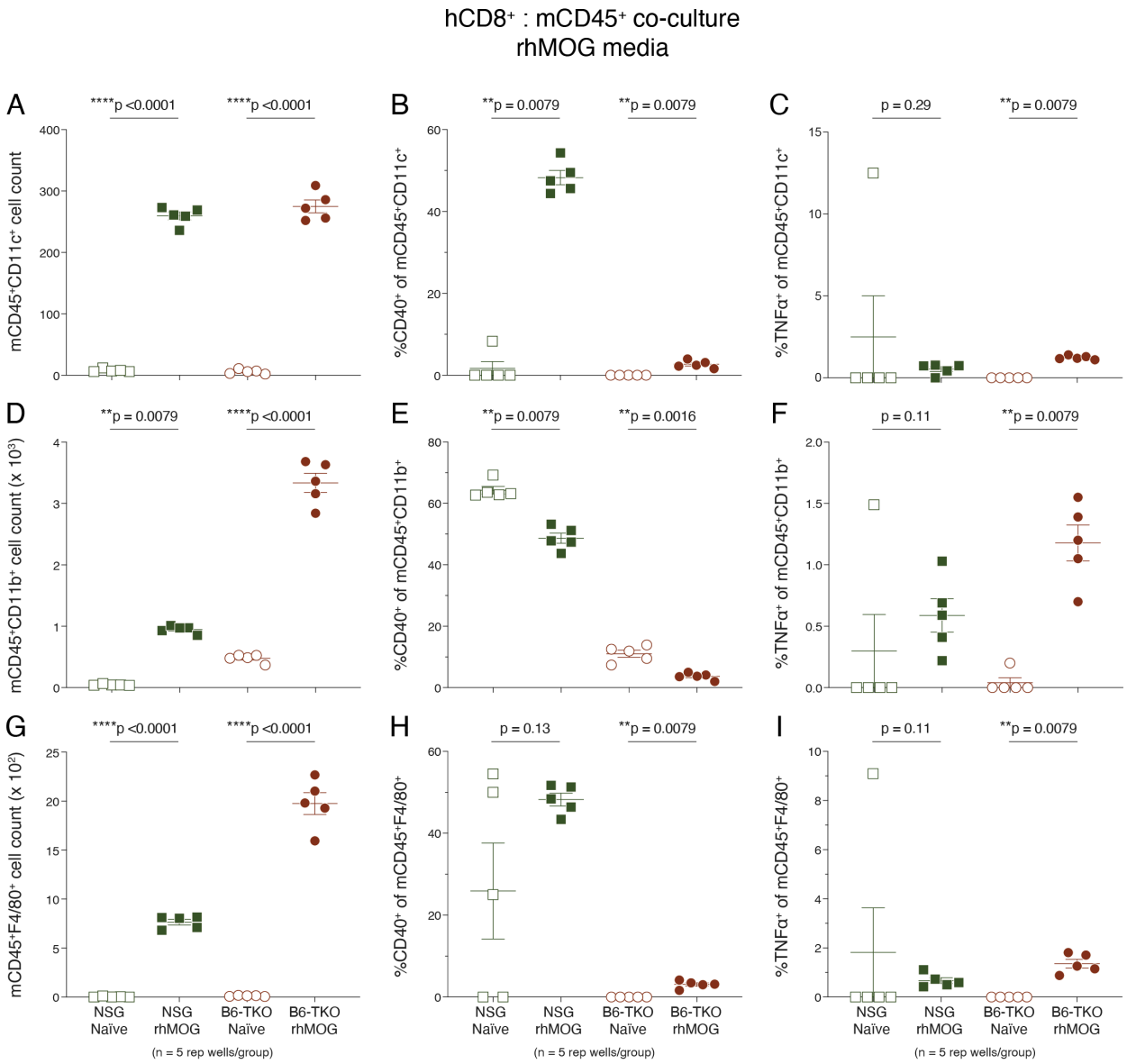

Figure 4.86 Strain-dependent murine APC responses to interspecies co-culture with human CD8$^+$ T cells and rhMOG supplemented media

FACS sorted mCD45$^+$ and hCD8$^+$ cells from the spleens of PBMC-engrafted B6-TKO or NSG mice (all male, derived from healthy female donor HD-04, HuPBMC cohort 30) were co-cultured at a 1:10 ratio in blank culture media (naïve) or media supplemented with rhMOG protein (n = 5 replicate wells per condition). For mCD45$^+$CD11c$^+$ cells (top row), mCD45$^+$CD11b$^+$ cells (middle row), and mCD45$^+$F4/80$^+$ (bottom row) figure shows the total number (left column), the proportion expressing mCD40 (middle column), and the proportion expressing mTNFα (right column) in the well after a 70-hour incubation. Data are shown as mean with SEM and the statistical differences between naïve and rhMOG wells for both strains were separately analyzed by Welch's unpaired t test or by Mann Whitney test.

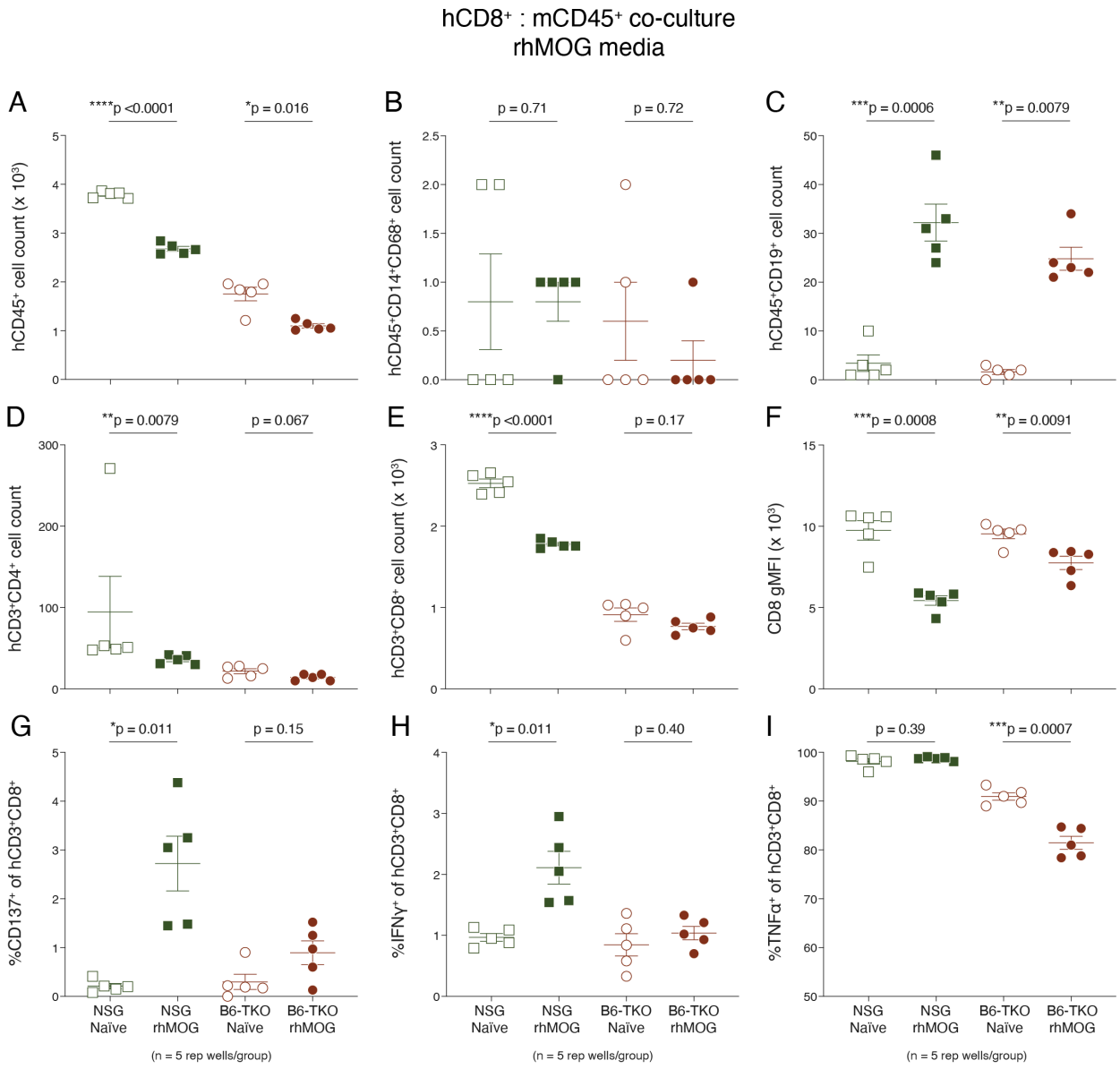

Figure 4.87 Human CD8$^+$ T cell responses to interspecies co-culture with murine NSG and B6-TKO derived APCs in rhMOG supplemented media

FACS sorted mCD45$^+$ and hCD8$^+$ cells from the spleens of PBMC-engrafted B6-TKO or NSG mice (all male, derived from healthy female donor HD-04, HuPBMC cohort 30) were co-cultured at a 1:10 ratio in blank culture media (naïve) or media supplemented with rhMOG protein (n = 5 replicate wells per condition). Figure shows the total number of (A) hCD45$^+$ cells, (B) hCD14$^+$CD68$^+$ myeloid cells, (C) hCD19$^+$ B cells, (D) hCD3$^+$CD4$^+$ T cells, and (E) hCD3$^+$CD8$^+$ T cells in each well after a 70-hour incubation. For the hCD3$^+$CD8$^+$ T cells, the figure also shows (F) the mean per cell expression of CD8 on these cells and the proportion expressing (G) hCD137, (H) hIFNγ, and (I) hTNFα. Data are shown as mean with SEM and the statistical differences between naïve and rhMOG wells for both strains were separately analyzed by Welch's unpaired t test or by Mann Whitney test. Abbr: Geometric median fluorescence intensity, gMFI.

The sorting process also removed most $hCD4^+$ T cells, typically leaving <50 cells per well, and the numbers were unchanged by protein antigen exposure or the source strain (Figure 4.87D). Interestingly, $hCD3^+CD8^+$ T cell counts were reduced with rhMOG media compared to blank media, specifically for wells containing T cells isolated from HuPBMC NSG spleens, whereas only a slight reduction in $hCD3^+CD8^+$ T cell numbers was seen in protein antigen exposed B6-TKO derived wells (Figure 4.87E). The reduced total $hCD3^+CD8^+$ T cell counts coincided with a significant reduction in the expression of hCD8 per cell (decreased geometric median fluorescence intensity, gMFI) for samples derived from both strains, but especially for the NSG wells (Figure 4.87F), indicative of TCR downregulation that occurs with antigen specific recognition and activation[716]. Correspondingly, the proportion of $hCD3^+CD8^+$ T cells expressing the co-stimulatory activation marker CD137, which is expressed only following recent TCR signal transduction[717], was significantly increased on NSG derived $hCD3^+CD8^+$ T cells with rhMOG media but not significantly so on B6-TKO derived $hCD3^+CD8^+$ T cells (Figure 4.87G). Furthermore, the frequency of IFNγ expressing $hCD3^+CD8^+$ T cells was significantly increased in wells from NSG mice with the addition rhMOG antigen but not wells derived from B6-TKO mice (Figure 4.87H). The proportion of $hCD3^+CD8^+$ T cells expressing TNFα was nearly 100% for NSG derived wells and was seemingly unaffected by rhMOG supplementation (Figure 4.87I). For B6-TKO wells, however, a reduced proportion of $hCD3^+CD8^+$ T cells expressing TNFα was observed following incubation with rhMOG, and TNFα expressing frequencies were overall lower for B6-TKO derived $hCD3^+CD8^+$ T cells relative to those from NSG spleens (Figure 4.87I).

Given the absence of mCD40 expression on murine myeloid cells derived from B6-TKO mice, reduced activation levels of co-cultured $hCD3^+CD8^+$ T cells is consistent with impaired APC functions observed in $CD47^{-/-}$ mice[474]. It is unclear how effective the rhMOG-exposed $hCD19^+$ cells would have been at cross-presenting antigen to $hCD8^+$ T cells over the professional $mCD11c^+$ cells. Assuming they had an outsized effect on $hCD8^+$ T cell responses, we would have expected the human B cells derived from both strains to be equally effective in doing so, given the equivalent numbers measured per well and the fact that the CD47 deletion only applies to $mCD45^+$ splenocytes from HuPBMC B6-TKO mice. It was therefore unlikely that the APC activities of the remaining human B cells could explain why $hCD8^+$ T cells cultured with NSG derived murine APCs exhibited greater activation than those from the B6-TKO mice. Clarification of the role of human B cells as APCs in HuPBMC EAE mice would be needed to draw a firm conclusion, which

could be accomplished by analyzing relevant markers expressed by hCD19^{+} B cells from both strains after rhMOG culture, adding a neutralizing anti-hCD19 antibody to the sample wells, and/or by culturing splenocytes derived from murine MHC knock out strains of NSG mice[505].

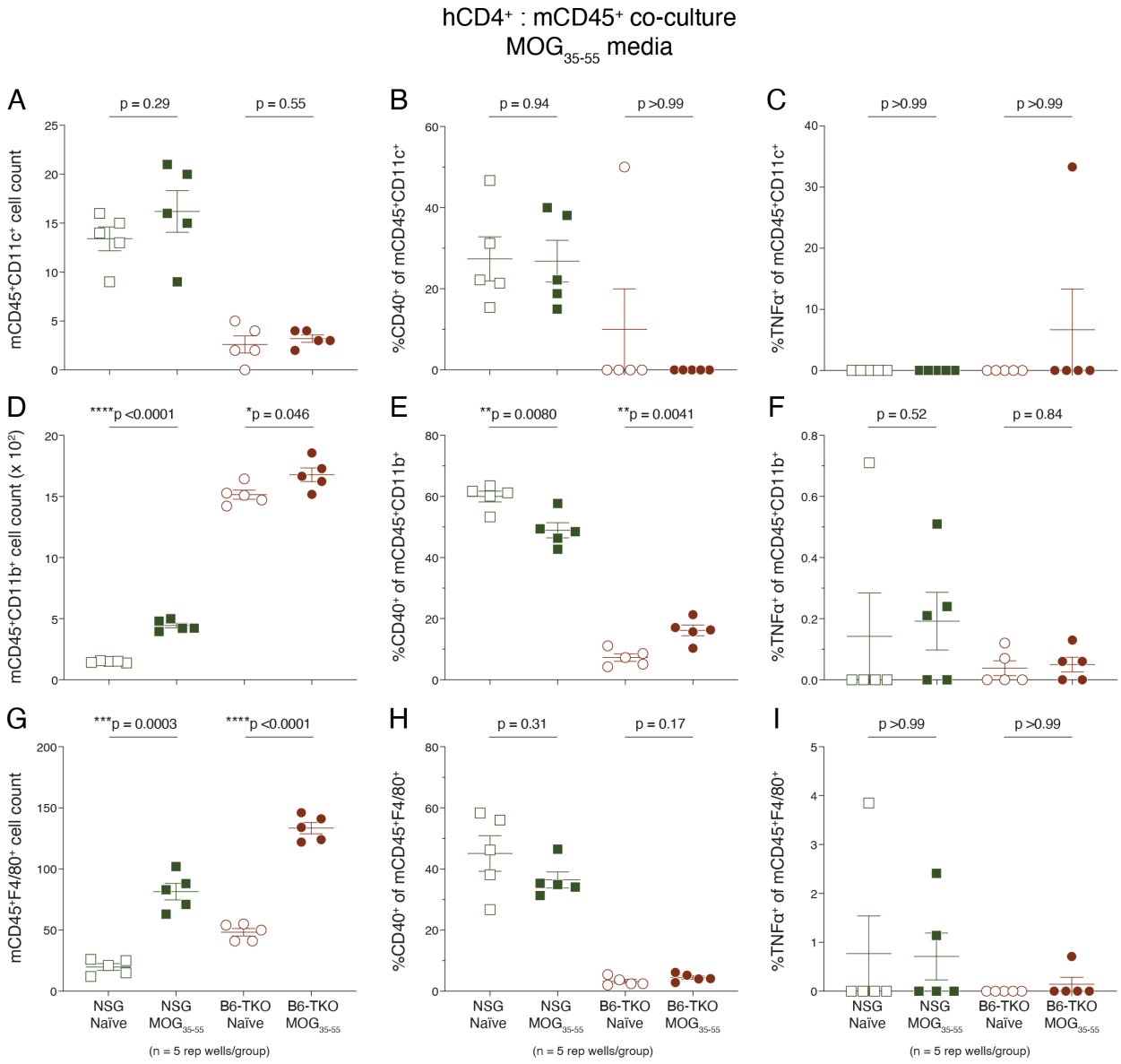

Figure 4.88 Strain-dependent murine APC responses to interspecies co-culture with human CD4^{+} T cells and MOG_{35-55} supplemented media

FACS sorted mCD45^{+} and hCD4^{+} cells from the spleens of PBMC-engrafted B6-TKO or NSG mice (all male, derived from healthy female donor HD-04, HuPBMC cohort 30) were co-cultured at a 1:10 ratio in blank culture media (naïve) or media supplemented with MOG_{35-55} peptide (n = 5 replicate wells per condition). For mCD45^{+}CD11c^{+} cells (top row), mCD45^{+}CD11b^{+} cells (middle row), and mCD45^{+}F4/80^{+} (bottom row) figure shows

the total number (left column), the proportion expressing mCD40 (middle column), and the proportion expressing mTNFα (right column) in the well after a 70-hour incubation. Data are shown as mean with SEM and the statistical differences between naïve and MOG_{35-55} wells for both strains were separately analyzed by Welch's unpaired t test or by Mann Whitney test.

Following a three-day exposure to MOG_{35-55} peptide, only a small, nonsignificant increase in the number of $mCD11c^+$ cells occurred in peptide supplemented NSG wells compared to blank media wells, with an even smaller effect seen with B6-TKO derived cells (Figure 4.88A). The proportion of these cells expressing mCD40 was unchanged by peptide antigen supplementation for both strains and was effectively absent on most B6-TKO derived $mCD11c^+$ cells, compared to consistent expression on ~25% $mCD40^+$ of $mCD11c^+$ NSG cells (Figure 4.88B). MOG_{35-55} peptide exposure did significantly increase the total number of $mCD11b^+$ cells from both strains, however, compared to blank media incubation (Figure 4.88D). $mCD11b^+$ cell counts were also higher in the B6-TKO wells compared to the NSG wells regardless of media treatments (Figure 4.88D). Interestingly, the proportion of $mCD11b^+$ cells expressing mCD40 decreased on NSG derived cells but slightly increased on B6-TKO derived cells with the addition of MOG_{35-55} peptide, though B6-TKO $mCD11b^+$ cell expression of mCD40 was less frequent (~15%) than NSG derived cells (~50%) under both conditions (Figure 4.88E). MOG_{35-55} exposure led to a significant increase in the number of $mF4/80^+$ cells from both strains (Figure 4.88G), while the proportion of $mF4/80^+$ cells expressing mCD40 trended similarly to the expression patterns seen on $mCD11b^+$ cells (Figure 4.88H). The proportion of murine myeloid cell subsets expressing TNFα was very low for all conditions for both strains and did not change with the addition of MOG_{35-55} peptide to the media. Under all media conditions, mCD40 expression on B6-TKO derived myeloid cells was much lower than on NSG derived myeloid cells (Figure 4.86 and Figure 4.88 middle columns).

Though $mCD45^+$ cell counts were moderately increased for both strains with the addition of MOG_{35-55} to culture media (Figure 4.88 left column), numbers of $hCD45^+$ cell from both strains were unaffected by MOG_{35-55} exposure (Figure 4.89A). To confirm the effectiveness of the FACS sort in isolating $hCD3^+CD4^+$ T cells, we also confirmed that relatively few $hCD14^+CD68^+$ macrophages (Figure 4.89B, max 1 cell per well), $hCD19^+$ B cells (Figure 4.89C, <20 cells per NSG well and <5 cells per B6-TKO well), and $hCD3^+CD8^+$ T cells (Figure 4.89D, <60 cells per NSG well and <20 cells per B6-TKO well) remained in the wells by endpoint. Moreover, within

these HIS subsets from each strain, MOG_{35-55} exposure did not change the total cell counts (Figure 4.89B – D). No expansion of $hCD3^+CD4^+$ T cells from either strain was observed with MOG_{35-55} media incubation (Figure 4.89E), and likewise, hCD4 gMFI was unaffected by peptide exposure (Figure 4.89F), suggesting they did not proliferate under these conditions.

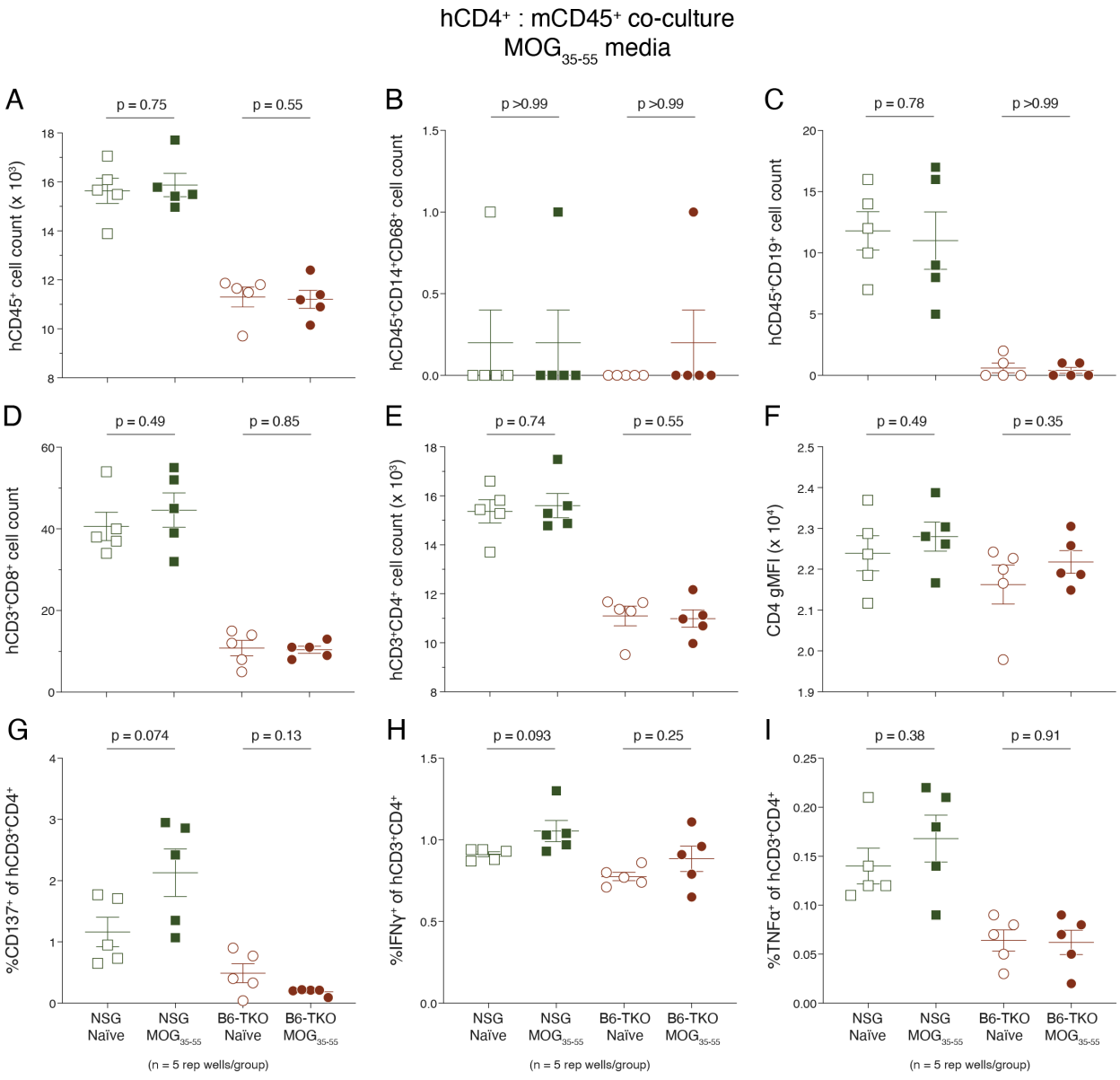

Figure 4.89 Human $CD4^+$ T cell responses to interspecies co-culture with murine NSG and B6-TKO derived APCs in MOG_{35-55} supplemented media

FACS sorted $mCD45^+$ and $hCD4^+$ cells from the spleens of PBMC-engrafted B6-TKO or NSG mice (all male, derived from healthy female donor HD-04, HuPBMC cohort 30) were co-cultured at a 1:10 ratio in blank culture media (naïve) or media supplemented with MOG_{35-55} peptide (n = 5 replicate wells per condition). Figure shows the

total number of (A) hCD45$^+$ cells, (B) hCD14$^+$CD68$^+$ myeloid cells, (B) hCD19$^+$ B cells, (D) hCD3$^+$CD8$^+$ T cells, and (E) hCD3$^+$CD4$^+$ T cells in each well after a 70-hour incubation. For the hCD3$^+$CD4$^+$ T cells, the figure also shows (F) the mean per cell expression of CD4 on these cells and the proportion expressing (G) hCD137, (H) hIFNγ, and (I) hTNFα. Data are shown as mean with SEM and the statistical differences between naïve and MOG$_{35-55}$ wells for both strains were separately analyzed by Welch's unpaired t test or by Mann Whitney test.

The proportion of hCD3$^+$CD4$^+$ T cells from NSG mice expressing hCD137 was moderately increased with MOG$_{35-55}$ exposure, indicating some degree of activation, whereas B6-TKO derived T cell expression was unchanged (Figure 4.89G). Similarly, the proportions of hCD3$^+$CD4$^+$ T cells from NSG mice expressing IFNγ and TNFα were non-significantly increased in MOG$_{35-55}$ media compared to blank media, with this trend being less striking with T cells from B6-TKO mice (Figure 4.89H, I). Antigen presentation by murine myeloid cells of either strain to hCD3$^+$CD4$^+$ T cells was likely ineffective due to the lack of mCD11c$^+$ cell expansion and lower mCD40 expression frequency with MOG$_{35-55}$ peptide media (Figure 4.88), resulting in fewer responding hCD3$^+$CD4$^+$ T cells (Figure 4.89). As noted by Lucas and colleagues, "It was found that although resting human T cells cannot respond effectively to resting murine APC, they can respond to activated murine stimulator populations… associated with increased expression of B7-2 on the xenogeneic stimulating cell populations"[718]. Repeating this assay with rhMOG protein supplemented media would better indicate if activated mCD11c$^+$ APCs from either strain could present antigen through MHC II to hCD3$^+$CD4$^+$ T cells.

4.9.3.3 hCD4$^+$ T cells from HuPBMC EAE mice do not bind murine I-A^{g7} MHC II tetramer complexes

To further assess whether hCD3$^+$CD4$^+$ T cell recognition of murine MHC II on host NSG APCs occurred in the HuPBMC-NSG EAE model, we stained CNS infiltrating hCD3$^+$CD4$^+$ T cells with NOD I-A^{g7} class II tetramers loaded with an immunodominant peptide epitope of (1) MOG$_{35-55}$ (indicative of specific epitope recognition), (2) PLP and MBP (indicative of epitope spreading to other myelin antigens), or (3) OVA (indicative of nonspecific I-A^{g7} complex recognition)[144,665,719]. For this assay, we analyzed cells isolated from the brains, spinal cords, spleens, liver, and intestinal lamina propria of PBMC-engrafted NSG mice after symptom onset from mixed rhMOG/MOG$_{35-55}$ EAE induction, to determine the tissue specificity of any observed

$hCD3^+CD4^+$ T cell tetramer binding (Figure 4.90). Based on optimization experiments performed using NOD EAE tissues, we anticipated an antigen specific MOG_{42-55} $I\text{-}A^{g7}$tetramer binding frequency of ~2 – 6% of $CD4^+$ T cells in the CNS, whereas nonspecific $OVA_{141-160}$ $I\text{-}A^{g7}$ tetramer binding was seen for <0.2% of $mCD4^+$ T cells in the brain and spinal cords (Appendix 11, Figure A.62 – Figure A.64). As epitope spreading is not observed in NOD WT mice immunized with MOG_{35-55} peptide[665], the expected binding frequency of PLP and MBP peptide loaded $I\text{-}A^{g7}$ tetramers by $mCD3^+CD4^+$ T cells was not pre-tested in our NOD EAE mice, so background staining levels were based on values measured in the spleens of HuPBMC-NSG EAE mice.

In HuPBMC-NSG mice immunized with mixed rhMOG/MOG_{35-55} antigens, <0.2% of $hCD3^+CD4^+$ T cells in most tissue samples were found to bind non-specifically to $OVA_{141-160}$ peptide loaded $I\text{-}A^{g7}$ tetramers, with higher frequency outliers occurring in two spinal cord samples at <0.6% (Figure 4.90A), suggesting $hCD3^+CD4^+$ T cells did not effectively bind the OVA tetramer. Similarly, very few samples from any tissue contained $hCD3^+CD4^+$ T cells positive for MOG_{42-55} $I\text{-}A^{g7}$ tetramer above the background staining level of ~0.2% (Figure 4.90B). In the intestinal samples that exceeded background levels, fluorophore matched CLIP peptide loaded control-stained samples also attained such frequencies (~0.4%), indicating any $hCD3^+CD4^+$ T cell binding to MOG_{42-55} $I\text{-}A^{g7}$ tetramers was likely nonspecific staining (Figure 4.90B). Based on the CLIP control loaded tetramers and staining of peripheral tissue samples, the background level of PLP_{56-70}, MBP_{74-85}, and MBP_{73-92} $I\text{-}A^{g7}$ tetramer staining (all bearing the same fluorophore to measure overall epitope spread) was ~0.3% (Figure 4.90C). The proportions of PLP/MBP $I\text{-}A^{g7}$ tetramer bound $hCD3^+CD4^+$ T cells in the brain did not exceed levels measured in the spleens and livers, suggesting $hCD3^+CD4^+$ T cells were not specifically binding to secondary myelin peptide loaded tetramers (Figure 4.90C). Three spinal cord samples contained tetramer-bound $hCD3^+CD4^+$ T cell frequencies above background, including one sample at 1.5% tetramer positive of infiltrating $hCD3^+CD4^+$ T cells (Figure 4.90C), though specific binding here would need to be confirmed by comparing results to NOD EAE mice actively immunized with these myelin peptides.

Murine MHCII I-A^{g7} tetramer binding of human T cells

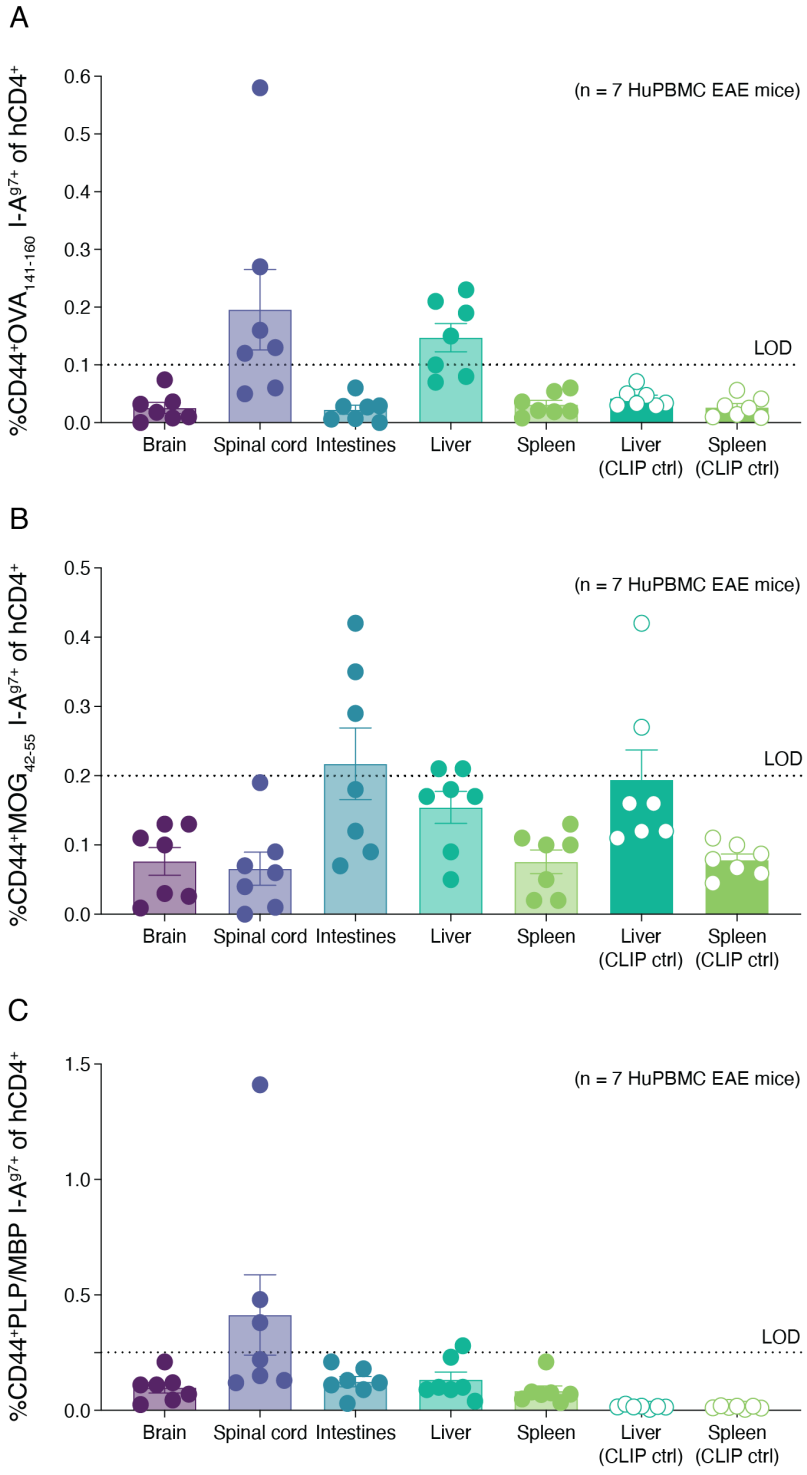

Figure 4.90 Human CD4$^+$ T cell binding to murine I-A^{g7} MHC II tetramers in the CNS and peripheral tissues of HuPBMC EAE mice

Figure shows the proportion of activated human $hCD3^+CD4^+(CD8^-)CD44^+$ T cells in the brain, spinal cord, intestinal lamina propria, liver, and spleen bound to NOD I-A^{g7} MHC II tetramers loaded with (A) $OVA_{141-160}$, (B) MOG_{42-55}, (C) PLP_{56-70}, MBP_{74-85}, and MBP_{73-92}, or respective fluorophore matched $CLIP_{87-101}$ control peptide, on days 19 – 22 post-immunization of mixed rhMOG/MOG_{35-55} EAE induced HuPBMC-NSG mice (n = 7 derived from HD-04 female PBMCs). Tissues were perfused prior to cell isolation. Data are shown as mean with SEM and the limit of detection (LOD) for nonspecific background staining shown as a dotted line.

These data suggested that $hCD3^+CD4^+$ T cells did not specifically recognize or did not bind any of the peptides loaded on the given I-A^{g7} tetramers with sufficient strength, which was further supported by the finding that, regardless of which combination (or removal of) antigen and adjuvant components was used to immunize HuPBMC mice, all tissues demonstrated similar binding frequencies in the processed tissues (see Appendix 11, Figure A.65 – Figure A.67). Though these data confirmed that nonspecific binding of $hCD3^+CD4^+$ T cells to I-A^{g7} tetramer complexes was low, it remained unclear if the negative result observed with the MOG_{42-55} I-A^{g7} tetramer was due to the lack of response of $hCD3^+CD4^+$ T cells to murine MHC II in HuPBMC mice following MOG immunization generally (MOG specific $hCD3^+CD4^+$ T cells are truly absent), or, if the MOG_{42-55} peptide was not the immunodominant epitope generated in this model (we did not load NOD I-A^{g7} tetramers with the recognized peptide sequence to detect MOG specific $hCD3^+CD4^+$ T cells in HuPBMC EAE mice), since the extracellular domain of rhMOG was also included in the inducing emulsion. In NOD I-A^{g7} expressing mice, the immunodominance of the MOG_{42-55} epitope was determined in MOG_{35-55} peptide immunized animals[665], but not those with full length protein.

In NOD WT mice immunized with either MOG_{35-55} peptide or $rhMOG_{1-120}$ protein, the frequency of $mCD3^+CD4^+$ T cells in spleen that bound to the MOG_{42-55} I-A^{g7} tetramer was <0.1%, as expected (Appendix 11, Figure A.68). In the CNS tissues, however, MOG_{35-55} peptide immunization produced MOG_{42-55} specific $mCD3^+CD4^+$ T cells in 5 of 7 mice, whereas rhMOG protein immunization only generated MOG_{42-55} specific $mCD3^+CD4^+$ T cells in 2 of 8 mice (Appendix 11, Figure A.68). Furthermore, in the CNS tissues containing MOG_{42-55} specific $mCD3^+CD4^+$ T cells, the proportions of total infiltrating $mCD3^+CD4^+$ T cells that bound to the MOG_{42-55} I-A^{g7} tetramer was ~1 – 5% with MOG_{35-55} peptide immunization but only ~0.25 – 2% with rhMOG protein immunization (see Appendix 11, Figure A.68). These data indicated that MOG_{42-55} was not the only and/or the predominant epitope recognized by CNS infiltrating

$mCD3^+CD4^+$ T cells or was not as strongly recognized when whole protein is processed, when NOD mice were induced with rhMOG protein instead of MOG_{35-55} peptide. Therefore, the absence of CNS infiltrating MOG_{42-55} I-A^{g7} tetramer positive $hCD3^+CD4^+$ T cells in the brains and spinal cords of HuPBMC-NSG mice immunized with mixed rhMOG/MOG_{35-55} was not necessarily a true negative result for MOG specific $hCD3^+CD4^+$ T cells. Determination of any or all immunodominant epitopes of $rhMOG_{1-120}$ that are presented by I-A^{g7} class II complexes would be required to evaluate if $hCD3^+CD4^+$ T cells are presented to and activated by murine MHC II expressing host cells in the HuPBMC-NSG rhMOG/MOG_{35-55} induced EAE model. The null tetramer data obtained in this analysis did reveal that nonspecific recognition of peptide loaded murine MHC II complexes by engrafted $hCD3^+CD4^+$ T cells was minimal and/or very infrequent in the tissues of HuPBMC-NSG EAE mice and was consistent with our findings in the prior section showing weak responses of co-cultured $hCD3^+CD4^+$ T cells to MHC II on murine myeloid cells when provided MOG_{35-55} peptide.

4.9.4 Summary and discussion of findings

Most studies investigating the immunological roles of SIRPα-CD47 signalling have focused on cancer cell evasion strategies involving CD47 upregulation and the administration of antibody therapies to interfere with these interactions, while studies in murine EAE models have pointed to a multifactorial role for SIRPα-CD47 signalling in the activation of encephalitogenic T cells in the periphery, mediating the demyelination of axons in the CNS, and facilitating neurological recovering by clearing out myelin debris within lesions[448,474,703,720,721]. We therefore compared EAE outcomes and antigen presentation in PBMC humanized and murine immune system reconstituted $CD47^{-/-}$ immunocompromised mice to determine the immunopathological similarity of the HuPBMC EAE model to existing murine EAE models, and to define the role of host murine myeloid cells more specifically in mediating disease in an interspecies chimeric model of autoimmune MS.

In comparison to PBMC engrafted NSG/SGM3 mice, HuPBMC B6-TKO ($mCD47^{-/-}$) mice showed overall lower levels of peripheral HIS reconstitution, which was consistent with the observation that "BRG mice transgenically expressing a human SIRPα increase engraftment to levels achieved in NSG and NRG mice, indicating that SIRPα is a causal factor in controlling engraftment levels"[465,471]. Although the specific protection from clinical paralysis observed in

HuPBMC B6-TKO EAE mice that was not observed with NSG/SGM3 mice may be due to the different MHC alleles expressed by the parent C57Bl/6 (*H-2b*) and NOD (*H2-g7*) strains, respectively, the observation that both NSG and BRG (*H-2d*) mice are susceptible to xGvHD implies a consistent ability of engrafted human T cells to respond to the murine MHC molecules of multiple haplotypes[612]. Moreover, some of the HuPBMC B6-TKO mice did develop clinical signs of xGvHD by EAE endpoint, including skin irritation and liver cirrhosis. Despite remaining entirely resistant to paralytic symptoms following EAE induction with MOG antigens, the brains and spinal cords of HuPBMC B6-TKO contained similar numbers of human effector T cells as those from donor matched HuPBMC NSG EAE mice. The absence of EAE symptom incidence in HuPBMC B6-TKO EAE mice was therefore seemingly not a result of insufficient effector $hCD3^{+}CD4^{+}$ T cell responses or proinflammatory polarization at the site of disease, as seen with EAE induced HuBLT-NSG mice. Furthermore, the HuPBMC B6-TKO CNS tissues contained greater numbers of both resident microglia and infiltrating myeloid cells than the NSG/SGM3 mice, pointing to the defect in murine myeloid cell phagocytosis in $mCD47^{-/-}$ B6-TKO mice as the main differential[474,699].

These findings were also reproduced using syngeneic murine immune system reconstituted B6-TKO mice, which underscored the similarity of the underlying disease pathology in the PBMC humanized of EAE to murine EAE, while eliminating the confounding xGvHD response observed in humanized mouse models. In alignment with previous findings in murine EAE models, the inability of the murine myeloid cells to phagocytose myelin and present antigen to infiltrating human T cells may have prevented the amplification and perpetuation of inflammation required to recruit additional effector T cells, as well as by precluding SIRPα expressing cells from mediating demyelination in the CNS[474,698,708,709]. The data indicated that regardless of the donor/species of the immune cells engrafted, B6-TKO mice are resistant to EAE induction, and suggests HuPBMC EAE in NSG/SGM3 mice proceeds similarly to regular EAE models in that CD47-SIRPα signalling through murine macrophages is needed for demyelination and EAE symptom precipitation.

It remained unclear, however, if the observed correlation between CNS infiltrating human effector T cells and myelin-phagocytosing murine myeloid cells in HuPBMC-NSG/SGM3 EAE mice was a consequence of indirect cooperation (i.e., human T cells produce cytotoxic factors that damage myelin, and separately, murine macrophages phagocytose this damaged myelin) or if

human T cells and murine macrophages were also capable of directly interacting via antigen presentation of myelin. To address these possibilities, and by harnessing the other known role of CD47 signalling in activation of encephalitogenic T cells in the periphery via antigen presentation[474], interspecies co-culture assays were performed using splenocytes isolated from PBMC humanized B6-TKO or NSG mice. The premise for this assay was based on separate but related findings that (1) "human T cells are able to recognize murine xeno-antigens presented by murine major histocompatibility complex (MHC)" and "human CD28 receptor is able to interact with murine B7.2 molecules [CD86] thus providing a second signal for human T cells"[493,609,722,723], (2) "engagement of SIRPβ2 on T cells by CD47 on antigen-presenting cells results in enhanced antigen-specific T-cell proliferation"[724] and (3) "impaired proliferation with WT T cells when co-cultured with irradiated $CD47^{-/-}$ splenocytes, suggesting T cells and APCs lacking in CD47 were defective in generating encephalitogenic T cells"[474]. These findings, along with our own obtained in the HuPBMC EAE model, indicate that the cooperation of human T cells and murine myeloid cells in mediating EAE is likely to be, at least in part, dependent on physical contact between these two subsets.

When cultured with $hCD8^+$ T cells in the presence of rhMOG protein antigen, $mCD45^+$ myeloid cells from HuPBMC NSG spleens upregulated markers of antigen presentation (mCD11c and mCD40), while the corresponding $hCD8^+$ T cells exhibited markers of activation, including reduced TCR expression and increased hCD137 and hIFNγ expression. $hCD8^+$ T cell activation, however, was significantly reduced in the presence of $mCD45^+$ myeloid cells from HuPBMC B6-TKO ($mCD47^{-/-}$) spleens, which failed to upregulate mCD40 in rhMOG supplemented media, potentially due to their inability to phagocytose and/or process antigen for subsequent presentation. These data affirmed the functional capacity of $hCD8^+$ T cells to recognize and respond to antigen in humanized mouse tissues containing scarce numbers of human HLA expressing APCs. On the other hand, $hCD4^+$ T cells seemingly did not respond to murine MHC II expression on $mCD45^+$ myeloid cells from either PBMC humanized strain in the presence of MOG_{35-55} peptide antigen. The null data indicating minimal $hCD4^+$ T cell and murine MHC II expressing APC interactions also corresponded with our finding that CNS infiltrating $hCD4^+$ T cells from HuPBMC EAE mice did not bind myelin specific or nonspecific peptide loaded NOD $I\text{-}A^{g7}$ MHC II tetramers to any measurable degree. Furthermore, the few remaining $hCD4^+$ T cells in the post-FACS sort $hCD8^+$ T cell culture wells containing rhMOG protein and activated NSG derived APCs did not

measurably proliferate, though repetition of this assay with greater numbers of hCD4$^+$ T cells and murine splenocytes with rhMOG protein may show otherwise.

Our co-culture assay results are consistent with the observation that "human CD8+ T cells were sufficient and required for xGVHD induction, while injection of purified CD4+ T-cells failed to induce xGVHD in NSG mice"[609,722]. Brehm, King, and colleagues have also shown that while hCD8$^+$ T cell recognition of murine MHC I is the predominant driving force behind xGvHD incidence in PBMC humanized NSG mice, knocking out MHC II does have a lesser but significant impact on development of clinical disease[493,505]. Addressing and distinguishing the role of nonspecific xGvHD reactivity in mediating clinical EAE symptoms, or protection therefrom, in the HuPBMC EAE model has proven to be a very difficult task. Dehmani and colleagues demonstrated that abrogating SIRPα-CD47 signalling in NSG mice via antibody blockage delayed the onset of xGvHD; reminiscent of how antibody blockade prior to EAE onset similarly protects from paralysis[720,721]. These data suggest the overlapping mechanisms of antigen recognition involved in xGvHD and HuPBMC EAE that depend on foreign MHC recognition and co-stimulation by cross-species interactions are highly conserved between the two disease processes and are difficult to dissect without more high throughput methods, such as TCR sequencing or large-scale overlapping peptide screens. As noted by Koyama and colleagues, "the pathways of antigen presentation leading to GVHD are highly promiscuous in xenograft systems where immune deficient mice (and their APC) stimulate a human T cell response"[712].

Though our findings do not rule out the possibility of atypical HLA expressing human T:T cell antigen presentation[499], our data suggests that T:T cell interactions do not present antigen with sufficient efficiency to affect the sum response we measured in culture, as genetic abrogation of murine CD47 was the sole modified factor in these assays (i.e. we would have expected to see similar hCD8$^+$ and hCD4$^+$ T cell responses regardless of the strain of murine APCs supplied if human HLA class II expressing T:T cell interactions were common and/or prevalent). The seemingly minimal role of atypical T:T cell antigen presentation is consistent with the findings of Halkias and colleagues in CD34$^+$ HuHSC-NSG mice, who did not observe this phenomenon in vivo by TCR repertoire analysis[488]. To fully discern the extent of myelin antigen specific hCD4$^+$ and hCD8$^+$ T cell recognition of murine MHC II and MHC I complexes, respectively, and/or human T:T cell antigen presentation following active EAE induction of HuPBMC mice would require more specific and comprehensive co-culture parameters, as well as the use of murine APCs

from genetically modified NSG strains such as donor matched HLA transgenic and murine MHC KO mice[487,493,505]. Collectively, however, our findings correspond with those of other groups demonstrating productive interspecies interactions in humanized mouse models[488,493,505,609,722,723] and suggests neuro-immunopathology proceeds similarly in HuPBMC EAE mice as it does in typical murine EAE models, requiring murine myeloid cells to both demyelinate the CNS and act as APCs to activate human T cells in order for EAE symptoms to develop.

4.10 Summary and discussion of major findings

In this chapter, we sought to optimize the protocol for generating HuPBMC EAE mice and characterize the underlying immunopathogenesis that results in clinical disease symptoms, which are known to vary between different EAE models[50,128,129]. For successful induction of EAE in PBMC humanized NSG mice, we determined that active myelin antigen immunization should be performed around 3 weeks post-engraftment, following an intravenous injection of recipient NSG mice with 5 million donor PBMCs (Section 4.2). We also determined that male recipient NSG mice were significantly more susceptible to myelin antigen immunization resulting in clinical EAE paralysis than female recipient mice, whereas female recipient mice were more prone to developing symptoms of xGvHD (Section 4.3). In terms of blood donor sex, the average overall EAE incidence of male PBMC-engrafted mice was approximately half of that in female PBMC engrafted mice, though once symptoms did develop, they tended to proceed similarly regardless of blood donor sex (Section 4.3). The clinical and immunological outcomes of engrafting and inducing NSG and NSG-SGM3 mice were comparable, and therefore, both strains were used interchangeably (noted as NSG/SGM3) to generate HuPBMC cohorts (Section 4.4). Regardless of the myelin antigen used to immunize HuPBMC-NSG/SGM3 mice, CNS infiltration and polarization of human T cells was similar, indicating T cell behaviour was largely dependent on the blood donor and the duration of time to experimental endpoint rather than the inducing antigen (Section 4.5).

In preliminary analyses, we determined that mixed rhMOG/MOG_{35-55} EAE induction of HuPBMC-NSG/SGM3 mice was preferable to the use of MOG_{35-55} peptide only or rhMBP protein, mainly because of the earlier onset of EAE paralysis that outpaced the onset of clinical symptoms of xGvHD (Section 4.5). PTx co-administration was also consistently increased the number of CNS infiltrating human immune cells in immunized HuPBMC mice (Section 4.8). Furthermore,

the addition of MOG antigen to the CFA emulsion significantly increased the incidence of clinical EAE symptoms, indicating that myelin immunization of HuPBMC mice preferentially directed the graft response to the CNS, resulting in EAE immunopathology (Section 4.8). Ultimately, our preliminary data revealed that the optimal protocol moving forward was: (1) engraftment of male NSG/SGM3 recipient mice with female blood donor PBMCs, in order to maximize the incidence of EAE symptoms and to minimize sex bias as a confounding factor, (2) reconstitution of HIS subsets in vivo for 3 weeks post-PBMC injection, and (3) SQ immunization of HuPBMC-NSG/SGM3 mice with CFA emulsion containing both rhMOG protein and MOG_{35-55} peptide, alongside two IP injections of PTx. Following this humanization and EAE induction protocol, the peripheral and CNS localized immune response in HuPBMC-NSG/SGM3 EAE mice was compared to C57Bl/6 and NOD mice, which are commonly used strains for studies of MOG-induced EAE models (Section 4.6). Clinically, EAE symptoms in HuPBMC-NSG/SGM3 mice generally reflected the disease course, onset, and incidence patterns observed in NOD EAE mice, mainly characterized by a monophasic, potentially relapsing phenotype. Comparative analysis of the phenotype of human effector T cells in the CNS and periphery revealed EAE symptoms in HuPBMC-NSG/SGM3 post-rhMOG/MOG_{35-55} immunization were predominantly a result of Th1 $hCD4^+$ and cytotoxic $hCD8^+$ T cell mediated disease, similar to established murine EAE models[131,134,139,688,689].

As confirmed by histological analysis, engrafted human $CD8^+$ T cells were able to migrate to and infiltrate the mouse CNS and localize to areas of microgliosis and myelin damage. The correlated numerical abundance and anatomical co-localization of myelin phagocytosing murine myeloid cells with cytotoxic $hCD8^+$ T cells within the CNS supported their cooperative role in mediating demyelination (Section 4.7), consistent with histological analysis of MS lesions in the human brain[36,37,697,725–727]. Moreover, the CNS of symptomatic mice was enriched for $hCD8^+$ relative to $hCD4^+$ T cells, which is commonly observed in post-mortem analysis of MS lesions[38,728] but is not usually observed in the CNS of classical murine EAE models[128]. Within the brain, $hCD8^+$ T cell infiltration was concentrated in the cerebellum, akin to murine EAE models where $mCD4^+$ T cells are known to infiltrate the vascularized cerebellar tissue[729,730]. We also observed equivalent numbers of infiltrating human T cells in the brain and the spinal cord, as opposed to the spinal cord dominant pathology of most murine EAE models[128]. The data collectively indicated that substantial human T cell infiltration of the CNS following MOG induction results in autoimmune

disease in HuPBMC-NSG/SGM3 mice and highlights the utility of HuPBMC EAE mice in modelling clinical and immunopathological aspects of MS.

A previous study that immunized PBMC humanized NSG mice with myelin antigens in CFA reported subclinical CNS inflammation when myelin antigen-pulsed autologous DCs were provided as human HLA expressing professional APCs[644]. Multiple discrepancies in the experimental design of this study may have accounted for the presence of human immune infiltrates without clinical EAE symptoms developing as a consequence (Figure 4.91). The most notable differences between their study and ours pertained to the engraftment route and reconstitution period for humanizing NSG mice with PBMCs, and the combination of myelin antigens and adjuvant components used to induce EAE. First, Zayoud and colleagues immunized NSG mice on day 7 post-PBMC injection, whereas we waited until 3 weeks post-engraftment to initiate immune challenge, similar to Ajith and colleagues[611]. One week may have been insufficient time to attain a suitable number of human T cells in the periphery before immunization. Moreover, IP injection of human PBMCs is considered less effective than IV injection to engraft NSG mice[429], which could have contributed to lower reconstitution levels at the time of immunization. Second, while the methods did not expressly state whether the culture-expanded DCs and injected autologous PBMCs had been previously frozen, a freeze-thaw step may have also reduced engraftment efficiency of certain HIS subsets. Third, the cages of humanized NSG mice included in their study were supplied with antibiotic treated water (trimethoprim and sulfadoxine) throughout the experiment, which could have impeded the development of EAE symptoms[731,732].

Lastly, the day 7 immunization formula included multiple myelin antigens emulsified in CFA, but PTx was not co-administered[644], which we found to be crucial for enhancing BBB permeability in HuPBMC-NSG/SGM3 mice. As noted by the authors, “In line with the lack of paralysis, analysis of H&E-stained sections revealed no signs of tissue damage and Kluver-Barrera-stained sections did not show demyelinated areas”[644]. For these reasons, it is possible that too few myelin reactive human T cells entered into the CNS following the humanization and induction regimen to generate sufficient inflammation for visible demyelination and clinical EAE symptoms to result. As far as the myelin antigens used to pulse autologous DCs, Zayoud and colleagues included a mixture of “PLP peptide 139–151, bovine MBP protein, human MBP peptide 87–99 (both have the same sequence at position 87–99 as mouse MBP87–99), rat/mouse MOG peptide 35–55 and rMOG protein 1–125 from rat (having the same sequence in the major

encephalitogenic epitope 35–55)"[644]. Our data suggests that mouse MOG_{35-55} does not elicit a strong $hCD4^+$ T cell response when cultured with murine MHC expressing myeloid cells, whereas recombinant human MOG protein did elicit a proinflammatory $hCD8^+$ T cell response. Zayoud and colleagues observed that a proinflammatory $hCD4^+$ T cell response occurred only with rat MOG protein when cultured with syngeneic pulsed DCs, while $hCD8^+$ T cells did not respond to any of the immunizing antigens presented by HLA matched DCs[644]. To note, however, rat MOG protein and human MOG protein are known to differ in their epitope specificities and B cell dependence in C57Bl/6 EAE mice, which could influence T cell activation[149].

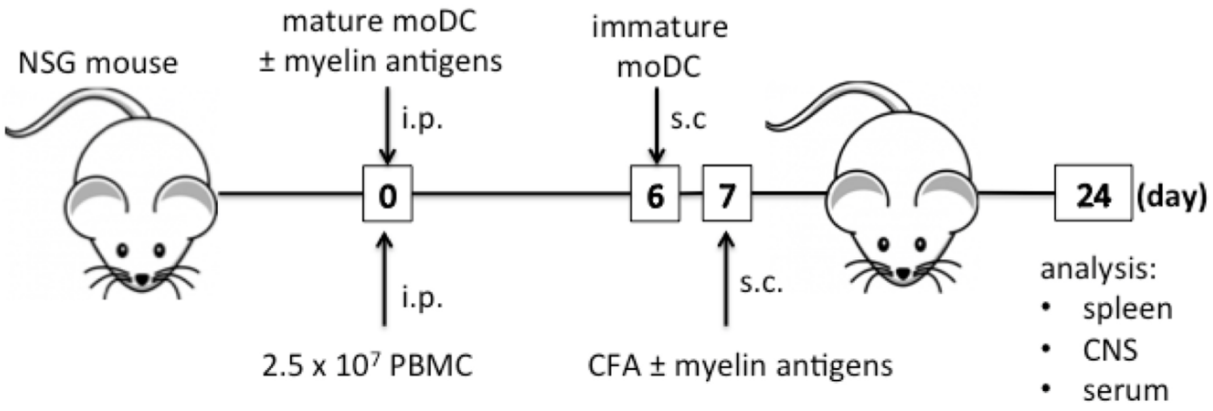

Figure 4.91 Schematic of experimental design employed by Zayoud and colleagues to immunize HuPBMC mice with myelin antigens

NSG mice were IP injected with healthy donor derived PBMCs pre-mixed with autologous myelin antigen-pulsed monocyte-derived DCs (expanded and matured ex vivo for 8 days and comprising ~2% of the total engrafted cells). Individual myelin antigens were used to pulse aliquots of the autologous DCs that were then combined in equal amounts for engraftment. Antigens included peptides and protein domains from PLP, MBP, and MOG, typically used in classical murine EAE models, or nonspecific antigens such as ovalbumin for control immunizations. Six days later, the engrafted HuPBMC NSG mice were then SQ injected with a second dose of non-pulsed immature DCs to promote antigen presentation, and 12 hours later on day 7 post-PBMC, mice were immunized with the same myelin antigen mix (50 µg of each) emulsified in CFA by SQ injection. At day 24 post-immunization, subclinical inflammatory infiltration of the brain and spinal cord was observed, comprised of human $CD4^+$ and $CD8^+$ T cells, though no clinical EAE symptoms like paresis or paralysis developed in any immunization group. Adapted from [644].

Though Zayoud and colleagues included the $PLP_{139–151}$ peptide typically used to immunize susceptible SJL mice (*H-2s*), NOD background mice (*H-2g7*) have been shown to be susceptible

to immunization with PLP_{56-70} peptide[144,733], and therefore, validation of the encephalitogenic capacity of each of these antigens separately in NOD WT mice (and/or human HLA type binding affinity for each antigen) would determine their suitability for use as EAE inducing antigens in HuPBMC-NSG mice. The authors noted that the number of donor cells required to engraft each recipient NSG mouse (25×10^6 PBMCs + 2.5×10^5 pulsed DCs + 2.5×10^5 immature DCs) was prohibitively too high to generate cohorts with MS patient derived PBMCs[644], and thus MS versus HD responses were not evaluated in their study. The authors concluded that "T and B cells from healthy human beings, which are specific for the MOG protein, are clonally expanded and readily activated when properly primed and migrate into their target tissue"[644].

The incorporation of professional autologous, human HLA expressing APCs alongside the engrafted donor PBMCs, was a logical addition designed to facilitate myelin antigen presentation to the engrafted human T cells through autologous HLA:TCR interactions. Multiple studies have demonstrated that human monocyte derived immune subsets generally do not survive in PBMC humanized NSG mice[429,465,644,734]. Yaguchi and colleagues have shown that beyond 10 days post-PBMC injection of NOG mice, human DCs are numerically scant[506]. It is therefore unclear if the pulsed autologous DCs would have survived long enough and/or in sufficient quantities to present myelin antigen to reconstituted human T cells when HuPBMC-NSG mice were immunized a week later, since the authors noted $hCD4^{lo}$ monocytes were not detectable in the CNS, blood, or spleen by endpoint[644]. SQ injection of immature DCs twelve hours before the myelin/CFA emulsion may have circumvented this issue of poor human myeloid cell survival in recipient NSG mice, but it may have also inadvertently distracted or sequestered myelin reactive T cells within the subcutaneous area where the only human HLA complexes were expressed, rather than promoting trafficking of these cells into the CNS to interact with the murine MHC complexes expressed locally. In culture, human T cells will preferentially interact with human APCs, favoring human HLA over murine MHC expressing cells when given the choice[718]. Our data suggests human DC priming is not necessary to produce clinical EAE symptoms in HuPBMC mice and supports existing data showing that productive interactions occur between human TCRs and murine MHC complexes[488,493,505,537].

A notable benefit to the inclusion of antigen primed human DCs, however, was the generation of a measurable serum anti-rat MOG IgG response in two of four immunized cohorts, indicating epitopes within rat MOG were presented to human B cells and co-administration of

autologous human DCs promoted B cell survival, maturation, and class switching in at least some HuPBMC-NSG mice[644]. Poor B cell maturation and class switching continues to be an issue in the development of representative humanized mouse models generally, so these findings are promising. Consistent with our findings, hCD45$^+$ cells, the majority of which were hCD3$^+$ T cells, comprised 75% of total immune cells in the spleen at day 24 post-humanization and human T cell subset proportions were similar in the spleens of both immunized and control mice ("both around 40–50 % of CD3$^+$ cells")[644]. These data further indicate that relative human T cell subset reconstitution is mainly a PBMC donor-based variable rather than one affected by EAE induction parameters. Within the CNS of immunized mice at endpoint, about 20% of isolated cells were hCD45$^+$ compared to 5% in controls[644], which fell on the lower end of the 10 – 90% hCD45$^+$ cells (average 52%) range measured in the CNS of our EAE induced HuPBMC-NSG/SGM3 mice and 23 – 38% in the CNS of antigen and adjuvant immunized controls (Section 4.8).

Zayoud and colleagues also identified "a significant increase of human CD3$^+$, CD4$^+$ and CD8$^+$ T cells in the parenchyma and also in the meninges of immunized PBMC-NSG mice compared to controls" histologically, as well as cerebellar clusters of mouse Iba-1$^+$(hCD45$^-$) activated microglia/macrophages in the myelin immunized HuPBMC-NSG mice[644], similar to our findings by IHC, suggesting gliosis in the CNS occurred following myelin CFA immunization whether or not there were primed human DCs present in the system. The authors also noted elevated human IFNγ mRNA levels in the CNS of immunized HuPBMC-NSG mice, whereas IL-17A mRNA was not detectable[644]. "Only scattered single CD20$^+$ B cells were detectable in the parenchyma and meninges of both groups"[644], which agrees with our flow cytometric data showing large numbers of Th1 cells and very few human CD19$^+$ B cells within the CNS of HuPBMC-NSG EAE mice. Furthermore, they noted that "neither the blood, nor the spleens or the CNS of both immunized and control mice contained human monocytes. The lack of demyelination and of overt neurological signs of EAE despite infiltration of human lymphocytes into the CNS of immunized mice might therefore be ascribed to the deficiency of human monocytes in this model"[644]. We too detected very few human monocytes in all of the tissues collected from HuPBMC-NSG/SGM3 mice at EAE endpoint, however, in their absence, host murine myeloid cells were able to infiltrate and phagocytose myelin in the CNS in association with human cytotoxic T cells.

Another key finding by Zayoud and colleagues was that xGvHD severity, as measured by H&E staining of various organs, was minimal at endpoint regardless of the myelin antigens, or

lack thereof, included in the immunization regimen[644]. They noted "during the time of our experiments, only a mild form of GvHD independent of the immunization" occurred[644]. These results are consistent with our data showing that the incidence of clinical signs of xGvHD was fairly consistent among groups of HuPBMC-NSG/SGM3 mice derived from the same PBMC donor when immunized with one or combinations of the EAE inducing antigens and/or adjuvant components (Section 4.8). The authors stated: "Analysis of GvHD pathology in skin, lung, liver, and gut using a histological index revealed rare infiltrates in the skin, mild infiltrates in the liver, and moderate infiltrates in the lung whereas infiltrates in the gut were absent. GvHD scores occurred at a similar level in myelin and in [random antigen] control-immunized animals, showing that CNS infiltration was a specific event due to the immunization with myelin antigens."

Following along this line, the additional use of PTx in our control groups likely enabled nonspecific human T cell infiltration of the CNS regardless of myelin antigen inclusion, though the addition of MOG antigen in the CFA emulsion specifically promoted EAE pathology. Similar average numbers of human and murine immune cell subsets were measured in the CNS tissues of all PTx treated groups, while only MOG immunized mice reliably developed clinical EAE symptoms. Therefore, the lack of symptom incidence in groups immunized without MOG emulsion could not be attributed to insufficient effector T cell infiltration of the CNS. If the incidence of EAE in HuPBMC mice was dependent simply on enabling the entry of xenoreactive human T cells into the mouse CNS, we would have expected to see equal or at least similar rates of paralysis in all PTx treated HuPBMC mice (Section 4.8). Moreover, the consistently higher incidence of clinical symptoms of xGvHD compared to symptoms of EAE in all immunized HuPBMC mice, independent of whether these mice also or separately developed paralysis, indicates that while xGvHD is an unavoidable feature of using the HuPBMC EAE model, CNS immunopathology likely cannot be attributed only to brain and spinal cord localized xGvHD.

In regular NOD EAE mice, only 2 – 6% of spinal cord infiltrating $mCD4^+$ T cells bind MOG specific MHC II tetramers, indicating the vast majority of the recruited T cells are not specific to the inducing antigen. If only a small fraction of MOG-specific human T cells in the CNS of HuPBMC EAE mice was present, it would not necessarily indicate that our model is simply an extension of xGvHD, but rather that EAE and xGvHD in the HuPBMC model exhibit common mechanisms of antigen presentation that depend on murine MHC complex recognition and co-stimulation through interspecies receptor: ligand interactions. Similar to our observations

in the HuPBMC EAE model, xGvHD development in PBMC engrafted BRG mice has been shown to depend on both human and murine immune cell cooperation[619]. Genetic overlap in susceptibility to xGvHD and autoimmunity has also been reported in HuHSC-NSG mice[607]. While some human and mouse signaling interactions can cross the species barrier (i.e., chemokines, hLFA-1/mICAM-1), others are noted to be incompatible (i.e., hFLT3R/mFLT3L, mLFA-1/hICAM-1)[488,542,735], demonstrating the evolutionarily divergence and complexity of species-specific immune responses.

Interspecies TCR: MHC interactions are also potentially less efficient than autologous TCR: HLA antigen presentation, as evidenced by a relatively lower rate of EAE symptom incidence compared to classical murine EAE models and the suspected reduced binding affinity of human TCRs for murine MHC complexes in humanized NSG mice[145,488]. These interactions are, however, sufficient to elicit $hCD8^+$ T cell activation ex vivo and produce demyelinating disease resulting in clinically measurable motor deficits. Ajith and colleagues also measured "a sizeable majority of naïve $CD8^+$ T cells unaffected by GVHD that are capable of mounting an allogeneic immune response" in HuPBMC-NSG mice, and that the $hCD8^+$ cytotoxic T cell response was sensitive and selectively attuned to different allogenic challenges[611]. More broad conclusions about the relative role of nonspecific xGvHD in the HuPBMC EAE model can likely only be made by repeating experiments with multiple donor cohorts and utilizing more sensitive measures of graft and myelin specific responses. The main findings of this chapter collectively indicate that infiltrating $hCD4^+$ T cells direct a Th1 polarized response in the CNS of HuPBMC EAE mice that leads to $hCD8^+$ T cell-mediated myelin damage and subsequent or concurrent phagocytosis by murine macrophages and microglia, resulting in a chimeric mouse model of autoimmune MS.

Chapter 5 – Epstein-Barr virus promotes T cell dysregulation in a humanized mouse model of multiple sclerosis

5.1 Rationale and experimental design

The significant association between previous infection with EBV and an elevated risk for developing MS later in life has been largely elucidated from epidemiological and clinical studies, comprised of population-based, serological, and post-mortem tissue analyses[74,109,323–325,355,357,367,736]. These studies have collectively demonstrated a strong, consistent correlation between a history of EBV infection and increased risk of MS, however, these data do not provide much additional insight as to the neuroimmunological mechanisms underlying this major risk factor for disease. A greater understanding of the inflammatory pathways affected by EBV infection over time is necessary to understand the contribution of viral infections to MS and autoimmune disease susceptibility generally, as well as to develop effective, targeted preventative and therapeutic interventions to reduce disease burden. Based on the average time delay of 5 – 8 years between EBV seroconversion or the incidence of clinically symptomatic IM and the onset of MS in affected individuals[109], as well as our group's data demonstrating that latent, rather than acute, gammaherpesvirus infection enhances disease outcomes following EAE induction of mice[415,418,420], we sought to evaluate the role of EBV latency specifically by using the HuPBMC EAE model, wherein the reconstituted human immune systems are derived from donor PBMCs that were naturally exposed to EBV.

EBV infection of humanized mice has recapitulated various aspects of the viral immune response and pathogenesis of EBV-associated diseases observed in humans, including lytic and latent infections[524,553,575], lymphoproliferation and tumor formation[552,554,560], and chronic and auto-inflammatory disorders[584,592,594,737]. Studies of EBV infection in humanized mice, however, have not reported CNS-localized inflammation leading to motor deficits, as seen in classical EAE models of MS[584,602,644]. Our EAE immunization protocol reproducibly generated EAE in PBMC humanized NSG/SGM3 mice with clinical and immunological characteristics similar to established murine EAE models (Section 4.6). To assess the effects of long-term latent EBV infection on immune function and neuroinflammation, we induced EAE in HuPBMC-NSG/SGM3 mice reconstituted with PBMCs isolated from healthy EBV seropositive (EBV^+) or EBV

seronegative (EBV$^-$) adults, as well as adults with a diagnosis of RRMS. Evaluation of EBV seronegative RRMS donors was determined not to be feasible for this initial study due to the near universal EBV seropositivity among adults with MS[109,319,738].

For the present study, we recruited blood donors diagnosed definitively with RRMS, rather than PPMS or SPMS, because of the increased prevalence of this clinical phenotype among women with MS and because the HuPBMC-NSG/SGM3 EAE mice developed a clinical disease course reminiscent of the relapsing phenotype seen with the background NOD strain for the recipient NSG/SGM3 (Section 4.6), which we anticipated would best reflect the immune response of individuals with an RRMS diagnosis. In order to limit the potential variable of sex as a confounding factor, we enrolled only female blood donors for this study, since male donor PBMCs resulted in reduced EAE incidence compared to female PBMCs in the HuPBMC-NSG/SGM3 EAE model in our preliminary analyses (Section 4.3), in addition to the known influence that sex can have on viral immune responses and MS-related gene expression in EBV infected B cells[739]. Women are also more susceptible to developing MS than men (~3:1), who are in turn more likely than women to be diagnosed with a progressive form of MS[9,10,73,740].

Figure 5.1 Schematic of experimental design to assess the immunomodulatory effect of donor history of EBV infection and RRMS diagnosis on CNS autoimmunity

Donor PBMCs isolated from women with or without a history of EBV infection and/or a diagnosis of RRMS were used to engraft immunocompromised male NSG/SGM3 mice at 5 x 10^6 PBMCs each by intravenous injection. Following a three-week reconstitution period and confirmation of circulating human CD45$^+$ cell repopulation, PBMC humanized NSG/SGM3 mice (referred to herein as HuPBMC mice) were immunized with mixed recombinant human myelin oligodendrocyte glycoprotein rhMOG$_{1-120}$ extracellular domain and MOG$_{35-55}$ peptide antigens emulsified in complete Freund's adjuvant to induce EAE.

In terms of the HuPBMC-NSG/SGM3 EAE model, we observed a greater incidence of graft-versus-host disease (GvHD) and reduced EAE symptom incidence in female NSG/SGM3 mice compared to male NSG/SGM3 mice engrafted with the same donor PBMCs (Section 4.3).

Moreover, NSG-SGM3 mice exhibited similar incidence of EAE and GvHD symptoms as NSG mice engrafted with the same donor PBMCs and were thus used interchangeably when randomized to recipient groups (Section 4.4). Therefore, female donor PBMCs from healthy individuals with or without a history of EBV infection, as well as those from female donors with a history of both RRMS and EBV infection, were used to humanize male NSG/SGM3 recipient mice (Figure 5.1).

Consenting female blood donors aged 19 – 39 years old were included in this study. Healthy donors (HDs) were classified as such based on a self-reported the lack of any diagnosed condition related to autoimmune, autoinflammatory, neuroinflammatory, or neurodegenerative diseases. For individuals with RRMS, we included participants that had (1) experienced a relatively short disease duration of less than 10 years from initial diagnosis, (2) had a low disability score (excluded individuals with an EDSS score ≥ 4), (3) were in remission at the time of donation, and (4) were DMT naïve throughout their lifetime up until the time of donation. Individuals with a progressive MS diagnosis (PPMS or SPMS) were excluded from the current study. The rationale behind these criteria were that (1) since EBV seroconversion is known to occur months to years prior to MS symptom onset[109], enrolling individuals early on in the disease process may better capture the immunomodulatory effects of latent EBV infection that promote the initiation of disease, (2) increasingly severe disability can be an indicator of a transition to SPMS, which is a form of MS with differing intrinsic neurological involvement than RRMS[51], and our current aim is to assess immunomodulation specifically, (3) active phases of MS are known to be associated with increased EBV reactivation[104], which is an as of yet unclear potential contributor or consequence of relapse that may confound our results, and (4) most currently approved DMTs for MS are immunomodulatory[62], and therefore the use of these medications was excluded as a confounding factor. The full inclusion and exclusion criteria are noted in the methods (Section 2.1). For the individuals whose PBMC samples were included in this study, relevant demographic and clinical information is reported in Table 5.1. The average ages of the donor groups were 31.5 ± 6.1 years for four RRMS EBV^+ donors, 28.8 ± 7.1 years for four HD EBV^+ donors, and 23.3 ± 3.8 years for three HD EBV^- donors. Among the four RRMS EBV^+ donors, the average duration of disease from initial diagnosis was 3.2 ± 3.3 years.

Table 5.1 Blood donor demographics, disease characteristics, and serology

All RRMS and healthy donors were female. RRMS participants were treatment naïve and in clinical remission at the time of donation. Abbreviations: Healthy donor, HD; Expanded Disability Status Scale, EDSS; Viral capsid antigen, VCA; Epstein-Barr nuclear antigen 1, EBNA-1; Cytomegalovirus, CMV.

Donor ID	Age (years)	Age (years) at MS symptom onset	EDSS score	Disease duration	EBV IgG serostatus	CMV IgG serostatus	Serum 25-OH (ng/mL)
MS-01	24	24	2.5	4 months	VCA + EBNA-1 +	+	29.7
MS-02	31	31	2.5	6 months	VCA + EBNA-1 -	+	34.9
MS-03	32	26	2.0	5 years	VCA + EBNA-1 +	-	19.9
MS-04	39	31	2.0	7 years	VCA + EBNA-1 +	-	66.5
HD-01	39	N/A	N/A	N/A	VCA + EBNA-1 +	-	27.7
HD-02	25	N/A	N/A	N/A	VCA - EBNA-1 -	-	35.0
HD-03	26	N/A	N/A	N/A	VCA - EBNA-1 -	-	29.8
HD-04	23	N/A	N/A	N/A	VCA + EBNA-1 +	+	37.5
HD-05	19	N/A	N/A	N/A	VCA - EBNA-1 -	+	18.9
HD-06	25	N/A	N/A	N/A	VCA + EBNA-1 -	+	38.4
HD-07	28	N/A	N/A	N/A	VCA + EBNA-1 +	-	27.5

5.2 EBV seropositive and RRMS donor derived PBMCs exacerbate clinical disease severity in HuPBMC EAE mice

Consistent with previous reports[109,314,741,742], the four donors diagnosed with RRMS were all EBV$^+$ and exhibited significantly elevated mean EBV-specific serum IgG titres to both acute phase VCA (Figure 5.2A) and latent phase EBNA-1 (Figure 5.2B) compared to previously infected, otherwise healthy EBV$^+$ donors. Uninfected EBV$^-$ HDs were identified and grouped based on the absence of serum IgM and IgG specific to both antigens (Figure 5.2A – B). We also assessed donor group differences in other serological factors associated with MS to identify confounding variables[69,82]. Seropositivity to CMV, which is a human herpesvirus closely related to EBV that establishes latent infection in human myeloid cells, has been linked with decreased risk for MS and relapse severity, though its potential pathogenic role in MS susceptibility is still debated[110–112,743]. Our donors showed 33 – 50% seropositivity for CMV within each donor group, which reflects the general population[744,745] (Table 5.1). Although there was no significant difference in anti-CMV IgG titres between EBV$^+$ HDs and the other two groups, RRMS EBV$^+$ donors had slightly elevated anti-CMV IgG compared to EBV$^-$ HDs (Figure 5.2C).

We also verified that the donors did not have any existing overt seroreactivity to the rhMOG inducing antigen that might otherwise impact recipient cohort responses to EAE induction post-PBMC engraftment (Figure 5.2D). See Appendix 2 for individual donor anti-EBV, anti-CMV, and anti-rhMOG IgG and IgM levels (Table A.1). Though a reduced serum vitamin D level is an important risk factor for MS[69,74,83,746], the donor groups had statistically similar serum 25-OH vitamin D levels at the time of donation (Figure 5.2E, Figure A.23). These data indicated that between our healthy and RRMS donor groups, a significantly increased humoral immune response to EBV infection in RRMS samples was the main serological variable at play. EBV viral load analysis of donor PBMCs using a viral DNA polymerase (BALF5) qPCR assay (Appendix 13, Figure A.73) confirmed that none of the donors had detectable levels of cell-associated EBV that might be indicative of a highly active infection or an EBV-associated disorder such as malignancy or infectious mononucleosis[190] (Figure 5.2F). Together with the serological data, these findings suggest all EBV$^+$ donors had cleared the acute infection by the time of donation.

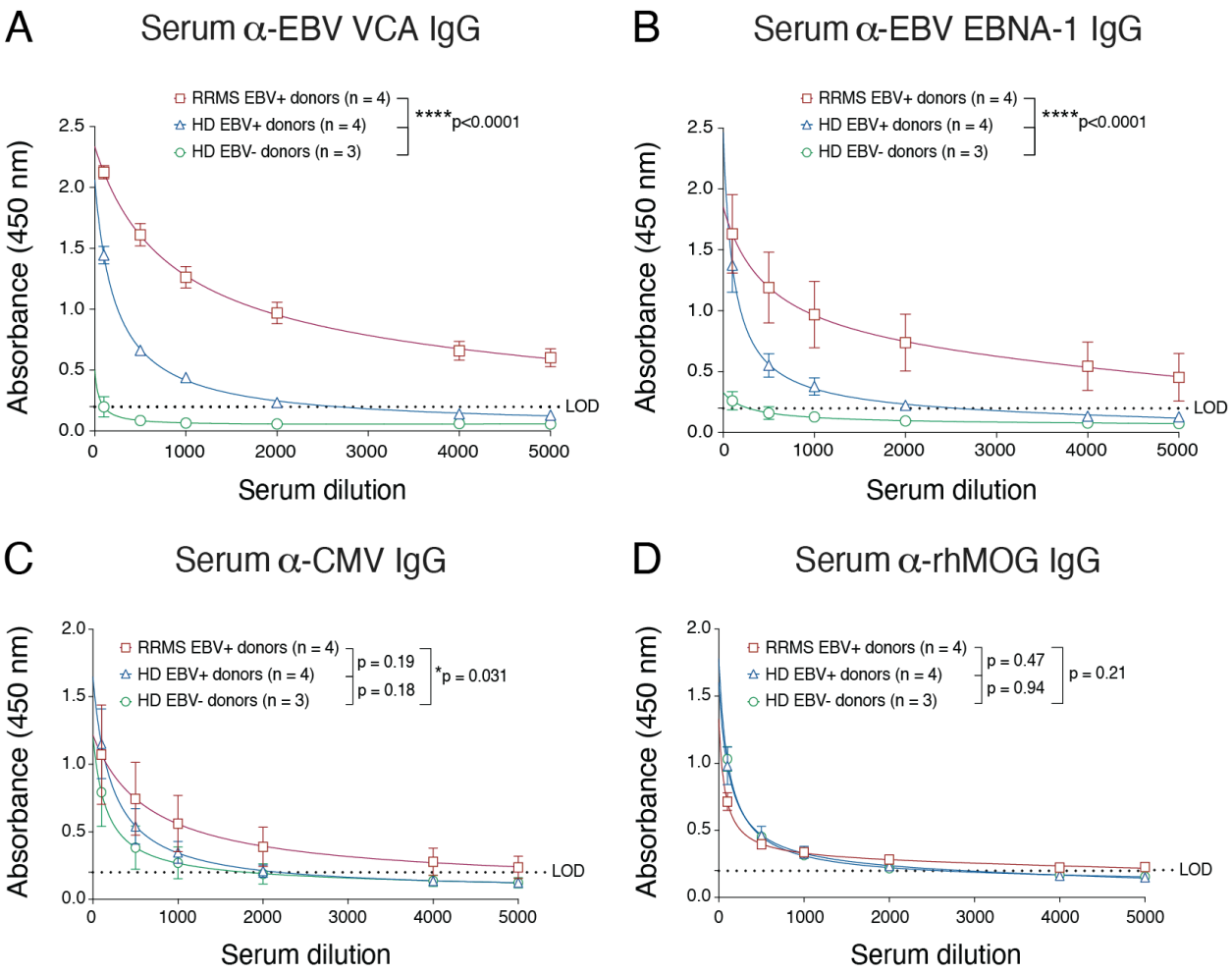

Figure 5.2 Blood donor assessment of previous herpesvirus infections and MS related serological risk factors

Figure shows donor serum IgG levels specific to (A) acute EBV antigen viral capsid antigen (VCA), (B) latent EBV antigen Epstein-Barr nuclear antigen 1 (EBNA-1), (C) cytomegalovirus (CMV) pp28 capsid protein and pp150 tegument protein antigens and (D) the inducing rhMOG$_{1\text{-}120}$ antigen. For A – D, group data are shown as mean with SEM (n = 3 – 4 donors/group) and were curve fit with a one-site total binding equation. Statistical differences in titre curves were assessed by ordinary two-way ANOVA. The lower limit of detection (LOD) is represented by a dashed line. (E) Donor serum 25-OH vitamin D levels are shown as mean with SEM for n = 3 – 4 donors/group and were analyzed by Brown-Forsythe and Welch ANOVA with Dunnett's T3 multiple comparisons test. (F) Cell-associated EBV viral loads in donor PBMCs measured by *BALF5* qPCR assay. Data are shown as mean with SEM and were analyzed by Kruskal-Wallis with Dunn's multiple comparisons test. The lower limit of detection (LOD) for each assay is represented by a dashed line.

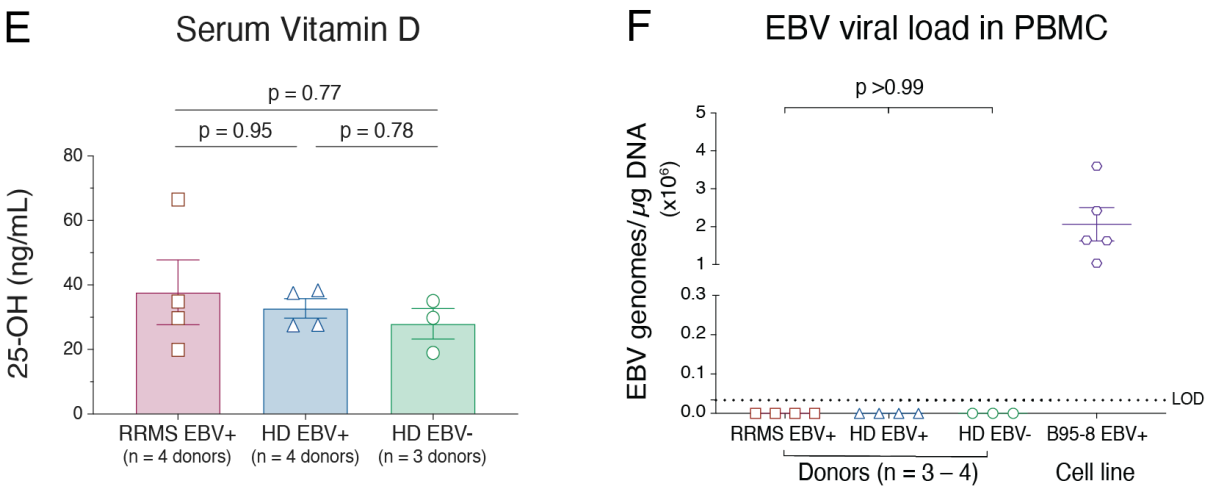

Figure 5.2 continued

Recipient NSG/SGM3 mice each received 5 x 10^6 total PBMCs each and were then induced with EAE using a mixture of $rhMOG_{1-120}$ and MOG_{35-55} after a three-week engraftment period post-PBMC injection (Figure 5.1). Flow cytometric analysis of transplanted PBMCs confirmed that recipient NSG/SGM3 mice were engrafted with a similar composition of immune cells from each donor (Figure 5.3). Individual donor PBMC composition and the number of human PBMCs injected per recipient mouse in each cohort is available in Appendix 1. HLA typing revealed that two of four RRMS donors carried the MS risk allele DRB1*15:01[80], whereas none of the healthy donors carried this allele (see Appendix 3, Table A.2 for individual HLA genotypes). As demonstrated in chapter 4, EAE induction of HuPBMC-NSG/SGM3 mice (henceforth referred to as HuPBMC EAE mice) resulted in an asynchronous, monophasic, possible relapsing, clinical phenotype alike the NOD EAE model. HuPBMC EAE mice demonstrated an exacerbation of clinical disease by multiple measures when engrafted with PBMCs from donors who were EBV^+ and had been diagnosed with RRMS (Figure 5.4). The overall disease course of EAE was significantly worsened in EBV^+ HD mice compared to EBV^- HD mice, which was in turn significantly more severe in the EBV^+ RRMS recipient cohorts compared to both HD groups (Figure 5.4A). The incidence of EAE symptoms was significantly greater in EBV^+ RRMS recipient mice compared to the HD groups, and moderately increased with EBV infection between HD groups (Figure 5.4B). HuPBMC EAE mice derived from EBV^- HD donors also exhibited a significantly delayed time to symptom onset compared to the EBV^+ recipient groups, which was

not significantly different between the EBV$^+$ recipient groups, regardless of an RRMS diagnosis (Figure 5.4C).

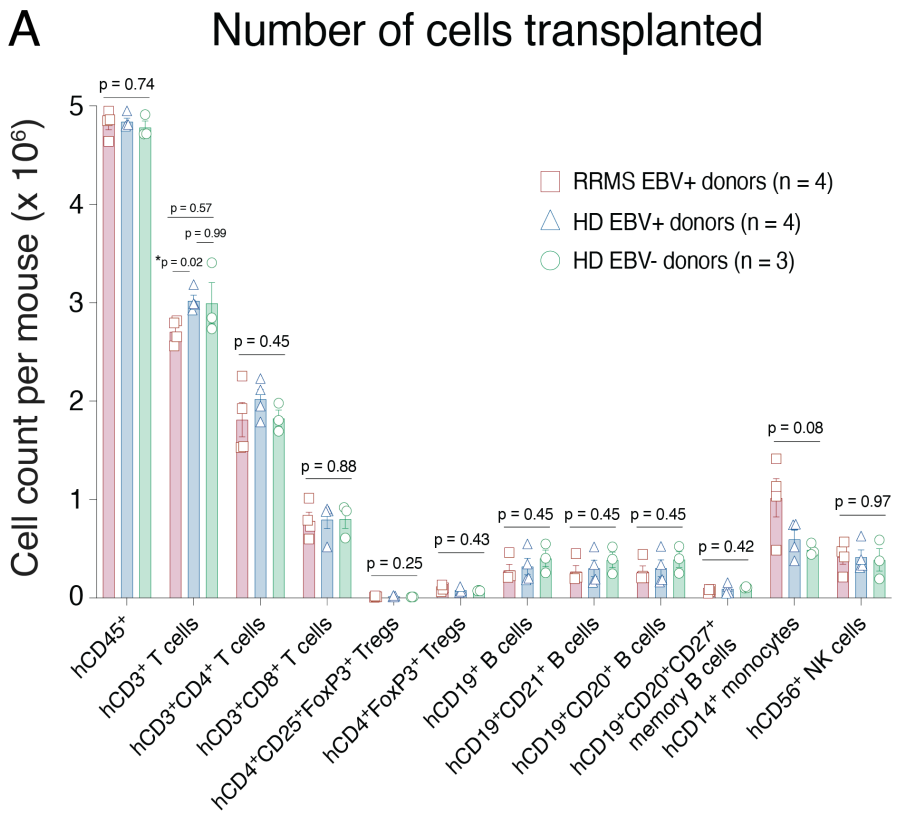

Figure 5.3 Phenotypic composition of donor PBMCs injected into recipient NSG/SGM3 mice is consistent regardless of EBV and RRMS status

Figure shows (A) the number of T cell, B cell, monocyte, and NK cell subsets transplanted per mouse and the relative proportions of (B) hCD4$^+$, hCD8$^+$, and hCD27$^+$ cells among hCD3$^+$ T cells, (C) hCD25$^+$ and/or hFOXP3$^+$ cells among hCD3$^+$CD4$^+$ regulatory T cells (Treg), and (D) hCD21$^+$, hCD20$^+$, and/or hCD27$^+$ cells among hCD19$^+$ B cells those transplanted cells. Data are shown as mean with SEM (n = 3 – 4 donors/group) and were analyzed by Brown-Forsythe and Welch ANOVA with Dunnett's T3 multiple comparisons test or by Kruskal-Wallis with Dunn's multiple comparisons test. Nonsignificant p values represent the overall test result for the three-group comparison, wherein each individual group comparison was also determined to be nonsignificant. The symbol legend in A is applicable to B – D.

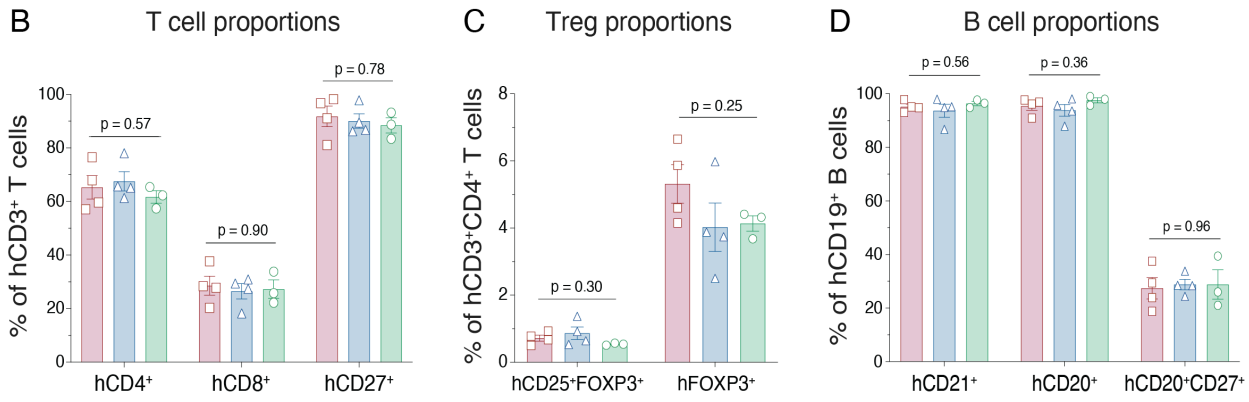

Figure 5.3 continued

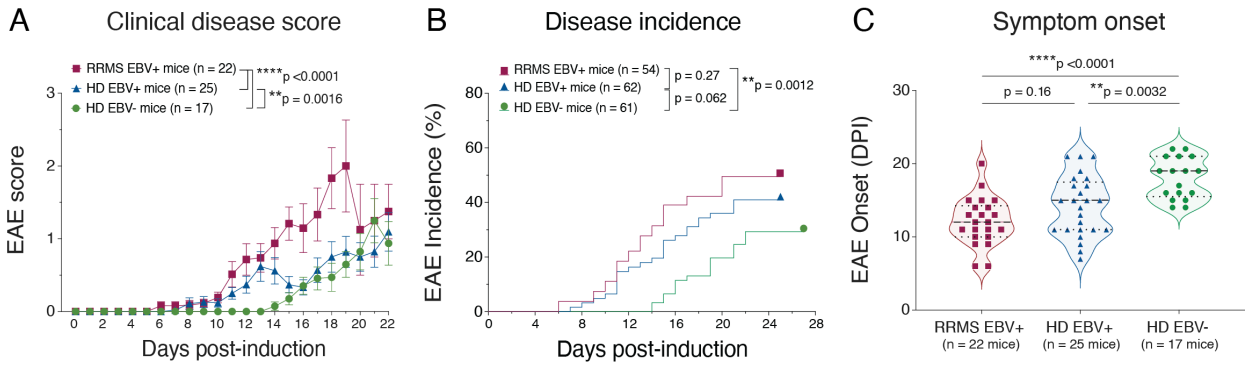

Figure 5.4 Clinical EAE outcomes in HuPBMC mice are worsened by donor RRMS and EBV status

Figure shows (A) the clinical disease scores post-induction for symptomatic HuPBMC EAE mice (n = 17 – 25 mice/group derived from 3 – 4 donors/group) and (B) the incidence of clinical EAE symptoms post-induction for all immunized mice (n = 54 – 62 mice/group derived from 3 – 4 donors/group), as well as (C) the day of EAE symptom onset post-induction (DPI), (D) the group average area and (E) the individual areas under clinical EAE disease curves, (F) the distribution of cumulative EAE disease scores, (G) the proportion of EAE scores attained at the peak of clinical disease, and (H) the average weight loss over time among symptomatic EAE mice (n = 17 – 25 mice/group derived from 3 – 4 donors/group). Recipient group average EAE symptom duration to endpoint was: RRMS EBV$^+$ mice 6.0 ± 1.6 days, HD EBV$^+$ mice 6.9 ± 2.4 days and HD EBV$^-$ mice 7.5 ± 1.4 days post-rhMOG/MOG$_{35-55}$ immunization. In A, D, E, and H, data are shown as mean with SEM. In B, data are shown as percentage of the group and curves were analyzed by Log-rank (Mantel-Cox) test. In C and F, distribution of individual data is shown with median and quartiles (dashed lines). In G, data are represented as proportions of all EAE scores attained in each group. Individual peak EAE scores per mouse were separately plotted and analyzed by Kruskal-Wallis with Dunn's multiple comparisons test. For A and H, curves were analyzed by ordinary two-way ANOVA. For C, E, and F, data were analyzed by Brown-Forsythe and Welch ANOVA with Dunnett's T3 multiple comparisons test. HuPBMC cohorts included: 10, 13 – 18, 20, 22, 24, 26, and 29.

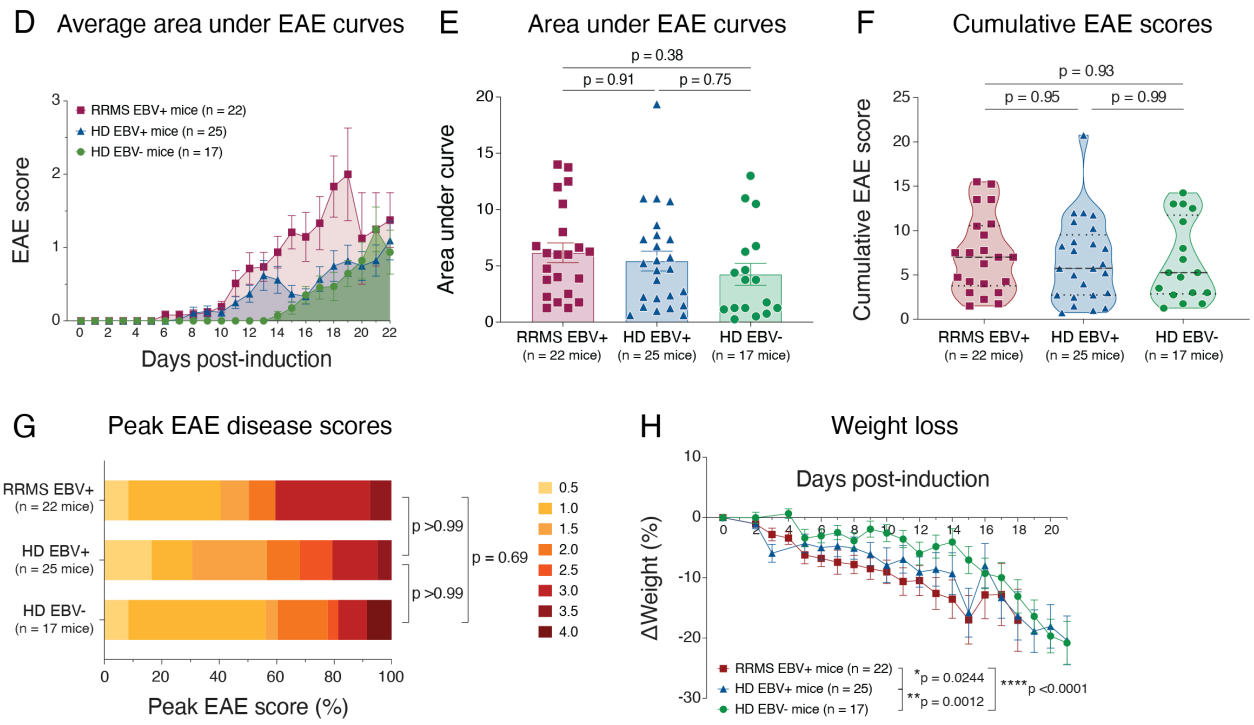

Figure 5.4 continued

The clinical outcomes of EAE indicated that donor EBV infection and RRMS diagnosis both increased disease susceptibility and severity in recipient HuPBMC EAE mice. In order to compare the immunopathological outcomes in HuPBMC EAE mice that might be altered by a donor history of EBV infection, endpoints per cohort were set to generate similar overall disease burden between groups, as demonstrated by similar average areas under the clinical disease curves and cumulative EAE scores between recipient groups by endpoint (Figure 5.4D – F). Similarly, peak EAE scores attained by individual mice and the progression of weight loss were statistically similar between the three recipient groups (Figure 5.4G – H). As weight loss is also key feature of non-specific graft reactivity that results in xGvHD in PBMC humanized NSG mice, we also compared the incidence of clinical signs of xGvHD, skin inflammation and hair loss, which were found to occur at similar rates in all three recipient groups (Figure 5.5). The approximate 20% incidence rate of xGvHD specific clinical symptoms also corresponded with the observed proportion of HuPBMC mice that developed EAE paralysis following myelin antigen-free immunization with CFA and PTx only (Section 4.8, Figure 4.53). Therefore, the differential incidence of EAE symptoms entirely to nonspecific infiltration and damage to the CNS could not be attributed entirely to localized xGvHD.

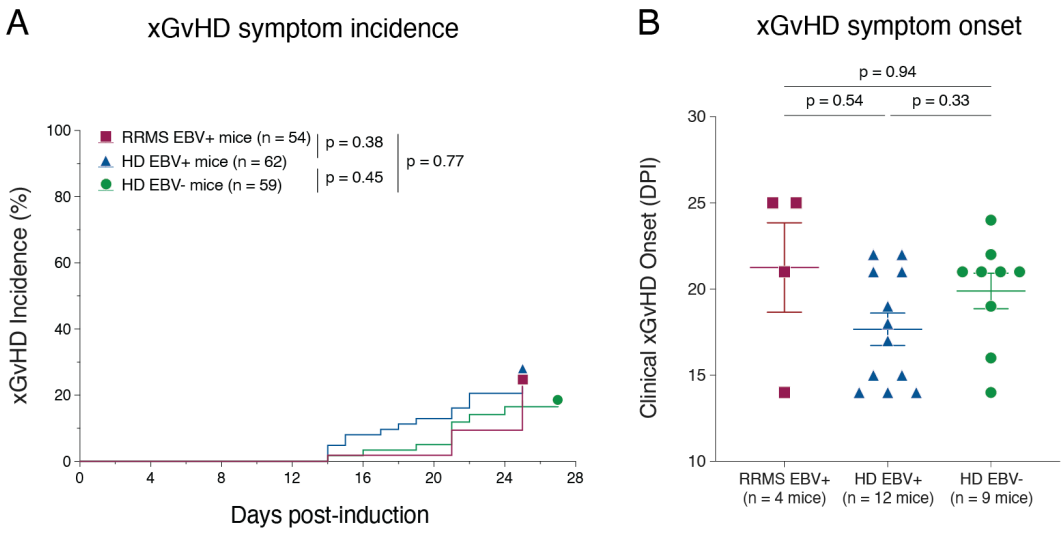

Figure 5.5 Clinical xGvHD outcomes in HuPBMC EAE mice are not differentially affected by donor RRMS and EBV status

Figure shows (A) the incidence of symptoms of xenogeneic graft-versus-host disease (xGvHD) over time (n = 54 – 62 mice/group derived from 3 – 4 donors/group) and (B) the time to xGvHD symptom onset (n = 4 – 12 symptomatic xGvHD mice/group derived from 3 – 4 donors/group), among the three HuPBMC EAE recipient groups immunized with rhMOG/MOG_{35-55} emulsion. In A, data are shown as percentage of the group and curves were analyzed by Log-rank (Mantel-Cox) test. In B, data are shown as mean with SEM and were analyzed by Brown-Forsythe and Welch ANOVA with Dunnett's T3 multiple comparisons test. HuPBMC cohorts included: 10, 13 – 18, 20, 22, 24, 26, and 29.

5.3 Donor EBV seropositivity and RRMS diagnosis promote demyelination and effector T cell accumulation in the CNS of HuPBMC EAE mice

To investigate the underlying cause of the clinical symptom differences associated with donor EBV and RRMS status, we first evaluated the degree of demyelination of the spinal cord among the three recipient HuPBMC EAE groups (see Appendix 7, Figure A.34 for quantification method). EAE induction of immunocompetent NOD mice and RRMS/HD EBV^+ HuPBMC mice led to a significant loss of total myelin content relative to unaffected NSG control mice throughout the length of the spinal cord (Figure 5.6). Both EBV^+ groups had significantly less myelin in the spinal cord compared to NSG controls, whereas EAE induction of EBV^- HD recipient HuPBMC mice did not significantly reduce myelination, suggesting greater protection from EAE consistent with diminished clinical disease severity in this group. We then assessed human immune cell

infiltration of the CNS and reconstitution in the periphery to identify immune subsets that may be contributing to the increased clinical disease severity and demyelination associated with EBV and RRMS status. In the brain, spinal cord, and spleen, HuPBMC EAE recipient cohorts followed a stepwise, increasing trend in total human $CD45^+$ immune cell counts with donor EBV seropositivity and RRMS diagnosis (Figure 5.7A). In all HuPBMC EAE mice, relatively few human B cells infiltrated the CNS relative to T cells: approximately 25 – 100 $hCD19^+$ B cells versus 10^3 – 10^5 $hCD3^+$ T cells per spinal cord (Figure 5.7B – C). Total human B cell infiltration of the CNS and peripheral reconstitution also did not differ between the three recipient groups (Figure 5.7B).

Though direct B cell involvement in causing disease differences appeared improbable due to low levels of reconstitution and infiltration of these cells regardless of the PBMC donor status, total $hCD3^+$ T cell counts comprised the majority of infiltrating human $CD45^+$ cells in the CNS and followed the same increasing trend of higher counts with donor EBV and RRMS status (Figure 5.7C). Among infiltrating human T cells, $hCD4^+$ T cells demonstrated the same increased trend in total counts in all three tissues with donor EBV seropositivity and RRMS (Figure 5.7D), whereas the numbers of $hCD4^+FOXP3^+$ Tregs remained fairly constant regardless of donor status (Figure 5.7E) and $hCD8^+$ T cell counts were increased only in the brain of RRMS recipient mice compared to both HD groups (Figure 5.7F). Increased $hCD8^+$ T cell counts in the RRMS recipient brains corresponded to greater numbers of infiltrating murine $mCD45^{hi}$ immune cells in these samples (Figure 5.8A), whereas $mCD45^{lo}$ microglia and human $hCD14^+CD68^+$ macrophage counts did not differ consistent with recipient cohort EBV and RRMS status in any tissue (Figure 5.8B – C).

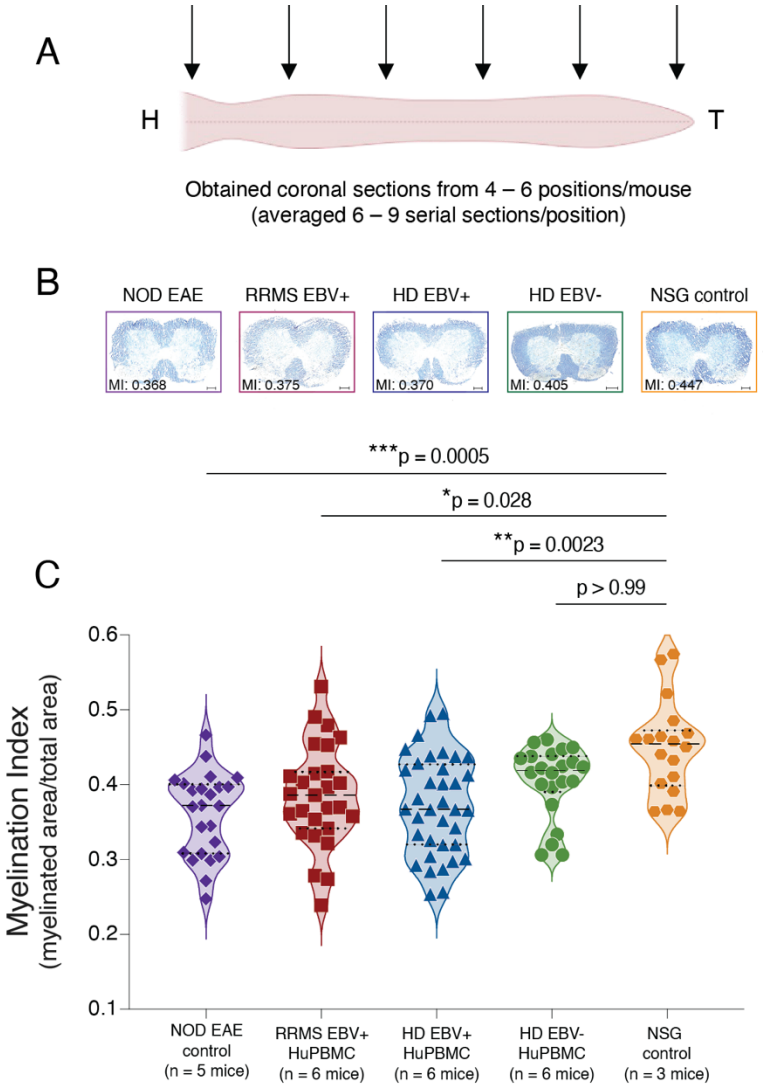

Figure 5.6 Donor EBV seronegativity is protective of spinal cord myelination in the HuPBMC EAE model

Figure shows (A) the sampling strategy used to obtain serial coronal sections from 4 – 6 equidistant regions along the entire length of each spinal cord (from head, H, to tail, T) for staining with myelin-labelling eriochrome cyanine. Perfused spinal cords were obtained days 19 – 25 post-induction (5 – 8 days post-symptom onset) from HuPBMC mice and days 15 – 25 post-induction from NOD mice (5 – 15 days post-symptom onset) immunized with rhMOG/MOG$_{35-55}$ EAE. (B) Representative eriochrome cyanine-stained sections obtained from the lower thoracic region of the spinal cord show myelination indices (MI – the myelinated area over the total area of the section) for each of the respective group means. (C) Myelination indices for HuPBMC EAE mice derived from donors with differential EBV and RRMS status (derived from n = 1 – 2 donors/group), as well as from NOD EAE positive control mice and NSG negative control mice. Individual data points represent the averages of serial sections obtained from each region along the spinal cord (n = 18 total regional points from 3 unengrafted and uninduced NSG control mice; n = 22 – 36 total regional points from 5 – 6 mice/group for EAE-induced NOD and HuPBMC groups). Distribution

of individual data are shown with median and quartiles (dashed lines) and were analyzed by Kruskal-Wallis with Dunn's multiple comparisons test. HuPBMC cohorts included: 13, 14, 16, 26, and 34.

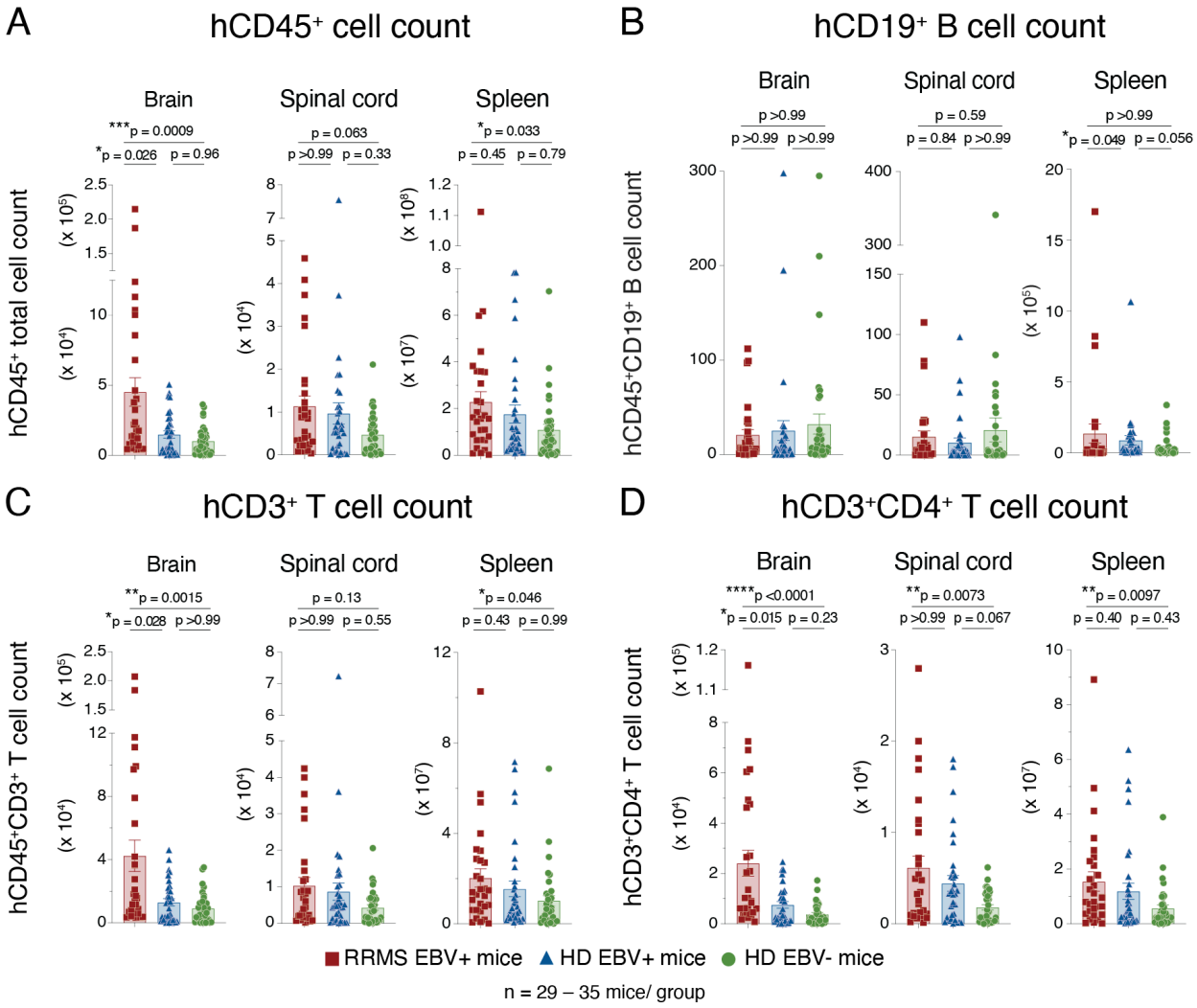

Figure 5.7 Human T cell infiltration of the CNS is increased in EBV seropositive and RRMS donor derived HuPBMC EAE mice

Figure shows total numbers of human (A) hCD45$^+$ immune cells, (B) hCD19$^+$ B cells, (C) hCD3$^+$ T cells, (D) hCD3$^+$CD4$^+$ T cells, (E) hCD4$^+$FOXP3$^+$ Tregs, and (F) hCD3$^+$CD8$^+$ T cells in the brain, spinal cord, and spleen of recipient HuPBMC EAE mice at endpoint, grouped by PBMC donor EBV serostatus and RRMS diagnosis (n = 29 – 35 mice/group derived from 2 – 3 donors/group). Perfused organs were collected days 14 – 27 post-rhMOG/MOG$_{35-55}$ immunization (average 5 – 10 days post-symptom onset). Data are shown as mean with SEM and were analyzed by Kruskal-Wallis with Dunn's multiple comparisons test. HuPBMC cohorts included: 15, 17, 18, 20, 22, 24, and 29.

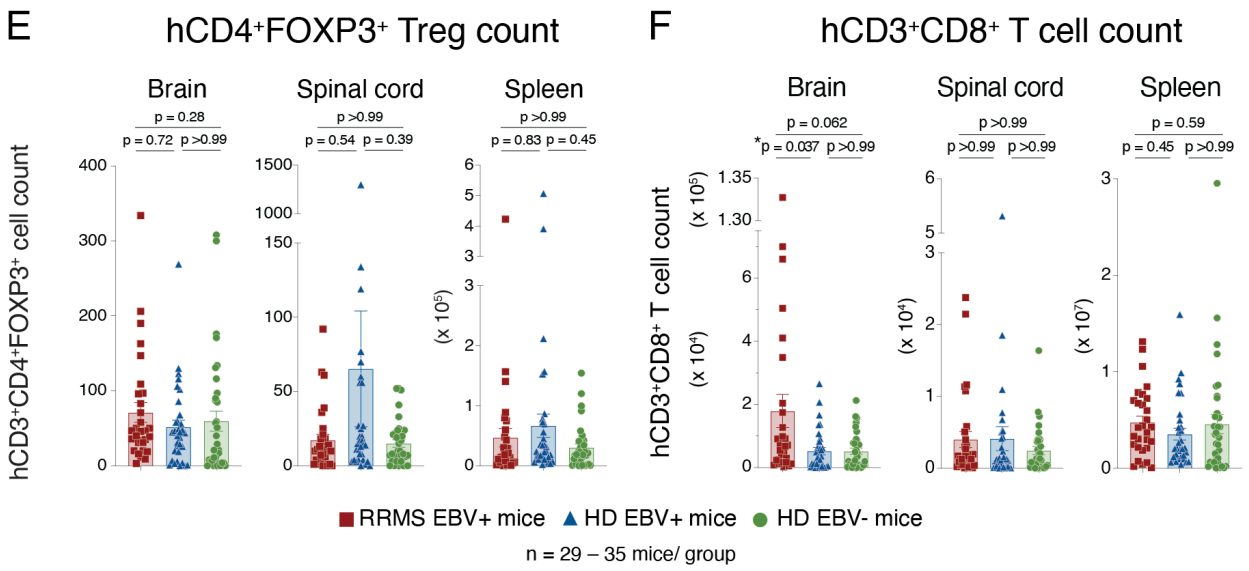

Figure 5.7 continued

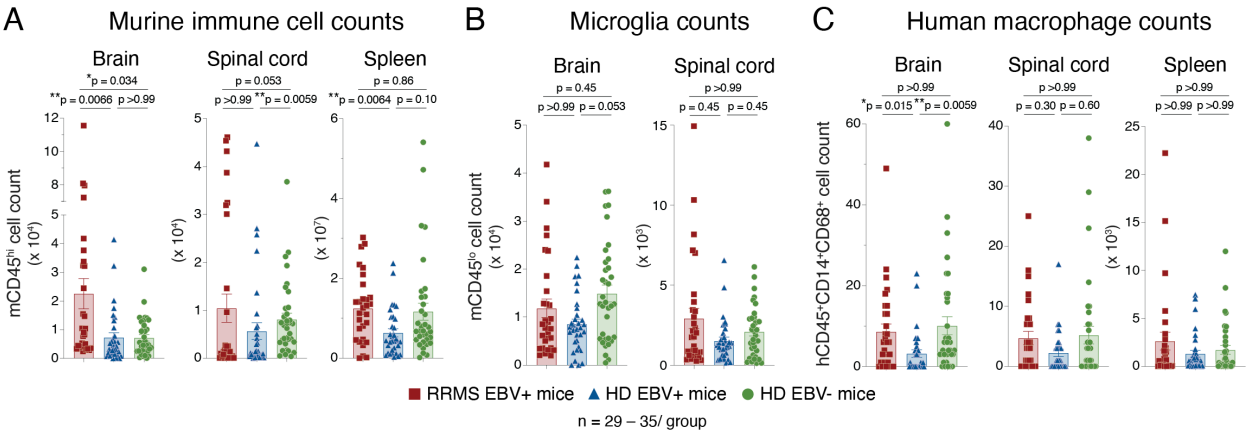

Figure 5.8 Murine and human myeloid cell abundance is similar in HuPBMC EAE derived from donors with differing EBV and RRMS status

Figure shows total numbers of (A) infiltrating murine mCD45^{hi} myeloid cells, (B) murine CNS resident mCD45^{lo} myeloid cells, and (C) human hCD45^{+}CD14^{+}CD68^{+} macrophages in the brain, spinal cord, and spleen of recipient HuPBMC EAE mice at endpoint, grouped by PBMC donor EBV serostatus and RRMS diagnosis (n = 29 – 35 mice/group derived from 2 – 3 donors/group). Perfused organs were collected days 14 – 27 post-rhMOG/MOG$_{35-55}$ immunization (average 5 – 10 days post-symptom onset). Data are shown as mean with SEM and were analyzed by Kruskal-Wallis with Dunn's multiple comparisons test. HuPBMC cohorts included: 15, 17, 18, 20, 22, 24, and 29.

EBV is known to intermittently reactivate from latently infected memory B cells to transmit to new cells[747], which has been suggested to potentially contribute to inciting onset and/or relapses

in MS[104]. Though engrafted B cells reconstituted the spleen at approximately 10^3 – 10^5 $hCD19^+$ B cells per organ (Figure 5.7B), EBV viral genomes were undetectable in the spleens of most mice at EAE endpoint in all recipient groups (Figure 5.9A), suggesting peripheral viral reactivation from engrafted B cells is unlikely to have influenced disease outcomes. We further assessed whether an active EBV infection may play a role in promoting disease by stimulating transferred EBV-specific B cells. Given that engrafted lymphocytes do not form organized GCs in NSG mouse lymphoid tissues, and are subsequently unable to promote class-switching and hypermutation of human B cells[509,510], any EBV-specific IgG produced in HuPBMC mice would indicate a reactivation of engrafted memory B cells rather than a novel response to infection post-engraftment. We confirmed the production of rhMOG-specific human IgM and the absence of rhMOG-specific human IgG in the serum of HuPBMC EAE mice (Figure 5.9B), indicating the engraftment of otherwise functionally responsive human B cells to immunization. In three separate EBV^+ recipient cohorts, no human IgG to the EBV antigen VCA could be detected in serum after EAE induction (Figure 5.9C), despite a strong response in the corresponding donor serum (Figure 5.2A).

These data are consistent with the relatively low rate of B cell infection by EBV in healthy individuals[172]. Based on the estimated proportion of 1 – 50 EBV infected cells per 10^6 B cells in the peripheral blood[172], we would anticipate the transfer of 1 – 15 EBV infected cells among ~3 x 10^5 total $hCD19^+$ B cells, on average (see Appendix 1, Figure A.1 – Figure A.22), into recipient NSG/SGM3 mice that received 5 x 10^6 whole PBMCs each. Though the number of infected B cells may be higher in the PBMC samples from some of the individuals diagnosed with RRMS, the participants included in this study were all in remission at the time of donation, which is when EBV viral loads have been shown to be lower in serum samples compared to active phases of disease, and with no significant elevation in cell-associated viral loads compared to HDs[748,749]. Given how ineffective human B cells reconstitute NSG/SGM3 mice following PBMC engraftment, it is unlikely that active EBV replication, or donor memory responses to an active infection, plays a role in the enhancement of clinical disease observed in EBV seropositive and RRMS diagnosed recipient HuPBMC EAE mice. We therefore assessed specific differences in the systemic and CNS infiltrating T cell response to elucidate the underlying cause of worsened clinical symptoms and spinal cord demyelination in HuPBMC EAE mice derived from EBV positive and RRMS diagnosed donors.

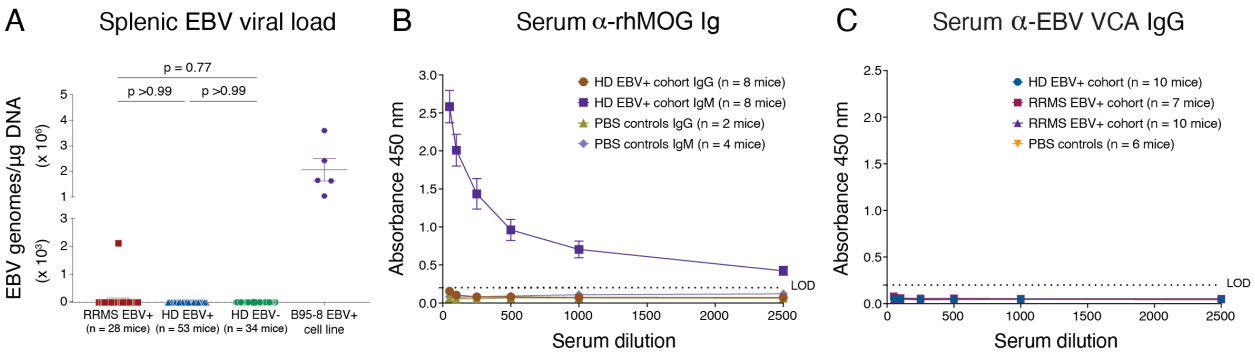

Figure 5.9 Active EBV infection is not detectable in the periphery of HuPBMC EAE mice

Figure shows (A) cell-associated EBV viral loads measured by *BALF5* qPCR assay in splenocytes grouped by donor EBV serostatus and RRMS diagnosis (n = 28 – 53 mice/group derived from 2 – 4 blood donors/group; n = 5 replicates for control EBV$^+$ B95-8 cell line). The LOD is represented by a dashed line. Data are shown as mean with SEM and were analyzed by Kruskal-Wallis with Dunn's multiple comparisons test. HuPBMC cohorts included: 10, 15, 17, 18, 20, 22, 24, 26, and 29. (B) Deficiency in human Ig class-switching from IgM to IgG in response to the rhMOG inducing antigen in HuPBMC EAE mice (n = 8 mice derived from one HD EBV$^+$ donor). (C) Absence of human IgG specific to EBV viral capsid antigen (VCA) in HuPBMC EAE mice derived from three unrelated EBV$^+$ donors (n = 6 – 10 mice/group derived from one donor each). For B and C, serum samples were collected days 15 – 25 post-rhMOG/MOG$_{35-55}$ immunization (average 5 – 8 days post-symptom onset) or from PBS-injected control NSG (n = 2 – 6 mice/group). Data are shown as mean with SEM. As most data points fell below the limit of detection (LOD, dashed line), data were not assessed statistically. HuPBMC cohorts included: 10, 15, and 17.

In the brain, spinal cord, and spleen, the infiltrating effector hCD4$^+$ T cells were mainly Th1 (~40%), with very few cells expressing IL-17A only (typically <1%) compared to double IFNγ$^+$IL-17A$^+$ cells (~2%) in all recipient groups (Figure 5.10A). The proportions of hCD4$^+$ T cells expressing cytokines indicative of Th1 or Th17 subset skewing did not follow any consistent trends with PBMC donor EBV or RRMS status (Figure 5.11A – B), indicating polarization toward a particular inflammatory Th subset was not the main driver of clinical group differences. Interestingly, the CNS of RRMS EBV$^+$ recipient mice did contain proportionally fewer dual Th1/Th17 cells compared to the HD recipient groups (Figure 5.11C). Among CNS infiltrating hCD8$^+$ T cells, however, there was a consistent increase in the proportion of Granzyme B expressing cells with donor EBV seropositivity compared to the HD EBV$^-$ recipient tissues (Figure 5.10B, Q2: GzmB$^+$IFNγ$^-$). Quantitatively, this effect was demonstrated by a significant shift from less IFNγ expression (Figure 5.11D) to more GzmB expression (Figure 5.11E) among hCD8$^+$ T cells in the brain and spinal cord. Interestingly, this trend was not further enhanced by donor RRMS

diagnosis, suggesting donor EBV seropositivity alone caused enhanced T cell cytotoxicity. In the spleen, single positive IFNγ$^+$ and GzmB$^+$ hCD8$^+$ T cell proportions were mostly similar between recipient groups (Figure 5.11D – E), however dual hIFNγ$^+$GzmB$^+$ cell proportions were significantly higher in the spleens of both EBV$^+$ groups compared to the HD EBV$^-$ group (Figure 5.11F).

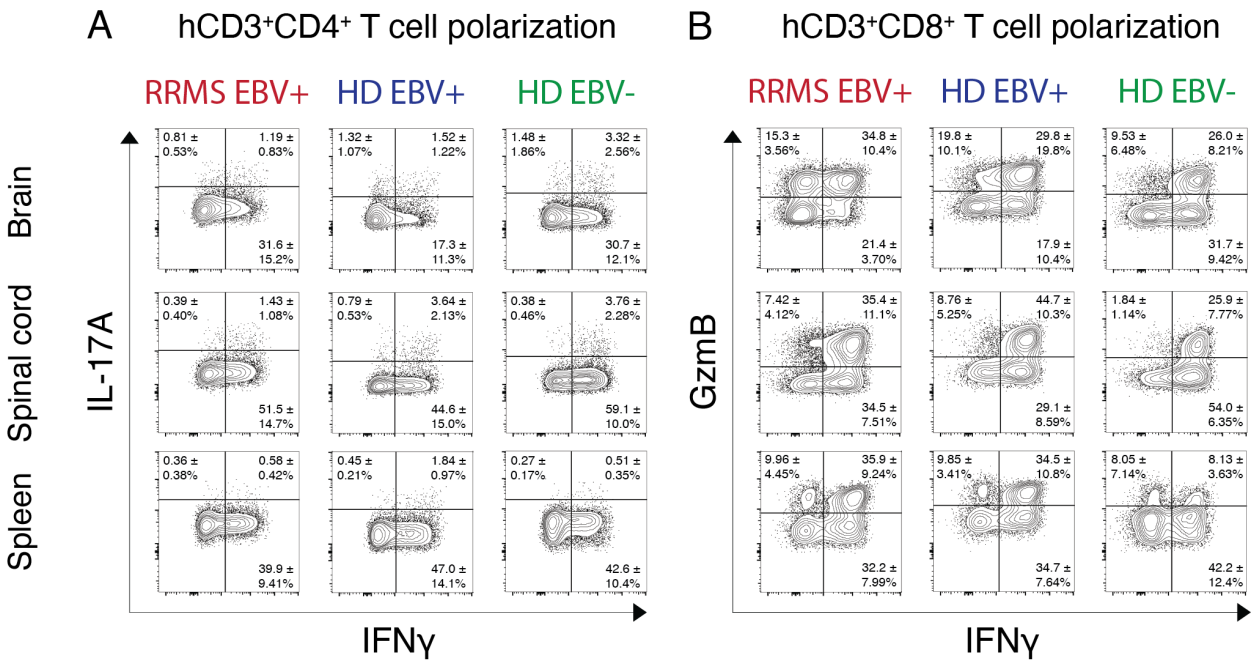

Figure 5.10 Patterns of proinflammatory and cytotoxic cytokine expression by infiltrating human T cells are consistent among HuPBMC EAE mice regardless of donor EBV and RRMS status

Figure shows concatenated flow cytometric plots of (A) IFNγ and IL-17A expression by hCD3$^+$CD4$^+$ T cells and (B) IFNγ and Granzyme B (GzmB) expression by hCD3$^+$CD8$^+$ T cells in the brain, spinal cord, and spleen of HuPBMC EAE mice grouped by PBMC donor EBV serostatus and RRMS diagnosis (n = 9 – 20 mice/group derived from 1 – 2 donors/group). Data are shown as mean frequency with SD. Perfused organs were collected days 14 – 27 post-rhMOG/MOG$_{35-55}$ immunization (average 5 – 10 days post-symptom onset). Isolated immune cells were stimulated with PMA and ionomycin for cytokine detection. HuPBMC cohorts included: 15, 18, 20, and 22.

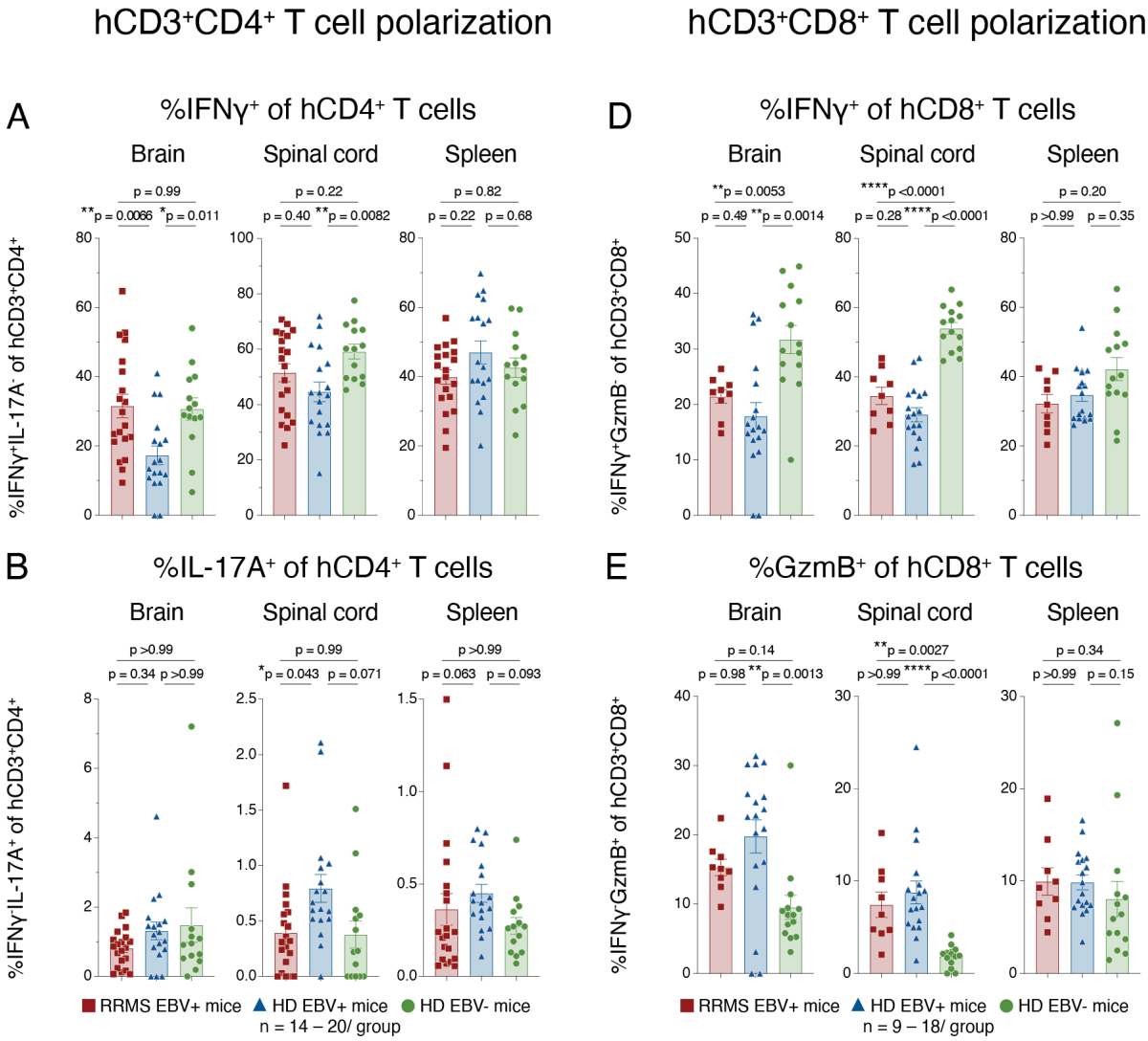

Figure 5.11 Frequencies of proinflammatory cytokine expressing human effector T cell subsets are altered in HuPBMC EAE mice by donor EBV and RRMS status

Figure shows the proportions of (A) IFNγ$^+$(IL-17A$^-$), (B) IL-17A$^+$(IFNγ$^-$), and (C) IFNγ$^+$IL-17A$^+$ among hCD3$^+$CD4$^+$ T cells (left column), as well as the proportions of (D) IFNγ$^+$(GzmB$^-$), (E) GzmB$^+$(IFNγ$^-$), and (F) IFNγ$^+$GzmB$^+$ among hCD3$^+$CD8$^+$ T cells (right column), in the brain, spinal cord, and spleen of HuPBMC EAE mice grouped by PBMC donor EBV serostatus and RRMS diagnosis (n = 9 – 20 mice/group derived from 1 – 2 donors/group). Perfused organs were collected days 14 – 27 post-rhMOG/MOG$_{35-55}$ immunization (average 5 – 10 days post-symptom onset). Isolated immune cells were stimulated with PMA and ionomycin for cytokine detection. Data are shown as mean with SEM and were analyzed by Brown-Forsythe and Welch ANOVA with Dunnett's T3 multiple comparisons or by Kruskal-Wallis test with Dunn's multiple comparisons test. HuPBMC cohorts included: 15, 18, 20, and 22.

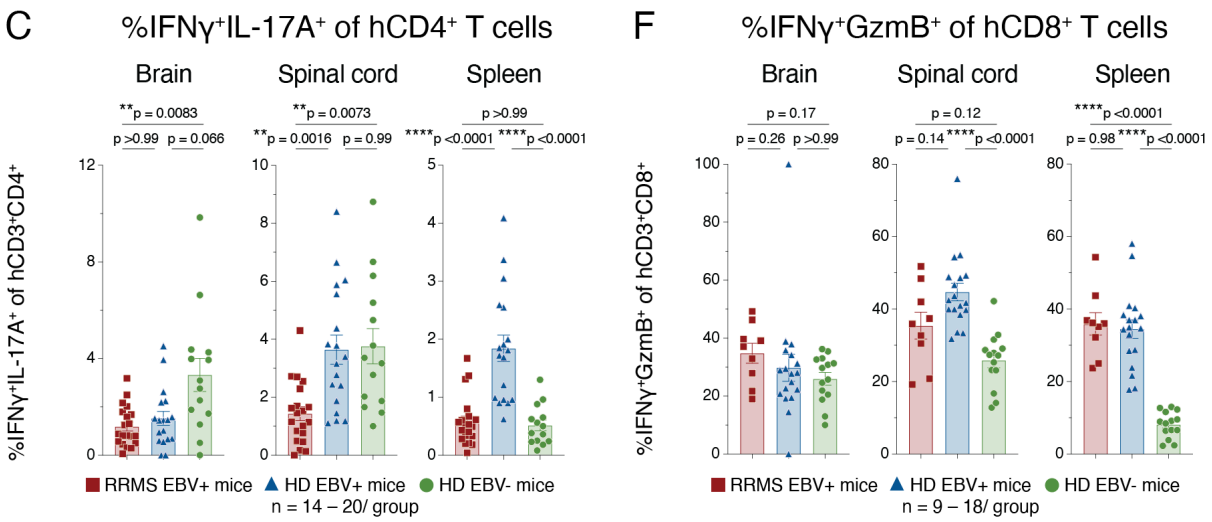

Figure 5.11 continued

Despite measuring a relatively similar frequency of Th1 and Th17 cells in the tissue samples from all three recipient groups (Figure 5.10A, Figure 5.11A – C), the increased total number of hCD4$^+$ T cells present in EBV$^+$ HD and RRMS recipient group tissues (Figure 5.7D) led to an overall greater abundance of effector Th1 cells in the spinal cords and spleens from the EBV$^+$ groups compared to the EBV$^-$ HD group (Figure 5.12A). In the brain, Th1 counts were elevated in the RRMS EBV$^+$ group compared to both HD groups (Figure 5.12A), consistent with increased hCD8$^+$ T cell and murine macrophage counts in these samples (Figure 5.7F, Figure 5.8A). The relatively fewer total numbers of Th17 (Figure 5.12B) and dual Th1/Th17 cells (Figure 5.12C) in the CNS showed some moderate, but not striking group specific trends that would otherwise suggest they underpinned the observed clinical disease differences. In the spleen, both IL-17A expressing populations were numerically more abundant in the EBV$^+$ HD and RRMS recipient group tissues compared to those from EBV$^-$ HD mice (Figure 5.12B – C).

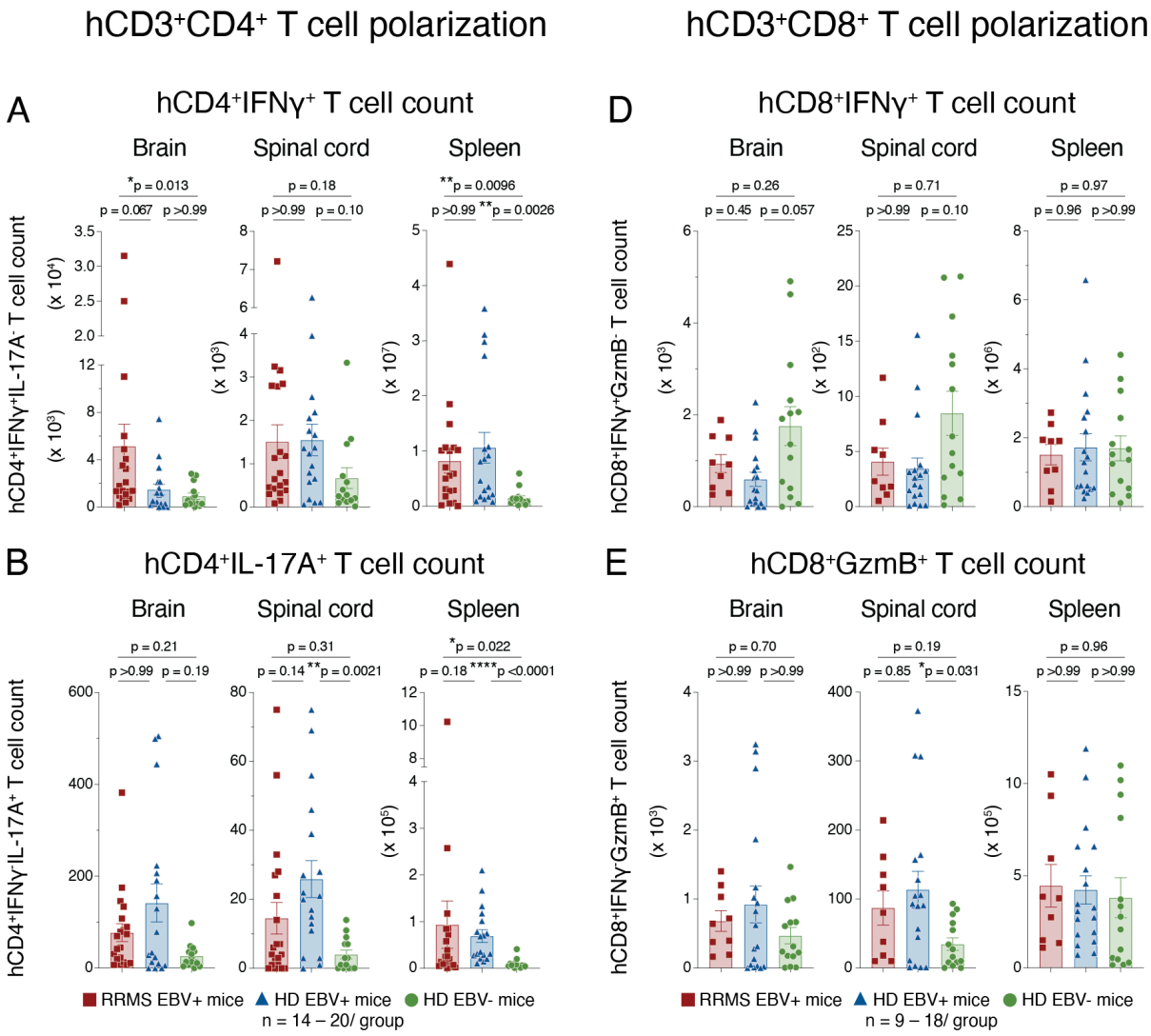

Figure 5.12 Abundance of proinflammatory cytokine expressing human effector T cell subsets is increased with donor EBV and RRMS status in HuPBMC EAE mice

Figure shows the total numbers of (A) hCD3$^+$CD4$^+$IFNγ$^+$(IL-17A$^-$), (B) hCD3$^+$CD4$^+$IL-17A$^+$(IFNγ$^-$), and (C) hCD3$^+$CD4$^+$IFNγ$^+$IL-17A$^+$ T cells (left column), as well as the total numbers of (D) hCD3$^+$CD8$^+$IFNγ$^+$(GzmB$^-$), (E) hCD3$^+$CD8$^+$GzmB$^+$(IFNγ$^-$), and (F) hCD3$^+$CD8$^+$IFNγ$^+$GzmB$^+$ T cells (right column), in the brain, spinal cord, and spleen of HuPBMC EAE mice grouped by PBMC donor EBV serostatus and RRMS diagnosis (n = 9 – 20 mice/group derived from 1 – 2 donors/group). Perfused organs were collected days 14 – 27 post-rhMOG/MOG$_{35-55}$ immunization (average 5 – 10 days post-symptom onset). Isolated immune cells were stimulated with PMA and ionomycin for cytokine detection. Data are shown as mean with SEM and were analyzed by Kruskal-Wallis test with Dunn's multiple comparisons test. HuPBMC cohorts included: 15, 18, 20, and 22.

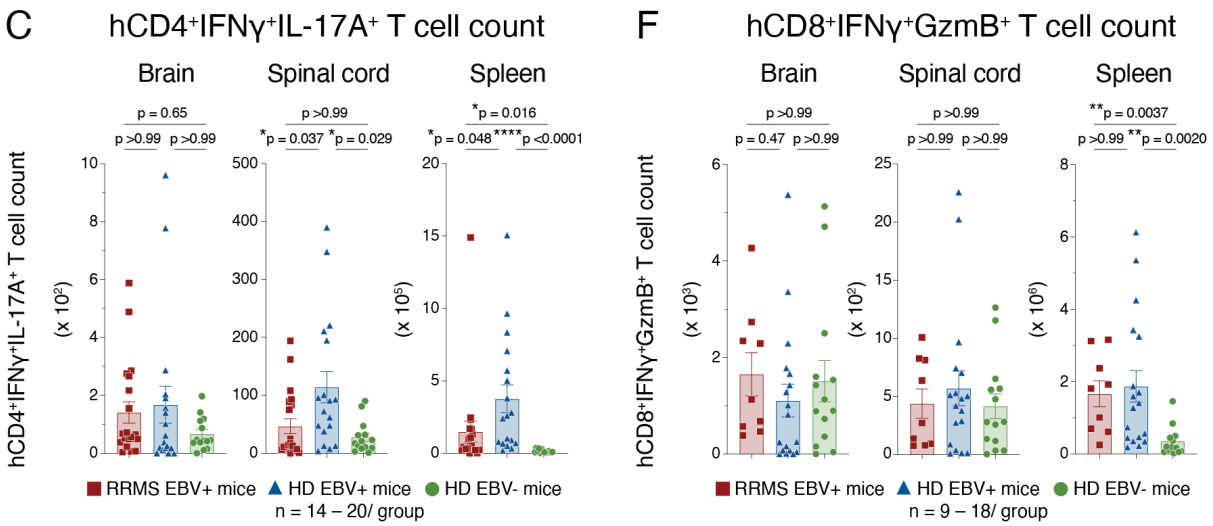

Figure 5.12 continued

In contrast, the total number of infiltrating hCD8$^+$ T cells in the CNS and spleen was mostly similar between recipient cohorts (Figure 5.7F), while the proportions of these cells expressing cytotoxic factors was increased by donor EBV seropositivity (Figure 5.10B, Figure 5.11D – F). In the brain and spinal cord, a nonsignificant trend of greater numbers of hCD8$^+$ T cells expressing IFNγ and fewer expressing GzmB was seen in EBV$^-$ HD mice compared to both EBV$^+$ recipient groups, whereas counts were similar between all three groups in the spleen (Figure 5.12D – E). In the CNS, dual IFNγ$^+$GzmB$^+$ hCD8$^+$ T cell counts were similar between groups, while the spleen of EBV$^-$ HD mice contained significantly fewer numbers compared to both EBV$^+$ recipient groups (Figure 5.12F). Although total effector hCD8$^+$ T cell counts were statically similar between recipient group CNS tissues (Figure 5.12D – F), the skewing toward increased cytotoxic capacity within the infiltrating hCD8$^+$ T cell population was consistent with the exacerbated extent of demyelination in the CNS of EBV$^+$ recipient mice (Figure 5.6). Overall, both a donor history of EBV infection and a diagnosis of RRMS led to incremental increases in the accumulation of pathogenic effector hCD4$^+$ and hCD8$^+$ T cells in the CNS of HuPBMC EAE mice associated with worsened clinical disease outcomes.

5.4 Donor EBV seropositivity and RRMS diagnosis limit regulatory T cell expansion in HuPBMC EAE mice

Alongside greater Th1 and cytotoxic T effector cell infiltration of the CNS, we observed a reduction in the proportion of $hCD4^+$ T cells expressing regulatory factors in EBV^+ recipient group tissues compared to those from EBV^- HD recipient mice. At 3 weeks post-PBMC injection, prior to the induction of EAE, blood samples obtained from HuPBMC mice show that $hCD3^+$ T cell subset frequencies among all engrafted and host leukocytes was reduced in EBV^- HD derived samples compared to both EBV^+ groups, between which reconstitution was similar (Figure 5.13A). Minorly engrafted non-T cell immune subset reconstitution levels, as well as the proportions of $hCD4^+$, $hCD8^+$, and $hCD27^+$ cells among engrafted $hCD3^+$ T cells, did not follow any donor EBV or RRMS status specific patterns (Figure 5.13B – C). Notably, however, the proportion of engrafted $hCD4^+$ T cells expressing the regulatory markers hCD25 and/or FOXP3 was significantly reduced in the blood of RRMS EBV^+ recipient mice, which showed an overall decreasing trend among the groups (Figure 5.13D) indicating peripheral Treg expansion was impaired with donor EBV and RRMS status. Initially, the $FOXP3^+$ proportion of $hCD4^+$ T cells from freshly isolated PBMCs was comparable between donor groups (Figure 5.13A) but was incrementally reduced in EBV^+ HD and RRMS $hCD4^+$ T cells in the blood following engraftment of PBMCs (Figure 5.14B). Following EAE induction of these HuPBMC mice, this trend of lower proportions of $FOXP3^+$ T cells was likewise observed in the CNS and spleen of EBV^+ HD and RRMS recipient mice (Figure 5.14C – E), even though total $hCD4^+FOXP3^+$ Treg counts were similar between groups (Figure 5.7E). These findings mimic data obtained from peripheral blood and CSF samples, which contained reduced frequencies of $FOXP3^+$ T cells from individuals with RRMS compared to unaffected controls[750].

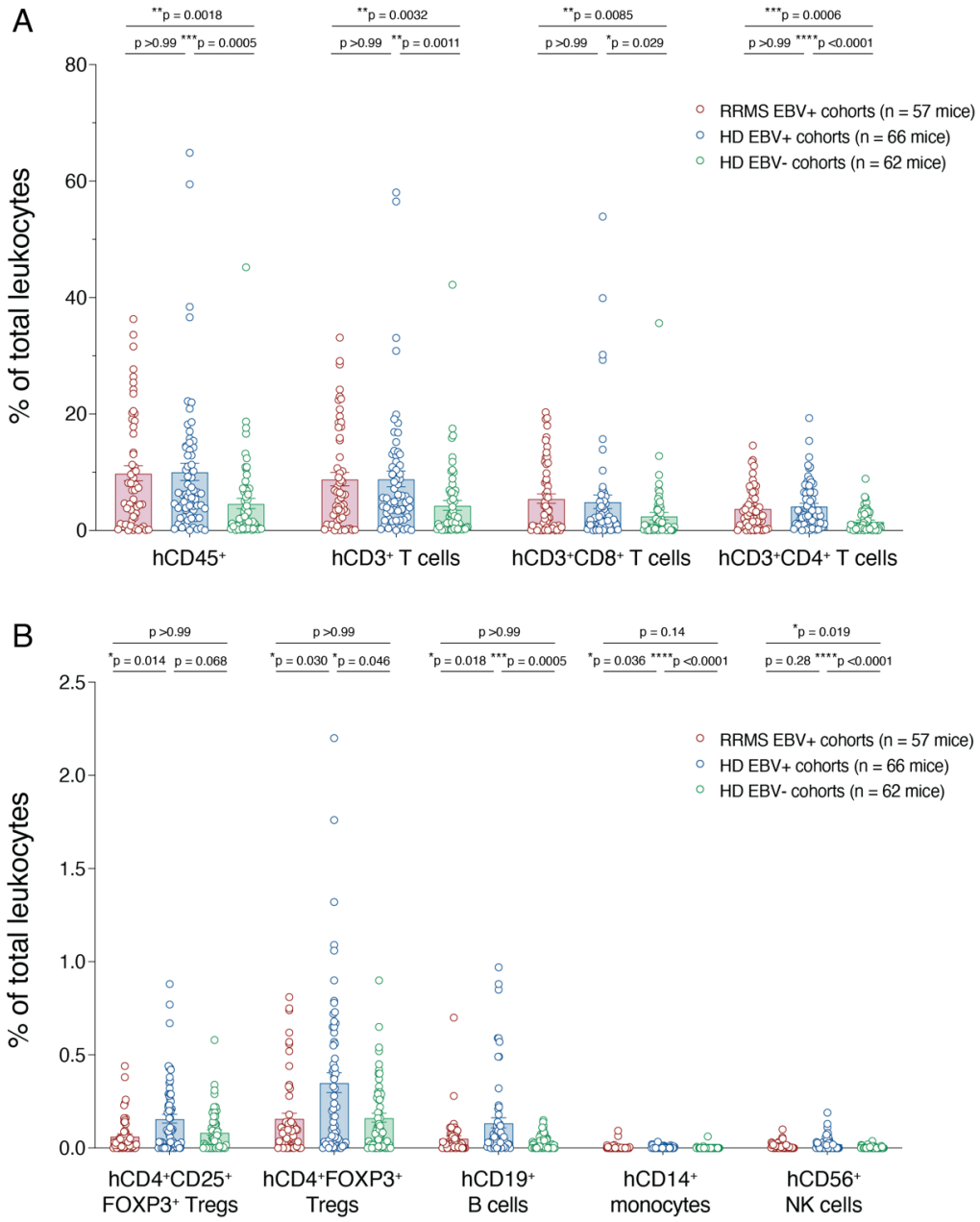

Figure 5.13 Peripheral blood reconstitution of HuPBMC mice derived from donors with differing EBV and RRMS status before EAE induction

Relative proportions of all measured human immune cell lineages are shown as a proportion of total leukocytes (murine and human) in the peripheral blood days 18 – 22 (3 weeks) post-PBMC engraftment of male NSG mice (n = 57 – 66 mice/group derived from 3 – 4 donors/group). Subsets are subdivided into (A) predominantly engrafted immune cell lineages and (B) minorly engrafted immune cell lineages to better illustrate relative frequencies. Proportions of (C) T cell subsets among hCD3$^+$ T cells and (D) regulatory T cell (Treg) subsets among hCD3$^+$CD4$^+$ T cells in each recipient group. Data are shown as mean with SEM and were analyzed by Kruskal-Wallis test with Dunn's multiple comparisons test. HuPBMC cohorts included: 10, 13 – 18, 20, 22, 24, 26, and 29.

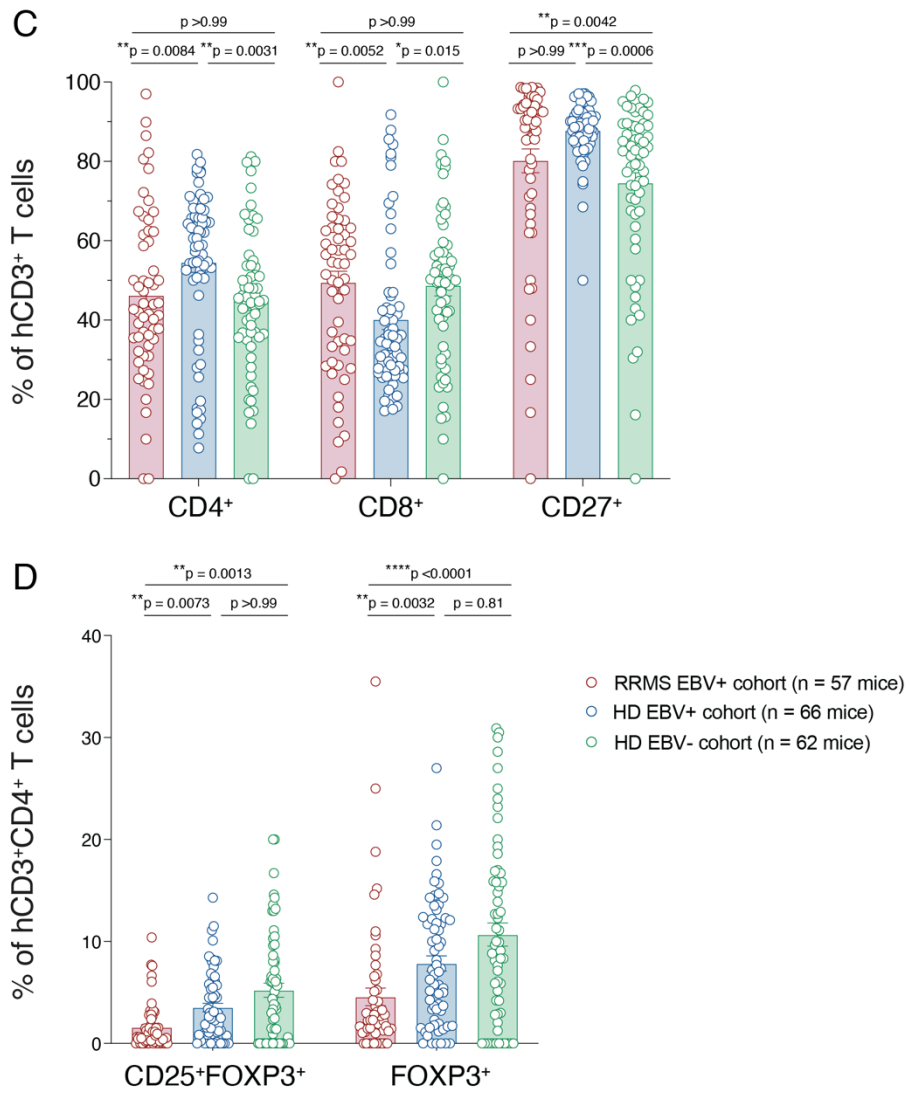

Figure 5.13 continued

The sum consequence of this incremental increase in pathogenic T cell infiltration of the CNS (Figure 5.11 – Figure 5.12) and simultaneous suppression of Treg expansion (Figure 5.14) was a significantly greater ratio of effector hCD4$^+$ and hCD8$^+$ T cells to regulatory hCD4$^+$ T cells in the CNS and periphery of EBV$^+$ HD and RRMS recipient mice compared to EBV$^-$ HD mice (Figure 5.15). As sample collection was timed to maintain similar overall cumulative EAE scores between groups at endpoint, differences in CNS infiltration could not be correlated with greater clinical disease burden for RRMS and EBV$^+$ recipient groups (Figure 5.4D – H). The data collectively suggest that a history of both EBV infection and an RRMS diagnosis among donors leads to a compounded reduction in the expansion of Tregs and a concomitant increase in effector

Th1 and cytotoxic T cell abundance following immune challenge, be that graft reactivity to murine antigens following PBMC engraftment or EAE immunization, and, subsequently, to systemic dysregulation of T cell-mediated inflammation resulting in excessive CNS damage and worsened clinical outcomes.

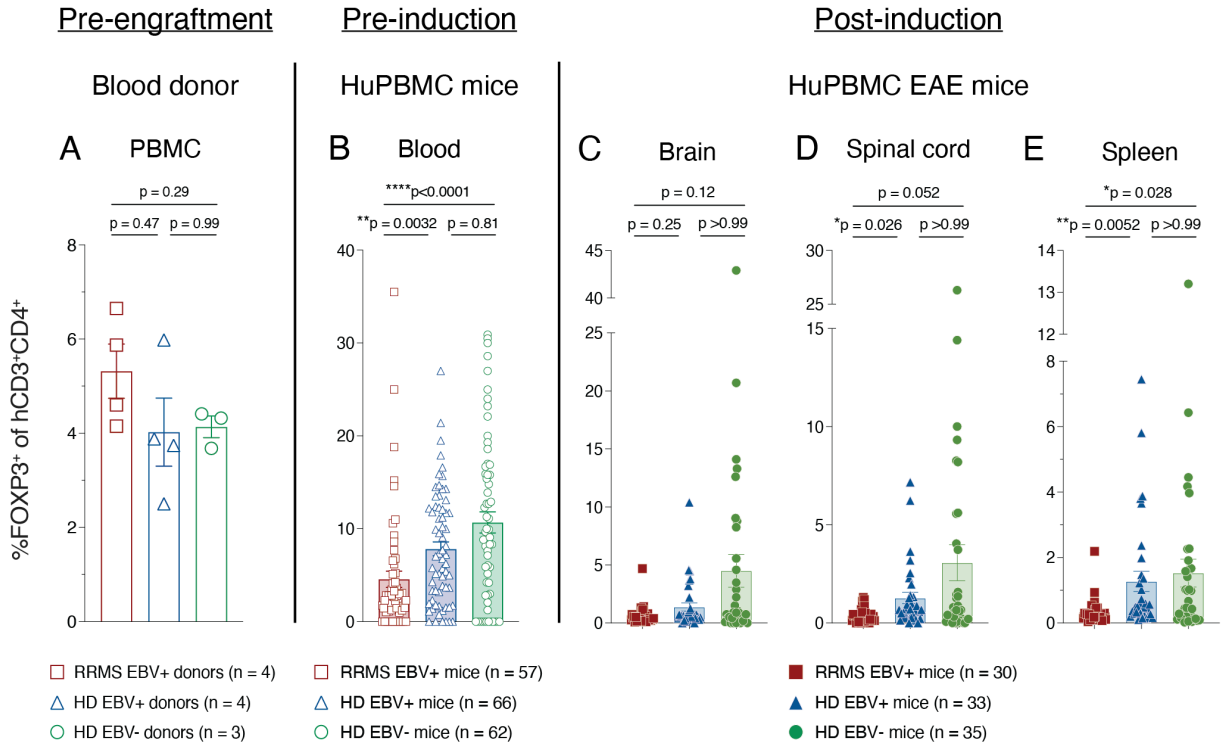

Figure 5.14 Donor EBV and RRMS status limit regulatory T cell expansion in HuPBMC mice following immunogenic antigen exposure

Figure shows the proportion of $hCD3^+CD4^+$ T cells expressing FOXP3 in (A) freshly isolated donor PBMCs (n = 3 – 4 donors/group), (B) in the peripheral blood of engrafted HuPBMC mice at 3 weeks (18 – 22 days) post-PBMC injection (n = 57 – 62 mice/group derived from 3 – 4 donors/group), and in the (C) brain, (D) spinal cord, and (E) spleen of recipient HuPBMC EAE mice grouped by PBMC donor EBV serostatus and RRMS diagnosis (n = 30 – 35 mice/group derived from 2 – 3 donors/group). For C – E, perfused organs were collected days 14 – 27 post-rhMOG/MOG_{35-55} immunization (average 5 – 10 days post-symptom onset). Data are shown as mean with SEM and were analyzed by Brown-Forsythe and Welch ANOVA with Dunnett's T3 multiple comparisons test or by Kruskal-Wallis with Dunn's multiple comparisons test. For B, HuPBMC cohorts included: 10, 13 – 18, 20, 22, 24, 26, and 29. For C – E, HuPBMC cohorts included: 15, 17, 18, 20, 22, 24, and 29.

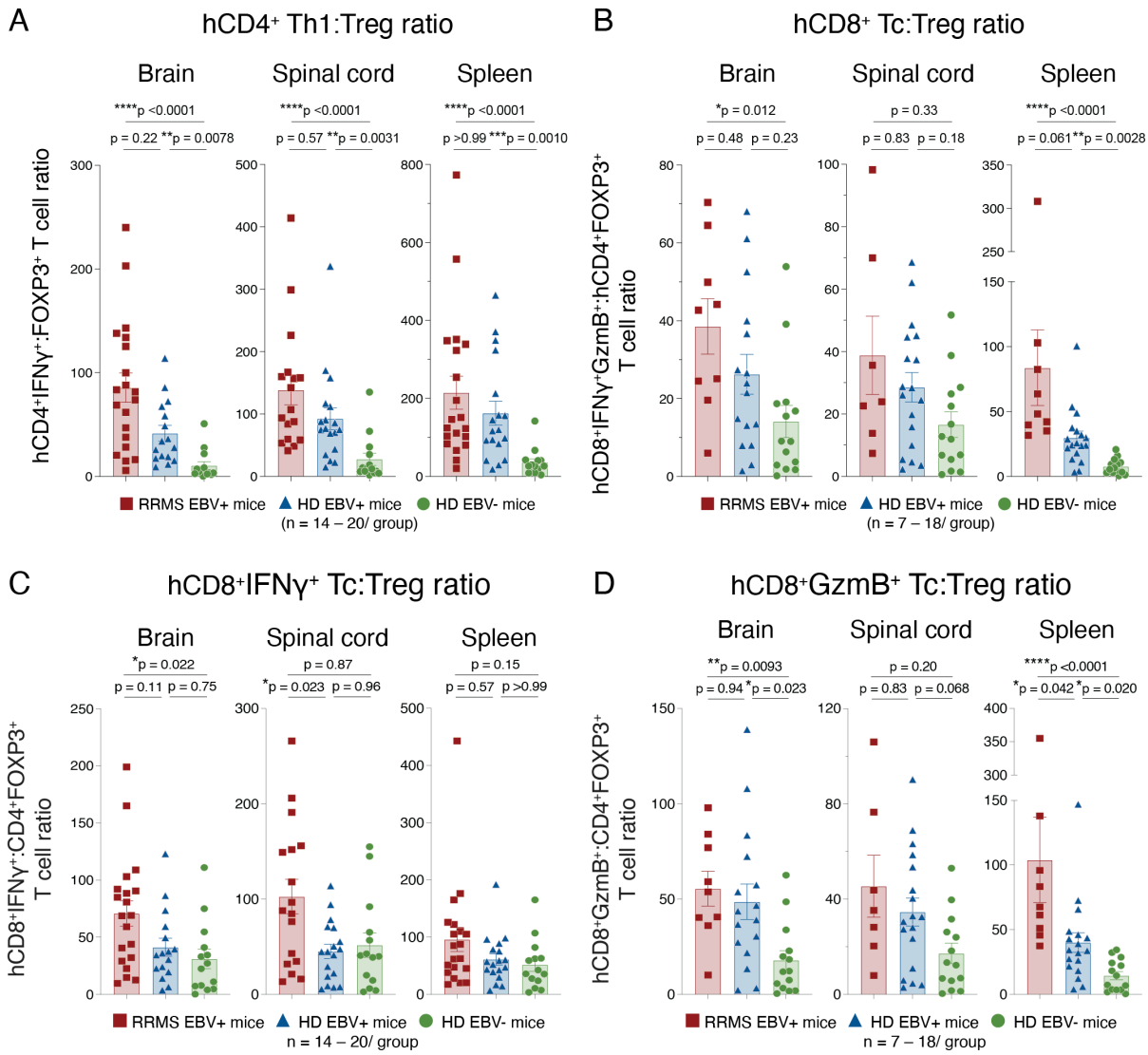

Figure 5.15 Donor EBV and RRMS both increase the effector T cell to regulatory T cell ratio in HuPBMC EAE mice

Figure shows the ratio of (A) hCD3⁺CD4⁺IFNγ⁺, (B) hCD3⁺CD8⁺IFNγ⁺GzmB⁺, (C) hCD3⁺CD8⁺IFNγ⁺, and (D) hCD3⁺CD8⁺GzmB⁺ effector T cells to hCD3⁺CD4⁺FOXP3⁺ regulatory T cells in the brain, spinal cord, and spleen of HuPBMC EAE mice grouped by PBMC donor EBV serostatus and RRMS diagnosis (n = 7 – 20 mice/group derived from 1 – 2 donors/group). Perfused organs were collected days 14 – 27 post-rhMOG/MOG_{35-55} immunization (average 5 – 10 days post-symptom onset). Isolated immune cells were stimulated with PMA and ionomycin for cytokine detection. Data are shown as mean with SEM and were analyzed by Brown-Forsythe and Welch ANOVA with Dunnett's T3 multiple comparisons test or by Kruskal-Wallis test with Dunn's multiple comparisons test. HuPBMC cohorts included: 15, 18, 20, and 22.

5.5 Gammaherpesvirus-68 infection skews effector and regulatory T cell infiltration in the CNS of C57Bl/6 mice induced with both B cell dependent and independent EAE

Our group has previously demonstrated that MOG_{35-55} peptide EAE induction of C57Bl/6 WT mice latently infected with γHV68, the murine homologue of EBV, results in a more severe CNS immunopathology compared to otherwise comparable, uninfected mice[415,418,420]. Other groups have separately demonstrated that EAE induction of C57Bl/6 mice with varying antigenic forms of the same myelin component can result in differential involvement of adaptive immune responses following EAE immunization. For instance, human MOG protein generates a B cell dependent EAE disease mechanism in C57Bl/6 WT mice that is abrogated when B cells are removed, while immunization of these mice with rat MOG protein, or the immunodominant rodent MOG_{35-55} peptide only, results in a B cell independent disease that proceeds similarly even if B cells are antibody depleted or genetically eliminated[149,155].

As we observed little to no effect of donor EBV or RRMS status on the ability of PBMC derived human B cells to engraft NSG/SGM3 mice and infiltrate the CNS of HuPBMC mice following EAE immunization, we were unable to evaluate the immunomodulatory effects of previous EBV exposure on T cell autoreactivity in the presence of an ongoing latent infection, as is the case for people with MS. We therefore sought to assess the potential dependency of the immunopathogenic effects of latent gammaherpesvirus infection on B cell engagement specifically by immunizing naïve and latent γHV68 infected mice with either MOG_{35-55} peptide or rhMOG protein. To do so, we first infected C57Bl/6 WT mice with γHV68 via intraperitoneal inoculation (or mock infected by blank media inoculation for uninfected controls) and waited 5 weeks for clearance of the acute infection and establishment of latency (Figure 5.16), as previously determined[415,418]. At 5 weeks post-infection, mice were immunized with either 200 μg of MOG_{35-55} peptide or 100 μg rhMOG protein emulsified in CFA (Figure 5.16). A delay of 2 – 3 days in the onset of clinical symptoms was observed for rhMOG induced mice compared to MOG_{35-55} induced mice (Appendix 13, Figure A.74A – B), and therefore endpoints were set as day 17 and 14 post-EAE induction, respectively, to ensure a similar cumulative disease burden for more accurate immunological comparisons between induction methods (Appendix 13, Figure A.74C). At endpoint, the presence of γHV68 DNA within the splenocytes of infected mice, as well as the absence in mock inoculated mice, was confirmed by PCR (Appendix 13, Figure A.75).

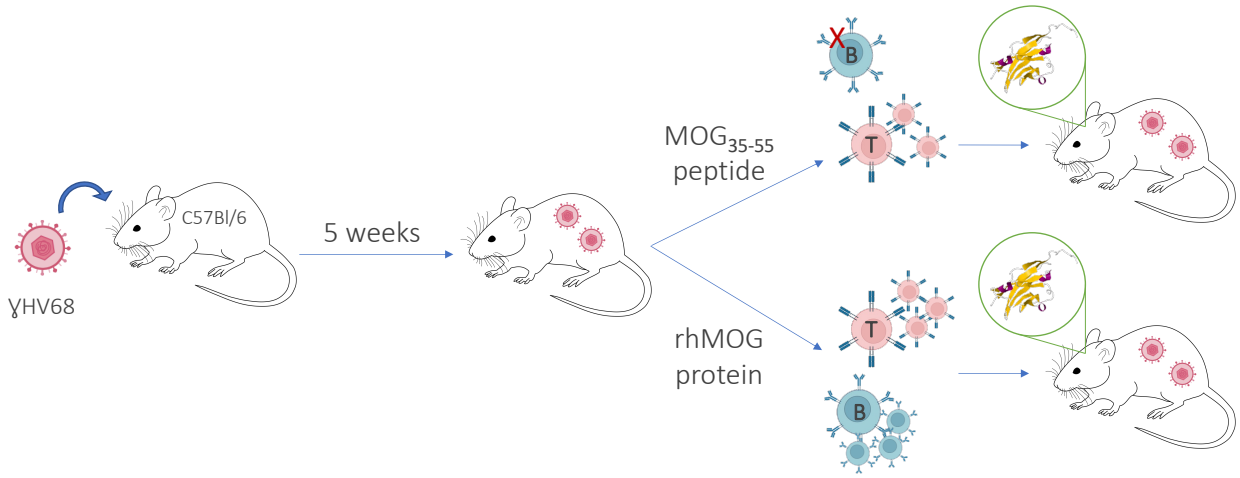

Figure 5.16 Schematic of experimental design for B cell dependent rhMOG EAE induction and B cell independent MOG_{35-55} EAE induction of latent γHV68 infected mice

Wild type C57Bl/6 mice are infected with 10^4 plaque forming units (PFU) of wild type gammaherpesvirus-68 (γHV68 WUMS strain) by intraperitoneal injection. Following a five-week incubation period, during which the virus establishes a latent infection in the periphery, mice are then actively immunized with myelin oligodendrocyte glycoprotein peptide MOG_{35-55} or recombinant human MOG_{1-120} (rhMOG) emulsified in complete Freund's adjuvant and co-administered two doses of pertussis toxin. B cell depletion of mice immunized with MOG_{35-55} does not abrogate disease incidence, whereas the presence of B cells is required for immunization with full length rhMOG protein [149,155].

As expected, the brains and spinal cords of uninduced control mice, regardless of their infection status, contained very few infiltrating $mCD19^+$ B cells (Figure 5.17A – B, D – E). While an increased number of B cells may have infiltrated the CNS of uninduced γHV68 infected mice relative to fully naïve mice, the low sample numbers available for the current analysis (n = 2 – 3 mice/group) precludes our ability to draw accurate conclusions about differences between the EAE control groups based solely on latent infection. B cell counts in the CNS did not significantly differ between infected and uninfected mice when induced with either MOG antigen (Figure 5.17A – B, D – E), though rhMOG EAE induction did result in higher numbers of B cells in the spinal cords of some γHV68 infected mice compared to uninfected rhMOG EAE mice (Figure 5.17E), and in comparison to all MOG_{35-55} induced mice (Figure 5.17B).

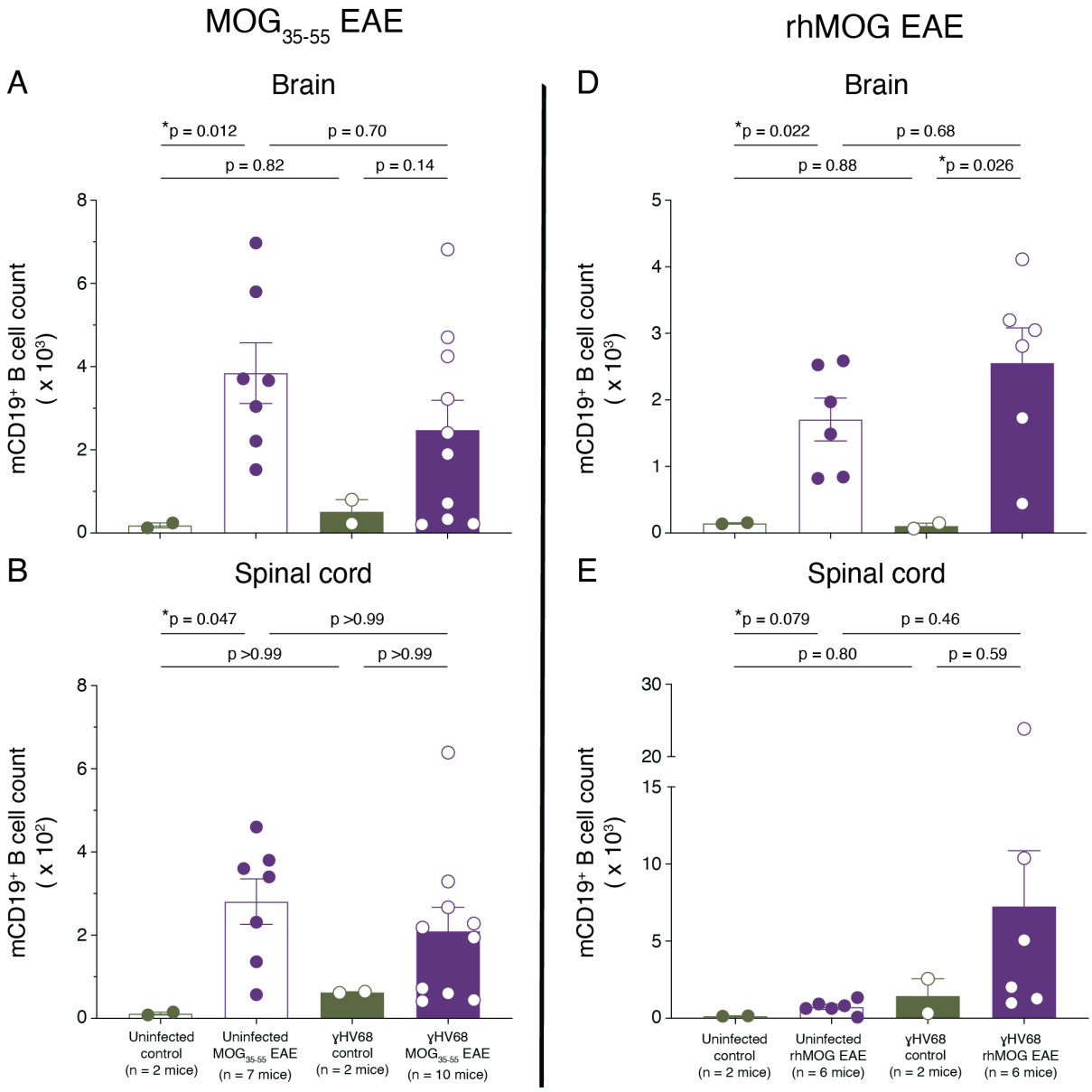

Figure 5.17 mCD19$^+$ B cell numbers are moderately elevated in the CNS of latently infected γHV68 mice after rhMOG but not MOG_{35-55} EAE induction

C57Bl/6 WT mice (mixed males and females) were injected intraperitoneally with either 10^4 PFU of γHV68 WUMS strain or with blank media for uninfected controls. At 5 weeks post-infection, EAE was induced with either 200 μg MOG_{35-55} peptide (n = 7 – 14 mice/group), 100 μg rhMOG protein (n = 6 – 10 mice/group) or remained as uninduced controls (n = 2 – 3 mice/group). Figure shows total numbers of mCD19$^+$ B cells in the (A, D) brain, (B, E) spinal cord, and (C, F) spleen on day 14 post-immunization with MOG_{35-55} peptide (left column) and day 17 post-immunization with rhMOG protein (right column). Data are shown as mean with SEM and were analyzed by Brown-Forsythe and Welch ANOVA with Dunnett's T3 multiple comparisons test or by Kruskal-Wallis with Dunn's multiple comparisons test.

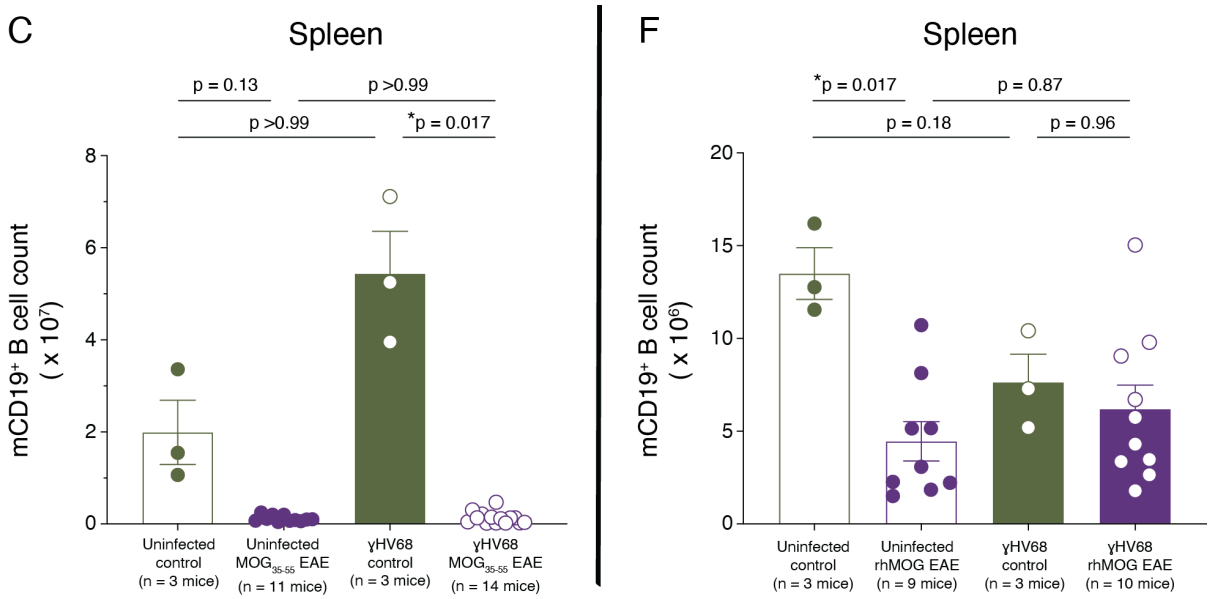

Figure 5.17 continued

In the spleen, mCD19$^+$ B cell counts were statistically similar in all control mice, with some variability by group. Independent of infection status, EAE induction of mice with MOG_{35-55} resulted in a contraction of the B cell population in the spleen (Figure 5.17C) that was far less pronounced following immunization with rhMOG at endpoint (Figure 5.17F). The difference in the degree of contraction based on immunizing antigen is potentially due to the more rapid onset of the priming and effector phases following peptide immunization compared to protein antigen, which must first be processed and loaded for antigen presentation to responding T cells. Alternatively, the B cell dependent EAE disease generated by rhMOG immunization may promote the survival of B cells that are otherwise outcompeted by proliferating T cells in the B cell independent MOG_{35-55} EAE model.

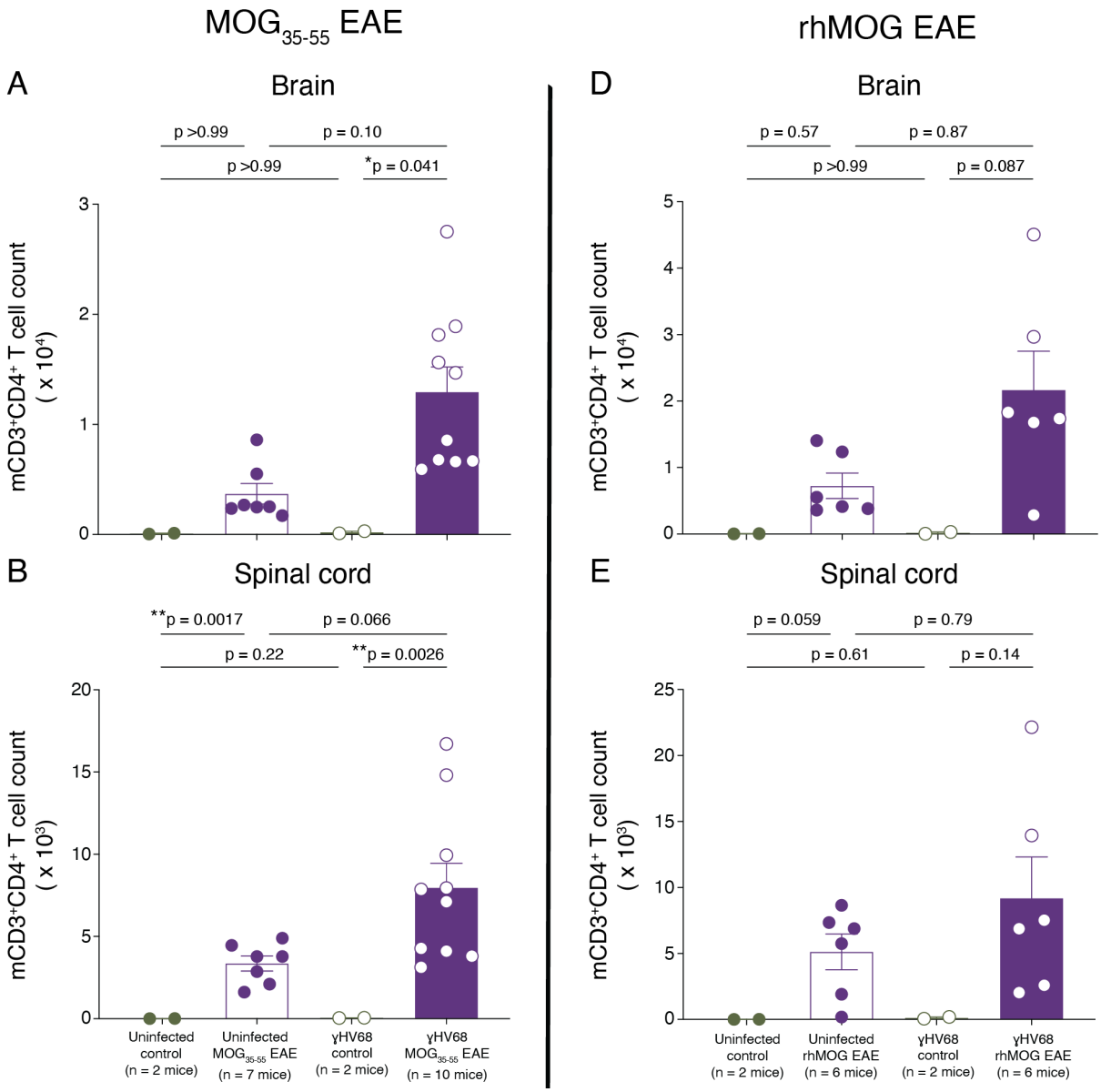

Figure 5.18 mCD3$^+$CD4$^+$ T cell numbers are moderately elevated in the CNS of latently infected γHV68-EAE mice regardless of the form of MOG EAE induction

C57Bl/6 WT mice (mixed males and females) were injected intraperitoneally with either 10^4 PFU of γHV68 WUMS strain or with blank media for uninfected controls. At 5 weeks post-infection, EAE was induced with either 200 µg MOG_{35-55} peptide (n = 7 – 14 mice/group), 100 µg rhMOG protein (n = 6 – 10 mice/group) or remained as uninduced controls (n = 2 – 3 mice/group). Figure shows total numbers of mCD3$^+$CD4$^+$ T cells in the (A, D) brain, (B, E) spinal cord, and (C, F) spleen on day 14 post-immunization with MOG_{35-55} peptide (left column) and day 17 post-immunization with rhMOG protein (right column). Data are shown as mean with SEM and were analyzed by Brown-Forsythe and Welch ANOVA with Dunnett's T3 multiple comparisons test or by Kruskal-Wallis with Dunn's multiple comparisons test.

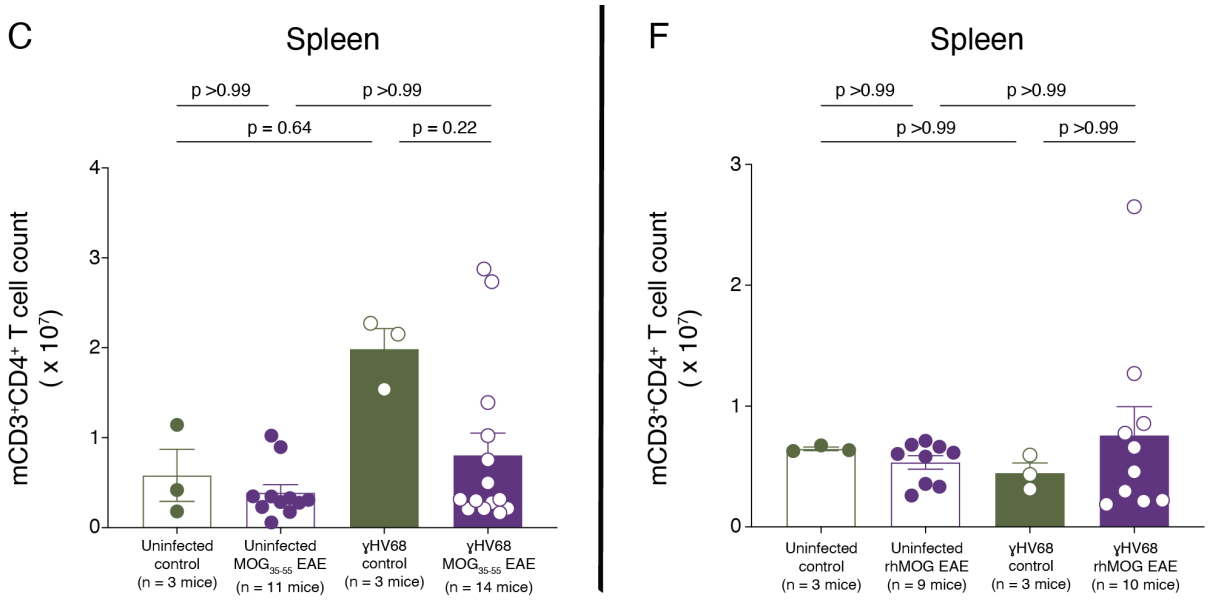

Figure 5.18 continued

Similarly, the CNS tissues of uninduced control mice contained very few mCD3$^+$CD4$^+$ T cells (Figure 5.18A – B, D – E). Following immunization with either MOG antigen, the total numbers of mCD3$^+$CD4$^+$ T cells were moderately elevated in γHV68-EAE CNS tissues compared to uninfected EAE mice (Figure 5.18A – B, D – E), whereas the relative abundance was very similar in the spleens from all groups (Figure 5.18C, F). Among CNS infiltrating mCD3$^+$CD4$^+$ T cells, an increased proportion expressed IFNγ in γHV68-EAE mice compared to uninfected EAE mice when induced with either MOG antigen (Figure 5.19A – B, D – E). The increased frequency of IFNγ expressing Th1 cells with latent infection was also observed in the spleens of both uninduced controls and EAE induced mice for both MOG antigens (Figure 5.19C, F). Quantitatively, CNS and peripheral tissues from γHV68-EAE mice contained consistently greater numbers of mCD3$^+$CD4$^+$IFNγ$^+$ Th1 cells compared to their respective uninfected control groups regardless of the MOG antigen used to induce EAE (Figure 5.20). In contrast, mCD4$^+$IL-17A$^+$ T cell counts in the CNS and periphery were largely unaffected by infection status in mice induced with either MOG antigen (Appendix 13, Figure A.76).

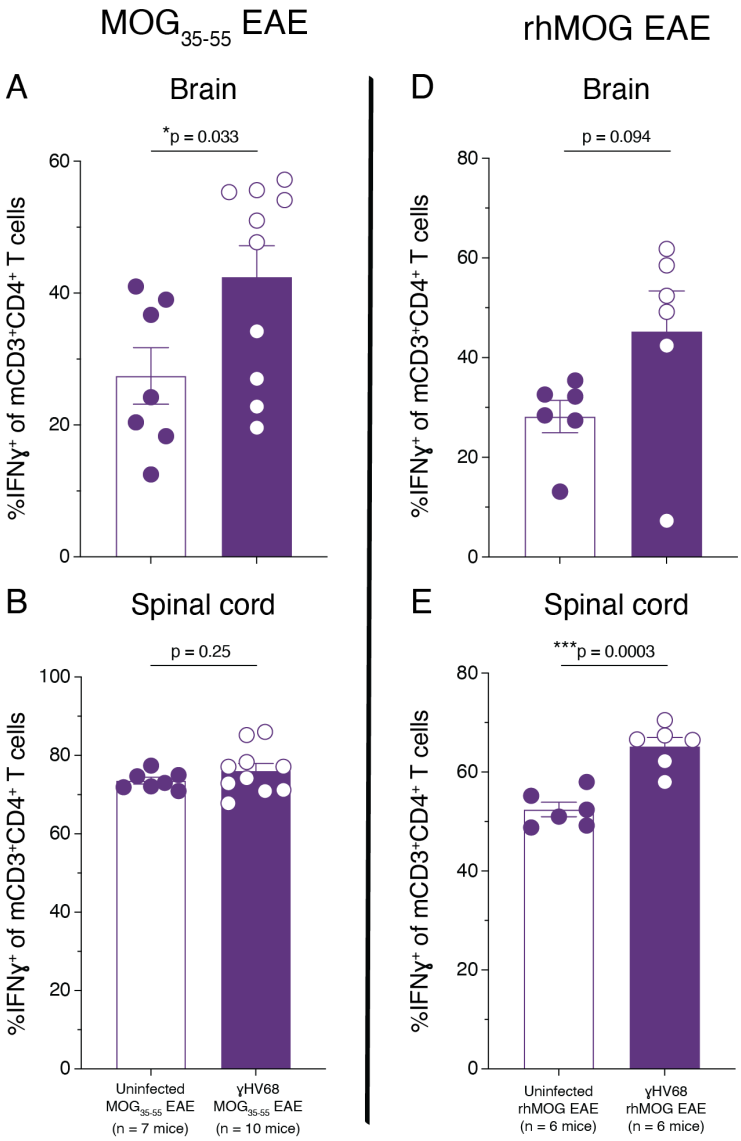

Figure 5.19 Proportions of IFNγ expressing mCD3$^+$CD4$^+$ T cells are increased in the CNS and periphery of γHV68-EAE mice regardless of the form of MOG EAE induction

C57Bl/6 WT mice (mixed males and females) were injected intraperitoneally with either 10^4 PFU of γHV68 WUMS strain or with blank media for uninfected controls. At 5 weeks post-infection, EAE was induced with either 200 µg MOG_{35-55} peptide (n = 7 – 14 mice/group), 100 µg rhMOG protein (n = 6 – 10 mice/group) or remained as uninduced controls (n = 2 – 3 mice/group). Figure shows the proportions of IFNγ expressing mCD3$^+$CD4$^+$ T cells in the (A, D) brain, (B, E) spinal cord, and (C, F) spleen on day 14 post-immunization with MOG_{35-55} peptide (left column) and day 17 post-immunization with rhMOG protein (right column). Data are shown as mean with SEM and were analyzed by (A, B, D, E) Welch's unpaired t test or by (C, F) Kruskal-Wallis with Dunn's multiple comparisons test.

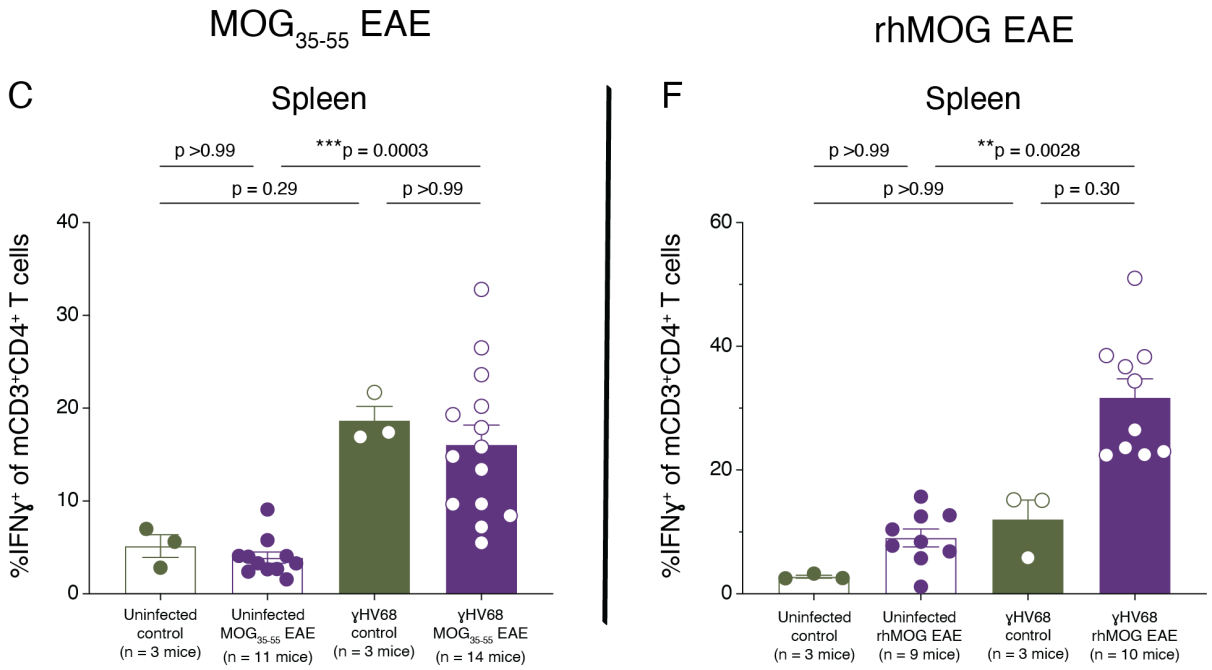

Figure 5.19 continued

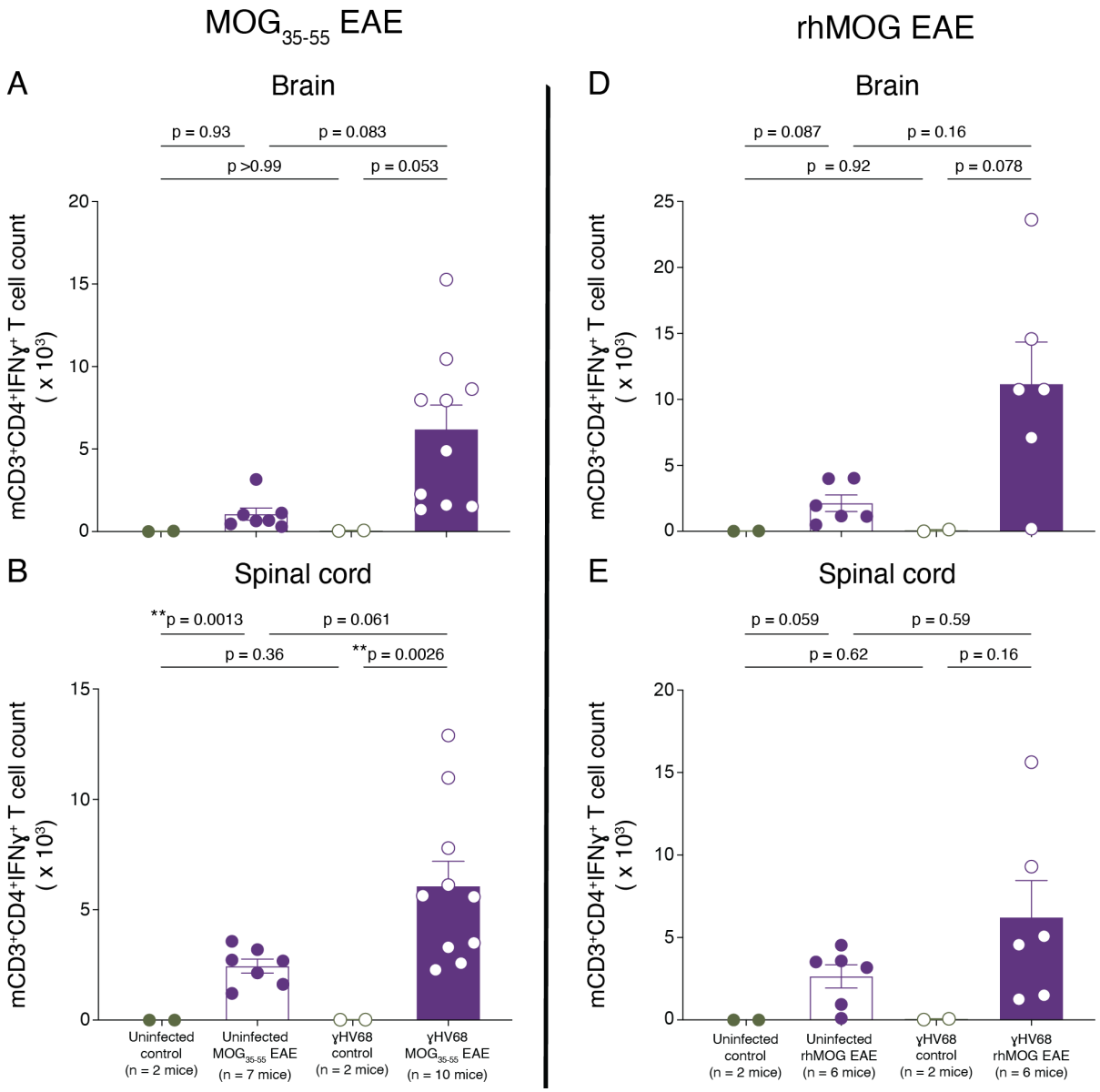

Figure 5.20 mCD3$^+$CD4$^+$IFNγ$^+$ Th1 cell numbers are increased in the CNS and periphery of latently infected γHV68-EAE mice regardless of the form of MOG EAE induction

C57Bl/6 WT mice (mixed males and females) were injected intraperitoneally with either 10^4 PFU of γHV68 WUMS strain or with blank media for uninfected controls. At 5 weeks post-infection, EAE was induced with either 200 µg MOG_{35-55} peptide (n = 7 – 14 mice/group), 100 µg rhMOG protein (n = 6 – 10 mice/group) or remained as uninduced controls (n = 2 – 3 mice/group). Figure shows total numbers of mCD3$^+$CD4$^+$IFNγ$^+$ Th1 cells in the (A, D) brain, (B, E) spinal cord, and (C, F) spleen on day 14 post-immunization with MOG_{35-55} peptide (left column) and day 17 post-immunization with rhMOG protein (right column). Data are shown as mean with SEM and were analyzed by Brown-Forsythe and Welch ANOVA with Dunnett's T3 multiple comparisons test or by Kruskal-Wallis with Dunn's multiple comparisons test.

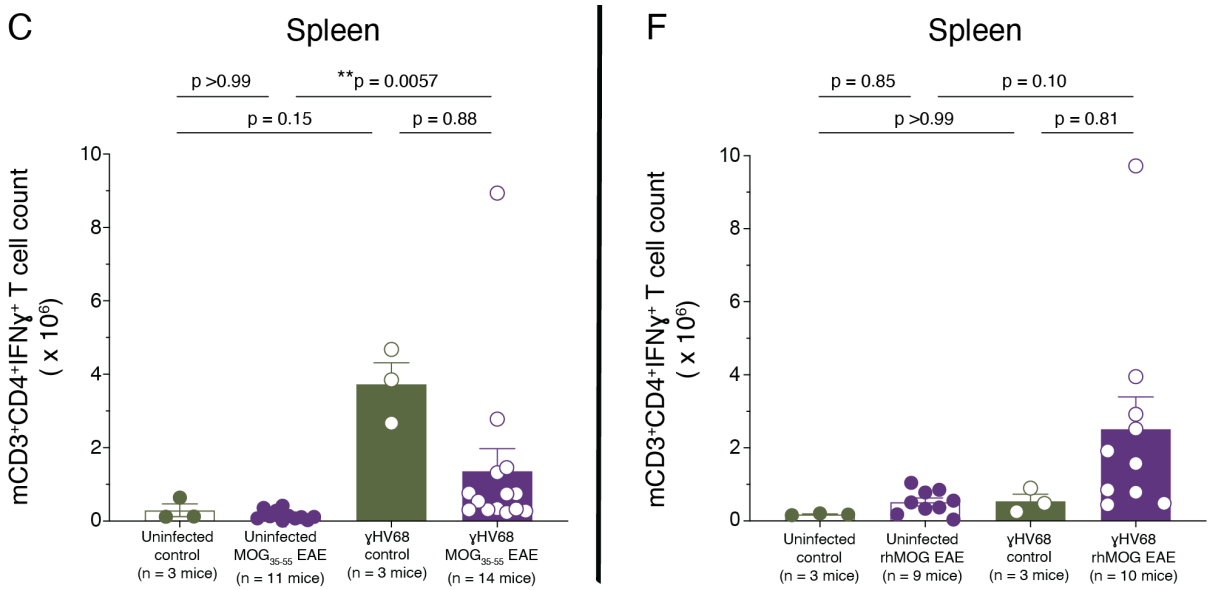

Figure 5.20 continued

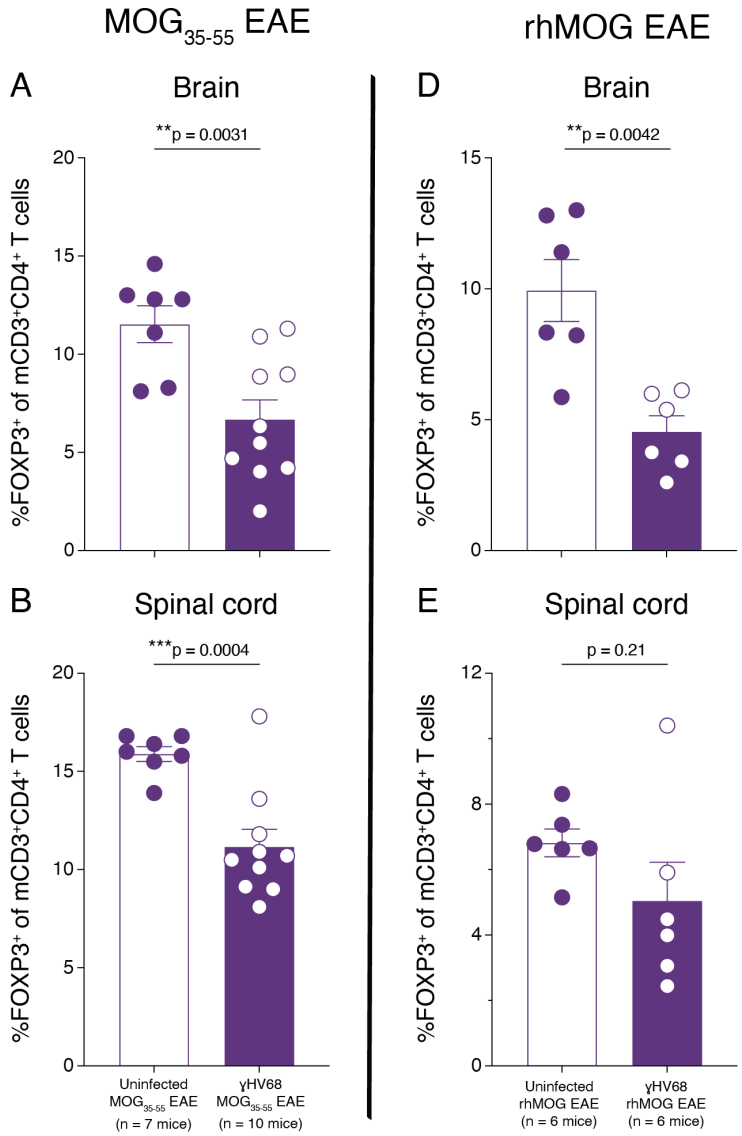

Figure 5.21 Proportions of FOXP3$^+$ expressing mCD3$^+$CD4$^+$ T cells are reduced in the CNS of γHV68-EAE mice regardless of the form of MOG EAE induction

C57Bl/6 WT mice (mixed males and females) were injected intraperitoneally with either 10^4 PFU of γHV68 WUMS strain or with blank media for uninfected controls. At 5 weeks post-infection, EAE was induced with either 200 µg MOG_{35-55} peptide (n = 7 – 14 mice/group), 100 µg rhMOG protein (n = 6 – 10 mice/group) or remained as uninduced controls (n = 2 – 3 mice/group). Figure shows the proportions of FOXP3 expressing mCD3$^+$CD4$^+$ T cells in the (A, D) brain, (B, E) spinal cord, and (C, F) spleen on day 14 post-immunization with MOG_{35-55} peptide (left column) and day 17 post-immunization with rhMOG protein (right column). Data are shown as mean with SEM and were analyzed (A, B, D, E) by Welch's unpaired t test, (C) by Brown-Forsythe and Welch ANOVA with Dunnett's T3 multiple comparisons test or (F) by Kruskal-Wallis with Dunn's multiple comparisons test.

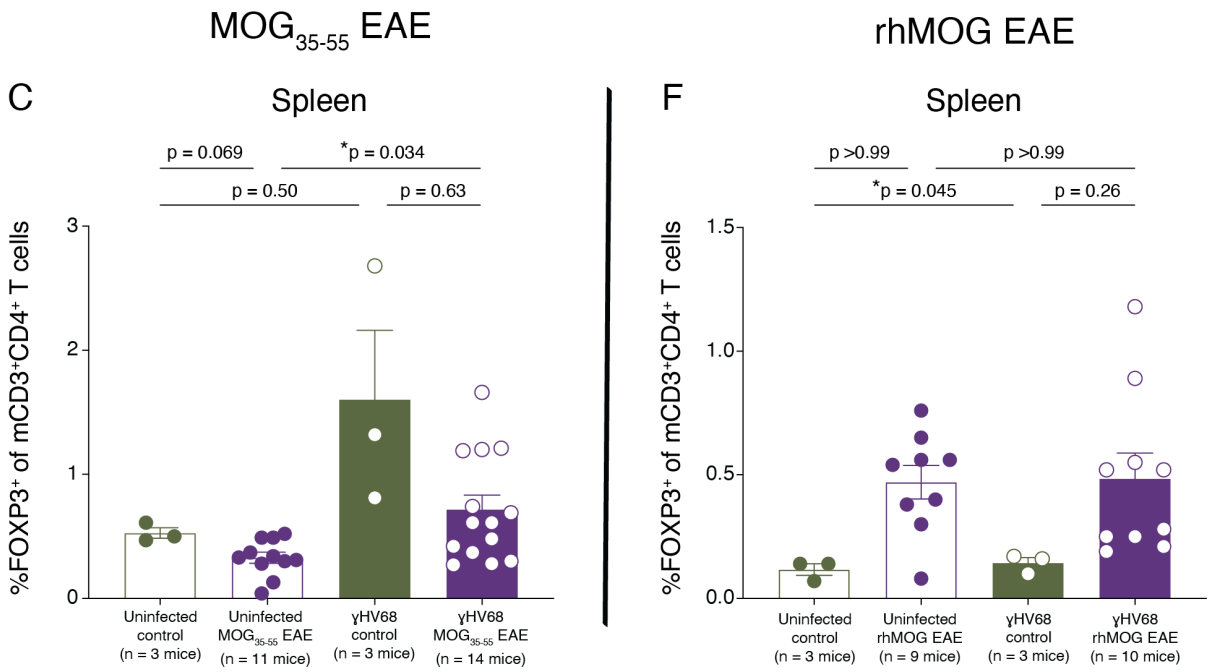

Figure 5.21 continued

Simultaneously, the proportion of CNS infiltrating mCD3$^+$CD4$^+$ T cells expressing the regulatory marker FOXP3 was significantly reduced in γHV68-EAE mice following immunization with either MOG antigen (Figure 5.21A – B, D – E), consistent with the relative rise in IFNγ$^+$ frequencies. FOXP3$^+$ proportions were slightly increased in the spleens of γHV68 mice compared to uninfected mice induced with MOG_{35-55} but were similar in the spleens of both infected and uninfected rhMOG EAE mice (Figure 5.21C, F). Numerically, however, the CNS and spleen tissues of all EAE induced mice contained similar numbers of mCD3$^+$CD4$^+$FOXP3$^+$ Tregs, regardless of the infection status or MOG antigen used to induce EAE (Figure 5.22). In some uninduced control γHV68 infected mice, mCD3$^+$CD4$^+$FOXP3$^+$ Treg counts were elevated compared to all other groups, though the underlying reason is unclear and may be related more to γHV68 specific T cell response kinetics at day 14 versus day 17 post-immunization (Figure 5.21C, Figure 5.22C).

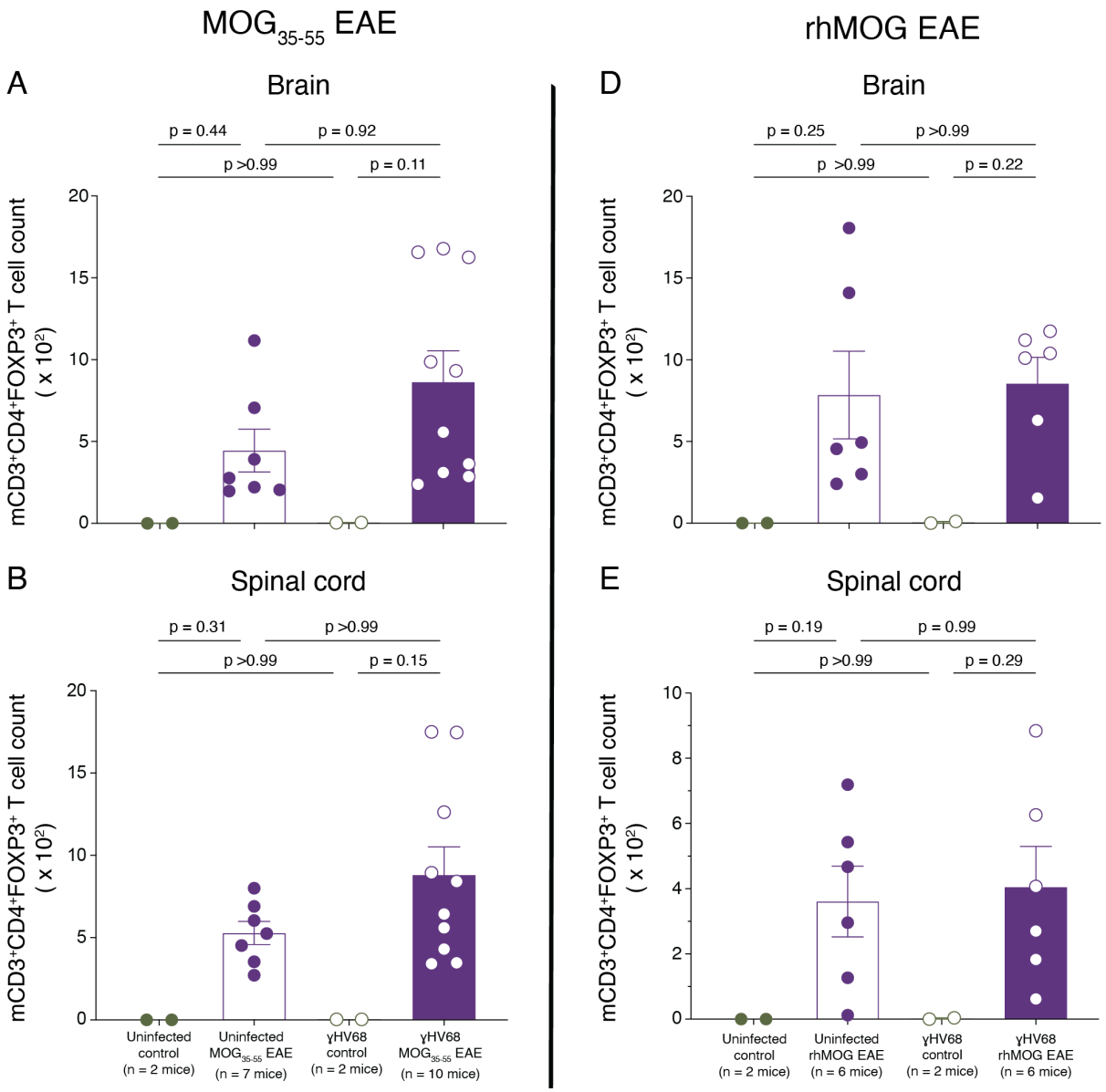

Figure 5.22 mCD3$^+$CD4$^+$FOXP3$^+$ Treg numbers are similar in the CNS and periphery of latently infected γHV68-EAE mice regardless of the form of MOG EAE induction

C57Bl/6 WT mice (mixed males and females) were injected intraperitoneally with either 10^4 PFU of γHV68 WUMS strain or with blank media for uninfected controls. At 5 weeks post-infection, EAE was induced with either 200 µg MOG_{35-55} peptide (n = 7 – 14 mice/group), 100 µg rhMOG protein (n = 6 – 10 mice/group) or remained as uninduced controls (n = 2 – 3 mice/group). Figure shows total numbers of mCD3$^+$CD4$^+$FOXP3$^+$ Tregs in the (A, D) brain, (B, E) spinal cord, and (C, F) spleen on day 14 post-immunization with MOG_{35-55} peptide (left column) and day 17 post-immunization with rhMOG protein (right column). Data are shown as mean with SEM and were analyzed by Kruskal-Wallis with Dunn's multiple comparisons test.

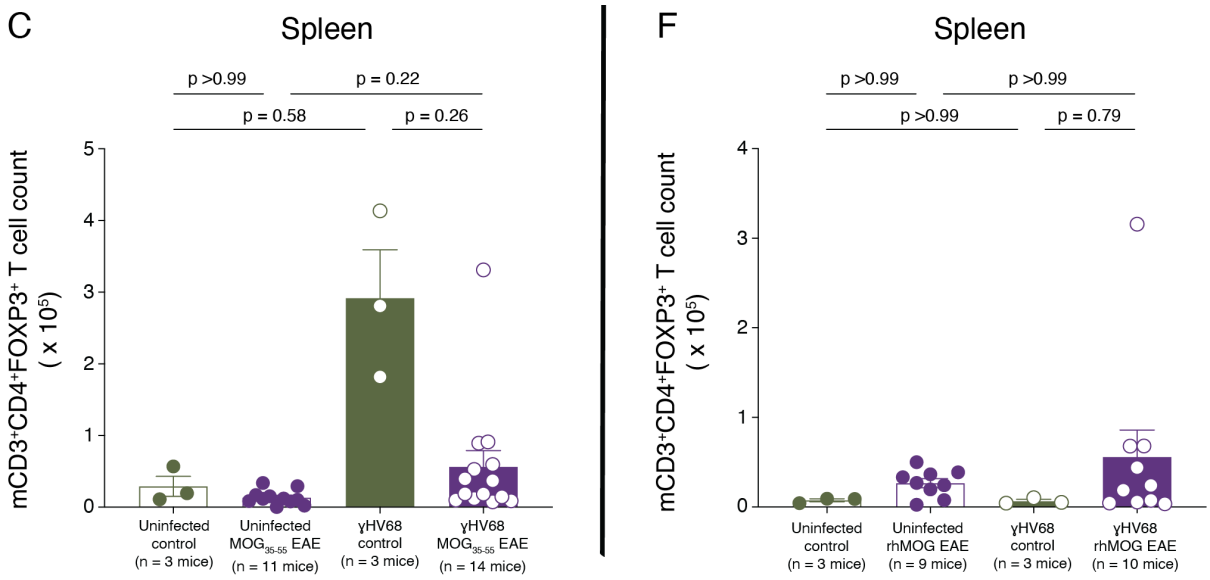

Figure 5.22 continued

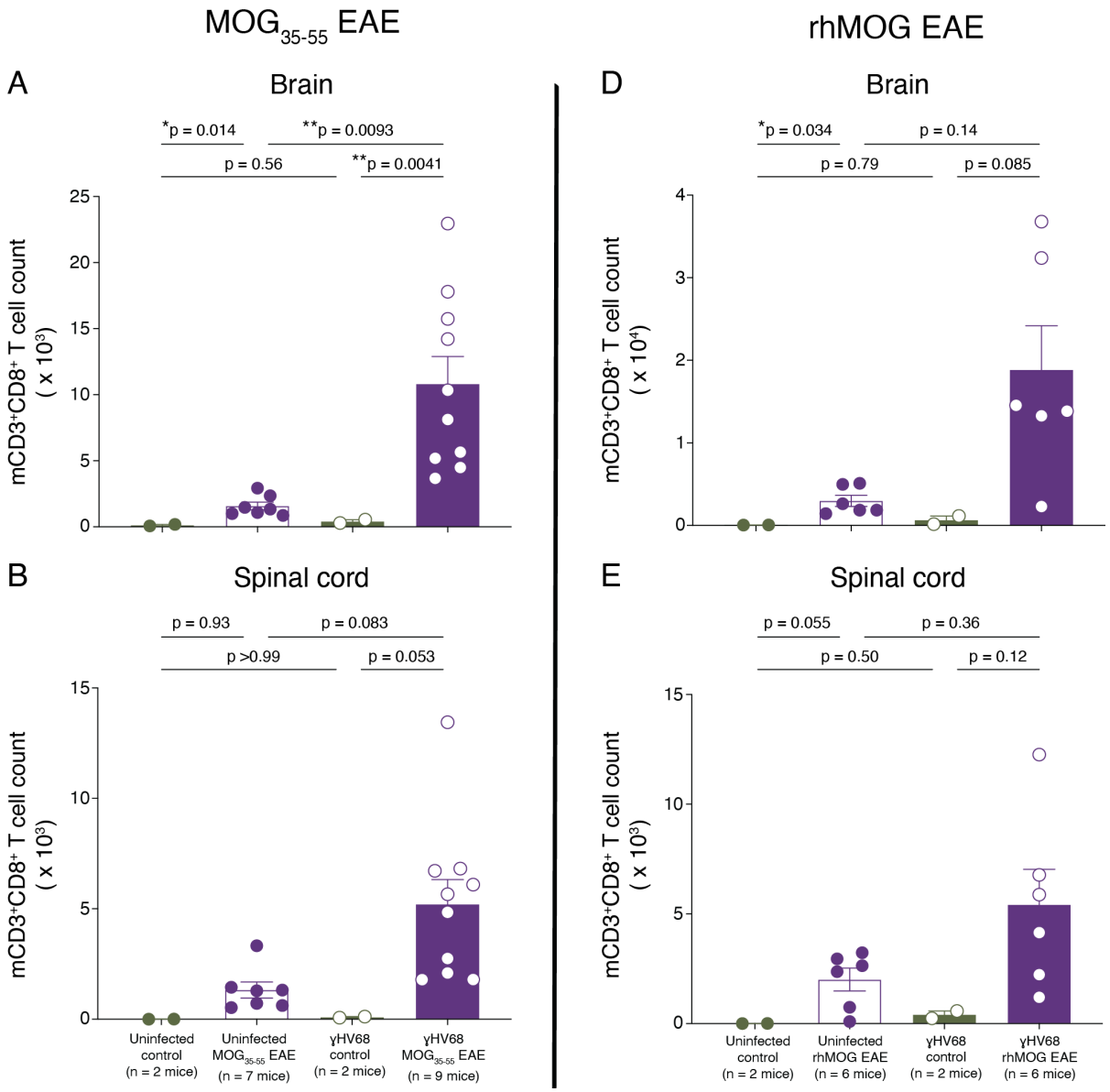

Figure 5.23 mCD3$^+$CD8$^+$ T cell numbers are increased in the CNS and periphery of latently infected γHV68-EAE mice regardless of the form of MOG EAE induction

C57Bl/6 WT mice (mixed males and females) were injected intraperitoneally with either 10^4 PFU of γHV68 WUMS strain or with blank media for uninfected controls. At 5 weeks post-infection, EAE was induced with either 200 µg MOG_{35-55} peptide (n = 7 – 14 mice/group), 100 µg rhMOG protein (n = 6 – 10 mice/group) or remained as uninduced controls (n = 2 – 3 mice/group). Figure shows total numbers of mCD3$^+$CD8$^+$ T cells in the (A, D) brain, (B, E) spinal cord, and (C, F) spleen on day 14 post-immunization with MOG_{35-55} peptide (left column) and day 17 post-immunization with rhMOG protein (right column). Data are shown as mean with SEM and were analyzed by Brown-Forsythe and Welch ANOVA with Dunnett's T3 multiple comparisons test or by Kruskal-Wallis with Dunn's multiple comparisons test.

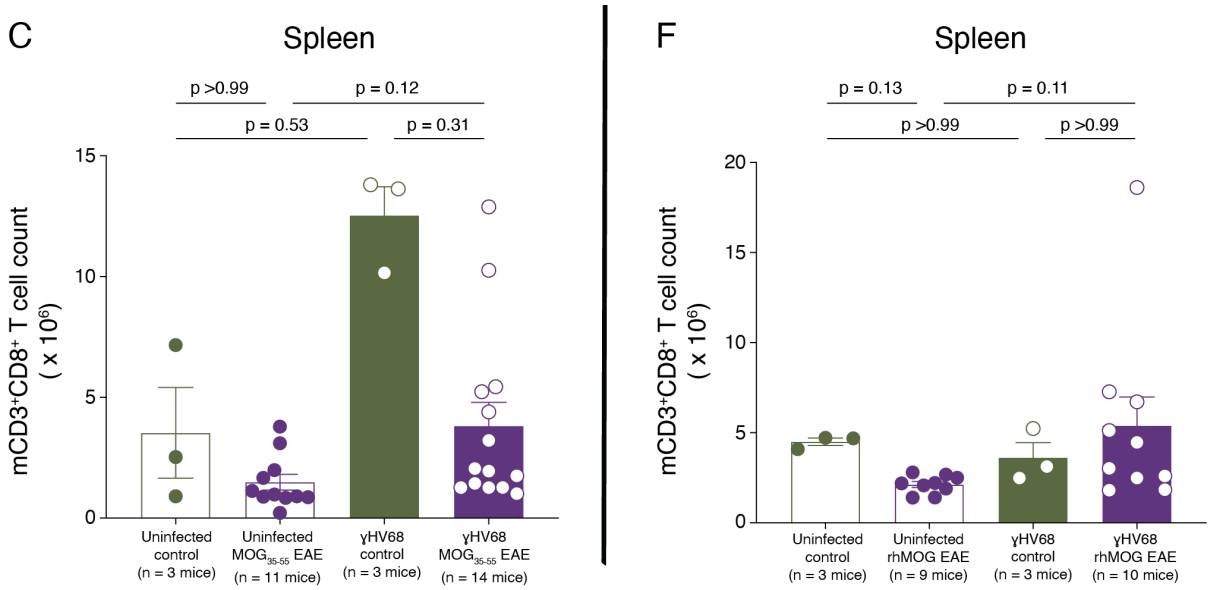

Figure 5.23 continued

CNS tissues from uninduced controls also contained very few total mCD3$^+$CD8$^+$ T cells, while EAE induction with either MOG antigen resulted in greater numbers of CNS infiltrating mCD3$^+$CD8$^+$ T cells in the latent γHV68 infected mice compared to uninfected mice (Figure 5.23A – B, D – E). The spleens of γHV68-EAE mice also contained moderately increased numbers of mCD3$^+$CD8$^+$ T cells compared to uninfected EAE mice, though less strikingly so than in the corresponding CNS tissues (Figure 5.23C, F). Interestingly, the proportion of CNS infiltrating mCD3$^+$CD8$^+$ T cells expressing IFNγ was reduced in γHV68-EAE mice compared to uninfected EAE mice when immunized with either MOG antigen (Figure 5.24A – B, D – E). Reduced overall IFNγ expressing mCD3$^+$CD8$^+$ T cell frequencies in the CNS may be due to a shift toward cells expressing a cytotoxic GzmB$^+$IFNγ$^-$ phenotype, and away from the GzmB$^+$IFNγ$^+$ and/or GzmB$^-$ IFNγ$^+$ phenotypes, as we observed in the HuPBMC EAE mice (Figure 5.10, Figure ***5.11***). Previous work in the γHV68-EAE model has shown that CNS infiltrating mCD3$^+$CD8$^+$ T cells were more cytotoxic than those from uninfected mice[415]. Assessment of infiltrating mCD3$^+$CD8$^+$ T cell cytotoxicity and inflammatory mediator expression would likely clarify the underlying inflammatory effects of γHV68 on IFNγ production by these T cells. Despite a reduction in the proportion of CNS infiltrating mCD3$^+$CD8$^+$ T cells expressing IFNγ in γHV68-EAE mice, numerically, the CNS of γHV68-EAE mice induced with either MOG antigen contained greater total amounts of mCD3$^+$CD8$^+$IFNγ$^+$ T cells than uninfected EAE mice (Figure 5.25A – B, D – E).

Likewise, the spleens of γHV68 infected mice contained greater numbers of mCD3$^+$CD8$^+$IFNγ$^+$ T cells compared to uninfected mice, whether or not these mice were also induced with EAE (Figure 5.25C, F).

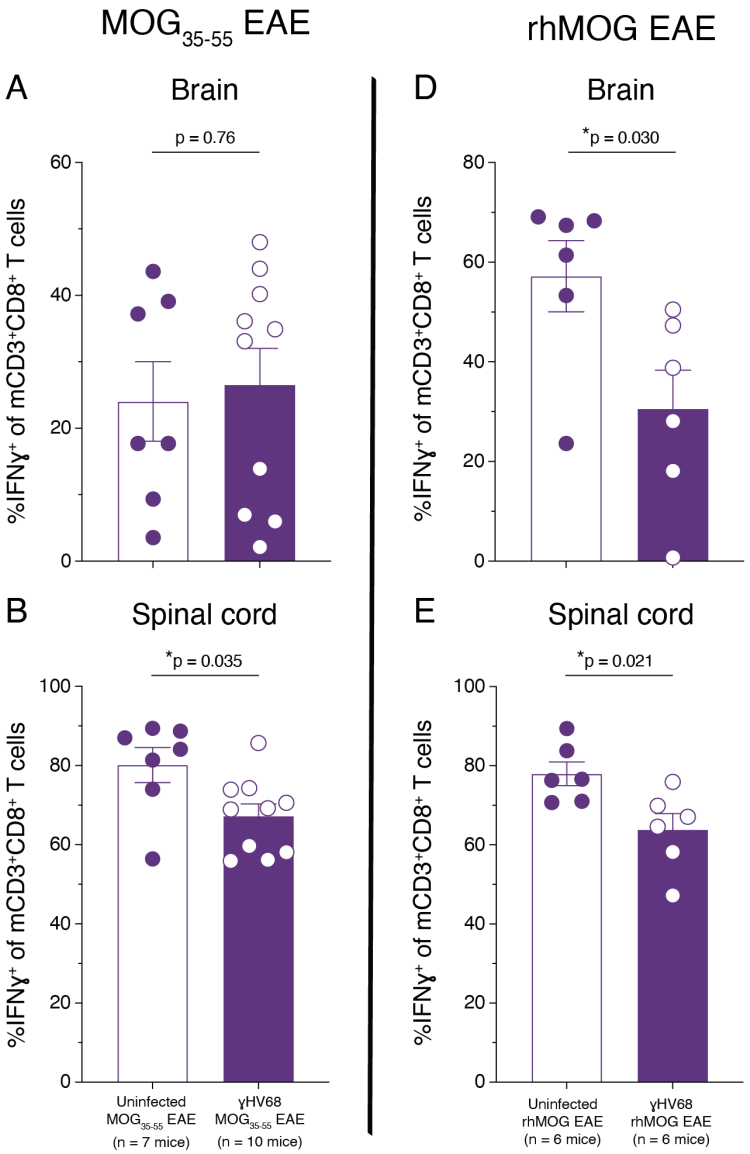

Figure 5.24 Proportions of IFNγ expressing mCD3$^+$CD8$^+$ T cells are reduced in the CNS and increased in the periphery of γHV68-EAE mice regardless of the form of MOG EAE induction

C57Bl/6 WT mice (mixed males and females) were injected intraperitoneally with either 10^4 PFU of γHV68 WUMS strain or with blank media for uninfected controls. At 5 weeks post-infection, EAE was induced with either 200 μg MOG_{35-55} peptide (n = 7 – 14 mice/group), 100 μg rhMOG protein (n = 6 – 10 mice/group) or remained as uninduced controls (n = 2 – 3 mice/group). Figure shows the proportions of IFNγ expressing mCD3$^+$CD8$^+$ T cells in

the (A, D) brain, (B, E) spinal cord, and (C, F) spleen on day 14 post-immunization with MOG_{35-55} peptide (left column) and day 17 post-immunization with rhMOG protein (right column). Data are shown as mean with SEM and were analyzed (A, B, D, E) by Welch's unpaired t test, (C) by Kruskal-Wallis with Dunn's multiple comparisons test, or (F) by Brown-Forsythe and Welch ANOVA with Dunnett's T3 multiple comparisons test.

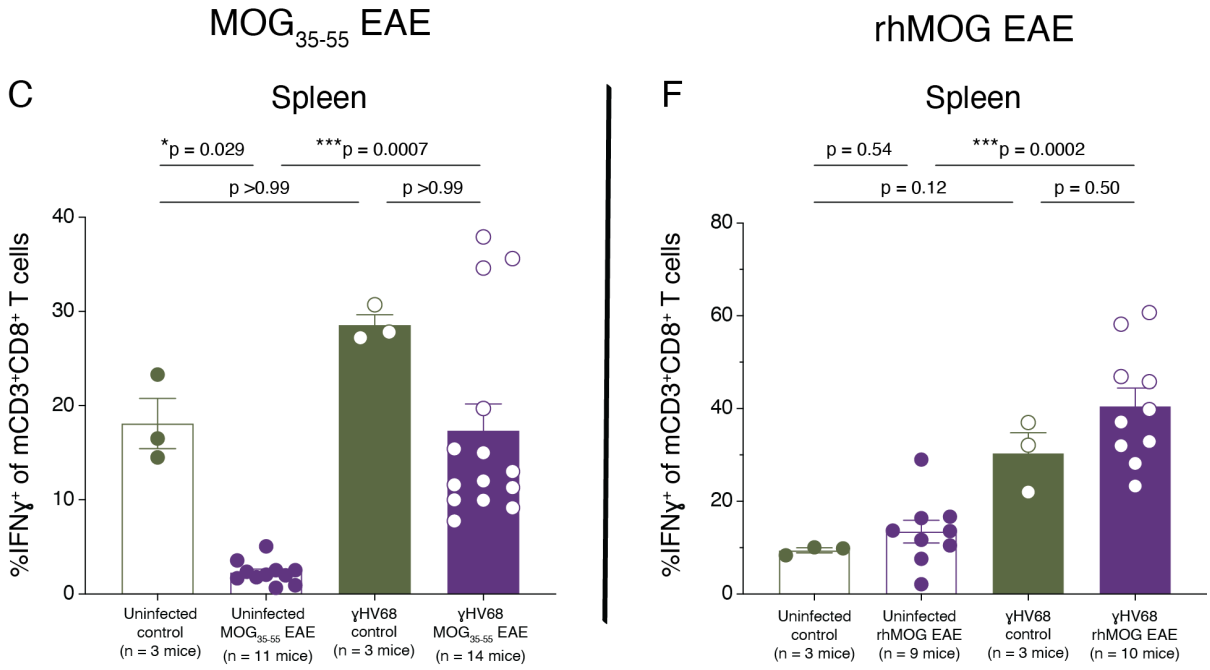

Figure 5.24 continued

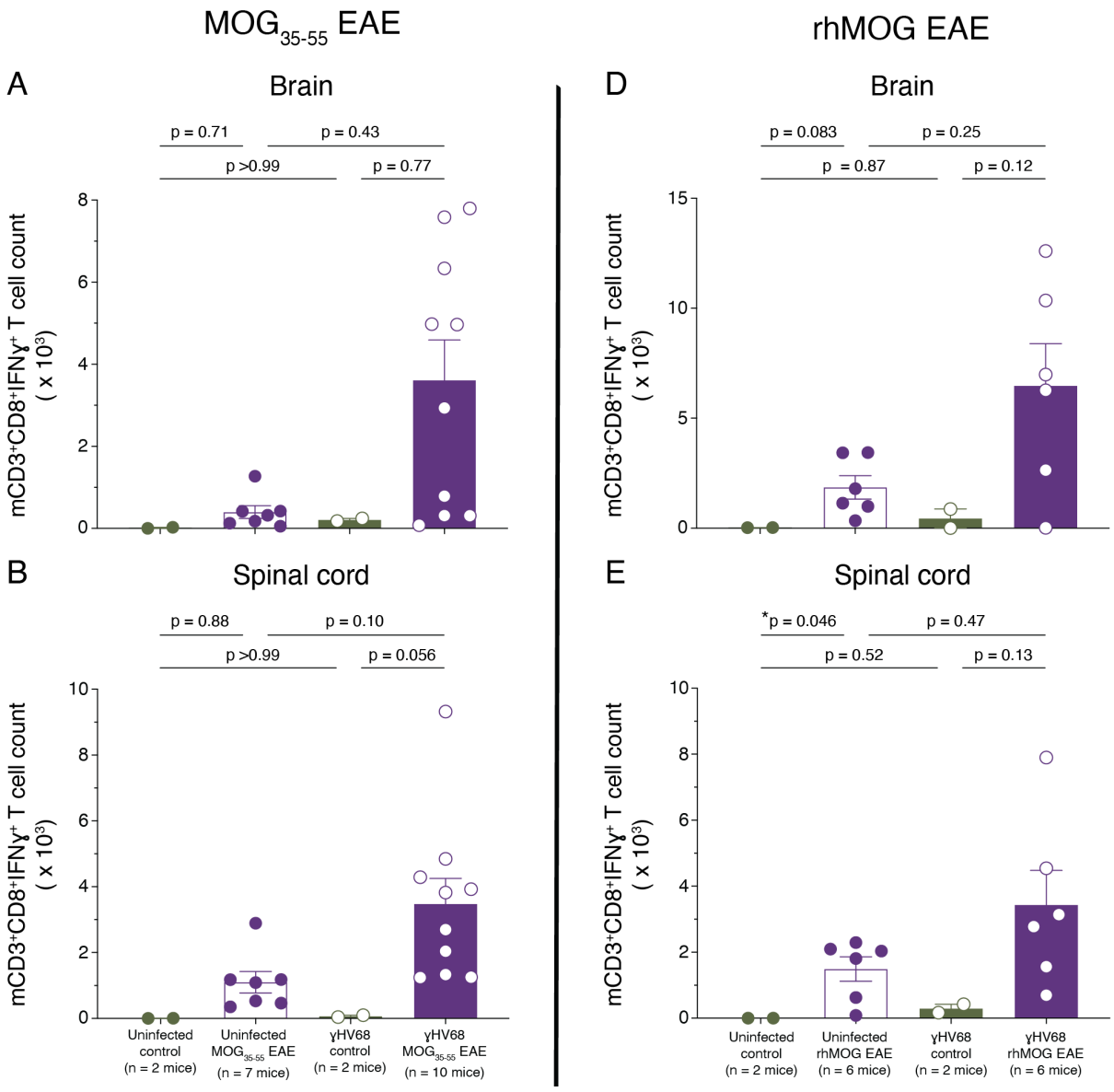

Figure 5.25 mCD3$^+$CD8$^+$IFNγ$^+$ Tc1 cell numbers are increased in the CNS and periphery of latently infected γHV68-EAE mice regardless of the form of MOG EAE induction

C57Bl/6 WT mice (mixed males and females) were injected intraperitoneally with either 10^4 PFU of γHV68 WUMS strain or with blank media for uninfected controls. At 5 weeks post-infection, EAE was induced with either 200 µg MOG_{35-55} peptide (n = 7 – 14 mice/group), 100 µg rhMOG protein (n = 6 – 10 mice/group) or remained as uninduced controls (n = 2 – 3 mice/group). Figure shows total numbers of mCD3$^+$CD8$^+$IFNγ$^+$ Tc1 cells in the (A, D) brain, (B, E) spinal cord, and (C, F) spleen on day 14 post-immunization with MOG_{35-55} peptide (left column) and day 17 post-immunization with rhMOG protein (right column). Data are shown as mean with SEM and were analyzed by Brown-Forsythe and Welch ANOVA with Dunnett's T3 multiple comparisons test or by Kruskal-Wallis with Dunn's multiple comparisons test.

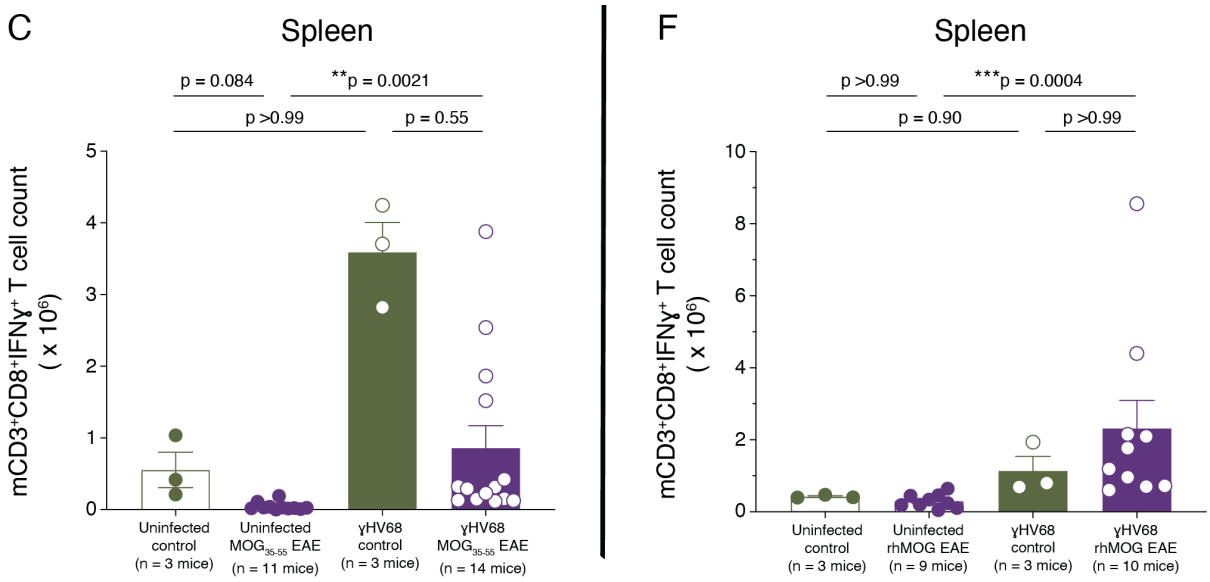

Figure 5.25 continued

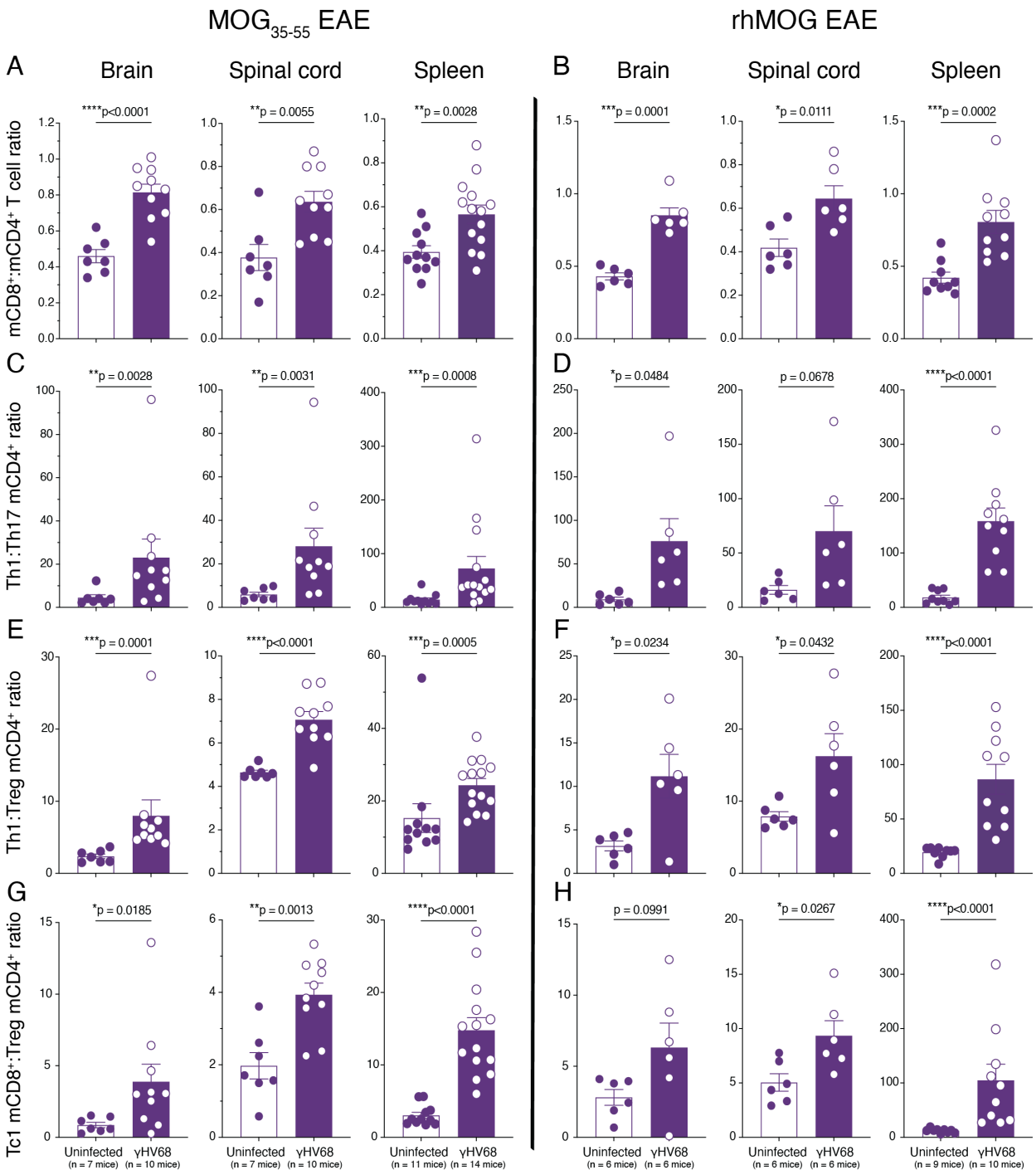

Figure 5.26 Effector to regulatory T cell subset ratios in the CNS and periphery are significantly increased in latently infected γHV68 mice regardless of the form of MOG EAE induction

C57Bl/6 WT mice (mixed males and females) were injected intraperitoneally with either 10^4 PFU of γHV68 WUMS strain or with blank media for uninfected controls. At 5 weeks post-infection, EAE was induced with either 200 μg MOG_{35-55} peptide (n = 7 – 14 mice/group) or 100 μg rhMOG protein (n = 6 – 10 mice/group). Figure shows

the ratios of (A, B) $mCD3^+CD8^+$ to $mCD3^+CD4^+$ T cells, (C, D) IFNγ (Th1) to IL-17A (Th17) expressing $mCD3^+CD4^+$ T cells, (E, F) IFNγ (Th1) to FOXP3 (Treg) expressing $mCD3^+CD4^+$ T cells, and (G, H) IFNγ (Tc1) expressing $mCD3^+CD8^+$ T cells to FOXP3 (Treg) expressing $mCD3^+CD4^+$ T cells in the brain, spinal cord, and spleen on day 14 post-immunization with MOG_{35-55} peptide (left column) and day 17 post-immunization with rhMOG protein (right column). Data are shown as mean with SEM and were analyzed by Welch's unpaired t test or by Mann-Whitney test.

In summary, latent γHV68 infection of mice prior to an autoimmune challenge specific to the CNS resulted in more proinflammatory $mCD3^+CD4^+$ and $mCD3^+CD8^+$ T cells infiltrating the brain and spinal cord compared to mice that were priorly naïve. The use of either B cell dependent rhMOG immunization or B cell independent MOG_{35-55} immunization to generate EAE disease[149,155] resulted in the same overall effects of an increased $mCD8^+$ to $mCD4^+$ T cell ratio and Th1 to Th17 cell ratio in the CNS and spleen of latently infected mice (Figure 5.26A – D). Concurrently, the same tissues contained a consistent number of regulatory $mCD3^+CD4^+FOXP3^+$ T cells that was seemingly unaltered by γHV68 infection, which ultimately resulted in a skewed, increased ratio of effector T cells relative to regulatory T cells in the CNS and periphery of latent γHV68 infected EAE mice compared to uninfected EAE mice, regardless of which MOG antigen was used to immunize the mice (Figure 5.26E – H). In alignment with our findings using the HuPBMC EAE model, these data collectively indicate that latent gammaherpesvirus infection skews neuroinflammatory responses toward a more pathogenic and less regulated Th1 response, regardless of whether the EAE inducing mechanisms is dependent on B cells or not, and suggests infection imparts a broad effect on T cell reactivity that is not dependent on priming with specific myelin antigens.

5.6 History of EBV infection and RRMS both enhance T cell proliferation following nonspecific TCR stimulation

In HuPBMC mice, the observation that FOXP3 positivity among the $hCD4^+$ T cell population is reduced even prior to EAE induction suggests the effector T cells may become more activated during reconstitution due to a lack of regulation, which then transfers to the CNS after MOG immunization (i.e., the effect on T cell responses was not epitope dependent). Based on our findings demonstrating that (1) human T cell reactivity to murine antigens following EBV^+ PBMC engraftment of NSG/SGM3 mice was sufficient to generate a reduction in peripheral Treg

proportions compared to EBV$^-$ PBMCs, (2) mixed MOG antigen EAE induction of HuPBMC mice derived from donors with a history of EBV infection and RRMS led to increased pathogenic T cell infiltration and simultaneous reduced Treg expansion in the CNS, and (3) both peptide and protein MOG antigen induced EAE in regular C57Bl/6 mice latently infected with murine γHV68 generated a similar dysregulation of effector and regulatory T cells systemically and within the CNS, we suspected that an existing latent EBV infection exerted a broad effect on T cell reactivity to subsequent immune challenge independent of the exact antigen supplied. Therefore, we assessed the response of EBV experienced donor PBMCs (pre-engraftment of recipient NSG/SGM3 mice) to nonspecific TCR stimulation to determine if T cell stimulation alone, separate from myelin antigen reactivity, was sufficient to generate differential donor T cell responses compared to EBV naïve donor PBMCs.

A subset of PBMCs was saved from each of the donors used to generate HuPBMC EAE recipient cohorts, the overall composition of which was apparently unchanged following preservation and freeze-thaw (Appendix 13, Figure A.77). Within the donor PBMC samples, hCD4$^+$ and hCD8$^+$ T cells did not differ significantly in their baseline expression of the activation markers HLA-DR, CD38, CD137, or CD154 based on donor EBV or RRMS status grouping (Figure 5.27, Figure 5.28). Likewise, baseline expression of T cell subset-specific transcription factors was similar between donor groups (Figure 5.29, Figure 5.30), with the one exception being a nonsignificant increasing trend in the frequency of Ki-67$^+$ hCD4$^+$ T cells with donor EBV seropositivity and an RRMS diagnosis (Figure 5.29C). Baseline cytokine expression, measured after a brief stimulation of PBMCs with PMA and ionomycin, did not follow any donor EBV or RRMS associated trends that would explain the clinical differences observed in the HuPBMC EAE mice (Figure 5.31, Figure 5.32), though inter-donor variability was high, especially in the EBV$^+$ HD group. We determined that the elevated proportions of T cell expressing activation markers, transcription factors, and cytokines in the EBV$^+$ HD group was not due to one or two donors specifically that consistently skewed the average for all measures, but that, within each measure, one or two different individuals in this group had higher expression levels compared to the others, which disproportionally skewed the mean due to the small 3-4 donors/group size for this initial assay. The samples in the EBV$^+$ HD group with increased frequencies of marker expression were determined not to be true outliers and were therefore included in all analyses.

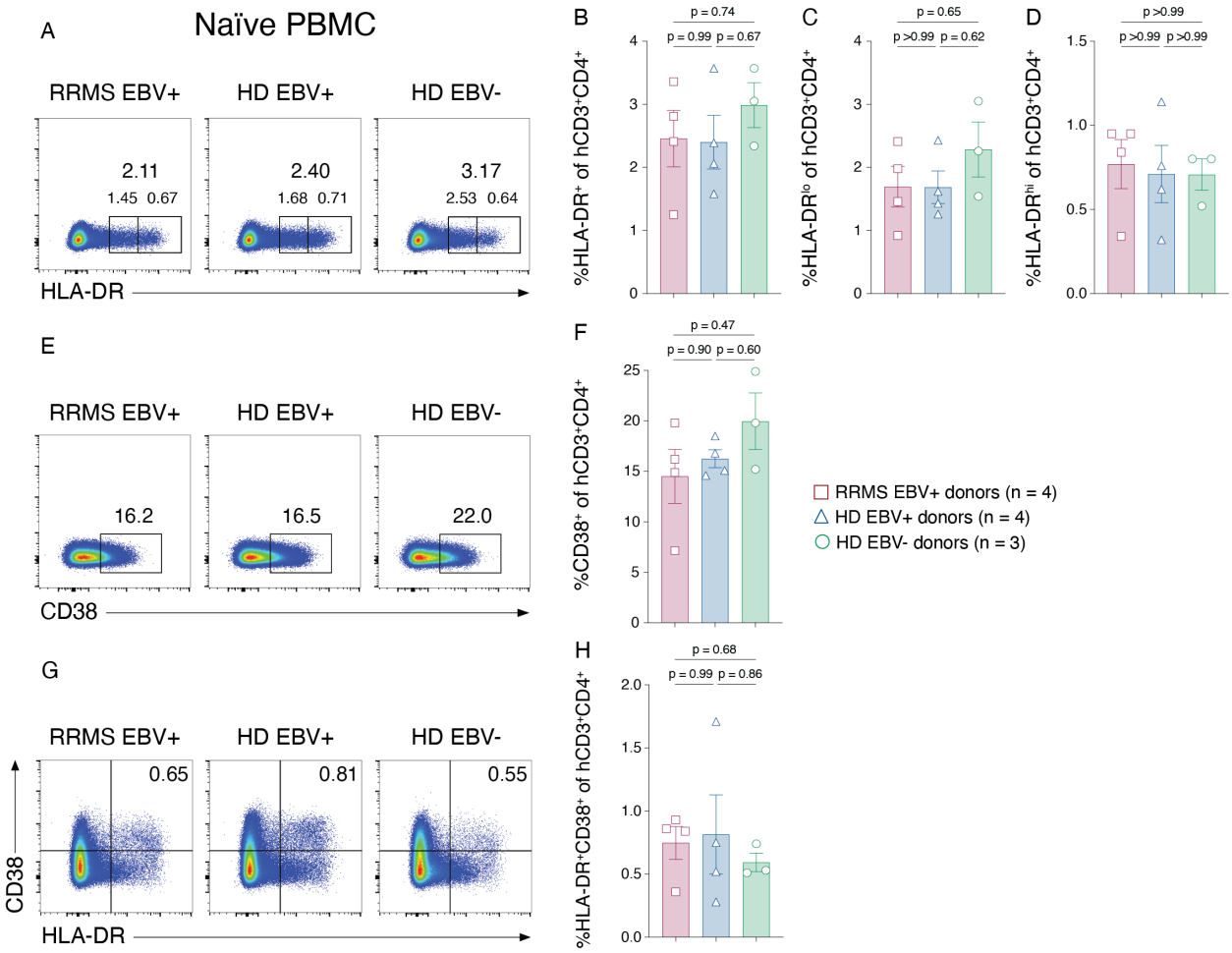

Figure 5.27 Baseline donor hCD3$^+$CD4$^+$ T cell activation

Following donor PBMC preservation in liquid nitrogen, baseline donor T cell activation was assessed by the proportion of naïve (untreated) hCD3$^+$CD4$^+$ T cells that express (A – D) HLA-DR, (E – F) CD38, (G – H) both HLA-DR and CD38, (I – J) CD137, and (K – L) CD154. For concatenated flow plots, the sum proportion of marker positive cells for all donors in each group is indicated. All plotted data are shown as mean with SEM (n = 3 – 4 blood donors/group) and were analyzed by Brown-Forsythe and Welch ANOVA with Dunnett's T3 multiple comparisons test or by Kruskal-Wallis with Dunn's multiple comparisons test.

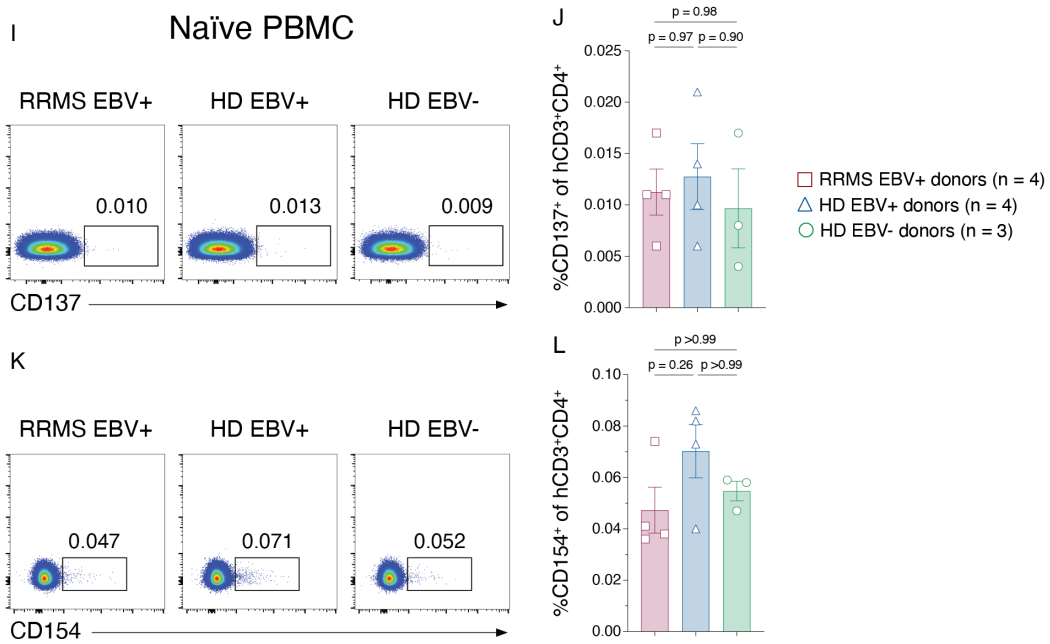

Figure 5.27 continued

We also ruled out the duration of sample storage as a potential factor as to why some of these samples had greater expression of certain markers compared to other PBMC samples in the EBV$^+$ HD group, since there was no consistent timeline nor reduced viability observed for any samples in particular. We suspect the variability observed in this group specifically is due to the broader donor availability for this population – most people are EBV$^+$ HDs and are likely more diverse compared to one another than for the other two groups, where populations affected by RRMS or that lack EBV infection could have more overlap in lifestyle or genetic characteristics. We thus theorize a potentially lower relative intra-donor variability in the RRMS and EBV$^-$ HD groups is due to similar confounding exposures, or lack thereof. To explore the baseline inflammatory variability among human T cells based on donor EBV and RRMS status more thoroughly would require greater participant numbers for all groups than were available in the present analysis.

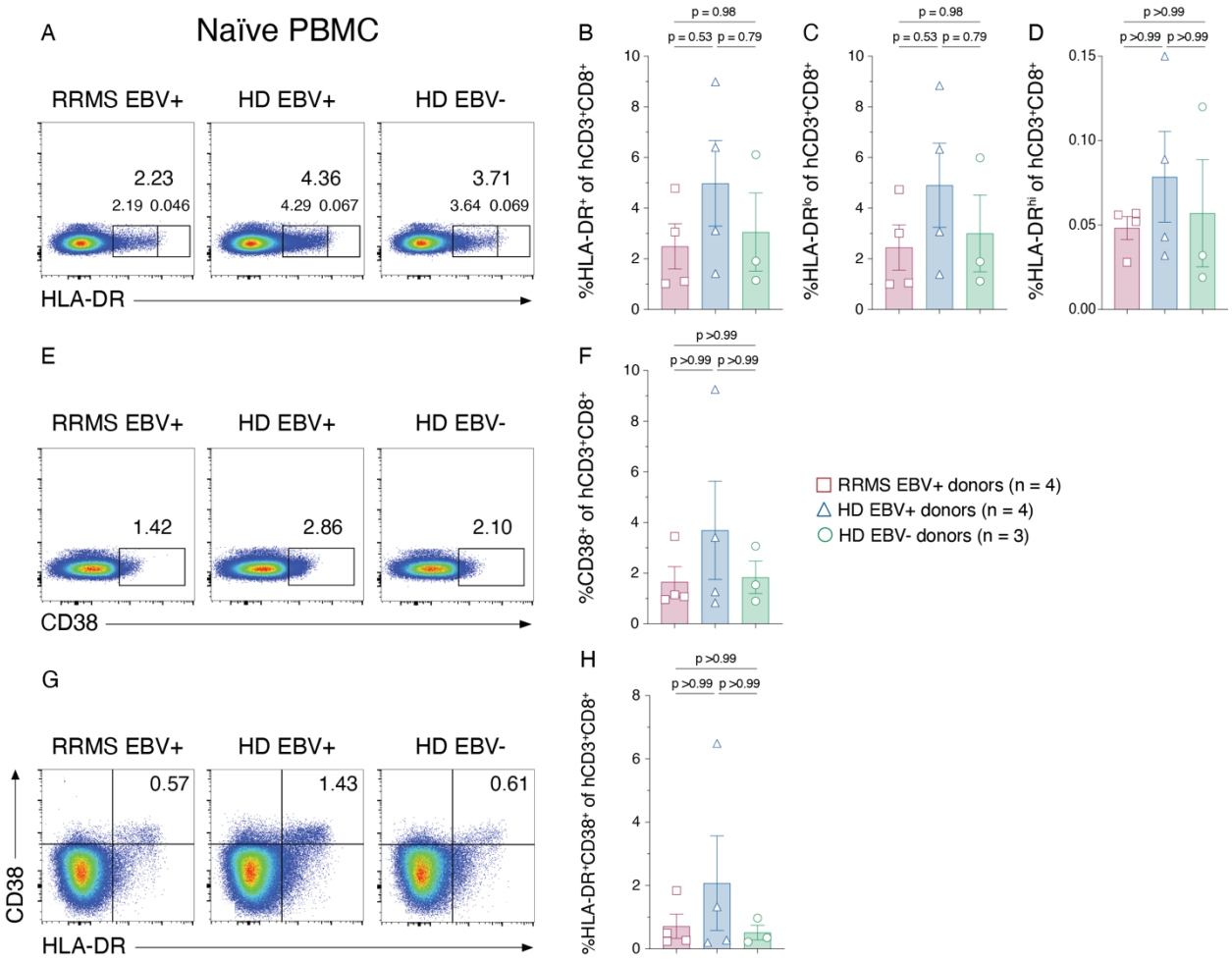

Figure 5.28 Baseline donor hCD3$^+$CD8$^+$ T cell activation

Following donor PBMC preservation in liquid nitrogen, baseline donor T cell activation was assessed by the proportion of naïve (untreated) hCD3$^+$CD8$^+$ T cells that express (A – D) HLA-DR, (E – F) CD38, (G – H) both HLA-DR and CD38, (I – J) CD137, and (K – L) CD154. For concatenated flow plots, the sum proportion of marker positive cells for all donors in each group is indicated. All plotted data are shown as mean with SEM (n = 3 – 4 blood donors/group) and were analyzed by Brown-Forsythe and Welch ANOVA with Dunnett's T3 multiple comparisons test or by Kruskal-Wallis with Dunn's multiple comparisons test.

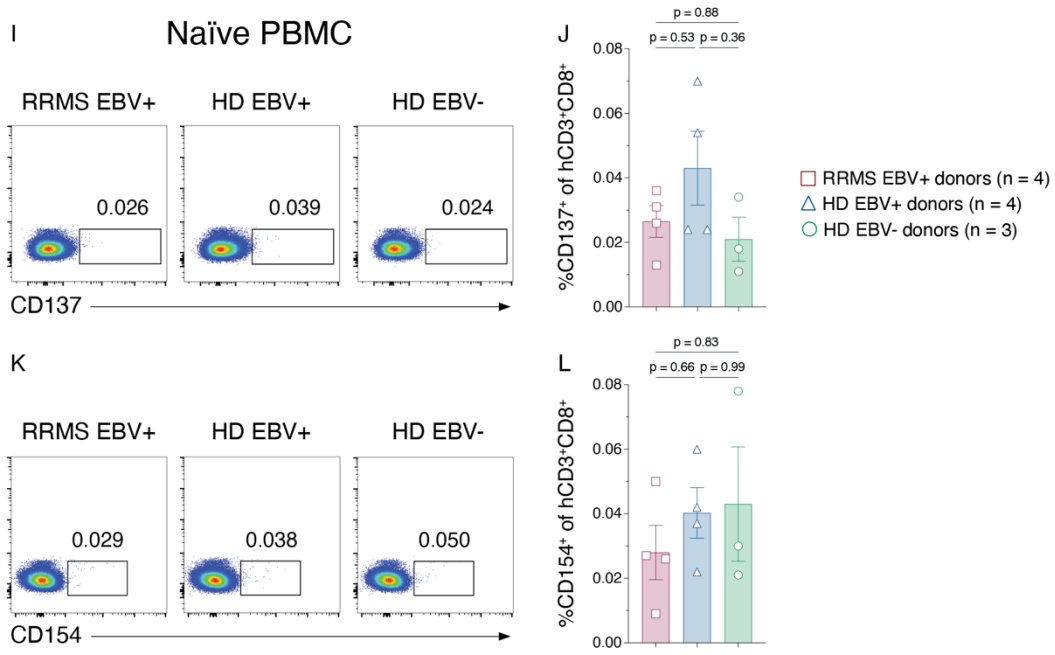

Figure 5.28 continued

To evaluate the possibility that T cells from an EBV-exposed host are more intensely activated following TCR engagement generally than those from an EBV naïve host, we stimulated donor PBMCs by anti-hCD3/CD28 stimulation in vitro (Figure 5.33, Figure 5.34). Interestingly, direct stimulation of the TCR by receptor engagement without introducing a specific antigen resulted in a trend of enhanced hCD4$^+$ T cell proliferation with donor EBV and RRMS status, as measured by a CFSE staining-based proliferation index and Ki-67 expression (Figure 5.33A – C), that emerged consistently despite the inter-donor variability observed in the baseline measurements. hCD4$^+$ T cells from HD EBV$^+$ PBMCs, and even more so from RRMS EBV$^+$ PBMCs, were able to attain a higher average number of cellular divisions during the incubation period compared to HD EBV$^-$ PBMCs (Figure 5.33B). Consistent with our findings in HuPBMC EAE mouse tissues, hCD4$^+$ T cells were not differentially polarized toward a Th1 or Th17 phenotype after bead stimulation, as determined by similar proinflammatory cytokine expression frequencies (Figure 5.33D, E). Moreover, the same effects were observed with hCD8$^+$ T cells, wherein an incremental increase in proliferation, as measured by CFSE staining and Ki-67 expression, was observed with donor EBV seropositivity and an RRMS diagnosis following anti-CD3/CD28 stimulation (Figure 5.34A – C). Bead-stimulated hCD8$^+$ T cell proinflammatory cytokine expression did not follow any clear donor group specific trends (Figure 5.34D, E).

Therefore, in addition to an EBV and RRMS associated deficiency in the expansion of Tregs in the HuPBMC EAE model, both hCD4$^+$ and hCD8$^+$ T cells from EBV experienced hosts were also more proliferative following general TCR stimulation, independent of the antigens involved and without alteration to the polarization proclivity of these cells.

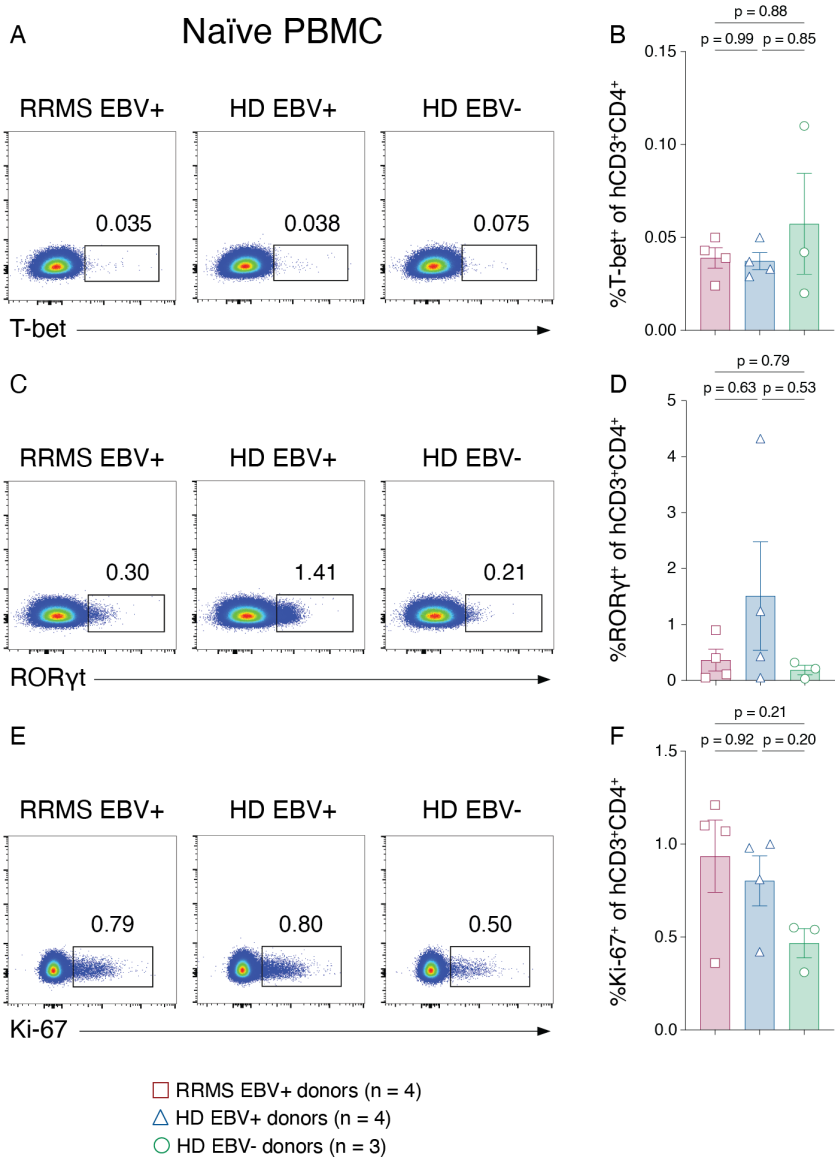

Figure 5.29 Baseline donor hCD3$^+$CD4$^+$ T cell transcription factor expression

Following donor PBMC preservation in liquid nitrogen, baseline donor T cell polarization and proliferation was assessed by the proportion of naïve (untreated) hCD3$^+$CD4$^+$ T cells that express (A – B) T-bet, (C – D) RORγt, and (E – F) Ki-67. For concatenated flow plots, the sum proportion of marker positive cells for all donors in each group is indicated. All plotted data are shown as mean with SEM (n = 3 – 4 blood donors/group) and were analyzed

by Brown-Forsythe and Welch ANOVA with Dunnett's T3 multiple comparisons test or by Kruskal-Wallis with Dunn's multiple comparisons test.

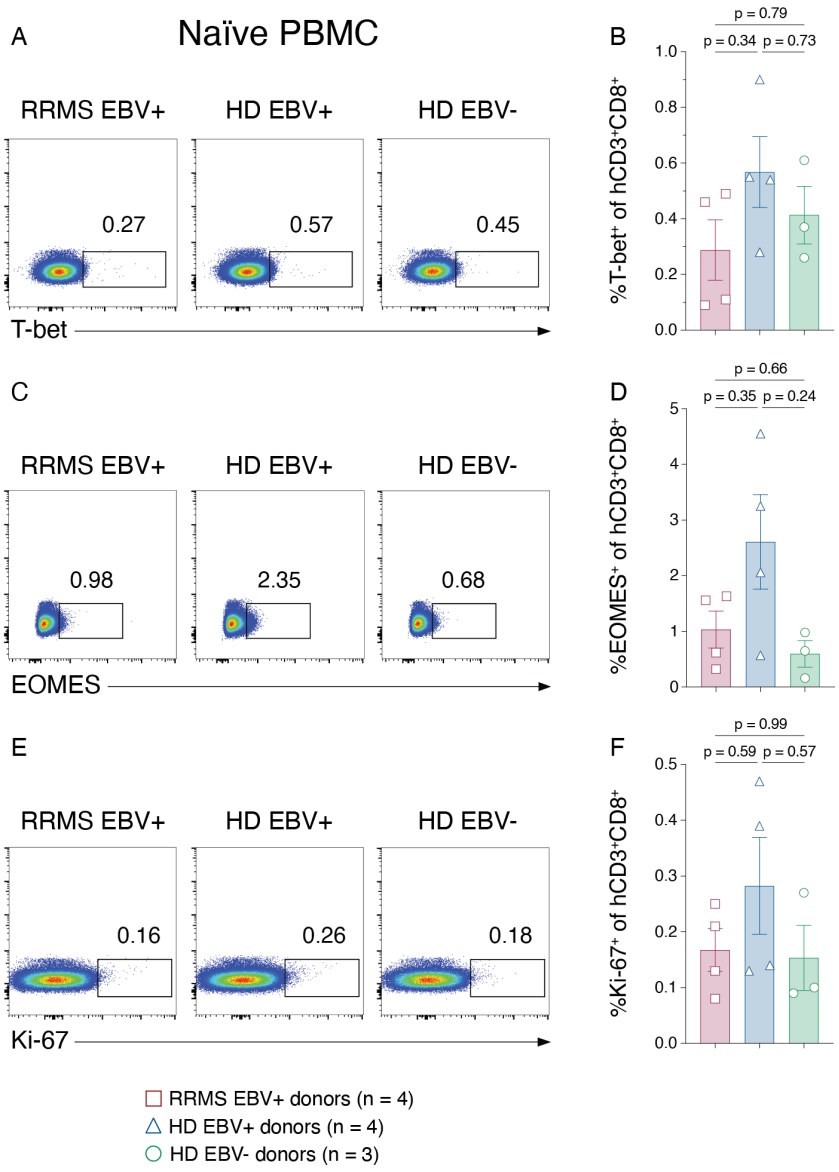

Figure 5.30 Baseline donor hCD3$^+$CD8$^+$ T cell transcription factor expression

Following donor PBMC preservation in liquid nitrogen, baseline donor T cell polarization and proliferation was assessed by the proportion of naïve (untreated) hCD3$^+$CD8$^+$ T cells that express (A – B) T-bet, (C – D) EOMES, and (E – F) Ki-67. For concatenated flow plots, the sum proportion of marker positive cells for all donors in each group is indicated. All plotted data are shown as mean with SEM (n = 3 – 4 blood donors/group) and were analyzed by Brown-Forsythe and Welch ANOVA with Dunnett's T3 multiple comparisons test or by Kruskal-Wallis with Dunn's multiple comparisons test.

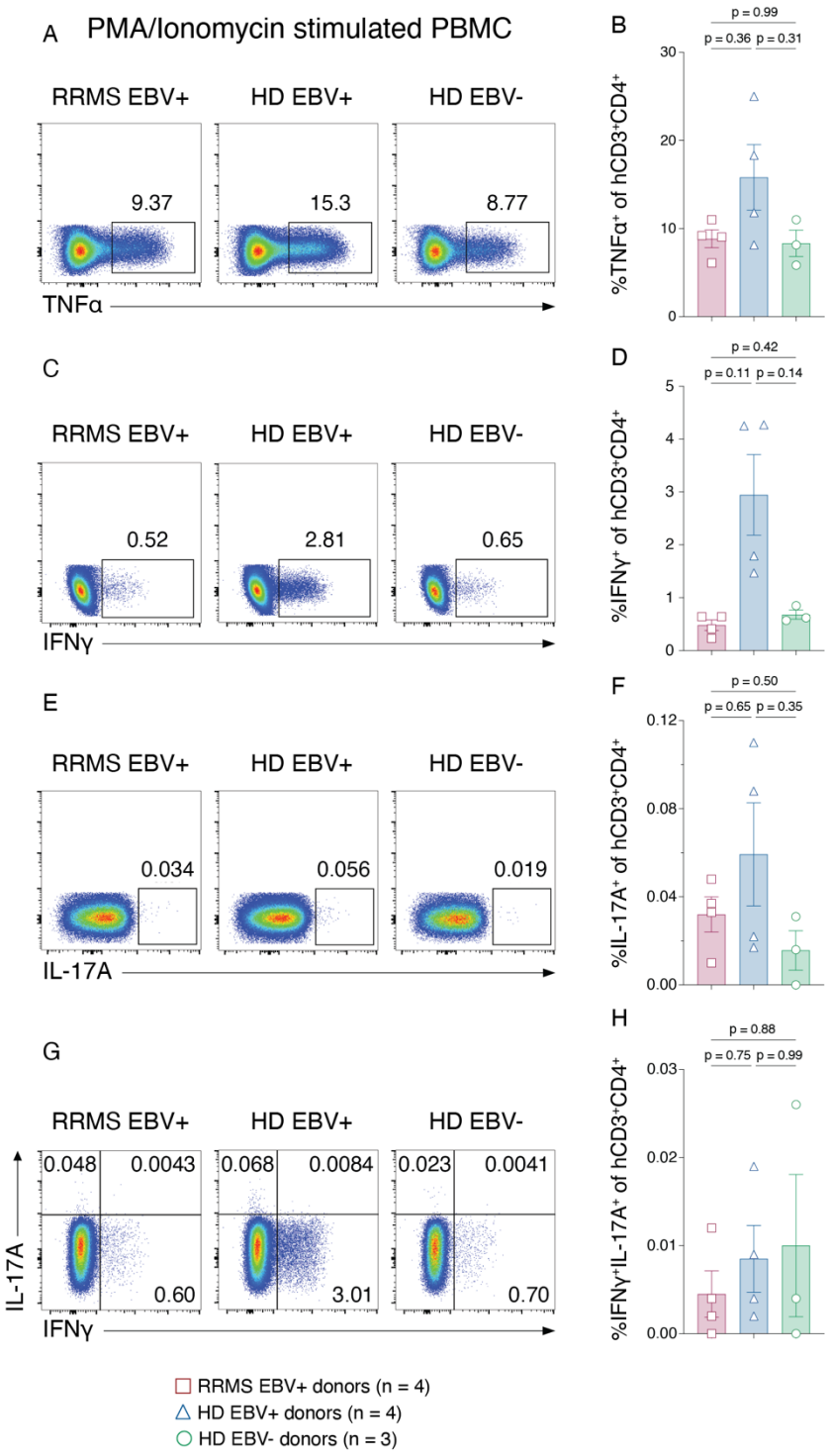

Figure 5.31 Baseline donor hCD3$^+$CD4$^+$ T cell inflammatory cytokine expression

Following donor PBMC preservation in liquid nitrogen, baseline donor T cell polarization was assessed by the proportion of PMA and ionomycin stimulated hCD3$^+$CD4$^+$ T cells that express (A – B) TNFα, (C – D) IFNγ, (E – F) IL-17A, and (G – H) both IFNγ and IL-17A. For concatenated flow plots, the sum proportion of marker positive cells for all donors in each group is indicated. All plotted data are shown as mean with SEM (n = 3 – 4 blood

donors/group) and were analyzed by Brown-Forsythe and Welch ANOVA with Dunnett's T3 multiple comparisons test or by Kruskal-Wallis with Dunn's multiple comparisons test.

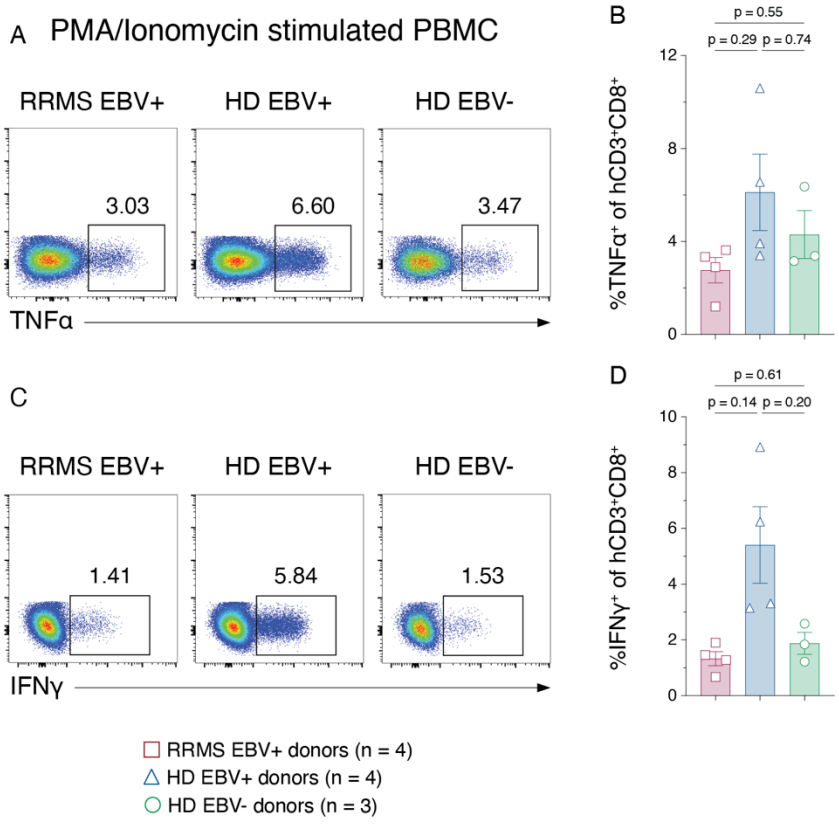

Figure 5.32 Baseline donor hCD3$^+$CD8$^+$ T cell inflammatory cytokine expression

Following donor PBMC preservation in liquid nitrogen, baseline donor T cell polarization was assessed by the proportion of PMA and ionomycin stimulated hCD3$^+$CD8$^+$ T cells that express (A – B) TNFα and (C – D) IFNγ. For concatenated flow plots, the sum proportion of marker positive cells for all donors in each group is indicated. All plotted data are shown as mean with SEM (n = 3 – 4 blood donors/group) and were analyzed by Brown-Forsythe and Welch ANOVA with Dunnett's T3 multiple comparisons test or by Kruskal-Wallis with Dunn's multiple comparisons test.

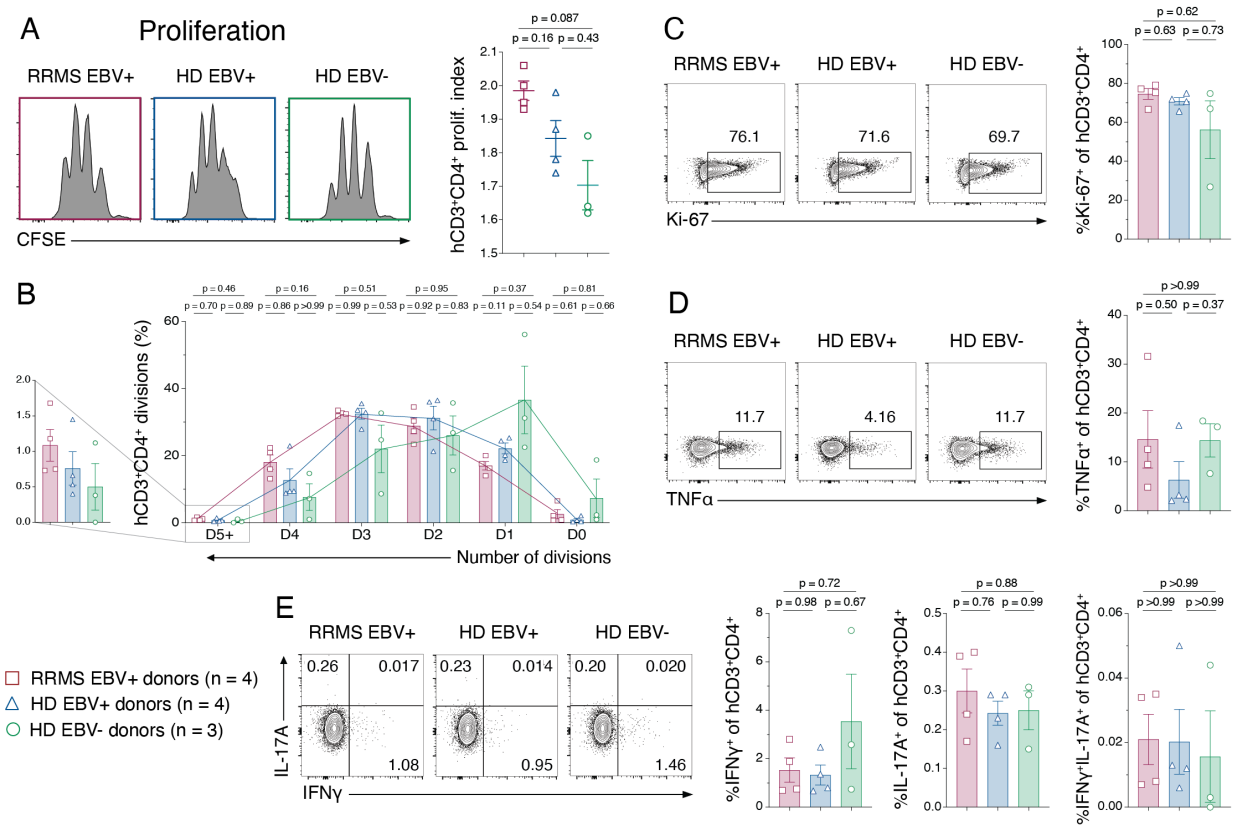

Figure 5.33 Donor hCD3⁺CD4⁺ TCR mediated cell proliferation is enhanced by both EBV seropositivity and an RRMS diagnosis

Previously frozen, whole PBMC samples from EBV⁺ RRMS, EBV⁺ HD, and EBV⁻ HD blood donors were incubated with anti-CD3/CD28 coated beads for 96 hours to stimulate human T cell receptors (TCR) in the absence of specific antigen. Figure shows (A) the proliferation index and (B) the proportion of hCD3⁺CD4⁺ T cells having undergone a specified number of cellular divisions, as determined by CFSE staining, as well as (C) Ki-67, (D) TNFα, and (E) IFNγ and/or IL-17A expression on bead stimulated hCD3⁺CD4⁺ T cells. For concatenated flow plots, the sum proportion of marker positive cells for all donors in each group is indicated. The colored symbol legend is applicable to all comparisons (n = 3 – 4 blood donors/group). All plotted data are shown as mean with SEM and were analyzed by Brown-Forsythe and Welch ANOVA with Dunnett's T3 multiple comparisons test or by Kruskal-Wallis with Dunn's multiple comparisons test.

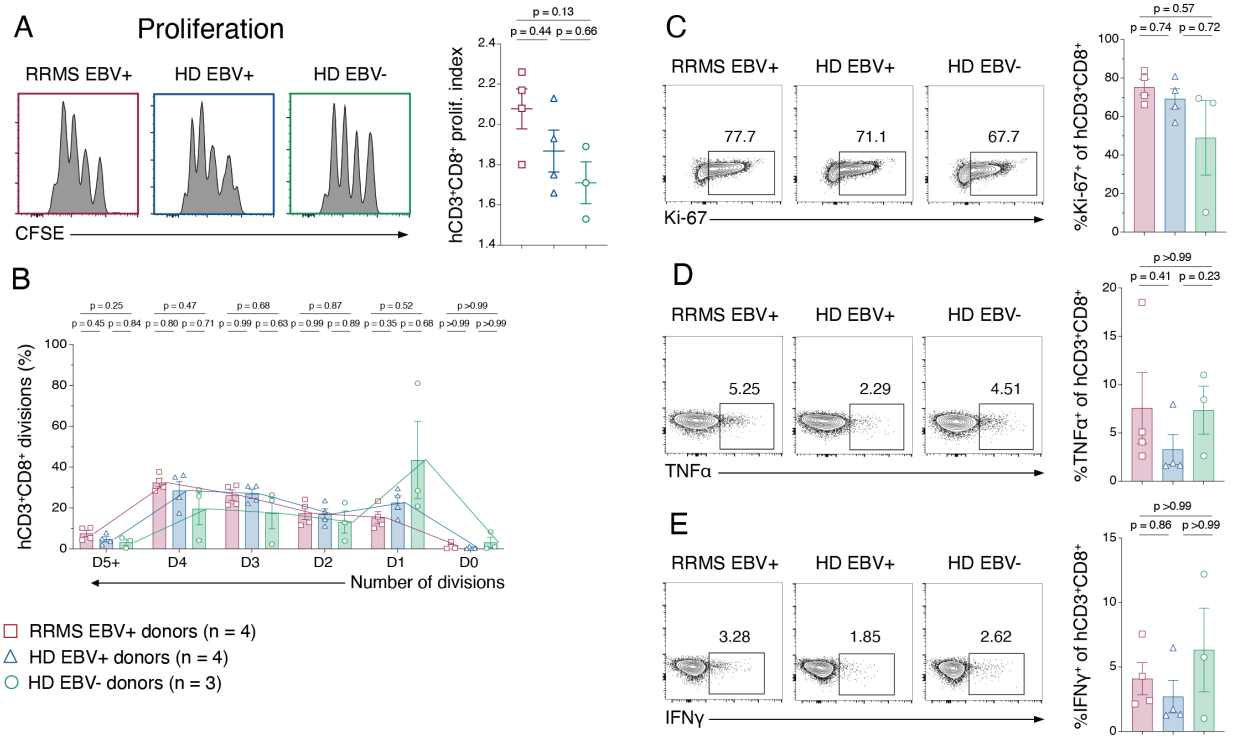

Figure 5.34 Donor hCD3$^+$CD8$^+$ TCR mediated cell proliferation is enhanced by both EBV seropositivity and an RRMS diagnosis

Previously frozen, whole PBMC samples from EBV$^+$ RRMS, EBV$^+$ HD, and EBV$^-$ HD blood donors were incubated with anti-CD3/CD28 coated beads for 96 hours to stimulate human T cell receptors (TCR) in the absence of specific antigen. Figure shows (A) the proliferation index and (B) the proportion of hCD3$^+$CD8$^+$ T cells having undergone a specified number of cellular divisions, determined by CFSE staining, and (C) Ki-67, (D) TNFα, and (E) IFNγ expression on bead stimulated hCD3$^+$CD8$^+$ T cells. For concatenated flow plots, the sum proportion of marker positive cells for all donors in each group is shown. The colored symbol legend is applicable to all graphs (n = 3 – 4 blood donors/group). All plotted data are shown as mean with SEM and were analyzed by Brown-Forsythe and Welch ANOVA with Dunnett's T3 multiple comparisons test or Kruskal-Wallis with Dunn's multiple comparisons test.

5.7 Summary and discussion of findings

PBMC donor history of EBV infection and a diagnosis of RRMS both exacerbated clinical disease susceptibility and severity in recipient HuPBMC EAE mice, which correlated with increased proinflammatory human T cell infiltration and a more profound loss of myelin in the CNS, compared to mice derived from EBV seronegative donors. We observed a significant enhancement in multiple measures of clinical disease severity in recipient HuPBMC EAE mice that correlated with the increasing serum EBV-specific IgG titres of the donor groups. Specifically, overall disease course, incidence of symptoms, and time to symptom onset, were significantly impacted by donor EBV and RRMS status. Clinical differences associated with donor EBV seropositivity in the HuPBMC EAE model are consistent with recent findings linking elevated humoral responses to EBV at disease onset with greater long-term disease severity and higher relapse rates in individuals with MS[110]. Similar to the findings of Bjornevik and colleagues[109], clinical EAE differences in our model could not be attributed to donor CMV infection status, nor to reduced serum vitamin D levels. Though EBV infection was not a necessary prerequisite to enable EAE development in HuPBMC mice following MOG immunization, the EBV^+ HD recipient group presented with an intermediate clinical phenotype that resembled RRMS recipient mice in some ways more than the EBV^- HD group.

The association between EBV and relapse risk has been suggested to be due to increased EBV-specific $CD8^+$ T cell activity during relapse following ineffective immune control of infection during the remission phase[387]. Interestingly, systemically active infection by EBV was not required to exacerbate disease severity, as demonstrated by undetectable viral loads in the PBMC samples from the donors with existing latent EBV infection, as well as the lack of reactivation and human memory B cell responses to EBV in the HuPBMC EAE mice derived from these donors. The data are also consistent with previous findings by our group showing that viral reactivation does not occur following EAE induction of C57Bl/6 mice latently infected with γHV68, and that γHV68 does not actively infect the CNS following immunization[415]. Human B cell accumulation in the CNS did not differ among HuPBMC EAE mice derived from donors with or without a history of RRMS and/or EBV infection. Though relatively few human B cells reconstituted the recipient mice peripherally, and even fewer infiltrated the CNS, compared to T cells following PBMC engraftment and EAE induction, the possibility remains that engrafted B cells of varying specificities and functionalities, which can act both protectively and

pathogenically in classical EAE models[336,751], may also contribute to the enhancement of disease and the increased CNS inflammation observed in EBV^+ and RRMS recipient mice. Clinical post-mortem evidence has suggested that EBV could contribute to the development and/or progression of MS through infection of CNS-infiltrating B cells and tertiary lymphoid structures, leading to local inflammation[52,355,357]. With minimal B cell accumulation in the CNS at endpoint, the HuPBMC EAE model likely reflects earlier stages of MS, where B cell-containing lymphoid structures have not yet formed. Further investigation will be required to assess the presence and influence of EBV-infected and EBV-specific B cells in HuPBMC EAE mice more precisely. Although there are multiple supported mechanisms by which EBV could promote an autoimmune environment through B cell-specific processes, our data obtained using two distinct mouse models of gammaherpesvirus infection and autoimmune MS suggest a critical role for inflammatory T cell modulation following latent infection.

The CNS tissues of HuPBMC EAE mice derived from EBV^+ HD and RRMS donors contained larger numbers of Th1 and cytotoxic T cells compared to EBV^- HD PBMC recipient mice. Additionally, the CNS and peripheral tissues of EBV^+ mice (both HD and RRMS) contained substantially reduced Treg frequencies among $hCD3^+CD4^+$ T cells, indicating an impairment of immune regulation resulting from latent infection. We therefore suppose that the skew toward increased abundance of effector T cells relative to regulatory T cells consequently promoted a more inflammatory environment in HuPBMC EAE mice derived from healthy donors with a history of EBV infection, which was further compounded when donors had also been diagnosed with RRMS. Unlike in classical EAE models, where inbred mice are effectively genetically identical and highly susceptible to EAE immunization[142,752], the genetic variability of engrafted human immune cells from multiple unrelated donors highlights the consistency and magnitude of the effect of EBV seropositivity on clinical and immunological disease outcomes in this model. Given that both clinical and immunological differences were observed between the healthy donor groups differing based on EBV serostatus, these effects are also not entirely due to existing autoimmunity among the donors. The increase in infiltrating T effector cells appeared to be due to a generalized enhanced proliferative capacity among T cells derived from EBV seropositive donors following TCR engagement independent of a specific antigen. Further analysis will be required to determine if engrafted human T cells that proliferate in the periphery express more CNS homing molecules and chemokine receptors when derived from RRMS and/or EBV^+ donors,

or, if upon infiltration of the CNS, EBV experienced T cells proliferate locally to a greater extent than those that are EBV naïve. Regulatory T cells control effector T cell proliferation and motility in the CNS following EAE induction[140], and thus assessment of the functional capacity of the engrafted cytotoxic T cell and Treg populations would also provide insight into mechanisms by which EBV suppresses regulation of effector cells following antigenic challenge.

In the γHV68-EAE model, we likewise observed greater proinflammatory $mCD8^+$ T cell infiltration of the CNS of latently infected mice, in addition to Th1-skewing of infiltrating $mCD4^+$ T cells, and reduced Treg proportions in the CNS and periphery using both B cell dependent and independent EAE immunization protocols. Similar Th1-skewing and $mCD8^+$ T cell involvement was observed by our group in latent γHV68-infected mice induced with a rheumatoid arthritis-like disease[417], suggesting a common role for gammaherpesviruses in the exacerbation of and predisposition for autoimmune disease independent of the inciting tissue-specific antigen that initially prompts autoreactivity. Given γHV68 and EBV are related but structurally distinct viruses that have become highly adapted to diverged mammalian species, these data suggest the immunomodulatory effects of latent gammaherpesvirus infection observed in both EAE models are not due to cross reactivity of viral and myelin antigens. Rather, as T cells are required for constant immune control of EBV-infected B cells[753], latent infection could promote lasting changes in the predisposition of T cells to activation generally, which alters the balance of effector and regulatory responses toward a more 'MS-like' state.

Other susceptibility factors for MS, including a history of obesity, smoking, and low vitamin D intake, have all been suggested to act in part by promoting T cell inflammation directly and by impeding regulatory processes[74,746,754,755]. A more generalized pathogenic effect on T cells of varying specificities would also explain the robust link between EBV and other, antigenically distinct autoimmune diseases[249,384,397,756]. An important next step is therefore to assess clinical outcomes and T cell inflammation in the model when engrafted with PBMCs derived from donors with other autoimmune disorders, especially those also linked to EBV infection, such as systemic lupus erythematosus and rheumatoid arthritis, to determine the generalizability of T cell immunomodulation by EBV in autoimmune disease susceptibility in humanized mice. Though EBV induced immunomodulation of T cell responses is a potential mechanism for inciting and potentiating inflammation in MS, it is also possible that immunomodulation occurs alongside additional virus-specific mechanisms, such as infection and immortalization of autoreactive B

cells, ineffective or aberrant immune control of EBV reactivation, and structural mimicry of CNS antigens by viral proteins[26,326,369,378,757]. Ingelfinger et al. recently identified increased CD25 expression on transitional helper T cells as a defining phenotype of MS-derived PBMCs in a monozygotic twin study, which the authors posit could be preferentially responsive to an environmental immune challenge such as EBV infection[758]. Zdimerova et al. also demonstrated a synergistic interaction between EBV infection and the MS risk allele HLA-DRB1*15:01 in stem cell-humanized mice, leading to increased T cell reactivity to myelin antigens[584]. Though two of four of the RRMS donors who provided samples to this study expressed the HLA-DRB1*15:01 risk allele, the absence of the variant among healthy donors in this small initial donor pool did not allow for an analysis of the downstream effects of this variant on outcomes in the HuPBMC EAE model. A tailored focus on the interplay of genetics and environmental exposures will enable more comprehensive investigation of MS risk factors and targeted therapies in the HuPBMC EAE model moving forward. HuPBMC EAE mice could be used for directly assessing DMTs specific to human immune targets, as well as indirectly by engrafting PBMCs derived from patients treated with potential or known anti-viral therapies such as teriflunomide, B cell monoclonal antibodies, or EBV-specific T cells[332,380,759].

In summary, we have shown for the first time that T cells derived from EBV infected people, as well as from those with a diagnosis of RRMS, are capable of mediating enhanced clinical symptoms and CNS immunopathology compared to T cells from uninfected people in a new human T cell transfer model of EAE. This effect was observed in the absence of an active EBV infection, indicating that lytic reactivation is not the only means by which EBV could pathogenically modulate an autoimmune response in the CNS. We also demonstrated an enhanced proliferative capacity of both $hCD4^+$ and $hCD8^+$ T cells derived from EBV exposed donors following direct TCR stimulation without a specific antigen, which links epidemiological and clinical data suggesting EBV risk for autoimmunity is not restricted only to MS but is also a risk factor for autoimmune diseases involving different tissues and distinct target antigens. Our findings highlight that EBV-mediated risk for disease in a humanized mouse model of MS occurs prior to autoimmune challenge and that either the establishment or maintenance of latent infection modulates subsequent T cell reactivity to autoantigen years later. The data support prevention of EBV infection and establishment of latency as a strong avenue for prevention of MS and other EBV-related autoimmune diseases.

Chapter 6 – Discussion and future directions

6.1 Summary of findings and significance

Previous infection with EBV has been repeatedly demonstrated to be a strong risk factor for the development of MS, though the precise mechanisms underlying this robust association remain unclear[82,109,110,313–315,318,325]. Evaluating co-factor mechanisms related to EBV infection has proven particularly difficult in clinical cases because primary infection is generally asymptomatic and predicting who will develop MS is not straightforward, in addition to the fact that individuals often experience a years-long prodrome prior to diagnosis, which obscures analysis of early autoimmune processes where latent EBV and/or infected B cells may be acting to incite disease[109,116,170,760]. Evaluating mechanisms pertinent to autoimmunity has also been hampered experimentally by the latent virus' narrow host tropism for human B cells and subsequent lack of experimental animal models that support EBV infection directly[273]. Exogenous infection of humanized mice has closely mimicked the pathology of various EBV-associated diseases, while the development of EAE models has enabled mechanistic investigation of the immunopathological and neurodegenerative pathways involved in MS[50,430,761]. We therefore applied the principles of both EAE mouse models of MS and EBV infection of humanized mice to evaluate the immunomodulatory effects of EBV infection on CNS autoimmunity directly in a tractable small animal model.

Three separate model methods were employed to generate humanized mice, each with distinct immunological characteristics, logistical limitations, and potential applications (Chapter 3). Consistent with published findings, side-by-side comparison of HuBLT, HuHSC, and HuPBMC mice on the NSG background demonstrated that mice from each model system reconstituted with varying levels of human immune cell subsets[429,493,499,505,509,524,531,552], with HSC engrafted models proving superior hosts for human B cells, while PBMC humanized mice were T cell dominant and readily susceptible to EAE induction resulting in clinically measurable motor deficits. We characterized the clinical phenotype and the peripheral and CNS localized immune cell responses in HuPBMC EAE mice compared to classical EAE models, addressed technical and sex-based considerations for permissive and reproducible active induction of EAE using myelin antigens, and defined the relative chimeric contributions of the engrafted human immune cell subsets and the residual murine myeloid cell compartment in mediating disease pathology (Chapter

4). Similar to established murine EAE models, MOG immunization of HuPBMC mice resulted in proinflammatory T cell infiltration of the CNS tissues, demyelination, and lower limb paralysis[128]. Our findings indicate that demyelinated lesion formation in this model occurred through the coordinated actions of reconstituted human IFNγ$^+$CD4$^+$ Th1 and IFNγ$^+$GzmB$^+$CD8$^+$ cytotoxic T cells, in conjunction with the antigen presenting and phagocytic activity of host murine macrophages. Furthermore, EAE induction of HuPBMC mice recapitulated key clinical and immunopathological aspects of MS more closely than in regular mice; specifically, the development of a phasic clinical disease coincident with CD8$^+$ T cell infiltration of the brain, rather than a CD4$^+$ T cell predominant invasion of the spinal cord observed in most murine EAE models[38,50,128,131].

By humanizing NSG mice with PBMCs from donors with differing EBV seropositivity and RRMS status, we observed that the HuPBMC EAE model reflected the epidemiological and clinical data describing the increased risk for MS incidence and disease severity following EBV seroconversion and the production of high virus-specific antibody titres, respectively (Chapter 5)[109,110,315]. Despite promoting a stepwise increase in clinical disease severity, PBMC donor EBV seropositivity and RRMS diagnosis did not affect the degree of human B cell infiltration in the CNS nor was viral reactivation detectable in the periphery; mechanisms that have been proposed to affect MS disease activity[104,387]. Donor EBV and RRMS status did, however, correspond to a significant incremental increase in the number of brain and spinal cord infiltrating effector T cells, due to enhanced proliferation of Th1 hCD4$^+$ and cytotoxic hCD8$^+$ T cells, and a correspondingly reduced expansion of hCD4$^+$FOXP3$^+$ regulatory T cells. The effect of latent infection on the effector to regulatory T cell ratio in the CNS was similarly modelled using the murine homologue of EBV, γHV68, in an established model of EAE[415,418], revealing a conserved immunomodulatory mechanism by which latent gammaherpesvirus infection could predispose an individual to the development of autoimmune disease. Since EBV is a potentially preventable infection, these findings have implications for reducing MS incidence by targeting EBV and its downstream effects on host immune responses. Therapeutic interventions aimed at reducing the proinflammatory T cell response prompted by EBV could effectively diminish disease activity in MS and other antigenically distinct EBV-associated autoimmune disorders. For example, the use of anti-CD20 B cell depletion therapy, which has been suspected to eliminate EBV infected cells[159], has the

additional effect of depleting memory $CD8^+$ T cells and reducing T cell inflammation generally[762,763].

Our findings also corroborate existing clinical and humanized mouse studies demonstrating a role for pathogenic T cell responses in driving autoimmunity generally. Our in vivo HuPBMC EAE data models the preferential Th1 phenotype observed in MS patients compared to controls, which is also upregulated during active disease phases relative to remission phases[764]. Vudattu and colleagues noted that in HuHSC-NSG mice, "co-administration of anti-CD3 with anti-CTLA-4 reversed all autoimmune manifestations induced by anti-CTLA-4 antibody. Our studies suggest three mechanisms that account for the development of autoimmunity including: T cell activation and proliferation, impaired localization of Tregs to pathologic sites, and recruitment and interaction with antigen presenting cells"[639]; aspects we observed to be specifically exacerbated in EBV^+ and RRMS PBMC engrafted mice compared to EBV^- HD derived HuPBMC EAE mice. Using an LPC-induced model of demyelination in NSG mice, El Behi and colleagues noted that engraftment of pre-existing lesions with PBMCs obtained from MS diagnosed individuals impaired remyelination compared to healthy donor PBMC engraftment[643]. Similar to our findings, El Behi and colleagues noted that "there is no major over-representation of certain circulating lymphocytes between multiple sclerosis patients and healthy donors", but that "their lymphocytes have a different intrinsic capacity to respond to stimulation"[643]. Data from the HuPBMC EAE model and analysis of donor T cell responses to TCR stimulation further suggest this intrinsic capacity is amplified by latent EBV infection, even among otherwise healthy donors.

As demonstrated herein, HuPBMC mice offer the possibility of pre-screening and selecting donors based on chosen genetic variants, environmental exposures, immunological conditions[636,765] to create a personalized human immune system model. The HuPBMC EAE model therefore provides a unique experimental platform that can factor in environmental exposures and immunogenetics known to be associated with MS but that are typically unaccounted for in classical EAE models due to species limitations and/or technical challenges. Instances of promising results from biological therapies in preclinical EAE models that have translated to worsened disease outcomes or serious side effects in humans could ideally be identified in mouse models with human immune systems, such as those discussed in this work, before advancement to clinical trials[335,404,646,647]. With continued improvement, optimization, and characterization, humanized

EAE models could narrow many of the gaps in our understanding of the causes of and contributing factors to MS development and provide researchers with new tools for testing promising DMTs.

6.2 Limitations and outstanding work

An important caveat to the use of humanized mice generally is that human immune system reconstitution of immunocompromised mice does not precisely replicate the composition of the donor PBMCs, nor all the nuanced contextual and site-specific complexities of the mammalian immune system[468,484,488,540,541,684]. Moreover, each humanized mouse reconstitutes variably, even among recipient mice derived from the same tissue or cell source, owing to both practical challenges in generating humanized mice and the inefficient engraftment of many immune subsets sensitive to species specific survival and developmental cues that are either absent or less potent in immunocompromised mouse tissues[465,540]. As a result, we observed considerable variability and heterogeneity in the incidence, time of onset, and severity of EAE symptoms in HuPBMC mice, as well as in the abundance and phenotype of CNS infiltrating human T cells. Despite the known caveats associated with humanized mouse models, the HuPBMC EAE model presents with certain advantages over classical EAE models, including the use of genetically diverse donor tissues that reflect variation in the human population more closely than inbred strains of mice. All EAE mouse model are known to present with pros and cons for certain types of studies, depending on which aspects of MS they most closely replicate[50,128], and thus the HuPBMC EAE model joins an existing repertoire of various MS models that have been used by many researchers to interrogate specific disease processes[41,62]. To reiterate the perspective of Constantinescu and colleagues, "usefulness is critically dependent on using appropriate models to answer the specific scientific or clinical questions that are being addressed"[50].

A practical consideration for generating the HuPBMC EAE model as described here is the logistical challenge of organizing and coordinating blood donors, clinical staff, and recipient mouse cohort availability, in order to engraft NSG mice with fresh donor PBMCs within an hour of donor blood collection. As such, running side by side group comparisons with sufficient numbers of mice per cohort derived from multiple donors is often not feasible. Future assessments of any differences in EAE outcomes between HuPBMC mice derived from fresh PBMCs and previously frozen and thawed donor PBMCs would clarify the necessity for day-of engraftment and potentially eliminate this consideration. A considerable experimental limitation of the

HuPBMC EAE model is the relatively short duration of experiments to 7 – 8 weeks post-engraftment of human PBMCs due to the onset of xGvHD. Therefore, the HuPBMC EAE model is better suited for studying factors affecting disease onset and the early phases of autoimmunity, rather than for studying long-term outcomes such as relapses or chronic disease. The co-occurrence of xGvHD in the HuPBMC EAE model also raises questions as to the antigen specificity of the T response within the CNS, and specifically, whether the differences in clinical symptoms observed between recipient groups were simply varying degrees of xGvHD depending on the activation status of the donor PBMCs. Though we did not observe any differences in xGvHD-specific clinical symptoms between our recipient groups, all human T cell responses to murine tissues in HuPBMC EAE mice are necessarily xenoreactive, involving interspecies recognition of murine MHC complexes.

Studies investigating human T cell development and murine MHC reactivity in humanized mouse tissues have generated nuanced and complex results supporting the occurrence of both canonical and atypical antigen responses compared to human HLA expressing tissues[488,607,712]. The data presented herein suggest that both myelin specific and nonspecific reactivity occurs following MOG immunization of HuPBMC mice. Total human T cell subset abundance was similar in the CNS tissues of all mice administered PTx, likely due to generalized BBB breach, however, the physical presence of human T cells within the CNS only produced clinical symptoms in 11% of HuPBMC mice immunized without MOG antigen. If the incidence of EAE in HuPBMC mice was dependent simply on enabling the entry of xenoreactive human T cells into the mouse CNS, we would have expected to see equal or at least similar rates of paralysis in all PTx treated HuPBMC mice. While CFA and PTX immunization alone was sufficient to generate clinical EAE paralysis in 20% of HuPBMC mice, the addition of MOG antigen to the CFA emulsion increased the incidence of paralysis to 50% of immunized HuPBMC mice, suggesting the inclusion of MOG preferentially directed the graft response to the CNS, resulting in more severe EAE pathology.

In NOD WT mice induced with MOG_{35-55} EAE, only 2 – 6% of spinal cord infiltrating $mCD4^+$ T cells bound to MOG_{42-55} peptide loaded MHC II tetramers, indicating the vast majority of T cells in CNS were not specific to the inducing antigen and were likely recruited secondarily to mediate damage to the CNS. If only a small fraction of MOG-specific human T cells infiltrated the CNS of HuPBMC EAE mice, it would not necessarily indicate that our model is simply an extension of xGvHD, but rather that EAE and xGvHD exhibit common mechanisms of antigen

presentation that both depend on murine MHC complex recognition and co-stimulation through interspecies receptor: ligand interactions. For example, Sonntag and colleagues identified genetic overlap in susceptibility to xGvHD and autoimmunity in HuHSC-NSG mice[607] and Hogenes and colleagues noted the development of xGvHD in PBMC engrafted BRG mice depended on human and murine immune cell cooperation[619]. Human Tregs have been previously shown to modulate human tissue transplant rejection in HuPBMC mice, while $hCD8^+$ T cells have been shown to mediate human allograft responses, neither of which required murine MHC recognition[465,493,611]. Furthermore, PBMC engrafted MHC KO NSG mice showed delayed onset of xGvHD but were not entirely resistance, demonstrating that human T cell responses in HuPBMC mice are not exclusively determined by murine MHC recognition[465,493,611]. As autoimmune disease and GvHD are both forms of immune mediated tissue rejection, more concrete conclusions about the relative role of myelin specific T cell reactivity versus nonspecific xGvHD in the HuPBMC EAE model can likely only be made by determining the epitopes of rhMOG protein presented by NSG host expressed MHC complexes and utilizing more sensitive measures to distinguish graft and myelin specific human T cell responses.

In the event that all CNS infiltrating human T cells in the HuPBMC EAE model are in fact xenoreactive, and evidence is obtained demonstrating that only nonspecific peptide-loaded murine MHC is recognized locally in the CNS, which then drives demyelination and clinical symptoms, the ultimate finding of chapter 5 would remain mostly unchanged. In this case, the HuPBMC EAE model should be characterized as a site-directed xGvHD of the CNS (or xEAE). In MOG immunized HuPBMC mice, the EBV and RRMS status of the donor PBMCs was shown to skew the overall ratio of effector and regulatory T cells and result in a more proinflammatory human T cell infiltrate composition in the CNS. Critically, we observed that stimulation of these donor T cells by three separate, antigenically distinct methods (direct anti-CD3/CD28 TCR stimulation, xenoreactivity following engraftment of NSG mice, and EAE immunization) all similarly resulted in excessive effector T cell expansion in EBV experienced donor PBMCs and corresponding recipient mice compared to those that were EBV naïve. Moreover, the same immunomodulatory effects were reproduced in the γHV68-EAE model, wherein xGvHD was not a factor, regardless of whether the EAE inducing antigen was a peptide or protein containing different immunodominant epitopes[149]. We have also observed this local and peripheral inflammatory T cell skewing in γHV68 infected mice immunized with collagen-induced arthritis, an antigenically

distinct model of autoimmunity affecting an anatomically distant tissue than does EAE[417]. Our data thus indicates that latent gammaherpesvirus does not mediate increased disease severity in EAE models through modulation of CNS antigen specific T cells, but rather through global, systemic skewing of the T cell compartment toward a more proinflammatory Th1/cytotoxic and less regulated response upon activation with an autoantigen in a susceptible individual.

Many of the outstanding questions that remain following our current work could be addressed by analyzing additional HuPBMC EAE and γHV68-EAE model cohorts, while some aspects of the EBV-MS relationship and the nature of T cell responses in HuPBMC mice will likely require more intensive investigation and have more complicated feasibility considerations. In general, the inclusion of additional donors for analysis in the HuPBMC EAE model will increase the strength and applicability of the current findings to the general and MS-affected population. Repetition of the study design in chapter 5 using CFA and PTx immunization only (without MOG antigen addition) would be a resource intensive but informative means of assessing differences in the donor T cell reactivity to nonspecific murine antigen stimulation and/or to assess existing CNS antigen reactivity conferred by donors with an RRMS diagnosis or history of EBV infection. Furthermore, while we do not suspect that EBV latency promotes activation of myelin epitope specific T cells exclusively, analysis of chemokine receptor expression by human T cells of the three recipient HuPBMC EAE groups, as well as murine T cells in γHV68 infected and uninfected EAE mice, could shed light on any effects infection exerts on the proclivity of activated T cells to migrate into the CNS following myelin autoantigen challenge. EBER staining (or TMER staining for γHV68) may also provide a more sensitive measure of potential EBV infected B cell transfer from seropositive donors to HuPBMC recipient mice and more accurately identify any infected B cells within the CNS. More broadly, continuation of this work should focus on dissecting the molecular and cellular mechanisms by which EBV infection results in dysregulated T cell responses following autoimmune challenge, in addition to optimizing and furthering the development of humanized mouse models of MS to study these mechanisms.

6.3 Future directions

The continued development of humanized EAE mice is a promising avenue for generating representative models of human immunity that can be used to address many of the genetic and environmental factors associated with MS and other autoimmune diseases. Given the ever

increasing availability of new immunocompromised mouse strains and the many reports of humanization protocols and analytical methods being generated and improved upon[429,431,602,766], specific aspects of disease pathogenesis could be readily assessed using specially adapted humanized EAE model variants. For instance, further optimization and induction of EAE in the HuHSC and HuBLT mice would enable investigation of the role of EBV infection in CNS autoimmunity on a consistent genetic background with more robust HIS subset reconstitution than can be obtained in HuPBMC mice, most notably of human B cells. Furthermore, HuHSC-NSG mice have been reported to be susceptible to intranasal infection with fluorescently tagged EBV virions (C. Münz, conference communication), which would permit the application of a physiologically relevant route of infection that mimics oral transmission between humans more closely than IV or IP inoculation. Specific next steps to generate HuBLT and HuHSC EAE models should focus on optimizing the method(s) to sufficiently activate and expand myelin reactive T cells following MOG immunization, as described in the summary and discussion section of Chapter 3. Additional modifications to the humanization procedures could also impact our understanding of the various immunological effects of EBV infection on disease outcomes in HSC-based models. While human B cell maturation and class switched antibody production is generally poor in humanized mice, the introduction of human transgene expressing immunocompromised mice with improved lymph node structures has led to considerable improvement in this regard[484,490,509,541]. The implantation of splenic fetal tissue has also been shown to improve B cell maturation in the HuBLT model by providing a suitable niche for productive T-B cell interactions[538]. Utilizing B cell promoting strains and humanization methods would thus be a reasonable next step in modeling EBV infected B cell behaviour more accurately in the context of CNS autoimmunity.

We anticipate that the use of murine MHC KO and human HLA transgenic NSG strains would also expand upon our understanding of the CNS infiltrating T cell response observed in the HuPBMC EAE model. Inducing EAE in HuPBMC mice on an MHC I and/or II KO background[493,505] would be helpful in confirming the role of human T cell recognition of murine MHC complexes following MOG immunization, either through initial antigen presentation and priming of the T cell response and/or via local restimulation in the CNS. Epitope specific MOG responses in HuPBMC-NSG EAE mice could then be probed using overlapping peptide screens and I-A^{g7} MHC I and II tetramer reagents, with MHC KO mice serving as negative controls for

interspecies human TCR: murine MHC interactions while accounting for the potential overlapping or predominant functions of any engrafted human APCs. Similarly, the engraftment of HLA transgenic NSG mice with pre-screened, genotype-matched donor PBMCs could improve the efficiency of MOG antigen presentation by murine APCs expressing human HLA complexes, as has been noted to occur in HuHSC HLA-A2 mice infected with EBV[470], and potentially, increase EAE symptom incidence. Though human HLA expression in recipient mice could reduce the confounding effects of interspecies APC interactions, the continued expression of murine MHC molecules and their recognition by engrafted human T cells along with human HLA molecules remains a potential issue, and thus engraftment of a dual human HLA transgenic and murine MHC KO NSG strain would be preferable. As noted by Ehx and colleagues in a report using the HLA-A2/HHD strain, expression of HLA-A0201 led to more severe xGVHD compared to regular NSG mice following engraftment of HLA type matched human PBMCs[609]. The development of reproducible clinical EAE symptoms in HuHSC mice would help resolve, in part, the role of myelin specific T cell responses in mediating disease pathology as human T cells are selected on murine MHC complexes in the host thymus of HuHSC mice during HSC differentiation.

Another option for determining the presence of MOG specific human T cells in actively immunized HuPBMC mice would be to passively transfer HuPBMC EAE spleen-derived $hCD4^+$ and/or $hCD8^+$ T cells, restimulated ex vivo with MOG, to naïve recipient NSG mice, without additional PTx treatment. In this case, the development of any EAE symptoms would most likely be due to MOG specific T cell entry into the CNS, as without PTx administration, the BBB would remain intact and engrafted human T cells would not infiltrate from the periphery unless myelin reactive. Passive EAE induction would be a logistically trickier protocol to establish using HuPBMC mice, in so far as the timing would be tight between reconstituting and actively immunizing donor HuPBMC mice, then adoptively transferring the ex vivo expanded MOG T cells into reconstituted recipient HuPBMC mice generated from the same blood donor, before the onset of xGvHD in recipients. If a passive immunization protocol can be reliably established, the ex vivo restimulation step presents an opportunity for investigating the effect of previous EBV infection on human T cell polarization, by supplementing EBV^+ and EBV^- HuPBMC EAE splenocyte cultures with MOG antigen in combination with Th1 and/or Th17 promoting cytokines[94,477,767]. Evidence from clinical and EAE studies have implicated both Th1 and Th17

cells in the pathogenesis of MS[40,55,694,768,769], though the impact of EBV on each of these autoinflammatory T cell populations in MS remains unknown.

In the γHV68-EAE model, latent infection shifts helper T cell polarization toward increased Th1 and reduced Th17 frequencies among total CNS infiltrating mCD4$^+$ T cells[415,418]. Delens and colleagues noted that engrafting NSG mice with whole donor PBMCs co-transplanted with naïve, in vivo polarized Th17 cells exacerbated xGvHD symptom severity and enhanced anti-tumor responses compared to Th1 polarized hCD4$^+$ T cells[677]. These findings are similar to reports describing more severe clinical EAE outcomes in recipient mice passively immunized with MOG-specific Th17 cells compared to MOG-specific Th1 cells[770,771]. As we observed relatively few hCD4$^+$IL-17A$^+$ T cells in the CNS of all HuPBMC EAE mice compared to classical EAE models, regardless of the PBMC donor EBV or RRMS status, the development of a humanized EAE model that improves Th17 responses could be more representative of human MS. Superior reconstitution of human Th17 cells has been reported to occur in HLA-A2 transgenic mice compared to regular NSG mice in the HuHSC model[487]. The inclusion of other human cytokine transgenes, such as for IL-23, IL-6, IL-1β, and TGF-β[772], may further enable expansion of Th17 cells following humanization and EAE induction in NSG mice.

The increased availability of next generation immunocompromised mouse strains also presents opportunities to investigate host tissue versus immune cell specific genetic differences in disease susceptibility in humanized EAE mice. As noted in Chapter 4, the C57Bl/6 background B6-TKO strain is an alternative genetic background to the NSG that has been used for humanization and HIV infection[500]. Our data indicates a critical role for murine macrophages in phagocytosing myelin in order to generate clinical EAE symptoms in HuPBMC-NSG EAE mice, and so HuPBMC-B6-TKO (*CD47*$^{-/-}$) mice were resistant to EAE induction. The acquisition of the newly developed C57Bl/6 background strain B6-RGS^{human}, expressing a human SIRPα transgene in addition to murine SIRPα gene deletion[501], would be an ideal comparator strain to the NSG that retains host compatible CD47 signalling and murine macrophage activity. Comparisons of NSG and B6-RGS^{human} mice engrafted with the same donor PBMCs could provide insights into host genetic and non-immune components of disease susceptibility that influence clinical phenotype and progression (e.g., sex bias, BBB integrity, CNS intrinsic factors, etc.) with immunogenetics normalized. As MOG immunization of C57Bl/6 WT mice results in a chronic monophasic clinical course[128,129], EAE induction of HuPBMC-B6-RGS^{human} mice could result in a phenotype more

akin to progressive forms of MS seen in the clinic, for which there are far fewer animal models and therapeutic options currently available[773].

Unlike NOD mice (and therefore NSG mice), C57Bl/6 mice (and therefore B6-RGS*human* mice) express an intact C5 gene required for complement activity[445], which has been described to play a role in lesion formation in MS[33,774]. Currently, JAX offers a C5 gene KI NSG strain, termed NSG-Hc1[476], that could also be used for studies investigating the role of complement in humanized EAE mice. HUMAMICE are another newer C57Bl/6 background immunocompromised mouse strain that expresses human *HLA-A2* and *HLA-DR1* with both murine MHC I and II expressing genes knocked out, which could further improve human T cell and murine host APC interactions in humanized EAE models, though they do not express human SIRPα[492]. Identifying and obtaining samples from individuals with these exact HLA genotypes could prove challenging for HuPBMC EAE model generation, but the use of different background strains could reveal important co-factor interactions between host and donor immunogenetics and concurrent environmental exposures, such as in the study performed by Zdimerova and colleagues demonstrating synergistic effects between EBV infection and HLA risk alleles on T cell activity in HuHSC-NSG mice[584]. While expanding the humanized EAE model variants into BRG background strains, including the MISTRG and BRGST[481], could be advantageous for certain studies, the resistance of the parent BALB/c strain to active EAE immunization with myelin antigens[143] does not offer much hope that BRG mice will serve as a reliable host strain for humanized EAE models.

Beyond the humanization and EAE induction of different immunocompromised strains of mice, more intensive modelling techniques could also be useful for generating model variants that reflect more complex site-specific immune responses and external factors that influence T cell autoreactivity. CNS intrinsic factors, such as mitochondrial defects and glial cell dysfunction, are proposed to play a role in disease susceptibility, though the evidence for a role of a primary neurodegenerative or demyelinating event in initiating some forms of MS remains contentious[775,776]. Unlike in EAE induction, where immunization with a specific exogenous myelin antigen is used to direct a peripheral immune response to the CNS, cuprizone autoimmune encephalomyelitis (CAE), is a model of MS wherein CNS antigens are supplied as a result of site-localized damage in the presence of nonspecific peripheral inflammation[777]. Our group has therefore begun investigating the immunopathological features of humanized CAE mice that are pre-treated with the demyelinating agent cuprizone prior to CFA immunization, in order to model

this phenomenon and evaluate the immunomodulatory effect latent EBV infection could exert on an inside-out mechanism of disease initiation, compared to the outside-in mechanism induced by EAE. In addition to the known deleterious effects of certain genetic risk alleles and prior infection with EBV, MS susceptibility and disease severity have also been linked to intestinal microbiome related environmental factors, such as diet and obesity[69], as well as to the composition of the microbiome itself[90,91,96,97]. Previous studies that have 'humanized' mice via FMT have revealed that MS patient derived fecal samples drive a more severe EAE pathology in genetically spontaneous and actively immunized recipient mice than if mice receive an FMT from a healthy donor[93,778]. Combined humanization of the immune system and microbiome by co-transfer of human PBMCs and fecal microbiota, from the same or a mismatched donor, into antibiotic treated NSG mice (the HuPooBMC model) could be used to interrogate temporal and disease dependent effects of microbial alterations on human T cell function in a model of CNS autoimmunity.

The role of human T cell activity, and the effects of currently employed DMTs for MS that are known to modulate T cell activity, could also be examined in HuPBMC EAE mice derived from select donor PBMCs. Administering the S1P receptor modulator fingolimod to HuPBMC EAE mice would further affirm the pathogenic role of CNS infiltrating human T cells by blocking their ability to traffic from lymph nodes to the CNS[57,58], and simultaneously allow for assessment of the resemblance of the therapeutic response in the model to that observed in the clinic. Likewise, anti-CD20 B cell depletion is only effective in some murine EAE models[155,157], which raises questions as to how representative these systems are of MS in people. We therefore plan to test the therapeutic effects of anti-CD20 B cell depletion in HSC-engrafted EAE models, in addition to comparing the immunopathological outcomes in the HuPBMC EAE model between NSG cohorts humanized with donor PBMCs from the same individual before and after receiving treatment for RRMS. Confirmation of the utility of known effective DMTs for MS in humanized EAE models will hopefully lend confidence to researchers in pursuit of representative systems to test novel DMTs that are difficult to evaluate in regular EAE models due to species limitations, such as monoclonal antibodies and vaccines. Furthermore, the impact of such DMTs can be further examined specifically in the context of EBV infection, as many currently used therapeutics, such as IFNβ, teriflunomide, and monoclonal antibodies, are suspected to modulate the viral reservoir in individuals with MS[104,159,350,759,779].

The development and optimization of multiple humanized EAE models could allow for direct and comprehensive investigation of the immunological mechanisms by which other human-specific risk factors influence immune cell function in the central nervous system during disease. Humanized EAE mice could also be used to circumvent the generation of costly transgenic mouse lines for immunogenetic studies. Further investigation of many proposed and suspected mechanisms by which EBV could promote disease activity in MS could likewise be interrogated in such models, in addition to assessing biomarkers of disease and personalized therapies specific to select donor genetics and immunophenotypes of interest. Ultimately, the ideal humanized mouse for studying the role of latent EBV infection in MS incorporates aspects of all above-mentioned factors and is therefore realistically achievable only by generating multiple humanized mouse models of MS covering each aspect. While no single humanized mouse model can capture the heterogeneity of MS and the full scope of human immune functions in one study, altering the combinations of humanization techniques, human immune cell donor sources, the autoimmune disease induction methods, and the immunodeficient recipient mouse strains (with differing genetic backgrounds and human transgenes that enable more complete adaptive and innate HIS reconstitution), will enable researchers to address specific neuroimmunological pathways of interest and elucidate the numerous possible roles EBV may play as a co-factor in autoimmune disease.

References

1. Dendrou, C. A., Fugger, L. & Friese, M. A. Immunopathology of multiple sclerosis. *Nat. Rev. Immunol.* **15**, 545–558 (2015).
2. Compston, A. The 150th anniversary of the first depiction of the lesions of multiple sclerosis. *J. Neurol. Neurosurg. Psychiatry* **51**, 1249–1252 (1988).
3. Cruveilhier, J. *Anatomie pathologique du corps humain; ou, Descriptions, avec figures lithographiées et coloriées, des diverses altérations morbides dont le corps humain est susceptible*. (Chez J.B. Baillière, 1842).
4. Carswell, S. R. *Pathological Anatomy: Illustrations of the Elementary Forms of Disease*. (Longman, Orme, Brown, Green and Longman, 1838).
5. Zalc, B. One hundred and fifty years ago Charcot reported multiple sclerosis as a new neurological disease. *Brain* **141**, 3482–3488 (2018).
6. Charcot, J. M. Histologie de la sclerose en plaque. *Gaz Hosp* **41**, 554–556 (1868).
7. Koch-Henriksen, N. The Danish Multiple Sclerosis Registry: a 50-year follow-up. *Mult. Scler. Houndmills Basingstoke Engl.* **5**, 293–296 (1999).
8. Banwell, B. *et al.* Clinical features and viral serologies in children with multiple sclerosis: a multinational observational study. *Lancet Neurol.* **6**, 773–781 (2007).
9. Ortona, E. *et al.* Sex-based differences in autoimmune diseases. *Ann. Ist. Super. Sanita* **52**, 205–212 (2016).
10. Rommer, P. S. *et al.* Relapsing and progressive MS: the sex-specific perspective. *Ther. Adv. Neurol. Disord.* **13**, 1756286420956495 (2020).
11. Browne, P. *et al.* Atlas of Multiple Sclerosis 2013: A growing global problem with widespread inequity. *Neurology* **83**, 1022–1024 (2014).

12. Gale, C. R. & Martyn, C. N. Migrant studies in multiple sclerosis. *Prog. Neurobiol.* **47**, 425–448 (1995).
13. Simpson, S., Blizzard, L., Otahal, P., Mei, I. V. der & Taylor, B. Latitude is significantly associated with the prevalence of multiple sclerosis: a meta-analysis. *J. Neurol. Neurosurg. Psychiatry* **82**, 1132–1141 (2011).
14. McLeod, J. G., Hammond, S. R. & Kurtzke, J. F. Migration and multiple sclerosis in immigrants to Australia from United Kingdom and Ireland: a reassessment. I. Risk of MS by age at immigration. *J. Neurol.* **258**, 1140–1149 (2011).
15. Government of Canada, S. C. Multiple sclerosis: Prevalence and impact. http://www.statcan.gc.ca/pub/82-003-x/2018001/article/54902-eng.htm (2018).
16. Walton, C. *et al.* Rising prevalence of multiple sclerosis worldwide: Insights from the Atlas of MS, third edition. *Mult. Scler. Houndmills Basingstoke Engl.* **26**, 1816–1821 (2020).
17. Nana, A. *et al.* Multiple sclerosis in Canada 2011 to 2031: results of a microsimulation modelling study of epidemiological and economic impacts. *Health Promot. Chronic Dis. Prev. Can. Res. Policy Pract.* **37**, 37–48 (2017).
18. Compston, A. & Coles, A. Multiple sclerosis. *The Lancet* **372**, 1502–1517 (2008).
19. Naci, H., Fleurence, R., Birt, J. & Duhig, A. Economic Burden of Multiple Sclerosis. *PharmacoEconomics* **28**, 363–379 (2010).
20. Feinstein, A. Multiple sclerosis and depression. *Mult. Scler. Houndmills Basingstoke Engl.* **17**, 1276–1281 (2011).
21. Klineova, S. & Lublin, F. D. Clinical Course of Multiple Sclerosis. *Cold Spring Harb. Perspect. Med.* **8**, a028928 (2018).

22. Poser, C. M. *et al.* New diagnostic criteria for multiple sclerosis: Guidelines for research protocols. *Ann. Neurol.* **13**, 227–231 (1983).

23. McDonald, W. I. *et al.* Recommended diagnostic criteria for multiple sclerosis: Guidelines from the international panel on the diagnosis of multiple sclerosis. *Ann. Neurol.* **50**, 121–127 (2001).

24. Polman, C. H. *et al.* Diagnostic criteria for multiple sclerosis: 2010 Revisions to the McDonald criteria. *Ann. Neurol.* **69**, 292–302 (2011).

25. Przybek, J., Gniatkowska, I., Mirowska-Guzel, D. & Członkowska, A. Evolution of diagnostic criteria for multiple sclerosis. *Neurol. Neurochir. Pol.* **49**, 313–321 (2015).

26. Lanz, T. V. *et al.* Clonally expanded B cells in multiple sclerosis bind EBV EBNA1 and GlialCAM. *Nature* **603**, 321–327 (2022).

27. Lumsden, C. E. Fundamental Problems in the Pathology of Multiple Sclerosis and Allied Demyelinating Diseases. *Br. Med. J.* **1**, 1035–1043 (1951).

28. Salama, S., Khan, M., Pardo, S., Izbudak, I. & Levy, M. MOG antibody associated encephalomyelitis. *Mult. Scler. Houndmills Basingstoke Engl.* **25**, 1427–1433 (2019).

29. Wingerchuk, D. M., Lucchinetti, C. F. & Noseworthy, J. H. Multiple sclerosis: current pathophysiological concepts. *Lab. Invest.* **81**, 263–281 (2001).

30. Holman, D. W., Klein, R. S. & Ransohoff, R. M. The Blood-Brain Barrier, Chemokines and Multiple Sclerosis. *Biochim. Biophys. Acta* **1812**, 220–230 (2011).

31. Bitsch, A., Schuchardt, J., Bunkowski, S., Kuhlmann, T. & Brück, W. Acute axonal injury in multiple sclerosis: Correlation with demyelination and inflammation. *Brain* **123**, 1174–1183 (2000).

32. Trapp, B. D., Bö, L., Mörk, S. & Chang, A. Pathogenesis of tissue injury in MS lesions. *J. Neuroimmunol.* **98**, 49–56 (1999).

33. Lucchinetti, C. *et al.* Heterogeneity of multiple sclerosis lesions: Implications for the pathogenesis of demyelination. *Ann. Neurol.* **47**, 707–717 (2000).

34. Beliën, J., Goris, A. & Matthys, P. Natural Killer Cells in Multiple Sclerosis: Entering the Stage. *Front. Immunol.* **13**, 869447 (2022).

35. Comi, G. *et al.* The role of B cells in Multiple Sclerosis and related disorders. *Ann. Neurol.* **89**, 13–23 (2021).

36. Koning, N., Bö, L., Hoek, R. M. & Huitinga, I. Downregulation of macrophage inhibitory molecules in multiple sclerosis lesions. *Ann. Neurol.* **62**, 504–514 (2007).

37. Mars, L. T., Saikali, P., Liblau, R. S. & Arbour, N. Contribution of CD8 T lymphocytes to the immuno-pathogenesis of multiple sclerosis and its animal models. *Biochim. Biophys. Acta* **1812**, 151–161 (2011).

38. Salou, M. *et al.* Expanded CD8 T-cell sharing between periphery and CNS in multiple sclerosis. *Ann. Clin. Transl. Neurol.* **2**, 609–622 (2015).

39. Viglietta, V., Baecher-Allan, C., Weiner, H. L. & Hafler, D. A. Loss of functional suppression by CD4+CD25+ regulatory T cells in patients with multiple sclerosis. *J. Exp. Med.* **199**, 971–979 (2004).

40. Lovett-Racke, A. E., Yang, Y. & Racke, M. K. Th1 Versus Th17: Are T Cell Cytokines Relevant in Multiple Sclerosis? *Biochim. Biophys. Acta* **1812**, 246–251 (2011).

41. Ben-Nun, A. *et al.* From classic to spontaneous and humanized models of multiple sclerosis: Impact on understanding pathogenesis and drug development. *J. Autoimmun.* **54**, 33–50 (2014).

42. Acs, P. & Kalman, B. Pathogenesis of Multiple Sclerosis: What Can We Learn from the Cuprizone Model. in *Autoimmunity* (ed. Perl, A.) 403–431 (Humana Press, 2012). doi:10.1007/978-1-60761-720-4_20.

43. Ponath, G., Park, C. & Pitt, D. The Role of Astrocytes in Multiple Sclerosis. *Front. Immunol.* **9**, 217 (2018).

44. Dong, Y. & Yong, V. W. When encephalitogenic T cells collaborate with microglia in multiple sclerosis. *Nat. Rev. Neurol.* **15**, 704–717 (2019).

45. Pinto, C., Cambron, M., Dobai, A., Vanheule, E. & Casselman, J. W. Smoldering lesions in MS: if you like it then you should put a rim on it. *Neuroradiology* **64**, 703–714 (2022).

46. Frischer, J. M. *et al.* Clinical and Pathological Insights into the Dynamic Nature of the White Matter Multiple Sclerosis Plaque. *Ann. Neurol.* **78**, 710–721 (2015).

47. Eshaghi, A. *et al.* Progression of regional grey matter atrophy in multiple sclerosis. *Brain* **141**, 1665–1677 (2018).

48. Andravizou, A. *et al.* Brain atrophy in multiple sclerosis: mechanisms, clinical relevance and treatment options. *Autoimmun. Highlights* **10**, 7 (2019).

49. ‘tHart, B. A., Kap, Y. S., Morandi, E., Laman, J. D. & Gran, B. EBV Infection and Multiple Sclerosis: Lessons from a Marmoset Model. *Trends Mol. Med.* **22**, 1012–1024 (2016).

50. Constantinescu, C. S., Farooqi, N., O’Brien, K. & Gran, B. Experimental autoimmune encephalomyelitis (EAE) as a model for multiple sclerosis (MS). *Br. J. Pharmacol.* **164**, 1079–1106 (2011).

51. Cree, B. A. C. *et al.* Secondary Progressive Multiple Sclerosis: New Insights. *Neurology* **97**, 378–388 (2021).

52. Pikor, N. B., Prat, A., Bar-Or, A. & Gommerman, J. L. Meningeal Tertiary Lymphoid Tissues and Multiple Sclerosis: A Gathering Place for Diverse Types of Immune Cells during CNS Autoimmunity. *Front. Immunol.* **6**, (2016).

53. Bieniek, M. *et al.* Cord atrophy separates early primary progressive and relapsing remitting multiple sclerosis. *J. Neurol. Neurosurg. Psychiatry* **77**, 1036–1039 (2006).

54. Antel, J., Antel, S., Caramanos, Z., Arnold, D. L. & Kuhlmann, T. Primary progressive multiple sclerosis: part of the MS disease spectrum or separate disease entity? *Acta Neuropathol. (Berl.)* **123**, 627–638 (2012).

55. Sweeney, C. M. *et al.* IL-27 mediates the response to IFN-β therapy in multiple sclerosis patients by inhibiting Th17 cells. *Brain. Behav. Immun.* **25**, 1170–1181 (2011).

56. Teitelbaum, D., Meshorer, A., Hirshfeld, T., Arnon, R. & Sela, M. Suppression of experimental allergic encephalomyelitis by a synthetic polypeptide. *Eur. J. Immunol.* **1**, 242–248 (1971).

57. Singer, B. A. Initiating oral fingolimod treatment in patients with multiple sclerosis. *Ther. Adv. Neurol. Disord.* **6**, 269–275 (2013).

58. Dominguez-Villar, M., Raddassi, K., Danielsen, A. C., Guarnaccia, J. & Hafler, D. A. Fingolimod modulates T cell phenotype and regulatory T cell plasticity in vivo. *J. Autoimmun.* **96**, 40–49 (2019).

59. Cinamon, G. *et al.* Sphingosine 1-phosphate receptor 1 promotes B cell localization in the splenic marginal zone. *Nat. Immunol.* **5**, 713–720 (2004).

60. Sic, H. *et al.* Sphingosine-1-phosphate receptors control B-cell migration through signaling components associated with primary immunodeficiencies, chronic lymphocytic leukemia, and multiple sclerosis. *J. Allergy Clin. Immunol.* **134**, 420–428 (2014).

61. van Oosten, B. W. *et al.* Treatment of multiple sclerosis with the monoclonal anti-CD4 antibody cM-T412: results of a randomized, double-blind, placebo-controlled, MR-monitored phase II trial. *Neurology* **49**, 351–357 (1997).

62. Allanach, J. R., Farrell, J. W., Mésidor, M. & Karimi-Abdolrezaee, S. Current status of neuroprotective and neuroregenerative strategies in multiple sclerosis: A systematic review. *Mult. Scler.* **28**, 29–48 (2022).

63. Regner-Nelke, L. *et al.* Real-world evidence on siponimod treatment in patients with secondary progressive multiple sclerosis. *Neurol. Res. Pract.* **4**, 55 (2022).

64. Khoy, K. *et al.* Natalizumab in Multiple Sclerosis Treatment: From Biological Effects to Immune Monitoring. *Front. Immunol.* **11**, (2020).

65. Hauser, S. L. *et al.* B-Cell Depletion with Rituximab in Relapsing–Remitting Multiple Sclerosis. *N. Engl. J. Med.* **358**, 676–688 (2008).

66. Miller, A. E. *et al.* Autologous Hematopoietic Stem Cell Transplant in Multiple Sclerosis: Recommendations of the National Multiple Sclerosis Society. *JAMA Neurol.* **78**, 241–246 (2021).

67. Rolfes, L. *et al.* Failed, Interrupted, or Inconclusive Trials on Immunomodulatory Treatment Strategies in Multiple Sclerosis: Update 2015–2020. *BioDrugs* **34**, 587–610 (2020).

68. Iwanowski, P. & Losy, J. Immunological differences between classical phenothypes of multiple sclerosis. *J. Neurol. Sci.* **349**, 10–14 (2015).

69. Olsson, T., Barcellos, L. F. & Alfredsson, L. Interactions between genetic, lifestyle and environmental risk factors for multiple sclerosis. *Nat. Rev. Neurol.* **13**, 25–36 (2017).

70. Dyment, D. A., Ebers, G. C. & Dessa Sadovnick, A. Genetics of multiple sclerosis. *Lancet Neurol.* **3**, 104–110 (2004).

71. Ebers, G. C., Sadovnick, A. D. & Risch, N. J. A genetic basis for familial aggregation in multiple sclerosis. *Nature* **377**, 150–151 (1995).

72. Parnell, G. P. & Booth, D. R. The Multiple Sclerosis (MS) Genetic Risk Factors Indicate both Acquired and Innate Immune Cell Subsets Contribute to MS Pathogenesis and Identify Novel Therapeutic Opportunities. *Front. Immunol.* **8**, (2017).

73. Willer, C. J., Dyment, D. A., Risch, N. J., Sadovnick, A. D. & Ebers, G. C. Twin concordance and sibling recurrence rates in multiple sclerosis. *Proc. Natl. Acad. Sci. U. S. A.* **100**, 12877–12882 (2003).

74. Ascherio, A., Munger, K. L. & Lünemann, J. D. The initiation and prevention of multiple sclerosis. *Nat. Rev. Neurol.* **8**, 602–612 (2012).

75. Gourraud, P.-A., Harbo, H. F., Hauser, S. L. & Baranzini, S. E. The genetics of multiple sclerosis: an up-to-date review. *Immunol. Rev.* **248**, 87–103 (2012).

76. Stürner, K. H. *et al.* Is multiple sclerosis progression associated with the HLA-DR15 haplotype? *Mult. Scler. J. - Exp. Transl. Clin.* **5**, 2055217319894615 (2019).

77. Frau, J., Coghe, G., Lorefice, L., Fenu, G. & Cocco, E. Infections and Multiple Sclerosis: From the World to Sardinia, From Sardinia to the World. *Front. Immunol.* **12**, 728677 (2021).

78. Grytten, N., Aarseth, J. H., Lunde, H. M. B. & Myhr, K. M. A 60-year follow-up of the incidence and prevalence of multiple sclerosis in Hordaland County, Western Norway. *J. Neurol. Neurosurg. Psychiatry* **87**, 100–105 (2016).

79. Sospedra, M. & Martin, R. IMMUNOLOGY OF MULTIPLE SCLEROSIS*. *Annu. Rev. Immunol.* **23**, 683–747 (2005).

80. Wang, J. *et al.* HLA-DR15 Molecules Jointly Shape an Autoreactive T Cell Repertoire in Multiple Sclerosis. *Cell* **183**, 1264-1281.e20 (2020).

81. Belman, A. L. *et al.* Characteristics of Children and Adolescents With Multiple Sclerosis. *Pediatrics* **138**, e20160120 (2016).

82. McKay, K. A., Jahanfar, S., Duggan, T., Tkachuk, S. & Tremlett, H. Factors associated with onset, relapses or progression in multiple sclerosis: A systematic review. *NeuroToxicology* **61**, 189–212 (2017).

83. Cortese, M. *et al.* Vitamin D, smoking, EBV, and long-term cognitive performance in MS. *Neurology* **94**, e1950–e1960 (2020).

84. Muris, A.-H. *et al.* Immune regulatory effects of high dose vitamin D3 supplementation in a randomized controlled trial in relapsing remitting multiple sclerosis patients receiving IFNβ; the SOLARIUM study. *J. Neuroimmunol.* **300**, 47–56 (2016).

85. Ramagopalan, S. V. *et al.* Expression of the Multiple Sclerosis-Associated MHC Class II Allele HLA-DRB1*1501 Is Regulated by Vitamin D. *PLoS Genet.* **5**, e1000369 (2009).

86. Povolo, C. A., Reid, J. N., Shariff, S. Z., Welk, B. & Morrow, S. A. Concussion in adolescence and the risk of multiple sclerosis: A retrospective cohort study. *Mult. Scler. Houndmills Basingstoke Engl.* **27**, 180–187 (2021).

87. Harroud, A. *et al.* The relative contributions of obesity, vitamin D, leptin, and adiponectin to multiple sclerosis risk: A Mendelian randomization mediation analysis. *Mult. Scler. J.* **27**, 1994–2000 (2021).

88. Hedström, A. K., Bäärnhielm, M., Olsson, T. & Alfredsson, L. Tobacco smoking, but not Swedish snuff use, increases the risk of multiple sclerosis. *Neurology* **73**, 696–701 (2009).

89. Noorimotlagh, Z., Azizi, M., Pan, H.-F., Mami, S. & Mirzaee, S. A. Association between air pollution and Multiple Sclerosis: A systematic review. *Environ. Res.* **196**, 110386 (2021).

90. Miyake, S. *et al.* Dysbiosis in the Gut Microbiota of Patients with Multiple Sclerosis, with a Striking Depletion of Species Belonging to Clostridia XIVa and IV Clusters. *PLoS ONE* **10**, (2015).

91. Tremlett, H. *et al.* Gut microbiota in early pediatric multiple sclerosis: a case−control study. *Eur. J. Neurol.* n/a-n/a (2016) doi:10.1111/ene.13026.

92. Berer, K. *et al.* Gut microbiota from multiple sclerosis patients enables spontaneous autoimmune encephalomyelitis in mice. *Proc. Natl. Acad. Sci.* 201711233 (2017) doi:10.1073/pnas.1711233114.

93. Cekanaviciute, E. *et al.* Gut bacteria from multiple sclerosis patients modulate human T cells and exacerbate symptoms in mouse models. *Proc. Natl. Acad. Sci. U. S. A.* 201711235 (2017) doi:10.1073/pnas.1711235114.

94. Fettig, N. M. *et al.* Inhibition of Th1 activation and differentiation by dietary guar gum ameliorates experimental autoimmune encephalomyelitis. *Cell Rep.* **40**, (2022).

95. Muszer, M., Noszczyńska, M., Kasperkiewicz, K. & Skurnik, M. Human Microbiome: When a Friend Becomes an Enemy. *Arch. Immunol. Ther. Exp. (Warsz.)* **63**, 287–298 (2015).

96. Bhargava, P. & Mowry, E. M. Gut Microbiome and Multiple Sclerosis. *Curr. Neurol. Neurosci. Rep.* **14**, 1–8 (2014).

97. Wang, Y. & Kasper, L. H. The role of microbiome in central nervous system disorders. *Brain. Behav. Immun.* **38**, 1–12 (2014).

98. Wendel-Haga, M. & Celius, E. G. Is the hygiene hypothesis relevant for the risk of multiple sclerosis? *Acta Neurol. Scand.* **136**, 26–30 (2017).

99. Charabati, M., Donkers, S. J., Kirkland, M. C. & Osborne, L. C. A critical analysis of helminth immunotherapy in multiple sclerosis. *Mult. Scler. J.* **26**, 1448–1458 (2020).

100. Kurtzke, J. F. & Heltberg, A. Multiple sclerosis in the Faroe Islands: an epitome. *J. Clin. Epidemiol.* **54**, 1–22 (2001).

101. Meier, U.-C., Cipian, R. C., Karimi, A., Ramasamy, R. & Middeldorp, J. M. Cumulative Roles for Epstein-Barr Virus, Human Endogenous Retroviruses, and Human Herpes Virus-6 in Driving an Inflammatory Cascade Underlying MS Pathogenesis. *Front. Immunol.* **12**, 757302 (2021).

102. Winger, R. C. & Zamvil, S. S. Antibodies in multiple sclerosis oligoclonal bands target debris. *Proc. Natl. Acad. Sci.* **113**, 7696–7698 (2016).

103. Brändle, S. M. *et al.* Distinct oligoclonal band antibodies in multiple sclerosis recognize ubiquitous self-proteins. *Proc. Natl. Acad. Sci.* **113**, 7864–7869 (2016).

104. Bar-Or, A. *et al.* Epstein–Barr Virus in Multiple Sclerosis: Theory and Emerging Immunotherapies. *Trends Mol. Med.* **26**, 296–310 (2020).

105. Xu, L. *et al.* Positive association of herpes simplex virus-IgG with multiple sclerosis: A systematic review and meta-analysis. *Mult. Scler. Relat. Disord.* **47**, 102633 (2021).

106. Kang, J.-H., Sheu, J.-J., Kao, S. & Lin, H.-C. Increased risk of multiple sclerosis following herpes zoster: a nationwide, population-based study. *J. Infect. Dis.* **204**, 188–192 (2011).

107. Ferrante, P. *et al.* Molecular evidences for a role of HSV-1 in multiple sclerosis clinical acute attack. *J. Neurovirol.* **6 Suppl 2**, S109-114 (2000).

108. Kofahi, R. M. *et al.* Prevalence of seropositivity of selected herpesviruses in patients with multiple sclerosis in the North of Jordan. *BMC Neurol.* **20**, 397 (2020).

109. Bjornevik, K. *et al.* Longitudinal analysis reveals high prevalence of Epstein-Barr virus associated with multiple sclerosis. *Science* **375**, 296–301 (2022).

110. Comabella, M. *et al.* Increased cytomegalovirus immune responses at disease onset are protective in the long-term prognosis of patients with multiple sclerosis. *J. Neurol. Neurosurg. Psychiatry* jnnp-2022-330205 (2022) doi:10.1136/jnnp-2022-330205.

111. Grut, V. *et al.* Cytomegalovirus seropositivity is associated with reduced risk of multiple sclerosis-a presymptomatic case-control study. *Eur. J. Neurol.* **28**, 3072–3079 (2021).

112. Langer-Gould, A. *et al.* Epstein-Barr virus, cytomegalovirus, and multiple sclerosis susceptibility. *Neurology* **89**, 1330–1337 (2017).

113. Perron, H. & Lang, A. The human endogenous retrovirus link between genes and environment in multiple sclerosis and in multifactorial diseases associating neuroinflammation. *Clin. Rev. Allergy Immunol.* **39**, 51–61 (2010).

114. Firouzi, R. *et al.* Multiple sclerosis-associated retrovirus particles cause T lymphocyte-dependent death with brain hemorrhage in humanized SCID mice model. *J. Neurovirol.* **9**, 79–93 (2003).

115. Diebold, M. & Derfuss, T. The monoclonal antibody GNbAC1: targeting human endogenous retroviruses in multiple sclerosis. *Ther. Adv. Neurol. Disord.* **12**, 1756286419833574 (2019).

116. Makhani, N. & Tremlett, H. The multiple sclerosis prodrome. *Nat. Rev. Neurol.* **17**, 515–521 (2021).

117. Goudarzvand, M. *et al.* Focal Injection of Ethidium Bromide as a Simple Model to Study Cognitive Deficit and Its Improvement. *Basic Clin. Neurosci.* **7**, 63–72 (2016).

118. Miller, R. H., Fyffe-Maricich, S. & Caprariello, A. C. Chapter 37 - Animal Models for the Study of Multiple Sclerosis. in *Animal Models for the Study of Human Disease (Second Edition)* (ed. Conn, P. M.) 967–988 (Academic Press, 2017). doi:10.1016/B978-0-12-809468-6.00037-1.

119. McCarthy, D. P., Richards, M. H. & Miller, S. D. Mouse Models of Multiple Sclerosis: Experimental Autoimmune Encephalomyelitis and Theiler's Virus-Induced Demyelinating Disease. *Methods Mol. Biol.* **900**, 381–401 (2012).

120. DePaula-Silva, A. B., Hanak, T. J., Libbey, J. E. & Fujinami, R. S. Theiler's Murine Encephalomyelitis Virus Infection of SJL/J and C57BL/6J Mice: Models for Multiple Sclerosis and Epilepsy. *J. Neuroimmunol.* **308**, 30 (2017).

121. Miller, S. D. *et al.* Persistent infection with Theiler's virus leads to CNS autoimmunity via epitope spreading. *Nat. Med.* **3**, 1133–1136 (1997).

122. Biswas, K. *et al.* Demyelinating strain of mouse hepatitis virus infection bridging innate and adaptive immune response in the induction of demyelination. *Clin. Immunol. Orlando Fla* **170**, 9–19 (2016).

123. Rivers, T. M., Sprunt, D. H. & Berry, G. P. OBSERVATIONS ON ATTEMPTS TO PRODUCE ACUTE DISSEMINATED ENCEPHALOMYELITIS IN MONKEYS. *J. Exp. Med.* **58**, 39–53 (1933).

124. Van Epps, H. L. Thomas Rivers and the EAE model. *J. Exp. Med.* **202**, 4 (2005).

125. Hurst, E. W. The Effects of the Injection of Normal Brain Emulsion into Rabbits, with Special Reference to the Aetiology of the Paralytic Accidents of Antirabic Treatment. *J. Hyg. (Lond.)* **32**, 33–44 (1932).

126. Kabat, E. A., Wolf, A. & Bezer, A. E. THE RAPID PRODUCTION OF ACUTE DISSEMINATED ENCEPHALOMYELITIS IN RHESUS MONKEYS BY INJECTION OF HETEROLOGOUS AND HOMOLOGOUS BRAIN TISSUE WITH ADJUVANTS. *J. Exp. Med.* **85**, 117–130 (1947).

127. Taylor, W. Experimental Allergic Encephalomyelitis. A Useful Model for Multiple Sclerosis. Progress in Clinical and Biological Research Vol 146. *J. Neurol. Neurosurg. Psychiatry* **49**, 339–340 (1986).

128. Simmons, S. B., Pierson, E. R., Lee, S. Y. & Goverman, J. M. Modeling the Heterogeneity of Multiple Sclerosis in Animals. *Trends Immunol.* **34**, 410–422 (2013).

129. Miller, S. D., Karpus, W. J. & Davidson, T. S. Experimental Autoimmune Encephalomyelitis in the Mouse. *Curr. Protoc. Immunol.* **CHAPTER**, Unit-15.1 (2007).

130. Muller, D. M., Pender, M. P. & Greer, J. M. A neuropathological analysis of experimental autoimmune encephalomyelitis with predominant brain stem and cerebellar involvement and differences between active and passive induction. *Acta Neuropathol. (Berl.)* **100**, 174–182 (2000).

131. Wagner, C. A., Roqué, P. J., Mileur, T. R., Liggitt, D. & Goverman, J. M. Myelin-specific CD8+ T cells exacerbate brain inflammation in CNS autoimmunity. *J. Clin. Invest.* **130**, 203–213 (2020).

132. Khare, P. *et al.* Myelin oligodendrocyte glycoprotein-specific antibodies from multiple sclerosis patients exacerbate disease in a humanized mouse model. *J. Autoimmun.* **86**, 104–115 (2018).

133. Bettelli, E. *et al.* Myelin oligodendrocyte glycoprotein-specific T cell receptor transgenic mice develop spontaneous autoimmune optic neuritis. *J. Exp. Med.* **197**, 1073–1081 (2003).

134. Anderson, A. C. *et al.* A transgenic model of central nervous system autoimmunity mediated by CD4+ and CD8+ T and B cells. *J. Immunol. Baltim. Md 1950* **188**, 2084–2092 (2012).

135. Bettelli, E., Baeten, D., Jäger, A., Sobel, R. A. & Kuchroo, V. K. Myelin oligodendrocyte glycoprotein–specific T and B cells cooperate to induce a Devic-like disease in mice. *J. Clin. Invest.* **116**, 2393–2402 (2006).

136. Awate, S., Babiuk, L. & Mutwiri, G. Mechanisms of Action of Adjuvants. *Front. Immunol.* **4**, (2013).

137. Root-Bernstein, R. Synergistic Activation of Toll-Like and NOD Receptors by Complementary Antigens as Facilitators of Autoimmune Disease: Review, Model and Novel Predictions. *Int. J. Mol. Sci.* **21**, 4645 (2020).

138. Wagner, C. A. & Goverman, J. M. Novel Insights and Therapeutics in Multiple Sclerosis. *F1000Research* **4**, (2015).

139. Ignatius Arokia Doss, P. M., Roy, A.-P., Wang, A., Anderson, A. C. & Rangachari, M. The Non-Obese Diabetic Mouse Strain as a Model to Study CD8+ T Cell Function in Relapsing and Progressive Multiple Sclerosis. *Front. Immunol.* **6**, (2015).

140. Koutrolos, M., Berer, K., Kawakami, N., Wekerle, H. & Krishnamoorthy, G. Treg cells mediate recovery from EAE by controlling effector T cell proliferation and motility in the CNS. *Acta Neuropathol. Commun.* **2**, 163 (2014).

141. Segal, B. M. *et al.* Repeated subcutaneous injections of IL12/23 p40 neutralising antibody, ustekinumab, in patients with relapsing-remitting multiple sclerosis: a phase II, double-blind, placebo-controlled, randomised, dose-ranging study. *Lancet Neurol.* **7**, 796–804 (2008).

142. Levine, S. & Sowinski, R. Experimental Allergic Encephalomyelitis in Inbred and Outbred Mice. *J. Immunol.* **110**, 139–143 (1973).

143. Hurwitz, A. A., Sullivan, T. J., Sobel, R. A. & Allison, J. P. Cytotoxic T lymphocyte antigen-4 (CTLA-4) limits the expansion of encephalitogenic T cells in experimental autoimmune encephalomyelitis (EAE)-resistant BALB/c mice. *Proc. Natl. Acad. Sci.* **99**, 3013–3017 (2002).

144. Baker, D. *et al.* Autoimmune encephalomyelitis in NOD mice is not initially a progressive multiple sclerosis model. *Ann. Clin. Transl. Neurol.* **6**, 1362–1372 (2019).

145. Dang, P. T., Bui, Q., D'Souza, C. S. & Orian, J. M. Modelling MS: Chronic-Relapsing EAE in the NOD/Lt Mouse Strain. in *Emerging and Evolving Topics in Multiple Sclerosis Pathogenesis and Treatments* (eds. La Flamme, A. C. & Orian, J. M.) 143–177 (Springer International Publishing, 2015). doi:10.1007/7854_2015_378.

146. Al-Izki, S. *et al.* Practical guide to the induction of relapsing progressive experimental autoimmune encephalomyelitis in the Biozzi ABH mouse. *Mult. Scler. Relat. Disord.* **1**, 29–38 (2012).

147. Zamvil, S. S. *et al.* T-cell epitope of the autoantigen myelin basic protein that induces encephalomyelitis. *Nature* **324**, 258–260 (1986).

148. Mendel, I., de Rosbo, N. K. & Ben-Nun, A. A myelin oligodendrocyte glycoprotein peptide induces typical chronic experimental autoimmune encephalomyelitis in H-2b mice: Fine specificity and T cell receptor Vβ expression of encephalitogenic T cells. *Eur. J. Immunol.* **25**, 1951–1959 (1995).

149. Oliver, A. R., Lyon, G. M. & Ruddle, N. H. Rat and Human Myelin Oligodendrocyte Glycoproteins Induce Experimental Autoimmune Encephalomyelitis by Different Mechanisms in C57BL/6 Mice. *J. Immunol.* **171**, 462–468 (2003).

150. Amor, S. *et al.* Identification of epitopes of myelin oligodendrocyte glycoprotein for the induction of experimental allergic encephalomyelitis in SJL and Biozzi AB/H mice. *J. Immunol.* **153**, 4349–4356 (1994).

151. Pham, H. *et al.* Experimental autoimmune encephalomyelitis (EAE) IN C57Bl/6 mice is not associated with astrogliosis. *J. Neuroimmunol.* **232**, 51–62 (2011).

152. Kuerten, S. & Angelov, D. N. Comparing the CNS morphology and immunobiology of different EAE models in C57BL/6 mice – A step towards understanding the complexity of multiple sclerosis. *Ann. Anat. - Anat. Anz.* **190**, 1–15 (2008).

153. Linker, R. A. & Gold, R. MBP-Induced Experimental Autoimmune Encephalomyelitis in C57BL/6 Mice. *J. Immunol.* **173**, 2896 (2004).

154. Berard, J. L., Wolak, K., Fournier, S. & David, S. Characterization of relapsing–remitting and chronic forms of experimental autoimmune encephalomyelitis in C57BL/6 mice. *Glia* **58**, 434–445 (2010).

155. Lyons, J.-A., San, M., Happ, M. P. & Cross, A. H. B cells are critical to induction of experimental allergic encephalomyelitis by protein but not by a short encephalitogenic peptide. *Eur. J. Immunol.* **29**, 3432–3439 (1999).

156. Marta, C. B., Oliver, A. R., Sweet, R. A., Pfeiffer, S. E. & Ruddle, N. H. Pathogenic myelin oligodendrocyte glycoprotein antibodies recognize glycosylated epitopes and perturb oligodendrocyte physiology. *Proc. Natl. Acad. Sci. U. S. A.* **102**, 13992–13997 (2005).

157. Weber, M. S. *et al.* B cell activation influences T cell polarization and outcome of anti-CD20 B cell depletion in CNS autoimmunity. *Ann. Neurol.* **68**, 369–383 (2010).

158. Axthelm, M. K. *et al.* Japanese macaque encephalomyelitis: a spontaneous multiple sclerosis-like disease in a nonhuman primate. *Ann. Neurol.* **70**, 362–373 (2011).

159. Jagessar, S. A. *et al.* The Different Clinical Effects of Anti-BLyS, Anti-APRIL and Anti-CD20 Antibodies Point at a Critical Pathogenic Role of γ-Herpesvirus Infected B Cells in the Marmoset EAE Model. *J. Neuroimmune Pharmacol.* **8**, 727–738 (2013).

160. Hart, 't *et al.* A B Cell-Driven Autoimmune Pathway Leading to Pathological Hallmarks of Progressive Multiple Sclerosis in the Marmoset Experimental Autoimmune Encephalomyelitis Model. *Front. Immunol.* **8**, (2017).

161. Kulkarni, P. *et al.* Novel Zebrafish EAE model: A quick in vivo screen for multiple sclerosis. *Mult. Scler. Relat. Disord.* **11**, 32–39 (2017).

162. Epstein, M. A., Achong, B. G. & Barr, Y. M. VIRUS PARTICLES IN CULTURED LYMPHOBLASTS FROM BURKITT'S LYMPHOMA. *Lancet Lond. Engl.* **1**, 702–703 (1964).

163. Epstein, M. A. Historical background. *Philos. Trans. R. Soc. Lond. Ser. B* **356**, 413–420 (2001).

164. McGeoch, D. J., Cook, S., Dolan, A., Jamieson, F. E. & Telford, E. A. Molecular phylogeny and evolutionary timescale for the family of mammalian herpesviruses. *J. Mol. Biol.* **247**, 443–458 (1995).

165. Cadwell, K. The virome in host health and disease. *Immunity* **42**, 805–813 (2015).

166. White, D. W., Beard, R. S. & Barton, E. S. Immune Modulation During Latent Herpesvirus Infection. *Immunol. Rev.* **245**, 189–208 (2012).

167. Whitley, R. J. Herpesviruses. in *Medical Microbiology* (ed. Baron, S.) (University of Texas Medical Branch at Galveston, 1996).

168. Gantt, S. *et al.* Prospective Characterization of the Risk Factors for Transmission and Symptoms of Primary Human Herpesvirus Infections Among Ugandan Infants. *J. Infect. Dis.* **214**, 36–44 (2016).

169. Carlson, A., Norwitz, E. R. & Stiller, R. J. Cytomegalovirus Infection in Pregnancy: Should All Women Be Screened? *Rev. Obstet. Gynecol.* **3**, 172–179 (2010).

170. Dunmire, S. K., Hogquist, K. A. & Balfour, H. H. Infectious Mononucleosis. *Curr. Top. Microbiol. Immunol.* **390**, 211–240 (2015).

171. Lang, D. J., Garruto, R. M. & Gajdusek, D. C. Early acquisition of cytomegalovirus and Epstein-Barr virus antibody in several isolated Melanesian populations. *Am. J. Epidemiol.* **105**, 480–487 (1977).

172. Hjalgrim, H., Friborg, J. & Melbye, M. The epidemiology of EBV and its association with malignant disease. in *Human Herpesviruses: Biology, Therapy, and Immunoprophylaxis* (eds. Arvin, A. et al.) (Cambridge University Press, 2007).

173. Ling, P. D. *et al.* The dynamics of herpesvirus and polyomavirus reactivation and shedding in healthy adults: a 14-month longitudinal study. *J. Infect. Dis.* **187**, 1571–1580 (2003).

174. McGeoch, D. J. Molecular evolution of the gamma-Herpesvirinae. *Philos. Trans. R. Soc. Lond. Ser. B* **356**, 421–435 (2001).

175. Correia, S. *et al.* Sequence Variation of Epstein-Barr Virus: Viral Types, Geography, Codon Usage, and Diseases. *J. Virol.* **92**, e01132-18 (2018).

176. Lin, Z. *et al.* Whole-Genome Sequencing of the Akata and Mutu Epstein-Barr Virus Strains. *J. Virol.* **87**, 1172–1182 (2013).

177. Walling, D. M., Brown, A. L., Etienne, W., Keitel, W. A. & Ling, P. D. Multiple Epstein-Barr Virus Infections in Healthy Individuals. *J. Virol.* **77**, 6546–6550 (2003).

178. Monteiro, T. A. F. *et al.* Genotypes of Epstein–Barr virus (EBV1/EBV2) in individuals with infectious mononucleosis in the metropolitan area of Belém, Brazil, between 2005 and 2016. *Braz. J. Infect. Dis.* **24**, 322–329 (2020).

179. Sixbey, J. W., Chesney, P. J., Shirley, P., Buntin, D. M. & Resnick, L. Detection of a second widespread strain of Epstein-Barr virus. *The Lancet* **334**, 761–765 (1989).

180. Skalsky, R. L. & Cullen, B. R. EBV Noncoding RNAs. *Curr. Top. Microbiol. Immunol.* **391**, 181–217 (2015).

181. Bu, G.-L., Xie, C., Kang, Y.-F., Zeng, M.-S. & Sun, C. How EBV Infects: The Tropism and Underlying Molecular Mechanism for Viral Infection. *Viruses* **14**, 2372 (2022).

182. Xiao, J., Palefsky, J. M., Herrera, R., Berline, J. & Tugizov, S. M. The Epstein-Barr Virus BMRF-2 Protein Facilitates Virus Attachment to Oral Epithelial Cells. *Virology* **370**, 430–442 (2008).

183. Zhang, H. *et al.* Ephrin receptor A2 is an epithelial cell receptor for Epstein–Barr virus entry. *Nat. Microbiol.* **3**, 1–8 (2018).

184. Hoover, S. E., Kawada, J., Wilson, W. & Cohen, J. I. Oropharyngeal shedding of Epstein-Barr virus in the absence of circulating B cells. *J. Infect. Dis.* **198**, 318–323 (2008).

185. Wang, X., Kenyon, W. J., Li, Q., Müllberg, J. & Hutt-Fletcher, L. M. Epstein-Barr Virus Uses Different Complexes of Glycoproteins gH and gL To Infect B Lymphocytes and Epithelial Cells. *J. Virol.* **72**, 5552–5558 (1998).

186. Borza, C. M. & Hutt-Fletcher, L. M. Alternate replication in B cells and epithelial cells switches tropism of Epstein-Barr virus. *Nat. Med.* **8**, 594–599 (2002).

187. Odumade, O. A., Hogquist, K. A. & Balfour, H. H. Progress and Problems in Understanding and Managing Primary Epstein-Barr Virus Infections. *Clin. Microbiol. Rev.* **24**, 193–209 (2011).

188. Yager, J. E. *et al.* Valganciclovir for the Suppression of Epstein-Barr Virus Replication. *J. Infect. Dis.* **216**, 198–202 (2017).

189. Baer, R. *et al.* DNA sequence and expression of the B95-8 Epstein—Barr virus genome. *Nature* **310**, 207–211 (1984).

190. Kimura, H. *et al.* Quantitative Analysis of Epstein-Barr Virus Load by Using a Real-Time PCR Assay. *J. Clin. Microbiol.* **37**, 132–136 (1999).

191. Kenney, S. C. Reactivation and lytic replication of EBV. in *Human Herpesviruses: Biology, Therapy, and Immunoprophylaxis* (eds. Arvin, A. et al.) (Cambridge University Press, 2007).

192. Lieberman, P. M. Keeping it quiet: chromatin control of gammaherpesvirus latency. *Nat. Rev. Microbiol.* **11**, 863–875 (2013).

193. Kang, M.-S. & Kieff, E. Epstein–Barr virus latent genes. *Exp. Mol. Med.* **47**, e131 (2015).

194. Kanda, T. EBV-Encoded Latent Genes. in *Human Herpesviruses* (eds. Kawaguchi, Y., Mori, Y. & Kimura, H.) 377–394 (Springer, 2018). doi:10.1007/978-981-10-7230-7_17.

195. Styles, C. T. *et al.* EBV epigenetically suppresses the B cell-to-plasma cell differentiation pathway while establishing long-term latency. *PLoS Biol.* **15**, e2001992 (2017).

196. Murata, T. Encyclopedia of EBV-Encoded Lytic Genes: An Update. in *Human Herpesviruses* (eds. Kawaguchi, Y., Mori, Y. & Kimura, H.) 395–412 (Springer, 2018). doi:10.1007/978-981-10-7230-7_18.

197. Wentink, M. W. J. *et al.* CD21 and CD19 deficiency: Two defects in the same complex leading to different disease modalities. *Clin. Immunol.* **161**, 120–127 (2015).

198. Cui, X. & Snapper, C. M. Epstein Barr Virus: Development of Vaccines and Immune Cell Therapy for EBV-Associated Diseases. *Front. Immunol.* **12**, 734471 (2021).

199. Klutts, J. S., Ford, B. A., Perez, N. R. & Gronowski, A. M. Evidence-Based Approach for Interpretation of Epstein-Barr Virus Serological Patterns. *J. Clin. Microbiol.* **47**, 3204–3210 (2009).

200. Middeldorp, J. M. Epstein-Barr Virus-Specific Humoral Immune Responses in Health and Disease. in *Epstein Barr Virus Volume 2: One Herpes Virus: Many Diseases* (ed. Münz, C.) 289–323 (Springer International Publishing, 2015). doi:10.1007/978-3-319-22834-1_10.

201. Liu, Z. *et al.* Multilaboratory Assessment of Epstein-Barr Virus Serologic Assays: the Case for Standardization. *J. Clin. Microbiol.* **57**, e01107-19 (2019).

202. Levitskaya, J., Sharipo, A., Leonchiks, A., Ciechanover, A. & Masucci, M. G. Inhibition of ubiquitin/proteasome-dependent protein degradation by the Gly-Ala repeat domain of the Epstein–Barr virus nuclear antigen 1. *Proc. Natl. Acad. Sci. U. S. A.* **94**, 12616–12621 (1997).

203. Tempera, I. & Lieberman, P. M. Chromatin Organization of Gammaherpesvirus Latent Genomes. *Biochim. Biophys. Acta* **1799**, 236–245 (2010).

204. Sarkari, F. *et al.* EBNA1-Mediated Recruitment of a Histone H2B Deubiquitylating Complex to the Epstein-Barr Virus Latent Origin of DNA Replication. *PLoS Pathog.* **5**, e1000624 (2009).

205. Laichalk, L. L. & Thorley-Lawson, D. A. Terminal Differentiation into Plasma Cells Initiates the Replicative Cycle of Epstein-Barr Virus In Vivo. *J. Virol.* **79**, 1296–1307 (2005).

206. Sausen, D. G., Bhutta, M. S., Gallo, E. S., Dahari, H. & Borenstein, R. Stress-Induced Epstein-Barr Virus Reactivation. *Biomolecules* **11**, 1380 (2021).

207. Moquin, S. A. *et al.* The Epstein-Barr Virus Episome Maneuvers between Nuclear Chromatin Compartments during Reactivation. *J. Virol.* **92**, e01413-17 (2018).

208. Kanda, T., Yajima, M. & Ikuta, K. Epstein-Barr virus strain variation and cancer. *Cancer Sci.* **110**, 1132–1139 (2019).

209. Romero-Masters, J. C. *et al.* B cells infected with Type 2 Epstein-Barr virus (EBV) have increased NFATc1/NFATc2 activity and enhanced lytic gene expression in comparison to Type 1 EBV infection. *PLoS Pathog.* **16**, e1008365 (2020).

210. Bornkamm, G. W., Delius, H., Zimber, U., Hudewentz, J. & Epstein, M. A. Comparison of Epstein-Barr virus strains of different origin by analysis of the viral DNAs. *J. Virol.* **35**, 603–618 (1980).

211. Bristol, J. A. *et al.* Reduced IRF4 expression promotes lytic phenotype in Type 2 EBV-infected B cells. *PLOS Pathog.* **18**, e1010453 (2022).

212. Coleman, C. B. *et al.* Epstein-Barr Virus Type 2 Latently Infects T Cells, Inducing an Atypical Activation Characterized by Expression of Lymphotactic Cytokines. *J. Virol.* **89**, 2301–2312 (2015).

213. Souza, T. A., Stollar, B. D., Sullivan, J. L., Luzuriaga, K. & Thorley-Lawson, D. A. Peripheral B cells latently infected with Epstein–Barr virus display molecular hallmarks of

classical antigen-selected memory B cells. *Proc. Natl. Acad. Sci. U. S. A.* **102**, 18093–18098 (2005).

214. Morbach, H., Eichhorn, E. M., Liese, J. G. & Girschick, H. J. Reference values for B cell subpopulations from infancy to adulthood. *Clin. Exp. Immunol.* **162**, 271–279 (2010).

215. Laichalk, L. L., Hochberg, D., Babcock, G. J., Freeman, R. B. & Thorley-Lawson, D. A. The Dispersal of Mucosal Memory B Cells: Evidence from Persistent EBV Infection. *Immunity* **16**, 745–754 (2002).

216. Thorley-Lawson, D. A., Hawkins, J. B., Tracy, S. I. & Shapiro, M. The Pathogenesis of Epstein-Barr Virus Persistent Infection. *Curr. Opin. Virol.* **3**, 227–232 (2013).

217. Hawkins, J. B., Delgado-Eckert, E., Thorley-Lawson, D. A. & Shapiro, M. The Cycle of EBV Infection Explains Persistence, the Sizes of the Infected Cell Populations and Which Come under CTL Regulation. *PLoS Pathog.* **9**, (2013).

218. Babcock, G. J., Hochberg, D. & Thorley-Lawson, D. A. The Expression Pattern of Epstein-Barr Virus Latent Genes In Vivo Is Dependent upon the Differentiation Stage of the Infected B Cell. *Immunity* **13**, 497–506 (2000).

219. Pich, D. *et al.* First Days in the Life of Naive Human B Lymphocytes Infected with Epstein-Barr Virus. *mBio* **10**, e01723-19 (2019).

220. Pratt, Z. L., Zhang, J. & Sugden, B. The Latent Membrane Protein 1 (LMP1) Oncogene of Epstein-Barr Virus Can Simultaneously Induce and Inhibit Apoptosis in B Cells. *J. Virol.* **86**, 4380–4393 (2012).

221. Ma, S.-D. *et al.* Latent Membrane Protein 1 (LMP1) and LMP2A Collaborate To Promote Epstein-Barr Virus-Induced B Cell Lymphomas in a Cord Blood-Humanized Mouse Model but Are Not Essential. *J. Virol.* **91**, e01928-16 (2017).

222. Chaganti, S. *et al.* Epstein-Barr virus colonization of tonsillar and peripheral blood B-cell subsets in primary infection and persistence. *Blood* **113**, 6372–6381 (2009).

223. Dunmire, S. K. *et al.* Primary EBV Infection Induces an Expression Profile Distinct from Other Viruses but Similar to Hemophagocytic Syndromes. *PLoS ONE* **9**, e85422 (2014).

224. Zheng, W. *et al.* Toll-like receptor-mediated innate immunity against herpesviridae infection: a current perspective on viral infection signaling pathways. *Virol. J.* **17**, 192 (2020).

225. Gent, M. van *et al.* EBV Lytic-Phase Protein BGLF5 Contributes to TLR9 Downregulation during Productive Infection. *J. Immunol.* **186**, 1694–1702 (2011).

226. Salamon, D. *et al.* Latency Type-Dependent Modulation of Epstein-Barr Virus-Encoded Latent Membrane Protein 1 Expression by Type I Interferons in B Cells. *J. Virol.* **86**, 4701–4707 (2012).

227. Münz, C. Immune Control and Vaccination against the Epstein-Barr Virus in Humanized Mice. *Vaccines* **7**, (2019).

228. Griffin, B. D. *et al.* Epstein-Barr virus BILF1 evolved to downregulate cell surface display of a wide range of HLA class I molecules through their cytoplasmic tail. *J. Immunol. Baltim. Md 1950* **190**, 1672–1684 (2013).

229. Azzi, T. *et al.* Role for early-differentiated natural killer cells in infectious mononucleosis. *Blood* **124**, 2533–2543 (2014).

230. Strowig, T. *et al.* Tonsilar NK cells restrict B cell transformation by the Epstein-Barr virus via IFN-gamma. *PLoS Pathog.* **4**, e27 (2008).

231. Crawford, D. H. Biology and disease associations of Epstein-Barr virus. *Philos. Trans. R. Soc. Lond. Ser. B* **356**, 461–473 (2001).

232. Long, H. M. *et al.* MHC II tetramers visualize human CD4+ T cell responses to Epstein-Barr virus infection and demonstrate atypical kinetics of the nuclear antigen EBNA1 response. *J. Exp. Med.* **210**, 933–949 (2013).

233. Steven, N. M. *et al.* Immediate early and early lytic cycle proteins are frequent targets of the Epstein-Barr virus-induced cytotoxic T cell response. *J. Exp. Med.* **185**, 1605–1617 (1997).

234. Hislop, A. D., Taylor, G. S., Sauce, D. & Rickinson, A. B. Cellular responses to viral infection in humans: lessons from Epstein-Barr virus. *Annu. Rev. Immunol.* **25**, 587–617 (2007).

235. Albanese, M. *et al.* Epstein–Barr virus microRNAs reduce immune surveillance by virus-specific CD8+ T cells. *Proc. Natl. Acad. Sci. U. S. A.* **113**, E6467–E6475 (2016).

236. Moore, K. W. *et al.* Homology of cytokine synthesis inhibitory factor (IL-10) to the Epstein-Barr virus gene BCRFI. *Science* **248**, 1230–1234 (1990).

237. Yajima, M. *et al.* T Cell-Mediated Control of Epstein-Barr Virus Infection in Humanized Mice. *J. Infect. Dis.* **200**, 1611–1615 (2009).

238. Fiala, M., Heiner, D. C., Turner, J. A., Rosenbloom, B. & Guze, L. B. Infectious Mononucleosis and Mononucleosis Syndromes. *West. J. Med.* **126**, 445–459 (1977).

239. Chan, C. W., Chiang, A. K. S., Chan, K. H. & Lau, A. S. Y. Epstein-Barr virus-associated infectious mononucleosis in Chinese children. *Pediatr. Infect. Dis. J.* **22**, 974–978 (2003).

240. Hoagland, R. J. The Incubation Period of Infectious Mononucleosis. *Am. J. Public Health Nations Health* **54**, 1699–1705 (1964).

241. Stuempfig, N. D. & Seroy, J. Monospot Test. in *StatPearls* (StatPearls Publishing, 2022).

242. Paul, J. R. & Bunnell, W. W. The presence of heterophile antibodies in infectious mononucleosis. *Am. J. Med. Sci.* **267**, 178–188 (1974).

243. Sprunt, T. P. & Evans, F. A. Mononuclear leukocytosis in reaction to acute infection (infectious mononucleosis). *Johns Hopkins Hosp. Bull.* 410–417 (1920).

244. Fafi-Kremer, S. *et al.* Long-Term Shedding of Infectious Epstein-Barr Virus after Infectious Mononucleosis. *J. Infect. Dis.* **191**, 985–989 (2005).

245. Bu, W. *et al.* Kinetics of Epstein-Barr Virus (EBV) Neutralizing and Virus-Specific Antibodies after Primary Infection with EBV. *Clin. Vaccine Immunol. CVI* **23**, 363–369 (2016).

246. Burton, E. M., Voyer, J. & Gewurz, B. E. Epstein–Barr virus latency programs dynamically sensitize B cells to ferroptosis. *Proc. Natl. Acad. Sci.* **119**, e2118300119 (2022).

247. Murata, T., Sato, Y. & Kimura, H. Modes of infection and oncogenesis by the Epstein–Barr virus. *Rev. Med. Virol.* **24**, 242–253 (2014).

248. Pope, J. H., Horne, M. K. & Scott, W. Transformation of foetal human keukocytes in vitro by filtrates of a human leukaemic cell line containing herpes-like virus. *Int. J. Cancer* **3**, 857–866 (1968).

249. Chen, M.-R. Epstein–Barr Virus, the Immune System, and Associated Diseases. *Front. Microbiol.* **2**, (2011).

250. Kaiser, C. *et al.* The Proto-Oncogene c-myc Is a Direct Target Gene of Epstein-Barr Virus Nuclear Antigen 2. *J. Virol.* **73**, 4481–4484 (1999).

251. Katsumura, K. R., Maruo, S. & Takada, K. EBV lytic infection enhances transformation of B-lymphocytes infected with EBV in the presence of T-lymphocytes. *J. Med. Virol.* **84**, 504–510 (2012).

252. Ma, S.-D. *et al.* A New Model of Epstein-Barr Virus Infection Reveals an Important Role for Early Lytic Viral Protein Expression in the Development of Lymphomas. *J. Virol.* **85**, 165–177 (2011).

253. Damania, B., Kenney, S. C. & Raab-Traub, N. Epstein-Barr virus: Biology and clinical disease. *Cell* **185**, 3652–3670 (2022).

254. Bechtel, D., Kurth, J., Unkel, C. & Küppers, R. Transformation of BCR-deficient germinal-center B cells by EBV supports a major role of the virus in the pathogenesis of Hodgkin and posttransplantation lymphomas. *Blood* **106**, 4345–4350 (2005).

255. Kanzler, H., Küppers, R., Hansmann, M. L. & Rajewsky, K. Hodgkin and Reed-Sternberg cells in Hodgkin's disease represent the outgrowth of a dominant tumor clone derived from (crippled) germinal center B cells. *J. Exp. Med.* **184**, 1495–1505 (1996).

256. Magrath, I., Jain, V. & Bhatia, K. Epstein-Barr virus and Burkitt's lymphoma. *Semin. Cancer Biol.* **3**, 285–295 (1992).

257. Brady, G., MacArthur, G. J. & Farrell, P. J. Epstein–Barr virus and Burkitt lymphoma. *J. Clin. Pathol.* **60**, 1397–1402 (2007).

258. Yone, C. L. R. P., Kube, D., Kremsner, P. G. & Luty, A. J. F. Persistent Epstein-Barr viral reactivation in young African children with a history of severe Plasmodium falciparum malaria. *Trans. R. Soc. Trop. Med. Hyg.* **100**, 669–676 (2006).

259. Epstein, M. A. Burkitt's lymphoma: Clues to the role of malaria. *Nature* **312**, 398–398 (1984).

260. Velavan, T. P. Epstein-Barr virus, malaria and endemic Burkitt lymphoma. *EBioMedicine* **39**, 13–14 (2018).

261. Kimura, H. & Cohen, J. I. Chronic Active Epstein–Barr Virus Disease. *Front. Immunol.* **8**, (2017).

262. Kimura, H. EBV in T-/NK-Cell Tumorigenesis. in *Human Herpesviruses* (eds. Kawaguchi, Y., Mori, Y. & Kimura, H.) 459–475 (Springer, 2018). doi:10.1007/978-981-10-7230-7_21.

263. Marsh, R. A. Epstein–Barr Virus and Hemophagocytic Lymphohistiocytosis. *Front. Immunol.* **8**, 1902 (2018).

264. Booth, C. *et al.* X-linked lymphoproliferative disease due to SAP/SH2D1A deficiency: a multicenter study on the manifestations, management and outcome of the disease. *Blood* **117**, 53–62 (2011).

265. Sharifi, R. *et al.* SAP mediates specific cytotoxic T-cell functions in X-linked lymphoproliferative disease. *Blood* **103**, 3821–3827 (2004).

266. Sun, C., Chen, X., Kang, Y. & Zeng, M. The Status and Prospects of Epstein–Barr Virus Prophylactic Vaccine Development. *Front. Immunol.* **12**, 677027 (2021).

267. Cohen, J. I. Vaccine Development for Epstein-Barr Virus. in *Human Herpesviruses* (eds. Kawaguchi, Y., Mori, Y. & Kimura, H.) 477–493 (Springer, 2018). doi:10.1007/978-981-10-7230-7_22.

268. Epstein, M. A., Morgan, A. J., Finerty, S., Randle, B. J. & Kirkwood, J. K. Protection of cottontop tamarins against Epstein-Barr virus-induced malignant lymphoma by a prototype subunit vaccine. *Nature* **318**, 287–289 (1985).

269. Sokal, E. M. *et al.* Recombinant gp350 vaccine for infectious mononucleosis: A phase 2, randomized, double-blind, placebo-controlled trial to evaluate the safety, immunogenicity, and efficacy of an Epstein-Barr virus vaccine in healthy young adults. *J. Infect. Dis.* **196**, (2007).

270. Kanekiyo, M. *et al.* Rational Design of an Epstein-Barr Virus Vaccine Targeting the Receptor-Binding Site. *Cell* **162**, 1090–1100 (2015).

271. Zhong, L. *et al.* Urgency and necessity of Epstein-Barr virus prophylactic vaccines. *Npj Vaccines* **7**, 1–14 (2022).

272. Haanstra, K. G., Wubben, J. A. M., Jonker, M. & Hart, B. A. 't. Induction of Encephalitis in Rhesus Monkeys Infused with Lymphocryptovirus-Infected B-Cells Presenting MOG34–56 Peptide. *PLOS ONE* **8**, e71549 (2013).

273. Fujiwara, S. Animal Models of Human Gammaherpesvirus Infections. in *Human Herpesviruses* (eds. Kawaguchi, Y., Mori, Y. & Kimura, H.) 413–436 (Springer, 2018). doi:10.1007/978-981-10-7230-7_19.

274. Ehlers, B. *et al.* Novel Simian Homologues of Epstein-Barr Virus. *J. Virol.* **77**, 10695–10699 (2003).

275. Lacoste, V., Lavergne, A., de Thoisy, B., Pouliquen, J.-F. & Gessain, A. Genetic diversity and molecular evolution of human and non-human primate Gammaherpesvirinae. *Infect. Genet. Evol.* **10**, 1–13 (2010).

276. Wang, F. Nonhuman primate models for Epstein-Barr virus infection. *Curr. Opin. Virol.* **3**, 233–237 (2013).

277. Moghaddam, A. *et al.* An animal model for acute and persistent Epstein-Barr virus infection. *Science* **276**, 2030–2033 (1997).

278. Cui, X. *et al.* Immunization with Epstein–Barr Virus Core Fusion Machinery Envelope Proteins Elicit High Titers of Neutralizing Activities and Protect Humanized Mice from Lethal Dose EBV Challenge. *Vaccines* **9**, (2021).

279. Wang, Z. *et al.* A study of Epstein-Barr virus infection in the Chinese tree shrew(Tupaia belangeri chinensis). *Virol. J.* **14**, 193 (2017).

280. Shi, N. *et al.* Cyclosporine A induces Epstein–Barr virus reactivation in tree shrew (Tupaia belangeri chinensis) model. *Microbes Infect.* 105212 (2023) doi:10.1016/j.micinf.2023.105212.

281. Xia, W. *et al.* Epstein Barr virus infection in tree shrews alters the composition of gut microbiota and metabolome profile. *Virol. J.* **20**, 177 (2023).

282. Xia, W. *et al.* Tree Shrew Is a Suitable Animal Model for the Study of Epstein Barr Virus. *Front. Immunol.* **12**, (2022).

283. Barton, E., Mandal, P. & Speck, S. H. Pathogenesis and Host Control of Gammaherpesviruses: Lessons from the Mouse. *Annu. Rev. Immunol.* **29**, 351–397 (2011).

284. Ackermann, M. Pathogenesis of gammaherpesvirus infections. *Vet. Microbiol.* **113**, 211–222 (2006).

285. Virgin, H. W. *et al.* Complete sequence and genomic analysis of murine gammaherpesvirus 68. *J. Virol.* **71**, 5894–5904 (1997).

286. De Leo, A., Calderon, A. & Lieberman, P. M. Control of Viral Latency by Episome Maintenance Proteins. *Trends Microbiol.* **28**, 150–162 (2020).

287. Milho, R. *et al.* In vivo imaging of murid herpesvirus-4 infection. *J. Gen. Virol.* **90**, 21–32 (2009).

288. Chen, L., Lai, K., Lomask, J. M., Jiang, B. & Zhong, N. Detection of Mouse Cough Based on Sound Monitoring and Respiratory Airflow Waveforms. *PLoS ONE* **8**, e59263 (2013).

289. François, S. *et al.* Illumination of Murine Gammaherpesvirus-68 Cycle Reveals a Sexual Transmission Route from Females to Males in Laboratory Mice. *PLoS Pathog* **9**, e1003292 (2013).

290. Peacock, J. W. & Bost, K. L. Infection of intestinal epithelial cells and development of systemic disease following gastric instillation of murine gammaherpesvirus-68. *J. Gen. Virol.* **81**, 421–429 (2000).

291. Sunil-Chandra, N. P., Efstathiou, S., Arno, J. & Nash, A. A. Virological and pathological features of mice infected with murine gamma-herpesvirus 68. *J. Gen. Virol.* **73 (Pt 9)**, 2347–2356 (1992).

292. Willer, D. O. & Speck, S. H. Long-Term Latent Murine Gammaherpesvirus 68 Infection Is Preferentially Found within the Surface Immunoglobulin D-Negative Subset of Splenic B Cells In Vivo. *J. Virol.* **77**, 8310–8321 (2003).

293. Flaño, E., Kim, I.-J., Moore, J., Woodland, D. L. & Blackman, M. A. Differential γ-Herpesvirus Distribution in Distinct Anatomical Locations and Cell Subsets During Persistent Infection in Mice. *J. Immunol.* **170**, 3828–3834 (2003).

294. Flaño, E., Woodland, D. L. & Blackman, M. A. A mouse model for infectious mononucleosis. *Immunol. Res.* **25**, 201–217 (2002).

295. Weck, K. E., Kim, S. S., Virgin, H. W. & Speck, S. H. Macrophages Are the Major Reservoir of Latent Murine Gammaherpesvirus 68 in Peritoneal Cells. *J. Virol.* **73**, 3273–3283 (1999).

296. Liang, X., Collins, C. M., Mendel, J. B., Iwakoshi, N. N. & Speck, S. H. Gammaherpesvirus-Driven Plasma Cell Differentiation Regulates Virus Reactivation from Latently Infected B Lymphocytes. *PLoS Pathog* **5**, e1000677 (2009).

297. Krug, L. T., Evans, A. G., Gargano, L. M., Paden, C. R. & Speck, S. H. The Absence of M1 Leads to Increased Establishment of Murine Gammaherpesvirus 68 Latency in IgD-Negative B Cells. *J. Virol.* **87**, 3597–3604 (2013).

298. Nash, A. A., Dutia, B. M., Stewart, J. P. & Davison, A. J. Natural history of murine gamma-herpesvirus infection. *Philos. Trans. R. Soc. Lond. Ser. B* **356**, 569–579 (2001).

299. Lee, K. S., Cool, C. D. & van Dyk, L. F. Murine Gammaherpesvirus 68 Infection of Gamma Interferon-Deficient Mice on a BALB/c Background Results in Acute Lethal Pneumonia That Is Dependent on Specific Viral Genes. *J. Virol.* **83**, 11397–11401 (2009).

300. Freeman, M. L. *et al.* Two Kinetic Patterns of Epitope-Specific CD8 T-Cell Responses following Murine Gammaherpesvirus 68 Infection. *J. Virol.* **84**, 2881–2892 (2010).

301. Yager, E. J. *et al.* γ-Herpesvirus-Induced Protection Against Bacterial Infection Is Transient. *Viral Immunol.* **22**, 67–71 (2009).

302. Marshall, W. L. *et al.* Epstein-Barr virus encodes a novel homolog of the bcl-2 oncogene that inhibits apoptosis and associates with Bax and Bak. *J. Virol.* **73**, 5181–5185 (1999).

303. AlQarni, S. *et al.* Lymphomas driven by Epstein-Barr virus nuclear antigen-1 (EBNA1) are dependant upon Mdm2. *Oncogene* **37**, 3998–4012 (2018).

304. Wilson, J. B., Bell, J. L. & Levine, A. J. Expression of Epstein-Barr virus nuclear antigen-1 induces B cell neoplasia in transgenic mice. *EMBO J.* **15**, 3117–3126 (1996).

305. Stevenson, D., Charalambous, C. & Wilson, J. B. Epstein-Barr Virus Latent Membrane Protein 1 (CAO) Up-regulates VEGF and TGFα Concomitant with Hyperlasia, with Subsequent Up-regulation of p16 and MMP9. *Cancer Res.* **65**, 8826–8835 (2005).

306. Balandraud, N. & Roudier, J. Epstein-Barr virus and rheumatoid arthritis. *Joint Bone Spine* **85**, 165–170 (2018).

307. Takei, M. *et al.* Are Viral Infections Key Inducers of Autoimmune Diseases? Focus on Epstein–Barr Virus. *Viruses* **14**, 1900 (2022).

308. James, J. A. *et al.* An increased prevalence of Epstein-Barr virus infection in young patients suggests a possible etiology for systemic lupus erythematosus. *J. Clin. Invest.* **100**, 3019–3026 (1997).

309. Jog, N. R. & James, J. A. Epstein Barr Virus and Autoimmune Responses in Systemic Lupus Erythematosus. *Front. Immunol.* **11**, (2021).

310. Hussain, N., Jaffery, G., Sabri, A. N. & Hasnain, S. HLA Association in SLE patients from Lahore-Pakistan. *Bosn. J. Basic Med. Sci.* **11**, 20–26 (2011).

311. Sorosina, M. *et al.* Risk HLA Variants Affect the T-Cell Repertoire in Multiple Sclerosis. *Neurol. Neuroimmunol. Neuroinflammation* **10**, e200093 (2023).

312. Warner, H. B. & Carp, R. I. Multiple Sclerosis and Epstein-Barr Virus. *The Lancet* **318**, 1290 (1981).

313. Ascherio, Munger, KL, Lennette, ET, & et al. Epstein-Barr virus antibodies and risk of multiple sclerosis: A prospective study. *JAMA* **286**, 3083–3088 (2001).

314. DeLorenze *et al.* Epstein-Barr virus and multiple sclerosis: Evidence of association from a prospective study with long-term follow-up. *Arch. Neurol.* **63**, 839–844 (2006).

315. Thacker, E. L., Mirzaei, F. & Ascherio, A. Infectious mononucleosis and risk for multiple sclerosis: A meta-analysis. *Ann. Neurol.* **59**, 499–503 (2006).

316. Handel, A. E. *et al.* An Updated Meta-Analysis of Risk of Multiple Sclerosis following Infectious Mononucleosis. *PLoS ONE* **5**, e12496 (2010).

317. Hernán, M. A., Zhang, S. M., Lipworth, L., Olek, M. J. & Ascherio, A. Multiple sclerosis and age at infection with common viruses. *Epidemiol. Camb. Mass* **12**, 301–306 (2001).

318. Alotaibi, S., Kennedy, J., Tellier, R., Stephens, D. & Banwell, B. Epstein-Barr virus in pediatric multiple sclerosis. *JAMA* **291**, 1875–1879 (2004).

319. Levin, L. I., Munger, K. L., O'Reilly, E. J., Falk, K. I. & Ascherio, A. Primary Infection with the Epstein-Barr Virus and Risk of Multiple Sclerosis. *Ann. Neurol.* **67**, 824–830 (2010).

320. Pohl, D. Epstein–Barr virus and multiple sclerosis. *J. Neurol. Sci.* **286**, 62–64 (2009).

321. Nourbakhsh, B. *et al.* MS is rare in EBV-seronegative children with CNS inflammatory demyelination. *Ann. Neurol.* **89**, 1234–1239 (2021).

322. Simon, K. C., Saghafian-Hedengren, S., Sverremark-Ekström, E., Nilsson, C. & Ascherio, A. Age at Epstein-Barr virus infection and Epstein-Barr virus nuclear antigen-1 antibodies in Swedish children. *Mult. Scler. Relat. Disord.* **1**, 136–138 (2012).

323. Lünemann, J. D. *et al.* EBNA1-specific T cells from patients with multiple sclerosis cross react with myelin antigens and co-produce IFN-γ and IL-2. *J. Exp. Med.* **205**, 1763–1773 (2008).

324. Lünemann, J. D. *et al.* Increased frequency and broadened specificity of latent EBV nuclear antigen-1-specific T cells in multiple sclerosis. *Brain* **129**, 1493–1506 (2006).

325. Lünemann, J. D. *et al.* Elevated Epstein-Barr virus-encoded nuclear antigen-1 immune responses predict conversion to multiple sclerosis. *Ann. Neurol.* **67**, 159–169 (2010).

326. Schneider-Hohendorf, T. *et al.* Broader Epstein–Barr virus–specific T cell receptor repertoire in patients with multiple sclerosis. *J. Exp. Med.* **219**, e20220650 (2022).

327. Pender, M., Csurhes, P., Burrows, J. & Burrows, S. Defective T-cell control of Epstein-Barr virus infection in multiple sclerosis., Defective T-cell control of Epstein–Barr virus infection in multiple sclerosis. *Clin. Transl. Immunol.* **6, 6**, e126, e126–e126 (2017).

328. Santón, A. *et al.* High frequency of co-infection by Epstein–Barr virus types 1 and 2 in patients with multiple sclerosis. *Mult. Scler. J.* **17**, 1295–1300 (2011).

329. Lindsey, J. W., Patel, S. & Zou, J. Epstein-Barr virus genotypes in multiple sclerosis. *Acta Neurol. Scand.* **117**, 141–144 (2008).

330. Zanella, L. *et al.* A reliable Epstein-Barr Virus classification based on phylogenomic and population analyses. *Sci. Rep.* **9**, 9829 (2019).

331. Zivadinov, R. *et al.* Effect of ocrelizumab on leptomeningeal inflammation and humoral response to Epstein-Barr virus in multiple sclerosis. A pilot study. *Mult. Scler. Relat. Disord.* **67**, 104094 (2022).

332. Kappos, L. *et al.* Ocrelizumab in relapsing-remitting multiple sclerosis: a phase 2, randomised, placebo-controlled, multicentre trial. *Lancet* **378**, 1779–1787 (2011).

333. Bar-Or, A. *et al.* Rituximab in relapsing-remitting multiple sclerosis: A 72-week, open-label, phase I trial. *Ann. Neurol.* **63**, 395–400 (2008).

334. St.Clair, E. W. Good and Bad Memories Following Rituximab Therapy. *Arthritis Rheum.* **62**, 1–5 (2010).

335. Kappos, L. *et al.* Atacicept in multiple sclerosis (ATAMS): a randomised, placebo-controlled, double-blind, phase 2 trial. *Lancet Neurol.* **13**, 353–363 (2014).

336. Rojas, O. L. *et al.* Recirculating Intestinal IgA-Producing Cells Regulate Neuroinflammation via IL-10. *Cell* **176**, 610-624.e18 (2019).

337. Pikor, N. & Gommerman, J. L. B cells in MS: Why, where and how? *Mult. Scler. Relat. Disord.* **1**, 123–130 (2012).

338. Vincent, F. B., Saulep-Easton, D., Figgett, W. A., Fairfax, K. A. & Mackay, F. The BAFF/APRIL system: Emerging functions beyond B cell biology and autoimmunity. *Cytokine Growth Factor Rev.* **24**, 203–215 (2013).

339. Barr, T. A. *et al.* B cell depletion therapy ameliorates autoimmune disease through ablation of IL-6–producing B cells. *J. Exp. Med.* **209**, 1001–1010 (2012).

340. Yokoi, T. *et al.* Epstein-Barr virus-immortalized B cells produce IL-6 as an autocrine growth factor. *Immunology* **70**, 100–105 (1990).

341. Steinmaurer, A., Wimmer, I., Berger, T., Rommer, P. S. & Sellner, J. Bruton's Tyrosine Kinase Inhibition in the Treatment of Preclinical Models and Multiple Sclerosis. *Curr. Pharm. Des.* **28**, 437–444 (2022).

342. Fish, K. *et al.* Rewiring of B cell receptor signaling by Epstein–Barr virus LMP2A. *Proc. Natl. Acad. Sci. U. S. A.* **117**, 26318–26327 (2020).

343. Ascherio, A. & Munger, K. L. Epstein–Barr Virus Infection and Multiple Sclerosis: A Review. *J. Neuroimmune Pharmacol.* **5**, 271–277 (2010).

344. Pakpoor, J. *et al.* The risk of developing multiple sclerosis in individuals seronegative for Epstein-Barr virus: a meta-analysis. *Mult. Scler. Houndmills Basingstoke Engl.* **19**, 162–166 (2013).

345. Rose, N. R. & Mackay, I. R. Molecular mimicry: a critical look at exemplary instances in human diseases. *Cell. Mol. Life Sci. CMLS* **57**, 542–551 (2000).

346. Benoist, C. & Mathis, D. Autoimmunity provoked by infection: how good is the case for T cell epitope mimicry? *Nat. Immunol.* **2**, 797–801 (2001).

347. Vaughan, J. H. *et al.* An Epstein Barr virus-related cross reactive autoimmune response in multiple sclerosis in Norway. *J. Neuroimmunol.* **69**, 95–102 (1996).

348. Esposito, M. *et al.* Human Transaldolase and Cross-Reactive Viral Epitopes Identified by Autoantibodies of Multiple Sclerosis Patients. *J. Immunol.* **163**, 4027–4032 (1999).

349. Jog, N. R. *et al.* Epstein Barr Virus Nuclear Antigen 1 (EBNA-1) peptides recognized by adult multiple sclerosis patient sera induce neurologic symptoms in a murine model. *J. Autoimmun.* **106**, 102332 (2020).

350. Bar-Or, A., Banwell, B., Berger, J. R. & Lieberman, P. M. Guilty by association: Epstein-Barr virus in multiple sclerosis. *Nat. Med.* **28**, 904–906 (2022).

351. Siloşi, I. *et al.* The role of autoantibodies in health and disease. *Romanian J. Morphol. Embryol. Rev. Roum. Morphol. Embryol.* **57**, 633–638 (2016).

352. Danke, N. A., Koelle, D. M., Yee, C., Beheray, S. & Kwok, W. W. Autoreactive T cells in healthy individuals. *J. Immunol. Baltim. Md 1950* **172**, 5967–5972 (2004).

353. Maple, P. A. *et al.* The Potential for EBV Vaccines to Prevent Multiple Sclerosis. *Front. Neurol.* **13**, 887794 (2022).

354. Stern, J. N. H. *et al.* B cells populating the multiple sclerosis brain mature in the draining cervical lymph nodes. *Sci. Transl. Med.* **6**, 248ra107 (2014).

355. Serafini, B. *et al.* Dysregulated Epstein-Barr virus infection in the multiple sclerosis brain. *J. Exp. Med.* **204**, 2899–2912 (2007).

356. Lassmann, H., Niedobitek, G., Aloisi, F. & Middeldorp, J. M. Epstein–Barr virus in the multiple sclerosis brain: a controversial issue—report on a focused workshop held in the Centre for Brain Research of the Medical University of Vienna, Austria. *Brain* **134**, 2772–2786 (2011).

357. Serafini, B., Rosicarelli, B., Magliozzi, R., Stigliano, E. & Aloisi, F. Detection of Ectopic B-cell Follicles with Germinal Centers in the Meninges of Patients with Secondary Progressive Multiple Sclerosis. *Brain Pathol.* **14**, 164–174 (2004).

358. Serafini, B. *et al.* Epstein-Barr virus latent infection and BAFF expression in B cells in the multiple sclerosis brain: implications for viral persistence and intrathecal B-cell activation. *J. Neuropathol. Exp. Neurol.* **69**, 677–693 (2010).

359. Peferoen, L. A. N. *et al.* Epstein Barr virus is not a characteristic feature in the central nervous system in established multiple sclerosis. *Brain* **133**, e137–e137 (2010).

360. Willis, S. N. *et al.* Epstein–Barr virus infection is not a characteristic feature of multiple sclerosis brain. *Brain* **132**, 3318–3328 (2009).

361. Sargsyan, S. A. *et al.* Absence of Epstein-Barr virus in the brain and CSF of patients with multiple sclerosis. *Neurology* **74**, 1127–1135 (2010).

362. Tzartos, J. S. *et al.* Association of innate immune activation with latent Epstein-Barr virus in active MS lesions. *Neurology* **78**, 15–23 (2012).

363. Moreno, M. A. *et al.* Molecular signature of Epstein-Barr virus infection in MS brain lesions. *Neurol. Neuroimmunol. Neuroinflammation* **5**, e466 (2018).

364. Hassani, A., Corboy, J. R., Al-Salam, S. & Khan, G. Epstein-Barr virus is present in the brain of most cases of multiple sclerosis and may engage more than just B cells. *PloS One* **13**, e0192109 (2018).

365. Serafini, B. *et al.* Massive intracerebral Epstein-Barr virus reactivation in lethal multiple sclerosis relapse after natalizumab withdrawal. *J. Neuroimmunol.* **307**, 14–17 (2017).

366. Serafini, B., Rosicarelli, B., Veroni, C., Mazzola, G. A. & Aloisi, F. Epstein-Barr Virus-Specific CD8 T Cells Selectively Infiltrate the Brain in Multiple Sclerosis and Interact

Locally with Virus-Infected Cells: Clue for a Virus-Driven Immunopathological Mechanism. *J. Virol.* **93**, e00980-19 (2019).

367. Veroni, C., Serafini, B., Rosicarelli, B., Fagnani, C. & Aloisi, F. Transcriptional profile and Epstein-Barr virus infection status of laser-cut immune infiltrates from the brain of patients with progressive multiple sclerosis. *J. Neuroinflammation* **15**, 18 (2018).
368. Evans, A. S. Causation and Disease: The Henle-Koch Postulates Revisited. *Yale J. Biol. Med.* **49**, 175–195 (1976).
369. Pender, M. P. Infection of autoreactive B lymphocytes with EBV, causing chronic autoimmune diseases. *Trends Immunol.* **24**, 584–588 (2003).
370. Pender, M. P. The Essential Role of Epstein-Barr Virus in the Pathogenesis of Multiple Sclerosis. *The Neuroscientist* **17**, 351–367 (2011).
371. Eriksson, C. *et al.* Autoantibodies predate the onset of systemic lupus erythematosus in northern Sweden. *Arthritis Res. Ther.* **13**, R30 (2011).
372. Höftberger, R., Lassmann, H., Berger, T. & Reindl, M. Pathogenic autoantibodies in multiple sclerosis — from a simple idea to a complex concept. *Nat. Rev. Neurol.* **18**, 681–688 (2022).
373. Samuels, J., Ng, Y.-S., Coupillaud, C., Paget, D. & Meffre, E. Impaired early B cell tolerance in patients with rheumatoid arthritis. *J. Exp. Med.* **201**, 1659–1667 (2005).
374. Volkov, M., van Schie, K. A. & van der Woude, D. Autoantibodies and B Cells: The ABC of rheumatoid arthritis pathophysiology. *Immunol. Rev.* **294**, 148–163 (2020).
375. Lambracht-Washington, D. *et al.* Antigen specificity of clonally expanded and receptor edited cerebrospinal fluid B cells from patients with relapsing remitting MS. *J. Neuroimmunol.* **186**, 164–176 (2007).

376. Tracy, S. I. *et al.* Persistence of Epstein-Barr Virus in Self-Reactive Memory B Cells. *J. Virol.* **86**, 12330–12340 (2012).

377. Pender, M. P., Csurhes, P. A., Pfluger, C. M. & Burrows, S. R. Decreased CD8+T cell response to Epstein-Barr virus infected B cells in multiple sclerosis is not due to decreased HLA class I expression on B cells or monocytes. *BMC Neurol.* **11**, 95 (2011).

378. Laurence, M. & Benito-León, J. Epstein–Barr virus and multiple sclerosis: Updating Pender's hypothesis. *Mult. Scler. Relat. Disord.* **16**, 8–14 (2017).

379. Nanbo, A., Sugden, A. & Sugden, B. The coupling of synthesis and partitioning of EBV's plasmid replicon is revealed in live cells. *EMBO J.* **26**, 4252–4262 (2007).

380. Ioannides, Z. A. *et al.* Sustained Clinical Improvement in a Subset of Patients With Progressive Multiple Sclerosis Treated With Epstein–Barr Virus-Specific T Cell Therapy. *Front. Neurol.* **12**, 652811 (2021).

381. Pender, M. P. *et al.* Epstein–Barr virus-specific adoptive immunotherapy for progressive multiple sclerosis. *Mult. Scler.* **20**, 1541–1544 (2014).

382. Márquez, A. C. & Horwitz, M. S. The Role of Latently Infected B Cells in CNS Autoimmunity. *Front. Immunol.* **6**, 544 (2015).

383. Hong, T. *et al.* Epstein–Barr virus nuclear antigen 2 extensively rewires the human chromatin landscape at autoimmune risk loci. *Genome Res.* **31**, 2185–2198 (2021).

384. Harley, J. B. *et al.* Transcription factors operate across disease loci, with EBNA2 implicated in autoimmunity. *Nat. Genet.* **50**, 699–707 (2018).

385. Keane, J. T. *et al.* The interaction of Epstein-Barr virus encoded transcription factor EBNA2 with multiple sclerosis risk loci is dependent on the risk genotype. *EBioMedicine* **71**, 103572 (2021).

386. Morandi, E., Jagessar, S. A., ’t Hart, B. A. & Gran, B. EBV Infection Empowers Human B Cells for Autoimmunity: Role of Autophagy and Relevance to Multiple Sclerosis. *J. Immunol.* **199**, 435–448 (2017).

387. Angelini, D. F. *et al.* Increased CD8+ T Cell Response to Epstein-Barr Virus Lytic Antigens in the Active Phase of Multiple Sclerosis. *PLOS Pathog.* **9**, e1003220 (2013).

388. van Nierop, G. P., Mautner, J., Mitterreiter, J. G., Hintzen, R. Q. & Verjans, G. M. G. M. Intrathecal CD8 T-cells of multiple sclerosis patients recognize lytic Epstein-Barr virus proteins. *Mult. Scler. Houndmills Basingstoke Engl.* **22**, 279–291 (2016).

389. Márquez, A. C., Croft, C., Shanina, I. & Horwitz, M. S. Influence of Type I Interferons in Gammaherpesvirus-68 and Its Influence on EAE Enhancement. *Front. Immunol.* **13**, 858583 (2022).

390. Szymczak, F., Colli, M. L., Mamula, M. J., Evans-Molina, C. & Eizirik, D. L. Gene expression signatures of target tissues in type 1 diabetes, lupus erythematosus, multiple sclerosis, and rheumatoid arthritis. *Sci. Adv.* **7**, eabd7600 (2021).

391. Pérez-Pérez, S. *et al.* Anti-Human Herpesvirus 6 A/B Antibodies Titers Correlate With Multiple Sclerosis-Associated Retrovirus Envelope Expression. *Front. Immunol.* **12**, 798003 (2021).

392. Christensen, T. Association of human endogenous retroviruses with multiple sclerosis and possible interactions with herpes viruses. *Rev. Med. Virol.* **15**, 179–211 (2005).

393. Frey, T. R., Akinyemi, I. A., Burton, E. M., Bhaduri-McIntosh, S. & McIntosh, M. T. An Ancestral Retrovirus Envelope Protein Regulates Persistent Gammaherpesvirus Lifecycles. *Front. Microbiol.* **12**, 708404 (2021).

394. Sutkowski, N., Conrad, B., Thorley-Lawson, D. A. & Huber, B. T. Epstein-Barr Virus Transactivates the Human Endogenous Retrovirus HERV-K18 that Encodes a Superantigen. *Immunity* **15**, 579–589 (2001).

395. Tai, A. K. *et al.* Human endogenous retrovirus-K18 Env as a risk factor in multiple sclerosis. *Mult. Scler. Houndmills Basingstoke Engl.* **14**, 1175–1180 (2008).

396. Fujinami, R. S., von Herrath, M. G., Christen, U. & Whitton, J. L. Molecular Mimicry, Bystander Activation, or Viral Persistence: Infections and Autoimmune Disease. *Clin. Microbiol. Rev.* **19**, 80–94 (2006).

397. Münz, C., Lünemann, J. D., Getts, M. T. & Miller, S. D. Antiviral immune responses: triggers of or triggered by autoimmunity? *Nat. Rev. Immunol.* **9**, 246–258 (2009).

398. Whiteside, S. K., Snook, J. P., Williams, M. A. & Weis, J. J. Bystander T Cells: A Balancing Act of Friends and Foes. *Trends Immunol.* **39**, 1021–1035 (2018).

399. van Noort, J. M., Bajramovic, J. J., Plomp, A. C. & van Stipdonk, M. J. B. Mistaken self, a novel model that links microbial infections with myelin-directed autoimmunity in multiple sclerosis. *J. Neuroimmunol.* **105**, 46–57 (2000).

400. Hassani, A., Reguraman, N., Shehab, S. & Khan, G. Primary Peripheral Epstein-Barr Virus Infection Can Lead to CNS Infection and Neuroinflammation in a Rabbit Model: Implications for Multiple Sclerosis Pathogenesis. *Front. Immunol.* **12**, 764937 (2021).

401. Flores, C., Fouquet, G., Moura, I. C., Maciel, T. T. & Hermine, O. Lessons to Learn From Low-Dose Cyclosporin-A: A New Approach for Unexpected Clinical Applications. *Front. Immunol.* **10**, (2019).

402. Polepole, P. *et al.* Epstein Barr virus-immortalized B lymphocytes exacerbate experimental autoimmune encephalomyelitis in xenograft mice. *J. Med. Virol.* **93**, 3813–3823 (2021).

403. Hjalgrim, H. *et al.* Familial Clustering of Hodgkin Lymphoma and Multiple Sclerosis. *J. Natl. Cancer Inst.* **96**, 780–784 (2004).

404. Jagessar, S. A. *et al.* Antibodies Against Human BLyS and APRIL Attenuate EAE Development in Marmoset Monkeys. *J. Neuroimmune Pharmacol.* **7**, 557–570 (2012).

405. ’t Hart, B. A. & Kap, Y. S. An essential role of virus-infected B cells in the marmoset experimental autoimmune encephalomyelitis model. *Mult. Scler. J. - Exp. Transl. Clin.* **3**, 2055217317690184 (2017).

406. Jagessar, S. A. *et al.* Induction of Progressive Demyelinating Autoimmune Encephalomyelitis in Common Marmoset Monkeys Using MOG34-56 Peptide in Incomplete Freund Adjuvant. *J. Neuropathol. Exp. Neurol.* **69**, 372–385 (2010).

407. ’t Hart, B. A. Experimental autoimmune encephalomyelitis in the common marmoset: a translationally relevant model for the cause and course of multiple sclerosis. *Primate Biol.* **6**, 17–58 (2019).

408. Jagessar, S. A. *et al.* Lymphocryptovirus Infection of Nonhuman Primate B Cells Converts Destructive into Productive Processing of the Pathogenic CD8 T Cell Epitope in Myelin Oligodendrocyte Glycoprotein. *J. Immunol. Baltim. Md 1950* **197**, 1074–1088 (2016).

409. Cho, Y.-G. *et al.* An Epstein–Barr-related herpesvirus from marmoset lymphomas. *Proc. Natl. Acad. Sci. U. S. A.* **98**, 1224–1229 (2001).

410. Gasper-Smith, N., Marriott, I. & Bost, K. L. Murine γ-Herpesvirus 68 Limits Naturally Occurring CD4+CD25+ T Regulatory Cell Activity following Infection. *J. Immunol.* **177**, 4670–4678 (2006).

411. Quan, T. E., Roman, R. M., Rudenga, B. J., Holers, V. M. & Craft, J. Epstein-Barr Virus Promotes Interferon-α Production by Plasmacytoid Dendritic Cells. *Arthritis Rheum.* **62**, 1693–1701 (2010).

412. Terry, L. A., Stewart, J. P., Nash, A. A. & Fazakerley, J. K. Murine gammaherpesvirus-68 infection of and persistence in the central nervous system. *J. Gen. Virol.* **81**, 2635–2643 (2000).

413. Kang, H.-R. *et al.* Persistent infection of a gammaherpesvirus in the central nervous system. *Virology* **423**, 23–29 (2012).

414. Cho, H.-J. *et al.* Age-dependent pathogenesis of murine gammaherpesvirus 68 infection of the central nervous system. *Mol. Cells* **27**, 105–111 (2009).

415. Casiraghi, C. *et al.* Gammaherpesvirus Latency Accentuates EAE Pathogenesis: Relevance to Epstein-Barr Virus and Multiple Sclerosis. *PLoS Pathog.* **8**, (2012).

416. Peacock, J. W., Elsawa, S. F., Petty, C. C., Hickey, W. F. & Bost, K. L. Exacerbation of experimental autoimmune encephalomyelitis in rodents infected with murine gammaherpesvirus-68. *Eur. J. Immunol.* **33**, 1849–1858 (2003).

417. Mouat, I. C., Morse, Z. J., Shanina, I., Brown, K. L. & Horwitz, M. S. Latent gammaherpesvirus exacerbates arthritis through modification of age-associated B cells. *eLife* **10**, e67024 (2021).

418. Casiraghi, C., Citlali Márquez, A., Shanina, I. & Steven Horwitz, M. Latent virus infection upregulates CD40 expression facilitating enhanced autoimmunity in a model of multiple sclerosis. *Sci. Rep.* **5**, 13995 (2015).

419. Márquez, A. C., Shanina, I. & Horwitz, M. S. Multiple Sclerosis-Like Symptoms in Mice Are Driven by Latent γHerpesvirus-68 Infected B Cells. *Front. Immunol.* **11**, 584297 (2020).

420. Mouat, I. C. *et al.* Gammaherpesvirus infection drives age-associated B cells toward pathogenicity in EAE and MS. *Sci. Adv.* **8**, eade6844 (2022).

421. Casiraghi, C., Dorovini-Zis, K. & Horwitz, M. S. Epstein-Barr virus infection of human brain microvessel endothelial cells: A novel role in multiple sclerosis. *J. Neuroimmunol.* **230**, 173–177 (2011).

422. Dalla Libera, D. *et al.* T Regulatory Cells Are Markers of Disease Activity in Multiple Sclerosis Patients. *PLoS ONE* **6**, e21386 (2011).

423. Norris, B. A. *et al.* Polyphasic innate immune responses to acute and chronic LCMV infection. *Immunity* **38**, 10.1016/j.immuni.2012.10.022 (2013).

424. Beura, L. K. *et al.* Lymphocytic choriomeningitis virus persistence promotes effector-like memory differentiation and enhances mucosal T cell distribution. *J. Leukoc. Biol.* **97**, 217–225 (2015).

425. Che, J. W., Daniels, K. A., Selin, L. K. & Welsh, R. M. Heterologous Immunity and Persistent Murine Cytomegalovirus Infection. *J. Virol.* **91**, e01386-16 (2017).

426. Jordan, M. C., Shanley, J. D. & Stevens, J. G. Immunosuppression reactivates and disseminates latent murine cytomegalovirus. *J. Gen. Virol.* **37**, 419–423 (1977).

427. Barton, E. S., Lutzke, M. L., Rochford, R. & Virgin, H. W. Alpha/Beta Interferons Regulate Murine Gammaherpesvirus Latent Gene Expression and Reactivation from Latency. *J. Virol.* **79**, 14149–14160 (2005).

428. Mouat, I. C., Shanina, I. & Horwitz, M. S. Age-associated B cells are long-lasting effectors that impede latent γHV68 reactivation. *Sci. Rep.* **12**, 21189 (2022).

429. Pearson, T., Greiner, D. L. & Shultz, L. D. Creation of "Humanized" Mice to Study Human Immunity. *Curr. Protoc. Immunol.* **CHAPTER**, Unit-15.21 (2008).

430. Dash, P. K. *et al.* Humanized Mice for Infectious and Neurodegenerative disorders. *Retrovirology* **18**, 13 (2021).

431. Koboziev, I. *et al.* Use of Humanized Mice to Study the Pathogenesis of Autoimmune and Inflammatory Diseases. *Inflamm. Bowel Dis.* **21**, 1652–1673 (2015).

432. Yue, F. *et al.* A Comparative Encyclopedia of DNA Elements in the Mouse Genome. *Nature* **515**, 355–364 (2014).

433. Shultz, L. D., Brehm, M. A., Bavari, S. & Greiner, D. L. Humanized mice as a preclinical tool for infectious disease and biomedical research. *Ann. N. Y. Acad. Sci.* **1245**, 50–54 (2011).

434. Stripecke, R. *et al.* Innovations, challenges, and minimal information for standardization of humanized mice. *EMBO Mol. Med.* **12**, e8662 (2020).

435. Flanagan, S. P. 'Nude', a new hairless gene with pleiotropic effects in the mouse. *Genet. Res.* **8**, 295–309 (1966).

436. Pantelouris, E. M. Absence of thymus in a mouse mutant. *Nature* **217**, 370–371 (1968).

437. Nehls, M., Pfeifer, D., Schorpp, M., Hedrich, H. & Boehm, T. New member of the winged-helix protein family disrupted in mouse and rat nude mutations. *Nature* **372**, 103–107 (1994).

438. Ganick, D. J., Sarnwick, R. D., Shahidi, N. T. & Manning, D. D. Inability of intravenously injected monocellular suspensions of human bone marrow to establish in the nude mouse. *Int. Arch. Allergy Appl. Immunol.* **62**, 330–333 (1980).

439. Bosma, M. J. & Carroll, A. M. The SCID mouse mutant: definition, characterization, and potential uses. *Annu. Rev. Immunol.* **9**, 323–350 (1991).

440. Matsumoto, Y., Asa, A. D. D. C., Modak, C. & Shimada, M. DNA-Dependent Protein Kinase Catalytic Subunit: The Sensor for DNA Double-Strand Breaks Structurally and Functionally Related to Ataxia Telangiectasia Mutated. *Genes* **12**, 1143 (2021).

441. Shultz, L. D. *et al.* Multiple defects in innate and adaptive immunologic function in NOD/LtSz-scid mice. *J. Immunol.* **154**, 180–191 (1995).

442. Kachapati, K., Adams, D., Bednar, K. & Ridgway, W. M. The Non-Obese Diabetic (NOD) Mouse as a Model of Human Type 1 Diabetes. in *Animal Models in Diabetes Research* (eds. Joost, H.-G., Al-Hasani, H. & Schürmann, A.) 3–16 (Humana Press, 2012). doi:10.1007/978-1-62703-068-7_1.

443. Thayer, T. C., Wilson, B. S. & Mathews, C. E. Use of NOD Mice to Understand Human Type 1 Diabetes. *Endocrinol. Metab. Clin. North Am.* **39**, 541–561 (2010).

444. Orr, M. T., Beilke, J. N., Proekt, I. & Lanier, L. L. Natural killer cells in NOD.NK1.1 mice acquire cytolytic function during viral infection and provide protection against cytomegalovirus. *Proc. Natl. Acad. Sci.* **107**, 15844–15849 (2010).

445. Baxter, A. G. & Cooke, A. Complement Lytic Activity Has No Role in the Pathogenesis of Autoimmune Diabetes in NOD Mice. *Diabetes* **42**, 1574–1578 (1993).

446. Alard, P. *et al.* Deficiency in NOD Antigen-Presenting Cell Function May Be Responsible for Suboptimal CD4+CD25+ T-Cell–Mediated Regulation and Type 1 Diabetes Development in NOD Mice. *Diabetes* **55**, 2098–2105 (2006).

447. Piganelli, J. D., Martin, T. & Haskins, K. Splenic macrophages from the NOD mouse are defective in the ability to present antigen. *Diabetes* **47**, 1212–1218 (1998).

448. Andrechak, J. C., Dooling, L. J. & Discher, D. E. The macrophage checkpoint CD47 : SIRPα for recognition of 'self' cells: from clinical trials of blocking antibodies to mechanobiological fundamentals. *Philos. Trans. R. Soc. B Biol. Sci.* **374**, 20180217 (2019).

449. Bosma, G. C. *et al.* Evidence of functional lymphocytes in some (leaky) scid mice. *J. Exp. Med.* **167**, 1016–1033 (1988).

450. Greiner, D. L., Hesselton, R. M. & Shultz, L. D. SCID mouse models of human stem cell engraftment. *Stem Cells Dayt. Ohio* (1998).

451. Kotloff, D. B., Bosma, M. J. & Ruetsch, N. R. V(D)J recombination in peritoneal B cells of leaky scid mice. *J. Exp. Med.* **178**, 1981–1994 (1993).

452. Rooney, S. *et al.* Leaky Scid Phenotype Associated with Defective V(D)J Coding End Processing in Artemis-Deficient Mice. *Mol. Cell* **10**, 1379–1390 (2002).

453. Carroll, A. M., Hardy, R. R., Petrini, J. & Bosma, M. J. T Cell Leakiness in Scid Mice. in *The Scid Mouse* (eds. Bosma, M. J., Phillips, R. A. & Schuler, W.) 117–123 (Springer, 1989). doi:10.1007/978-3-642-74974-2_15.

454. Mombaerts, P. *et al.* RAG-1-deficient mice have no mature B and T lymphocytes. *Cell* **68**, 869–877 (1992).

455. Shultz, L. D. *et al.* Human Lymphoid and Myeloid Cell Development in NOD/LtSz-scid IL2Rγnull Mice Engrafted with Mobilized Human Hemopoietic Stem Cells 12. *J. Immunol.* **174**, 6477–6489 (2005).

456. Traggiai, E. *et al.* Development of a Human Adaptive Immune System in Cord Blood Cell-Transplanted Mice. *Science* **304**, 104–107 (2004).

457. Brehm, M. A., Wiles, M. V., Greiner, D. L. & Shultz, L. D. Generation of improved humanized mouse models for human infectious diseases. *J. Immunol. Methods* **0**, 3–17 (2014).

458. Ito, M. *et al.* NOD/SCID/γcnull mouse: an excellent recipient mouse model for engraftment of human cells. *Blood* **100**, 3175–3182 (2002).

459. Watanabe, S. *et al.* Hematopoietic stem cell-engrafted NOD/SCID/IL2Rgamma null mice develop human lymphoid systems and induce long-lasting HIV-1 infection with specific humoral immune responses. *Blood* **109**, 212–218 (2007).

460. Lin, J.-X. & Leonard, W. J. The Common Cytokine Receptor γ Chain Family of Cytokines. *Cold Spring Harb. Perspect. Biol.* **10**, a028449 (2018).

461. Christianson, S. W. *et al.* Role of natural killer cells on engraftment of human lymphoid cells and on metastasis of human T-lymphoblastoid leukemia cells in C57BL/6J-scid mice and in C57BL/6J-scid bg mice. *Cell. Immunol.* **171**, 186–199 (1996).

462. Shultz, L. D. *et al.* Regulation of human short-term repopulating cell (STRC) engraftment in NOD/SCID mice by host CD122+ cells. *Exp. Hematol.* **31**, 551–558 (2003).

463. King, M. *et al.* A new Hu-PBL model for the study of human islet alloreactivity based on NOD-scid mice bearing a targeted mutation in the IL-2 receptor gamma chain gene. *Clin. Immunol. Orlando Fla* **126**, 303–314 (2008).

464. Onder, L. *et al.* IL-7–producing stromal cells are critical for lymph node remodeling. *Blood* **120**, 4675–4683 (2012).

465. Shultz, L. D., Brehm, M. A., Garcia, J. V. & Greiner, D. L. Humanized mice for immune system investigation: progress, promise and challenges. *Nat. Rev. Immunol.* **12**, 786–798 (2012).

466. van Lent, A. U. *et al.* IL-7 enhances thymic human T cell development in 'human immune system' Rag2-/-IL-2Rgammac-/- mice without affecting peripheral T cell homeostasis. *J. Immunol. Baltim. Md 1950* **183**, 7645–7655 (2009).

467. Coppin, E. *et al.* Enhanced differentiation of functional human T cells in NSGW41 mice with tissue-specific expression of human interleukin-7. *Leukemia* **35**, 3561–3567 (2021).

468. Li, Y. *et al.* A human immune system mouse model with robust lymph node development. *Nat. Methods* **15**, 623–630 (2018).

469. McDermott, S. P., Eppert, K., Lechman, E. R., Doedens, M. & Dick, J. E. Comparison of human cord blood engraftment between immunocompromised mouse strains. *Blood* **116**, 193–200 (2010).

470. Strowig, T. *et al.* Priming of protective T cell responses against virus-induced tumors in mice with human immune system components. *J. Exp. Med.* **206**, 1423–1434 (2009).

471. Strowig, T. *et al.* Transgenic expression of human signal regulatory protein alpha in Rag2−/−γc−/− mice improves engraftment of human hematopoietic cells in humanized mice. *Proc. Natl. Acad. Sci.* **108**, 13218–13223 (2011).

472. Wang, H. *et al.* Lack of CD47 on nonhematopoietic cells induces split macrophage tolerance to CD47null cells. *Proc. Natl. Acad. Sci.* **104**, 13744–13749 (2007).

473. Legrand, N. *et al.* Functional CD47/signal regulatory protein alpha (SIRP(alpha)) interaction is required for optimal human T- and natural killer- (NK) cell homeostasis in vivo. *Proc. Natl. Acad. Sci. U. S. A.* **108**, 13224–13229 (2011).

474. Han, M. H. *et al.* Janus-like opposing roles of CD47 in autoimmune brain inflammation in humans and mice. *J. Exp. Med.* **209**, 1325–1334 (2012).

475. Shultz, L. D. *et al.* Humanized Mouse Models of Immunological Diseases and Precision Medicine. *Mamm. Genome Off. J. Int. Mamm. Genome Soc.* **30**, 123–142 (2019).

476. Verma, M. K. *et al.* A Novel Hemolytic Complement-Sufficient NSG Mouse Model Supports Studies of Complement-Mediated Antitumor Activity In Vivo. *J. Immunol. Methods* **446**, 47–53 (2017).

477. Doss, P. M. I. A. *et al.* Male sex chromosomal complement exacerbates the pathogenicity of Th17 cells in a chronic model of central nervous system autoimmunity. *Cell Rep.* **34**, 108833 (2021).

478. Billerbeck, E. *et al.* Development of human CD4+FoxP3+ regulatory T cells in human stem cell factor–, granulocyte-macrophage colony-stimulating factor–, and interleukin-3–expressing NOD-SCID IL2Rγnull humanized mice. *Blood* **117**, 3076–3086 (2011).

479. Nicolini, F. E., Cashman, J. D., Hogge, D. E., Humphries, R. K. & Eaves, C. J. NOD/SCID mice engineered to express human IL-3, GM-CSF and Steel factor constitutively mobilize engrafted human progenitors and compromise human stem cell regeneration. *Leukemia* **18**, 341–347 (2004).

480. Matsuda, M. *et al.* Human NK cell development in hIL-7 and hIL-15 knockin NOD/SCID/IL2rgKO mice. *Life Sci. Alliance* **2**, e201800195 (2019).

481. Rongvaux, A. *et al.* Development and function of human innate immune cells in a humanized mouse model. *Nat. Biotechnol.* **32**, 364–372 (2014).

482. Sefik, E. *et al.* A humanized mouse model of chronic COVID-19. *Nat. Biotechnol.* **40**, 906–920 (2022).

483. Yu, H. *et al.* A novel humanized mouse model with significant improvement of class-switched, antigen-specific antibody production. *Blood* **129**, 959–969 (2017).

484. Li, Y. *et al.* A novel Flt3-deficient HIS mouse model with selective enhancement of human DC development. *Eur. J. Immunol.* **46**, 1291–1299 (2016).

485. Lopez-Lastra, S. *et al.* A functional DC cross talk promotes human ILC homeostasis in humanized mice. *Blood Adv.* **1**, 601–614 (2017).

486. Tarrant, J. C. *et al.* Pathology of macrophage activation syndrome in humanized NSGS mice. *Res. Vet. Sci.* **134**, 137–146 (2021).

487. Shultz, L. D. *et al.* Generation of functional human T-cell subsets with HLA-restricted immune responses in HLA class I expressing NOD/SCID/IL2rγnull humanized mice. *Proc. Natl. Acad. Sci. U. S. A.* **107**, 13022–13027 (2010).

488. Halkias, J. *et al.* Conserved and divergent aspects of human T-cell development and migration in humanized mice. *Immunol. Cell Biol.* **93**, 716–726 (2015).

489. Presa, M. *et al.* The presence and preferential activation of Tregs diminishes adoptive transfer of autoimmune diabetes by polyclonal NOD T cell effectors into NSG versus NOD-scid mice. *J. Immunol. Baltim. Md 1950* **195**, 3011–3019 (2015).

490. Danner, R. *et al.* Expression of HLA Class II Molecules in Humanized NOD.Rag1KO.IL2RgcKO Mice Is Critical for Development and Function of Human T and B Cells. *PLoS ONE* **6**, e19826 (2011).

491. Covassin, L. *et al.* Human peripheral blood CD4 T cell-engrafted non-obese diabetic-scid IL2rγnull H2-Ab1 tm1Gru Tg (human leucocyte antigen D-related 4) mice: a mouse model of human allogeneic graft-versus-host disease. *Clin. Exp. Immunol.* **166**, 269–280 (2011).

492. Zeng, Y. *et al.* Creation of an immunodeficient HLA-transgenic mouse (HUMAMICE) and functional validation of human immunity after transfer of HLA-matched human cells. *PLOS ONE* **12**, e0173754 (2017).

493. King, M. A. *et al.* Human peripheral blood leucocyte non-obese diabetic-severe combined immunodeficiency interleukin-2 receptor gamma chain gene mouse model of xenogeneic graft-versus-host-like disease and the role of host major histocompatibility complex. *Clin. Exp. Immunol.* **157**, 104–118 (2009).

494. Rongvaux, A. *et al.* Human Hemato-Lymphoid System Mice: Current Use and Future Potential for Medicine. *Annu. Rev. Immunol.* **31**, 635–674 (2013).

495. Adigbli, G. *et al.* Humanization of Immunodeficient Animals for the Modeling of Transplantation, Graft Versus Host Disease, and Regenerative Medicine. *Transplantation* **104**, 2290 (2020).

496. Mosier, D. E., Gulizia, R. J., Baird, S. M. & Wilson, D. B. Transfer of a functional human immune system to mice with severe combined immunodeficiency. *Nature* **335**, 256–259 (1988).

497. Ye, C. *et al.* A rapid, sensitive, and reproducible in vivo PBMC humanized murine model for determining therapeutic-related cytokine release syndrome. *FASEB J.* **34**, 12963–12975 (2020).

498. Schmidt, M. R. *et al.* Human BLyS Facilitates Engraftment of Human PBL Derived B Cells in Immunodeficient Mice. *PLoS ONE* **3**, e3192 (2008).

499. Ishikawa, Y. *et al.* Functional engraftment of human peripheral T and B cells and sustained production of autoantibodies in NOD/LtSzscid/IL-2Rγ−/− mice. *Eur. J. Immunol.* **44**, 3453–3463 (2014).

500. Lavender, K. J. *et al.* BLT-humanized C57BL/6 Rag2−/−γc−/−CD47−/− mice are resistant to GVHD and develop B- and T-cell immunity to HIV infection. *Blood* **122**, 4013–4020 (2013).

501. Jinnouchi, F. *et al.* A human SIRPA knock-in xenograft mouse model to study human hematopoietic and cancer stem cells. *Blood* **135**, 1661–1672 (2020).

502. McIntosh, B. E. *et al.* Nonirradiated NOD,B6.SCID Il2rγ−/−KitW41/W41 (NBSGW) Mice Support Multilineage Engraftment of Human Hematopoietic Cells. *Stem Cell Rep.* **4**, 171–180 (2015).

503. Dagur, R. S. *et al.* Human-like NSG mouse glycoproteins sialylation pattern changes the phenotype of human lymphocytes and sensitivity to HIV-1 infection. *BMC Immunol.* **20**, 2 (2019).

504. Aryee, K.-E., Shultz, L. D., Burzenski, L. M., Greiner, D. L. & Brehm, M. A. NOD-scid IL2rγnull mice lacking TLR4 support human immune system development and the study of human-specific innate immunity. *J. Leukoc. Biol.* qiac020 (2023) doi:10.1093/jleuko/qiac020.

505. Brehm, M. A. *et al.* Lack of acute xenogeneic graft-versus-host disease, but retention of T-cell function following engraftment of human peripheral blood mononuclear cells in NSG mice deficient in MHC class I and II expression. *FASEB J.* **33**, 3137–3151 (2019).

506. Yaguchi, T. *et al.* Human PBMC-transferred murine MHC class I/II-deficient NOG mice enable long-term evaluation of human immune responses. *Cell. Mol. Immunol.* **15**, 953–962 (2018).

507. Serr, I. *et al.* Type 1 diabetes vaccine candidates promote human Foxp3+Treg induction in humanized mice. *Nat. Commun.* **7**, 10991 (2016).

508. Majji, S. *et al.* Differential effect of HLA class-I versus class-II transgenes on human T and B cell reconstitution and function in NRG mice. *Sci. Rep.* **6**, 28093 (2016).

509. Jangalwe, S., Shultz, L. D., Mathew, A. & Brehm, M. A. Improved B cell development in humanized NOD-scid IL2Rγnull mice transgenically expressing human stem cell factor, granulocyte-macrophage colony-stimulating factor and interleukin-3. *Immun. Inflamm. Dis.* **4**, 427–440 (2016).

510. Lang, J. *et al.* Replacing mouse BAFF with human BAFF does not improve B-cell maturation in hematopoietic humanized mice. *Blood Adv.* **1**, 2729–2741 (2017).

511. Svoboda, D. S. *et al.* Human iPSC-derived microglia assume a primary microglia-like state after transplantation into the neonatal mouse brain. *Proc. Natl. Acad. Sci. U. S. A.* **116**, 25293–25303 (2019).

512. Borel, F. *et al.* Survival Advantage of Both Human Hepatocyte Xenografts and Genome-Edited Hepatocytes for Treatment of α-1 Antitrypsin Deficiency. *Mol. Ther. J. Am. Soc. Gene Ther.* **25**, 2477–2489 (2017).

513. Jangphattananont, N. *et al.* Distinct Localization of Mature HGF from its Precursor Form in Developing and Repairing the Stomach. *Int. J. Mol. Sci.* **20**, 2955 (2019).

514. Tellez, K. *et al.* In vivo studies of glucagon secretion by human islets transplanted in mice. *Nat. Metab.* **2**, 547–557 (2020).

515. Maykel, J. *et al.* NOD-scidIl2rgtm1Wjl and NOD-Rag1nullIl2rgtm1Wjl: A Model for Stromal Cell–Tumor Cell Interaction for Human Colon Cancer. *Dig. Dis. Sci.* **59**, 1169–1179 (2014).

516. Walcher, L. *et al.* Humanized mouse model: Hematopoietic stemcell transplantation and tracking using short tandem repeat technology. *Immun. Inflamm. Dis.* **8**, 363–370 (2020).

517. Hess, N. J. *et al.* Different Human Immune Lineage Compositions Are Generated in Non-Conditioned NBSGW Mice Depending on HSPC Source. *Front. Immunol.* **11**, (2020).

518. Biedermann, K. A., Sun, J. R., Giaccia, A. J., Tosto, L. M. & Brown, J. M. scid mutation in mice confers hypersensitivity to ionizing radiation and a deficiency in DNA double-strand break repair. *Proc. Natl. Acad. Sci. U. S. A.* **88**, 1394–1397 (1991).

519. Lagresle-Peyrou, C. *et al.* Long-term immune reconstitution in RAG-1-deficient mice treated by retroviral gene therapy: a balance between efficiency and toxicity. *Blood* **107**, 63–72 (2006).

520. Shultz, L. D. *et al.* NOD/LtSz-Rag1null mice: an immunodeficient and radioresistant model for engraftment of human hematolymphoid cells, HIV infection, and adoptive transfer of NOD mouse diabetogenic T cells. *J. Immunol. Baltim. Md 1950* **164**, 2496–2507 (2000).

521. Ponomaryov, T. *et al.* Induction of the chemokine stromal-derived factor-1 following DNA damage improves human stem cell function. *J. Clin. Invest.* **106**, 1331–1339 (2000).

522. Volk, V. *et al.* Multidimensional Analysis Integrating Human T-Cell Signatures in Lymphatic Tissues with Sex of Humanized Mice for Prediction of Responses after Dendritic Cell Immunization. *Front. Immunol.* **8**, 1709 (2017).

523. Lan, P., Tonomura, N., Shimizu, A., Wang, S. & Yang, Y.-G. Reconstitution of a functional human immune system in immunodeficient mice through combined human fetal thymus/liver and CD34+ cell transplantation. *Blood* **108**, 487–492 (2006).

524. Melkus, M. W. *et al.* Humanized mice mount specific adaptive and innate immune responses to EBV and TSST-1. *Nat. Med.* **12**, 1316–1322 (2006).

525. McCune, J. M. *et al.* The SCID-hu mouse: murine model for the analysis of human hematolymphoid differentiation and function. *Science* **241**, 1632–1639 (1988).

526. Moffat, J. F., Stein, M. D., Kaneshima, H. & Arvin, A. M. Tropism of varicella-zoster virus for human CD4+ and CD8+ T lymphocytes and epidermal cells in SCID-hu mice. *J. Virol.* **69**, 5236–5242 (1995).

527. Gobbi, A. *et al.* Human Herpesvirus 6 (HHV-6) Causes Severe Thymocyte Depletion in SCID-hu Thy/Liv Mice. *J. Exp. Med.* **189**, 1953–1960 (1999).

528. Farr Zuend, C., Nomellini, J. F., Smit, J. & Horwitz, M. S. A Caulobacter crescentus Microbicide Protects from Vaginal Infection with HIV-1JR-CSF in Humanized Bone Marrow-Liver-Thymus Mice. *J. Virol.* **93**, e00614-19 (2019).

529. Wang, L.-X. *et al.* Humanized-BLT mouse model of Kaposi's sarcoma-associated herpesvirus infection. *Proc. Natl. Acad. Sci. U. S. A.* **111**, 3146–3151 (2014).

530. Zhang, J. *et al.* Human Microglia Extensively Reconstitute in Humanized-BLT Mice with Human Interleukin-34 Transgene and Support HIV-1 Brain Infection. *Front. Immunol.* **12**, 672415 (2021).

531. Smith, D. J. *et al.* Propagating Humanized BLT Mice for the Study of Human Immunology and Immunotherapy. *Stem Cells Dev.* **25**, 1863–1873 (2016).

532. Wahl, A. *et al.* Precision mouse models with expanded tropism for human pathogens. *Nat. Biotechnol.* **37**, 1163–1173 (2019).

533. Wang, W. *et al.* Modulation of host CD59 expression by varicella-zoster virus in human xenografts in vivo. *Virology* **491**, 96–105 (2016).

534. Vatakis, D. N. *et al.* Using the BLT Humanized Mouse as a Stem Cell based Gene Therapy Tumor Model. *J. Vis. Exp.* (2012) doi:10.3791/4181.

535. Morvan, M. G. *et al.* Genetically edited CD34+ cells derived from human iPS cells in vivo but not in vitro engraft and differentiate into HIV-resistant cells. *Proc. Natl. Acad. Sci. U. S. A.* **118**, e2102404118 (2021).

536. Drake, A. C., Chen, Q. & Chen, J. Engineering humanized mice for improved hematopoietic reconstitution. *Cell. Mol. Immunol.* **9**, 215–224 (2012).

537. Covassin, L. *et al.* Human immune system development and survival of non-obese diabetic (NOD)-scid IL2rγnull (NSG) mice engrafted with human thymus and autologous haematopoietic stem cells. *Clin. Exp. Immunol.* **174**, 372–388 (2013).

538. Chung, Y. S. *et al.* Transplantation of human spleen into immunodeficient NOD/SCID IL2Rγnull mice generates humanized mice that improve functional B cell development. *Clin. Immunol.* **161**, 308–315 (2015).

539. Huang, S.-Y., Tien, H.-F., Su, F.-H. & Hsu, S.-M. Nonirradiated NOD/SCID-Human Chimeric Animal Model for Primary Human Multiple Myeloma: A Potential in Vivo Culture System. *Am. J. Pathol.* **164**, 747–756 (2004).

540. Martinov, T. *et al.* Building the Next Generation of Humanized Hemato-Lymphoid System Mice. *Front. Immunol.* **12**, (2021).

541. Lang, J. *et al.* Studies of Lymphocyte Reconstitution in a Humanized Mouse Model Reveal a Requirement of T Cells for Human B Cell Maturation. *J. Immunol.* **190**, 2090–2101 (2013).

542. Ding, Y. *et al.* FLT3-Ligand Treatment of Humanized Mice Results in the Generation of Large Numbers of CD141+ and CD1c+ Dendritic Cells In Vivo. *J. Immunol.* **192**, 1982–1989 (2014).

543. Namikawa, R., Kaneshima, H., Lieberman, M., Weissman, I. L. & McCune, J. M. Infection of the SCID-hu mouse by HIV-1. *Science* **242**, 1684–1686 (1988).

544. Mosier, D. E. *et al.* Human immunodeficiency virus infection of human-PBL-SCID mice. *Science* **251**, 791–794 (1991).

545. Akkina, R. New generation humanized mice for virus research: Comparative aspects and future prospects. *Virology* **435**, 14–28 (2013).

546. Berges, B. K. & Tanner, A. Modelling of human herpesvirus infections in humanized mice. *J. Gen. Virol.* **95**, 2106–2117 (2014).

547. Leung, C. *et al.* Infectious diseases in humanized mice. *Eur. J. Immunol.* **43**, 2246–2254 (2013).

548. Skelton, J. K., Ortega-Prieto, A. M. & Dorner, M. A Hitchhiker's guide to humanized mice: new pathways to studying viral infections. *Immunology* **154**, 50–61 (2018).

549. Mosier, D. E. *et al.* EBV-induced human B cell lymphomas in hu-PBL-SCID mice. *AIDS Res. Hum. Retroviruses* **8**, 735–740 (1992).

550. Johannessen, I. & Crawford, D. H. In vivo models for Epstein-Barr virus (EBV)-associated B cell lymphoproliferative disease (BLPD). *Rev. Med. Virol.* **9**, 263–277 (1999).

551. Rowe, M. *et al.* Epstein-Barr virus (EBV)-associated lymphoproliferative disease in the SCID mouse model: implications for the pathogenesis of EBV-positive lymphomas in man. *J. Exp. Med.* **173**, 147–158 (1991).

552. Islas-Ohlmayer, M. *et al.* Experimental Infection of NOD/SCID Mice Reconstituted with Human CD34+ Cells with Epstein-Barr Virus. *J. Virol.* **78**, 13891–13900 (2004).

553. Yajima, M. *et al.* A New Humanized Mouse Model of Epstein-Barr Virus Infection That Reproduces Persistent Infection, Lymphoproliferative Disorder, and Cell-Mediated and Humoral Immune Responses. *J. Infect. Dis.* **198**, 673–682 (2008).

554. Lim, W. H., Kireta, S., Russ, G. R. & Coates, P. T. H. Human plasmacytoid dendritic cells regulate immune responses to Epstein-Barr virus (EBV) infection and delay EBV-related mortality in humanized NOD-SCID mice. *Blood* **109**, 1043–1050 (2007).

555. Lei, H. *et al.* Identification and characterization of EBV genomes in spontaneously immortalized human peripheral blood B lymphocytes by NGS technology. *BMC Genomics* **14**, 804 (2013).

556. Fujiwara, S., Matsuda, G. & Imadome, K.-I. Humanized Mouse Models of Epstein-Barr Virus Infection and Associated Diseases. *Pathogens* **2**, 153–176 (2013).

557. Zeng, M.-S. *et al.* Genomic Sequence Analysis of Epstein-Barr Virus Strain GD1 from a Nasopharyngeal Carcinoma Patient. *J. Virol.* **79**, 15323–15330 (2005).

558. Chijioke, O. *et al.* Human natural killer cells prevent infectious mononucleosis features by targeting lytic Epstein-Barr virus infection. *Cell Rep.* **5**, 1489–1498 (2013).

559. Gujer, C. *et al.* Plasmacytoid dendritic cells respond to Epstein-Barr virus infection with a distinct type I interferon subtype profile. *Blood Adv.* **3**, 1129–1144 (2019).

560. Heuts, F. *et al.* T Cells Modulate Epstein-Barr Virus Latency Phenotypes during Infection of Humanized Mice. *J. Virol.* **88**, 3235–3245 (2014).

561. Antsiferova, O. *et al.* Adoptive Transfer of EBV Specific CD8+ T Cell Clones Can Transiently Control EBV Infection in Humanized Mice. *PLoS Pathog.* **10**, (2014).

562. Parker, B. D., Bankier, A., Satchwell, S., Barrell, B. & Farrell, P. J. Sequence and transcription of Raji Epstein-Barr virus DNA spanning the B95-8 deletion region. *Virology* **179**, 339–346 (1990).

563. Weiss, E. R. *et al.* Early Epstein-Barr Virus Genomic Diversity and Convergence toward the B95.8 Genome in Primary Infection. *J. Virol.* **92**, e01466-17 (2018).

564. Skare, J., Edson, C., Farley, J. & Strominger, J. L. The B95-8 isolate of Epstein-Barr virus arose from an isolate with a standard genome. *J. Virol.* **44**, 1088–1091 (1982).

565. Miller, G., Shope, T., Lisco, H., Stitt, D. & Lipman, M. Epstein-Barr Virus: Transformation, Cytopathic Changes, and Viral Antigens in Squirrel Monkey and Marmoset Leukocytes. *Proc. Natl. Acad. Sci. U. S. A.* **69**, 383–387 (1972).

566. Blacklow, N. R., Watson, B. K., Miller, G. & Jacobson, B. M. Mononucleosis with heterophil antibodies and EB virus infection: Acquisition by an elderly patient in hospital. *Am. J. Med.* **51**, 549–552 (1971).

567. Takada, K. *et al.* An Epstein-Barr virus-producer line Akata: Establishment of the cell line and analysis of viral DNA. *Virus Genes* **5**, 147–156 (1991).

568. Kanda, T., Yajima, M., Ahsan, N., Tanaka, M. & Takada, K. Production of High-Titer Epstein-Barr Virus Recombinants Derived from Akata Cells by Using a Bacterial Artificial Chromosome System. *J. Virol.* **78**, 7004–7015 (2004).

569. Shimizu, N., Yoshiyama, H. & Takada, K. Clonal propagation of Epstein-Barr virus (EBV) recombinants in EBV-negative Akata cells. *J. Virol.* **70**, 7260–7263 (1996).

570. Gregory, C. D., Murray, R. J., Edwards, C. F. & Rickinson, A. B. Downregulation of cell adhesion molecules LFA-3 and ICAM-1 in Epstein-Barr virus-positive Burkitt's lymphoma underlies tumor cell escape from virus-specific T cell surveillance. *J. Exp. Med.* **167**, 1811–1824 (1988).

571. Desgranges, C., Lavoué, M. F., Patet, J. & de-Thé, G. In vitro transforming activity of Epstein-Barr virus (EBV). II. Differences between M81 and B95-8 EBV strains. *Biomed. Publiee Pour AAICIG* **30**, 102–108 (1979).

572. Church, T. M., Verma, D., Thompson, J. & Swaminathan, S. Efficient Translation of Epstein-Barr Virus (EBV) DNA Polymerase Contributes to the Enhanced Lytic Replication Phenotype of M81 EBV. *J. Virol.* **92**, e01794-17 (2018).

573. Volk, V. *et al.* PD-1 Blockade Aggravates Epstein–Barr Virus+ Post-Transplant Lymphoproliferative Disorder in Humanized Mice Resulting in Central Nervous System Involvement and CD4+ T Cell Dysregulations. *Front. Oncol.* **10**, (2021).

574. Tsai, M.-H. *et al.* Spontaneous Lytic Replication and Epitheliotropism Define an Epstein-Barr Virus Strain Found in Carcinomas. *Cell Rep.* **5**, 458–470 (2013).

575. Lin, X. *et al.* The Epstein-Barr Virus BART miRNA Cluster of the M81 Strain Modulates Multiple Functions in Primary B Cells. *PLoS Pathog.* **11**, (2015).

576. Dolan, A., Addison, C., Gatherer, D., Davison, A. J. & McGeoch, D. J. The genome of Epstein–Barr virus type 2 strain AG876. *Virology* **350**, 164–170 (2006).

577. Pizzo, P. A., Magrath, I. T., Chattopadhyay, S. K., Biggar, R. J. & Gerber, P. A new tumour-derived transforming strain of Epstein-Barr virus. *Nature* **272**, 629–631 (1978).

578. Toomey, N. L. *et al.* Induction of a TRAIL mediated suicide program by interferon alpha in primary effusion lymphoma. *Oncogene* **20**, 7029–7040 (2001).

579. Kurokawa, M. *et al.* Azidothymidine inhibits NF-κB and induces Epstein-Barr virus gene expression in Burkitt lymphoma. *Blood* **106**, 235–240 (2005).

580. Heuts, F. & Nagy, N. Mice with Reconstituted Human Immune System Components as a Tool to Study Immune Cell Interactions in EBV Infection. in *Epstein Barr Virus* (eds. Minarovits, J. & Niller, H. H.) 229–240 (Springer New York, 2017). doi:10.1007/978-1-4939-6655-4_17.

581. Danisch, S. *et al.* Spatiotemporally Skewed Activation of Programmed Cell Death Receptor 1-Positive T Cells after Epstein-Barr Virus Infection and Tumor Development in Long-Term Fully Humanized Mice. *Am. J. Pathol.* **189**, 521–539 (2019).

582. Chatterjee, B. *et al.* CD8+ T cells retain protective functions despite sustained inhibitory receptor expression during Epstein-Barr virus infection in vivo. *PLoS Pathog.* **15**, e1007748 (2019).

583. Ma, S.-D. *et al.* PD-1/CTLA-4 Blockade Inhibits Epstein-Barr Virus-Induced Lymphoma Growth in a Cord Blood Humanized-Mouse Model. *PLoS Pathog.* **12**, (2016).

584. Zdimerova, H. *et al.* Attenuated immune control of Epstein–Barr virus in humanized mice is associated with the multiple sclerosis risk factor HLA-DR15. *Eur. J. Immunol.* **51**, 64–75 (2021).

585. Yuling, H. *et al.* EBV-Induced Human CD8+ NKT Cells Suppress Tumorigenesis by EBV-Associated Malignancies. *Cancer Res.* **69**, 7935–7944 (2009).

586. Whitehurst, C. B. *et al.* Knockout of Epstein-Barr Virus BPLF1 Retards B-Cell Transformation and Lymphoma Formation in Humanized Mice. *mBio* **6**, (2015).

587. Zhang, X. *et al.* PLK1-dependent phosphorylation restrains EBNA2 activity and lymphomagenesis in EBV-infected mice. *EMBO Rep.* **22**, e53007 (2021).

588. White, R. E. *et al.* EBNA3B-deficient EBV promotes B cell lymphomagenesis in humanized mice and is found in human tumors. *J. Clin. Invest.* **122**, 1487–1502 (2012).

589. Accardi, R. *et al.* The mycotoxin aflatoxin B1 stimulates Epstein–Barr virus-induced B-cell transformation in in vitro and in vivo experimental models. *Carcinogenesis* **36**, 1440–1451 (2015).

590. McHugh, D. *et al.* Persistent KSHV Infection Increases EBV-Associated Tumor Formation In Vivo via Enhanced EBV Lytic Gene Expression. *Cell Host Microbe* **22**, 61-73.e7 (2017).

591. McHugh, D. *et al.* EBV renders B cells susceptible to HIV-1 in humanized mice. *Life Sci. Alliance* **3**, e202000640 (2020).

592. Sato, K. *et al.* A novel animal model of Epstein-Barr virus–associated hemophagocytic lymphohistiocytosis in humanized mice. *Blood* **117**, 5663–5673 (2011).

593. Chellapandian, D. *et al.* Treatment of Epstein Barr virus-induced haemophagocytic lymphohistiocytosis with rituximab-containing chemo-immunotherapeutic regimens. *Br. J. Haematol.* **162**, 376–382 (2013).

594. Kuwana, Y. *et al.* Epstein-Barr Virus Induces Erosive Arthritis in Humanized Mice. *PLoS ONE* **6**, (2011).

595. Nagasawa, Y. *et al.* Human osteoclastogenesis in Epstein-Barr virus-induced erosive arthritis in humanized NOD/Shi-scid/IL-2Rγnull mice. *PLoS ONE* **16**, (2021).

596. van Zyl, D. G. *et al.* Immunogenic particles with a broad antigenic spectrum stimulate cytolytic T cells and offer increased protection against EBV infection ex vivo and in mice. *PLoS Pathog.* **14**, e1007464 (2018).

597. Wei, C.-J. *et al.* A bivalent Epstein-Barr virus vaccine induces neutralizing antibodies that block infection and confer immunity in humanized mice. *Sci. Transl. Med.* **14**, eabf3685 (2022).

598. Malhi, H. *et al.* Immunization with a self-assembling nanoparticle vaccine displaying EBV gH/gL protects humanized mice against lethal viral challenge. *Cell Rep. Med.* **3**, 100658 (2022).

599. Liu, W. N. *et al.* Establishment and Characterization of Humanized Mouse NPC-PDX Model for Testing Immunotherapy. *Cancers* **12**, (2020).

600. Schuhmachers, P. & Münz, C. Modification of EBV Associated Lymphomagenesis and Its Immune Control by Co-Infections and Genetics in Humanized Mice. *Front. Immunol.* **12**, (2021).

601. Villaudy, J., Schotte, R., Legrand, N. & Spits, H. Critical assessment of human antibody generation in humanized mouse models. *J. Immunol. Methods* **410**, 18–27 (2014).

602. Alves da Costa, T., Lang, J., Torres, R. M. & Pelanda, R. The development of human immune system mice and their use to study tolerance and autoimmunity. *J. Transl. Autoimmun.* **2**, 100021 (2019).

603. Walsh, N. C. *et al.* Humanized Mouse Models of Clinical Disease. *Annu. Rev. Pathol. Mech. Dis.* **12**, 187–215 (2017).

604. Huntington, N. D. *et al.* Autonomous and extrinsic regulation of thymopoiesis inhuman immune system (HIS) mice. *Eur. J. Immunol.* **41**, 2883–2893 (2011).

605. Brugman, M. H. *et al.* Development of a diverse human T-cell repertoire despite stringent restriction of hematopoietic clonality in the thymus. *Proc. Natl. Acad. Sci.* **112**, E6020–E6027 (2015).

606. Onoe, T. *et al.* Human Natural Regulatory T Cell Development, Suppressive Function, and Postthymic Maturation in a Humanized Mouse Model. *J. Immunol.* **187**, 3895–3903 (2011).

607. Sonntag, K. *et al.* Chronic graft-versus-host-disease in CD34(+)-humanized NSG mice is associated with human susceptibility HLA haplotypes for autoimmune disease. *J. Autoimmun.* **62**, 55–66 (2015).

608. Khosravi-Maharlooei, M. *et al.* Cross-reactive public TCR sequences undergo positive selection in the human thymic repertoire. *J. Clin. Invest.* **129**, 2446–2462 (2019).

609. Ehx, G. *et al.* Xenogeneic Graft-Versus-Host Disease in Humanized NSG and NSG-HLA-A2/HHD Mice. *Front. Immunol.* **9**, 1943 (2018).

610. Lang, J. *et al.* Receptor editing and genetic variability in human autoreactive B cells. *J. Exp. Med.* **213**, 93–108 (2015).

611. Ajith, A. *et al.* Humanized Mouse Model as a Novel Approach in the Assessment of Human Allogeneic Responses in Organ Transplantation. *Front. Immunol.* **12**, 687715 (2021).

612. Ali, N. *et al.* Xenogeneic Graft-versus-Host-Disease in NOD-scid IL-2Rγnull Mice Display a T-Effector Memory Phenotype. *PLoS ONE* **7**, e44219 (2012).

613. Pino, S. *et al.* Development of Novel Major Histocompatibility Complex Class I and Class II-Deficient NOD-SCID IL2R Gamma Chain Knockout Mice for Modeling Human Xenogeneic Graft-Versus-Host Disease. *Methods Mol. Biol. Clifton NJ* **602**, 105–117 (2010).

614. Nakauchi, Y. *et al.* Effective treatment against severe graft-versus-host disease with allele-specific anti-HLA monoclonal antibody in a humanized mouse model. *Exp. Hematol.* **43**, 79-88.e4 (2015).

615. Tary-Lehmann, M., Lehmann, P. V., Schols, D., Roncarolo, M. G. & Saxon, A. Anti-SCID mouse reactivity shapes the human CD4+ T cell repertoire in hu-PBL-SCID chimeras. *J. Exp. Med.* **180**, 1817–1827 (1994).

616. Mutis, T. *et al.* Human Regulatory T Cells Control Xenogeneic Graft-versus-Host Disease Induced by Autologous T Cells in RAG2−/−γc−/− Immunodeficient Mice. *Clin. Cancer Res.* **12**, 5520–5525 (2006).

617. Reading, J. L. *et al.* Augmented Expansion of Treg Cells From Healthy and Autoimmune Subjects via Adult Progenitor Cell Co-Culture. *Front. Immunol.* **12**, 716606 (2021).

618. Lockridge, J. L. *et al.* Mice Engrafted With Human Fetal Thymic Tissue And Hematopoietic Stem Cells Develop Pathology Resembling Chronic GVHD. *Biol. Blood Marrow Transplant. J. Am. Soc. Blood Marrow Transplant.* **19**, 1310–1322 (2013).

619. Hogenes, M. C. H. *et al.* Histological Assessment of the Sclerotic Graft-versus-Host Response in the Humanized RAG2−/−γc−/− Mouse Model. *Biol. Blood Marrow Transplant.* **18**, 1023–1035 (2012).

620. Ono, R. *et al.* Co-activation of macrophages and T cells contribute to chronic GVHD in human IL-6 transgenic humanised mouse model. *eBioMedicine* **41**, 584–596 (2019).

621. Schinnerling, K., Rosas, C., Soto, L., Thomas, R. & Aguillón, J. C. Humanized Mouse Models of Rheumatoid Arthritis for Studies on Immunopathogenesis and Preclinical Testing of Cell-Based Therapies. *Front. Immunol.* **10**, (2019).

622. Brehm, M. A. *et al.* Human immune system development and rejection of human islet allografts in spontaneously diabetic NOD-Rag1null IL2rgammanull Ins2Akita mice. *Diabetes* **59**, 2265–2270 (2010).

623. Zhao, Y. *et al.* Selective destruction of mouse islet beta cells by human T lymphocytes in a newly-established humanized type 1 diabetic model. *Biochem. Biophys. Res. Commun.* **399**, 629–636 (2010).

624. Dai, C. *et al.* Stress-impaired transcription factor expression and insulin secretion in transplanted human islets. *J. Clin. Invest.* **126**, 1857–1870 (2016).

625. Whitfield-Larry, F. *et al.* HLA-A2–Matched Peripheral Blood Mononuclear Cells From Type 1 Diabetic Patients, but Not Nondiabetic Donors, Transfer Insulitis to NOD-scid/γcnull/HLA-A2 Transgenic Mice Concurrent With the Expansion of Islet-Specific CD8+ T cells. *Diabetes* **60**, 1726–1733 (2011).

626. Chen, J. *et al.* Humanized Mouse Models of Systemic Lupus Erythematosus: Opportunities and Challenges. *Front. Immunol.* **12**, 816956 (2022).

627. Freitas, E. C., de Oliveira, M. S. & Monticielo, O. A. Pristane-induced lupus: considerations on this experimental model. *Clin. Rheumatol.* **36**, 2403–2414 (2017).

628. Andrade, D. *et al.* Engraftment of PBMC from SLE and APS Donors into BALB-Rag2−/−IL2Rgc−/− Mice: a Promising Model for Studying Human Disease. *Arthritis Rheum.* **63**, 2764–2773 (2011).

629. Mihaylova, N. *et al.* Suppression of autoreactive T and B lymphocytes by anti-annexin A1 antibody in a humanized NSG murine model of systemic lupus erythematosus. *Clin. Exp. Immunol.* **199**, 278–293 (2020).

630. O'Boyle, G. *et al.* Chemokine receptor CXCR3 agonist prevents human T-cell migration in a humanized model of arthritic inflammation. *Proc. Natl. Acad. Sci. U. S. A.* **109**, 4598–4603 (2012).

631. Ye, Z. *et al.* Arachidonic acid-regulated calcium signaling in T cells from patients with rheumatoid arthritis promotes synovial inflammation. *Nat. Commun.* **12**, 907 (2021).

632. Shen, Y. *et al.* Metabolic control of the scaffold protein TKS5 in tissue-invasive, pro-inflammatory T cells. *Nat. Immunol.* **18**, 1025–1034 (2017).

633. Misharin, A. V. *et al.* Development of a new humanized mouse model to study acute inflammatory arthritis. *J. Transl. Med.* **10**, 190 (2012).

634. Chang, N.-H., Inman, R. D., Dick, J. E. & Wither, J. E. Bone marrow-derived human hematopoietic stem cells engraft NOD/SCID mice and traffic appropriately to an inflammatory stimulus in the joint. *J. Rheumatol.* **37**, 496–502 (2010).

635. Young, N. A. *et al.* A chimeric human-mouse model of Sjögren's syndrome. *Clin. Immunol. Orlando Fla* **156**, 1–8 (2015).

636. Unterweger, A. L. *et al.* NOD/scid IL-2Rγnull mice reconstituted with peripheral blood mononuclear cells from patients with Crohn's disease reflect the human pathological phenotype. *Immun. Inflamm. Dis.* **9**, 1631–1647 (2021).

637. Taconic Biosciences. Webinar Q&A — Case Study: Variance and its Implications on Study Design in the huNOG-EXL. https://www.taconic.com/taconic-insights/oncology-immuno-oncology/webinar-qa-variance-implications-study-design-hunog-exl.html (2021).

638. Little, M. A. *et al.* Anti-proteinase 3 anti-neutrophil cytoplasm autoantibodies recapitulate systemic vasculitis in mice with a humanized immune system. *PloS One* **7**, e28626 (2012).

639. Vudattu, N. K. *et al.* Humanized mice as a model for aberrant responses in human T cell immunotherapy. *J. Immunol. Baltim. Md 1950* **193**, 587–596 (2014).

640. Gorantla, S., Gendelman, H. E. & Poluektova, L. Y. Can Humanized Mice Reflect the Complex Pathobiology of HIV-Associated Neurocognitive Disorders? *J. Neuroimmune Pharmacol.* **7**, 352–362 (2012).

641. Manocha, G. D. *et al.* Defining the contribution of neuroinflammation to Parkinson's disease in humanized immune system mice. *Mol. Neurodegener.* **12**, 17 (2017).

642. Fugger, L., Friese, M. A. & Bell, J. I. From genes to function: the next challenge to understanding multiple sclerosis. *Nat. Rev. Immunol.* **9**, 408–417 (2009).

643. El Behi, M. *et al.* Adaptive human immunity drives remyelination in a mouse model of demyelination. *Brain J. Neurol.* **140**, 967–980 (2017).

644. Zayoud, M. *et al.* Subclinical CNS Inflammation as Response to a Myelin Antigen in Humanized Mice. *J. Neuroimmune Pharmacol.* **8**, 1037–1047 (2013).

645. Hartung, H.-P. & Kieseier, B. C. Atacicept: targeting B cells in multiple sclerosis. *Ther. Adv. Neurol. Disord.* **3**, 205–216 (2010).

646. Schmidt, J. *et al.* Treatment and prevention of experimental autoimmune neuritis with superagonistic CD28-specific monoclonal antibodies. *J. Neuroimmunol.* **140**, 143–152 (2003).

647. Suntharalingam, G. *et al.* Cytokine storm in a phase 1 trial of the anti-CD28 monoclonal antibody TGN1412. *N. Engl. J. Med.* **355**, 1018–1028 (2006).

648. Zorzella, S. F. G., Seger, J., Martins, D. R., Pelizon, A. C. & Sartori, A. Resistance to experimental autoimmune encephalomyelitis development in Lewis rats from a conventional animal facility. *Mem. Inst. Oswaldo Cruz* **102**, 931–936 (2007).

649. Salvador, F. *et al.* A Spontaneous Model of Experimental Autoimmune Encephalomyelitis Provides Evidence of MOG-Specific B Cell Recruitment and Clonal Expansion. *Front. Immunol.* **13**, (2022).

650. Jayaraman, S. & Jayaraman, A. Long-Term Provision of Acidified Drinking Water Fails to Influence Autoimmune Diabetes and Encephalomyelitis. *J. Diabetes Res.* **2018**, e3424691 (2018).

651. Breithaupt, C. *et al.* Structural insights into the antigenicity of myelin oligodendrocyte glycoprotein. *Proc. Natl. Acad. Sci. U. S. A.* **100**, 9446–9451 (2003).

652. Weck, K. E., Barkon, M. L., Yoo, L. I., Speck, S. H. & Virgin HW, I. V. Mature B cells are required for acute splenic infection, but not for establishment of latency, by murine gammaherpesvirus 68. *J. Virol.* **70**, 6775–6780 (1996).

653. Liu, S., Pavlova, I. V., Virgin, H. W. & Speck, S. H. Characterization of Gammaherpesvirus 68 Gene 50 Transcription. *J. Virol.* **74**, 2029–2037 (2000).

654. Greijer, A. E., van de Crommert, J. M. G., Stevens, S. J. C. & Middeldorp, J. M. Molecular Fine-Specificity Analysis of Antibody Responses to Human Cytomegalovirus and Design of Novel Synthetic-Peptide-Based Serodiagnostic Assays. *J. Clin. Microbiol.* **37**, 179–188 (1999).

655. Prior, H., Sewell, F. & Stewart, J. Overview of 3Rs opportunities in drug discovery and development using non-human primates. *Drug Discov. Today Dis. Models* **23**, 11–16 (2017).

656. Mostarica-Stojković, M., Petrović, M. & Lukić, M. L. Resistance to the induction of EAE in AO rats: its prevention by the pre-treatment with cyclophosphamide or low dose of irradiation. *Clin. Exp. Immunol.* **50**, 311–317 (1982).

657. van Bekkum, D. W. Effectiveness and risks of total body irradiation for conditioning in the treatment of autoimmune disease with autologous bone marrow transplantation. *Rheumatology* **38**, 757–761 (1999).

658. Vitale, B., Allegretti, N. & Matošić, M. Influence of X-Irradiation on Experimental Allergic Encephalomyelitis in Rats. *Radiat. Res.* **28**, 727–734 (1966).

659. Fujiwara, S., Imadome, K.-I. & Takei, M. Modeling EBV infection and pathogenesis in new-generation humanized mice. *Exp. Mol. Med.* **47**, e135 (2015).

660. Hohlfeld, R. & Steinman, L. T Cell–Transfer Experimental Autoimmune Encephalomyelitis: Pillar of Multiple Sclerosis and Autoimmunity. *J. Immunol.* **198**, 3381–3383 (2017).

661. Brehm, M. A. *et al.* Parameters for Establishing Humanized Mouse Models to Study Human Immunity: Analysis of Human Hematopoietic Stem Cell Engraftment in Three Immunodeficient Strains of Mice Bearing the IL2rγnull Mutation. *Clin. Immunol. Orlando Fla* **135**, 84–98 (2010).

662. Liang, Z., Dong, X., Zhang, Z., Zhang, Q. & Zhao, Y. Age-related thymic involution: Mechanisms and functional impact. *Aging Cell* **21**, e13671 (2022).

663. Hasgur, S., Aryee, K. E., Shultz, L. D., Greiner, D. L. & Brehm, M. A. Generation of Immunodeficient Mice Bearing Human Immune Systems by the Engraftment of Hematopoietic Stem Cells. *Methods Mol. Biol. Clifton NJ* **1438**, 67–78 (2016).

664. Ford, M. L. & Evavold, B. D. Specificity, magnitude, and kinetics of MOG-specific CD8+ T cell responses during experimental autoimmune encephalomyelitis. *Eur. J. Immunol.* **35**, 76–85 (2005).

665. Kersh, A. E., Edwards, L. J. & Evavold, B. D. Progression of relapsing-remitting demyelinating disease does not require increased TCR affinity or epitope spread. *J. Immunol. Baltim. Md 1950* **193**, 4429–4438 (2014).

666. Klein, S. L. & Flanagan, K. L. Sex differences in immune responses. *Nat. Rev. Immunol.* **16**, 626–638 (2016).

667. Lyons, P. A. *et al.* The NOD Idd9 Genetic Interval Influences the Pathogenicity of Insulitis and Contains Molecular Variants of Cd30, Tnfr2, and Cd137. *Immunity* **13**, 107–115 (2000).

668. Wang, L. *et al.* Epitope-Specific Tolerance Modes Differentially Specify Susceptibility to Proteolipid Protein-Induced Experimental Autoimmune Encephalomyelitis. *Front. Immunol.* **8**, (2017).

669. Huntemann, N. *et al.* An optimized and validated protocol for inducing chronic experimental autoimmune encephalomyelitis in C57BL/6J mice. *J. Neurosci. Methods* **367**, 109443 (2022).

670. Molnarfi, N. *et al.* MHC class II–dependent B cell APC function is required for induction of CNS autoimmunity independent of myelin-specific antibodies. *J. Exp. Med.* **210**, 2921–2937 (2013).

671. Stromnes, I. M. & Goverman, J. M. Active induction of experimental allergic encephalomyelitis. *Nat. Protoc.* **1**, 1810–1819 (2006).

672. Svensson, L. *et al.* A comparative analysis of B cell-mediated myelin oligodendrocyte glycoprotein-experimental autoimmune encephalomyelitis pathogenesis in B cell-deficient mice reveals an effect on demyelination. *Eur. J. Immunol.* **32**, 1939–1946 (2002).

673. Bernard, C. C. *et al.* Myelin oligodendrocyte glycoprotein: a novel candidate autoantigen in multiple sclerosis. *J. Mol. Med. Berl. Ger.* **75**, 77–88 (1997).

674. Girvin, A. M. *et al.* A Critical Role for B7/CD28 Costimulation in Experimental Autoimmune Encephalomyelitis: A Comparative Study Using Costimulatory Molecule-Deficient Mice and Monoclonal Antibody Blockade1. *J. Immunol.* **164**, 136–143 (2000).

675. Slavin, A. *et al.* Induction of a Multiple Sclerosis-Like Disease in Mice with an Immunodominant Epitope of Myelin Oligodendrocyte Glycoprotein. *Autoimmunity* **28**, 109–120 (1998).

676. Glatigny, S. & Bettelli, E. Experimental Autoimmune Encephalomyelitis (EAE) as Animal Models of Multiple Sclerosis (MS). *Cold Spring Harb. Perspect. Med.* **8**, a028977 (2018).

677. Delens, L. *et al.* In Vitro Th17-Polarized Human CD4+ T Cells Exacerbate Xenogeneic Graft-versus-Host Disease. *Biol. Blood Marrow Transplant.* **25**, 204–215 (2019).

678. Koarada, S., Wu, Y. & Ridgway, W. M. Increased Entry into the IFN-γ Effector Pathway by CD4+ T Cells Selected by I-Ag7 on a Nonobese Diabetic Versus C57BL/6 Genetic Background. *J. Immunol.* **167**, 1693–1702 (2001).

679. Pender, M. P., Csurhes, P. A., Burrows, J. M. & Burrows, S. R. Defective T-cell control of Epstein–Barr virus infection in multiple sclerosis. *Clin. Transl. Immunol.* **6**, e126 (2017).

680. Legroux, L. & Arbour, N. Multiple Sclerosis and T Lymphocytes: An Entangled Story. *J. Neuroimmune Pharmacol.* **10**, 528–546 (2015).

681. Huseby, E. S., Huseby, P. G., Shah, S., Smith, R. & Stadinski, B. D. Pathogenic CD8 T Cells in Multiple Sclerosis and Its Experimental Models. *Front. Immunol.* **3**, (2012).

682. Mars, L. T. *et al.* CD8 T Cell Responses to Myelin Oligodendrocyte Glycoprotein-Derived Peptides in Humanized HLA-A*0201-Transgenic Mice1. *J. Immunol.* **179**, 5090–5098 (2007).

683. Yamasaki, R. *et al.* Differential roles of microglia and monocytes in the inflamed central nervous system. *J. Exp. Med.* **211**, 1533–1549 (2014).

684. Morillon, Y. M., Sabzevari, A., Schlom, J. & Greiner, J. W. The Development of Next-generation PBMC Humanized Mice for Preclinical Investigation of Cancer Immunotherapeutic Agents. *Anticancer Res.* **40**, 5329–5341 (2020).

685. Gresle, M. M. *et al.* Serum phosphorylated neurofilament-heavy chain levels in multiple sclerosis patients. *J. Neurol. Neurosurg. Psychiatry* **85**, 1209–1213 (2014).

686. Shehab, A. A., Solima, D. A., Abdel-Hafeez, M. A. & Mohamed, S. M. Serum Phosphorylated Neurofilament Heavy Chain Level in Relapsing Remitting Multiple Sclerosis in Correlation to Disease Activity and Disability. *Egypt. J. Immunol.* **26**, 1–13 (2019).

687. Gresle, M. M. *et al.* Validation of a novel biomarker for acute axonal injury in experimental autoimmune encephalomyelitis. *J. Neurosci. Res.* **86**, 3548–3555 (2008).

688. Furtado, G. C. *et al.* Swift Entry of Myelin-Specific T Lymphocytes into the Central Nervous System in Spontaneous Autoimmune Encephalomyelitis. *J. Immunol.* **181**, 4648–4655 (2008).

689. Leuenberger, T. *et al.* The Role of CD8+ T Cells and Their Local Interaction with CD4+ T Cells in Myelin Oligodendrocyte Glycoprotein35–55–Induced Experimental Autoimmune Encephalomyelitis. *J. Immunol.* **191**, 4960–4968 (2013).

690. Bourekas, E. C. *et al.* Lesions of the Corpus Callosum: MR Imaging and Differential Considerations in Adults and Children. *Am. J. Roentgenol.* **179**, 251–257 (2002).

691. Constantinescu, C. S. & Hilliard, B. A. Adjuvants in EAE. in *Experimental Models of Multiple Sclerosis* (eds. Lavi, E. & Constantinescu, C. S.) 73–84 (Springer US, 2005). doi:10.1007/0-387-25518-4_5.

692. Fontes, J. A. *et al.* Complete Freund's adjuvant induces experimental autoimmune myocarditis by enhancing IL-6 production during initiation of the immune response. *Immun. Inflamm. Dis.* **5**, 163–176 (2017).

693. Lazarević, M. *et al.* Complete Freund's adjuvant-free experimental autoimmune encephalomyelitis in Dark Agouti rats is a valuable tool for multiple sclerosis studies. *J. Neuroimmunol.* **354**, 577547 (2021).

694. Tigno-Aranjuez, J. T., Jaini, R., Tuohy, V. K., Lehmann, P. V. & Tary-Lehmann, M. Encephalitogenicity of Complete Freund's Adjuvant Relative to CpG Is Linked to Induction of Th17 Cells. *J. Immunol.* **183**, 5654–5661 (2009).

695. Verlaat, L. *et al.* Novel pre-clinical mouse models for chronic Graft-versus-Host Disease. *Front. Immunol.* **13**, (2023).

696. Haque, M. *et al.* Modelling Graft-Versus-Host Disease in Mice Using Human Peripheral Blood Mononuclear Cells. *Bio-Protoc.* **12**, e4566 (2022).

697. Rawji, K. S. & Yong, V. W. The Benefits and Detriments of Macrophages/Microglia in Models of Multiple Sclerosis. *Clin. Dev. Immunol.* **2013**, 948976 (2013).

698. Ajami, B., Bennett, J. L., Krieger, C., McNagny, K. M. & Rossi, F. M. V. Infiltrating monocytes trigger EAE progression, but do not contribute to the resident microglia pool. *Nat. Neurosci.* **14**, 1142–1149 (2011).

699. Wang, H. *et al.* CD47 antibody blockade suppresses microglia-dependent phagocytosis and monocyte transition to macrophages, impairing recovery in EAE. *JCI Insight* **6**, (2021).

700. Tsang, J. Y. S., Chai, J. G. & Lechler, R. Antigen presentation by mouse CD4+ T cells involving acquired MHC class II:peptide complexes: another mechanism to limit clonal expansion? *Blood* **101**, 2704–2710 (2003).

701. Schooten, E., Klous, P., van den Elsen, P. J. & Holling, T. M. Lack of MHC-II expression in activated mouse T cells correlates with DNA methylation at the CIITA-PIII region. *Immunogenetics* **57**, 795–799 (2005).

702. Holguin, L., Echavarria, L. & Burnett, J. C. Novel Humanized Peripheral Blood Mononuclear Cell Mouse Model with Delayed Onset of Graft-versus-Host Disease for Preclinical HIV Research. *J. Virol.* **96**, e01394-21 (2022).

703. Chao, M. P. *et al.* Therapeutic Targeting of the Macrophage Immune Checkpoint CD47 in Myeloid Malignancies. *Front. Oncol.* **9**, (2020).

704. Kwant-Mitchell, A., Pek, E. A., Rosenthal, K. L. & Ashkar, A. A. Development of Functional Human NK Cells in an Immunodeficient Mouse Model with the Ability to Provide Protection against Tumor Challenge. *PLoS ONE* **4**, e8379 (2009).

705. Junker, A. *et al.* MicroRNA profiling of multiple sclerosis lesions identifies modulators of the regulatory protein CD47. *Brain J. Neurol.* **132**, 3342–3352 (2009).

706. Cho, M.-J. *et al.* Steady-state memory-phenotype conventional CD4+ T cells exacerbate autoimmune neuroinflammation in a bystander manner via the Bhlhe40/GM-CSF axis. *Exp. Mol. Med.* **55**, 1033–1045 (2023).

707. Sato-Hashimoto, M. *et al.* Microglial SIRPα regulates the emergence of CD11c+ microglia and demyelination damage in white matter. *eLife* **8**, e42025 (2019).

708. Bauer, J., Sminia, T., Wouterlood, F. G. & Dijkstra, C. D. Phagocytic activity of macrophages and microglial cells during the course of acute and chronic relapsing experimental autoimmune encephalomyelitis. *J. Neurosci. Res.* **38**, 365–375 (1994).

709. Montilla, A. *et al.* Microglia and meningeal macrophages depletion delays the onset of experimental autoimmune encephalomyelitis. *Cell Death Dis.* **14**, 1–13 (2023).

710. Schroeder, M. A. & DiPersio, J. F. Mouse models of graft-versus-host disease: advances and limitations. *Dis. Model. Mech.* **4**, 318–333 (2011).

711. Lucas, P. J., Shearer, G. M., Neudorf, S. & Gress, R. E. The human antimurine xenogeneic cytotoxic response. I. Dependence on responder antigen-presenting cells. *J. Immunol. Baltim. Md 1950* **144**, 4548–4554 (1990).

712. Koyama, M. & Hill, G. R. Mouse Models of Antigen Presentation in Hematopoietic Stem Cell Transplantation. *Front. Immunol.* **12**, (2021).

713. Stevanović, S. *et al.* Donor T cells administered over HLA class II barriers mediate antitumor immunity without broad off-target toxicity in a NOD/scid mouse model of acute leukemia. *Biol. Blood Marrow Transplant. J. Am. Soc. Blood Marrow Transplant.* **19**, 867–875 (2013).

714. Zhang, W., Young, A. C., Imarai, M., Nathenson, S. G. & Sacchettini, J. C. Crystal structure of the major histocompatibility complex class I H-2Kb molecule containing a single viral peptide: implications for peptide binding and T-cell receptor recognition. *Proc. Natl. Acad. Sci. U. S. A.* **89**, 8403–8407 (1992).

715. Weiss, E. *et al.* The DNA sequence of the H-2kb gene: evidence for gene conversion as a mechanism for the generation of polymorphism in histocompatibilty antigens. *EMBO J.* **2**, 453–462 (1983).

716. Kroger, C. J. & Alexander-Miller, M. A. Dose-dependent modulation of CD8 and functional avidity as a result of peptide encounter. *Immunology* **122**, 167–178 (2007).

717. Wolfl, M. *et al.* Activation-induced expression of CD137 permits detection, isolation, and expansion of the full repertoire of CD8+ T cells responding to antigen without requiring knowledge of epitope specificities. *Blood* **110**, 201–210 (2007).

718. Lucas, P. J., Bare, C. V. & Gress, R. E. The human anti-murine xenogeneic cytotoxic response. II. Activated murine antigen-presenting cells directly stimulate human T helper cells. *J. Immunol. Baltim. Md 1950* **154**, 3761–3770 (1995).

719. Mayo, S. & Quinn, A. Altered susceptibility to EAE in congenic NOD mice: Altered processing of the encephalitogenic MOG35–55 peptide by NOR/LtJ mice. *Clin. Immunol.* **122**, 91–100 (2007).

720. Dehmani, S. *et al.* SIRPγ-CD47 Interaction Positively Regulates the Activation of Human T Cells in Situation of Chronic Stimulation. *Front. Immunol.* **12**, (2021).

721. Velazquez, F. E., Autio, A., Newton, G. & Luscinskas, F. W. Antibody blockade of CD47-SIRPα axis is protective in the murine model of Experimental Autoimmune Encephalomyelitis. *FASEB J.* **33**, 375.2-375.2 (2019).

722. Søndergaard, H., Kvist, P. H. & Haase, C. Human T cells depend on functional calcineurin, tumour necrosis factor-α and CD80/CD86 for expansion and activation in mice. *Clin. Exp. Immunol.* **172**, 300–310 (2013).

723. Tsunetsugu-Yokota, Y. *et al.* Analysis of function of a human antigen-presenting cell by xenogeneic interaction with mouse T cells. *Immunol. Lett.* **40**, 73–77 (1994).

724. Piccio, L. *et al.* Adhesion of human T cells to antigen-presenting cells through SIRPbeta2-CD47 interaction costimulates T-cell proliferation. *Blood* **105**, 2421–2427 (2005).

725. Carson, M. J., Reilly, C. R., Sutcliffe, J. G. & Lo, D. Disproportionate Recruitment of CD8+ T Cells into the Central Nervous System by Professional Antigen-Presenting Cells. *Am. J. Pathol.* **154**, 481–494 (1999).

726. Crawford, M. P. *et al.* High prevalence of autoreactive, neuroantigen-specific CD8+ T cells in multiple sclerosis revealed by novel flow cytometric assay. *Blood* **103**, 4222–4231 (2004).

727. Prineas, J. W. & Wright, R. G. Macrophages, lymphocytes, and plasma cells in the perivascular compartment in chronic multiple sclerosis. *Lab. Invest.* **38**, 409–421 (1978).

728. Babbe, H. *et al.* Clonal Expansions of CD8+ T Cells Dominate the T Cell Infiltrate in Active Multiple Sclerosis Lesions as Shown by Micromanipulation and Single Cell Polymerase Chain Reaction. *J. Exp. Med.* **192**, 393–404 (2000).

729. Tonra, J. R. Cerebellar susceptibility to experimental autoimmune encephalomyelitis in SJL/J mice: Potential interaction of immunology with vascular anatomy. *The Cerebellum* **1**, 57–68 (2002).

730. Archambault, A. S., Sim, J., McCandless, E. E., Klein, R. S. & Russell, J. H. Region-specific regulation of inflammation and pathogenesis in experimental autoimmune encephalomyelitis. *J. Neuroimmunol.* **181**, 122–132 (2006).

731. Yogev, N. *et al.* CD4+ T-cell-derived IL-10 promotes CNS inflammation in mice by sustaining effector T cell survival. *Cell Rep.* **38**, 110565 (2022).

732. Seifert, H. A. *et al.* Antibiotics Protect against EAE by Increasing Regulatory and Anti-inflammatory Cells. *Metab. Brain Dis.* **33**, 1599–1607 (2018).

733. Greve, B., Reddy, J., Waldner, H.-P., Sobel, R. A. & Kuchroo, V. K. Dissimilar background genes control susceptibility to autoimmune disease in the context of different

MHC haplotypes: NOD.H-2s congenic mice are relatively resistant to both experimental autoimmune encephalomyelitis and type I diabetes. *Eur. J. Immunol.* **34**, 1828–1838 (2004).

734. Verma, B. & Wesa, A. Establishment of Humanized Mice from Peripheral Blood Mononuclear Cells or Cord Blood CD34+ Hematopoietic Stem Cells for Immune-Oncology Studies Evaluating New Therapeutic Agents. *Curr. Protoc. Pharmacol.* **89**, e77 (2020).
735. Johnston, S. C., Dustin, M. L., Hibbs, M. L. & Springer, T. A. On the species specificity of the interaction of LFA-1 with intercellular adhesion molecules. *J. Immunol. Baltim. Md 1950* **145**, 1181–1187 (1990).
736. Loosen, S. H. *et al.* Infectious mononucleosis is associated with an increased incidence of multiple sclerosis: Results from a cohort study of 32,116 outpatients in Germany. *Front. Immunol.* **13**, 937583 (2022).
737. Münz, C. EBV Infection of Mice with Reconstituted Human Immune System Components. in *Epstein Barr Virus Volume 2* (ed. Münz, C.) 407–423 (Springer International Publishing, 2015). doi:10.1007/978-3-319-22834-1_14.
738. Abrahamyan, S. *et al.* Complete Epstein-Barr virus seropositivity in a large cohort of patients with early multiple sclerosis. *J. Neurol. Neurosurg. Psychiatry* **91**, 681–686 (2020).
739. Keane, J. T. *et al.* Gender and the Sex Hormone Estradiol Affect Multiple Sclerosis Risk Gene Expression in Epstein-Barr Virus-Infected B Cells. *Front. Immunol.* **12**, 732694 (2021).
740. Ribbons, K. A. *et al.* Male Sex Is Independently Associated with Faster Disability Accumulation in Relapse-Onset MS but Not in Primary Progressive MS. *PLoS ONE* **10**, e0122686 (2015).

741. Mouhieddine, T. H. *et al.* Risk factors for multiple sclerosis and associations with anti-EBV antibody titers. *Clin. Immunol.* **158**, 59–66 (2015).

742. Pender, M. P. & Burrows, S. R. Epstein–Barr virus and multiple sclerosis: potential opportunities for immunotherapy. *Clin. Transl. Immunol.* **3**, e27 (2014).

743. Vanheusden, M., Stinissen, P., Hart, B. A. 't & Hellings, N. Cytomegalovirus: a culprit or protector in multiple sclerosis? *Trends Mol. Med.* **21**, 16–23 (2015).

744. Staras, S. A. S. *et al.* Seroprevalence of Cytomegalovirus Infection in the United States, 1988–1994. *Clin. Infect. Dis.* **43**, 1143–1151 (2006).

745. Lachmann, R. *et al.* Cytomegalovirus (CMV) seroprevalence in the adult population of Germany. *PLoS ONE* **13**, e0200267 (2018).

746. Fisher, S. A. *et al.* The role of vitamin D in increasing circulating T regulatory cell numbers and modulating T regulatory cell phenotypes in patients with inflammatory disease or in healthy volunteers: A systematic review. *PLoS ONE* **14**, e0222313 (2019).

747. Hadinoto, V. *et al.* On the dynamics of acute EBV infection and the pathogenesis of infectious mononucleosis. *Blood* **111**, 1420–1427 (2008).

748. Cocuzza, C. E. *et al.* Quantitative Detection of Epstein-Barr Virus DNA in Cerebrospinal Fluid and Blood Samples of Patients with Relapsing-Remitting Multiple Sclerosis. *PLoS ONE* **9**, e94497 (2014).

749. Wandinger, K. *et al.* Association between clinical disease activity and Epstein-Barr virus reactivation in MS. *Neurology* **55**, 178–184 (2000).

750. Venken, K. *et al.* Compromised CD4+ CD25high regulatory T-cell function in patients with relapsing-remitting multiple sclerosis is correlated with a reduced frequency of FOXP3-

positive cells and reduced FOXP3 expression at the single-cell level. *Immunology* **123**, 79–89 (2008).

751. Jain, R. W. & Yong, V. W. B cells in central nervous system disease: diversity, locations and pathophysiology. *Nat. Rev. Immunol.* 1–12 (2021) doi:10.1038/s41577-021-00652-6.
752. Marín, N. *et al.* Regulatory Lymphocytes Are Key Factors in MHC-Independent Resistance to EAE. *J. Immunol. Res.* **2014**, e156380 (2014).
753. Long, H. M., Meckiff, B. J. & Taylor, G. S. The T-cell Response to Epstein-Barr Virus–New Tricks from an Old Dog. *Front. Immunol.* **10**, 2193 (2019).
754. Correale, J. & Farez, M. F. Smoking worsens multiple sclerosis prognosis: Two different pathways are involved. *J. Neuroimmunol.* **281**, 23–34 (2015).
755. Marrodan, M., Farez, M. F., Balbuena Aguirre, M. E. & Correale, J. Obesity and the risk of Multiple Sclerosis. The role of Leptin. *Ann. Clin. Transl. Neurol.* **8**, 406–424 (2021).
756. Bogers, L., Kuiper, K. L., Smolders, J., Rip, J. & van Luijn, M. M. Epstein–Barr virus and genetic risk variants as determinants of T-bet+ B cell-driven autoimmune diseases. *Immunol. Lett.* (2023) doi:10.1016/j.imlet.2023.07.006.
757. Lang, H. L. E. *et al.* A functional and structural basis for TCR cross-reactivity in multiple sclerosis. *Nat. Immunol.* **3**, 940–943 (2002).
758. Ingelfinger, F. *et al.* Twin study reveals non-heritable immune perturbations in multiple sclerosis. *Nature* **603**, 152–158 (2022).
759. Gold, J. *et al.* Effect of teriflunomide on Epstein-Barr virus shedding in relapsing-remitting multiple sclerosis patients: Outcomes from a real-world pilot cohort study. *Mult. Scler. Relat. Disord.* **68**, 104377 (2022).

760. Hone, L., Giovannoni, G., Dobson, R. & Jacobs, B. M. Predicting Multiple Sclerosis: Challenges and Opportunities. *Front. Neurol.* **12**, (2022).

761. Imadome, K.-I. & Fujiwara, S. Generation and Analysis of Humanized Mouse Model of EBV Infection. in *Epstein Barr Virus* (eds. Minarovits, J. & Niller, H. H.) 241–254 (Springer New York, 2017). doi:10.1007/978-1-4939-6655-4_18.

762. Fernández-Velasco, J. I. *et al.* Effect of Ocrelizumab in Blood Leukocytes of Patients With Primary Progressive MS. *Neurol. - Neuroimmunol. Neuroinflammation* **8**, (2021).

763. Mathias, A. *et al.* Ocrelizumab Impairs the Phenotype and Function of Memory CD8+ T Cells: A 1-Year Longitudinal Study in Patients With Multiple Sclerosis. *Neurol. Neuroimmunol. Neuroinflammation* **10**, e200084 (2023).

764. Frisullo, G. *et al.* pSTAT1, pSTAT3, and T-bet expression in peripheral blood mononuclear cells from relapsing-remitting multiple sclerosis patients correlates with disease activity. *J. Neurosci. Res.* **84**, 1027–1036 (2006).

765. Jodeleit, H. *et al.* Head-to-head study of oxelumab and adalimumab in a mouse model of ulcerative colitis based on NOD/Scid IL2Rγnull mice reconstituted with human peripheral blood mononuclear cells. *Dis. Model. Mech.* **14**, dmm046995 (2021).

766. Del Rio, N. M. *et al.* Generation of the NeoThy mouse model for human immune system studies. *Lab Anim.* **52**, 149–168 (2023).

767. Tanaka, Y. *et al.* EAE Induction by Passive Transfer of MOG-specific CD4+ T Cells. *Bio-Protoc.* **7**, e2370 (2017).

768. Passos, G. R. D. *et al.* Th17 Cells Pathways in Multiple Sclerosis and Neuromyelitis Optica Spectrum Disorders: Pathophysiological and Therapeutic Implications. *Mediat. Inflamm. Mediat. Inflamm.* **2016, 2016**, e5314541 (2016).

769. Rangachari, M. & Kuchroo, V. K. Using EAE to better understand principles of immune function and autoimmune pathology. *J. Autoimmun.* **45**, 31–39 (2013).

770. Domingues, H. S., Mues, M., Lassmann, H., Wekerle, H. & Krishnamoorthy, G. Functional and Pathogenic Differences of Th1 and Th17 Cells in Experimental Autoimmune Encephalomyelitis. *PLoS ONE* **5**, e15531 (2010).

771. Jäger, A., Dardalhon, V., Sobel, R. A., Bettelli, E. & Kuchroo, V. K. Th1, Th17 and Th9 effector cells induce experimental autoimmune encephalomyelitis with different pathological phenotypes. *J. Immunol. Baltim. Md 1950* **183**, 7169–7177 (2009).

772. Tesmer, L. A., Lundy, S. K., Sarkar, S. & Fox, D. A. Th17 cells in human disease. *Immunol. Rev.* **223**, 87–113 (2008).

773. Hart, B. A. 't, Luchicchi, A., Schenk, G. J., Killestein, J. & Geurts, J. J. G. Multiple sclerosis and drug discovery: A work of translation. *eBioMedicine* **68**, (2021).

774. Saez-Calveras, N. & Stuve, O. The role of the complement system in Multiple Sclerosis: A review. *Front. Immunol.* **13**, 970486 (2022).

775. Kamma, E., Lasisi, W., Libner, C., Ng, H. S. & Plemel, J. R. Central nervous system macrophages in progressive multiple sclerosis: relationship to neurodegeneration and therapeutics. *J. Neuroinflammation* **19**, 45 (2022).

776. Luchicchi, A., Preziosa, P. & 't Hart, B. Editorial: "Inside-Out" vs "Outside-In" Paradigms in Multiple Sclerosis Etiopathogenesis. *Front. Cell. Neurosci.* **15**, (2021).

777. Caprariello, A. V. *et al.* Biochemically altered myelin triggers autoimmune demyelination. *Proc. Natl. Acad. Sci. U. S. A.* **115**, 5528–5533 (2018).

778. Berer, K. *et al.* Commensal microbiota and myelin autoantigen cooperate to trigger autoimmune demyelination. *Nature* **479**, 538–541 (2011).

779. Sedaghat, N. & Etemadifar, M. Revisiting the antiviral theory to explain interferon-beta's effectiveness for relapsing multiple sclerosis. *Mult. Scler. Relat. Disord.* **67**, 104155 (2022).

780. Mosca, L. *et al.* HLA-DRB1*15 association with multiple sclerosis is confirmed in a multigenerational Italian family. *Funct. Neurol.* **32**, 83–88 (2017).

781. Liu, X. & Quan, N. Immune Cell Isolation from Mouse Femur Bone Marrow. *Bio-Protoc.* **5**, e1631 (2015).

Appendices

Appendix 1. Human donor PBMC composition and HuPBMC cohort engraftment

Individual blood donor PBMC composition and respective numbers of human immune cells injected into each recipient HuPBMC mouse per cohort are included herein.

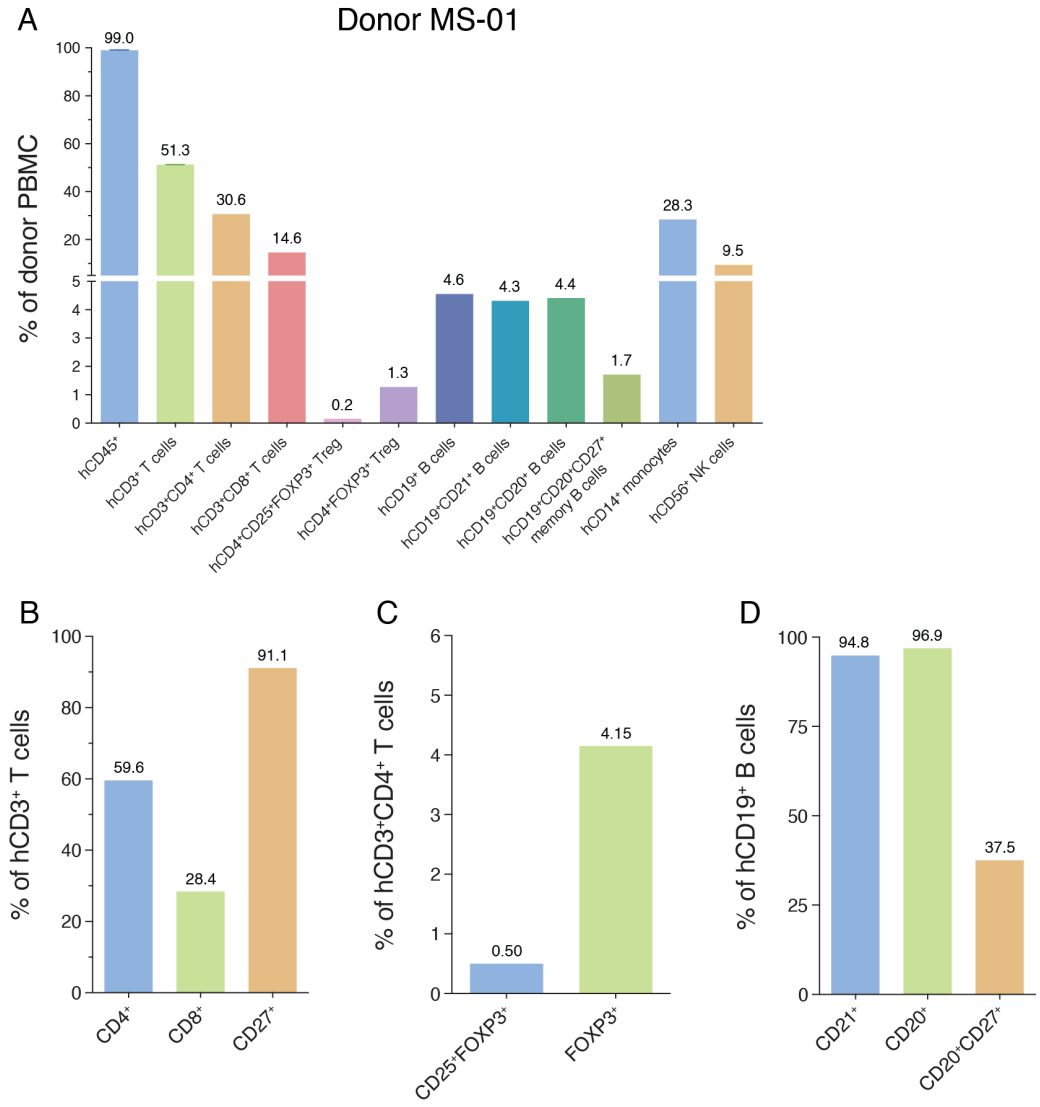

Figure A.1 Blood donor MS-01 PBMC composition and HuPBMC cohort 15 engraftment

(A) Relative composition of human immune cell lineages in the PBMCs of donor MS-01 as a percentage of total leukocytes immediately after isolation from whole blood. (B) Proportions of $hCD4^+$, $hCD8^+$, and $hCD27^+$ T cell subsets among $hCD3^+$ T cells. (C) Proportions of $hCD25^+$ and/or $hFOXP3^+$ regulatory T cell (Treg) subsets among

hCD3^{+}CD4^{+} T cells. (D) Proportions of hCD21^{+}, hCD20^{+}, and/or hCD27^{+} B cell subsets among hCD19^{+} B cells. (E) Total number of human immune cell subsets injected per recipient mouse in HuPBMC Cohort 15.

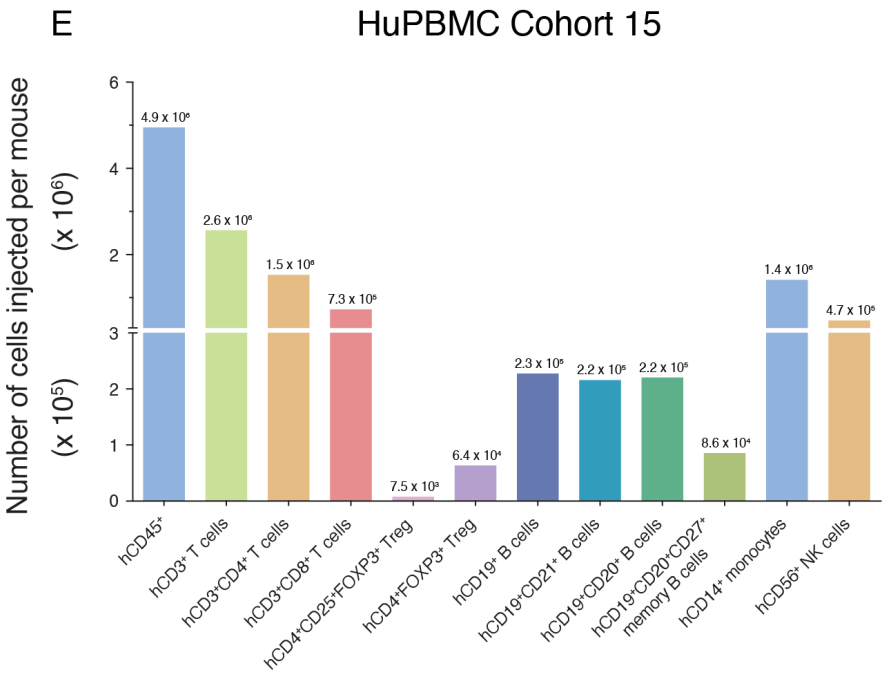

Figure A.1 continued

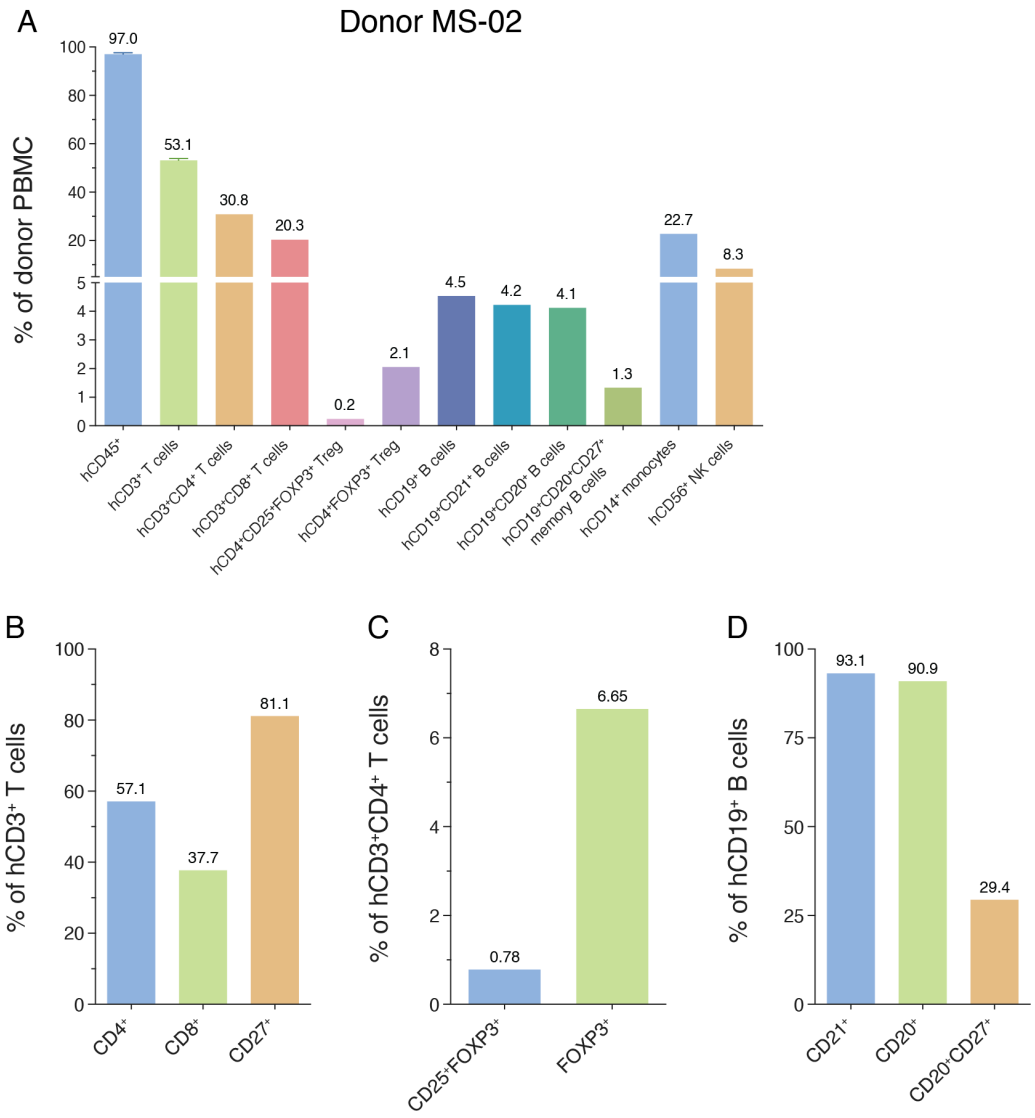

Figure A.2 Blood donor MS-02 PBMC composition and HuPBMC cohort 16 engraftment

(A) Relative composition of human immune cell lineages in the PBMCs of donor MS-02 as a percentage of total leukocytes immediately after isolation from whole blood. (B) Proportions of hCD4$^+$, hCD8$^+$, and hCD27$^+$ T cell subsets among hCD3$^+$ T cells. (C) Proportions of hCD25$^+$ and/or hFOXP3$^+$ regulatory T cell (Treg) subsets among hCD3$^+$CD4$^+$ T cells. (D) Proportions of hCD21$^+$, hCD20$^+$, and/or hCD27$^+$ B cell subsets among hCD19$^+$ B cells. (E) Total number of human immune cell subsets injected per recipient mouse in HuPBMC Cohort 16.

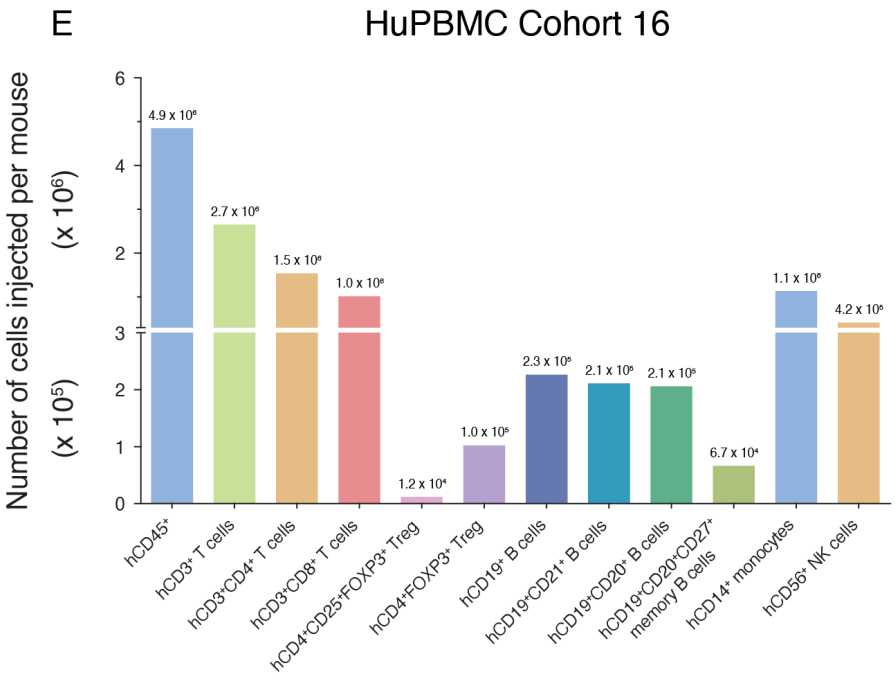

Figure A.2 continued

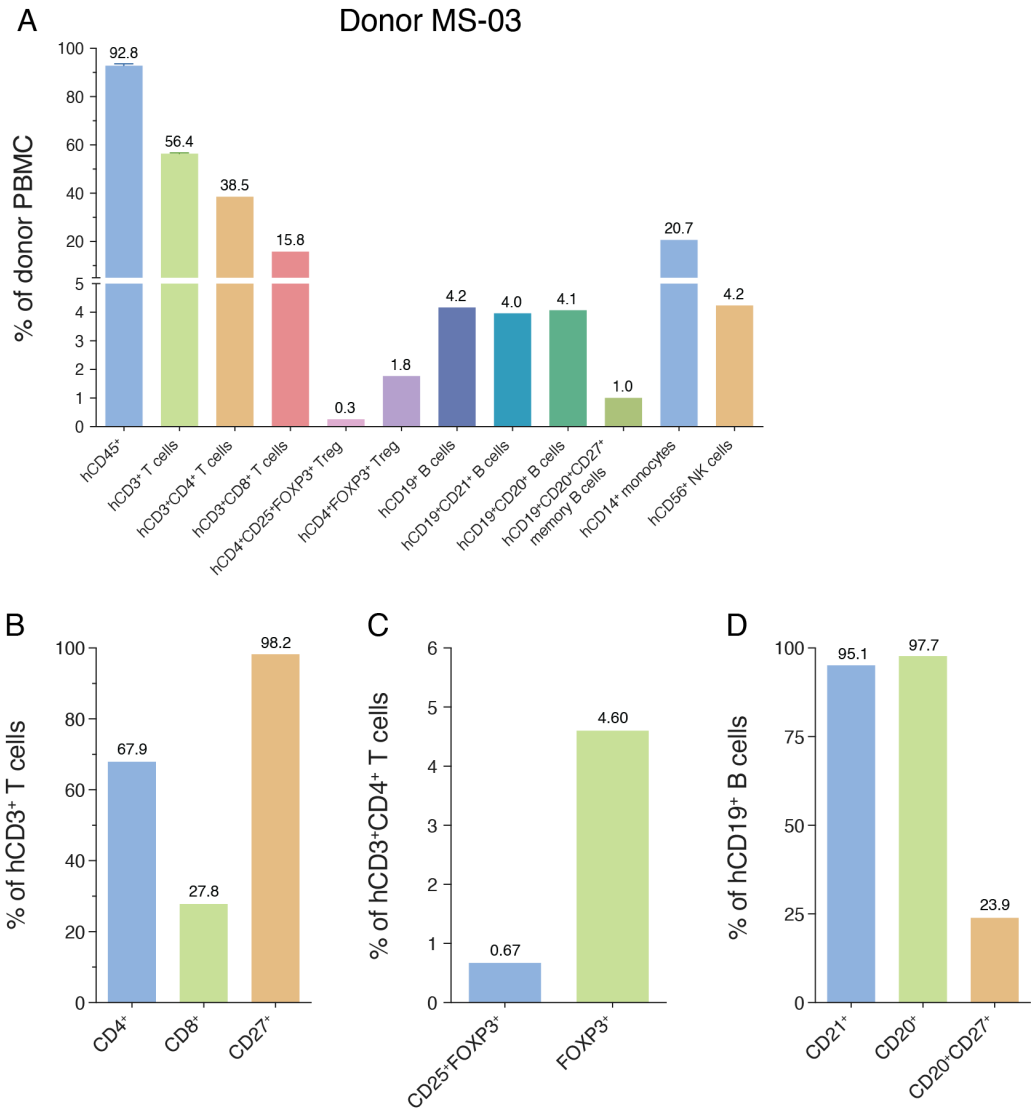

Figure A.3 Blood donor MS-03 PBMC composition and HuPBMC cohort 17 engraftment

(A) Relative composition of human immune cell lineages in the PBMCs of donor MS-03 as a percentage of total leukocytes immediately after isolation from whole blood. (B) Proportions of hCD4$^+$, hCD8$^+$, and hCD27$^+$ T cell subsets among hCD3$^+$ T cells. (C) Proportions of hCD25$^+$ and/or hFOXP3$^+$ regulatory T cell (Treg) subsets among hCD3$^+$CD4$^+$ T cells. (D) Proportions of hCD21$^+$, hCD20$^+$, and/or hCD27$^+$ B cell subsets among hCD19$^+$ B cells. (E) Total number of human immune cell subsets injected per recipient mouse in HuPBMC Cohort 17.

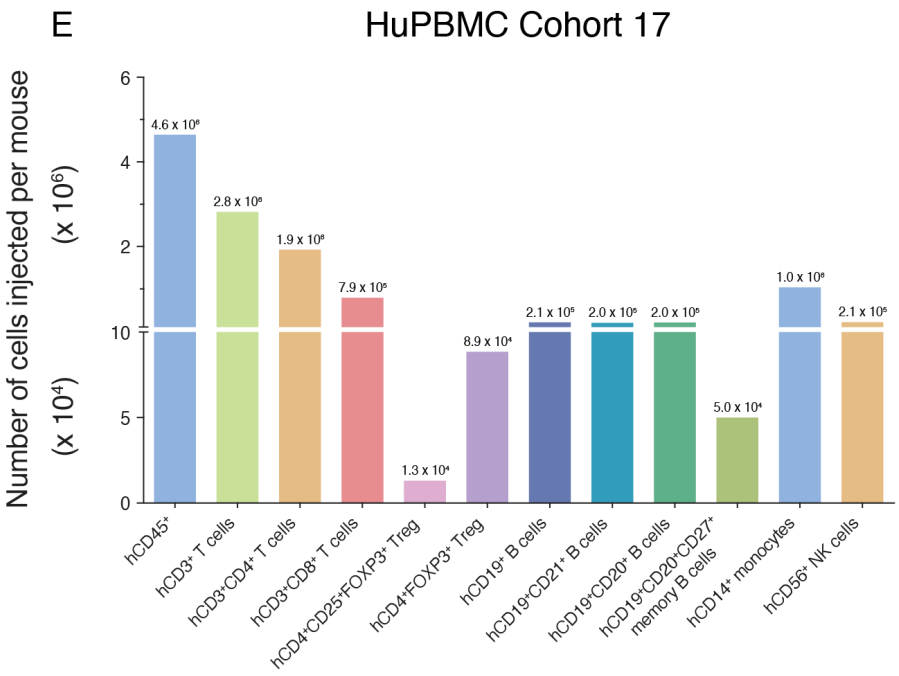

Figure A.3 continued

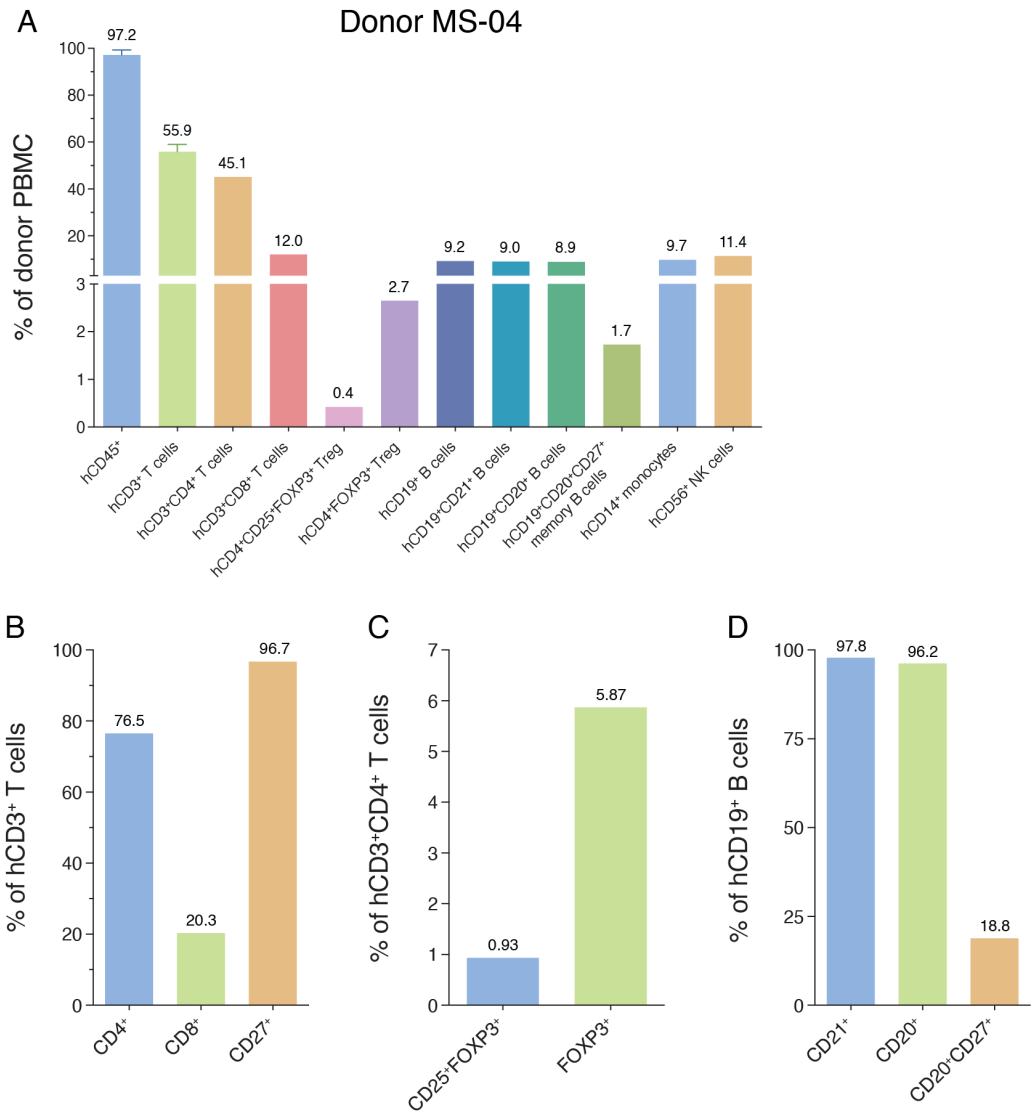

Figure A.4 Blood donor MS-04 PBMC composition and HuPBMC cohort 20 engraftment

(A) Relative composition of human immune cell lineages in the PBMCs of donor MS-04 as a percentage of total leukocytes immediately after isolation from whole blood. (B) Proportions of hCD4$^+$, hCD8$^+$, and hCD27$^+$ T cell subsets among hCD3$^+$ T cells. (C) Proportions of hCD25$^+$ and/or hFOXP3$^+$ regulatory T cell (Treg) subsets among hCD3$^+$CD4$^+$ T cells. (D) Proportions of hCD21$^+$, hCD20$^+$, and/or hCD27$^+$ B cell subsets among hCD19$^+$ B cells. (E) Total number of human immune cell subsets injected per recipient mouse in HuPBMC Cohort 20.

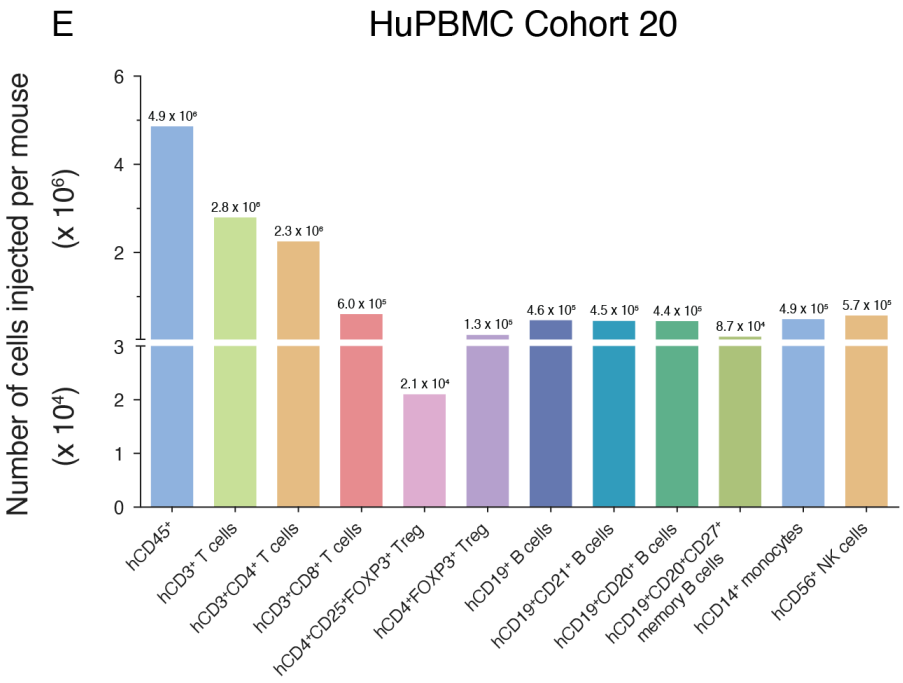

Figure A.4 continued

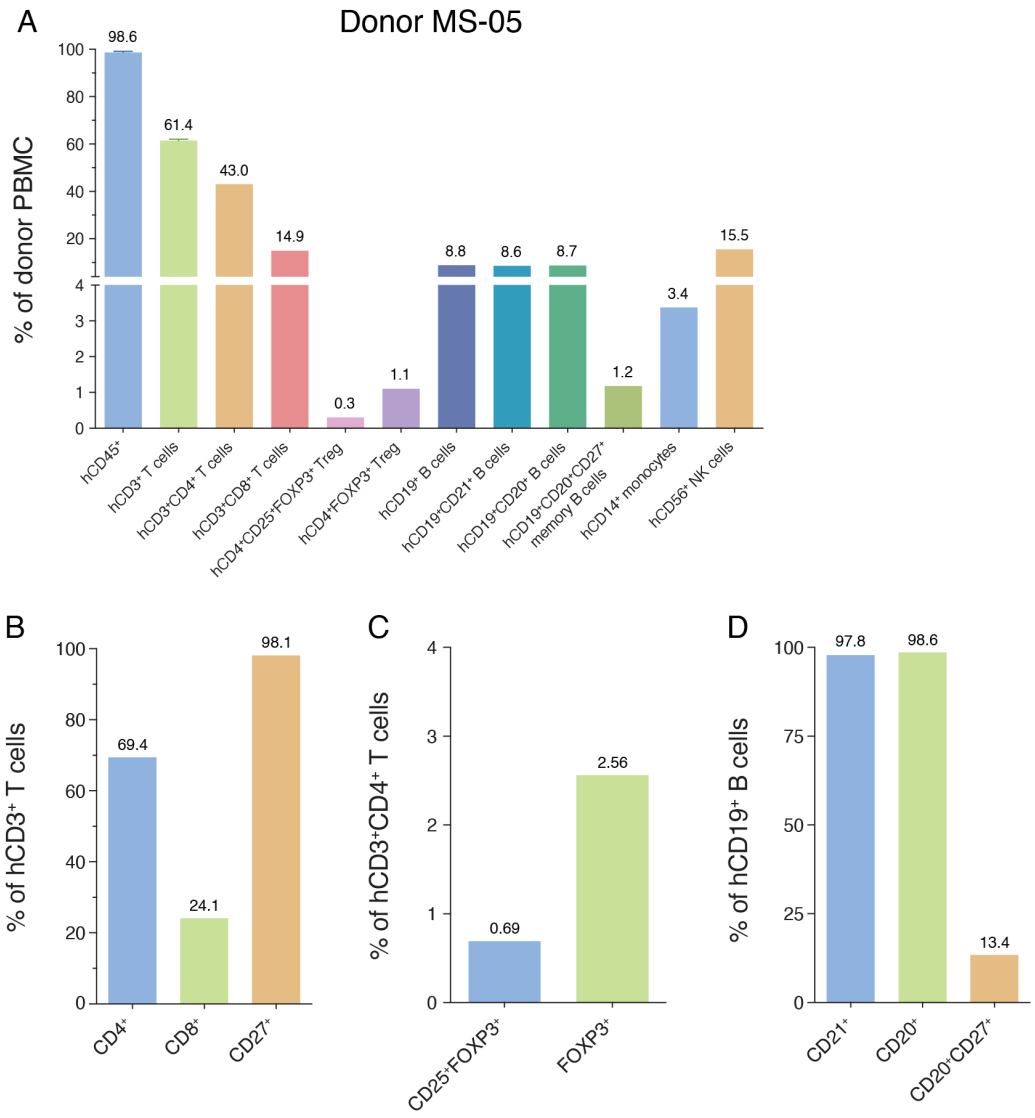

Figure A.5 Blood donor MS-05 PBMC composition and HuPBMC cohort 34 engraftment

(A) Relative composition of human immune cell lineages in the PBMCs of donor MS-05 as a percentage of total leukocytes immediately after isolation from whole blood. (B) Proportions of hCD4$^+$, hCD8$^+$, and hCD27$^+$ T cell subsets among hCD3$^+$ T cells. (C) Proportions of hCD25$^+$ and/or hFOXP3$^+$ regulatory T cell (Treg) subsets among hCD3$^+$CD4$^+$ T cells. (D) Proportions of hCD21$^+$, hCD20$^+$, and/or hCD27$^+$ B cell subsets among hCD19$^+$ B cells. (E) Total number of human immune cell subsets injected per recipient mouse in HuPBMC Cohort 34.

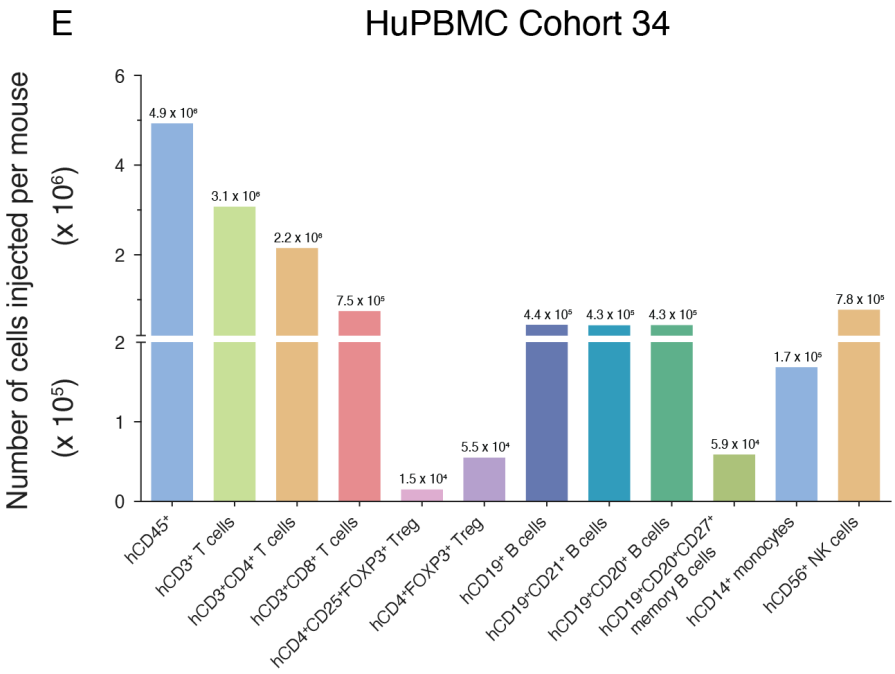

Figure A.5 continued

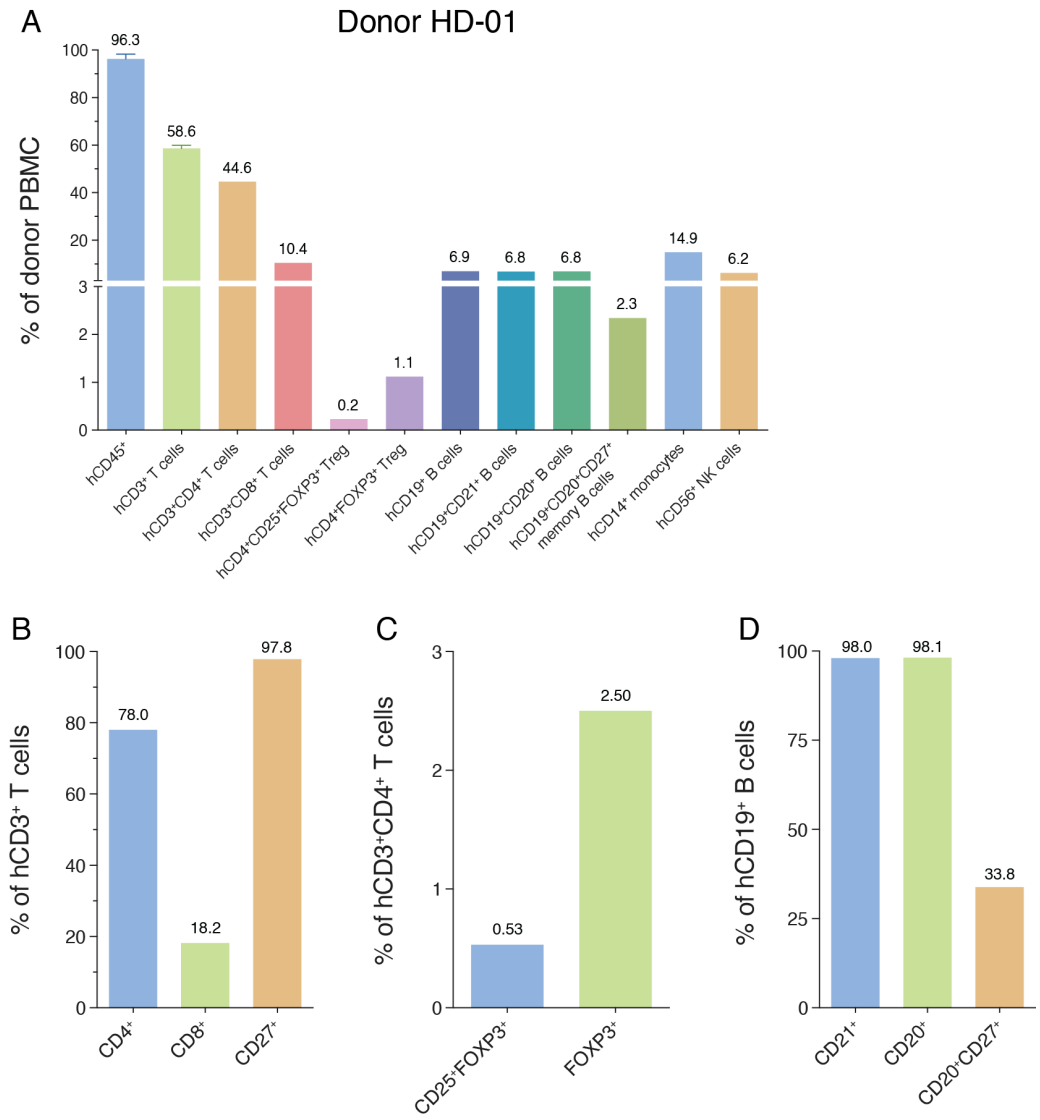

Figure A.6 Blood donor HD-01 PBMC composition and HuPBMC cohort 10 engraftment

(A) Relative composition of human immune cell lineages in the PBMCs of donor HD-01 as a percentage of total leukocytes immediately after isolation from whole blood. (B) Proportions of hCD4$^+$, hCD8$^+$, and hCD27$^+$ T cell subsets among hCD3$^+$ T cells. (C) Proportions of hCD25$^+$ and/or hFOXP3$^+$ regulatory T cell (Treg) subsets among hCD3$^+$CD4$^+$ T cells. (D) Proportions of hCD21$^+$, hCD20$^+$, and/or hCD27$^+$ B cell subsets among hCD19$^+$ B cells. (E) Total number of human immune cell subsets injected per recipient mouse in HuPBMC Cohort 10.

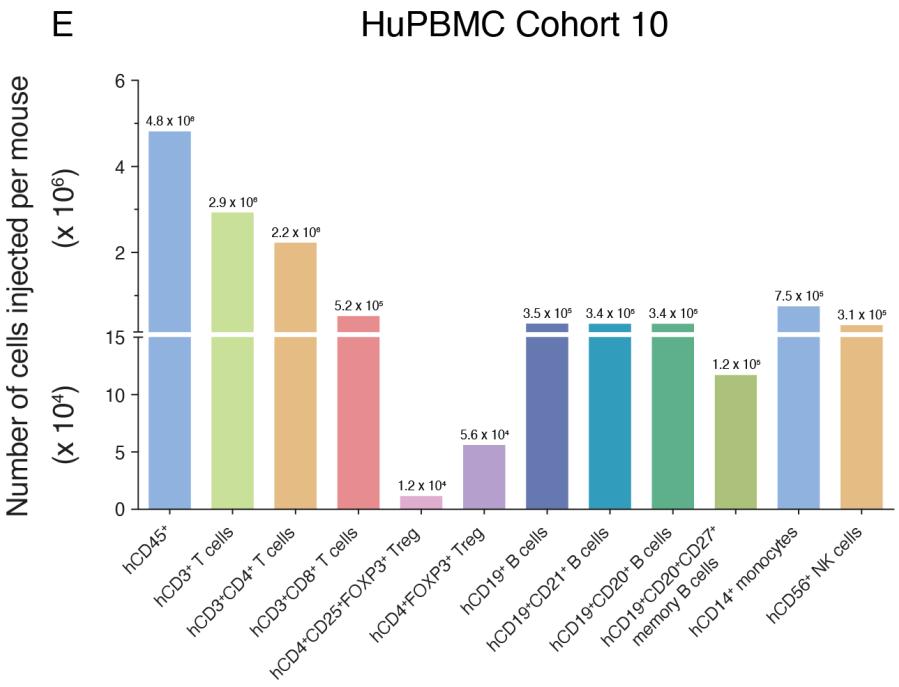

Figure A.6 continued

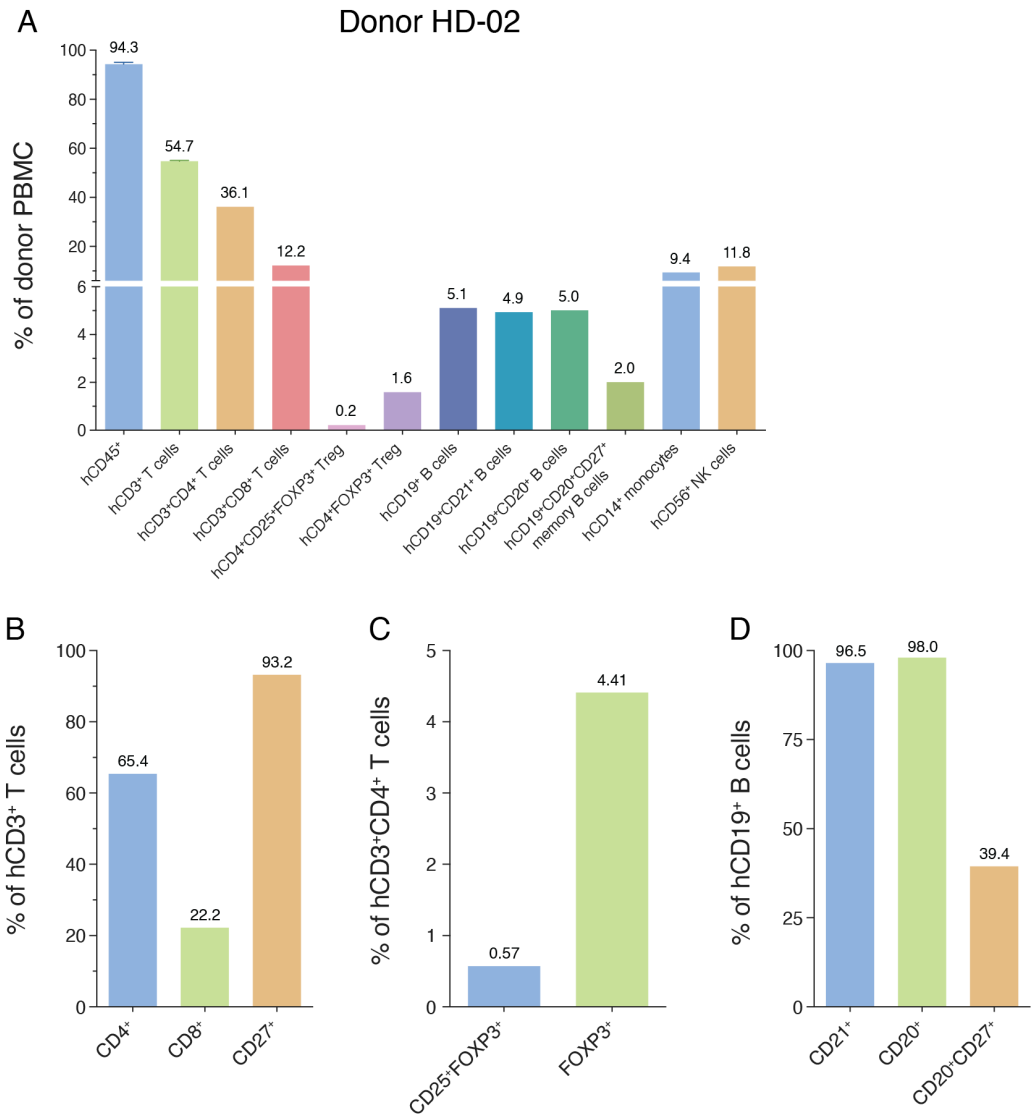

Figure A.7 Blood donor HD-02 PBMC composition and HuPBMC cohort 13 engraftment

(A) Relative composition of human immune cell lineages in the PBMCs of donor HD-02 as a percentage of total leukocytes immediately after isolation from whole blood. (B) Proportions of hCD4$^+$, hCD8$^+$, and hCD27$^+$ T cell subsets among hCD3$^+$ T cells. (C) Proportions of hCD25$^+$ and/or hFOXP3$^+$ regulatory T cell (Treg) subsets among hCD3$^+$CD4$^+$ T cells. (D) Proportions of hCD21$^+$, hCD20$^+$, and/or hCD27$^+$ B cell subsets among hCD19$^+$ B cells. (E) Total number of human immune cell subsets injected per recipient mouse in HuPBMC Cohort 13.

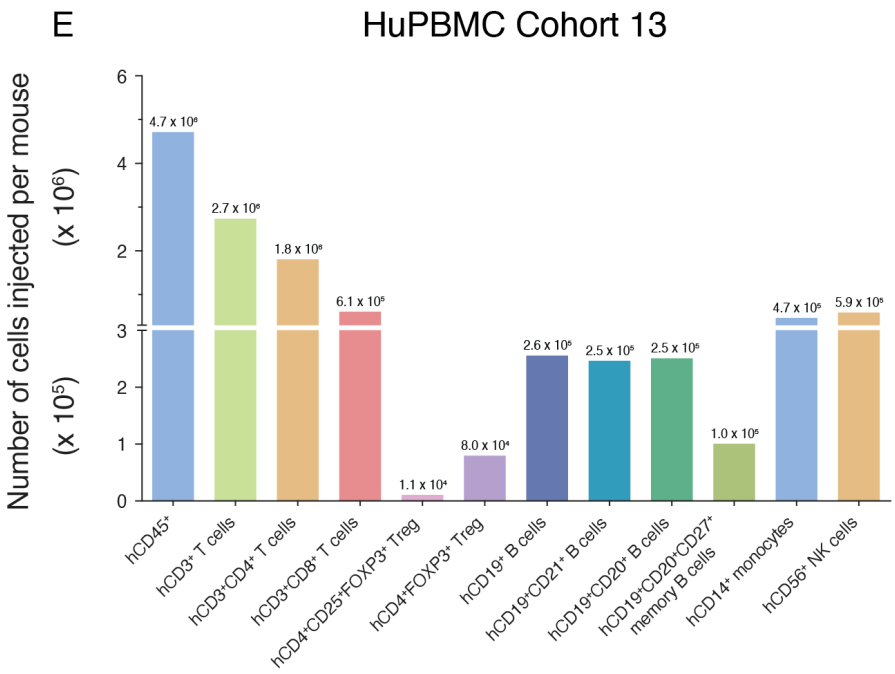

Figure A.7 continued

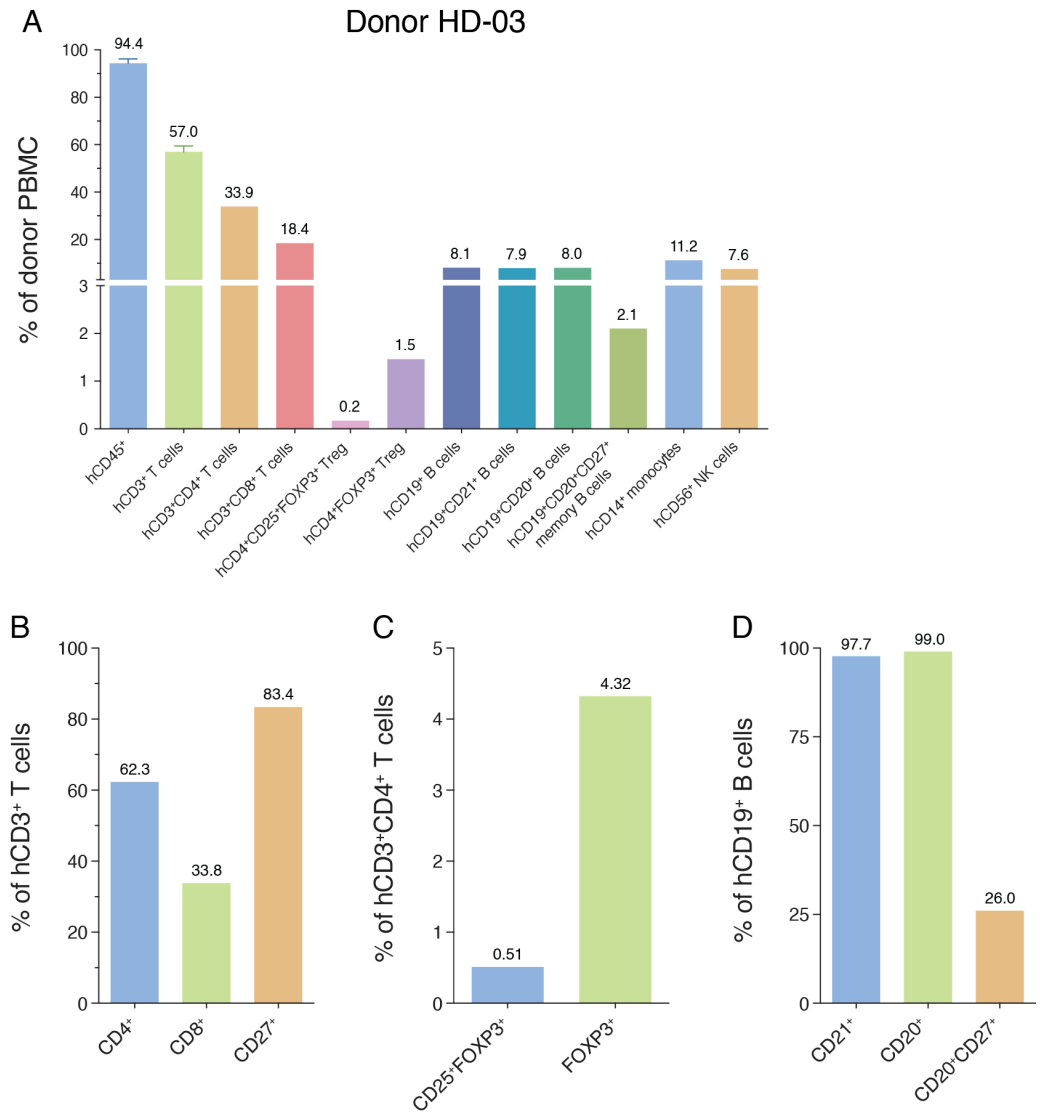

Figure A.8 Blood donor HD-03 PBMC composition and HuPBMC cohort 14 engraftment

(A) Relative composition of human immune cell lineages in the PBMCs of donor HD-03 as a percentage of total leukocytes immediately after isolation from whole blood. (B) Proportions of hCD4$^+$, hCD8$^+$, and hCD27$^+$ T cell subsets among hCD3$^+$ T cells. (C) Proportions of hCD25$^+$ and/or hFOXP3$^+$ regulatory T cell (Treg) subsets among hCD3$^+$CD4$^+$ T cells. (D) Proportions of hCD21$^+$, hCD20$^+$, and/or hCD27$^+$ B cell subsets among hCD19$^+$ B cells. (E) Total number of human immune cell subsets injected per recipient mouse in HuPBMC Cohort 14.

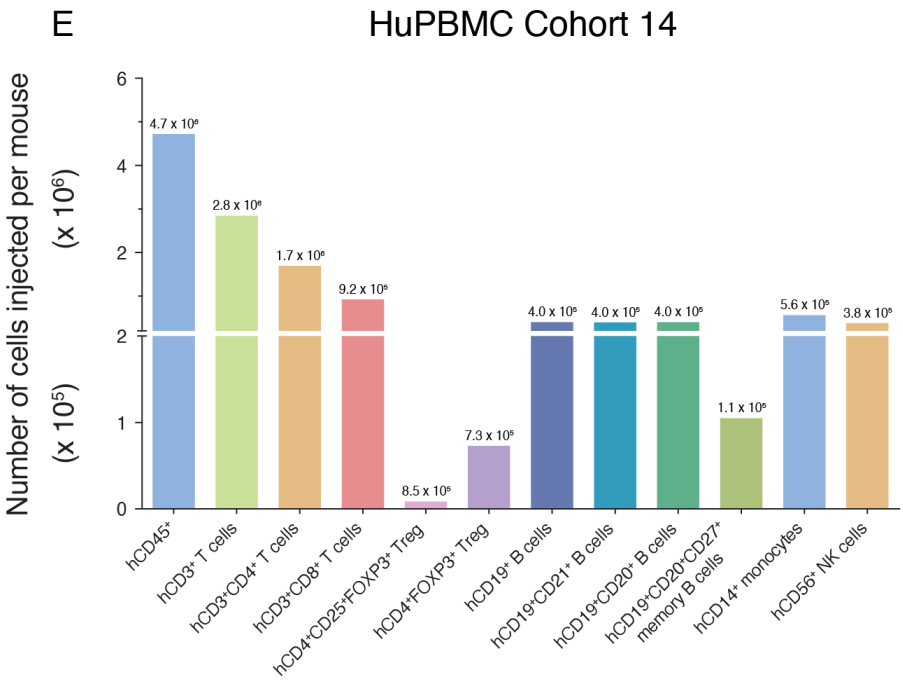

Figure A.8 continued

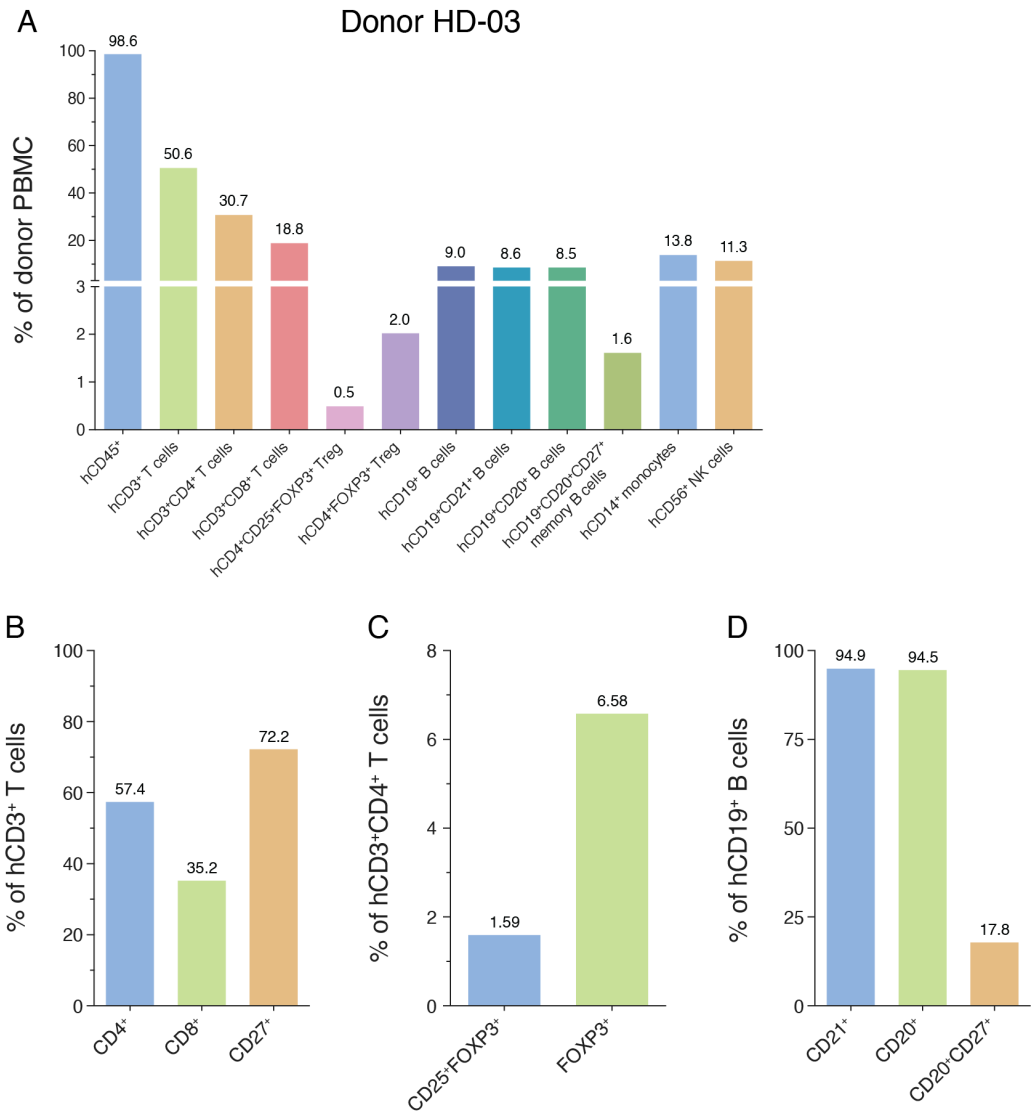

Figure A.9 Blood donor HD-03 PBMC composition and HuPBMC cohort 29 engraftment

(A) Relative composition of human immune cell lineages in the PBMCs of donor HD-03 as a percentage of total leukocytes immediately after isolation from whole blood. (B) Proportions of hCD4$^+$, hCD8$^+$, and hCD27$^+$ T cell subsets among hCD3$^+$ T cells. (C) Proportions of hCD25$^+$ and/or hFOXP3$^+$ regulatory T cell (Treg) subsets among hCD3$^+$CD4$^+$ T cells. (D) Proportions of hCD21$^+$, hCD20$^+$, and/or hCD27$^+$ B cell subsets among hCD19$^+$ B cells. (E) Total number of human immune cell subsets injected per recipient mouse in HuPBMC Cohort 29.

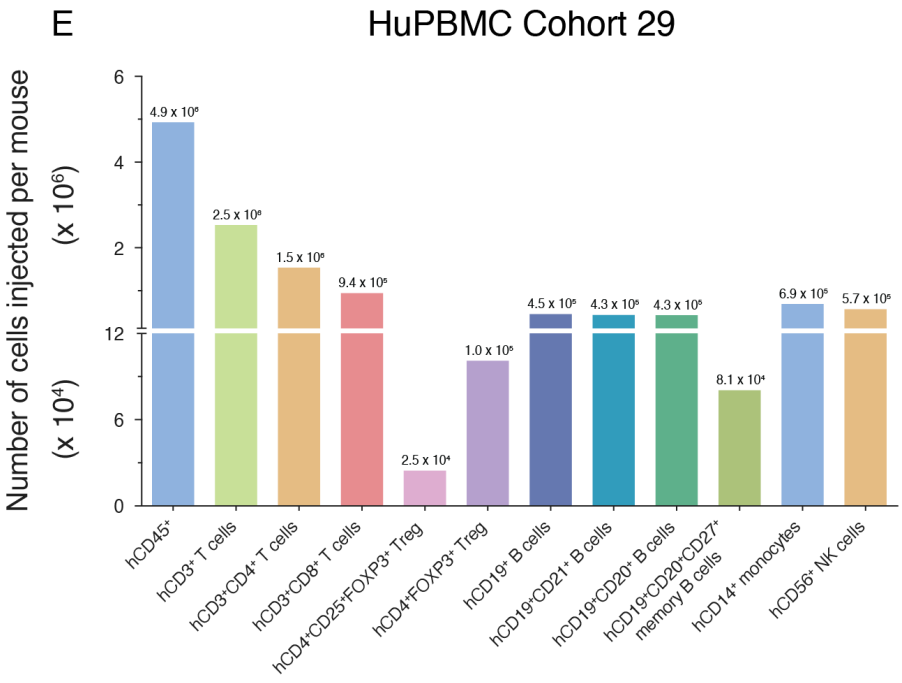

Figure A.9 continued

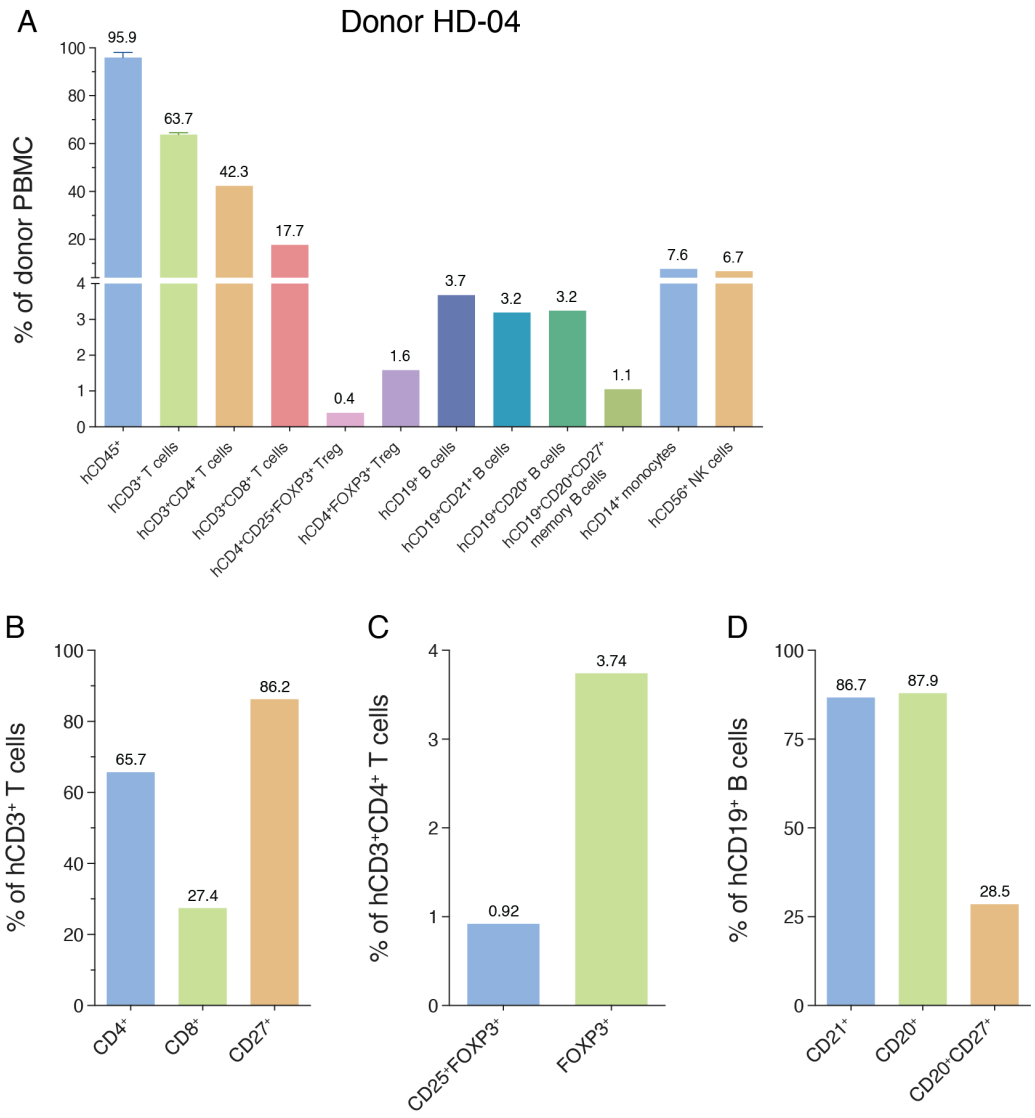

Figure A.10 Blood donor HD-04 PBMC composition and HuPBMC cohort 18 engraftment

(A) Relative composition of human immune cell lineages in the PBMCs of donor HD-04 as a percentage of total leukocytes immediately after isolation from whole blood. (B) Proportions of hCD4$^+$, hCD8$^+$, and hCD27$^+$ T cell subsets among hCD3$^+$ T cells. (C) Proportions of hCD25$^+$ and/or hFOXP3$^+$ regulatory T cell (Treg) subsets among hCD3$^+$CD4$^+$ T cells. (D) Proportions of hCD21$^+$, hCD20$^+$, and/or hCD27$^+$ B cell subsets among hCD19$^+$ B cells. (E) Total number of human immune cell subsets injected per recipient mouse in HuPBMC Cohort 18.

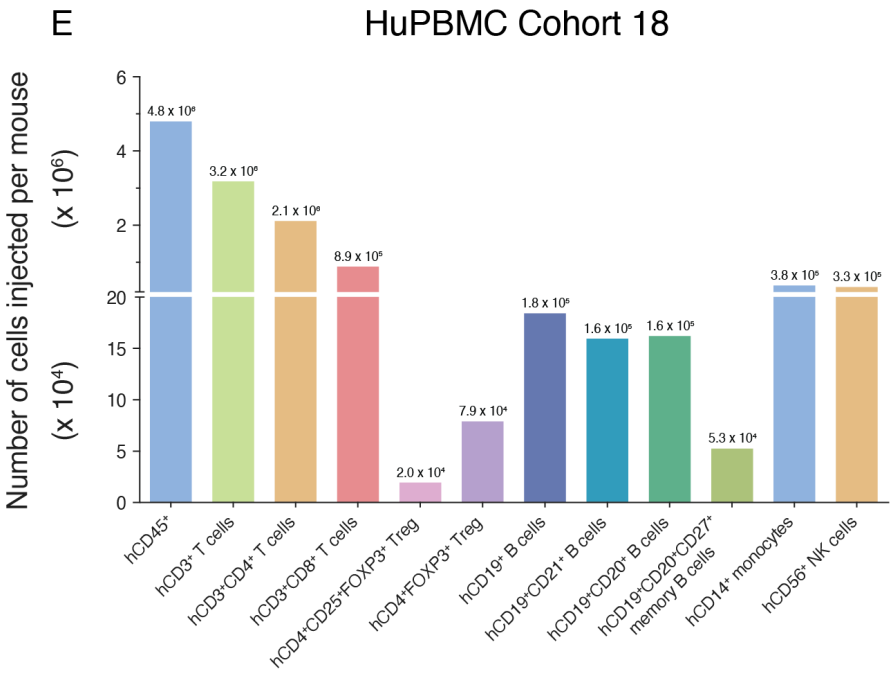

Figure A.10 continued

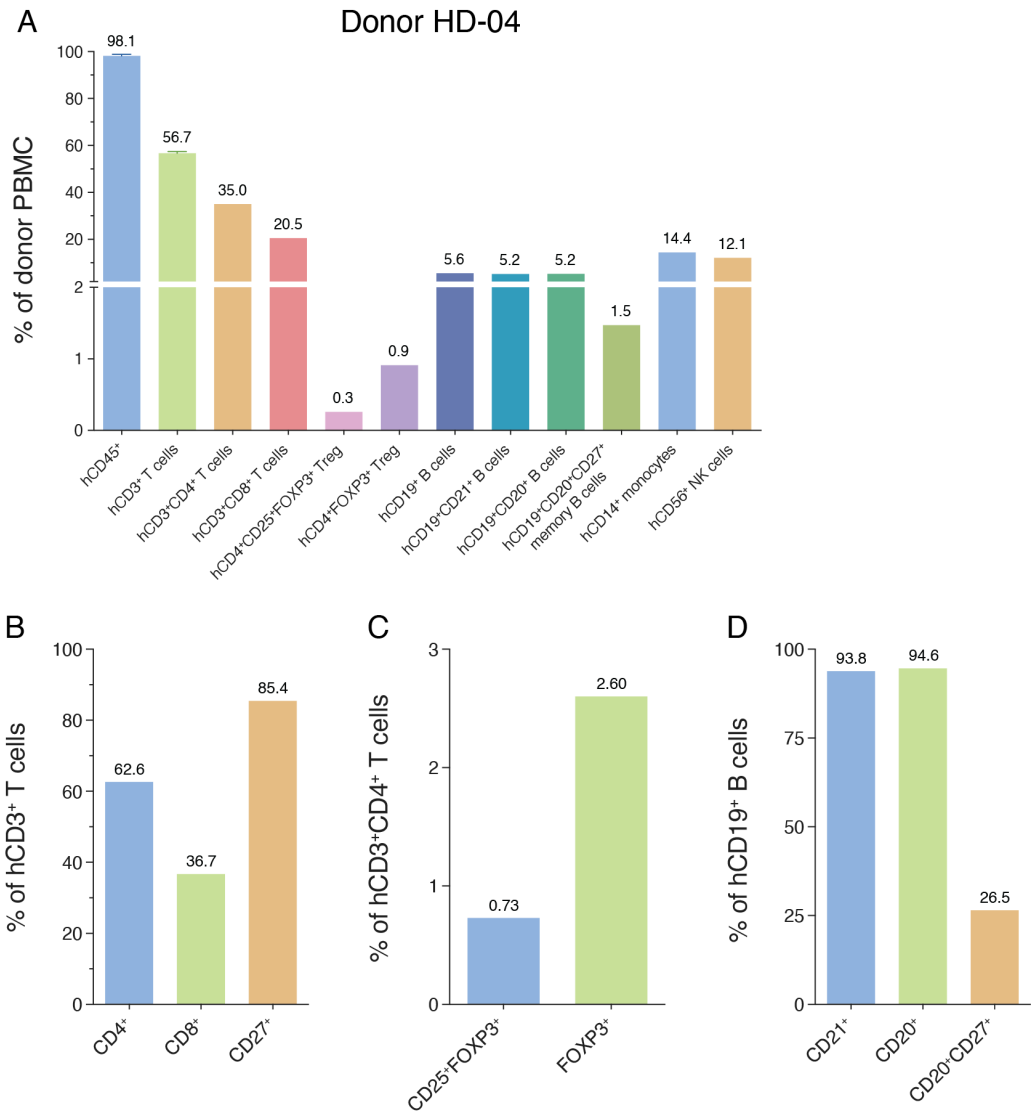

Figure A.11 Blood donor HD-04 PBMC composition and HuPBMC cohort 23 engraftment

(A) Relative composition of human immune cell lineages in the PBMCs of donor HD-04 as a percentage of total leukocytes immediately after isolation from whole blood. (B) Proportions of hCD4$^+$, hCD8$^+$, and hCD27$^+$ T cell subsets among hCD3$^+$ T cells. (C) Proportions of hCD25$^+$ and/or hFOXP3$^+$ regulatory T cell (Treg) subsets among hCD3$^+$CD4$^+$ T cells. (D) Proportions of hCD21$^+$, hCD20$^+$, and/or hCD27$^+$ B cell subsets among hCD19$^+$ B cells. (E) Total number of human immune cell subsets injected per recipient mouse in HuPBMC Cohort 23.

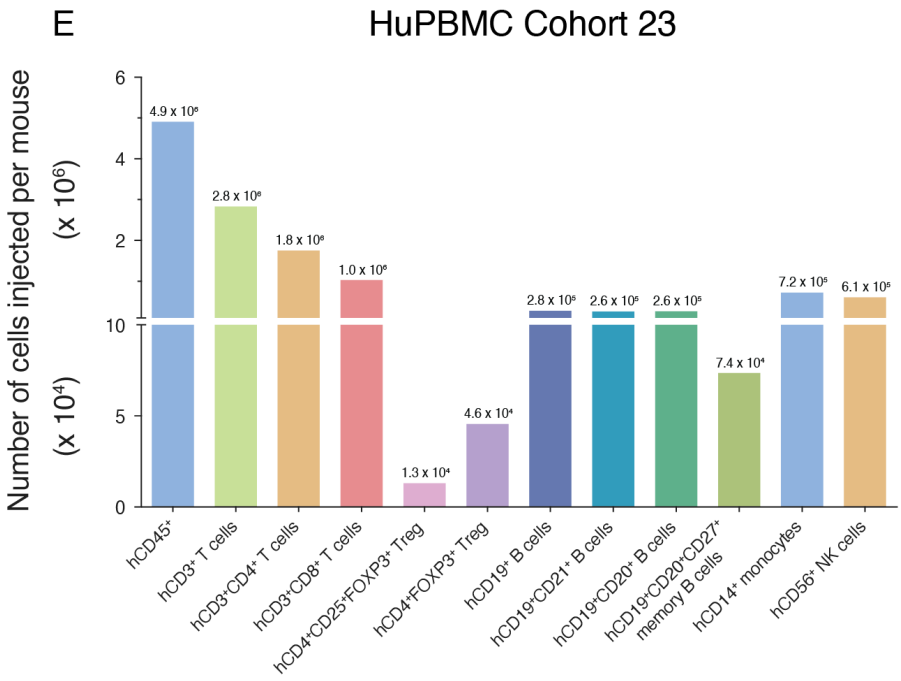

Figure A.11 continued

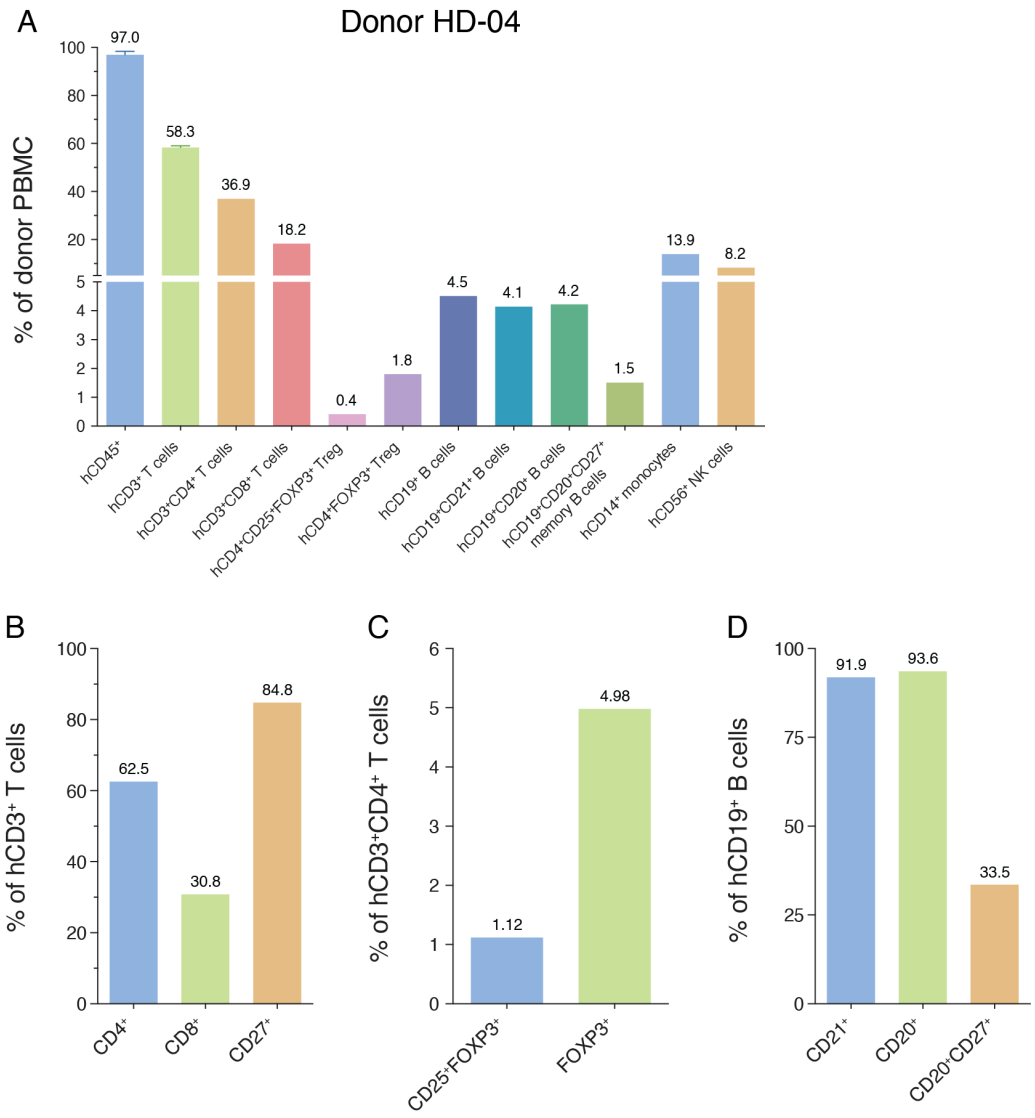

Figure A.12 Blood donor HD-04 PBMC composition and HuPBMC cohort 25 engraftment

(A) Relative composition of human immune cell lineages in the PBMCs of donor HD-04 as a percentage of total leukocytes immediately after isolation from whole blood. (B) Proportions of hCD4$^+$, hCD8$^+$, and hCD27$^+$ T cell subsets among hCD3$^+$ T cells. (C) Proportions of hCD25$^+$ and/or hFOXP3$^+$ regulatory T cell (Treg) subsets among hCD3$^+$CD4$^+$ T cells. (D) Proportions of hCD21$^+$, hCD20$^+$, and/or hCD27$^+$ B cell subsets among hCD19$^+$ B cells. (E) Total number of human immune cell subsets injected per recipient mouse in HuPBMC Cohort 25.

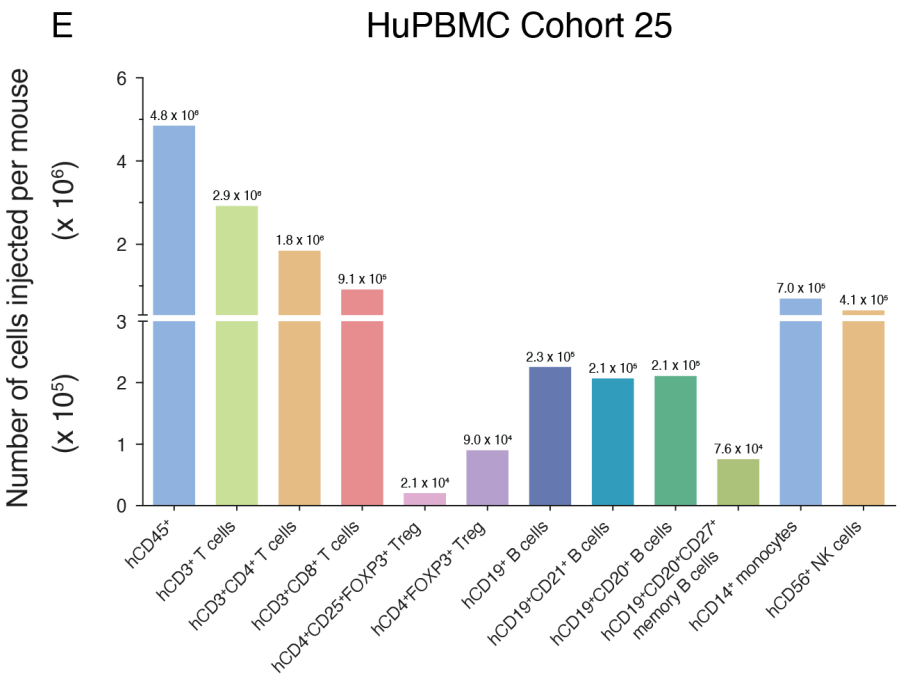

Figure A.12 continued

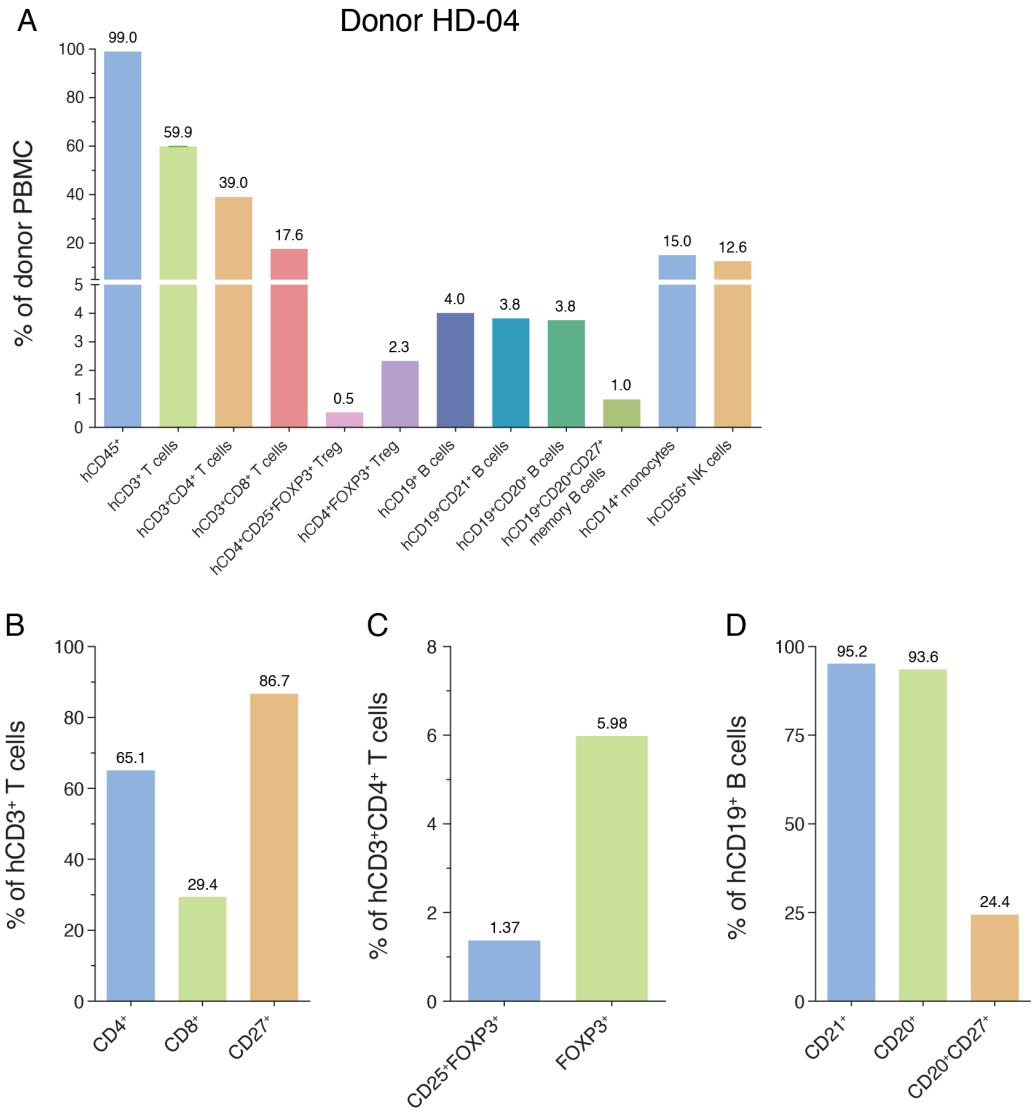

Figure A.13 Blood donor HD-04 PBMC composition and HuPBMC cohort 27 and 28 engraftment

(A) Relative composition of human immune cell lineages in the PBMCs of donor HD-04 as a percentage of total leukocytes immediately after isolation from whole blood. (B) Proportions of hCD4$^+$, hCD8$^+$, and hCD27$^+$ T cell subsets among hCD3$^+$ T cells. (C) Proportions of hCD25$^+$ and/or hFOXP3$^+$ regulatory T cell (Treg) subsets among hCD3$^+$CD4$^+$ T cells. (D) Proportions of hCD21$^+$, hCD20$^+$, and/or hCD27$^+$ B cell subsets among hCD19$^+$ B cells. (E) Total number of human immune cell subsets injected per recipient mouse in HuPBMC Cohorts 27 and 28.

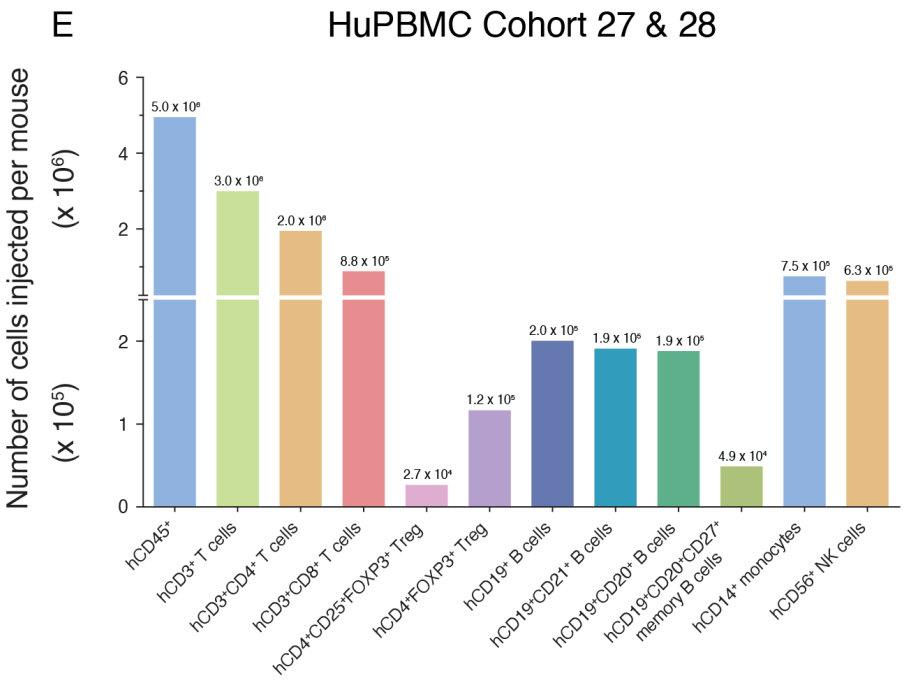

Figure A.13 continued

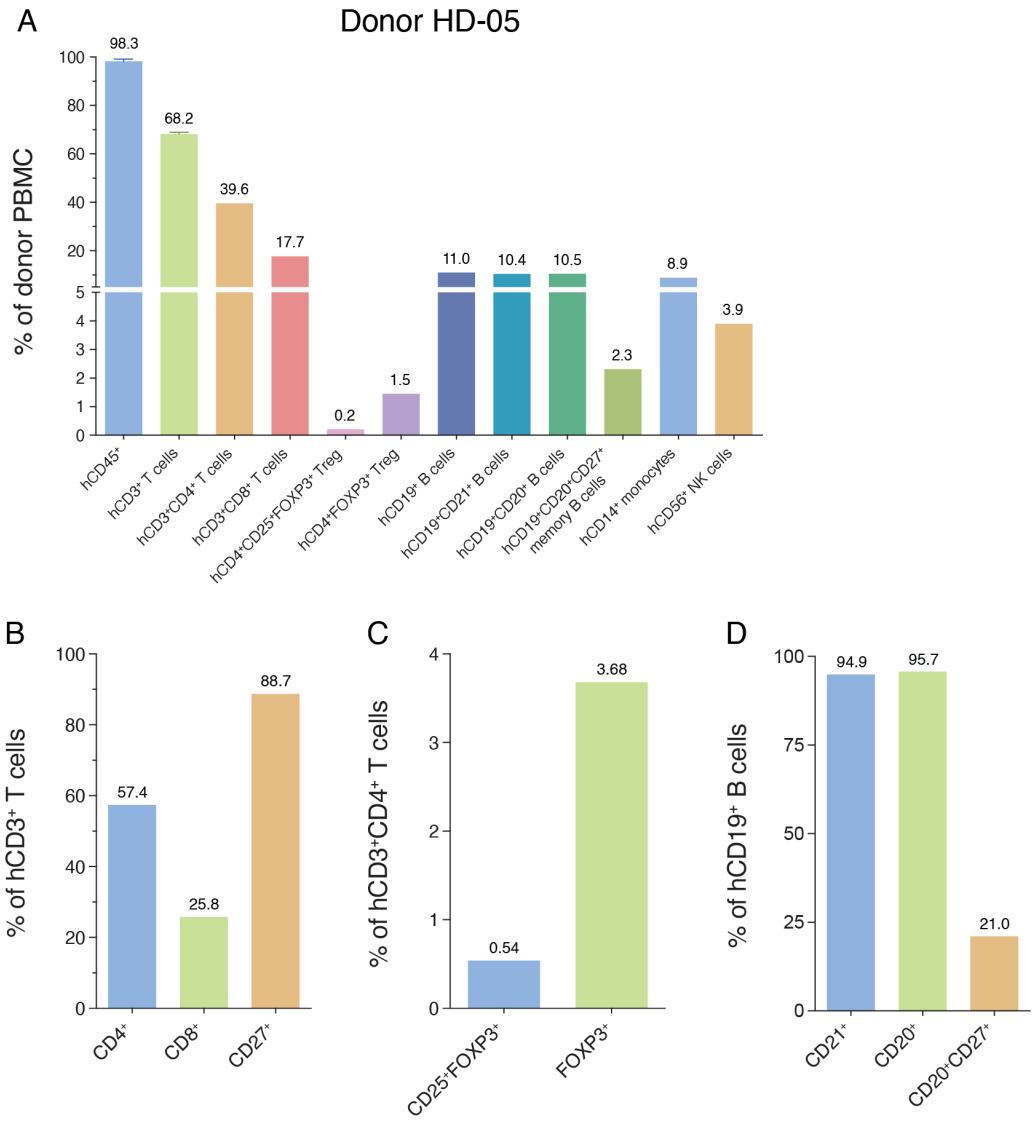

Figure A.14 Blood donor HD-05 PBMC composition and HuPBMC cohort 22 engraftment

(A) Relative composition of human immune cell lineages in the PBMCs of donor HD-05 as a percentage of total leukocytes immediately after isolation from whole blood. (B) Proportions of hCD4$^+$, hCD8$^+$, and hCD27$^+$ T cell subsets among hCD3$^+$ T cells. (C) Proportions of hCD25$^+$ and/or hFOXP3$^+$ regulatory T cell (Treg) subsets among hCD3$^+$CD4$^+$ T cells. (D) Proportions of hCD21$^+$, hCD20$^+$, and/or hCD27$^+$ B cell subsets among hCD19$^+$ B cells. (E) Total number of human immune cell subsets injected per recipient mouse in HuPBMC Cohort 22.

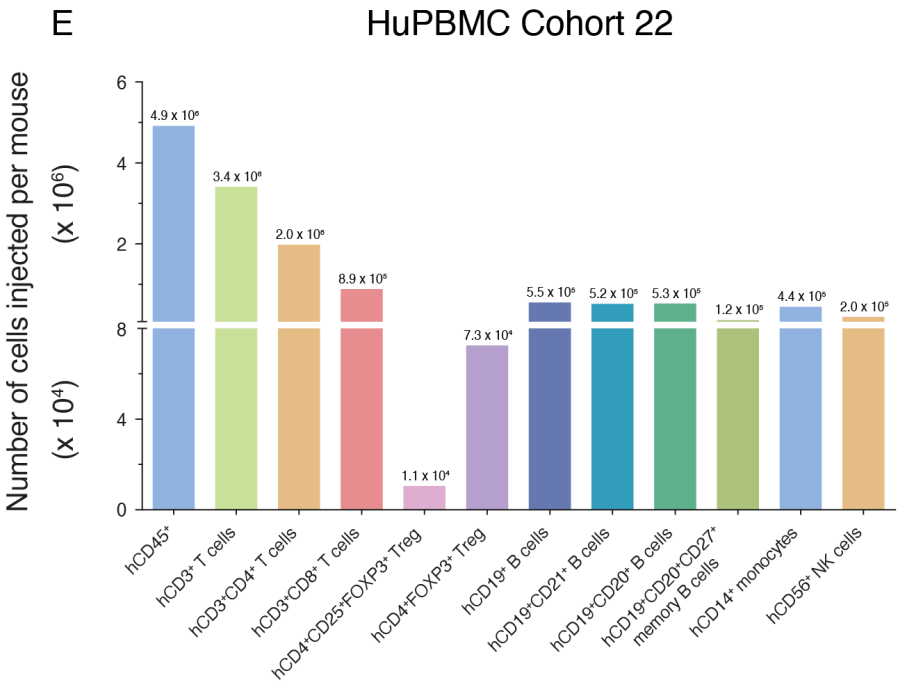

Figure A.14 continued

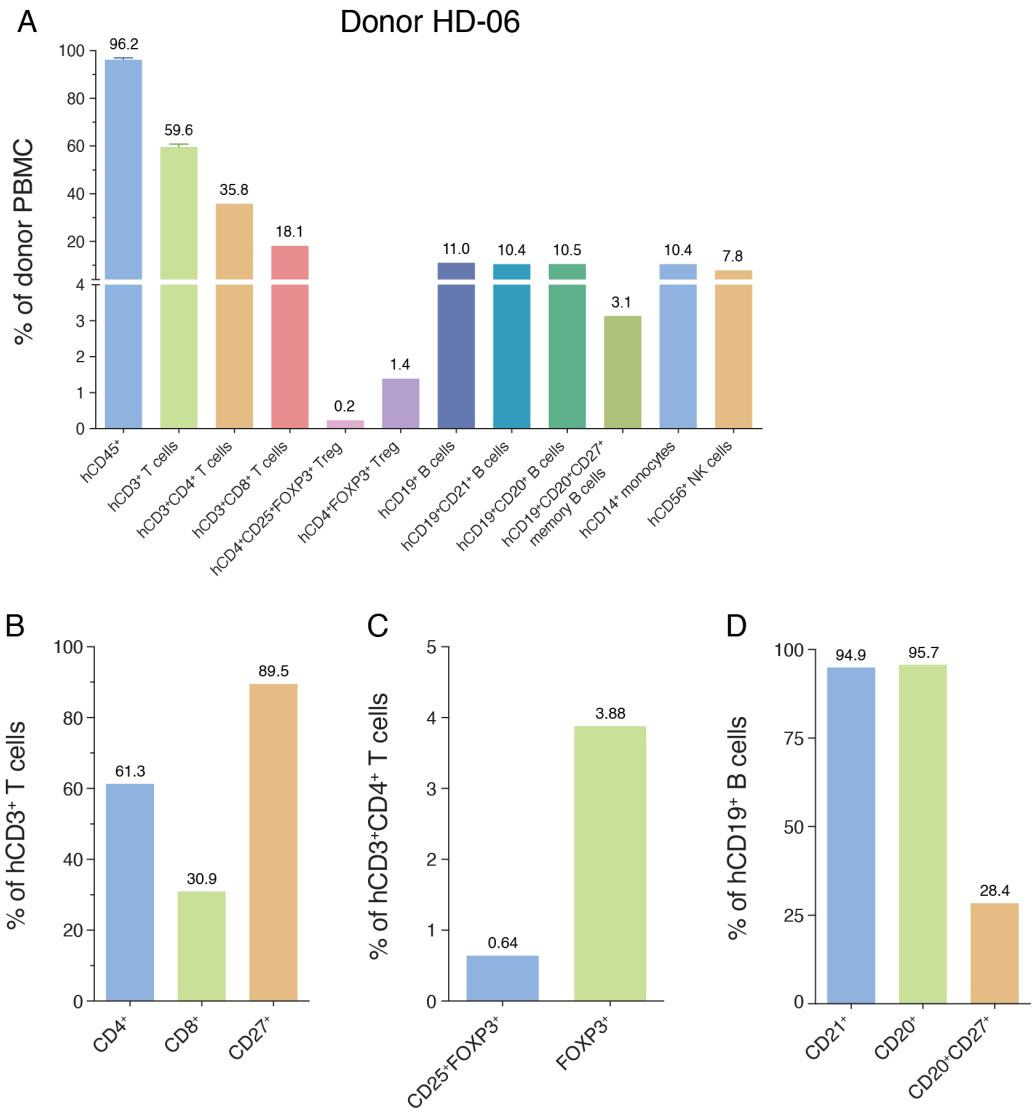

Figure A.15 Blood donor HD-06 PBMC composition and HuPBMC cohort 24 engraftment

(A) Relative composition of human immune cell lineages in the PBMCs of donor HD-06 as a percentage of total leukocytes immediately after isolation from whole blood. (B) Proportions of $hCD4^+$, $hCD8^+$, and $hCD27^+$ T cell subsets among $hCD3^+$ T cells. (C) Proportions of $hCD25^+$ and/or $hFOXP3^+$ regulatory T cell (Treg) subsets among $hCD3^+CD4^+$ T cells. (D) Proportions of $hCD21^+$, $hCD20^+$, and/or $hCD27^+$ B cell subsets among $hCD19^+$ B cells. (E) Total number of human immune cell subsets injected per recipient mouse in HuPBMC Cohort 24.

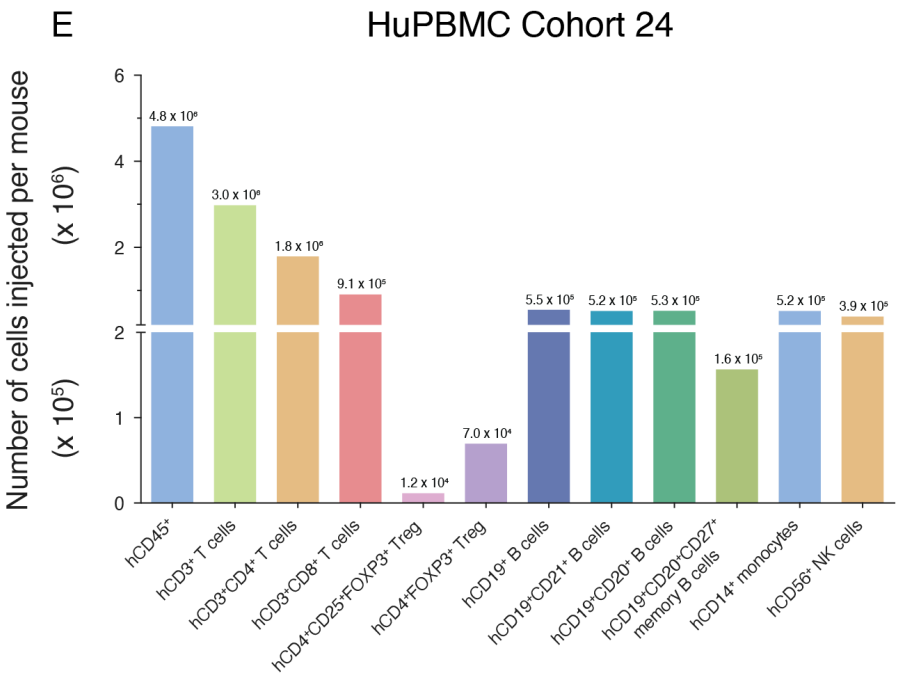

Figure A.15 continued

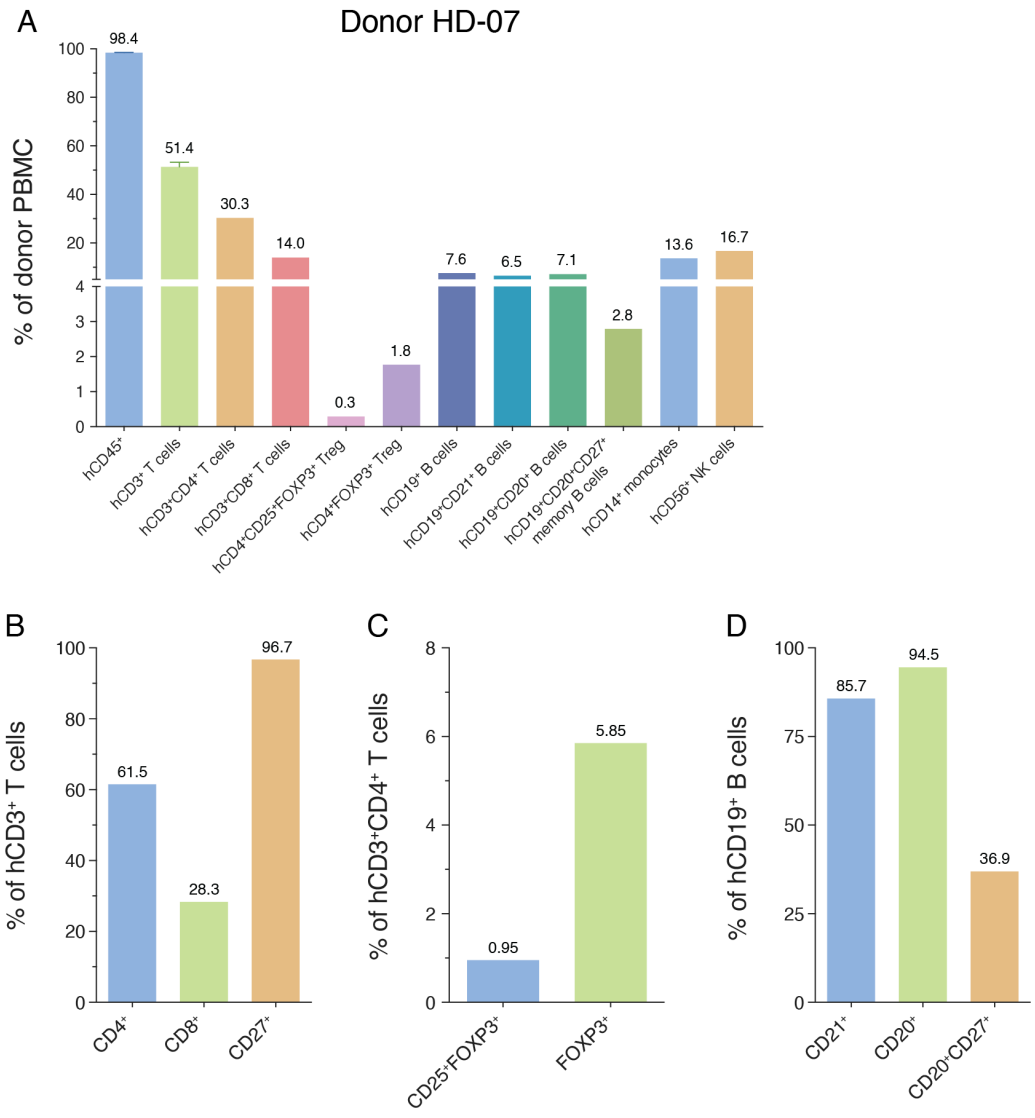

Figure A.16 Blood donor HD-07 PBMC composition and HuPBMC cohort 26 engraftment

(A) Relative composition of human immune cell lineages in the PBMCs of donor HD-07 as a percentage of total leukocytes immediately after isolation from whole blood. (B) Proportions of hCD4$^+$, hCD8$^+$, and hCD27$^+$ T cell subsets among hCD3$^+$ T cells. (C) Proportions of hCD25$^+$ and/or hFOXP3$^+$ regulatory T cell (Treg) subsets among hCD3$^+$CD4$^+$ T cells. (D) Proportions of hCD21$^+$, hCD20$^+$, and/or hCD27$^+$ B cell subsets among hCD19$^+$ B cells. (E) Total number of human immune cell subsets injected per recipient mouse in HuPBMC Cohort 26.

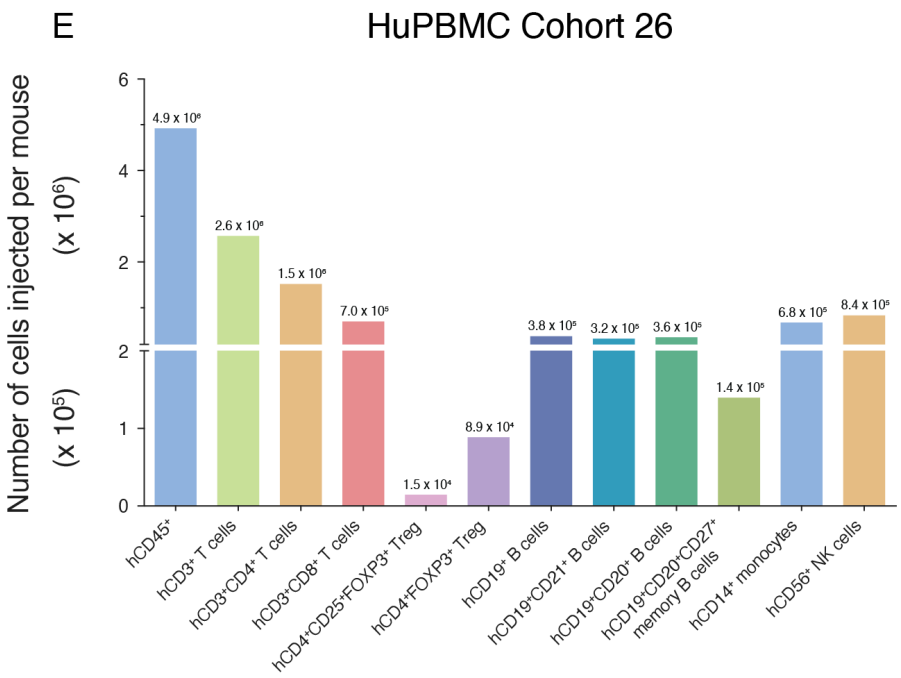

Figure A.16 continued

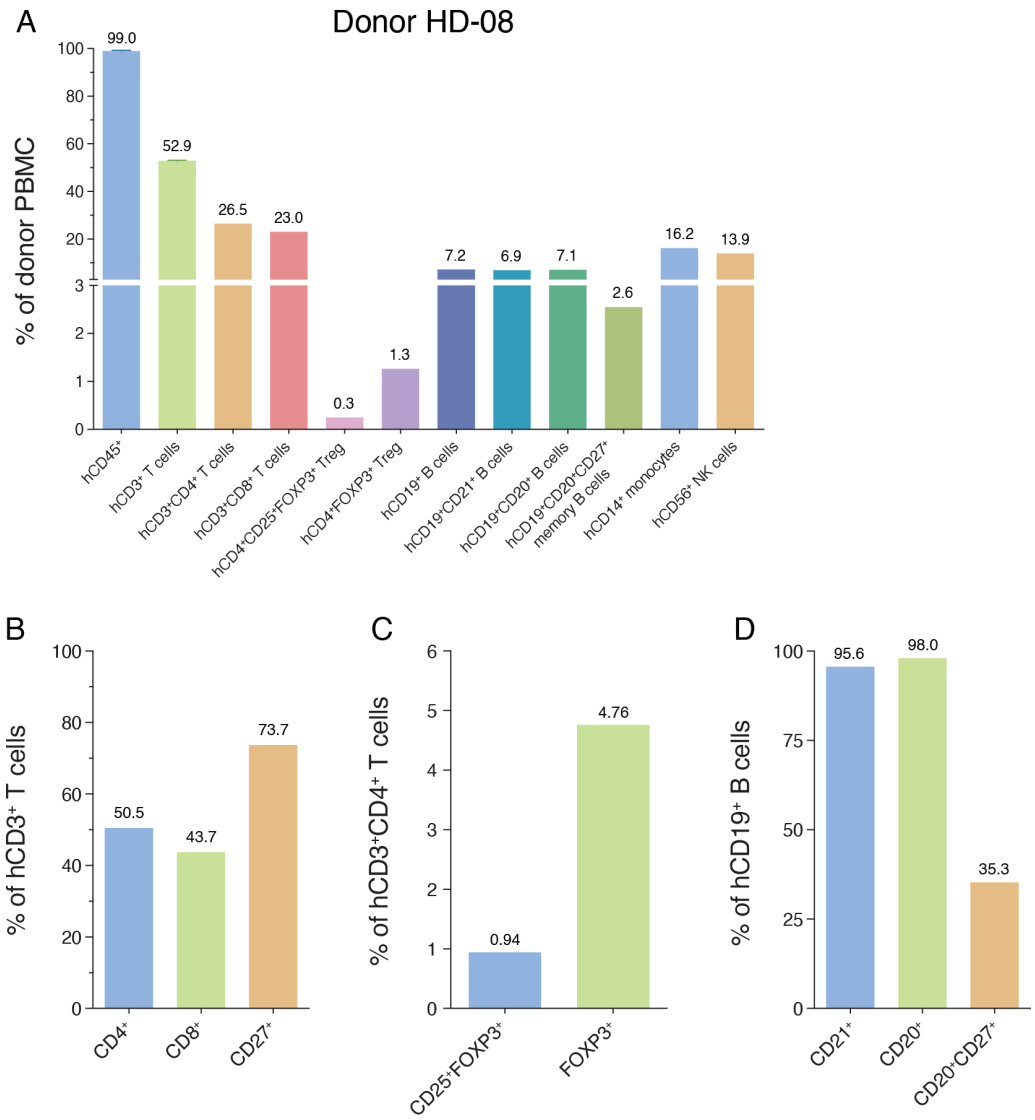

Figure A.17 Blood donor HD-08 PBMC composition and HuPBMC cohort 12 engraftment

(A) Relative composition of human immune cell lineages in the PBMCs of donor HD-08 as a percentage of total leukocytes immediately after isolation from whole blood. (B) Proportions of hCD4$^+$, hCD8$^+$, and hCD27$^+$ T cell subsets among hCD3$^+$ T cells. (C) Proportions of hCD25$^+$ and/or hFOXP3$^+$ regulatory T cell (Treg) subsets among hCD3$^+$CD4$^+$ T cells. (D) Proportions of hCD21$^+$, hCD20$^+$, and/or hCD27$^+$ B cell subsets among hCD19$^+$ B cells. (E) Total number of human immune cell subsets injected per recipient mouse in HuPBMC Cohort 12.

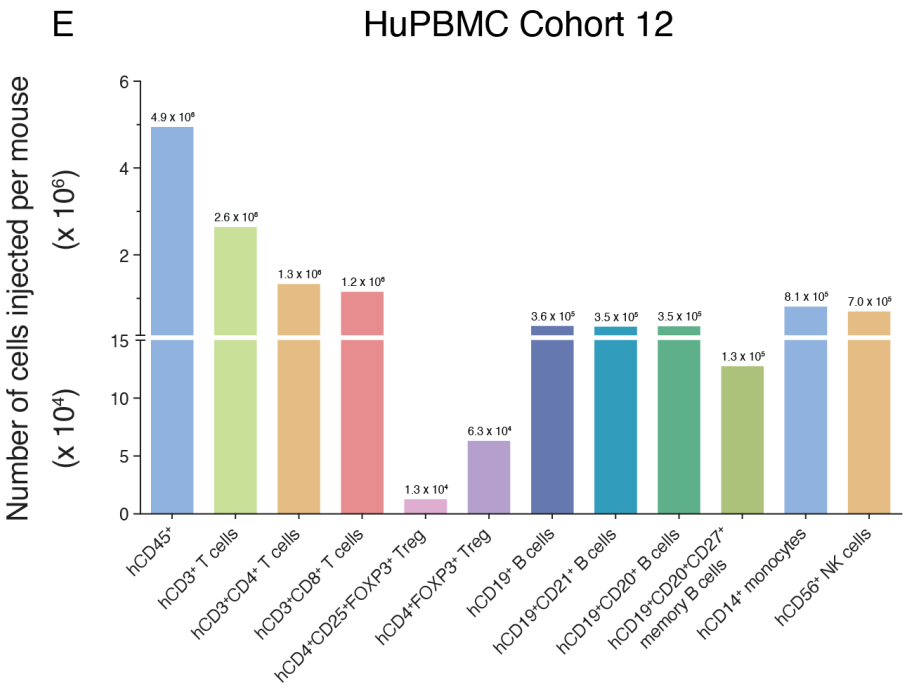

Figure A.17 continued

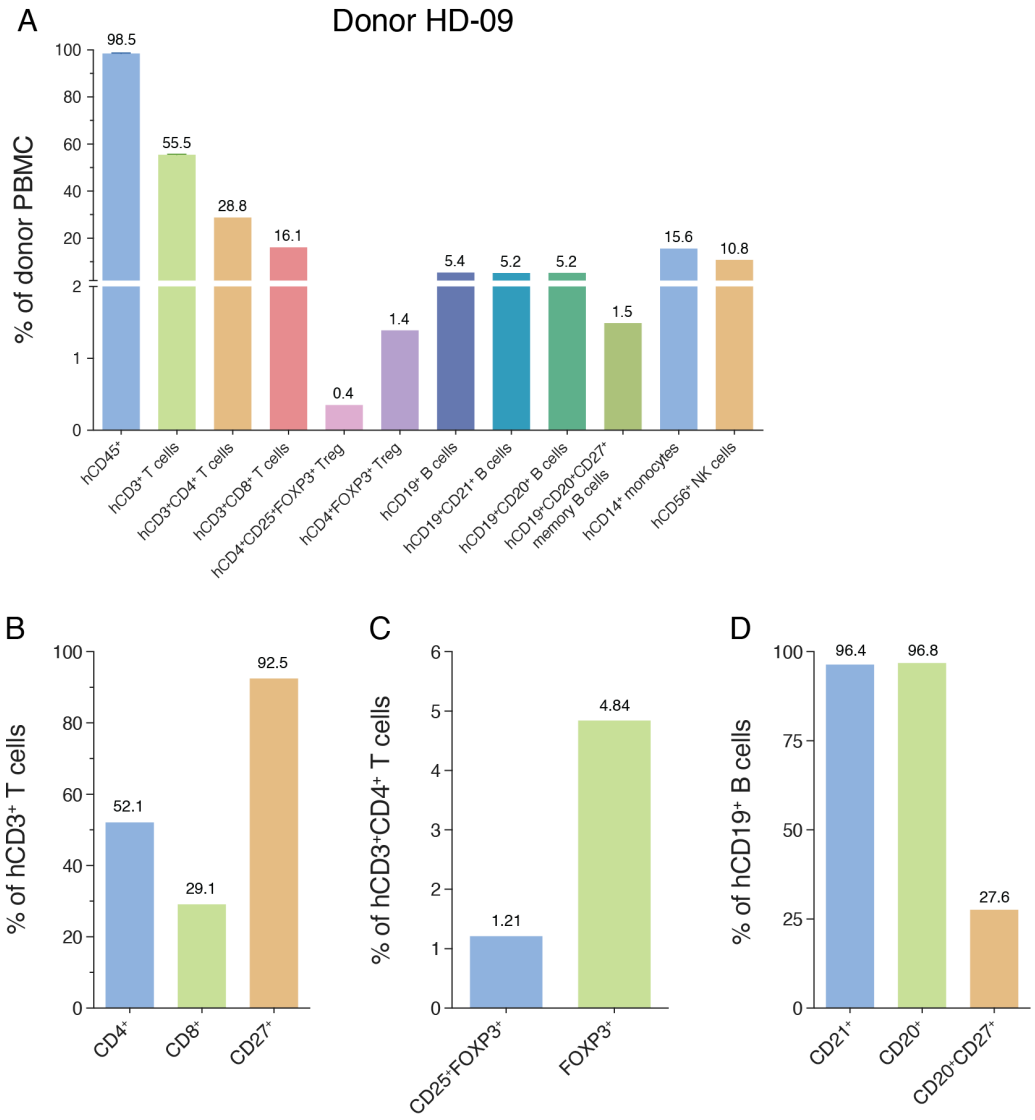

Figure A.18 Blood donor HD-09 PBMC composition and HuPBMC cohort 11 engraftment

(A) Relative composition of human immune cell lineages in the PBMCs of donor HD-09 as a percentage of total leukocytes immediately after isolation from whole blood. (B) Proportions of hCD4$^+$, hCD8$^+$, and hCD27$^+$ T cell subsets among hCD3$^+$ T cells. (C) Proportions of hCD25$^+$ and/or hFOXP3$^+$ regulatory T cell (Treg) subsets among hCD3$^+$CD4$^+$ T cells. (D) Proportions of hCD21$^+$, hCD20$^+$, and/or hCD27$^+$ B cell subsets among hCD19$^+$ B cells. (E) Total number of human immune cell subsets injected per recipient mouse in HuPBMC Cohort 11.

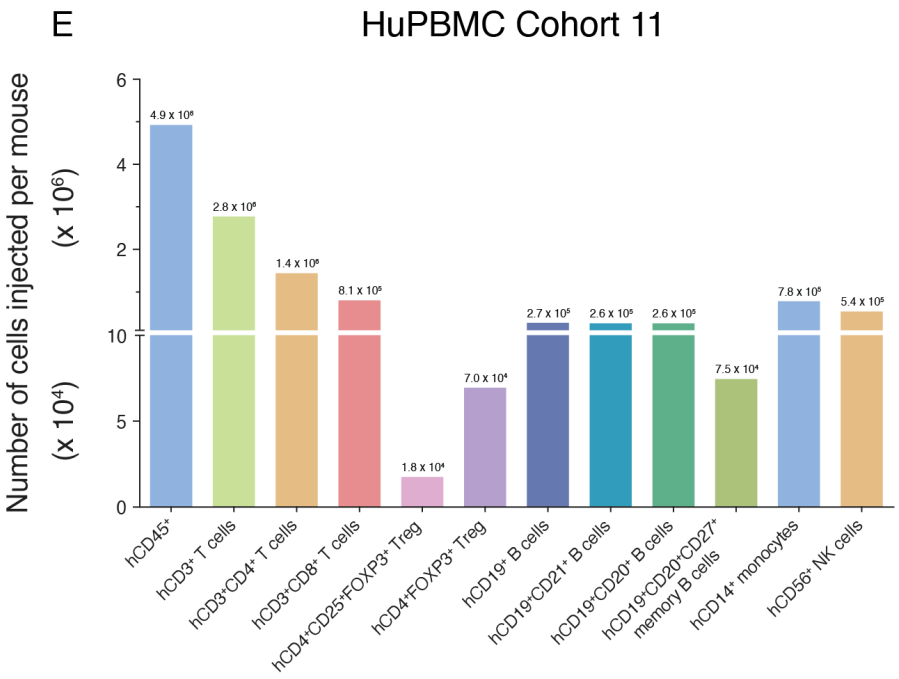

Figure A.18 continued

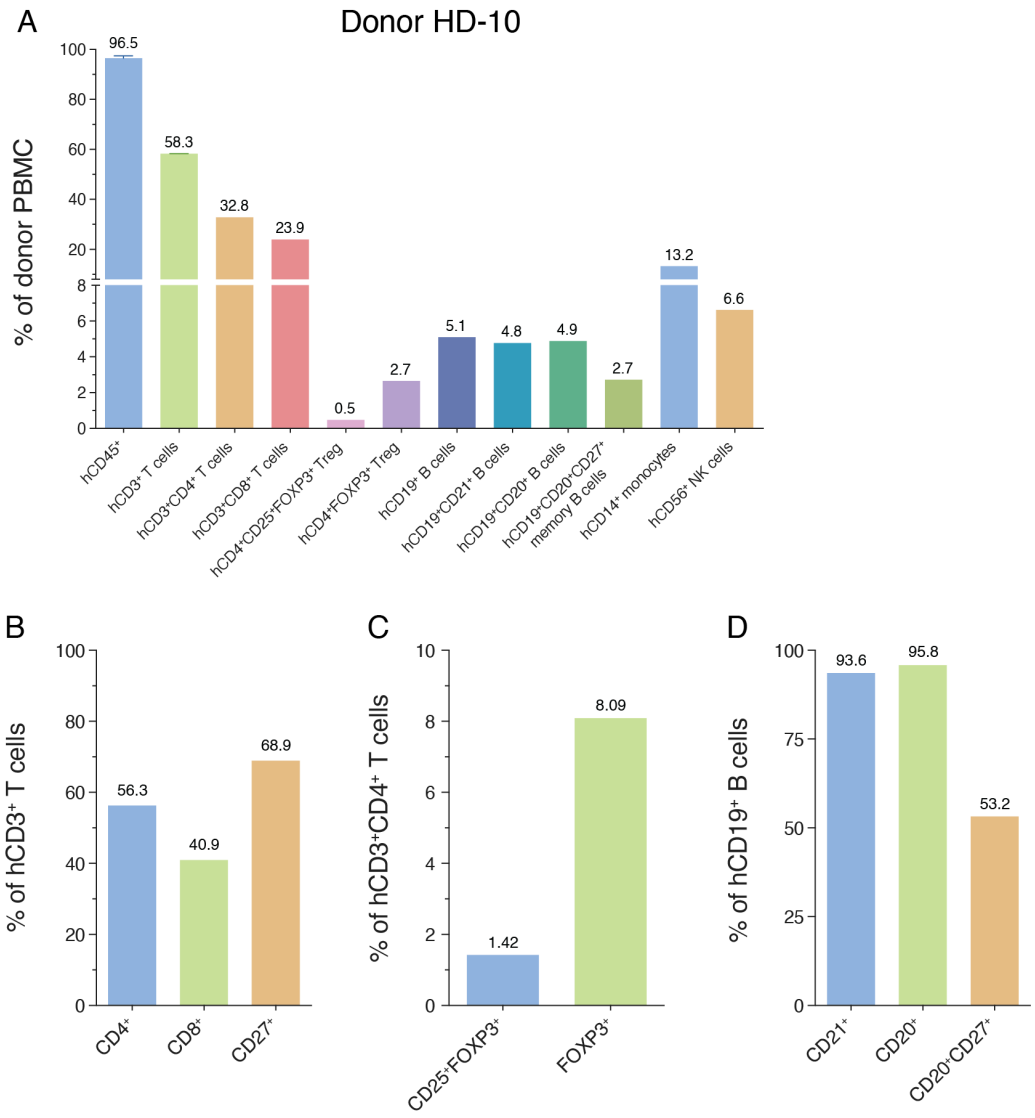

Figure A.19 Blood donor HD-10 PBMC composition and HuPBMC cohort 19 engraftment

(A) Relative composition of human immune cell lineages in the PBMCs of donor HD-10 as a percentage of total leukocytes immediately after isolation from whole blood. (B) Proportions of hCD4$^+$, hCD8$^+$, and hCD27$^+$ T cell subsets among hCD3$^+$ T cells. (C) Proportions of hCD25$^+$ and/or hFOXP3$^+$ regulatory T cell (Treg) subsets among hCD3$^+$CD4$^+$ T cells. (D) Proportions of hCD21$^+$, hCD20$^+$, and/or hCD27$^+$ B cell subsets among hCD19$^+$ B cells. (E) Total number of human immune cell subsets injected per recipient mouse in HuPBMC Cohort 19.

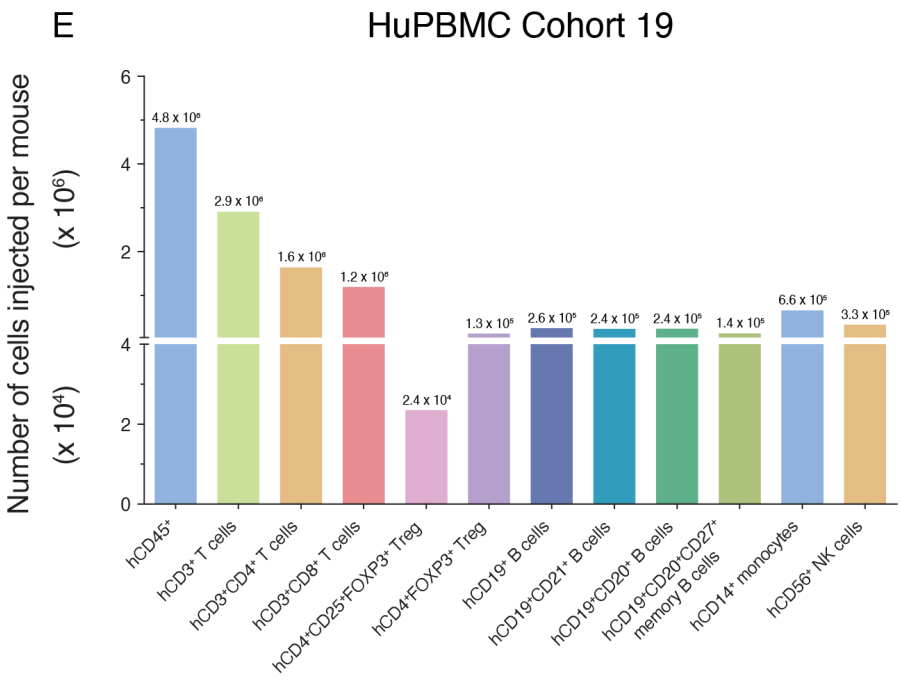

Figure A.19 continued

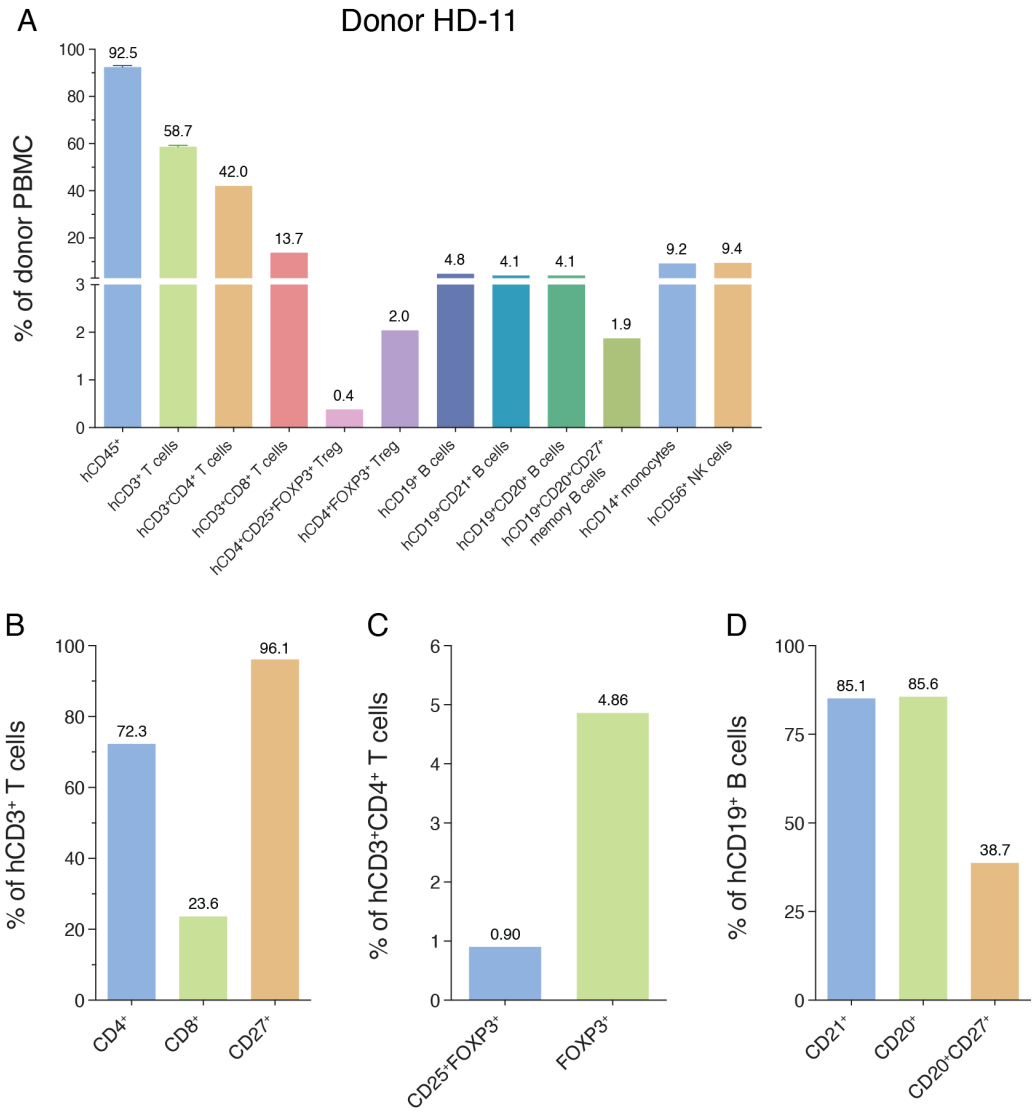

Figure A.20 Blood donor HD-11 PBMC composition and HuPBMC cohort 21 engraftment

(A) Relative composition of human immune cell lineages in the PBMCs of donor HD-11 as a percentage of total leukocytes immediately after isolation from whole blood. (B) Proportions of hCD4$^+$, hCD8$^+$, and hCD27$^+$ T cell subsets among hCD3$^+$ T cells. (C) Proportions of hCD25$^+$ and/or hFOXP3$^+$ regulatory T cell (Treg) subsets among hCD3$^+$CD4$^+$ T cells. (D) Proportions of hCD21$^+$, hCD20$^+$, and/or hCD27$^+$ B cell subsets among hCD19$^+$ B cells. (E) Total number of human immune cell subsets injected per recipient mouse in HuPBMC Cohort 21.

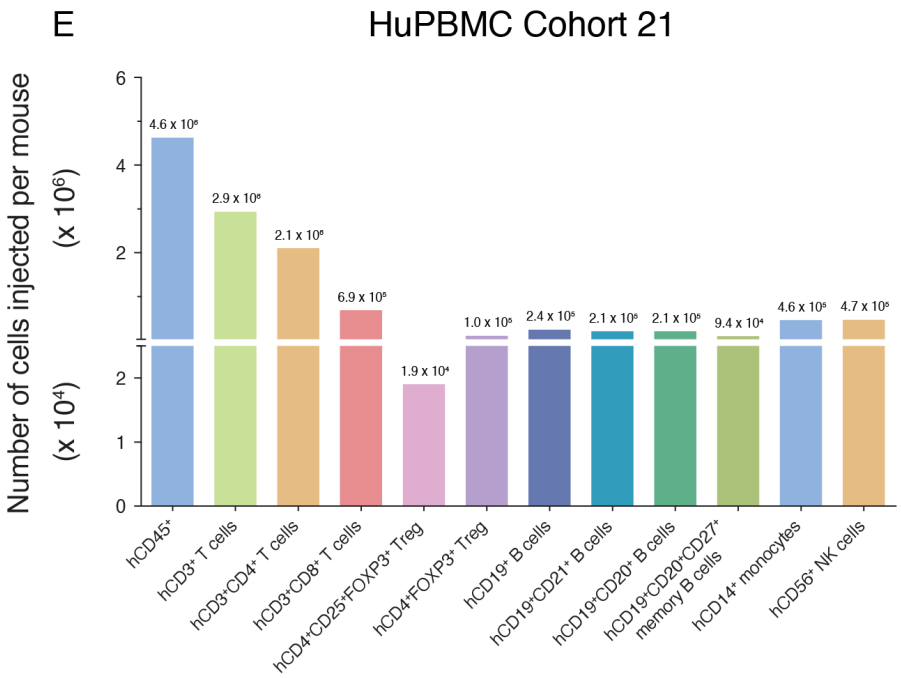

Figure A.20 continued

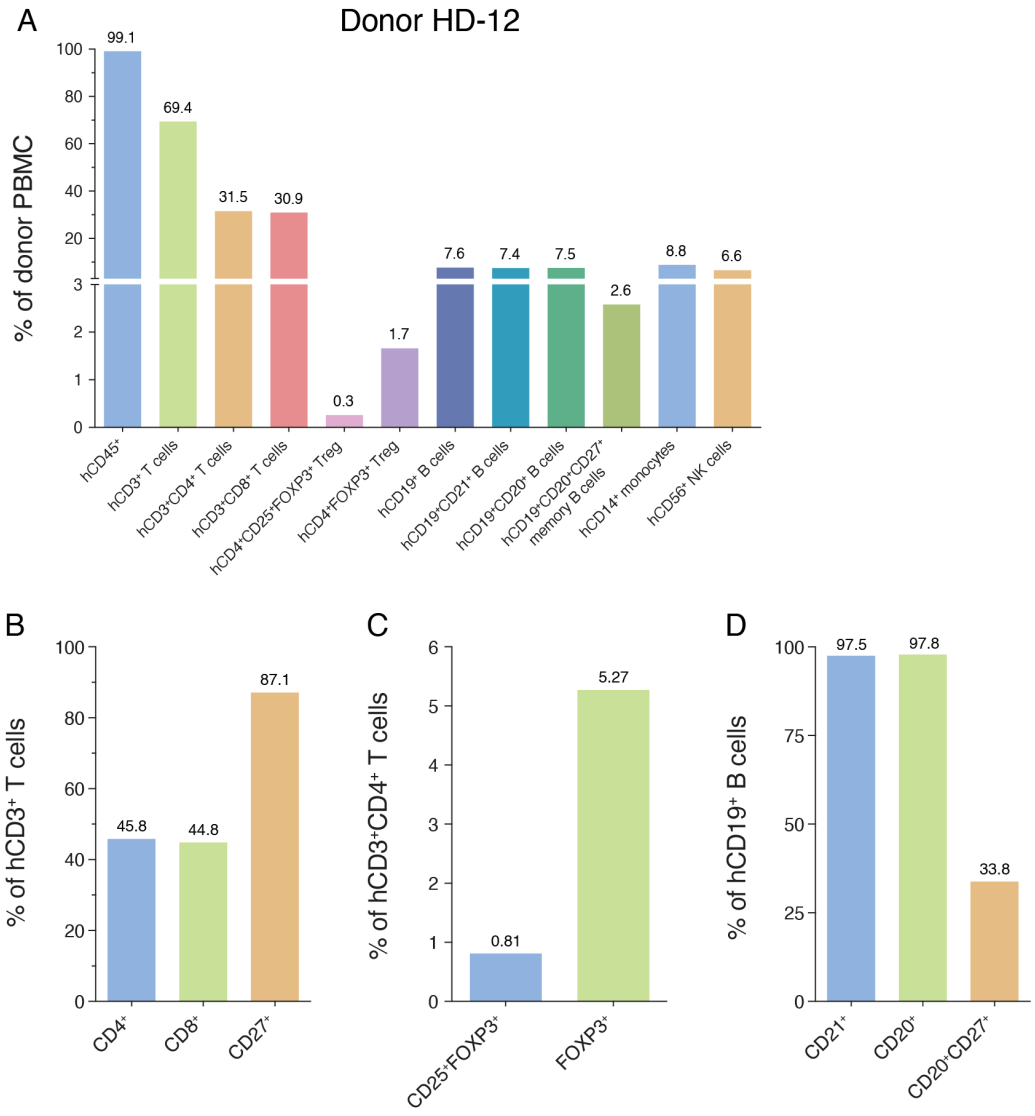

Figure A.21 Blood donor HD-12 PBMC composition and HuPBMC cohort 31 engraftment

(A) Relative composition of human immune cell lineages in the PBMCs of donor HD-12 as a percentage of total leukocytes immediately after isolation from whole blood. (B) Proportions of hCD4$^+$, hCD8$^+$, and hCD27$^+$ T cell subsets among hCD3$^+$ T cells. (C) Proportions of hCD25$^+$ and/or hFOXP3$^+$ regulatory T cell (Treg) subsets among hCD3$^+$CD4$^+$ T cells. (D) Proportions of hCD21$^+$, hCD20$^+$, and/or hCD27$^+$ B cell subsets among hCD19$^+$ B cells. (E) Total number of human immune cell subsets injected per recipient mouse in HuPBMC Cohort 31.

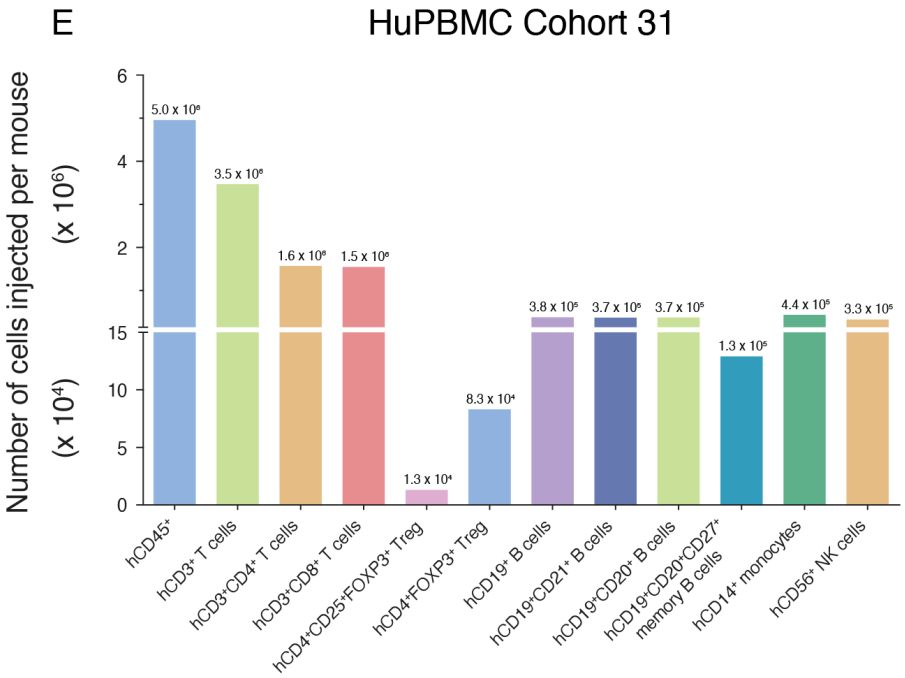

Figure A.21 continued

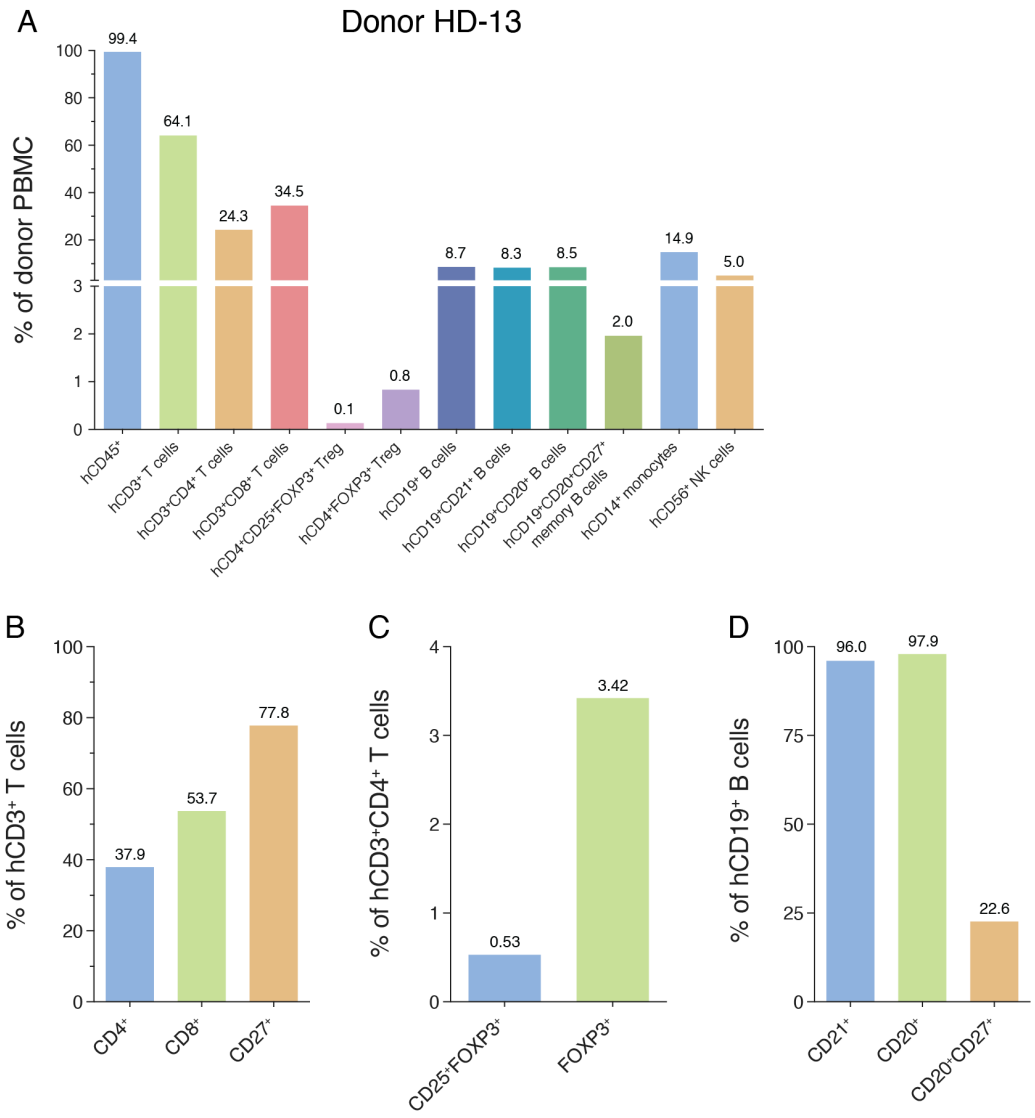

Figure A.22 Blood donor HD-13 PBMC composition and HuPBMC cohort 32 engraftment

(A) Relative composition of human immune cell lineages in the PBMCs of donor HD-13 as a percentage of total leukocytes immediately after isolation from whole blood. (B) Proportions of hCD4$^+$, hCD8$^+$, and hCD27$^+$ T cell subsets among hCD3$^+$ T cells. (C) Proportions of hCD25$^+$ and/or hFOXP3$^+$ regulatory T cell (Treg) subsets among hCD3$^+$CD4$^+$ T cells. (D) Proportions of hCD21$^+$, hCD20$^+$, and/or hCD27$^+$ B cell subsets among hCD19$^+$ B cells. (E) Total number of human immune cell subsets injected per recipient mouse in HuPBMC Cohort 32.

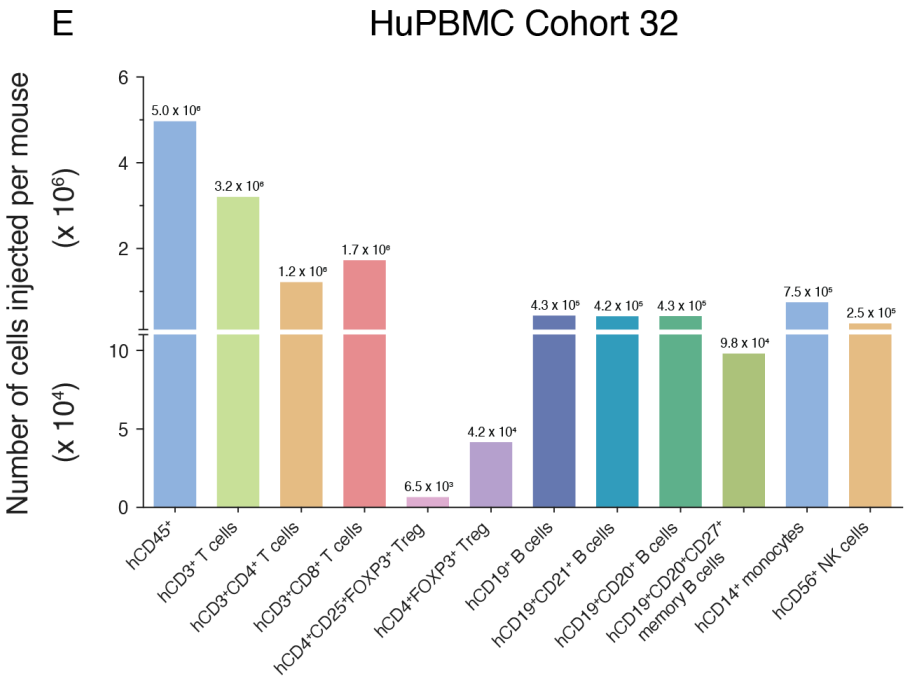

Figure A.22 continued

Appendix 2. Human blood donor serology

Table A.1 Blood donor serum anti-EBV, anti-CMV, and anti-rhMOG IgG and IgM levels

Values shown are mean of duplicate wells per sample obtained at the time of PBMC donation. Nonspecific anti-human IgG binding and anti-human IgM binding were determined to have a background 450 nm absorbance signal (A450) of 0.2 and 0.4, respectively, at a serum dilution of 1:1000. Cytomegalovirus, CMV; Epstein-Barr nuclear antigen 1, EBNA-1; viral capsid antigen, VCA; recombinant human myelin oligodendrocyte glycoprotein, rhMOG.

		A450 at 1:1000 serum dilution						
		α-rhMOG	α-EBV VCA		α-EBV EBNA-1		α-CMV	
Donor ID	Date of serum collection	IgG	IgG	IgM	IgG	IgM	IgG	IgM
HD-01	November 13, 2018	0.229	0.580	-	0.505	-	0.064	0.562
HD-02	February 13, 2019	0.260	0.055	0.448	0.070	0.452	0.059	0.325
HD-03	February 13, 2019	0.278	0.051	0.286	0.055	0.248	0.097	0.638
HD-03	February 3, 2021	0.361	0.104	0.415	0.318	0.433	0.118	0.663
HD-04	July 23, 2019	0.388	0.446	-	0.301	-	0.451	-
HD-04	January 21, 2020	0.414	0.498	-	0.368	-	0.485	-
HD-05	January 8, 2020	0.366	0.054	0.533	0.070	0.223	0.808	-
HD-06	March 5, 2020	0.154	0.363	-	0.052	0.732	0.674	-
HD-07	July 22, 2020	0.497	0.313	-	0.665	-	0.066	0.187
HD-08	January 29, 2019	0.243	0.755	-	0.934	-	0.087	0.298
HD-09	January 29, 2019	0.215	0.688	-	0.107	0.364	0.063	0.248
HD-10	July 29, 2019	0.295	1.249	-	0.488	-	0.741	-
HD-11	October 16, 2019	0.152	0.108	0.241	0.072	0.251	0.061	0.161
HD-12	March 1, 2021	0.348	1.010	-	0.325	-	0.093	0.233
HD-13	March 1, 2021	0.303	0.310	-	0.927	-	0.162	0.687
MS-01	April 1, 2019	0.304	1.123	-	0.614	-	1.406	-
MS-02	April 24, 2019	0.350	1.503	-	0.082	0.420	0.692	-
MS-03	April 29, 2019	0.326	1.470	-	2.025	-	0.072	0.168
MS-04	October 7, 2019	0.365	0.956	-	1.156	-	0.073	0.733

Note: Donor MS-05 recipient HuPBMC cohort samples were collected only for histological analysis and therefore serotyping was not performed.

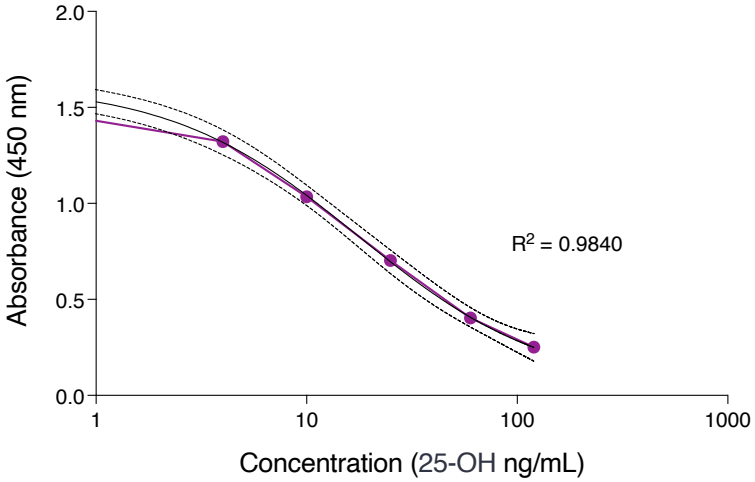

Figure A.23 Competitive ELISA standard curve for quantification of vitamin D in donor serum

Donor serum 25-OH concentration was determined by inversely interpolating sample absorbance values from the standard curve. Data points shown the mean of three replicates. The dashed lines indicate the 95% confidence interval.

Appendix 3. Human blood donor HLA genotypes

Table A.2 Blood donor HLA genotypes

HLA alleles were determined for class I HLA-A, -B, and -C, as well as for class II DRB1, DRB3, DRB4, DRB5, DQB1, DQA1, DPB1, and DPA1. Each cell contains typing results for alleles 1 and 2, if applicable. Occurrence of the MS risk allele DRB1*15:01 is highlighted red[780].

Donor ID	HLA-I			HLA-II							
	HLA-A	HLA-B	HLA-C	DRB1	DRB3	DRB4	DRB5	DQB1	DQA1	DPB1	DPA1
MS-01	02:01:01:01 11:01:01:01	41:01:01:01 50:01:01:01	06:02:01:02 17:01:01:05	03:01:01:01 03:01:01:01	02:02:01:01 03:01:01:01	-- --	-- --	02:01:01:01 02:01:01:01	05:01:01:03 05:01:01:03	14:01:01:01 104:01:01:01	01:03:01:02 02:01:01:01
MS-02	02:01:01:01 02:01:01:01	08:01:01:02 08:01:01:02	07:02:01:01 07:02:01:01	03:01:01:01 03:01:01:01	-- --	-- --	-- --	02:01:01:01 02:01:01:01	05:01:01:03 05:01:01:03	04:01:01:01 04:01:01:01	01:03:01:02 01:03:01:04
MS-03	02:01:01:01 68:02:01:01	07:02:01:01 14:02:01:01	05:01:01:02 08:02:01:01	13:03:01:01 15:01:01:01	01:01:02:01 --	-- --	01:01:01:01 --	03:01:01:03 06:02:01:01	01:02:01:01 05:05:01:13	02:01:02:01 04:01:01:01	01:03:01:01 01:03:01:02
MS-04	02:01:01:18 26:01:01:01	07:02:01:01 35:03:01:01	04:01:01:01 07:02:01:03	11:15:01:01 15:01:17	-- --	-- --	-- --	03:01:01:03 06:02:01:01	01:02:01:01 05:05:01:01	02:01:02:01 02:01:02:10	01:03:01:01 01:03:01:04
HD-01	02:01:01:01 11:01:01:01	08:01:01:01 44:02:01:01	05:01:01:02 07:01:01:01	03:01:01:01 13:01:01:01	01:01:02:01 02:02:01:02	-- --	-- --	02:01:01:01 06:03:01:01	01:03:01:02 05:01:01:02	01:01:01:01 19:01:01:01	02:01:02:02 02:07:01:01
HD-02	01:01:01:01 01:01:01:01	08:01:01:01 15:17:01:01	07:01:01:01 07:01:02:01	01:01:01:01 13:03:01:01	-- --	-- --	-- --	03:01:01:03 05:01:01:03	01:01:01:01 05:05:01:13	03:01:01:01 04:02:01:02	01:03:01:03 01:03:01:05
HD-03	01:01:01:01 26:01:01:01	08:01:01:01 44:03:01:01	07:01:01:01 16:01:01:01	03:01:01:01 07:01:01:01	-- --	01:01:01:01 --	-- --	02:01:01:01 02:02:01:01	02:01:01:01 05:01:01:02	04:01:01:01 04:01:01:01	01:03:01:02 01:03:01:02
HD-04	01:01:01:01 32:01:01:01	08:01:01:01 40:02:01:01	02:02:02:01 07:01:01:01	03:01:01:01 14:01:01	-- --	-- --	-- --	02:01:01:01 05:03:01:01	01:04:01:01 05:01:01:02	03:01:01:01 04:01:01:01	01:03:01:01 01:03:01:03
HD-05	24:02:01:01 24:02:01:01	48:03:01:01 54:01:01:01	01:02:01:01 08:01:01:01	09:01:02:01 11:01:01:01	02:02:01:03 --	01:03:02 --	-- --	03:01:01:03 03:03:02:02	03:02:01:01 05:05:01:01	05:01:01:01 05:01:01:01	01:03:01:01 02:02:02:01
HD-06	01:01:01:01 02:01:01:01	08:01:01:01 40:01:02:01	03:04:01:01 07:01:01:01	07:01:01:01 08:03:02:01	-- --	01:03:01:01 --	-- --	02:02:01:01 03:01:01:17	02:01:01:01 06:01:01:03	04:01:01:01 06:01:01:01	01:03:01:02 01:03:01:03
HD-07	02:01:01:01 31:01:02:01	27:05:02:01 44:02:01:01	02:02:02:01 05:01:01:02	12:01:01:01 13:02:01:02	02:02:01:06 03:01:01:01	-- --	-- --	03:01:01:05 06:04:01:01	01:02:01:04 05:05:01:03	02:01:02:01 03:01:01:01	01:03:01:01 01:03:01:03
HD-08	01:01:01:01 03:01:01:01	07:02:01:01 08:01:01:01	07:01:01:01 07:02:01:03	03:01:01:01 15:01:01:01	-- --	-- --	01:01:01:01 --	02:01:01:01 06:02:01:01	01:02:01:01 05:01:01:02	03:01:01:01 04:01:01:03	01:03:01:03 01:03:01:04
HD-09	03:01:01:01 29:02:01:01	07:02:01:01 44:03:01:01	07:02:01:03 16:01:01:01	07:01:01:01 15:01:01:01	-- --	01:01:01:01 --	01:01:01:01 --	02:02:01:01 06:03:01:01	01:02:01:01 02:01:01:01	11:01:01:01 14:01:01:01	02:01:01:01 02:01:01:02
HD-10	02:01:01:01 02:01:01:01	07:02:01:01 27:05:02:01	02:02:02:01 07:02:01:03	08:01:01 08:63	-- --	-- --	-- --	04:02:01:04 04:02:01:04	04:01:01:01 04:02	04:01:01:03 10:01:01:01	01:03:01:04 02:01:01:02
HD-11	01:01:01:01 03:01:01:01	35:01:01:02 50:01:01:01	04:01:01:01 06:02:01:02	01:01:01:01 03:01:01:01	02:02:01:01 --	-- --	-- --	02:01:01:01 05:01:01:03	01:01:01:01 05:01:01:03	02:01:02:01 04:02:01:02	01:03:01:01 01:03:01:05
HD-12	02:01:01:05 26:01:01:01	39:01:01:03 44:02:01:01	05:01:01:02 12:03:01:01	11:01:01:01 16:01:01	02:02:01:02 --	-- --	02:02:01 --	03:01:01:19 05:02:01:01	01:02:02:01 05:05:01:01	04:02:01:02 05:01:01:01	01:03:01:05 02:02:02:01
HD-13	02:01:01:01 33:01:01:01	14:02:01:01 40:01:02:01	03:04:01:01 08:02:01:01	01:02:01:01 13:02:01:02	03:01:01:01 --	-- --	-- --	05:01:01:01 06:04:01:01	01:01:02:01 01:02:01:04	03:01:01:01 04:02:01:02	01:03:01:03 01:03:01:05

Note: Donor MS-05 recipient HuPBMC cohort samples were collected only for histological analysis and therefore HLA genotyping was not performed.

Appendix 4. Human $CD34^+$ hematopoietic stem cell purity analysis

Human $CD34^+$ stem cells were isolated from fetal liver at 19 weeks' gestation (ID 743001) using magnetic bead separation. Based on flow cytometric analysis, the CD34 positive fraction appeared over 90% pure and 12% of the negative fraction is $CD34^+$ indicating some but not significant loss during selection (Figure A.24). Lineage (Lin) and differentiation markers expected to have low or no expression (Table A.3) on $hCD34^+$ HSCs were present on only a fraction of the positive fraction cells – 2% were slightly Lin^+ and $CD45RA^+$ while 7% expressed CD38 (Figure A.24).

Table A.3 Expected cell surface marker expression on isolated $hCD34^+$ hematopoietic stem cells
Hematopoietic stem cells, HSCs.

Cell marker	Expected expression on HSCs	Expressed on
CD34	Positive	Hematopoietic stem cells
CD45	Positive	General immune cells
Lineage (CD3, CD14, CD16, CD19, CD20, CD56)	Negative	Mature immune cells
CD38	Negative – low expression	Differentiated progenitor cells
CD45RA	Negative – low expression	Differentiated progenitors for myeloid cells

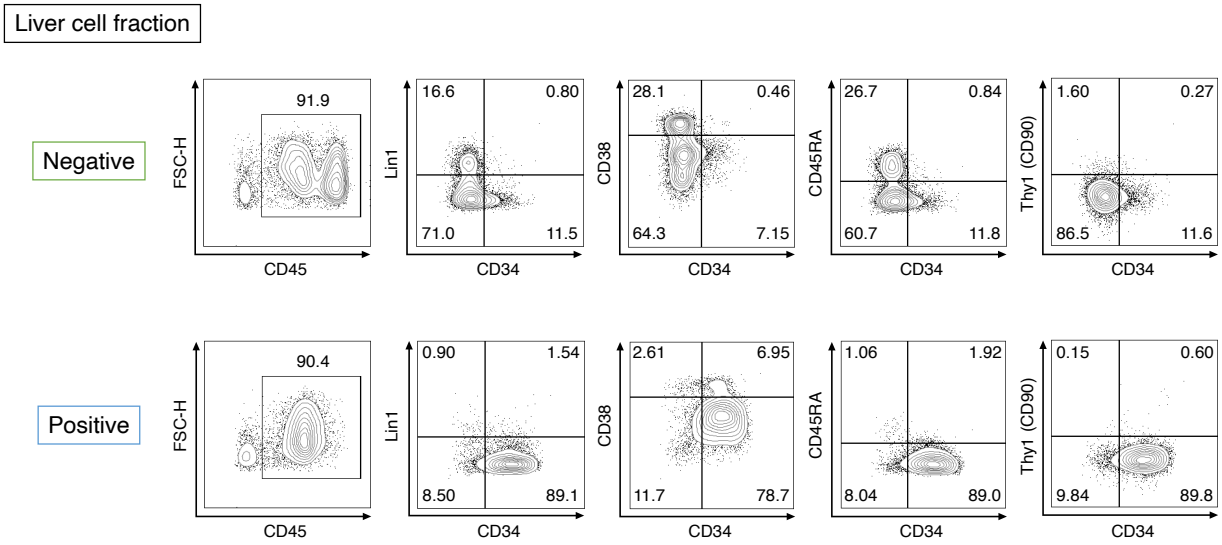

Figure A.24 Fetal liver derived human CD34^{+} hematopoietic stem cell purity by flow cytometric analysis

Figure shows the expression of human CD45, CD34, lineage markers (CD3, CD14, CD16, CD19, CD20, and CD56), CD38, CD45RA and Thy1 on the CD34 negative and positive selection fractions following EasySep magnetic bead separation from total fetal liver cells.

Appendix 5. Generation of the HuProBLT model

Based on the protocol published by Smith and colleagues, reconstituted HuBLT-NSG mice are used as implant tissue and immune cell donors to humanize multiple naïve recipient NSG mice, which were noted to reconstitute by 6 weeks post-surgery and quadruple the humanized mouse yield from a single tissue donation[531]. To assess the utility of such a protocol, we adapted this method to transfer the enlarged kidney implant and the total bone marrow (BM) and spleen derived cells from one donor HuBLT-NSG female mouse to four naïve female NSG mice (Figure A.25).

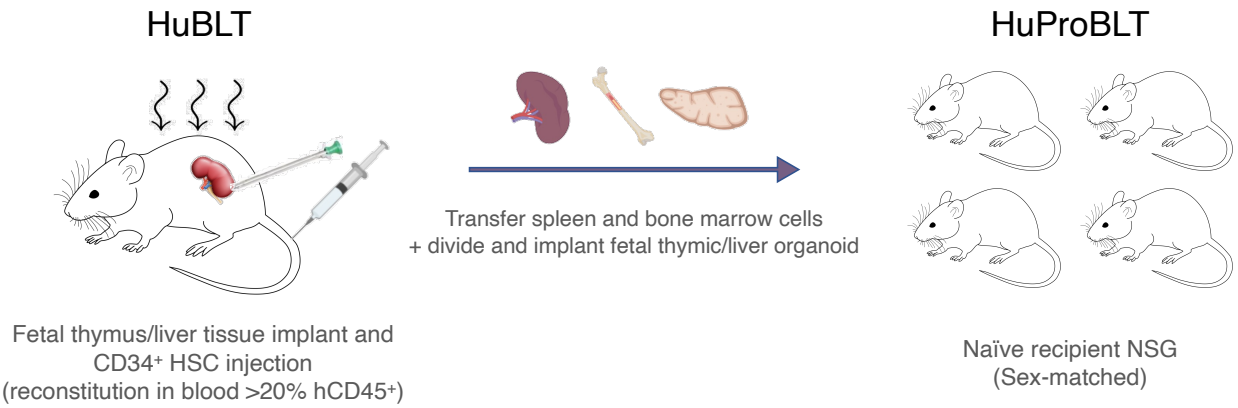

Figure A.25 Schematic representation of the generation of HuProBLT mice

Reconstituted HuBLT-NSG mice (containing >20% $hCD45^+$ cells among total leukocytes in peripheral blood) are used as tissue and immune cell donors to each generate 4 – 5 sex-matched derivative HuProBLT-NSG mice. The fetal liver and thymus organoid is removed from the kidney capsule of reconstituted HuBLT mice and divided equally into 4 – 5 pieces, which are then implanted into x-ray preconditioned recipient HuProBLT-NSG mouse kidney capsules. Total isolated bone marrow cells and splenocytes were also isolated, divided equally, and injected into recipients immediately following implantation of the human tissue organoid. Created in part with BioRender.

Processing HuBLT donor samples

The donor HuBLT mouse was assessed for reconstitution levels in the peripheral blood at 14 weeks post-HSC injection, wherein 81.6% of leukocytes were hCD45$^+$, indicating successful engraftment and suitability as a tissue donor. Total immune cells were isolated from the BM of both dissected hind leg femurs and tibias following the protocol by Liu and Quan[781]. A total of 7.6 x10^6 cells were isolated from the BM and reconstitution of various human immune cell lineages was assessed by flow staining (Figure A.26). Splenocytes were isolated per standard protocol, resulting in 8.2 x10^6 cells total, which were also analyzed for reconstitution (Figure A.27). Lastly, the enlarged kidney implanted organoid was dissected whole for transfer to recipient mice. Both the donor BM and spleen contained human T cells, B cells, monocytes, and NK cells (Table A.4).

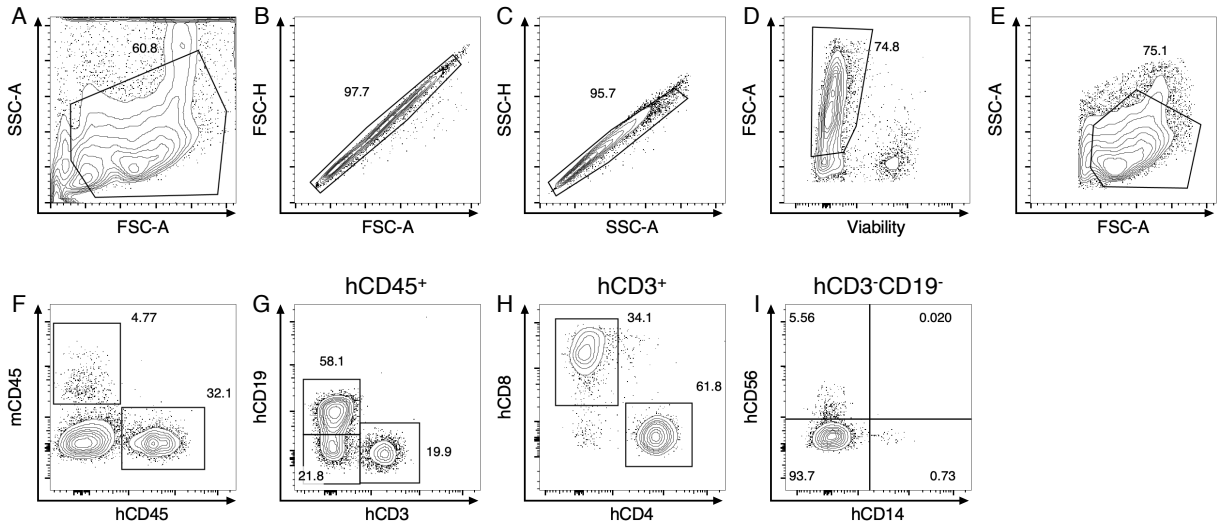

Figure A.26 Gating strategy for flow cytometric analysis of human immune cells in donor HuBLT mouse bone marrow

Figure shows (A – E) General cleanup steps applied to all samples. Gates were drawn successively from left to right: exclusion of cellular debris and doublets, by both size and complexity, followed by selection of viable cells and leukocytes in bone marrow cells isolated from a HuBLT mouse at 14 weeks post-HSC injection. (F) Identification of human (h) and mouse (m) CD45$^+$ cell subsets, (G) hCD3$^+$ T and hCD19$^+$ B cell populations, (H) hCD3$^+$CD4$^+$ and hCD3$^+$CD8$^+$ T cell subsets, and (I) hCD56$^+$ NK cell and hCD14$^+$ monocyte populations. The parent population for each plot is noted above.

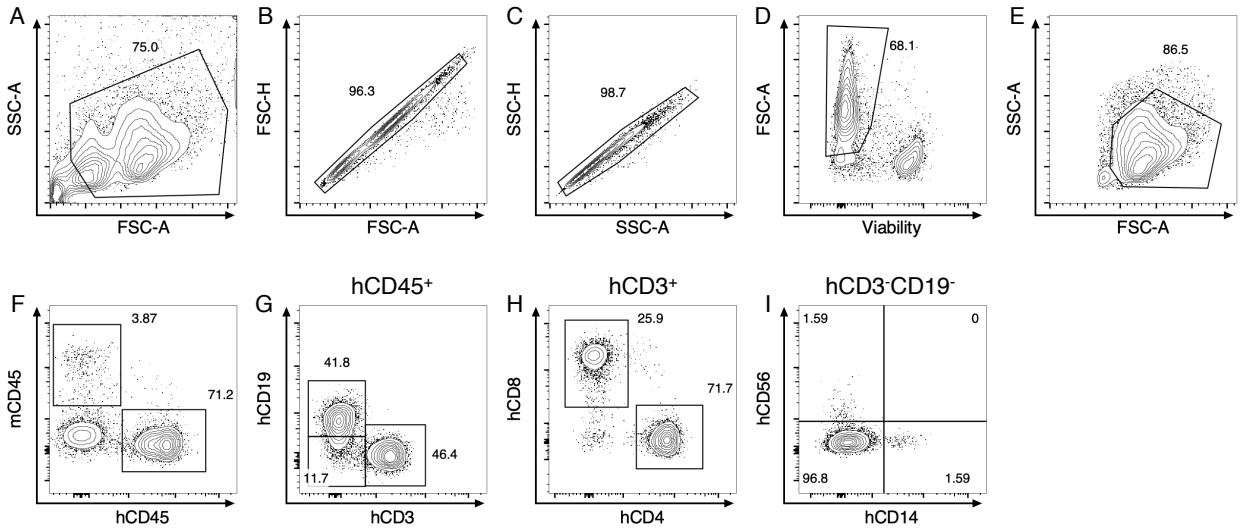

Figure A.27 Gating strategy for flow cytometric analysis of human immune cells in donor HuBLT mouse splenocytes

Figure shows (A – E) General cleanup steps applied to all samples. Gates were drawn successively from left to right: exclusion of cellular debris and doublets, by both size and complexity, followed by selection of viable cells and leukocytes in splenocytes isolated from a HuBLT mouse at 14 weeks post-HSC injection. (F) Identification of human (h) and mouse (m) $CD45^+$ cell subsets, (G) $hCD3^+$ T and $hCD19^+$ B cell populations, (H) $hCD3^+CD4^+$ and $hCD3^+CD8^+$ T cell subsets, and (I) $hCD56^+$ NK cell and $hCD14^+$ monocyte populations. The parent population for each plot is noted above.

Table A.4 Proportional human immune cell lineage reconstitution of the bone marrow and spleen of the donor HuBLT mouse

Tissue	**%hCD45$^+$ of leukocytes**	**%CD3$^+$ of hCD45$^+$**	**%CD3$^+$CD4$^+$ of hCD45$^+$**	**%CD3$^+$CD8$^+$ of hCD45$^+$**	**%CD19$^+$ of hCD45$^+$**	**%CD14$^+$ of hCD45$^+$**	**%CD56$^+$ of hCD45$^+$**
Bone marrow	32.1	19.9	12.3	6.80	58.1	0.16	1.21
Spleen	71.2	46.4	33.3	12.0	41.8	0.19	0.19

Humanization of HuProBLT mice

The cage of recipient NSG mice was placed on Baytril treated water (0.2 mg/mL enrofloxacin) three days before surgery and maintained for 2 weeks, after which, acidified water was provided. Recipients were also irradiated with 100 cGy the day before surgery. Control NSG mice, which received an IV injection of sterile PBS only, were not irradiated and stayed on acidified water throughout the experiment. Surgery to humanize the recipient HuProBLT mice was performed as usual to engraft the donor organoid tissue, which was evenly divided and implanted under kidney capsule immediately following isolation and processing of all donor HuBLT tissues. Recipient mice all received one piece of donor thymus/liver organoid tissue, an IP injection of splenocytes (evenly divided for four recipients) in 200 μL of PBS, and an IV injection of BM cells (evenly divided for four recipients) in 100 μL PBS, all under isoflourane anesthesia. Procedures, post-operative care, and monitoring proceeded as usual for generating HuBLT mice. At 5 weeks post-surgery, the peripheral blood of recipient HuProBLT mice contained very few $hCD45^+$ cells (Table A.5). At 16 weeks post-surgery, high levels of 30 – 50 % $hCD45^+$ cells were detected in the blood of 2 out of 4 recipients, whereas the other two did not humanize (Table A.6). Within the reconstituted blood samples, human T cell, B cell, monocyte, and NK cell subsets were detected, indicating multilineage expansion (Table A.7).

Table A.5 Peripheral blood reconstitution of recipient HuProBLT-NSG mice at 5 weeks post-transplant

Mouse ID	Group	%$mCD45^+$ of leukocytes	%$hCD45^+$ of leukocytes
873	PBS control	41.8	0.08
874	PBS control	9.16	0.07
875	ProBLT-NSG	76.8	0.44
876	ProBLT-NSG	92.3	0.00
877	ProBLT-NSG	86.6	0.31
878	ProBLT-NSG	85.4	0.08

Table A.6 Peripheral blood reconstitution of recipient HuProBLT-NSG mice at 16 weeks post-transplant

Mouse ID	Group	%mCD45$^+$ of leukocytes	%hCD45$^+$ of leukocytes
873	PBS control	94.8	0.00
874	PBS control	97.8	0.02
875	ProBLT-NSG	56.3	38.9
876	ProBLT-NSG	98.6	0.00
877	ProBLT-NSG	97.5	0.15
878	ProBLT-NSG	43.6	52.7

Table A.7 Human immune cell proportions in the peripheral blood of reconstituted HuProBLT-NSG mice at 16 weeks post-transplant

Mouse ID	%CD3$^+$ of hCD45$^+$	%CD3$^+$CD4$^+$ of hCD45$^+$	%CD4$^+$CD25$^+$ FOXP3$^+$ of hCD45$^+$	%CD4$^+$FOXP3$^+$ of hCD45$^+$	%CD3$^+$CD8$^+$ of hCD45$^+$	%CD3$^+$CD27$^+$ of hCD45$^+$
875	72.5	25.9	0.49	3.12	42.0	57.0
878	21.1	20.3	0.06	0.34	0.52	9.04

Mouse ID	%CD19$^+$ of hCD45$^+$	%CD19$^+$CD20$^+$ of hCD45$^+$	%CD19$^+$CD21$^+$ of hCD45$^+$	%CD19$^+$CD20$^+$ CD27$^+$ of hCD45$^+$	%CD14$^+$ of hCD45$^+$	%CD56$^+$ of hCD45$^+$
875	8.15	7.26	4.10	0.32	1.20	0.51
878	63.5	59.8	28.9	1.73	2.12	0.50

At 18 weeks post-surgery, endpoint spleen analysis confirmed that 2 of 4 recipient HuProBLT mice fully humanized, while the other two did not at all (Table A.8). As this experiment was a pilot study, technical error is likely the cause of the incomplete humanization of recipients. With procedural experience, generation of HuProBLT mice should be near 100%. Moreover, no symptoms of wasting (chronic xGvHD) were observed up to 18 weeks post-surgery, though reconstitution may be sufficient as early as 8 weeks post-surgery with improved surgical technique. Major cell subsets in the BM and spleen of the donor HuBLT mouse appear at similar frequencies in the spleen of the two humanized HuProBLT recipients, within the expected variability range for the HuBLT model (Table A.9). Given the similarity in reconstitution, HuProBLT mice likely

function comparably to the HuBLT mice, though tissue specific composition and function would also need to be assessed to verify (intestines, vaginal tract, etc.).

Table A.8 Spleen reconstitution of recipient HuProBLT-NSG mice at 18 weeks post-transplant

Mouse ID	Group	%mCD45$^+$ of leukocytes	%hCD45$^+$ of leukocytes
873	PBS control	95.9	0.007
874	PBS control	96.4	0.008
875	ProBLT-NSG	21.9	76.5
876	ProBLT-NSG	95.8	0.011
877	ProBLT-NSG	96.0	0.24
878	ProBLT-NSG	11.4	85.3

Table A.9 Human immune cell proportions in the spleens of reconstituted HuProBLT-NSG mice at 18 weeks post-transplant

Mouse ID	%CD3$^+$ of hCD45$^+$	%CD3$^+$CD4$^+$ of hCD45$^+$	%CD4$^+$CD25$^+$ FOXP3$^+$ of hCD45$^+$	%CD4$^+$FOXP3$^+$ of hCD45$^+$	%CD3$^+$CD8$^+$ of hCD45$^+$	%CD3$^+$CD27$^+$ of hCD45$^+$
875	67.0	18.3	0.37	2.67	45.1	52.2
878	32.7	24.9	0.09	0.40	7.16	19.3

Mouse ID	%CD19$^+$ of hCD45$^+$	%CD19$^+$CD20$^+$ of hCD45$^+$	%CD19$^+$CD21$^+$ of hCD45$^+$	%CD19$^+$CD20$^+$ CD27$^+$ of hCD45$^+$	%CD14$^+$ of hCD45$^+$	%CD56$^+$ of hCD45$^+$
875	16.1	13.9	8.07	0.40	0.60	0.39
878	54.2	40.7	25.1	0.79	0.11	0.78

Appendix 6. Intracellular detection of myelin basic protein in myeloid cells

The detection of intracellular MBP within murine myeloid cells was used as a proxy to assess the extent of myelin damage and debris phagocytosis occurring in the CNS of EAE induced mice. To measure MBP within cellular phagosomes by flow cytometry, an anti-mouse MBP purified primary antibody and conjugated secondary antibody were used in combination. Target antigen specificity of the primary and secondary antibodies, tissue specific detection of MBP, and the suitability of the analysis to be used as an indicator of inflammatory damage in the CNS was confirmed by comparing C57Bl/6 WT mice immunized with MOG_{35-55} EAE emulsion or with blank CFA emulsion. Perfused brains, spinal cords, and spleens were collected for single cell processing on day 15 post-immunization.

The gating scheme used to identify and quantify CNS $mCD45^{lo}$ resident and $mCD45^{hi}$ infiltrating myeloid cells expressing CD11b and/or F4/80 that contain intracellular MBP indicative of phagocytosis (Figure A.28). T cell subset markers were also included to determine correlations between infiltrating subsets and myelin damage and uptake by myeloid cells. Within the spinal cord, MOG_{35-55} EAE induction results in an expansion in the abundance of resident and infiltrating myeloid cells compared to blank CFA immunization (Figure A.29). Moreover, CFA immunization did not result in substantial MBP detection within myeloid cells in the spinal cord as was observed for MOG EAE samples (Figure A.29). Among MOG EAE tissues, intracellular MBP within myeloid cells was only measured in the brains and spinal cords and not the spleens, confirming tissue appropriate detection of myelin specifically in the CNS (Figure A.30).

To further confirm the primary and secondary antibodies did not generate substantial nonspecific background staining, full minus one (FMO) antibody panels were used to analyze certain samples. CNS and spleen tissues collected for FMO analysis were obtained from mice that had similar disease burden to those collected for full staining, therefore the absence of non-specific staining is not due to reduced or minimal clinically measurable disease activity in the mice assigned to the FMO stain groups (Figure A.31A). None of the blank CFA immunized mice developed clinical EAE symptoms. The proportion of $mCD11b^{hi}F4/80^{+}$ myeloid cells in the spleen positive for MBP was nearly zero, whereas the brain and spinal cord both contained MBP^{+} myeloid cells, confirming the tissue specificity of MBP detection using this method (Figure A.31B). The spinal cords of MOG EAE induced mice contained a greater fraction of $mCD11b^{hi}F4/80^{+}MBP^{+}$

myeloid cells compared to blank CFA immunized mice, indicating this is likely a specific measure of EAE pathology (Figure A.31B). In the brain, however, general peripheral inflammation caused by CFA immunization led to increased MBP phagocytosis, regardless of MOG_{35-55} inclusion, beyond the proportions seen in the spinal cord, where MOG_{35-55} EAE induction is known to generate demyelinated lesions in C57Bl/6 mice (Figure A.31B). Though the proportion of $mCD11b^{hi}F4/80^{+}$ myeloid cells containing MBP is similar between CFA immunized and MOG EAE induced mice in the brain, the CNS tissues from CFA-immunized mice contains fewer total infiltrating $mCD45^{hi}$ cells compared to MOG EAE induced tissues, and accordingly, overall fewer myeloid cells that contain intracellular myelin (Figure A.31C – F).

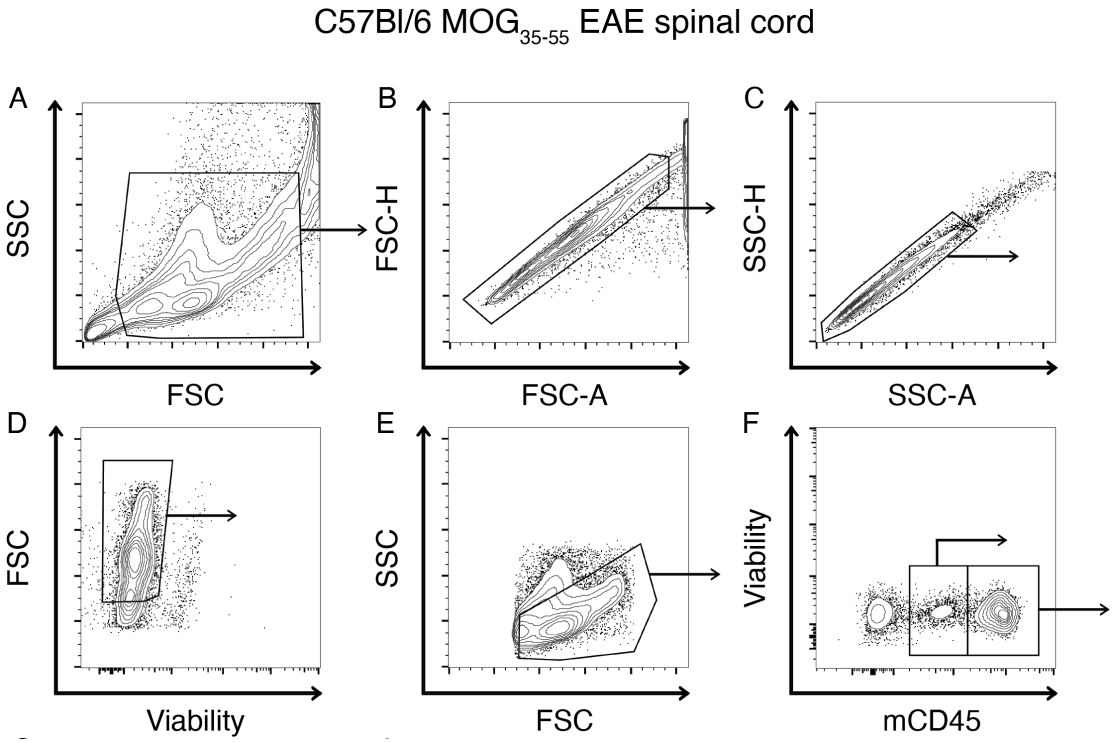

Figure A.28 General gating scheme to identify myelin basic protein phagocytosing myeloid cells in the spinal cord of C57Bl/6 EAE mice

Figure shows representative gated flow cytometric plots for measuring murine myeloid cell populations that have phagocytosed and contain intracellular myelin basic protein (MBP) in the spinal cord of a C57Bl/6 mouse induced with MOG_{35-55} EAE on day 15 post-immunization. Cells were isolated from perfused spinal cord tissue. (A – E) General cleanup steps applied to all samples. Gates were drawn successively from left to right: exclusion of cellular debris and doublets, by both size and complexity, followed by selection of viable cells and leukocytes. (F) Identification of resident $mCD45^{lo}$ and infiltrating $mCD45^{hi}$ populations. (G) Within the $mCD45^{hi}$ population, $mCD3^{+}$ T cells, $mCD19^{+}$ B cells, and double $mCD3^{-}CD19^{-}$ cells were gated. (H) $mCD3^{+}$ T cell populations expressing mCD4

or mCD8. (I) mCD3^{-}CD19^{-} myeloid cells expressing mCD11b and/or mF4/80 and (J) MBP positive staining for these myeloid populations. For G – J, the parent population for each plot is noted in the top right corner.

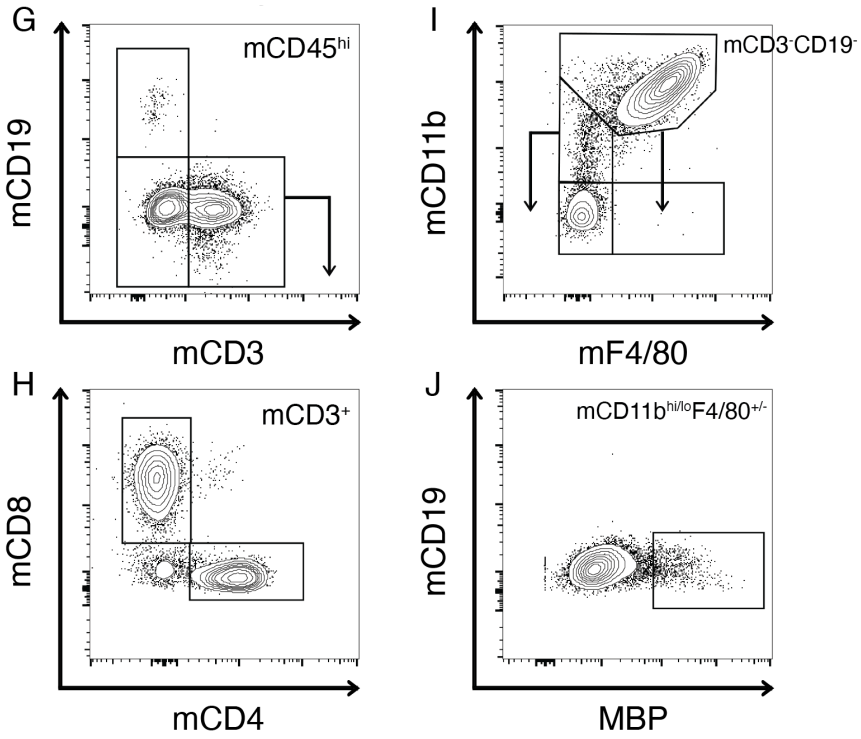

Figure A.28 continued

In the spinal cord, MOG EAE induction in C57Bl/6 mice led to increased proportions of myeloid cells that contain intracellular MBP as compared to blank CFA immunized mice (Figure A.32 left column). The proportions are more similar in the brain between treatments (Figure A.32 right column), however the staining appears accurate, given that none of the FMO combinations in either tissue show much background staining with very few MBP^{+} cells. In summary, FMO data confirms that both primary and secondary antibodies are required to detect intracellular MBP in myeloid cells in the tissues of MOG EAE mice and the secondary is not binding non-specifically to other antibody Fc regions in the panel.

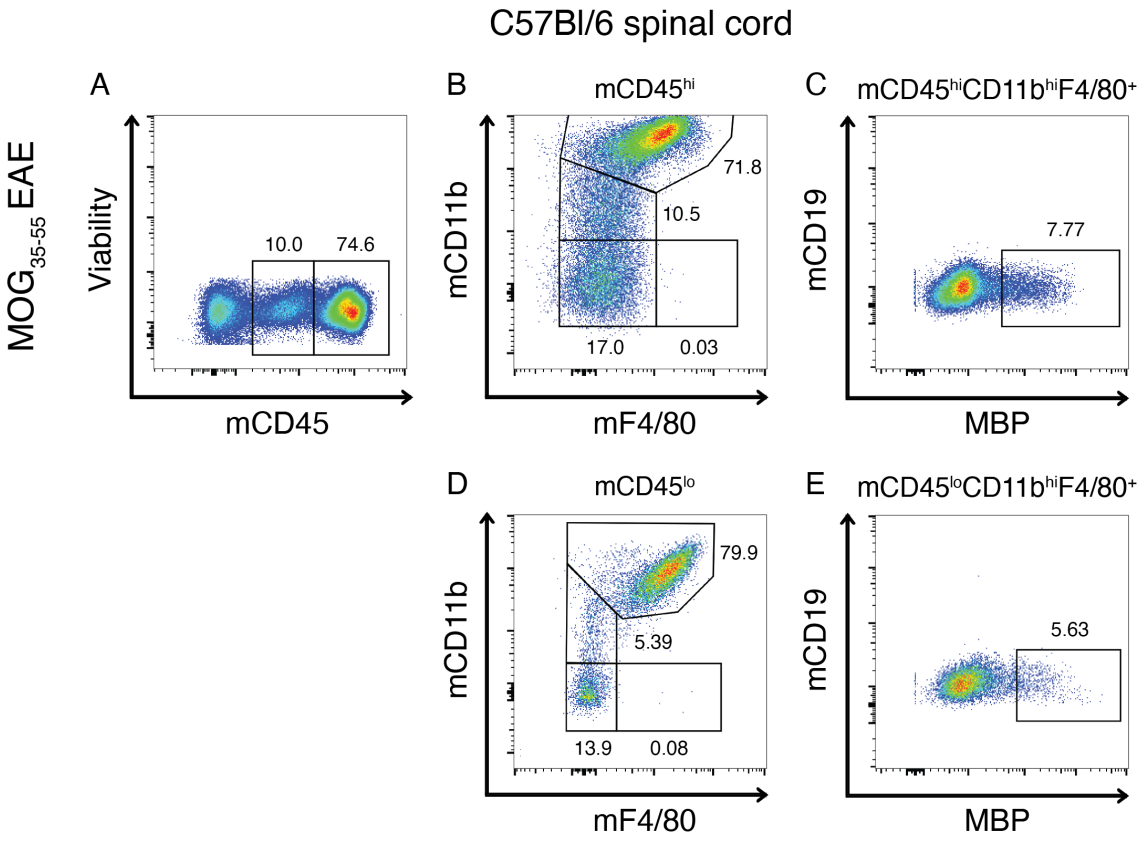

Figure A.29 Intracellular myelin basic protein positive staining of myeloid cell populations in the spinal cord of C57Bl/6 MOG_{35-55} EAE and CFA immunized mice

Figure shows representative flow cytometric plots for gating murine myeloid cell populations containing intracellular myelin basic protein (MBP) in the spinal cord of C57Bl/6 mice induced with MOG_{35-55} EAE (A – E) or blank CFA (F – J) on day 15 post-immunization. Cells were isolated from perfused spinal cord tissues. (A, F) Identification of resident $mCD45^{lo}$ and infiltrating $mCD45^{hi}$ populations. (B, G) Infiltrating $mCD45^{hi}$ myeloid cells expressing mCD11b and/or mF4/80, as well as (C, H) $mCD45^{hi}CD11b^{hi}F4/80^{+}$ cells containing myelin basic protein (MBP^{+}). (D, I) CNS resident $mCD45^{lo}$ myeloid cells expressing mCD11b and/or mF4/80, as well as (E, J) $mCD45^{lo}CD11b^{hi}F4/80^{+}$ cells containing myelin basic protein (MBP^{+}). The parent population for each plot is noted above.

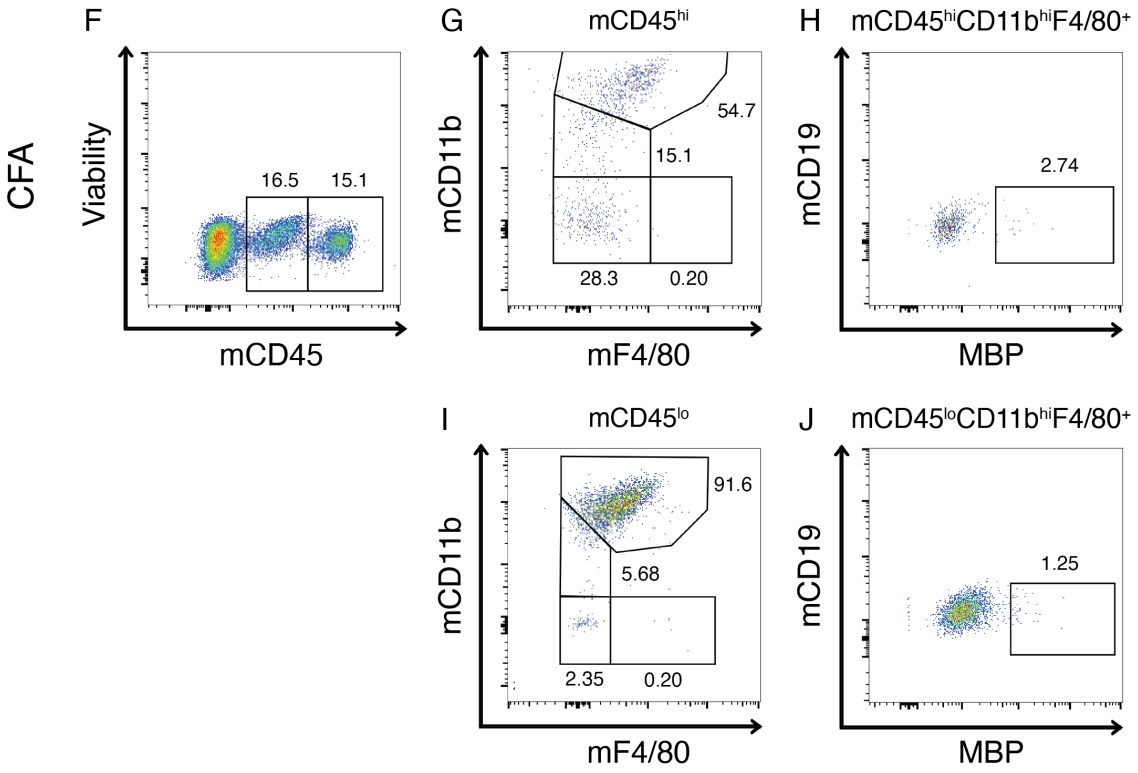

Figure A.29 continued

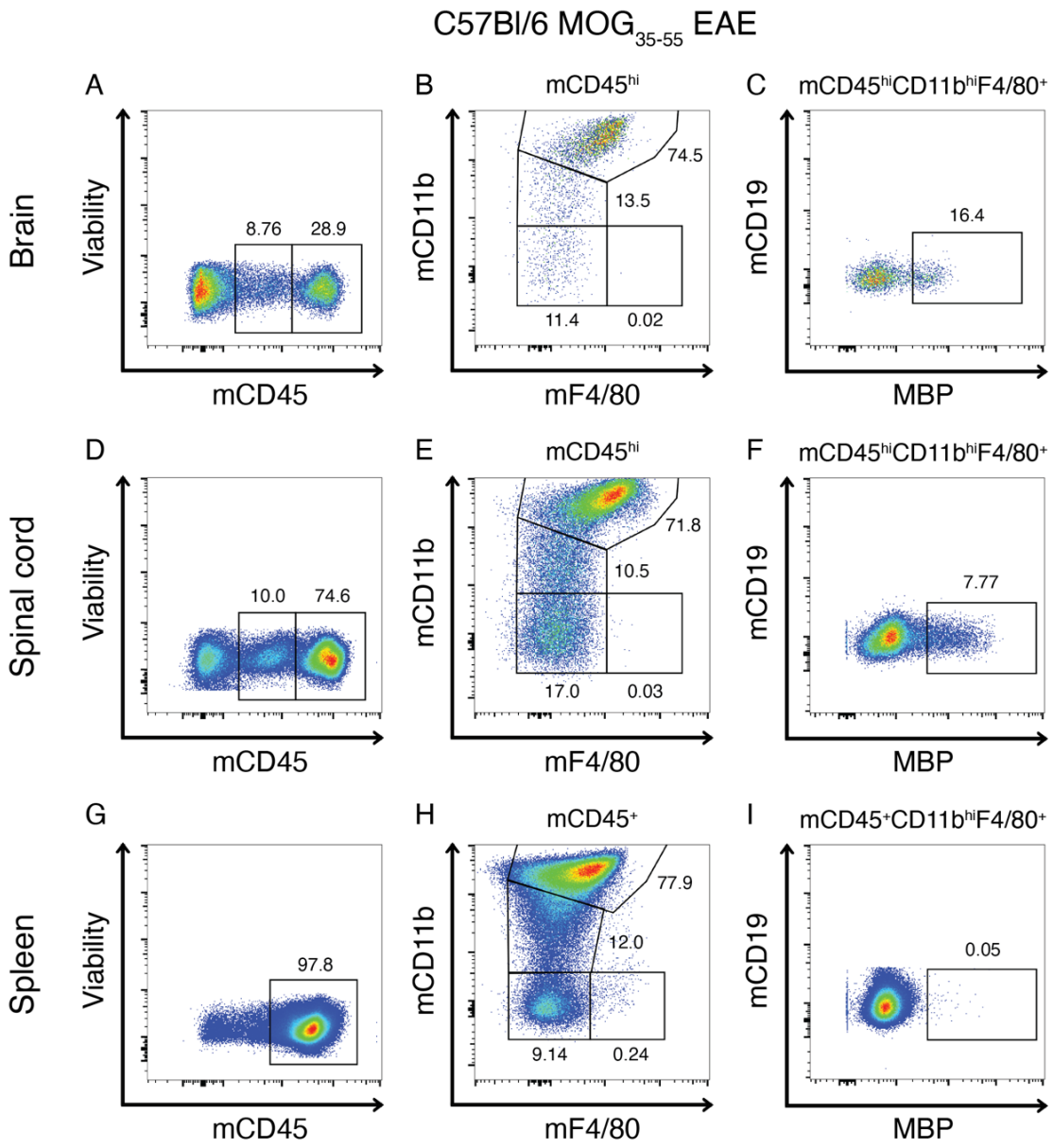

Figure A.30 Tissue specific detection of myelin basic protein within myeloid cells in the CNS of C57Bl/6 EAE mice

Figure shows representative flow cytometric plots for gating murine myeloid cell populations containing intracellular myelin basic protein (MBP) in the brain, spinal cord, and spleen of a C57Bl/6 mouse induced with MOG_{35-55} EAE on day 15 post-immunization. Cells were isolated from perfused CNS tissues. (A, D, G) Identification of resident $mCD45^{lo}$ and infiltrating $mCD45^{hi}$ populations in the CNS, and peripheral $mCD45^{+}$ cells in the spleen. (B, E, H) $mCD45^{hi/+}$ myeloid cells expressing mCD11b and/or mF4/80 and (C, F, I) $mCD45^{hi/+}CD11b^{hi}F4/80^{+}$ myeloid cells containing intracellular myelin basic protein (MBP). The parent population for each plot is noted above.

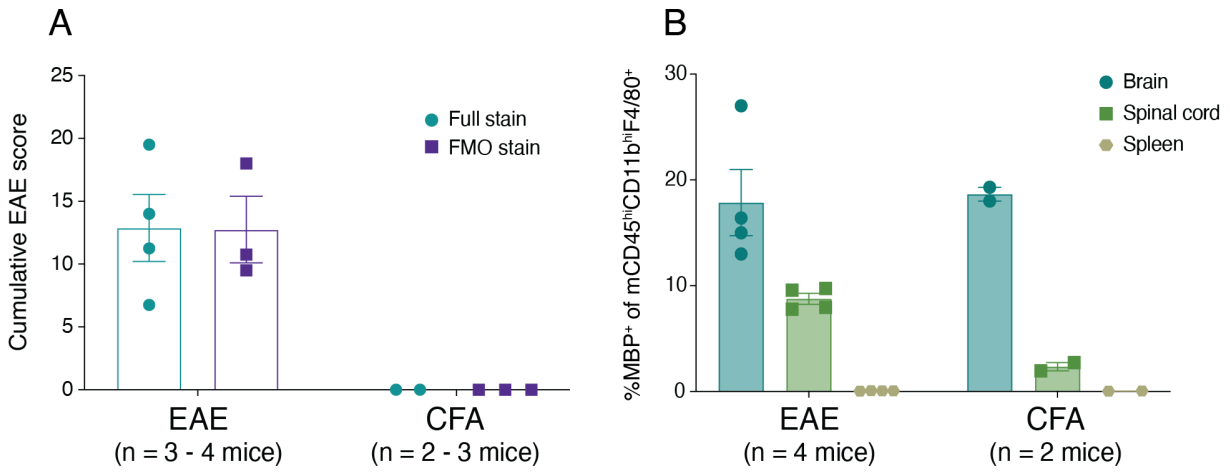

Figure A.31 CNS tissue localized and MOG immunization specific detection of intracellular myelin basic protein in phagocytic cells by flow cytometry

Figure shows (A) the cumulative clinical EAE disease scores attained by C57Bl/6 WT mice immunized with MOG_{35-55} antigen replete CFA emulsion (EAE, n = 3 – 4 mice for full stain analysis group or FMO stain analysis group) and blank, antigen-free CFA emulsion (CFA, n = 2 – 3 mice/group) up to and including day 15 post-induction. All induced mice were co-administered pertussis toxin per the standard immunization protocol. (B) The proportion of $mCD45^{hi}CD11b^{hi}F4/80^{+}$ cells in the brains, spinal cords, and spleens of EAE induced (n = 4) and CFA induced (n = 2) C57Bl/6 WT mice containing intracellular myelin basic protein (MBP^{+}) day 15 post-immunization. The total number of infiltrating $mCD45^{hi}$ and resident $mCD45^{lo}$ myeloid cells expressing CD11b and/or F4/80 in the spinal cord (C) and brain (D), as well as the total numbers of these myeloid cells containing intracellular MBP in the spinal cord (E) and brain (F), of EAE induced (n = 4) and CFA induced (n = 2) C57Bl/6 WT mice day 15 post-immunization. Immune cells were isolated from perfused CNS tissues. All data are shown as mean with SEM.

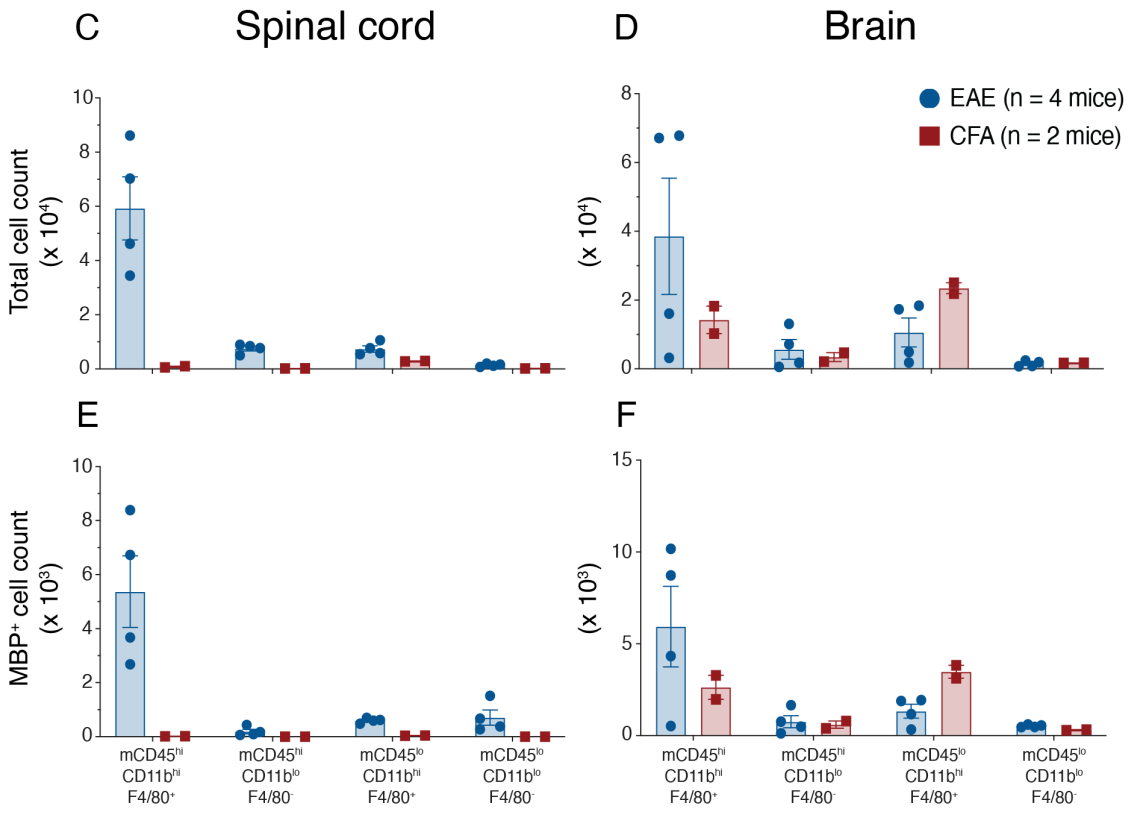

Figure A.31 continued

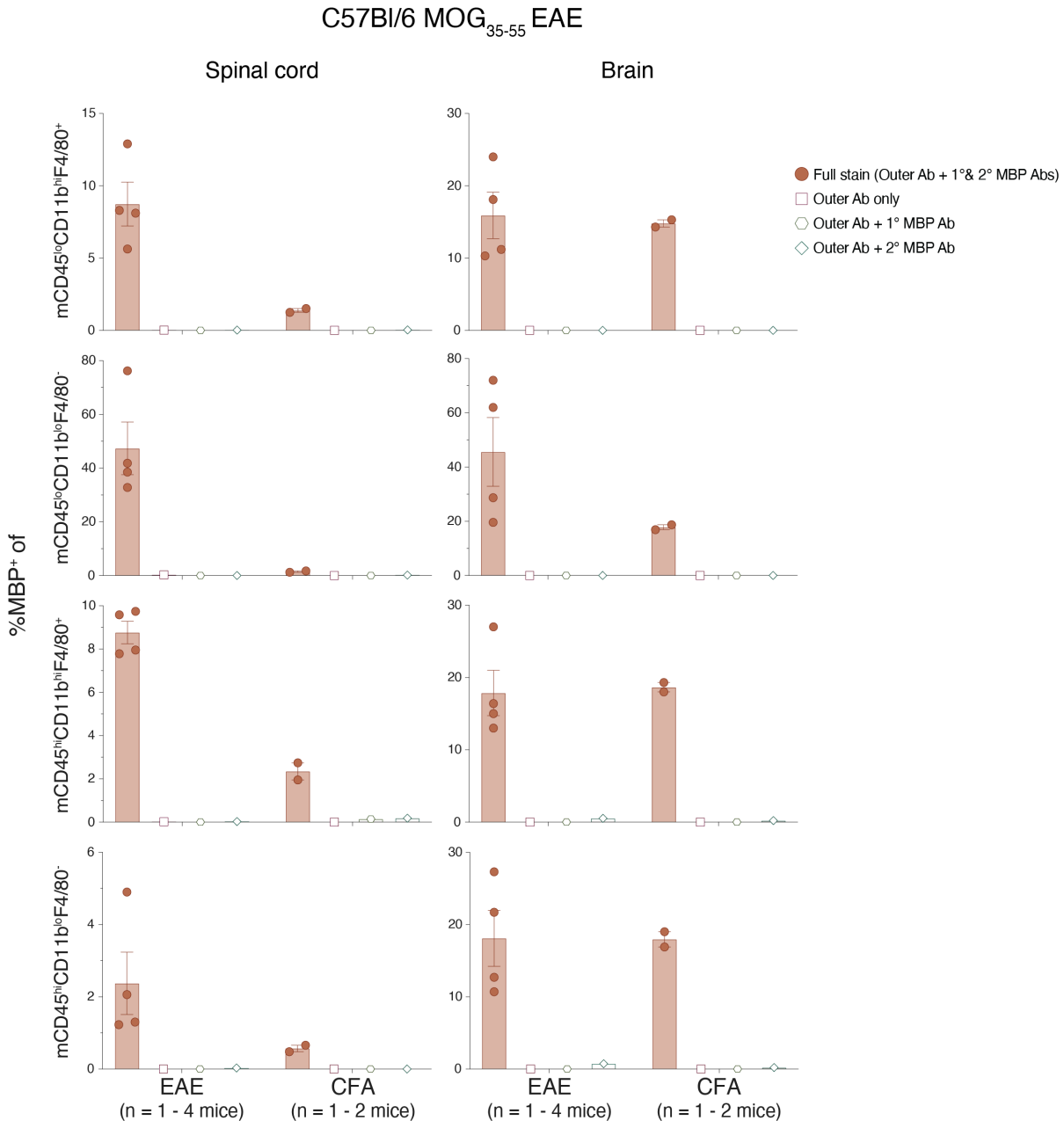

Figure A.32 Flow cytometric detection of murine myeloid cell phagocytosis of myelin basic protein in the CNS of EAE and CFA immunized C57Bl/6 mice

Figure shows the proportion of resident mCD45^{lo} and infiltrating mCD45^{hi} myeloid cells expressing CD11b and/or F4/80 in the spinal cord (left) and brain (right) containing detectable intracellular myelin basic protein (MBP^{+}) day 15 post-immunization (n = 1 – 4 mice per induction treatment and staining panel). Cells isolated from perfused CNS tissue were stained with one of four antibody panels: the full panel (Outer Ab + 1° & 2° MBP Abs), the panel minus the intracellular primary antibody specific to MBP and conjugated secondary antibody specific to the primary antibody's Fc domain (FMO Outer Ab only), the panel minus the secondary antibody (FMO Outer Ab + 1° MBP Ab), or the panel minus the primary antibody (FMO Outer Ab + 2° MBP Ab). Data are shown as mean with SEM.

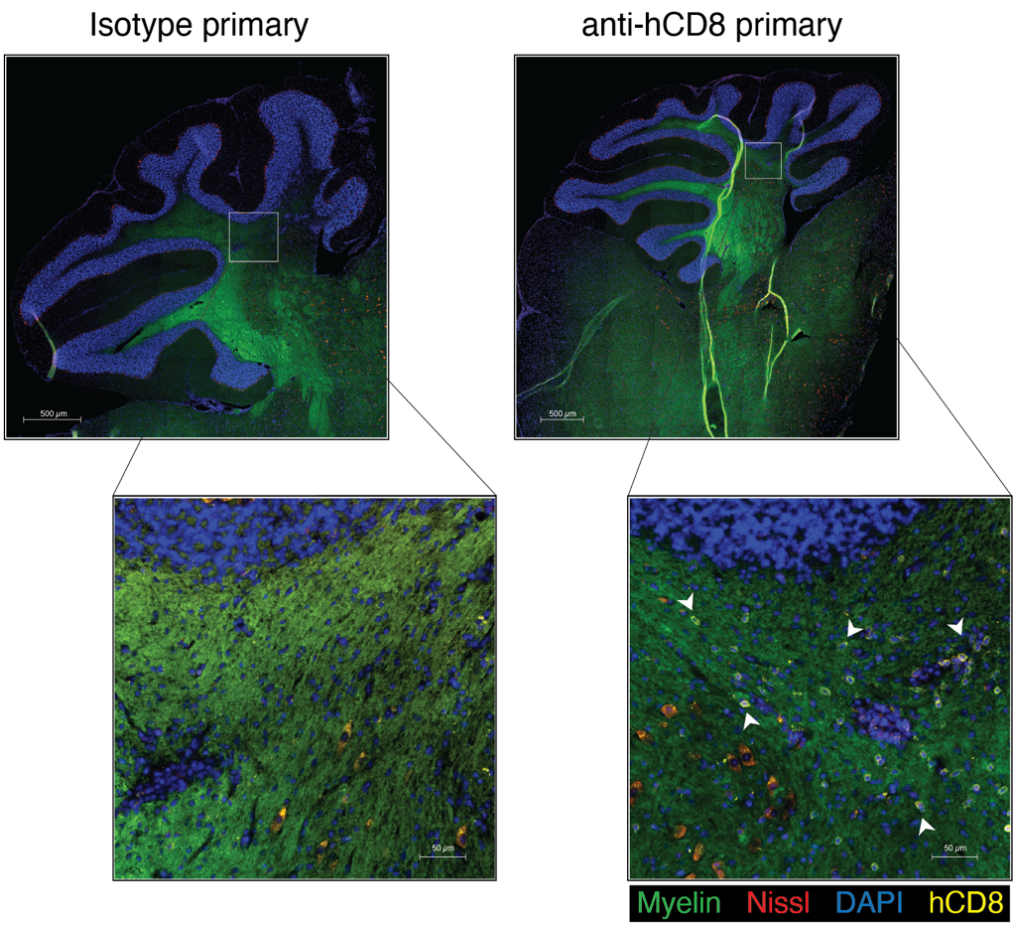

Figure A.33 Isotype control staining to confirm specific human CD8$^+$ T cell detection in the CNS of HuPBMC EAE mice by IHC

Representative images of sagittal cerebellar sections from a symptomatic HuPBMC EAE mouse (right) derived from a female donor with RRMS (MS-05). Perfused tissues were collected day 15 post-EAE induction (day 4 post-symptom onset). Serial sections were labelled with FluoroMyelin (green), NeuroTrace 530/615 (red), DAPI (blue), and either an isotype IgG control antibody (left) or an anti-hCD8 antibody (right) in yellow. Example hCD8$^+$ T cells are indicated by white arrows. Scale bars indicate size as specified per panel, showing 500 µm sections and 50 µm insets.

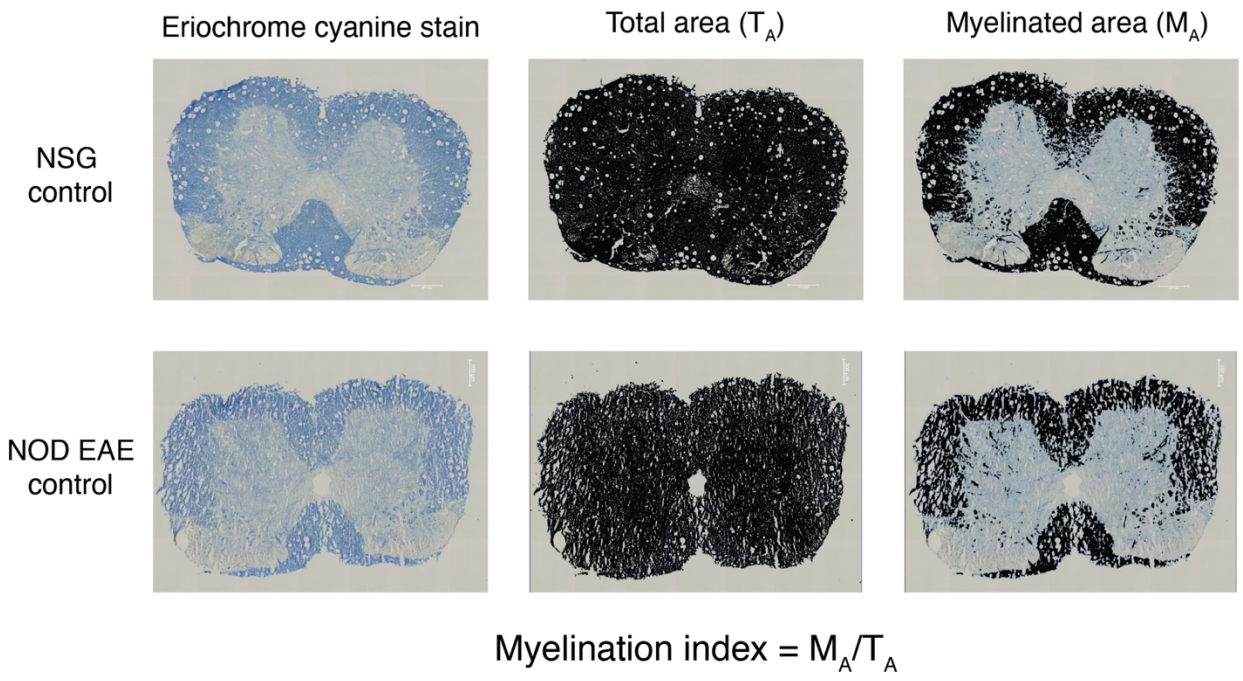

Figure A.34 Histological quantification of spinal cord myelination

Representative images of coronal lumbar spinal cord sections from an unengrafted NSG control mouse (top row) and a NOD mouse induced with MOG_{35-55} (bottom row) stained with eriochrome cyanine. Intensity thresholds were set consistently for total tissue area (T_A) and myelinated area (M_A), as measured based on individual scale bars, for all sections using ImageJ, and myelination index was calculated as a fraction of myelinated area of total tissue area. Scale bars indicate 200 μm.

Appendix 8. Supplemental data to section 4.8

The following data are supplemental to section 4.8.4.

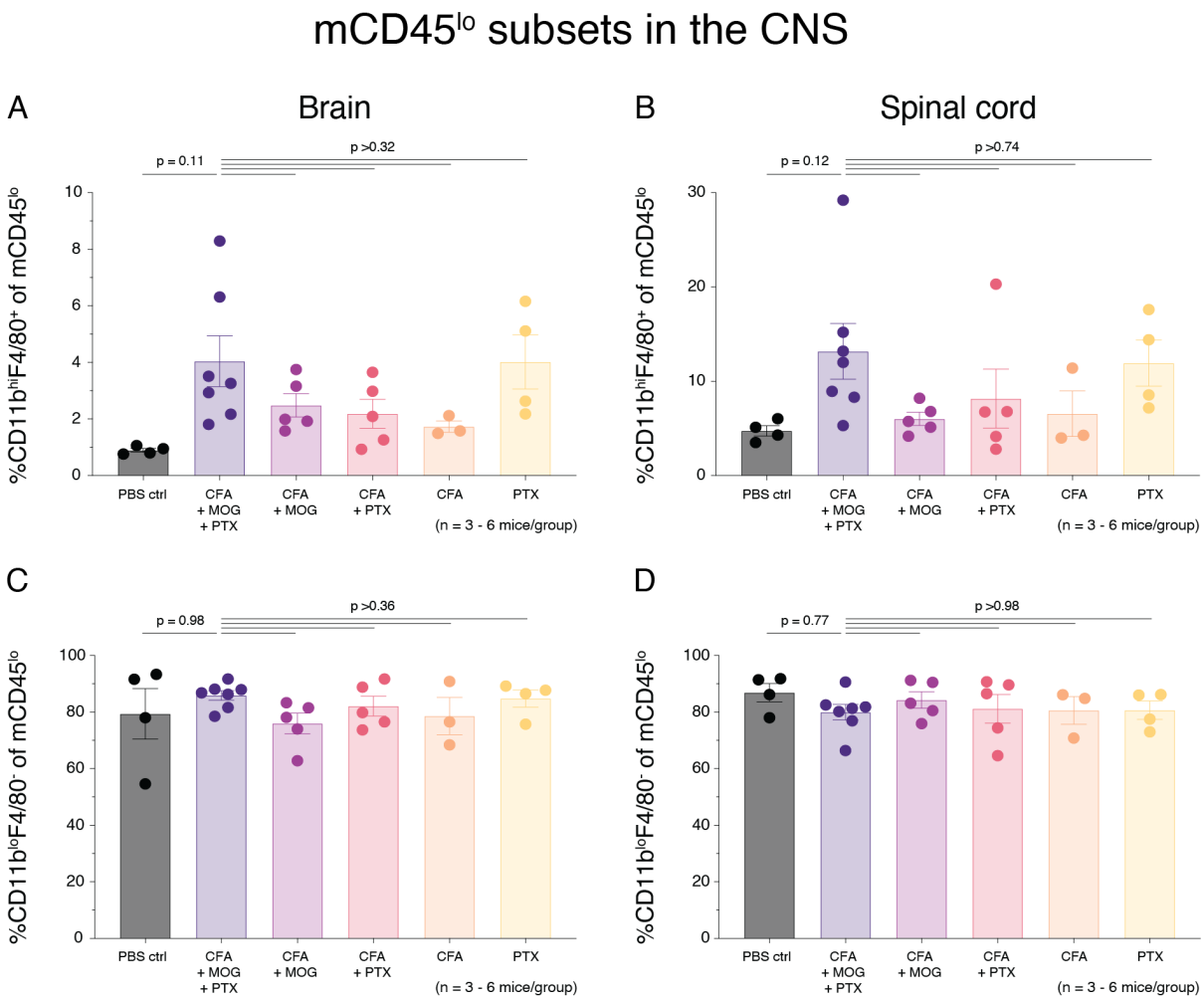

Figure A.35 CD11b and F4/80 expression on CNS resident mCD45^{lo} cells in HuPBMC mice induced with different EAE adjuvant components

Figure shows the proportion of resident murine mCD45^{lo} myeloid cells that are (A, B) CD11b^{hi}F4/80^{+} or (C, D) CD11b^{lo}F4/80^{-} in the brain (left column) and spinal cord (right column) on days 19 – 22 post-immunization of PBS engrafted control NSG mice induced with the full mixed MOG EAE immunization containing rhMOG and MOG$_{35-55}$ antigen emulsified in CFA, co-administered PTx (n = 4 mice) and HuPBMC mice (n = 26 mice all derived from HD-04 female PBMCs) induced with full mixed EAE immunization (CFA + MOG + PTx, n = 7 mice), mixed MOG emulsion without PTx (CFA + MOG, n = 5 mice), blank CFA emulsion and PTx without antigen (CFA + PTx, n = 5 mice), blank CFA emulsion only without antigen or PTx (CFA, n = 3 mice), or PTx only without emulsion (PTx, n = 4 mice). Tissues were perfused prior to cell isolation. Data are shown as mean with SEM and were analyzed by Brown-

Forsythe and Welch ANOVA with Dunnett's T3 multiple comparisons test or by Kruskal-Wallis with Dunn's multiple comparisons test.

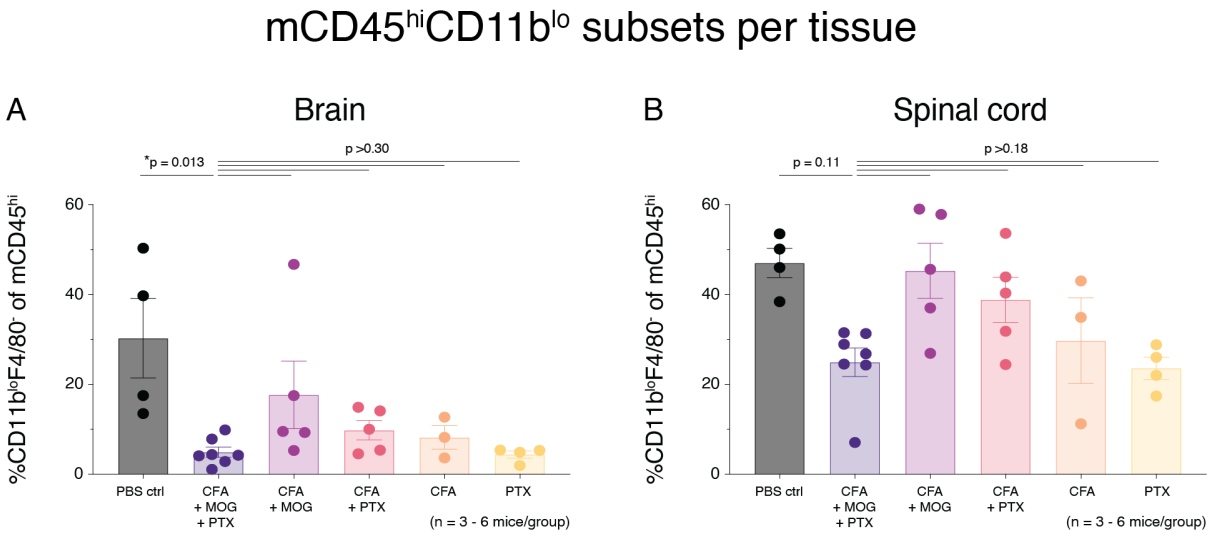

Figure A.36 CD11b^{lo} expression on infiltrating and peripheral mCD45^{hi} cells in HuPBMC mice induced with different EAE adjuvant components

Figure shows the proportion of peripherally derived murine mCD45$^{hi/+}$ myeloid cells that are CD11b^{lo}F4/80^{-} expressing in the (A) brain, (B) spinal cord, (C) spleen, (D) liver, and (E) intestinal lamina propria on days 19 – 22 post-immunization of PBS engrafted control NSG mice induced with the full mixed MOG EAE immunization containing rhMOG and MOG$_{35-55}$ antigen emulsified in CFA, co-administered PTx (n = 4 mice) and HuPBMC mice (n = 26 mice all derived from HD-04 female PBMCs) induced with full mixed EAE immunization (CFA + MOG + PTx, n = 7 mice), mixed MOG emulsion without PTx (CFA + MOG, n = 5 mice), blank CFA emulsion and PTx without antigen (CFA + PTx, n = 5 mice), blank CFA emulsion only without antigen or PTx (CFA, n = 3 mice), or PTx only without emulsion (PTx, n = 4 mice). Tissues were perfused prior to cell isolation. Data are shown as mean with SEM and were analyzed by Brown-Forsythe and Welch ANOVA with Dunnett's T3 multiple comparisons test or by Kruskal-Wallis with Dunn's multiple comparisons test.

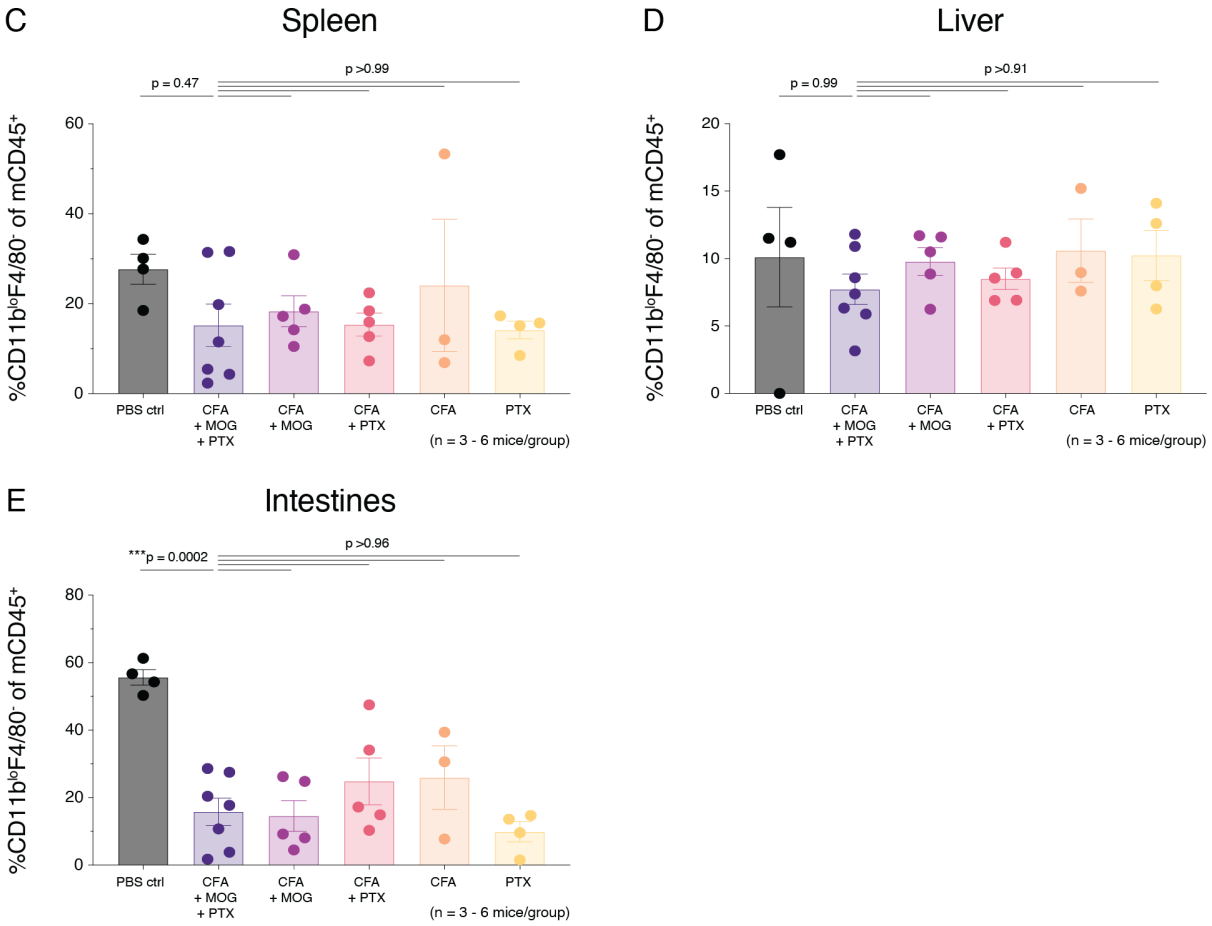

Figure A.36 continued

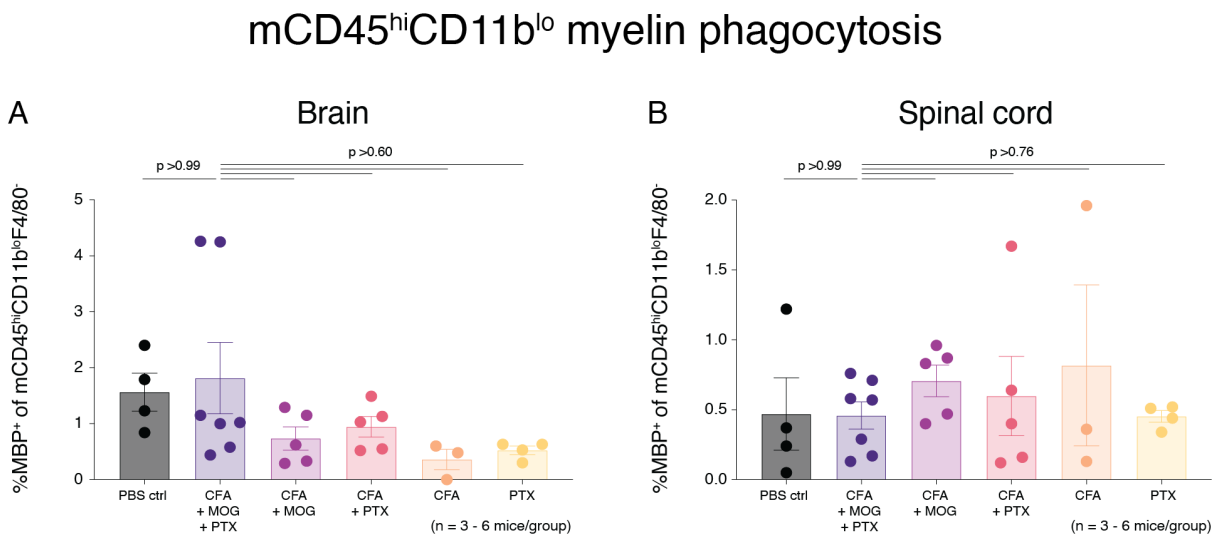

Figure A.37 Myelin phagocytosis by infiltrating and peripheral mCD45^{hi}CD11b^{lo} cells in HuPBMC mice induced with different EAE adjuvant components

Figure shows the proportion of peripherally derived murine mCD45$^{hi/+}$CD11b^{lo}F4/80^{-} myeloid cells containing intracellular myelin basic protein (MBP) in the (A) brain, (B) spinal cord, (C) spleen, (D) liver, and (E) intestinal lamina propria on days 19 – 22 post-immunization of PBS engrafted control NSG mice induced with the full mixed MOG EAE immunization containing rhMOG and MOG$_{35-55}$ antigen emulsified in CFA, co-administered PTx (n = 4 mice) and HuPBMC mice (n = 26 mice all derived from HD-04 female PBMCs) induced with full mixed EAE immunization (CFA + MOG + PTx, n = 7 mice), mixed MOG emulsion without PTx (CFA + MOG, n = 5 mice), blank CFA emulsion and PTx without antigen (CFA + PTx, n = 5 mice), blank CFA emulsion only without antigen or PTx (CFA, n = 3 mice), or PTx only without emulsion (PTx, n = 4 mice). Tissues were perfused prior to cell isolation. Data are shown as mean with SEM and were analyzed by Brown-Forsythe and Welch ANOVA with Dunnett's T3 multiple comparisons test or by Kruskal-Wallis with Dunn's multiple comparisons test.

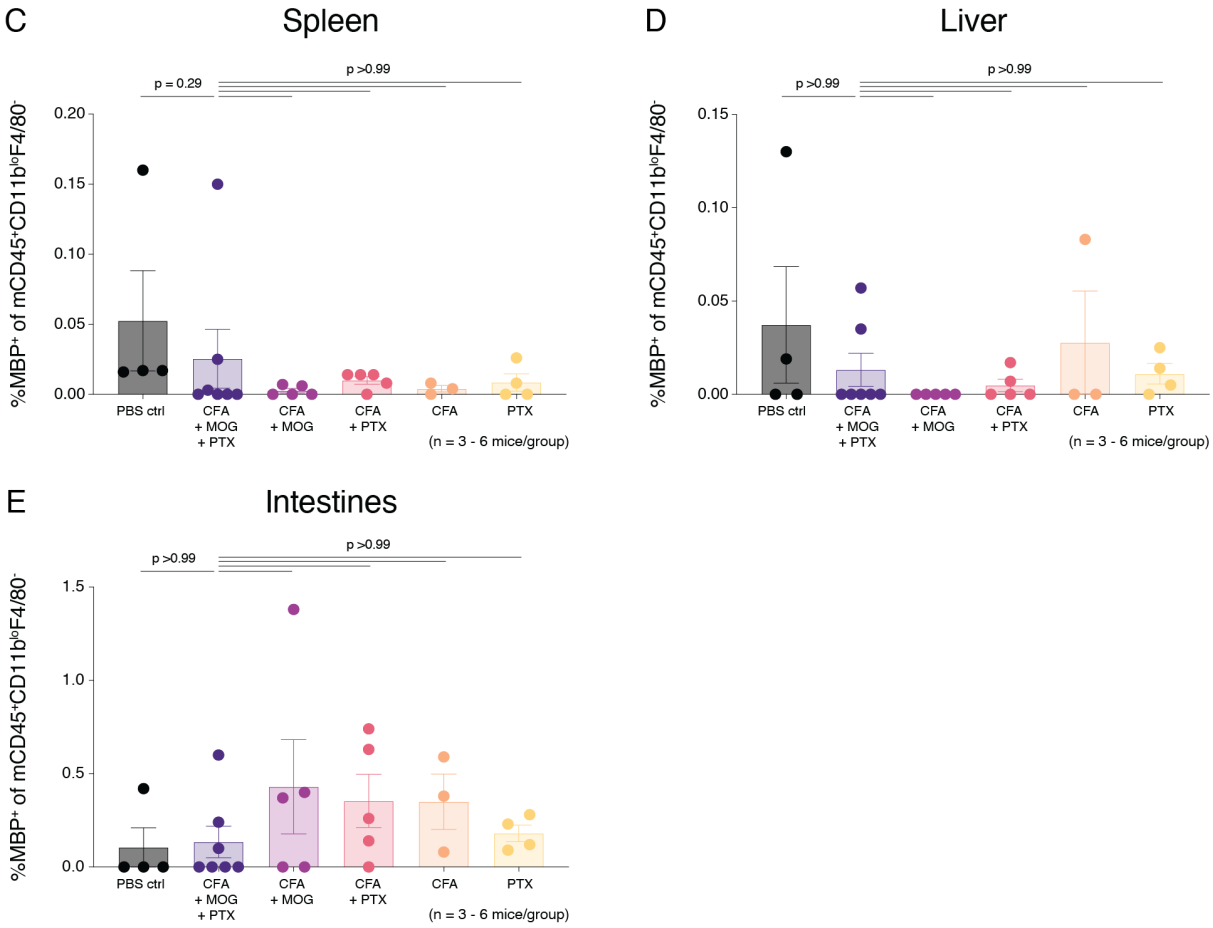

Figure A.37 continued

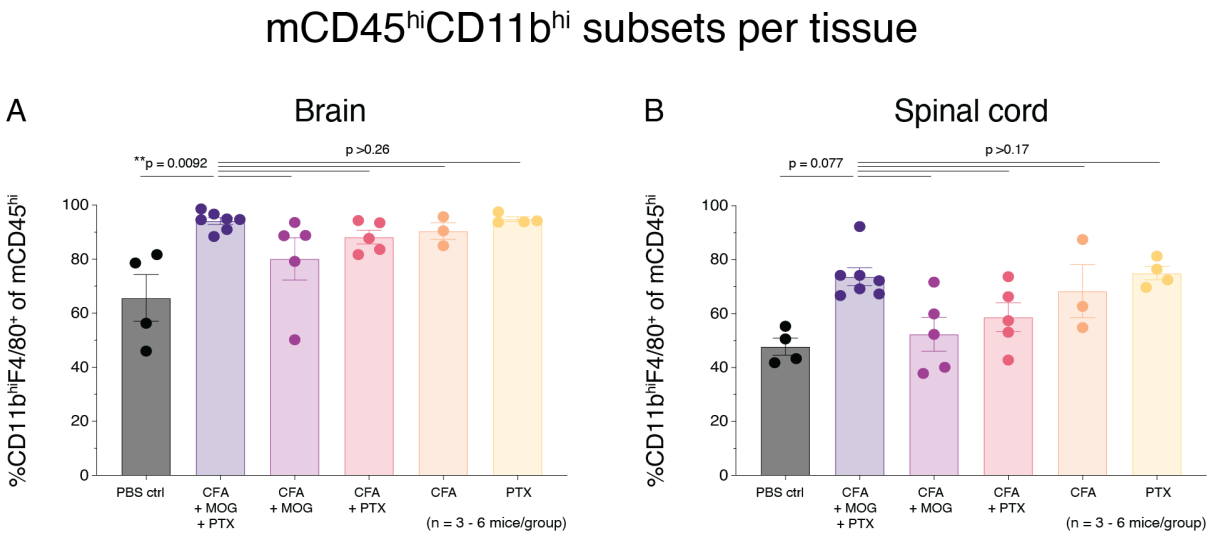

Figure A.38 CD11b and F4/80 expression on infiltrating and peripheral mCD45^{hi} cells in HuPBMC mice induced with different EAE adjuvant components

Figure shows the proportion of peripherally derived murine mCD45$^{hi/+}$ myeloid cells that are CD11b^{hi}F4/80^{+} expressing in the (A) brain, (B) spinal cord, (C) spleen, (D) liver, and (E) intestinal lamina propria on days 19 – 22 post-immunization of PBS engrafted control NSG mice induced with the full mixed MOG EAE immunization containing rhMOG and MOG$_{35-55}$ antigen emulsified in CFA, co-administered PTx (n = 4 mice) and HuPBMC mice (n = 26 mice all derived from HD-04 female PBMCs) induced with full mixed EAE immunization (CFA + MOG + PTx, n = 7 mice), mixed MOG emulsion without PTx (CFA + MOG, n = 5 mice), blank CFA emulsion and PTx without antigen (CFA + PTx, n = 5 mice), blank CFA emulsion only without antigen or PTx (CFA, n = 3 mice), or PTx only without emulsion (PTx, n = 4 mice). Tissues were perfused prior to cell isolation. Data are shown as mean with SEM and were analyzed by Brown-Forsythe and Welch ANOVA with Dunnett's T3 multiple comparisons test or by Kruskal-Wallis with Dunn's multiple comparisons test.

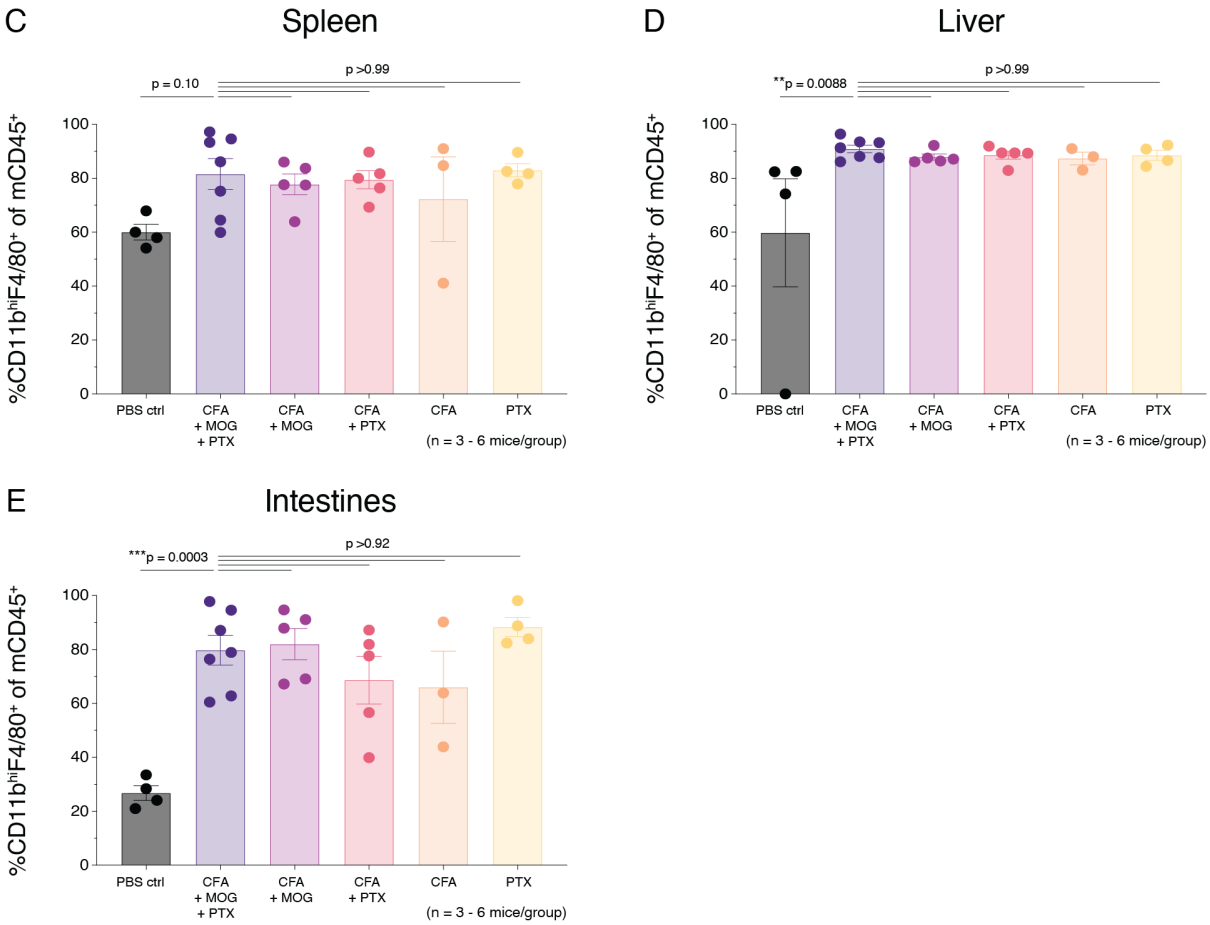

Figure A.38 continued

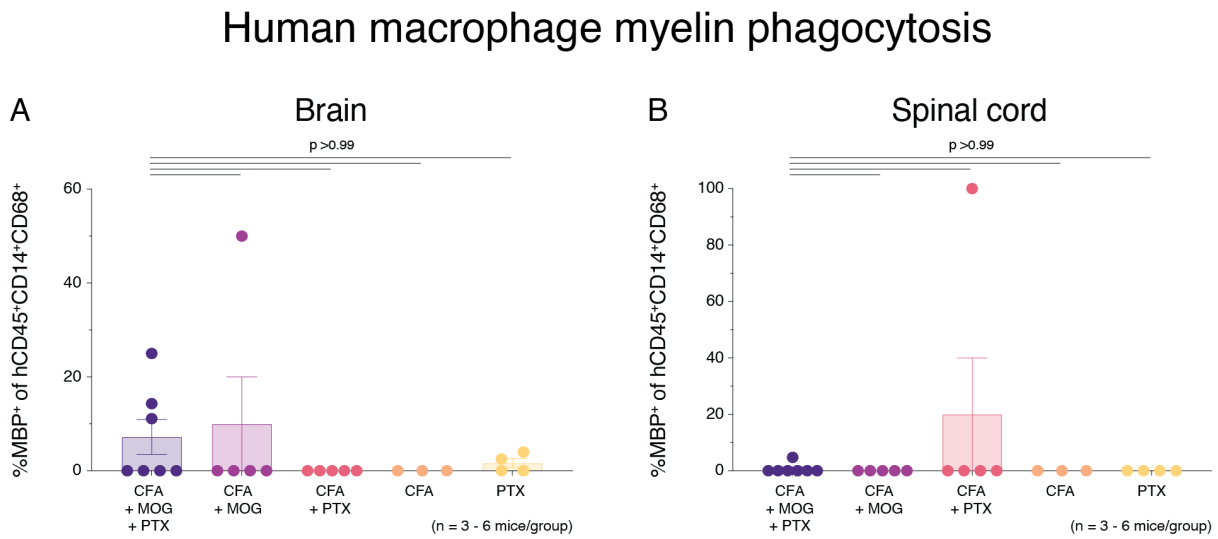

Figure A.39 Myelin phagocytosis by infiltrating and peripheral hCD45^{+}CD14^{+}CD68^{+} cells in HuPBMC mice induced with different EAE adjuvant components

Figure shows the proportion of peripherally derived human hCD45^{+}CD14^{+}CD68^{+} macrophages containing intracellular myelin basic protein (MBP) in the (A) brain, (B) spinal cord, (C) spleen, (D) liver, and (E) intestinal lamina propria on days 19 – 22 post-immunization of PBS engrafted control NSG mice induced with the full mixed MOG EAE immunization containing rhMOG and MOG$_{35-55}$ antigen emulsified in CFA, co-administered PTx (n = 4 mice) and HuPBMC mice (n = 26 mice all derived from HD-04 female PBMCs) induced with full mixed EAE immunization (CFA + MOG + PTx, n = 7 mice), mixed MOG emulsion without PTx (CFA + MOG, n = 5 mice), blank CFA emulsion and PTx without antigen (CFA + PTx, n = 5 mice), blank CFA emulsion only without antigen or PTx (CFA, n = 3 mice), or PTx only without emulsion (PTx, n = 4 mice). Tissues were perfused prior to cell isolation. Data are shown as mean with SEM and were analyzed by Brown-Forsythe and Welch ANOVA with Dunnett's T3 multiple comparisons test or by Kruskal-Wallis with Dunn's multiple comparisons test.

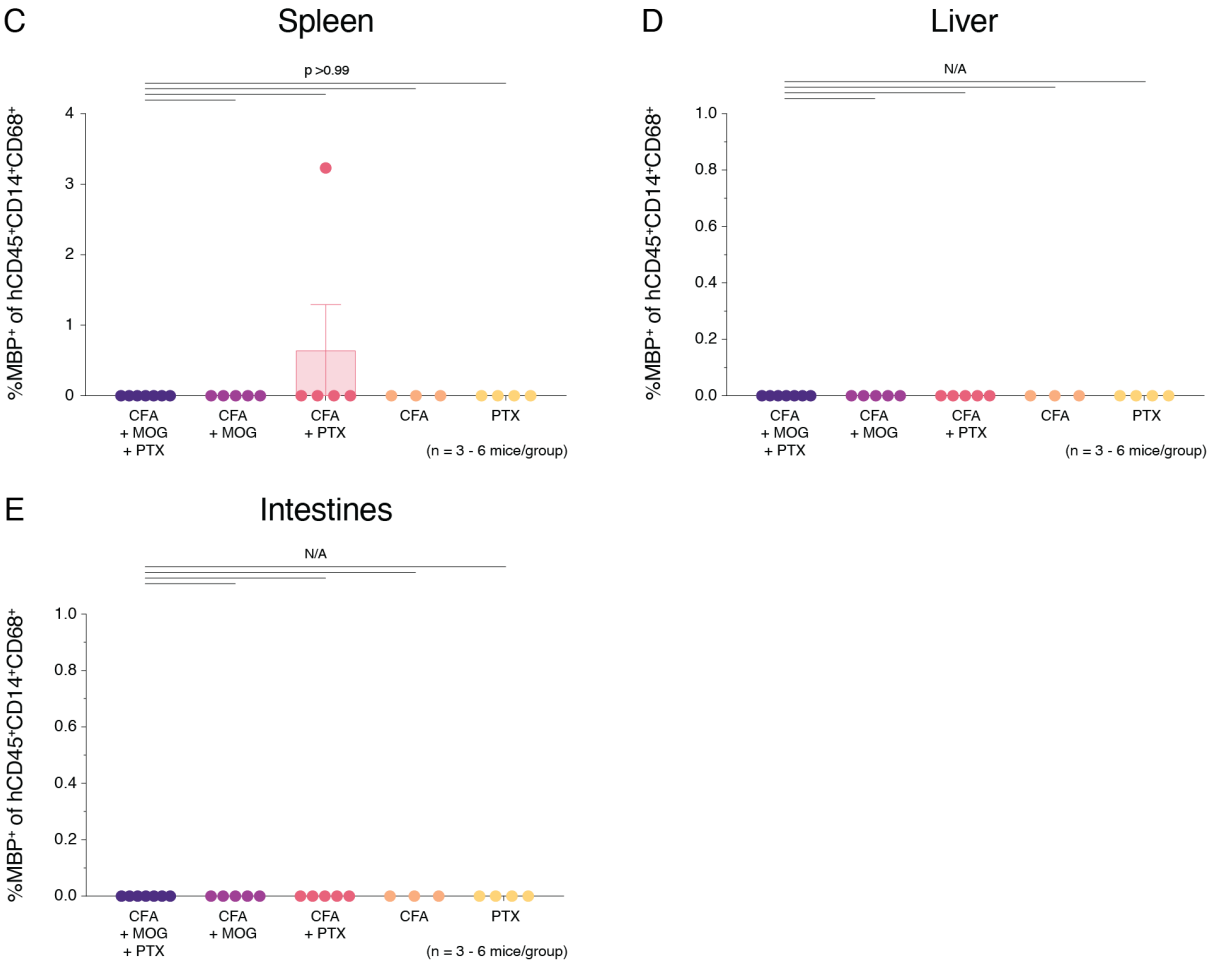

Figure A.39 continued

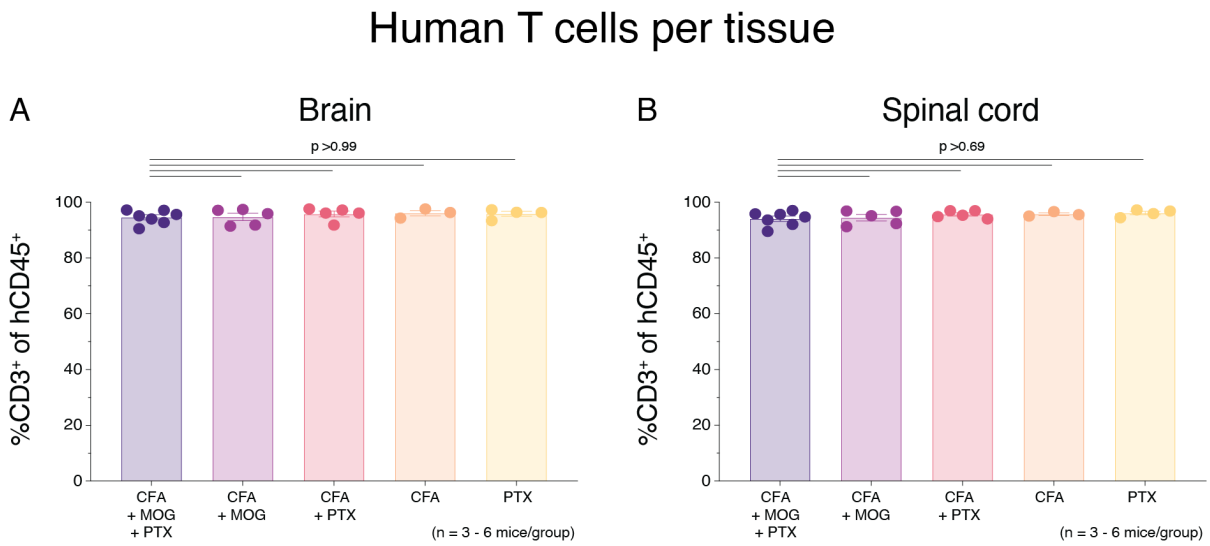

Figure A.40 Proportions of human CD3$^+$ T cells in the CNS and periphery of HuPBMC mice induced with different EAE adjuvant components

Figure shows the proportion of hCD45$^+$ immune cells that are hCD3$^+$ in the (A) brain, (B) spinal cord, (C) spleen, (D) liver, and (E) intestinal lamina propria on days 19 – 22 post-immunization of PBS engrafted control NSG mice induced with the full mixed MOG EAE immunization containing rhMOG and MOG$_{35-55}$ antigen emulsified in CFA, co-administered PTx (n = 4 mice) and HuPBMC mice (n = 26 mice all derived from HD-04 female PBMCs) induced with full mixed EAE immunization (CFA + MOG + PTx, n = 7 mice), mixed MOG emulsion without PTx (CFA + MOG, n = 5 mice), blank CFA emulsion and PTx without antigen (CFA + PTx, n = 5 mice), blank CFA emulsion only without antigen or PTx (CFA, n = 3 mice), or PTx only without emulsion (PTx, n = 4 mice). Tissues were perfused prior to cell isolation. Data are shown as mean with SEM and were analyzed by Brown-Forsythe and Welch ANOVA with Dunnett's T3 multiple comparisons test or by Kruskal-Wallis with Dunn's multiple comparisons test.

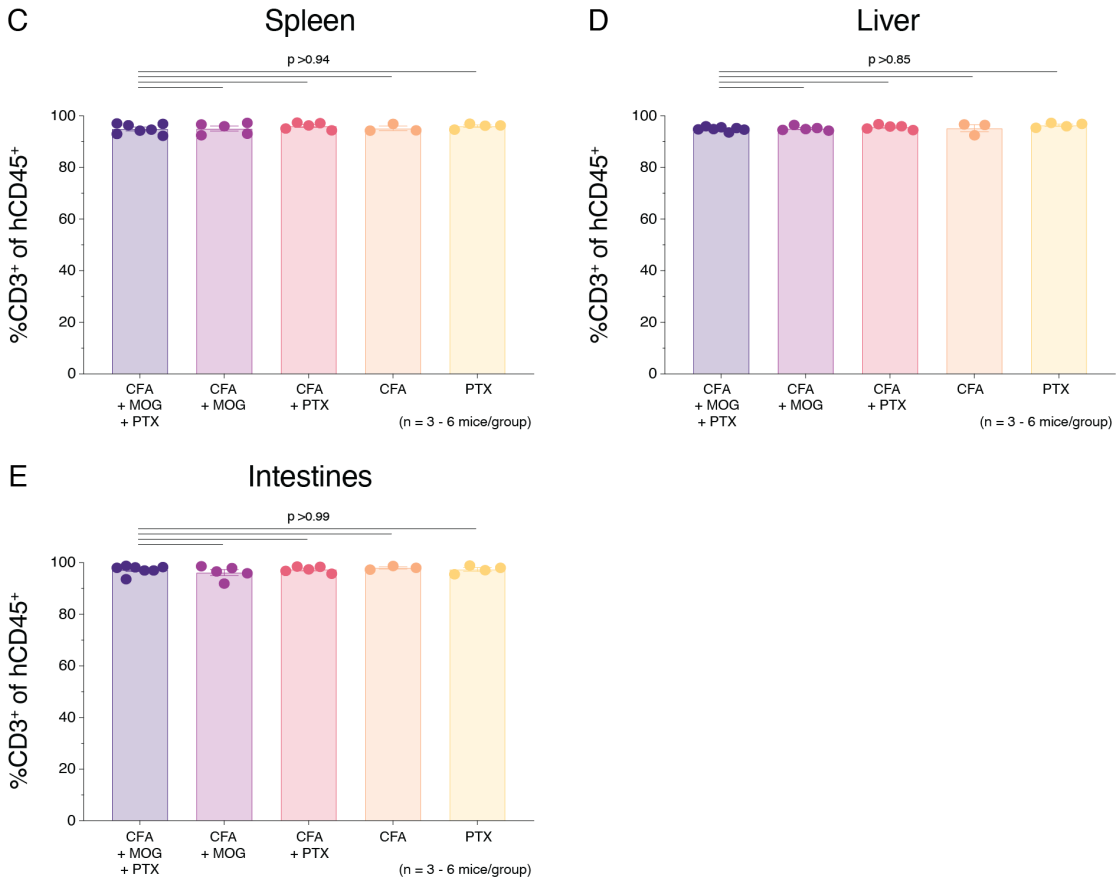

Figure A.40 continued

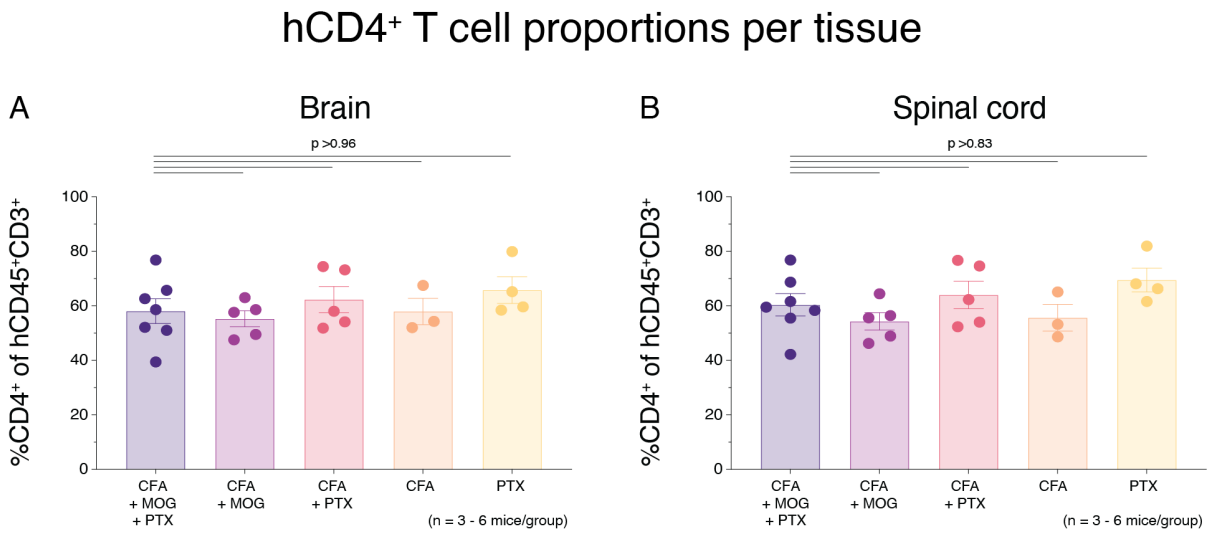

Figure A.41 Proportions of CD4 expressing human T cells in the CNS and periphery of HuPBMC mice induced with different EAE adjuvant components

Figure shows the proportion of $hCD45^+CD3^+$ T cells that are $hCD4^+$ in the (A) brain, (B) spinal cord, (C) spleen, (D) liver, and (E) intestinal lamina propria, as well as (F) $hCD8^-$ in the intestinal lamina propria, on days 19 – 22 post-immunization of PBS engrafted control NSG mice induced with the full mixed MOG EAE immunization containing rhMOG and MOG_{35-55} antigen emulsified in CFA, co-administered PTx (n = 4 mice) and HuPBMC mice (n = 26 mice all derived from HD-04 female PBMCs) induced with full mixed EAE immunization (CFA + MOG + PTx, n = 7 mice), mixed MOG emulsion without PTx (CFA + MOG, n = 5 mice), blank CFA emulsion and PTx without antigen (CFA + PTx, n = 5 mice), blank CFA emulsion only without antigen or PTx (CFA, n = 3 mice), or PTx only without emulsion (PTx, n = 4 mice). Tissues were perfused prior to cell isolation. Data are shown as mean with SEM and were analyzed by Brown-Forsythe and Welch ANOVA with Dunnett's T3 multiple comparisons test or by Kruskal-Wallis with Dunn's multiple comparisons test.

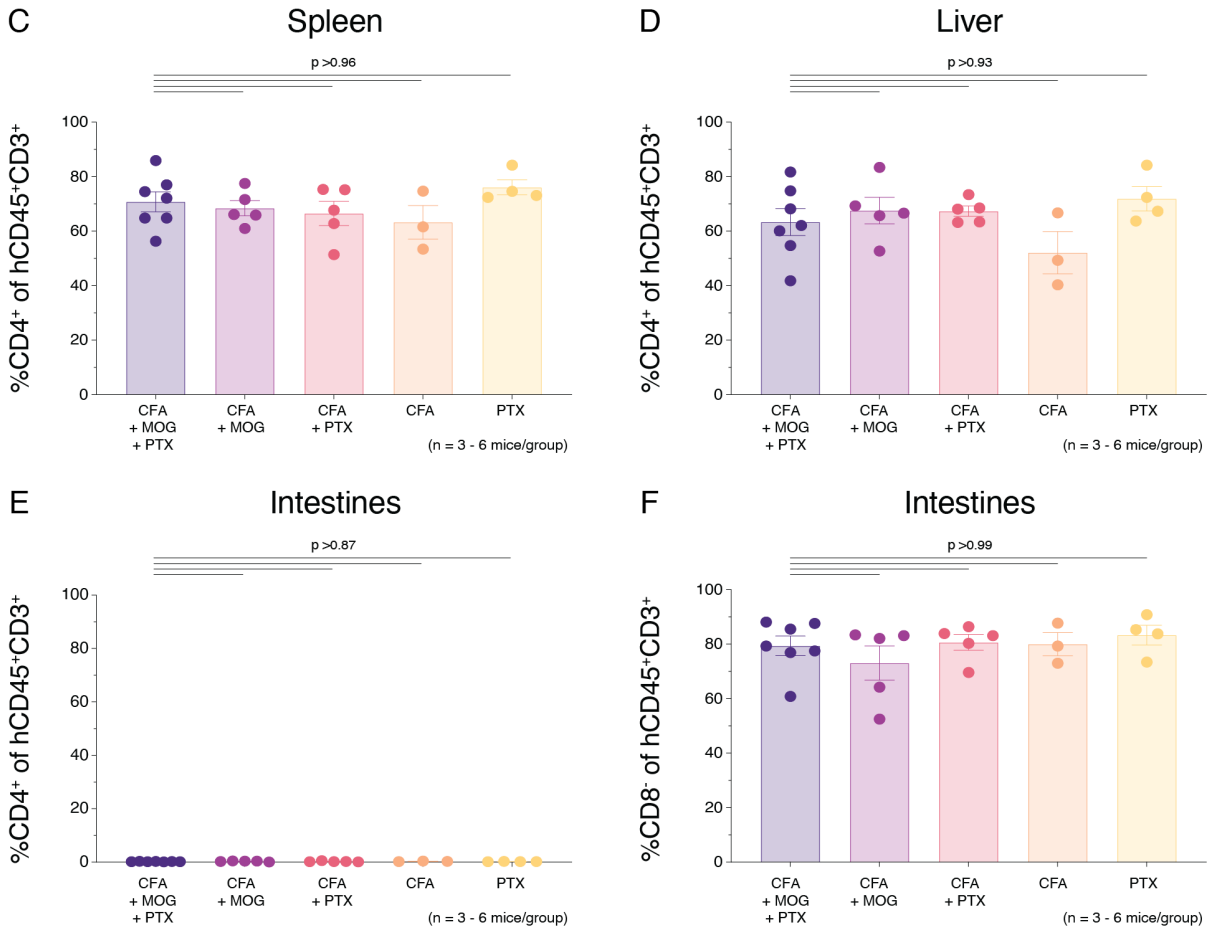

Figure A.41 continued

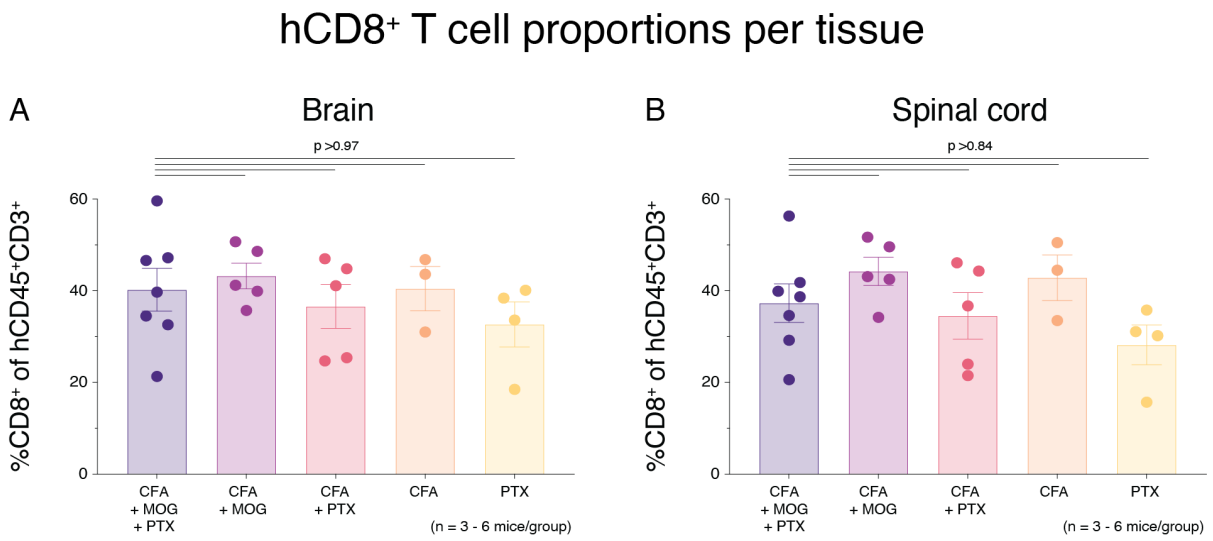

Figure A.42 Proportions of CD8 expressing human T cells in the CNS and periphery of HuPBMC mice induced with different EAE adjuvant components

Figure shows the proportion of $hCD45^+CD3^+$ T cells that are $hCD8^+$ in the (A) brain, (B) spinal cord, (C) spleen, (D) liver, and (E) intestinal lamina propria on days 19 – 22 post-immunization of PBS engrafted control NSG mice induced with the full mixed MOG EAE immunization containing rhMOG and MOG_{35-55} antigen emulsified in CFA, co-administered PTx (n = 4 mice) and HuPBMC mice (n = 26 mice all derived from HD-04 female PBMCs) induced with full mixed EAE immunization (CFA + MOG + PTx, n = 7 mice), mixed MOG emulsion without PTx (CFA + MOG, n = 5 mice), blank CFA emulsion and PTx without antigen (CFA + PTx, n = 5 mice), blank CFA emulsion only without antigen or PTx (CFA, n = 3 mice), or PTx only without emulsion (PTx, n = 4 mice). Tissues were perfused prior to cell isolation. Data are shown as mean with SEM and were analyzed by Brown-Forsythe and Welch ANOVA with Dunnett's T3 multiple comparisons test or by Kruskal-Wallis with Dunn's multiple comparisons test.

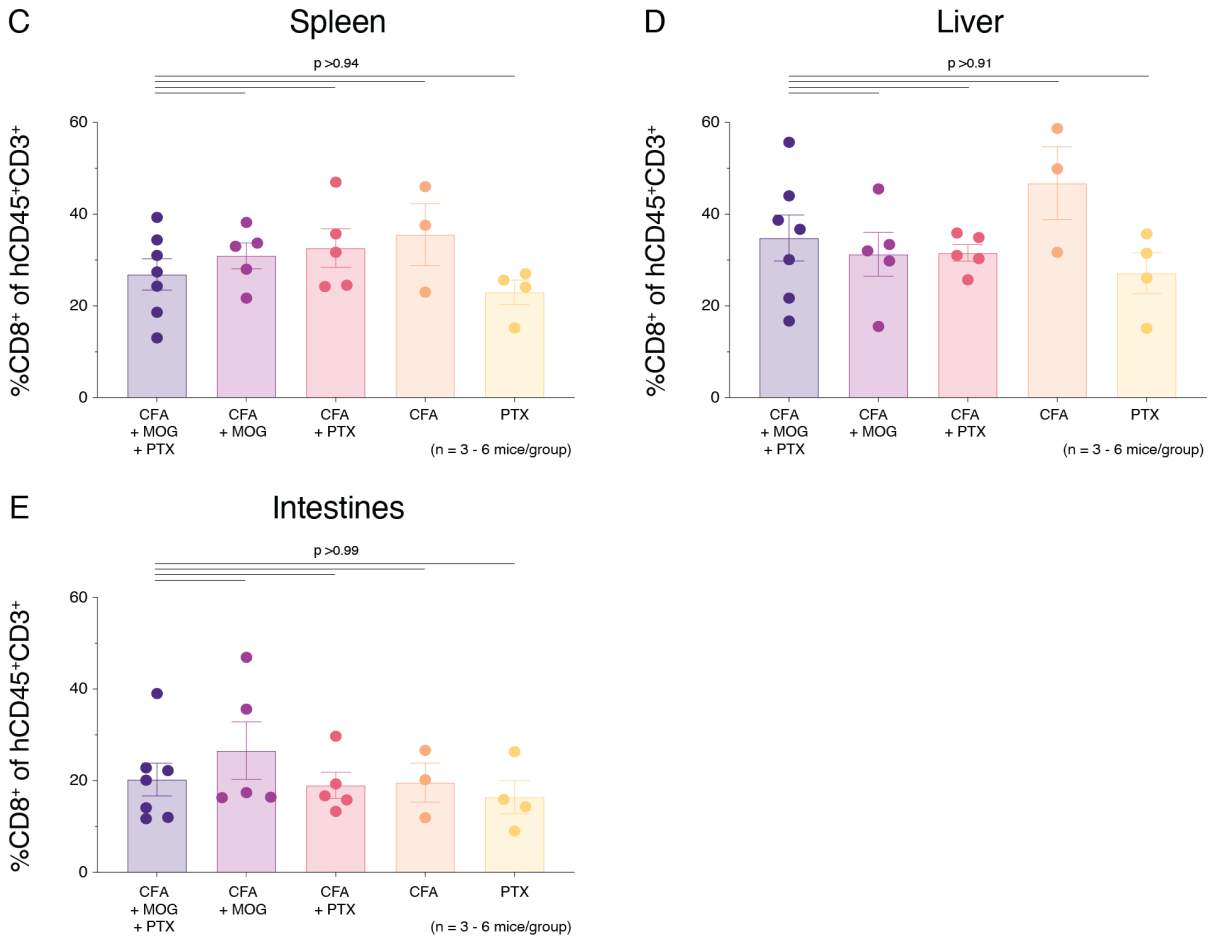

Figure A.42 continued

The following data are supplemental to section 4.8.5.

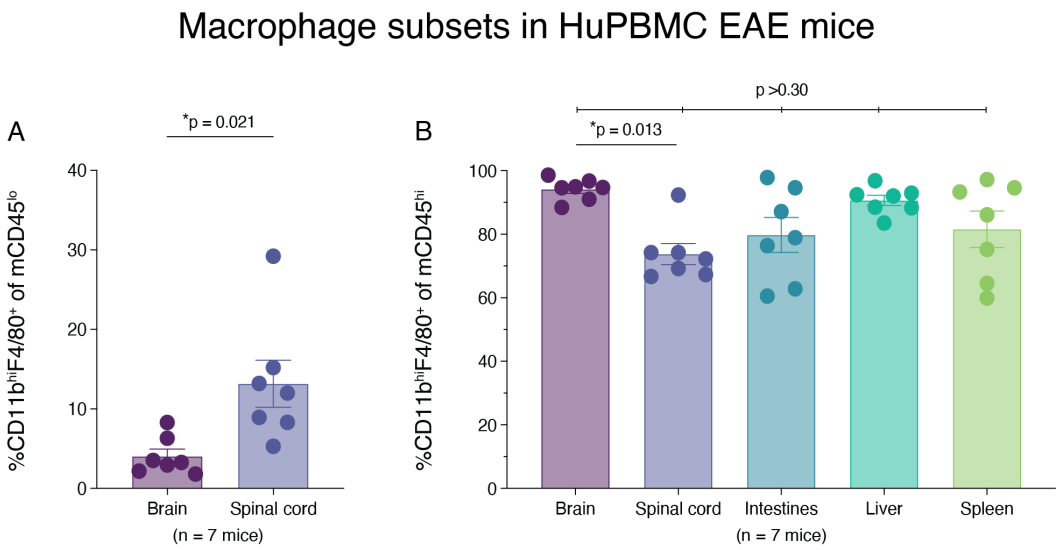

Figure A.43 Human and murine myeloid cell population frequencies in the CNS and periphery of HuPBMC EAE mice

Figure shows the proportion of (A) mCD45^{lo} cells and (B) mCD45^{hi} cells that are CD11b^{hi}F4/80^{+} in the brain, spinal cord, intestinal lamina propria, liver, and spleen on days 19 – 22 post-immunization of HuPBMC mice (n = 7 males derived from HD-04 female PBMCs) induced with the full mixed MOG EAE immunization containing rhMOG and MOG$_{35-55}$ antigen emulsified in CFA with PTx co-administered. Figure also shows the proportion of (C) mCD45^{lo} and (B) mCD45^{hi} cells that are CD11b^{lo}F4/80^{-} in the brain, spinal cord, intestinal lamina propria, liver, and spleen. (E) Shows the proportion of hCD45^{+} cells that are hCD14^{+}CD68^{+} in the brain, spinal cord, intestinal lamina propria, liver, and spleen. All tissues were perfused prior to cell isolation. Data are shown as mean with SEM and were analyzed by (A, C) Welch's unpaired t test or by (B, D, E) Kruskal-Wallis with Dunn's multiple comparisons test.

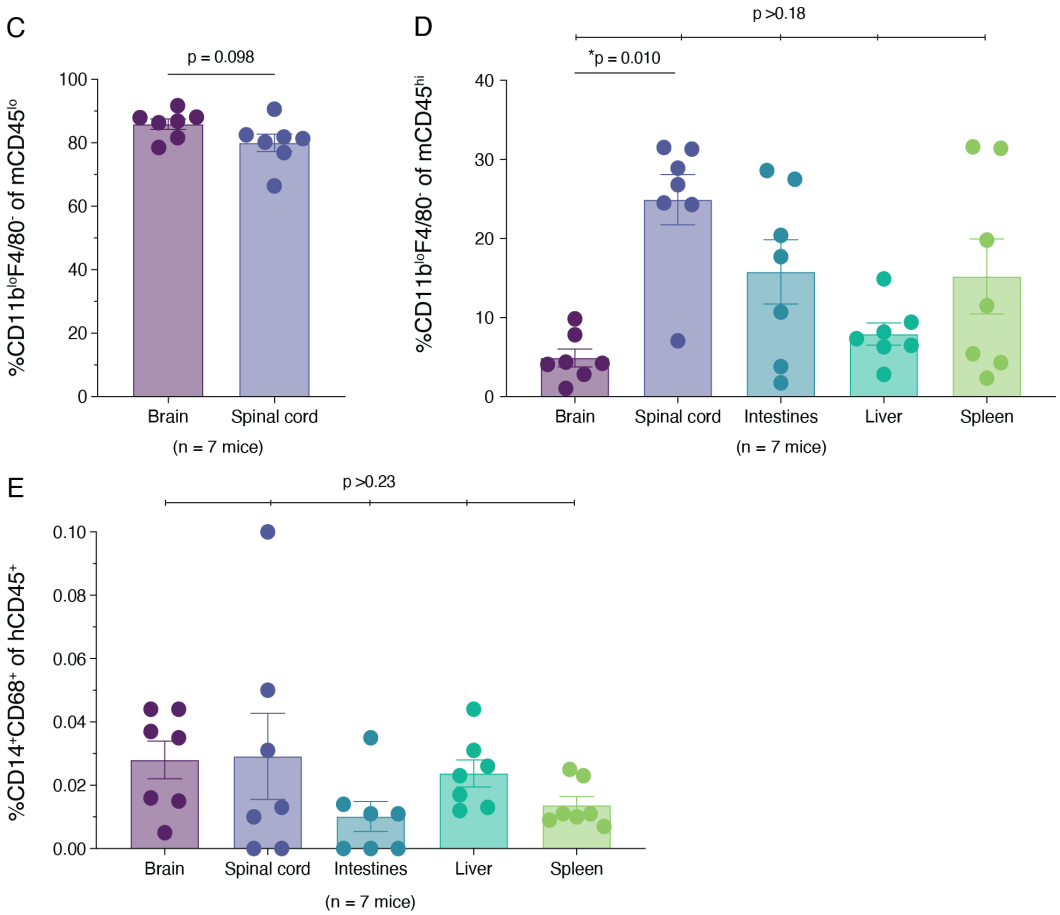

Figure A.43 continued

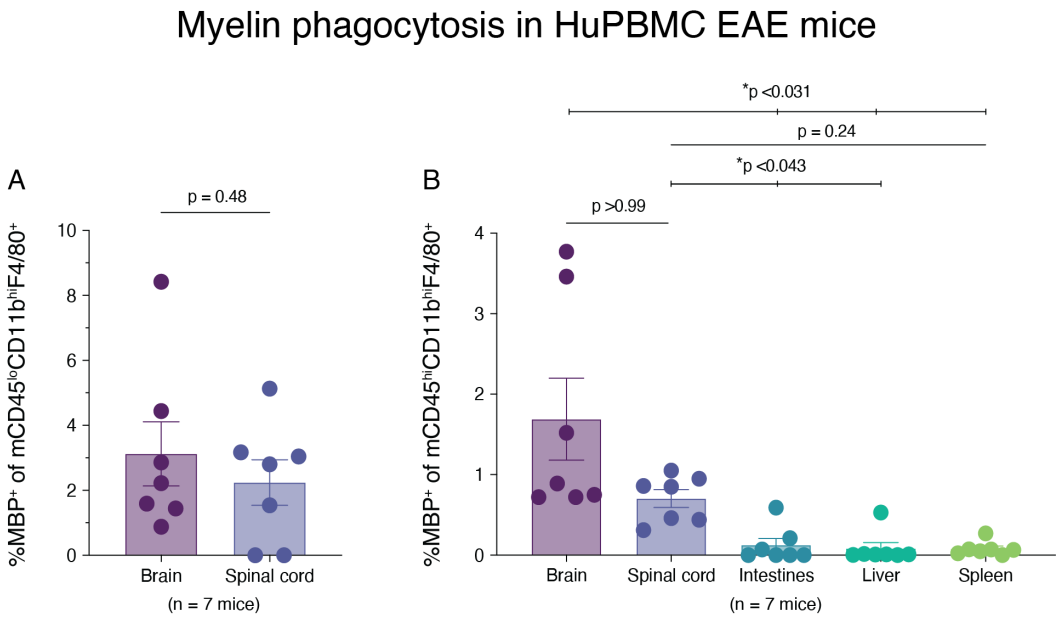

Figure A.44 Myelin phagocytosing human and murine myeloid cell populations in the CNS and periphery of HuPBMC EAE mice

Figure shows the proportion of (A) mCD45^{lo}CD11b^{hi}F4/80^{+} and (B) mCD45^{hi}CD11b^{hi}F4/80^{+} cells that are positive for myelin basic protein staining (MBP^{+}) in the brain, spinal cord, intestinal lamina propria, liver, and spleen on days 19 – 22 post-immunization of HuPBMC mice (n = 7 males derived from HD-04 female PBMCs) induced with the full mixed MOG EAE immunization containing rhMOG and MOG$_{35-55}$ antigen emulsified in CFA with PTx co-administered. Figure also shows the proportion of (C) mCD45^{lo}CD11b^{lo}F4/80^{-}, (B) mCD45^{hi}CD11b^{lo}F4/80^{-}, and (E) hCD45^{+}CD14^{+}CD68^{+} cells that are MBP^{+} in the brain, spinal cord, intestinal lamina propria, liver, and spleen. All tissues were perfused prior to cell isolation. Data are shown as mean with SEM and were analyzed by (A) Welch's unpaired t test, (C) Mann-Whitney test, or (B, D, E) Kruskal-Wallis with Dunn's multiple comparisons test.

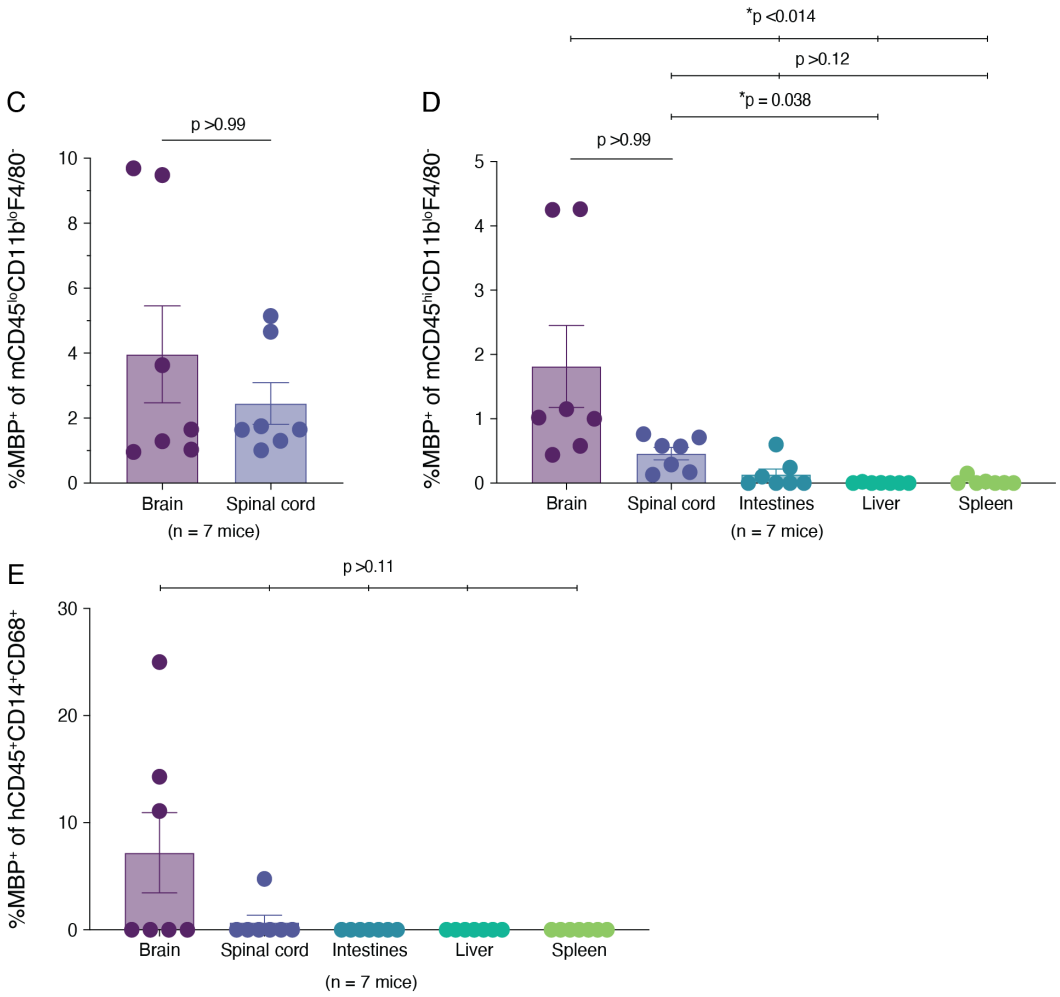

Figure A.44 continued

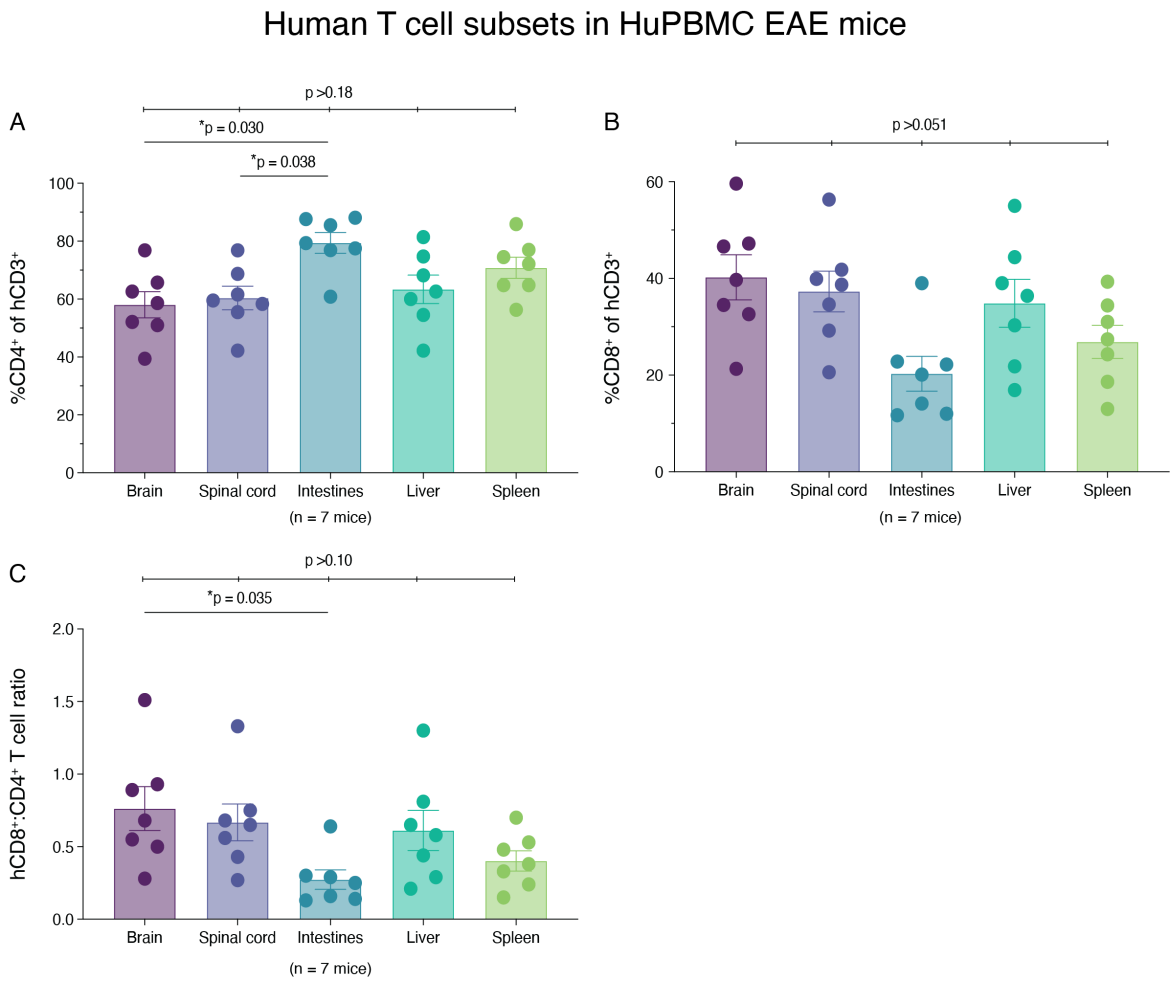

Figure A.45 Relative proportions and ratios of CD8 and CD4 expressing human T cells in the CNS and periphery of HuPBMC mice induced with different EAE adjuvant components

Figure shows the proportion of $hCD45^+CD3^+$ T cells that are (A) $hCD4^+$ or (B) $hCD8^+$ in the brain, spinal cord, spleen, liver, and intestinal lamina propria, as well as (C) the ratio of $hCD8^+$:$hCD4^+$ T cell subsets in these tissues, on days 19 – 22 post-immunization of HuPBMC mice (n = 7 males derived from HD-04 female PBMCs) induced with the full mixed MOG EAE immunization containing rhMOG and MOG_{35-55} antigen emulsified in CFA with PTx co-administered. All tissues were perfused prior to cell isolation. Data are shown as mean with SEM and were analyzed by Brown-Forsythe and Welch ANOVA with Dunnett's T3 multiple comparisons test or by Kruskal-Wallis with Dunn's multiple comparisons test.

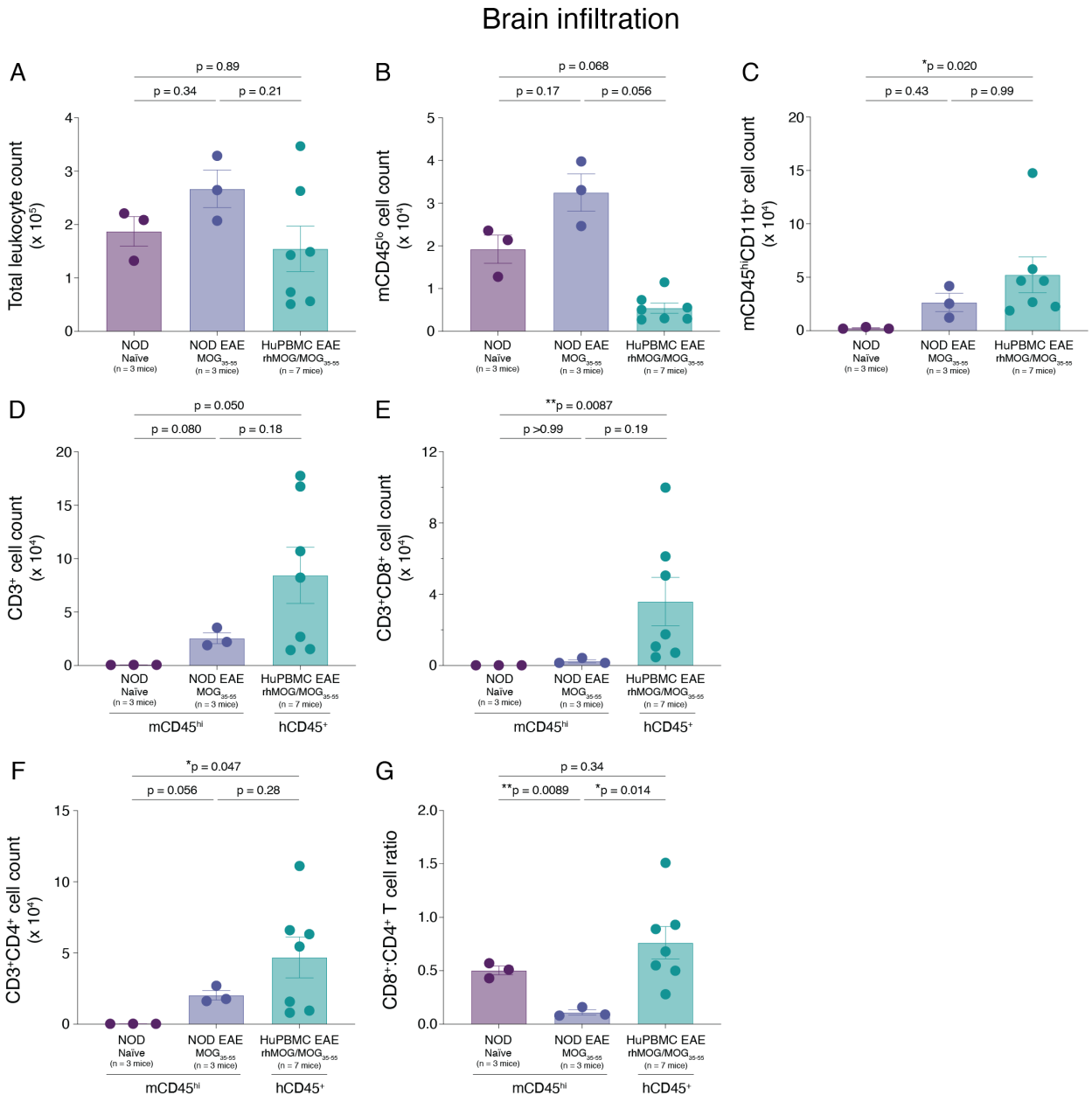

Figure A.46 Immune infiltration of the brain of EAE induced NOD and HuPBMC mice

Figure shows the total numbers of (A) all leukocytes (murine and human), (B) mCD45^{lo} resident myeloid cells (B) mCD45^{hi}CD11b^{+} myeloid cells, (C) m/hCD3^{+} T cells, (D) m/hCD3^{+}CD8^{+} T cells, (E) m/hCD3^{+}CD4^{+} T cells, and (F) the ratio of m/hCD3^{+}CD8^{+} to m/hCD3^{+}CD4^{+} T cells in the brains of naïve (untreated) NOD mice (n = 3 WT), MOG$_{35-55}$ EAE induced NOD mice (n = 3 WT) day 24 post-immunization, and mixed rhMOG/MOG$_{35-55}$ EAE induced HuPBMC mice (n = 7 derived from HD-04 female PBMCs) day 19 – 22 post-immunization. Tissues were perfused prior to cell isolation. Data are shown as mean with SEM and were analyzed by Brown-Forsythe and Welch ANOVA with Dunnett's T3 multiple comparisons test or by Kruskal-Wallis with Dunn's multiple comparisons test.

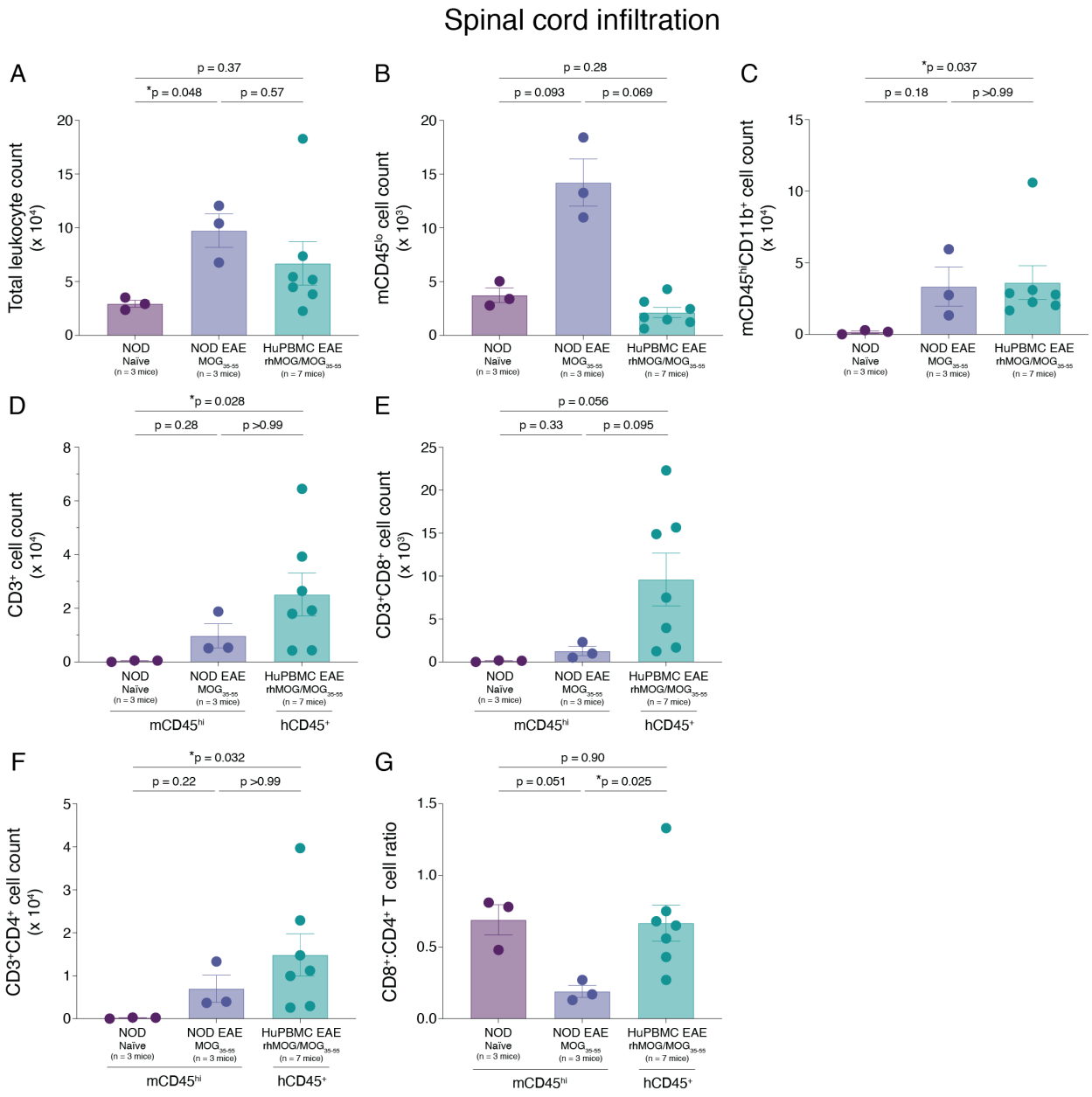

Figure A.47 Immune infiltration of the spinal cord of EAE induced NOD and HuPBMC mice

Figure shows the total numbers of (A) all leukocytes (murine and human), (B) mCD45^{lo} resident myeloid cells (B) mCD45^{hi}CD11b^{+} myeloid cells, (C) m/hCD3^{+} T cells, (D) m/hCD3^{+}CD8^{+} T cells, (E) m/hCD3^{+}CD4^{+} T cells, and (F) the ratio of m/hCD3^{+}CD8^{+} to m/hCD3^{+}CD4^{+} T cells in the spinal cords of naïve (untreated) NOD mice (n = 3 WT), MOG$_{35-55}$ EAE induced NOD mice (n = 3 WT) day 24 post-immunization, and mixed rhMOG/MOG$_{35-55}$ EAE induced HuPBMC mice (n = 7 derived from HD-04 female PBMCs) day 19 – 22 post-immunization. Tissues were perfused prior to cell isolation. Data are shown as mean with SEM and were analyzed by Brown-Forsythe and Welch ANOVA with Dunnett's T3 multiple comparisons test or by Kruskal-Wallis with Dunn's multiple comparisons test.

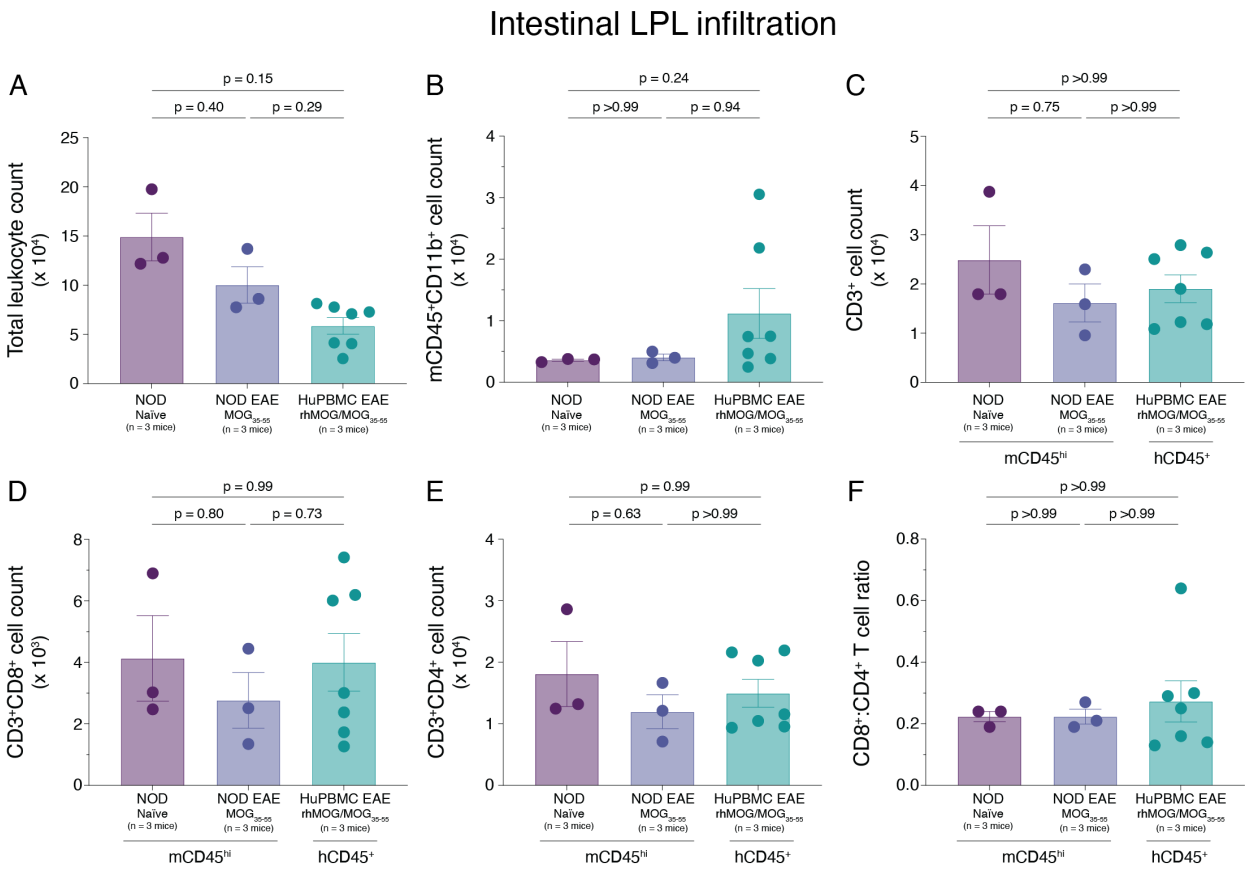

Figure A.48 Immune infiltration of the intestinal lamina propria of EAE induced NOD and HuPBMC mice

Figure shows the total numbers of (A) all leukocytes (murine and human), (B) mCD45$^+$CD11b$^+$ myeloid cells, (C) m/hCD3$^+$ T cells, (D) m/hCD3$^+$CD8$^+$ T cells, (E) m/hCD3$^+$CD4$^+$ T cells, and (F) the ratio of m/hCD3$^+$CD8$^+$ to m/hCD3$^+$CD4$^+$ T cells in the intestinal lamina propria of naïve (untreated) NOD mice (n = 3 WT), MOG_{35-55} EAE induced NOD mice (n = 3 WT) day 24 post-immunization, and mixed rhMOG/MOG_{35-55} EAE induced HuPBMC mice (n = 7 derived from HD-04 female PBMCs) day 19 – 22 post-immunization. Tissues were perfused prior to cell isolation. Data are shown as mean with SEM and were analyzed by Brown-Forsythe and Welch ANOVA with Dunnett's T3 multiple comparisons test or by Kruskal-Wallis with Dunn's multiple comparisons test.

Appendix 9. Sex differences in HuPBMC B6-TKO EAE mice

As noted in section 4.3, PBMC engrafted NSG mice displayed an effect of the recipient mouse sex on the susceptibility of developing clinical EAE and xGvHD symptoms. Based on two replicate cohorts of B6-TKO mice engrafted with PBMCs from the same donor healthy female donor, there was no considerable effect of recipient B6-TKO strain sex on the composition or abundance of spleen engrafted or CNS infiltrating human immune cells at endpoint (days 22 or 33 post-induction). Human T cell subset proportions did not differ based on recipient sex in any tissue (Figure A.49), though female recipients did have a small relative skew toward more $hCD4^+$ over $hCD8^+$ T cells compared to male recipients (Figure A.49A, B). Reconstitution of the spleen and infiltration of the CNS by the major murine and human immune cells subsets were also not different between HuPBMC B6-TKO EAE mice based on recipient sex (Figure A.50, Figure A.51). Overall, very few differences are seen based on recipient sex that would suggest a bias similar to that seen in NSG recipient mice. Due to the lack of symptom generation, any sex bias could not be determined based on incidence of disease. Given there are essentially no immunological differences, female and male HuPBMC B6-TKO mice were both included in analyses comparing to HuPBMC NSG males.

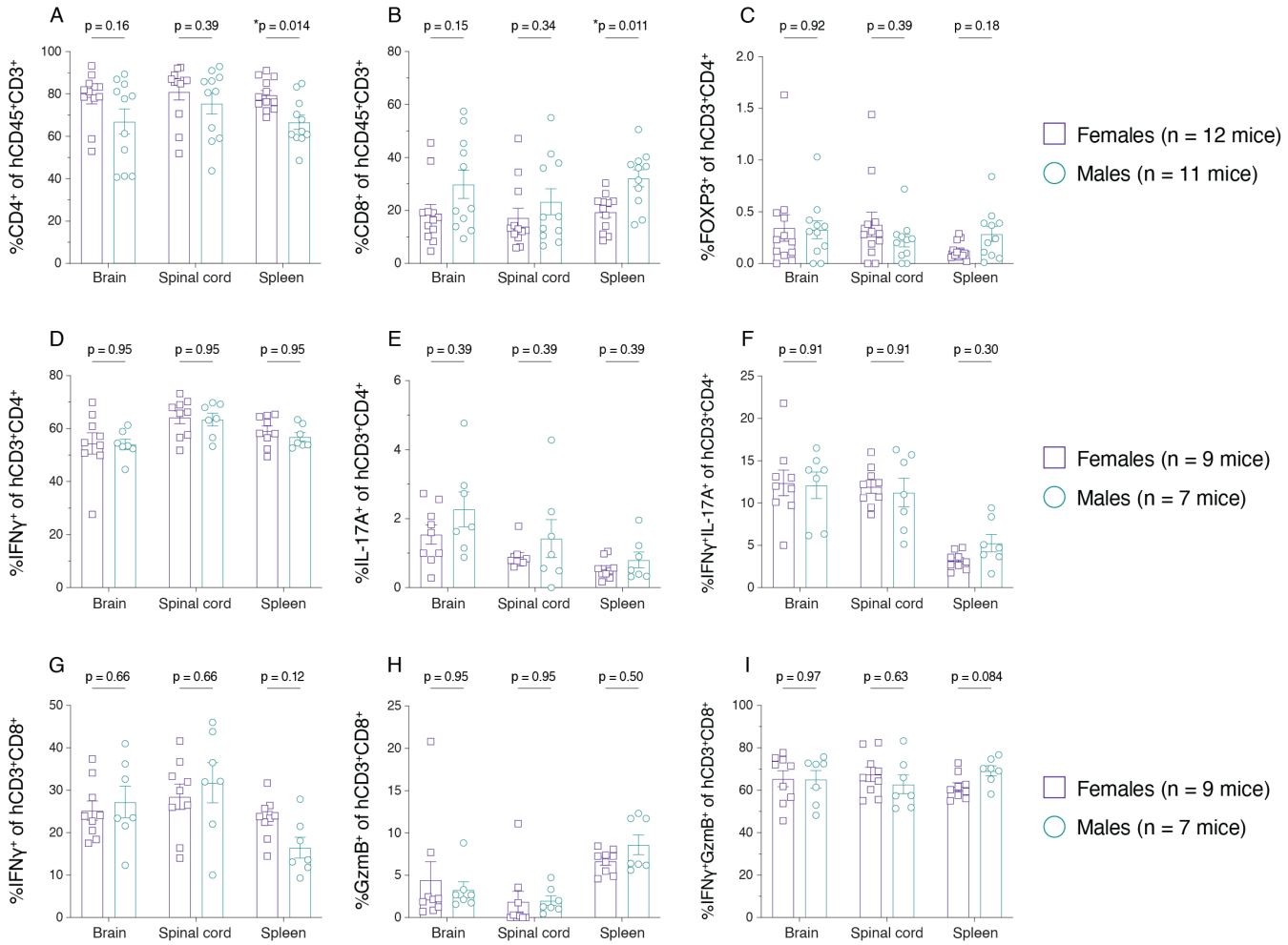

Figure A.49 Sex differences in human T cell subset proportions in the CNS and periphery of HuPBMC B6-TKO EAE mice at endpoint

Figure shows the proportions of (A) $hCD4^+$ and (B) $hCD8^+$ cells among $hCD45^+CD3^+$ T cells, the proportions of (C) $FOXP3^+$, (D) $IFN\gamma^+(IL\text{-}17A^-)$, (E) $IL\text{-}17A^+(IFN\gamma^-)$, and (F) $IFN\gamma^+IL\text{-}17A^+$ cells among $hCD3^+CD4^+$ T cells, and the proportions of (G) $IFN\gamma^+(GzmB^-)$, (H) $GzmB^+(IFN\gamma^-)$, and (I) $IFN\gamma^+GzmB^+$ cells among $hCD3^+CD8^+$ T cells in the brains, spinal cords, and spleens of PBMC-engrafted female (n = 9 – 12) and male (n = 7 – 11) B6-TKO mice derived from a healthy female donor (HD-04) day 22 or 33 post-rhMOG/$MOG_{35\text{-}55}$ EAE induction. All mice remained asymptomatic until endpoint. Tissues were perfused prior to cell isolation. Data are shown as mean with SEM and were analyzed by Welch's unpaired t test. HuPBMC cohorts included: 23 and 28.

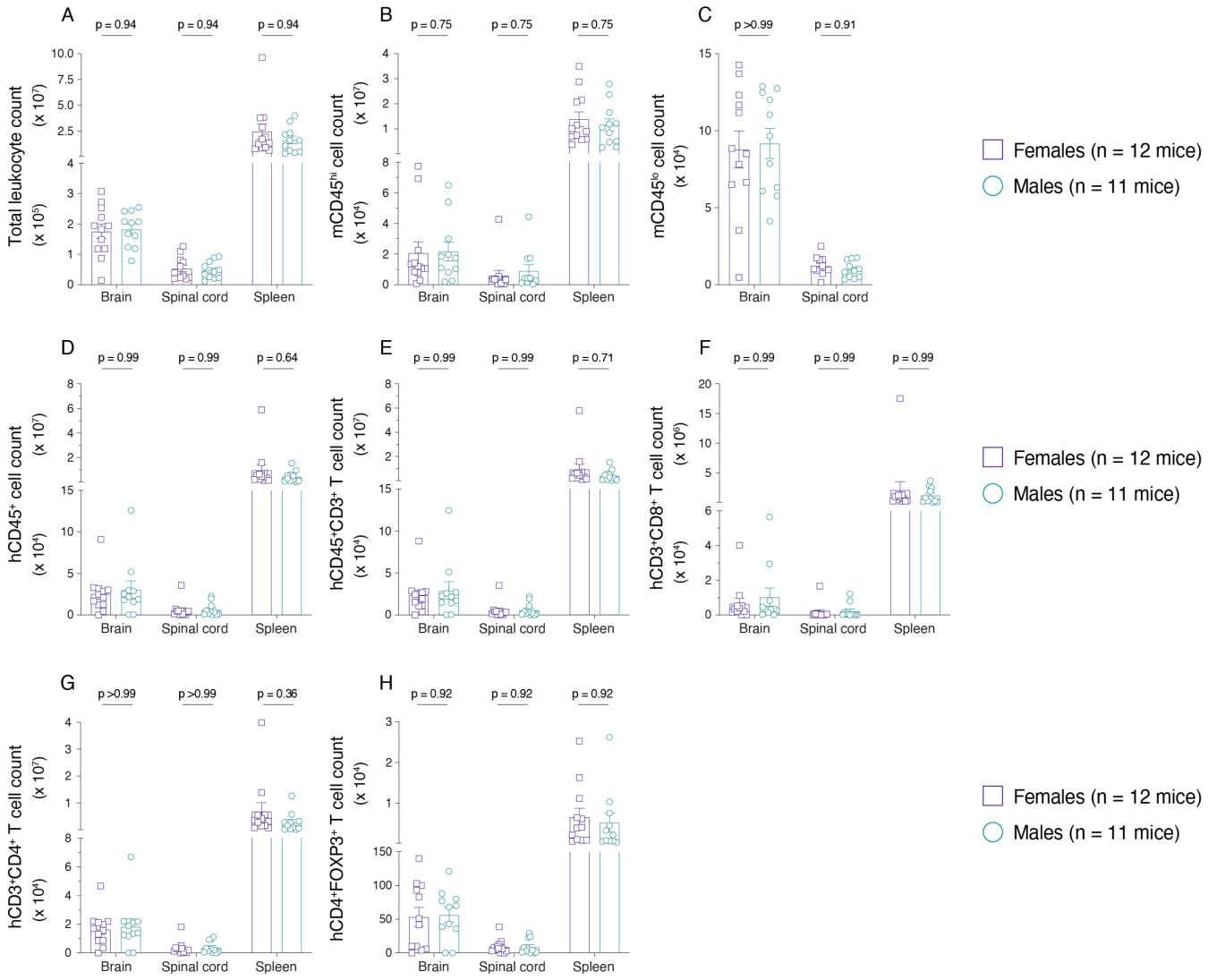

Figure A.50 Sex differences in human and murine immune cell abundance in the CNS and periphery of HuPBMC B6-TKO EAE mice at endpoint

Figure shows total cell counts for (A) all leukocytes (murine and human), (B) mCD45$^{hi/+}$ cells, (C) mCD45^{lo} resident myeloid cells, (D) hCD45^{+} cells, (E) hCD3^{+} T cells, hCD3^{+}CD8^{+} T cells, (F) hCD3^{+}CD4^{+} T cells, and (H) hCD3^{+}CD4^{+}FOXP3^{+} regulatory T cells in the brains, spinal cords, and spleens of PBMC-engrafted female (n = 12) and male (n = 11) B6-TKO mice derived from a healthy female donor (HD-04) day 22 or 33 post-rhMOG/MOG$_{35-55}$ EAE induction. All mice remained asymptomatic until endpoint. Tissues were perfused prior to cell isolation. Data are shown as mean with SEM and were analyzed by Mann Whitney test. HuPBMC cohorts included: 23 and 28.

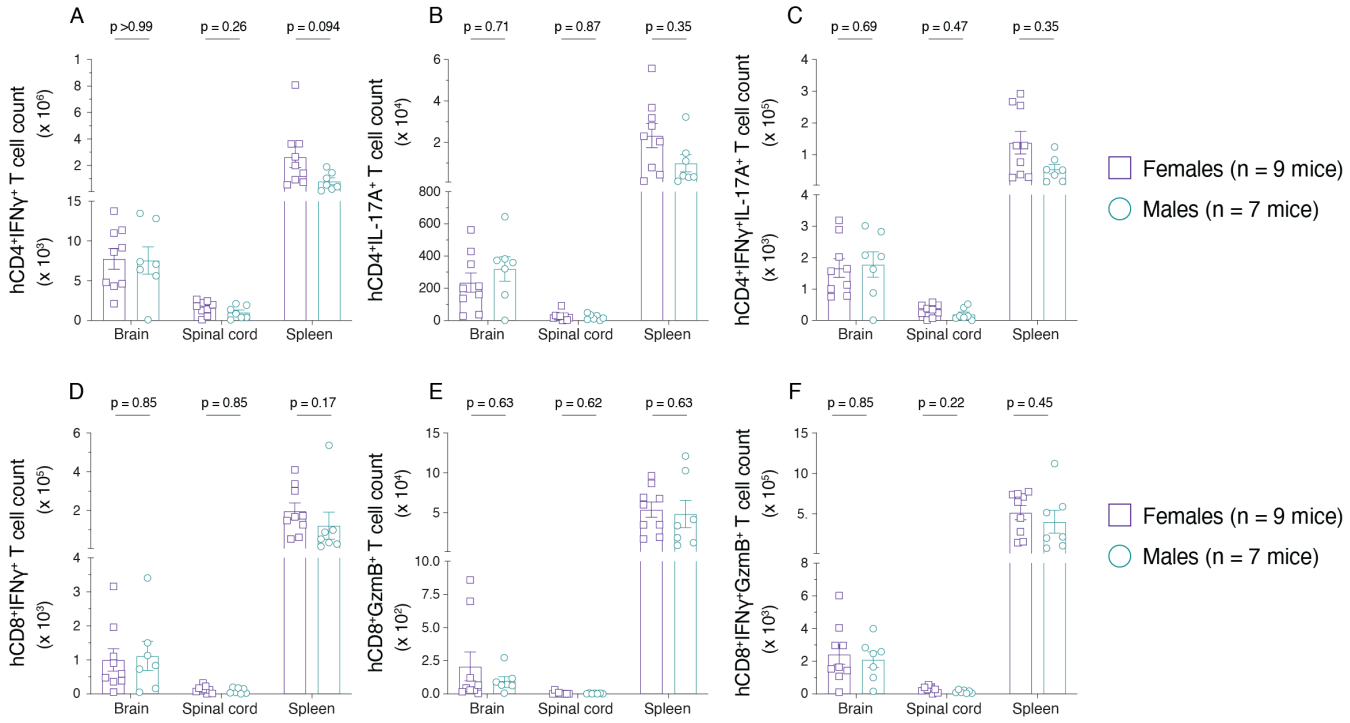

Figure A.51 Sex differences in human T cell subset abundance in the CNS and periphery of HuPBMC B6-TKO EAE mice at endpoint

Figure shows total cell counts for (A) hCD4$^+$IFNγ$^+$(IL-17A$^-$), (B) hCD4$^+$IL-17A$^+$(IFNγ$^-$), (C) hCD4$^+$IFNγ$^+$IL-17A$^+$, (D) hCD8$^+$IFNγ$^+$(GzmB$^-$), (E) hCD8$^+$GzmB$^+$(IFNγ$^-$), and (F) hCD8$^+$IFNγ$^+$GzmB$^+$ T cells in the brains, spinal cords, and spleens of PBMC-engrafted female (n = 9) and male (n = 7) B6-TKO mice derived from a healthy female donor (HD-04) day 22 or 33 post-rhMOG/MOG$_{35-55}$ EAE induction. All mice remained asymptomatic until endpoint. Tissues were perfused prior to cell isolation. Data are shown as mean with SEM and were analyzed by Mann Whitney test. HuPBMC cohorts included: 23 and 28.

Appendix 10. Supplemental data to section 4.9

The following data are supplemental to section 4.9.2.3. In order to identify immune cell populations in murine and human immune system reconstituted B6-TKO EAE tissue samples (Figure A.52 – Figure A.55), gates varied in their position between cohorts due to different fluorophore containing antibody panels having been used for each experimental endpoint.

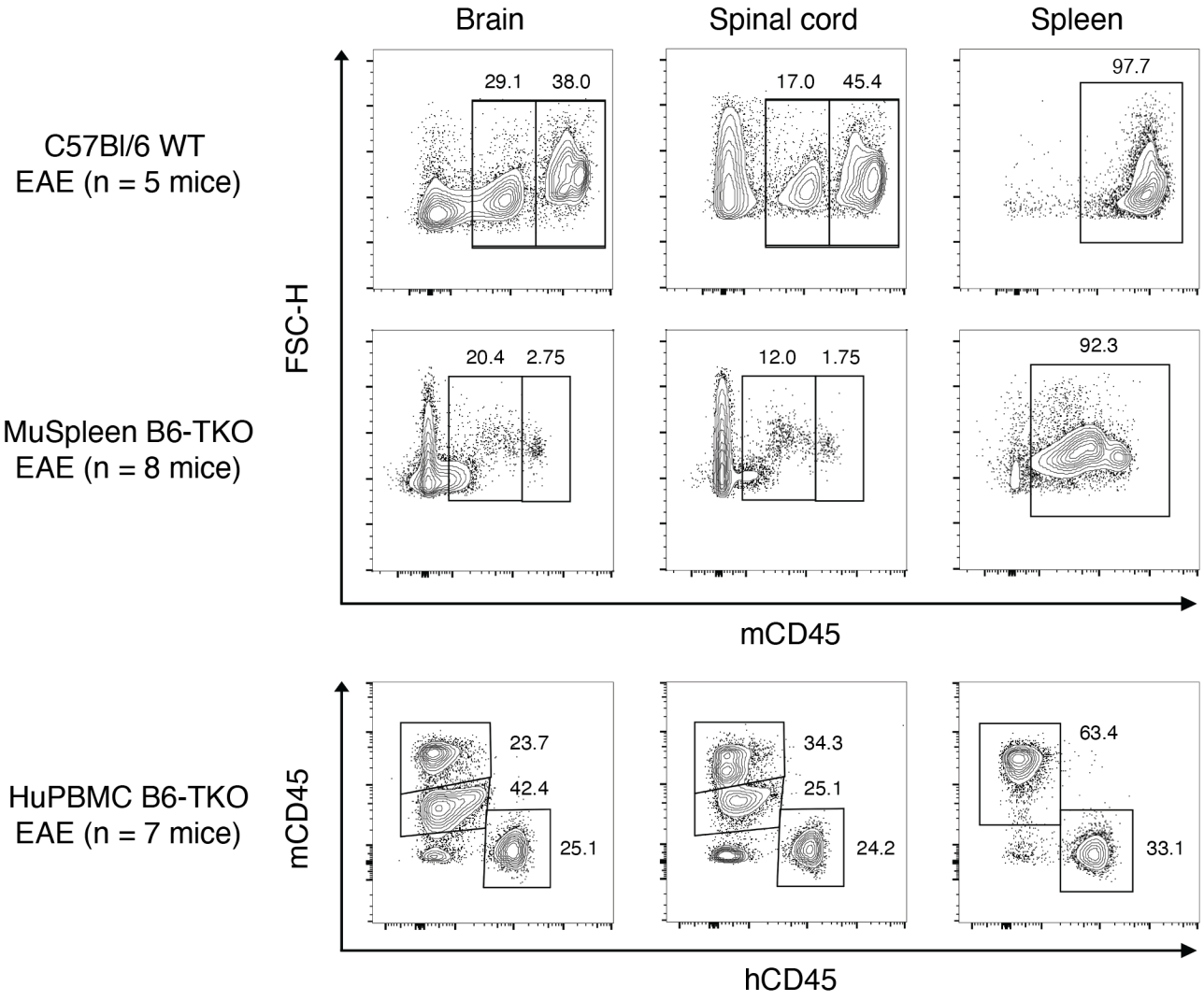

Figure A.52 Flow cytometric gating strategy to identify human and murine immune cell populations in reconstituted B6-TKO mouse tissues

Figure shows concatenated flow cytometric plots illustrating the gating strategy for and the overall frequencies of $mCD45^{lo}$ and $mCD45^{hi}$ cells in the brain, spinal cord, and spleen of immunocompetent C57Bl/6 mice (n = 5 WT males, endpoint day 15 post-induction with rhMOG/MOG_{35-55} EAE) and B6-TKO mice engrafted with

sex-matched syngeneic C57Bl/6 WT derived splenocytes (n = 8 MuSpleen females and males mixed, endpoint day 41 post-induction with MOG_{35-55} EAE). Figure also shows the gating strategy and overall frequencies for $mCD45^{lo}$, $mCD45^{hi}$, and $hCD45^{+}$ cells in the brain, spinal cord, and spleen of human PBMC engrafted B6-TKO mice (n = 7 females and males mixed derived from healthy female donor HD-04, cohort 23, endpoint day 33 post-induction with rhMOG/MOG_{35-55} EAE). The parent population gated is all live leukocytes.

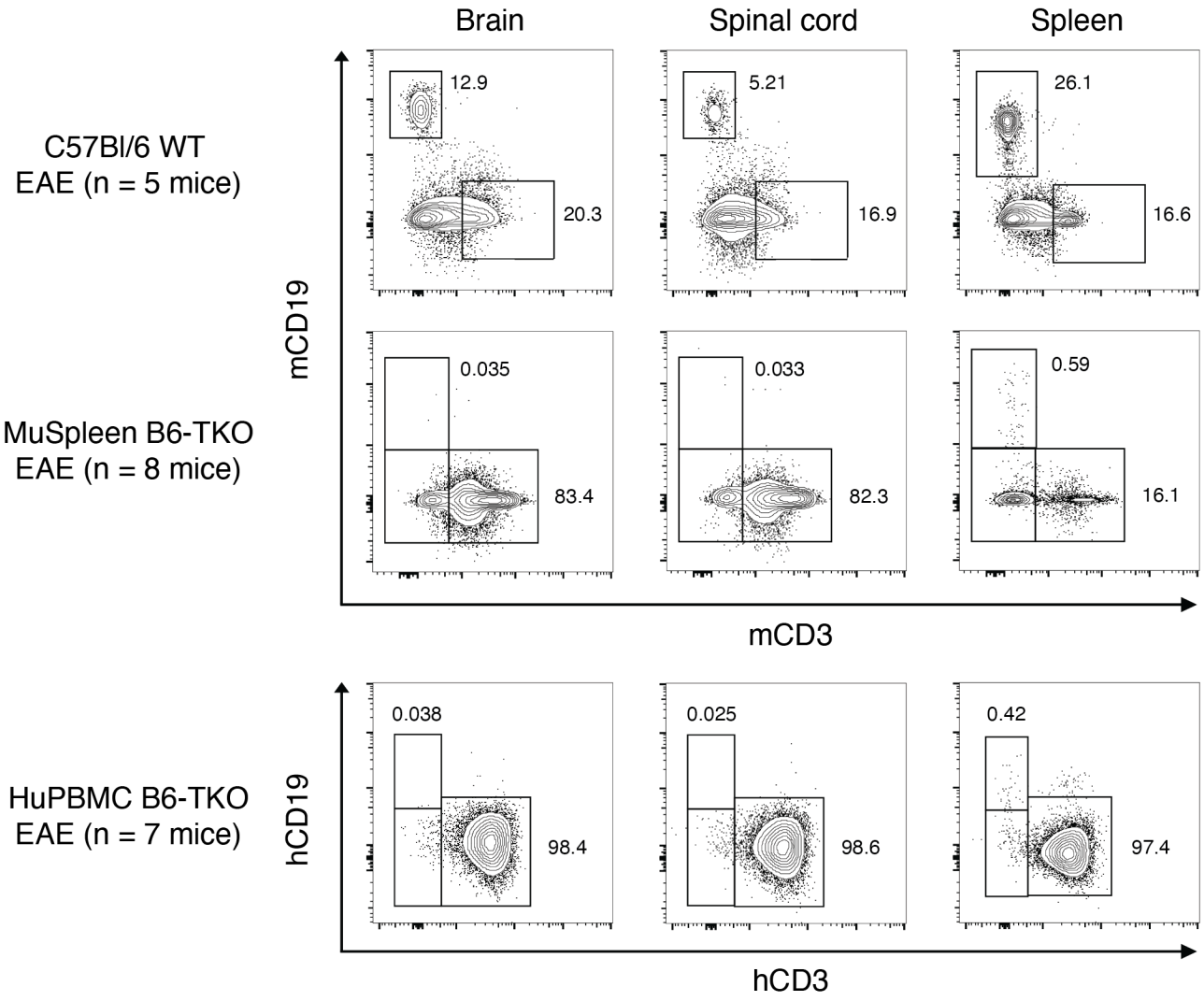

Figure A.53 Flow cytometric gating strategy to identify T and B cell populations in human and murine immune system reconstituted B6-TKO mouse tissues

Figure shows concatenated flow cytometric plots illustrating the gating strategy for and the overall frequencies of $mCD3^{+}$ T cells and $mCD19^{+}$ B cells in the brain, spinal cord, and spleen of immunocompetent C57Bl/6 mice (n = 5 WT males, endpoint day 15 post-induction with rhMOG/MOG_{35-55} EAE) and B6-TKO mice engrafted with sex-matched syngeneic C57Bl/6 WT derived splenocytes (n = 8 MuSpleen females and males mixed, endpoint day 41 post-induction with MOG_{35-55} EAE). Figure also shows the gating strategy and overall frequencies for $hCD3^{+}$

T cells and hCD19^{+} B cells in the brain, spinal cord, and spleen of human PBMC engrafted B6-TKO mice (n = 7 females and males mixed derived from healthy female donor HD-04, cohort 23, endpoint day 33 post-induction with rhMOG/MOG$_{35-55}$ EAE). The parent population gated is mCD45^{hi} cells for fully murine samples and hCD45^{+} cells for humanized mouse samples.

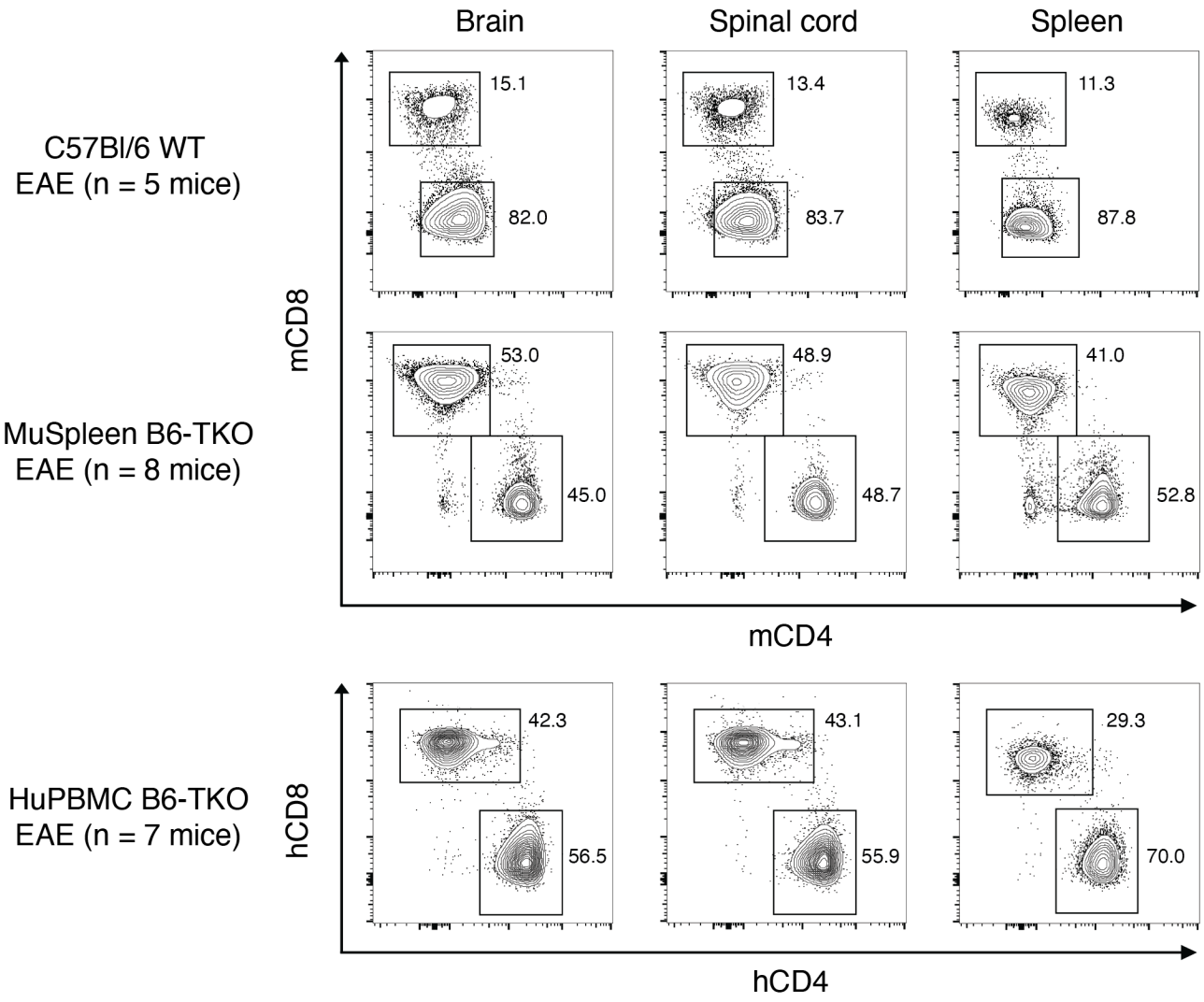

Figure A.54 Flow cytometric gating strategy to identify T cell populations in human and murine immune system reconstituted B6-TKO mouse tissues

Figure shows concatenated flow cytometric plots illustrating the gating strategy for and the overall frequencies of mCD4^{+} and mCD8^{+} T cells in the brain, spinal cord, and spleen of immunocompetent C57Bl/6 mice (n = 5 WT males, endpoint day 15 post-induction with rhMOG/MOG$_{35-55}$ EAE) and B6-TKO mice engrafted with sex-matched syngeneic C57Bl/6 WT derived splenocytes (n = 8 MuSpleen females and males mixed, endpoint day 41 post-induction with MOG$_{35-55}$ EAE). Figure also shows the gating strategy and overall frequencies for hCD4^{+} and hCD8^{+} T cells in the brain, spinal cord, and spleen of human PBMC engrafted B6-TKO mice (n = 7 females and males

mixed derived from healthy female donor HD-04, cohort 23, endpoint day 33 post-induction with rhMOG/MOG_{35-55} EAE). The parent population gated is $mCD45^{hi}CD3^{+}$ T cells for fully murine samples and $hCD45^{+}CD3^{+}$ T cells for humanized mouse samples.

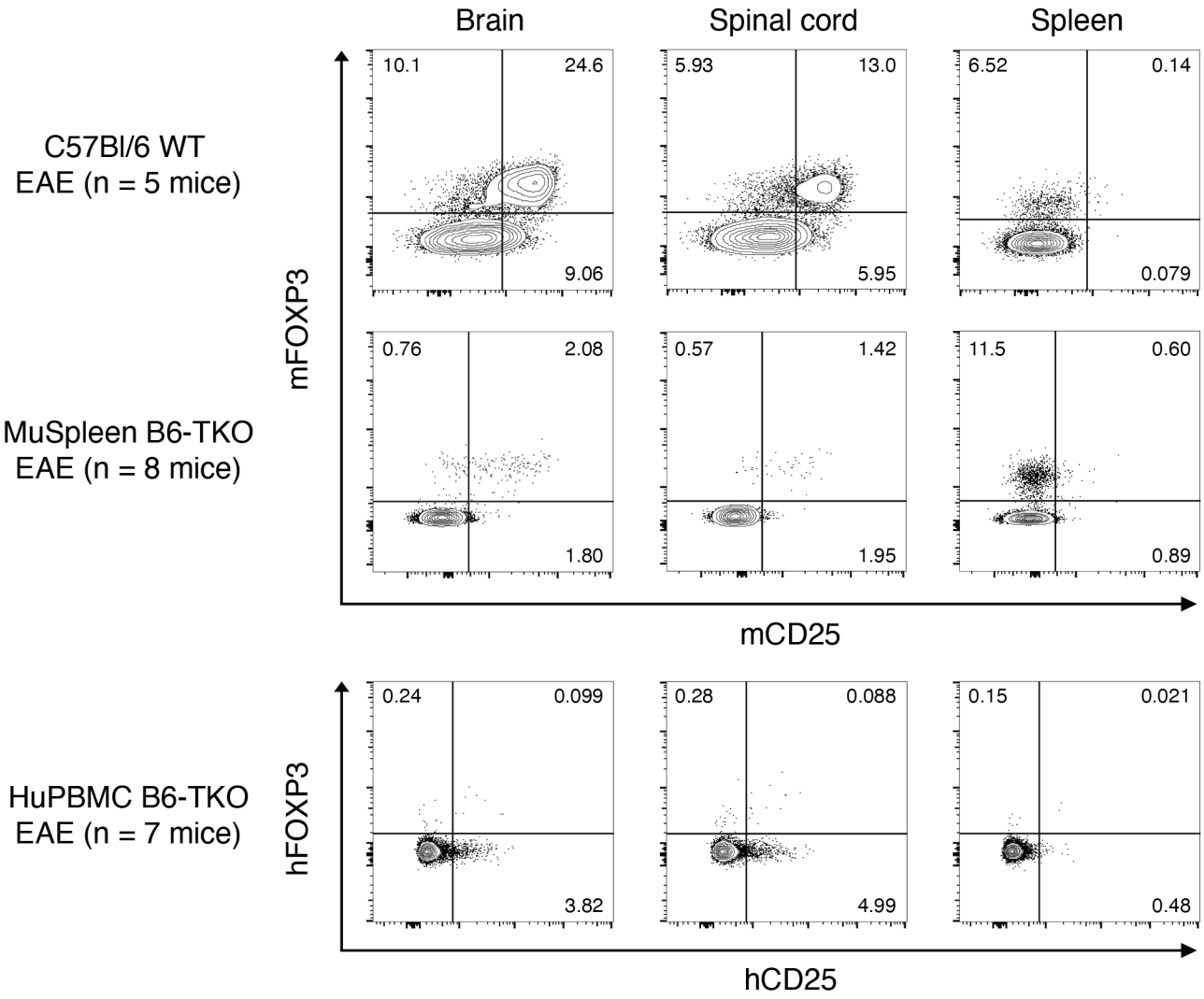

Figure A.55 Flow cytometric gating strategy to identify regulatory T cell populations in human and murine immune system reconstituted B6-TKO mouse tissues

Figure shows concatenated flow cytometric plots illustrating the gating strategy for and the overall frequencies of $mCD25^{+}$ and/or $mFOXP3^{+}$ regulatory T cells in the brain, spinal cord, and spleen of immunocompetent C57Bl/6 mice (n = 5 WT males, endpoint day 15 post-induction with rhMOG/MOG_{35-55} EAE) and B6-TKO mice engrafted with sex-matched syngeneic C57Bl/6 WT derived splenocytes (n = 8 MuSpleen females and males mixed, endpoint day 41 post-induction with MOG_{35-55} EAE). Figure also shows the gating strategy and overall frequencies for $hCD25^{+}$ and/or $hFOXP3^{+}$ regulatory T cells in the brain, spinal cord, and spleen of human PBMC engrafted B6-TKO mice (n = 7 females and males mixed derived from healthy female donor HD-04, cohort 23, endpoint day 33

post-induction with rhMOG/MOG$_{35-55}$ EAE). The parent population gated is mCD45^{hi}CD3^{+}CD4^{+} T cells for fully murine samples and hCD45^{+}CD3^{+}CD4^{+} T cells for humanized mouse samples.

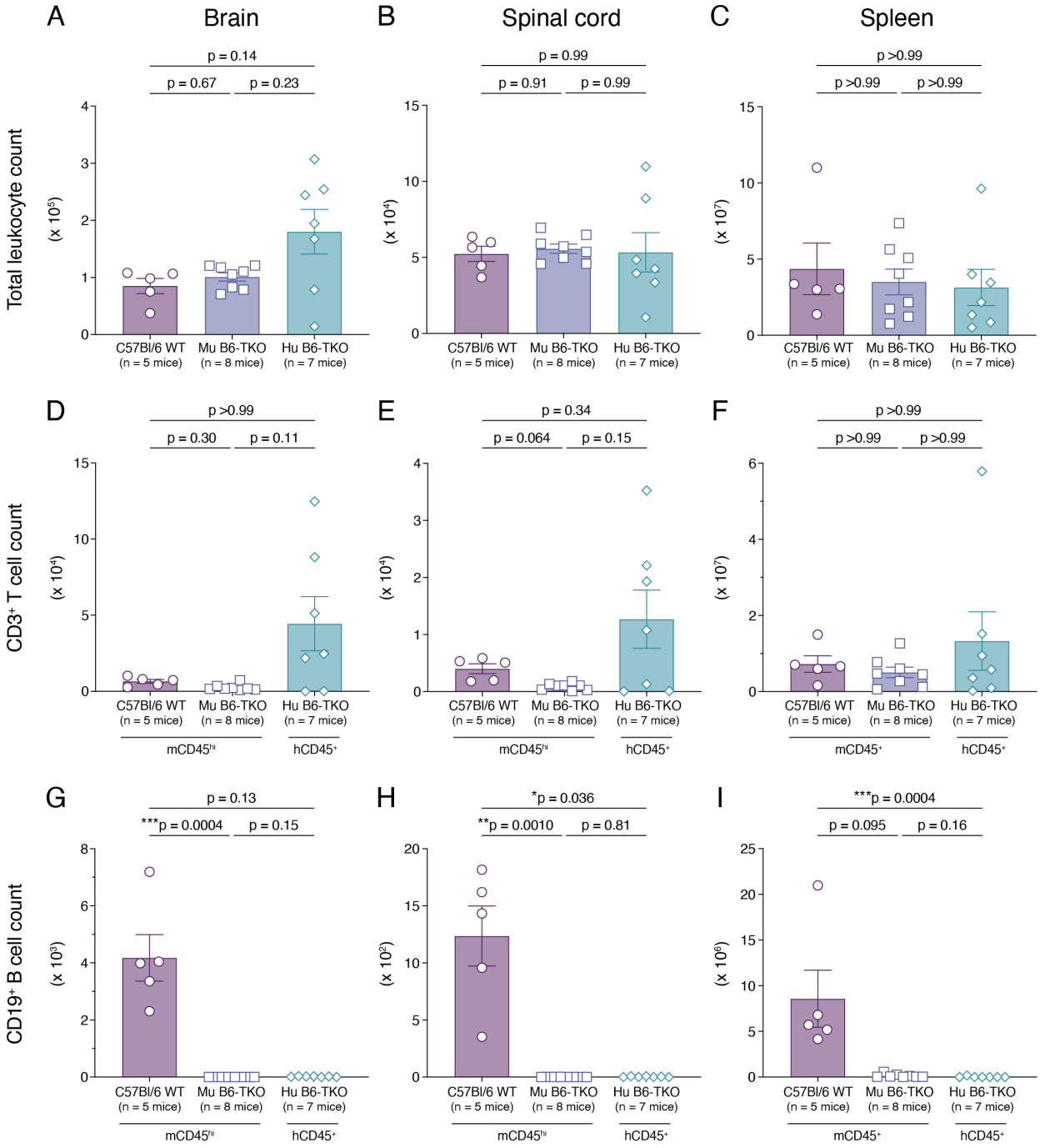

Figure A.56 Abundance of T and B cell populations in the CNS and periphery of human and murine immune system reconstituted B6-TKO mice

Figure shows the total number of (A – C) leukocyte (murine and/or human combined), (D – F) m- or h-$CD3^+$ T cells, and (G – I) m- or h-$CD19^+$ B cells in the brain (left column), spinal cord (middle column), and spleen (right column) of EAE induced groups of C57Bl/6 background mice. Groups include immunocompetent C57Bl/6 WT mice (n = 5 males) day 15 post-induction with rhMOG/MOG_{35-55} EAE, B6-TKO mice engrafted with sex-matched syngeneic C57Bl/6 WT derived splenocytes (n = 8 Mu B6-TKO females and males mixed) day 41 post-induction with MOG_{35-55} EAE, and human PBMC engrafted Hu B6-TKO mice (n = 7 females and males mixed derived from healthy female donor HD-04, cohort 23) day 33 post-induction with rhMOG/MOG_{35-55} EAE. The parent population gated for T and B cells is $mCD45^{hi}$ cells for C57Bl/6 WT and Mu B6-TKO samples and $hCD45^+$ cells for Hu B6-TKO samples. Data are shown as mean with SEM and were analyzed by Brown-Forsythe and Welch ANOVA with Dunnett's T3 multiple comparisons test or by Kruskal-Wallis with Dunn's multiple comparisons test.

Total leukocyte counts in the CNS tissues were statistically similar between all groups, suggesting an absence of immune cells in the CNS was not due to a lack of neuroinflammation nor due to an undisrupted blood-brain barrier or reduced migration in EAE induced reconstituted B6-TKO cohorts (Figure A.56A, B). Though T cell counts were higher in some of the Hu B6-TKO EAE CNS samples, T cell counts were similar between groups (Figure A.56D, E). Likewise, the spleens all contained similar number of leukocytes and $CD3^+$ T cells, indicating that ineffective peripheral reconstitution was not a determining factor for symptom development (Figure A.56C, F). $CD19^+$ B cell counts in all tissues, however, were much lower in both immune system reconstituted B6-TKO EAE cohorts, demonstrating inefficient engraftment of B cells following adoptive transfer from both murine and human donor sources (Figure A.56G – I).

Though levels were variably higher in some humanized B6-TKO EAE mice, total numbers of both $CD4^+$ and $CD8^+$ T cells were statistically similar between groups in all tissues, indicating similar degrees of peripheral reconstitution and CNS infiltration of these T cell subsets (Figure A.57A – F). Interestingly, the $CD8^+$:$CD4^+$ T cell ratio was higher in immune system reconstituted B6-TKO EAE groups compared to C57Bl/6 WT EAE mice in all tissues, suggesting differential reconstitution of T cell subset proportions when transferred and/or antigenically challenged (Figure A.57G – I). Most CNS samples contained an equivalent number or fewer $CD8^+$ T cells compared to $CD4^+$ T cells (ratio <1).

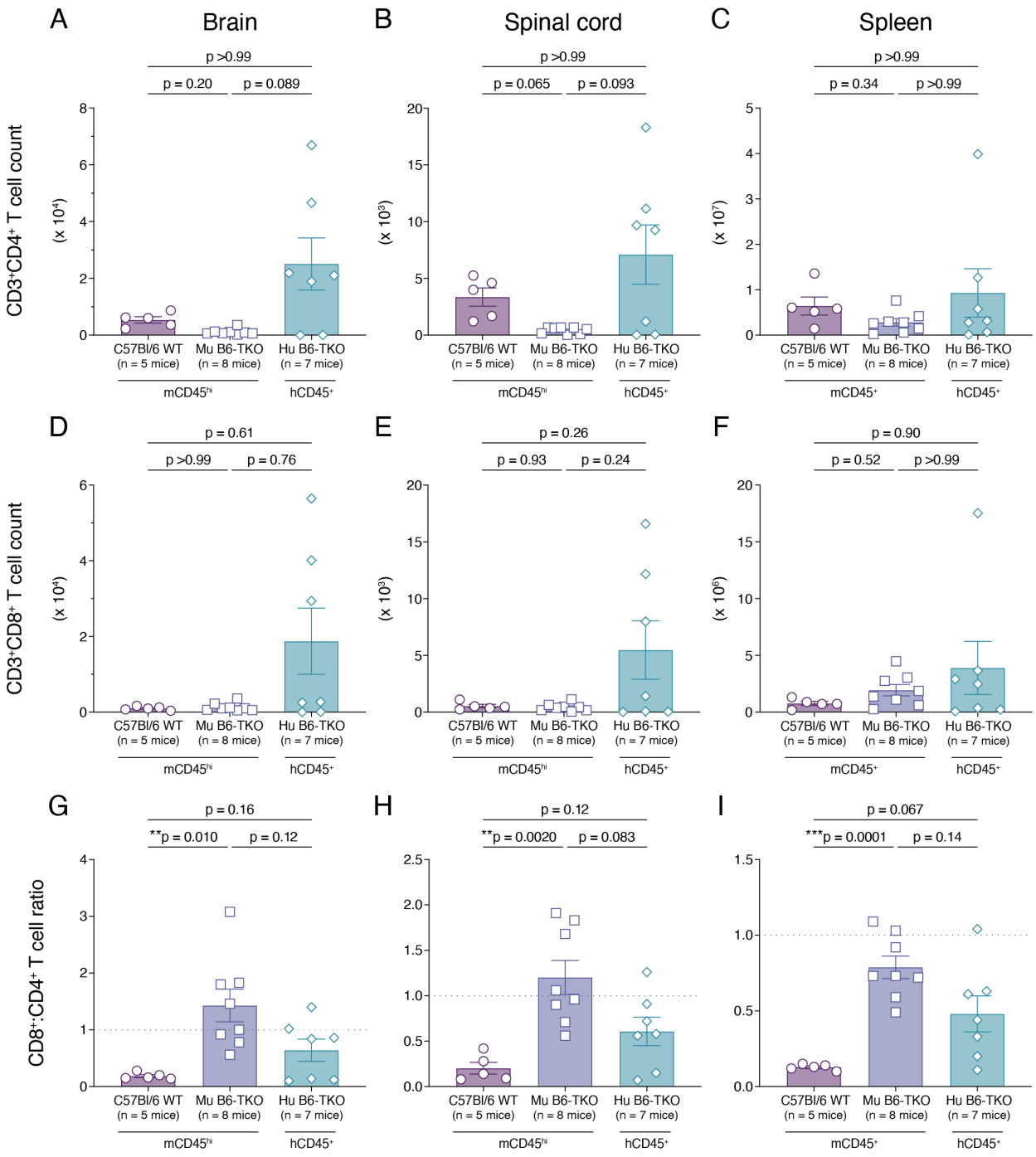

Figure A.57 Abundance of T cell subsets in the CNS and periphery of human and murine immune system reconstituted B6-TKO mice

Figure shows the total number of (A – C) m- or h-CD3$^+$CD4$^+$ T cells and (D – F) m- or h-CD3$^+$CD8$^+$ T cells, as well as (G – I) the ratio of m- or h-CD3$^+$CD8$^+$ to CD3$^+$CD4$^+$ T cells in the brain (left column), spinal cord (middle column), and spleen (right column) of EAE induced groups of C57Bl/6 background mice. Groups include immunocompetent C57Bl/6 WT mice (n = 5 males) day 15 post-induction with rhMOG/MOG$_{35-55}$ EAE, B6-TKO

mice engrafted with sex-matched syngeneic C57Bl/6 WT derived splenocytes (n = 8 Mu B6-TKO females and males mixed) day 41 post-induction with MOG_{35-55} EAE, and human PBMC engrafted Hu B6-TKO mice (n = 7 females and males mixed derived from healthy female donor HD-04, cohort 23) day 33 post-induction with rhMOG/MOG_{35-55} EAE. The parent population gated is $mCD45^{hi}CD3^{+}$ T cells for C57Bl/6 WT and Mu B6-TKO samples and $hCD45^{+}CD3^{+}$ T cells for Hu B6-TKO samples. Data are shown as mean with SEM and were analyzed by Brown-Forsythe and Welch ANOVA with Dunnett's T3 multiple comparisons test or by Kruskal-Wallis with Dunn's multiple comparisons test.

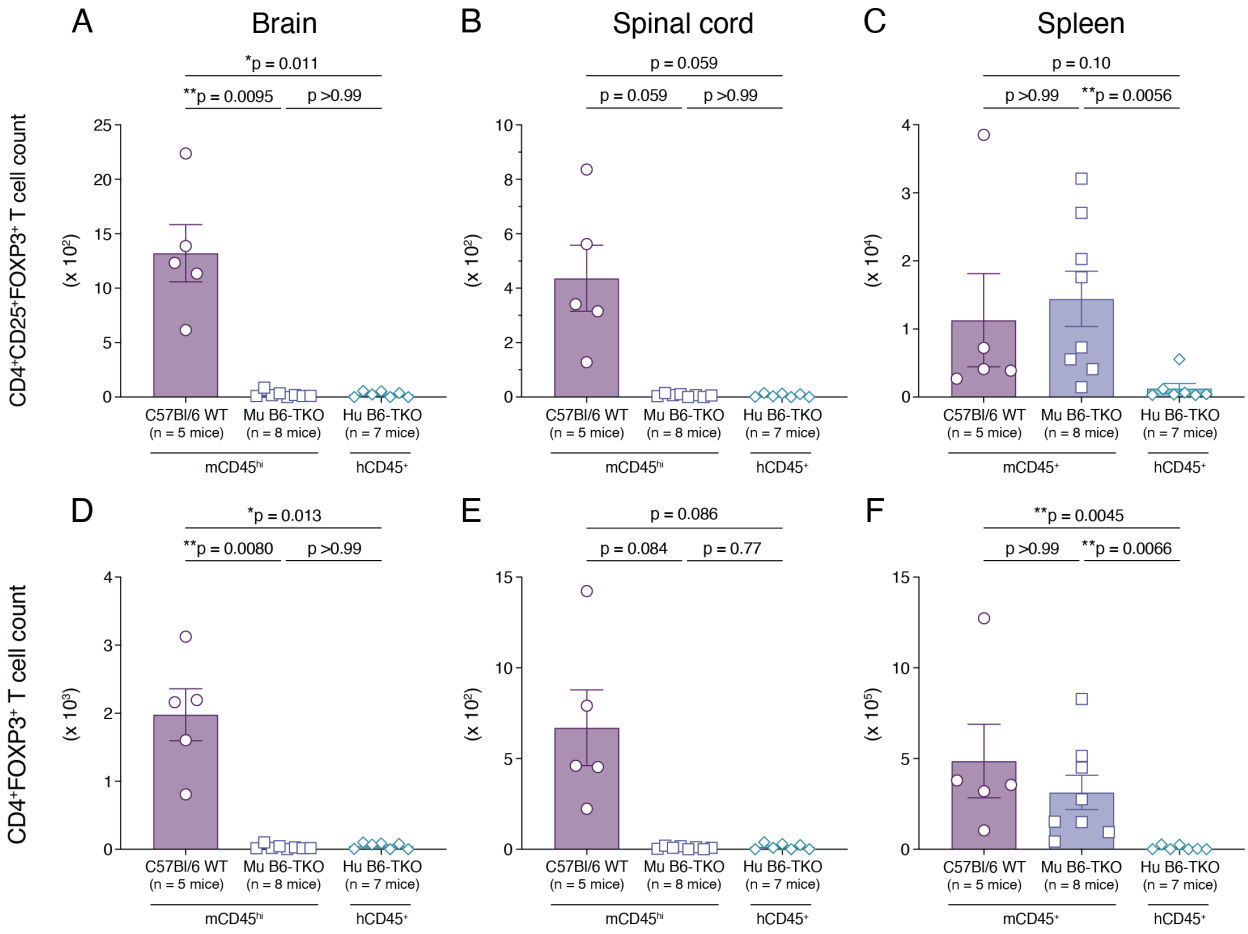

Figure A.58 Abundance of regulatory T cell subsets in the CNS and periphery of human and murine immune system reconstituted B6-TKO mice

Figure shows the total number of (A – C) m- or h-$CD4^{+}CD25^{+}FOXP3^{+}$ T cells and (D – F) m- or h-$CD4^{+}FOXP3^{+}$ T cells in the brain (left column), spinal cord (middle column), and spleen (right column) of EAE induced groups of C57Bl/6 background mice. Groups include immunocompetent C57Bl/6 WT mice (n = 5 males) day 15 post-induction with rhMOG/MOG_{35-55} EAE, B6-TKO mice engrafted with sex-matched syngeneic C57Bl/6 WT derived splenocytes (n = 8 Mu B6-TKO females and males mixed) day 41 post-induction with MOG_{35-55} EAE, and human PBMC engrafted Hu B6-TKO mice (n = 7 females and males mixed derived from healthy female donor HD-

04, cohort 23) day 33 post-induction with rhMOG/MOG_{35-55} EAE. The parent population gated is $mCD45^{hi}CD3^+$ T cells for C57Bl/6 WT and Mu B6-TKO samples and $hCD45^+CD3^+$ T cells for Hu B6-TKO samples. Data are shown as mean with SEM and were analyzed by Brown-Forsythe and Welch ANOVA with Dunnett's T3 multiple comparisons test or by Kruskal-Wallis with Dunn's multiple comparisons test.

In the CNS, C57Bl/6 WT EAE mice contained far more total Tregs than both immune system reconstituted B6-TKO EAE groups (Figure A.58A, B, D, E). An overabundance of Tregs dampening the immune response is thus not likely responsible for the lack of symptoms in EAE induced reconstituted B6-TKO mice. In the spleen, murine immune system reconstituted B6-TKO EAE mice (Mu B6-TKO) contained similar numbers of Tregs as C57Bl/6 WT EAE mice, whereas these numbers are significantly reduced in the human immune system reconstituted B6-TKO EAE mice (Hu B6-TKO). The data suggest that symptom resistance in the Mu B6-TKO group is likely not due to ineffective immunization given that peripheral Tregs expanded to similar levels in the spleen as C57Bl/6 WT EAE, and the reduced number in the Mu B6-TKO CNS samples indicates insufficient local inflammation needed to draw in or expand a large number of Tregs.

Among the CNS infiltrating immune cells, most were $CD3^+$ T cells in Mu B6-TKO and Hu B6-TKO mice (Figure A.59A, B), with very few $CD19^+$ B cells comprising the infiltrating populations compared to C57Bl/6 WT EAE mice (Figure A.59D, E). In the spleen, T cell proportions were similar between the murine groups regardless of reconstitution, but T cell frequencies were relatively higher in the Hu B6-TKO mice (Figure A.59C, F). Confirming the cell count data, the proportions of both T cell subsets was much higher in B6-TKO reconstituted mice than WT B6 mice due to a corresponding absence of B cells, which were underrepresented following adoptive transfer (Figure A.59G – L). In the CNS, both double $CD25^+FOXP3^+$ and single $FOXP3^+$ $CD4^+$ Treg populations comprised a larger proportion of infiltrating immune cells in the C57Bl/6 WT EAE mice than either of the reconstituted B6-TKO EAE groups, though the Hu B6-TKO CNS samples contained even fewer Tregs relative to Mu B6-TKO CNS samples (Figure A.60A, B, D, E). In the spleen, $CD25^+FOXP3^+$ Treg frequencies are similar between all groups, but for total $FOXP3^+$ Tregs, C57Bl/6 WT EAE and Mu B6-TKO mice contain similar Treg frequencies that are both much higher than that observed in Hu B6-TKO spleens (Figure A.60C, F).

In all three tissues, reconstituted Mu B6-TKO and Hu B6-TKO mice displayed a skew toward CD8 expression relative to CD4 expression on $CD3^+$ T cells compared to C57Bl/6 WT EAE mice. T cell subset proportions were similar between Mu B6-TKO and Hu B6-TKO tissues (Figure A.61A – F). The proportional reduction in Treg populations in reconstituted B6-TKO CNS samples compared to C57Bl/6 WT EAE CNS samples is consistent with cell count data and suggests minimal inflammation in the CNS of reconstituted B6-TKO EAE mice (Figure A.61G, H, J, K). In the spleen, Mu B6-TKO and C57Bl/6 WT EAE mice contained similar frequencies of Tregs among total $CD3^+CD4^+$ T cells, and Hu B6-TKO spleens contain proportionally very few Tregs (Figure A.61C, F).

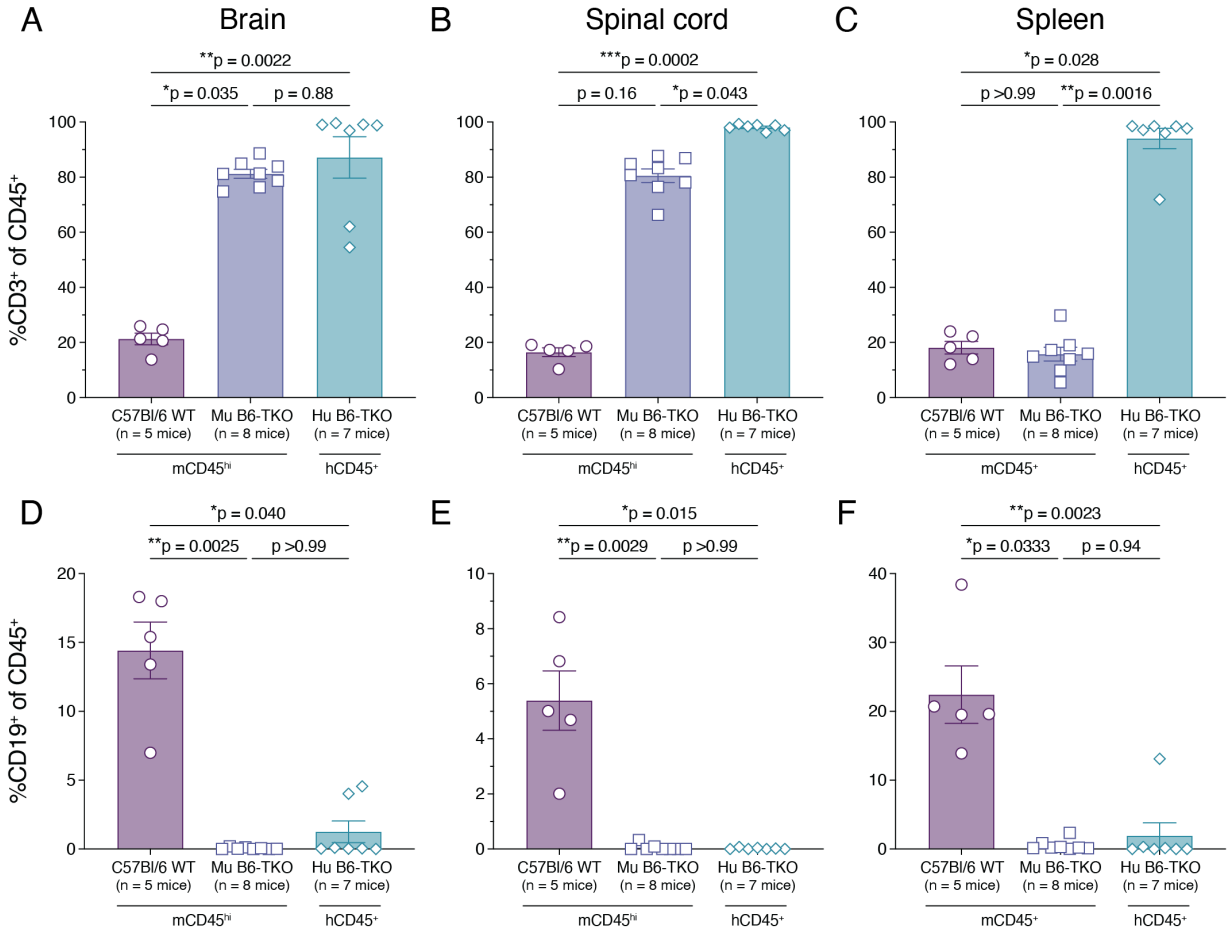

Figure A.59 Proportions of T and B cells in the CNS and periphery of human and murine immune infiltrates in reconstituted B6-TKO mice

Figure shows the proportions of (A – C) m- or h-$CD3^+$ T cells, (D – F) m- or h-$CD19^+$ B cells, (G – I) m- or h-$CD3^+CD4^+$ T cells, and (J – L) m- or h-$CD3^+CD8^+$ T cells among total m- or h-$CD45^{hi/+}$ cells in the brain (left

column), spinal cord (middle column), and spleen (right column) of EAE induced groups of C57Bl/6 background mice. Groups include immunocompetent C57Bl/6 WT mice (n = 5 males) day 15 post-induction with rhMOG/MOG_{35-55} EAE, B6-TKO mice engrafted with sex-matched syngeneic C57Bl/6 WT derived splenocytes (n = 8 Mu B6-TKO females and males mixed) day 41 post-induction with MOG_{35-55} EAE, and human PBMC engrafted Hu B6-TKO mice (n = 7 females and males mixed derived from healthy female donor HD-04, cohort 23) day 33 post-induction with rhMOG/MOG_{35-55} EAE. The parent population gated for T and B cells is $mCD45^{hi}$ cells for C57Bl/6 WT and Mu B6-TKO samples and $hCD45^{+}$ cells for Hu B6-TKO samples. Data are shown as mean with SEM and were analyzed by Brown-Forsythe and Welch ANOVA with Dunnett's T3 multiple comparisons test or by Kruskal-Wallis with Dunn's multiple comparisons test.

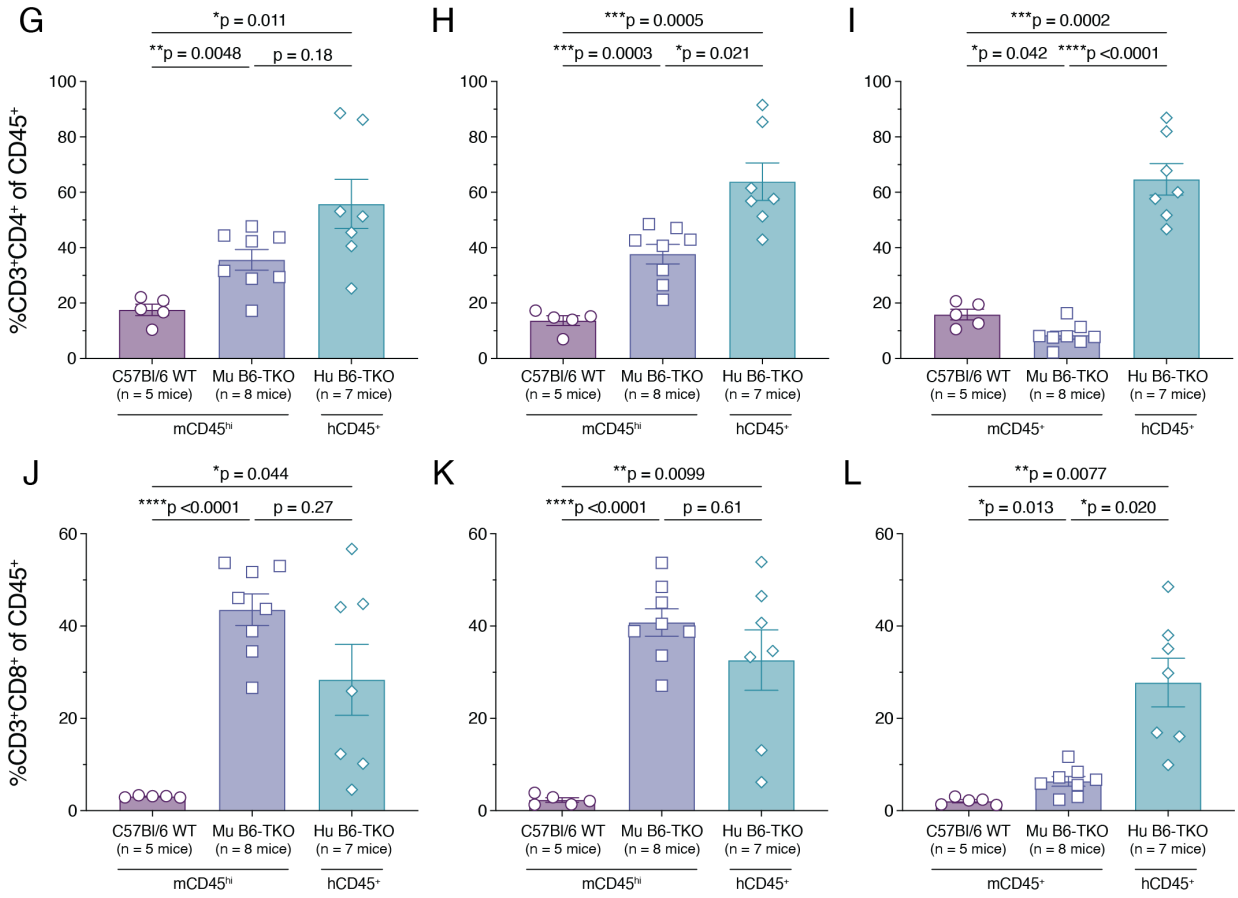

Figure A.59 continued

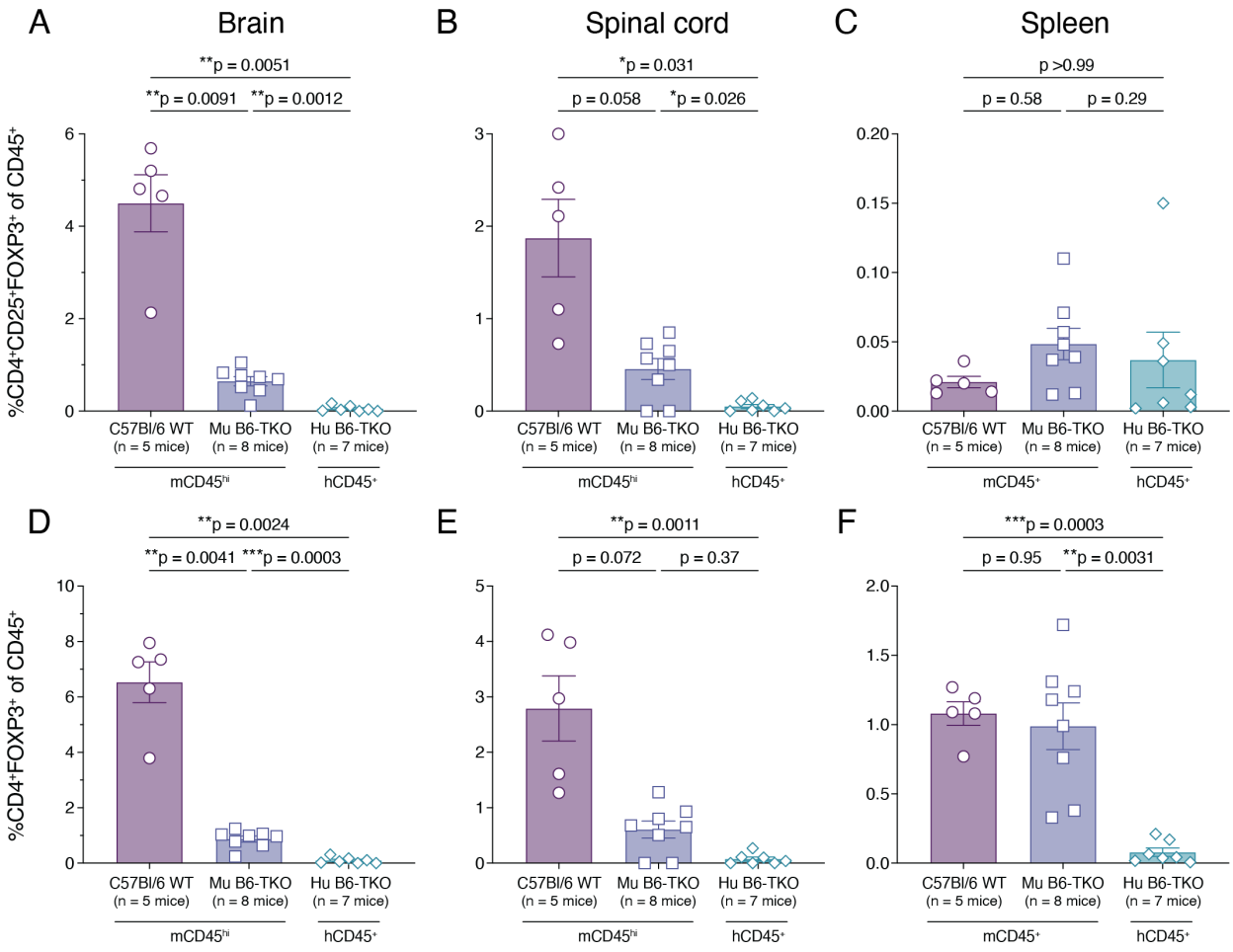

Figure A.60 Proportions of regulatory T cells in the CNS and periphery of human and murine immune infiltrates in reconstituted B6-TKO mice

Figure shows the proportions of (A – C) m- or h-$CD4^+CD25^+FOXP3^+$ and (D – F) m- or h- $CD4^+FOXP3^+$ T cells among total m- or h-$CD45^{hi/+}$ cells in the brain (left column), spinal cord (middle column), and spleen (right column) of EAE induced groups of C57Bl/6 background mice. Groups include immunocompetent C57Bl/6 WT mice (n = 5 males) day 15 post-induction with rhMOG/MOG_{35-55} EAE, B6-TKO mice engrafted with sex-matched syngeneic C57Bl/6 WT derived splenocytes (n = 8 Mu B6-TKO females and males mixed) day 41 post-induction with MOG_{35-55} EAE, and human PBMC engrafted Hu B6-TKO mice (n = 7 females and males mixed derived from healthy female donor HD-04, cohort 23) day 33 post-induction with rhMOG/MOG_{35-55} EAE. The parent population gated for T and B cells is $mCD45^{hi}CD3^+$ cells for C57Bl/6 WT and Mu B6-TKO samples and $hCD45^+CD3^+$ cells for Hu B6-TKO samples. Data are shown as mean with SEM and were analyzed by Brown-Forsythe and Welch ANOVA with Dunnett's T3 multiple comparisons test or by Kruskal-Wallis with Dunn's multiple comparisons test.

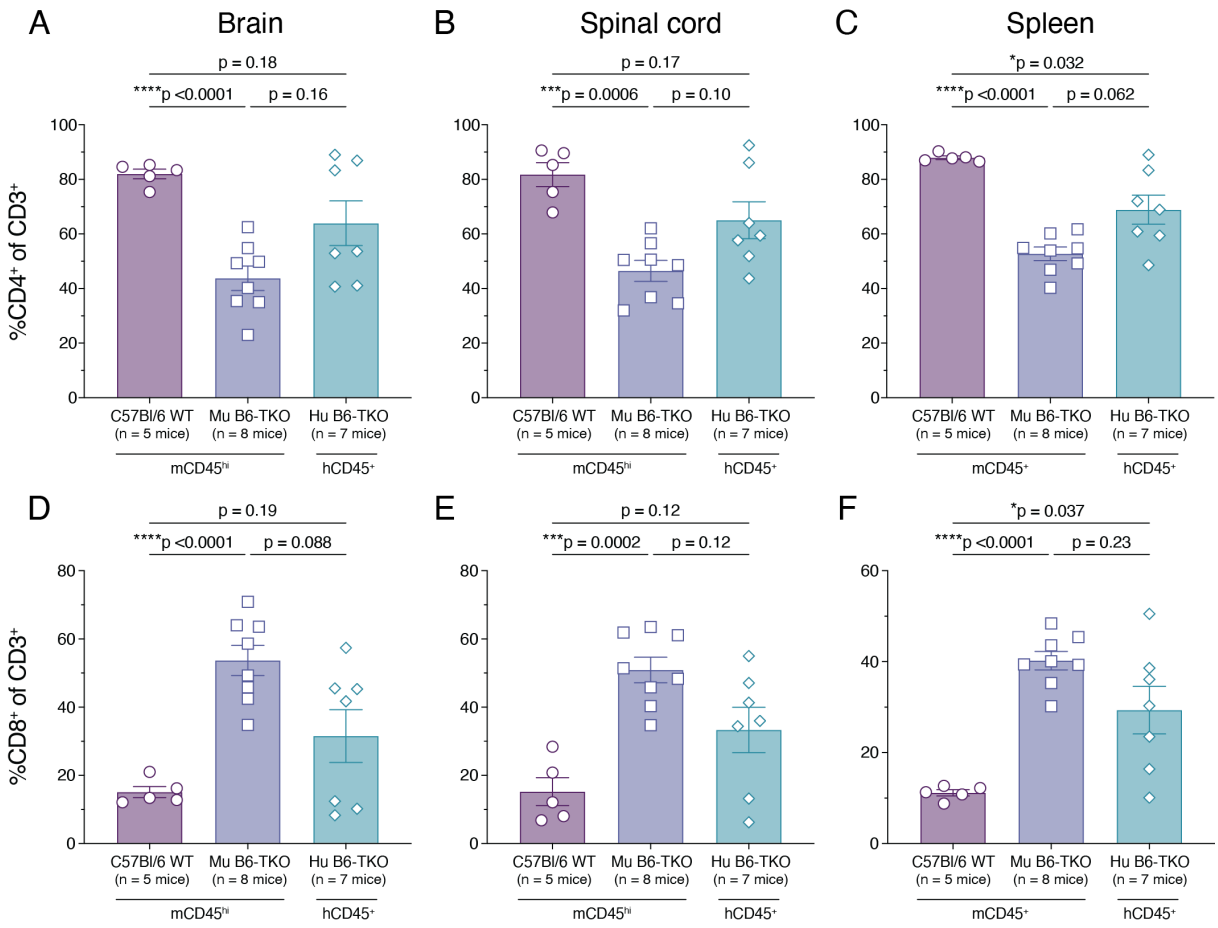

Figure A.61 Proportions of T cell subsets in the CNS and periphery of human and murine immune system reconstituted B6-TKO mice

Figure shows the proportions of (A – C) $CD4^+$ and (D – F) $CD8^+$ T cells among m- or h-$CD3^+$ T cells, as well as (G – I) $CD25^+FOXP3^+$ and (J – L) $FOXP3^+$ T cells among m- or h-$CD3^+CD4^+$ T cells in the brain (left column), spinal cord (middle column), and spleen (right column) of EAE induced groups of C57Bl/6 background mice. Groups include immunocompetent C57Bl/6 WT mice (n = 5 males) day 15 post-induction with rhMOG/MOG_{35-55} EAE, B6-TKO mice engrafted with sex-matched syngeneic C57Bl/6 WT derived splenocytes (n = 8 Mu B6-TKO females and males mixed) day 41 post-induction with MOG_{35-55} EAE, and human PBMC engrafted Hu B6-TKO mice (n = 7 females and males mixed derived from healthy female donor HD-04, cohort 23) day 33 post-induction with rhMOG/MOG_{35-55} EAE. The parent population gated for T and B cells is $mCD45^{hi}CD3^+$ cells for C57Bl/6 WT and Mu B6-TKO samples and $hCD45^+CD3^+$ cells for Hu B6-TKO samples. Data are shown as mean with SEM and were analyzed by Brown-Forsythe and Welch ANOVA with Dunnett's T3 multiple comparisons test or by Kruskal-Wallis with Dunn's multiple comparisons test.

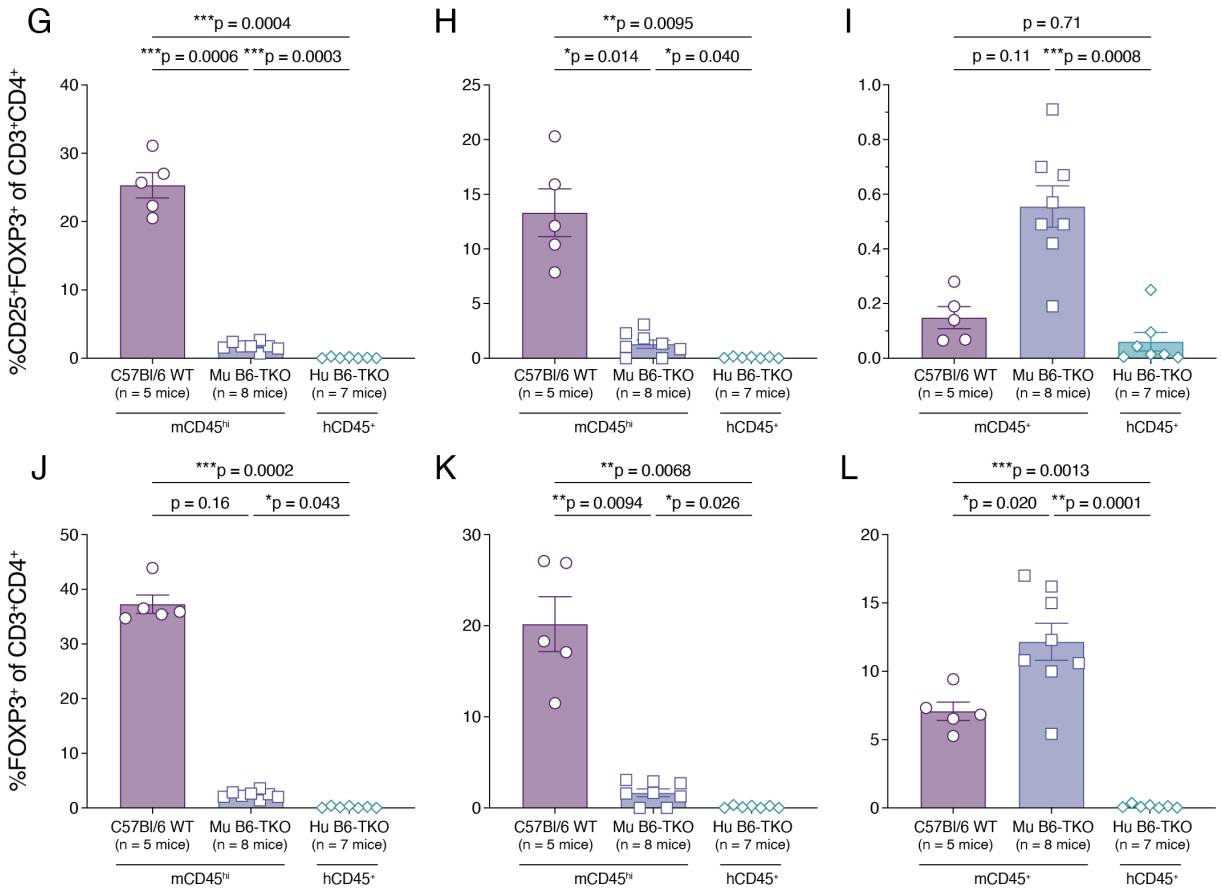

Figure A.61 continued

Appendix 11. Optimization and validation of MOG_{42-55} I-A^{g7} tetramer staining

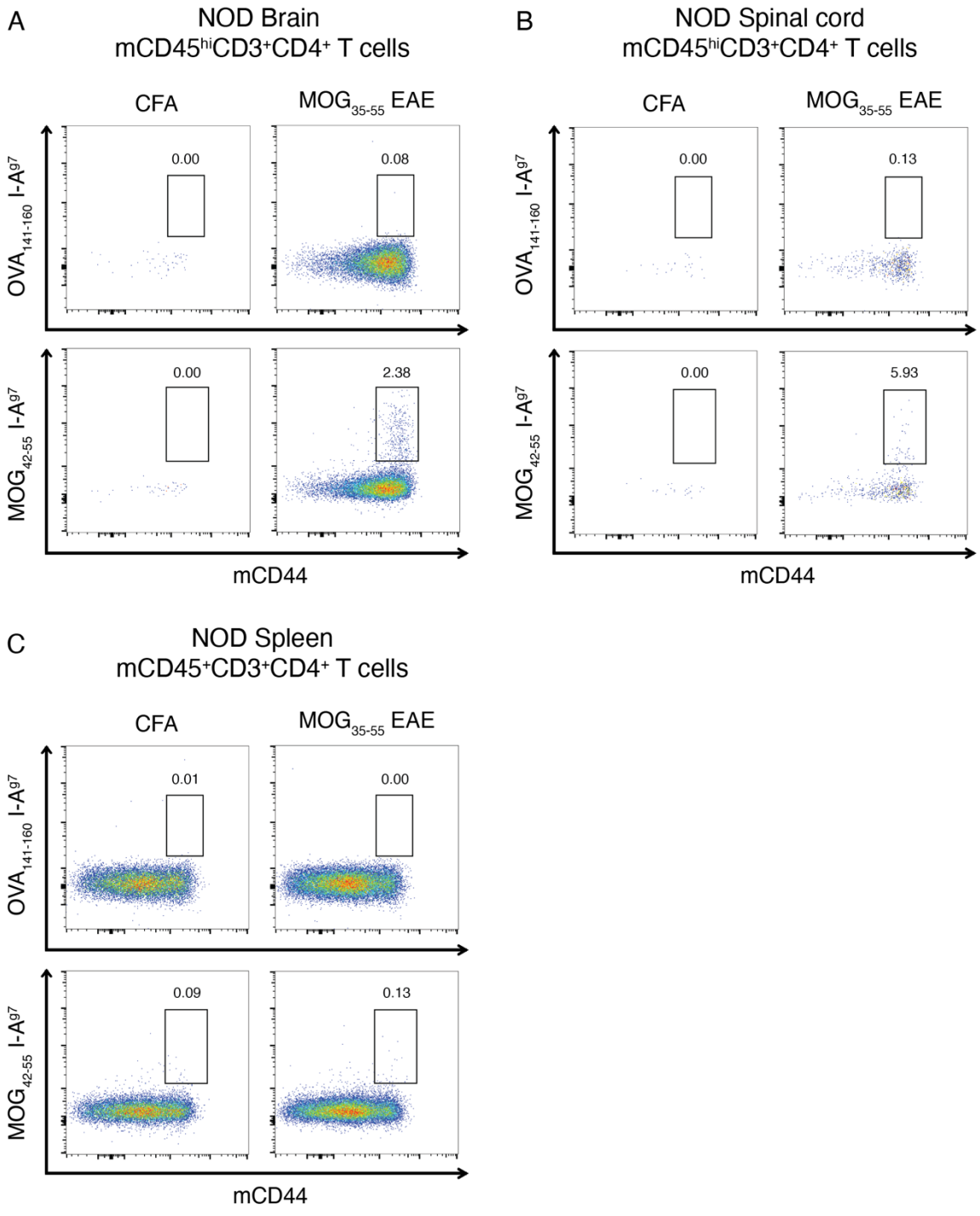

Figure A.62 Flow cytometric analysis of MOG_{42-55} I-A^{g7} MHC II tetramer binding by $mCD4^+$ T cells from blank CFA and MOG_{35-55} immunized NOD mice

Figure shows representative flow cytometric plots indicating the proportions of mCD45$^{hi/+}$CD3^{+}CD4^{+}CD44^{hi} T cells bound to OVA$_{141-160}$ I-A^{g7} and MOG$_{42-55}$ I-A^{g7} tetramers in the (A) brain, (B) spinal cord, and (C) spleen on day 35 post-immunization of NOD mice with either blank CFA or 200 µg MOG$_{35-55}$ peptide. Cell suspensions were isolated from perfused tissues and stained with 4.6 µg/mL I-A^{g7} tetramer for 3 hours at room temperature.

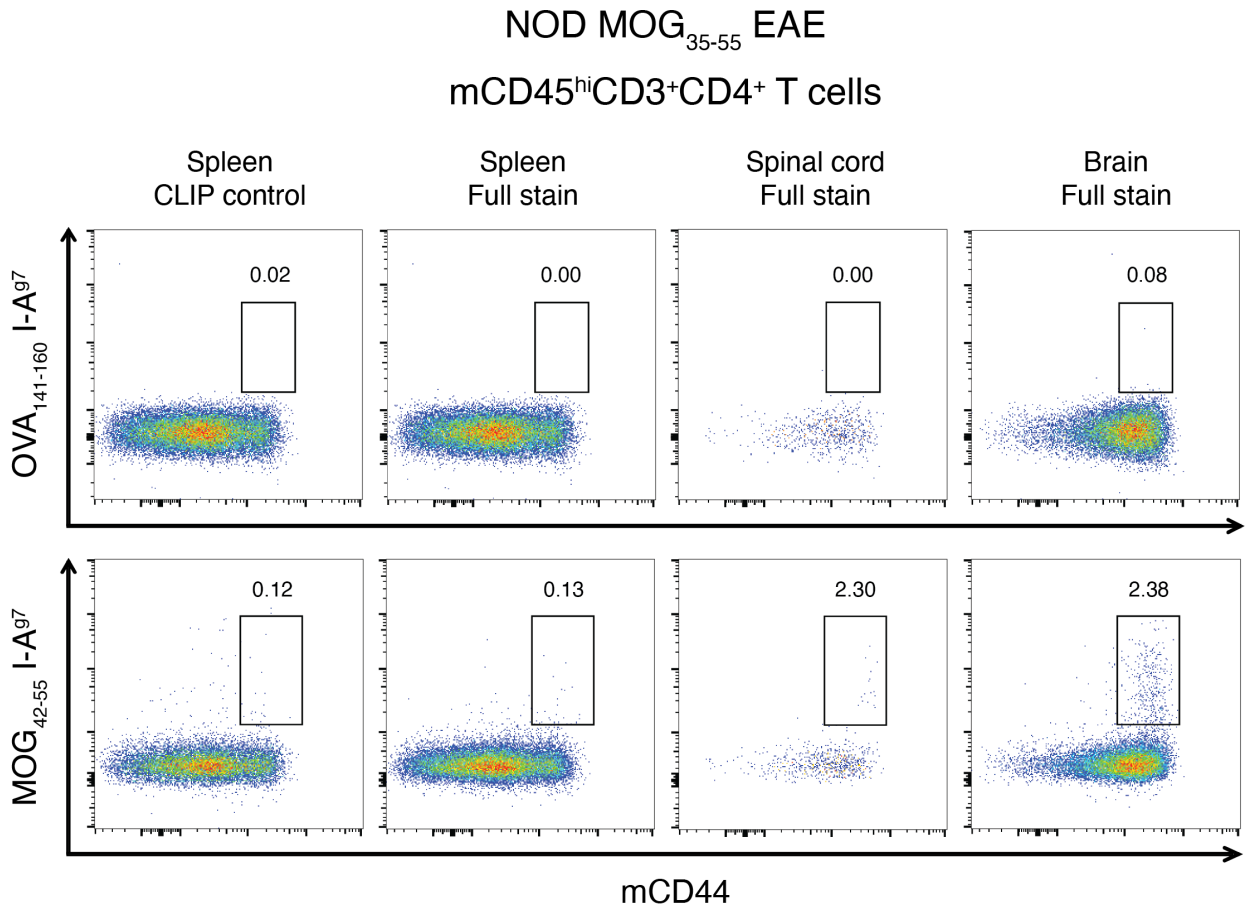

Figure A.63 CNS specific binding of MOG$_{42-55}$ bound I-A^{g7} MHC II tetramer by mCD4^{+} T cells from MOG$_{35-55}$ immunized NOD mice

Figure shows flow cytometric plots from the spleen, brain, and spinal cord of an individual NOD mouse immunized with 200 µg MOG$_{35-55}$ peptide, which indicate the proportions of mCD45$^{hi/+}$CD3^{+}CD4^{+}CD44^{hi} T cells bound to OVA$_{141-160}$ I-A^{g7} and MOG$_{42-55}$ I-A^{g7} tetramers, or respective fluorophore matched control tetramers loaded with human CLIP$_{87-101}$ peptide, on day 35 post-induction. Cell suspensions were isolated from perfused tissues and stained with 4.6 µg/mL I-A^{g7} tetramer for 3 hours at room temperature.

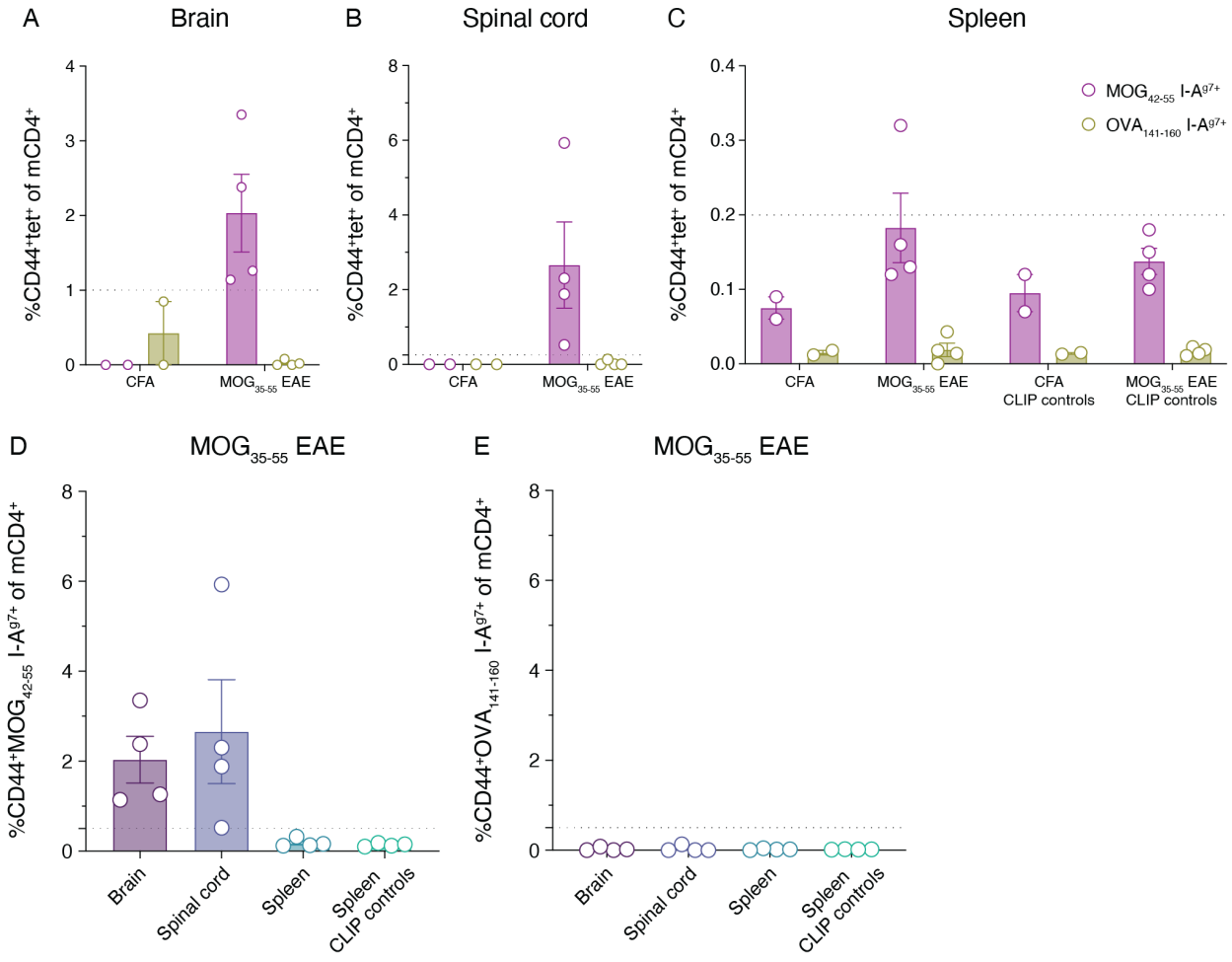

Figure A.64 Quantification of MOG_{42-55} and nonspecific peptide loaded I-A^{g7} MHC II tetramer binding by $mCD4^+$ T cells from MOG_{35-55} and blank CFA immunized NOD mice

Figure shows the proportions of $mCD45^{hi/+}CD3^+CD4^+CD44^{hi}$ T cells bound to $OVA_{141-160}$ I-A^{g7} and MOG_{42-55} I-A^{g7} tetramers in the (A) brain, (B) spinal cord, and (C) spleen, day 35 post-immunization of NOD mice with either blank CFA (n = 2 mixed sex) or 200 µg MOG_{35-55} peptide (n = 4 mixed sex). Proportions of (D) MOG_{42-55} I-A^{g7} tetramer and (E) $OVA_{141-160}$ I-Ag7 tetramer, or respective fluorophore matched control tetramers loaded with human $CLIP_{87-101}$ peptide, bound to $mCD45^{hi/+}CD3^+CD4^+CD44^{hi}$ T cells in each tissue of MOG_{35-55} immunized NOD mice (n = 4 mixed sex). Cell suspensions were isolated from perfused tissues and stained with 4.6 µg/mL I-A^{g7} tetramer for 3 hours at room temperature. Data are shown as mean with SEM.

Table A.10 Antibody staining panel for flow cytometric detection of intracellular myelin basic protein and I-A^{g7} MHC II tetramer binding human CD4^{+} T cells in HuPBMC EAE mouse tissues

Target	Fluorophore	Attune laser	Clone	Isotype	Vol per well (µL)	Cat no.
MBP (2.9 mg/mL)	FITC	BL1	MBP101	Mouse IgG2b	0.1	ab62631
+ 2° α-Mu IgG2b			m2b-25G4	---	0.5	11-4220-82
mCD45	PerCP-Cy5.5	BL2	30-F11	Rat IgG2b	0.5	45-0451-82
$OVA_{141-160}$ class II I-A(g7)	APC	R1	N/A	N/A	0.33	NIH t.o. 61886 (or 61888 for CLIP)
hCD3	Alexa 700	R2	OKT3	Mouse IgG2a	1	56-0037-42
mF4/80	APC-e780	R3	BM8	Rat IgG2a	0.5	47-4801-82
hCD4			RPA-T4	Mouse IgG1	1	47-0049-42
PLP_{56-70}	BV421	V1	N/A	N/A	0.33	NIH t.o. 61883
MBP_{74-85}					0.33	NIH t.o. 61884
MBP_{73-92} class II I-A(g7)					0.33	NIH t.o. 61885 (or 61889 for CLIP)
Live/Dead	*eFluor 506*	*V2*	---	---	*100 (of 2X dye)*	*65-0866-14*
---	SB600	V3	---	---	---	---
hCD8	BV650	V4	RPA-T8	Mouse IgG1	1	563821
m/hCD44	SB702	V5	IM7	Rat IgG2b	0.5	67-0441-82
hCD14	BV785	V6	63D3	Mouse IgG1	1	367142
hCD68			Y1/82A	Mouse IgG2b	1	333826
MOG_{42-55} class II I-A(g7)	PE	Y1	N/A	N/A	0.33	NIH t.o. 61882 (or 61887 for CLIP)
hCD45	PE-Texas Red	Y2	HI30	Mouse IgG1	1	MHCD4517
mCD11b	PE-Cy7	Y3	M1/70	Rat IgG2b	0.5	25-0112-82

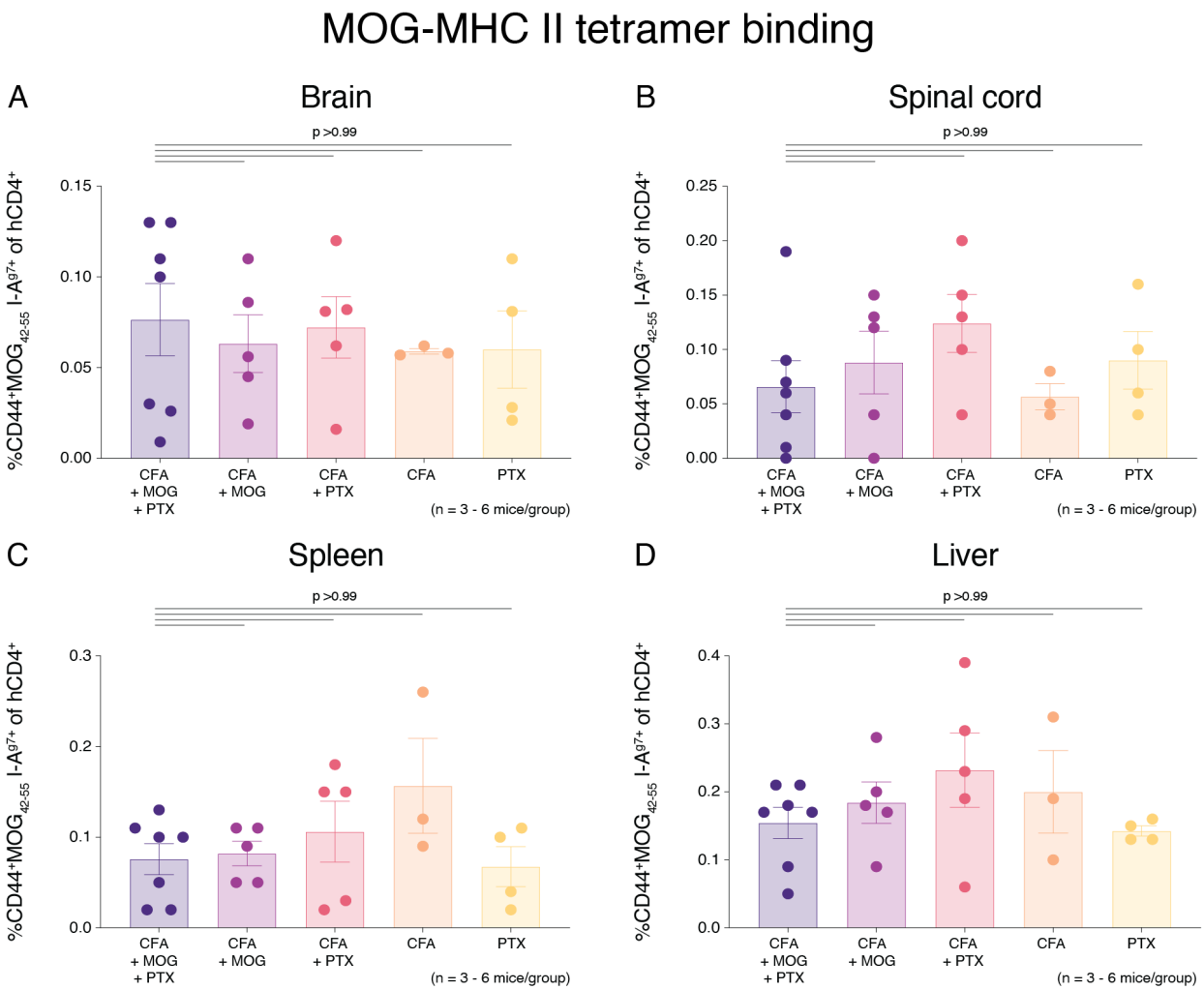

Figure A.65 MOG peptide-loaded MHC II tetramer binding by human $CD4^+$ T cells in the CNS and periphery of HuPBMC mice induced with different EAE adjuvant components

Figure shows the proportion of activated human $hCD3^+CD4^+(CD8^-)CD44^+$ T cells in the (A) brain, (B) spinal cord, (C) spleen, (D) liver, and (E) intestinal lamina propria positive for MOG_{42-55} $I\text{-}A^{g7}$ MHC II tetramer staining on days 19 – 22 post-immunization of PBS engrafted control NSG mice induced with the full mixed MOG EAE immunization containing 100 µg rhMOG and µg MOG_{35-55} antigen emulsified in CFA, co-administered PTx (n = 4 mice) and HuPBMC mice (n = 26 mice all derived from HD-04 female PBMCs) induced with full mixed EAE immunization (CFA + MOG + PTx, n = 7 mice), mixed MOG emulsion without PTx (CFA + MOG, n = 5 mice), blank CFA emulsion and PTx without antigen (CFA + PTx, n = 5 mice), blank CFA emulsion only without antigen or PTx (CFA, n = 3 mice), or PTx only without emulsion (PTx, n = 4 mice). Control $hCD3^+CD4^+(CD8^-)CD44^+$ T cell staining with a fluorophore matched $CLIP_{87-101}$ $I\text{-}A^{g7}$ MHC II tetramer is shown in the spleen (F) and liver (G) for the same immunization groups. Tissues were perfused prior to cell isolation. Data are shown as mean with SEM and were analyzed by Brown-Forsythe and Welch ANOVA with Dunnett's T3 multiple comparisons test or by Kruskal-Wallis with Dunn's multiple comparisons test.

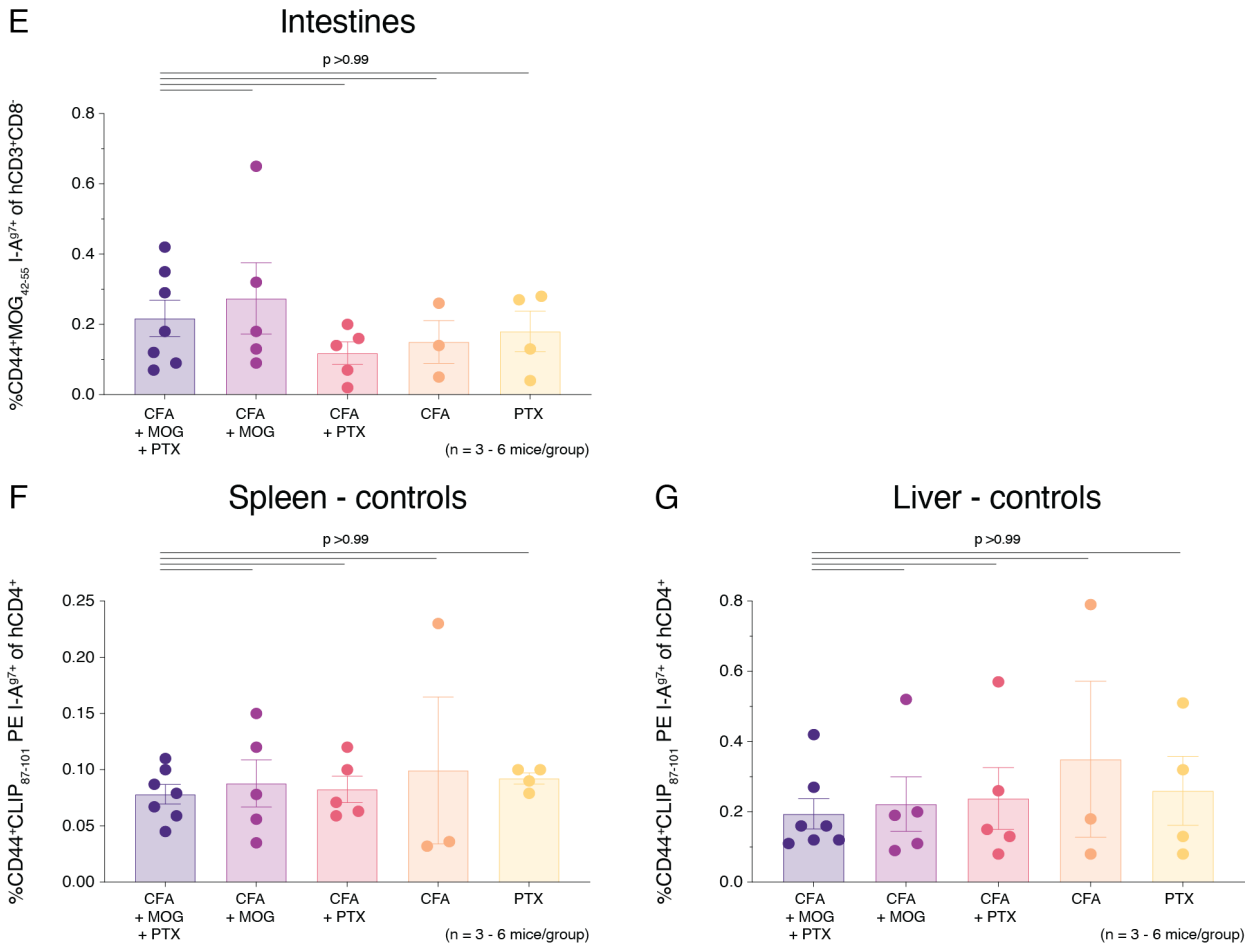

Figure A.65 continued

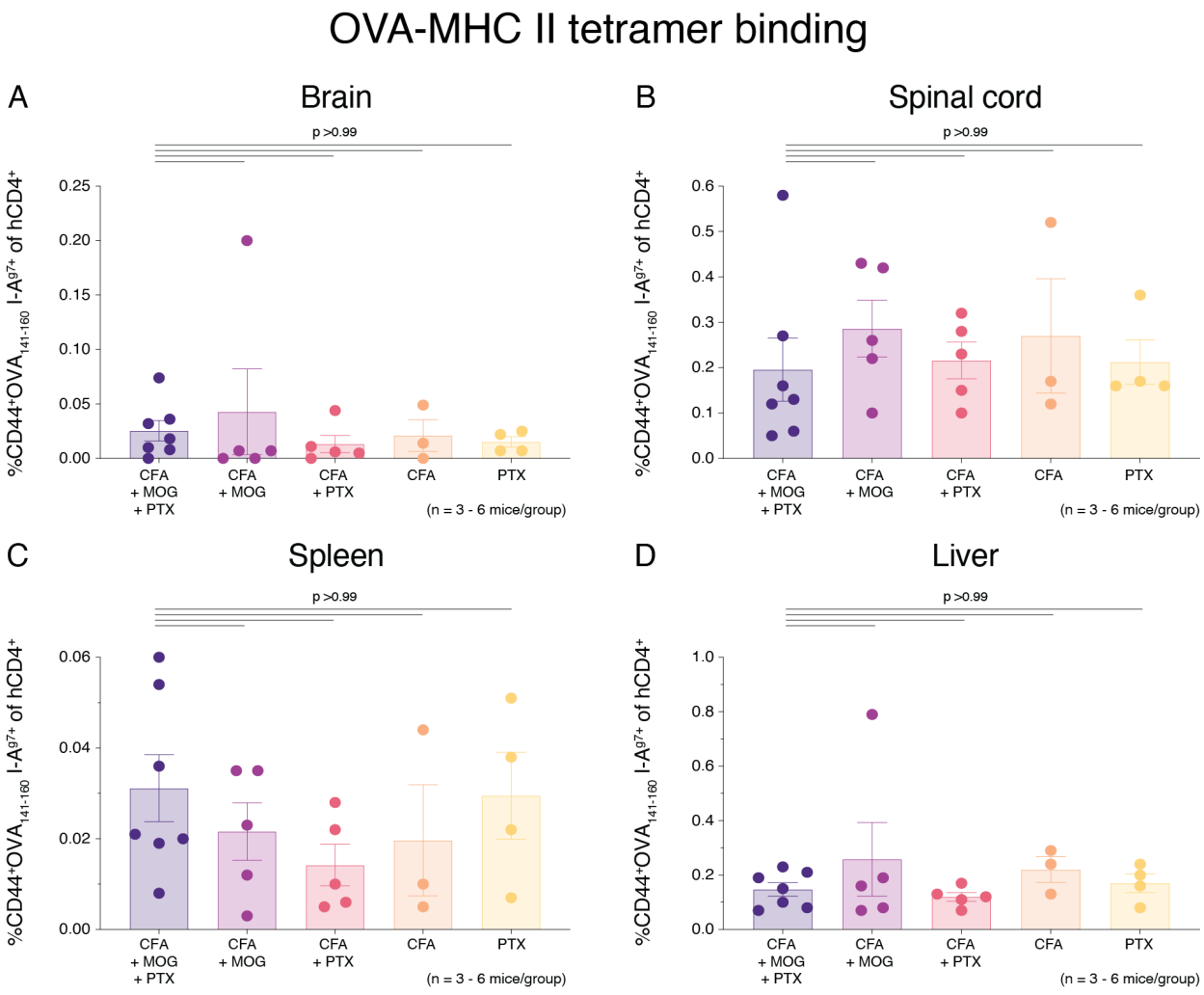

Figure A.66 OVA peptide-loaded MHC II tetramer binding by human $CD4^+$ T cells in the CNS and periphery of HuPBMC mice induced with different EAE adjuvant components

Figure shows the proportion of activated human $hCD3^+CD4^+(CD8^-)CD44^+$ T cells in the (A) brain, (B) spinal cord, (C) spleen, (D) liver, and (E) intestinal lamina propria positive for $OVA_{141\text{-}160}$ $I\text{-}A^{g7}$ MHC II tetramer staining on days 19 – 22 post-immunization of PBS engrafted control NSG mice induced with the full mixed MOG EAE immunization containing 100 µg rhMOG and µg $MOG_{35\text{-}55}$ antigen emulsified in CFA, co-administered PTx (n = 4 mice) and HuPBMC mice (n = 26 mice all derived from HD-04 female PBMCs) induced with full mixed EAE immunization (CFA + MOG + PTx, n = 7 mice), mixed MOG emulsion without PTx (CFA + MOG, n = 5 mice), blank CFA emulsion and PTx without antigen (CFA + PTx, n = 5 mice), blank CFA emulsion only without antigen or PTx (CFA, n = 3 mice), or PTx only without emulsion (PTx, n = 4 mice). Control $hCD3^+CD4^+(CD8^-)CD44^+$ T cell staining with a fluorophore matched $CLIP_{87\text{-}101}$ $I\text{-}A^{g7}$ MHC II tetramer is shown in the spleen (F) and liver (G) for the same immunization groups. Tissues were perfused prior to cell isolation. Data are shown as mean with SEM and were analyzed by Brown-Forsythe and Welch ANOVA with Dunnett's T3 multiple comparisons test or by Kruskal-Wallis with Dunn's multiple comparisons test.

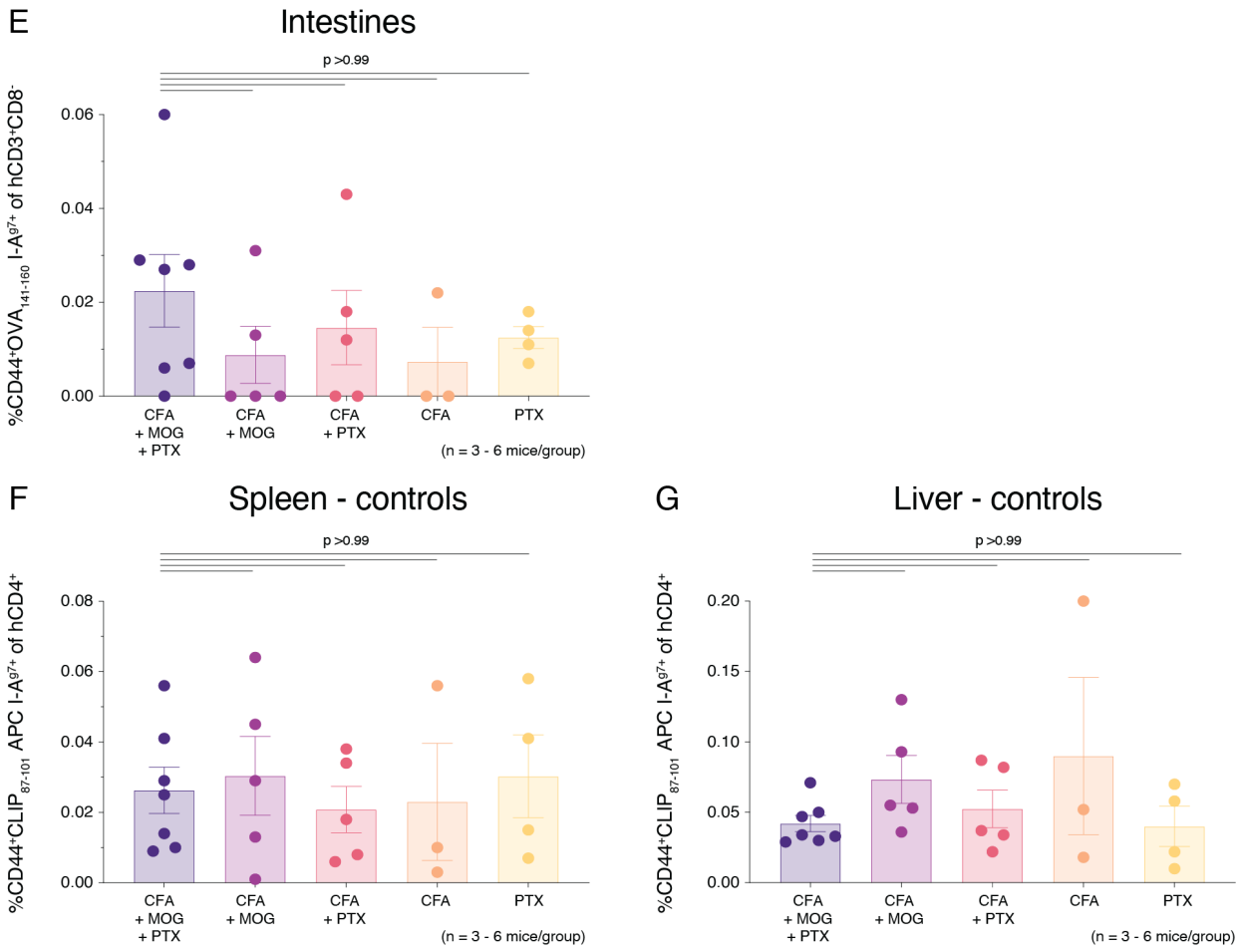

Figure A.66 continued

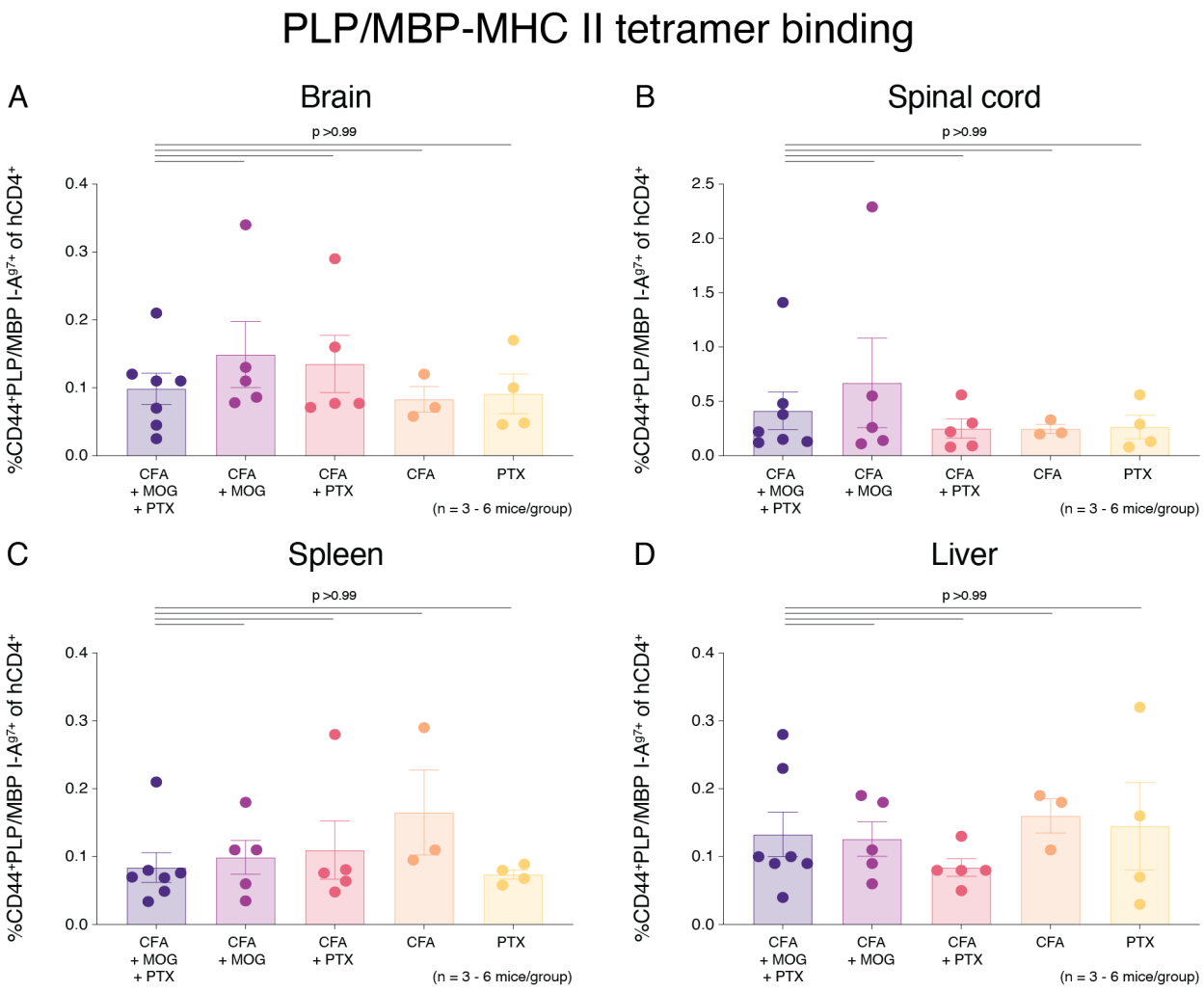

Figure A.67 PLP and MBP peptide-loaded MHC II tetramer binding by human $CD4^+$ T cells in the CNS and periphery of HuPBMC mice induced with different EAE adjuvant components

Figure shows the proportion of activated human $hCD3^+CD4^+(CD8^-)CD44^+$ T cells in the (A) brain, (B) spinal cord, (C) spleen, (D) liver, and (E) intestinal lamina propria positive for PLP_{56-70}, MBP_{74-85}, and MBP_{73-92} I-A^{g7} MHC II tetramer staining on days 19 – 22 post-immunization of PBS engrafted control NSG mice induced with the full mixed MOG EAE immunization containing 100 µg rhMOG and µg MOG_{35-55} antigen emulsified in CFA, co-administered PTx (n = 4 mice) and HuPBMC mice (n = 26 mice all derived from HD-04 female PBMCs) induced with full mixed EAE immunization (CFA + MOG + PTx, n = 7 mice), mixed MOG emulsion without PTx (CFA + MOG, n = 5 mice), blank CFA emulsion and PTx without antigen (CFA + PTx, n = 5 mice), blank CFA emulsion only without antigen or PTx (CFA, n = 3 mice), or PTx only without emulsion (PTx, n = 4 mice). Control $hCD3^+CD4^+(CD8^-)CD44^+$ T cell staining with a fluorophore matched $CLIP_{87-101}$ I-A^{g7} MHC II tetramer is shown in the spleen (F) and liver (G) for the same immunization groups. Tissues were perfused prior to cell isolation. Data are shown as mean with SEM and were analyzed by Brown-Forsythe and Welch ANOVA with Dunnett's T3 multiple comparisons test or by Kruskal-Wallis with Dunn's multiple comparisons test.

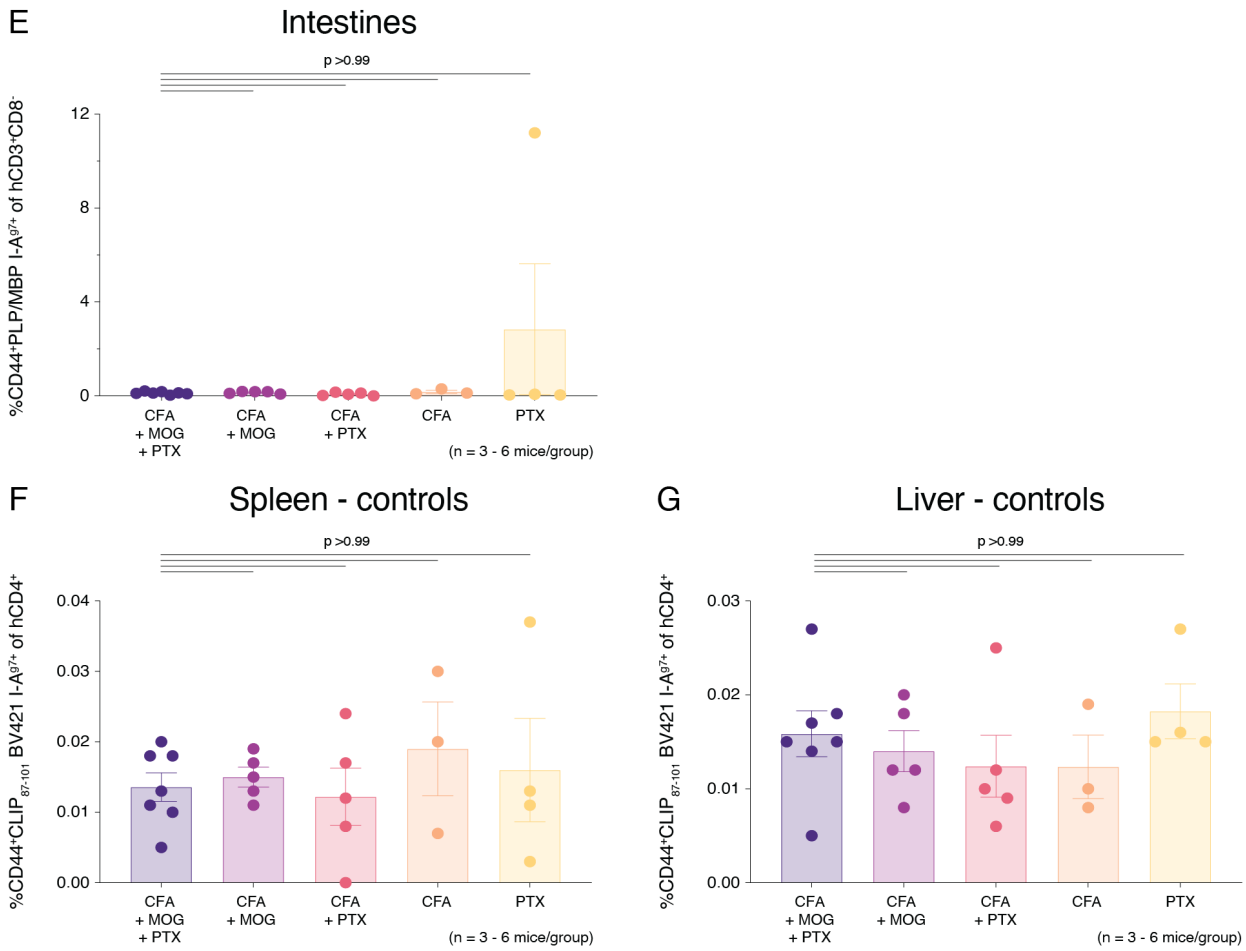

Figure A.67 continued

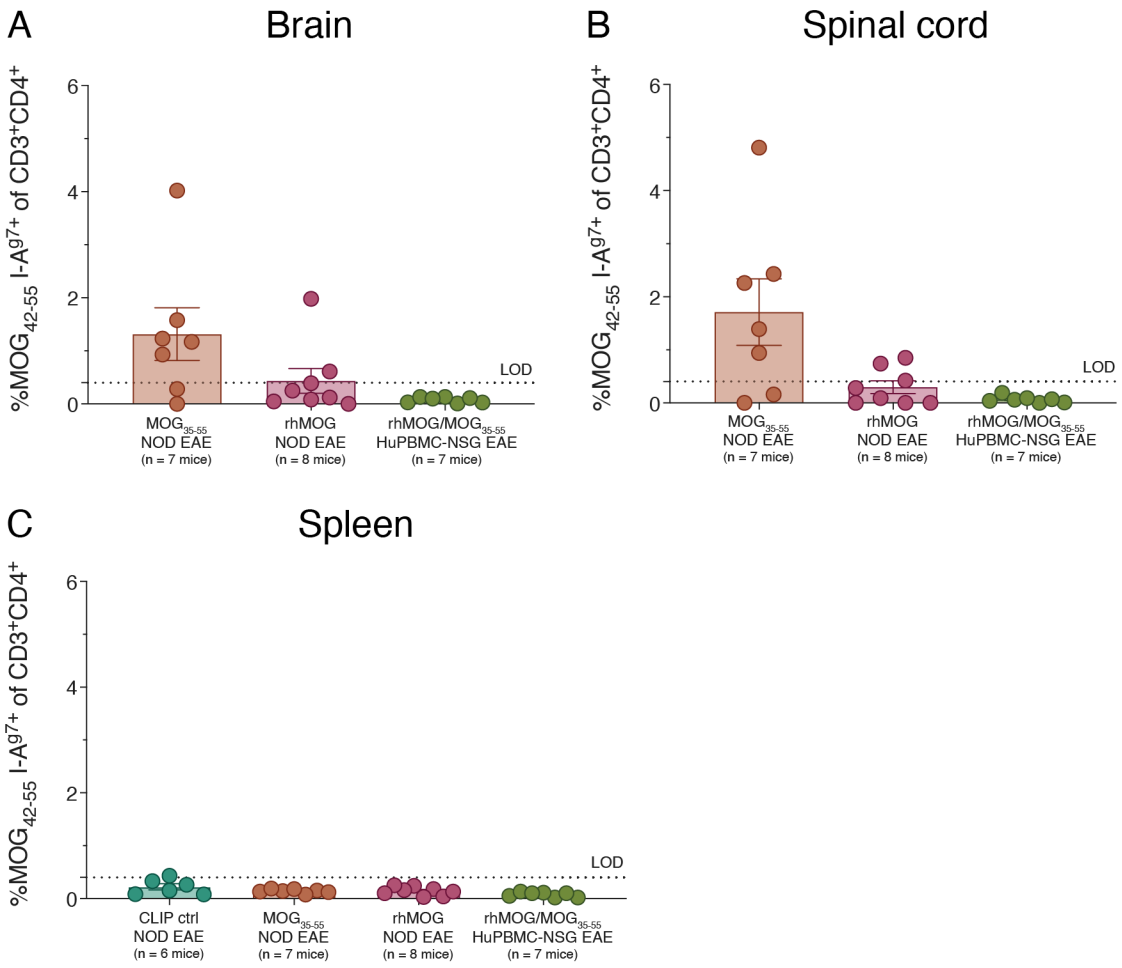

Figure A.68 Murine and human $CD4^+$ T cell recognition of $MOG4_{2-55}$ I-A^{g7} tetramers in NOD and HuPBMC mice induced with MOG peptide and/or protein EAE

Figure shows the proportion of murine (for NOD mice) and human (for HuPBMC-NSG mice) $CD3^+CD4^+$ T cells in the (A) brain, (B) spinal cord, and (C) spleen bound to NOD I-A^{g7} MHC II tetramers loaded with the immunodominant epitope MOG_{42-55} of NOD mice (n = 7 WT males and females mixed) induced with 200 µg MOG_{35-55} peptide EAE on day 20 post-immunization, NOD mice (n = 8 WT males and females mixed) induced with 100 µg $rhMOG_{1-120}$ EAE on day 18 post-immunization, and HuPBMC mice (n = 7 NSG derived from HD-04 female PBMCs) induced with mixed rhMOG/MOG_{35-55} EAE on days 19 – 22 post-immunization. Tissues were perfused prior to cell isolation. Data are shown as mean with SEM and the limit of detection (LOD) for nonspecific background staining, determined using fluorophore matched, control $CLIP_{87-101}$ loaded I-A^{g7} tetramers, is shown as a dotted line. At endpoint, EAE symptoms were observed in 5 of 7 MOG_{35-55} immunized mice (71% incidence), 4 of 8 rhMOG immunized mice (50% incidence), and 4 of 8 HuPBMC rhMOG/MOG_{35-55} immunized mice (50% incidence).

Appendix 12. Flow cytometry gating strategy for interspecies co-culture assay

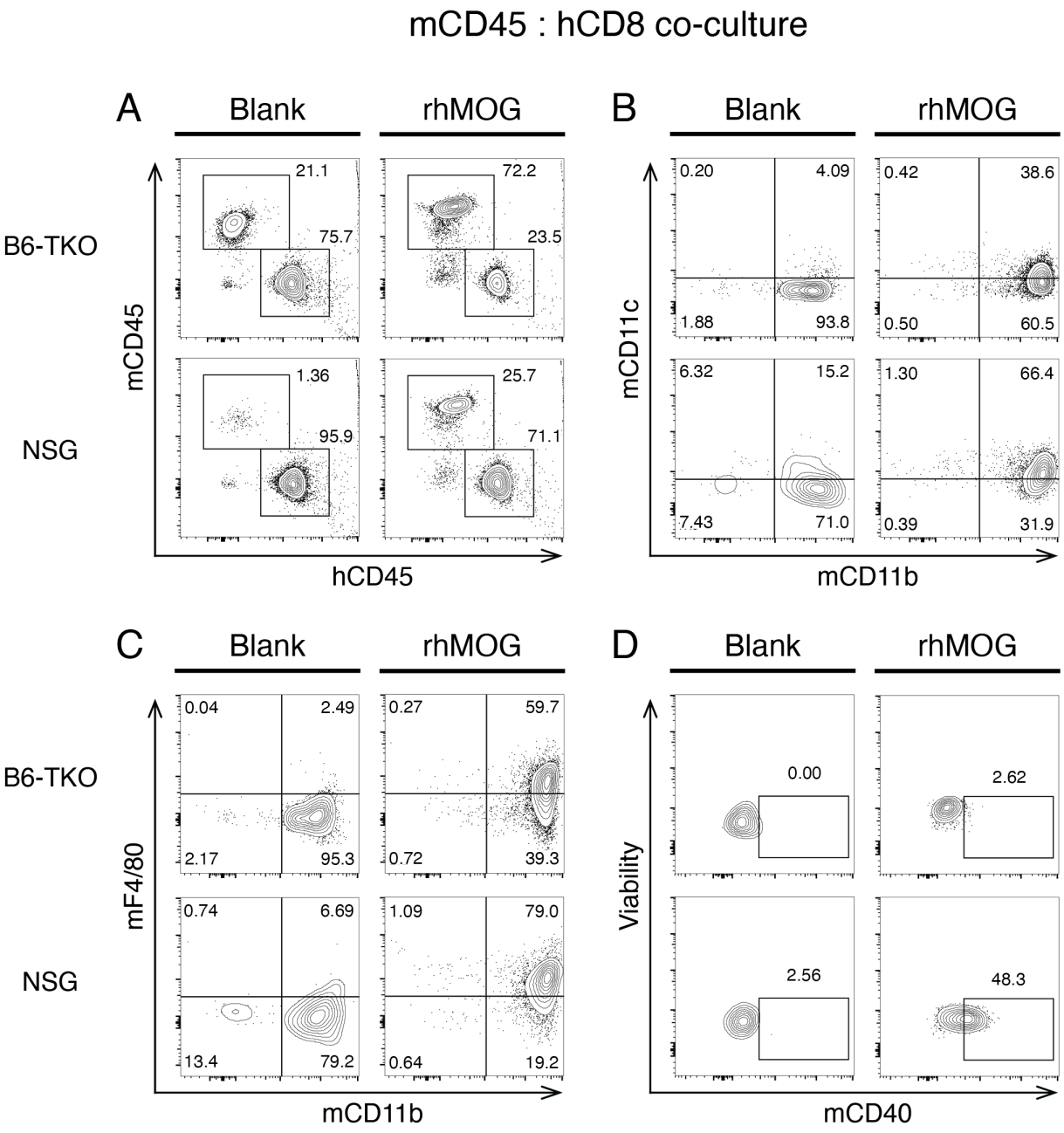

Figure A.69 Flow cytometric gating strategy to identify strain dependent murine myeloid cell marker expression following co-culture with human $CD8^+$ T cells and rhMOG protein

FACS sorted $mCD45^+$ and $hCD8^+$ cells from the spleens of PBMC-engrafted B6-TKO or NSG mice (all male, derived from healthy female donor HD-04) were co-cultured at a 1:10 ratio in blank culture media or media supplemented with rhMOG protein (n = 5 replicates per condition). Figure shows concatenated flow cytometric plots illustrating the gating strategy for and the overall frequencies of (A) $hCD45^+$ and $mCD45^+$ cells, (B) $mCD11b^+$ and/or

mCD11c^{+} cells (mCD45^{+} parent gate), (C) mCD11b^{+} and/or mF4/80^{+} cells (mCD45^{+} parent gate), and (D) mCD11c^{+}CD40^{+} cells (mCD45^{+}mCD11c^{+} parent gate) after 70 hours incubation.

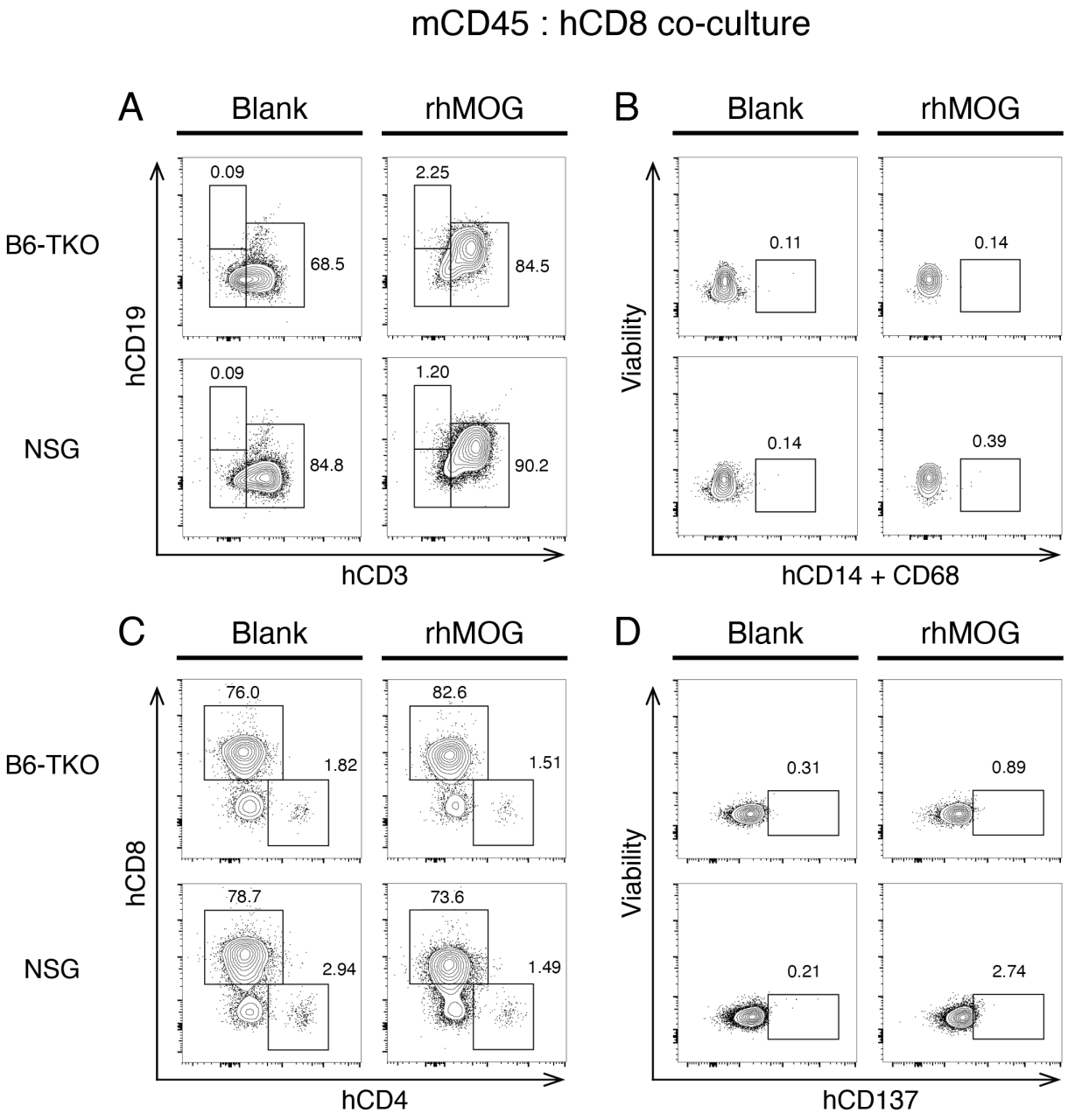

Figure A.70 Flow cytometric gating strategy to identify human CD8^{+} T cell marker expression following co-culture with strain specific murine myeloid cells and rhMOG protein

FACS sorted mCD45^{+} and hCD8^{+} cells from the spleens of PBMC-engrafted B6-TKO or NSG mice (all male, derived from healthy female donor HD-04) were co-cultured at a 1:10 ratio in blank culture media or media supplemented with rhMOG protein (n = 5 replicates per condition). Figure shows concatenated flow cytometric plots

illustrating the gating strategy for and the overall frequencies of (A) $hCD3^+$ T cells and $hCD19^+$ B cells ($hCD45^+$ parent gate), (B) $hCD14^+CD68^+$ macrophages ($hCD45^+CD3^-CD19^-$ parent gate), (C) $hCD4^+$ and $hCD8^+$ T cells ($hCD45^+CD3^+$ parent gate), (D) $hCD8^+CD137^+$ T cells ($hCD45^+CD3^+CD8^+$ parent gate), and (E) $hCD8^+IFN\gamma^+$ T cells ($hCD45^+CD3^+CD8^+$ parent gate) after 70 hours incubation.

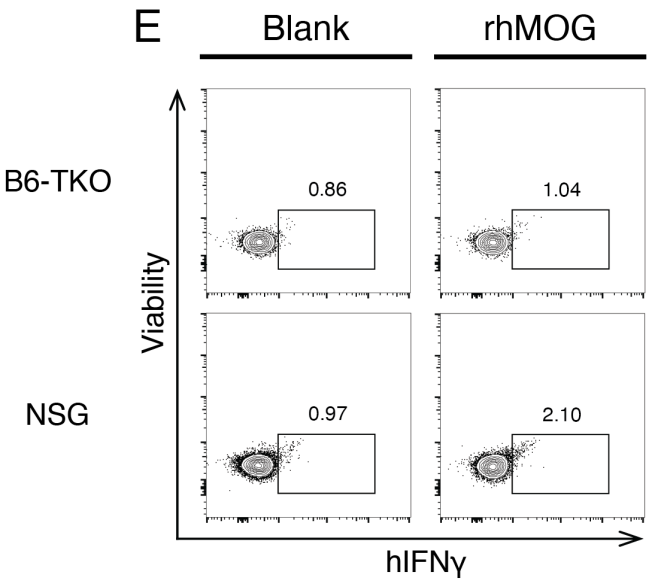

Figure A.70 continued

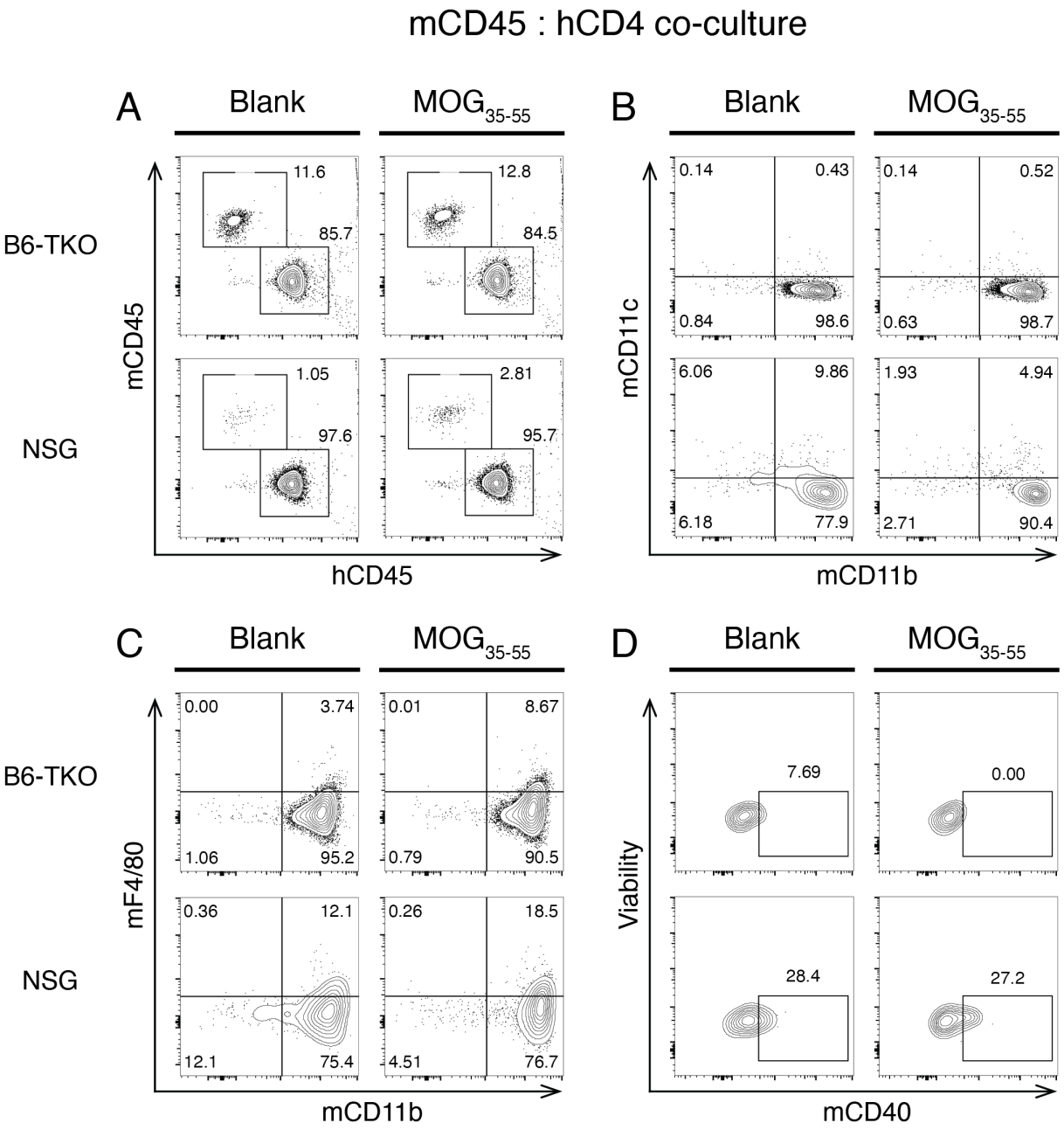

Figure A.71 Flow cytometric gating strategy to identify strain dependent murine myeloid cell marker expression following co-culture with human $CD4^+$ T cells and MOG_{35-55} peptide

FACS sorted $mCD45^+$ and $hCD4^+$ cells from the spleens of PBMC-engrafted B6-TKO or NSG mice (all male, derived from healthy female donor HD-04) were co-cultured at a 1:10 ratio in blank culture media or media supplemented with MOG_{35-55} peptide (n = 5 replicates per condition). Figure shows concatenated flow cytometric plots illustrating the gating strategy for and the overall frequencies of (A) $hCD45^+$ and $mCD45^+$ cells, (B) $mCD11b^+$ and/or $mCD11c^+$ cells ($mCD45^+$ parent gate), (C) $mCD11b^+$ and/or $mF4/80^+$ cells ($mCD45^+$ parent gate), and (D) $mCD11c^+CD40^+$ cells ($mCD45^+mCD11c^+$ parent gate) after 70 hours incubation.

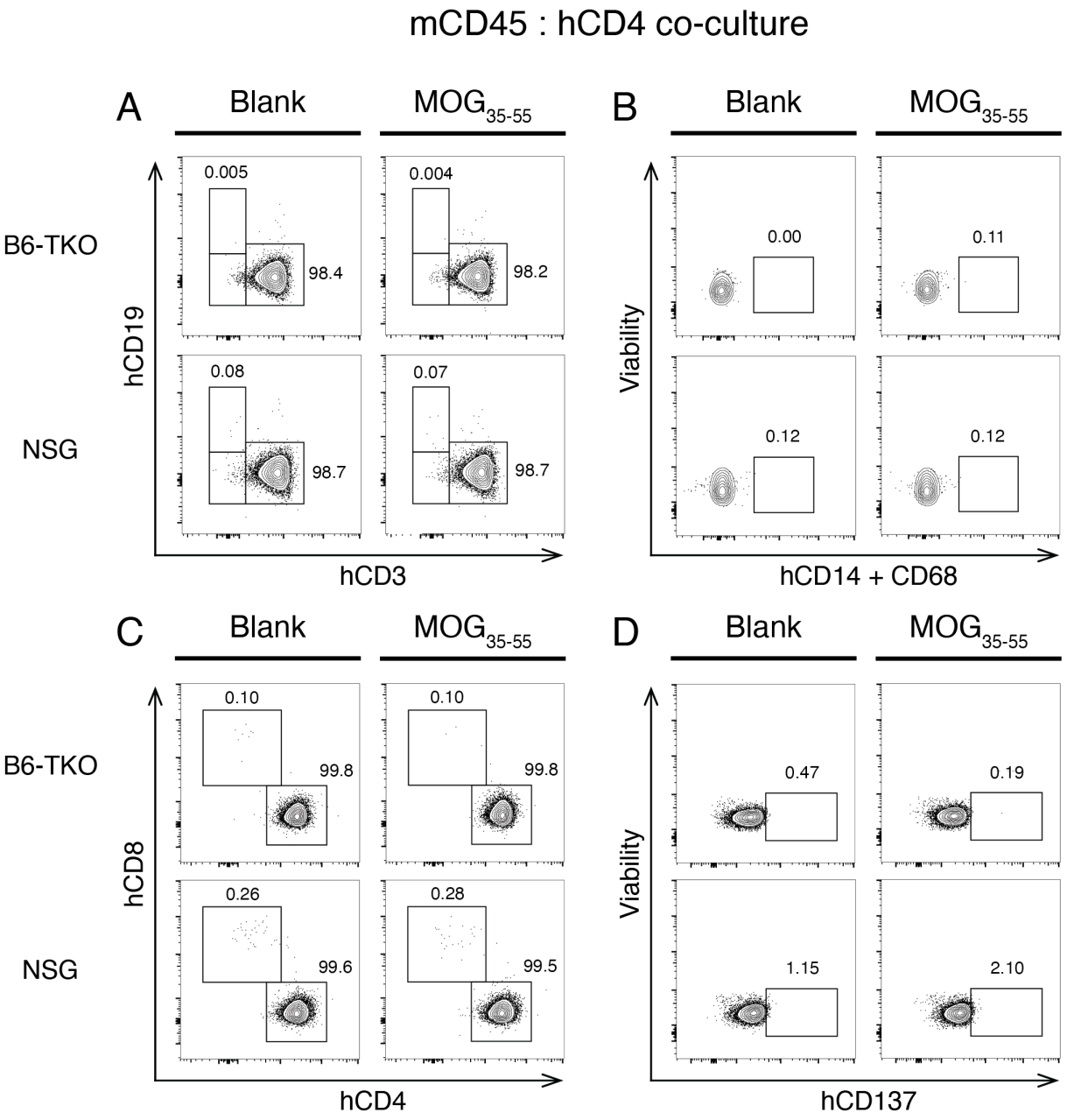

Figure A.72 Flow cytometric gating strategy to identify human CD5$^+$ T cell marker expression following co-culture with strain specific murine myeloid cells and MOG_{35-55} peptide

FACS sorted mCD45$^+$ and hCD5$^+$ cells from the spleens of PBMC-engrafted B6-TKO or NSG mice (all male, derived from healthy female donor HD-04) were co-cultured at a 1:10 ratio in blank culture media or media supplemented with MOG_{35-55} peptide (n = 5 replicates per condition). Figure shows concatenated flow cytometric plots illustrating the gating strategy for and the overall frequencies of (A) hCD3$^+$ T cells and hCD19$^+$ B cells (hCD45$^+$ parent gate), (B) hCD14$^+$CD68$^+$ macrophages (hCD45$^+$CD3$^-$CD19$^-$ parent gate), (C) hCD4$^+$ and hCD8$^+$ T cells (hCD45$^+$CD3$^+$ parent gate), (D) hCD4$^+$CD137$^+$ T cells (hCD45$^+$CD3$^+$CD4$^+$ parent gate), and (E) hCD4$^+$IFNγ^+ T cells (hCD45$^+$CD3$^+$CD4$^+$ parent gate) after 70 hours incubation.

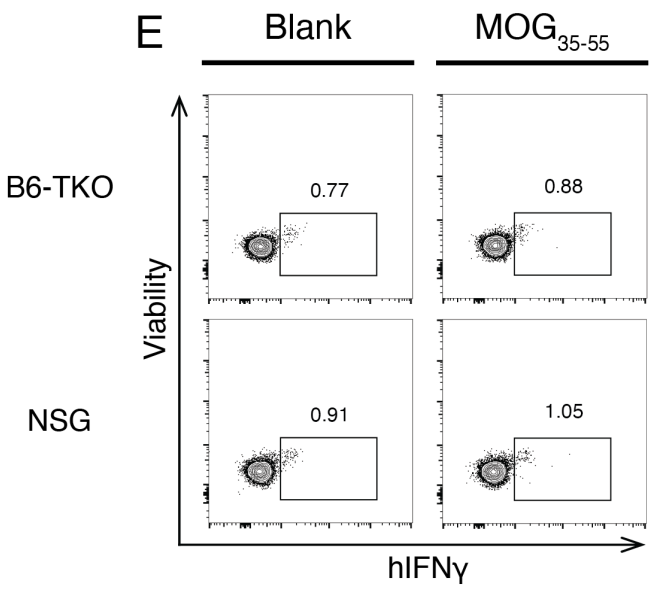

Figure A.72 continued

Appendix 13. Supplemental data to Chapter 5

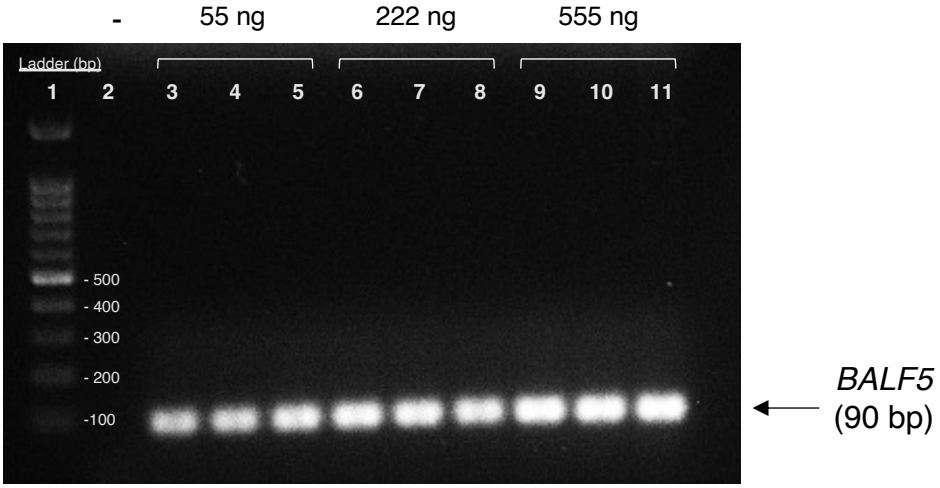

Figure A.73 Detection of Epstein-Barr virus *BALF5* gene in DNA isolated from B95-8 cells

Genomic DNA was extracted from cultured B95-8 EBV positive cells for qPCR detection of infection. Figure shows (1) a 100 bp DNA ladder, (2) a negative control with water instead of DNA, and product amplified from triplicate reactions with (3 – 5) 55 ng, (6 – 8) 222 ng, and (9 – 11) 555 ng of genomic DNA. The expected band size for the *BALF5* gene is 90 bp.

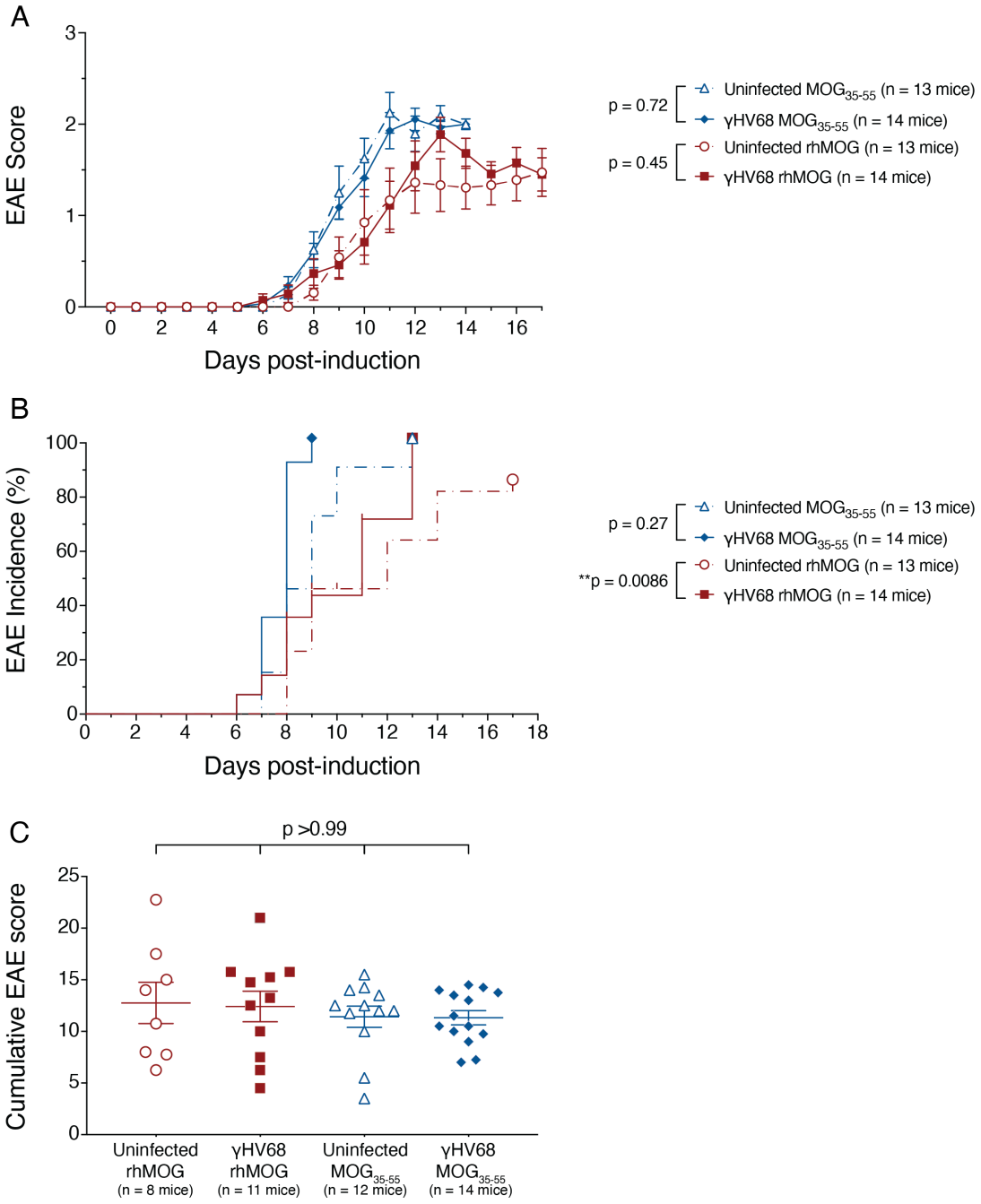

Figure A.74 Clinical EAE outcomes for B cell dependent rhMOG and independent MOG_{35-55} EAE induction of latent γHV68 infected mice

C57Bl/6 WT mice were injected intraperitoneally with either 10^4 PFU of γHV68 WUMS strain or with blank media for uninfected controls. At 5 weeks post-infection, EAE was induced with either 200 µg MOG_{35-55} peptide or 100 µg rhMOG protein. Figure shows (A) clinical disease scores over time and (B) EAE symptom incidence over time (n = 13 – 14 mice/group, mixed males and females). (C) The cumulative EAE disease scores attained by

symptomatic mice up to day 14 with MOG_{35-55} peptide (n = 12 – 14 mice/group) and day 17 post-induction with rhMOG protein (n = 8 – 11 mice/group). In A, data are shown as mean with SEM and were analyzed by mixed-effects analysis with Geisser-Greenhouse correction. In B, data are shown as percentage of the group and were analyzed by Log-rank (Mantel-Cox) test. In C, data are shown as mean with SEM and were analyzed by Kruskal-Wallis with Dunn's multiple comparisons test.

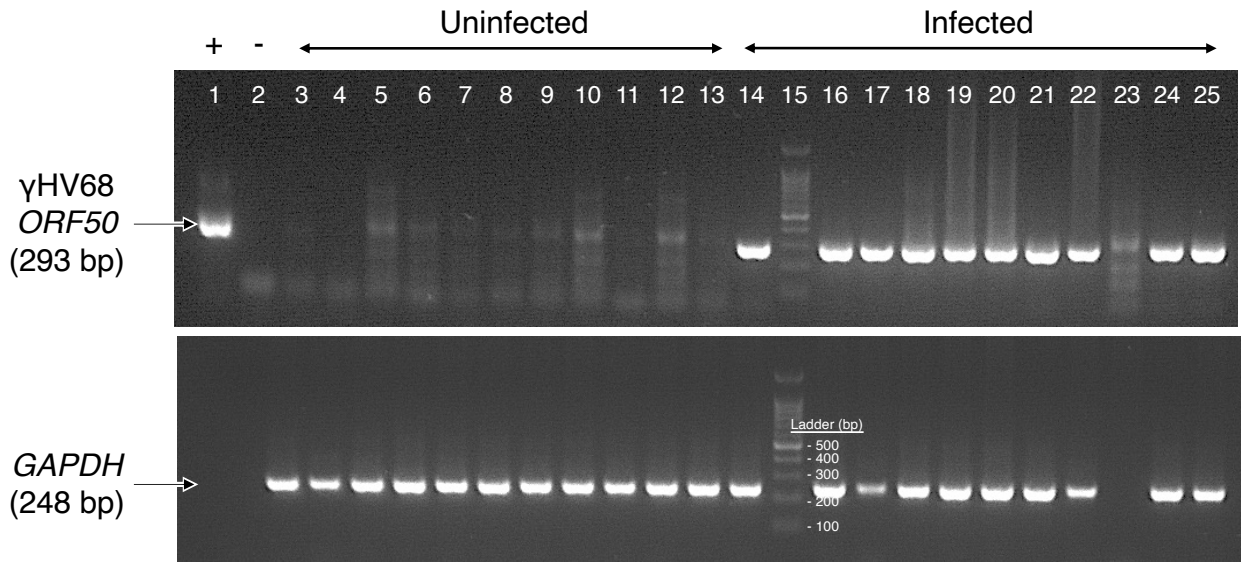

Figure A.75 Confirming latent γHV68 infection in C57Bl/6 splenocytes at EAE endpoint

C57Bl/6 WT mice were injected intraperitoneally with either 10^4 PFU of γHV68 WUMS strain or with blank media for uninfected controls (n = 11 males and females mixed per group). At 5 weeks post-infection, EAE was induced with either MOG_{35-55} peptide or rhMOG protein. On day 14 or 17 post-induction, genomic DNA was extracted from total splenocyte cell suspensions for PCR analysis. Figure shows reactions to detect γHV68 gene *ORF50* (top row) or *GAPDH* control gene (bottom row) containing (1) a positive control plasmid with the γHV68 *ORF50* gene, (2) a negative control with water instead of DNA, (3 – 13) uninfected EAE spleen DNA, (14, 16 – 25) γHV68-infected EAE spleen DNA, and (15) a 100 bp DNA ladder. The expected band size for γHV68 gene *ORF50* is 293 bp and 248 bp for *GAPDH*.

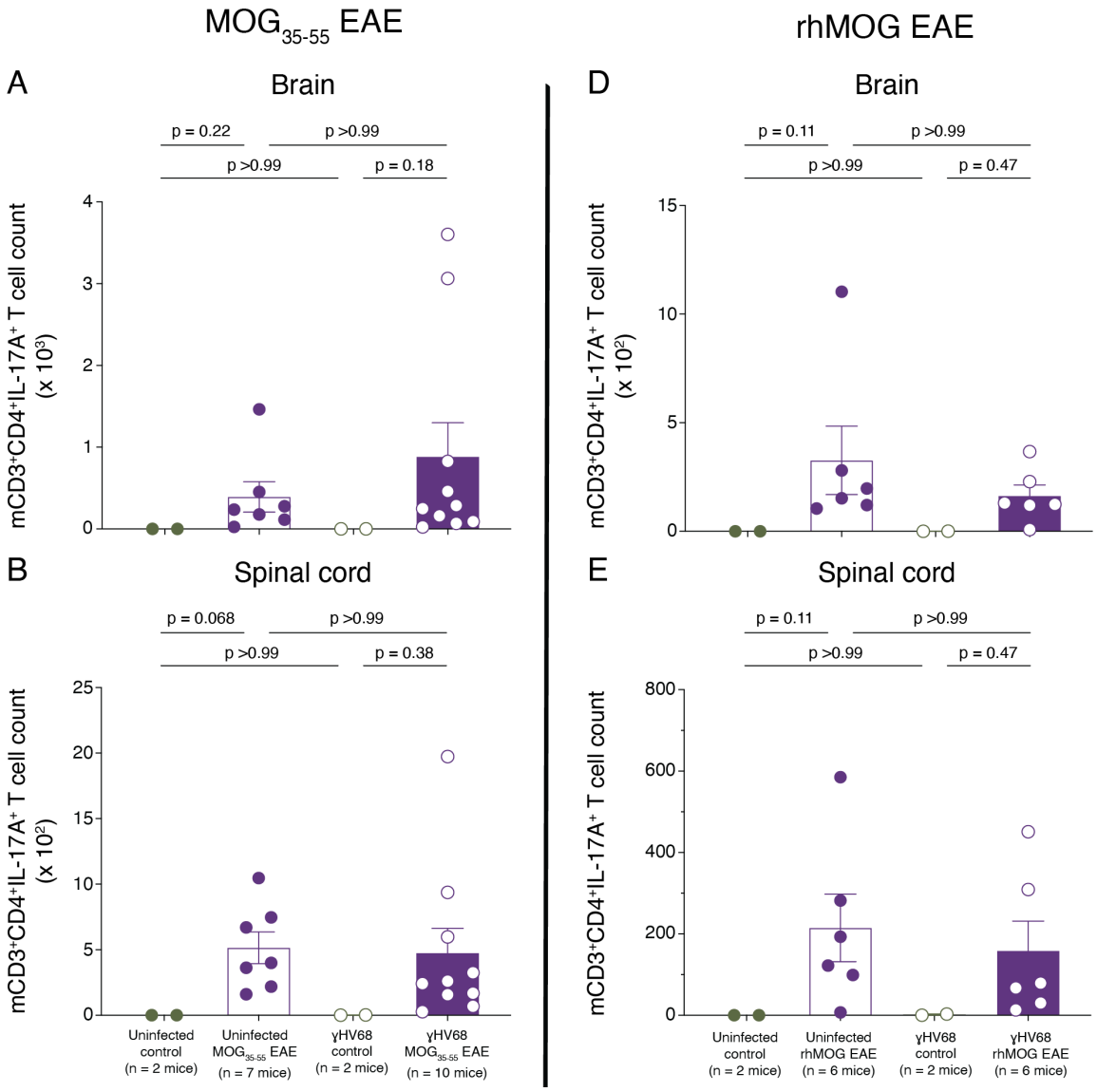

Figure A.76 mCD3$^+$CD4$^+$IL-17A$^+$ Th17 cell numbers are similar in the CNS and periphery of EAE mice regardless of their infection status and the form of MOG EAE induction

C57Bl/6 WT mice (mixed males and females) were injected intraperitoneally with either 10^4 PFU of γHV68 WUMS strain or with blank media for uninfected controls. At 5 weeks post-infection, EAE was induced with either 200 µg MOG_{35-55} peptide (n = 7 – 14 mice/group), 100 µg rhMOG protein (n = 6 – 10 mice/group) or remained as uninduced controls (n = 2 – 3 mice/group). Figure shows total numbers of mCD3$^+$CD4$^+$IL-17A$^+$ Th17 cells in the (A, D) brain, (B, E) spinal cord, and (C, F) spleen on day 14 post-immunization with MOG_{35-55} peptide (left column) and day 17 post-immunization with rhMOG protein (right column). Data are shown as mean with SEM and were analyzed by Brown-Forsythe and Welch ANOVA with Dunnett's T3 multiple comparisons test or by Kruskal-Wallis with Dunn's multiple comparisons test.

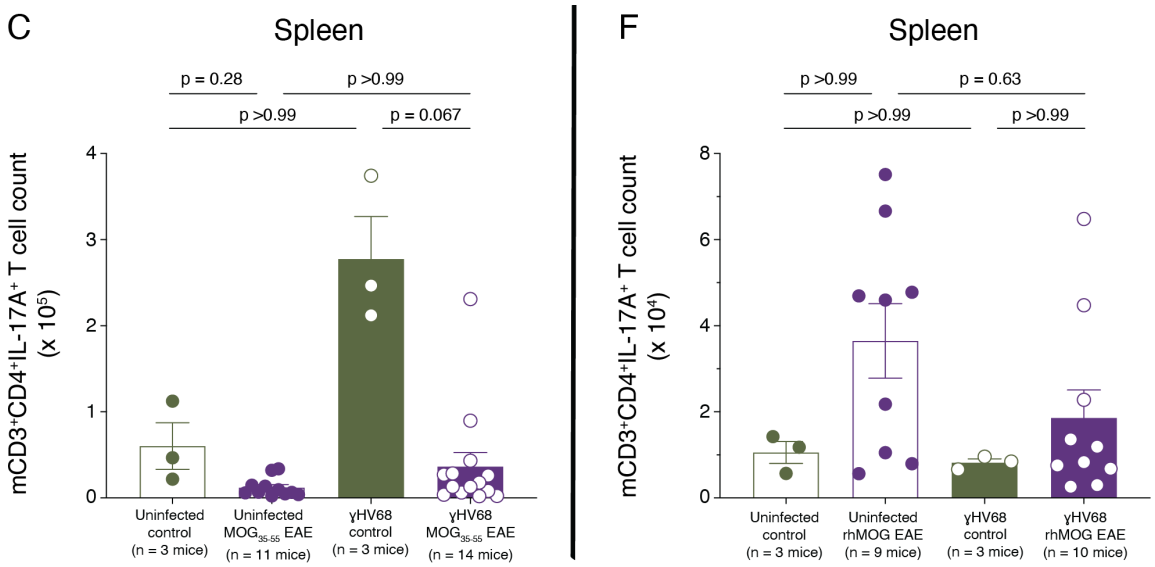

Figure A.76 continued

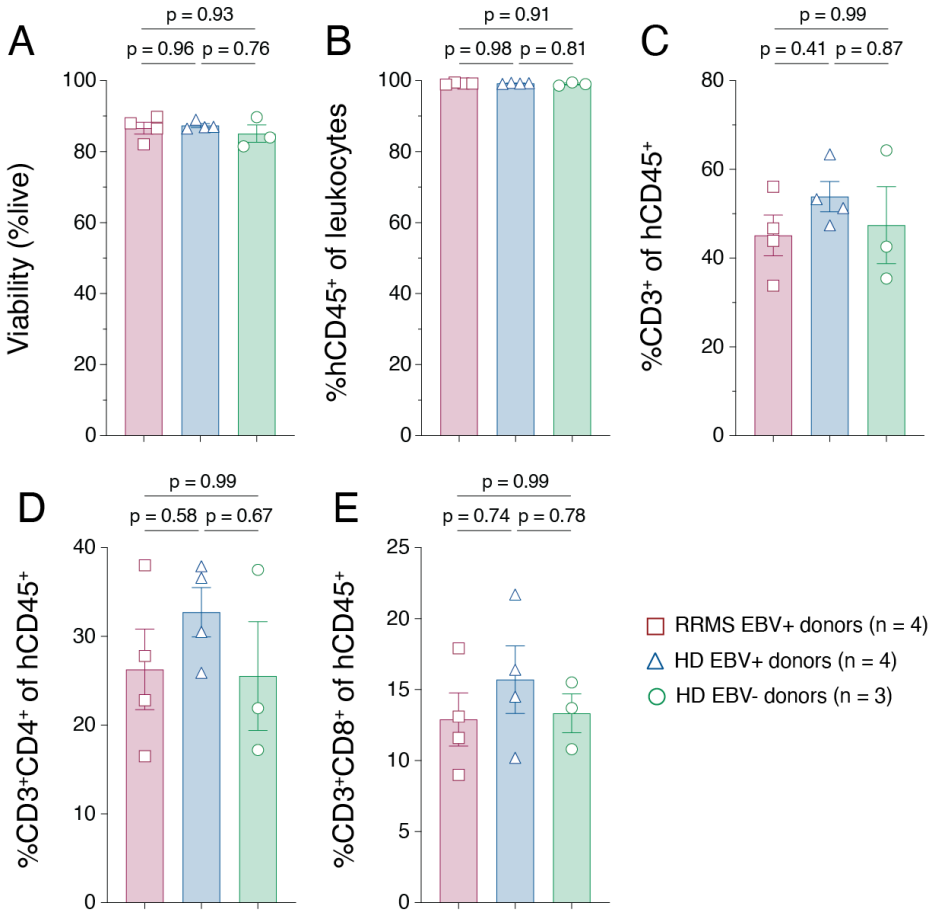

Figure A.77 Donor PBMC T cell composition after freeze-thaw

Following preservation in liquid nitrogen, donor group differences in PBMC composition were assessed by the proportion of (A) viable cells after recovery, (B) $hCD45^+$ cells among all leukocytes, (C) $hCD3^+$ T cells among $hCD45^+$ cells, (D) $hCD3^+CD4^+$ T cells among $hCD45^+$ cells, and (E) $hCD3^+CD8^+$ T cells among $hCD45^+$ cells. Data are shown as mean with SEM (n = 3 – 4 blood donors/group) and were analyzed by Brown-Forsythe and Welch ANOVA with Dunnett's T3 multiple comparisons test or by Kruskal-Wallis with Dunn's multiple comparisons test.